

Editor
Necia Grant Cooper

Managing Editor
Ileana G. Buican

Science Writer
Jay A. Schecker

Designer
Gloria E. Sharp

Distribution Manager
Donna L. Spitzmiller

Illustrators
Andrea J. Kron
David R. Delano
Annie T. Loweree

Editorial Support
Judyth K. Prono
Martha L. DeLanoy
Brian H. Fishbine
Wendy M. Burditt
Christopher L. Percy
Octavio Ramos, Jr.

Photographers
Michael D. Greenbank
John A. Flower
Gary A. Warren

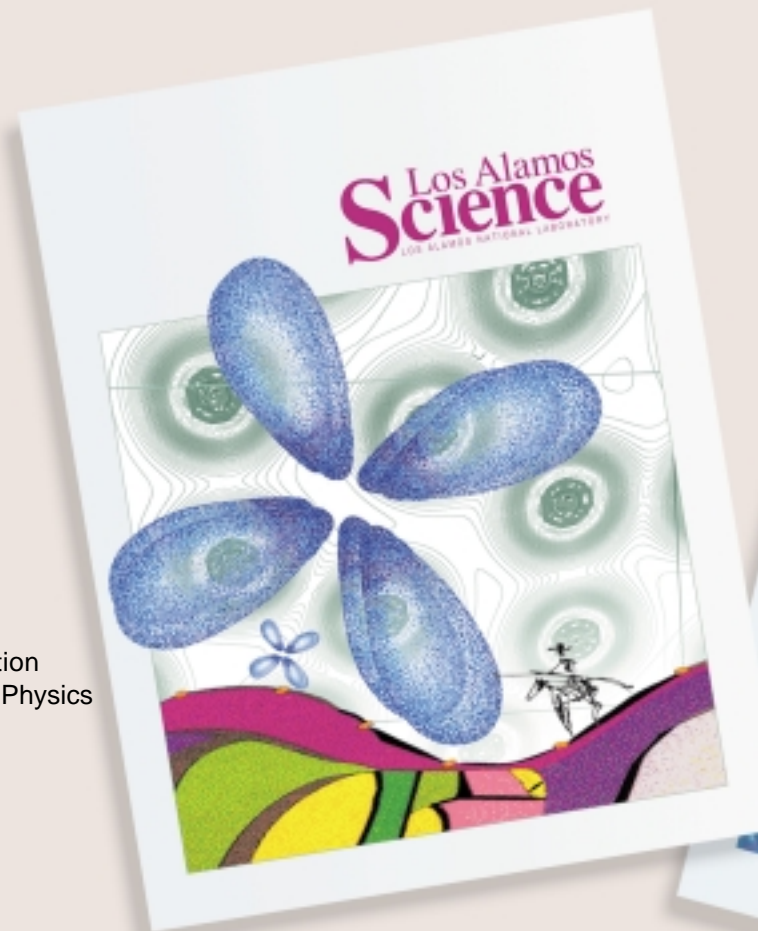
Printing Coordination
Guadalupe D. Archuleta

Address mail to
Los Alamos Science
Mail Stop M711
Los Alamos National Laboratory
Los Alamos, NM 87545

lascience@lanl.gov
FAX: 505-665-4408
Tel: 505-667-1447

Challenges in Plutonium Science

Los Alamos Science Number 26, 2000



Volume I
Historical Introduction
Condensed-Matter Physics
Plutonium Aging



Volume II
Plutonium Metallurgy
Actinide Chemistry and the Environment
The Yucca Mountain Project

For past issues of *Los Alamos Science*, see our Web site:
www.lanl.gov/external/science/lascience/index.html

Download Acrobat 4.0

Los Alamos
NATIONAL LABORATORY
LA-UR-00-4100

Volume I

An Update: Plutonium and Quantum Criticality *George Chapline and James L. Smith* 1

Historical Introduction, Condensed-Matter Physics, and Plutonium Aging

Historical Introduction

Plutonium—A Historical Overview *Siegfried S. Hecker with the Los Alamos Science staff* 2

In the Beginning 3

A Factor of Millions—Why We Made Plutonium—with *André F. Michaudon and Ileana G. Buican* 4

Plutonium in Use—From Single Atoms to Multiton Amounts 10

Plutonium—An Element at Odds with Itself 16

The Plutonium Challenge—Stockpile Stewardship 24

The Plutonium Challenge—Avoiding Nuclear Weapons Proliferation 28

The Plutonium Challenge—Environmental Issues 36

The Taming of “49”—Big Science in Little Time 48

Recollections of Edward F. Hammel

Reflections on the Legacy of a Legend—Glenn T. Seaborg (1912–1999) 56

David L. Clark and David E. Hobart

From Alchemy to Atoms—The Making of Plutonium 62

André F. Michaudon

Plutonium and Health—How Great Is the Risk? 74

George L. Voelz as told to Ileana G. Buican

Plutonium Condensed-Matter Physics

Plutonium Condensed-Matter Physics—A Survey of Theory and Experiment 90

A. Michael Boring and James L. Smith

Actinide Ground-State Properties—Theoretical Predictions 128

John M. Wills and Olle Eriksson

Basics of the Density Functional Theory (DFT) Approach 135

Electronic Structure of α - and δ -Plutonium—Theory vs Experiment 152

Aloysius J. Arko, John J. Joyce, and John M. Wills

A Possible Model for δ -Plutonium—Self-Induced Anderson Localization, δ -Phase Stability, and the Melting Temperature of Plutonium 154

Bernard R. Cooper

Photoelectron Spectroscopy of α - and δ -Plutonium 168

Aloysius J. Arko, John J. Joyce, Luis A. Morales, Jeffrey H. Terry, and Roland K. Schulze

Laser-Plasma Light Source—Design and Operation 186

John J. Joyce, Aloysius J. Arko, and Luis A. Morales

Actinide Photoemission Measurements at the Advanced Light Source 188

Roland K. Schulze and Jeffrey H. Terry

Atomic Vibrations and Melting in Plutonium 190

*Andrew C. Lawson, Barbara Martinez, Joyce A. Roberts, James W. Richardson, Jr.,
and Bard I. Bennett*

Equations of State—Theoretical Formalism 192

Bard I. Bennett

Microstrain in δ' -Plutonium 201

Andrew C. Lawson

Vibrational Softening in α -Uranium 202

Michael E. Manley

Elasticity, Entropy, and the Phase Stability of Plutonium 208

Albert Migliori, Joseph P. Baiardo, and Timothy W. Darling

Preparing Single Crystals of Gallium-Stabilized Plutonium 226

Jason C. Lashley, Michael S. Blau, and Roger L. Moment

A Single-Crystal Saga 233

Roger L. Moment

Plutonium Aging

Aging of Plutonium and Its Alloys 238

Siegfried S. Hecker and Joseph C. Martz

A Tale of Two Diagrams 244

Siegfried S. Hecker and Lidia F. Timofeeva

Surface and Corrosion Chemistry of Plutonium 252

John M. Haschke, Thomas H. Allen, and Luis A. Morales

Catalyzed Corrosion of Plutonium: Hazards and Applications 266

John M. Haschke and Joseph C. Martz

Radiation Effects in Plutonium—What Is Known? Where Should We Go from Here? 274

Wilhelm G. Wolfer

Transmission Electron Microscopy of Plutonium Alloys 286

Thomas G. Zocco

Volume II

Plutonium Metallurgy, Actinide Chemistry and the Environment, and the Yucca Mountain Project

Plutonium Metallurgy

Plutonium and Its Alloys—From Atoms to Microstructure 290

Siegfried S. Hecker

Mechanical Behavior of Plutonium and Its Alloys 336

Siegfried S. Hecker and Michael F. Stevens

Where Is the Gallium?—Searching the Plutonium Lattice with XAFS 356

Steven D. Conradson

Actinide Chemistry and the Environment

The Chemical Complexities of Plutonium 364

David L. Clark

Computational Studies of Actinide Chemistry 382

P. Jeffrey Hay and Richard L. Martin

The Chemical Interactions of Actinides in the Environment 392

Wolfgang H. Runde

Spectroscopies for Environmental Studies of Actinide Species 412

Wolfgang H. Runde

Siderophore-Mediated Chemistry and Microbial Uptake of Plutonium 416

Mary P. Neu

Characterizing the Plutonium Aquo Ions by XAFS Spectroscopy 418

Steven D. Conradson, David L. Clark, Mary P. Neu, Wolfgang H. Runde, and C. Drew Tait

XAFS—A Technique to Probe Local Structure 422

Steven D. Conradson as told to Jay A. Schecker

A Vision for Environmentally Conscious Plutonium Processing 436

Larry R. Avens and P. Gary Eller

Salt Distillation 449

Eduardo Garcia, Vonda R. Dole, James A. McNeese, and Walter J. Griego

Hydrothermal Processing 450

Laura A. Worl, Steven J. Buelow, and Dennis D. Padilla

Enhanced Pyrolysis for Converting Polystyrene or Cellulose Polymers 451

Daniel J. Kathios

Treatment of Liquid Wastes 452

Gordon D. Jarvinen, Geraldine M. Purdy, Barbara F. Smith, and Thomas C. Robinson

Electrochemical Decontamination of Metallic Wastes 453

Douglas E. Wedman and Jerry L. Lugo

Molecularly Engineered Resins for Plutonium Recovery 454

S. Fredric Marsh, D. Kirk Veirs, Gordon D. Jarvinen, Mary E. Barr, and Eddie W. Moody

The Yucca Mountain Project

Yucca Mountain—Looking Ten Thousand Years into the Future 464

by Roger C. Eckhardt for David L. Bish, Gilles Y. Bussod, June T. Fabryka-Martin, Schön Levy, Paul W. Reimus, Bruce A. Robinson, Wolfgang H. Runde, Inés Triay, and David T. Vaniman

Mesh Generation for Yucca Mountain 472

Carl W. Gable

Colloids—Carriers of Actinides into the Environment 490

Analyzing Volcanic Hazards at Yucca Mountain 492

Frank V. Perry, Bruce M. Crowe, and Greg A. Valentine

Element 94 has baffled scientists since the days of the Manhattan Project. When the first ponderable quantities of reactor-made plutonium arrived at Los Alamos in 1944, the pure metal showed wildly differing densities, and the molten state was so reactive that it corroded almost every container it came in contact with. The engineering challenge was to prepare a stable metallic form and fashion it into a pair of hemispheres for the first implosion nuclear bomb. That task was accomplished in about 15 months, a remarkable feat considering how little was known about plutonium at the time.

Experimental work since then has revealed the unusual ground-state structure of plutonium, its seven distinct crystallographic phases, its dimensional changes with temperature, pressure, and impurity content, its ability to combine with virtually every other element, its pyrophoricity, its multitude of oxidation states, its highly anomalous resistivity, its resemblance to heavy-fermion compounds and other correlated-electron materials, and on and on. This body of data has only added to plutonium's reputation for being the most perplexing element in the periodic table and, arguably, the most interesting. The solid-state, chemical, and metallurgical properties appear to be in a class of their own and, until recently, much too complex to be understood from first principles.

Ironically, the fissile properties of plutonium-239, which render it useful for nuclear bombs and nuclear reactors, are not nearly as difficult to understand. In fact, those nuclear properties had been predicted even before plutonium was made and isolated at Berkeley in 1941 and well before Enrico Fermi and Leo Szilard demonstrated the first self-sustaining fission chain reaction in December 1942.

The inspiration for this issue of *Los Alamos Science* is threefold. First, recent developments in understanding the chemistry and condensed-matter physics of plutonium at a fundamental level call for even greater involvement.

Second, three missions of Los Alamos National Laboratory—stewardship of the nuclear weapons stockpile, reducing the threat of nuclear weapons proliferation, and cleanup of the nation's nuclear weapons complex—demand that we develop a deeper understanding of plutonium. Third, as Los Alamos has the only remaining national facility fully equipped for all aspects of plutonium research, it is our job to document the recent progress and to interest the next generation of scientists in keeping our nation at the frontier of this very difficult but dynamic field.

A few recent Los Alamos achievements will illustrate the new directions in research. Electronic-structure calculations from first principles have finally reproduced the ground-state properties of plutonium, including its atypical crystal structure. These calculations predict that the f-shell electrons of neighboring atoms overlap, but just barely, forming a narrow conduction band, a picture that has been confirmed directly at Los Alamos through the first photoemission measurements of electronic structure. Narrow bands are associated with strong electron-electron correlations, and the next step is to probe the nature of those correlations and their effects on the phase stability of plutonium and its alloys. Resonant ultrasound spectroscopy, a technique developed at Los Alamos, has yielded very accurate measurements of the elastic constants of both the α - and the δ -phase of new and aged plutonium. It should prove very useful in the study of aging effects as well as fundamental properties. X-ray absorption fine-structure (XAFS) spectroscopy is revealing the possible existence of new substructures in plutonium and its alloys and is proving to be extremely useful in characterizing chemical species in the environment. Surface studies are revealing new modes of corrosion in plutonium that must be understood for the safe disposal of plutonium over the long term.

If we can support the experimental work that needs to be done, our scien-

tists are likely to predict, within the next decade, such critical matters as the aging of plutonium in weapons components and the rates at which colloidal forms might carry actinide wastes from particular locations underground. At the same time, the truly unique electronic features of plutonium are challenging established paradigms, and we can expect this element to influence the science of condensed-matter physics for a long time to come.

The larger context for plutonium research is covered in a sweeping overview by former Laboratory Director Sig Hecker. In tracing the history of plutonium on the planet, its use in nuclear weapons and nuclear energy, and the mission-oriented challenges facing our scientists, Hecker emphasizes the particular need to help the Russians safeguard their weapons-grade plutonium and to collaborate with them on health and environmental problems that have resulted from the excesses of the Cold War. The international forces that will determine the future of plutonium on the planet should also be kept in mind. The 200 tonnes of weapons-grade plutonium is dwarfed by the 1000 tonnes of plutonium present in spent fuel from nuclear reactors. Much of the world wants to use that plutonium in civilian power reactors. France and Japan are currently burning MOX fuel (mixed oxides of uranium and plutonium). Even in nuclear reactors now operating in the United States, about a third of the power comes from the fissioning of plutonium that has "grown in" within the uranium fuel through neutron irradiation.

U.S. policy notwithstanding, plutonium is likely to be used and coveted for the foreseeable future, and this Laboratory must continue its historic role—to prepare for all potential uses and abuses of this unique element.



Volume I

An Update: Plutonium and Quantum Criticality *George Chapline and James L. Smith* 1

Historical Introduction, Condensed-Matter Physics, and Plutonium Aging

Historical Introduction

Plutonium—A Historical Overview *Siegfried S. Hecker with the Los Alamos Science staff* 2

In the Beginning 3

A Factor of Millions—Why We Made Plutonium—with *André F. Michaudon and Ileana G. Buican* 4

Plutonium in Use—From Single Atoms to Multiton Amounts 10

Plutonium—An Element at Odds with Itself 16

The Plutonium Challenge—Stockpile Stewardship 24

The Plutonium Challenge—Avoiding Nuclear Weapons Proliferation 28

The Plutonium Challenge—Environmental Issues 36

The Taming of “49”—Big Science in Little Time 48

Recollections of Edward F. Hammel

Reflections on the Legacy of a Legend—Glenn T. Seaborg (1912–1999) 56

David L. Clark and David E. Hobart

From Alchemy to Atoms—The Making of Plutonium 62

André F. Michaudon

Plutonium and Health—How Great Is the Risk? 74

George L. Voelz as told to Ileana G. Buican

Plutonium Condensed-Matter Physics

Plutonium Condensed-Matter Physics—A Survey of Theory and Experiment 90

A. Michael Boring and James L. Smith

Actinide Ground-State Properties—Theoretical Predictions 128

John M. Wills and Olle Eriksson

Basics of the Density Functional Theory (DFT) Approach 135

Electronic Structure of α - and δ -Plutonium—Theory vs Experiment 152

Aloysius J. Arko, John J. Joyce, and John M. Wills

A Possible Model for δ -Plutonium—Self-Induced Anderson Localization, δ -Phase Stability, and the Melting Temperature of Plutonium 154

Bernard R. Cooper

Photoelectron Spectroscopy of α - and δ -Plutonium 168

Aloysius J. Arko, John J. Joyce, Luis A. Morales, Jeffrey H. Terry, and Roland K. Schulze

Laser-Plasma Light Source—Design and Operation 186

John J. Joyce, Aloysius J. Arko, and Luis A. Morales

Actinide Photoemission Measurements at the Advanced Light Source 188

Roland K. Schulze and Jeffrey H. Terry

Atomic Vibrations and Melting in Plutonium 190

*Andrew C. Lawson, Barbara Martinez, Joyce A. Roberts, James W. Richardson, Jr.,
and Bard I. Bennett*

Equations of State—Theoretical Formalism 192

Bard I. Bennett

Microstrain in δ' -Plutonium 201

Andrew C. Lawson

Vibrational Softening in α -Uranium 202

Michael E. Manley

Elasticity, Entropy, and the Phase Stability of Plutonium 208

Albert Migliori, Joseph P. Baiardo, and Timothy W. Darling

Preparing Single Crystals of Gallium-Stabilized Plutonium 226

Jason C. Lashley, Michael S. Blau, and Roger L. Moment

A Single-Crystal Saga 233

Roger L. Moment

Plutonium Aging

Aging of Plutonium and Its Alloys 238

Siegfried S. Hecker and Joseph C. Martz

A Tale of Two Diagrams 244

Siegfried S. Hecker and Lidia F. Timofeeva

Surface and Corrosion Chemistry of Plutonium 252

John M. Haschke, Thomas H. Allen, and Luis A. Morales

Catalyzed Corrosion of Plutonium: Hazards and Applications 266

John M. Haschke and Joseph C. Martz

Radiation Effects in Plutonium—What Is Known? Where Should We Go from Here? 274

Wilhelm G. Wolfer

Transmission Electron Microscopy of Plutonium Alloys 286

Thomas G. Zocco

Volume II

Plutonium Metallurgy, Actinide Chemistry and the Environment, and the Yucca Mountain Project

Plutonium Metallurgy

Plutonium and Its Alloys—From Atoms to Microstructure 290

Siegfried S. Hecker

Mechanical Behavior of Plutonium and Its Alloys 336

Siegfried S. Hecker and Michael F. Stevens

Where Is the Gallium?—Searching the Plutonium Lattice with XAFS 356

Steven D. Conradson

Actinide Chemistry and the Environment

The Chemical Complexities of Plutonium 364

David L. Clark

Computational Studies of Actinide Chemistry 382

P. Jeffrey Hay and Richard L. Martin

The Chemical Interactions of Actinides in the Environment 392

Wolfgang H. Runde

Spectroscopies for Environmental Studies of Actinide Species 412

Wolfgang H. Runde

Siderophore-Mediated Chemistry and Microbial Uptake of Plutonium 416

Mary P. Neu

Characterizing the Plutonium Aquo Ions by XAFS Spectroscopy 418

Steven D. Conradson, David L. Clark, Mary P. Neu, Wolfgang H. Runde, and C. Drew Tait

XAFS—A Technique to Probe Local Structure 422

Steven D. Conradson as told to Jay A. Schecker

A Vision for Environmentally Conscious Plutonium Processing 436

Larry R. Avens and P. Gary Eller

Salt Distillation 449

Eduardo Garcia, Vonda R. Dole, James A. McNeese, and Walter J. Griego

Hydrothermal Processing 450

Laura A. Worl, Steven J. Buelow, and Dennis D. Padilla

Enhanced Pyrolysis for Converting Polystyrene or Cellulose Polymers 451

Daniel J. Kathios

Treatment of Liquid Wastes 452

Gordon D. Jarvinen, Geraldine M. Purdy, Barbara F. Smith, and Thomas C. Robinson

Electrochemical Decontamination of Metallic Wastes 453

Douglas E. Wedman and Jerry L. Lugo

Molecularly Engineered Resins for Plutonium Recovery 454

S. Fredric Marsh, D. Kirk Veirs, Gordon D. Jarvinen, Mary E. Barr, and Eddie W. Moody

The Yucca Mountain Project

Yucca Mountain—Looking Ten Thousand Years into the Future 464

by Roger C. Eckhardt for David L. Bish, Gilles Y. Bussod, June T. Fabryka-Martin, Schön Levy, Paul W. Reimus, Bruce A. Robinson, Wolfgang H. Runde, Inés Triay, and David T. Vaniman

Mesh Generation for Yucca Mountain 472

Carl W. Gable

Colloids—Carriers of Actinides into the Environment 490

Analyzing Volcanic Hazards at Yucca Mountain 492

Frank V. Perry, Bruce M. Crowe, and Greg A. Valentine

An Update

Plutonium and Quantum Criticality

George Chapline and James L. Smith

After more than fifty years of plutonium research at Los Alamos, we might be expected to understand the strange properties of this metal. Instead, we are still stumped. One might also expect that we could catalog the engineering properties of plutonium and use them to predict, for example, how the plutonium in the stockpile will age. However, its properties depend too sensitively on variables such as impurity content, temperature, and method of fabrication to be predictable. As a result, we have not been able to treat plutonium as a typical engineering material such as steel and aluminum.

Plutonium's strange behavior is generally attributed to its numerous competing states near the ground state. The different competing states are possible because the f electrons in plutonium are strongly interacting and can self-organize in different ways. This situation has a very important practical consequence—small changes in the parameters of the system can cause the properties of the material to change dramatically. But can we predict these changes? As it happens, recent experiments on heavy-fermion metals and high-temperature superconductors have led to a new perspective on the kind of complexity we see in plutonium.

At zero temperature, sudden changes in the ground-state wave function of a system that result from small changes in an external parameter such as pressure or doping are called quantum phase transitions (Sachdev 2000). A material near a quantum phase transition, much like one near an ordinary critical point, exhibits characteristically anomalous behavior independent of the material—a phenomenon referred to as quantum criticality. On the other hand, unlike ordinary phase transitions, quantum transitions occur between ground states and involve negligible changes in entropy.

Anomalously large resistivity near a quantum phase transition has recently been demonstrated for metallic heavy-fermion compounds of cerium (Mathur et al. 1998) and uranium (Saxena et al. 2000). Although this resistivity is not yet explained theoretically, it is almost certainly a type of quantum critical behavior relating to the way the f electrons self-organize in these materials. The changes in f-electron organization are also reflected in changes in magnetic properties. Therefore, one might suspect that these examples of anomalous behavior near a quantum phase transition are not particularly relevant to plutonium, for which magnetism is either absent or extremely weak. However, it is important to remember that plutonium has an unusually large magnetic susceptibility in addition to showing other hints of heavy-fermion behavior.

The anomalous temperature dependence of the electrical resistivity of plutonium is particularly suggestive of quantum critical behavior. In ordinary metals, the resistivity decreases as the material is cooled from room temperature because the vibrational motion of the atoms is decreasing. In plutonium and extreme heavy-fermion materials, the resistivity increases with decreasing temperature over part of the cooling range.

Laughlin et al. (2000) have argued that it is virtually impossible to calculate from first principles the properties of a system whose behavior is dominated by a quantum phase transition. To uncover the properties of plutonium, therefore, we must rely heavily on experiments. The implications for stockpile stewardship are important. As evidenced by this volume, much has already been accomplished, but there is a lot more work to do. We need to find and characterize the quantum critical point

responsible for the strange properties of plutonium. We need metal of higher purity than ever before because impurities blur the properties just as raising the temperature does. With this cleaner metal in hand, we need to apply high magnetic fields and pressure and to lower the temperature close to absolute zero. We need new ways to measure fundamental properties under these conditions.

It is clear that a large number of exciting and important issues in condensed-matter physics revolve around plutonium. Los Alamos is one of the few laboratories in the world that can do experiments with plutonium, and it is certainly part of our mission to understand the properties of this metal. We are poised at the frontier of new physics, and this issue of *Los Alamos Science* is your guide to that frontier. ■

Further Reading

- Laughlin, R. B., G. G. Lonzarich, P. Monthoux, and D. Pines. "The Quantum Criticality Conundrum" (submitted to *Phys. Rev. Lett.*).
- Mathur, N. D., F. M. Grosche, S. R. Julian, I. R. Walker, D. M. Freye, R. K. W. Haselwimmer, and G. G. Lonzarich. 1998. *Nature* **394**: 39.
- Sachdev, S. 2000. *Science* **288**: 475.
- Saxena, S. S., P. Agarwal, K. Ahilan, F. M. Grosche, R. K. W. Haselwimmer, M. J. Steiner et al. 2000. *Nature* **406**: 587.



Plutonium

A historical overview

Siegfried S. Hecker

with the Los Alamos Science staff

A Factor of Millions

Why we made plutonium

with André F. Michaudon and Ileana G. Buican



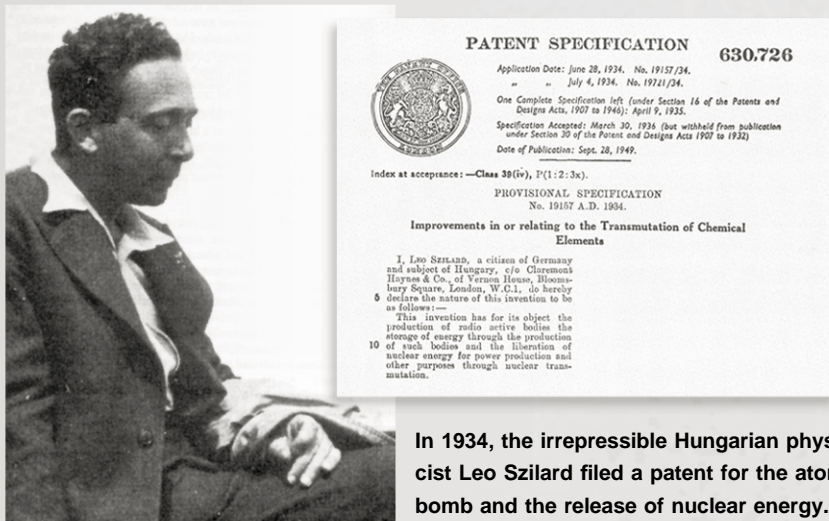
The seminal work of (from the top) Irène Curie and Frédéric Joliot, Ernest Rutherford, James Chadwick, and Niels Bohr opened the modern era of nuclear physics.

Until the middle of the 20th century, humans had managed to extract only chemical energy from atoms. That energy is carried by electrons orbiting around the heavy, tiny nucleus at the atom's center. Released when conventional fuel is burnt or explosives are detonated, that energy is on the order of electron volts per atom. Yet early in the century, scientists—particularly those educated in the great European school of physics—were already engaged in probing the secrets of the nucleus. In 1938, they discovered that the nucleus could be split through a process called fission, unleashing huge amounts of energy. Suddenly, the scale of energy release changed from electron volts to millions of electron volts, which became available for powerful explosives and civilian energy production. And it was the Manhattan Project pioneers who managed to extract the millionfold advantage of nuclear over conventional explosives during a wartime race with Nazi Germany.

The Discovery of Nuclear Fission

When James Chadwick discovered the neutron in 1932, he paved the way for a greater understanding of nuclear reactions. Indeed, in September 1933, the Hungarian physicist Leo Szilard envisioned that neutrons could be absorbed by a nucleus and induce a repeatable chain reaction that would lead to the controlled release of atomic energy. Szilard then also thought of using neutron-induced chain reactions to create explosions. In 1934, while in London, he filed and was awarded a patent on that concept, thus becoming the legally recognized inventor of the atomic bomb.

That same year, Frédéric Joliot and Irène Curie demonstrated that stable elements could be made radioactive. After irradiating aluminum nuclei with α -particles, they detected the neutrons produced but also a signal of radioactivity. The scientists deduced that the signal was coming from a short-lived phosphorus isotope into which some of the aluminum must have transmuted. Using a chemical precipitation



In 1934, the irrepressible Hungarian physicist Leo Szilard filed a patent for the atomic bomb and the release of nuclear energy.



A nucleus, mimicked here by a drop of oil, can deform and break in two.

method, Joliot and Curie separated the source of the radioactive signal from the aluminum target and proved that the signal was indeed coming from phosphorus. Their technique for studying nuclear transmutations was adopted universally, and the neutron, which has no electric charge, was immediately seen as an ideal “projectile” for inducing nuclear transformations.

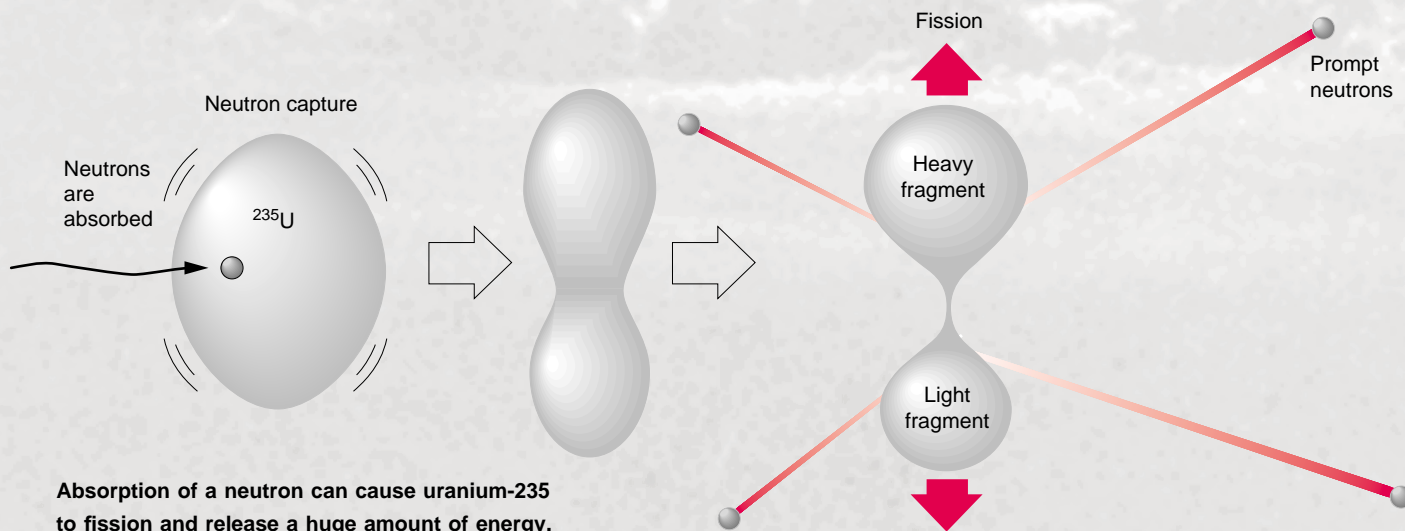
In Rome, Enrico Fermi, Edoardo Amaldi, Emilio Segrè, and Franco Rasetti systematically bombarded all the elements in the periodic table with neutrons. Finally, they bombarded uranium, hoping to create elements beyond uranium (or transuranic elements). Although Fermi had shown that slow neutrons (those whose energies are on the order of electron volts or less) created more radioactivity than fast ones, the Italian scientists did not identify any clear signal of transuranic elements from the array of induced radioactivities. Nor did they know that, in the process of bombarding uranium with neutrons, they must have produced nuclear fission. Later, Emilio Segrè reminisced about those events and admitted that, “We did not seriously entertain the possibility of nuclear fission although it had been mentioned by Ida Noddack, who sent us a reprint of her work. The reason for our blindness, shared by Hahn, Meitner, the Joliot-Curies, and everybody else working on the subject, is not clear to me even today.” (*A Mind Always in Motion: the Autobiography of Emilio Segrè*, 1993, Berkeley, CA: University of California Press.)



(From top left): Enrico Fermi, Fritz Strassmann, Otto Hahn and Lise Meitner, and Otto Frisch.

In December 1938, the German chemists Otto Hahn and Fritz Strassmann discovered that one of the induced activities in neutron-irradiated uranium came from an isotope of barium, a nucleus with roughly half the mass and charge of the uranium nucleus. The scientists were astonished at their findings.

Their collaborator Lise Meitner, then in exile in Sweden, and her nephew Otto Frisch quickly explained the new phenomenon in terms of Niels Bohr’s liquid-drop model. When it absorbs a neutron, the positively charged nucleus begins to vibrate, behaving like a drop of liquid. As shown in the illustration below, the vibration deforms the large uranium nucleus so much that the nucleus splits into two smaller nuclei that fly apart, a process accompanied by a tremendous release of



Absorption of a neutron can cause uranium-235 to fission and release a huge amount of energy.

Plutonium Overview

After Ed McMillan discovered neptunium, he started the process of making plutonium. But it was wartime, and McMillan was summoned to work on radar at the Massachusetts Institute of Technology. As Joseph Kennedy (below, right photo) later put it, McMillan got on the train, and the others found plutonium.



Art Wahl (left) vividly remembers his excitement the night he and Kennedy first isolated plutonium. “By the time I finished the second part of the experiment—reducing the oxide and recovering the plutonium—Kennedy had gone home. So, I went to bed with the secret of the discovery of plutonium all to myself.”



(From center to right): Glenn Seaborg, Art Wahl, and Ed McMillan accept a plaque from Undersecretary of the Interior John Carver, Jr., on the occasion of the 25th anniversary of plutonium’s discovery. The ceremony took place in Gilman Hall, in front of Room 307, where plutonium had been isolated.

energy. After talking with biologist William Arnold about fissioning bacteria, Frisch borrowed the terminology for splitting nuclei.

On January 26, 1939, Niels Bohr publicly announced the discovery of fission at an annual theoretical-physics conference at George Washington University. Physicists from the United States, the Soviet Union, and Western Europe immediately understood the implications—building an atomic bomb from uranium became a possibility. The fission products are created in an excited state and would likely lose energy by “boiling off” neutrons (referred to as prompt neutrons). These neutrons could be captured by other nuclei and induce more fission events, as Szilard had envisioned in 1933. Depending primarily on the arrangement and density of the fissile material, fission could proceed in either a controlled, self-sustaining manner and produce nuclear power or in a “runaway” fashion and result in a nuclear explosion.

By February 1939, Niels Bohr had deduced that uranium-235 is the only naturally occurring fissile uranium isotope (a fissile isotope is one in which fission can be induced by neutrons of any energy, no matter how small). In September that same year, Bohr and Wheeler published a theoretical analysis of fission. The nuclear physics is such that the odd number of neutrons (143) in uranium-235—as opposed to the even number of neutrons (146) in uranium-238 (both isotopes have 92 protons, an even number)—makes all the difference. But natural uranium contains only 0.7 percent uranium-235. The rest is uranium-238. Using natural uranium for a bomb was clearly inefficient because too few fission events could occur in 99.3 percent of the material.

A successful fission bomb would require a few kilograms of uranium-235, but obtaining those quantities was difficult because the fissile isotope could not be chemically separated from uranium-238. In the meantime, however, the 1939 paper by Bohr and Wheeler had inspired several scientists to postulate that a transuranic element with 94 protons and 145 neutrons—plutonium-239—should also be fissile. Plutonium offered the attractive alternative of a fissile element that could be chemically separated from uranium. But every atom of plutonium would have to be made.



(From the left): Donald Cooksey and Ernest O. Lawrence stand in front of the historic 60-in. cyclotron designed by Lawrence. The primary deuterons and secondary neutrons from the cyclotron were used to irradiate uranium samples. The uranium decayed to neptunium, which decayed to plutonium. Plutonium amounts made here in 1941 were too small to be seen but sufficient for initial analysis of chemical properties. The inset shows a 2.7- μg sample of plutonium oxide produced by Seaborg at the Washington University cyclotron. It is placed on a platinum weighing boat and has been magnified 40-fold.

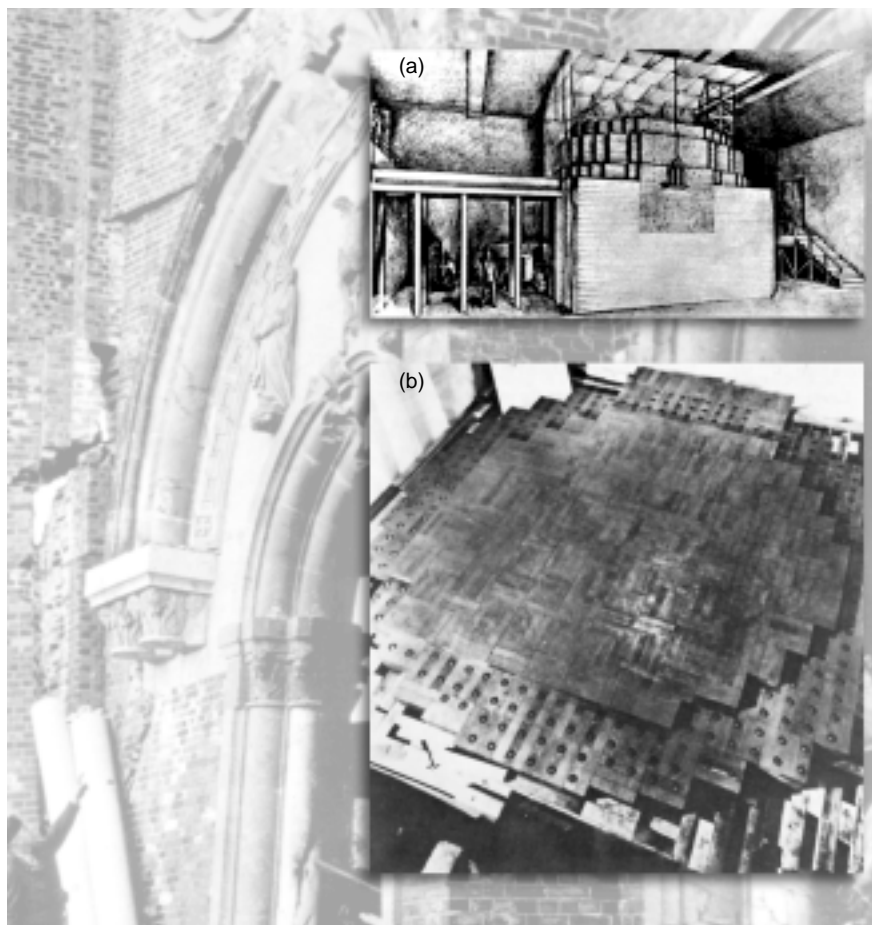
Creating Plutonium

Until 1939, the worldwide attempt to identify transuranic elements had not been successful. That year, however, the American scientists Ed McMillan and Philip Abelson were the first to prove the existence of element 93. After bombarding uranium-238 with neutrons in the 60-inch cyclotron at the University of California at Berkeley, they used a clever sequence of measurements to prove that element 93 was growing in from the decay of uranium-239. They called it neptunium, after the planet Neptune. Neptunium was expected to decay to element 94 (plutonium), which would signal its presence through α -decay. Although minute quantities of the long-lived plutonium-239 must have been made, its radioactivity could not be detected. Shortly thereafter, McMillan's colleagues Seaborg, Kennedy, Wahl, and Segrè bombarded uranium-238 with deuterons and detected α -decay from the shorter-lived plutonium-238. Finally, on the night of 23 February 1941, Seaborg, Kennedy, and Wahl isolated a minute quantity of element 94, which a year later they officially named plutonium for the planet Pluto.

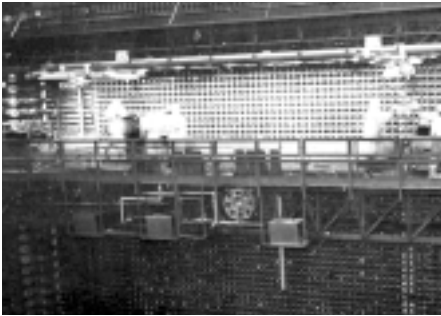
As early as 1939, American scientists, many of whom were refugees from Fascist regimes in Europe, had already started organizing a secret project that would take advantage of the newly discovered fission process for military purposes. Under the code name the Manhattan Project, it was officially established in August 1942. The Metallurgical Laboratory (Met Lab) at the University of Chicago became one of four Manhattan Project secret sites. It was tasked with producing plutonium-239 from uranium-238 in a reactor pile. The low neutron flux available at cyclotrons can produce only minute amounts of plutonium. A self-sustaining chain reaction in a reactor pile, on the other hand, would produce an extremely high neutron flux that could transform large amounts of uranium-238 into plutonium-239. But first, as told in the caption to the right, the fission chain reaction would have to be demonstrated.



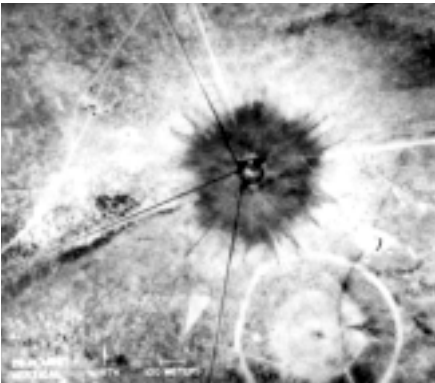
Relying on their experience with building a uranium-graphite lattice at Columbia University, Fermi (above) and Szilard codesigned the Chicago pile—an artist's rendition is shown in (a). Fermi and coworkers built it. Stagg Field (background picture to the left), a Gothic-style monument to the university's football pride was chosen as the site for the chain-reacting pile. The work for building the pile was slow, laborious, and dirty. Made of uranium oxide and uranium metal components held by graphite bars in a lattice arrangement—see (b)—the pile contained 349,263 kg of graphite, 36,507 kg of uranium oxide, and 5,617 kg of uranium metal. On December 2, 1942, after the last cadmium control rod had been pulled out to the next required position to allow the neutron intensity to increase, the pile went critical. And so, what had begun as Szilard's scientific speculation turned into a wartime reality. Inevitably, plutonium must have been created in the pile, but the goal of this experiment was to prove the fission chain reaction.



Making the Atomic Bomb



This is one of the first three plutonium production reactors at Hanford, Washington.



During the Trinity Test, crater and heat effects scarred the desert at Ground Zero.

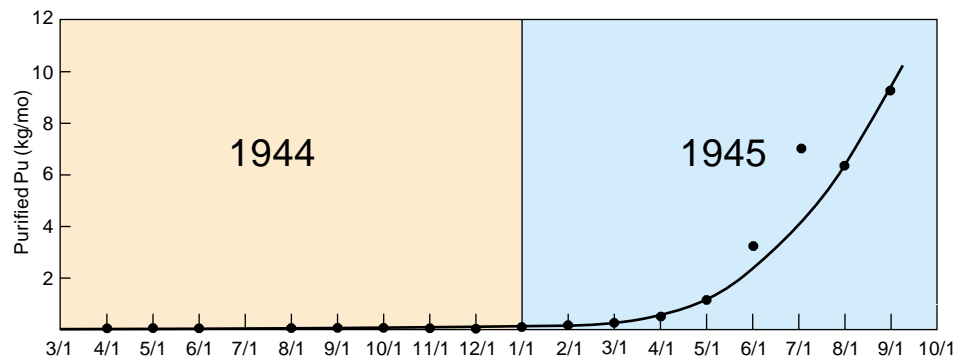


At Los Alamos, the world's first atomic bombs were designed and built.

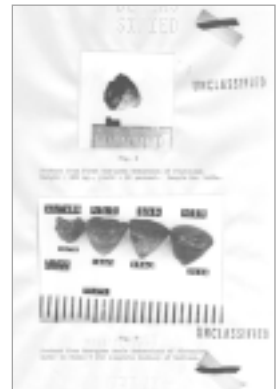
After Fermi and coworkers had demonstrated that natural uranium could sustain a fission chain reaction, the scaled-up uranium-graphite piles at Hanford, Washington, started producing plutonium-239. Hanford was the second site of the Manhattan Project. Eventually, there would be enough plutonium for three bombs—one to be tested at Trinity Site, another that would destroy Nagasaki, and a third that would end up not being used. Simultaneously, at Clinton (later to be called Oak Ridge), Tennessee, uranium-235 was being separated from uranium-238 for the bomb that would destroy Hiroshima. At this third secret site, there was also a plutonium-producing reactor. Los Alamos became the Manhattan Project's fourth site. In October 1942, following Gen. Groves's proposal, J. Robert Oppenheimer was named director of Project Y at Los Alamos, where the world's first atomic bombs were to be designed and built with material shipped from Clinton and Hanford.

Once the neutron-irradiated fuel elements in the reactor had been dissolved in an aqueous solution of mostly nitric acid, the plutonium nitrate slurry extracted would be shipped to Los Alamos and converted to plutonium chloride or fluoride. That compound would then be reduced to plutonium metal, whose material properties would have to be studied and understood. Ted Magel and Nick Dallas were the first to solve the plutonium reduction problem on a scale larger than a few micrograms. They obtained plutonium metal in a graphite centrifuge.

However, to scale up the reduction process, Dick Baker adapted the "bomb" reduction technique, which had been developed at Iowa State University for uranium, to the reduction of plutonium. He reduced plutonium halide to metal in a metallothermic reaction of the type $\text{PuF}_4 + 2\text{Ca} \rightarrow \text{Pu} + 2\text{CaF}_2$. The reaction took place inside a sealed steel container with a refractory liner in an inert-gas atmosphere at high temperatures. That is why it was nicknamed the bomb reduction technique. Plutonium



During 1944, monthly deliveries of plutonium metal were minuscule (see graph above). From these quantities, Magel and Dallas produced a 50-mg button on March 9, 1944. By March 23, they had produced the first 1-g button (to the right, upper half of photo). Four more plutonium metal buttons made by Magel and Dallas during the spring of 1944 are pictured to the right (lower half of photo). Kilogram quantities did not arrive at Los Alamos until May 1945, when the Hanford reactor started making plutonium in large quantities. Ed Hammel eloquently tells the remarkable story (see page 48) of how the Manhattan Project pioneers learned just enough about this enormously complex metal to be able to craft it into a nuclear device in a very short time.



metal was a precious commodity. In a letter to Gen. Groves, Oppenheimer pointed out that, by the end of August 1944, “we have received 51 grams of this material. The material has been used for approximately 2500 separate experiments. The overall loss per experiment has been about 1 percent.” After each experiment, plutonium had to be recycled. In Oppenheimer’s words, the “material we have dissipated” (that is, the 1 percent per experiment) “will be paid for many times over by the effectiveness with which we can deal with production lots when they become available.”

At Los Alamos, work had initially centered on developing a gun-type bomb, which required high purification limits for plutonium. But in July 1944, plutonium produced in the Hanford reactor was found to contain not only the isotope 239 but also enough of the isotope 240 to create a problem. The heavier isotope would spontaneously fission and produce neutrons, which would trigger the bomb prematurely. The gun design was therefore promptly abandoned for the plutonium bomb, and the effort shifted toward an implosion design. Ironically, not only did the new work ease some impurity constraints, but it also required that metallurgists add an “impurity”—a few atomic percent gallium—to stabilize the cubic crystal form of plutonium that could be easily pressed into the final shape for the Trinity and Nagasaki bombs.

By July 1945, Los Alamos chemists and metallurgists had learned enough about the mysteries of plutonium to shape it into hemispheres and trust that a plutonium pit would hold together for the required number of weeks before the atomic bomb was to be used. Yet, the fact that the scientists decided to test the plutonium bomb and thus use almost half the quantity of material available at that time is a measure of how uncertain they were that the bomb would work as expected. The test at Trinity Site on July 16, 1945, was completely successful. On August 9, 1945, the plutonium bomb destroyed Nagasaki. ■



Some of the leaders of the Los Alamos Project are pictured here. (Top row from the left): J. Robert Oppenheimer was the first director of Los Alamos (1942–1945). Physicist Seth Neddermeyer laid the foundations of the implosion program at Los Alamos. John von Neumann, a consultant to the Manhattan Project, was a great mathematician and physicist who invented the concept for a rapid implosion device. Cyril Smith was in charge of metallurgy. He suggested adding a second element to stabilize the δ -phase of plutonium. Hans Bethe led the Theoretical Division in predicting critical masses and explosive yields. (Bottom row from the left): Eric Jette, a physical chemist, headed the section in which plutonium reductions, remelting, alloying, and casting were conducted. George Kistiakowsky developed the explosives lenses that made the implosion concept work.

Plutonium in Use

From single atoms to multiton amounts

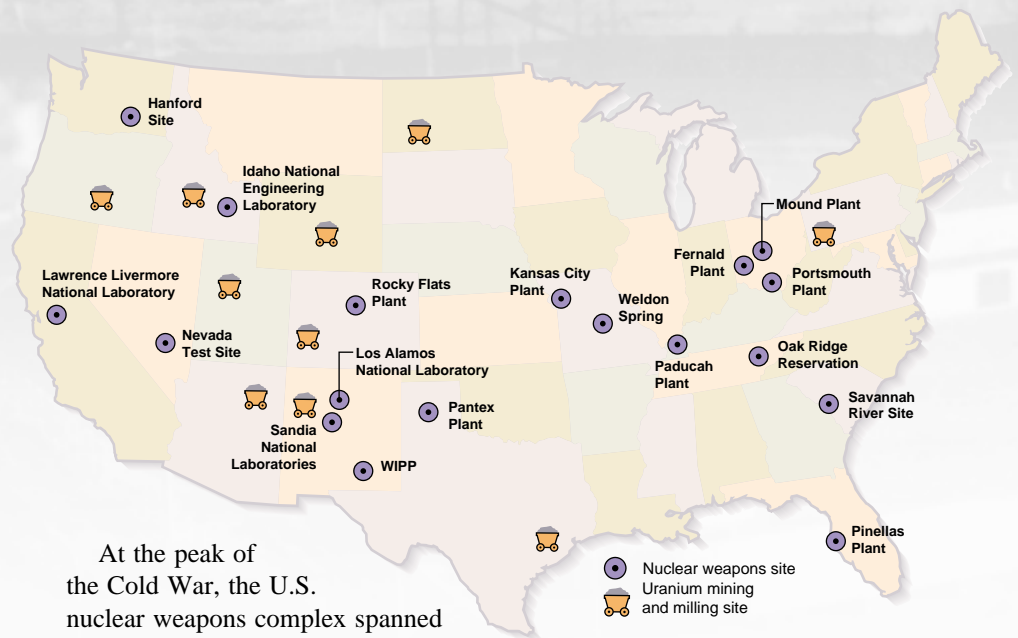
Plutonium is highly toxic and radioactive, virtually nonexistent in nature, and very expensive to produce. Clearly, one must have good reason to justify its use. The only significant applications for plutonium to date, therefore, are those capitalizing on the “factor of millions” gained by using the energy of the nucleus: nuclear explosives and nuclear power. Moreover, the persistent radioactive decay of plutonium has also made this metal useful as a compact heat source to produce electricity for deep-space missions.



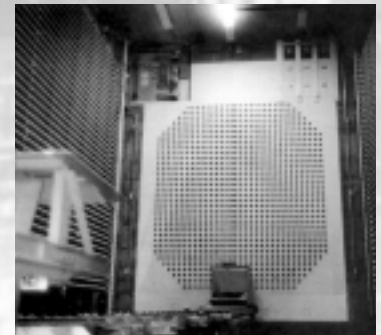
The U.S. nuclear triad: submarine launched missiles, land-based missiles, and air-dropped bombs.

Nuclear Weapons

During the Manhattan Project, the plutonium challenge was to produce sufficient material for a few bombs and to fabricate it into the desired shape. But in the years that followed, the effort shifted to the mass production of plutonium, and the designing, building, and testing of large numbers of nuclear weapons.



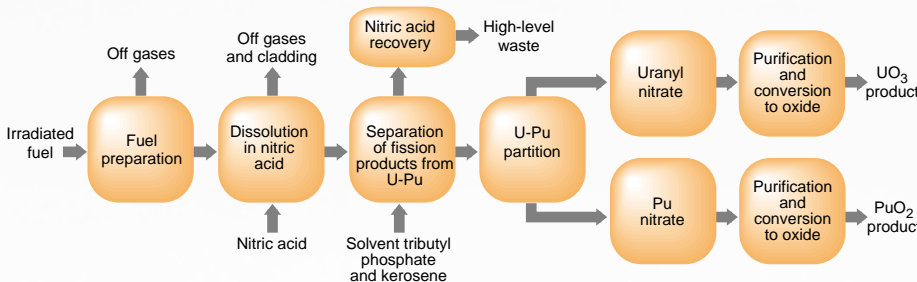
At the peak of the Cold War, the U.S. nuclear weapons complex spanned the country with 18 facilities. Nine plutonium production reactors were in operation at the Hanford Site in Washington, and five more at the Savannah River site (top of opposite page) that was established in 1950 near Aiken, SC. Those two sites also hosted seven reprocessing facilities to extract the plutonium from the irradiated uranium fuel rods. Weapon parts were manufactured in Colorado, Florida, Missouri, Ohio, Tennessee, and Washington, and the final warhead assembly took place at the Pantex Plant near Amarillo, TX. The national laboratories in New Mexico and California designed the warheads, which were subsequently tested at the site in Nevada. In more than 50 years of operation, the nuclear weapons complex created over 100 tonnes of plutonium, produced tens of thousands of nuclear warheads, and oversaw more than 1000 detonations.



All plutonium production reactors in the United States are now shut down. The U.S. government declared nearly half of the 99.5 tonnes still in the inventory (in forms ranging from plutonium pits in stockpiled weapons systems to oxides, scrap, residues, and waste) as excess to the nation's defense needs. The United States has, however, more than an adequate supply of plutonium for the triad of land-based missiles, submarine-launched missiles, and air-delivered bombs that constitute the U.S. nuclear deterrent.

The Soviet nuclear weapons program began in earnest right after Hiroshima. The nuclear bomb first tested by the Soviets was a copy (obtained through espionage) of the U.S. plutonium design tested at Trinity Site on July 16, 1945. During the Cold War, the Soviets built an enormous plutonium production infrastructure at three major sites: Chelyabinsk-65 (in the South Urals), Tomsk-7 (in Siberia), and Krasnoyarsk-26 (in Siberia). The Soviet Union matched the United States step by step in developing its nuclear arsenal. The Soviets also created the ultimate doomsday weapon, a 100-megaton device (tested at half yield in 1961).

We do not know how much plutonium was produced in the Soviet Union and how much remains in Russia today because Russia still considers its plutonium inventories to be state secrets. Our best estimate is that today Russia has between 125 and 200 tonnes of plutonium in its military program in many different forms. The stockpiles of military plutonium in the rest of the world, including the United Kingdom, France, China, India, Pakistan, Israel and North Korea, are small and total about 18 tonnes.



Plutonium is created in nuclear reactors, such as the N reactor (upper right) at the Hanford Site (top left). Once the fuel is removed from the reactor core, it is placed in a cooling tank (middle right) to allow shortest-lived fission products to decay. The PUREX process (lower left) is used to separate plutonium and uranium from the remaining fission products in the irradiated nuclear fuel. The highly radioactive waste from PUREX is stored in enormous tanks (lower right) located on-site.

Nuclear Reactors



Mark I, a prototype reactor that could be used in a submarine, became the first U.S. reactor to produce substantial amounts of power on May 31, 1953. Two years later, under the able leadership of Admiral Hyman G. Rickover, the United States launched its naval reactor program with the first sea trials of the U.S.S. Nautilus, a nuclear-power submarine.

Shortly after the discovery of radioactivity, people started dreaming about the peaceful use of atomic energy for virtually inexhaustible power production. In his book *The Interpretation of Radium*, published in 1909, Frederick Soddy referred to nuclear energy as being “the real wealth of the world. It is a legitimate aspiration to believe that one day [man] will attain the power to regulate for his own purposes the primary fountains of energy which Nature now so jealously conserves for the future.” Enrico Fermi also dreamed about the potential of limitless nuclear energy shortly after his reactor, CP-1, sustained the first controlled-fission reaction on December 2, 1942. (See the article “From Alchemy to Atoms” on page 62.)

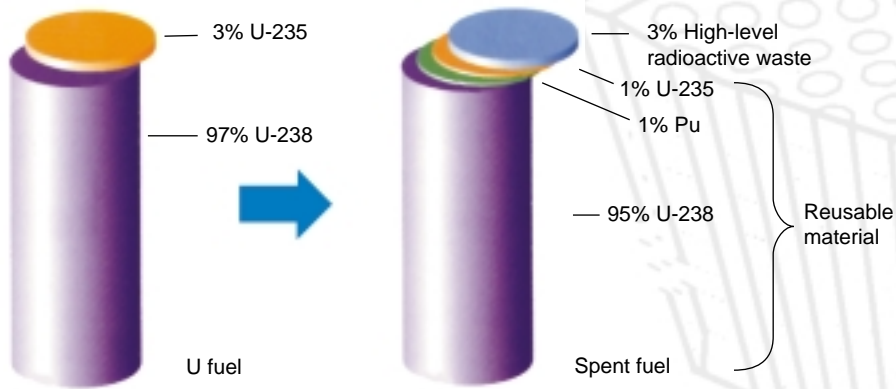
Commercial nuclear power received a significant boost when President Eisenhower launched the Atoms for Peace Program with a speech at the United Nations on December 8, 1953. Although nuclear power has not expanded at the rate it was projected during Eisenhower’s years, it nevertheless has become an indispensable part of the world’s energy supply. Some 430 nuclear power reactors around the world supply nearly 20 percent of the world’s electricity today, providing electric power for nearly one billion people. One hundred and four reactors are in service today in the United States. However, no new nuclear power plants have been ordered in the United States for over 20 years.

Nuclear reactors were also developed to power the Navy’s submarines under the able leadership of Admiral Hyman G. Rickover. The United States launched its naval reactor program in January 1955 with the sea trials of the first nuclear-power submarine, the U.S.S. Nautilus. The Soviets not only followed suit with a nuclear submarine program of their own, but they built many other seafaring vessels, including the first nuclear-powered ice breaker, the Lenin, in 1959.

Nuclear reactors are designed to foster a fission chain reaction and to extract the nuclear energy in a controlled manner. Commercial reactors typically use fuel that is 95 to 98 percent uranium-238, with the fissile isotope uranium-235 making



The Soviet Union claimed it demonstrated the world’s first nuclear power plant at Obninsk (a) commissioned on June 27, 1954. It was a graphite-moderated, water-cooled reactor designed to produce 5 MW of electric power. The United Kingdom was first to operate a truly commercial nuclear power plant at Sellafield (b) in 1956. The first U.S. commercial power plant was commissioned at Shippingport, Pennsylvania (c), in December 1957.



Fuel that has been through one reactor burn cycle is called spent fuel even though it contains 2% fissile material and 95% fertile material. (This illustration was adapted with permission from *PowerLine*, Japan.)

up the rest. To be fissile means that the nucleus fissions when it absorbs a neutron of any energy, including low-energy neutrons that are in thermal equilibrium with the environment (known as thermal neutrons). Fertile isotopes, which can be transmuted into fissile isotopes, will fission only with high-energy neutrons. Uranium-238 and thorium-232 are fertile isotopes.

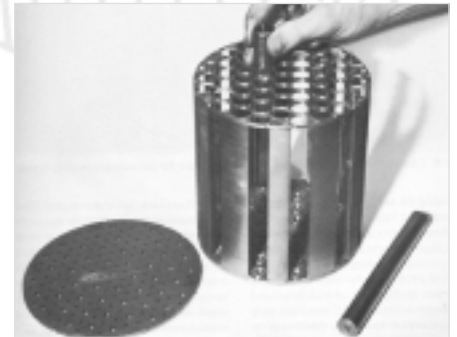
Thermal reactors use thermal neutrons to “burn” the fissile component of the uranium fuel. Atoms of uranium-235 that absorb the low-energy neutrons fission into two nuclei of nearly equal mass. These fission products fly away from each other with tremendous energy, most of which is converted to heat as the product nuclei come to rest in the fuel rod. The heat is extracted by a coolant (typically water) that is run through a heat-exchanger. Water on the other side of the heat exchanger is converted to steam, which drives a turbine coupled to an electric generator. Today’s large commercial reactors have an electrical generating capacity of more than a billion watts.

On average, about 2.5 neutrons are released when uranium-235 fissions. Only one of those neutrons needs to be absorbed by another uranium-235 atom to maintain the chain reaction. The other neutrons are absorbed by the many uranium-238 atoms, which subsequently decay to plutonium-239. Since plutonium-239 is fissile, it too can fission and release energy. In modern reactors, the “in-grown” plutonium accounts for approximately 30 percent of the generated power.

Within the civilian sector, worldwide plutonium inventories are currently estimated at over 1000 tonnes—an amount that dwarfs military inventories. This commercial, or reactor-grade, plutonium contains nearly 40 percent nonfissile isotopes. In contrast, the weapons-grade plutonium produced in military reactors consists of over 93 percent fissile plutonium-239 and less than 7 percent other plutonium isotopes.

In the generic thermal reactor described above, only a small fraction of the uranium-235 and the in-grown plutonium is actually consumed during one cycle of power generation. The fertile uranium-238 that makes up most of the fuel rod is essentially inert—its energy potential is tapped only after it absorbs a neutron and is transmuted to fissile plutonium-239. Thus, most of the energy potential of the fuel is unused. Shortly after World War II, Fermi and other scientists recognized the possibility of enhancing plutonium production and creating more fissile fuel than was consumed. After fuel has burnt for one cycle, the excess plutonium could be extracted, separated from uranium-238, and reprocessed into fuel rods. By “breeding” plutonium within a closed fuel cycle, we can tap most of the nuclear energy.

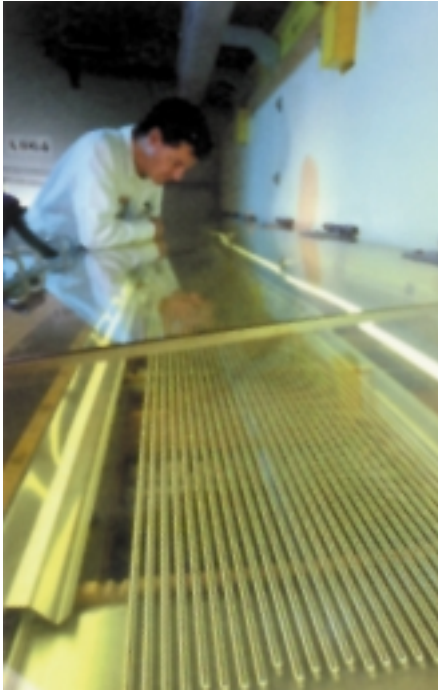
A breeder reactor uses high-energy (fast) neutrons, rather than thermal neutrons, to sustain the chain reaction. The fission cross section decreases with neutron energy, so the chain reaction is maintained by increased amounts of fissile material (either uranium-235 or plutonium-239). Because each fission event produces an excess of neutrons, the net effect is that, within the reactor, many neutrons are available to transmute uranium-238 and breed plutonium.



Several research reactors were developed at Los Alamos. They were designed to produce a high-neutron flux that could be used to obtain neutron cross-section data relevant for nuclear weapons. Of note was the Clementine reactor that was built toward the end of 1946. It used plutonium metal as fuel and fast neutrons to achieve the chain reaction. The plutonium fuel led to severe corrosion problems, and Clementine ceased operations in 1952.



The first fast reactor to fully explore the breeder concept and to produce usable power was the Experimental Breeder Reactor I (EBR-I), located at Arco, Idaho. On December 20, 1951, the reactor powered up and initially produced enough electricity to light four 150-W light bulbs. Its output later reached 100 kW of electric power.



For 35 years, plutonium has been recycled by burning of mixed-oxide (MOX) fuel in nuclear reactors. Today, European conventional water-cooled nuclear reactors are licensed to load around one-third of the core with MOX fuel. In the photo above, a technician is checking MOX fuel rods. (This photo was reproduced courtesy of Nuclear Recycling.)

The Soviet Union responded to the U.S. Plowshare Project with its own “industrial nuclear explosion” carried out in 1965 at the Semipalatinsk Test Site in Kazakhstan. The purpose of the test was to build a dam across a small river. The lip of the test crater was to form the dam during spring runoff. The test created a major lake of some 10 million cubic meters of water. It released substantial radioactivity into the atmosphere. Today, the lake is known as Lake Balapan, is used for water control, and supplies water to cattle in the area. Modern PNE nuclear devices, such as those shown here from the Atomic Museum in Snezhinsk, were designed to minimize the fission yields in order to reduce radiological contamination.

Breeder reactors are much more difficult to control and far more expensive to build than thermal reactors. For several decades, the breeder reactor program was pursued aggressively in the United States, the Soviet Union, and France. But the Carter Administration strongly opposed the U.S. breeder program, which finally came to a halt in 1983 with the cancellation of the Clinch River Breeder Reactor program. France, Russia, and Japan are still pursuing breeder technology today with the hope of reviving commercial interest early in this century.

Another way to fully utilize the power potential of the uranium is to recycle or reprocess the spent fuel. Unburned uranium and plutonium grown in during reactor operation are chemically separated from each other and from the radioactive fission products. (The fission products poison the chain reaction by absorbing neutrons and must therefore be removed.) However, the efficiency gained by recycling nuclear fuel is offset by the fact that the separated plutonium can be used to make nuclear weapons.

In 1977, President Carter judged the proliferation risk too great, and he decided not to allow U.S. commercial nuclear power plants to recycle plutonium from spent fuel. He hoped to set an example, which the other nuclear power nations would follow. However, they did not. Instead, they followed the economic incentive to reprocess plutonium from spent fuel.

Reprocessed plutonium can be mixed with uranium to form a mixed-oxide (MOX) fuel. One gram of MOX fuel will produce as much electricity as burning one ton of oil, and oil is a commodity that countries such as France and Japan have to import. Today, 32 reactors in Belgium, France, Germany, and Switzerland use MOX fuel. Japan has also begun to burn MOX fuel.

Peaceful Nuclear Explosives

The Atoms for Peace program also led to the exploration of nuclear explosions for peaceful purposes known as peaceful nuclear explosions (PNEs). The U.S. Plowshare Project began in 1957 and initially explored using PNEs for large-scale earth moving, including excavating a second Atlantic-to-Pacific canal through Central America. Additional peaceful applications, such as oil and gas stimulation, were also considered.

The United States detonated 27 PNEs. However, a PNE with a yield of about 10 kilotons injects several kilograms of fission products and actinides into the local environment. Radioactive contamination is therefore part of the risk associated with the detonations. The program was abandoned in the mid-1970s because the risks were considered to outweigh the benefits.



The Soviet Union carried out 124 underground PNEs. They were used as giant excavation tools for creating dams and lakes or diverting rivers. With PNEs, geologic mapping was completed throughout vast regions of the Soviet Union, and huge underground cavities were created for the storage of gas condensates. Russian nuclear scientists have continued to advocate using PNEs for the destruction of chemical weapons, chemical wastes, or even nuclear devices. However, following the recommendation of the United States, all nuclear explosions, including PNEs, were banned by the 1996 Comprehensive Test Ban Treaty.

Nuclear Batteries

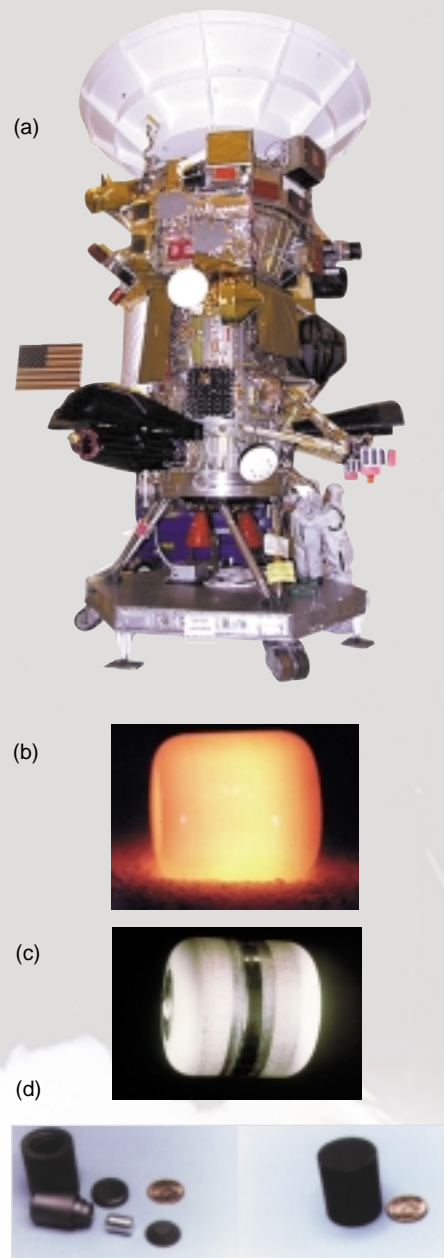
Plutonium is the power source for nuclear batteries that provide heat and electricity. When plutonium decays by α -particle emission, the α -particles lose most of their 5 million electron volts of energy to electrons in the plutonium lattice. As a result, heat is generated. Each gram of plutonium-239 produces a modest 0.002 watt as a result of its intrinsic α -particle decay. But plutonium-238, which is also produced in nuclear reactors, has a half-life of 89 years and an α -activity roughly 280 times greater than that of plutonium-239. Its intrinsic heat output is approximately 0.5 watt per gram. A thermoelectric device can convert the heat to electricity, and a few hundred grams of plutonium-238 is sufficient to generate usable amounts of electric power.

Several applications were initially considered for nuclear batteries, including powering heart pacemakers and remote terrestrial power stations. However, the difficulties of dealing with plutonium in commercial applications are such that today nuclear batteries are used only for deep-space missions. The spectacular photographs and scientific data sent back from the Pioneer and Voyager satellites were made possible by the extremely dependable performance of plutonium-238 power sources.

A modern battery, known as a general purpose heat source (GPHS) consists of a 150-gram pellet of plutonium-238 dioxide encased in many layers of protective materials. Seventy-two GPHS are stacked together with a set of thermocouples to make a radioisotope thermoelectric generator (RTG), which has an output of 285 watts of electricity. The RTG unit is compact and extremely reliable. Smaller capsules (known as radioisotope heater units, RHU) contain 2.7 grams of plutonium-238 dioxide. These are used as heat sources to keep equipment warm and functioning. Three RHUs, for example, were on the small Mars robot lander. ■



For several decades, both the Soviet Union and the United States operated compact, uranium-fueled nuclear reactors in space for applications requiring much greater power than those delivered by the thermoelectric generators. These reactors have had a checkered safety history. Today, interest in them is maintained only at a research level.



(a) By 2004, the Cassini spacecraft, shown here during assembly, should reach Saturn, where it will collect scientific data for four years. Aboard Cassini, almost 1 kW of electricity is supplied by three thermoelectric generators, each powered by a general-purpose heat source containing 72 plutonium-238 dioxide pellets. Each pellet produces 62 W of heat from the natural radioactive decay of plutonium-238. When thermally isolated, each pellet glows a brilliant orange, as shown in (b). The pellets are clad with iridium and welded as shown in (c) before they are further protected with several graphite shells for heat and impact resistance. (d) Lightweight, 1-W plutonium-238 heater units are used to warm sensitive electrical and mechanical systems aboard the spacecraft.

Plutonium

An element at odds with itself



Plutonium is a physicist's dream but an engineer's nightmare. With little provocation, the metal changes its density by as much as 25 percent. It can be as brittle as glass or as malleable as aluminum; it expands when it solidifies—much like water freezing to ice; and its shiny, silvery, freshly machined surface will tarnish in minutes. It is highly reactive in air and strongly reducing in solution, forming multiple compounds and complexes in the environment and during chemical processing. It transmutes by radioactive decay, causing damage to its crystalline lattice and leaving behind helium, americium, uranium, neptunium, and other impurities. Plutonium damages materials on contact and is therefore difficult to handle, store, or transport. Only physicists would ever dream of making and using such a material. And they did make it—in order to take advantage of the extraordinary nuclear properties of plutonium-239.

Plutonium, the Most Complex Metal

Plutonium, the sixth member of the actinide series, is a metal, and like other metals, it conducts electricity (albeit quite poorly), is electropositive, and dissolves in mineral acids. It is extremely dense—more than twice as dense as iron—and as it is heated, it begins to show its incredible sensitivity to temperature, undergoing dramatic length changes equivalent to density changes of more than 20 percent.

Six Distinct Solid-State Phases of Plutonium

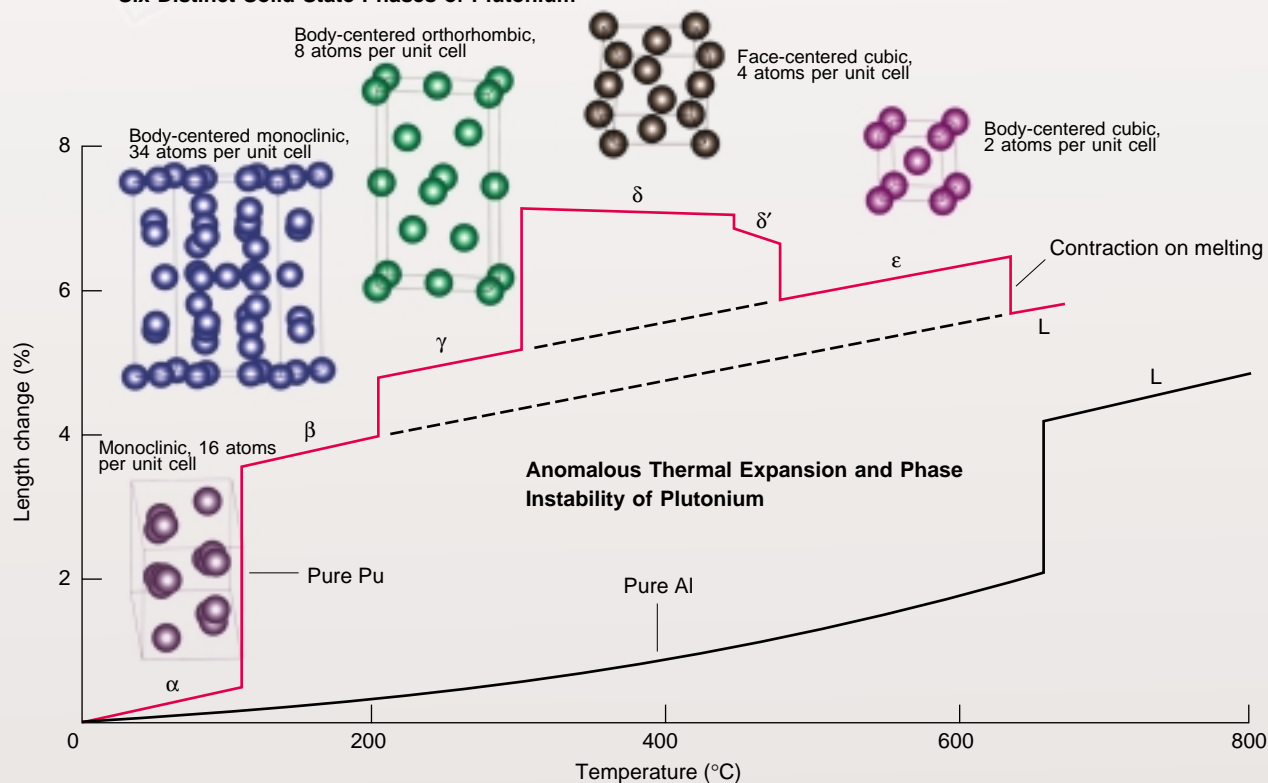


Table I. Physical Properties of Plutonium Compared with Other Metals

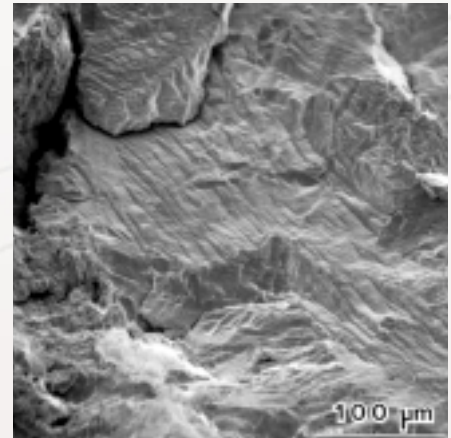
Metal	Thermal Conductivity (cal/cm-s-K)	Electrical Resistivity (Ω cm $\times 10^{-6}$)	Compressibility (GPa $^{-1}$)	Young's Modulus (GPa)
Aluminum	0.530	2.9	0.015	70
Stainless Steel	0.036	70	0.0007	180
α -Plutonium	0.010	145	0.020	100
δ -Plutonium (Pu-Ga)	0.022	100	0.033	42

At certain temperatures, the density changes are discontinuous as plutonium suddenly transforms into a new phase, or crystal structure. As it is being heated to its melting point at atmospheric pressure, plutonium will take on six distinct crystal structures; at higher pressures, it will take on a seventh structure. At room temperature and below, it is in the brittle α -phase, which has an unusual low-symmetry monoclinic structure typical of minerals. At 583 kelvins, it takes on the highly symmetric face-centered-cubic structure of the δ -phase, a close-packed structure typical of metals such as aluminum and copper.

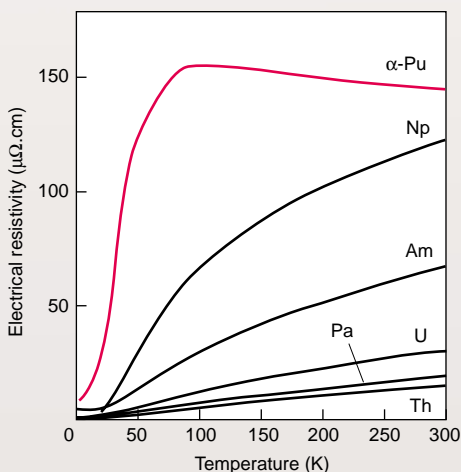
Even in a single phase, plutonium demonstrates unusual behavior—expanding when heated in the α -phase at a rate almost 5 times the rate in iron and contracting while being heated in the δ -phase. Then, at an unusually low 913 kelvins, plutonium melts. While melting, it contracts because the liquid is denser than the previous solid phase. In the liquid state, plutonium has a very high surface tension and the greatest viscosity of any element.

The table above compares plutonium with other metals. Like stainless steel, plutonium is a poor electrical and thermal conductor, and it is very soft, or compressible—even more so than aluminum. In addition, recent measurements have shown that the softening increases much more rapidly than expected with increasing temperature.

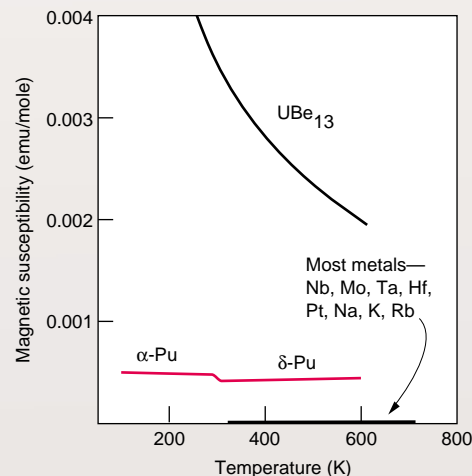
Cooling below room temperature brings out other atypical behaviors. Plutonium's electrical resistivity, already very high at room temperature, increases as the temperature is lowered to 100 kelvins. The energy required to heat plutonium (its specific heat) is 10 times higher than normal at temperatures close to absolute zero. Its magnetic susceptibility, also atypically high, remains constant with perhaps a slight increase as the temperature is lowered, indicating a tendency toward magnet-



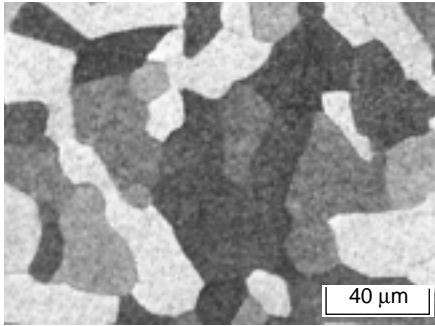
The α -phase has undergone brittle fracture under torsion.



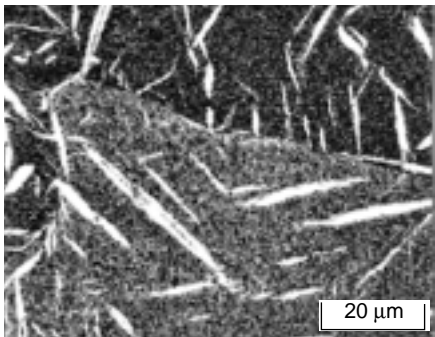
Anomalous Resistivity



High Magnetic Susceptibility



Grains of Pu-2 at. % Ga δ -phase alloy are shown in this micrograph.



Illustrated here is the formation of α' -phase platelets in δ -phase grains.

ism. But even at the lowest temperatures, plutonium never settles down to a state of long-range order (either magnetic or superconducting) as other metals do.

Plutonium is sensitive not only to temperature and pressure but also to chemical additions. In fact, much of its density and structural instability can be circumvented by additions of a few atomic percent of aluminum or gallium. These additions retain the face-centered-cubic δ -phase to room temperature, making plutonium malleable and easily pressed into different shapes. Yet, this most useful and familiar phase is the least understood theoretically. It has a close-packed structure, but the lowest density. Also, the δ -phase alloys exhibit phase instability, transforming readily between the δ - and α -phase (see micrographs) as temperature is changed or stress is applied. And the electronic structure of δ -plutonium, which may be unique in the periodic table, remains unexplained.

It's the 5f Electrons

Why does plutonium metal behave so strangely? Knowing that electronic structure determines nonnuclear properties, we turn to the periodic table and recent insights from modern calculations. The actinides mark the filling of the 5f atomic subshell much like the rare earths mark the filling of the 4f subshell. Yet, the 5f electrons of the light actinides behave more like the 5d electrons of the transition metals than the 4f electrons of the rare earths. Atomic volumes are the best indicators of what these electrons are doing, and the graph on the opposite page clearly demonstrates the similarity between the early actinides through plutonium and the transition metals. Each additional 5f electron in the early actinides leads to a decrease in atomic volume. The reason was guessed decades ago. Like the 5d electrons, the 5f electrons go into the conduction band, where they increase the chemical bonding forces, pulling the atoms closer together. In contrast, at americium, the 5f electrons start behaving like the 4f electrons of the rare earths, localizing at each lattice site and becoming chemically inert.

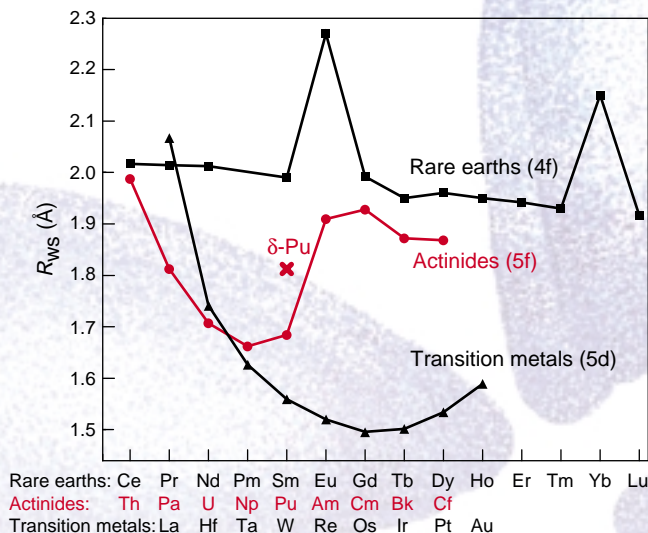
With no 5f contribution to bonding, the atomic volume suddenly increases at americium and contracts only slightly with increasing atomic number because the 5f electrons remain localized in the remainder of the series. The pattern of local magnetic moments confirms this picture. The light actinides show no local moments (as expected if all the valence electrons are in the conduction band), whereas the heavy actinides and the rare earths generally have local moments that are produced by their localized 5f and 4f electrons, respectively.

1	H											2	He																							
3	Li	4	Be											10	Ne																					
11	Na	12	Mg											18	Ar																					
19	K	20	Ca	21	Sc	22	Ti	23	V	24	Cr	25	Mn	26	Fe	27	Co	28	Ni	29	Cu	30	Zn	31	Ga	32	Ge	33	As	34	Se	35	Br	36	Kr	
37	Rb	38	Sr	39	Y	40	Zr	41	Nb	42	Mo	43	Tc	44	Ru	45	Rh	46	Pd	47	Ag	48	Cd	49	In	50	Sn	51	Sb	52	Te	53	I	54	Xe	
55	Cs	56	Ba	57	La	72	Hf	73	Ta	74	W	75	Re	76	Os	77	Ir	78	Pt	79	Au	80	Hg	81	Tl	82	Pb	83	Bi	84	Po	85	At	86	Rn	
87	Fr	88	Ra	89	Ac	104	Rf	105	Db	106	Sg	107	Bh	108	Hs	109	Mt	110	111	112	113	114	115	116	117	118										
				58	Ce	59	Pr	60	Nd	61	Pm	62	Sm	63	Eu	64	Gd	65	Tb	66	Dy	67	Ho	68	Er	69	Tm	70	Yb	71	Lu					
				89	Ac	90	Th	91	Pa	92	U	93	Np	94	Pu	95	Am	96	Cm	97	Bk	98	Cf	99	Es	100	Fm	101	Md	102	No	103	Lr			
				—	—	—	6d	6d	6d	6d	6d	6d	6d	—	—	—	—	—	—	—	—	—	—	—	—	—	—	—	—	—	—	—	—	—		
				—	—	—	7s ²	7s ²	7s ²	7s ²	7s ²	7s ²	7s ²	—	—	—	—	—	—	—	—	—	—	—	—	—	—	—	—	—	—	—	—	—	—	
				—	—	—	—	—	—	—	—	—	—	—	—	—	—	—	—	—	—	—	—	—	—	—	—	—	—	—	—	—	—	—	—	—

Periodic table showing the valence electrons in isolated atoms of the actinides.

We now have rigorous first-principles calculations that reproduce the general trends in atomic volumes, local moments, and ground-state structures. These calculations also hint at the origin of instability in plutonium and its lighter neighbors. We can therefore begin to make sense of the intriguing temperature-composition phase diagram connecting all the actinides that was drawn almost 20 years ago (see the connected phase diagram on the opposite page).

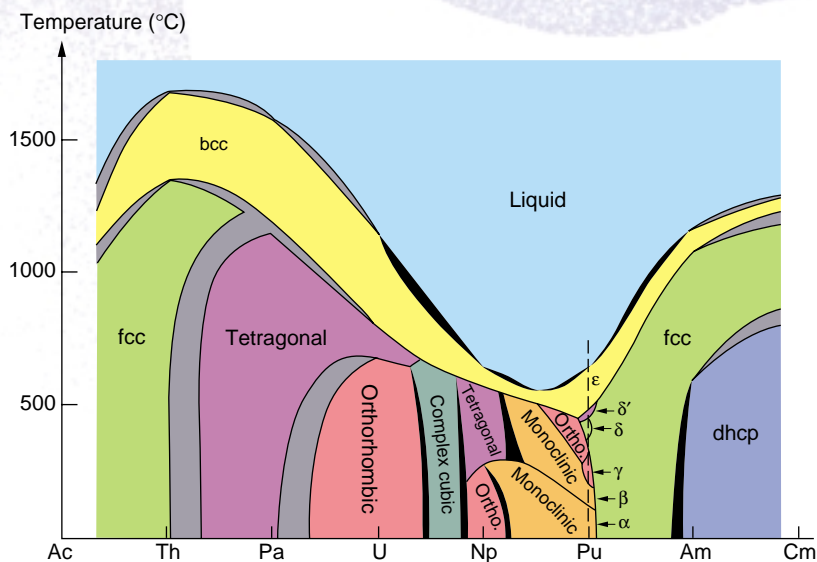
The most important insight from calculations is that, in the early actinides, the 5f electrons from different atoms overlap—but just barely. They therefore



The atomic radii of the actinide metals are compared with those of the rare earths and transition metals.

occupy a very narrow conduction (or energy) band, which has a very high density of states near the Fermi energy. As the number of 5f electrons populating that band increases, the specific properties of the band begin to dominate the bonding properties of the metal. For example, lattice distortions, or low-symmetry structures, are favored in narrow-band materials because they split the band in certain regions and thereby lower the total energy. Thus, the connected phase diagram shows that uranium, neptunium, and plutonium exhibit low-symmetry ground-state structures rather than high-symmetry structures, which are found in most metals. Before this new insight, the low-symmetry ground state of plutonium was attributed to directional or covalent-like bonding resulting from the angular characteristics of f electrons. Also, because the narrow 5f band overlaps the s, p, and d bands, a number of electronic configurations have nearly equal energy, leading to the multiple allotropic forms of uranium, neptunium, and plutonium and their great sensitivity to external influences.

Thus, many of the peculiarities of plutonium (anomalously low melting point, astonishingly high number of allotropes, and an unusual preference for low-symmetry crystal structures) are not part of a single anomaly but the culmination of a systematic trend in the early actinides resulting from the narrow 5f band. After plutonium, the 5f electrons are completely localized, and typical metallic structures and behaviors return. Right at plutonium, however, between the monoclinic α -phase, which is stable at room temperature, and the fcc δ -phase, which is stable at elevated temperatures, there appears to be a major transition in the 5f electronic structure from bonding to partial localization. It is that tendency toward partial localization that seems to contribute to plutonium's dramatic variability and sensitivity to external influences. The fundamental nature of the transition is at the research frontier of condensed matter physics. The consequences of the transition are critically important to the structural properties of plutonium—particularly to phase stability.



The connected binary-phase diagram of the actinides illustrates the transition from typical metallic behavior at thorium to complex behavior at plutonium and back to typical metallic behavior past americium.

Complex Chemistry of Plutonium



Each plutonium oxidation state has a characteristic color in solution.

The chemical behavior of plutonium, like its solid-state behavior, is controlled by its electronic structure. The lowest energy configuration of the valence electrons is nominally $5f^67s^2$, but the energy levels of the 6d and 5f orbitals are similar, and the $5f^67s^2$ and $5f^56d7s^2$ electronic configurations compete. In fact, as one moves from thorium to plutonium in the periodic table, the orbital energies invert—the 5f orbitals become lower in energy than the 6d orbitals. Unlike the 4f orbitals in the lanthanides (rare earths), the 5f and 6d orbitals in the light actinides up to americium extend far enough to be accessible for chemical bonding. Consequently, the light actinides exhibit complex chemical behavior reminiscent of the d-transition elements. In the heavy actinides beyond americium, the 5f orbitals are pulled in and not involved in chemical bonding, and therefore the chemical behavior of those heavy actinides and the lanthanides are quite similar.

In the metal, multiple electronic configurations of nearly equal energy lead to multiple solid-state phases. In the atom, they produce a tendency to supply more bonding electrons in chemical reactions and thus to exhibit a very complex chemistry. A plutonium atom in aqueous solution will readily lose between three and seven of its outer electrons to form positively charged cations in five formal oxidation states ranging from Pu(III) to Pu(VII). Many different oxidation states, however,

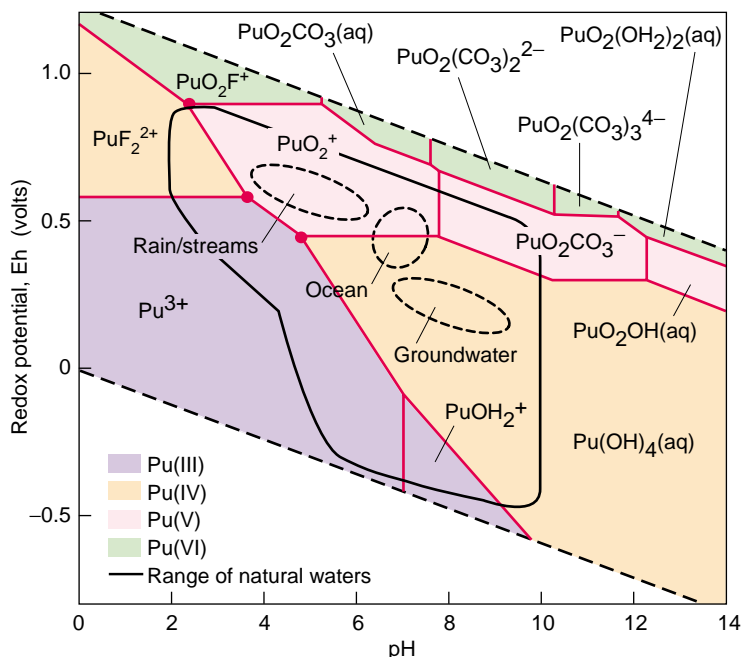
make solution chemistry very complex because each of them forms different compounds or complexes. The plutonium complexes span a broad range of structural motifs and typically have high coordination numbers (that is, the plutonium cation surrounds itself with many anions). Coordination numbers from 3 to 12 have been observed for various oxidation states.

Moreover, under acidic conditions, the energy needed to add or subtract electrons (the reduction-oxidation, or redox potential) and thereby change oxidation states is very similar (approximately 1 volt). Thus, plutonium will often change oxidation states in solution and follow several different chemical pathways simultaneously. It can also exist in several oxidation states within the same solution and, at very low pH, can even exhibit four oxidation states simultaneously. This last feature makes plutonium unique among the elements.

The shapes of 5f and 6d orbitals, in addition to their radial extents, affect molecular (not metallic) bonding. The f- and d-electron wave functions with three and two quanta of angular momentum, respectively, are nonspherical and have highly directional lobes, producing certain unique covalent

motifs. For example, in water, actinides in the (V) and (VI) oxidation state immediately bond with two oxygens to form the linear “actinyl” motif. Plutonyl $O=Pu=O$, uranyl $O=U=O$, and neptunyl $O=Np=O$ are examples. Once formed, other ligands bond in the equatorial plane bisecting the actinyl motif (see figure).

Each oxidation state can form various molecular complexes, each with a characteristic solubility and chemical reactivity. The instabilities of plutonium’s oxidation states, coupled with the creation of free radicals through its radioactive decay, yield solution chemistry that is constantly changing and affecting chemical processing operations, nuclear waste storage and treatment, and the reactivity and mobility of plutonium in the environment. Over the years, the redox states of plutonium have been controlled by complexation with various ligands. Some of these, such as



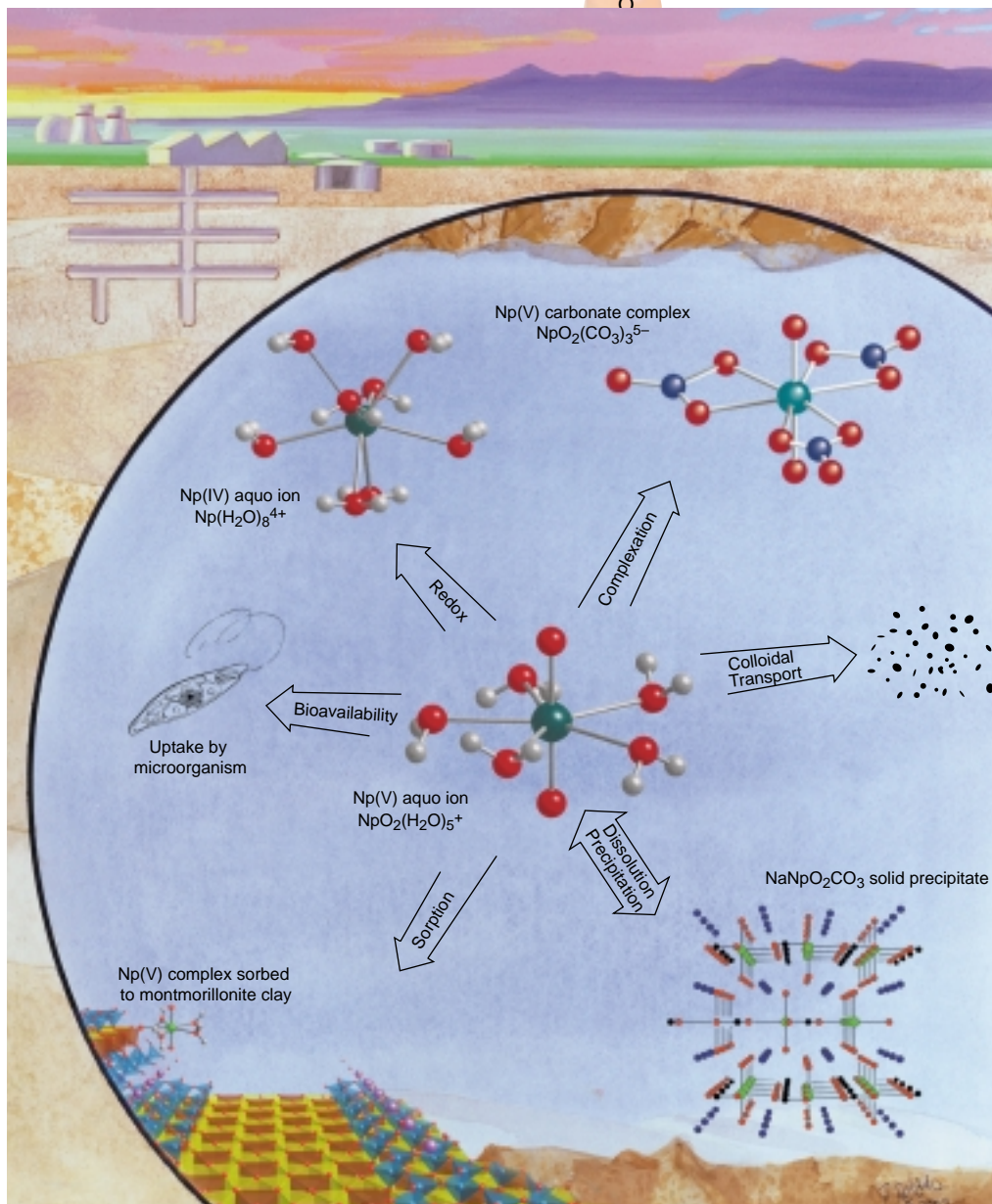
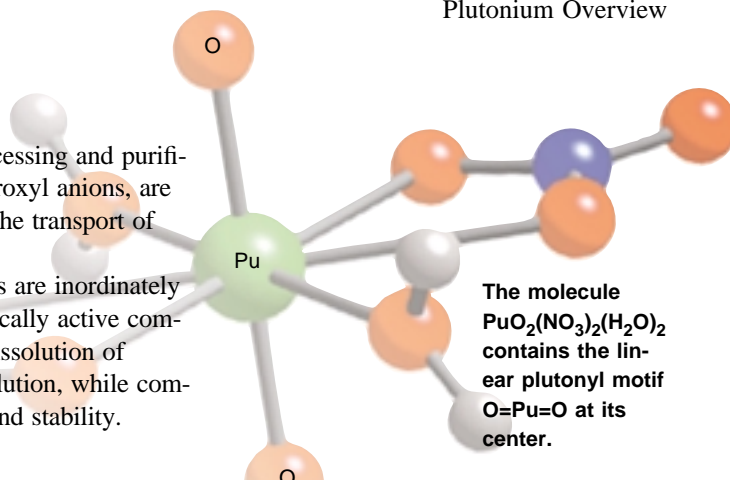
The range of plutonium complexes and oxidation states in water containing carbonate, hydroxyl, and fluoride ions is evident in the redox potential vs pH diagram. In many natural waters, plutonium will be in the relatively insoluble IV state. Redox reactions, however, will allow plutonium to assume any of the oxidation states III, V, and VI. Overall therefore, the environmental behavior of plutonium is extremely complicated. The red dots mark conditions under which plutonium can coexist in three different oxidation states simultaneously.

the nitrate anion, have played a historically critical role in the processing and purification of plutonium. Other ligands, such as the carbonate and hydroxyl anions, are ubiquitous in natural groundwaters and play an influential role in the transport of plutonium in the natural environment.

When actinides enter the environment, the chemical interactions are inordinately complex because, in addition to natural waters, hundreds of chemically active compounds and minerals exist in earth formations. Precipitation and dissolution of actinide-bearing solids limit the upper actinide concentration in solution, while complexation and redox reactions determine the species' distribution and stability.

The interaction of a dissolved species with mineral and rock surfaces and/or colloids determines if and how those species will migrate through the environment. The prevalent oxidation state in groundwater is Pu(IV), whereas Pu(III), Pu(V), and Pu(VI) are also common in streams, brines, or bogs. The light actinides, including plutonium, form the strongest, most stable complexes in the IV oxidation state. (See the article "The Chemical Interactions of Actinides in the Environment" on page 392.)

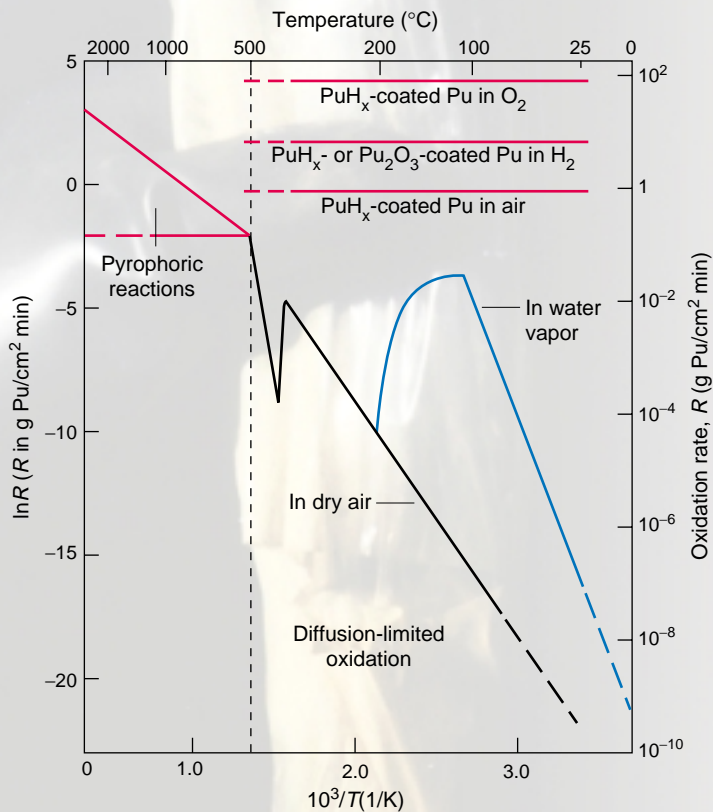
In general, actinide solubilities are so low in most natural waters—below micromolar concentrations—that only advanced spectroscopic techniques can detect the species present, a prerequisite for understanding environmental chemistry. Studies have shown that actinides in the V oxidation state have the highest solubilities; those in the IV state, the lowest. Actinides in the IV oxidation state also show the strongest sorption onto mineral and rock surfaces. The actinides' very low solubility and high sorption create two key natural barriers to actinide transport in the environment. Less-studied microorganisms represent a potential third barrier because plutonium binds with such organisms and their metabolic byproducts. However, recent observations at the Nevada Test Site showed that colloid-facilitated transport of plutonium in groundwater can play an important role in migration (see the box on page 490). Clearly, we must continue to apply modern chemical techniques to better understand the fundamental interactions of plutonium and the actinides in the environment.



This is an artist's rendition of the interactions that affect actinide mobility in the underground environment.

Plutonium Surfaces and Ceramics

Although plutonium is a very reactive metal, a protective surface layer of plutonium dioxide forms almost instantly in dry air (much as aluminum is protected by its oxide) so that further corrosion occurs at a miniscule rate of less than 0.2 micrometer per year. In moist air, however, the corrosion rate is 200 times faster at room temperature and 100,000 faster at 100°C. Rapid oxidation of plutonium is induced because water dissociates on the surface producing hydrogen and a plutonium hyperoxide (having more oxygen than the dioxide). The excess oxygen at the surface creates a high oxygen gradient across the oxide interface, enhancing the diffusion rate through the oxide layer and thus the rate of oxidation at the oxide/metal interface.



The graph above illustrates corrosion rates for plutonium metal. Surface hydrides and oxides can catalyze reactions with hydrogen, oxygen, and water vapor and make those reactions extremely fast. See the article “Surface and Corrosion Chemistry of Plutonium” on page 252.

Hydrogen reacts with plutonium metal at unprecedented rates. If the entire metal surface is covered with hydride, the reaction occurs very rapidly—at rates of 20 centimeters per hour linear penetration for hydrogen at atmospheric pressure, which is 10^{10} (ten billion) times faster than the reaction in dry air. We do not fully understand the fundamental physics and chemistry driving these surface reactions, but they likely involve the metallic bonding state of the substrate and the chemical bonding behavior of the surface in a certain environment.

Plutonium is also pyrophoric—it ignites spontaneously in air at 500°C. Plutonium particulates, such as powder or machining chips, ignite at temperatures as low as 150°C to 200°C. These potentially catastrophic surface reactions make it imperative that plutonium be protected from hydrogen or moisture in sealed containers.

Combining plutonium with nonmetallic elements, such as oxygen, in a bulk solid promotes a strong sharing of electronic charge between the plutonium cation and the oxygen anion. Hence, the oxide has a strong ionic character in contrast to the metallic character resulting from electrons in the conduction band of plutonium metal. The oxides are no longer dominated by the peculiarities of the 5f electrons. Plutonium oxides (as well as carbides and nitrides) are refractory—that is, heat resistant. Plutonium dioxide (PuO_2), the most important plutonium ceramic compound, melts at

2673 kelvins (plutonium metal melts at 913 kelvins), and is much less reactive than plutonium metal. The properties of these compounds are determined primarily by the type of crystal lattice (which is governed by the oxidation state and atomic sizes of cations and anions) and their defect structure. Consequently, plutonium ceramic compounds are still quite complex, but no longer the most complex.

Aging of Plutonium—Alchemy at Work

Like many other metals, plutonium ages from the outside in by corrosion. However, because of its radioactive nature, plutonium also ages from the inside out by self-irradiation damage. Plutonium-239 decays mainly by α -particle decay (emitting an α -particle, or He^{++} , and becoming a uranium nucleus), which damages the crystal lattice. The most severe damage occurs when a uranium nucleus recoils

from α -particle decay. The α -particles pick up electrons to become helium atoms, which can associate with crystal defects such as vacancies. Most of the roughly 5 million electron volts of energy released in each decay event is converted into heat, making plutonium noticeably warm to the touch.

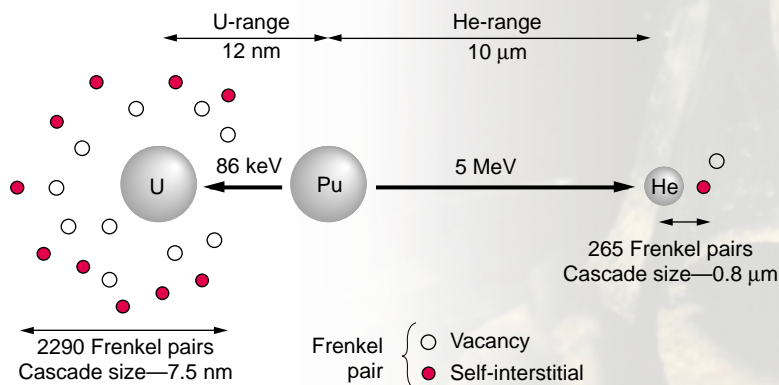
The relentless deposition of energy from the radioactive decay of plutonium damages its crystal lattice and transmutes some of the plutonium into other elements. For example, at standard temperature and pressure, 1 kilogram of plutonium accumulates almost 0.2 liter of helium in 50 years. Fortunately, much of the lattice damage is annealed out or “healed” at room temperature. Nevertheless, the defects resulting from the residual lattice damage and the changes in chemistry can affect plutonium’s delicate balance of stability with changes in temperature, pressure, or chemistry. Such defects may also influence diffusion rates and cause plutonium metal to swell.

Chemical and surface behaviors are also affected by radioactive decay. At high plutonium concentrations in solution, such decay can induce oxidation-state changes by radiolysis, even in the absence of redox agents. Radiolytic decomposition of the surrounding water can lead to the reduction of Pu(VI) and Pu(V) to Pu(IV) and Pu(III) and, consequently, to a change in the chemical behavior of plutonium over time. Radiolysis of hydrogenous materials in the vicinity of plutonium metal can also speed up surface corrosion dramatically by making hydrogen available. Therefore, it is especially important to avoid access to hydrogenous materials when storing plutonium. In geologic media, plutonium may also cause lattice damage and amorphization of the host solid leading to potentially increased leaching rates.

The plutonium challenges ahead—stockpile stewardship, nonproliferation, environmental issues, and nuclear power—require a better fundamental understanding of plutonium in metals or ceramics, on surfaces, in solution, and in the environment. ■



These glowing embers are small pieces of plutonium metal burning spontaneously in air under static conditions.



When a plutonium nucleus undergoes α -decay, the recoiling uranium and helium nuclei knock plutonium atoms from their lattice sites. Displaced plutonium atoms come to rest at interstitial sites and leave lattice vacancies behind. Each displaced plutonium atom creates a Frenkel pair—consisting of a vacancy and a self-interstitial. Each decay event creates more than 2000 Frenkel pairs. The cascade size is the space occupied by the Frenkel pairs created during a certain decay event.

Acknowledgments

Many of the exciting ideas summarized here originate with the authors of the following articles: “Plutonium Condensed-Matter Physics” by A. Michael Boring and James L. Smith; “Actinide Ground-State Properties” by John M. Wills and Olle Eriksson; “The Chemical Complexities of Plutonium” by David L. Clark; “The Chemical Interactions of Actinides in the Environment” by Wolfgang H. Runde; “Surface and Corrosion Chemistry of Plutonium” by John M. Haschke, Thomas H. Allen, and Luis A. Morales; and “Radiation Effects in Plutonium” by Wilhelm G. Wolfer.

The Plutonium Challenge

Stockpile stewardship

Challenging as it may be to understand and mitigate the problems of plutonium aging, by far the most difficult problem we face today is the aging of our technical staff. Because plutonium science is enormously complex, we are just now beginning to understand it at a fundamental level. Our approach has therefore been largely empirical. But experience rests with the practitioners, and unfortunately, these practitioners are aging. We are in danger of losing their expertise and advice before we develop a more fundamental understanding of plutonium—one that can more easily be taught and sustained over time.

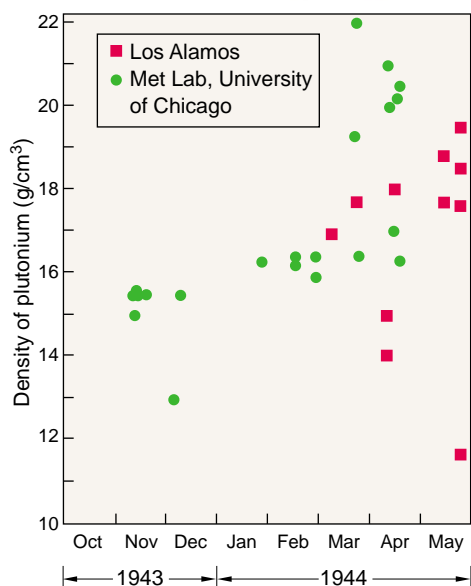
The plutonium pit is at the heart of the bomb. Fabrication of the first pits during the Manhattan Project was a tour de force. In 1944 and 1945, when gram and kilogram quantities of plutonium became available, this metal was found to be at odds not only with itself but also with everyone who touched it. Just enough was learned about this mysterious new element that the chemists and metallurgists were able to reduce the reactor product to metal. They could subsequently purify it, alloy it (so they could stabilize it and press it into shape), coat it (so they could handle it), and keep it together long enough before the plutonium bomb exploded at Trinity and Nagasaki.

Over the following 50 years, Los Alamos scientists and many other scientists around the world tried to decipher the mysteries of plutonium. Fortunately, many of the great academics recruited to Los Alamos during the Manhattan Project kept an affiliation with the Laboratory. Numerous professors spent their summers at Los Alamos and sent their best graduates to work at the Laboratory. Willi Zachariasen, probably the best crystallographer of all times, came from the University of Chicago to continue his wartime quest for understanding plutonium. He eventually determined the incredibly complex monoclinic crystal structure of the α -phase.

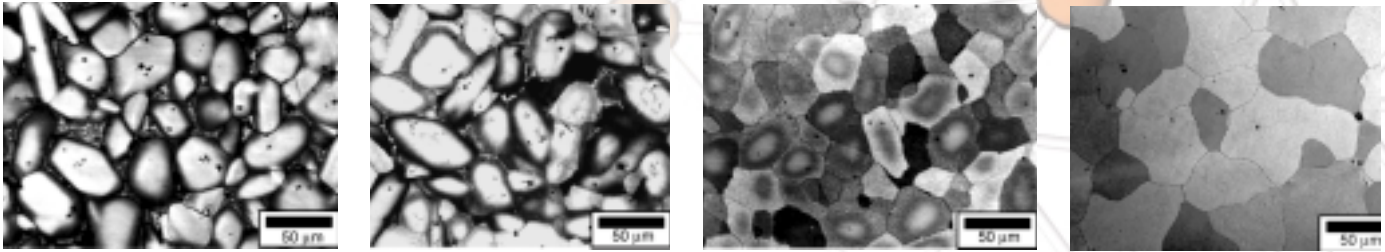
It seemed that the more we learned about plutonium, the deeper its mysteries became. The sensitivity of plutonium to thermal changes was matched by similar sensitivities to the application of pressure and to the addition of chemical elements. In fact, plutonium appeared to change phase with very little provocation at all and by almost every transformation mechanism known to scientists.

From the 1950s through the 1970s, Los Alamos, Livermore, and Rocky Flats metallurgists, chemists, and engineers extracted as much as possible from the international scientific work on plutonium to help shape the U.S. classified research program. That program provided sufficient knowledge to enable the development of increasingly sophisticated physics designs required by the drive for devices with a constantly higher yield-to-weight ratio. In fact, the drive for improved performance was so relentless that it far surpassed our progress in understanding plutonium at a fundamental level. As a result, much of the engineering performance requirements were met through empirical knowledge and day-to-day experience. Manufacturing plutonium was more of an art than a science. Fortunately, however, some of the engineering requirements experienced during manufacturing, storage, and delivery could be tested in the laboratory.

Because the implosion performance has never been adequately simulated,



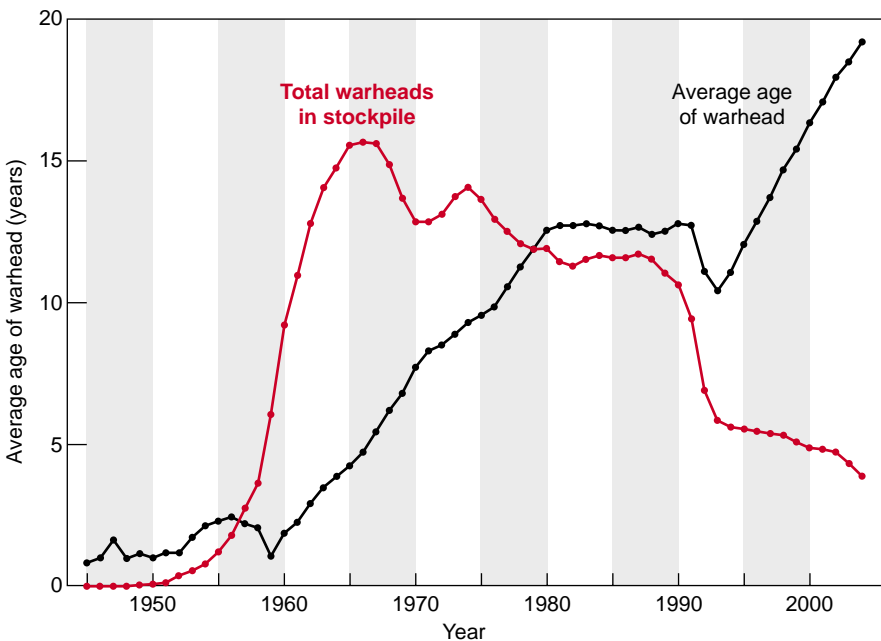
The variations in plutonium density baffled Manhattan Project chemists and metallurgists until about midway through 1944, when they discovered that plutonium had no less than five allotropic phases between room temperature and the melting point.



we relied heavily on nuclear testing—first, in the atmosphere and, after 1963, underground. Yet we had to develop great skills in modeling the physics and, with the aid of large-scale computing, we “calibrated” the performance of plutonium during the extraordinarily complex conditions of a nuclear explosion. Problems that were often discovered through calculations or stockpile surveillance were fixed, but they often required nuclear tests to ensure the adequacy of the fix. Some expected concerns about the aging of plutonium were most easily addressed by the replacement of old systems with new, more-capable systems.

The enormous geopolitical changes of the past decade have brought about an entirely different approach to our nuclear weapons responsibilities at Los Alamos. Nuclear weapons remain the cornerstone of U.S. national security strategy, and our job is to keep them safe and reliable into the indefinite future. But we must do so without nuclear testing, according to the provisions of the Comprehensive Test Ban

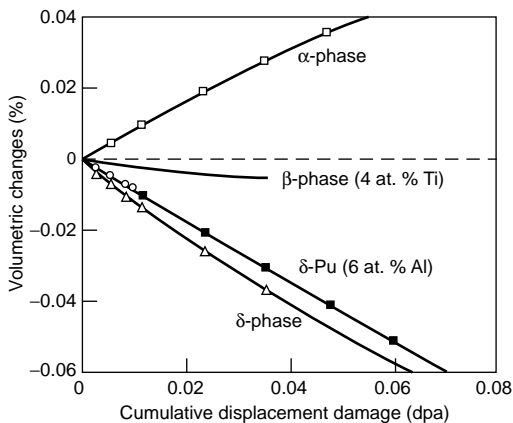
A few atomic percent gallium is typically added to plutonium to retain the face-centered-cubic phase, which is easily shaped into components. However, as Pu-Ga alloys cool during casting, gallium segregates and leaves a nonuniform distribution across the metallic grains. This sequence of micrographs demonstrates gradual gallium homogenization during annealing for long times at 460°C. The as-cast sample on the left exhibits regions high in gallium in the grain centers (etched to appear very light). At longer times, the gallium concentration becomes more uniform, as demonstrated by the more uniform coloration within the grains. After 720 h, the sample is completely uniform—the variations from grain to grain result strictly from differences in crystalline orientation.



The number of weapons in the stockpile is decreasing, and in another decade, the ages of most weapons will be well beyond their original design lifetimes.



The plutonium facility at Los Alamos is developing the capability to remanufacture small lots of plutonium pits and now carries out all surveillance activities necessary for stockpile stewardship. All experiments and tests are conducted inside a glove-box environment (inset).



Self-irradiation produced these volume changes in plutonium at cryogenic temperatures. The volume changes eventually saturated at approximately 10% for the α -phase and 15% for the δ -phase. Fortunately, much of the lattice damage from self-irradiation anneals out at ambient temperature. However, we are still studying the effects of helium and transmutation products such as americium, uranium, and neptunium.

Treaty. In addition, in 1992, President Bush adopted the policy of not fielding weapons of new design, so we must also forgo the practice of fixing stockpile problems by replacing old designs with new ones. Although the number of weapons in our stockpile is decreasing because of arms reductions agreements with Russia, the remaining weapons are approaching or exceeding their original design lifetimes.

Nuclear Weapons Certification

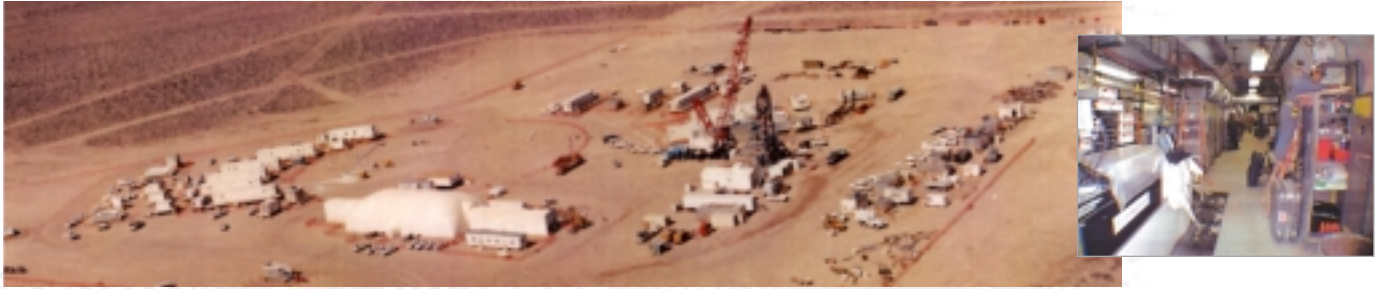
Yearly, the directors of the three nuclear weapons laboratories—Los Alamos National Laboratory, Lawrence Livermore National Laboratory, and Sandia National Laboratories—certify the weapons designed by their labs as safe and reliable without testing. This annual certification drives the stewardship challenge. Plutonium is a particularly demanding part of that challenge because it is the component that we cannot test under conditions that produce a nuclear yield. Many of the other components can be adequately tested under simulated conditions.

Our approach to stewardship is to extend the lifetimes of pits (requalify) or remanufacture the pits in the warheads scheduled to remain in the stockpile. The United States is currently establishing a pit production capability of very limited capacity at Los Alamos. Extending the lifetimes of pits to 50 years and beyond provides a substantial financial incentive because of the high construction costs for new plutonium facilities. Certification of requalified or remanufactured pits is a major challenge for metallurgists, chemists, engineers, and weapon designers.

Because the pits in the stockpile are aging, we must significantly upgrade our surveillance. It is therefore imperative that we develop new, more-sophisticated nondestructive techniques to assess changes caused by aging. New diagnostic capabilities under development may allow detecting changes early and predicting the lifetimes of pits. Several age-related issues about plutonium concern us. Among them are surface changes caused by corrosion and dimensional changes caused by potential phase instabilities. In addition, plutonium undergoes continuous radioactive decay during which it transmutes itself. This radioactive decay leads to long-term chemical changes, as well as short-term self-irradiation damage. To have any hope of assessing the effects of these complex events on the already hypersensitive plutonium lattice, we must develop a better fundamental understanding of plutonium.

Remanufacturing the plutonium pits is another challenging task. The United States has not manufactured a war-reserve plutonium pit in 12 years. Because the Rocky Flats plant is no longer operational, remanufacture will be done at Los Alamos with new people, new equipment, and some new processes. Certifying that such pits are functionally equivalent to those originally manufactured and tested is one of the principal challenges of stockpile stewardship.

When nuclear tests were allowed, we could work around what we did not understand about plutonium by testing its performance. Now, we must understand plutonium better, then test it in every conceivable way permitted, and finally have the designers test their confidence by comparing the new computational results with those stored in the archives. Better understanding necessarily means incorporating the influence of microstructure on performance. Consequently, computational requirements will increase by several orders of magnitude if microstructure-based materials models are to be incorporated into the physics design codes. Such increased sophistication in materials behavior drives much of the need for the Accelerated Strategic Computing Initiative (ASCI) of the Department of Energy.



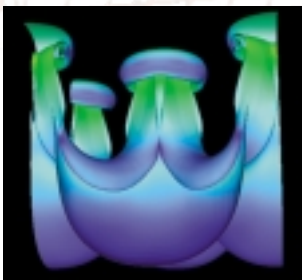
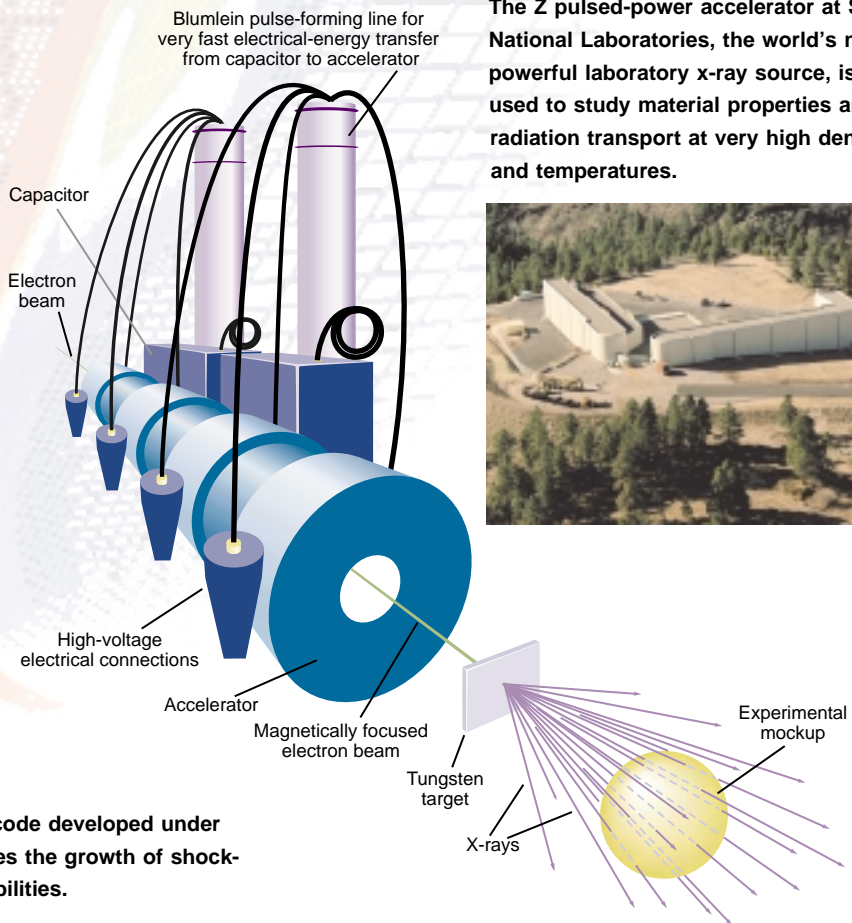
The U1A tunnel complex at the Nevada Test Site (above) is being used to study the response of plutonium alloys to shock loading. The results are incorporated into computer simulations of the nuclear-weapon implosion process. Experimental alcoves for these experiments and the diagnostics alcove (top right) are approximately 1000 feet underground.

DARHT (photo below), a dual-axis x-ray facility now under construction at Los Alamos, will provide 3-D digital x-ray images of nonnuclear implosion tests. The 4000-A, 20-MeV pulsed-electron beam from an advanced accelerator (diagram below, left) produces intense nanosecond x-ray pulses that can capture very high resolution images of the detonation and implosion. The National Ignition Facility (NIF) at Lawrence Livermore National Laboratory will produce high-energy densities that overlap those produced in nuclear weapons and will eventually be used to implode tiny fusion capsules. The Z pulsed-power accelerator at Sandia National Laboratories, the world's most powerful laboratory x-ray source, is being used to study material properties and radiation transport at very high densities and temperatures.

The Challenge

The technical challenge is to keep the stockpile weapons safe and reliable without nuclear testing. To predict the lifetimes of existing pits or to remanufacture pits so that they can be certified will require a better understanding of how plutonium ages and how microstructure affects performance. To succeed in our stockpile stewardship mission, we will have to combine such understanding with significantly increased computing power and permissible experiments. Improving our fundamental understanding of plutonium requires that we continue to work closely at the frontiers of actinide science with the academic community and the international research community. Indeed, we must continue to attract and retain the best and the brightest of the next generation of scientists and engineers.

From a policy and societal point of view, the U.S. government must deter all our country's potential adversaries with a smaller number of nuclear weapons. We, who work at the nuclear weapons laboratories, must be able to assure our leaders that the weapons we designed and retained in the stockpile will work reliably if they ever have to be used. ■



RAGE, a 3-D code developed under ASCI, simulates the growth of shock-induced instabilities.

The Plutonium Challenge

Avoiding nuclear weapons proliferation

Today, the basic knowledge about building and manufacturing an atomic bomb is within reach of any industrialized nation. During the Gulf War (1991), for example, there was little doubt that Iraqi scientists and engineers could duplicate the Manhattan Project feats of more than half a century ago. And so, the main uncertainty before that war was whether the Iraqis had obtained sufficient weapons-usable nuclear material to build nuclear weapons.

Limiting Access to Weapons-Usable Materials

Along with political dissuasion, denying access to weapons-usable materials is the best barrier to the spread of nuclear weapons in aspiring states and among rogue leaders and terrorists. As Saddam Hussein discovered, clandestine efforts to produce weapons-usable material are costly. They are also difficult to conceal for long. Uranium has to be enriched to high levels of the isotope 235 (highly enriched uranium, or HEU) by industrial processes whose signatures are clearly visible. Production of substantial quantities of plutonium requires construction of nuclear reactors—an undertaking that is large, visible, and expensive.

Production of plutonium and highly enriched uranium in the five original nuclear powers—the United States, Russia, the United Kingdom, France, and China—has been stopped except at three remaining production reactors in Russia that generate much needed heat and electricity as byproducts. It appears that production in Israel, India, and Pakistan continues. In North Korea, it is currently frozen. South Africa has taken its HEU out of military programs. Table I lists stockpiled amounts of weapons-usable materials.

An obvious alternative to the clandestine production of weapons-usable nuclear materials is theft or diversion from existing HEU or plutonium stockpiles. Kilogram quantities of plutonium or HEU pose a significant proliferation concern. However, materials produced for the nuclear weapons programs of the original five nuclear powers have been well protected for many decades. The United States and the western powers developed nuclear safeguards—a stringent system of

President Eisenhower's "Atoms for Peace" speech has become a landmark in the history of international cooperation. To ensure that "the miraculous inventiveness of man shall not be dedicated to his death but consecrated to his life," President Eisenhower proposed setting up an international atomic energy agency whose responsibility would be to protect fissionable materials and develop methods whereby those materials "would be allocated to serve the peaceful pursuits of mankind."

Table I. Stockpiles of Weapons-Usable Materials^a

Country	Plutonium (tonnes)	Uranium Equivalent (tonnes)
United States	99.5	635
Russia	130 ^b	1000
United Kingdom	7.6	15
France	5	24
China	4	20
Israel	~0.5	Not known
India	~0.35	Small quantity
Pakistan	Negligible	0.21
North Korea	0.03	None
South Africa	None	0.4

^aAdapted with permission from *The Challenges of Fissile Material Control*, David Albright and Kevin O'Neill (Eds.), Washington, DC: Institute for Science and International Security Press, 1999.

^bHecker believes this amount could be in the range 125–200 tonnes.

protection, control, and accounting for nuclear materials. When the Atoms for Peace Program and the 1954 amendment to the Atomic Energy Act cleared the way for the United States to export nuclear materials for peaceful purposes, our government stipulated strict safeguards measures to be enforced by the recipient nations. In 1957, the International Atomic Energy Agency (IAEA) was established under the umbrella of the United Nations to promote peaceful applications of atomic energy and to help safeguard civilian nuclear materials from military use. The role of the IAEA has been increasingly important and assertive in safeguarding civilian nuclear materials around the world. The agency, however, has no jurisdiction over defense nuclear materials.

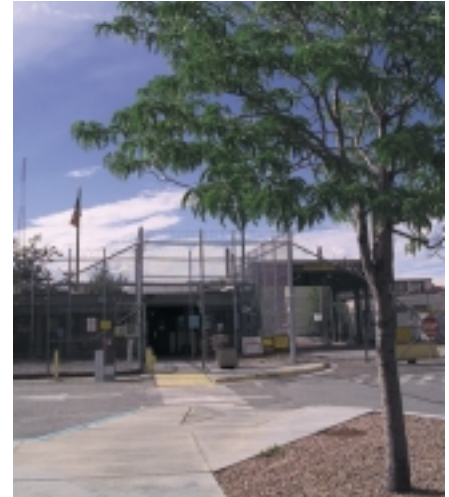
The United States has exercised its own rigorous nuclear safeguards system intended to prevent, deter, detect, or respond to attempts at unauthorized possession or use of nuclear materials. This system provides physical protection, personnel security, control and accountability of nuclear materials, and administrative controls. To be effective, the system is backed up by federal government laws. In the United States, nuclear materials have never been diverted or stolen. The IAEA has adopted a civilian safeguards system very similar to that practiced in the United States. We believe that the United Kingdom and France operate similarly effective systems.



At the Los Alamos Plutonium Facility, rigorous assaying and accounting procedures within the glove-box system record plutonium as it is moved from one location to another.



A security police officer controls access to a secure area by verifying a photo ID badge.



Located at Technical Area 55, the Los Alamos Plutonium Facility is a state-of-the-art R&D facility for plutonium processing and handling. Activities conducted here range from chemical and metallurgical research to surveillance of plutonium pits from the U.S. nuclear stockpile and from small-scale production of pits to pilot-scale demonstration of technologies that support arms control agreements. The facility is surrounded by barbed wire fences and has portal monitors equipped with neutron and gamma-ray sensors that detect nuclear materials. Strict assaying and accounting procedures protect nuclear materials from outsider and insider threats.



The robotic nondestructive-assay system includes a large overhead gantry robot to move plutonium to and from several instruments, such as the large cylindrical calorimeter pictured here. With this calorimeter, Los Alamos personnel measure the heat generated by the radioactive decay of plutonium and thus determine the quantity of plutonium present.



A Clear and Present Danger in Russia

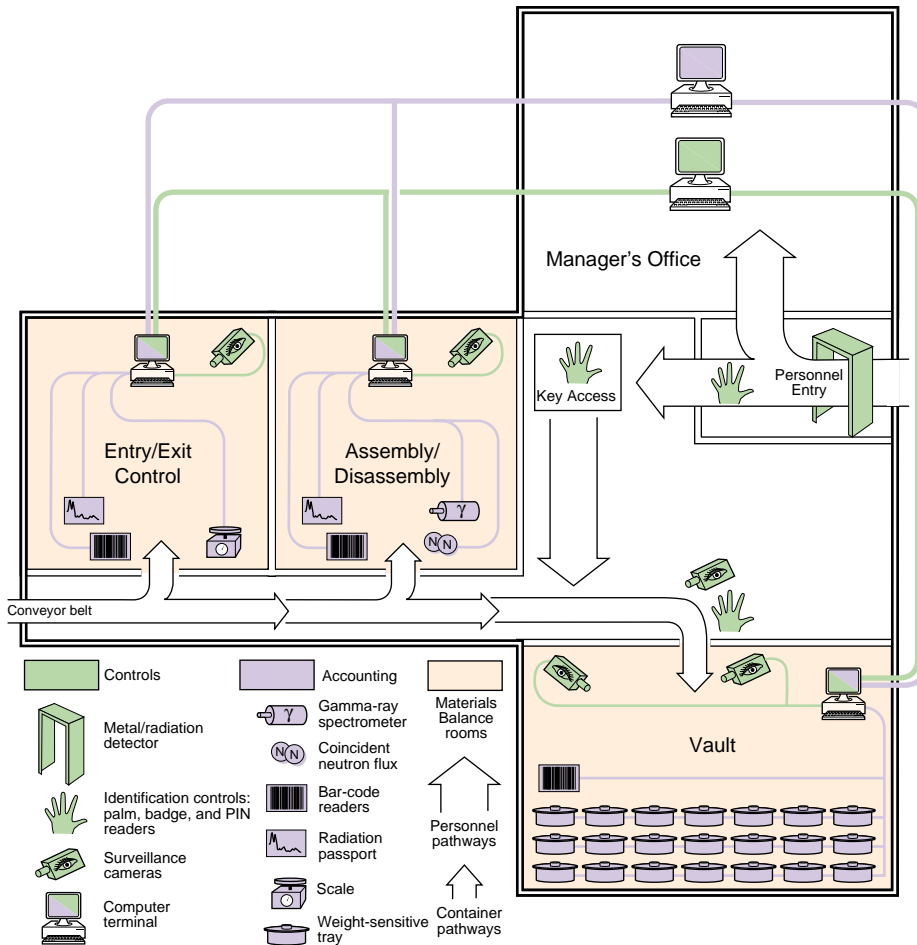


The BN-350 fast breeder reactor outside Aktau in western Kazakhstan is one of the sites where the United States has helped install advanced nuclear materials protection, control, and accounting (MPC&A) systems. The output power (350 MW) of the reactor is used to desalinate Caspian seawater for drinking and industrial purposes, to generate heat for commercial and residential use, and to generate electricity for the local area. The BN-350 achieved first criticality in 1973 and was operational until mid-1999.

Russia inherited the Soviet system that had been designed for a centrally controlled police state. It was often called the system of “grave consequences” or “guns, guards, and gulags”—that is, anyone who might dare challenge it would face serious personal repercussions. Based on rigorous personnel scrutiny and physical protection backed up by impenetrable borders, this system did not rely on modern technology in case the other protective means failed. The Chinese government also appears to have adopted the Soviet safeguards system. Only in the past few years has China begun to learn about more rigorous systems from the West.

Nevertheless, the Soviet system worked during Soviet days—its record for protecting weapons-usable materials was impressive. Today, the dramatic political, economic, and social changes resulting from the breakup of the Soviet Union pose a new and serious proliferation threat—some of Russia’s 125 to 200 tonnes of plutonium or its 1000 (or more) tonnes of highly enriched uranium are at risk of being stolen or diverted. When the police state was dissolved, the gulags disappeared and the borders became penetrable, but the custodians of the nuclear materials and the guards protecting the storage facilities were seldom paid, suffered severe personal hardship, and became demoralized. Not surprisingly, the breakdown of a system that relied mainly on the conduct of people ushered in the ingredients for potential disaster.

Generally, weapons-usable materials are more difficult to protect than nuclear weapons. Unlike the weapons, which have serial numbers, nuclear materials exist in forms difficult to analyze, account, and protect. Waste and scrap are two examples of such forms. In Russia, some nuclear sites—such as those of the nuclear navy—became particularly vulnerable because financial support for the entire program dissolved almost overnight. Many of the vessels, storage facilities, and transportation



(Opposite page): The map of the former Soviet Union shows the main sites with nuclear-material inventories—nuclear weapons facilities (including nuclear materials, nuclear military R&D, and weapons assembly and disassembly), naval fuel-cycle facilities, and civilian reactor and R&D facilities. All these sites have been involved in the cooperative U.S.-Russian MPC&A program whose mission has been to reduce the threat of nuclear proliferation and terrorism by improving the security of all weapons-usable nuclear materials in Russia and the other countries of the former Soviet Union. (Left): This is a conceptual diagram of the Arzamas-16 (in Sarov) demonstration system for nuclear MPC&A. The United States has helped Russia set it up. Controls (shown in green) limit and monitor access to materials. Accounting instruments are shown in blue, and the three material-balance rooms are shown in peach. Bar-code readers identify containers, and they also track the movements of materials through the facility.

systems were left vulnerable. To make a western-style safeguards system work in Russia, it is imperative for Russia to downsize its huge nuclear complex and consolidate the nuclear materials sites.

Much of the Soviet nuclear enterprise is now housed in independent nations of the former Soviet Union. With the help of the cooperative threat-reduction program funded by the United States, all the Soviet nuclear weapons have been returned to Russia by the nations of Ukraine, Kazakhstan, and Belarus. These and other countries continue to have weapons-usable materials on their soil—much of it in research reactors and facilities that are even more underfunded and overstressed than those in Russia. In Kazakhstan, for example, several reactors and the huge former nuclear test site at Semipalatinsk are no longer under Russian control.

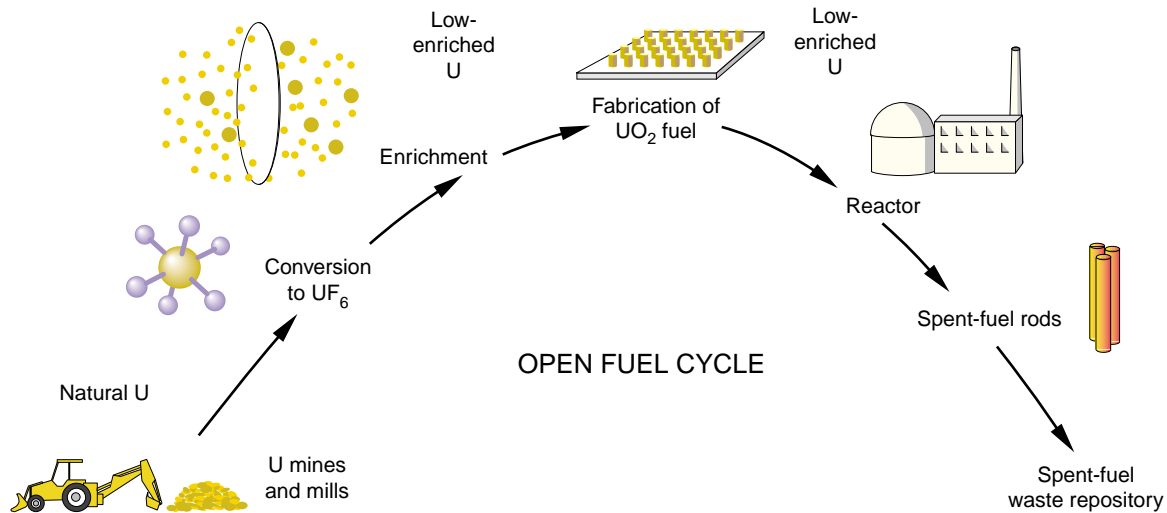
Over the past eight years, the United States—mainly through the Department of Energy and its laboratories—has helped Russia and other states of the former Soviet Union develop a more rigorous safeguards system although Russian officials showed resistance at first. Fortunately, in the midst of uncertainty and turmoil, no major loss of weapons-usable materials is known to have occurred in these countries. The present danger can be overcome only by close collaboration between Russia and the United States and by support from the international community.



Pictured here is the dismantlement of a missile in Ukraine. This work was done as part of the cooperative threat-reduction program. (Photo reproduced courtesy of AFP.)



The test site at Semipalatinsk, Kazakhstan, was ground zero of the first Soviet nuclear explosion (August 29, 1949). The infrastructure for nuclear testing at Semipalatinsk has been dismantled or destroyed with U.S. help. The nuclear “Stonehenge” on the left shows the remains of the diagnostic towers left standing at Semipalatinsk after one of the Soviet tests.



OPEN FUEL CYCLE

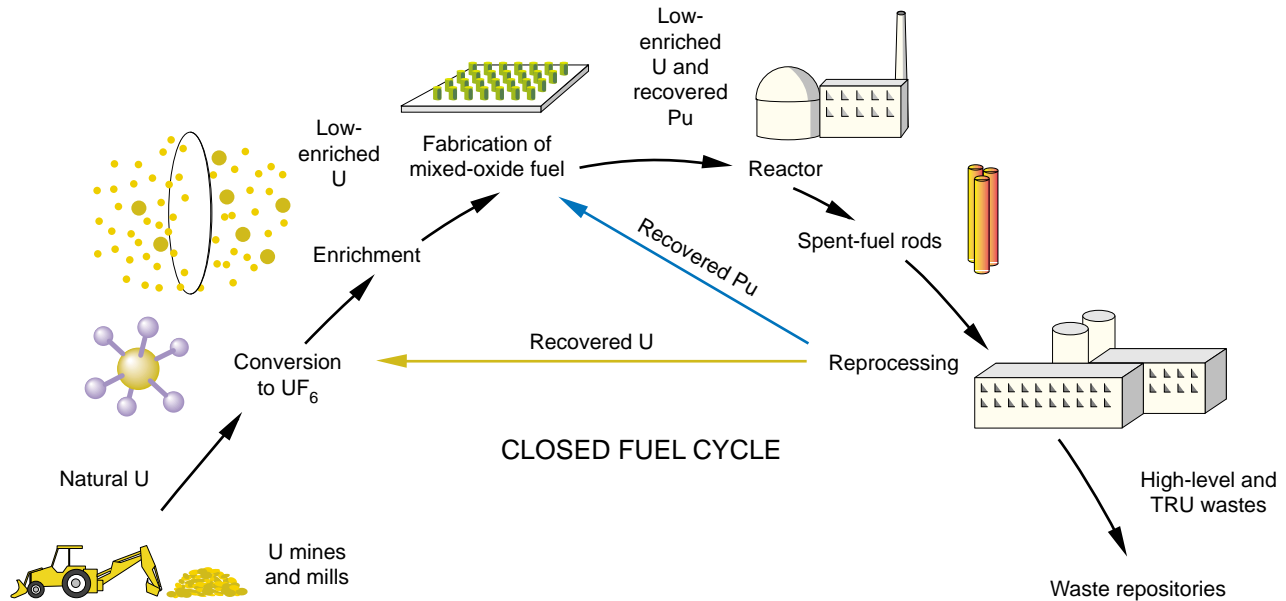
In 1977, the open fuel cycle was the standard chosen for commercial nuclear-power reactors in the United States. Less than 2% of the energy content of the uranium fuel is extracted during one reactor cycle. The spent fuel, together with the fission products, is disposed of geologically.

Strict Control on Civilian Plutonium Is Imperative

In 1970, 170 nations implemented the Nonproliferation Treaty (NPT), a nuclear agreement that no nation beyond the five original nuclear powers would acquire nuclear weapons. In return, access to civilian nuclear technology would be granted to all nations, which would have to comply with IAEA monitoring of international safeguards. The original five states agreed to negotiate in good faith to disarm their nuclear arsenals. In 1995, this treaty was extended indefinitely by 185 nations, with the notable exception of states such as India, Pakistan, and Israel. Controversy is still alive about best ways to control the proliferation risk inherent in the commercial nuclear fuel cycle. How well it is resolved will to a large extent determine the future of commercial nuclear power.

What are the risks and what safeguards are in place in the commercial nuclear-power industry? The enriched fuel used in most commercial power reactors—containing 3 to 4 percent uranium-235—presents no proliferation danger. According to the IAEA, only fuel that has been enriched in uranium-235 to greater than 20 percent is weapons usable. Naval-reactor and research-reactor fuels are often enriched to much more than 20 percent uranium-235—mostly to achieve compactness. Unused fresh fuel intended for such reactors is therefore at risk from diversion for military purposes. However, diluting HEU with uranium-238, which is abundantly present in nature, is an easy remedy for rendering HEU unsuitable for weapons. Moreover, the blended material can be used as commercial-reactor fuel. However, we must continue to monitor the proliferation risk posed by advanced, more-compact enrichment technologies that could reverse the benefits of blending or that could more easily enrich natural uranium.

Plutonium is produced by the transmutation of uranium-238 in power reactors. It is therefore intimately interspersed with uranium and fission products. The fuel rods in power reactors are “burned” to a greater extent than those in plutonium production reactors, so they contain a significantly larger fraction of the higher isotopes of plutonium. For example, weapons-grade plutonium is typically greater than 93 percent plutonium-239, whereas reactor-grade plutonium contains as little as 60 percent plutonium-239 (with as much as 25 percent plutonium-240). For many years, the hope had been that the isotopic mixtures of reactor-grade plutonium would prove to be unattractive for weapons use. However, it is now widely recog-



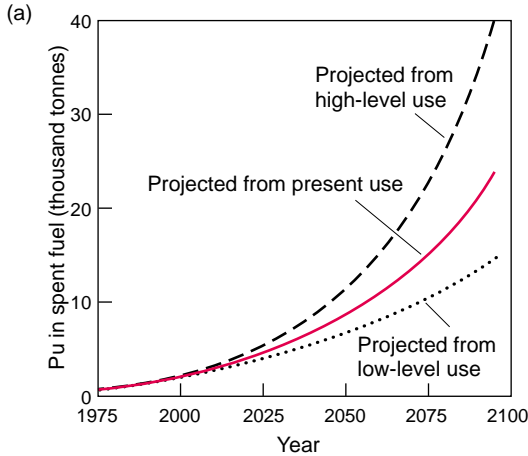
nized that, once plutonium is separated from uranium and fission products, most isotopic mixtures provide little deterrent for weapons use. The IAEA classifies as weapons usable all isotopic mixtures except those containing more than 80 percent plutonium-238, which would literally melt before being of use as weapons materials. Because blending plutonium-239 is not a viable solution to the risk of proliferation, plutonium is the material posing the greatest long-term proliferation concern. In recent years, the U.S. government has also expressed its concerns over the potential availability of neptunium-237 and americium, both of which are byproducts of nuclear reactors.

To date, commercial nuclear reactors in the world have produced more than 1000 tonnes of plutonium, growing at a rate of about 75 tonnes per year. Approximately 200 tonnes of the total civilian plutonium has been separated from the remaining uranium and fission products, mostly in the United Kingdom and France. The Soviet Union made little distinction between military and commercial reactors, but Russia has now declared 30 tonnes of separated civilian plutonium.

One approach to protecting plutonium produced in power reactors from diversion to military use is not to separate it from the fission products in spent fuel. These products exhibit intense penetrating radiation—mostly from cesium-137 and strontium-90 with half-lives of approximately 30 years. This self-protecting feature provides a significant barrier for several decades because remote manipulators and heavy shielding are required to chemically separate plutonium. Other protective methods are often compared with the spent-fuel standard, which is defined as greater than 100 rads per hour at a distance of 1 meter. However, after more than 50 to 100 years, this self-protection will be reduced to the point at which spent fuel also becomes an attractive source of plutonium. We must also recognize that a technologically sophisticated adversary is able to overcome the self-protecting barrier of even fresher fuel.

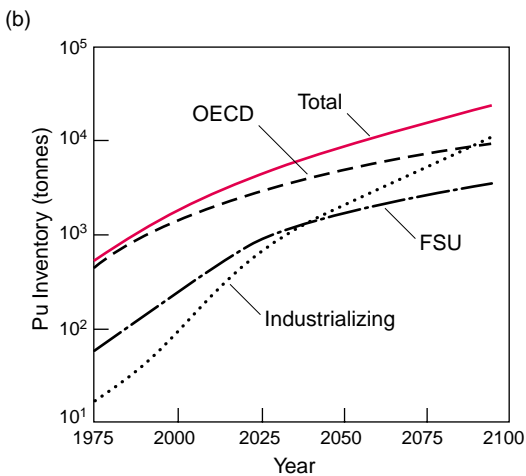
The principal issue then is the nature of the fuel cycle used in commercial nuclear power reactors. Proponents of the spent-fuel standard for proliferation resistance favor the “once-through” or open fuel cycle. In this case, only 2 percent of the energy content of the uranium fuel is extracted during one reactor burn cycle. The spent fuel is allowed to cool off (from its radioactive decay). Then, it is disposed of geologically, together with the fission products. In 1977, President Carter chose this option for the United States to set an example for the rest of the world.

In the closed fuel cycle, which has been adopted by most countries, the spent fuel is reloaded into the reactor and reprocessed to burn the remaining uranium fuel and the newly bred plutonium.



In the United States, however, there are also numerous advocates of a closed fuel cycle—one in which the spent fuel is reprocessed so that the remaining uranium fuel and the newly bred plutonium can be burned in a reactor. More important, most nations that have commercial nuclear power programs are not willing to forego the energy content of the spent fuel. They want to extract the energy inherent in uranium more efficiently and favor developing plutonium breeder reactors as the ultimate future power source. Besides, those countries view the closed fuel cycle as more benign environmentally because the highly radioactive products are separated out, making nuclear-waste disposal easier.

The fuel-cycle controversy has no simple solution. The United States and much of the rest of the world have gone in different directions for nearly a quarter of a century. Perhaps the most serious consequence of President Carter's decision not to allow reprocessing of civilian spent fuel is that the United States has become much less influential in global decisions that affect the future of nuclear power. And those future developments would benefit from greater U.S. influence.



Fight Proliferation through International Cooperation

Technical advances are required at each stage of the fight against nuclear proliferation. The continuous radioactive decay of plutonium allows passive measurements. The plutonium signature is distinct and thus easy to recognize. However, increasingly sensitive and reliable passive measurements would allow detection of constantly smaller amounts of plutonium at greater distances. Likewise, improved systems of verification, monitoring, and real-time accounting are required. In addition, we must continue to develop increased proliferation barriers inherent in the fuel cycle—such as proliferation-resistant fuels and alternative reactors or reactor operations. For example, a fuel cycle based on thorium instead of uranium offers potential proliferation benefits because it does not produce plutonium. Also, several reactor schemes and accelerator-based systems are being developed, which may dramatically reduce the inventory and availability of plutonium from the civilian reactor cycle.

Any effective safeguards system must include strict control over all stockpiles of weapons-usable materials. Clearly, each of the five original nuclear powers will insist on managing its own military stockpile of nuclear materials. As already pointed out, the Russian safeguards program is in a state of transition. It is of the utmost importance that its nuclear materials—military and civilian—are fully protected at all times. Continued cooperation with the United States will help the Russian Federation make a safe and secure transition to a modern system of nuclear materials safeguards. Although the Russian Federation and the United States have agreed to remove from their stockpiles substantial quantities of nuclear materials no longer required for military purposes, it is crucial that materials protection be given highest priority because all nuclear materials disposition schemes will require decades to complete.

The IAEA has played a seminal role in managing the proliferation risks inherent in the civilian nuclear fuel cycle. This role will become more important as the amount of plutonium produced in currently operating civilian reactors continues to increase (see graphs to the left). And the challenge becomes even greater if nuclear power takes on an increasing share of energy production in the future. Although very few nuclear power plants are currently being constructed in the industrialized nations of the West, it will be difficult to meet the projected doubling of energy demand over the next 50 years without an increasing share from nuclear power and without doing irreparable damage to the environment.

Increased international cooperation and an even-stronger future role for the IAEA will be necessary to deal with potential proliferation threats. The U.S. government pursued international control of nuclear materials immediately following the end of World War II. Bernard Baruch offered such a plan to the United Nations Atomic

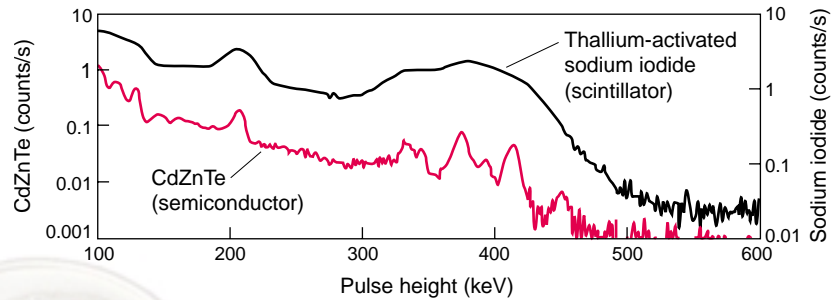
(a) Global inventories of plutonium in spent fuel are certain to rise even if use of nuclear energy stays at present or lower levels. However, that use may increase because of increased energy demand from industrializing nations as well as efforts to control fossil fuel emissions and thereby minimize global climate change. Compared with its present level, nuclear energy use could quadruple by 2050. (b) Although today the primary users are the developed nations belonging to the Organization for Economic Cooperation and Development (OECD)—the United States, Western Europe, and Japan—recent Los Alamos analyses suggest that, by 2075, the former Soviet Union and other industrializing nations such as China will become the primary users of nuclear energy and will have the largest inventories of plutonium in spent reactor fuel. (These graphs are courtesy of Ed Arthur of Los Alamos.)

Energy Commission in 1946, but the Soviet Union rejected it. Several years later, however, President Eisenhower's Atoms for Peace initiative ushered in a new era of international cooperation on nuclear matters. And today, the end of the Cold War opens the possibility of exploring novel international-management approaches to the nuclear fuel cycle. For example, the idea of creating several internationally monitored, well-protected storage facilities for retrievable spent fuel in a few key locations around the world is being evaluated. The cost of such facilities is substantial, but it is much less than the cost of building numerous smaller storage facilities. The concept of a "world plutonium bank" has also been considered as a way to deal with mounting inventories of civilian reprocessed plutonium. In addition to shaping its own nuclear complex, the United States would have to play a leading role in shaping the international nuclear complex.

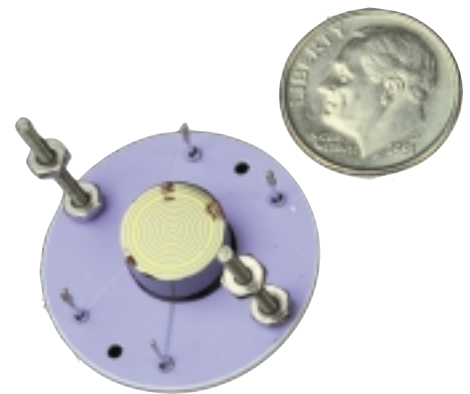
International cooperation is also needed to deal with the challenge posed by the 1998 nuclear tests conducted by India and Pakistan. Specifically, reaching an international agreement for a cutoff in the production of fissile materials would help stem the arms race escalation in South Asia. In addition, close cooperation among the current nuclear powers on the export of civilian nuclear technology to India or Pakistan will be necessary to adequately safeguard the potential use of civilian nuclear materials for military applications. In all these areas, close cooperation between the United States and Russia and a stronger IAEA presence are essential.

The proliferation danger posed by the dissolution of the former Soviet Union can be resolved in the near term only by close cooperation between Russia and the United States. It is time to tackle the immediate threats—namely, loss of nuclear weapons, materials, or knowledge—with a greater sense of urgency. Fighting nuclear terrorism and nuclear emergencies is also best accomplished jointly by the United States and Russia. Likewise, shrinking Russia's huge nuclear military complex can be expedited if the West helps convert military activities in Russia's closed nuclear cities into commercial and civilian ventures. Working together, Russia and the United States could help complete the removal of all weapons-usable materials from the other states of the former Soviet Union and thus lessen a serious, immediate proliferation threat.

In the long term, current U.S. programs that help Russia reduce its huge inventories of weapons-usable materials become increasingly important. And so does reaching an agreement on ending the production of fissile materials. The United States and the West have now an opportunity to increase their help. The price tag may seem large, but it is truly insignificant compared with the amounts to be spent if a nuclear catastrophe were to occur. ■



This graph compares two gamma-ray spectra from low-burnup plutonium measured by the CdZnTe detector and a sodium iodide scintillation detector. For the first time, we can obtain isotopic information needed for nuclear-material safeguards by using a hand-held detector.



The CdZnTe (or "cad-zinc-tel" for short) detector developed at Los Alamos has opened the way for a new generation of compact, low-power gamma-ray sensors to be used in nuclear-material safeguards. In this photo, the detector is shown next to a dime. The circular pattern of electrodes (gold on platinum) allows high-quality measurements of gamma-ray spectra. (For details on the CdZnTe detector, see T. H. Prettyman et al. 1999. In *Hard X-Ray, Gamma-Ray, and Neutron Detector Physics* Vol. 3768, p. 339. Bellingham, WA: SPIE.)



(Left): Video portal monitors guard the departure area at Sheremetyevo Airport in Moscow to help prevent nuclear smuggling. (Right): An official with the United Nations Special Commission uses a hand-held radiation detector at an inspection site in Iraq. The detector was originally developed at Los Alamos.



The Plutonium Challenge

Environmental issues

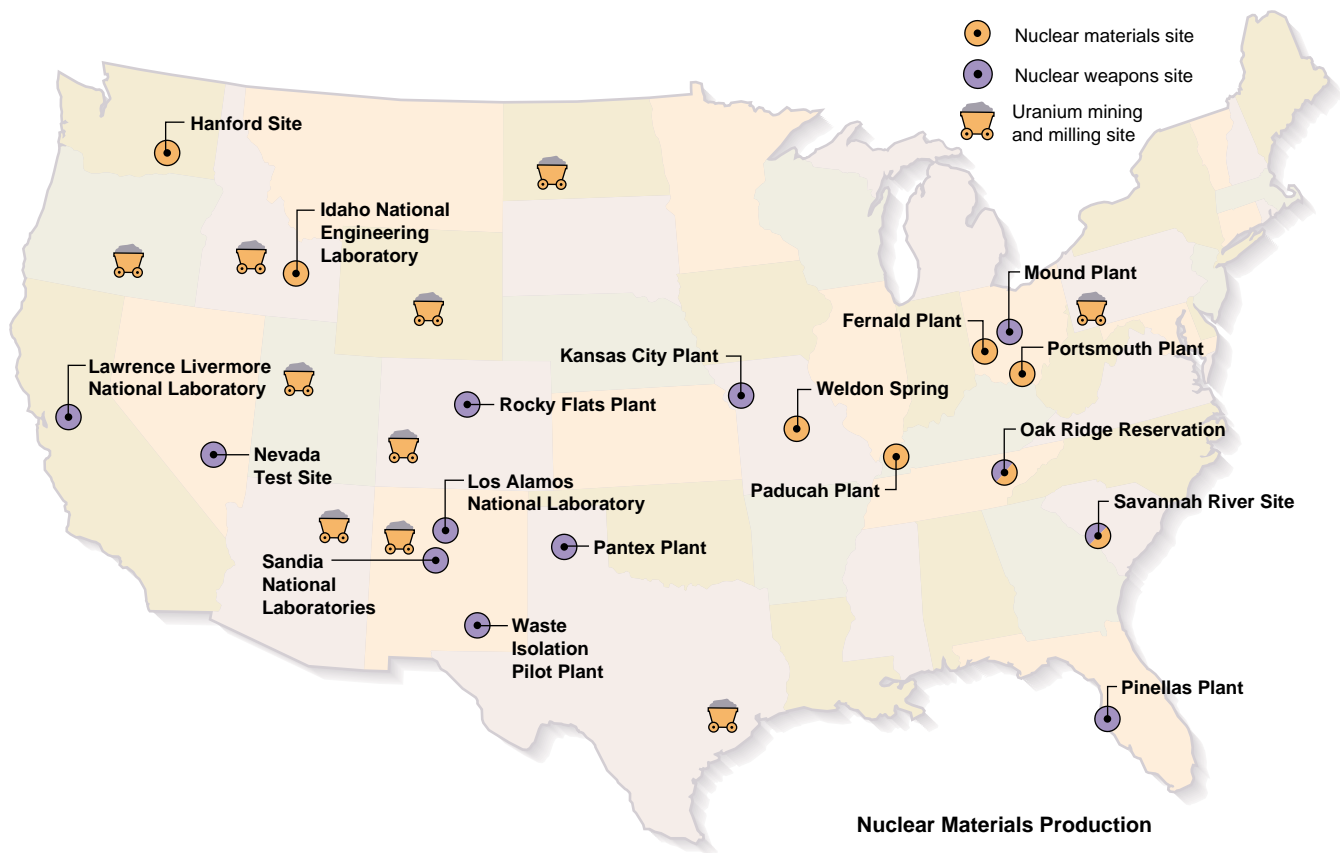
The environmental concerns about plutonium stem from its potentially harmful effects on human health. Unlike many industrial materials whose toxicity was discovered only after years of use, plutonium was immediately recognized as dangerous and as requiring special handling care. Consequently, the health effects on plutonium workers in the United States and the general public have been remarkably benign. Nevertheless, the urgency of the wartime effort and the intensity of the arms race during the early years of the Cold War resulted in large amounts of radioactivity being released into the environment in the United States and Russia. These issues are being addressed now, especially in the United States. Science and international cooperation will play a large role in minimizing the potential health effects on future generations.

Environmental Consequences of the Cold War

The environmental problems resulting from wartime and Cold War nuclear operations were for the most part kept out of public view during the arms race between the United States and the Soviet Union. On the other hand, concerns over health effects from atmospheric testing were debated during the 1950s, leading to the 1963 Limited Test Ban Treaty, which banned nuclear testing everywhere except underground. The U.S. nuclear weapons complex was not opened for public scrutiny until the late 1980s, following a landmark court decision on mercury contamination at the Oak Ridge, Tennessee, facilities of the Department of Energy (DOE) in 1984. In the Soviet Union, all nuclear matters, including environmental problems in the nuclear weapons complex, were kept secret. The huge Soviet environmental problems were not recognized until the curtain of secrecy began to lift in post-Soviet times. I believe we can most effectively address nuclear environmental issues resulting from the Cold War by close collaboration with the Russian nuclear complex because we have a lot to learn from our respective experiences and practices. Moreover, it is in each country's interest and in the interests of the whole world to avoid nuclear accidents and environmental catastrophies.

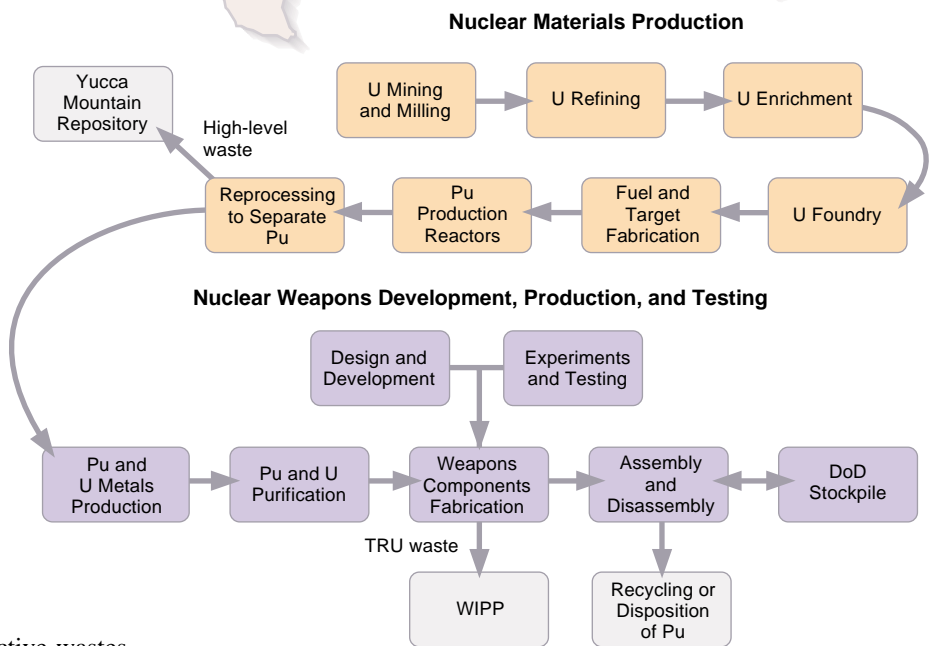
Nuclear Weapons Complex Sites. Most radioactive contamination of current concern resulted from poor nuclear-waste disposal practices within the U.S. and Russian nuclear weapons complexes during the Cold War.

Nuclear weapons complexes have two sectors—one for nuclear materials production and the other for nuclear weapons development, production, and testing (see map of U.S. complex). Nuclear materials production consists of uranium mining and milling, processing and enrichment, fabrication into fuel elements, burning uranium fuel elements in reactors, separating plutonium from leftover uranium and fission products in spent fuel, and disposing of all the nuclear wastes associated with these steps. This cycle generates high-level waste, that is, the short-lived, intensely radioactive fission products associated with spent fuel and waste streams resulting from separating plutonium from spent fuel. Among these fission products, strontium-90 and cesium-137 pose a particular health hazard because they can be transferred from soil through the food chain.

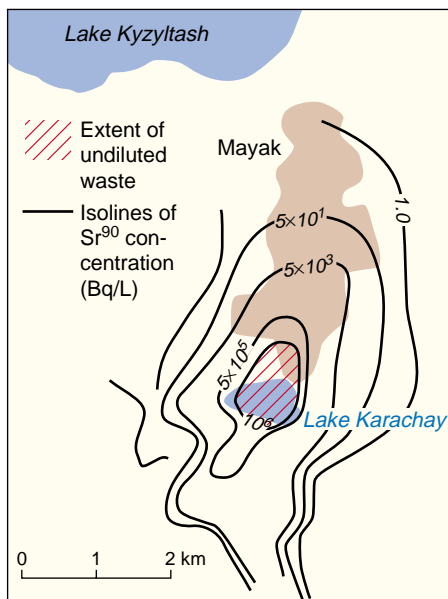


Chemical compounds of plutonium and enriched uranium from the materials production complex are fed to the nuclear weapons development, production, and testing part of the complex. The activities in this part of the complex include reduction of plutonium and uranium compounds to metal, purification of plutonium and uranium metal, manufacture of weapons components, design and development of weapons, related experiments and nuclear testing, the maintenance of the stockpile (including transportation), recycling or disposition of plutonium, and storage and disposal of nuclear wastes. The radioactive wastes generated during these activities are primarily transuranic (TRU) wastes, that is, wastes containing actinide elements heavier than uranium. Over the years, some of the residual uranium and transuranic radionuclides from the plutonium-handling facilities and temporary-storage areas have been released into the environment.

Plutonium and other long-lived transuranics decay by the emission of α -particles, which have very little penetrating power. As long as they do not enter the human body, those particles have little effect on humans. Plutonium α -particles have an energy of 5 million electron volts and travel only 3 to 5 centimeters in air. A sheet of paper, or plastic, or even human skin will stop them. However, once inside the body, plutonium can cause acute or long-term health



High-level waste results from reprocessing spent fuel. It contains highly radioactive fission products, hazardous chemicals, and toxic heavy metals. Transuranic (TRU) waste contains alpha-emitting transuranic elements with half-lives of more than 20 years, in concentrations of more than 100 nCi/g of waste.



By 1990, the strontium-90 contamination from Lake Karachay had migrated a distance of about 2 km.

problems, and because its half-life is 24,400 years, it is important to isolate plutonium as much as possible from the environment.

Releases of High-Level Waste from Spent-Fuel Reprocessing. The highest inventories of radioactive waste in terms of their radioactivity measured in curies (1 curie = 37 billion becquerels or radioactive nuclear decays per second—the number of decays for 1 gram of radium) are in spent fuel and in the high-level waste generated during the separation of plutonium from spent fuel. In the early years, waste streams from fuel reprocessing were often discharged directly into the environment. Consequently, high-level waste from reprocessing is the dominant source of releases to the environment, as shown in a recent study by D. J. Bradley (*Behind the Nuclear Curtain: Radioactive Waste Management in the Former Soviet Union*, 1997, Columbus, OH: Battelle Press) and represented in the pie charts on the opposite page. The largest releases by far have been from sites engaged in reprocessing spent fuel from military production reactors, specifically, the DOE sites at Hanford and Savannah River and the Russian sites at Chelyabinsk-65 (Mayak) in the South Urals as well as Tomsk-7 (Seversk) and Krasnoyarsk-26 (Zheleznogorsk) in Siberia.

More than 99 percent of the high-level waste consists of radionuclides with half-lives of less than 50 years. In the United States, about 1 billion curies of high-level waste are stored temporarily at the production sites in tanks as liquid, sludge, or solid and below ground in temporary structures—cribs, tanks, and other interim facilities. Environmental releases include the approximately 700,000 curies that were dumped or injected into the ground at the Hanford site during the 1940s and 1950s, and the approximately 500,000 curies that had leaked from the Hanford

storage tanks by the late 1980s. Final disposition of all U.S. high-level wastes awaits approval and commissioning of a permanent high-level waste repository.

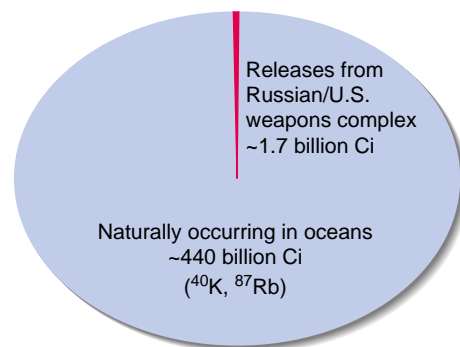
In Russia, deep-well injection was used in the late 1960s to isolate high-level waste at three reprocessing facilities—the two defense facilities at Seversk and Zheleznogorsk and the civilian facility at Dimitrovgrad. It was deemed important to inject into porous geologic media with sufficient capacity and filtration properties, sufficient isolation from the surface, and small enough rates of underground water movement to ensure containment within the site boundaries. Favorable absorbent geologic layers were found at depths of roughly 300 to 450 meters at Seversk and 1400 to 1600 meters at Zhelznogorsk and Dimitrovgrad. The Russians believe that this practice is superior to the interim storage of high-level waste in tanks. This difference in practice, however, accounts for the much greater radioactivity discharged to the environment in Russia than in the United States. The long-term effects of deep-well injection are far from understood today and constitute a potentially fruitful area of collaboration between Russian and U.S. scientists.

Although the waste disposal practices at Zheloznogorsk and Seversk have caused significant radioactive contamination of the nearby areas and river systems, the Mayak site in the Chelyabinsk region currently has the most serious environmental and health problems. Because the geology at the Mayak site was judged not suitable for deep-well injection, all wastes were either directly discharged into the local rivers and lakes or stored in tanks. Russian officials report that, between 1949 and 1956, the Mayak production complex drained 76 million cubic meters of contaminated industrial waste with an activity of 2.75 million curies into the Techa-Iset-Tobol river system. In 1951, the radiation level at the discharge site was 1.8 sieverts per hour and levels up to 540 millisieverts per hour were reported downstream. The people living along the river were using those waters for drinking and agriculture. Approximately 124,000 persons were exposed to elevated levels of radiation. Not until 1953 did the government begin to relocate the residents. The range from internal and external exposures was 74 to 1400 millisieverts. For the 1200 people living in the village of Metlino, 7 kilometers from the point of discharge, the average effective dose was 1400 millisieverts (about ten times the average lifetime dose from natural background radiation, which is 150 millisieverts). Preliminary data suggest a measurable increase in leukemia incidence 5 to 20 years after contamination of the local population began, and that increase appears to be linked to the discharges of high-level waste directly into the river primarily in the period 1949 to 1951.

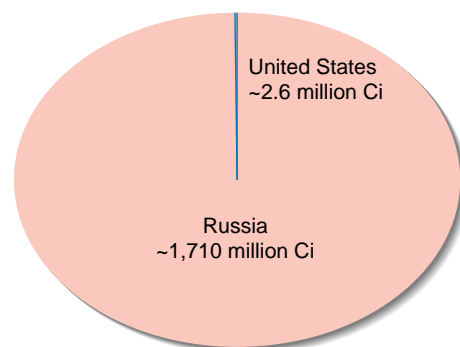
The practice of dumping liquid radioactive waste into the river system ceased in the early 1950s in Russia. High-level waste was being stored in cooled underground steel storage tanks. On September 29, 1957, the failure of a cooling pipe at Mayak led to overheating and a violent explosion that released 20 million curies into the environment. Most of the contamination was spread over a small area near the tank. However, 2 million curies of activity were swept up to a height of one kilometer contaminating an area of 23,000 square kilometers. At the time, the Mayak complex was secret and did not appear on any map. Although 10,200 people were evacuated, the accident was kept secret for decades. It eventually became known as the 1957 Kyshtym accident, named for the large town near the complex, which was on the map. The residents in the most contaminated areas were evacuated within 7 to 10 days following the explosion and the last group of residents, not until two years later. It is estimated that the inhabitants in the most contaminated areas received doses of approximately 520 millisieverts. Agricultural production was also affected in the nearby areas. In 1958, approximately 100 square kilometers of agricultural land was laid fallow. Some areas in the Chelyabinsk region still cannot be used because of the accident.

In addition to being stored in tanks, liquid waste with a radioactivity of about

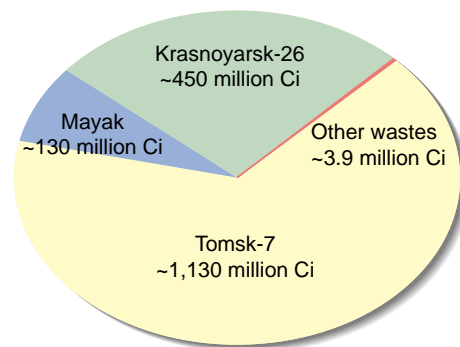
Global Inventory of Radionuclides



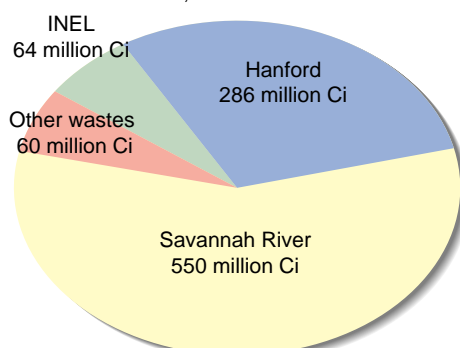
Releases in the United States and Russia

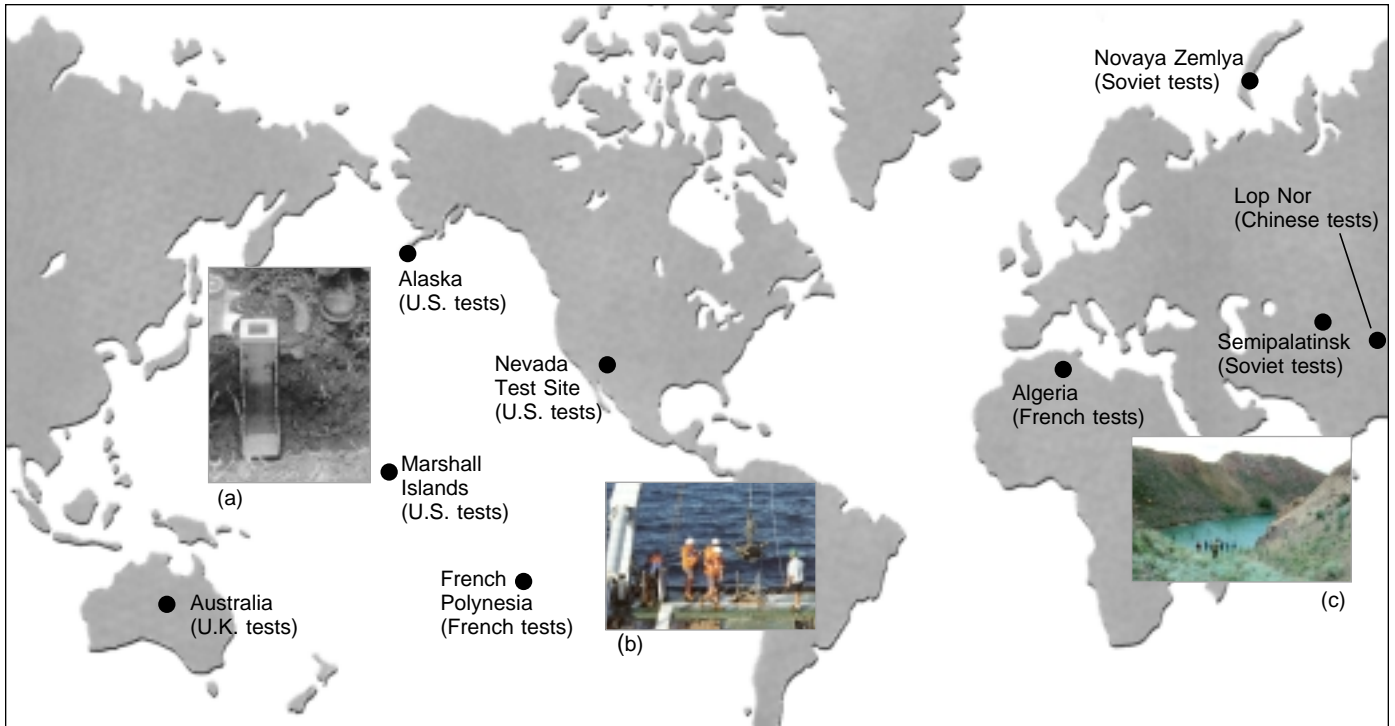


Russian Reprocessing Wastes Released to the Environment

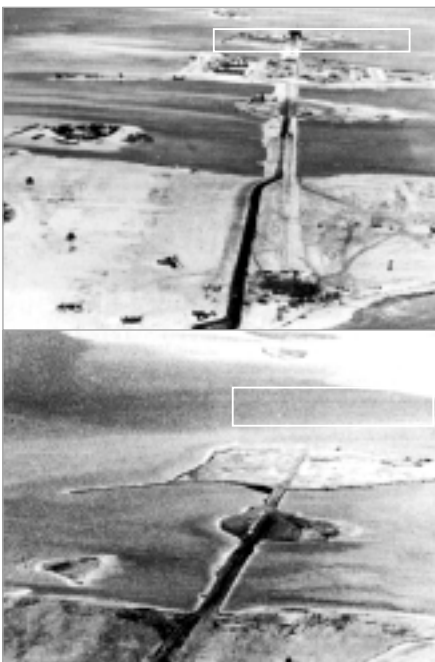


U.S. Reprocessing Wastes in Storage





The IAEA evaluation of test site lands included (a) soil-profile sampling on Bikini Island, (b) drilling for samples of coral bedrock core in French Polynesia, and (c) determining radiation doses near the Semipalatinsk test site.



The island on which the Mike shot was detonated at Eniwetok Atoll disappeared completely.

120 million curies was discharged into the closed water system of Lake Karachay instead of the river system. Another accidental release occurred in 1967, when a major dust storm injected significant levels of radioactivity from the banks of Lake Karachay into the atmosphere after the water level of the lake had been drastically lowered by a severe drought. The inhabitants of the most-contaminated nearby areas received an effective dose of 130 millisieverts. All in all, the accidents described, along with routine discharges, contaminated an area of 26,000 square kilometers with a total radioactivity of 5 million curies.

All defense nuclear-material production facilities in the United States have now been shut down because the government has decided it has more than sufficient quantities of plutonium and highly enriched uranium. Thus, the job that remains is to decommission the facilities and clean up the production sites. In Russia, three production reactors (two in Seversk and another in Zheleznogorsk) and their reprocessing facilities are still operating because the byproducts of reactor operations (heat and electricity) are needed by the local communities.

Within the U.S. nuclear weapons development, production, and testing complex, the principal waste concern are the 850,000 barrels of transuranic waste in temporary storage, waiting for shipment to the permanent storage facility at the Waste Isolation Pilot Plant (WIPP). U.S. weapons production practices have yielded defense scrap and wastes that contain many tons of plutonium. Several weapons production facilities involved with nuclear materials have also been shut down. The Rocky Flats site is on the national superfund cleanup list because of radioactive and chemical contamination. The Fernald, Ohio, site is on the Environmental Protection Agency national priority list because of uranium contamination in the soil. Plutonium operations are being consolidated at the Savannah River site and the Los Alamos National Laboratory (augmented by a research capability at Lawrence Livermore National Laboratory).

It appears that three facilities in the Russian complex still have full-scale plutonium fabrication capabilities. However, the Russian government has announced its intention to close down the plutonium fabrication operations at Zheleznogorsk. Although little is known about plutonium inventories in Russian waste streams,

the Russian practice of extracting as much plutonium as possible for weapons use undoubtedly leaves little scrap plutonium destined for disposal.

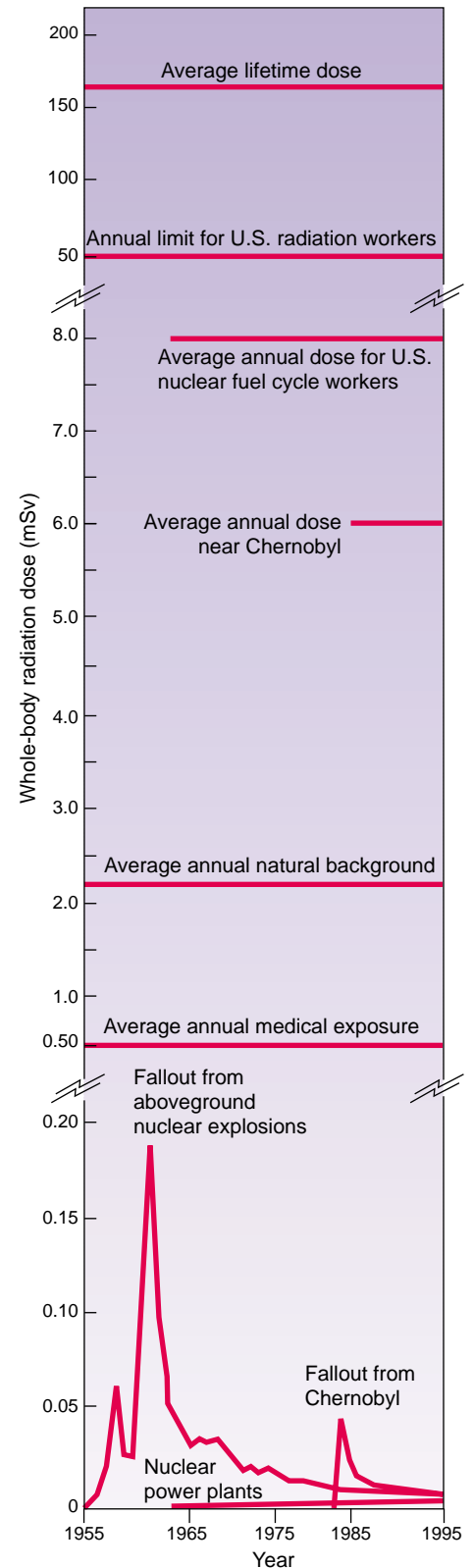
In the late 1980s, the United States embarked on the cleanup of its entire nuclear weapons complex. It has become the world's most costly environmental cleanup. The recently published (June 1998) Department of Energy report "Accelerating Cleanup: Paths to Closure" lists 353 cleanup projects at 53 sites in 22 states. The current projected cost for the cleanup is about \$147 billion through the year 2070. By any standard of comparison, the Russian nuclear complex has not only caused significantly greater environmental damage than that of the United States, but it also faces greater future cleanup problems. Unfortunately, because of the dire state of the Russian economy, the Russian government's most recent 30-year projection for nuclear cleanup is only \$3.6 billion. Both U.S. and Russian production sites will remain ecological hazards for many years to come. The U.S. program, which currently enjoys strong financial support from Congress, would benefit immensely from collaborations with Russian scientists at the Russian sites. For example, as a result of the discharges into Lake Karachay and the deep-well injection practice, the Russians have an enormous amount of data on the migration of numerous radionuclides in different geologic media. The United States has developed several sophisticated models for radionuclide migration. Scientific exchange and cooperation in areas such as these could benefit both countries.

Releases from Atmospheric Testing. Before the Limited Test Ban Treaty was implemented in 1963, atmospheric nuclear testing posed the greatest environmental and health concern to the general public. A total of 541 atmospheric nuclear tests have been acknowledged (conducted principally between 1945 and 1963 by the United States and the Soviet Union), dispersing more than 4 tonnes of plutonium (about 360 kilocuries) and 95 kilograms of americium into the environment.

Most of the global fallout settled rather uniformly in the temperate regions of the Northern Hemisphere at the minuscule level of 3 to 30 picocuries per kilogram of soil. For comparison, the average natural level of thorium and uranium in soil is approximately 50 picocuries per kilogram. Also, because radioactivity decreases with time, the risk from these sources has been declining continuously. The U.S. National Council on Radiation Protection and Measurements reported that, in 1962, global fallout from fission products, actinides, and activation products accounted for 7 percent of the annual mean dose of radiation for humans (see graph to the right). By 1989, this level had dropped to 1 percent.

On the other hand, near the test sites and at unpredictable locations (where rain deposited the fallout), exposures were sometimes much higher than average. A 1997 National Cancer Institute study reported that American children received radiation doses to the thyroid gland from radioactive iodine-131 that were 15 to 70 times greater than previously reported. The cumulative dose to the thyroid was 60–140 millisieverts on average and 270–1120 millisieverts in the most contaminated areas. Areas near the Nevada Test Site were the most contaminated, but surprisingly, the entire continental United States was affected, and many "hot spots" occurred at places far from the test site.

Atmospheric and underground nuclear tests as well as near-surface nuclear experiments have left radioactive residues at the test sites themselves (a total of 2048 nuclear tests and experiments have been reported to the United Nations Scientific Committee on the Effects of Atomic Radiation, UNSCEAR). The sites of the five declared nuclear powers span the globe from the atolls of French Polynesia to the Marshall Islands, Algeria, Australia, and the former Soviet Semipalatinsk test site now in Kazakhstan. The test sites in Nevada, Novaya Zemlya above the Arctic Circle in Russia, and Lop Nor in China are still being used for nuclear experiments permitted by the Comprehensive Test Ban Treaty. Much has been



The variation of annual doses from natural background radiation is represented by purple shading. Around the world, these doses vary from as little as 0.1 mSv to as much as 220 mSv, or 100 times the average worldwide dose.

Table I. Accidental Releases in Decreasing Order of Radioactivity^a

Source and Location	Date	Radioactivity (Ci)	Radionuclides	Radioactivity in 1996 (Ci)
Chernobyl Explosion, Ukraine	Apr. 1986	50–80 million 1.5 million	All Long-lived	1.2 million
Mayak Explosion, Russia	Sept. 1957	~2 million	All	~44,000
SNAP-9A Accident, USA	Apr. 1964	~17,000	Pu-238	13,400
Three Mile Island, USA	Mar. 1979	3–17 2.4–13 million	I-131 Noble gases ^b	0 200–2000
Windscale Accident, the United Kingdom	Oct. 1957	597	All	249
Soviet Cosmos954 Satellite, Canada	Jan. 1978	46,000	All	Not known
Tomsk-7 Explosion, Russia	Apr. 1993	~40	All	≤40
B-52 Crash, Greenland	Jan. 1968	~27	Pu-240 and Pu-239	~27
Pu Fire, Rocky Flats, USA	May 1969	≤5.8	Pu-239	≤5.8
B-52 Crash, Spain	Jan. 1966	2.7	Pu-240 and Pu-239	2.7

^a This table was adapted with permission from Battelle Press.

^b Because their half-lives are short and they are not retained in the body, noble gases do not present a health hazard when released into the atmosphere.



Work is under way to remove spent-fuel assemblies from the reactor in this laid-up submarine at the Zvezdochka shipyard in Severodvinsk. However, existing facilities are not equipped to adequately treat and store spent fuel. Operations at Severodvinsk include maintenance of active submarines and building of new ones in addition to decommissioning the older ones.

done to clean up the effects of radioactive contamination at the former test sites, including decontamination efforts and digging up and disposing of large quantities of soil, in Australia, the Marshall Islands, and French Polynesia. The International Atomic Energy Agency (IAEA) has been asked to evaluate the residual radiation exposure risks at many of the former test sites. A recent IAEA report (IAEA Bulletin, 1998, vol. 40, no. 4) shows that most of the sites no longer pose a health concern for the nearby populations bordering the test sites. In some cases, the sites are suitable (or nearly so, pending some additional cleanup) for human habitation. However, other sites, such as Semipalatinsk, have many hot spots that require continued isolation and monitoring.

Releases into the Open Seas. The Soviets dumped large quantities of liquid wastes and spent reactor fuel from their nuclear navy program into the Arctic Seas and Pacific Ocean, including one million curies into the Kara Sea alone. Concern in neighboring Norway has led the IAEA, other international organizations, and the Norwegian government to monitor the Arctic Seas for pollution and accompanying potential health effects. A recent IAEA study of the Kara Sea contamination concludes: “Although the amount of radioactive material dumped is large, the project results were not alarming for public health and safety...the potential radiation doses to humans would be minute.” Dispersal was probably a major component in reducing the risk, but binding of radionuclides, especially plutonium, to ocean floors could also have been effective.

Considerable risk remains, however, because 183 Russian nuclear-power military submarines have been taken out of service (110 in the Northern Fleet and 73 in the Pacific Fleet), and two-thirds of these still have nuclear fuel in their reactors. Thirty have been laid up as long as 30 years with little maintenance, and they are currently in danger of sinking. Other vessels, such as floating barges, carry significant nuclear-material inventories without adequate protection from theft or diversion. Today, the Russian government is ill equipped to handle the spent fuel brought back on land. Consequently, northern regions, such as the Kola Peninsula and some Pacific regions, face serious environmental problems and continue to require international help.

Releases from Nuclear Accidents. Nuclear accidents, including the 1957 Mayak explosion, have also released significant quantities of radioactive materials into the environment (see table at left). The largest release, 50 to 60 million curies, occurred during the Chernobyl accident in 1986. Early consequences were seen only in the firemen and plant personnel exposed at the plant site. Of the 237 people immediately hospitalized, 134 had clinical symptoms attributable to acute radiation exposure, and of these 28 persons died almost immediately. Approximately 135,000 people were evacuated from the regional area, and even now the area within 30 kilometers of the plant is largely uninhabited. The principal radiation doses resulted from cesium-137 and iodine-131. The average dose near Chernobyl has been about 6 millisieverts, three times the average background dose but below the average dose received by nuclear-fuel-cycle workers in the United States (see graph on page 41). According to the latest assessment of UNSCEAR, there have been about 1,800 cases of thyroid cancer in children who were exposed at the time of the accident (clinical experience indicates that 5 to 10 percent of these children will die of thyroid cancer). The report states: "Apart from this increase, there is no evidence of a major public-health impact attributable to radiation exposure 14 years after the accident." Nevertheless, the long-term health effects require continued monitoring. And the psychological effects of the accident, especially in Europe, were devastating. The Chernobyl accident had a chilling effect on the public's confidence in the future of nuclear power.

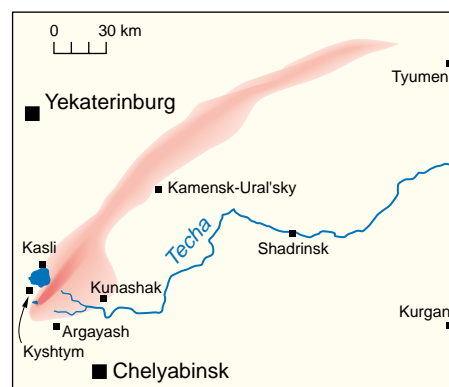
The table on the opposite page lists other accidental global and regional airborne releases of radioisotopes. With the exception of Chernobyl, these accidents showed no measurable health effects. The releases of radioactive noble gases from the Three Mile Island reactor accident in 1979 were not considered a significant health threat, although the psychological impact was enormous. These accidents have reinforced Admiral Rickover's philosophy of utmost attention to nuclear safety practiced by the U.S. nuclear navy program. Over the years, the safety record of nuclear enterprises around the world has improved. Unfortunately, however, the 1993 explosion in the reprocessing plant in Seversk (Tomsk-7) and the recent criticality accident at the reprocessing plant in Tokai in Japan that killed two people but posed no risk to the public again shake the public's confidence in nuclear operations.

Storing Nuclear Waste. Many of today's environmental threats stem from not having a long-term repository for high-level waste and therefore retaining "interim" solutions long past their design lifetime. Because these wastes contain long-lived transuranics, a permanent solution must isolate them from the biosphere for tens of thousands of years. Admittedly, it is very difficult to make convincing predictions for times that far into the future, but careful analysis has led to a worldwide scientific and political consensus that deep geologic disposal is the best option for permanent disposition.

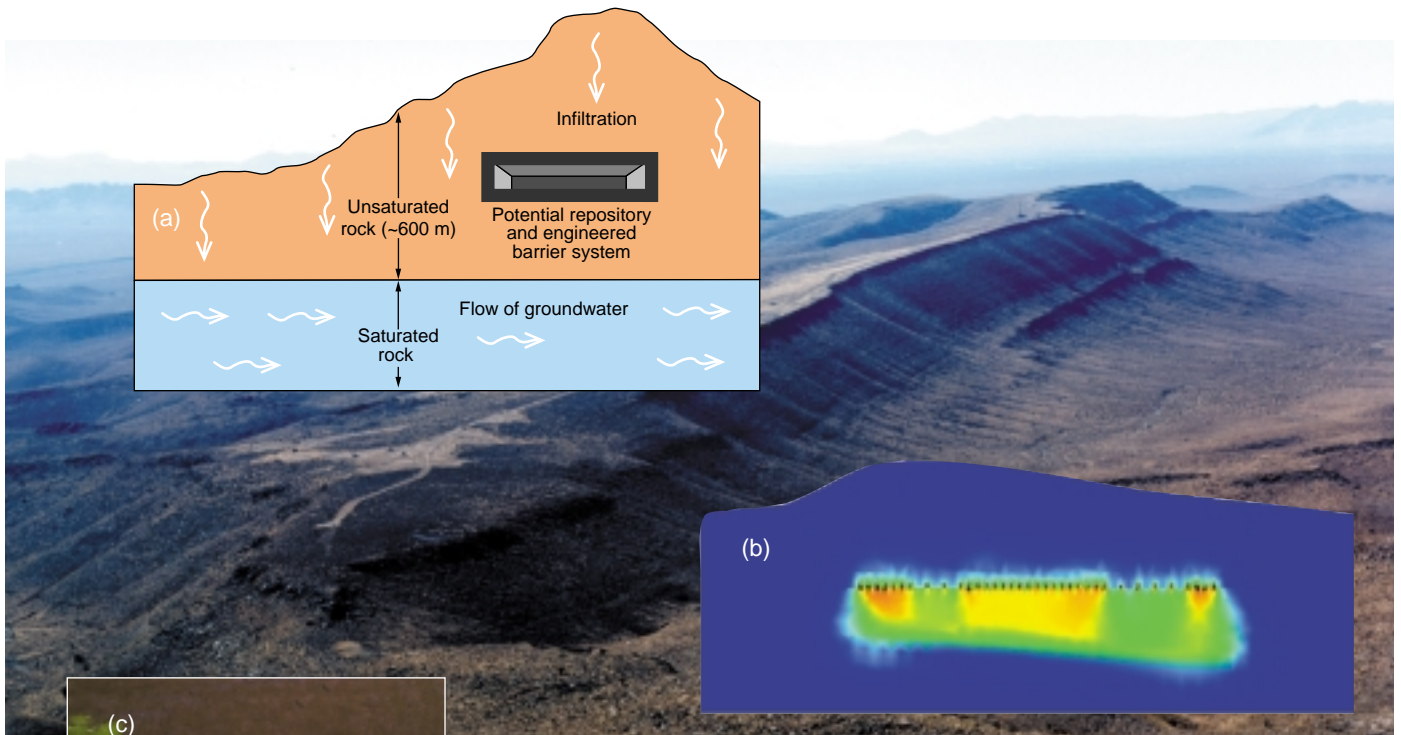
In 1987, the United States Congress chose Yucca Mountain in the deserts of Nevada as the proposed site for the initial high-level waste repository. The repository is being designed to contain 70,000 tonnes of uranium equivalent nuclear waste, 90 percent derived from commercial-reactor spent fuel (sufficient to include all spent fuel generated until the year 2010) and 10 percent from reprocessing spent fuel for defense production reactors and naval propulsion reactors. The proposed repository is to be located in the densely welded, devitrified tuff 200 to 400 meters above the water table in the unsaturated (vadose) zone.



Unit 4 of the Chernobyl Nuclear Power Plant is shown several days after it suffered two explosions that destroyed the 200-tonne reactor core and the reactor building. Five to 10 tonnes of relatively heavy radioactive particles (predominantly strontium, plutonium, and other nonsoluble radionuclides) were blown out of the burning reactor and settled in the 30-kilometer exclusion zone around the plant. Smaller particles were carried great distances by a plume of smoke and debris ascending from the burning reactor.



The radioactive plume from the 1957 Kyshtym accident contaminated an area of 23,000 km².



(a) This cross section of Yucca Mountain shows the potential high-level waste repository at 200 m above the water table in unsaturated volcanic rock.
(b) Los Alamos computer simulations of actinide migration show that, should the engineered containment fail and water infiltrate the repository, it would take over 10,000 years for the most mobile actinides to reach the water table.
(c) Fluorescent tracers are injected into the rock matrix at Yucca Mountain to track water movements through the rock. Results from these field tests are used to calibrate theoretical models of potential radionuclide migration. (See the article “Yucca Mountain” on page 464.)

The tuff itself provides desirable containment characteristics, and the fracture zones in this area contain zeolites and other minerals that have a high sorption affinity for most of the actinides. Based on extensive field data and state-of-the-art modeling of worst-case scenarios, researchers have predicted that the waste would take at least 10,000 years to migrate to the water table (saturated zone). This prediction is consistent with experience at the nearby Nevada Test Site, which indicates that the mobility of radionuclides is generally very small—that is, for the most part, the actinides injected into underground test holes from nuclear explosions have remained close to where they were deposited. However, recent experiments found one exception, whereby transport of plutonium was most likely enhanced by its tendency to bind and hitch rides with natural colloids. Ongoing scientific studies of the Yucca Mountain Site will help determine whether this site will be licensed to accept nuclear waste by 2010.

Located near Carlsbad, New Mexico, WIPP was authorized in Congress in 1979 to store transuranic waste generated principally during nuclear weapons production. WIPP is a mined geologic repository located in the 600-meter thick Salado Formation of marine-bedded salt. The bedded salts consist of thick halite (NaCl) and interbeds of minerals such as clays and anhydrites of the late Permian period (about 225 million years ago) that do not support flowing water. Salt formations have a very low water content and impermeability characteristics that reduce the potential for groundwater radionuclide migration. WIPP is designed to take advantage of natural geologic barriers and imposed chemical controls to ensure that waste radionuclides do not migrate to the accessible environment. It was licensed to receive waste in 1998 and received its first shipment in 1999.

Environmental Pathways and Human Health

Some observed health effects from environmental releases of the relatively short-lived fission products have already been mentioned. Here, the discussion will be limited to plutonium and the actinides because they present the greatest long-term concern. To adversely affect human health, plutonium and the other

actinides must find a pathway into the human body through air, water, or land. Airborne plutonium constitutes the most immediate threat because the pathway to humans is directly by inhalation. Plutonium released into land or water undergoes numerous reactions with chemicals and minerals that retard its migration along the path to human uptake. Because actinide solubilities are low in most natural waters—below micromolar concentrations—and sorption to many minerals is high, solubility and sorption of actinides pose two key natural barriers to actinide transport in the environment. Less-studied microorganisms represent a potential third barrier because plutonium binds with such organisms and their metabolic byproducts. Uptake of actinides into most plants is also very limited—plants typically take up only one ten-thousandth of the plutonium concentration present in soil.

The body itself provides some additional protection. Only about 5 to 25 percent of inhaled plutonium particles are retained, and depending on their size and chemical form, they will either remain lodged in the lung or lymph system or be absorbed by the blood and delivered to the liver or bones (the smaller the plutonium particles, the higher the risk of being retained). In adults, only about 0.05 percent of ingested plutonium in soluble compounds (and 0.001 percent in insoluble compounds) enters the blood stream; the rest passes through the body. However, absorption through skin cuts, a danger mainly for plutonium workers, is a serious risk because it can result in complete plutonium retention in the body.

Very high doses of ionizing radiation are harmful—in fact, doses of 3 to 5 sieverts delivered in one hour are lethal to humans. Lethal doses can be delivered by criticality accidents, in which quantities of fissile plutonium or enriched uranium accidentally assemble into a critical mass. Almost instantly, a fission chain reaction in the material produces very intense fluxes of penetrating neutron and gamma radiation that will rapidly lead to death. Exposure to unshielded spent fuel or high-level waste can also produce lethal doses.

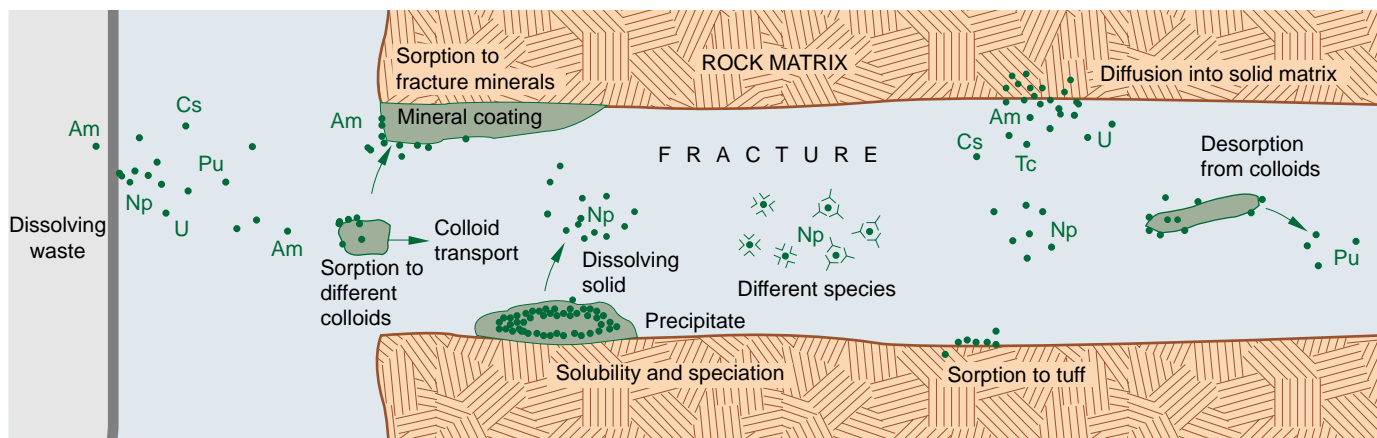
Being an alpha emitter, plutonium must enter the body to deliver a radiation dose. Animal studies indicate that inhaling 20 milligrams of respirable plutonium particles (less than 3 micrometers in diameter) could cause death within a month from pulmonary fibrosis or pulmonary edema. Ingestion of 0.5 gram of plutonium could deliver an acutely lethal dose to the gastrointestinal tract. No one has ever come close to taking up such amounts of plutonium, and no humans have ever died from acute toxicity due to plutonium uptake.

If plutonium is inhaled, it deposits preferentially in the lung, liver, or bones and becomes an internal radiation source. All ionizing radiation can alter a living cell's genetic makeup. That alteration, in turn, has some probability of either being repaired, killing the cell, or triggering uncontrolled cell growth and cell multiplication, leading to cancer. Consequently, the plutonium exposure standards for radiation workers and for the public were set conservatively on the basis of a linear



The Waste Isolation Pilot Plant (WIPP) located in southern New Mexico has been receiving TRU and low-level waste since 1999. The U.S. Environmental Protection Agency oversees WIPP to ensure that it continues to protect human health and the environment.

The cartoon below depicts the geochemical factors that would accelerate and retard migration of radioactive wastes dissolving from a breached underground waste canister near a water-filled rock fracture. Sorption onto colloids and complexation with various ligand species would increase mobility, whereas sorption to minerals that coat the fracture and diffusion into the rock matrix would retard migration.



no-threshold (LNT) model of the effects of ionizing radiation on human health. That is, the risk of cancer is assumed to increase in proportion to the increase in dose, no matter how small. Current regulations for nuclear facilities call for a maximum dose of 50 millisieverts per year for radiation worker exposures and 1 millisievert per year for the public. For comparison, on average, the body is bombarded by about a billion particles of radiation daily, or 2.2 millisieverts per year.

To date, no cancer fatalities among the public have been directly attributable to plutonium exposure. Also, studies of plutonium workers in the United States show no increase in the incidence of cancer resulting from plutonium exposure. So far, only one plutonium worker has died of cancer (a rare bone cancer), which may have been caused by exposure to plutonium. However, the rigorous precautions for handling plutonium in the United States have kept exposures very low. Interestingly, extensive studies on rats suggest that there may be a threshold for radiation-induced lung cancer several hundred times higher than the occupational limit for humans.

Some plutonium workers at the Mayak plant in Russia were exposed to very high cumulative lung doses from plutonium (100–740 sieverts). Thanks to the U.S.-Russian cooperation initiated by the Nuclear Regulatory Commission and the DOE, some of the health effects on Russian workers are being analyzed. Two recent Russian studies report increased incidence of lung cancer with exposure (see the article “Plutonium and Health” on page 74). One study shows a linear correlation with dose, whereas the other shows a threshold as well as a suggestion that low levels may even be beneficial. The possibility of a beneficial effect, known as hormesis, might result from stimulating the body’s immune system. Studies of the survivors of Hiroshima and Nagasaki suggest a threshold for harmful health effects, as does the fact that populations in regions of Brazil, India, and Iran have experienced no adverse health effects from living with background radiation levels as much as 100 times higher than the world average. On the other hand, there is no convincing biological model that predicts a threshold for radiation effects.

The Mayak worker registry for 1948–1958 covering 8800 workers offers an extremely important database for studying radiation effects on humans. Mean external doses of nearly 1.7 sieverts received over reasonably short time periods resulted in clinically observable effects including cardiovascular, gastrointestinal, and neural system disorders in 20 percent of the workers. A registry of 2283 plutonium workers shows a mean accumulated dose to the lungs of 8 sieverts for male workers and 14 sieverts for female workers. These levels are far beyond anything seen in the West, and have caused plutonium pneumosclerosis.

The Challenge

Large amounts of radioactivity have been released into the environment as a result of Cold War operations and poor waste disposal practices. The extent of long-term adverse health effects will depend on the mobility of actinides in the environment and on our ability to develop cost-effective scientific methods of removing or isolating actinides from the environment. The very low solubility and high sorption of plutonium and the actinides provide some natural barriers to migration. However, the recent evidence of colloidal transport demonstrates the need for better understanding and caution, especially if we must predict effects spanning

thousands of years. Studying the complex chemistry of plutonium and the actinides interacting with their environment is one of the most important technological challenges and one of the greatest scientific challenges in actinide science today.

Likewise, the effects of ionizing radiation must be understood at a more fundamental level and be coupled to epidemiological studies of low-level ionizing radiation on human beings. The Russian experience offers a very special opportunity to study the validity of the LNT model that drives international radiation standards. However, significant effort is required to preserve the data in the worker registries because they exist mostly in single-paper copies. Significant research is also required to reconstruct actual doses and analyze health effects. The current collaboration between Russian and U.S. researchers is woefully underfunded.

We must find an acceptable method for long-term disposal of nuclear waste. Fortunately, the “factor of millions” advantage of nuclear energy means that the amount of waste generated is relatively small. The problem is technically challenging but certainly manageable if we give science and technology a chance. Over the next few decades, a better understanding of the actinide mobility in geologic media will surely provide some answers. Likewise, some of the options to separate the long-lived actinides from nuclear waste may prove financially viable and may obviate the need for guaranteeing waste isolation over eons of time. In the meantime, we can gain substantial experience relevant to geologic repositories by joining the Russians in studies of actinide migration at both Russian and U.S. sites.

We should also develop the scientific basis for converting our nuclear facilities so that they create little or no future contamination of the environment. Advances in plutonium chemistry in the past few years have made it possible to create molecules that combine with or extract target metal ions, such as plutonium, with a high degree of specificity. These techniques must be taken from the laboratory and used in our enduring plutonium facilities (see the article “A Vision for Environmentally Conscious Plutonium Processing” on page 436).

Finally, the societal challenge of dealing with the environmental problems is perhaps the greatest. Technically, we must strive to establish the risks of ionizing radiation on human health. Then, we must communicate the risks clearly to the public and the policy makers. It will be necessary to reevaluate the principles and concepts of radiation protection—specifically, the application of the LNT model—because the current regulations are seriously impacting the cost and viability of all nuclear facilities, including the future of nuclear power. However, overcoming the public’s fear of all things nuclear will require a level of trust and confidence that the nuclear scientific community does not enjoy today. The lifting of the veil of secrecy that has shrouded the nuclear weapons sites and providing the public with an accurate accounting of the environmental problems resulting from the Cold War were important first steps. ■

The Department of Energy has established the Office of Long-Term Stewardship to oversee the 109 “legacy”-waste sites that it deems can never be made clean enough for unrestricted use even after remediation. These sites are located in 27 states, Puerto Rico, and territorial islands in the Pacific. A recent National Research Council committee report cautions, however, that containment strategies for these sites are not likely to function as expected for the indefinite future. Consequently, the report recommends that the long-term stewardship plan include the monitoring of waste migration and changes in landscape and human activity around each site as well as contaminant reduction and physical isolation of waste. The DOE is also encouraged to engage the public in developing stewardship plans.

The Taming of “49”

Big science in little time

Recollections of Edward F. Hammel



During the Manhattan Project, plutonium was often referred to, simply, as 49. Number 4 was for the last digit in 94 (the atomic number of plutonium) and 9 for the last digit in plutonium-239, the isotope of choice for nuclear weapons. The story that unfolds was adapted from *Plutonium Metallurgy at Los Alamos, 1943–1945*, as Edward F. Hammel remembers the events of those years.

The work in plutonium chemistry and metallurgy carried out at Los Alamos (Site Y) between 1943 and 1945 had a somewhat controversial history. The controversy was about who was going to do what. At the time Los Alamos was being organized, most of the expertise in plutonium chemistry resided at Berkeley, where plutonium was discovered in December 1940, and at the Met Lab in Chicago. Consequently, most of the original Los Alamos chemistry staff came from these two laboratories. At the Met Lab, the existing body of information on plutonium was constantly being upgraded and extended to optimize the plutonium extraction processes,¹ which were initially carried out at Oak Ridge (Site X) and finally at Hanford (Site W). At the Met Lab, attention was also being given to the production and properties of plutonium metal.

When Los Alamos began operations in April 1943, the division of labor between its chemical and metallurgical R&D programs and similar programs under way elsewhere in the Manhattan Project (particularly those at the Met Lab) had not been agreed upon. The issue was not settled until May of that year, when a special review committee appointed by General Groves and chaired by W. K. Lewis of the Massachusetts Institute of Technology recommended that the final purification of plutonium, the reduction to its metallic state, the determination of the metal's relevant physical and metallurgical properties, and the development of the necessary weapon-fabrication technologies be carried out at Los Alamos. This recommendation was triggered by two main reasons: First, the Los Alamos Project was responsible for the correct functioning of the weapon, and second, a considerable amount of plutonium reprocessing and repurifica-

tion work was an inevitable consequence of the nuclear and physical research that was still to be conducted on the metal. It would clearly have been inefficient and time consuming to ship small amounts of plutonium metal back to Chicago for repurification and refabrication into different sizes and shapes for the next-scheduled nuclear physics experiment.

Minimizing the time spent to solve weapons R&D problems was a constant concern for the Los Alamos staff. Many of us had already participated in the costly uranium isotope separation or the plutonium production projects (at sites



Ed Hammel in 1944

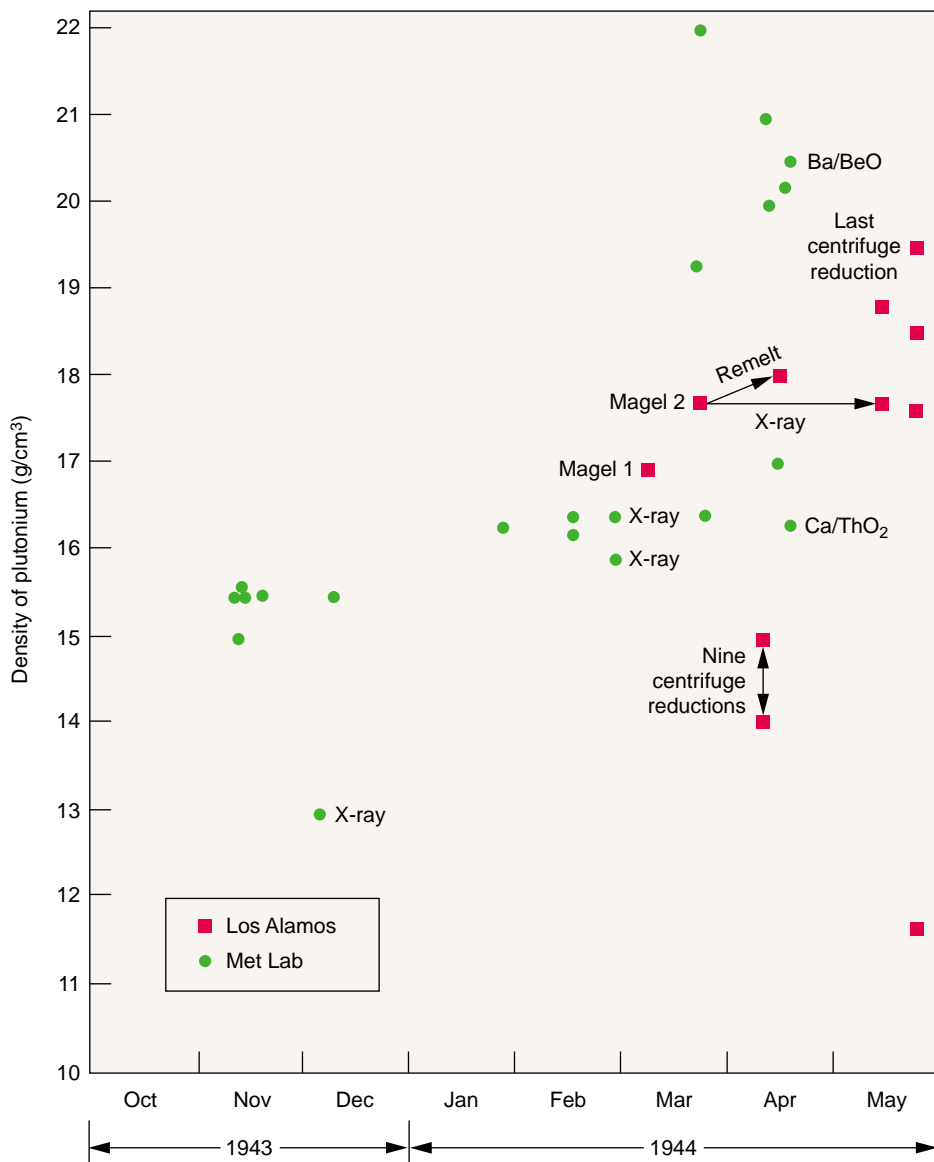
X or W or at their parent university laboratories), and we therefore knew that their engineering and construction phases were proceeding more or less on schedule. We also knew when their production phases were likely to begin and what the expected production rates would be. Our primary task was to make sure that, after enough active material had been delivered to Los Alamos to fabricate a weapon, the weapon could and would be built without further delay and then would be either tested or delivered to the Air Force for combat use. For the Chemistry and Metallurgy (CM) Division personnel, these concerns were intensified because important questions about plutonium's chemical and metallurgical properties had to be answered before

the metal could be fabricated into satisfactory weapon components. In addition, not until January 1944 did the first few milligrams of pile-produced plutonium arrive at Los Alamos. The first 1-gram shipment arrived in February 1944, and quantity shipments of plutonium did not begin to arrive at Los Alamos until May 1945.

From the outset, it was clear that the purification of plutonium was the most important task of the CM-Division staff at Los Alamos. Achieving the impurity limits originally specified (on the order of a few parts per 10 million by weight for each of the lightest impurity elements) was essential for the success of the project. But this task was expected to be extremely difficult. To avoid a predetonation, we needed highly purified plutonium. The emission rate for plutonium α -particles is very high, well over 1000 times that of enriched-uranium α -particles. When the α -particles collide with an impurity nucleus (especially with that of a light element), neutrons are created. Unless each of the impurities is reduced to about 10 percent of the already very low levels specified before, the resulting neutron background will increase the chance of initiating a fission chain reaction in the plutonium well before the planned postfiring condition of maximum supercriticality is attained. The result will be a predetonation, or a "fizzle," in which little of the active material fissions before the entire assembly is blown apart.

Although we were fully aware of the impurity problem, we conducted little research on it during the first eight or nine months because adequate supplies of plutonium were nonexistent during that period. One project undertaken almost immediately, however, was the design and construction of a facility in which the projected chemistry and metallurgy work could be carried out with minimal contamination of the active materials by light-element dust particles settling out from the air. This facility was designated "D-Building." In May 1943, after the committee chaired by

¹ In addition to many other assignments, the Met Lab had prime responsibility for developing processes for separating plutonium from the uranium and the radioactive fission products in the reactor (pile) fuel elements.



Variations in measured plutonium metal densities finally provided convincing evidence for the high allotropy found in plutonium (six allotropes).

Lewis decided on the construction of this facility, some of the important tasks of the senior CM-Division staff, in collaboration with the architect and, in particular, with C. A. Thomas,² were to help set specifications for the building, participate in the design work, and

² Thomas, Research Director of the Monsanto Chemical Company, had been appointed by General Groves as coordinator for all the plutonium purification work being carried out throughout the Manhattan Project.

subsequently, monitor the construction phase. The result was a laboratory as nearly dust-free as the air-conditioning technology available at that time permitted. The building was occupied in December 1943.

Working in temporary quarters through March 1944, when the division was more formally organized, CM-Division members were engaged in a variety of tasks, most of which have already been described in other accounts of the Laboratory's early days.

It may be of interest, however, to comment on the general modus operandi during the first eight to ten months of the division's existence. April, May, and June 1943 were spent primarily on the acquisition of personnel, equipment, and materials; on organizational details; and on getting highly specialized laboratories in operation. J. W. Kennedy was appointed as acting leader of the CM-Division, and C. S. Smith served as acting associate division leader for metallurgy. Initially, there were about 20 chemists and metallurgists in this division, who would soon be assisted by roughly an equal number of technicians (by the end of the year, the division's size had approximately doubled). During this same period, the functional structure of the division began to emerge. The two main organizational entities were obviously chemistry and metallurgy, but within those categories, small specialized groups were soon established. In the chemistry area, for example, a clear need arose for expertise in radiochemistry, analytical chemistry, purification chemistry, and general or service-related chemistry. Then, in addition to synthesizing materials requested by other parts of the project, CM-Division staff had to fabricate those materials into various shapes. The physical and chemical properties of those materials were specified and had to be confirmed. These tasks—including the reduction of purified plutonium compounds to plutonium metal and the final remelting, casting, and fabrication of the plutonium metal into the desired shape—were carried out by the metallurgical and analytical groups.

Because of the informality of the division's organizational structure, its early accomplishments were recorded in a series of Los Alamos series reports, each dealing with a problem assigned to and reported on by an individual member (or members) of the division. Very brief (one- or two-page) semi-monthly or monthly memoranda were also filed by the division leader. They summarized the results of those topical reports. It is also worth noting that

essentially all the technical personnel in CM-Division were experimentalists. Not surprisingly, much of their work had a strong empirical content.

Summary of Events between March 1944 and August 1945

In this section, I summarize plutonium metallurgy research, development, and production in D-Building by providing an abbreviated time line of the events that unfolded from March 1944 until the end of World War II. This time line also lists some of the associated problems that occurred and were solved by CM-Division personnel. The graph on the next page spread will assist you in achieving a better perspective of these events. Each numbered paragraph below refers to the corresponding number under the ordinate axis of the graph, and the short vertical line above each number points to the date when each event occurred.

1. Before any plutonium became available at Los Alamos, experience was sought with reduction techniques on related materials. Uranium and other plutonium "stand-ins" were used. But as it eventually turned out, such experience proved to be neither relevant nor very helpful. When it became fairly certain that the first macroscopic amounts (50 milligrams to 1 gram) of plutonium would be arriving at Project Y in late February or early March 1944, the metallurgists realized that they would first have to deal with the scaling problem. In other words, they would have to apply procedures and techniques that worked well on "large-scale" uranium reductions (>10 grams of uranium) to very small samples of plutonium. And it became immediately obvious that those techniques were not likely to work well at all on the first plutonium samples, which would be considerably smaller. In January 1944, therefore, Los Alamos staff conducted experiments to explore small-scale reductions, but these attempts were

unsuccessful. The only individuals known to be familiar with such reductions were T. T. Magel and his assistant N. Dallas, who had been using centrifuge techniques to solve similar problems at the Met Lab in Chicago. Arrangements were therefore made for their immediate transfer to Los Alamos, and they arrived at the Laboratory in early February 1944.

2. Using their centrifuge to help force the coalescence of the molten metal produced into a single well-formed button, Magel and Dallas produced their first 50-milligram button of metallic plutonium on March 9, 1944.

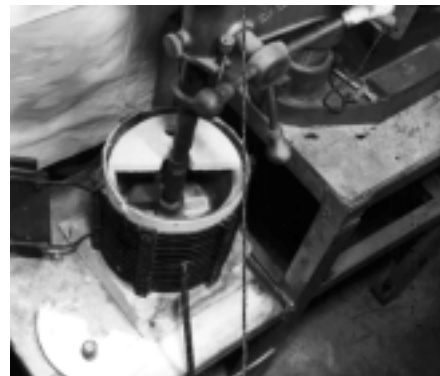
3. Using their centrifuge, Magel and Dallas produced the first 1-gram specimen of plutonium metal on March 23, 1944.

4. From these first metallic buttons, many of the first estimates of the physical properties of plutonium were obtained. By far, the most significant and inexplicable property exhibited by both of these samples, as well as the others that followed, was widely differing densities (see graph on page 50). This phenomenon had already been observed at the Met Lab, but the samples used were so small that the results were simply indicative of a problem, without an explanation for it.

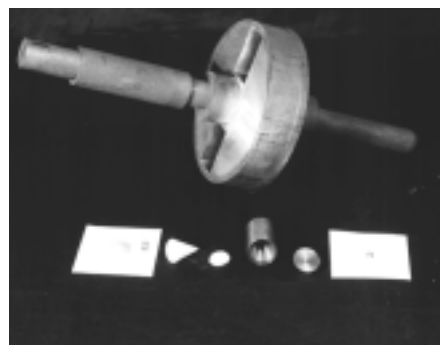
5. At Los Alamos, F. Schnettler made the first tentative suggestion that the conflicting density results might be attributable to allotropism.³

6. By the end of May 1944, R. D. Baker had solved his reduction problems for the "stationary-bomb" approach to small (0.5- to 1.0-gram) plutonium samples. Because his technique appeared equally efficient and intrinsically safer, the centrifuge program was phased out. Shortly thereafter, Magel and Dallas left Los Alamos. Important physical properties still remained to be determined. Among them were ductility, tensile strength, melting point, thermal-expansion

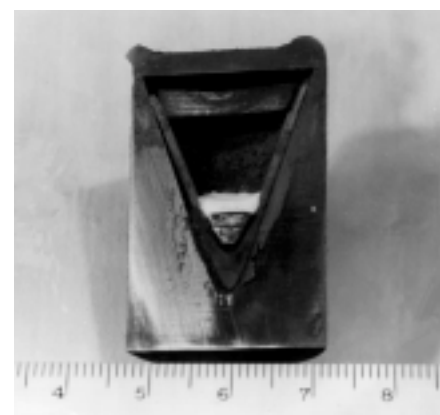
³ A similar suggestion had previously been advanced at the Met Lab in Chicago.



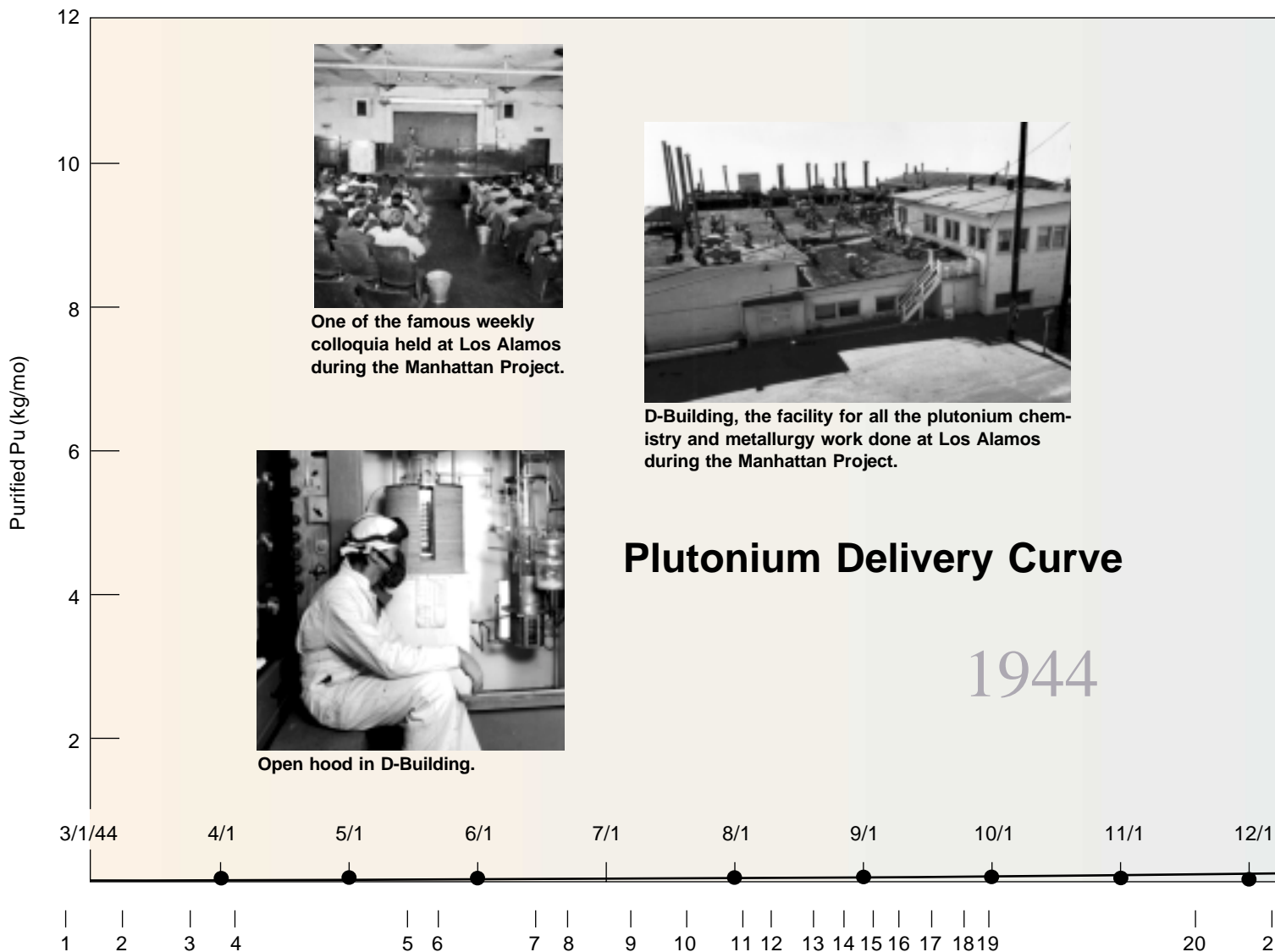
The centrifuge used by Magel and Dallas for small-scale reductions of plutonium compounds.



Components of Magel and Dallas's centrifuge.



The plutonium compound was placed inside a graphite crucible and was then reduced in the centrifuge. The longitudinal cross-section view above shows the button of plutonium metal obtained after reduction.



coefficients, compressibility, metallographic properties, and others. From the outset, nuclear physics requirements for plutonium purity levels were so high that they were previously unheard of. This problem was being studied by high-temperature, high-vacuum remelting of the metal in various new and exotic crucibles believed to be incapable of adding refractory-derived impurities to the molten metal. Also during May, M. Kolodney demonstrated that the melting point of plutonium was less than 660°C, far below previous estimates.

7. In June 1944, using careful dilatometric measurements, F. Schnettler unambiguously demonstrated that transformations into at least two different



The infirmary

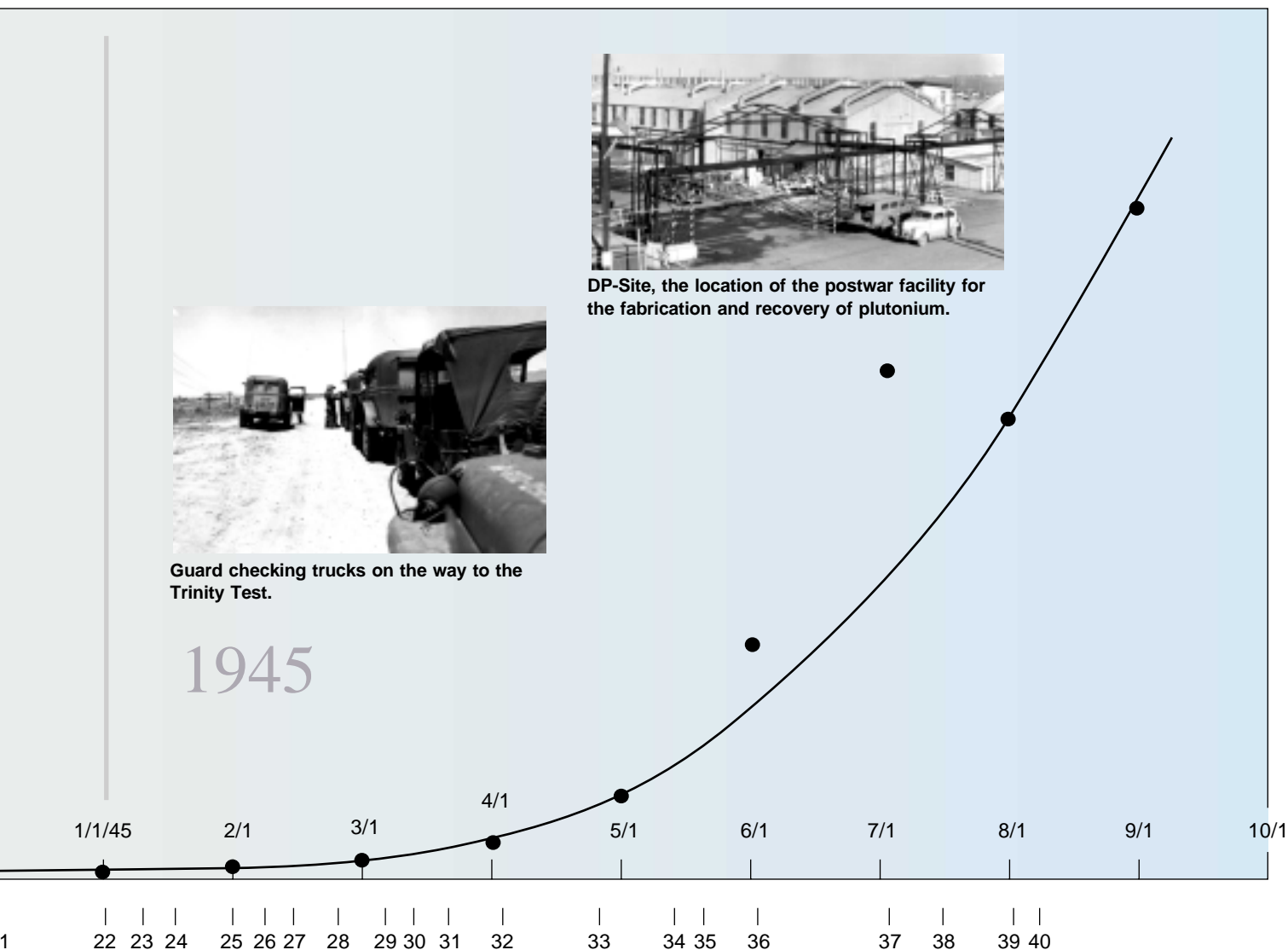
allotropic forms were associated with the progressive heating of plutonium and that the transition temperature was in the range of 130°C–140°C.

8. Later in June, two additional phase changes were identified.

9. In July 1944, Segrè and his group confirmed the expectation of many nuclear physicists that the plutonium produced in the Hanford piles would contain substantial amounts of plutonium-240, an isotope whose spontaneous-fission rate was very high and would result in a high neutron background and therefore a predetonation, or fizzle, of the bomb.

10. Therefore, on July 20, 1944, R&D work on the plutonium gun program was formally terminated.

11. By the beginning of August 1944, the Laboratory had been reorganized to facilitate the design, construction, testing, and deployment of a plutonium implosion weapon, which would compress so rapidly that



the increased neutron background became irrelevant.

12. In a memorandum sent to J. W. Kennedy on August 8, 1944, C. S. Smith casually mentioned, perhaps as an afterthought, that consideration was being given to the addition of a small amount of some impurity to a plutonium melt with the hope that such an addition might retard the transformation to the α -phase. Smith subsequently noted that, if such a stratagem were found to work, one would, of course, be always dealing with a metastable state but that, nevertheless, it might be worth pursuing. Only long after the war was over did the scientists learn that δ -plutonium so stabilized was thermo-

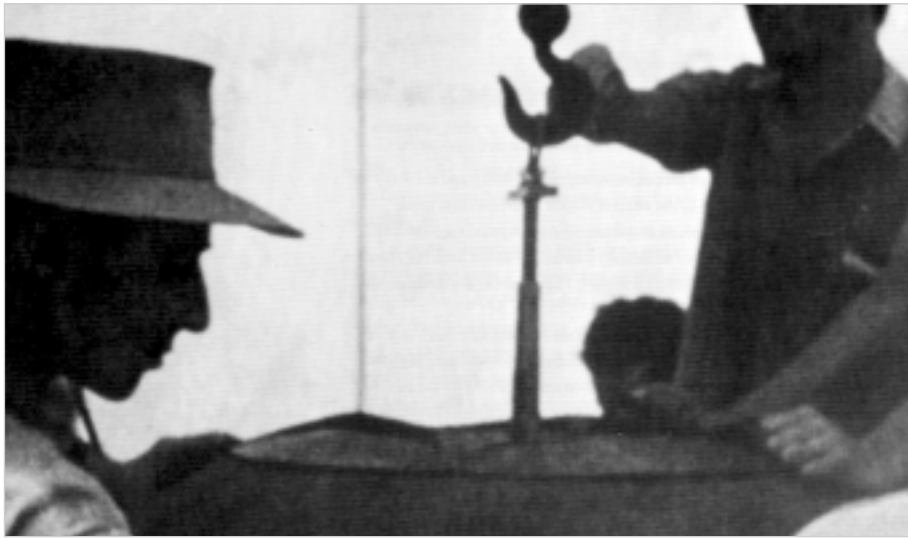


Technical area near Ashley Pond

dynamically stable—or perhaps it was not (see the article “A Tale of Two Diagrams” on page 244). Despite Smith’s suggestion, no action was taken to initiate an alloy survey program until the end of October 1944,

and it was not until mid-December that aluminum was found to retard the transformation to the α -phase.

13. Beginning in August 1944 and continuing for the rest of that year, problems were encountered in fabricating plutonium specimens for various research activities. Attempting to fabricate the specimens at room temperature was hopeless because α -plutonium was much too hard and brittle at ambient temperatures, but the scientists had some success by carrying out the fabrication process at 250°C–300°C and retaining the forming pressure while the metal was cooling. Unfortunately, as the specimens fabricated became larger and more complicated, this technique became less reliable.



J. R. Oppenheimer at the Trinity Test

14. By the end of August, the research program on the corrosion, cleaning, and development of a permanent and impervious coating for plutonium metal moved into high gear. Although this research had been in progress for months with evaporative techniques investigated by the CM-6 group and electrolytic methods investigated by M. Kolodney and his section, little success had been achieved in solving the problem.

15. During September, an extensive R&D program was initiated to study the rates of transition between different adjacent phases of plutonium upon both the heating and the cooling of the specimen.

16. R. D. Baker successfully carried out the largest reduction of plutonium by the stationary-bomb technique to date (6.5 grams).

17. An extensive new series of crucible testing was initiated.

18. Phase transition studies were expanded and extended.

19. Toward the end of September 1944, the Alloy Survey Program was formally initiated.

20. During November, the Alloy Survey Program was significantly enlarged.

21. In December, aluminum was discovered to retard the $\delta \rightarrow \alpha$ transformation. Silicon was also found to be

effective in this regard but not as effective as aluminum.

22. In early January 1945, additional aluminum alloys (with differing atomic percentages of aluminum) were made and tested for their ability to retain the δ -phase at low temperatures.

23. Preparations were under way during the first week of January for making two 0.9-inch-diameter hemispheres of δ -plutonium for multiplication measurements. After having been pressed, they were cooled under load and, upon removal from the die, appeared entirely satisfactory.

24. On January 18, 1945, the roof of C-Shop caught fire. Because C-Shop was only a few yards away from D-Building, where plutonium was being

processed, Kennedy worried about the safety of the community and the workers should that building catch fire as well. He immediately enlisted C. A. Thomas's help for the design of a new plutonium-processing facility.

25. In early February, General Groves approved the construction of this new facility, which was called DP-Site.

26. The most complete and detailed set of measurements of the phase transition temperatures of plutonium was carried out in February. Dilatometry and electrical resistance measurements monitored the progression of the phase transitions at each temperature at which they occurred.

27. A number of aluminum and silicon alloys of plutonium were also prepared and tested in February.

28. At the end of February, the Christy core design (a solid plutonium sphere) for the newly proposed implosion device was approved.

29. On March 9, 1945, CM-Division received a new set of impurity tolerances for the plutonium core of the implosion device.

30. CM-Division officially remained cautious and uncertain about guaranteeing the long-term stability of a weapon core fabricated from stabilized δ -phase plutonium.

31. Toward the end of March, it was recognized that the amount of aluminum required to stabilize δ -phase plutonium would exceed the latest impurity-tolerance levels and hence could not be used.

32. In early April 1945, barely four months before Nagasaki, it was decided that the substitution of gallium for aluminum should be investigated. Gallium was considered another element likely to be effective in stabilizing δ -phase plutonium because it was immediately below aluminum in the periodic table and hence should behave similarly in comparable chemical and physical situations. Simultaneously, gallium would more than satisfy the impurity-tolerance criteria. The substitution was totally successful. Nevertheless, at that time,



the weapon designers were still intending to use an α -phase plutonium core—density 19.8 grams per cubic centimeter (g/cm^3).

33. During the last week of April, the physicists requested four 2-inch-diameter α -phase plutonium hemispheres for neutron multiplication measurements.

34. Fabrication of the four hemispheres was completed by mid-May. Despite having been cooled under load, however, all the hemispheres transformed more completely to the α -phase upon removal from the die. And that transformation triggered serious warping and cracking of the diametral planes.

35. Within days, it was decided that the 3.0–3.5 atomic percent (at. %) gallium alloy should be used for the cores of the Trinity device and the combat weapon.

36. On June 1, 1945, an extensive, systematic, and rigorous long-time surveillance study of the gallium alloy was initiated.

37. On July 1, 1945, the hemispheres for the Trinity Test were completed and delivered.

38. On July 14, 1945, the Trinity Test was carried out, and the combat hemispheres were completed and delivered.

39. On August 1, 1945, additional hemispheres were completed and delivered.

40. On August 6, 1945, the plutonium bomb was dropped at Nagasaki.

A Final Comment

In retrospect, the plutonium delivery curve illustrated on pages 52–53 and the explanatory notes in the “Summary of Events between March 1944 and August 1945” present more dramatically than any words alone can convey how much science and technology were accomplished in so short a time and with so little material with which to work. Indeed, the immense body of data obtained could only have been accumulated by the recycling of every metal specimen immediately after every planned measurement had been completed. The used specimens went back through the Recovery and the Chemical Purification Groups, which in turn immediately proceeded to synthesize new plutonium tetrafluoride for Baker to reduce once again to more metal and for the rest of us to make new test specimens, carry out more tests, and measure more properties. ■

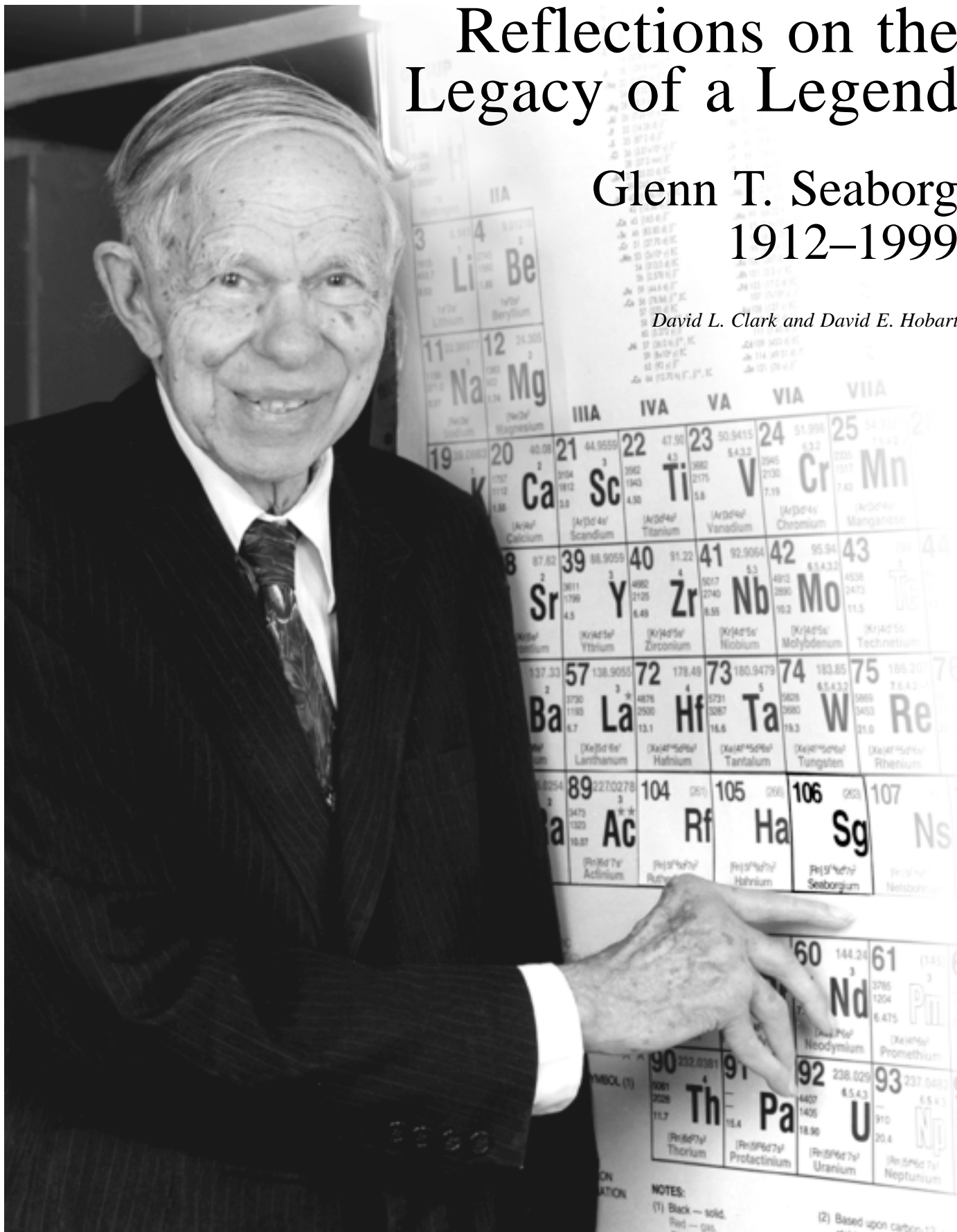


Edward F. Hammel completed all the formal requirements for a Ph.D. in physical chemistry at Princeton in 1941 (but actually received the diploma in the mail in 1944). He began working on the heavy-water portion of the S-1 Project (directed by the Office of Scientific Research and Development) in May 1941 at Princeton. During the first half of 1942, he served as the scientific representative of the Columbia/Princeton Substitute Alloy Materials (SAM) Laboratories at the Consolidated Mining and Smelting Corporation’s plant at Trail, British Columbia, where a new facility to produce heavy water in tonnage quantities had been constructed and was being brought on line. Deuterium was a candidate, along with graphite, for use as a neutron moderator in achieving the first controlled-fission chain reaction. After returning to Princeton, Hammel participated in diffusion barrier research and development for one of the uranium-235 separation plants at Oak Ridge, Tennessee. At the end of May 1944, Hammel transferred to Los Alamos and was assigned responsibility for the remelting, alloying, and casting of plutonium metal. After the end of the war, he and his group undertook a program to determine, with the highest precision, the physical properties of plutonium (among these were its very low temperature properties). While preparing to carry out these experiments, however, Hammel’s interests shifted to low-temperature physics research. In 1948, he and colleagues E. R. Grilly and S. G. Sydorik were the first to liquefy and study many of the properties of pure helium-3. For 25 years Hammel headed the Los Alamos Low-Temperature Physics and Cryoengineering Group. In 1970, he moved to energy-related research and, for several years, directed the Los Alamos program in superconducting energy technology. Shortly thereafter, Hammel was appointed Associate Leader of the newly formed Energy Division. In 1974, he became the Laboratory’s Assistant Director for Energy. Hammel retired from Los Alamos in 1979 and has continued his association with the Laboratory ever since.

Reflections on the Legacy of a Legend

Glenn T. Seaborg
1912–1999

David L. Clark and David E. Hobart

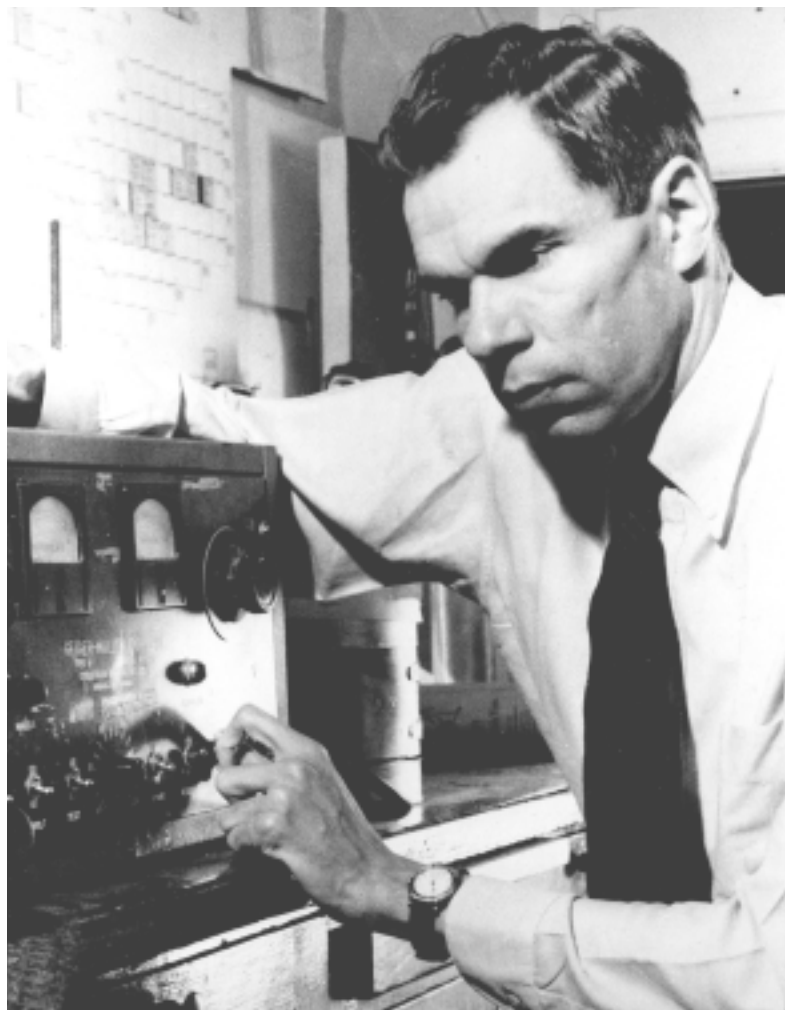


On February 25th, 1999, chemist, educator, administrator, humanitarian, and Nobel Prize recipient Glenn T. Seaborg died in his home in Lafayette, California, at the age of 86. Many know of the scientific accomplishments of the man who has become a legend, and anyone who has attended his lectures can attest to how informative and entertaining Seaborg was. He had an enticing, whimsical sense of humor and used this talent to drive home his points and to share his passion for “hard” science and his quest for discovery. Seaborg was the architect of the actinide series of the periodic table of elements and codiscoverer of 10 transuranium elements—one of which bears his name (element 106, seaborgium)—and of numerous radioisotopes. His work and achievements have touched many lives, and his discoveries and legacy will continue to touch many lives for generations to come.

Glenn T. Seaborg was born in Ishpeming, Michigan, on April 19th, 1912. His family moved to Los Angeles, California, where Seaborg was first exposed to science in high school. Later, he dedicated his life to this endeavor. Seaborg received his A.B. degree from the University of California (U.C.) at Los Angeles in 1934 and his Ph.D. in chemistry from U.C. at Berkeley in 1937. He served as a faculty member at Berkeley from 1939 until his death and was chancellor of that campus from 1958 to 1961.

In 1940, when Edwin M. McMillan, Seaborg’s fellow Berkeley researcher, was called away to the Massachusetts Institute of Technology to work on radar, young Seaborg was left in charge of the program to prepare new elements by bombarding uranium atoms with deuterons. In late 1940, working with Joseph Kennedy and graduate student Art Wahl, Seaborg succeeded in identifying element 94, now known as plutonium. A letter sent to Washington, DC, in 1941 and signed by Seaborg, McMillan, Kennedy, and Wahl described the discovery. But a self-imposed cover of secrecy shrouded the research because of the potential military applications of element 94.

In his lectures, Seaborg often noted that throughout 1941, the year that marked the beginning of the U.S. involvement in World War II, element 94 was referred to by the code name of “copper.” This name was satisfactory until it was necessary to use the real element copper in some of the experiments. The scientists circumvented the problem of distinguishing between the two elements by referring to element 94 as “copper” and to real copper as “honest-to-God copper!” The naming of element 94 followed the tradition of naming transuranium elements after consecutive planets in the solar system. Element 93 was dubbed neptunium (Np) after the planet Neptune, and element 94 was named plutonium (Pu). Seaborg and coworkers considered the name “plutium” but it “[d]idn’t roll off of the tongue like the name plutonium,” said Seaborg in one of his lectures. The obvious choice for the symbol would have been Pl, but facetiously, Seaborg suggested Pu, like the words a child would exclaim, “Pee-yoo!” when smelling something bad. Seaborg thought that he would receive a great deal of flak over that suggestion, but the naming committee accepted the symbol without a word.



Seaborg is at a Geiger-Müller counter and amplifier at Berkeley in 1941. A chart of isotopes with replaceable colored entry cards is on the wall in the background.

In the spring of 1941, it was determined that the newly discovered isotope plutonium-239 could undergo fission and had potential as a powerful nuclear-energy source. Consequently, Seaborg left Berkeley to head the University of Chicago's Metallurgical Laboratory (known as Met Lab) and develop the chemical separation process that would provide plutonium-239 for the Manhattan Project, which was aimed at creating a secret nuclear weapon. Still in Chicago after completion of the plutonium project, Seaborg focused his attention on looking for new elements heavier than plutonium.



At the White House, Seaborg is briefing President George Bush on cold fusion (April 14, 1989).

In an effort to prepare elements 95 and 96, now known as americium and curium, Seaborg and coworkers were unsuccessful in separating and identifying these elements from bombarded targets. Their failure was a result of assuming that the chemical properties of those elements resembled those of iridium and platinum, as suggested by their placement at that time in the d-block of the periodic table. Seaborg then considered that perhaps the actinides were in the wrong location in the periodic table and should actually be, like the lanthanides, a separate rare-earth-like series. Based on the assumption that elements 95 and 96 were rare-earth-like, Seaborg and coworkers successfully separated and identified americium and curium in 1945. Purely by chance, the announcement of the discovery of elements 95 and 96 did not take place as planned, at the 1945 American Chemical Society (ACS) meeting, but a few days earlier. Seaborg revealed the discovery on a nationally broadcast radio program, "The Quiz Kids." Seaborg subsequently prepared a communication for the periodical *Chemical and Engineering News*, proposing his actinide series theory. He ran the concept past some of his colleagues knowledgeable in inorganic chemistry, who told him something to the effect that, should he propose this revolutionary concept, he would ruin his reputation. "Fortunately, I really didn't have a reputation to ruin at that time, and even more fortunate, I was right," quipped Seaborg. He published the article and changed the appearance of the periodic table forever.

After World War II, Seaborg returned to Berkeley's chemistry department to direct the search for new elements at the U.C. Radiation Laboratory, now known as Lawrence Berkeley National Laboratory (LBNL). In 1951, Seaborg and Edwin McMillan shared the Nobel Prize in Chemistry for their discovery of plutonium and other elements. During his career, Seaborg codiscovered the actinide elements through nobelium (element 102), the transactinide element 106, seaborgium, and many new isotopes (including iodine-131, technetium-99m, cobalt-57, cobalt-60, iron-55, iron-59, zinc-65, cesium-137, manganese-54, antimony-124, californium-252, americium-241, plutonium-238, and the fissile isotopes plutonium-239 and uranium-233).

Seaborg was quite fond of telling the story (complete with the right accent) of how he was in his office at Berkeley one day, when he received a phone call from someone "claiming" to be the President of the United States. Curious and suspicious that his friends were pulling a joke on him, Seaborg listened. A man with a distinc-

tively Bostonian accent said, “Ahh, Professor Seaborg, thish ish-ah, Jack Kennedy.” Seaborg was highly amused and replied, “Yeah! Right, and who are you really?” The voice said, “I’m sorry, but this ah-really ish-ah Jack Kennedy, and I would like you to come to Washington and serve as the ah chairman of the Atomic Energy Commission!” Seaborg finally realized that this was no joke, went to Washington, and served as Chairman of the Commission from 1961–1971. He also served as scientific consultant to eleven U.S. Presidents—from Franklin D. Roosevelt to William J. Clinton.

Seaborg was always eager to welcome visitors, great and small, into his LBNL office to chat about current events, discuss some late-breaking research, or to counsel young scientists. He was always quick with a joke or a twist on words and had a sharp wit till the end. Seaborg’s office walls were covered with numerous photographs of himself with prominent scientists and great world leaders, as well as many of the U.S. Presidents he served. On one occasion, his staff faked an impressive photograph of Seaborg standing next to President Abraham Lincoln and unobtrusively placed it on his wall. The Lincoln photo remained unnoticed for some time until, one day, Seaborg was proudly showing a visitor his photographs and noticed this new one. He suddenly burst out laughing. More amusing was the fact that an obviously naive young student actually thought the photograph was authentic! “How old did she think I was?” Seaborg chuckled.

For all of the awards, prizes, and recognition that Seaborg received in his career, nothing surpassed the naming of element 106 as seaborgium.

Indeed, Seaborg was the first living scientist to be so recognized. “This is the greatest honor ever bestowed upon me,” he declared. A great deal of unnecessary controversy followed this announcement, along with helter-skelter renaming of the heaviest elements at the end of the periodic table. In effect, the International Union of Pure and Applied Chemistry (IUPAC) naming committee declared that no new elements could be named after living persons. This decision temporarily left the name seaborgium off the periodic table. Undaunted and maintaining his pervasive sense of humor, Seaborg joked that the IUPAC refused to name the element after him “because I was alive, and, furthermore, they could prove it!” In 1997, however, sanity prevailed, and the name seaborgium was reinstated for element 106. Seaborg’s immortality was thus secured for as long as there is civilization and a periodic table.

As an educator, Seaborg was tireless in his efforts to inspire young people in science. “A hard working individual will succeed where a lazy genius may fail,” he said to a young student concerned about her chances in science.

He was also tireless in informing the public about the benefits of nuclear energy and the use of radionuclides in industry, medicine, and the physical, chemical, and



(Top) To Glenn from his staff on his 81st anniversary.



(Bottom) John F. Kennedy and Glenn T. Seaborg during the President’s visit to the Nevada Test Site on December 8, 1962. This was one of Seaborg’s favorite pictures with President Kennedy.

biological sciences. He was one of the Manhattan Project scientists that advocated the use of the atomic bomb on a deserted island as a demonstration to Japan to end World War II.

Seaborg advocated a ban on nuclear weapons testing and argued for nuclear arms reduction and dismantlement. He strongly advocated the conversion of weapons-grade plutonium into mixed-oxide (MOX) fuel to “burn” in nuclear power reactors for peaceful purposes. In concert with the work of Russian counterparts, Seaborg’s work would help ensure a lasting peace after the Cold War and reduce threats of proliferation and potential acts of terrorism. “I was a codiscoverer of plutonium in 1941 at Berkeley. I have always felt a parental pride in its potential for good—its ability to provide the world with a clean energy source virtually forever. But I also am fully aware of the great threat it can pose in the wrong hands...” said Seaborg (1997)



The King of Sweden presents the Nobel Prize to Glenn T. Seaborg.

Seaborg served as member of the National Commission on Excellence in Education, was active in the ACS throughout his career, and served as president of the ACS in 1976. He was also president of the American Association for the Advancement of Science and Associate Director-at-Large at LBNL. His awards include the 1951 Nobel Prize, the ACS 1979 Priestley Medal, the 1991 Medal of Science, and the George C. Pimentel Award in chemical education in 1994. The

readers of *Chemical and Engineering News* voted Seaborg one of the “Top 75 Distinguished Contributors to the Chemical Enterprise” in 1998. His acceptance of this prestigious award at the ACS meeting in Boston marked one of his last public appearances. A legend has left us, but his legacy will live on forever. ■

Further Reading

Gutin, J. C. 1995. “The Man Who Would Be an Element.” In *San José Mercury News West Magazine*, March 5 Issue.

Hoffman, D. C., A. Ghiorso, and G. T. Seaborg. 2000. *The Transuranium People: The Inside Story*. London: Imperial College Press.

Jacobs, M. 1999. “In Memory of Glenn Seaborg.” *Chemical and Engineering News*. March 8 Issue, p. 5.

Seaborg, G. T. 1997. “Adopt Plutonium Policy of Mutual Assured Destruction.” *The Washington Post*. August 24 Issue.

Wilkinson, S. L. 1999. “A Legend Has Left Us.” In *Chemical and Engineering News*. March 8 Issue, p. 29.



(From left) David Clark, David Hobart, and Glenn Seaborg at a conference in Honolulu, Hawaii (December 1989).

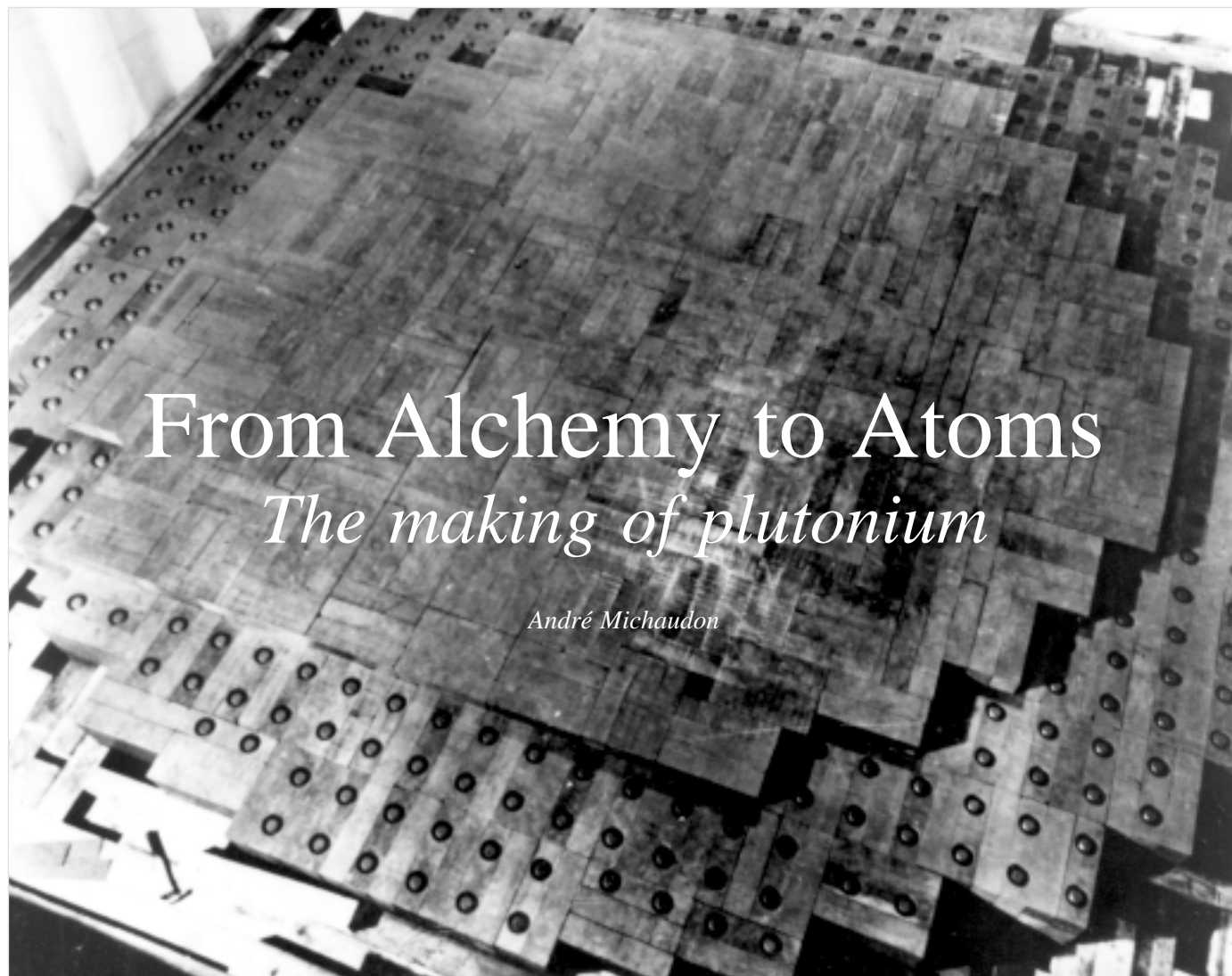
All photos are courtesy of Ernest Orlando Lawrence Berkeley National Laboratory.

David E. Hobart received a B.S. in chemistry from Rollins College in 1971 and a Ph.D. in analytical chemistry from the University of Tennessee, Knoxville, in 1981. After spending two years as a postdoctoral research associate at Oak Ridge National Laboratory, David became a technical staff member at Los Alamos National Laboratory in the Isotope and Nuclear Chemistry Division. In 1993, David served as group leader of the Actinide Geochemistry Group at Lawrence Berkeley National Laboratory. From 1995 to 1999, as a contract consultant, David assisted in the successful licensing of the Waste Isolation Pilot Plant (WIPP). He is now a technical lead in the Analytical Chemistry Group at Los Alamos and a participating guest scientist at the Seaborg Institute for Transactinium Science. His research interests include lanthanide and actinide element solution and solid state chemistries, speciation, solubility, spectroscopy, redox behavior, thermodynamics, and complexation.



Glenn Seaborg and the Discovery of Plutonium

- 1789** Klaproth discovers element 92, uranium.
- 1869** Mendeleev arranges the then known elements in a “periodic table.”
- 1895** Becquerel discovers that uranium undergoes radioactive decay.
- 1912** Seaborg is born in Ishpeming, Michigan, on April 19th.
- 1934** Fermi and coworkers irradiate uranium with neutrons and mistakenly believe they have produced transuranium elements.
- 1937** Seaborg receives his Ph.D. degree from the University of California (U.C.), Berkeley.
- 1938** Hahn, Meitner, and Strassmann discover nuclear fission by bombarding uranium with neutrons.
- 1939** Seaborg joins the faculty at U.C. Berkeley.
- 1940** McMillan and Abelson synthesize neptunium, element 93 (the first transuranic element), by bombarding uranium with slow neutrons.
- 1940-41** Seaborg, McMillan, Kennedy, and Wahl discover element 94, plutonium, by irradiating uranium with deuterons.
- 1941** Seaborg heads University of Chicago’s Metallurgical Laboratory (Met Lab) to provide quantities of pure plutonium for the Manhattan Project.
- 1944-45** Seaborg conceives and publishes the controversial “Actinide Concept.” Seaborg, James, Morgan, and Ghiorso discover americium and curium by using separation methods based on the Actinide Concept.
- 1945** The plutonium bomb is detonated at Trinity, in the desert near Alamogordo, New Mexico, on July 16th.
- 1946** Following his return to work at the U.C. Radiation Laboratory (now known as Lawrence Berkeley National Laboratory), Seaborg prematurely announces the discovery of elements 95 (americium) and 96 (curium) on the nationally broadcasted “Quiz Kids” radio program.
- 1945-50** Thompson, Street, Ghiorso, and Seaborg discover elements 97, berkelium, and 98, californium.
- 1951** Seaborg and Edwin McMillan win the Nobel Prize in chemistry for their research in transuranic elements.
- 1952-58** Ghiorso, Seaborg, and others discover elements 99 (einsteinium), 100 (fermium), 101 (mendelevium), and 102 (nobelium). The discovery of nobelium was shared by Donets et al.
- 1954** Seaborg becomes Associate Director of the Lawrence Radiation Laboratory.
- 1958** Seaborg is named Chancellor of U.C. Berkeley.
- 1961-71** Seaborg goes to Washington, D.C., to serve the nation as the chairman of the Atomic Energy Commission.
- 1971-97** Seaborg rejoins the staff at U.C. Berkeley and also serves as President of the American Chemical Society and the American Association for the Advancement of Science, Associate Director-at-Large at Lawrence Berkeley National Laboratory, member of the National Commission on Excellence in Education, and science advisor to eleven U.S. presidents.
- 1997** In honor of Seaborg’s contributions to science, element 106 is officially named “seaborgium.”
- 1999** Seaborg dies in his home in Lafayette, California, on February 25th at the age of 86.



From Alchemy to Atoms

The making of plutonium

André Michaudon

To this day, plutonium—the famous isotope plutonium-239 in particular—continues to play a crucial role in nuclear weapons and peaceful nuclear energy. Having atomic number $Z = 94$, plutonium is the next element after neptunium in the periodic table and is two elements up from uranium. Yet until 1940, no elements beyond uranium were known to exist. They were not found because all transuranic elements are radioactive, with lifetimes that are short compared with geologic times. While large quantities may have existed very early in Earth's history, all natural accumulations have long since disappeared.¹

The understanding of how to create plutonium and other transuranic ele-

ments was the result of several breakthroughs in nuclear physics in the 1930s, including the discovery of the neutron in 1932 and of artificial radioactivity in 1934. Those remarkable developments encouraged nuclear scientists, the modern-day alchemists, to pursue the lofty goal of reintroducing these elements to the Earth. But with the discovery of fission in 1938 came the potential to liberate huge amounts of nuclear energy. Once it was realized that plutonium-239 might undergo fission by slow neutrons, the erudite desire to simply create it was quickly superseded by another: to create enough material to build a weapon, one so powerful that it would change the affairs of man.

Chain Reactions

The year 1932 is considered the beginning of modern nuclear physics. In that *annus mirabilis*, the neutron was discovered by James Chadwick, the positron was identified by Carl Anderson, and the particle accelerator of John Cockroft and Ernest Walton was first used to perform artificial disintegrations of the atomic nucleus.

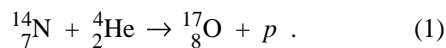
Before the discovery of the neutron,

¹Minute amounts of transuranic elements are continuously produced on Earth. Through a process described in this article, uranium in uranium ore will absorb neutrons from natural radioactivity and get transmuted into neptunium and plutonium. Also, transuranic elements formed in violent cosmic explosions may spread into the cosmos and fall to Earth.

several groups had shown that bombarding boron and beryllium with α -particles resulted in the emission of a penetrating radiation—one that could knock out protons from absorbers containing hydrogen. Through numerous experiments, Chadwick was able to demonstrate that this radiation was actually a neutral particle with a mass nearly identical to that of the proton.

Dubbed a neutron, such a particle had already been envisaged by Ernest Rutherford as early as 1920, but as a proton-electron combination. Together with Roys, Rutherford had already proved (in 1908) that α -particles were helium nuclei. By 1911, Rutherford showed that essentially the entire mass of an atom was contained in a tiny, positively charged nucleus. After the discovery of the neutron as an uncharged elementary particle, the nucleus was understood to consist of neutrons and protons. The number of protons Z determines the electric charge, or elemental identity, of the nucleus, whereas the mass number A determines the isotopic identity (see Figure 1).

Chadwick's discovery also opened the door to neutron-induced nuclear transmutations. The alchemists' dream of transmuting the elements had already become a reality as early as 1919, when Rutherford demonstrated that bombarding nuclei with α -particles resulted in reaction products that were different from the target nuclei. For example, nitrogen-14 was transformed into oxygen-17 by the reaction



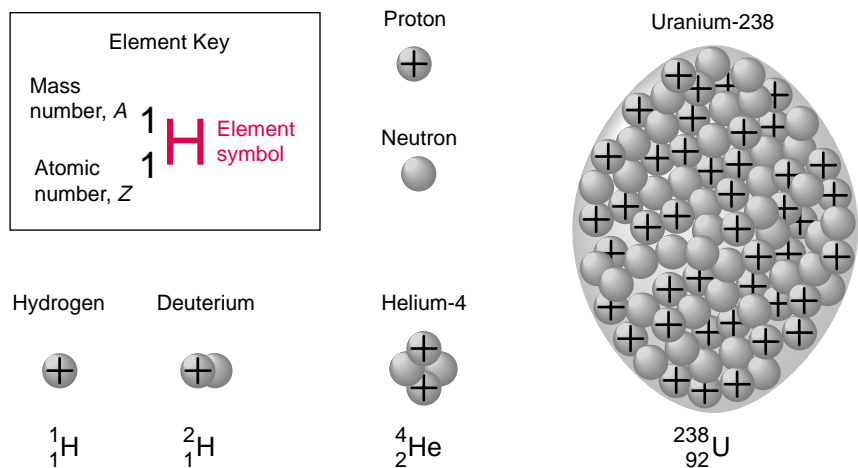
The α -particle (helium-4 nucleus) is absorbed by the nitrogen to create a fleeting, unstable nuclear state, which rapidly decays to oxygen-17 by emitting a proton. This reaction and the others known at the time were induced with positively charged projectiles—namely, protons or α -particles—whose energy had to be sufficient to overcome the

Periodic Table of the Elements—1941

Periodic Table of the Elements—1941

*Lanthanides

58	Ce	59	Pr	60	Nd	61	Pm	62	Sm	63	Eu	64	Gd	65	Tb	66	Dy	67	Ho	68	Er	69	Tm	70	Yb	71	Lu
----	----	----	----	----	----	----	----	----	----	----	----	----	----	----	----	----	----	----	----	----	----	----	----	----	----	----	----


Figure 1. Elements and Nuclei

The top portion of the figure shows the periodic table in 1941. Each column contains elements with similar chemical properties. Each row contains elements arranged in order of increasing atomic number Z , the number of protons in the atomic nucleus. In 1941, no elements beyond uranium had been identified, and thorium, protactinium, and uranium were thought to be transition metals. James Chadwick discovered the neutron, a neutral particle with nearly the same mass as the positively charged proton. His discovery led to a concise model of the nucleus. Each has Z protons, N neutrons, and a mass number $A = Z + N$. Hydrogen, the first element, has the simplest nucleus (a lone proton). Deuterium is an isotope of hydrogen. (Isotopes of the same element have the same number of protons but different numbers of neutrons.) The nucleus of the next element, helium, is also known as an α -particle. Nuclei increase in size roughly as $A^{1/3}$. Thus, uranium-238 (with 238 nucleons—protons plus neutrons) is a huge nucleus, and it is distorted like a football. Uranium has two common isotopes, uranium-235 and uranium-238.



James Chadwick

Coulomb repulsion from the target nucleus. But neutrons have no electric charge and, consequently, no Coulomb barrier to overcome. Therefore, they can penetrate matter and be absorbed by nuclei more easily than charged particles.

The first to realize that the neutron was also the key to releasing the energy embedded in the nucleus was Leo Szilard, a Hungarian physicist. On September 12, 1933, Szilard envisioned neutron-mediated chain reactions. A neutron could induce a nuclear reaction that would emit two or more neutrons and thus act as a neutron multiplier. This nuclear reaction would also liberate energy. Because they are uncharged, emitted neutrons would not lose energy

lard, a Hungarian physicist. On September 12, 1933, Szilard envisioned neutron-mediated chain reactions. A neutron could induce a nuclear reaction that would emit two or more neutrons and thus act as a neutron multiplier. This nuclear reaction would also liberate energy. Because they are uncharged, emitted neutrons would not lose energy

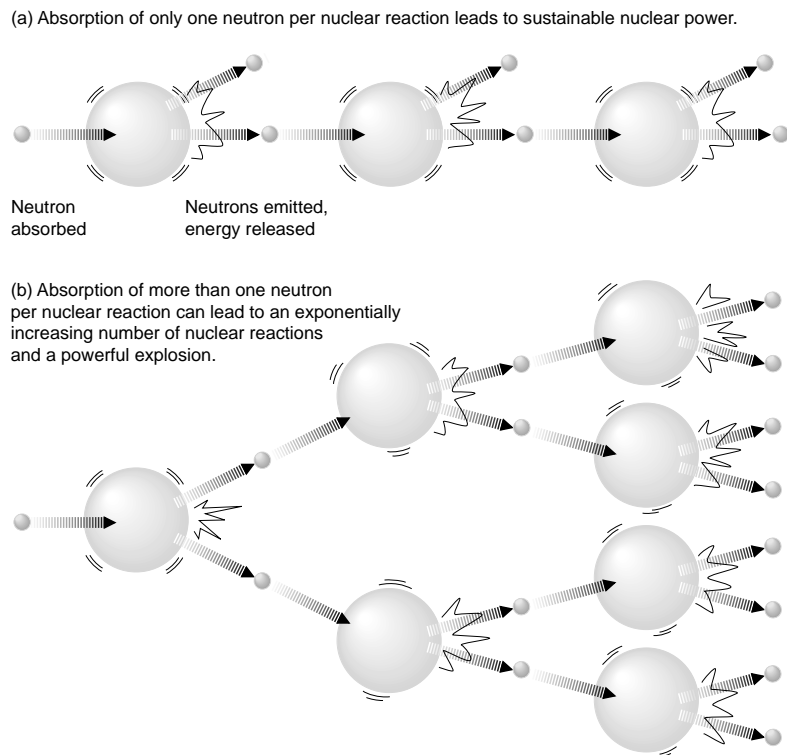


Figure 2. A Nuclear Chain Reaction

Leo Szilard realized that a self-sustaining chain reaction could occur if absorption of one neutron causes a nucleus to emit several others. Each reaction releases energy, and the amount of energy released per unit time depends on the rate at which emitted neutrons are reabsorbed, inducing more reactions. (a) If one neutron is reabsorbed per reaction on average, the chain proceeds in a linear fashion. This is the concept of a nuclear reactor, wherein the number of neutrons is purposely limited to keep the chain reaction under control. (b) If more than one neutron is reabsorbed, on average, the number of nuclear reactions increases geometrically. Without controls, the chain can grow so quickly and release so much energy that a massive explosion occurs.



Leo Szilard

to electrons in matter and would therefore race through a material until they collide with other nuclei. These neutrons could then induce similar reactions, again followed by neutron multiplication. The same process would continue with more and more reactions. If two neutrons were emitted, one reaction would be followed by two, which would be followed by four, then eight, sixteen, thirty-two, sixty-four, and so on. The number of reactions would increase geometrically, as would the total energy released. A self-sustaining chain reaction would be established, resulting in an enormous release of

nuclear energy (see Figure 2). If the neutrons were fast, each generation of the chain reaction would occur in a short time, and there would be many generations before the energy liberated by the process blew the material apart. A massive explosion would occur with a force millions of times greater than anything man had previously unleashed.

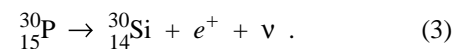
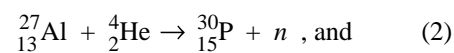
Harnessing nuclear energy was therefore inextricably linked to creating a nuclear bomb, and Szilard accepted this woeful connection as he began looking for elements that could act as neutron multipliers when bombarded by neutrons. He thought that beryllium, for

example, might emit two neutrons when it absorbed one. Szilard also realized that neutrons had to induce neutron-multiplying reactions before diffusing out of the material. Along those lines, Szilard introduced the concept of critical mass (of still unknown elements), or the minimum amount of material needed to sustain a chain reaction. Although Rutherford had stated that energy could not possibly be released from atomic nuclei, by 1934 Szilard had filed a patent on this subject.

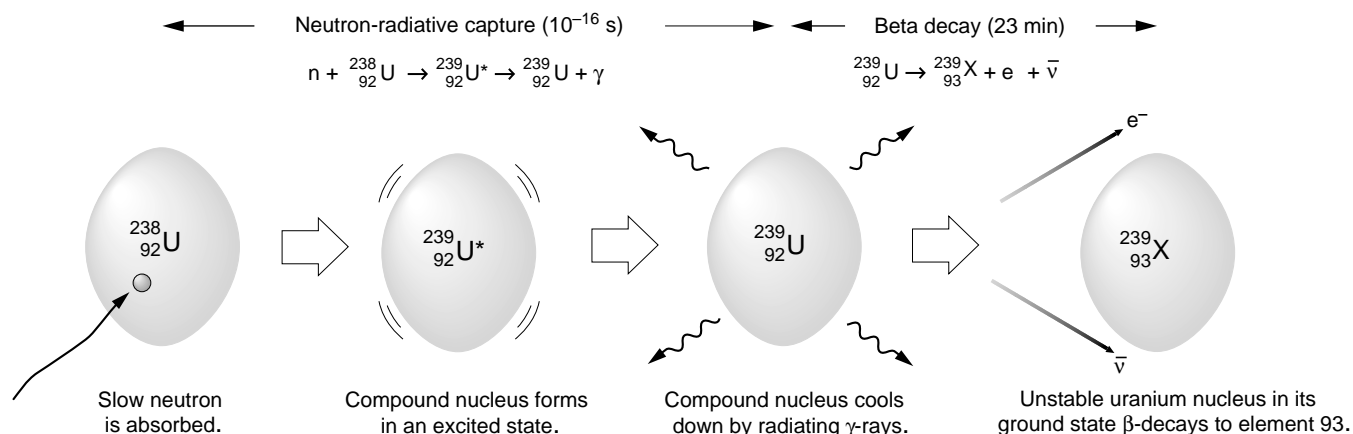
Nuclear Transmutations

Before Szilard began thinking about chain reactions, nuclear transmutations had been achieved but were initially thought to produce stable nuclei like the oxygen-17 of Reaction (1). In further studies, positrons were observed after light elements such as boron, aluminum, or magnesium had been bombarded with α -particles. Positrons (e^+) are the antimatter counterparts of electrons. They are positively charged and have a mass equal to that of the electron. Frederic Joliot and Irène Curie observed that positron emission continued after α -ray irradiation had been stopped. Furthermore, the number of emitted positrons decreased exponentially with time. The positron signal was therefore similar to what would be expected from the decay of a radioactive element.

Using a chemical precipitation method, Joliot and Curie separated the source of this persistent positron emission from an irradiated aluminum target and showed that the source was an unstable isotope of phosphorus that subsequently decayed into silicon-30 by positron emission:



Joliot and Curie had thus discovered artificial radioactivity (1934). Whereas



Enrico Fermi

Figure 3. Creating Transuranic Elements

Enrico Fermi discovered that irradiating elements with low-energy (slow) neutrons greatly increased the probability of neutron capture. Often, the result was the creation of an unstable nucleus that would radioactively decay. If uranium-238 captured a slow neutron, it would become the compound nucleus uranium-239* (an excited state of uranium-239), which would cool down to the ground state by emitting γ -rays. It was expected that uranium-239 would then undergo β -decay, wherein a neutron in uranium-239 decays into a proton, an electron, and an electron antineutrino, thus creating the first transuranic element, X-239, with atomic number $Z = 93$.

natural radioactivity had been observed in many of the heaviest elements (from thallium to uranium), artificially induced nuclear transmutations could now create new nuclei across the periodic table. Furthermore, Joliot-Curie had rigorously proved their result by chemically isolating their product. In this way, they established a precedent for identifying transmuted nuclei.

Spurred on by these remarkable events, several groups pursued using neutrons, rather than charged particles, to induce nuclear transmutations. The idea was given its greatest impetus in Rome, under Fermi's leadership. Beginning in early 1934, Fermi and his collaborators carried out a systematic study of nearly every element in the periodic table. Stable elements would be bombarded with neutrons, and Fermi would measure the activity, that is, the intensity of the radiation induced in the irradiated sample.

A major step forward occurred when Fermi and colleagues accidentally discovered that the activity increased dramatically when the incident neutrons were slowed down. Neutrons lose

energy when they scatter from hydrogen or other light elements, and the insertion of paraffin (which contains lots of hydrogen atoms) between a neutron source and the irradiated sample was sufficient to slow the neutrons down. Even neutrons that had slowed down to room temperature—so-called thermal neutrons with energies of only a fraction of an electron volt (eV)—would lead to a high activity.

The enhanced activity, an indication that many unstable nuclei were being created, was the result of neutron-radiative capture. A slow neutron can be absorbed by a target nucleus to form a relatively long-lived intermediate state known as the compound nucleus. (The compound nucleus model was proposed by Niels Bohr in 1936.) The binding energy of the absorbed neutron is converted into excitation energy of the compound nucleus, which quickly decays by γ -ray emission to its ground state (or sometimes to an isomeric state). The newly created nucleus—an isotope one mass unit higher than the target nucleus—can be unstable, in which case it decays after a characteris-

tic half-life by emitting either α -particles (α -decay) or β -particles (β -decay).

When neutron absorption is followed by β -decay, a neutron (or a proton) in the unstable nucleus transforms into a proton (neutron), creating a β -particle and a type of neutrino. If a neutron transforms, the β -particle is an electron and the neutrino an electron antineutrino, both of which flee the nucleus. The newly created proton remains in the nucleus, so that a new element—one atomic number higher but with the same mass number—is created. Neutron bombardment could therefore be used to produce transuranic elements. As seen in Figure 3, neutron irradiation of uranium-238 would create uranium-239, which was expected to β -decay to element X-239 with atomic number $Z = 93$.

Confident that he would produce the first transuranic element, Fermi tried his neutron source on uranium. But while he observed β -activity to come from the sample, direct confirmation of a new element escaped him. The chemistry of transuranic elements was not known at that time, and separation of β -emitters from irradiated samples

proved difficult. Using chemical separation techniques, Fermi could only prove that the activity did not come from uranium, lead, or any element between them in the periodic table. Fermi postulated that an unexplained β -activity with a half-life of 13 minutes came from a transuranic element, but in the absence of chemical proof would not go beyond this suggestion.

More troublesome was the fact that the radiations emitted by the neutron-activated samples were remarkably complex. Besides the 13-minute activity were several others that could not be identified nor simply interpreted in terms of transuranic radioactive decays.

In September 1934, Ida Noddack suggested that the complex radiations might be coming from nuclear products lighter than lead. Because lead has 10 protons less than uranium, Noddack was suggesting that absorption of a single low-energy neutron resulted in a substantial breakup of the uranium nucleus. This was unimaginable. At the time, all known nuclear reactions resulted in only minor changes of the nucleus. Noddack's suggestion was largely ignored and Fermi himself, after some calculations, patently dismissed the idea.

Noddack was correct however, and ironically, Fermi could have seen evidence for such a nuclear breakup within his own laboratory in early 1935. At that time, Fermi's group made another attempt to detect transuranic elements from irradiated uranium samples, using a recently built ionization chamber. They postulated that, if neutron absorption followed by β -decay produced transuranic nuclei and if those nuclei had a short half-life for α -decay, they would emit energetic α -particles (according to the Geiger-Nuttall law). To reduce low-energy background from natural α -radioactivity, the Italian scientists placed a thin aluminum foil between the uranium sample and the detector. While stopping low-energy α -particles of natural radioactivity, this foil would be partially transparent to the higher-energy α -particles that might be emitted from short-lived transuranic

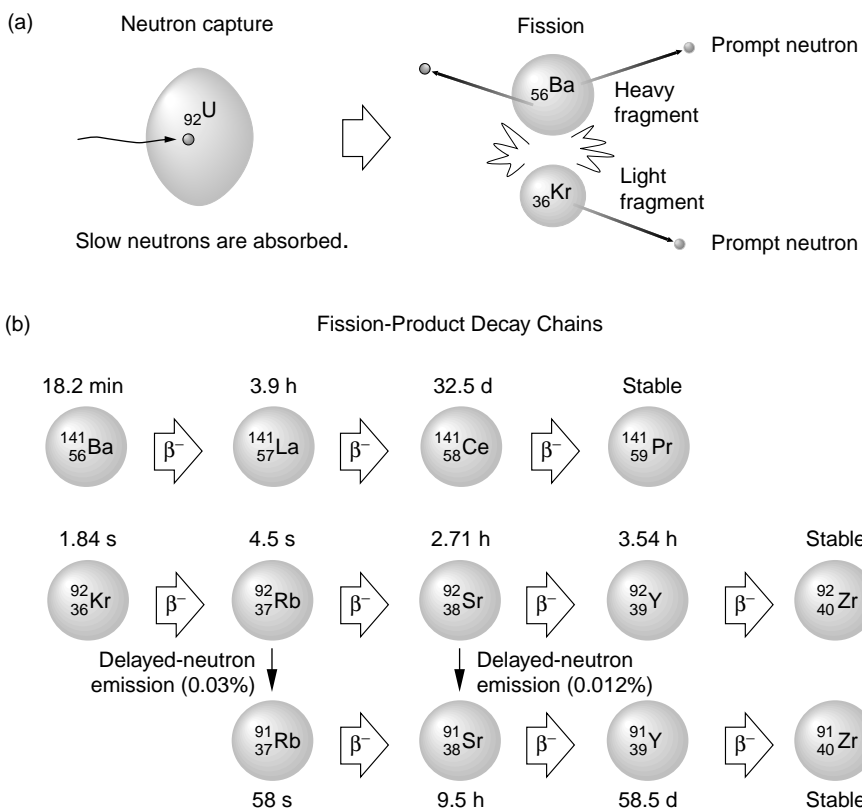
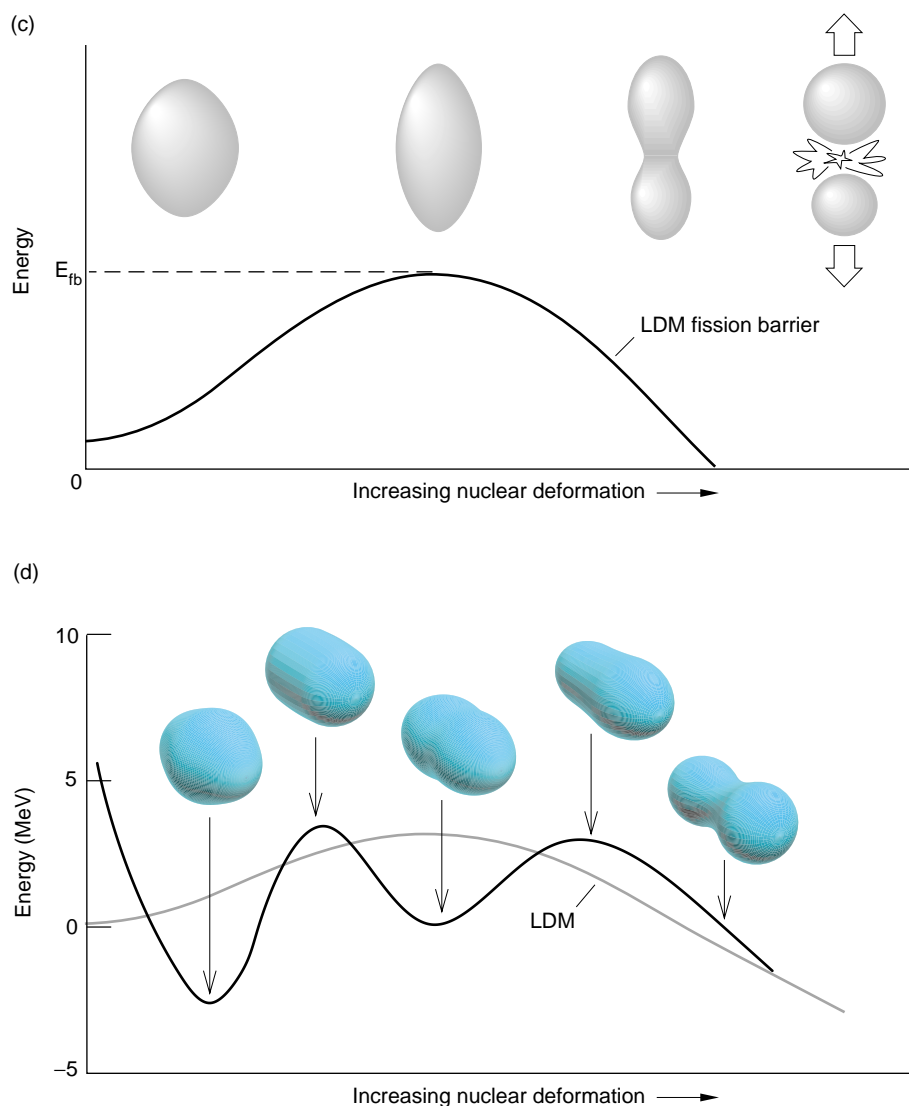


Figure 4. Fission

(a) Hahn and Strassmann chemically isolated radioactive barium from a neutron-irradiated sample of pure uranium. They realized that the uranium nucleus had split into two nuclei, one of which was barium. Fission could explain the confusing activity of neutron-irradiated uranium samples that was observed by groups in Rome, Paris, and Berlin. The fission fragments are born with a significant amount of excitation energy that is dissipated through prompt-neutron and γ -ray emission. Because de-excited fission products are far from the β -stability valley, they subsequently β -decay, and then always emit γ -rays and sometimes delayed neutrons. Also, fission does not produce a unique pair of primary fission fragments before prompt-neutron emission or a unique pair of fission products after prompt-neutron emission. (b) The β -decay chains of fission products are illustrated here for barium-141 ($Z = 56$) and krypton-92 ($Z = 36$). They were obtained after prompt emission of 3 neutrons from the primary fission fragments produced in uranium-235 neutron-induced fission. The γ -ray emission that follows β -decay is not shown. The β -decays from krypton-92 and rubidium-92 ($Z = 37$) are also followed by neutron emission (the delayed neutrons) from rubidium-92 and strontium-92, respectively. Later, experiments proved that both prompt



and delayed neutrons were emitted during fission. (c) Lise Meitner and Otto Frisch used the liquid drop model (LDM) to explain fission. The nucleus is considered to be a positively charged drop of fluid acted upon by two opposing forces. The attractive strong force holds the nucleons together and results in a surface tension that shapes the drop into a compact sphere. The electric (Coulomb) force tries to break the drop apart. As the size of the nucleus increases, the surface tension grows less rapidly than the long-range Coulomb force because the strong force has very limited range. The net result is that larger nuclei become increasingly unstable with respect to shape distortions. It requires additional energy to further distort the nucleus, seen by the fission barrier in the potential-energy diagram. When uranium absorbs a neutron, the excitation energy sets the nucleus oscillating, and the extra energy allows it to deform so much that it tops the fission barrier ($E > E_{fb}$). The nucleus breaks in two. The fission fragments carry off about 170 MeV of kinetic energy, more than a factor of 20 greater than the energy released by α - or β -decay, and tens of millions of times greater than that released by breaking chemical bonds. (d) A modern calculation of the fission barrier and nuclear deformation in plutonium-240 is shown here. The double hump (solid line) arises from considering the detailed quantum mechanics of the nucleus. (Calculation courtesy of Peter Möller, Los Alamos National Laboratory.)

elements. The experiment proved unsuccessful—no α -particles were detected—but fission products were undoubtedly produced and would have been detected if the aluminum foil had not been there to stop them!

The multitude of β -activities from neutron-irradiated uranium remained a mystery for quite a while. Indeed, by 1935, two other groups had observed similar startling results: Irene Curie and Pavel Savitch in Paris, and Lise Meitner, Otto Hahn, and Fritz Strassmann in Berlin. A 23-minute activity seemed to originate from uranium-239 and would imply the creation of X-239, but neither the Paris nor the Berlin scientists could explain their results convincingly.

All these studies and speculations took a radically different turn with the discovery of fission by Hahn and Strassmann in December 1938. (Lise Meitner, who was Jewish, had to flee the Nazi regime. She left Berlin in July.) Using radiochemical methods, the team clearly demonstrated that a pure uranium sample contained radioactive barium ($Z = 56$) after having been irradiated by neutrons. The barium could only come from the splitting, or fission, of the uranium nucleus. Fission could explain the confusing spectrum of radiation that was observed after neutron-induced activation of uranium—the radiation came in part from the great variety of fission fragments and their descendants (see Figure 4). Also, Szilard's vision of nuclear energy released from nuclear chain reactions suddenly switched from dream to reality. The prompt emission of neutrons from the hot fission fragments would provide the neutron multiplication mechanism needed for a chain reaction.

Fission

Although nuclear fission had escaped theoretical prediction, it was immediately explained in terms of existing nuclear models. Like neutron-radiative capture, neutron-induced fission was interpreted as one mode of decay of the compound nucleus. The details could easily

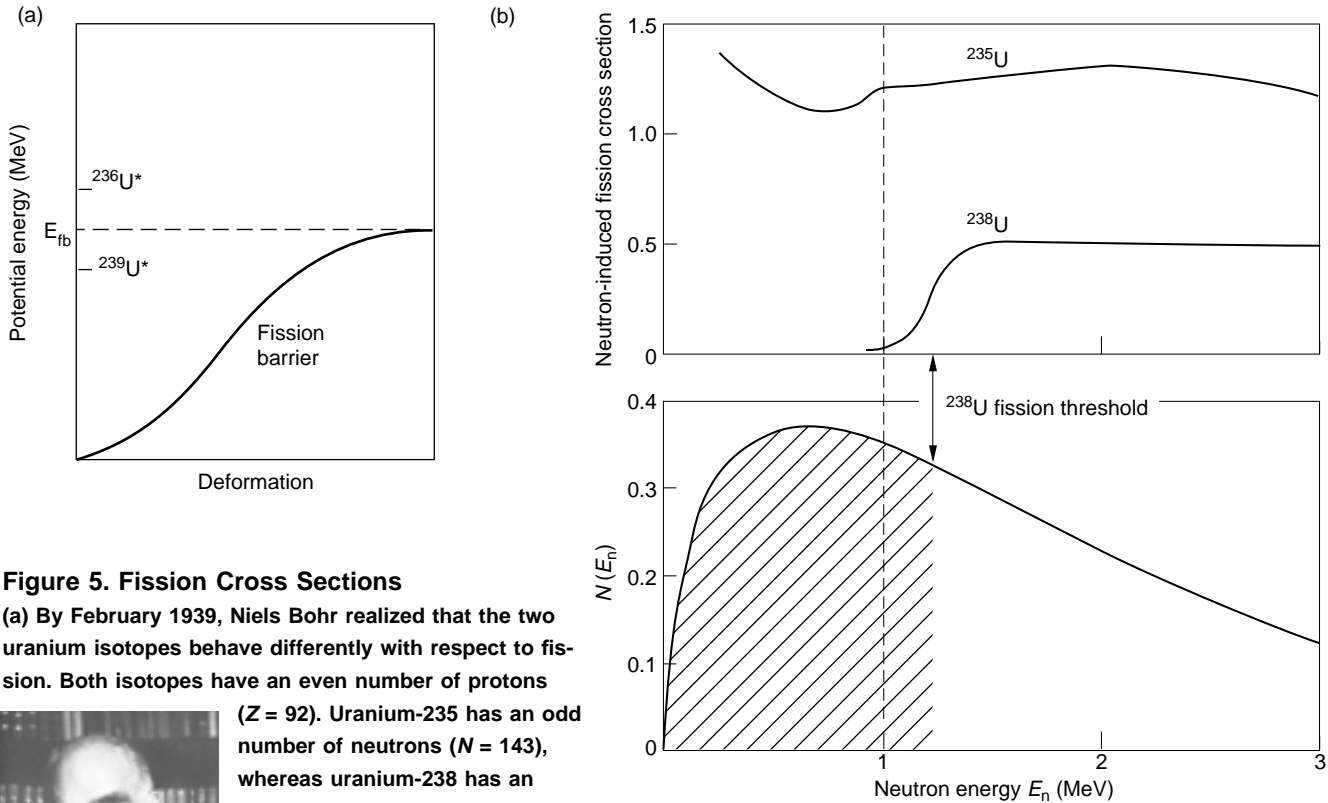


Figure 5. Fission Cross Sections

(a) By February 1939, Niels Bohr realized that the two uranium isotopes behave differently with respect to fission. Both isotopes have an even number of protons

($Z = 92$). Uranium-235 has an odd number of neutrons ($N = 143$), whereas uranium-238 has an even number ($N = 146$). When



Niels Bohr

uranium-238 absorbs a neutron, it forms the even-odd nucleus uranium-239 and gains about 4.8 MeV of binding energy, which goes into nuclear excitation. This amount of energy is not enough to top the fission barrier of about 6 MeV, so uranium-238 needs to absorb a neutron with kinetic energy greater than about 1 MeV in order to fission. But the strong force that binds the nucleus together “likes” to pair up protons and neutrons; hence, when uranium-235 absorbs a neutron to form the even-even nucleus uranium-236, it gains about 6.5 MeV of binding energy. That amount is more than enough to allow the excited nucleus to fission regardless of the incident-neutron energy. Uranium-235 is fissile. (b) The top graph shows the different fission cross-sections for uranium isotopes as a function of neutron energy. At thermal energies of about 0.025 eV, the uranium-235 cross section is about 500 barns. In the bottom graph, the energy spectrum of prompt neutrons emitted in the slow-neutron-induced fission of uranium-235 is quite wide, with an average energy of about 2 MeV. About half of these neutrons cannot induce fission in uranium-238 (hatched area). The fraction that cannot induce fission is even higher in nuclear devices because the neutrons lose energy through nuclear interaction with device components.

be described within the context of the liquid-drop model (LDM), originally put forward by George Gamow in 1928 and then given a much more serious development by Bohr in 1937. The LDM ignores the discrete nature of the protons and neutrons. Instead, it models the nucleus as an electrically charged liquid drop that can deform, vibrate, or split. It can also merge with another drop as in fusion reactions. The model provided a straightforward prescription for calculating basic nuclear properties, such as the mass and size of nuclei.

Meitner had remained in close com-

munication with the Berlin group, and within a week of the discovery of fission, she and her nephew Otto Frisch used the LDM to describe the process. In the heuristic picture presented in Figure 4, the drop-like compound nucleus deforms so much upon absorbing a neutron that it elongates into a dumbbell shape that finally scissions into two droplets, also known as fission fragments. (Frisch was the one who coined the term “fission” after a discussion with the American biologist William Arnold about the splitting of bacterial cells.) The electrically charged droplets repel

each other, and they instantly fly apart to rapidly reach about 170 million electron volts (MeV) of total kinetic energy after full acceleration. By mid-January of 1939, Frisch had observed these energetic fission fragments with an ionization chamber, and subsequently observed neutron-induced fission in thorium-232.

Experimental studies quickly focused on whether neutron emission accompanied fission. R. B. Roberts, R. C. Meyer, and P. Wang in the United States first showed that “delayed” neutrons were emitted following the β -decay of fission products. But other studies soon revealed

that, as the initial fission fragments form, they immediately release “prompt” neutrons. Fermi, Szilard and collaborators at Columbia University, and Joliot and his collaborators at Paris demonstrated that more than one prompt neutron was emitted during fission. Joliot and collaborators first reported this finding for uranium, with the precise average number of 3.5 ± 0.7 prompt neutrons. The modern figure is now an average of 2.4 prompt neutrons per fission.

Therefore, the prospect of nuclear energy liberated from fission chain reactions came within reach, but as understood by groups in the United States, Western Europe, the Soviet Union, and later Japan, the prospects of achieving an explosive chain reaction using natural uranium were dim. Shortly after the discovery of fission in thorium, Bohr had analyzed the available data and concluded that only uranium-235, not uranium-238, fissioned when bombarded with slow neutrons. Neutrons of any energy could induce the lighter isotope to fission (it was said to be a fissile material), whereas neutrons had to have energies on the order of 1 MeV or more to induce uranium-238 to fission.

The difference stems from the fact that uranium-235 has an odd number of neutrons and uranium-238 has an even number (both isotopes have an even number of protons). Thus, when uranium-235 absorbs a neutron, it pairs with the odd neutron, creating additional excitation energy (or pairing energy) and pushing the resulting uranium-236 compound nucleus above the fission barrier (see Figure 5). Uranium-238 has no unpaired neutron to match up with the absorbed neutron, and thus no pairing energy and no fission results until the incident neutron brings in the needed energy. Bohr and John Wheeler used the LDM to strengthen the argument in their 1939 landmark paper on fission. In March 1940, by comparing slow-neutron-induced fission in separated uranium isotopes, Alfred O. Nier et al. finally provided experimental proof that uranium-235 was fissile.

In a nuclear device, however, fast neutrons would have to induce enough fission reactions and release enough energy before the material is blown off. In this respect, the role of the two uranium isotopes strongly depends on the energy spectrum of fission neutrons. It was later shown that fission neutrons have a wide energy spectrum with an average energy of about 2 MeV. Given this spectrum, only half of these fission neutrons can induce fission in uranium-238 but this fraction would be even lower in a nuclear device, where the neutron energy is degraded through nuclear interactions with the components of the device (see Figure 5). Even with nuclear data available at that time, uranium-238 appeared unsuitable for nuclear detonations. Uranium-235 is much more suitable, but its isotopic abundance in natural uranium is only 0.7 percent. Thus, a bomb made of natural uranium would be very inefficient. In May 1940, French physicist Francis Perrin estimated the critical mass of natural uranium to be on the order of tens of tons. Shortly thereafter, more-precise calculations by Rudolf Peierls reduced this number to some tons. But similar calculations for pure uranium-235 made by Frisch and Peierls led to a critical mass of a few pounds for this isotope. This was well within the realm of a bomb.

Obtaining pure uranium-235, however, was a severe problem. Because the chemical properties of isotopes are identical, chemical separation of uranium-235 from uranium-238 was not possible. The fissile isotope could be obtained in large amounts only through a separation process that exploited the slight 1.2 percent difference in mass between uranium-235 and uranium-238. The most promising method was a gaseous diffusion method, which had previously been developed by the German physical chemist Klaus Clusius. But the equipment and facilities needed to achieve the separation would have to be constructed on a gigantic scale. Frisch estimated that approximately 100,000 tubes would be necessary. This number

was, however, drastically reduced to 5,000 tubes in subsequent developments. Still, with the European continent at war and the possibility that German scientists might be developing a bomb, plans were made to separate uranium isotopes and build a uranium-235 bomb.

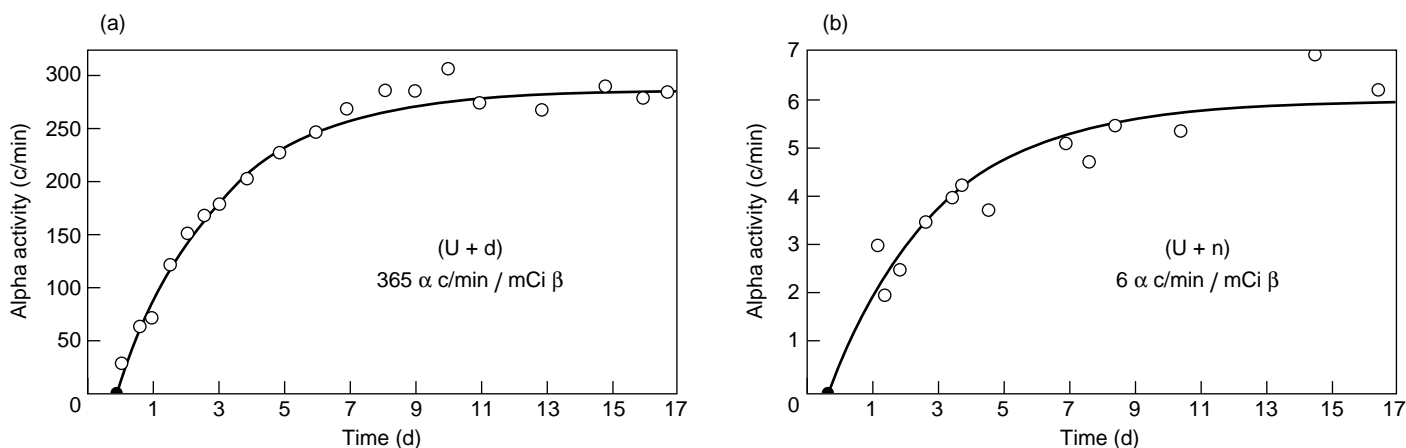
Almost as these plans were being drawn up, Bohr’s analysis of fissionable nuclei had another implication. The transuranic element 239 with $Z = 94$ protons and 145 neutrons, could also be fissile. In May 1940, Turner outlined this possibility in a letter to Szilard, who urged secrecy, for he realized that if element-239 with $Z = 94$ were created, subsequent separation of this transuranic element from uranium could be done through chemistry, thus obviating the difficult and expensive need to separate isotopes.

Seven months later, Fermi and Segrè came to the same conclusion. They also understood that the neutron flux within a nuclear reactor—a device that allows for a self-sustaining, controlled chain reaction—would be extremely high. Fermi had believed that a controlled chain reaction could be achieved in natural uranium if slow neutrons were used. He realized that neutron-radiative capture by the uranium-238 reactor fuel would then produce large quantities of element-239.

Studies on chain reactions were soon concentrated at Columbia. The use of graphite as a neutron moderator proved feasible when measurements of neutron attenuation in a large graphite assembly proved that the absorption of neutrons by carbon was lower than anticipated. Also, measurements of the multiplication factor in a lattice structure of graphite and uranium gave hope that a multiplication factor greater than 1 could be achieved. Therefore, a nuclear reactor could possibly be made with such a lattice.

The Discovery of Neptunium

The discovery of fission in the waning days of 1938 had cleared the way for more-precise studies on transuranic



Glenn Seaborg



Art Wahl

Figure 6. Discovery of Plutonium at Berkeley

After failing to detect plutonium-239 from the neptunium-239 sample produced in neutron-irradiated uranium, the Berkeley team irradiated uranium with deuterons. This deuteron-induced reaction produced two neptunium isotopes—neptunium-239 with a β -decay half-life of 2.3 days and neptunium-238 with a β -decay half-life of 2.1 days. The data in (a) show the α -activity in the neptunium sample from deuteron-irradiated uranium. It was observed with a new high-sensitivity ionization chamber. Although neptunium-238 contributed only 5% of the total β -activity, the product of that decay (plutonium-238) produced more than 98% of the observed α -activity. The α -activity in (b) originated from plutonium-239 that had grown in a neptunium sample from neutron-irradiated uranium. (Early experiments by McMillan and Abelson were not sensitive enough to detect this small plutonium-239 α -activity.)

elements. Taking into account the radioactivity of fission products, the German team confirmed that a previously observed β -activity with a 23-minute half-life actually came from uranium-239. While they failed to detect the first transuranic, their work helped an American research effort to succeed.

At Berkeley, Edwin McMillan began using cyclotron-produced neutrons to irradiate a thin foil of uranium. The energetic fission fragments would fly out of the foil. McMillan discovered that the foil retained some activity. In addition to the known 23-minute activity, indicative of uranium-239, another 2.3-day activity remained. Although this last activity could not have originated from fission fragments, the source behaved chemically like the rare earths, which are abundant in most fission fragments. This puzzling inconsistency led McMillan and Philip Abelson to repeat the experiment. The second time, they found that the 2.3-day activity came from an element with chemical properties different from

those of any other element but close to those of uranium.

Moreover, McMillan and Abelson demonstrated in May 1940 that the 2.3-day activity grew from uranium-239. They carefully purified the activated uranium sample and then obtained precipitates at 23-minute intervals, using equal amounts of cerium as a carrier. The activity of the precipitate was measured a day later to allow any uranium-239 to totally decay away while preserving most of the 2.3-day activity. The intensity of the latter activity showed a 23-minute exponential decay as a function of the time the precipitate was taken from the activated uranium sample. This demonstrated that uranium-239 decays with a 23-minute half-life to a new radioactive transuranic element that has a 2.3-day half-life.

McMillan and Abelson had thus discovered the first transuranic element with mass number 239 and atomic number $Z = 93$. They called it neptunium—after the planet Neptune, which was next in line beyond Uranus in the solar system.

Because the chemical properties of neptunium-239 were different from those of rare earths but close to those of uranium, McMillan and Abelson suggested for the first time that neptunium might belong to a second “rare earth” group of similar elements starting with uranium.

Their suggestion was prophetic. Glenn Seaborg later proved that this second “rare earth” group actually starts after actinium ($Z = 89$). Today, the group is referred to as the actinides. (See the box “The Actinide Concept” on page 368.)

The Discovery of Plutonium

The next step was the formation and identification of the transuranic element with $Z = 94$, soon to be dubbed “plutonium” even before its discovery. (The new element was named after Pluto, after the next planet beyond Neptune in the solar system.) As a follow-up of their studies on neptunium-239, McMillan and Abelson had already attempted to identify plutonium-239 as

the product of the 2.3-day decay of neptunium-239. Plutonium was expected to decay by emission of α - rather than β -particles, and so McMillan and Abelson looked for radiation from α -decay (or spontaneous fission²) from a purified sample of neptunium-239 obtained from neutron-irradiated uranium. They failed to detect any, and the negative result led them to postulate that the half-life for these two processes in plutonium-239 was greater than a million years.

McMillan left Berkeley shortly thereafter to help develop radar for the war effort while Kennedy, Seaborg, Segrè, and graduate student Art Wahl continued the pursuit of plutonium. A major step forward occurred when the group used the 60-inch cyclotron at Berkeley to irradiate uranium with deuterons with the hope that another plutonium isotope, shorter-lived than plutonium-239, could be formed, whose α -decay could be more easily detected. Studies of γ -rays and β -rays emitted from these deuteron-irradiated uranium samples revealed the presence of two neptunium isotopes—neptunium-239 and another that accounted for about 5 percent of the β -ray activity. This other isotope (later identified as neptunium-238) had a half-life of 2.1 days, close to that of neptunium-239. These neptunium samples also showed the existence of an α -emitter whose chemical properties were found to be different from those of neptunium, uranium, and all other known elements. The only possibility was that this α -emitter was the second transuranic element—plutonium—which was created by the β -decay of neptunium.

The growth of plutonium from the neptunium samples was later studied in the spring of 1941 from the radiation emitted by these samples with the help of a newly developed ionization chamber that could be placed behind the poles of the magnet. With this arrangement, β -rays were deflected away from the ionization chamber but

not the α -rays, which could then be more easily detected. The growth studies showed that the α -decay detected from neptunium chemically separated from deuteron-irradiated uranium samples came mostly from plutonium-238, which was produced by the β -decay of the neptunium-238. (see Figure 6). Although this decay accounted only for 5 percent of the total β -decay in the sample, the grown-in plutonium-238 has a relatively short half-life (88 years) and therefore a relatively high α -activity.

The same sensitive technique was used with neptunium samples chemically separated from neutron-irradiated uranium, and the α -ray activity from plutonium-239 was finally detected. Previous experiments with neutron-irradiated uranium were not sensitive enough to detect the relatively small α -activity of plutonium-239, which is due to its relatively long half-life (24,000 years).

Making Bulk Plutonium

Small but ponderable quantities of plutonium-239 (0.5 microgram), produced using cyclotrons, soon became available and were used to demonstrate that fission induced by thermal neutrons was larger by a factor of 1.28 than for uranium-235. A larger plutonium-239 sample (3.5 micrograms) was used in July 1941 to demonstrate that its fission cross section with fast neutrons was also larger than that for uranium-235. Although uncertainties still existed about the number of prompt fission neutrons emitted, it already appeared that plutonium-239 was a strong competitor to uranium-235 for nuclear explosives.

Then, a remarkable effort followed for making enough plutonium to build a bomb. At the beginning of 1942, all work on plutonium was supervised by the Metallurgical Laboratory at the University of Chicago and was placed under the leadership of Arthur Compton. Three missions were given to this laboratory: (1) to find a system using natural uranium in which a controlled chain reaction could take place, (2) to find a

chemical separation technique for plutonium formed in the irradiated uranium fuel, and (3) to obtain theoretical and experimental nuclear data relevant to an explosive chain reaction with uranium or plutonium.

The first objective, which had already been started by Fermi and Szilard at Columbia, gained momentum when the work shifted to the University of Chicago. In an abandoned squash court, Fermi assembled what he knew would be a self-sustaining nuclear reactor. Twenty-five feet high and 20 feet wide, the reactor was built from 349,263 kilograms of pure carbon cut as large graphite bricks. Blind holes were drilled into about a quarter of the bricks, and about 36,500 kilograms of uranium oxide and 5600 kilograms of pure uranium metal were pressed into thousands of fuel elements and dropped into the holes. An active brick layer contained an array of evenly spaced uranium plugs. These were sandwiched between two dead layers of solid graphite. As the two types of layers were alternated and stacked, a full 3-dimensional lattice of uranium plugs was formed (see photo on article's opening page).

Collisions with the carbon atoms in the graphite would slow the neutrons to thermal energies, whereupon they would diffuse until they encountered a uranium-235 atom. The chain reaction was held in check by cadmium control rods that would absorb neutrons without fissioning. As the number of layers increased, the reactor came increasingly close to critical mass. On December 2, 1942, with the final layers in place and the control rods removed, the reactor went critical and sustained the world's first manmade nuclear chain reaction.

Several steps were taken to meet the second objective—the bulk-scale chemical separation of plutonium from reactor fuel. By the end of 1942, about 500 micrograms of mostly plutonium-239 had been obtained from large quantities of neutron-irradiated uranium. The irradiation had been carried out at the cyclotrons at Berkeley and Wash-

²Spontaneous fission, wherein the nucleus undergoes fission without an initiating neutron, was discovered in uranium by George Flerov and K. A. Petrjak of the Soviet Union in June, 1940.

ington University. Chemical studies with these first milligram samples showed that it would be possible to separate plutonium from other elements in the reactor fuel.

Subsequent developments on a larger scale included the construction of a pilot nuclear plant at Clinton, Tennessee. This plant was to produce plutonium in quantities larger than the fraction of a milligram obtained from cyclotrons in order to demonstrate the possibility of plutonium separation on an industrial scale and study the biological effects of radiation. The Clinton reactor started operation on November 4, 1943, by producing 500 kilowatts, and it reached 1800 kilowatts in May 1944. Plutonium was separated from slugs of irradiated uranium fuel by remote control and behind thick shields. The first slug was treated for plutonium separation on December 20, 1943, and by March 1944, several grams of plutonium were available. These larger quantities of plutonium were also essential in obtaining nuclear data on plutonium.

The last step toward the production and separation of plutonium-239 was the construction of three nuclear piles on the Hanford site, whose purchase was approved by General Groves almost immediately after the creation of Met Lab. These reactors were designed to supply enough plutonium-239 for nuclear devices. The first pile started operation in September 1944, and the three piles were in operation by the summer of 1945.

Met Lab's third objective—obtaining precise nuclear data on plutonium-239—was met by experiments carried out at Berkeley and at the new, secret Los Alamos site, where J. Robert Oppenheimer had been appointed director. Although early data already indicated that plutonium would be fissile, more precise and sometimes new data were needed to design a weapon. Most of these data were obtained by measurements of fission cross sections and fission neutrons. The number of prompt neutrons emitted per fission of plutonium-239 proved to be higher than for uranium-235, which enhanced the potential for using plutonium-239 as a weapons material.

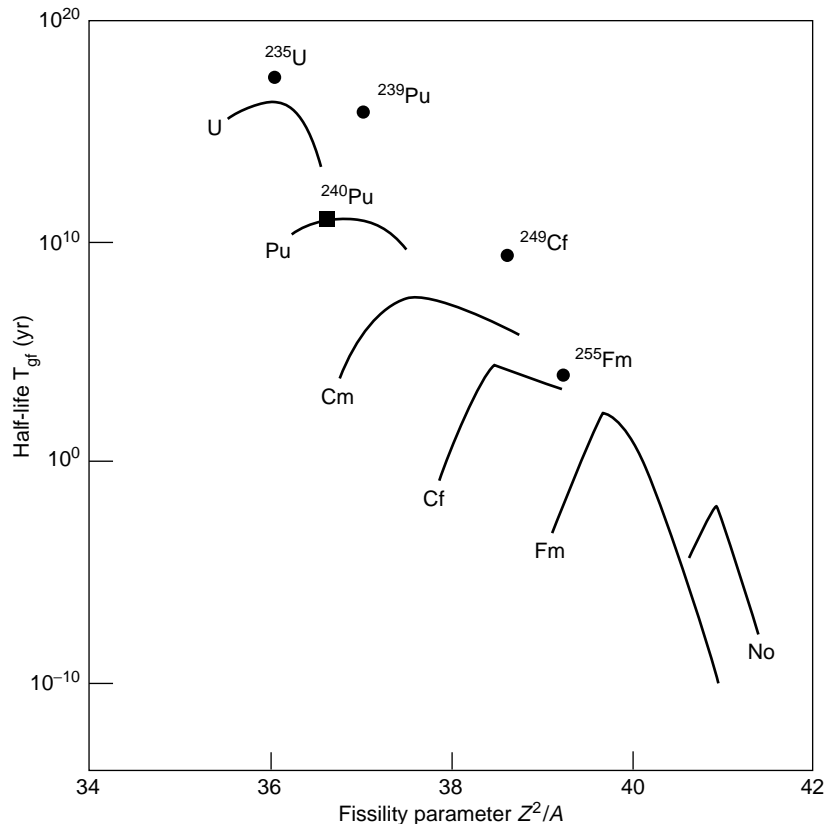


Figure 7. Spontaneous Fission Half-Lives

Experimental spontaneous-fission half-lives T_{gr} for isotopes of transuranic elements are plotted as a function of the fissility parameter Z^2/A (Z and A are the atomic and mass number, respectively, for each isotope). The solid lines are drawn through the half-lives of isotopes having even numbers of protons (Z) and neutrons (N). These even-even isotopes have spin 0 and positive parity. The solid square is for plutonium-240. The spontaneous fission half-lives of isotopes having even Z but odd N (such as uranium-235, plutonium-239, californium-249, and fermium-255), indicated by filled circles, are systematically higher than those for the even-even isotopes of the same element. These even-odd isotopes have a spin different from zero and a parity that can be either positive or negative. Their spontaneous-fission half-lives are longer because the fission barrier is higher to accommodate their spin and parity. Similarly, the α -decay half-life of even-odd isotopes is higher than for neighboring even-even isotopes (see the discussion of plutonium-238 and plutonium-239 in the text) because the α -particles have to penetrate a higher potential barrier—another manifestation of a spin effect—in these even-odd nuclei.

um-239 as a weapons material.

Although these plutonium-239 data were encouraging, other data seemed to indicate that plutonium-239 might not be used in the weapon that was being designed at Los Alamos. The plutonium samples obtained from the Clinton pilot plant were emitting an unexpectedly high neutron intensity from spontaneous fission, which had not been seen in the samples from the Berkeley cyclotron.

The high neutron flux and long irradiation times in the Clinton reactor allowed plutonium-239 itself to capture neutrons and become plutonium-240, which has a high spontaneous fission rate. The spontaneous fission rate in plutonium-239 is hindered by a spin effect that makes the fission barrier higher than for plutonium-240 (see Figure 7). The plutonium from the Hanford piles would have an isotopic composition similar to that of the

plutonium produced in the Clinton pile.

At the time of this discovery, the favored weapon design was the “gun-type” design, wherein a subcritical amount of fissile material would be literally fired—like a bullet from a gun—into another subcritical mass. The rapid assembly of a critical mass from these two fissile pieces would result in a run-away chain reaction and a nuclear explosion. But the ever-present emission of neutrons from spontaneous fission would cause premature fissioning of the plutonium before a critical mass was achieved. A plutonium gun-type weapon would thus fizzle.

The use of plutonium in a nuclear detonation, therefore, required the formation of the critical mass with a faster method. This new method was found with the implosion of a plutonium shell, whose efficiency was later demonstrated at the Alamogordo test. ■

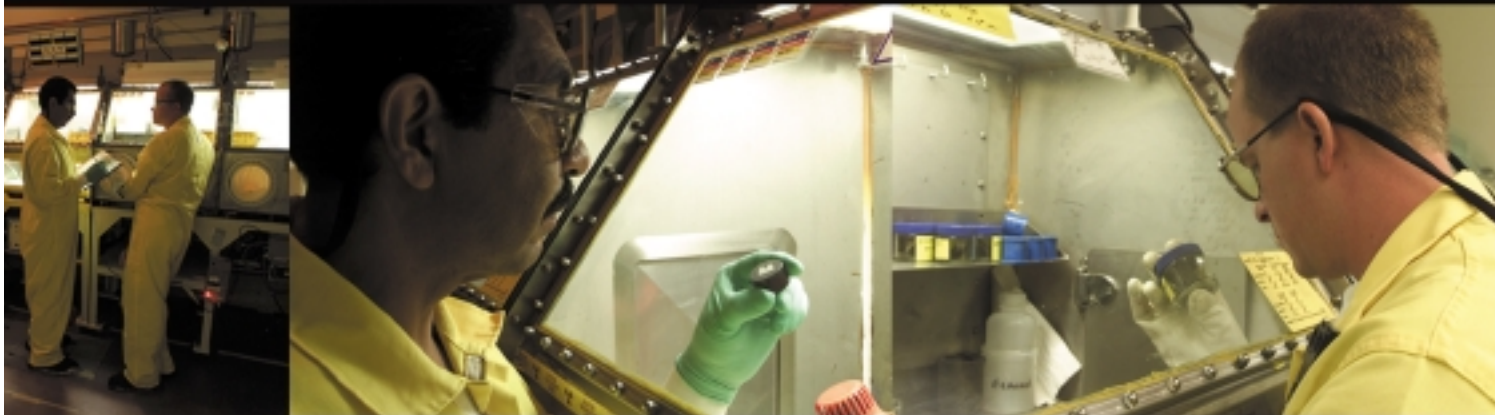
Further Reading

- Amaldi, E. 1984. *Physics Reports* **111**: 1.
- Bohr, N., and Wheeler, J. A. 1939. *Phys. Rev.* **56**: 426.
- Chamberlain, O., G. W. Farwell, and E. Segrè, 1944. “ $^{94}_{240}$ and Its Spontaneous Fission” (September). Los Alamos Scientific Laboratory report LAMS-131.
- Curie, I., and F. Joliot. 1934a. *Comptes Rendus* **198**: 254.
- . 1934b. *Comptes Rendus* **198**: 559.
- Fermi, E. 1934a. *Nature*. **133**: 757.
- . 1934b. *Nature*. **133**: 898.
- Flerov, G. N., and K. A. Petrjak 1940. *Phys. Rev.* **58**: 89.
- Frisch, O. R. 1939. *Nature* **143**: 276.
- Frisch, O. 1979. *What Little I Remember*. New York: Cambridge University Press.
- Goldschmidt, B. 1982. *La Recherche* **131** (13): 366.
- Hahn, O., and F. Strassmann. 1939. *Naturwissenschaften* **27**: 11.
- Holloway, D. 1994. *Stalin and the Bomb—the Soviet Union and Atomic Energy 1939–1956*. New Haven: Yale University Press.
- Hughes, J. 2000. *Phys. World*. July issue: 43.
- Joliot, F., and I. Curie. 1934. *Nature* **133**: 201.
- Kennedy, J. W., G. T. Seaborg, E. Segrè, and A. C. Wahl. 1946. *Phys. Rev.* **70**: 555.
- Lanouette, W., and B. Silard. 1994. *Genius in the Shadows, A Biography of Leo Szilard*. Chicago: The University of Chicago Press.
- McMillan, E., and P. H. Abelson. 1940. *Phys. Rev.* **57**: 1185.
- Meitner, L., and O. R. Frisch. 1939. *Nature* **143**: 239.
- Nier, A. O., E. T. Booth, J. R. Dunning, and A. V. Grosse. 1940. *Phys. Rev.* **57**: 546.
- Noddack, I. 1934. *Angew. Chemie* **47**: 653.
- Rhodes, R. 1987. *The Making of the Atomic Bomb*. New York: Simon & Schuster.
- Roberts, R., R. Meyer, and P. Wang. 1939. *Phys. Rev.* **55**: 510.
- Seaborg, G. T., and E. Segrè. 1947. *Nature* **4052**: 863.
- Kathren, R. L. J. B. Gough, and G. T. Benefiel, eds. 1994. *The Plutonium Story: The Journals of Professor Glenn T. Seaborg*. Columbus, OH: Battelle Press.
- Seaborg, G. T., E. M. McMillan, J. W. Kennedy, and A. C. Wahl. 1946. *Phys. Rev.* **69**: 367.
- Segré, E. 1970. *Enrico Fermi: Physicist*. Chicago: The University of Chicago Press.
- Segré, R. 1993. *A Mind Always in Motion: The Autobiography of Emilio Segrè*. Los Angeles: The University of California Press.
- Sime, R. L. 1998. *Scientific American*. January issue: 80.
- Szilard, L., and W. H. Zinn. 1939. *Phys. Rev.* **55**: 799.
- Turner, L. A. 1940. *Rev. Mod. Phys.* **12**: (1): 1.
- von Halban, H., F. Joliot, and L. Kowarski. 1939. *Nature* **143**: 680.
- Wahl, A. Discovery of Plutonium. 1990. In *Proceedings of the Robert A. Welch Foundation Conference on Chemical Research XXXIV, Fifty Years with Transuranium Elements*, October 22–23, Houston, Texas.
- Wheeler, J. A. 1989. *Ann. Rev. Nucl. Part. Sci.* **39**: xiii.

André Michaudon obtained two engineering degrees from the French Grandes Ecoles. He then served as Lieutenant in the French Navy. After a short appointment as a microwave research engineer in a private company, he had a long career at the Commissariat à l’Energie Atomique. He served as a group leader at the Centre d’Etudes Nucléaires at Saclay, where he pioneered neutron time-of-flight work with an electron linear accelerator



used as a pulsed-neutron source. Results of these studies, which focused on fission, formed the backbone of a Ph.D. thesis submitted at the Sorbonne. Intermediate resonances in the neptunium-237 subthreshold fission cross section were discovered in the course of these studies. Work at Saclay was interrupted by a sabbatical year of studies in theoretical nuclear physics at the Massachusetts Institute of Technology under the supervision of H. Feshbach. André then moved to Bruyères le Chatel, as Head of the Nuclear Physics Division, and later to Limeil as Deputy Head of the Department of General Physics. Later, André was appointed as French co-Director of the Institut Laue Langevin, in Grenoble. In this position, he was instrumental in obtaining the decision to build the European Synchrotron Research Facility at Grenoble. André Michaudon was a Professor of Nuclear Physics at the Institut des Sciences et Techniques Nucléaires. In addition, he was a member and chairman of many national and international scientific committees and served on the Executive Council of the European Science Foundation. He has been associated with the Los Alamos National Laboratory first as a consultant and then a staff member. André Michaudon is a Fellow of the American Physical Society and of the American Nuclear Society.



Plutonium and Health

How great is the risk?

George L. Voelz as told to Ileana G. Buican

At Los Alamos, some 100 men and women work with plutonium routinely in the only remaining plutonium-processing facility in the United States. As shown on these pages, from the moment they enter the facility, they follow rigid safety precautions. Protected by specially designed clothes, gloves, and goggles, these experts use glove boxes for their work with plutonium, handling even minute quantities with amazing dexterity. At the end of the day, their radiation levels are thoroughly monitored. Our people are well protected, but their work has its risks. Therefore, the Laboratory places the highest importance on providing more-accurate answers to the question of how dangerous plutonium is to human health. This article summarizes our findings over several decades.





Pictured here are Jason Lashley and Ramiro Pereyra, two of the contributors to this volume.

Ever since its discovery in 1941, plutonium has been known as a very dangerous material. Because it is capable of sustaining a nuclear chain reaction, plutonium is used in atomic weapons. Indeed, the first atomic bomb detonated at Trinity Site on July 16, 1945, was made of plutonium. At Trinity, scientists experienced firsthand the awesome power of the metal they had made. And feelings were profoundly ambivalent—joy at a remarkable scientific achievement and horror at having created a deadly instrument of war. J. Robert Oppenheimer was reminded of words from the Hindu scripture, the *Bhagavad-Gita*, “Now I am become Death, the destroyer of worlds.”

But concerns about plutonium are only partly related to its use in atomic weapons. Because it is radioactive, plutonium is dangerous when it finds its way into the human body. Driven by knowledge of the possible harmful health effects of plutonium, scientists carefully warned the public about them and established procedures to protect the workers in plutonium-processing facilities. In fact, their care was so extreme that many believe it was the scientists themselves who promoted an overstated idea that became well known at the end of the 1940s: “Plutonium is the most toxic substance known to man.”

In this article, we will give a realistic assessment of the health risks of plutonium. We will also stress that, because these risks were immediately anticipated, protective measures were taken soon after macroscopic amounts of plutonium had been produced. Most of the article, however, will explore related topics on plutonium that are of much concern to the general public: What are the health risks of plutonium? What is the likelihood of exposure to plutonium? What is the metabolism of plutonium once it enters the body?

The Health Risks of Plutonium

Background. Much of our early understanding of the health risks of plutonium comes from knowledge of the effects of radium, a radioactive element discovered by Marie Curie in 1899. (An element is radioactive if its nucleus is unstable, decays, and emits radiation.) Having a half-life¹ of 1620 years, radium-226 remains a relatively intense and constant source of radiation for hundreds of years. These features triggered its use in the treatment of cancer as early as 1906. Applicators that contained radium salts would be placed on the surface of tumors to shrink or eliminate them. When scientists later discovered that the radiation penetrating the applicators was primarily composed of gamma rays from the daughter nuclei of radium decay, other gamma-emitting radioisotopes replaced radium in this application. The new radioisotopes became available from nuclear reactors during the 1960s.

But the use of radium as a cure for cancer was so much publicized in the press at the time that people thought its healing powers had no limits. Radium became known as the elixir of life and a cure for every ailment. Even when stories surfaced about the dangers of radium’s “emanations,” people would still hail the new element as a “miracle.”

Radium-laced water, radium baths, or radium-containing facial creams were the latest fashion throughout Europe and the United States in the first decades of the 20th century. Thousands of people were exposed to this element before 1932. Whatever the merits of low doses of radium, the tragic effects of high-dose exposures became evident after only a few years.

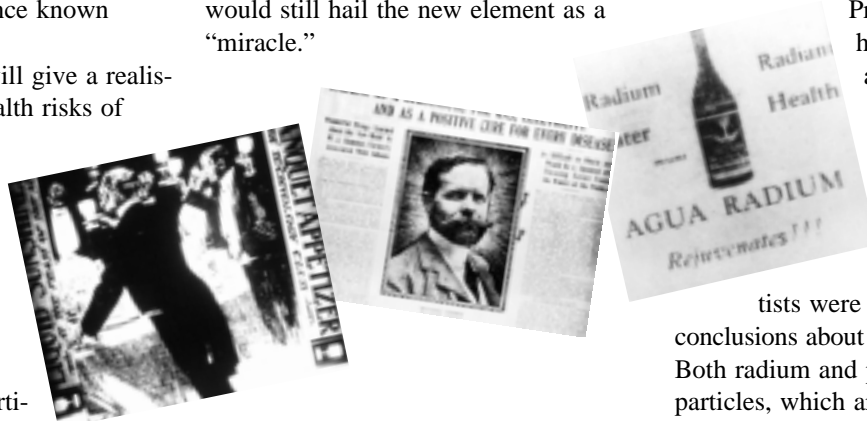
Acute cases of radium poisoning ended in rapid death, whereas other cases followed a much slower course: Victims suffered from infections of the jaw bones, pathological bone fractures, or cancers of the bone. The stories of those who had been exposed to radium—the young radium-dial workers being best known among them—made a deep impression on the scientists and contributed to awakening the public to the dangers of radium. (See “Radium—The Benchmark of Alpha Emitters” in *Los Alamos Science* No. 23, 1995.)

Radium was considered so dangerous that the National Bureau of Standards formed a nine-member committee to come up with an occupational standard for radium. On May 2, 1941, the standard for radium-226 was adopted—only two months before the discovery of plutonium. The publicity regarding the new standard alerted sci-

entists on the Manhattan Project to the potential hazards of plutonium, a radioisotope similar to radium. Gram for gram, plutonium would be roughly as dangerous as radium. By extrapolation, the sci-

tists were able to draw conclusions about the risks of plutonium. Both radium and plutonium emit alpha particles, which are positively charged helium nuclei ejected during radioactive decay. Helium nuclei are doubly charged because they are composed of two protons and two neutrons.

Tunneled out of a nucleus with a kinetic energy of about 5 million electron volts (MeV), the alpha particles



¹ The half-life of a radioisotope is the time it takes for half the number of atoms present to decay into another element and release particulate radiation (alpha or beta particles) and electromagnetic radiation (gamma rays). It will take 1620 years for half a quantity of radium-226 to decay, and another 1620 years for half of the remaining half to decay, and so on.

from plutonium-239 move at a speed of about 1.5×10^7 meters per second (5 percent of the speed of light). Because of their relatively low speed and their double charge, the alpha particles travel only a short distance, depositing their energy by ionization—they collide with molecules, break those molecules apart through electrical forces, and leave a trail of ion pairs in their wake.

The density of the ion pairs is essentially the same for most of the distance covered by the alphas but then increases sharply for an instant, as the particles seemingly “stumble” and dump—all at once—what is left of their energy. As shown in Figure 1(a), their travel has come to a halt. It has been much like the journey of a person running through sand—at first the run is smooth, progress then turns awkward, and the stop comes with a stumble. In air, alphas travel only 3 to 5 centimeters and in living tissue only about 30 micrometers (which is equal to 3 to 5 cell diameters) before they expend their energy and come to rest. The latter distance is less than the thinnest part of the epidermis (the dead layer of external skin cells). It is also less than the thickness of a standard piece of paper (about 100 micrometers). Fortunately, therefore, the penetration power of alpha particles is limited. A mere sheet of paper or the outer layers of our skin will block their passage—see Figure 1(b). To be harmful, alpha emitters have to be inside the body, but there are other types of radiation—

x-rays, gamma rays, and beta particles—that are harmful by hitting the body from the outside. They deposit their energies by ionization as well. The amount of energy for external radiation depends on the particle. Energy ranges for x-rays vary from less than 30 kilo-electron-volts (keV) to 25 MeV; for gamma rays, from 1 keV to 10 MeV; and for beta particles, from 1 keV to 2 MeV. Unlike alpha particles, x-rays, gammas, and betas generally travel farther and leave a less-dense track of ion pairs in their wake. For all types of ionizing radiation, the effects depend on

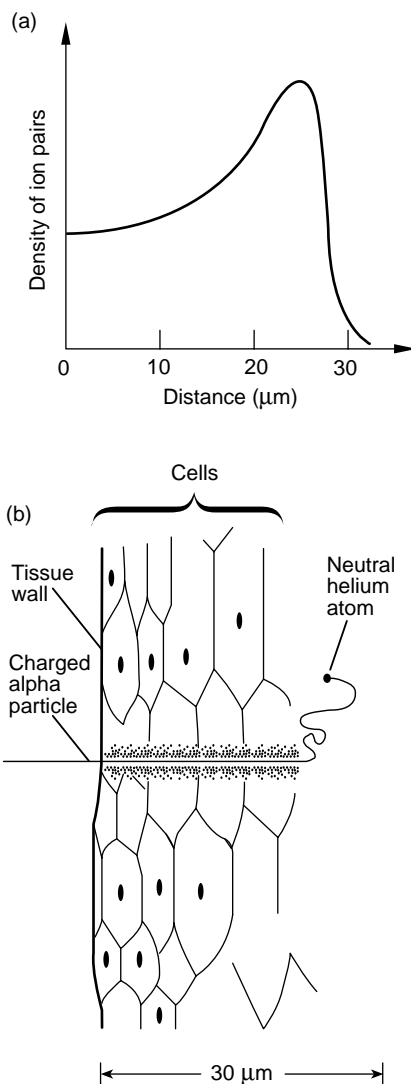


Figure 1. Emitters of α -Particles
(a) The density of the ion pairs created as the alphas pass through a substance or through air is essentially the same for most of the distance covered by the alphas but then increases sharply as the particles dump, all at once, what is left of their energy. (b) Emitted with an energy of about 5 MeV, plutonium α -particles travel in air 3 to 5 cm and in living tissue about 30 μm before they expend their energy and come to rest. A mere sheet of paper (typically about 100 μm thick) or the outer layers of intact skin will block their passage. Therefore, when plutonium (or any other α -emitter) is external to the body, it is not a health hazard.

the dose. High radiation doses usually manifest their effects soon after a person has been exposed. These effects are deterministic, or predictable, and their severity increases with dose. External radiation may cause skin burns, a temporary decrease in the number of blood cells, cataracts,² and even death—only a few possible health effects triggered by the severe dysfunction or death of large numbers of cells.

If enough cells are involved, tissues may be affected or entire organs may be impaired. Early symptoms of acute external-radiation doses are fatigue, nausea, and vomiting. Radiation primarily affects systems that contain rapidly dividing cells, such as the blood-forming system (whose cells originate from the bone marrow) or the gastrointestinal system (the cells that line the small intestine). It also affects the central nervous system. For example, bone-marrow stem cells can die when they are irradiated. Their death diminishes or stops the resupply of circulating red and white blood cells and other blood constituents. After about three weeks, the reduction in blood cell supply leads to immune deficiencies, infections, fever, bleeding, and even death unless the bone marrow starts to regenerate.

At lower doses, acute radiation effects become less noticeable, and below certain levels of exposure, effects cannot be predicted. It is at these low levels of exposure that stochastic, or probabilistic, effects become apparent. Cancer is best known among them. Ionizing radiation of any kind can lead to alterations of a living cell's genetic makeup, and sometimes those alterations trigger the uncontrolled growth and multiplication of that cell's progeny, more commonly known as cancer. Stochastic effects occur randomly and are assumed to have no threshold dose. Their probability increases with dose. Their severity, however, does not. Moreover, there is

² Cataracts are densities that form within the eye lens and do not allow the light to penetrate.

a substantial delay between the time of exposure and the appearance of the effect. If the effect is cancer, the delay ranges from several years for leukemia to decades for solid tumors.

Plutonium Toxicity. It is important to remember that, because their power of penetration is limited, alpha emitters are hazardous to human health only when they have found their way into the body. When inhaled, ingested, or passed into the blood stream through a wound, plutonium deposits in the lung, liver, or bones. Only about 10 percent of it is distributed to other organs. The plutonium atoms remain in the body for many decades, a fraction of them emitting alpha ionizing radiation and damaging the surrounding cells. The long radioactive half-lives of the plutonium isotopes and the amounts retained in the body make plutonium a long-term source of radiation to nearby cells and thus a biological hazard.

The half-life of plutonium-239 is 24,065 years. This half-life is short enough that 1 microgram of material will undergo more than 2000 decay events per second, but it is long enough to allow that microgram to decay at an approximately constant rate for thousands of years. If plutonium had uranium's half-life of 4 billion years, there would be so few decays over the span of a human's lifetime that the radiological toxicity of plutonium would be much less severe.³ However, that is not the case.

No humans have ever died from acute toxicity due to plutonium uptake.⁴ Nevertheless, lethal doses⁵ have been estimated from research on dogs, rats, and mice. Animal studies indicate that a few milligrams of plutonium per

kilogram of tissue is a lethal dose. For example, the LD₅₀(30) for dogs after intravenous injection of plutonium is about 0.32 milligram per kilogram of tissue. Assuming this animal dose also applies to humans, an LD₅₀(30) by intravenous injection for an average human of 70 kilograms would be about 22 milligrams. By inhalation, the uptake would have to be about 4 times higher.

Because the levels of plutonium exposure have been kept extremely low, even cancer cannot be linked to such exposure with any certainty in epidemiological studies⁶ of workers in the United States. So far, only one plutonium worker in the United States has died of a rare bone cancer, which may have been caused by exposure to plutonium. But epidemiological studies are not very sensitive to low risks, especially because the number of plutonium workers is small. As a precaution in setting radiation standards, the International Commission on Radiation Protection (ICRP) assumes that some risk may be involved in any exposure.

Although dangerous, plutonium is not "the most toxic substance known to man." On a weight-by-weight basis, plutonium is less toxic than the unforgiving bacterial toxins that cause botulism, tetanus, and anthrax. And yet, plutonium's position is frighteningly high on the lethal ladder. A few millionths of a gram (or a few micrograms) distributed through the lungs, liver, or bones may increase the risk for developing cancer in those organs. Airborne, soluble chemical compounds of plutonium are considered so dangerous by the Department of Energy (DOE) that the maximum permissible occupational concentration in air is an infinitesimal 32 trillionths of a gram per cubic meter! By comparison, the national standard for air concentrations of inorganic lead is 50 millionths of a gram per cubic

meter, which suggests that inorganic lead is a million times less dangerous by weight than plutonium.

The Plutonium Standard. By 1945, when plutonium was being produced in kilogram quantities to enable the development of a plutonium-implosion bomb that would help put an end to the war, scientists had become sensitive to the risks of radiation, particularly through previous experience with radium, and were educating the workers about those risks.

Moreover, the experience with radium also provided a quantitative basis for the creation of a plutonium standard. Robert Stone, the head of the Plutonium Project Health Division at the Metallurgical Laboratory (Met Lab) in Chicago,⁷ made the earliest estimate of a permissible plutonium body burden—the total amount of plutonium that can be present in the body over a lifetime without causing ill effects—by scaling the radium standard on the basis of the radiological differences between radium and plutonium. Those included differences in their radioactivities⁸ and those of their daughter nuclei and the difference in the average energy of their alpha particles. Results indicated that, gram for gram, plutonium was less toxic than radium by a factor of 50, and the permissible body burden was therefore set to 5 micrograms, or 0.3 microcurie.⁹

In July 1945, in the wake of disturbing animal experiments, which

⁷ In 1942, A. H. Compton consolidated the Plutonium Project at the University of Chicago under the cryptic name of Met Lab, which was to become one of the important sites of the Manhattan Project. The Met Lab's goals were to demonstrate a nuclear chain reaction for plutonium-239 using natural uranium and to develop chemical procedures for isolating the plutonium that would be produced in the reactor fuel.

⁸ Radioactivity is the rate at which a radionuclide decays and emits radiation. That rate is expressed as a number of disintegrations per second and depends on the material's half-life and on the amount of material present.

⁹ The quantity of plutonium present may be expressed either by weight (for example, in micrograms) or by radioactivity (for example, in microcuries). Because 5 micrograms of plutonium has a radioactivity of 0.3 microcurie, that quantity of plutonium may be expressed either way.

³ Uranium is also much more soluble than plutonium and leaves the body rapidly.

⁴ Plutonium uptake is the amount of the metal retained by the body after some has been rapidly eliminated from the lungs and gastrointestinal tract, whereas plutonium intake is the total amount of plutonium that enters a person's body.

⁵ The amount of material that causes death in 50 percent of the animals after n days is known as the LD₅₀(n), that is, the lethal dose 50 percent.

⁶ Epidemiology is the study of the number and distribution of health events in a given population.

Units of Radiation Dose

To measure the absorbed dose of radiation from sources external to the body (for example, beta, gamma, or x-ray emissions), health physicists calculate the amount of energy absorbed per kilogram of tissue for specific organs or the whole body. The unit of energy used is the joule, and 1 joule = 10^6 ergs. The absorbed dose is called a gray,* and 1 gray is the deposition of 1 joule of energy per kilogram of tissue. An earlier conventional unit for this same measurement was the radiation absorbed dose (rad), and 100 rad = 1 gray.

The biological damage done by 1 gray of ionizing radiation depends on the type and energy of that radiation. The more energy carried by the radiation and deposited in the tissue, the more damage done to the cells. However, the different types of radiation are not equally effective at producing biological damage. For example, 1 gray of neutron radiation is 2 to over 20 times more damaging than 1 gray of gamma radiation. To account for biological effects, health physicists multiply the absorbed dose (given in gray) by appropriate weighting factors and obtain an adjusted dose that has the same biological effect for different types and energies of radiation. The unit for this adjusted dose is called a sievert. An earlier conventional unit was the roentgen equivalent man (rem), and 100 rem = 1 sievert.

Doses from radioactive sources inside the body depend on the amount of the radionuclide in the body. And that amount is inferred from the radionuclide's activity, which is the number of decays per second. For external radiation sources (x-rays, gammas, or betas), the radioactivity is measured with dosimeters; for alpha emitters, it is inferred from measurements of the radioactivity of excreta, such as urine or fecal samples; and for gamma radiation coming from a person's body, it is measured by whole-body counting. The person is placed in a shielded room whose background radiation is low. Gamma radiation penetrates a detection crystal, excites a scintillator, and gives a direct measure of the person's internal gamma radioactivity. The unit of radioactivity is the becquerel, and 1 becquerel = 1 disintegrating atom per second. A historical unit for measuring the radioactivity in the body is the curie (1 curie = 37×10^9 becquerels).

To obtain doses from the amount of radionuclide in the body, health physicists use biokinetic models. These models take into account the radioactive half-life of the radionuclide, the type and energy of the radiation the radionuclide emits, the metabolism it undergoes once it is in the body, and the time it takes for half the amount of the radionuclide (or half time) to leave the body. Because internal doses to organs are often nonuniform, the composite health detriments from them are converted to a value that is equivalent to an equal health detriment from an external radiation dose to the whole body. This adjusted internal dose is called effective dose equivalent, or simply effective dose, and is distributed over the period in which the radionuclide is present in the body. And the sum of these doses over future years is called the committed dose. The committed dose generally spans 50 years for occupational exposures and 70 years for children and the general population.

* All the modern radiation units described in this box were named after scientists in radiation research.

indicated that plutonium was distributed in bones differently and more dangerously than radium, a group of scientists—among whom were Drs.

H. Friedell, L. H. Hempelmann, J. W. Kennedy, and W. H. Langham—met at Los Alamos to discuss these results. The outcome of this meeting was that the 5-microgram standard was reduced by a factor of 5. The permissible body burden for plutonium was thus set to 1 microgram, or 0.06 microcurie. This limit was intended to better protect plutonium workers in the United States.

Later, however, discussions at the Chalk River Conferences in Ontario, Canada (1949 to 1953), led to further reductions in the plutonium standard, which was set at 0.65 microgram, or 0.04 microcurie, for a permissible lifetime body burden.

This standard remained unchanged for more than two decades. In 1977, however, the International Commission on Radiation Protection (ICRP) described a new radiation-protection concept (ICRP 26, 1977) based on plutonium dose rather than plutonium deposition. The guideline for a maximum occupational dose is based on a calculated effective whole-body dose equivalent, and because it uses weighting factors, it does take into account organ doses. The overall guideline is that the maximum occupational plutonium dose is not to exceed an effective whole-body dose equivalent of 0.05 sievert, or 5 rem, annually from all types of occupational radiation exposure—internal and external (see the box “Units of Radiation Dose”).

Published between 1979 and 1988, a series of reports known collectively as ICRP 30 contains the derived annual limits of radionuclide intake¹⁰ for the protection of workers. Although the conceptual basis for limiting exposure to plutonium has changed drastically, the limit on internal deposition has not.

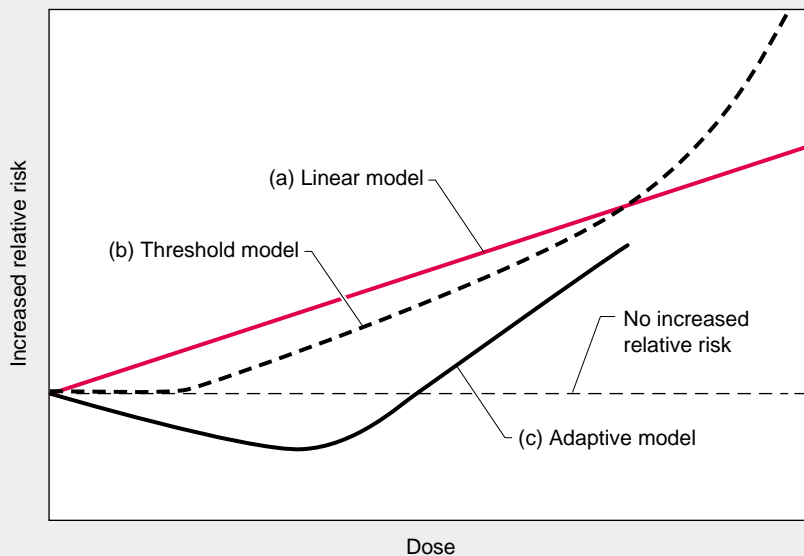
¹⁰ The annual limit of intake is the activity of a radionuclide that, taken internally, would irradiate a person, organ, or tissue to the limit set by the ICRP for each year of occupational exposure.

Models Predicting Risk of Carcinogenesis

When radiation protection standards are set, cancer risk from exposure to ionizing radiation is the factor that determines the allowed dose. Does a threshold dose exist below which cancer is not induced by radiation? The answer to this question is crucial, but the evidence is not strong enough to allow a definite “yes.” Although one Russian study of plutonium workers at the Mayak nuclear plant in Russia (Tokarskaya et al. 1997) concludes that a threshold value does exist (at around 16 sieverts) below which plutonium radiation does not induce lung cancer, most scientists advise for caution. They embrace a more-conservative approach by assuming that there is no threshold dose and that the relationship between dose and effect is linear. In this way, they assume that any exposure to radiation will carry some risk (see graph below). Because the nonthreshold model gives a higher risk per unit dose in the low-dose range than does a threshold model, radiation protection standards are set at lower-dose limits as a prudent measure for protection.

Interestingly, animal and human epidemiological studies often show a reduction in the overall mortality rate or the rate from cancer deaths for individuals with small radiation doses. Scientists attribute this beneficial response to a stimulatory effect of the radiation on the body’s natural defense mechanisms such as the immune system. This adaptive response is called hormesis. Although observed frequently, the hormetic response is usually not great enough to be statistically significant and is not used in setting regulatory standards. Its validity is the subject of heated scientific debate.

The current standards limit plutonium intake to keep the increased lifetime cancer risk to an imperceptible level. The limit set by occupational radiation guidelines for exposures to all sources of radiation (internal and external) is 0.05 sievert per year. If the radiation were due to plutonium exclusively, the lifetime deposition of plutonium would be about 0.5 microgram. In practice, plutonium workers are also exposed to some external radiation, so the actual lifetime deposition of plutonium should be less than that.



Three Models for Predicting Cancer Risk

The ICRP protection concept requires calculation of organ doses. For plutonium, these doses are uncertain because the internal distribution of plutonium varies greatly from one case to the next and the microdistribution of dose within organs is poorly understood. Therefore, the effective dose equivalent for plutonium is calculated with standard models, as recommended by ICRP 30 (see the box “Models Predicting Risk of Carcinogenesis”). This revised worker-protection guidance was placed into effect for DOE facilities at the beginning of 1989.

In the spring of 1991, the ICRP published new recommendations (ICRP 60) according to which the occupational exposure limit will be reduced to 0.02 sievert, or 2 rem, per year, which includes external and internal radiation doses. So far, the United States has not adopted this latest recommendation.

The Likelihood of Exposure to Plutonium

The largest amount of plutonium that has entered the environment is, by far, from radioactive fallout caused by aboveground nuclear weapons tests. From the Trinity Test in 1945 until atmospheric testing was banned in 1963, over 5 tons of plutonium were dispersed in the atmosphere in the form of small particles blown around the globe by the wind.

Most of this plutonium dust fell into the oceans, and approximately 96 percent of that amount simply sank as sediment onto the ocean floors because plutonium is not readily soluble in seawater. The fact that plutonium dissolves very slowly in water also explains why the plutonium concentration in our oceans is low and will continue to be so. The rest of the plutonium dust fell on land.

At present, surface soils everywhere contain minute quantities of plutonium. Plutonium attaches itself to

Nuclear Accident at Chernobyl

On April 26, 1986, one of the four reactors at the Chernobyl nuclear power station in the Ukraine (formerly part of the Soviet Union) melted down and exposed millions of people to the single largest radiation event in world history. The facts leading up to the explosion are well known. Reactor 4 produced steam that drove generators to make electricity. On the night of the accident, operators were testing the generators to determine how long they could run without power. To this end, they reduced the power produced in reactor 4 and stopped the steam flow to the generators. But the RBMK-1000 design of reactor 4 has a flaw that makes its operation at low power unstable. Moreover, in violation of existing rules, the operators withdrew most control and safety rods from the core and switched off some important safety systems so that those should not interfere with test results. Ironically, the safety systems could have averted the destruction of the reactor's core.

Power production in the reactor's core surged to 100 times the maximum permissible level, temperature increased in a couple of seconds, and two explosions blew off the metal plate sealing the reactor's top and destroyed the building housing the reactor. Within seconds, the explosions showered the environment with hot and highly radioactive gases. The gases contained aerosolized fuel and fission products, the radioactive nuclei created when uranium atoms split.

Early health consequences of this disaster were seen only in the firemen and power plant personnel exposed at the plant site. Of the 237 persons immediately hospitalized, 134 had clinical symptoms and signs attributable to radiation exposure. From among these 134 acute cases, 28 persons died as a result of exposure to high levels of radiation. The off-site environmental contamination levels were high enough to require, within about 10 days of the accident, that about 135,000 people leave their homes. Ten years after the accident, the area within 30 kilometers of the Chernobyl plant was largely uninhabited, and people in 60 settlements outside this zone had also been relocated (Shcherbak 1996).

Most of the reactor fuel was uranium. Mixed with it was plutonium (about 580 kilograms) created as a by-product of normal operations. And yet, in spite of the large quantity of plutonium present in the reactor, this metal has seldom been mentioned in accounts of the Chernobyl accident. Plutonium is not very volatile, and even the red hot meltdown of the Chernobyl reactor core did not disperse much of it. About 3.5 percent of the plutonium (or a volume equivalent of about 1 liter) in the reactor was released to the environment. Plutonium was

detected with sensitive measurement techniques in contaminated areas, but the levels were below those that would cause health concerns.

Instead, the main radioisotopes that caused significant radiation doses during this accident were two uranium fission products: cesium-137 and iodine-131. About 50 to 60 percent of the iodine-131 and 20 to 40 percent of the cesium-137 were released to the environment. Because cesium-137 has a half-life of 30 years, scientists believe it will account for the largest radiation doses in the long run. Having a relatively short half-life (only 8 days), iodine-131 caused large radiation exposures in the weeks immediately after the accident. Ten years after the accident, health studies showed an increased incidence of thyroid cancer among infants who were in the most-contaminated off-site zones immediately after the accident. By the end of 1995, close to 800 children in Belarus, northern Ukraine, and Russia were reported to have thyroid cancer. Clinical experience indicates that 5 to 10 percent of these children will die of thyroid cancer, but only a handful have so far. No significant rise in leukemia has yet been detected among the inhabitants of those same zones or among the emergency workers and evacuees exposed to the highest initial doses of radiation.

Indeed, so far, the Chernobyl experience has not validated the opinions of either optimists or pessimists. The former predicted no long-term medical consequences from the explosion; the latter predicted well over 100,000 cancer cases. However, previous experience with long-term radiation effects at Hiroshima and Nagasaki suggests that the current toll will continue to rise and that the health effects triggered by this accident will be fully understood only a few decades into the future.

Interestingly, a gamut of psychosomatic disorders became widespread after the Chernobyl accident. The hushing up of the dangers from this accident in Soviet propaganda caused people to live in constant fear for their lives and the lives of their children. Indeed, a 10- to 15-fold increase has been observed in the incidence of psychosomatic disorders (Shcherbak 1996). Even in less-contaminated areas, there has been a large upswing in stress-related physical ailments. In the end, the morbidity* and mortality caused by psychosomatic disorders may become far reaching. Perhaps, they may even exceed the number of sicknesses and deaths caused by exposure to radiation.

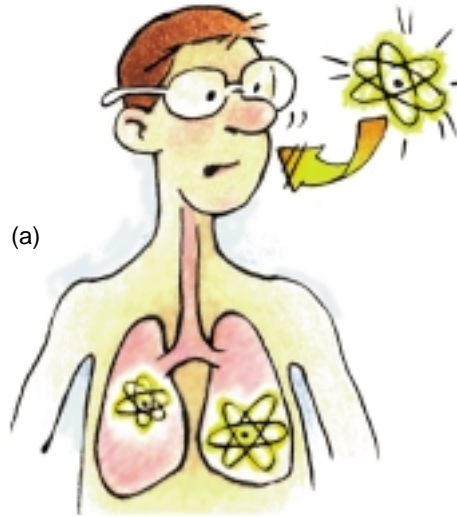
* The ratio of the number of sick individuals to the total population of a community.

soil particles through ion-exchange processes—minerals in the soil can be exchanged for plutonium, which will stick to the soil and move only when the soil does. This chemical property of plutonium restricts its movement through soil and limits its uptake into most plants. For example, if soil were to contain 10,000 parts of plutonium, approximately 1 part would be taken up by a plant. The highest plutonium contamination on leafy vegetables or grains comes from wind-blown dust and rain splash.

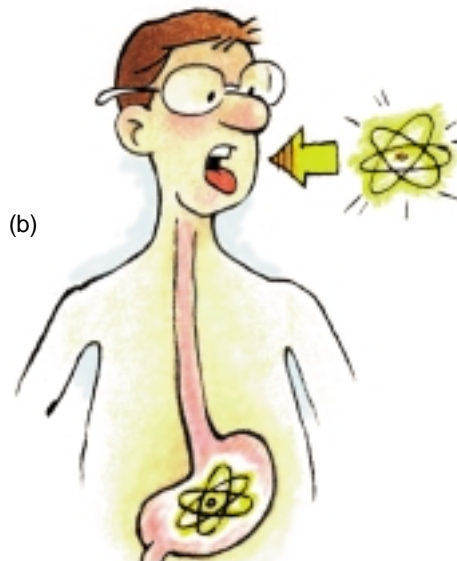
People are exposed to plutonium mainly when they inhale small particles from the top soil kicked up by the wind or by some human activity. Measurements of the plutonium uptake have been derived from autopsy tissues, and scientific data indicate that the levels of plutonium in the general population of the United States are very small. On average, the committed effective dose from the plutonium content of a person living in the northern hemisphere is an insignificant 0.00006 sievert compared with the background radiation dose, which can be as high as 0.21 sievert. The committed effective dose is the estimated amount of radiation a person in the general population receives from a given source, in this case plutonium, over a 70-year period. Involved in this study were primarily people who lived in the 1950s and 1960s, decades during which radioactive fallout was being generated from atmospheric weapons testing.

But fallout from weapons testing is not the only possible source of plutonium dust in the environment. Nuclear accidents, such as the 1986 Chernobyl accident, may cause plutonium dust to enter the environment. And yet, although the meltdown of the Chernobyl reactor was a potentially large source of plutonium dust, scientific data indicate that cesium-137 and iodine-131, rather than plutonium, were the major sources of hazard following that accident (see the box “Nuclear Accident at Chernobyl”).

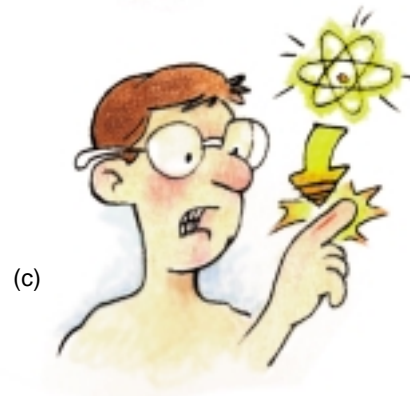
Scientists who work with plutonium and are familiar with its properties will



(a)



(b)



(c)

Figure 2. Plutonium Entry Routes into the Body

(a) Inhalation is the most likely and dangerous entry route for plutonium particles. Approximately 5% to 25% of the inhaled particles are retained by the body. Depending on particle size (the smaller the particle, the higher its risk to be retained) and chemical form (soluble forms are more easily absorbed by the blood), inhaled plutonium will remain lodged in the lung or lymph system, or it will be absorbed by the blood and delivered mainly to the liver or bones.

(b) Ingestion of plutonium is the least likely entry route for plutonium particles. In adults, only about 0.05% of the ingested soluble plutonium compounds and a mere 0.001% of the ingested insoluble ones enter the blood stream. The rest passes through the gastrointestinal tract and is excreted.

(c) Absorption of plutonium through skin cuts is a serious risk but mainly for workers who handle highly contaminated items in glove boxes. Up to 100% of the plutonium absorbed in this way will be retained by the body.

argue that, although highly dangerous, plutonium is handled safely. In occupational terms, therefore, plutonium is no more of a hazard than other industrial toxins. In terms of the general public, barring serious accidents and nuclear war, another way in which people in the United States or elsewhere could possibly increase their levels of plutonium would be by eating dirt! And there are people who suffer from an eating disorder called pica, or the compulsive ingestion of large quantities of dirt. While eating dirt, these people will ingest greater than normal plutonium quantities. However, even then, they are significantly protected because the human gastrointestinal tract absorbs only about 1 part of plutonium out of 5000 to 10,000 parts swallowed.

And yet, none of the above should detract from the fact that

plutonium is a very hazardous material. Great attention is paid to providing safe workplaces and work practices for plutonium operations. More than 50 years have passed since plutonium was discovered, and experience with this dangerous metal proves that people can be protected.

Data from Plutonium Exposures

Suppose for a moment that, in spite of safe standards and handling procedures for plutonium, one is accidentally exposed to low levels of plutonium. What is the risk for developing cancer or suffering any other detectable effects, such as chromosomal instabilities or cell dysfunctions? To answer that question, we shall first have to discuss plutonium metabolism, once this metal enters the body.

Plutonium Metabolism. The ease with which plutonium is absorbed in the body depends significantly on two factors—the means of entry and the type of plutonium compound that has entered the body. In general, soluble forms such as nitrates, citrates, and certain oxides are absorbed more readily by the body's fluids than insoluble forms. Figure 2 summarizes the plutonium entry routes into the body.

Absorption of plutonium through intact skin is very low. But puncture wounds, cuts, and to a lesser extent, skin burns contaminated with plutonium favor deposition of the element into tissues within and below the skin. The amount of plutonium picked up in the blood circulation depends on the chemical form of the plutonium. Soluble forms start being distributed throughout the body within minutes or hours of the uptake. Some of the plutonium may be transferred to lymph nodes near the wound, where it may stay for years. Even some insoluble forms of plutonium are taken up into the blood circulation quickly, but most remain at the site and are slowly mobi-

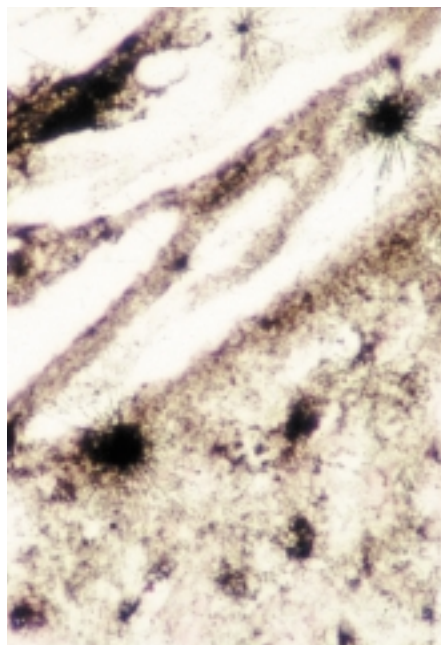


Figure 3. Distribution of Inhaled Plutonium in the Lung and Lymph Nodes

If the inhaled plutonium particles are in a relatively insoluble chemical form, most will remain in the lung tissue or the lymph nodes around the lungs and thus increase a person's risk for developing lung cancer. This autoradiograph of a tracheobronchial lymph node from a former worker at Los Alamos shows alpha tracks radiating in a typical star pattern from tiny alpha-active clumps of material. Chemical analyses of the radioisotopes in this person's lungs and lymph nodes indicated that those clumps most likely consisted of an aggregate of plutonium particles.

lized over weeks and months. The plutonium absorbed in the blood circulation is called the systemic burden because it gets redistributed throughout the body. About 90 percent of the systemic burden gets deposited in the liver and bones. Urine, produced in the kidneys, reflects the concentration of the plutonium circulating in the blood. Plutonium measurements from urine are therefore the major source of data about the overall systemic plutonium deposition in the body over time.

Ingesting plutonium is perhaps the least likely means for plutonium to enter the body. But even if plutonium is ingested, the gastrointestinal tract provides a natural barrier, and in adults only about 0.05 percent of the soluble plutonium compounds and a mere 0.001 percent of the insoluble ones enter the blood stream. The rest of the plutonium simply moves out of the body in feces. In babies under 1 year of age, however, the plutonium uptake may be as much as 10 times greater than in adults.

It is the inhalation of plutonium dust that is the most likely way for plutonium to enter the body. The size of the inhaled particles affects the ease with which plutonium is absorbed: the smaller the particle, the higher its likelihood to be retained. Most particles over 10 micrometers in diameter (considered large) are filtered out in the nose and upper respiratory region, then swallowed, and eventually passed out of the gastrointestinal tract in feces. Particles less than 10 micrometers in diameter are called respirable particles. When inhaled, some of them are deposited on the mucus layer of the bronchial tubes, whose lining contains numerous hair-like structures called cilia. The natural wave motion of the cilia transports the mucus layer and its dust particles up to the throat. This process, known as lung clearance, removes much of the foreign material deposited in the bronchial tubes.

Even smaller particles, especially those under 1 micrometer in diameter, or about one-tenth the thickness of a typical human hair, are carried down into the tiniest airways of the lung and into alveoli (also known as air sacs). Because all these structures have no cilia on their surfaces and no effective lung-clearance mechanisms, scavenger cells called phagocytes move in on the inhaled plutonium particles, engulf them, and transport them into lymph nodes or into lung tissues, which are sites of longer-term retention (see Figure 3). The plutonium particles

retained in lung tissues might increase a person's risk for developing lung cancer.

The rate of absorption from the lung into the blood is directly determined by the plutonium compound's solubility. An oxide produced at high temperatures is not very soluble and remains for very long periods in the lung tissue or the lymph nodes, the filter system around the lung. In tissue samples taken during autopsy from three plutonium workers known to have inhaled plutonium dust, 35 to 60 percent of the plutonium in the body at the time of death was in the lung or the tracheobronchial lymph nodes. The plutonium remained there for about 40 years after inhalation.

Soluble forms of plutonium in wounds or lungs dissolve into surrounding tissue fluids, are picked up in the bloodstream, and will then be circulated around the body. About 90 percent of the plutonium picked up from the lung is deposited about equally into the liver and bones. The remaining 10 percent or so is quite uniformly deposited in soft tissues, and a small fraction of it is excreted in urine and feces.

Autopsy studies reveal that, initially, plutonium is not deposited throughout bone tissues. Instead, it is mostly deposited on the bone surfaces and, in particular, on the interlaced surfaces of the so-called trabecular bone (see Figure 4). Less than 5 percent of the plutonium is typically found within the bone marrow, the soft material that is the site of the blood-forming cells (the hematopoietic stem cells). Given this pattern of deposition, the primary carcinogenic risk from plutonium in the skeleton is bone cancer. There is no conclusive evidence that plutonium increases the risk for leukemia, which is the unchecked proliferation of certain blood cells produced in the bone marrow.

Once sequestered in the bone, plutonium remains there for a very long time. Normal remodeling of the bone structure results in plutonium being gradually redistributed more uniformly throughout the bone. Current models

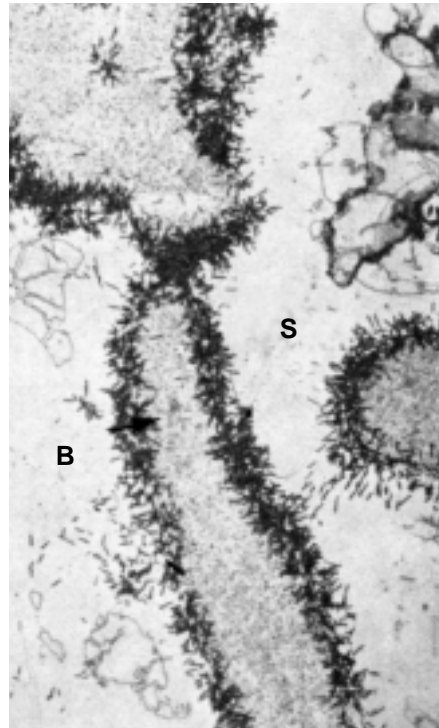


Figure 4. Plutonium Deposition in the Bone

This neutron-induced autoradiograph (magnified 190 times) of portions of the trabecular bone (B) in a dog shows fission tracks from particles of plutonium deposited on the bone surface (S). Bones have two kinds of tissue: one is dense and is called compact bone whereas the other is made of slender spicules, trabeculae, and lamellae joined into a convoluted matrix and is called trabecular bone. Although plutonium deposits on both types of tissue, the trabecular bone has a larger surface area and thus acquires a greater fraction. And because bone-producing cells reside at bone surfaces, the risk for developing bone cancer increases. (This photo, obtained courtesy of the University of Utah, is from *Radiobiology of Plutonium*, 1972.)

(based on observation of exposed persons and autopsy data) estimate a half time of about 50 years for plutonium retention—that is, 50 years after it was initially deposited, half of the plutonium would still remain in the bone. A small fraction is excreted.

The plutonium deposited in the

liver is eventually transformed from relatively soluble forms in hepatic cells into insoluble forms (hemosiderin deposits), which are sequestered in the cells that form the linings of liver ducts (reticuloendothelial cells). The retention half time for the plutonium deposited in the liver is approximately 20 years.

Low-Level Exposures. So, what are the actual chances for developing cancer as a result of low-level exposures to plutonium? (Low-level exposures are those less than 0.05 sievert per year from external and internal radiation sources combined.) We can answer this question by looking at data from studies of persons exposed to plutonium, other alpha-emitting radionuclides such as radium or thorium, and external radiation as well as by looking at data from experimental studies of animals exposed to plutonium. If taken separately, each approach has its own limitations, but the combined information gathered from them all will give a fuller answer to our question.

All approaches rely on epidemiological methods, that is, statistical studies of health events in a given population. The principal events from plutonium exposure are cancer incidence and mortality. However, medical tests cannot distinguish between the same type of cancer in a group that has been exposed to radiation and another that has not. Interpretation of epidemiological data hinges therefore on the ability to identify a statistically higher cancer rate for the exposed group than for the unexposed group. And the ability to detect increased cancer risk is based on the number of people observed—the higher that number, the better the chance for results to be statistically significant. Ideally, epidemiological studies of occupational groups will therefore involve tens of thousands of persons. If only few individuals can be analyzed, those studies are hampered.

Moreover, epidemiology is not a very sensitive analytical tool, especially at exposure levels at which risks are small. Other significant issues must

also be considered when interpreting epidemiological data. We shall stop to look at only two of them: bias and confounding factors.

Bias is any trend in the collection, analysis, interpretation, publication, or review of data that can lead to conclusions systematically different from the truth. Often encountered is the "healthy-worker effect," a bias that results from comparing employed people with persons in the general population. Employed people should be healthy enough to be in the workforce, whereas the general population will include some persons who are disabled or ill. Thus, unless it experiences strong, detrimental effects from exposures, the employed group generally looks healthier by statistical analysis than the general population.

A confounding factor is any risk factor, other than the risk under study, that influences the outcome. Smoking, for example, is a strong confounding factor because it increases the chance for cardiovascular diseases and the incidence of and mortality rate from lung and other cancers. Unless data are available and adjustments are made for differences in smoking between different populations, smoking may account for the differences in the observed frequency of smoking-related diseases rather than other factors such as exposure to radiation. So, interpreting epidemiological data is complex and potentially controversial. Although it may establish a statistical association between some agent or activity and health effects, this finding does not, by itself, establish causation. Causation decisions are judgments made on the strength of the data, confirmation by other studies, and biological credibility.

To date, there have been only few epidemiological studies of workers exposed to plutonium. Studies of workers at Los Alamos National Laboratory (Wiggs et al. 1994) and Rocky Flats (Wilkinson et al. 1987) are the only ones in the United States to have used quantitative measurements of plutonium exposures, but they involved few work-

ers: 303 at Los Alamos and 1450 at Rocky Flats. These two studies showed no evidence of statistically increased rates of lung, liver, and bone cancers, which are shown in animal experiments to be the highest-risk cancers due to plutonium exposure. A study by Reyes et al. (1984) indicates that an increased brain-cancer rate in Rocky Flats workers was not caused by plutonium exposure or external radiation.

Over the years, there have been a few other studies on Los Alamos workers exposed to plutonium, but most of them are smaller in scope. Published in 1983, one such study by Voelz et al. was conducted on 224 males exposed to plutonium between 1944 and 1974. Their plutonium deposition was greater than 0.16 microgram, or 0.01 microcurie. None of the people involved in this study developed bone or liver cancer, and by 1980, the final year of the study, only one person had died of lung cancer. This study did not confirm earlier opinions of some nuclear-industry critics who predicted a very high risk for lung cancer at low plutonium doses.

Another study involved 26 chemists, metallurgists, and technicians at Los Alamos, who were accidentally exposed to plutonium between 1944 and 1946. The plutonium body burdens of these men were from 5 to more than 360 times the current annual limit of intake set by DOE. By weight, the corresponding body burdens, 50 years after exposure, ranged from 0.02 to 1.4 micrograms and were estimated by analysis of the men's urine. Estimates are that the men took up about twice this amount at the time of exposure. Wright Langham, the originator of this ongoing study, roguishly called this tiny cohort of men the UPPU (or U-P-Pu!) club, a name by which they have been known since.

It is important to note that the mortality rate of the club members has been lower than that of the population in general. In 1996, the most recent year of our data analysis, 19 members were still alive. To this day, their health is being monitored periodically by

Los Alamos physicians. Overall, it is typical of men their age.

Of the individuals in this club who are no longer alive, one man died of lung cancer in 1989, at the age of 66. Two men died of prostate cancer and congestive heart failure, respectively, but both had lung cancer at the time of death. All three men were very heavy smokers. Significantly, three cases of lung cancer are consistent with the national cancer incidence rate, over the same period, in U.S. white males of the same age. The national cancer incidence rate is the rate at which new cases of lung cancer emerge.

Another club member, who had an estimated plutonium deposition of 0.245 microgram, developed a rare bone cancer 43 years after exposure and died in 1990. This last finding is statistically significant for a small group like the UPPU club. But in the 1994 Los Alamos study (Wiggs et al.) of 303 workers, this same individual remained the only one to have developed bone cancer. Statistical analysis indicates that one death caused by bone cancer in this larger group may well be due to chance and is not statistically significant.

Finally, three more club members died of causes unrelated to cancer: one of a heart attack, another of viral pneumonia, and a third in a car accident. As shown in Table I, according to the national mortality rate, one would have expected 19.8 deaths in the UPPU club at the time of the latest data analysis. In this table, we did not include the pneumonia and car accident deaths in the breakdown on causes of death because plutonium clearly played no part in those deaths. We did, however, include the death from a heart attack because, as shown later, cardiovascular illnesses are significantly low for this small group.

The table gives standardized mortality ratios, which compare the mortality rates of the exposed group with those of an unexposed group. Both groups were composed of U.S. white males. Should the mortality rates

Table I. Number of Deaths and Mortality Rates among 26 Plutonium Workers^a in the United States

Causes of Death	Observed Deaths	Expected Deaths	Standardized Mortality Ratios	95% Confidence Intervals	p-Values
All causes	7	19.8	0.37	0.15–0.77	0.0009 ^b
Cancer	3	4.6	0.65	0.13–1.9	0.326
Lung	1		0.60	0.01–3.4	0.509
Prostate	1		2.7	0.04–15	0.309
Bone	1		90	1.18–502	0.01 ^b
Cardiovascular illness	2	9.1	0.22	0.02–0.80	0.006 ^b

^aAnalyses of results through 1996
^bSignificant p-values

of the exposed and the comparison groups be identical, the standardized mortality ratio will have a value of 1. A value of 0.37, as shown in the first line of the table, for example, indicates that the mortality rate in the workers exposed to plutonium is 37 percent that of the white male population of the United States. The potential error associated with this rate is given by the 95 percent confidence intervals. These intervals have a 95 percent statistical probability of including the true value of the standardized mortality ratio. And the probability values, or p-values for short, shown in the far-right column of the table are the probability that a particular finding—in this case, the mortality rate—has occurred by chance. A p-value of less than 0.05 has therefore less than a 5 percent chance of having been caused by random events and is considered statistically significant. With less than a probability of 1 percent to have been caused by chance, a p-value of less than 0.01 is considered very significant. In Table I, there are three such values. The first (0.0009) indicates that a generally low mortality rate among the 26 workers exposed to plutonium is not due to chance. But that outcome may have been influenced by the healthy lifestyles of the people who were still alive—less

smoking, plenty of exercise, and good food. The second statistically significant finding is a p-value of 0.01 for one death from bone cancer. Because bone cancer was also present in experimental animals exposed to plutonium, this finding has biological credibility. However, no other bone tumors have been reported in U.S. plutonium workers. The third significant p-value (0.006) indicates a very low rate of cardiovascular deaths in this small group of people, which was probably caused by a confounding factor—most likely smoking. A higher percentage of white males in the United States tend to smoke than in the small UPPU club. The rate of expected cardiovascular deaths in the general population is therefore high.

Overall, data from the several studies of persons exposed to low levels of plutonium radiation in the United States do not show a relationship between dose and effect. They merely indicate that such a relationship does not exist or cannot be confirmed. If plutonium is harmful at these low levels, its health risks are so small that, given the small number of workers involved, epidemiological methods cannot differentiate between effects triggered by plutonium radiation and variations in a group of people unexposed to such radiation.

We need to stress that cancer risk from low doses of radiation and low-dose rates is not known precisely. When an individual who has had a history of radiation exposures—occupational and/or medical—plus other possible additive and synergistic insults is diagnosed with cancer, no specific cause is readily attributable. In case of litigation, the medical testimony will rest on opinions about the probability that the occupational radiation dose may or may not have been a major cause. In the future, when radiation risk coefficients for low doses are better defined, it may be easier to form these medical opinions.

Although studies conducted on plutonium workers in the United States did not yield data that demonstrate the risk from plutonium radiation, there are such data from much higher doses to which Russian plutonium workers have been exposed.

High-Level Exposures. Russian scientists have recently published two studies (Tokarskaya et al. 1997, Koshurnikova et al. 1998) of workers who had been exposed to plutonium at the Mayak Plant, the first nuclear facility in the former Soviet Union. The authors demonstrate that an increased risk for lung cancer is associated with higher exposures. Although both studies investigate this risk on many of the same workers, their conclusions about the relationship between dose and risk are different (see Figure 5).

Koshurnikova et al. analyzed data from a cohort of 1479 workers who had been exposed to high doses of various types of radiation, including plutonium radiation, between 1948 and 1993. The control group was composed of 3333 other workers at Mayak who had also been exposed to radiation but within occupational limits. As illustrated in Figure 5(a), the authors found a linear relationship between lung doses from 0.5 to 30 sieverts (or 50 to 3000 rem) and standardized mortality ratios. This result means that no threshold was found, that is, no dose value

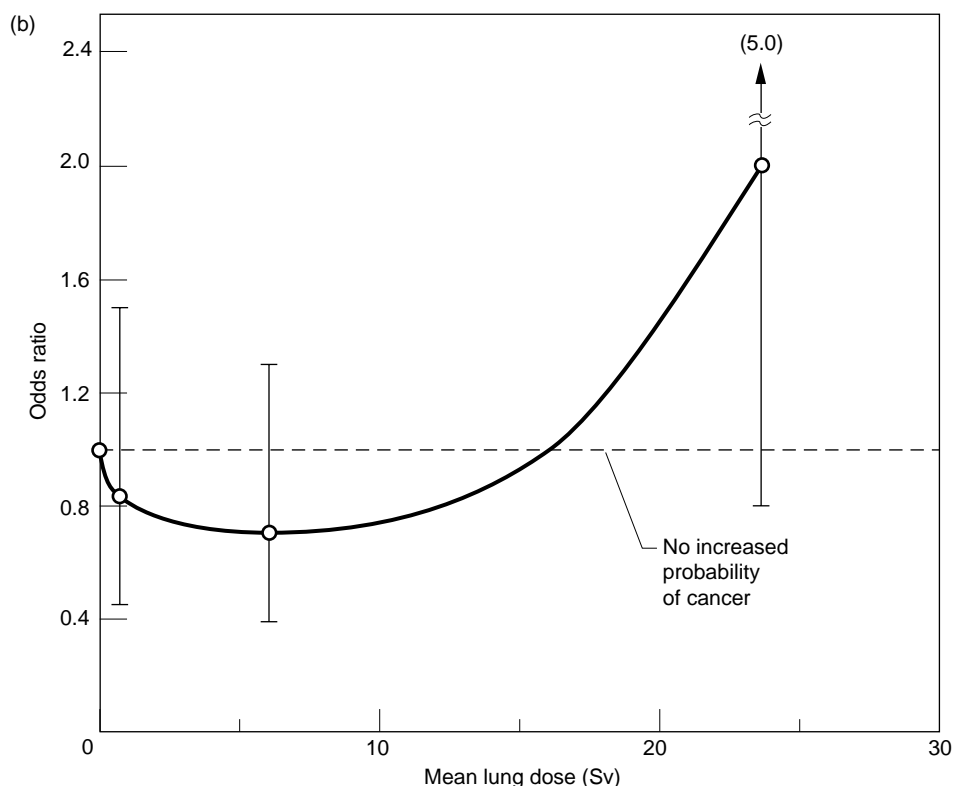
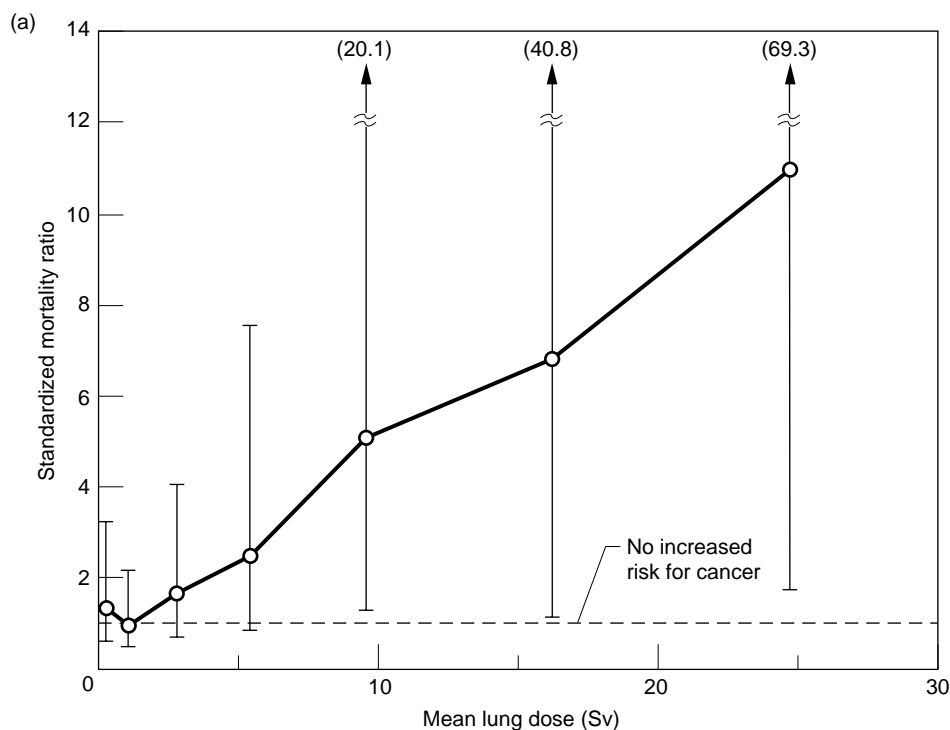


Figure 5. Plutonium Dose vs Lung Cancer Risk at Mayak—Two Results

(a) Results of an epidemiological cohort study at the Mayak Plant in Russia (Koshurnikova et al. 1998) show standardized mortality ratios—the ratio of the observed to the expected deaths adjusted for age distributions and calendar years of death—as a function of lung doses of up to 30 sieverts (Sv). The horizontal dotted line marks a mortality rate of 1, which indicates that no increase in lung cancer risk was observed. The mortality rate appears to increase linearly with dose and, at a dose of about 25 Sv, has risen to 11 times the normal rate. The statistical bars here and in (b) show the 95% confidence intervals. In other words, the true mortality rate has a 95% probability of falling within that interval.

(b) In the case-control study by Tokarskaya et al. (1997), increased lung-cancer risk from plutonium radiation is shown to exhibit a threshold effect. The odds ratios for lung cancer are shown as a function of lung doses up to 30 Sv. The odds ratio is the exposed group's probability divided by the control group's probability of developing cancer. Up to a dose of about 7 Sv, the curve shows odds ratios less than 1—that is, no increased risk from plutonium radiation. Above 7 Sv, however, the curve begins to turn up, and at 16 Sv there is a threshold above which the risk increases rapidly. Some scientists have speculated that the dip below a value of 1 at low doses may be due to the adaptive response described in the box "Models Predicting Risk of Carcinogenesis" on page 80.

was found within the given range below which cancer risk from plutonium radiation would be completely eliminated. To obtain the mortality rates, the authors calculated the ratio of the observed to the expected deaths and then adjusted the result for age distributions and calendar years of death. The observed deaths (105) are those of workers who had been exposed to total lung doses of up to 30 sieverts. The expected deaths (40.67) are from the control group whose lung doses totaled only about 0.5 sievert. According to the data, in the dose range between 0.5 and 30 sieverts, lifetime risk from lung cancer increases by 1.2 percent for each additional sievert in that range, which is about double the lifetime risk quoted by the ICRP (ICRP 60, 1991). Shown in this graph are also 95 percent confidence intervals. The lowest values of these intervals for the first four sets of data points are less than 1. Below a mean dose of about 5 sieverts, therefore, the observed mortality rates in exposed workers have a reasonable likelihood of having been caused by chance. Nevertheless, the trend of increasing rates with increasing dose is impressive.

But Tokarskaya et al. (1997) found a nonlinear threshold relationship between dose and lung cancer risk. Their results are shown in Figure 5(b). This is a case-control study devoted to 162 plutonium workers who developed lung cancer between 1966 and 1991 and a control group of 338 Mayak workers who, during the same period, did not. As mentioned before, there was much overlap of workers between the two Russian studies because those people worked at the same Mayak Plant. Tokarskaya and her colleagues analyzed three risk factors for lung cancer: smoking (most of these workers were heavy smokers), plutonium radiation, and external gamma radiation. They determined relative risks by using a different methodology, namely, odds ratios. They calculated the ratio of the probability that lung cancer was the result of exposure to plutonium by juxtaposing the exposed and control

groups. The authors found no lung-cancer risk up to a threshold dose of 16 sieverts, which corresponds to a deposition of about 1.6 micrograms of plutonium. Above this threshold value, however, the risk rises rapidly. The initial portion of the curve, up to a lung dose of at least 7 sieverts, has odds ratio values of less than 1. This finding suggests that there is no increased risk from plutonium radiation and that a possible beneficial effect cannot be ruled out. Above 7 sieverts, however, the curve begins to turn up, and above 16 sieverts, the risk rises dramatically. The 95 percent confidence intervals reveal that the lower and upper values of those intervals encompass the value 1 for all mean doses under 30 sieverts. This result indicates that slight variations in odds ratios, such as the initial dip below 1 and even the later increase to 2 may simply have been caused by chance.

The two curves based on Russian data are very different in shape. However, differences notwithstanding, the Mayak data demonstrate that lung cancer risk does indeed increase with higher doses. No studies have yet been published on the Mayak workers' risk for developing bone or liver cancer.

Summary

It has been almost six decades since plutonium was first made, and people's fears about this material are still strong today. No doubt, the dangers of plutonium are real. The fact that the defense and nuclear power industries have been able to limit the extent of exposures is a direct result of the foresight and careful planning on the part of the physicists and chemists who first isolated and produced plutonium. Almost from the moment plutonium was isolated, scientists worried about the possible health effects of this radioactive substance. Since then, plutonium has been handled in different chemical forms, fabricated as a metal, machined, and used successfully in

many applications primarily because standards and procedures were soon established to prevent people from being exposed. There has been no instance of acute death from plutonium radiation except for external-radiation deaths resulting from criticality accidents. That is a remarkable achievement.

Precisely because it is conservative in its assumptions, the linear nonthreshold model for risk from low levels of plutonium radiation is at the basis of permissible plutonium occupational doses. Workers in the United States are well protected, but accidents can happen. From our extensive experience with plutonium and other radioactive materials, we know that effective communication with persons involved in radiation accidents is very important. Indeed, open communication with the general population is equally important.

Los Alamos has been leading the way in providing the world with facts about plutonium. Does the population at large need to be concerned about being exposed to plutonium radiation? Exposures to high levels of plutonium radiation can happen only during accidents. Should they occur, such exposures are dangerous as they can induce cancer in humans. Exposures to low levels of plutonium radiation are a real possibility for plutonium workers. Epidemiological studies, however, have not yielded data that would allow us to establish a clear relationship between plutonium dose and its possible health effects. And this kernel of uncertainty is the very reason for radiation protection measures to stay conservative—perhaps more conservative than is actually needed. Barring an act of sabotage, nuclear war, or a nuclear accident more severe than Chernobyl, the general public is not likely to be significantly exposed to plutonium. Plutonium is around only in negligible amounts. Hopefully, this excellent track record will continue indefinitely. ■

Further Reading

- Clarke, R. H., J. Dunster, J.-C. Nenot, H. Smith, and G. Voelz. 1996. *J. Radiological Protection* **16** (2): 91.
- ICRP Publication 48. Radiation Protection—The Metabolism of Plutonium and Related Elements. 1986. *Annals of the ICRP*. **16** (2–3).
- ICRP Publication 60. Recommendation of the International Commission on Radiological Protection. 1991. *Annals of the ICRP*. **21** (1–3).
- Koshurnikova, N. A., M. G. Bolotnikova, L. A. Ilyin, I. B. Keirim-Markus, Z. S. Menshikh, P. V. Okatenko, et al. 1998. *Radiat. Res.* **149**: 366.
- Reyes, M., G. S. Wilkinson, G. Tietjen, G. L. Voelz, J. F. Acquavella, and R. Bistline. 1984. *J. Occupational Med.* **26**: 721.
- Shcherbak, Y. 1996. Ten Years of the Chernobyl Era. *Scientific American*. April issue: 44.
- Stover, B. J., and W. S. S. Jee, ed. 1972. *Radiobiology of Plutonium*. University of Utah, Salt Lake City: J. W. Press.
- Tokarskaya, Z. B., N. D. Okladnikova, Z. D. Belyaeva, and E. G. Drozhko. 1997. *Health Phys.* **73** (6): 899.
- Voelz, G. L., and J. N. P. Lawrence. 1991. *Health Phys.* **61** (2): 181.
- Voelz, G. L., J. N. P. Lawrence, and E. R. Johnson. 1997. *Health Phys.* **73** (4): 611.
- Voelz, G. L., G. S. Wilkinson, J. W. Healy, J. F. McInroy, and G. L. Tietjen. 1983. Mortality Study of Los Alamos Workers with Higher Exposures to Plutonium. In *Proceedings of the 16th Midyear Topical Meeting of the Health Physics Society*. Washington, DC: Technical Information Service.
- Wiggs, L. D., E. R. Johnson, C. A. Cox-DeVore, and G. L. Voelz. 1994. *Health Phys.* **67**: 577.
- Wilkinson, G. S., G. L. Tietjen, L. D. Wiggs, W. A. Galke, J. F. Acquavella, M. Reyes, et al. 1987. *Am. J. Epidemiology* **125**: 231.

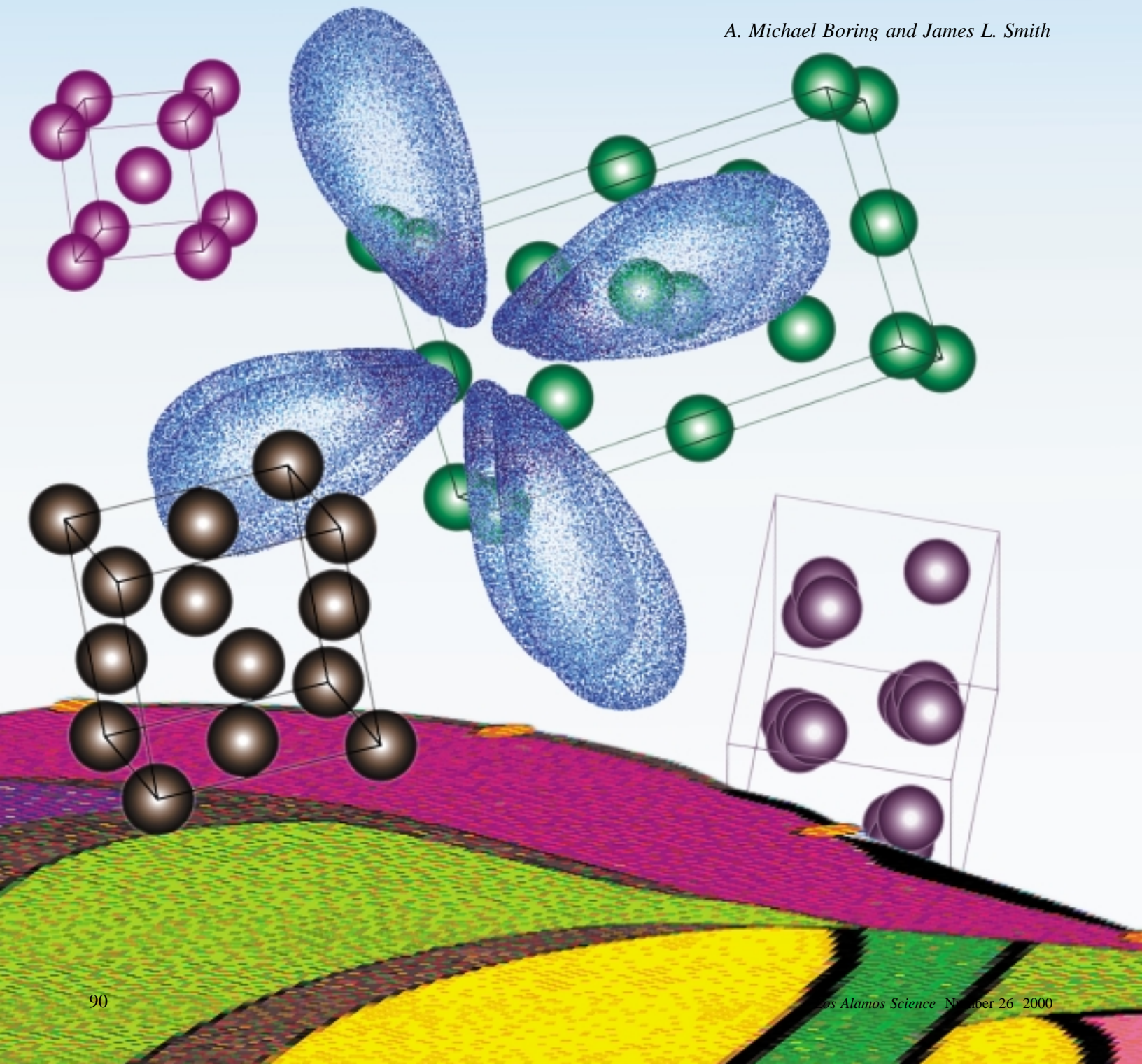


George Voelz, a native of Wisconsin, received his M.D. degree from the University of Wisconsin Medical School in 1950 and then did an internship at the University of Oregon Medical School Hospital and Clinics. After having completed an Atomic Energy Commission fellowship in occupational medicine at the Kettering Laboratory of the University of Cincinnati in 1951, George completed another fellowship at the Los Alamos Scientific Laboratory in 1952. From 1957 to 1970, George worked at the National Reactor Testing Station for the U.S. Atomic Energy Commission, Idaho Operations Office, where he organized and became director of the Health Services Laboratory in 1967. George returned to Los Alamos in 1970 to serve as leader of the Health Division until 1982. For the next five years, he was Health Division deputy leader, working primarily in the administration of research programs. From 1987 to 1990, George led the epidemiology section of the Occupational Medicine Group at Los Alamos. In 1990, he retired from the Laboratory. Since then, he has actively continued his research as a Laboratory associate, studying the health of nuclear industry workers. His special interest has been the effects of plutonium exposure on human health. George has been certified as a diplomat of the American Board of Preventive Medicine since 1959 and has served on numerous committees. He is a lifetime honorary member of the National Council on Radiation Protection and Measurements. He also served as a committee member for the International Commission on Radiological Protection and, in 1994, as a team member of the Los Alamos Human Study Project.

Plutonium Condensed-Matter Physics

A survey of theory and experiment

A. Michael Boring and James L. Smith



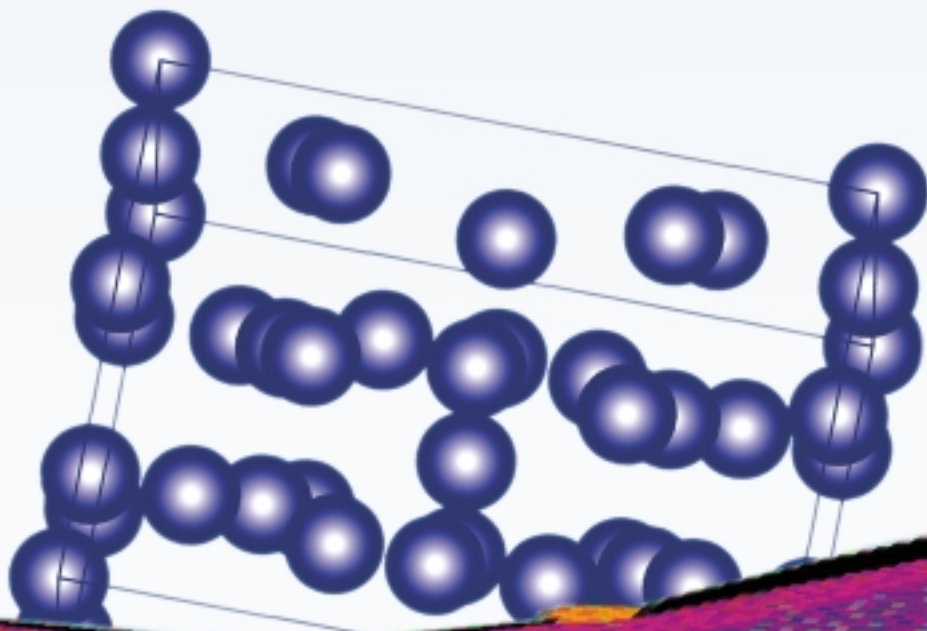
Systems like to be in the lowest-energy state, but plutonium metal has trouble getting there. It has many states close to each other in energy but dramatically different in structure, and so a portion of a sample can change its structure and density in response to minor changes in its surroundings. We probably have yet to see a sample near room temperature that has reached true equilibrium. This metastability and its huge effects are part of the story of the strange properties of plutonium metal, alloys, and metallic compounds, and they are extremely important if we want to leave nuclear weapons untouched for decades.

Here, we will put plutonium metal in perspective by comparing it to the other actinides and to other metals in the periodic

table of the elements. Plutonium has many unusual properties. Instead of having the cubic structure found in familiar metals, its ground state has a very low symmetry monoclinic structure with 16 atoms in the unit cell. Its instability is legendary among metallurgists—plutonium goes through six distinct crystallographic phases when heated to its melting point under atmospheric pressure. One of those phases is the face-centered-cubic δ -phase, which can be stabilized down to relatively low temperatures by alloying it with a tiny amount of gallium metal. The δ -phase is itself a tremendous puzzle, having an unusually low density, as well as a negative thermal-expansion coefficient; that is, δ -plutonium contracts when heated. Below room temperature, plutonium continues to display

anomalous properties. In particular, it has an unusually high resistivity and an elevated specific heat, suggesting novel interactions and correlations among its electrons. Because they are probably the root for much of plutonium's unusual behavior, we will bring up these unusual electron correlations in connection with both high- and low-temperature phenomena. Figure 1 shows plutonium sitting at the crossover of many properties. As we survey those properties, we will consider the following questions: Is plutonium fundamentally different from other metals? Do we need an entirely new theory to explain its behavior?

Definitive answers must await better and more-complete experimental data leading to a full theory of plutonium and its compounds. We show, however, that the two underlying concepts of modern theories of metals, the one-electron “band-structure” approach and the correlated-electron approach, are relevant to plutonium.



Moreover, many ground-state properties of plutonium can be predicted from modern one-electron band theory. Other problems remain to be solved. As you read this and other papers in this volume, you will learn not only about the successes but also about the ongoing mysteries that place plutonium at a frontier of condensed-matter physics.

The f Electrons and the Role of Narrow Conduction Bands. All metals, including plutonium, are held together by the electronic, or chemical, bonding between the conduction electrons and the positively charged ion cores that constitute the crystal lattice. Conduction electrons are not localized at individual lattice sites. Instead, they are itinerant and travel almost freely through the crystal. They are the “glue” that binds the ions together. We do not think of glue as moving around, so metals are a bit tougher conceptually than other solids. Nevertheless, it is possible to calculate the specific bands of energy levels that are occupied by the conduction electrons. The structure of those bands determines many properties of metals.

In pure plutonium and other light actinides, the conduction electrons include not only the s, p, and d valence electrons, as in the transition metals, but also the valence electrons unique to the actinides, namely, those in the 5f valence shell. Each plutonium atom has five 5f electrons to contribute to bonding. However, the roles of those 5f electrons in the various solid phases of pure plutonium metal and in its metallic compounds and alloys seem to vary. The 5f electrons can be localized (or bound) at lattice sites, in which case they do not contribute to the bonding, or they can occupy a narrow conduction band and contribute to the glue. Pinning down the exact interactions and correlations among the electrons that lead to this variability between localization and itinerancy is currently the subject of intense studies.

For decades, scientists thought that the pointed shape (angular variation) of

f-electron atomic orbitals and the likelihood that those orbitals would form directional bonds were the source of the anomalies in plutonium metal. That concept was used for solids because it worked so well for molecules and molecular complexes. In fact, when you read the articles on actinide chemistry, you will see the importance of the shape of f orbitals for those molecular systems. In this article, however, we explain how modern band-structure calculations of plutonium in its low-symmetry ground state (the α -phase) have led to a less atomic-like view of at least some of its properties. Those calculations demonstrate that, for plutonium, as for other metals, it is the energy bands that determine such ground-state ($T = 0$) properties as the cohesive energy, the stability of the crystal structure, and the elastic properties. Furthermore, plutonium’s very low symmetry crystal structure in the ground state can be traced to a very particular feature of its energy bands—its dominant conduction band, the one that contributes the most to holding the metal together, is the rather narrow f electron band.

In the latter half of the article, we examine the phase instabilities in pure plutonium, as the metal is heated, and their possible origin in f-electron narrow-band behavior. We then introduce the low-temperature properties that place plutonium among the correlated-electron materials. Finally, we discuss the exotic “heavy-fermion behavior” of cerium and light actinide compounds because, if we can understand these extremely narrow band materials, we may understand plutonium. In general, the low-temperature behavior of correlated-electron materials including plutonium appears to be dominated by as yet unexplained interactions involving their narrow-band electrons. For that reason, the ground states, which in more typical materials are either magnetic or superconducting, are often not well determined and certainly not understood for these materials.

Every few years, condensed-matter physicists find a material with a new

ground state that challenges accepted paradigms, and the community turns its attention to this new challenge. But there is also a compelling need to keep working on plutonium: This metal presents some of the most puzzling behaviors of all the elements, and those behaviors bear on the national security mission of the Los Alamos National Laboratory. Although theory can be done anywhere, plutonium cannot be measured at most laboratories, and so we, at Los Alamos, are working on experiment and theory with renewed intensity.

The ideas in our survey of plutonium range in acceptance from firm science to outright speculation. We will try to make clear which is which, but we include both in order to cover our deepest understanding of this complex element efficiently and, we hope, with more interest.

Basic Properties of Metals

For the most part, metals form in a crystalline state. Unlike amorphous or glassy materials, the atoms in a crystal are arranged in a periodic (repeating) array of identical structural units known as unit cells. The repetition in space means that metals have translational symmetry, and this symmetry underlies all metallic behaviors. Most theoretical models of metals are tractable because they exploit the translational symmetry. For example, even with modern computers, one cannot calculate the electronic structure of a piece of wood because it has no underlying symmetry. The translational symmetry of crystalline solids (not just metals) leads to electron wave functions (or Bloch states) that have that same translational symmetry up to a phase factor. These wave functions are macroscopic, extending over the entire crystal lattice, and they serve as the solid-state equivalents of molecular orbitals. That is, just as electrons in molecular orbitals are the glue that bond atoms into a molecule, electrons in Bloch states are the glue that bond atoms into a crystal.

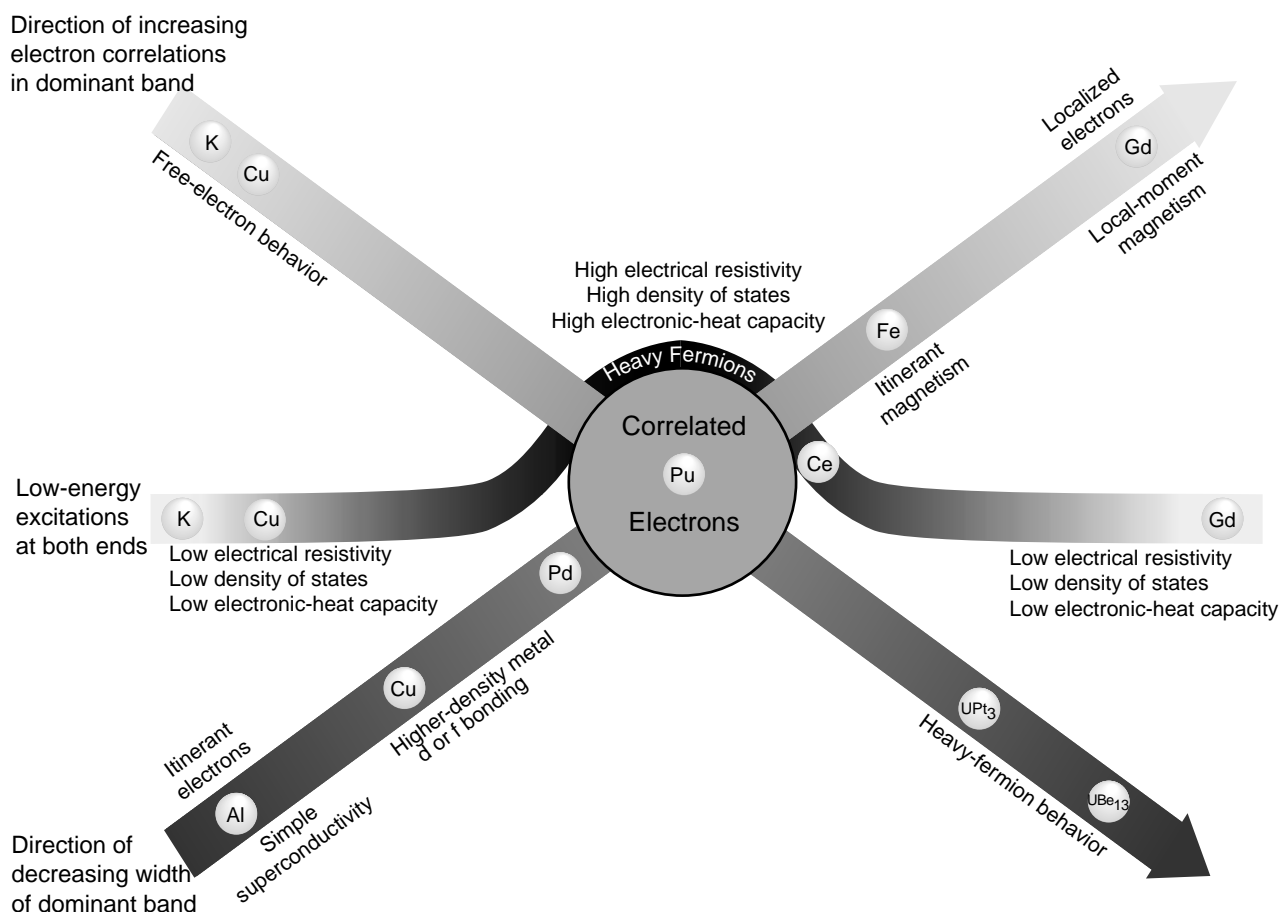


Figure 1. Plutonium at a Crossover in Electronic Properties

This figure summarizes some of the unusual electronic properties of plutonium, stemming from the dominant role of its narrow 5f band. Along one diagonal, plutonium stands midway between simple metals, whose conduction electrons are essentially uncorrelated and exhibit free-electron behavior, and heavy-fermion materials, whose conduction electrons exhibit very strong correlations leading to extremely high effective masses. Along the other diagonal, plutonium stands at the crossover between materials whose itinerant broad-band electrons form superconducting ground states and magnetic materials, whose fully localized electrons (infinitely narrow-band) form local moments and magnetic ground states. Along the horizontal line, plutonium and other correlated-electron narrow-band materials are distinguished from the elements on either side through their high resistivity and specific heat, high density of states at the Fermi energy, and enhanced electronic mass.

The big difference between molecular orbitals and Bloch states lies in their numbers: In a molecule, there are only a few molecular orbitals, but there are on the order of 10^{23} Bloch states. Therefore, one does not focus on individual Bloch states (it is difficult to choose a particular one) but on averages over these states, such as the density-of-states functions discussed in the next section.

Formation of Energy Bands. When light metallic elements, such as lithium or sodium, condense into the solid state, they typically have cubic struc-

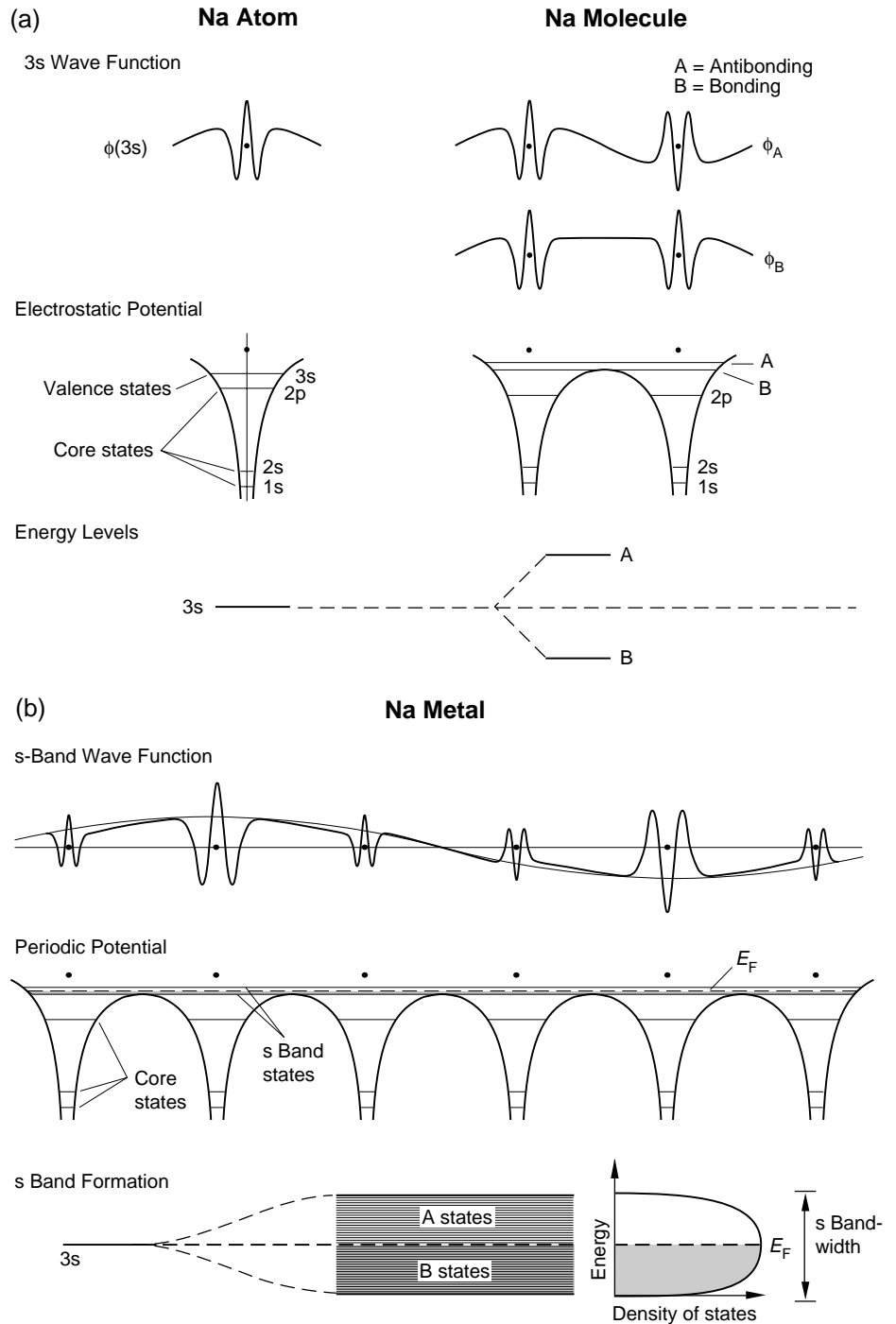
tures at room temperature, and the electrons from their atomic valence shells become conduction electrons traveling almost freely through the lattice. That is, these valence electrons occupy one-electron Bloch states, and they are therefore responsible for bonding the solid. The allowed energies of those Bloch states form a broad band of energy levels. In a metal, this energy band is a conduction band because it is only partially filled. Because many empty states are available, the conduction electrons with the highest energies respond to low-energy thermal and electrical excitations as if they were

a gas of free particles.

Figure 2 illustrates band formation and the formation of Bloch states in sodium. The top of the figure shows that, when two sodium atoms are brought together, their 3s-electron wave functions (orbitals) overlap, and the valence electrons feel a strong electrostatic pull from both atoms (depicted as the double-well electrostatic potential). The atomic orbitals combine to form molecular orbitals that may bind the two atoms into a diatomic molecule. The single atomic energy level splits into two: one lower in energy, or bonding, and the other higher in energy, or antibonding.

Figure 2. The Formation of an Energy Band in Sodium

The figure shows the transformation of electronic structure when two sodium atoms are brought into close proximity and when numerous atoms condense to form sodium metal. (a) When two sodium atoms are brought together to form a diatomic molecule, the atomic wave function for the 3s valence electron changes into two molecular wave functions—one is bonding (ϕ_B) and the other antibonding (ϕ_A)—corresponding to the sum and the difference of the 3s atomic wave functions, respectively. The single potential well of the isolated sodium atom with its 3s-valence energy level and its core energy levels becomes a double-welled potential, with bonding (B) and antibonding (A) molecular energy levels replacing the valence energy level. Finally, the energy level diagram shows the 3s atomic energy level becoming molecular energy levels A and B, which correspond to the molecular wave functions ϕ_A and ϕ_B , respectively. (b) When N atoms are brought together, the 3s radial wave function becomes a Bloch state made up of a 3s atomic wave function at each atomic site modulated by a plane wave. The single potential well becomes a periodic potential well with core level states at atomic sites and the energy levels of the Bloch (conduction electron) states above the potential wells. The energy level diagram shows the original 3s level becoming a band of N very closely spaced energy levels, whose width is approximately equal to the energy difference between levels A and B in the diatomic molecule. That energy difference or bandwidth is proportional to the amount of overlap between atomic wave functions from neighboring sites. In sodium metal, the 3s conduction band is only half full, and the highest occupied state at $T = 0$ is denoted by E_F , the Fermi energy. Also shown is the number of energy levels per unit energy, or the density of states, for this s-electron conduction band.



The energy difference between these two levels is proportional to the amount of overlap of the two s-electron atomic orbitals, and the molecular orbitals (wave functions) corresponding to the bonding and antibonding energy levels are sum and difference, respectively, of the atomic orbitals.

Similarly, when N atoms are brought close together to form a perfect crystal (bottom of Figure 2), a single valence

electron sees the periodic electrostatic potential due to all N atoms. Its wave function (Bloch state) is now a combination of overlapping 3s wave functions from all the atoms and extends over the entire volume occupied by those atoms. As in the molecular case, that wave function can be a bonding state or an antibonding state. The original atomic valence levels generalize to a band of very closely spaced energy levels, half

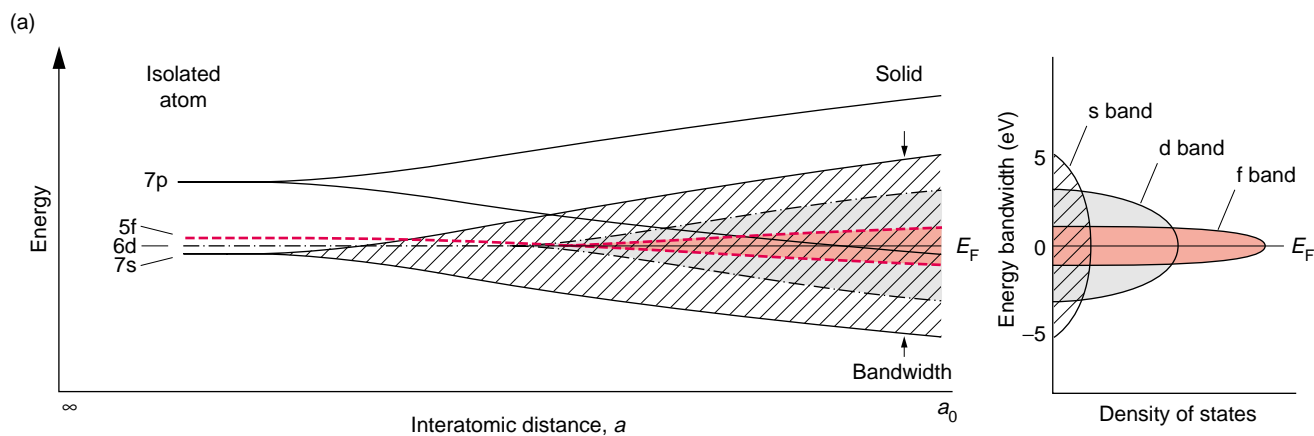
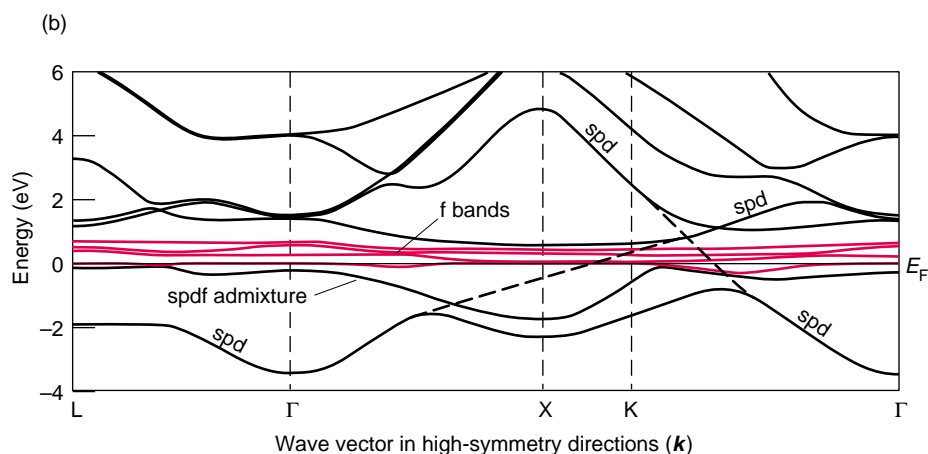


Figure 3. Multiband Formation in the Light Actinides

(a) Illustrated here are the multiple energy bands that form in going from a single actinide atom to a solid. Multiple bands always form when an atom has more than one valence electron. Note that the s and p bands are much wider than the d band, which is much wider than the f band. Also, because the s, p, d, and f states overlap in energy, they can hybridize with each other. That is, any Bloch state with wave vector $k(\Psi_k)$ can be a linear combination of states

from the different bands with that same wave vector. Finally, the density-of-states functions show that the narrow f band dominates at the Fermi energy because it is so much narrower than the other bands and therefore has many more states at that energy.

(b) The energy bands, one-electron energies as a function of wave vector k , are shown for cerium. The very narrow f bands at the Fermi energy are shown in red. The spd bands are broad. States with the same symmetry cannot cross the Fermi energy level. We therefore show by dashed lines how the spd bands would connect if no f bands of like symmetry were present.



of them bonding and half of them antibonding, and the width of the energy band is approximately equal to the energy split between the bonding and antibonding energy levels in the diatomic molecule. This broad band forms whether the crystal is an insulator, a metal, or a semiconductor.

Because in a macroscopic sample the number of levels in the energy band is large (approximately 10^{23}) and the spacing between those levels is small, we can consider the electron energies to be a continuous variable. We describe the number of electron energy levels per unit energy in terms of a density of states that varies with energy. Because each electron must have at least a slightly different energy (the Pauli exclusion principle), electrons fill up

the energy levels one by one, in order of increasing energy.

A Bloch state, or the three-dimensional extended wave function of a valence electron in a solid, is represented in Figure 2 in one dimension. In this example, the 3s valence electron wave function of sodium appears at every atomic site along a line of sodium atoms, but its amplitude is modulated by the plane wave $e^{ik \cdot r}$. As we mentioned before, this general form for a Bloch state in a solid emerges from the requirement of translational invariance. That is, the electron wave function in a given unit cell must obey the Bloch condition $u_k(\mathbf{r} + \mathbf{T}_n) = u_k(\mathbf{r})$, where \mathbf{T}_n is a set of vectors connecting equivalent points of the repeating unit cells of the solid. It must therefore be of the form

$\Psi_k(\mathbf{r}) = e^{ik \cdot \mathbf{r}} u_k(\mathbf{r})$, where a plane wave with wave vector \mathbf{k} modulates the atomic wave function in a solid. The wave vector \mathbf{k} , or the corresponding crystal momentum $\mathbf{p} = \hbar\mathbf{k}$, is the quantum number characterizing that Bloch state, and the allowed magnitudes and directions of \mathbf{k} reflect the periodic structure of the lattice. Similar Bloch states exist in all crystalline materials, and their occupation by valence electrons is what binds the atoms into a single crystal.

The electronic structure gets more complicated in metals containing more than one type of valence electron. For example, Figure 3 shows that multiple overlapping bands are created when the conduction electrons in a solid originate from, say, the s, p, d, and f valence orbitals of an atom, as in the light

actinides. The width of each band increases from left to right, as the interatomic distance decreases and the overlap of the wave functions increases. Also, the s and p bands are always wider (span a wider energy range) than the d band, which in turn is always wider than the f band. The overlapping bands in Figure 3 imply that the Bloch functions with a given quantum number (wave vector) \mathbf{k} could be linear combinations of states originating from the s, d, p, and f atomic orbitals. In other words, the Bloch states could be “hybridized” states containing many angular-momentum components, in contrast to atomic orbitals that contain only one angular-momentum component. Figure 3 also shows the density of states $D(\epsilon)$ resulting from this multi-band structure. Note that the f states outnumber all the others at the Fermi energy E_F , which is defined as the highest energy level occupied by a conduction electron at the absolute lowest energy of the metal ($T = 0$). Later, when we discuss cohesion, we will show that these f states dominate the bonding of plutonium in the ground state (or α -phase), primarily because there are five f electrons per atom and only one d electron per atom occupying the Bloch states and participating in bonding. (There are, of course, two electrons in s and p bands but they contribute little to the bonding.) For that reason, we refer to the narrow f band in plutonium as the dominant band. Because narrow bands correspond to small overlaps of wave functions, these f band electrons may be easily pushed toward localization by various effects, in which case they do not contribute to bonding.

If an energy sub-band is filled (electrons occupy all its energy levels), the solid is an insulator. If a band is only partially filled, the solid is a metal. Thus, in a metal there are many empty states close in energy to the occupied states, and so the electrons can easily change their motion (energy) in response to small temperature and electromagnetic perturbations.

The Free-Electron Model and Departures from It. Beyond contributing to bonding, conduction electrons are also thermally excited. In simple broad-band metals such as potassium and copper, the free-electron model describes these low-energy excitations. In that model, the electrons occupying the Bloch states in the conduction band are treated as a gas of identical free particles. That is, the periodic electrostatic potential seen by the conduction electrons and the interactions and correlations among the electrons have no explicit role. However, the model does account for the conduction electrons obeying the Pauli exclusion principle, and therefore at $T = 0$, they fill in the conduction band in order of increasing energy up to the Fermi energy E_F . If we draw the energy states in the three-dimensional space defined by the crystal momentum $\hbar\mathbf{k}$, as in Figure 3(b), then E_F traces a surface in momentum space (or \mathbf{k} -space) known as the Fermi surface. In the free-electron model, each state corresponds to an electron with crystal momentum $\mathbf{p} = \hbar\mathbf{k}$ and with kinetic energy given by the free-particle formula, $\epsilon = (\hbar\mathbf{k})^2/2m_e$.

For a gas of free particles heated from absolute zero to a temperature T , classical statistical mechanics would predict that, on the average, the kinetic energy of each particle would increase by an amount $k_B T$. But because of the exclusion principle, the electrons respond differently. Only those conduction electrons occupying states within $k_B T$ of the Fermi level E_F can be heated (by phonon scattering) because only they can access states not occupied by other electrons (see Figure 4). The number of electrons that participate in properties such as electrical conduction and electronic heat capacity decreases to a fraction T/T_F of the total number of conduction electrons in the metal (here, the temperature at the Fermi surface T_F is defined by the relation $k_B T_F = E_F$). At room temperature, T/T_F is about 1/200 in most metals. Thus, replacing the classical Maxwell-Boltzmann statistics with the Fermi-Dirac quantum sta-

tistics implied by the exclusion principle has a profound impact on the electronic properties of metals.

The factor T/T_F shows up explicitly in the low-temperature specific heat of a metal. In general, the specific heat is the sum of a lattice vibrational term (proportional to T^3), which is due to the thermal excitation of the ions, and an electronic term γT , which is due to the thermal excitation of the electrons. The classical coefficient of the electronic term is $\gamma = Nk_B$, but because of the exclusion principle, it becomes $\gamma = Nk_B T/T_F$, and only electrons near the Fermi energy can be heated. Thus, in simple metals obeying the free-electron model, γ is inversely proportional to T_F , or equivalently, E_F , and therefore proportional to the rest mass of the free electron, m_e . Later, when we discuss the low-energy excitations in correlated-electron materials including plutonium, we show that the conduction electrons depart from free-particle behavior. They behave more like the strongly interacting particles of a liquid, more like a Fermi liquid. Because the interactions slow down the electrons, the effective mass of the electrons appears larger, and it shows up as an increase in the value of γ over that predicted by the free-electron model. Thus, low-temperature specific-heat measurements reveal the strength of the electron-electron correlations in a metal and therefore provide a major tool for identifying unusual metals.

Electrical resistivity at low temperatures tells us about the quality of the metal. In a perfect crystal, electrical resistance would be zero at the classical $T = 0$ because the noninteracting conduction electrons, acting as waves, would move through the perfect lattice unimpeded. Above $T = 0$, the thermal excitations of lattice vibrations (phonons) make the lattice imperfect and scatter the electrons. The electrical resistance increases linearly with temperature, as will be shown later in this article. In general, anything that destroys the perfect translational invariance of the crystal lattice will scatter

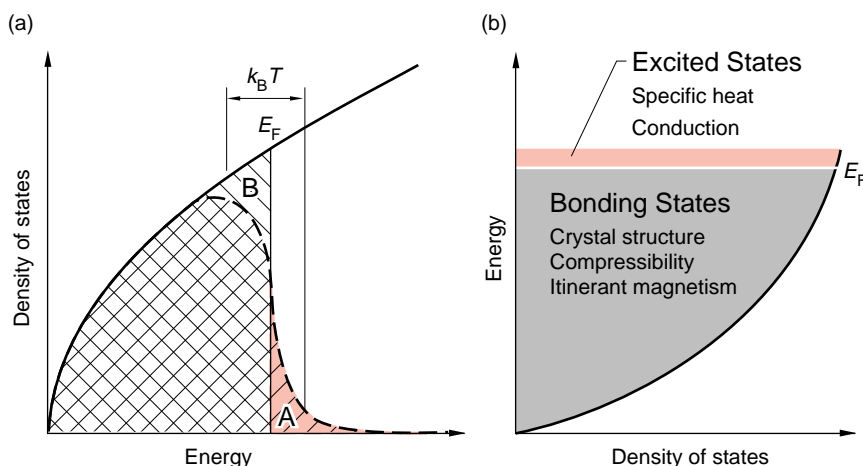


Figure 4. Density of States for a Free-Electron Gas

(a) The solid line is the density of single-particle states for a free-electron gas plotted as a function of one-electron energy ϵ . At $T = 0$, electrons occupy all the states up to the Fermi energy E_F . The dashed curve shows the density of filled states at a finite temperature T , where $k_B T$, the average thermal energy per particle, is much less than the Fermi energy. Only electrons within $k_B T$ of the Fermi level can be thermally excited from states below the Fermi energy (region B) to states above that level (region A). (b) This plot of the density of states emphasizes that all electrons in the conduction band participate in bonding, whereas only those with energies near the Fermi energy contribute to low-energy excitations, such as specific heat, and conduct electricity.

electrons. Foreign atoms, lattice vacancies, more-complicated defects such as stacking faults, and finally, magnetic moments in an array without the full symmetry of the lattice can scatter electrons. Many of these imperfections are temperature independent and lead to a finite limiting resistance as $T = 0$ is approached. Hence, this limit is used as a measure of the quality of metal samples, for which the lowest residual resistance signifies the most perfect sample. We will show that correlated-electron materials often have anomalously high resistivities and very small or zero magnetic moments at low temperatures.

Models of Conduction Electrons

We have suggested that the electrostatic forces holding the metal together can be considered averaged forces between the ions and conduction electrons and that these forces can be modeled by a periodic electrostatic

potential. On the other hand, once a metal is formed, its conduction electrons (approximately 10^{23} per cubic centimeter) can act collectively or in a correlated manner, giving rise to what is called quasiparticle or free-electron behavior (not determined by averaged electrostatic forces) and to collective phenomena such as superconductivity and magnetism.

These two seemingly opposing views of conduction electrons and their behavior in solids first appeared in the scientific literature in 1937 and 1957. John Slater (1937) proposed calculating the electronic states—the energy bands in Figures 2 and 3(b)—of solids by the same self-consistent method that had been applied so successfully to describing the electronic states of atoms and molecules. In this method, one treats electrons as independent particles and calculates the average Coulomb forces on a single electron. The other electrons and all the ions in the solid are the source of these Coulomb forces on one electron. This calculation, repeated for all the electrons in the unit cell, leads to

a charge distribution from which the electrostatic potential seen by the electrons can be obtained as a solution of Poisson's equation. Using the new electrostatic potential, one then repeats the calculations for each electron until the charge density (distribution of electrons) and the crystal potential (forces on the electrons) have converged to self-consistent values. Slater's approach led to all the modern electronic-band-structure calculations commonly labeled one-electron methods. These one-electron band-structure methods are adaptations of the familiar Hartree-Fock methods that work so well for atoms and molecules. They were put on a more rigorous footing through Walter Kohn's development of density functional theory (DFT). For his achievement, Kohn became one of the recipients of the 1998 Nobel Prize in Chemistry.

Lev Landau (1957) took a different view and argued that the collective motion of electrons in a solid's conduction band was very different from the motion of electrons in atomic or molecular orbitals. He pointed out that particles in the conduction band act as if they were nearly free even though the individual electrons are subject to strong Coulomb forces. Landau's way out of this paradox was to argue that the effect of the electrons' correlated motions from mutual interactions in the solid was to "clothe" themselves, which screens their charge. In heuristic terms, a conduction electron is very much like an onion with many layers. When the electromagnetic force is weak, the interaction penetrates only a few layers, and the electron appears to be clothed. When the force becomes stronger, however (as in the ejection of conduction electrons by photons in photoemission experiments), the interaction penetrates many more layers until the bare electron with its Coulomb force becomes visible, as it does in the one-electron models.

And yet, the conserved quantum numbers characterizing the single-particle states of the clothed electrons—such as spin, momentum, and charge—are unchanged by the

Electron Correlations vs Correlated-Electron Materials

Electron correlations are always mentioned in discussions of electronic structure or excitations, but their physical origin is not always explained. Here, we will give a simple argument for the need to include electron correlations. We will also give some examples of such correlations.

Assume that we have a container of electrons (no ions) that are noninteracting and that we can remove the container and turn on the interactions. At that point, the electron cloud will expand indefinitely because of the Coulomb repulsion between the electrons. No correlations are needed to describe this motion of free electrons. Note that the term free-electron behavior as applied to conduction electrons really means that the electrons act like neutral particles (no charge) that obey Fermi-Dirac statistics—that is, they act like Landau's quasiparticles.

Now suppose that we have a container with an equal number of ions and electrons and that the ions are on closely spaced lattice sites, as in a real solid. Again, we remove the container and turn on the interactions. We assume that our electrons are in random positions and their de Broglie wavelengths are greater than the ion spacings when the interactions are turned on. In this case, the electrons' motion is much more complex because the electrons are simultaneously attracted to the ions and repelled from each other. To minimize the total energy of the system, the electrons must minimize the electron-electron repulsion while maximizing the electron-ion attraction, and the way to minimize the Coulomb repulsion is for them to stay as far from each other as possible. Below, we will demonstrate how electrons are kept apart in real calculations, and the reader will thus get a feel for what we mean by electron correlations.

We will first consider the helium atom, which has two occupied atomic orbitals—one for each electron. Helium was the first many-electron system for which a quantum mechanical calculation was attempted. In developing a model that would predict the observed spectral lines of helium, physicists discovered two unanticipated properties of the electrons. First, the two electrons are indistinguishable—that is, electron 1 can be in

orbital A or B, and so can electron 2. Second, the electrons have to obey the Pauli exclusion principle, which means that the total wave function for the two electrons has to be antisymmetric, and that antisymmetry implies that the Hamiltonian must contain an exchange term. This exchange term is what separates the Hartree-Fock calculations of many-electron atoms from the original Hartree calculations of those atoms.

When the exchange term was included in the calculation of an electron gas, it was found that around each electron, there is a “hole,” or depression, in the probability of finding another electron close by. The accompanying figure shows the “exchange” hole, which is the probability of finding an electron of the same spin near a given electron. That probability is one-half the value it would have without the exchange term. This exchange hole demonstrates that the electron motion is correlated, in the sense that electrons with the same spin cannot get close to each other. In the 1930s, Wigner performed similar calculations for electrons of opposite spins,

which led to a “correlation” hole (very similar to the exchange hole) for the probability of finding an electron of opposite spin near a given electron. The picture of an exchange hole and a correlation hole around each electron is a great visual image of electron correlations in solids. Modern one-electron calculations include these correlations in an average way

because these terms can be calculated from the average electron density around a given electron.

Having given a physical basis for the need to include electron correlations, we now refer to the modern usage of the phrase. Any theory that includes interactions beyond the one-electron method is now considered a correlated-electron theory. Likewise, any solid (metal, insulator, and so on) that exhibits behavior not explained by either the free-electron model or the one-electron band model is considered a correlated-electron system. If the properties of a solid deviate strongly from the predictions of free-electron or band models, that solid is called a strongly correlated system. Figure 1 in the main text shows examples of such systems.

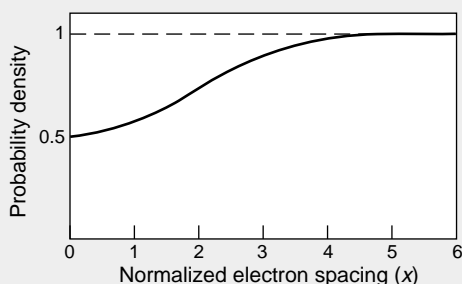


Table I. Solid-State Excitations

Excitation	Excitation Energy	Typical Theoretical Method
Photoemission	20–1500 eV	One-electron/many-electron
Band formation	2–10 eV	One-electron
Cohesion	2–10 eV	One-electron
Phase stability	1–25 meV	One-electron
Elastic constants	1–25 meV	One-electron
Magnetic moments (band)	1–25 meV	One-electron
Magnetic moments (local)	1–25 meV	One-electron
dHvA signals	0.1 meV	One-electron/many-electron
Resistivity	0.1 meV	One-electron/many-electron
Specific heat (at low temperature)	0.1 meV	One-electron/many-electron
Magnetic ordering	0.1 meV	Many-electron
Superconductivity	0.01–0.1 meV	Many-electron

interactions. This argument led Landau to propose a one-to-one correspondence between the interacting and noninteracting systems. That is, the number of energy levels in the interacting system (labeled by the conserved quantum numbers of the noninteracting system) and the number of elementary excitations (or clothed particles) in the interacting system would be the same as those in the noninteracting system. The clothed electrons, called quasiparticles, with their physical properties modified, would then interact very weakly and thus have almost-free-particle behavior.

Landau's original argument was meant to explain the nearly-free-electron behavior seen in the conduction electrons in simple metals, in the atoms in liquid helium-3, and in the protons and neutrons in nuclear matter. Later, scientists realized that the same conceptual framework could be applied to small-energy electronic excitations of solids in which the conduction electrons do not exhibit nearly-free-electron behavior but behave more like a liquid. For this reason, the Landau method can be considered a correlated-electron method. Landau's genius was to recognize that these correlations did not have to be calculated directly. Instead, one could assume that the correlations were built into the behavior of the quasiparticles, which could therefore no longer

be identified as electrons. The small deviations of those quasiparticles from free-particle behavior were the sign of residual interactions, and the effects of those interactions on the quasiparticle behavior could be determined directly from experimental data. The downside of this theory is that the measurable parameters are not easily derived from first-principles calculations, and so their meaning is not always clear.

Although the one-electron band theories and the correlated-electron theories seem incompatible, we have learned that both are correct and that their relevance depends on the energy and time scale used to view the conduction electrons. We also know that all theories of conduction electrons must include clothing, or correlations. The one-electron methods include averaged correlations, which produce an averaged exchange hole and correlation hole around each electron (these terms are defined in the box "Standard Electron Correlations vs Correlated-Electron Materials"). For higher energies and longer times, such as those involved in bonding, these one-electron methods work well because the averaged correlations dominate the behavior of the electrons. For low-energy excitations, spin and charge fluctuations become more important than averaged values, and the Landau method, which incorpo-

rates these fluctuations in the behavior of the quasiparticles, becomes more useful.

Models for Correlated-Electron Materials. Until 1980, we had these two general methods for calculating phenomena involving higher and lower energies, and they worked quite well—except for some isolated systems. But, in the early 1980s, we began finding new metallic materials, the heavy-fermion and mixed-valence materials, whose behavior was as anomalous as that of the light actinides. Resistivities, specific heats, magnetic susceptibilities, electron masses, and other low-energy excitations were different in different materials of the same class and had strange temperature dependencies. Some of these anomalies had been seen before, but they seemed isolated. Almost every new material appeared to exhibit odd behaviors that could not be explained by one-electron models or the Landau treatment.

We now recognize that the central feature of all these materials, including plutonium, is the presence of a dominant, narrow conduction band. We also recognize that the exotic behavior of these materials has a common source: the spin and charge fluctuations associated with the low-energy excitations in those narrow bands. As indicated

before, narrow bands mean that the wave functions from different atoms are barely overlapping, and the electrons are thus bordering on being localized. These materials are now collectively called correlated-electron materials, and those with the most extreme behavior are the heavy fermions. (In the late 1980s, another class of materials was discovered, namely, high-temperature superconductors. Although they are complicated and interesting, high-temperature superconductors are not narrow-band materials. Their exotic behavior is therefore unrelated to that of plutonium.)

Along with the discovery of correlated-electron materials came a new class of many-electron models to describe the exotic behaviors of those materials. The Kondo, Hubbard, and Anderson models are among them. These models stand between the one-electron methods and the Landau method in the sense that they can be used to add electron-electron interactions (correlations) to either the semi-clothed electrons of one-electron theory or to the quasiparticles of the Landau theory. Originally, the Kondo and Anderson models were invented to solve specific mysteries in materials containing impurities, and they can be generically classed as two-electron “impurity” models. That is, they introduce interactions between pairs of electrons, one localized on an impurity atom and one in a conduction band.

Unfortunately, these impurity models break the translational invariance of the crystal lattice. To become applicable to correlated-electron systems, these models must allow translational invariance to be restored. In the standard approach, the localized (or “almost localized”) *f* electrons become the impurity, and one postulates a lattice of couplings between conduction electrons and the *f* electrons, which are either located at every lattice site or distributed randomly among the sites. In principle, translational symmetry makes these extended impurity models soluble, but in practice, the models present

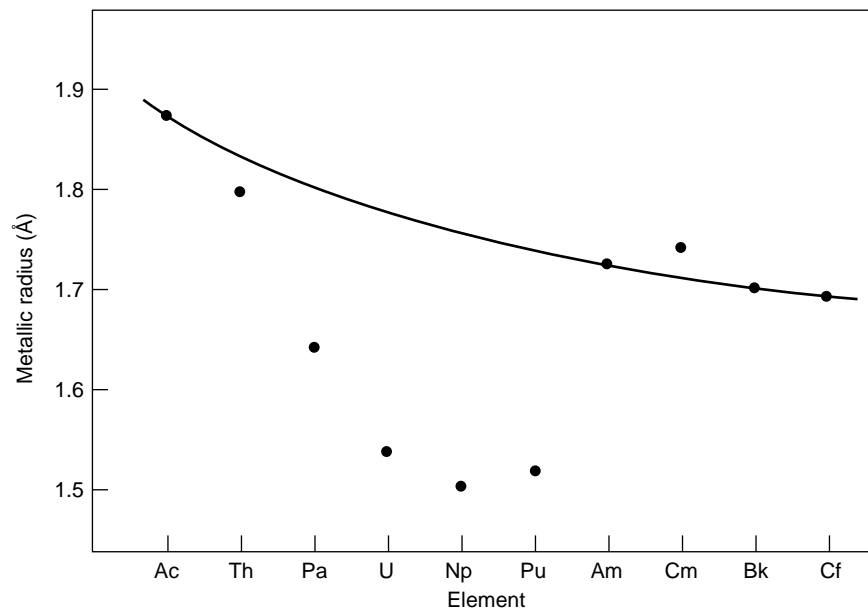


Figure 5. The Metallic Radii of the Actinide Elements in the Ground State The metallic radius is half the average distance between the atoms in the solid. The line follows the smoothly varying metallic radii of the simple trivalent actinide metals, whose *f* electrons are localized and therefore nonbonding. The metallic radii of the light actinides—thorium through plutonium—fall on a parabolic curve below the trivalent line, showing the contribution of the *f* electrons in the bonding, that is, in pulling the atoms closer together.

enormous calculational difficulties, and progress in solving them has been slow.

Energy Scales of Electronic Phenomena. Table I lists solid-state excitations or effects, along with the energy scale and theory most applicable for each effect. Effects for relatively high energies—2 to 10 electron-volts (eV)—include the ground-state crystal structures, as well as the particular bonding energies and stability of those structures. Those properties are modeled with one-electron methods as are the elastic constants, which are among the effects for moderate energies—1 to 25 milli-electron-volts (meV). Low-energy (0.1 meV) excitations and phenomena such as resistivity, magnetic ordering, and specific heat can be described by either one-electron or many-electron models, whereas the very low energy (0.1 to 0.01 meV), collective electronic ground states such as superconductivity and magnetism can only be

described by many-electron models.

Not all phenomena in solids, however, can be fully treated by a single approach. For example, the de Haas–van Alphen (dHvA) effect¹, as seen in heavy-fermion materials, requires both. The oscillations can be explained by one-electron theories, whereas the very heavy electron masses are explained only by correlated-electron theories. Another example is provided by the spectra obtained from photoemission experiments, which are performed at relatively high energies but for short times. Photoemission spectra measure the one-electron density of states predicted from one-electron methods, but because of the short time, spin and charge fluctuations may add small features to the overall spectra (see the article “Photoelectron Spectroscopy of α - and δ -Plutonium” on

¹The dHvA effect is the oscillation in magnetic susceptibility at low temperatures, as an applied magnetic field changes.

page 168). Clearly, we need both theoretical techniques to explain the properties of metallic plutonium and its compounds.

To convey an overall picture of the actinide metals, we first discuss their bonding properties, for which we use one-electron methods. Later in the article, when we look at phase instabilities and other lower-energy phenomena, we will need arguments and concepts from correlated-electron theories.

Cohesion in the Light Actinides—Similarity with the Transition Metals

Our discussion of the bonding properties in the actinides focuses on the role of the 5f valence electrons. The 5f electrons in the light actinides (thorium through plutonium) are itinerant, just like the 5d electrons in the transition metals, participating in the bonding of the solid and affecting most of the high-energy properties such as cohesion, crystal structure, and elastic properties. In contrast, the heavy-actinide metals (americium through lawrencium) have localized (atomic-like as opposed to itinerant) 5f electrons, and they are thus the true counterpart to the rare-earth metals. (The presence of localized magnetic moments in both the lanthanides and the heavy actinides is a direct sign that f electrons are localized.)

Figure 5 is a plot of the metallic radii of the actinides, and it gives explicit evidence for the bonding behavior of the 5f electron series in the ground state. Notice that the light actinides have smaller metallic radii (therefore, higher densities) than the heavy actinides. The reason is that the f electrons in the light actinides contribute to the bonding. Also, the metallic radius of the light actinides gets smaller with increasing atomic number (Z) because each additional f electron per atom pulls the atoms closer together. This trend stops at americium. The metallic radii of the heavy actinides are all about the same,

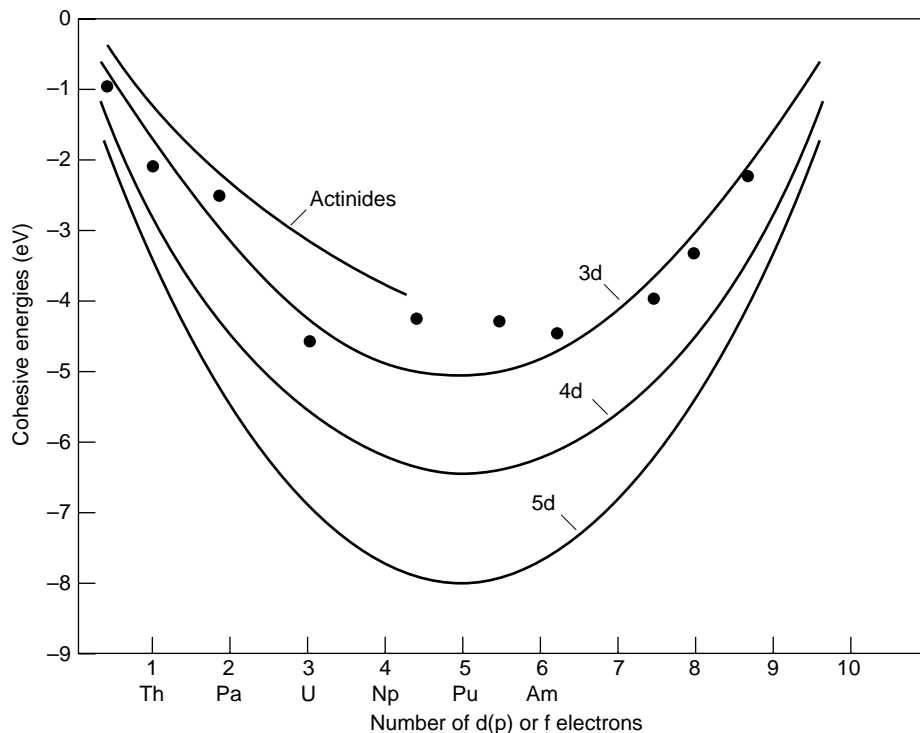


Figure 6. One-Electron and Friedel Model Results for the Cohesive Energies of the d and f Series

The calculated cohesive energies per atom of the 3d metals (dots) are equal to the calculated difference between the binding energy of an isolated atom (excluding atomic valence-electron coupling) and the binding energy of an atom in its solid. For pedagogical reasons, in these LDA one-electron calculations, the metals were assumed to be in the fcc crystal structure. (The cohesion of the other structures differs by up to 10% from that of the fcc phase.) The Friedel model predicts a parabolic curve for the 3d metals. This simplified model of bonding assumes that the density of states in the d band of the transition metals is constant over its width. The model also assumes that the d electrons fill the energy band in order of increasing energy: First the bonding d states are filled, which increase the binding, and then the antibonding d states, which decrease the binding. Thus, maximum stability is reached when the band is half full. (Refer to the article “Actinide Ground-State Properties” on page 128 for a more detailed discussion of this model.) The LDA one-electron results agree with the predictions of the Friedel model. We show only the parabolic curves for the 3d, 4d, and 5d elements and for the light actinides. The cohesive energies of the light actinides look similar to those of the transition metals—that is, they show increased bonding as the f shell is being filled.

and that value is larger than that for the radii of the light actinides because the localized 5f electrons have no effect on bonding.

Ironically, before the Manhattan Project, when thorium and uranium were the only actinides whose physical properties were known, these metals were thought to belong to a 6d metal series to be placed below hafnium and tungsten in the periodic table of the ele-

ments. The similarities between thorium and uranium and the 5d transition metals were the cause for this misconception. After McMillan and Abelson discovered neptunium in 1940 and after the discoveries of plutonium, americium, and curium during the Manhattan Project, measurements of atomic spectra showed that the valence electrons in this ever-lengthening series were filling a 5f shell and not a 6d shell of atomic

orbitals. These 5f electrons were expected to be localized in the solid state, like the 4f electrons of the rare earths. Long after the Manhattan Project, the pendulum swung back, as scientists realized that the similarities between the light actinides and the 5d transition-metal elements meant that the 5f electrons in those early actinides did indeed form a conduction band.

The cohesive energy per atom holding a crystal together is defined as the difference between the electrostatic binding energy per isolated atom (ignoring coupling among electrons) and the total internal (electrostatic binding) energy per atom in a crystal. Both binding energies, and thus the cohesive energy, are calculated self-consistently by one-electron methods. Figure 6 shows the one-electron predictions for the cohesive energy per atom of 3d transition metals in a hypothetical face-centered-cubic (fcc) structure (dots) and the Friedel model predictions for the 3d, 4d, 5d, and 5f elements (parabolic curves). The Friedel Model, a simplified model of bonding, assumes that the d electrons are conducting and are filling an energy band in order of increasing energy: first, the bonding d states, which increase the amount of binding, and then the antibonding d states, which decrease that amount. Note that the Friedel model predictions for the 3d elements fit the results from quantum mechanical one-electron calculations quite well. And the bonding in the 4d and 5d metals is greater than that in the 3d metals because 4d and 5d electronic states have a greater radial extent (more overlap) than 3d states (a feature not obtained from the simple Friedel model). The cohesive energies of the light actinides look similar. That is, they show increased bonding with the filling of the beginning of the 5f shell. However, the parabolic trend in the early actinides ends at americium because the 5f electrons are no longer contributing to bonding.

Similarly, the lattice constants (length of the edge of the basic cubes in a cubic crystal structure) tend to

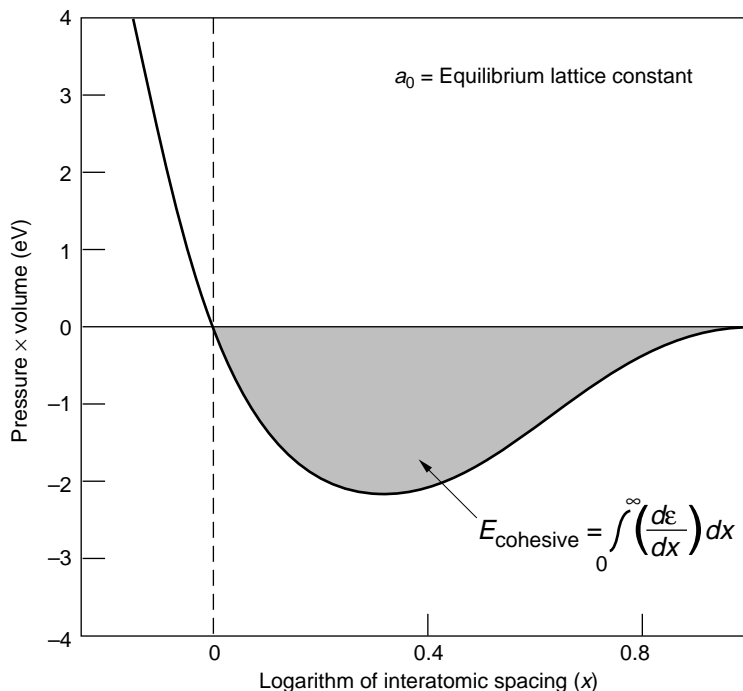


Figure 7. The Bonding Curve for Potassium

The plot shows LDA one-electron calculations of the bonding curve for potassium in the fcc structure, which is the change in cohesive energy per atom, dE/dx , as isolated potassium atoms at infinite separation are brought together to form a solid. We plot this quantity as $P\Omega$ (pressure times volume or force times length) vs the separation between atoms (or lattice constant a). The shaded area under the bonding curve is the cohesive energy to bond the atom in the solid. To compress the bonding curve, the horizontal axis is a logarithmic scale $x = \ln(a/a_0)$. Equilibrium occurs when $dE/dx = P = F/A = 0$, at which point $a = a_0$ and $x = 0$ (the dashed line in the figure). The bulk modulus (average elastic constant) is given by the slope of the curve at equilibrium (that is, at $x = 0$ and $dE/dx = 0$). At the minimum in the curve, the attractive forces between the atoms are the greatest. Those forces weaken as the atoms move together until they vanish at the equilibrium separation.

decrease as one goes across the first half of all the d and the 5f series, again indicating that each additional electron increases the bonding or cohesion. Recall that metallic radii also decrease parabolically across the early part of the 5f series, as revealed in Figure 5.

Plutonium and the Universal Bonding Curve of Metals

The parabolic trend in cohesion and lattice constant extends to the bulk modulus, which is the average elastic (or spring) constant of the solid. The bulk modulus thus gives the strength of

the restoring forces, or interatomic forces, that bind the solid together as the ion cores vibrate about their equilibrium positions. For most metals, the bulk modulus, the cohesive energy, and the lattice constant can be related to each other through the “universal bonding curve.” We will show next that plutonium fits this curve as well.

First developed as a parameterized equation, the bonding curve is a plot of pressure (cohesive force per unit area) on an atom vs the distance between the atoms. Figure 7 shows the bonding curve for potassium metal calculated from one-electron band-structure calculations in the atomic-sphere approxima-

tion (the electrostatic potential around each lattice site is assumed to be spherical). Here, the bonding forces are for atoms arranged in an fcc structure, and they are plotted as a function of x , the natural log of the lattice spacing a normalized by a_0 . At very large interatomic distances, the atoms are isolated, and the pressure on any atom is zero. As the atoms approach each other, their electronic wave functions overlap, and there is an attraction, or pressure, that pulls them together. Finally, they reach equilibrium at the lattice constant a_0 , where again the pressure on the atoms is zero. In Figure 7, the cohesive energy is the area between the bonding curve and the line indicating zero pressure; the equilibrium lattice spacing is at $x = 0$ (or $a = a_0$), the value at which the bonding curve crosses the zero pressure line; and the bulk modulus is the slope of the bonding curve at this equilibrium spacing. Remember that this curve represents the forces on an atom in the solid. Therefore, the minimum in the curve is the lattice constant at which the attractive force between the atoms is the greatest. As the atoms move closer together, the attractive force becomes weaker and vanishes at the equilibrium lattice constant a_0 .

We will next illustrate that there is only one bonding curve for all metals, including plutonium. We first calculate the bonding curve for molybdenum because, among metals, it has the largest cohesion. We then plot all other metals on this curve, by drawing the zero pressure line for each metal so that the area between that line and the bonding curve is equal to its cohesive energy. The results, shown in Figure 8 for several metals, reveal the following relationships: First, if the cohesion of one metal is greater than that of another, then its lattice constant is smaller. Next, the bonding curve becomes steeper as the interatomic distances get smaller (see the part of the curve to the left of the maximum force point). This means that the tangent to the curve (bulk modulus) becomes larger as one moves up the curve. So, if the cohesion of one

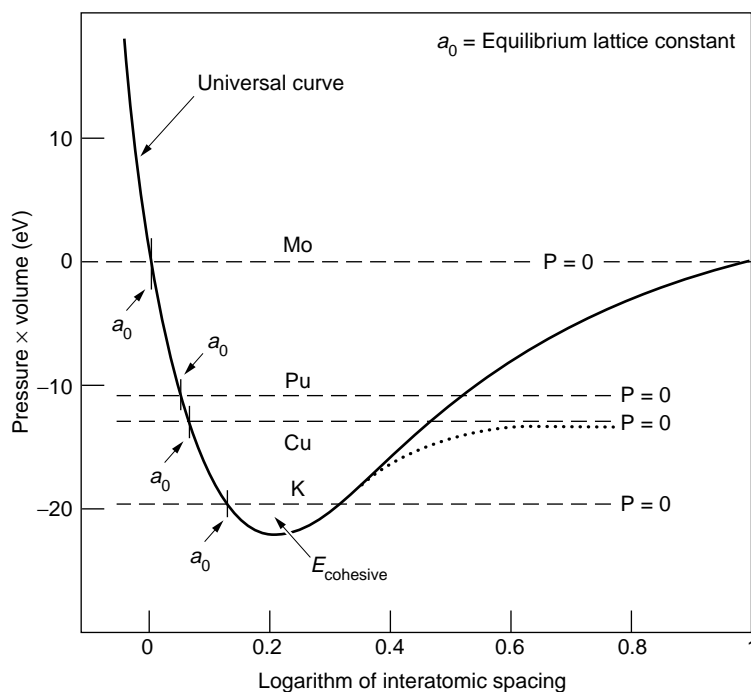


Figure 8. A Universal Bonding Curve

LDA one-electron calculations of the bonding curves for potassium, copper, plutonium, and molybdenum in fcc structures are overlaid on the same curve. The horizontal axis for each metal is placed at zero pressure for that metal, and the area between that axis and the curve gives the correct cohesive energy per atom. (The dotted curve for copper shows that, in this construction, we are ignoring the large distance tails of the bonding curve for each element.) A number of relationships are apparent in this figure. As the cohesive energy increases from one metal to the next, the $P = 0$ axis moves up, and the equilibrium lattice constant a_0 decreases (moves to the left). At the same time that a_0 moves to the left, the force curve at a_0 becomes steeper, and the bulk modulus, which is the tangent to the curve at a_0 , increases. So, if the cohesion of one metal is larger than that of another, its lattice constant will be smaller and its bulk modulus will be larger.

metal is larger than that of another, its bulk modulus will be larger. This universal bonding applies to all metals in the periodic table. When considering cohesion and bulk modulus, we can see that plutonium and the other light actinides fit the universal curve just like any other metal. We note that plutonium and the light actinides have relatively small bulk moduli because they have large lattice parameters, which, as we shall see, are due to the electrons in the s and p bands and are consistent with the universal curve.

More exact calculations of bonding in plutonium are now available and are presented in the article “Actinide

Ground-State Properties” (page 128), but a few general remarks are in order. Those modern calculations, as well as the ones we presented above, are based upon the local density approximation (LDA) of the DFT approach to band-structure calculations. But in contrast to our simplified, pedagogical approach, Wills and Eriksson have performed full-potential calculations (that is, no constraints are put on the form of the crystal potential), so that all types of crystal structures can be handled. Their modern calculations are fully relativistic (as were our pedagogical calculations), which is necessary for crystals with high Z -number atoms. For example, a

nonrelativistic calculation of the plutonium atom gives a wrong ordering of the s, p, d, and f valence levels.

One of the expected connections between electronic-structure calculations based on one-electron methods and experiment has been provided by the values for the energy levels of the one-electron states, which can be measured by photoemission experiments. In the atomic case, for example, it has been proved that the energy eigenvalues of the one-electron Hartree-Fock equations (see the box on page 98) are equal to the electron-removal, or ionization, energies (Koopman's theorem), which are directly measurable quantities. Unfortunately, when those atomic eigenvalues are calculated with the LDA, they do not have the same physical meaning.

Instead, they are equal to the removal energies plus a small calculable correction, and this correction has not been shown to vanish for atomic energy levels nor has it been calculated for the one-electron Bloch (periodic) states of a solid. Therefore, we have to rely on a comparison with experimental data to determine how close the LDA-calculated energies are to the electron removal energies measured from photoemission experiments. Any disagreements do not mean that the theory is wrong.

Finally, we remind the reader that all one-electron methods automatically predict the hybridization between the s, p, d, and f states when those states overlap. The LDA results we reported here agree with experimental data at the 90 percent level, whereas full-potential calculations, such as those in the article "Actinide Ground-State Properties" on page 128, are often in better agreement. However, it is not only the calculated values that are important but also the deeper understanding that LDA calculations enable. Because these calculations are efficient, we can repeat them for many variations of the parameters, thereby uncovering detailed bonding features that determine the structures and bulk properties of all the metals in the periodic table.

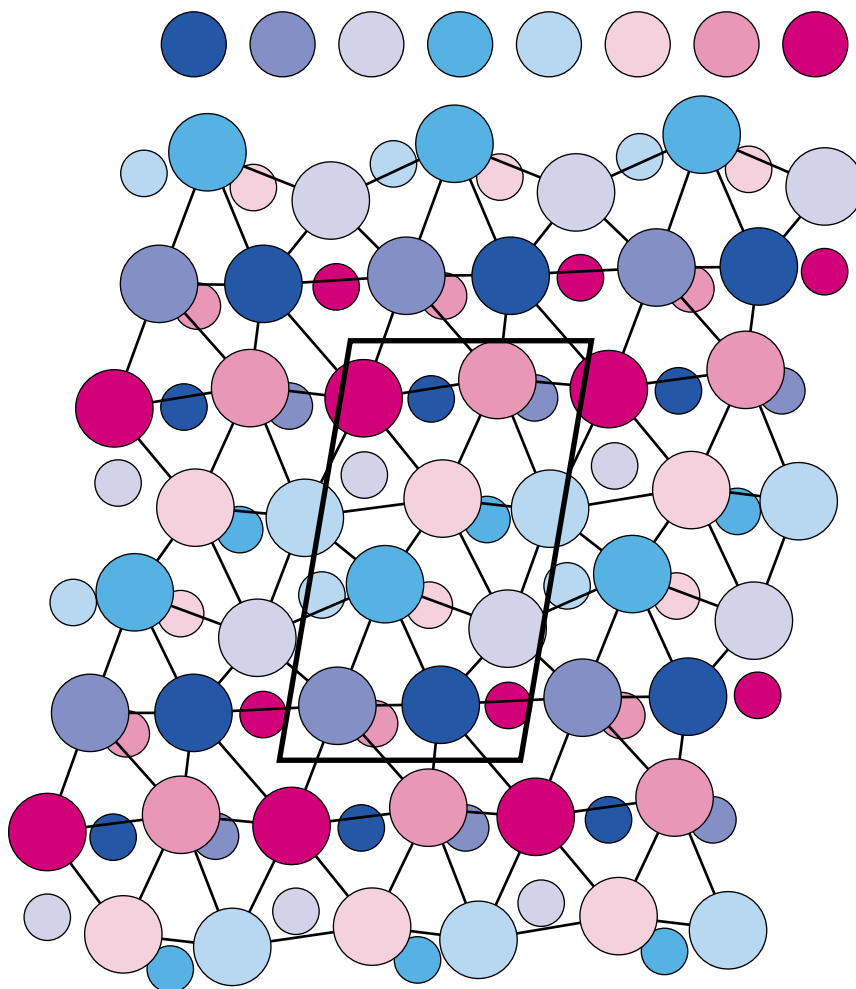


Figure 9. The Crystal Structure of α -Plutonium

The α -phase, the equilibrium phase of pure plutonium at room temperature and below, has a monoclinic crystal structure. The parallelogram outlining the 16-atom unit cell shows 2 flat layers (or planes) of atoms, and 8 distinct atomic sites. The larger numbers label the distinct sites in the top plane of atoms, and the smaller numbers label the equivalent sites in the next layer down into the crystal. The lines between the atoms show that the layers are somewhat similar to a hexagonal structure. For atoms numbered 2 through 7, one side of each atom has only short lengths to its nearest neighbors (2.57–2.78 Å), and the other side has only longer lengths (3.19–3.71 Å). This pattern could be viewed as a strange packing of individual “half dimers,” which is what a three-dimensional Peierls distortion might be.

Low-Symmetry Structures from Narrow Bands

One of the striking anomalies of plutonium metal is its very low symmetry crystal structure. In fact, the light actinides exhibit the lowest-symmetry ground states of all elemental metals: from orthorhombic for α -uranium to monoclinic for α -plutonium. Figure 9

shows the room-temperature monoclinic crystal structure of α -plutonium and its departure from a hexagonal structure.

In contrast, the transition metals, despite their relatively complex behavior, form high-symmetry cubic ground states such as bcc (body-centered cubic), fcc, or hcp (a hexagonal close-packed variation of fcc). These high-symmetry structures look like spheres stacked in an

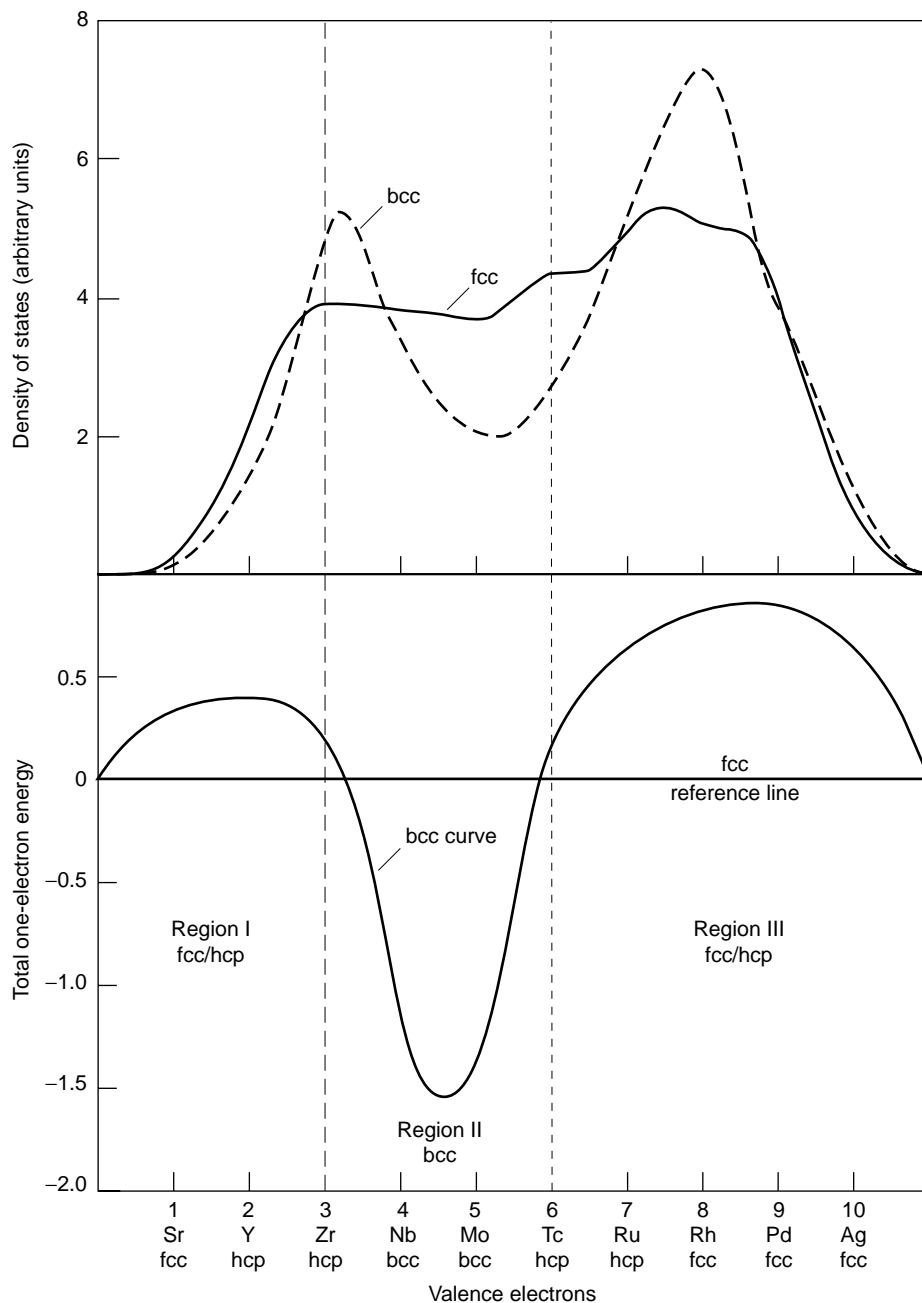
Figure 10. Stability of bcc, fcc, and hcp 4d Transition Metal Structures Determined from the Density of States

(Top) The LDA fcc (hcp) and bcc electronic density of states for the d conduction band of the 4d transition metals are plotted as a function of energy and display their unique signatures. For pedagogical purposes, we ignore the relatively small differences between the fcc and hcp density of states. The d-band density of states is the same for all 4d elements, but the Fermi level, or highest occupied level, for each element (dashed vertical lines shown for Zr and Mo) increases with the number of 4d electrons. (Bottom)

The total one-electron energy contributions for each element in both the fcc (hcp) and bcc structures were calculated from the first moment, $\int \epsilon D(\epsilon) d\epsilon$ for that crystal structure, where each ϵ is a one-electron energy eigenvalue from LDA calculations. The fcc (hcp) results are the reference line, the bcc results are plotted relative to that reference, and the lower value of the two is the prediction of the stable structure for that element. Note that the predicted sequence of structures matches the observed sequence (listed below each element) if we ignore the difference between fcc and hcp. The lines through the top and bottom figures mark the level of band filling (E_F) at which the crystal stability changes from fcc (hcp) to bcc or vice versa. In Region I, the number of 4d electrons per atom contributing to the band increases from 1 to 3. For each element in Region I, the fcc centroid (average value of ϵ) for the filled states is always lower in energy (farther away from

the highest filled level at E_F) than the bcc centroid. Therefore, for those elements, there is more bonding in the fcc (hcp) phase. In Region II, the situation is reversed because the E_F for these elements goes above the first bcc density-of-states peak, and therefore the bcc centroid goes below the fcc (hcp) centroid. Finally, for the elements in Region III, E_F reaches the second bcc peak, the bcc centroid shifts closer to E_F than the fcc centroid, and so the fcc (hcp) phases become more stable again. Thus, the d band filling and the unique signatures of the electronic density of states determine the crystal structures of the 4d transition metals.

efficient space-filling manner with no directional bonding (increased electron density) between the atoms. Once metallurgists know the stacking pattern (or crystal structure), they can predict many of the metallurgical properties. To illustrate the connection between electronic



structure and crystal structure, we show how LDA electronic-structure calculations correctly predict the sequence of ground-state crystal structures for all the transition metals.

The LDA calculations predict that the one-electron density-of-states func-

tions for the fcc and hcp transition-metal structures are very similar. For this discussion, we will treat those crystal structures as equivalent and compare the one-electron energy contributions of the bcc structures with those of the fcc (or hcp) structures. The one-electron

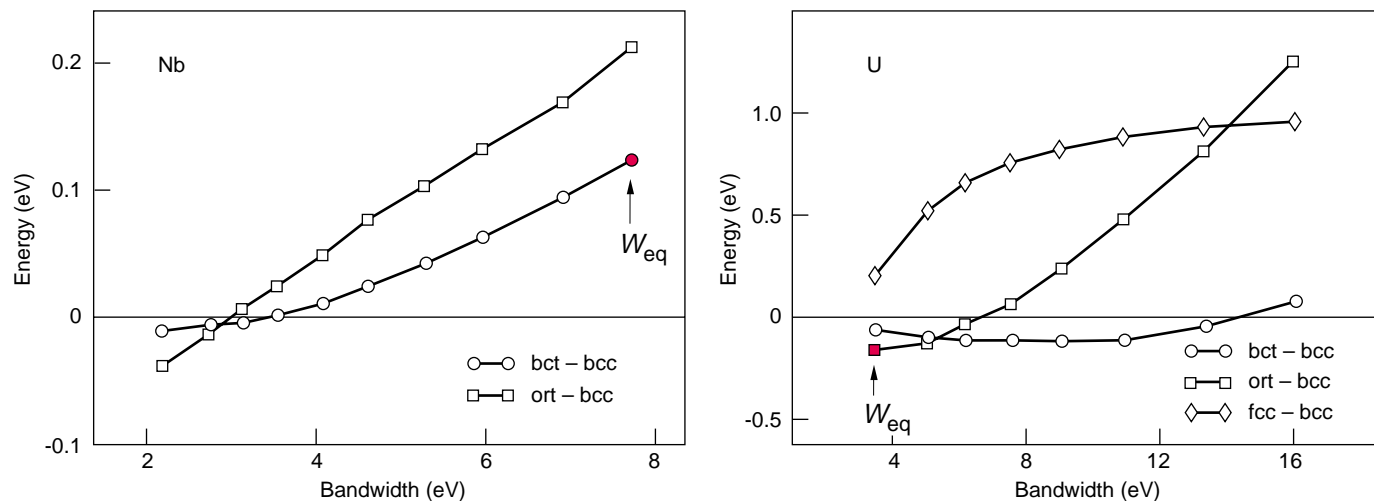


Figure 11. Internal Ground-State Energies as a Function of Bandwidth

DFT results for bonding energy vs bandwidth demonstrate that narrow bands produce low-symmetry ground states and wide bands produce high-symmetry ground states. Results are shown here for niobium (a d-banded metal), and uranium (an f-banded metal).

The atomic number, crystal structure, and lattice constant (or volume) are inputs to these calculations, and the bandwidth and energy are outputs. The input structures are bcc, bct, and orthorhombic, and in the case of uranium, fcc. The results for the bcc structure are plotted as the horizontal reference line, and those for the other structures are plotted relative to the bcc results.

Thus, a structure is more stable than bcc when its bonding energy appears below the reference line. Note that for niobium, the low-symmetry orthorhombic structure becomes stable when we force the d band to be narrower than 3 eV by decreasing the input volume. Likewise, when we force the f band in uranium to be broader than 7 eV by increasing the input volume, the high-symmetry bcc structure becomes stable. The calculated bandwidth at the experimental equilibrium volume is labeled W_{eq} . The results in the figure suggest that transition metals have broad bandwidths and symmetric structures, whereas the light actinides have narrow bandwidths and low-symmetry structures. (This figure was reproduced courtesy of *Nature*.)

energy contribution for a given element is equal to the one-electron energy ε averaged over the portion of the one-electron density-of-states function $D(\varepsilon)$ that is filled for that particular element ($\varepsilon D(\varepsilon)d\varepsilon$). The upper half of Figure 10 shows the approximate forms of $D(\varepsilon)$ for the 4d transition-metal series in the bcc and fcc (or hcp) crystal structures. The lower half of that figure presents the one-electron energy contribution for the 4d series, with the fcc (hcp) results plotted as the horizontal reference line and the bcc results plotted relative to that line. The structure that gives the lower-energy value for each element is the LDA prediction for that element's ground-state structure. In all cases, the LDA prediction agrees with the observed structure. The same methods yield similar agreement between predicted and observed crystal structures for the 3d and 5d metals.

We remind the reader that the total internal energy is equal to this one-electron contribution plus other terms (double counting, exchange, and correlation terms). Our results suggest, however, that the one-electron contribution is the dominant factor in determining the crystal structure. The physical reason for its dominance is that the states at the bottom of the conduction band are the most bonding, so the crystal structure whose average one-electron energy is lowest, or closest to the bottom of the band, should be the most stable.

Figure 10 shows that one-electron theory predicts the right crystal structures for the transition metals, and it also illustrates why crystal structures in the 4d series occur in the sequences observed. In principle, we could perform the same calculations for the low-symmetry structures of the actinide series, but the density-of-states functions for

those elements are more complicated, so those calculations would not be as easy to interpret.

Because electronic structure determines crystal structure, we will consider how the electronic structure of the light actinides, of plutonium in particular, differs from that of the transition metals. An obvious difference is the angular character and symmetry of the orbitals associated with their dominant electron bands—that is, d orbitals with even symmetry for the transition metals vs f orbitals with odd symmetry for the light actinides. Perhaps the odd symmetry of the f orbitals causes the ground states to have low symmetry, as do p-bonded metals such as indium, tin, antimony, and tellurium. In these metals, the odd-symmetry p orbitals seem to produce directional covalent-like bonds and low-symmetry noncubic structures. With no way to check this conjecture

for plutonium, metallurgists and physicists alike long held on to the notion that directional bonding plays the dominant role in explaining the low symmetry of the light actinides.

Recent LDA electronic-structure calculations of ground-state properties have demonstrated that the narrow width (approximately 2 to 4 eV) of the f bands leads to the low-symmetry ground states of the actinides. The d bands of the transition metals are much broader—approximately 5 to 10 eV. From our discussion of band formation, one intuitively knows that bandwidths are a function of volume. They become narrower for large volumes (the wave functions barely overlap between lattice sites), they turn into a single energy value for fully separated atoms, and they become broader for small volumes. Using the LDA, one can calculate the total bonding energy of a given element in any crystal structure and across a range of volumes (with their concomitant bandwidths) and thereby demonstrate the dependence of energy on bandwidth.

The results of such calculations are plotted in Figure 11. The ground-state (or internal) energy is plotted as a function of bandwidth for niobium and uranium in several structures: the bct (body-centered tetragonal) and ort (orthorhombic) structures for niobium and the bct, ort, and fcc structures for uranium. In both plots, the ground-state energy of the bcc (body-centered cubic) phase is the horizontal reference line. A structure is more stable than bcc when its internal energy goes below the reference line. Figure 11 shows that, when the d band is forced to be narrower than 3 eV because an expanded volume is used as input to the calculation, the low-symmetry orthorhombic structure becomes stable. Likewise, when the f band in uranium is forced to be broader than 7 eV, the high-symmetry bcc structure becomes stable. This is simply a demonstration that narrow bands favor lower-symmetry structures, not that niobium would form in the orthorhombic structure of α -uranium. That particular

structure is used only for convenience in the calculations, and we expect that some other low-symmetry structure would be even more stable. Figure 11 also indicates that the true equilibrium bandwidths (W_{eq}) are broad (small volumes) for the transition metals and narrow (larger volumes) for the light actinides.

Lowering the Electronic Energy through a Peierls-like Distortion. In metals, narrow bandwidths (and their high density-of-states functions) lead to low-symmetry structures through a Peierls-like distortion. The original Peierls-distortion model occurs in a one-dimensional lattice: A row of perfectly spaced atoms can lower the total energy by forming pairs (or dimers). The lower periodicity causes the otherwise degenerate electronic-energy levels to split, some becoming lower and others becoming higher in energy. The lowered levels are occupied by electrons, and therefore the distortion increases the bonding and lowers the total energy of the system. In this one-dimensional system, the distortion opens an energy gap at the Fermi level and makes the system an insulator. In the higher dimensional systems, which we will discuss next, the material remains a metal after the distortion because there are other Bloch states that fill this gap.

In real three-dimensional lattices, the energy levels are degenerate along high-symmetry directions. If those levels lie close to E_F , a crystal structure distortion (Peierls-like) would increase the one-electron contribution to bonding, again because the degenerate levels in the band would split, pushing some levels above E_F and others below E_F . This mechanism is very effective if there are many degenerate levels near E_F —that is, if the energy bands are narrow and therefore the density of states is large. Materials with broad bands (wider than 4 eV), gain less energy from level splitting because there are fewer levels near E_F , and therefore symmetry-lowering distortions are rare in these materials.

Stabilizing Wide Bands into High-Symmetry Structures. Besides the one-electron contribution, there is another important contribution to the ground-state energy, namely, the electrostatic Madelung energy. This term is generated because the conduction electrons do not completely shield the ions on the lattice sites. The unshielded positive charge leads to a long-range attractive force on the conduction electrons that lowers their energy. This negative Madelung energy is largest for high-symmetry crystals, opposing the Peierls-like term. So, for the broad s-p² and d band metals with few degenerate levels near E_F , the Madelung term dominates the effects of the Peierls-like distortion, and these metals are stabilized in high-symmetry structures. Although the Madelung term stabilizes these high-symmetry structures, remember from our discussion of crystal structures that the one-electron contribution determines which structure (fcc, hcp, or bcc) will be stable. For the light actinides with their narrow 5f bands and a very high density of states near E_F , the Peierls distortion wins out, and these metals form low-symmetry structures. A closer look at Figure 9, for example, shows that six of the eight different atoms in the α -plutonium unit cell have neighboring atoms that fall into near distances on one side and far distances on the other. It is as if one hemisphere around the atom were smaller and the other larger, and it is difficult to imagine how to pack such objects efficiently. But this type of problem is just what one might expect to solve with the three-dimensional version of the Peierls distortion.

Why Are the 5f Bands Narrow?

By considering the contribution of each energy band (s, p, d, and f) to the bonding curve of the universal bonding picture, we can understand why the 5f bands are narrow at the ground-state equilibria of the light actinides.

—————

²The broad s and p bands often mix strongly and are therefore referred to as the s-p band.

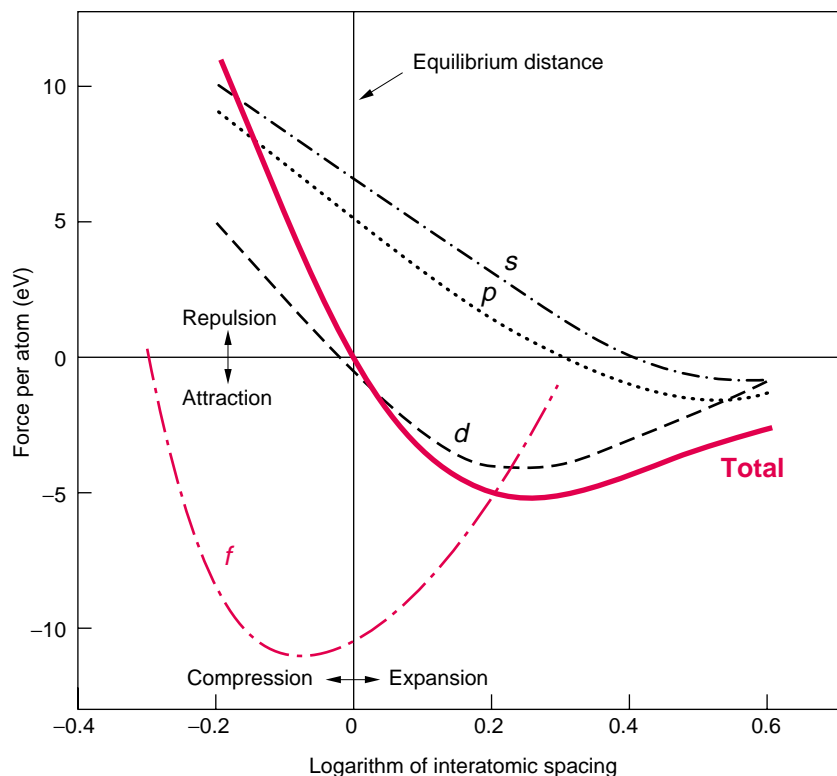


Figure 12. Contributions of Different Electrons to δ -Pu Bonding

LDA predictions for the bonding curves of δ -Pu (fcc structure) are plotted as a function of the interatomic spacing $x = \ln(a/a_0)$. The figure includes the curve for the total cohesive energy per atom, as well as the individual contributions from the s, p, d, and f energy bands. Note that, if the bonding came from the f band alone, the equilibrium lattice constant of Pu would correspond to the value of x at which the f band contribution crosses the horizontal axis; that is, the lattice constant would be well below a_0 . At this smaller volume, the f band would be wider, and Pu would stabilize in a high-symmetry crystal structure. In the true equilibrium represented by the vertical line at $x = 0$, the s-p bands contribute a repulsive term and therefore help stabilize Pu at the larger volume. The f band is narrow at that larger volume, and the narrowness leads to the low-symmetry ground-state crystal structure of δ -Pu. It may seem strange that the s-p bands are not bonding at equilibrium, but we must remember that they are also not bonding in d-electron transition metals, which form the bulk of metals in the periodic table.

We used the atomic-sphere approximation to calculate the contributions from individual bands, and for simplicity, we performed those calculations in the fcc phase. Figure 12 shows the results for plutonium. To understand this figure, consider that, if the metal had only one energy band, the lattice constant in the ground state would be given by the point at which the bonding curve for that band crossed the zero pressure line. From Figure 12, you can see that, if plutonium had only an f band contribution, its equilibrium lattice constant

would be smaller than it actually is, its f band would be wider, and this metal would stabilize in a high-symmetry crystal structure. In reality, the contribution from the s-p band (a repulsive term at true equilibrium) helps to stabilize plutonium at a larger volume; the f band is narrow at that larger volume, and the narrowness leads to the low-symmetry crystal structure. This argument is universal for multiband metals. In the transition metals, the s-p band is repulsive at equilibrium and leads to slightly larger volumes than would be

the case if these metals had only d bands.

We conclude that the width of the dominant band determines the symmetry of the ground state, and one does not need to invoke directional bonding to obtain low-symmetry structures. When Willie Zachariasen and Finley Ellinger first identified the crystal structure of α -plutonium in 1957, they called it a covalent structure, suggestive of directional bonds, but they never repeated that name. (We note that this was one of the most difficult structure identifications ever done because single crystals were not available, the x-ray pattern had many lines, other phases in the samples contributed to the pattern, and the x-ray lines were terribly broadened by strain.) In recent years, John Wills and collaborators (see the article “Actinide Ground-State Properties” on page 128) have been able to calculate the charge density for several actinides using the full-potential DFT method. They find no dominant directional 5f bonds and, most important, no charge buildup between atoms. Instead, the calculated ground-state properties of α -plutonium indicate that this metal is quite average.

We already have hinted, however, that plutonium may not be so average. The strong competition between the repulsive s-p band contribution and the attractive f band term in Figure 12 is the first sign of instability near the ground state. The second sign is the fact that the density-of-states functions for different low-symmetry crystal structures are very similar. Thus, the total energies for different low-symmetry crystal structures are likely to be very close to each other—that is, many states lie close to the ground state.

The Landscape of Actinide Phases

Knowing that the ground states of the light actinides are in a very shallow minimum of energy, we might expect these metals to change phase as they

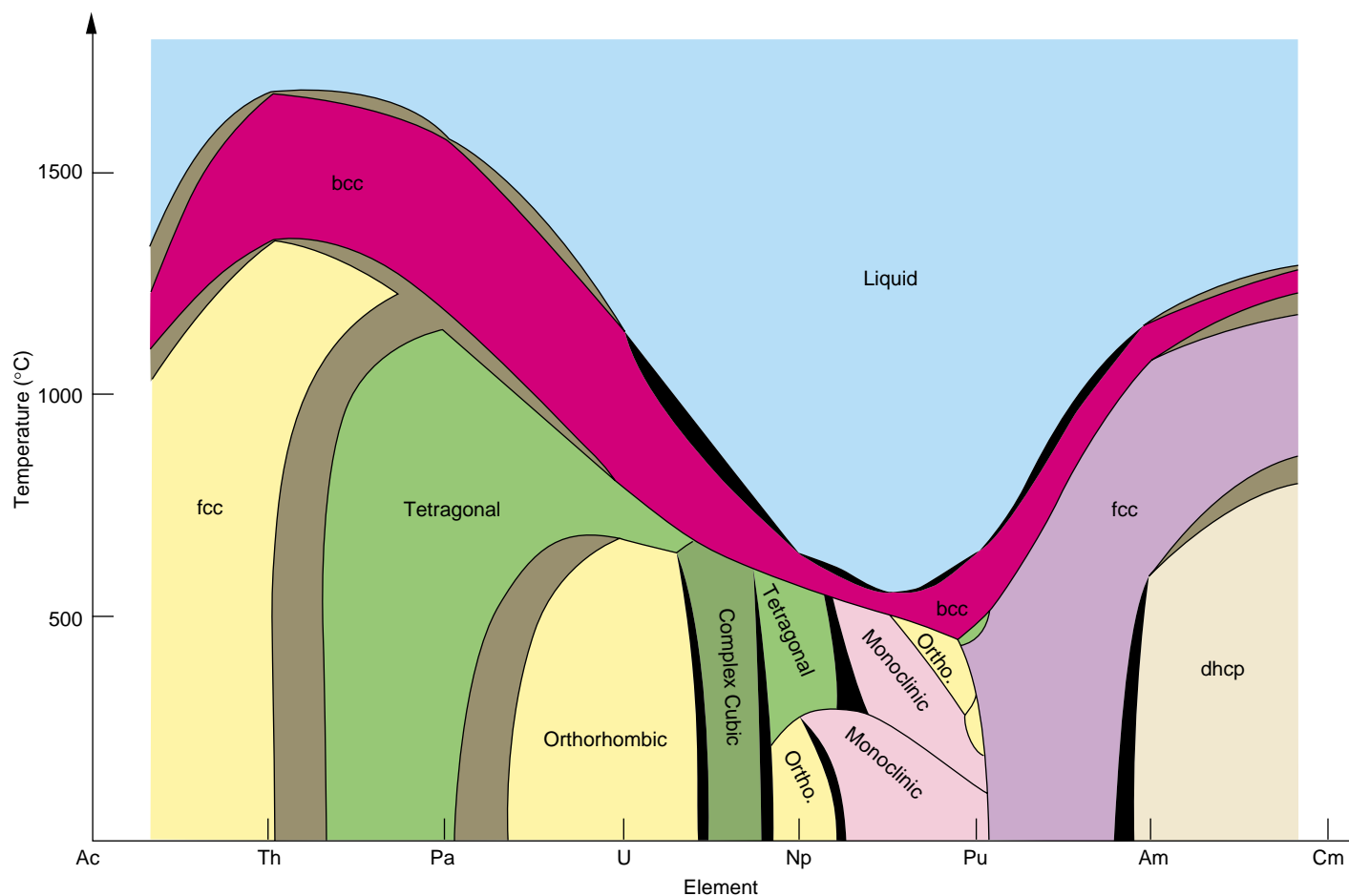


Figure 13. Schematic Phase Diagram of the Light Actinides

This phase diagram connects individual binary alloy diagrams of the light actinide series. The black areas are two-phase regions; the brown are regions where the details are unknown. Whereas the trend in phases is rather ordinary at either end of this series, the phase variation in the middle (at neptunium and plutonium) is very complex (also revealed by the opening illustration to “Atomic Vibrations and Melting in Plutonium” on page 190). In these two elements, the 5f electrons play a major role in bonding because they are so numerous. This widely reproduced and compelling figure shows nature in action, and we have yet to match it with an equally appealing theory.

are perturbed by heating or alloying. An atomic argument leads to the same conclusion. In the actinides, two or three different shells of electrons in an atom are partially filled, producing more states to compete with the lowest-energy ground state. Also, the heavier the atom (or the higher the value for Z), the smaller the energy difference between the last few valence electrons in different shells, and hence the greater the chance for metamorphosis.

A composite phase diagram for the entire actinide series is drawn in Figure 13. This plot was constructed from individual-alloy phase diagrams for the actinide neighboring-element pairs. Each original diagram showed the

change in phase as the temperature and the binary composition were varied.

In Figure 13, these diagrams have been simplified and drawn side by side. The gray areas represent guesses for unidentified details. The resulting “landscape” of the actinides has been reprinted widely since Smith and Kmetko drew it in 1980 because anything with such a pretty pattern was something the actinide community needed to understand.

Phase Instability and the f-f Interaction. One striking feature of Figure 13 is the large number of allotropes, or solid-state phases. In fact, the actinides have the largest number of allotropes of any series in the periodic table. Note

also that most of the allotropes occur at neptunium and plutonium, the elements having the highest number of bonding f electrons. Figure 14, a replotting of the actinide metallic radii in Figure 5 that now includes some of the allotropes, emphasizes the effects of the f electrons on bonding. The f electron bonding begins at thorium, with a fraction of an f electron in the energy bands, and increases all the way to plutonium, which has the highest phase instability. Thus, in the ground-state phases of the early actinides, each additional f electron increases the bonding and decreases the interatomic distance. At americium, the f electrons localize completely and become nonbonding

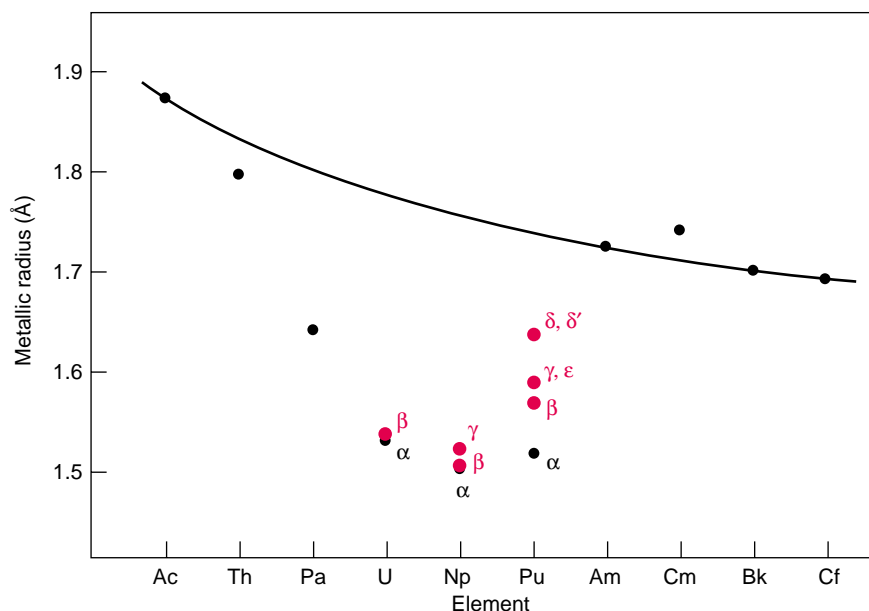


Figure 14. Metallic Radii of Actinide Allotropes

Here, we have replotted Figure 5 to include additional allotropes (red) of the actinides. As in Figure 5, the metallic radius is half the average distance between the atoms in the solid, and the line represents simple trivalent metals with nonbonding f electrons. The points falling below the line show the involvement of the f electrons in the bonding, which pulls the atoms closer together. Notice that the various allotropes of uranium and neptunium have similar metallic radii. In contrast, the radii of the phases from α - to δ -plutonium increase monotonically. The δ -phase still departs from the trivalent line but is much larger than the α -phase, indicating that the f electrons are not completely localized and therefore still contribute to bonding.

because Coulomb forces have at last become strong enough to pull the f electrons inside the valence shell, leaving only the three (or sometimes two) valence electrons in the s-p and d bands to form the glue that holds the atoms together for the rest of the actinides. The metallic radii increase at this crossover to localization, and as shown in Figure 14, the low-temperature phases of the heavier actinides (beginning with americium) form close-packed or bcc structures.

The upper (high-temperature) part of Figure 13 shows the liquid phase, and the melting curve separating the liquid from the solid state goes through a minimum between neptunium and plutonium, at which point the crystal structures are least stable. In its broadest features, the pattern shows the light actinides forming low-symmetry ground states

but melting out of high-symmetry structures as the heavy actinides and most other metals do. This observation is striking, but the really difficult aspect to explain is that the transition from low symmetry to high symmetry occurs over an extremely small temperature range, small enough that the f band remains narrow. What property of narrow bands (or, specifically, narrow f bands) enables them to stabilize high-symmetry structures at modest temperatures?

We know from standard Wigner-Seitz rules that, for electrons in narrow bands, the radial portion of the electronic wave function measured from a given lattice site must change rapidly as a function of energy. These rules also tell us that the electrons in the upper half of a band are less bonding, so we can use the molecular concept of bonding and antibonding orbitals to under-

stand the Bloch states of solids.³ Also, the electronic wave functions of atoms on different lattice sites overlap less for narrow bands than for wide bands.

Cerium, the only 4f metal with a narrow f band, is a good example.

The f-electron wave functions overlap only the nearest-neighbor sites, whereas the s-p and d wave functions, which are associated with wide bands, overlap sites that are far from a given site.

In other words, narrow f bands imply a short-range, rapidly changing interaction among the f electrons. This means less overlap between f electrons on different sites and also weaker hybridization of electrons in f orbitals with electrons in s, p, and d orbitals.

The many phase transformations in the center of the actinide landscape suggest that the f-f interaction varies dramatically with very small changes in the interatomic distances, such as those produced by lattice vibrations or heating. Also, electron-phonon coupling appears to be very strong in these narrow bands. We would even suggest that the variation with temperature in the f-f interaction (and f-spd interactions) might cause some of the f orbitals to become localized as plutonium transforms from the α - to the δ -phase. The situation is complicated by several different interatomic distances in the low-symmetry structures of the light actinides (see the crystal structure of plutonium in Figure 9). Unlike the phase transformations in the transition metals, which follow simple, well-understood routes, such as the Bain path (fcc \leftrightarrow bcc) or the fcc \leftrightarrow hcp path, the individual transformations in plutonium (say, $\alpha\leftrightarrow\beta$ or $\beta\leftrightarrow\gamma$) are difficult to characterize. And the whole path from the α - to the δ -phase is even more difficult to characterize. We need more detailed analysis and many more calculations to work out the details of these phase transformations. But we do know

³According to the Wigner-Seitz rules, the radial part of the wave function at the top of the band is zero at the Wigner-Seitz radius (a radius that is roughly half the interatomic distance). At the bottom of the band, the derivative of that radial part is zero at that same radius.

that the short-range nature of the f-f interaction in the light actinides and the partial transition from bonding (itinerancy) to localization (rather than directional bonding) are key ingredients for a better understanding of plutonium.

The Role of Entropy in Phase Stability. To understand fully the stability of these different phases as a function of temperature, we must go beyond the one-electron methods. Remember that those methods determine only the internal energies of solids (they describe the system at $T = 0$), whereas phase stability depends on the free energy, which is the internal energy plus the entropy of the system. So far, theorists have not been able to calculate the free energy from first principles. Nevertheless, we can make some general comments about the role of entropy.

For the low-symmetry structures of the light actinides, which have similar density-of-states functions and therefore similar internal energies, the internal-energy path between different low-symmetry phases is very shallow. That is, the lower-energy phase sits in a relatively flat potential well connecting it to the higher-energy phase. For that reason, it often has very soft (low-frequency) vibrational modes in its phonon spectrum. Low-frequency modes imply large numbers of phonons per mode and therefore lots of entropy. For example, entropy is a driver in the first three solid-to-solid phase transformations in plutonium (α to β , β to γ , and γ to δ), in which low-symmetry structures are involved. (A recent measurement on phonons in uranium gave the entropies for uranium. See the article “Vibrational Softening in α -Uranium” on page 202).

The δ - to ϵ -phase transformation in plutonium is between two high-symmetry structures, following the standard Bain’s path (fcc \leftrightarrow bcc) seen in most transition metals. Typically, the internal-energy path between cubic structures is not shallow. However, experimental data indicate that this path is shallow in plutonium. In Figure 15,

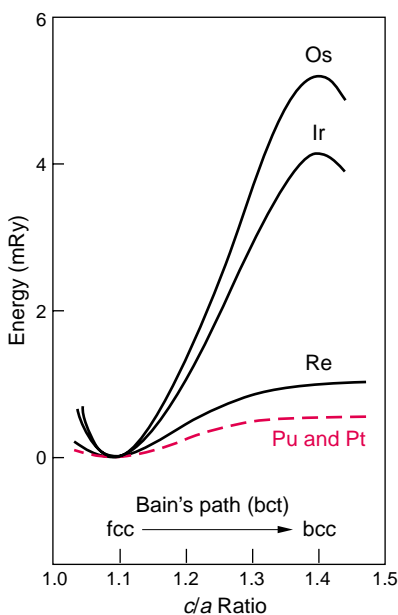


Figure 15. The Bain Paths for Typical Transition Metals and for the δ - to ϵ -Plutonium Transformation

We performed these calculations by varying the c/a ratio in the bct structure to go from the fcc to the bcc phase. The calculated internal energy as a function of the c/a ratio yields the path the solid must follow to get from the fcc to the bcc phase. As shown, the Bain’s paths for typical transition metals (5d), such as osmium and iridium, are steep. The platinum path is very shallow, and we use it as our model for the plutonium path (red dotted lines). The shallow well in the fcc phase for platinum and plutonium leads to soft modes and large entropy. The observation that plutonium goes through the δ' -phase (bct) in going from δ - to ϵ -phase implies that the Bain’s path for plutonium is flat enough to make the δ' -phase metastable at least at some value of c/a .

we show the Bain’s path for a few typical transition metals and the postulated path for the δ - to ϵ -phase in plutonium. When the internal-energy path between phases is shallow and the entropy is large, the range of stability of a phase can be small. And that is exactly what is seen in the δ - to ϵ -phase transformation. The δ -phase remains stable for

only 160°C, whereas in a typical transition metal, the fcc phase remains stable for around 1000°C before becoming bcc. (See the article “Elasticity, Entropy, and the Phase Stability of Plutonium” on page 208 for a discussion of how to estimate the vibrational entropy through measurements of elastic constants.)

The actinides are not unique in having shallow internal-energy paths between them. The same is true of some transition metals (see Figure 15) and even simple metals such as lithium. In all these metals, entropy plays a big a role. We emphasize, however, that in all the actinides, and particularly in plutonium, the initial instabilities (leading to high entropy and frequent phase changes) are due to the role of the f electrons and the existence of many internal-energy states whose energy values are very close.

Low Melting Temperatures and Electron-Phonon Coupling. The last remarkable feature of Figure 13 that we will comment on is the pronounced dip in the melting curve at neptunium and plutonium. We suggest that two effects may lead to this reduction in melting temperature: the strong electron-phonon coupling in narrow-band materials (which in a one-electron theory would be seen as the large variation of the f-f interaction with temperature) and the instability of the phases due to the large entropy term. Strong electron-phonon coupling implies that small temperature changes lead to larger-than-usual electronic changes. As a result, the effective temperature is larger than the actual one, and therefore the material melts at a relatively low temperature. Evidence for strong electron-phonon coupling is seen in the strong temperature dependence of the elastic constants of gallium-stabilized δ -plutonium deduced from neutron diffraction measurements (see the article “Atomic Vibrations and Melting in Plutonium” on page 190). Strong electron-phonon coupling is also implied by the high resistivity of pure plutonium just below room temperature.

The large entropies (soft vibrational modes) in these materials also imply that relatively small temperature changes produce relatively large changes in free energy. As a result, the average temperature change between phases in plutonium is 85°C, whereas in typical transition metals, it is around 1000°C. In other words, a free-energy change large enough to cause melting requires only a small temperature change—that is, the melting temperature is relatively low. These general insights notwithstanding, Migliori is right to emphasize that much more work is needed to quantify the vibrational energy and entropy contributions to the free energy and phase stability. We now return to the problem of how electronic structure affects the phase stability of plutonium, especially its δ -phase.

Delta Plutonium, f Electron Localization, and Plutonium Metallurgy

Delta-phase plutonium is of special interest because its fcc structure allows plutonium to be formed into shapes as easily as aluminum. Used in building nuclear weapons, this phase is most important to understand from first principles. Ironically, although electronic-structure calculations of plutonium have improved, the δ -phase has been the toughest one to get right in spite of its simple cubic structure because its f electron behavior does not fit the usual categories. The plot of metallic radii in Figure 14 indicates the dramatic increase in the metallic radius (decrease in density) of the δ -phase, suggesting that f electron bonding decreases markedly from the α - to the δ -phase. On the other hand, f electron localization is not complete because the interatomic distance for δ -plutonium is still below the trivalent line defined by actinium and the heavier actinides, whose f electrons are fully localized. (The side a_0 of the cube of the unit cell is 4.637 angstroms in δ -plutonium and 4.894 angstroms in cubic americium.) Thus, the f electrons

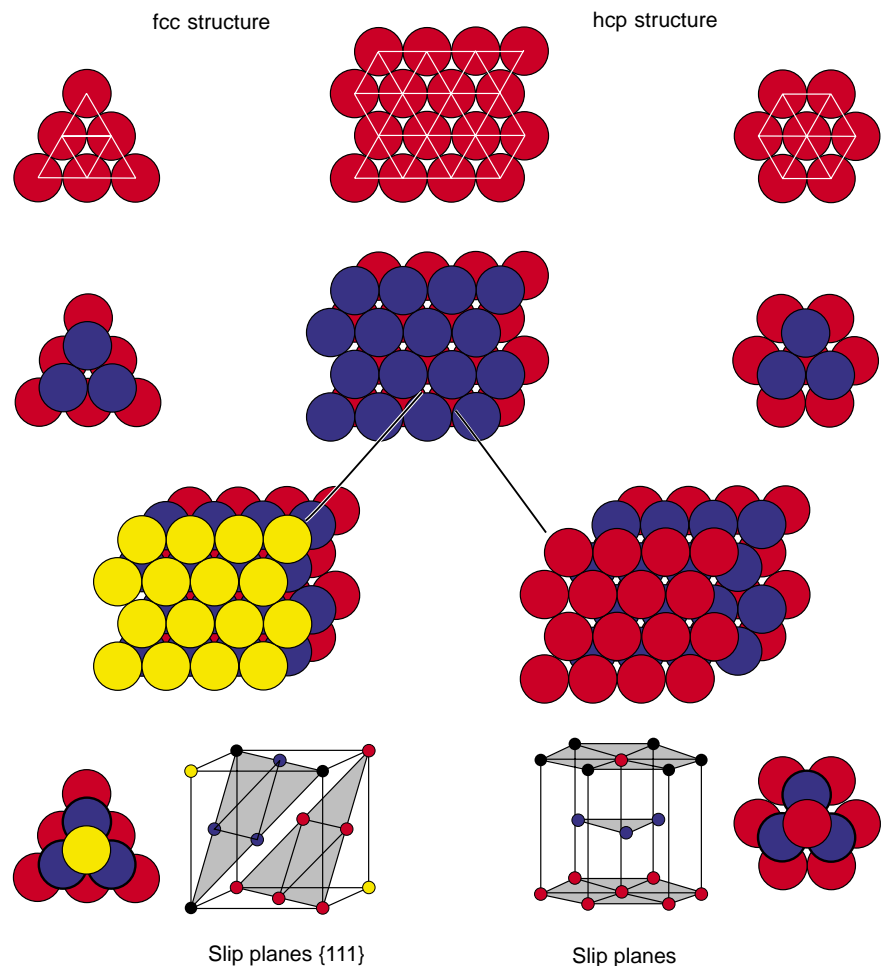


Figure 16. Stacking Close-Packed Crystal Structures

The red and blue layers of the fcc and hcp crystal structures are stacked identically. In the fcc structure, the third layer (yellow) is in a new position; in the hcp structure, it is perfectly aligned with the first layer (both are red). The ability of one plane to slide (slip) over another leads to the ductility of fcc metals. It takes a bit of practice to visualize the close-packed planes (shaded) within the fcc unit cell. The many slip systems in fcc metals are discussed in the box “Atomic Packing and Slip Systems in Metals” on page 308.

in δ -plutonium are in limbo between localization and itinerancy, a state that has yet to be modeled in any convincing way. Plutonium can easily change its crystal structure and density in response to its surroundings, and the δ -phase is the most sensitive.

The only other transformation that comes close to producing the 26 percent volume expansion seen in the transformation from α - to δ -plutonium is the isostructural expansion from the fcc α -phase to the fcc γ -phase of cerium. This transition produces a 20 percent volume expansion. Before f bands were known

to exist, the reverse transition in cerium—the collapse from the fcc γ -phase to the denser fcc α -phase near room temperature and under pressure—was attributed to a change of an f electron (localized) to a d electron (itinerant), which would explain the volume change and the magnetic properties. However, accumulating data showed no change in the number of f electrons through the change in volume. In 1974, Börje Johansson suggested that the collapse in cerium involved a Mott transition. Mott had described how the localization of conducting electrons turned conductors

into insulators, and delocalization did the reverse. Johansson saw that cerium's fcc isostructural expansion involved localization and its collapse involved delocalization just as in the Mott metal-insulator transition, but for cerium, only the f electrons were involved. The s-p and d electrons remain conducting in both fcc phases, and thus this Mott-like transformation is between two metallic phases of cerium. Many theorists believe that a similar localization mechanism is probably responsible for the series of phase transitions from α - to δ -plutonium, except that the net result falls short of the more complete transformation to localization seen in the transformation from α - to γ -cerium because five, instead of one, f electrons are involved (see the article "A Possible Model for δ -Plutonium" on page 154).

Despite its weird electronic state, δ -plutonium signals the return of the actinides to the typical metallic close-packed crystal structures. That is, it forms the tip of the "iceberg" of the fcc phases at the right in Figure 13. The fcc structure is what makes metals such as copper, aluminum, stainless steel, and δ -plutonium very useful. It is a high-symmetry, close-packed structure that one can easily construct by stacking marbles, as in Figure 16. The first layer of marbles (red) forms hexagons made of triangles. The second layer (blue) falls naturally into a set of first-layer depressions. The marbles in the third layer can be either directly above those in the first layer (red) or in a third set of positions not found in the layers below (yellow). The hcp structure is formed if the third layer is on top of the first one; the fcc structure, if the third layer is in the third position. Notice that, in all cases, it would be fairly easy to slide one layer across the next one because the marbles do not have to move up and down too much in order to land into the next set of holes. Sliding them across some other plane would not work as well because there are fewer atoms in all other nonequivalent planes and the wells are deeper. It is precisely because one plane can easily slide across the next

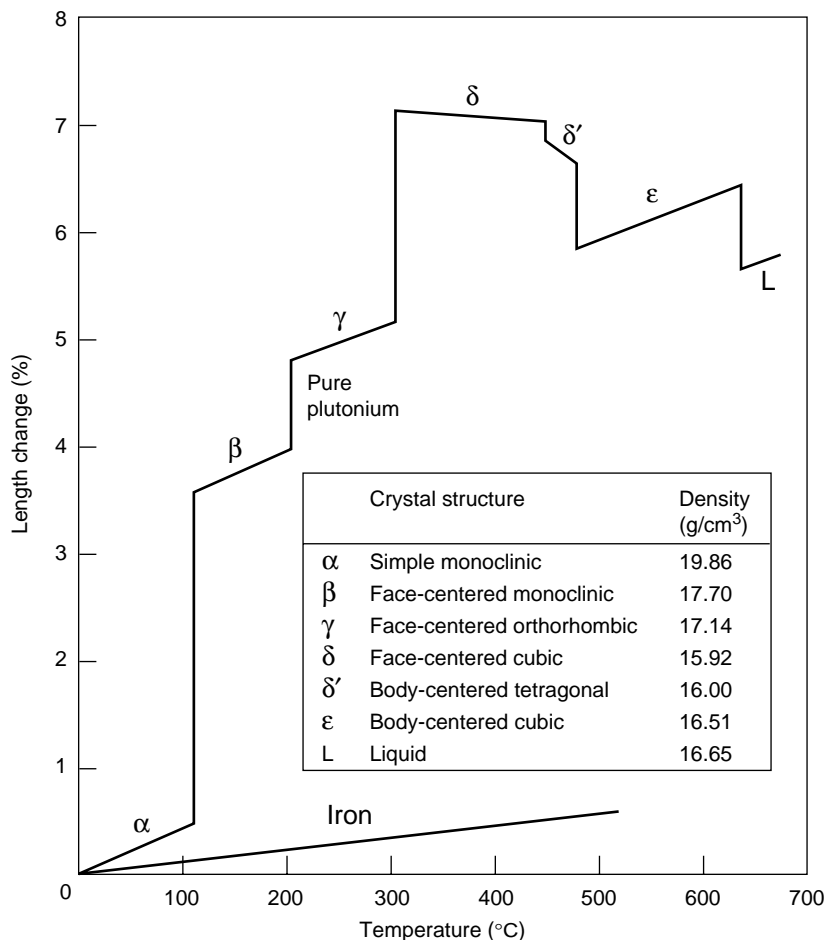


Figure 17. Thermal Expansion of Plutonium

The percentages by which the lengths of plutonium and iron have changed are shown as a function of temperature for 0°C to 660°C. Abrupt changes in the curve for plutonium denote phase transitions, and each of the smooth segments is in the labeled structures. The crystal structures and densities of each phase are also listed. Note that plutonium's thermal expansion is very large, the material goes through six solid-state phases before melting, the δ -phase contracts as it is heated, and plutonium contracts as it melts. These features are in stark contrast to the small linear expansion of iron and most metals.

one that fcc metals are ductile and therefore easy to shape.

Ductility, a remarkable feature of metals, is not necessarily long lasting. As a plane of atoms slides, some of the atoms may not move uniformly. And as more and more planes "misalign" in this way, the misfits accumulate, and the metal gets stronger—that is, it takes greater force to deform it or to make it fail. This process is called work hardening. Alpha plutonium is an example of a naturally brittle and strong material.

From the α -plutonium structure shown in Figure 9, it is easy to see that sliding planes across each other in any direction would be extremely difficult because the atoms would no longer fit. In contrast, the planes of δ -plutonium slide very easily, like those of aluminum.

On the other hand, new single crystals of very pure α -uranium were shown to bend easily when squeezed by hand. Single crystals are expected to be easier to bend because there are no grain boundaries and dislocations to pin

the sliding. However, these uranium crystals seem softer than expected. We do know that uranium deforms by making twins, which are structures that look like mirror images of each other separated by planar boundaries. In general, low-symmetry structures have more planes across which twins can form, and this may mean that, if we had single crystals of very pure α -plutonium, they would be far softer than any crystals we have ever seen. For a more complete description of these metallurgical properties, see the article “Plutonium and Its Alloys” on page 290.

Unfortunately, δ -plutonium is not very stable. It takes only about 1 kilobar of pressure to transform δ -plutonium into a lower-symmetry phase such as α -plutonium. A fascinating reversal of this transformation was seen during the fracture of α -plutonium and is described in “Plutonium and Its Alloys.” The surface of fractured typical-purity α -plutonium appears jagged and broken, as would be expected for a brittle monoclinic metal. However, under a scanning electron microscope, the surface looks covered by ductile dimples, like a peanut butter sandwich that has been pulled apart. Such dimples are never seen in brittle materials because the plastic flow needed to make them does not occur. So, where did the dimples come from? Although the following explanation has not been proved so far, it is believed that a region of hydrostatic expansion preceding the tip of the crack is created during the fracture of α -plutonium. The expansion, or effective negative pressure, in this region instantaneously transforms the α - into the δ -phase. After the fracture has propagated through the region, the material relaxes and returns to the α -phase. These fracture results show that plutonium easily moves back and forth from the α - to the δ -phase and that spreading out the atoms (during hydrostatic expansion) stabilizes the fcc phase, as one would guess. Yet, this quick transformation to the δ -phase increases the volume by 26 percent.

Figure 17 shows the complex pattern of length changes produced by heating

Plutonium in the Liquid State

Plutonium must be happier (have lower energy) in the liquid because it has a higher density than the phase from which it melts. It seems likely that plutonium forms clusters in the liquid (as water does) because it has the highest viscosity of any molten metal and because it forms complexes, as discussed in the article “The Complex Chemistry of Plutonium” on page 364. We note that the bcc crystal structure has its second-nearest neighbor atoms almost as close as the closest neighbor atoms and has little shear strength; that is, it is the most liquidlike crystal structure and the highest-temperature solid phase for most metals. That is why bcc sodium cuts with a butter knife. Because water and plutonium are both good solvents, it may be fair to draw a comparison between the polar molecules of water and the atomic misfits of plutonium. To find the nature of liquid plutonium, we therefore need to use neutrons or some other probe. We remind the reader that, if plutonium were not such a good solvent, we would have more usable containers in which to put it while we make measurements at high temperatures.

plutonium metal. Plutonium goes through six solid phases before it reaches its melting point, with the δ -phase having the lowest density (and the most-localized f electrons) of all the phases including the liquid state. These changes in volume are not only challenging for physicists to explain but also extremely troublesome to metallurgists. For example, when castings are made from plutonium in the liquid state, the metal expands as it solidifies (see the box “Plutonium in the Liquid State”) and thus helps fill a mold. During subsequent cooling, however, the many changes in volume lead to the formation of voids, which reduce the structural integrity of cast plutonium.

Another surprising feature is that δ -plutonium contracts when heated, as revealed in Figure 17. Remember that thermal expansion is an anharmonic effect and therefore not predicted by the usual harmonic models of a solid. In harmonic models, a solid is described as a set of masses held together by springs. That is, the potential energy as a function of distance between neighboring atoms is a parabola, and the forces are linear in the displacement from equilibrium, as they are for springs. In these models, the coefficient of thermal expansion is always zero, and this is true for all even powers of the potential energy

as a function of interatomic spacing.

So, the common belief that atoms vibrate more at higher temperatures and therefore take up more room is not correct. Instead, when atomic excursions become large enough to run into the “hard core” of the filled-shell electrons of the neighboring ions, the interatomic potential becomes steeper than a parabola, and this anharmonicity, or increase in pressure, leads to an expansion in volume with increasing temperature. Conversely, a potential that increases more slowly than a parabola (including higher even powers) at large atomic excursions yields a contraction in volume with increasing temperature and reflects a change in electronic structure. We will return to this topic when we discuss magnetism. For the moment, we can say that a negative thermal-expansion coefficient may be due to a conversion of magnetic into bonding energy as in Invar (see the box “Itinerant Magnetism, Invar, and δ -Plutonium” on page 120).

New Models for Delta Plutonium

As yet, there has been no established model for the unusual features of the fcc δ -phase. Here, we suggest that both the unusual thermal properties and

the absence of measured magnetism in δ -plutonium may be related to the delicate balance of forces between the repulsive s-p bands and the attractive f band (and the sensitivity of the f-f interactions) shown in Figure 12. First principles ground-state calculations have shown that all five 5f electrons are bonding in the α -phase. Because it has never been demonstrated that plutonium has less than five 5f electrons in its atoms, molecules, and solids, we must assume that the δ -phase also has five.

In the δ -phase, some or all of these electrons may be localized, a fact consistent with Figure 12. Localization would reduce the contribution of the five 5f electrons to pressure, and the lattice would expand. If their number were reduced from five to, say, one, then the three electrons in the spd broad bands would become more important in determining the crystal structure (see Figure 18). And because broad bands favor cubic structures, the δ -phase is a reasonable outcome of localization. The real problem, however, is to determine a mechanism for such localization in the f shell.

Wills and Eriksson (see the article "Actinide Ground-State Properties" on page 128) have used one-electron calculations to show that localizing four of the five 5f electrons leads to a correct prediction of the δ -phase volume. Through a separate atomic calculation, they show that the energy gain from localizing those four electrons yields the lowest-energy state at the δ -phase volume. However, those calculations provide no mechanism for the localization.

In "A Possible Model for δ -Plutonium" (page 154), Cooper presents the self-induced Anderson localization model, a two-electron impurity-like model. According to this model, all the 5f electrons on some plutonium sites become localized. The strong scattering from these "impurity sites" can disrupt the coherence of the 5f band states and drive the whole system toward localized 5f states. The Anderson Hamiltonian, as used by Cooper, has both the Hubbard repulsive Coulomb term and a Kondo-

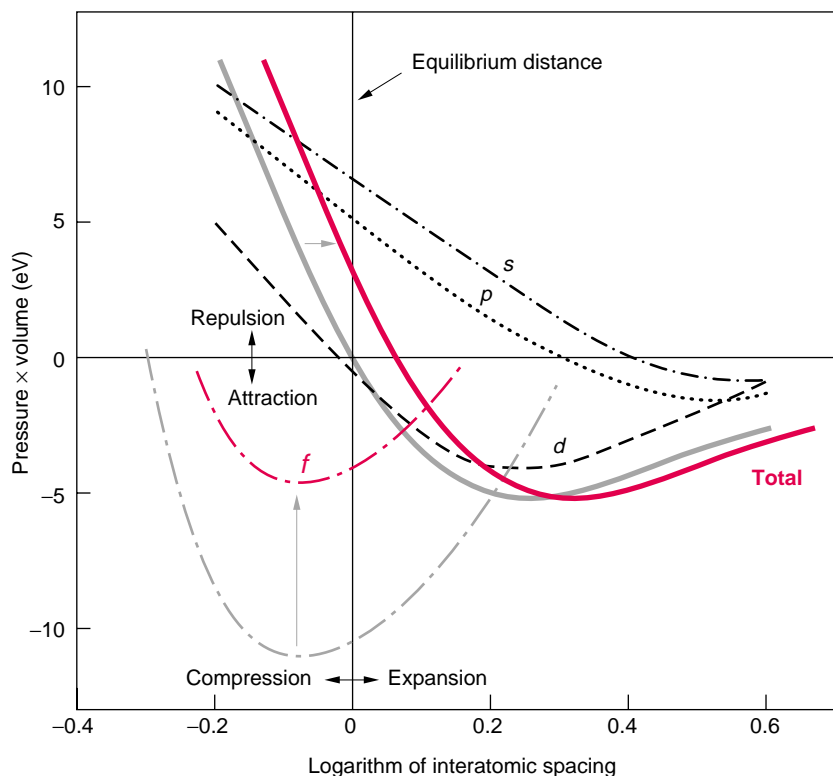


Figure 18. Modified Bonding in Plutonium with Fewer 5f Bonding Electrons In this figure, we show how the bonding would change if only one 5f electron is in the conduction band instead of the usual five, and the other four are localized at lattice sites. We illustrate the effect of this localization by artificially reducing the f band contribution to bonding by roughly 80% relative to the results plotted in Figure 12. In this case, the s-p repulsion term is not balanced by the f bonding term, and the lattice must expand to reach a new equilibrium.

like two-electron term (originally invented to treat the spin-spin interaction between an electron on an impurity atom and a conduction electron). The Hubbard term keeps the 5f electrons localized, and the two-electron term leads to a partial localization of the conduction electrons. This model has therefore all the right ingredients for yielding localization in going from the α - to the δ -phase, but it may take years before it could be used for realistic calculations. Moreover, to start the calculation, one must have some impurity sites. In effect, this prerequisite helps avoid the question of how the five 5f electrons become localized.

Can we obtain a translationally invariant solution for fcc plutonium in which the five 5f electrons are localized by starting from a calculable Hamiltonian?

The usual one-electron calculation (translationally invariant) at the δ -phase density predicts itinerant 5f electrons. So, we must modify the Hamiltonian to predict localization. In the Anderson model, the Hubbard term prevents the f electrons on other sites from hopping onto a given site. This is the impurity view, but as we have pointed out, it is almost impossible to obtain translationally invariant solutions from impurity models. Instead, let us find out what will keep the 5f electrons from leaving a site. Clearly, we need to add an attractive Coulomb term. We therefore propose a model with a small attractive Coulomb term added (in the f states only) to the band Hamiltonian in a one-electron calculation. Such a calculation would have to be performed

self-consistently so that the hybridization of the *f* states with the non-*f* states could change in value as the 5*f* electrons become more localized. We believe such a calculation is feasible within the standard codes of electronic-structure calculations. Having such a solution, we could then apply the two-electron model to obtain the dynamics of partial localization.

A feasible approach closer to the impurity models would be an electronic-structure calculation of an alloy, in which there are two plutonium sites: One has an added attractive Coulomb term, and the other does not. Such a self-consistent calculation would demonstrate whether random sites with localized *f* states could drive all the *f* states to localization on all sites. The physical basis for an attractive term may be the poor screening of the nuclear charge by the 5*f* states, as it is by the 4*f* states in the case of the lanthanide contraction. As we are looking at new models for the δ -phase, we must also consider the alloy-stabilized δ -phase.

Gallium-Stabilized δ -Plutonium.

Although no one understands the electronic structure of δ -plutonium, people in the nuclear weapons program work with this phase all the time. In fact, the secret to stabilizing this phase down to room temperature dates back to the Manhattan Project. At room temperature, pure plutonium would be in the very brittle α -phase, but as luck would have it, one of the very first “high-purity” samples made by Manhattan Project workers had enough impurities to become ductile. Those pioneers knew therefore from the start that they could deform the new metal into a required shape. They soon figured out that it was the addition of a few percent of a trivalent metal at high temperature that held plutonium in the δ -phase down to room temperature.

But why should the addition of those small atoms stabilize a phase with a dramatically low density and the desired malleability? The answer is not known yet, so we can only make suggestions. The impurity picture suggests that atoms

at random lattice sites create strong scattering, thereby blurring the periodicity of the lattice and killing the coherence of band states. Applying this mechanism to plutonium, we would say that the addition of impurity atoms containing no *f* electrons would destroy the coherence of the *f* band. Without its narrow *f* band, plutonium could no longer lower its energy by lowering its symmetry through a Peierls-like distortion into the α -phase; it would therefore remain in the δ -phase. Another view is that plutonium atoms relax and move toward the smaller non-*f* atoms, thereby reducing the *f*-*f* interactions that stabilize the α -phase. So, the solid remains stable in the high-symmetry fcc phase even as the temperature is lowered. In this cubic structure, only 3 atomic percent aluminum or gallium dissolved in plutonium (the replacement of one plutonium atom by a gallium atom in every three-atom-sided cube) is enough to hold the fcc structure down to room temperature. Roughly, any atoms that are soluble in pure δ -plutonium at its elevated temperatures and that have no *f* electrons should stabilize the δ -phase to lower temperatures. (Like plutonium, cerium and americium have *f* electrons, but they also stabilize the δ -plutonium. Understanding how their more-localized *f* electrons interact with the itinerant *f* electrons in plutonium, however, is best left to band or alloy calculations that can include some of these effects.)

Our discussion of the plutonium δ -phase and other phases highlights the complexity of the 5*f* bonding in plutonium and its impact on metallurgical properties. We believe that improved one-electron methods, along with new measurements conducted with modern techniques, will clarify our understanding of bonding in all plutonium phases. One might also have to go beyond the average electron correlations inherent in one-electron methods to include specific spin interactions and specific interactions between more-localized and less-localized electrons, as in the two-electron dynamics described in the article by Cooper.

We now leave the topic of phase instabilities, the least understood aspect of the light actinides, and turn to the low-temperature properties of the light actinides. Recently, these properties have been recognized as similar to the low-temperature properties of other correlated-electron materials.

A Revised View of the Periodic Table

Plutonium is not alone in having its electrons precariously balanced between bonding and localized states although it exhibits this property better than any other element. If the periodic table is arranged to show only the *d* and *f* electron series, and the *f* series are put on top and squeezed together to fit as in Figure 19, then the elements highlighted by the white diagonal stripe are the rough dividing line between localized (local moment magnetism) and itinerant (superconductivity) long-range collective behavior. This is a good indication that the *f* and *d* electrons of the diagonal elements may be balanced between being localized and itinerant, and their behavior is therefore interesting. We will discuss the “normal metals” off the diagonal before we consider the diagonal elements.

Normal Behavior off the Diagonal: Magnetism vs Superconductivity. Figure 19 indicates that the *f* and *d* electron metals away from the diagonal divide neatly into two categories. In one category, the *f* and *d* electrons are itinerant and fully bonding, and they tend to form a superconducting ground state at very low temperatures. In the other category, the *f* and *d* electrons are fully localized, usually forming local magnetic moments and ordering into a magnetic ground state at some temperature.

This association of localized electrons with local magnetic moments and of shared electrons with bonding is familiar to chemists. When chemists make a new insulator or organic compound containing an *f* or *d* electron atom, they can

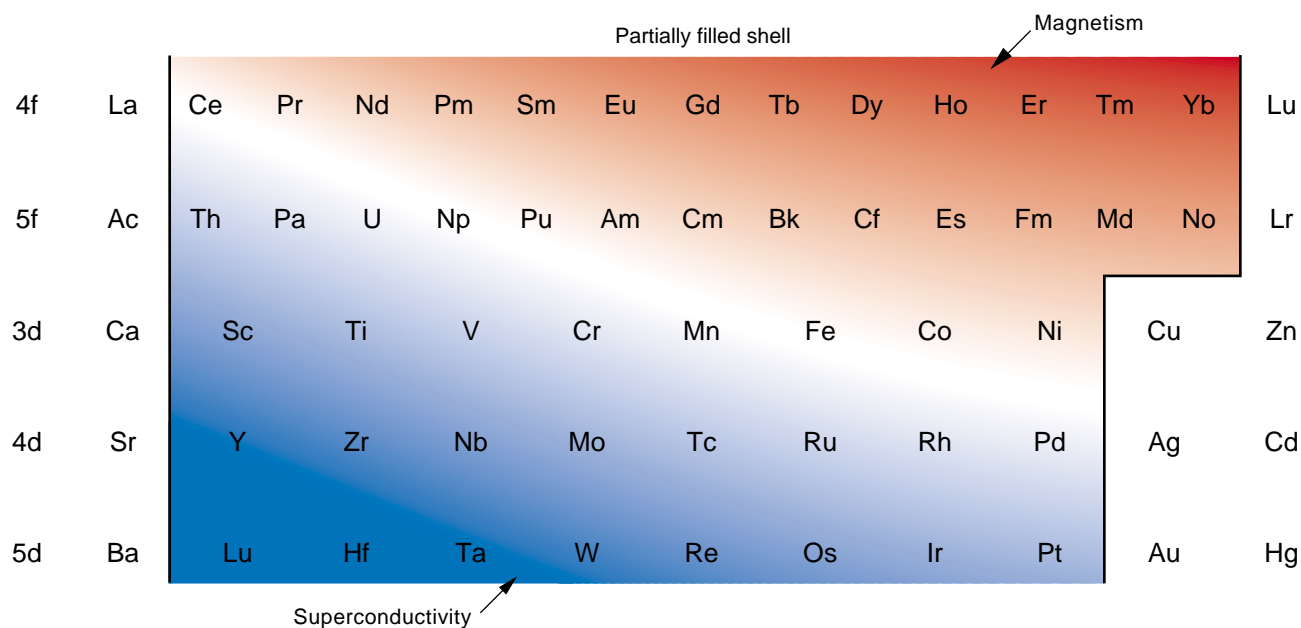


Figure 19. A Revised Periodic Table of the f and d Series

The periodic table is rearranged with the rare-earth, or lanthanide, elements in the top row, the actinides in the second row, and the d-electron transition elements below them. Most metals have predictable ground states and become superconducting (blue) or magnetic (red) as the temperature is lowered. But the low-temperature metallic properties of the elements along the diagonal are difficult to explain because, in the solid-state, their f or d valence electrons are poised between localization and itinerancy.

deduce the valence state of that atom by measuring the magnetic moment of the compound. The measured value tells them the number of electrons contributing to the moment and therefore the number of electrons localized on the atom. The remaining f or d electrons are participating in bonding, and their count gives the valence. Usually, metals are not so simple, but it is useful to think of electrons as magnetic or bonding.

So, how do we know if there are local magnetic moments in a material? Magnetic susceptibility χ measures the internal response of a material to an applied magnetic field. That is, $M = \chi B$, where M is the magnetization of the material and B is the magnetic field intensity. In 1845, Michael Faraday showed that some materials were drawn to the high-field region of his magnet and others were repelled. He called the former behavior paramagnetic with a positive susceptibility and the latter diamagnetic with a negative susceptibility. Most common metals have no magnetic moments and are weakly paramagnetic or diamag-

netic. As shown in Figure 20, these non-magnetic metals have low susceptibilities, which are roughly temperature independent. Magnetic materials have positive, much larger susceptibilities, and because thermal motion counters the tendency for moments to align with the applied field, this positive susceptibility is inversely proportional to temperature, as shown in Figure 21. We can extract the size of the magnetic moment in a magnetic material from the slope of χ vs T .

In the solid state of metals or insulators, local moments at lattice sites tend to line up at some temperature as the material is cooled, producing a state of long-range order called magnetism. (Following Hund's rules, the local magnetic moments at each lattice site are proportional to a vector sum of the total spin and total orbital angular momentum of the localized electrons.) In particular, each magnetic material has a critical temperature, at which the free energy of the system is lowered through an alignment of the local moments. If the moments line up parallel to each other,

forming a ferromagnetic state, the transition temperature is called the Curie point T_C . If the moments line up antiparallel, forming an antiferromagnetic state, the temperature is called the Néel temperature T_N . Magnetic transition temperatures range from close to absolute zero to about 1000 kelvins, and a ferromagnetic material whose T_C is above room temperature is called a permanent magnet. Figure 21, a generic plot of the inverse susceptibility vs temperature, shows how the temperature intercept can indicate whether a material will be a ferromagnet or an antiferromagnet at lower temperatures. If the intercept is at a positive temperature, the material should be ferromagnetic, and if it is at a negative temperature, antiferromagnetic.

Local moments in one of these magnetic ground states in a metal are arranged following the symmetry of the lattice, and they do not scatter the conduction electrons well. As a crystal is heated above T_C or T_N , the magnetic ordering disappears, the local moments point in random directions, and those

Figure 20. Magnetic Susceptibility of Plutonium and Other Materials

The susceptibility of most metals is close to zero on this plot, but that of UBe_{13} is very large as though this heavy-fermion compound had local moments. It was therefore conjectured that UBe_{13} would become an antiferromagnet at low temperatures. Instead, however, UBe_{13} becomes a superconductor at low temperatures, and the reason for its high susceptibility is not well understood. The susceptibilities of plutonium's various phases are also higher than those of most metals, but they are lower than those of materials with local moments. The blowup of the plutonium curve (see inset) displays more clearly the variation in susceptibility as plutonium changes phase. Although essentially temperature independent, the susceptibility of plutonium appears to increase slightly as the temperature decreases. It is fair to say that plutonium behaves as if it were almost magnetic.

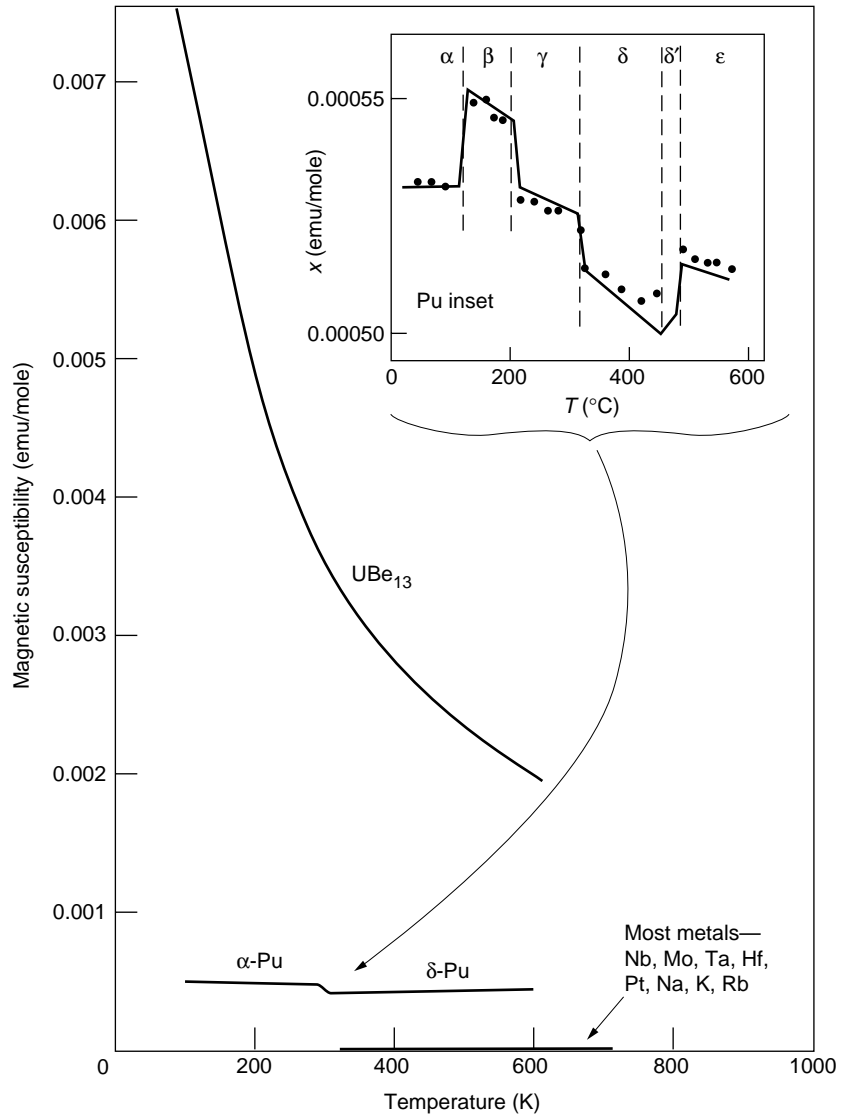
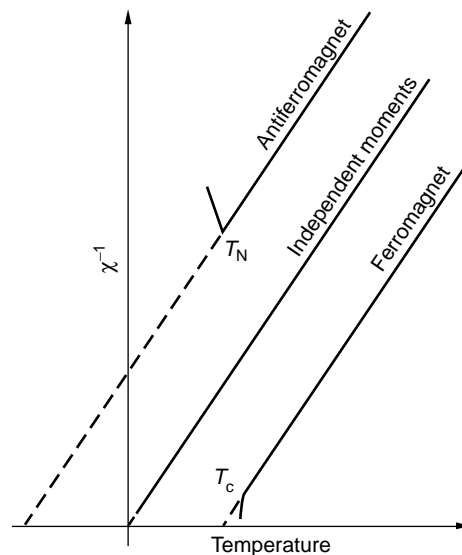


Figure 21. Curie-Weiss Plots of Inverse Magnetic Susceptibility

The magnetic susceptibility due to local moments follows the Curie-Weiss law: It is inversely proportional to temperature because thermal motion tends to wash out the natural alignment of local moments as temperature increases. The inverse susceptibility is plotted for several cases. If there is no interaction among local moments, the inverse susceptibility extrapolates to zero at $T = 0$. If there is a ferromagnetic interaction among the local moments, it extrapolates to zero at a positive temperature intercept, and if there is an antiferromagnetic interaction, it extrapolates to a negative intercept. The absolute value of the intercept tends to correlate with the magnetic ordering temperatures.



moments can now scatter the conduction electrons. The scattering occurs through a magnetic interaction that can flip the spins of the conduction electrons. We shall see that plutonium scatters the conduction electrons very well although it does not have local moments.

Superconductivity is a state of truly perfect conductivity that can exist in an electrical conductor at low temperatures. In general, materials with magnetic moments do not become superconductors at low temperatures because magnetism in any form is inimical to superconductivity. The typical superconducting state forms at temperatures of a few kelvins and consists of pairs of conduction electrons with opposite spins and momenta that are bound together through their interaction with the crystal lattice. These pairs act like a Bose condensate and travel through the lattice with no resistance whatsoever. This low-energy collective state was explained in the Bardeen-Cooper-Schrieffer (BCS) theory of superconductivity (1957). However, if a material has ordered moments, a net magnetization, or spins from random impurities, the magnetic field resulting from any of these sources would tend to flip one of the two opposing spins in the pair and prevent the pairs from forming. Thus, elements with localized d or f electrons typically have magnetic ground states, and those with conducting d or f electrons typically have superconducting ground states.

Anomalous Properties of Elements on the Diagonal. Now, we turn our attention to the elements on the diagonal in Figure 19. On the atomic level, these elements are like plutonium because they have two or more incompletely filled atomic shells that are close in energy. The electrons can therefore shift between shells relatively easily. As a result, these elements show giant resonances in their atomic optical spectra, reflecting their many close-lying energy levels.

These energy levels in the atom

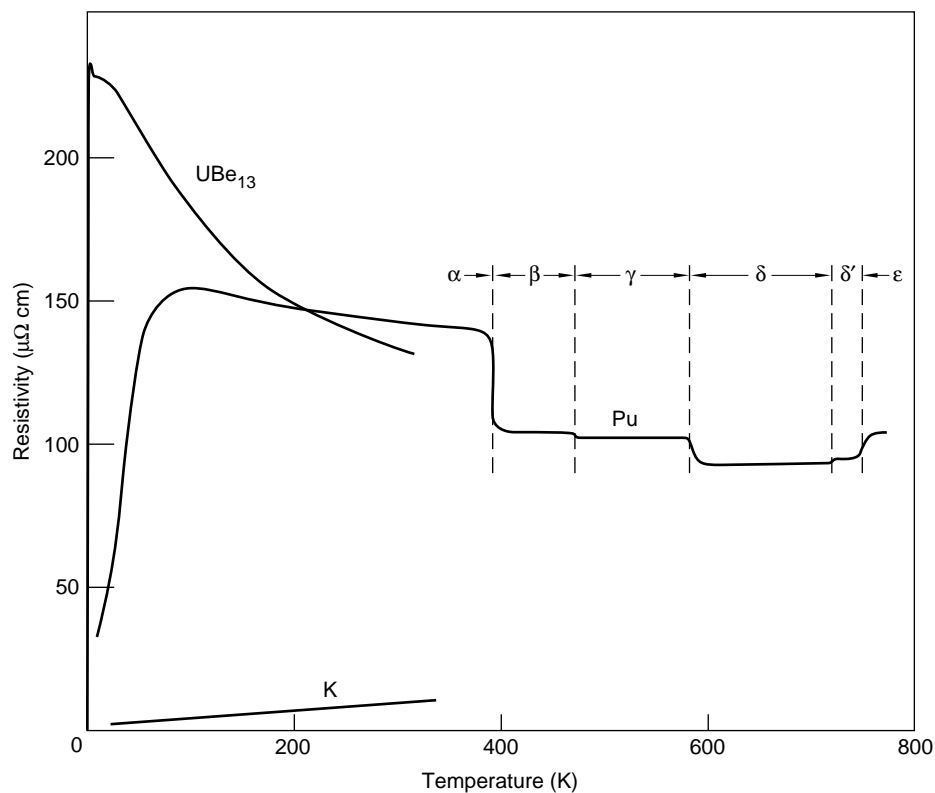


Figure 22. Resistivity of UBe_{13} , Plutonium, and Potassium

Electrical resistance in most metals increases linearly with temperature because electrons are scattered by phonons, as shown for potassium. Imperfections such as foreign atoms, lattice vacancies, and more-complicated defects, which are temperature independent, also scatter electrons and lead to a finite limiting resistance as $T = 0$. Plutonium has much higher resistivity values at all temperatures, showing enhanced scattering of the conduction electrons. The electron scattering comes from electron correlations. The compound UBe_{13} yields one of the most extreme examples of electron scattering in a metal.

translate into a multiband system with one relatively narrow band and a high density of states at the Fermi energy in the metal. This description is true of the transition metals on the diagonal, even though their d bands are not quite as narrow as the f bands in elements along the diagonal. Narrow bands tend to mix or hybridize with other close-lying bands (a phenomenon that is predicted by one-electron band calculations). Moreover, weakening or strengthening the hybridization can push the d or f electrons in these narrow bands toward greater localization or greater itinerancy, respectively. Thus, the electrons in these narrow bands are highly sensitive to small perturbations. This sensitivity

can lead to many allotropic crystal structures in the same element and to catalytic activity. It can also lead to the metal's ability to absorb hydrogen easily and to spark when struck. Catalytic activity and hydrogen absorption occur when perturbations can modify the chemical state, and the diagonal is the place to look for those behaviors.

First, let us consider a metal's ability to make sparks. All metals shower off burning pieces when put to a grinding wheel because the wheel heats the pieces as they break off, and most hot, finely divided metals burn. However, steel, cerium, uranium, neptunium, and plutonium make sparks under far more gentle conditions. For example, it is the cerium

Itinerant Magnetism, Invar, and δ -Plutonium

In some magnetic materials such as iron, conduction electrons rather than localized electrons produce ferromagnetic ground states. In these "itinerant magnets," the conduction band splits into two distinct bands, one composed of spin-up states and the other of spin-down states. Although those two sets of states exist in all materials, in most they remain degenerate, except in the presence of an applied magnetic field. In iron, for example, the somewhat narrow d band splits spontaneously (without an applied magnetic field) into spin-up and spin-down bands. As in the Peierls distortion described in the main text, the separation of degenerate states into two bands lowers the total energy of the filled states. (Note that itinerant magnetism does not follow Hund's rules because the orbital angular momentum of conduction electrons is quenched.) Itinerant magnets are less robust than local-moment magnets because the split conduction bands remain close to each other in energy and various perturbations can easily overwhelm the energy advantage from the split. The ferromagnetic state of iron, for example, disappears when iron is alloyed with other elements to make stainless steel.

We note the little-appreciated correlation between corrosion and magnetism. Most stainless steels are nonmagnetic and, of course, do not corrode. After welding or deformation, they sometimes rust in exactly those spots that have converted to a magnetic form of iron, martensite. Why? We suggest that any electrons that are not fully participating in bonding, including localized electrons or conducting electrons that are magnetically ordered, are more available for chemical reaction and thus for corrosion. We also note that, if the electrons in an itinerant magnet become less bonding and more magnetic, the lattice becomes bigger and vice versa. It is this effect that made Invar possible. Invar, as well as being an itinerant magnet, is an alloy with a zero coefficient of thermal expansion around room temperature. Accurate pocket watches were made of Invar a century ago. As an itinerant magnet is heated, thermal motion interferes with the spin alignment of electrons in the narrow bands, and this decrease in magnetic ordering makes those electrons a little more bonding (van Schilfgaarde et al. 1999), thus countering the normal thermal expansion. By choosing the correct combination of elements, one can make an alloy that maintains its

size over some temperature range because these competing effects exactly balance out over that temperature range. It is now clear that Invar watches had to be kept out of magnetic fields because those fields could have bent the parts. We will not discuss the Invar effect in detail but will give a simple example that illustrates the electronic-structure changes leading to this effect.

The energy contained in the magnetic field of a permanent magnet can become noticeable on the scale of the cohesive energy. When dropped, modern neodymium-iron-boron permanent magnets break not because the metal is weak but because the huge magnetic energy decreases dramatically.

Consider the itinerant magnets iron, cobalt, and nickel. By one-electron calculations, we can determine the volumes of the true ferromagnetic state and of the hypothetical paramagnetic state. We calculate the ferromagnetic state by including spin, and thus we have spin-up and spin-down bands as mentioned before. In the paramagnetic calculation, we do not include spin, and the spin-up and spin-down bands are degenerate. In all cases, the calculated volume of the paramagnetic state is smaller than that of the ferromagnetic state. In other words, if the itinerant electrons contribute to magnetism, their contribution to bonding is reduced. Can this tradeoff be related to the contraction upon heating that is seen in the δ -phase of pure plutonium?

Although plutonium has no local magnetic moments, one might ask whether its conduction electrons could make it an itinerant magnet, like iron. There is little evidence now for magnetism in pure plutonium, but many plutonium compounds are magnetic and tend to be itinerant magnets. Simply dissolving hydrogen in plutonium is enough to make the electrons localize and the system ferromagnetic. Also, a comparison of the light actinides with the transition metals indicates that the light actinides should be superconductors unless they have local moments. So, the fact that plutonium is not a superconductor may indicate that plutonium is an incipient, weak itinerant magnet and that the loss of magnetic ordering with heating plays a role in the contraction of the δ -phase.

in a lighter flint that makes the sparks for lighting fires. We argue without proof that the high density of states near the Fermi surface causes the transfer of electrons to or from a tiny piece of highly deformed metal as it breaks off from a large piece, no matter how gently the breaking occurs. The resulting voltage difference produces a tiny electrical discharge across

the gap, which then ignites the shard. Lanthanum, which is mechanically similar to cerium and is far more chemically active, does not make sparks because it has no f electrons and its density of states is low. The uranium-manganese compound UMn_2 , which is made of two narrow-band elements from the diagonal in Figure 19, sparks so readily that its pow-

der burns as soon as it is poured in air.

The most-common anomalous property, and the simplest one to measure, is the departure from the usual linear relation between electrical resistivity and temperature that occurs below room temperature. In Figure 22, we compare the resistivities of potassium and plutonium. Over the temperature range shown,

potassium's resistivity increases linearly with temperature, as expected from the interaction of conduction electrons with lattice vibrations (phonons). Instead of following this simple linear increase, plutonium's resistivity bulges high above linearity at temperatures below room temperature and remains extremely high above room temperature, where it shows off its many phase transitions. The resistivity of plutonium at the bulge is of the order of 150 micro-ohm centimeters ($\mu\Omega$ cm), which means, microscopically, that an electron is scattered by roughly every atom in the lattice. This type of scattering is considered the highest possible simple resistance that can be seen in a metal and is called the unitary limit. Many correlated-electron metals show higher resistivities, which can only be explained by correlated-electron models such as the Kondo and Anderson models for extended systems. These models add electron interactions and correlations beyond those included in one-electron methods.

This puzzling enhanced electrical resistivity upon cooling began receiving attention thirty-five years ago, when it was noticed that a small amount of iron dissolved in gold showed an increasing electrical resistance as it was cooled at temperatures of a few kelvins. At the same time, the iron atoms had no magnetic moments. (The increase in the resistance of plutonium from room temperature down had already been measured, but this curve was neither as reproducible as the curve for the iron-gold alloy nor as easy for everyone to check.)

Jun Kondo was the first scientist to have come up with an explanation for the increase in the gold alloy's resistivity: The missing magnetic moment in iron was responsible for it. Kondo then made a model in which the spins of conduction electrons could flip the spins of the electrons on the iron atoms and thereby cancel the magnetic moment within the small volume around each iron atom impurity. This model predicted the desired increase in resistivity with decreasing temperature. In time, theories with a characteristic Kondo temperature

were used for explaining not only the increase in resistivity upon cooling but also the leveling off in magnetic susceptibility upon further cooling, once a high value had been reached. They could also explain why magnetic moments were missing in so many materials. So, the Kondo impurity model was expanded to a Kondo lattice model, an extended system, in which crystallographically ordered moments could again be made to disappear, even though there seemed not to be enough conduction electrons to do the job. The most extreme example are the "Kondo insulators," in which no conduction electrons are present, but their spins are assumed to make magnetic moments vanish. We believe that these are examples of overworking a model simply because it fits the data. Such situations would not occur if we had a comprehensive theory for these phenomena. We note that the disappearance of the iron moment in the gold alloy should have come as no surprise because that moment is also known to disappear when iron is alloyed to make stainless steel. Indeed, it has been well known since the 1930s that the magnetism of iron is not robust (see the box "Itinerant Magnetism, Invar, and δ -Plutonium" on page 120). However, we are so used to calling iron a permanent magnet that even today many people believe iron is an archetypal example of a magnetic atom or metal.

Correlated-Electron Materials. Despite exaggerated claims, the Kondo model and all its offshoots have shown the condensed-matter physics community that there are very interesting anomalies going on in metallic systems, especially the metals on the diagonal in Figure 19, and this group includes plutonium. Although we do not have a simple predictive model to explain the origin of high resistivities, the materials exhibiting these conundrums are now lumped under the single category of correlated-electron materials. As shown in Figure 1, apart from high resistivities, these materials exhibit high magnetic susceptibilities, and they have no local moments at low

temperatures. Other anomalies include tiny magnetic moments (as much as 1000 times smaller than expected), higher-than-expected magnetic ordering temperatures, failure to follow the quadratic temperature dependence of resistivity predicted by the Fermi-liquid model, and high specific heats indicating enhanced electron masses. All the signatures of correlated-electron materials are believed to result from strong electron-electron correlations involving spin and charge interactions.

Plutonium is probably the clearest example of a pure element in the correlated-electron category. Figure 22 shows its anomalous resistivity. Plutonium also has the most enhanced low-temperature specific heat of any pure element. The specific heat shown in Figure 23 indicates that the electron effective mass of plutonium is 10 times larger than that of most metals. Finally, plutonium has a relatively large magnetic susceptibility in all its solid-state phases, as seen in the inset on Figure 20.

The relatively large paramagnetic susceptibilities of the various phases of plutonium suggest that phases with magnetic moments or itinerant magnetism must have similar internal energies. Perhaps all the phases in pure plutonium above the α -phase have magnetic moments, but because the temperature range of each phase is so narrow, we have not been able to demonstrate them by magnetic susceptibility or neutron diffraction measurements. Correlated-electron materials usually show increases in susceptibility as they cool, but that susceptibility levels out within a few kelvins of absolute zero. Our best chance of finding out whether plutonium has local moments is to do synchrotron x-ray and neutron-scattering experiments on single crystals. Those measurements would be adequately sensitive to magnetic moments. We note that Méot-Raymond and Fournier (1996) claim to have found the signature of local moments on top of a huge paramagnetic background in δ -plutonium. Although the presence of local moments is consistent with the model of δ -plutonium described in Cooper's article, we

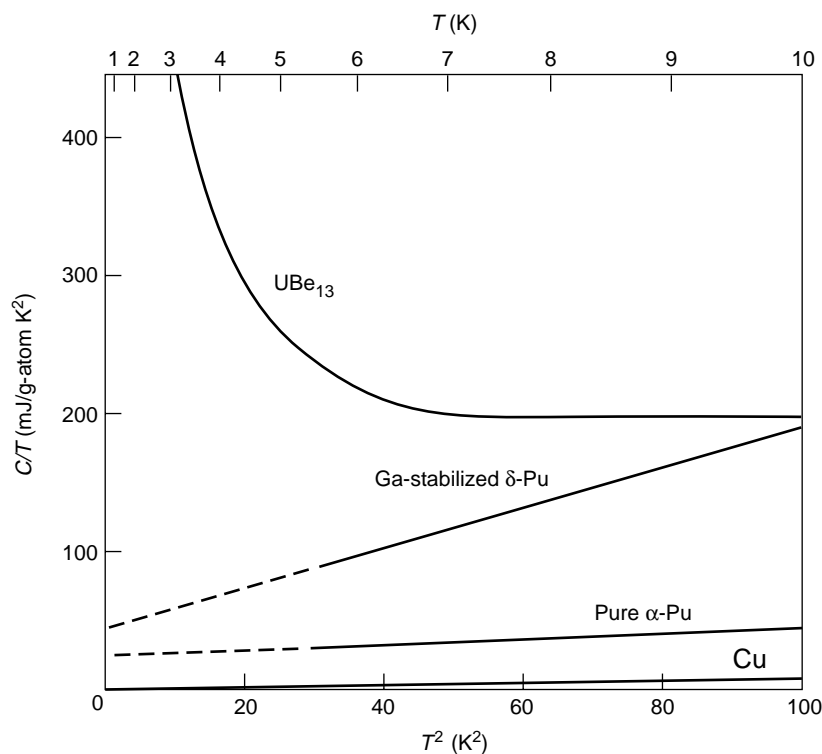


Figure 23. The Specific Heat of Plutonium and Other Metals

The low-temperature specific heat of a metal is the sum of a lattice term proportional to T^3 and an electronic term γT ; that is, $C_V = \gamma T + AT^3$. Hence, when we plot C_V divided by T vs T^2 , we get a straight line that has an intercept equal to γ at $T = 0$ and a slope equal to A . That slope yields the Debye temperature Θ_D via the relation $\Theta_D^3 = 1944 \text{ \AA}^{-1} \text{ J-mol}^{-1} \cdot \text{K}^{-1}$. As we explained in the section on the free-electron model, the specific-heat coefficient γ is proportional to T/T_F , and T_F is inversely proportional to the mass of the electron. So, γ is proportional to the electron mass. In this figure, the line for copper represents the behavior of most metals whereas the lines for α - and δ -plutonium have the highest values of γ (intercept values) of any pure element, indicating that conduction electrons have an enhanced effective mass. The compound UBe_{13} has an extremely high electronic specific heat, which continues to increase until it is cut off by the compound's transition to superconductivity just below 1 K (not shown). The superconductivity of UBe_{13} proves that its large heat capacity must be associated with the conduction electrons rather than the local moments and that the anomalously large values of γ are enhanced electron masses, or heavy-fermion masses, m^* .

remain somewhat skeptical of this data interpretation because so many correlated-electron systems show the same type of susceptibility even when they do not have local moments.

Magnetism and local moments do become manifest in plutonium if we spread out the plutonium atoms. As mentioned in the box "Itinerant Magnetism, Invar, and δ -Plutonium," plutonium hydride is ferromagnetic because the increased separation between plutonium atoms causes the f electrons to localize and pushes their behavior across the diagonal limit in

Figure 19 and into the magnetic regime. This last statement leads us into a discussion of actinide compounds that exhibit localized 5f states or whose ground states become superconducting.

Hill Plots and Actinide Compounds

The crossover from itinerant to localized electrons can clearly be achieved if the atoms are spread out. Before 1970, investigators could not

guess or understand whether cerium and uranium compounds would be superconducting or magnetic. In 1970, at Los Alamos, Hunter Hill explained under what conditions metallic compounds containing f electron elements would be superconducting or magnetic. Until then, the light-actinide and lanthanide compounds seemed to show these two collective ground states in an unpredictable manner.

Hill realized that in cerium and light-actinide compounds, the distance between the f electron elements determined whether their ground states were superconducting or magnetic, usually quite independently of which atoms containing non-f electrons were separating them. Figure 24 shows what is now called a Hill plot for uranium compounds. Superconducting or magnetic transition temperatures are plotted vertically, and the spacing between the f electron elements is plotted horizontally. In Hill's original plot, the known behaviors fell into two of the four quadrants—large spacing correlated with magnetism and short spacing with superconductivity.

At the time, it was quite strange to think that superconductivity did not depend on the intervening atoms containing non-f electrons. Energy band calculations were just beginning to show that the f electrons would be in bands, but those calculations were limited to the simplest structures. Hill conjectured that the f electrons could hybridize only with f electrons at other sites and that the intervening non-f electron atoms were just spacers to change the degree of overlap between the f-electron wave functions. In this way, Hill's plot became a major step toward understanding the light actinides. This picture is far more general in Figure 19, where we see that elements on or near the diagonal can have their properties easily modified.

Figure 24 shows many more materials than were plotted in Hill's original version, including two superconducting compounds that, based on the relatively large distance between two f-electron atoms, should have been magnetic. These two, namely, the uranium-platinum and

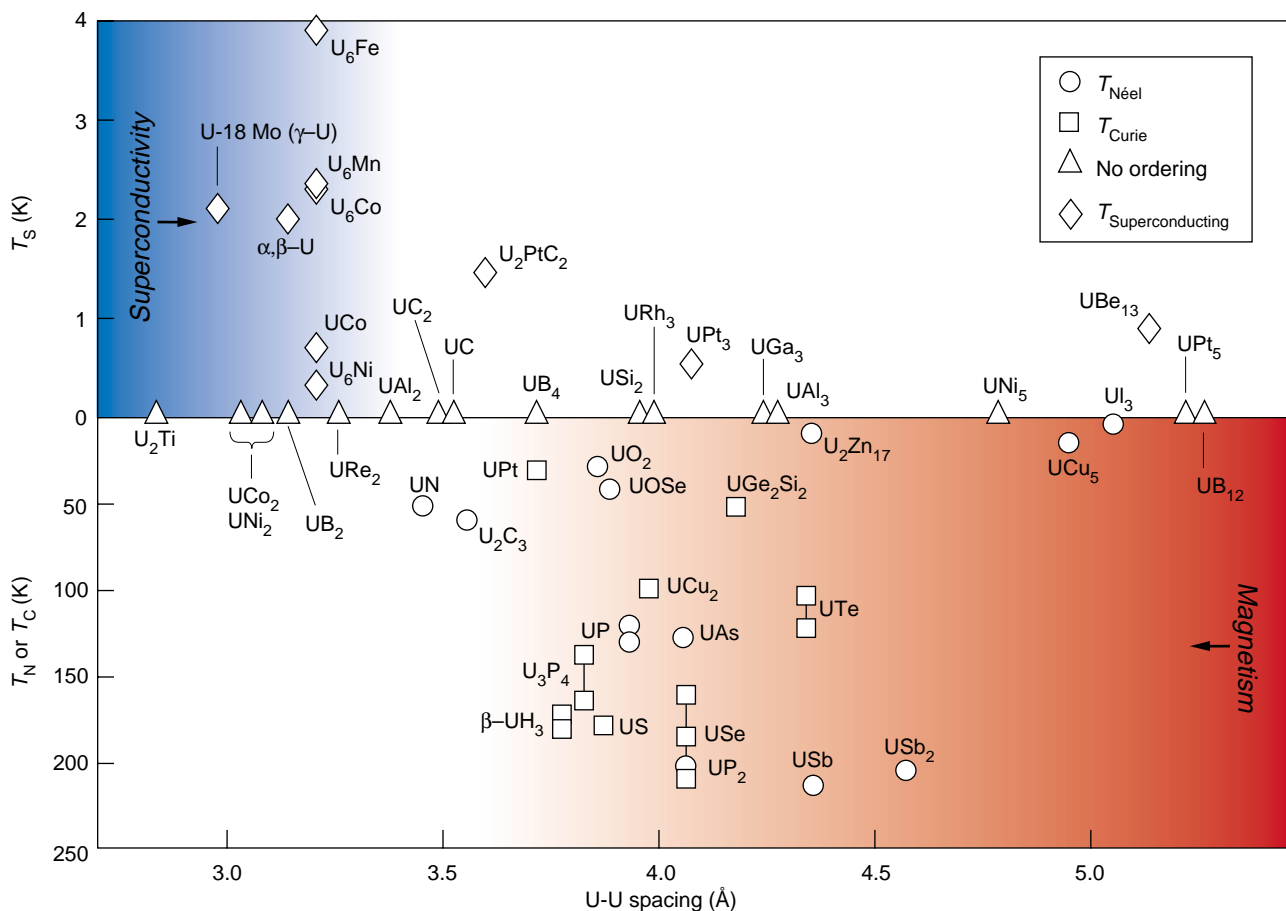


Figure 24. Hill Plot for Uranium Compounds

The Hill plot shows the superconducting or magnetic transition temperatures vs interatomic spacing separating the f electron atoms. We augmented the original Hill plot for uranium compounds to include more data—in particular, the transition temperatures of the two superconducting heavy-fermion compounds UPt_3 and UBe_{13} . Hill conjectured that the overlap of the f-electron wave functions between the uranium atoms determines whether the f electrons are localized (magnetic) or itinerant (superconducting) independent of the intervening atoms. Most compounds behaved as Hill expected. The superconducting compounds occurred at short f-electron spacings (blue quadrant), and the magnetic compounds at large f-electron spacings. The heavy-fermion superconducting compounds are exceptions. Although the spacing between the uranium atoms in those compounds is fairly large, the f electrons are still not fully localized and can condense into a superconducting state.

uranium-beryllium compounds UPt_3 and UBe_{13} , are examples of heavy-fermion superconductors.

Heavy-Fermion Materials

Many compounds and alloys containing elements near the diagonal in Figure 19 are called heavy-fermion materials, which means that their conduction electrons behave as if they had extremely heavy masses. The very high heat capacity of UBe_{13} shown in Figure 23 indicates that the electrons have an effective

mass hundreds of times larger than that of conduction electrons in normal metals. Heavy-fermion materials also show very strange magnetic and superconducting ground states. All these materials are narrow-band metallic systems. So, their unusual collective ground states arise from very strong electron correlations involving the electrons in their narrow bands. Also, their low-energy excitations are associated with the spin and charge fluctuations in that narrow band. One difference between these materials and the light actinides is that the former do not exhibit crystal structure instabilities

because their narrow bands are not the dominant bonding bands. This feature can be seen in UPt_3 , whose wide d band has roughly 27 electrons (9 electrons for each platinum atom) and its narrow f band has only 3 electrons. So, it is the low-energy excitations (mostly at low temperatures) that make the heavy-fermion materials resemble the light actinides. We will discuss the discovery of the heavy-fermion materials and the significant role played by the Los Alamos scientists, as well as the exotic properties of these materials.

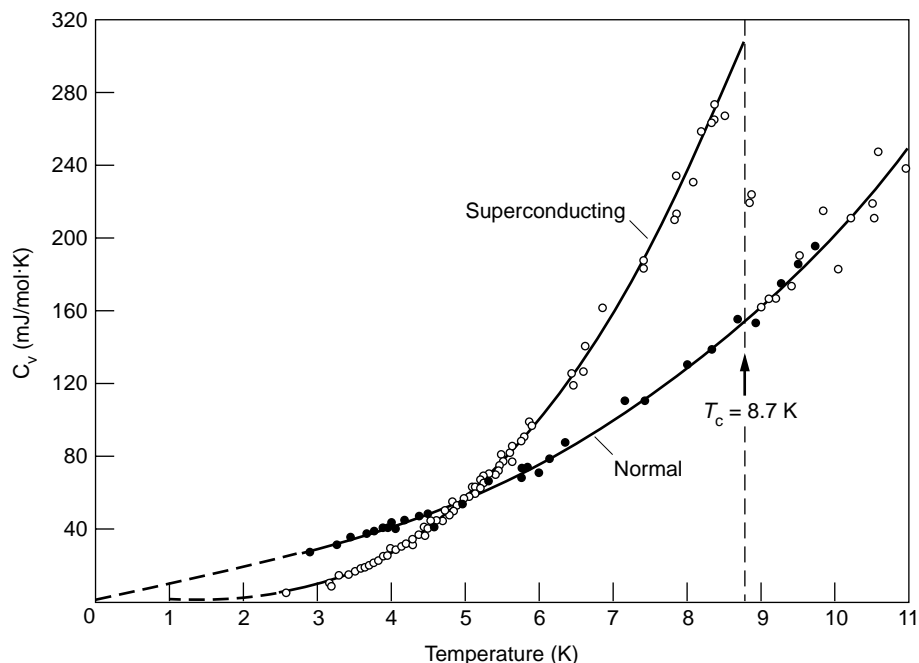


Figure 25. Specific Heat Signature of the Superconducting Transition in Niobium

Common superconductors, such as niobium, show a drop in specific heat as the superconducting transition temperature is reached because a gap opens in the spectrum of possible electronic energies. It is this energy gap that makes the resistance of the material vanish. That is, once in the superconducting state, conduction electrons cannot be scattered as they move through the material because the scattering would cause them to have energies within the energy gap. If an external magnetic field is applied to the material, the superconducting transition will be suppressed, and the specific heat will vary with temperature as in a normal metal. Note that this plot is not a straight line because C , rather than C/T , is plotted on the vertical axis. The same specific-heat signatures of superconducting transitions occur in heavy-fermion compounds such as CeCu_2Si_2 and UPt_3 but at temperatures that are 10 times lower and with changes in specific heat that are 10 times larger.

In the late 1970s, in Cologne, Germany, Frank Steglich and coworkers were the first scientists to observe an anomalous superconducting ground state. They were measuring the low-temperature properties of the cerium-copper-silicon compound CeCu_2Si_2 . The behavior of this compound at temperatures above 100 kelvins suggested that, at very low temperatures, CeCu_2Si_2 would become an antiferromagnet. That is, this compound showed the standard inverse temperature dependence of the magnetic susceptibility, as shown in Figure 21, with a negative intercept on the temperature axis. It also had a huge heat capacity at low temper-

atures, of the order of joules per mole-kelvin, the size associated with localized magnetic moments.⁴ On the other hand, the magnetic susceptibility of CeCu_2Si_2 became temperature independent at low temperatures, implying that magnetic ordering never took place. The real surprise was a large jump in the specific heat, as the compound went supercon-

⁴The electronic heat capacity of a magnetic material is much larger than that of a normal metal because the moments on all the atoms contribute to the former whereas only T/TF of the conduction electrons contribute to the latter. The low-temperature electronic specific heat of normal metals is of the order of 1–10 millijoules per mole-kelvin.

ducting just below 1 kelvin. The specific heat of a superconductor at its transition point is shown in Figure 25. The opening of a large gap in the midst of the huge heat capacity of CeCu_2Si_2 meant that the electrons that presumably were localized and associated with large magnetic moments had become superconducting. But that conclusion simply did not make sense. Localized electrons cannot even conduct electricity, much less be superconducting. These properties were considered so unlikely that they were discounted as artifacts of bad samples, but Steglich defended his results.

Then, in the early 1980s, Los Alamos scientists found that the compounds UPt_3 and UPt_3 have the same properties: very large heat capacities and a superconducting transition at low temperatures. The Los Alamos results made clear that a new ground state of matter existed, one in which electron interactions were so highly correlated that only an extreme quasiparticle picture could cause that behavior. That is, the electrons were so heavily clothed by interactions that they acted as if their masses were 1000 times larger than the mass of a free electron. A heat capacity that should typically belong to magnetic moments belonged, in this case, to the electrons moving through the metal.

The existence of this new ground state blurred forever the distinction between localized and itinerant electrons. Fully localized electrons, with their definite energy levels, can be thought of as belonging to an infinitely narrow band. Because no energy levels are near by, those electrons act as if they had infinite mass—that is, they cannot move at all. By analogy, the f electrons in heavy-fermion materials occupy such a narrow energy band that the electrons act as if they had a huge mass—that is, as if they were almost localized.

Zachary Fisk, Hans Ott, Al Giorgi, Greg Stewart, Joe Thompson, Jeff Willis, and other Los Alamos scientists went on to identify more compounds that had the same heavy-fermion, or

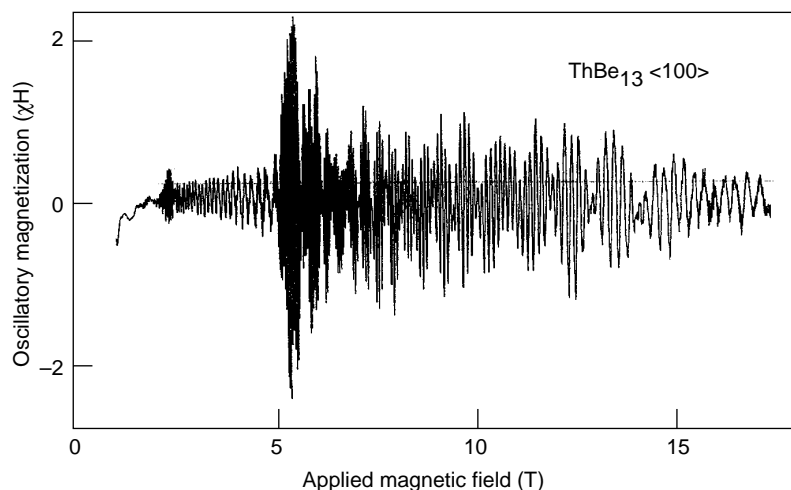


Figure 26. The de Haas–van Alphen (dHvA) Effect

At low temperature and in a high magnetic field, the susceptibility of a metal oscillates with a period that is inversely proportional to the field. This oscillation occurs because the field imposes a quantization condition on the allowed levels of the electrons. The Fermi surface can be extracted in this way. Illustrated here are the oscillations for the ThBe_{13} compound, which is a noncorrelated-electron counterpart of UBe.

enhanced-mass, behavior but did not become superconductors. Some of these heavy-fermion materials became antiferromagnetic and others, as measured then, had neither magnetic ordering nor superconducting ground states. Heavy-fermion compounds had been seen earlier, but until some were seen to be superconducting, there was no way to distinguish them from the magnetic materials, which have large heat capacities. Indeed, in the mid 1970s, Jim Trainor⁵ and coworkers noticed that the antiferromagnetism of the neptunium-tin compound NpSn_3 showed, at its magnetic ordering temperature, a heat capacity anomaly in the shape of a superconducting anomaly, similar to the one shown in Figure 25 for a superconductor. Because they could fit the shape of a magnetic anomaly with that of a superconducting one, the scientists knew that something quite unusual was occurring. However, no one was listening then, and the puzzling result went unnoticed.

⁵At that time, Trainor was a postdoctoral fellow at Argonne National Laboratory.

Several many-body theory groups have tried to understand the unusual metallic properties of the heavy-fermion compounds by developing Fermi-liquid descriptions. In the mid 1990s at Los Alamos, Kevin Bedell and his coworkers Gerry Brown, David Meltzer, Chris Pethick, David Pines, Khandker Quader, and Carlos Sanchez-Castro carried out the most detailed theoretical study of this kind. They developed very simplified one- and two-band Fermi-liquid models of heavy-fermion compounds such as UPt_3 . The surprise was that these simplified models yielded quantitative results in agreement with the low-energy and low-temperature physics of these materials. Again, like the Kondo model, the Fermi-liquid quasiparticle turns out to be a far more useful model than originally expected. Lev Landau's principle of one-to-one correspondence between electron and quasiparticle states continues to be correct and to yield profound insights into systems of strongly interacting particles.

The series of discoveries on heavy-fermion materials established Los Alamos as an institution for leading-

edge research into condensed-matter physics and turned the attention of theorists and experimentalists worldwide to the actinide elements. High interest in these materials continues today.

High Magnetic Fields for Measuring Enhanced Masses.

In the early 1930s, W. J. de Haas and P. M. van Alphen were measuring the magnetic susceptibility of a bismuth crystal and observed oscillations in susceptibility as they varied the field. The period of the oscillations varied as the inverse of the applied magnetic field. The explanation is now simple. Placing a metal in a large magnetic field at low temperatures triggers a new quantization condition. The continuum of energy levels in the conduction band becomes a new set of discrete Landau levels with a splitting between levels given by $\hbar e H / 2\pi m c$. For most experiments, the number of these levels ranges from 1 to 10^{10} . This new set of available states affects all the properties of the metal, provided the applied field is very large and the temperature very low. As the magnetic field increases, one discrete level at a time rises above the Fermi energy and causes the fixed number of electrons (or quasiparticles) to be redistributed on the remaining levels. This electron redistribution is seen as an oscillation in all metallic properties. By measuring the periodicity of the oscillations in different crystallographic directions, we can map the shape of a metal's Fermi surface. And by measuring the temperature dependence of the oscillations, we can determine the effective masses of the electrons on the Fermi surface. Figure 26 shows the dHvA oscillations in ThBe_{13} .

This dHvA effect was used in the 1950s and 1960s to show that Fermi surfaces existed and to measure their shape for simple metals. Later, however, scientists stopped using this technique because most pure metals had been measured. And then, in the late 1980s, the dHvA effect became fashionable again because verifying

the heavy-fermion masses in cerium and uranium compounds was of interest and the higher magnetic fields necessary for that work became available at the National High Magnetic Field Laboratory in Tallahassee, Gainesville, and at Los Alamos. It was thus immediately clear that dHvA methods would allow measuring the heavy-electron masses in heavy-fermion compounds. In the early 1990s, at the Cavendish Laboratory in Cambridge, England, Gil Lonzarich, Stephen Julian, and Louis Taillefer resurrected the 20-year-old technique and used high magnetic fields (up to 20 tesla) and the very low temperatures of a dilution refrigerator (down to 10 millikelvins). After much work, they saw effective electron masses as high as 210 in UPt_3 . This mass is so large that the highest oscillations visible at a temperature of 10 millikelvins were gone by 30 millikelvins. This means that the highest fields, lowest temperatures, and highest-quality samples are a must. Although many groups have looked for similar oscillations in UBe_{13} , such oscillations have never been reported in credible work because UBe_{13} masses are much larger than UPt_3 masses, and the oscillations are already gone at the lowest temperature attainable at this time.

In 1998, Jason Detwiler, George Schmeideshoff, and Neil Harrison observed dHvA oscillations in the praseodymium-beryllium and thorium-beryllium compounds PrBe_{13} and ThBe_{13} by working with a 70-tesla pulsed magnet at the National High-Magnet Laboratory at Los Alamos. These compounds do not have the heavy electrons of UBe_{13} , and so the scientists focused on measuring the Fermi surface and showed that their results agreed with one-electron calculations. Then, to try and sneak up on UBe_{13} , they next tried the thorium-uranium-beryllium compound $\text{Th}_{0.95}\text{U}_{0.05}\text{Be}_{13}$ and saw nothing. They did, however, see oscillations in $\text{Th}_{0.995}\text{U}_{0.005}\text{Be}_{13}$, but much work lies ahead before the masses of UBe_{13} can be seen. We will have to create the following mandatory conditions: very low temperatures, very high fields, and sam-

ples of even higher quality. Because the one-electron behavior of PrBe_{13} and ThBe_{13} has already been confirmed, the natural next step is to measure the clothed masses in UBe_{13} .

Future Steps

If researchers think of narrow-band phenomena when thinking of plutonium, we have succeeded in making our point. The narrow 5f bands lead to all the unusual behaviors of plutonium at all energy scales. At higher energies, the narrow bands predicted by one-electron DFT calculations lead to low-symmetry crystal structures but normal elastic properties. At low temperatures and energies, strong spin and charge fluctuations connected to the excitations from those narrow bands lead to all the anomalous heavy-fermion-like behaviors. The strong electron-phonon coupling of narrow-band electrons may lead to higher effective temperatures, which form a depressed melting curve in the light actinides. The instability of these band states (due to the small radial overlap of the f-electron wave functions and the many states with similar energies) leads to the many-phase transitions in these materials. This instability most likely leads to the partial localization of these 5f states suspected to exist in δ -plutonium.

For the past 40 years, we focused on the difference between the angular character of d and f wave functions as the key to understanding the light actinides although, for most of that time, we knew that the 5f electrons go from being itinerant in plutonium to being localized in americium. That change to localization occurs only because of a change in the radial part of the wave function. We have also known for almost 10 years that the low-symmetry crystal structures are less related to the angular character than to the narrow bonding bands in these metals. Therefore, we need to study other features, such as the short-range nature of the f-f interactions in Bloch states. How can we construct states with partial localization, that is,

with two kinds of 5f electrons (localized and itinerant) in the same metal?

Over the next few years, improved one-electron theories will better describe the short-range nature of the 5f interactions. To determine the range of the f-f interactions, these theories might involve some Slater-Koster fitting of the f bands. Such a scheme could also be used in determining the variation of the f-f interaction as a function of volume. Some calculations of this nature have been performed, but details of the f-f interactions have not yet been extracted. Also, the modern electronic-structure calculations have only demonstrated that the angular character of the single-atom orbitals is not a main factor in determining crystal structures. Indeed, it appears to be washed out when a large number of states build up to form bands, and for that reason little or no charge buildup is seen between atoms in the actinide metals. However, improved calculations may show some small charge buildup, and then we would have to reconsider this feature. Models of localization of the 5f states need to be developed.

Many low-energy properties are still so poorly understood that existing correlated-electron theories need to be improved and new theories might have to be developed. Theorists are still unable to predict the collective ground states in many of these materials. Also, we cannot explain why neptunium and plutonium are the only f electron elements that do not develop a collective magnetic or superconducting state. After examining heavy-fermion materials more closely, we now believe that all may have a magnetic ground state. By using the most-modern experimental tools, we now can try and measure magnetic moments that are 1000 times smaller than they should be. From this work, we hope that new insights into plutonium will emerge.

But right now, the most-modern experimental techniques cannot be applied to plutonium because they require large single crystals, and those are not yet available for plutonium. Learning how to grow such crystals in a repeatable fashion would be a real break-

through in plutonium studies. One could then use the crystals in neutron-scattering experiments to measure the entire phonon spectrum of plutonium and in photoemission experiments to measure its energy bands as a function of crystal momentum. Photoemission (photon in and electron out) is now sufficiently accurate to determine the widths and structure of the narrow 5f bands in materials such as plutonium. In all the earlier photoemission experiments, the instrument resolution for x-rays was so poor and the surface contamination for ultraviolet rays so high that the result was merely featureless spectra. Now, with some of the new photoemission machines and improved surface-cleaning techniques, we should obtain actinide spectra that show the structure predicted by the electronic-structure calculations. At Los Alamos, we are currently making tiny single crystals of plutonium and related materials with techniques that had been used decades ago at Rocky Flats and Argonne National Laboratory. As reported in this volume, we are measuring these tiny samples with ultrasound, neutrons, and x-rays.

Although we may eventually understand the electronic structure of plutonium single crystals, the landscape of close-lying but different states cannot be removed to give homogeneity when we make a large plutonium casting. And because plutonium is radioactive, its atoms will always be converted into impurities, and this process damages the lattice. Nevertheless, if we know how single crystals behave, it is much simpler to model a collection of them in a large casting than to reverse-engineer a large piece to see its components. This is why we are looking forward to more progress in these areas.

We must study plutonium and its neighbors, alloys, and compounds because we deal with them all in weapons. We may never know what ideal plutonium is. However, the gift from nature is that this most-complicated element teaches us about all the elements and shows us that there still is new science to discover. ■

Further Reading

- Fisk, Z., D. W. Hess, C. J. Pethick, D. Pines, J. L. Smith, J. D. Thompson, and J. O. Willis. 1988. *Science* **239**: 33.
- Harrison, N., A. L. Cornelius, H. Harima, K. Takegahara, J. A. Detwiler, G. M. Schmiedeshoff, and J. C. Cooley. 2000. *Phys. Rev. B* **61**: 1779.
- Hess, D.W., P. S. Riseborough, and J. L. Smith. 1993. In *Encyclopedia of Applied Physics* Vol. 7, p. 435. Edited by G. L. Trigg. New York: VCH Publishers.
- Johansson, B. 1974. *Phil. Mag.* **30**: 469.
- Lander, G. H., E. S. Fisher, and S. D. Bader. 1994. *Adv. Phys.* **43**: 1.
- Méot-Reymond, S., and J. M. Fournier. 1996. *J. Alloys and Compounds* **232**: 119.
- Ott, H. R., H. Rudigier, Z. Fisk, and J. L. Smith. *Phys. Rev. Lett.* **50**: 1595.
- Smith, J. L., and R. G. Haire. 1978. *Science* **200**: 535.
- Smith, J. L., and E. A. Kmetko. 1983. *J. Less-Common Metals* **90**: 83.
- Söderlind, P. 1998. *Adv. Phys.* **47**: 959.
- Söderlind, P., O. Eriksson, B. Johansson, J. M. Wills, and A. M. Boring. 1995. *Nature* **374** (6522): 524.
- Stewart, G. R., Z. Fisk, J. O. Willis, and J. L. Smith. 1984. *Phys. Rev. Lett.* **52**: 679.
- van Schilfgaarde, M., I. A. Abrikosov, and B. Johansson. 1999. *Nature* **400**: 46.

A. Michael Boring received a B.S. in mathematics and physics, an M.S. in experimental nuclear physics, and a Ph.D. in theoretical solid-state physics from the University of Florida.

Mike came to Los Alamos as a staff member directly from the University of Florida. He worked on solid state and neutron transport problems as well as theoretical chemistry and atmospheric chemical reactions. Mike organized a re-



search effort into the electronic structure of solids (energy band theory) for actinide materials and went on to become Deputy Director of the Center for Materials Science at Los Alamos. For most of his career at Los Alamos, his research focused on the quantum theory of atoms, molecules, and solids. In 1993, he retired from the Laboratory after 25 years of service. Since retiring, he has maintained his connection with the Laboratory as an affiliate working with staff members and post-doctoral fellows on condensed-matter physics problems.

James L. Smith received his B.S. in Physics from Wayne State University and his Ph.D. in Physics from Brown University. He is currently a Los Alamos Laboratory Fellow in the Materials Science and Technology Division. Jim is also an adjunct professor at several universities, editor of *Philosophical Magazine B*, and member on the board of the Brown University Alumni Association. His research interests include superconductivity, magnetism, actinides, high magnetic fields, electronic properties of metals, experimental physics, and new materials. During his career, Jim published more than 350 papers. For his work, he received the E. O. Lawrence Award from the Department of Energy in 1986 and the American Physical Society International Prize for New Materials in 1990.



Actinide Ground-State Properties

Theoretical predictions

John M. Wills and Olle Eriksson

For nearly fifty years, the actinides defied the efforts of solid-state theorists to understand their properties. These metals are among the most complex of the long-lived elements, and in the solid state, they display some of the most unusual behaviors of any series in the periodic table. Very low melting temperatures, large anisotropic thermal-expansion coefficients, very low symmetry crystal structures, many solid-to-solid phase transitions—the list is daunting. Where does one begin to put together an understanding of these elements?

In the last 10 years, together with our colleagues, we have made a breakthrough in calculating and understanding the ground-state, or lowest-energy, properties of the light actinides, especially their cohesive and structural properties. For all metals, including the light actinides, the conduction electrons produce the interatomic forces that bind the atoms together. In the light actinides, it is the *s*, *p*, and *d* valence electrons and also the 5*f* valence electrons that contribute to chemical bonding (binding). When they are valence electrons in isolated atoms, the 5*f* electrons have an orbital angular momentum $\ell = 3$, and they orbit around the atomic nuclei at speeds approaching the speed of light. In the solid, these electrons are thought to be at least partially shared by all the atoms in the crystal. Therefore, they are thought to be participating in bonding. Moreover, their relativistic motion and their

electron-electron correlations—the interactions among the 5*f* electrons and between them and other electrons—are expected to affect the bonding.

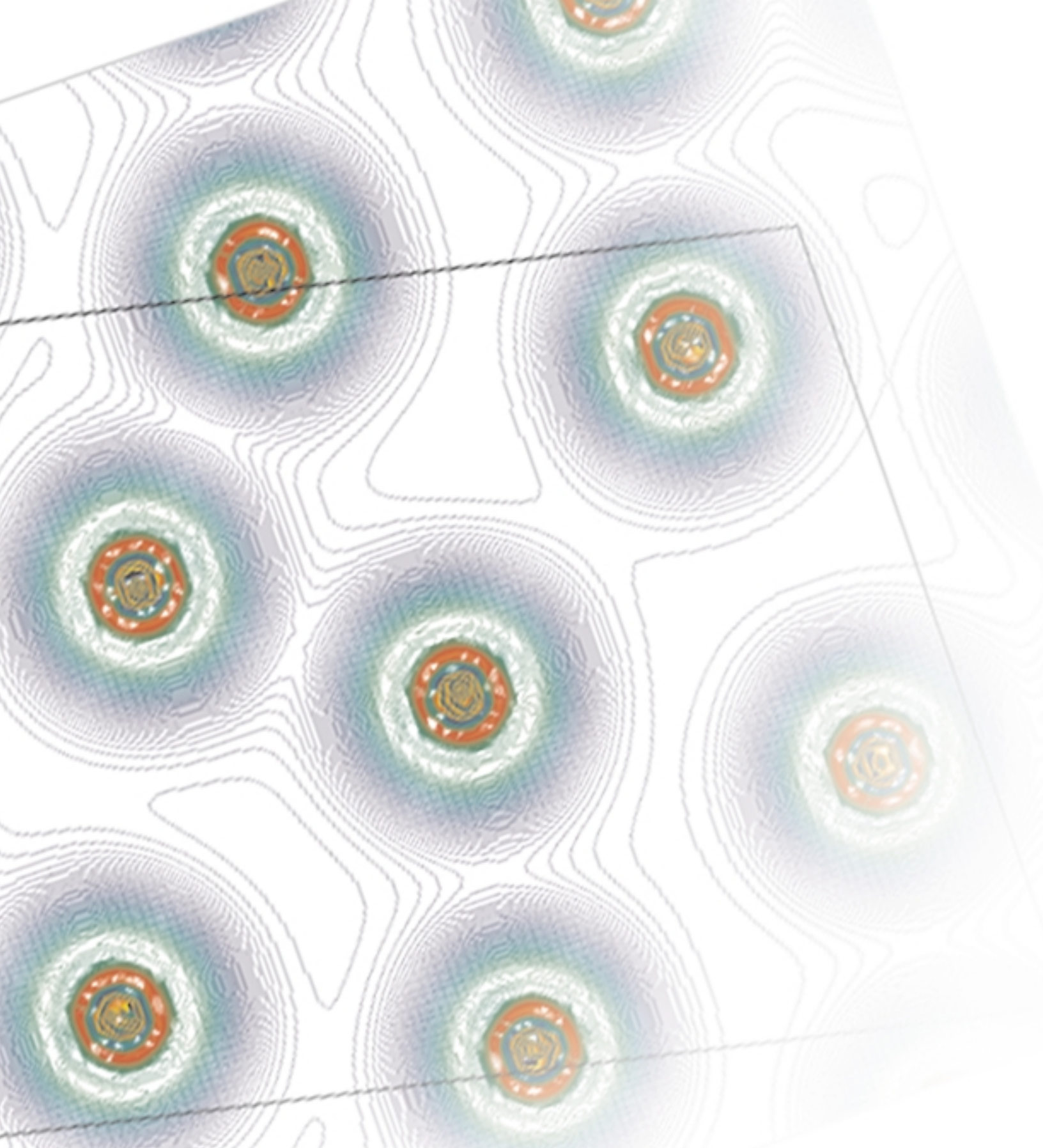
Low-symmetry crystal structures, relativistic effects, and electron-electron correlations are very difficult to treat in traditional electronic-structure calculations of metals and, until the last decade, were outside the realm of computational ability. And yet, it is essential to treat these effects properly in order to understand the physics of the actinides. Electron-electron correlations are important in determining the degree to which 5*f* electrons are localized at lattice sites. If they are localized, the 5*f* electrons are atomic-like and do not contribute to bonding; if they are not localized, they are itinerant, or conducting, and contribute to bonding. Many of the fundamental properties of the actinides hinge on the properties of the 5*f* electrons and on the question of whether those electrons are localized or delocalized.

During the past 10 to 15 years, however, there has been a minirevolution in electronic-structure calculations. It has become possible to calculate from first principles (that is, without experimental input) and with high accuracy the total ground-state energy of the most complicated solids, including the actinides. Density functional theory, or DFT (Hohenber and Kohn 1964, Kohn and Sham 1965), the variational formulation of the electronic-structure problem, enabled this accomplishment. DFT gives a rigorous description of the total

electronic energy of the ground state of solids, molecules, and atoms as a functional of electron density. The DFT prescription has had such a profound impact on basic research in both chemistry and solid-state physics that Walter Kohn, its main inventor, was one of the recipients of the 1998 Nobel Prize in Chemistry.

In general, it is not possible to apply DFT without some approximation. But many man-years of intense research have yielded reliable approximate expressions for the total energy in which all terms, except for a single-particle kinetic-energy term, can be written as a functional of the local electron density. Even the complicated electron-electron exchange term arising from the Pauli exclusion principle and the electron-electron electrostatic interactions can be approximated in this way. Called the local density approximation, or LDA, this development has yielded more accurate results than anyone ever dreamed possible. We have developed bases, algorithms, and software to perform the calculation efficiently and accurately.¹ The efficiency allows us to get solutions for arbitrary geometries, including low crystal symmetry and complex unit cells, and to vary the inputs and thereby investigate the trends and the microscopic mechanisms behind the chemical bonding of solids. Once we know the total energy,

¹ One of the most reliable and robust theoretical methods and software packages for performing such calculations is the FP-LMTO software package developed by John Wills at Los Alamos.



We calculated this contour plot of electron density for α -plutonium from first principles by using density functional theory. The parallelepiped outlines the 16-atom simple monoclinic unit cell. The contours show more charge buildup away from the bonds, indicating that covalent bonding is not prevalent in α -plutonium.

nisms behind the chemical bonding of solids. Once we know the total energy, we can easily calculate all the quantities related to the energy as a function of position, such as pressures and interatomic forces. Our calculations are highly accurate and often predictive.

In this article, we present our calculations of the light actinides (thorium through plutonium) in their observed low-symmetry structures. We have developed a firm theoretical understanding of the equilibrium volume, structural stability, cohesive energy, and magnetic properties of these elements at $T = 0$. We have been able to reproduce the observed lattice constants of the light actinides to within about 5 percent, to determine structural stabilities—including pressure-induced phase transitions—that agree well with experiment, to predict high-pressure structural phase transitions, and to reproduce magnetic susceptibilities that agree with observations. We have also developed a modified version of our methodology that describes with some accuracy the δ -phase of plutonium, that is, the face-centered-cubic (fcc) phase of the metal used in nuclear weapons. Perhaps more important than the numerical results is a new understanding about why the actinides form in the structures in which they do. In particular, our results contradict the old adage that the low-symmetry crystal structures of the actinides are a consequence of the directional character of the 5f spherical harmonic functions.

The success of DFT in reproducing and sometimes even predicting the ground-state properties of the actinides suggests that accurate computer simulations of the properties of other materials might become feasible. In the concluding section, we discuss the possibility of simulating defect formation, grain boundaries, segregation of specific atomic impurities in plutonium to the surface or to grain boundaries, and alloy formation. From the point of view of stockpile stewardship, simulating the material properties of the actinides would, of course, be valuable.

Background to the Modern Developments

Despite the brilliant accomplishment of nuclear physics in predicting the existence of plutonium and its fission properties and then creating this new material, it took a long time before the chemistry of element 94 was understood well enough to enable scientists to place plutonium in the periodic table. It was initially speculated that plutonium and the other light actinides—actinium, thorium, protactinium, uranium, and neptunium—were the early part of a 6d transition metal series in analogy with the 3d, 4d, and 5d transition metal series. That is, an increase in the atomic number of the element would correspond to an increase in the number of

electrons in the 6d electronic shell. For this reason, the manmade element with atomic number 94 was initially named eka-osmium and was expected to have the same valence configuration and thus the same chemical properties as osmium. Then, Seaborg suggested (1945) that the elements from actinium through plutonium were the early part of a new series called “the actinide series.” In this series, by analogy with the lanthanide series, the f rather than the d shell was being filled. The 4f electrons in the lanthanides tend to be localized at lattice sites; in other words, they are chemically inert and do not contribute to the cohesion of the solid. Hence, the electronic bonding for the lanthanides is provided by three (and sometimes only two) conduction-band electrons.

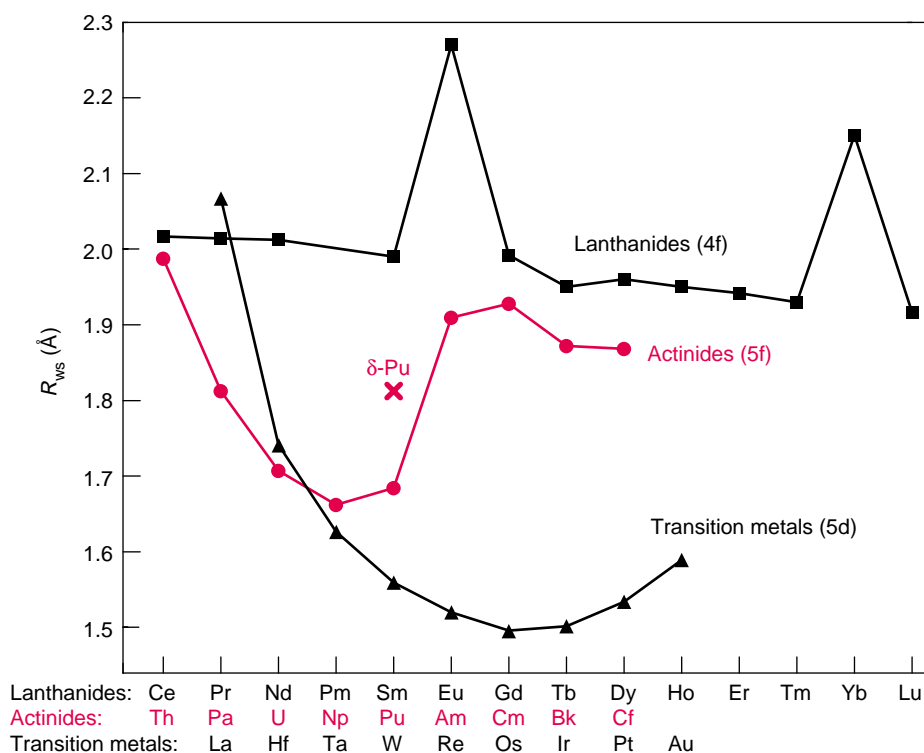


Figure 1. Experimental Wigner-Seitz Radius of Actinides, Lanthanides, and Transition Metals

The Wigner-Seitz radius R_{WS} (the radius of the volume per atom in a solid) is defined as $(4\pi/3)R_{WS}^3 = V$, where V is the equilibrium volume of the primitive unit cell.

The atoms of the actinides, lanthanides, and transition metals are aligned so that elements that lie on top of each other have the same number of valence electrons.

The volumes of the light actinides and the light transition metals decrease with increasing atomic number, whereas the volumes of the lanthanides remain about constant. For that reason, it was originally thought that the light actinides were the beginning of a 6d transition-metal series.

Figure 1 compares the experimental equilibrium volumes of the lanthanides and actinides with those of the 5d transition metals. From this figure, it is easy to see why it was tempting to think of the light actinides as a d transition series rather than an f series. The equilibrium volumes are similar for the transition metals and the light actinides, decreasing parabolically as a function of increasing atomic number, which indicates that the valence electrons in the light actinides contribute to bonding.

The first calculations of the electronic structure of the actinides, which were made almost three decades ago (Kmetko and Waber 1965, Hill and Kmetko 1970, Koelling et al. 1970), finally resolved questions about the nature of the chemical bonding in the light actinides and about the role played by the 5f electrons. Those calculations showed that the 5f electrons do not have sharp energies characteristic of atomic-like energy levels. Instead, they occupy a band of energy levels whose energy spread is 3 to 4 electron volts (eV). Occupancy in an energy band signifies that the 5f electrons are not localized at lattice sites but are itinerant and, hence, chemically active in binding the solid together. As we will outline later, the Friedel model (Friedel 1969), which is a simplified model of bonding by conduction electrons, has successfully explained the equilibrium volumes of both the transition metals and the light actinides. Thus, the nature of the chemical bonding appears to be similar in both series of elements.

A closer examination of the ground states shows some important differences between these different series. First, the parabolic dependence in the equilibrium volumes of the actinides ends abruptly between plutonium and americium. Second, the transition metals and actinides differ in their low-temperature crystal structures. The transition metals² form in close-packed, high-symmetry

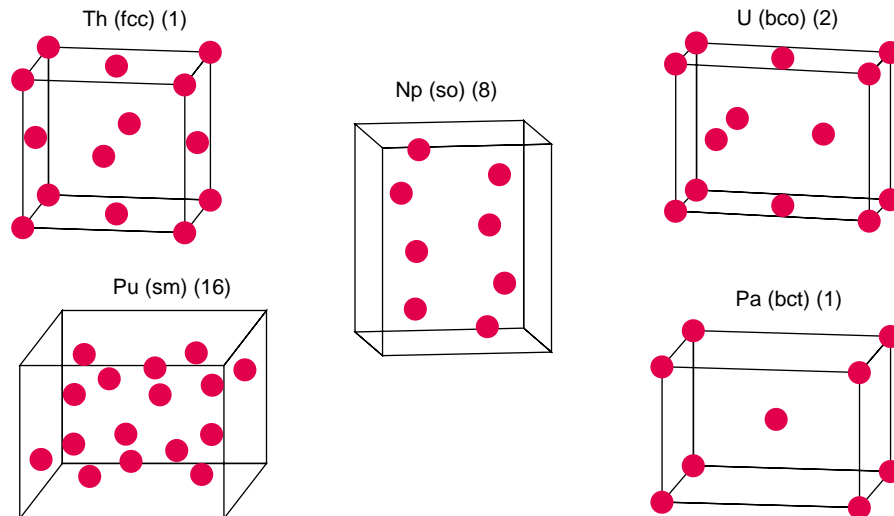


Figure 2. Experimental Crystal Structures of the Light Actinides

Illustrated here are the conventional unit cells of the ground-state crystal structures of the light actinides (thorium through plutonium). The number in parentheses represents the number of atoms in the primitive cell. Notice that most of these structures are open in contrast to the close-packed hcp, fcc, and bcc structures of the transition metals.

structures, such as hexagonal close-packed (hcp), face-centered cubic (fcc), and body-centered cubic (bcc), whereas the light actinides form at low temperatures in the low-symmetry, open-packed structures shown in Figure 2. For instance, protactinium forms in a body-centered-tetragonal (bct) structure, and uranium and neptunium form in orthorhombic structures with 2 and 8 atoms per cell, respectively. At low temperatures, plutonium forms in a monoclinic structure with 16 atoms per cell. Of all the actinide metals, plutonium shows by far the most complex structural properties. Given the similarities between the transition metals and the light actinides regarding equilibrium volumes and chemical bonding, one may ask why the two series are so different in structural properties. Below, we will explain the origin of this difference.

Figure 1 also shows that the equilibrium volumes of the actinides past plutonium resemble those of the lanthanides, remaining relatively constant as a function of atomic number. The usual explanation is that, like the 4f electrons in the lanthanides, the 5f elec-

trons in the heavy actinides become localized, or atomic-like, through a Mott transition (Skriver et al. 1978, Skriver et al. 1980, Brooks et al. 1984). In this picture, localization occurs because 5f (or 4f) electron-electron correlations at a given lattice site become large enough to prevent those electrons from hopping between sites. This phenomenon has actually motivated some scientists to call the heavy actinides a second rare-earth series. It is interesting to note that the famous isostructural expansion in cerium from the alpha to the gamma phase appears to be a Mott transition, in which strong correlations at lattice sites cause the electrons in the 4f¹ conduction band to become localized (Johansson 1974).

The δ -phase of plutonium, the fcc phase that is malleable and therefore of interest for nuclear weapons, is stabilized at room temperature by the addition of, for instance, a few percent atomic weight of gallium. In this phase, plutonium appears to be different from the light and heavy actinides. Figure 1 shows that the equilibrium volume of δ -plutonium is between that of α -plutonium and americium. Electron-electron

² Manganese, which has a very complex crystallographic and magnetic structure, is an exception to this rule.

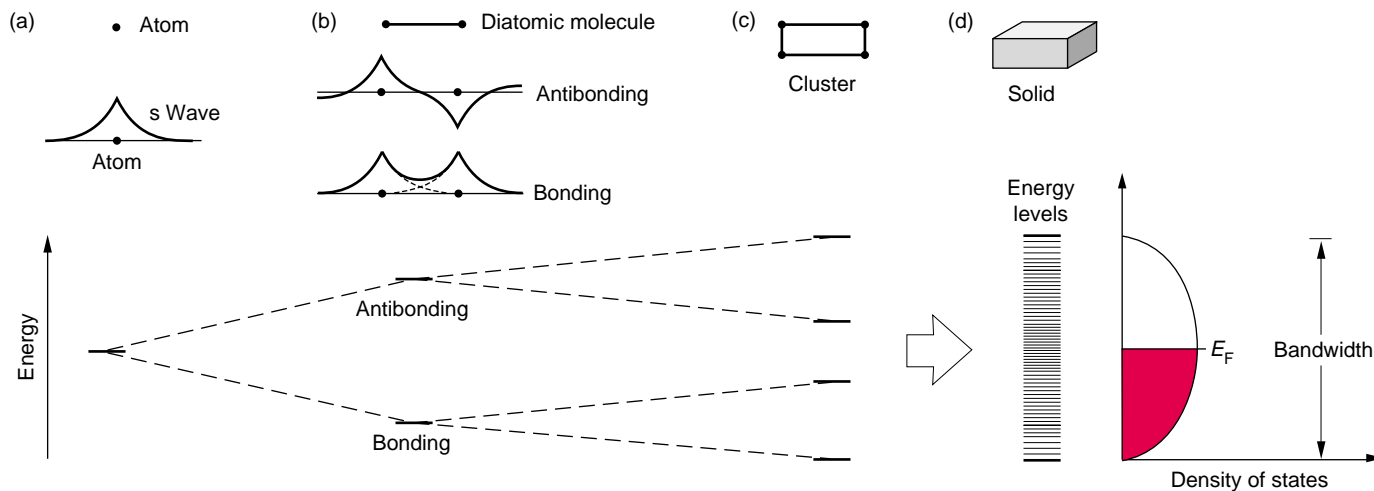


Figure 3. Formation of Energy Bands in Solids

(a) Shown here are the radial wave function and the energy level for a 1s valence electron in an isolated atom. (b) When two such atoms are brought together, their s-electron wave functions will hybridize to form the bonding and antibonding orbitals of a diatomic molecule. The bonding orbital is the sum of the two atomic wave functions, whereas the antibonding orbital is the difference between them. The original energy level has split into two: The lower level is the energy of

the bonding orbital, and the upper, the energy of the antibonding orbital. As shown in (c), the energy levels split again when four atoms are brought together to form a cluster, and again they correspond to bonding and antibonding states. When a very large number of atoms are brought together into a solid (d), their energy levels form a closely spaced band corresponding to both the bonding and the antibonding states. Note that the width of the energy band is

about equal to the difference between the bonding and antibonding energy levels in the diatomic molecule. The levels in the energy band are so tightly packed that we consider the one-electron energy e to be a continuous variable and enumerate the levels in terms of a density of states function $D(e)$. The shaded region of $D(e)$ represents the occupied levels at $T = 0$, that is, all levels are occupied up to the Fermi level, E_F .

correlations are apparently very important in this phase and produce a non-magnetic state, in which the electrons are neither fully localized nor fully delocalized. Thus, the electronic configuration of δ -plutonium may be unique among the configurations of the other elements in the periodic table.

At the end of this paper, we review our recent attempt (Eriksson et al. 1999) at describing the δ -phase and demonstrate that a specific approximation to DFT reproduces the equilibrium volume, energy, and elastic properties of this unusual state. Our approach is based on the model of electron-electron correlations associated with a Mott transition. That is, some of the f electrons in plutonium localize at lattice

sites through very strong correlations. This localization occurs in a bath of spd conduction electrons, ensuring metallic behavior on both sides of the transition (Johansson 1974, Skriver et al. 1978, Skriver et al. 1980, Brooks et al. 1984). Is this a correct description of the electron correlations in plutonium? This question is very much open to investigation. Other attempts at describing the electron correlations in plutonium might include the following: the GW approximation, which uses a Green's function approach and a screened Coulomb interaction (Hedin 1965), a perturbation series in the occupation fluctuation (Steiner et al. 1992), the dynamical mean-field theory (Georges et al. 1996), and an

ab initio treatment of the Anderson model, which includes strong electron correlations (Sandalov et al. 1995).

Energy Bands in Metals

Just as the energy levels and the corresponding electron states (atomic orbitals) provide a fundamental basis for understanding and predicting the properties of atoms, the allowed states of the conduction electrons provide a basis for understanding most properties unique to metals. In the one-electron theory of metals, the allowed states of conduction electrons are single-particle wave functions spread throughout the crystal, and the allowed energies of

those itinerant electrons are grouped into sets of very closely spaced energy levels referred to as energy bands. At $T = 0$, the states within an energy band are occupied by electrons in increasing order of energy, and in a metal, there are only enough valence electrons to partially fill the conduction band. The highest occupied energy level (called the Fermi level, E_F) is defined in such a way that the number of energy levels below E_F is equal to the number of electrons.

Although energy bands are not rigorously meaningful in the DFT approach, we can obtain an often-useful approximation to the physical spectrum from our solution for the total energy and charge density. In fact, whenever we seek to understand the physical mechanisms behind our density functional results on structural stability and other properties, we return to the energy bands and examine their behavior.

Formation of Energy Bands. One may think of how an energy band is formed in the following simple terms. Consider an atom with its discrete spectrum of single-electron energy levels, for instance, of s angular character (the orbital angular momentum is $\ell = 0$). Figure 3(a) shows the energy level and the radial shape of the s electron wave function. If two such atoms are brought together to form a diatomic molecule—Figure 3(b)—the s electron wave functions of each atom will overlap and combine, or hybridize, to form two new states: the bonding and antibonding wave functions of the diatomic molecule. The bonding state is the sum of the two atomic s wave functions, whereas the antibonding state is the difference between those wave functions. In this simplified model, the energy of the bonding state is $E_{\text{bond}} = E_{\text{atom}} - h$, and the energy of the antibonding state is $E_{\text{anti}} = E_{\text{atom}} + h$, where h is the magnitude of the integral between the wave functions ψ on the two sites (A and B) and the potential V . In other words, $h = |(\psi_A|V|\psi_B)|$. The closer the atoms or the larger the overlap between

the atomic wave functions, the bigger is the hybridization parameter h , and the larger is the energy difference between the bonding and antibonding states. The lowered state is called a bonding state because occupying it lowers the energy and stabilizes the system; the raised state is called an antibonding state because occupying it raises the energy and destabilizes the system.

Figure 3(c–d) shows that a similar pattern ensues if more atoms are brought together to form a cluster of atoms. The number of energy levels increases, and the levels divide into a set of bonding states and a set of antibonding states. Finally, if very large numbers of atoms are brought together into a solid, the atomic levels evolve into a band of closely spaced energy levels containing both bonding and antibonding states. Although the set of energy levels remains discrete, the number of levels in the band is so large (on the order of 10^{23}) and the spacing between levels so small that it is more useful to consider the energy as a continuous variable and to enumerate the electron energy levels (states) in terms of a density of states at a given energy.

The width of the energy band in a metal can be related to the energy levels of the diatomic molecule. Just as in the case of two atoms, the smaller the interatomic distance, the larger the overlap of the electron wave functions and the wider the spread in energies from the top to the bottom of the energy band. Notice also that, if the bonding electron states were the only states occupied, reducing the interatomic distance would, according to the discussion above, always lower the total energy and lead to an infinitely contracted lattice or molecule. But the total energy of the solid is not equal to the sum of energies shown in Figure 3. Other terms, such as the electrostatic Hartree term—see Equation (9) in the box “Basics of the DFT Approach”—balance the band-formation term, preventing the molecule or solid from collapsing. For those readers familiar with second quantization,

we include the box “A Model Hamiltonian for Conduction Electrons,” which presents a particle picture (as opposed to a wave picture) of the essential physics of band formation in an analytically solvable form.

The actinides do not have just one energy band. Instead, they have a set of bands, each typically labeled by the orbital quantum numbers (s , p , d , or f) of the atomic valence state from which the band originated. However, angular momentum is ill-defined for a conduction electron moving through the lattice, and so the energy bands that overlap in energy tend to lose their original identity and behave as a single energy band, especially when the bands are broad.

In calculating these conduction bands, one can usually neglect the effects of the surface and treat the solid as if it had periodic boundary conditions and as if its extent were infinite. The atoms in this idealized solid are arrayed on a perfect crystalline lattice (also called a Bravais lattice), with lattice vectors \mathbf{R} . Because the crystal looks the same from any lattice site (that is, it is translationally invariant), the wave function of an electron can only differ by a phase $e^{i\mathbf{k}\cdot\mathbf{R}}$ from one periodic cell to the next. The wave vector \mathbf{k} must lie within the unit cell of the lattice reciprocal to the Bravais lattice (the unit cell is equivalent to the Brillouin zone). For that reason, the electron states (also known as the Bloch states) in a crystal are characterized by the modulation vector \mathbf{k} , and the energy levels in an energy band are described by a function of the wave vector $e(\mathbf{k})$.³

The wave vector \mathbf{k} is often called the electron’s crystal momentum because it enters conservation laws that are analo-

³ When the atoms in the solid are arrayed on a crystalline (Bravais) lattice, electron states are representations of the (Abelian) translation group and, hence, can acquire a phase $e^{i\mathbf{k}\cdot\mathbf{R}}$ on being translated by lattice vectors \mathbf{R} , with \mathbf{k} lying in the unit cell of the lattice reciprocal to the Bravais lattice. We thus arrive at the conventional description of the energy of an electron in a crystal $e(\mathbf{k})$, which is a function of the translation quantum number, or crystal momentum \mathbf{k} .

A Model Hamiltonian for Conduction Electrons

One can think of conduction electrons as waves traveling through the crystal, but one can also think of them as particles hopping from one lattice site to the next. The model Hamiltonian in Equation (1) embodies this particle picture.

$$H = e \sum_i \hat{n}_i + h \sum_i \sum_{i' \neq i} \hat{c}_{i'}^\dagger \hat{c}_i, \quad (1)$$

where \hat{c}_i^\dagger (\hat{c}_i) is the creation (destruction) operator for site i and $\hat{n}_i = \hat{c}_i^\dagger \hat{c}_i$ is the number operator for site i .

This Hamiltonian describes a set of N valence electrons from N neutral atoms that have condensed into a solid and are located at lattice sites i . The electrons in their atomic state have only one degenerate energy level with energy e . The first term in the Hamiltonian contains the number operator \hat{n}_i , which counts the number of electrons at site i . Thus, the first term is the sum of the energies of all the electrons located at lattice sites. The second term contains the creation operator $\hat{c}_{i'}^\dagger$, which creates an electron at site i' , and the annihilation operator \hat{c}_i , which annihilates an electron at site i . Thus, the second term in the Hamiltonian causes an electron to jump from site i to site i' . The likelihood of that jump is proportional to h , the hopping strength, or hybridization strength (we take h to be non-negative).

This Hamiltonian is interesting because it is simple enough to solve analytically, and yet it captures the most important aspects of the interactions in the system—in particular, the formation of energy bands. For example, suppose $N = 2$ so that only two such atoms are brought in proximity. If one solves for the energy levels of this model two-atom system (by diagonalizing a 2×2 matrix), one finds that the single energy level e will split into a bonding level $e - h$ and an antibonding level $e + h$. If many such atoms are brought together to form a solid, the atomic levels evolve into a set of levels falling approximately in the range spanned by a simple, two-atom bonding-antibonding picture. The eigenstates (electron wave functions) of this Hamiltonian are itinerant—that is, their density is spread among all the atoms of the system. When the atoms are far apart and the atomic wave functions barely overlap, h in Equation (1) is small, and the energy levels fall into a narrow range. In this case, the eigenstates, though itinerant, retain much of the character of the atomic states from which they evolve and are usually (and loosely) labeled by the atomic orbital quantum number from which they evolve (s, p, d, or f). As the atoms are brought still closer together, the strength of the hybridization potential— h in Equation (1)—increases, the range of energy levels broadens, and the electronic states lose much of their atomic character and become, in essence (though not in detail), free-electron-like.

In the section describing the Mott transition in the actinide elements, we will show how correlation effects can be added to the model Hamiltonian of Equation (1).

gous to the momentum conservation law for free particles. In contrast to the orbital labels (s, p, d, and f), the crystal momentum is a true quantum number of electrons in a perfect periodic

lattice. For narrow bands, however, whose electrons can be thought of as partially localized, the orbital labels inherited from atomic orbitals are useful and meaningful characterizations.

Density Functional Theory (DFT)

The general features of energy bands and the reasons for their existence are not difficult to grasp, but solving the equations for the bands is complicated. For many decades, band calculations were limited to the simplest crystal structures with unit cells containing only one or two atoms and with spherically symmetric potentials around each atom. In the absence of a total energy functional of DFT, the cohesive energy of a solid could not be calculated with any degree of accuracy. Instead, one focused on determining the dispersion curves for the energy bands $\epsilon(\mathbf{k})$ and the shape of the Fermi surface, which is just the portion of \mathbf{k} -space occupied by electrons at the Fermi energy level, E_F .

As we mentioned in the introduction, the application of DFT has led to a tremendous simplification of band structure calculations. In its pure form, DFT outlines a rigorous prescription for calculating the total electronic energy of solids, molecules, and atoms in the ground state (at $T = 0$) in terms of a functional of the total charge density. In most practical applications, however, one can get excellent results by using local functions of the density to express the entire DFT energy functional, including the usual nonlocal exchange and correlation terms. The LDA approximates the exchange and correlation term as a local function of density, and the general gradient approximation, or GGA, expresses that term as a local function of density and density gradient. Because of this simplification, calculating the total energy of an electronic system becomes possible. The box on the next page briefly outlines the mathematical framework of density functional calculations.

We must also note that most implementations of DFT have a strong connection to energy band theory in the form used before DFT was invented. As a matter of fact, the Kohn-Sham equation, the crucial equation normally

continued on page 138

Basics of the Density Functional Theory (DFT) Approach

To calculate the ground-state electronic energy of an atomic system, one normally starts from the time-independent Schrödinger equation. In addition, the Born-Oppenheimer approximation is frequently used because it neglects the motion of the nuclei and allows calculating the total energy of the electrons in the potential created by the nuclei. Therefore, one could calculate the ground-state (lowest-energy configuration) total electronic energy from

$$H\Psi(r_1, r_2, \dots, r_n) = E\Psi(r_1, r_2, \dots, r_n) \quad (2)$$

where H is the Hamiltonian containing the kinetic energy and all the interactions of the system (electron-electron correlation and exchange and electron-nuclei interactions), $\Psi(r_1, r_2, \dots, r_n)$ is a many-electron wave function of the n -electron system, and E is the total electron energy of the ground state. The input parameters in Equation (2) are the atomic numbers of the atoms and the geometry of the crystal (the lattice constant, the crystal structure, and the atomic positions).

To determine the equilibrium volume theoretically, one could keep the crystal structure fixed and calculate the ground-state electronic energy for different input volumes (or lattice constants). The volume that produced the lowest energy would represent the theoretical equilibrium volume. Similarly, one could compare the total energy of different structures at different volumes and draw conclusions about structural stability and possible structural phase transitions that might occur when the volume is changed (experimentally, one can compress the volume by applying an external pressure). In addition, one could calculate the energy gain when free atoms condense to a solid (the cohesive energy). Unfortunately, there is no practical way to solve Equation (2) for a solid.

Nevertheless, we have been able to carry out this program of calculations because there is an alternative theoretical formulation for determining the electronic structure. In two important theorems (Hohenberg and Kohn 1964, Kohn and Sham 1965, Dreitzler and Gross 1990), it has been shown that the total energy of a solid (or atom) may be expressed uniquely as a functional of the electron density. We can therefore minimize this functional with respect to the density in order to determine the ground-state energy. Therefore, instead of working with a many-electron wave function, $\Psi(r_1, r_2, \dots, r_n)$, one can express the ground-state energy in terms of the electron density at a single point $n(r)$, where that density is due to all the electrons in the solid:

$$n(r) = \sum_{i=1}^n \int \Psi^*(r_1, r_2, \dots, r_n) \delta(r-r_i) \Psi(r_1, r_2, \dots, r_n) dr_1 dr_2 \dots dr_n \quad (3)$$

In addition, Hohenberg and Kohn (1964), Kohn and Sham (1965), and Dreitzler and Gross (1990) demonstrated that, instead of calculating the electron density from the many-electron wave function $\Psi(r_1, r_2, \dots, r_n)$, one may work with the solutions to an effective one-electron problem.

The trick is to use the form of the total-energy functional to identify an effective potential $V_{\text{eff}}(r)$ for one-electron states and then solve for the one-electron states to produce a density equal to the many-electron density. The equation for the one-electron states is

$$\left(\hat{T} + V_{\text{eff}}\right)\psi_i(r) = \epsilon_i \psi_i(r) \quad (4)$$

where \hat{T} is a kinetic energy operator (for example, $-\hbar^2\nabla^2/2m$ in a nonrelativistic approximation)

and the resulting total electron density is given by

$$n(r) = \sum_i |\psi_i(r)|^2 . \quad (5)$$

To include relativistic effects important in the actinides, one replaces the nonrelativistic, Schrödinger-like one-electron equation—see Equation (4)—by the relativistic Dirac equation. By finding the correct form for the effective potential, the electron density in Equation (5) will be the same as that in Equation (3).

As mentioned in the section “Density Functional Theory” in the main text, the one-electron problem defined by Equation (4) has the same form as the equations solved by band theorists before DFT was invented, and the eigenvalues of those equations as a function of crystal momentum are precisely the energy bands. The contribution of DFT is to provide a rigorous prescription for determining the effective potential and for calculating the total ground-state energy. The DFT prescription for the effective potential in Equation (4) is

$$V_{\text{eff}}(r) = \frac{\delta}{\delta n(r)} \left[E_H(n(r)) + E_{xc}(n(r)) + E_{eN}(n(r)) \right] , \quad (6)$$

where the different terms are derived from the total-energy functional $E(n(r))$:

$$E(n(r)) = T(n(r)) + E_H(n(r)) + E_{xc}(n(r)) + E_{eN}(n(r)) + E_{NN} . \quad (7)$$

In this equation, $T(n(r))$ represents the kinetic energy of the effective one-electron states and is calculated from

$$T(n(r)) = \sum_i \int \psi_i^\dagger(r) \hat{T} \psi_i(r) dr . \quad (8)$$

$E_H(n(r))$ is the classical Hartree interaction (the electrostatic interaction between two charge clouds):

$$E_H(n(r)) = \frac{1}{2} e^2 \int \frac{n(r_1)n(r_2)}{|r_1 - r_2|} dr_1 dr_2 . \quad (9)$$

$E_{eN}(n(r))$ is the electron-nuclei interaction:

$$E_{eN}(n(r)) = -e^2 \sum_R Z_R \int \frac{n(r)}{|r - R|} dr . \quad (10)$$

$E_{xc}(n(r))$ is the part of the interaction that goes beyond the classical Hartree term as well as the difference between the true kinetic energy and the one-electron kinetic energy. In the LDA, this term has the form

$$E_{xc}(n(r)) = \int n(r) \mathcal{E}_{xc}(n(r)) dr . \quad (11)$$

Finally, E_{NN} is the Coulomb interaction between the different atomic nuclei of the lattice:

$$E_{NN} = \frac{1}{2} e^2 \sum_R \sum_{R' \neq R} \frac{Z_R Z_{R'}}{|R - R'|} . \quad (12)$$

From these definitions, it becomes obvious that the effective potential in which the electron moves has contributions from the electron's interaction with the nuclei and the other electrons in the solid both by the classical Hartree term and by the quantum mechanical exchange and correlation term.

Because all electron-electron interactions that go beyond the classical Hartree term are found in $E_{XC}(n(r))$, it is crucial to have a good approximation for this term (unfortunately, there is no exact form of this term for a real solid). However, if one assumes the functional to be local, a numerical form may be obtained from many-body calculations (quantum Monte Carlo or perturbation series expansion), and very good values may be obtained for the ground-state energy for different values of the electron density. If the electron density of a real system varies only smoothly in space, one expects that a form of E_{XC} taken from a uniform electron gas should be applicable to the real system as well. This approximation is no other than the LDA. The good agreement, for many solids,* on cohesive energy, equilibrium volume, and structural properties between this approximate theoretical approach and experimental values suggests that the LDA form of E_{XC} works even if the electron density varies rapidly in space. As an example of how E_{XC} might look, we quote the full form of the exchange and correlation energy density in Equation (11), as given by Hedin and Lundqvist, with parameters calculated in the random-phase approximation:

$$\mathcal{E}_{XC}(n(r)) = \mathcal{E}_X(r_s) + \mathcal{E}_C(r_s) \quad ,$$

where

$$r_s = \left(\frac{3}{4\pi n(r)} \right)^{\frac{1}{3}}$$

$$\mathcal{E}_X(r_s) = \frac{-0.91633}{r_s}$$

$$\mathcal{E}_C(r_s) = -0.045 G\left(\frac{r_s}{21}\right)$$

$$G(x) = (1+x^3) \ln\left(1 + \frac{1}{x}\right) - x^2 + \frac{x}{2} - \frac{1}{3} \quad . \quad (13)$$

Thus, one can calculate the total ground-state energy by solving an effective one-electron equation. This tremendous simplification of replacing interacting electrons with effective one-electron states will work only if one can find the correct, effective one-electron potential. ■

* Among such solids are simple metals, transition metals, actinides, p electron elements, and thousands of compounds formed between these elements.

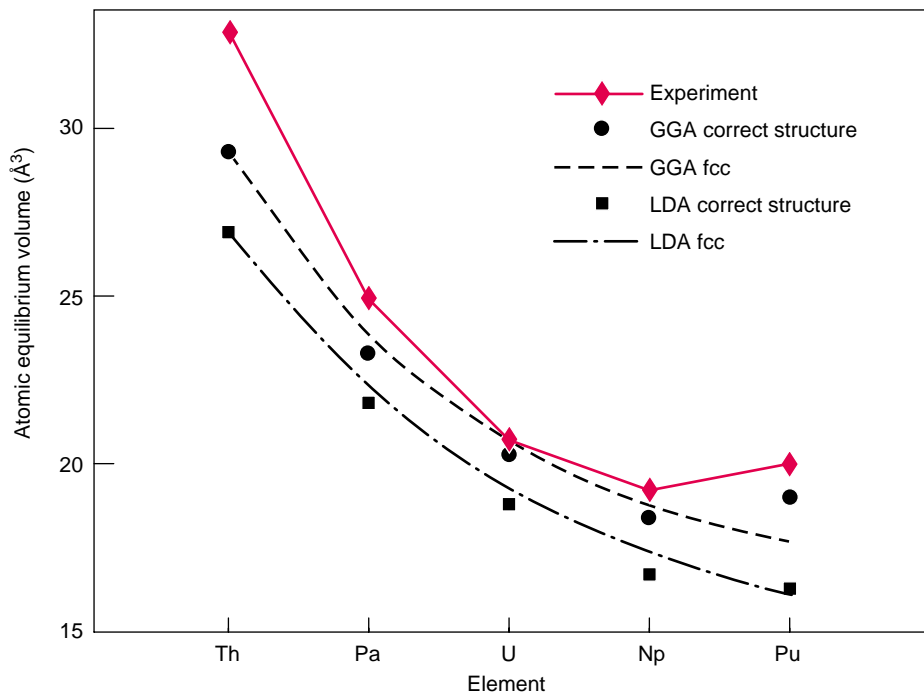


Figure 4. DFT and Experimental Equilibrium Volumes for the Light Actinides We used DFT to compute the equilibrium volume of each light actinide in its observed crystal structure and in a hypothetical fcc structure. In each calculation, we used first the local density approximation (LDA) and then the generalized gradient approximation (GGA). Our LDA values are systematically smaller than the experimental ones, but the GGA results are typically a few percent larger and in better agreement with observation. In fact, our GGA calculations reproduce some of the finer details of the observations, including the small increase in equilibrium volume between α -neptunium and α -plutonium. This result implies that the 5f electrons in α -plutonium, like the 5f electrons in α -uranium, are delocalized.

continued from page 134

solved in DFT, is identical in form to the one solved by the Slater X- α method, as is any one-electron-like equation. In addition, the exchange part of the effective potential is very similar in the two methods. Unlike traditional approaches, however, DFT derives its strength from the fact that it gives an explicit and well-founded form for the total energy of the electrons in the lattice in terms of a functional of the total electron density. Hence, DFT could be said to have two outputs: first, and most important, the total energy and charge density of the electrons in the solid and second (and less rigorously comparable to experiment), the energy bands and density of states. The latter set of properties can also be calculated from band theory with the Slater X- α method.

Equilibrium Volumes from DFT Calculations. In Figure 4, we display the calculated equilibrium volumes of all the light actinides for several different inputs in order to show the results from the DFT energy functional defined in Equation (7). We used both the observed crystal structure as well as a hypothetical fcc structure for each element (for thorium, the observed structure is fcc). We then repeated the calculation using the two most common approximate forms for the DFT energy functional, the LDA and GGA. These two approximations designate specific forms of the exchange and correlation term E_{xc} shown in Equations (11) and (13). In the LDA, E_{xc} is a local function of density; in the GGA, it is a local function of density and density gradient.

Notice that, without any experimental information, one can reproduce the observed equilibrium volumes with good accuracy. Our LDA-calculated values for the volumes of the actinides are systematically smaller than the experimental values. This shortcoming is true for most materials, but it can be corrected if we use the GGA, which normally gives equilibrium volumes that are a few percent larger.

Considering the approximations that enter practical calculations, we expect some disagreement between theory and experiment. But the real power of these types of calculations is not the accurate reproduction of experimental data to within the second or third decimal point but the ability to identify the physical mechanisms underlying the general trends in cohesion, magnetism, superconductivity, or any other phenomenon one is interested in. Having said this, we note that our present calculational scheme reproduces the finer details of the observations, including the small increase in volume between α -neptunium and α -plutonium. This result is important because it implies that the 5f electrons in α -plutonium are delocalized in much the same way as the 5f electrons in α -uranium. Before our calculations, that point was a matter of some controversy.

The one-electron energies from Equation (4), or the energy bands $e(\mathbf{k})$, are another output from the DFT prescription. Figure 5 displays our DFT results for the energy bands in α -uranium. The figure also shows the density of states as a function of energy that results from the α -uranium band structure and the calculated Fermi energy E_F for this metal.

The Friedel Model

The calculated density of states in Figure 5 is very complicated, and often one wants to estimate various metallic properties analytically, by using a simplified version of the density of states. Figure 6 shows such a simplified ver-

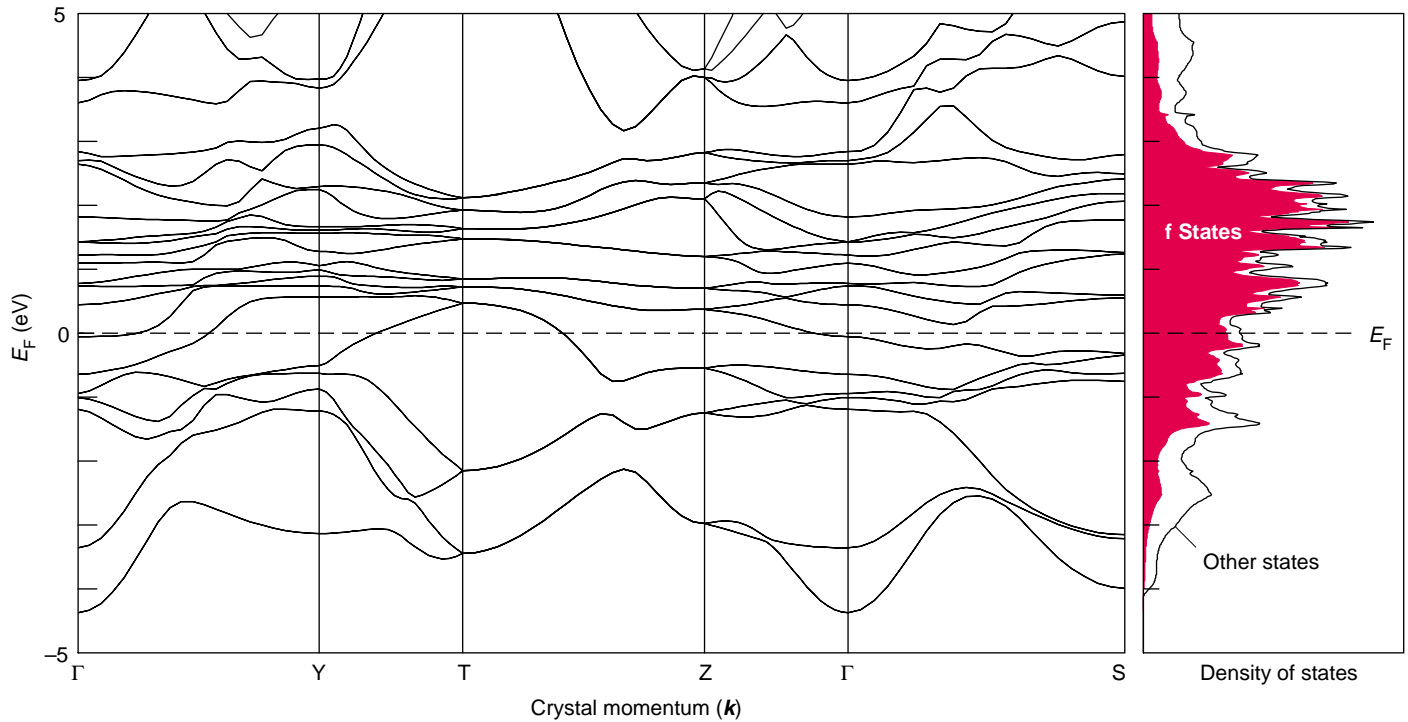


Figure 5. Calculated Energy Bands and Density of States of α -Uranium

DFT predictions for the energy bands $\epsilon(\mathbf{k})$ are plotted along several different directions in the unit cell of the reciprocal lattice. The labels on the \mathbf{k} -axis denote different high-symmetry points of the Brillouin zone: $\Gamma = (000)$, $Y = (110)$, and $T = (111)$. The narrow bands close to the Fermi level (dashed line) are dominated by the 5f orbitals. The fact that some of the bands cross the Fermi level demonstrates that α -uranium is a metal. The shaded area of the density of states curve represents the contribution from the 5f orbitals.

sion called the Friedel model, which is applicable to the transition metals. The d band is represented by a constant density of states over a relatively narrow energy range, and the s and p bands are represented by a much-broader, combined band. The figure also indicates the atomic energy level from which the d or f band originated. The band states at energies lower than the atomic energy level are bonding, and those at higher energies are antibonding.

Three decades ago, Friedel (1969) used this simplified density of states to explain the parabolic behavior of the equilibrium volumes of the 5d transition metals. He suggested that the cohesive energy of those metals varies with increasing atomic number because of the filling of a d-electron conduction band. The occupied states for the lighter elements would be bonding

whereas for the heavier elements the occupied states would be both bonding and antibonding. Assuming a constant density of states for the d band as shown in Figure 6, Friedel wrote down the following analytical expression to approximate the contribution of the d band to the cohesive energy as a function of N_d , the number of valence electrons of the element (Friedel 1969):

$$E_{coh}(N_d) = -\frac{1}{2} W_d N_d \left(1 - \frac{N_d}{10}\right), \quad (14)$$

where W_d is the width of the d band. Note that 10 is the maximum value of N_d because an atom's d shell can have 10 electrons (5 orbitals \times 2 spin states) at the most. This expression for the cohesive energy demonstrates that the chemical bonding is maximized for a half-filled shell ($N_d = 5$) and that the cohesive energy varies as $(N_d)^2$, or parabolically, when plotted as a function

of N_d (see Figure 7). It also shows correctly that the cohesive energy is zero for a filled or an empty band. Because there is an inverse relationship between bond length (lattice constant or atomic radius) and bond strength (Pettifor 1995), the parabolic trend in the observed equilibrium volumes of the transition metals (see Figure 1) follows directly from this result for the cohesive energy.

The Friedel model also explains the parabolic behavior of the volumes of the actinides, but the 5- to 10-eV width of the d band must be replaced with the 3- to 4-eV width of the f band (Skriver et al. 1978, Skriver et al. 1980, Brooks et al. 1984). The agreement between theory and experiments suggests that the chemical binding of the transition metals and the light actinides is predominantly similar to the binding of metals; that is, the 5f electrons of the

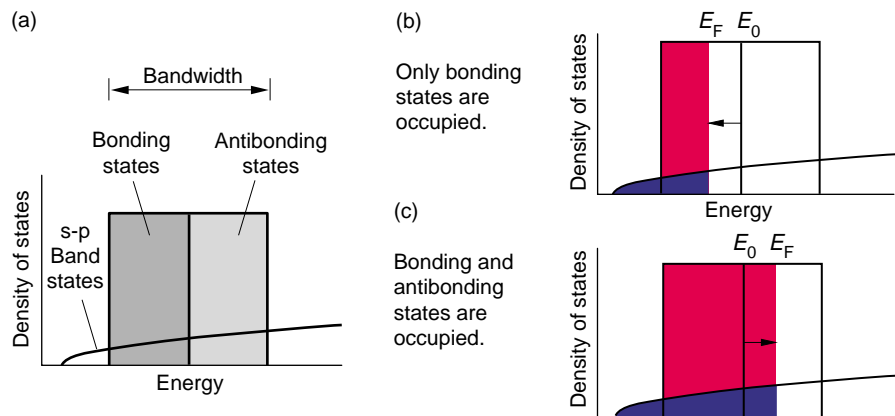


Figure 6. Density of States in the Friedel Model

(a) Shown here is a simplified form for the density of states called the Friedel model, which is applicable to the transition metals. The d band has a constant density of states over a relatively narrow energy range, and the s and p bands are represented by a broader, combined s-p band. E_0 is the atomic energy level from which the d band originated. The band states at energies lower than E_0 are bonding, and those at higher energies are antibonding. (b) For elements in the first half of the series, the Fermi level is below E_0 , and all occupied states are bonding. (c) For elements in the second half of the series, the Fermi level is above E_0 , and both bonding and antibonding states are occupied.

light actinides are conduction electrons participating in bonding.

The behavior of the light actinides deviates in one way from the parabolic behavior predicted by the Friedel model: The volume of plutonium is actually larger than that of neptunium even though the f band is not yet half filled (the f shell can have a maximum of 14 electrons—(7 orbitals \times 2 spin states)—whereas plutonium in the solid state has only five 5f electrons). It was first thought that very strong spin-orbit interactions in the light actinides might split the single, narrow band in the Friedel-like density of states shown in Figure 6. In that case, the lower energy band would extend from thorium to americium, the cohesive energy would reach a maximum between uranium and neptunium, and plutonium would have a larger volume than neptunium (Skriver et al. 1978, Skriver et al. 1980, Brooks et al. 1984). Our subsequent, more-accurate calculations have shown that the spin-orbit interactions alone are insufficient for explaining the upturn in volume between neptunium and plutonium. Indeed, we had to use both the correct crystal structure of α -plutonium and the best available estimate of the exchange and correlation potential (obtained with the GGA) to reproduce that observation (see our results in Figure 4). This modification of the Friedel model, however, is very slight, and in no way alters the main conclusion that the 5f states in α -plutonium are delocalized in very much the same way as those in α -neptunium and α -uranium.

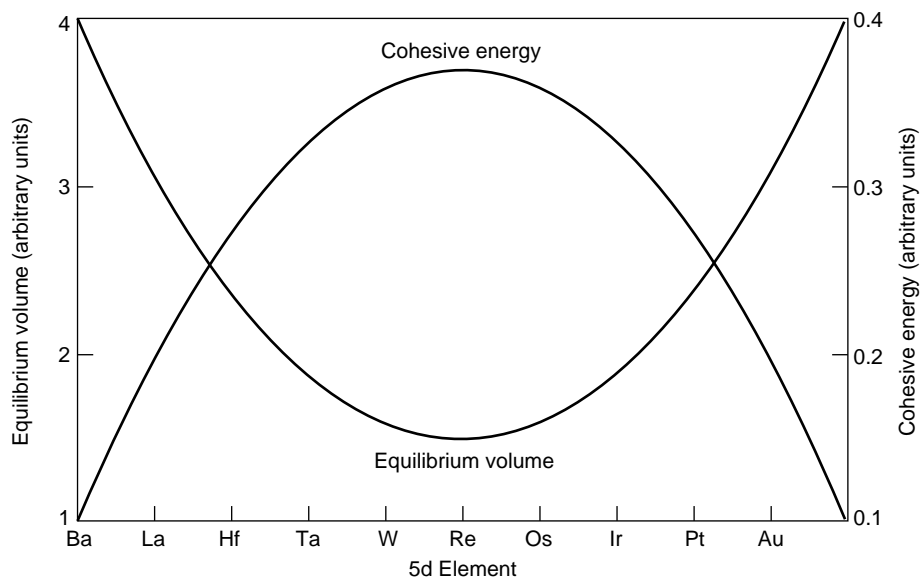


Figure 7. Friedel Model Predictions for the Cohesive Energies and Equilibrium Volumes of the 5d Transition Metals

The contribution of the d band to the cohesive energy is plotted as a function of N_d , the number of valence d electrons in each 5d transition metal according to Equation (14). The chemical bonding reaches a maximum for a half-filled d shell ($N_d = 5$), the cohesive energy from the d band varies parabolically, and its value is zero for a filled or an empty band. Because the equilibrium volume varies inversely to the cohesive energy, the parabolic trend in the observed equilibrium volumes of the transition metals (see Figure 1) follows directly from this result for the cohesive energy.

Actinide Structures

Having shown that the light actinides and the transition metals agree with the Friedel model of chemical bonding, we return to the question of whether this similarity in bonding is compatible with the very different structural properties of the actinides and transition metals. Recently, together with our collaborators, we have investigated the structural stability of the

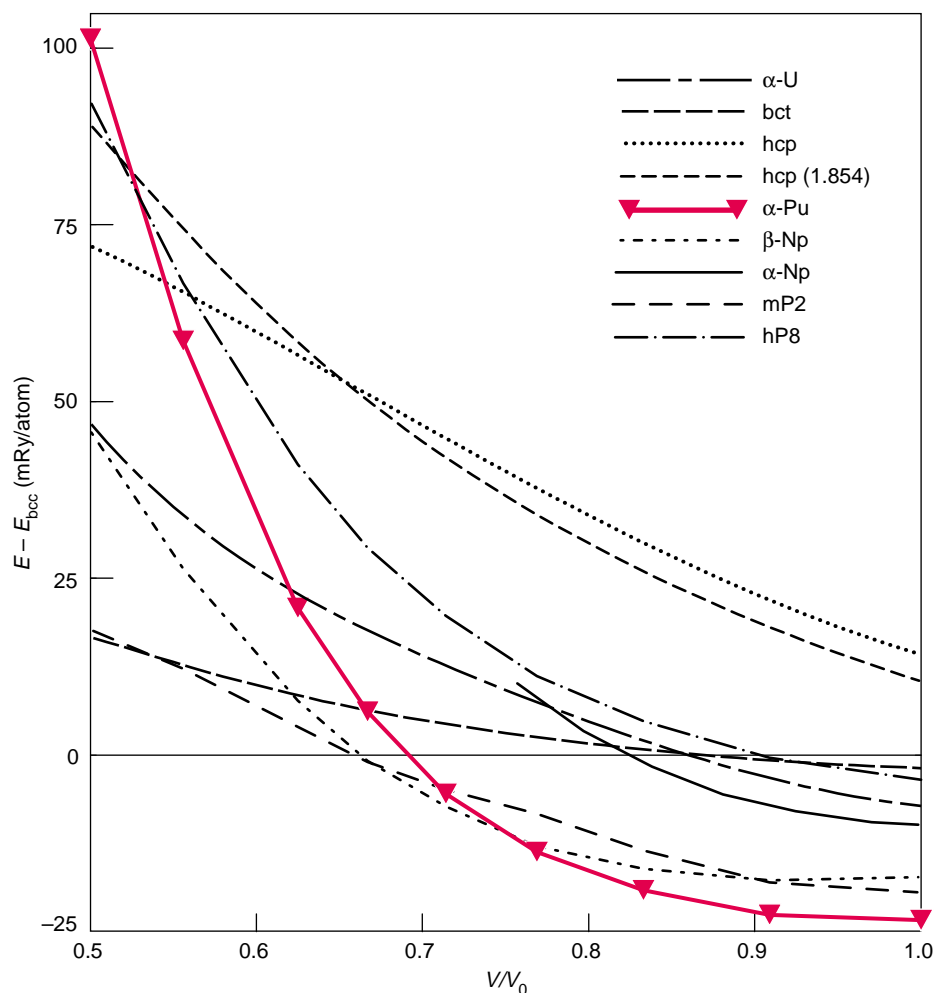


Figure 8. DFT Energies for Plutonium in Different Crystal Structures as a Function of Compressed Volume

Of all the plutonium structures used as input to the calculations, the α -plutonium structure yielded the lowest energy at the equilibrium volume. The delocalized bcc phase is the reference level and is set to zero. V_0 , the equilibrium volume of α -plutonium, is 19.49 \AA^3 . Under a sufficiently high pressure, calculation predicts that most of the light actinides—uranium, neptunium, and plutonium—revert to a highly symmetric bcc structure.

actinides (Wills and Eriksson 1992, Söderlind et al. 1995, Söderlind 1998). Using our DFT methodology, we were able to calculate the total energy of the transition metals and the light actinides in various crystal structures to an accuracy of thousandths of an electron-volt, or approximately 0.1 to 0.5 millirydberg (mRy). With this theory, we successfully reproduced the stability of the low-symmetry structures of the light actinides. As an example, Figure 8 displays the calculated energies of

different structures of the most complex actinide material, plutonium. Of all the investigated structures, the α -plutonium structure (which is monoclinic with 16 atoms per unit cell) is correctly calculated to have the lowest energy. We also predict that, under a sufficiently high pressure, most of the light actinides (uranium, neptunium, and plutonium) will revert to the highly symmetric bcc structure. Recent diamond-anvil-cell experiments confirm these predictions for neptunium.⁴

In 1970, Hunter Hill proposed that the unusual structures found in the light actinides resulted from covalent bonding between the highly angular, or “pointed,” orbitals of the 5f electrons (Hill and Kmetko). We have used first principles calculations to investigate this argument in detail and found that Hill’s proposed mechanism is not correct. If Hill were right, one would expect the charge density, which is dominated by 5f electron states, to pile up between the actinide atoms. The contour plots in Figure 9 display the calculated charge density of α -uranium and silicon. The α -uranium plots (a–c) are in the 010-plane for three different cases. The first case includes the effects of the 5f binding, and the second one excludes the 5f binding. The two plots are almost identical. Hence, the shape of the charge density does not appear to be affected by the pointed 5f orbitals. In fact, the third charge-density contour plot, which shows the results of overlapping the charge densities of isolated atoms and therefore carries no information about the chemical bonding of the crystal, looks very similar to the first two plots. We conclude that, for α -uranium and other light actinides, the geometry of the underlying lattice determines the shape of the charge density. By contrast, for the heavy actinides, the charge density of the 5f atomic orbitals determines the geometry of the lattice. Finally, Figure 9(d) shows the charge density of silicon in the diamond structure, in which case strong covalent bonds do indeed cause a visible buildup of charge between the silicon atoms. The bond in α -uranium, on the other hand, is very weakly covalent (the chemical bonding in all materials has some degree of covalency), and the binding is best described as metallic.

Recently, R. C. Albers of Los Alamos and coworkers made calculations for aluminum that seem to support Hill’s conjecture. By using an enlarged

⁴ J. Akella, Lawrence Livermore National Laboratory (private communication).

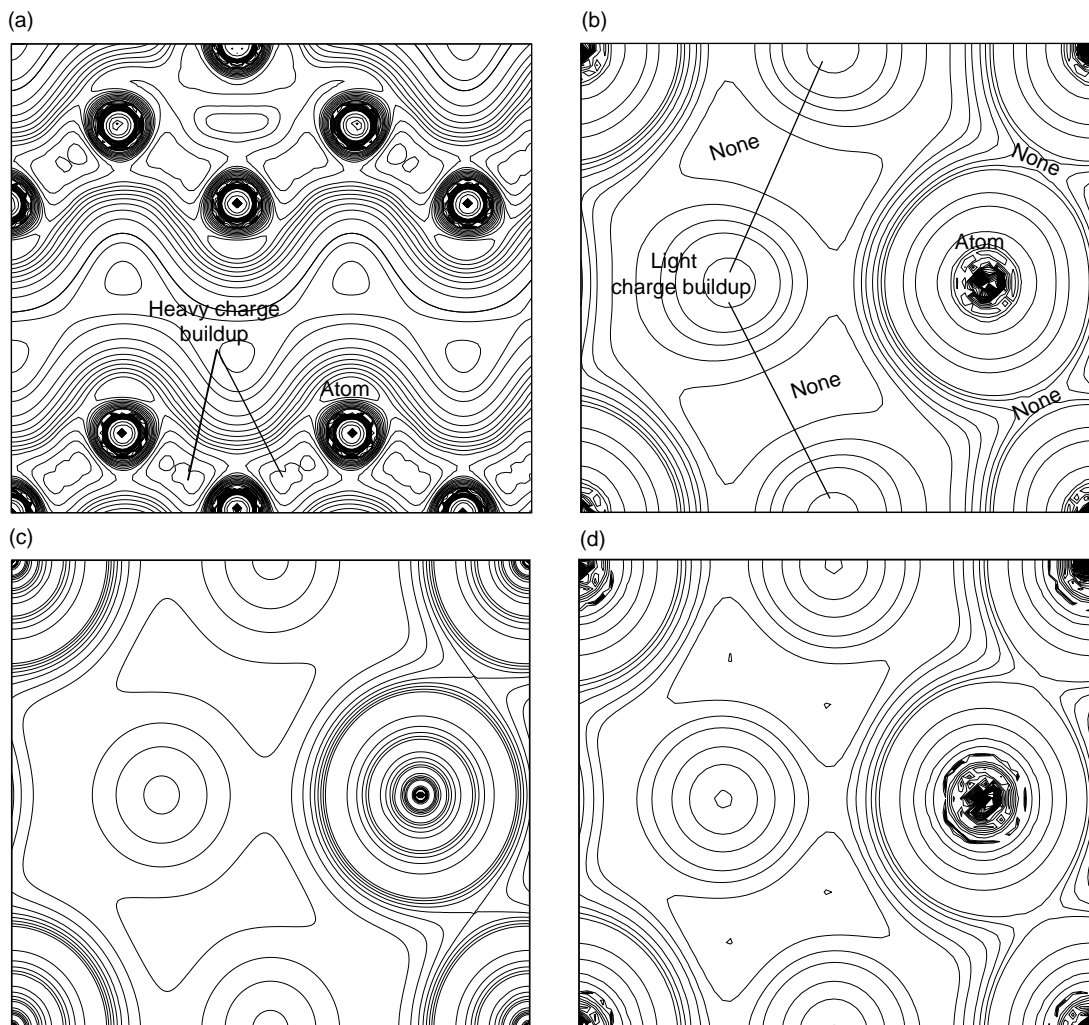


Figure 9. Calculated Charge Density of α -Uranium and Silicon in the 010-Plane

We compare three electron-density contour plots of α -uranium with a similar plot for silicon in the diamond structure. Shown in (a) is the plot for silicon. In the diamond structure, silicon provides an excellent example of covalent bonding, the signature of which is a buildup of charge along bonds. In contrast, the uranium contours (b–d) show a buildup of charge away from the bonds, in the interstices. This type of buildup is characteristic of metallic bonding. However, the underlying lattice often determines the appearance of an electron-density contour. We are, therefore, showing three kinds of calculations for uranium: In (b), we calculated the electron density with itinerant 5f electrons, in (c) with core (spherical) 5f electrons, and in (d) by overlapping atomic densities. Clearly, the presence or absence of asymmetric 5f orbitals has little effect on the shape of the charge density and on the character of the bonds in α -uranium.

volume as the input, these scientists found the ground-state structure of aluminum to be the highly symmetric diamond structure. They suggested that, at the expanded volume, the very small overlap between atomic orbitals reduces the effects of the valence electrons on the nearest neighbors, and the angular character of the orbitals stabilizes the diamond structure. We have checked this conjecture by calculating the total

energy of aluminum first in the diamond structure and then in a series of lower symmetry orthorhombic structures. This crystal distortion actually leads to a structure resembling that of γ -plutonium. Plotted in Figure 10, our results show that the diamond structure is not the lowest energy structure of aluminum at expanded volumes. Instead, a low-symmetry actinide-like structure is the most stable.

A Mechanism for Stabilizing Low-Symmetry Structures. Our results for aluminum jibe with our understanding that the light actinides form in unique, low-symmetry open-packed structures because their f electrons occupy very narrow conduction bands (Wills and Eriksson 1992, Söderlind et al. 1995). The mechanism producing the low symmetry resembles a Peierls-Jahn-Teller distortion of the energy bands

and may be viewed as follows: Suppose an actinide metal is in a hypothetical bcc structure at ambient conditions and has an energy band shaped like the black curve in Figure 11. This band describes energy levels along a high-symmetry direction of the bcc crystal and therefore has a high degeneracy, say 2. In other words, there are two states for each energy level, and the energy band is really two bands of energy levels that lie on top of each other. (This type of degeneracy always occurs along high-symmetry directions of fcc and bcc structures). If the bcc structure were changed to a slightly distorted (say tetragonal or orthorhombic) bcc structure, the lowered symmetry would break the degeneracy. As shown in Figure 11, the original band would split into two nondegenerate bands: One would be slightly raised (the red curve) and the other slightly lowered in energy (the blue curve).

The hypothetical bands in Figure 11 are conduction bands; that is, they are intersected by the Fermi level E_F .

Consequently, when the original band splits, some states are pushed above the Fermi level and others below that level. In fact, there is a range of wave vectors k , in which the occupied states (those below the Fermi level) of the distorted structure are lower in energy than the occupied states of the symmetric structure. Thus, the energy contribution of those regions of k -space is less in the distorted than in the undistorted structure. In other regions of k -space, the contribution to the total energy is the same regardless of symmetry: Either both split bands are above E_F and therefore unoccupied (and not affecting the total energy), or they both are below E_F . In the latter case, the energy from the two split bands is equal to two times the average energy of those two bands, which is exactly the energy of the two degenerate bands of the high-symmetry structure. Thus, only regions of k -space that straddle the Fermi level contribute to lowering the total energy of the low-symmetry structure. This energy-lowering mechanism is similar to the

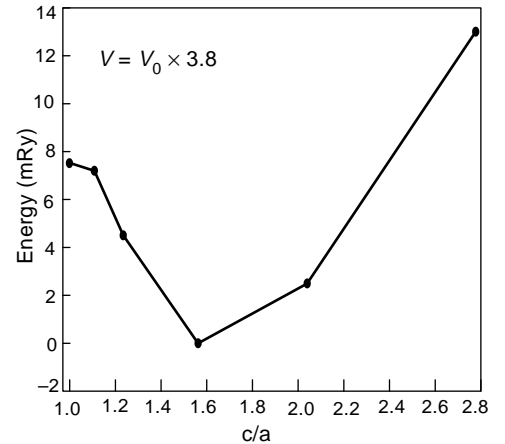


Figure 10. Calculated Total Energy of Aluminum as a Function of Orthorhombic Shear

Illustrated here is the energy of aluminum at 3.8 times its equilibrium volume. Starting from the diamond structure, we allowed the atoms to have orthorhombic and internal positional freedom. The resulting relaxed structure is very similar to that of γ -plutonium. This similarity illustrates the point that actinide structures are favored at narrow bandwidths even in non-f-bonded metals.

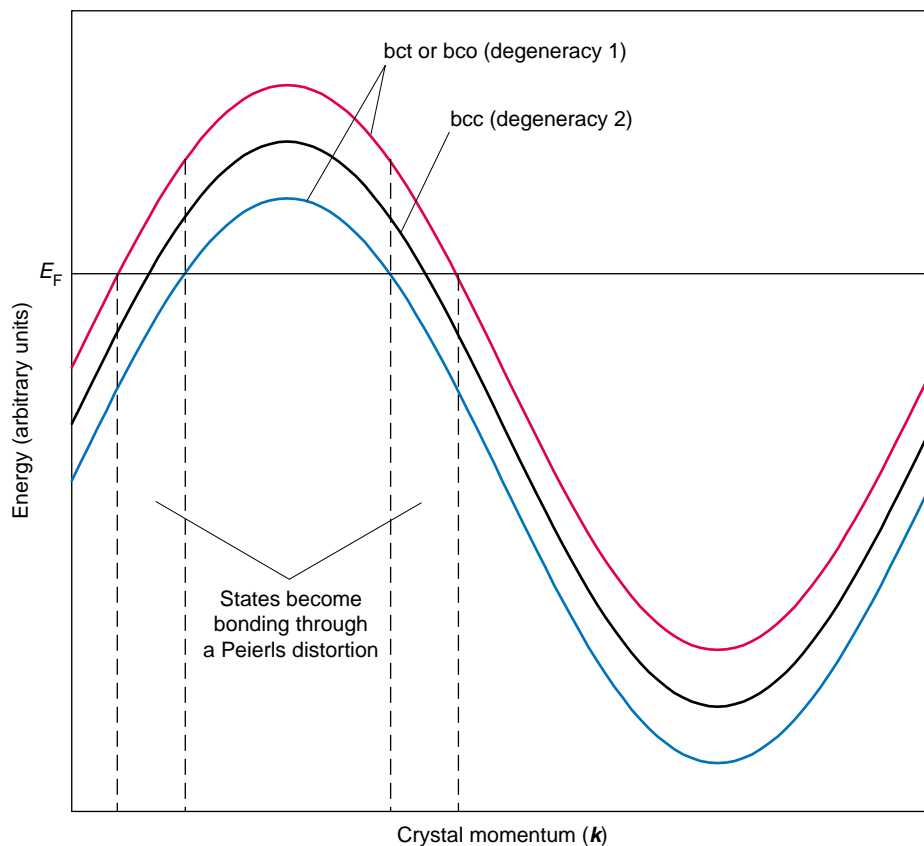


Figure 11. Lowering the Energy through a Peierls Distortion

The black curve is a hypothetical narrow energy band $\epsilon(k)$ along a direction of high symmetry in a highly symmetric (bcc) crystal. The band passes through the Fermi energy and has a degeneracy of 2. If the crystal is distorted from a bcc to a bct or boc structure, the band splits into two nondegenerate bands (red and blue). In the two regions of k -space marked by dashed lines, occupied states that were near the Fermi energy in the bcc structure are lowered in energy and therefore lower the total energy. Other unoccupied states are lowered and become occupied. Therefore, the one-electron contribution to the total energy in those regions is lowered by a distortion to a lower-symmetry structure. In other regions of k -space, the contribution to the total energy is the same regardless of symmetry.

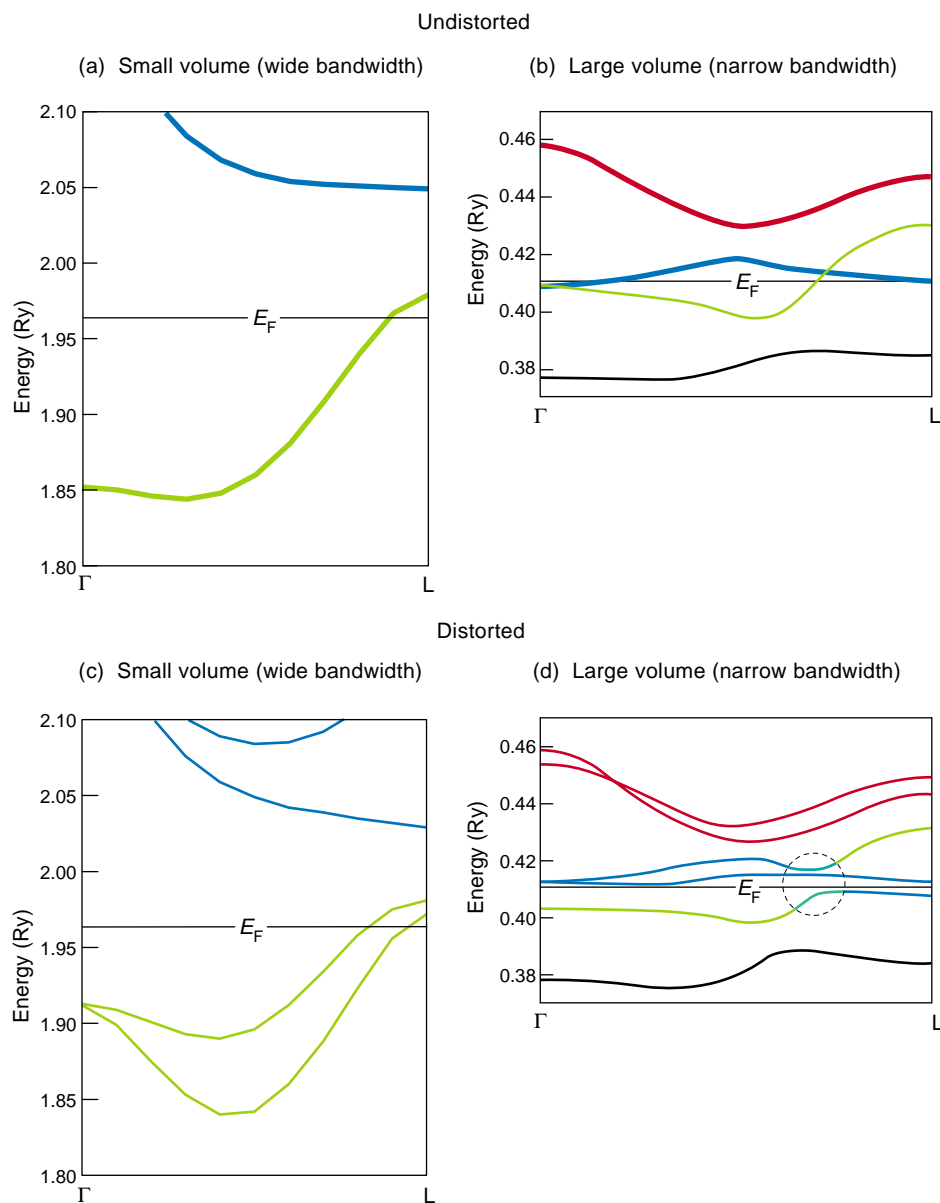


Figure 12. Calculated Energy Bands for Neptunium (bcc vs bct Structures)

We display the energy band structure in neptunium for two input volumes and two crystal structures. In the graphs to the right, the input volume is close to the equilibrium value for neptunium, the bands are narrow, and a distortion from bcc to bct pushes some states from just above to just below the Fermi level (see region within dashed circle), thereby lowering the one-electron contribution to the energy. In the graphs to the left, the input volume is compressed, the bands are therefore broader, and the splitting of these bands by a crystal distortion has no effect on the one-electron energy contribution. Thus, the narrow bands in neptunium explain its low-symmetry ground-state structure.

Peierls distortion and Jahn-Teller effect.

If the energy bands in Figure 11 were narrower (that is, if the curves were flatter), more states (or a larger region of the horizontal axis) would contribute to lowering the total energy of the distorted structure. This effect

is seen in Figure 12, in which the calculated energy bands are shown for bcc neptunium and for a slightly tetragonally distorted (bct) structure of neptunium, each at two different volumes. For both the large and the small input volumes, the crystal distortion

lifts degeneracies, lowering the energy of one band and raising the energy of the other, but at expanded volumes, the bands are flatter (narrower), and more electron states contribute to lowering the energy of the distorted structure.

The tendency toward expanded volumes and low-symmetry structures is balanced by other contributions to the total energy (such as electrostatic interactions and overlap repulsion) that favor broader bands and close-packed structures. Thus, the energy-lowering mechanism described here will lead to low symmetry only in systems with bands that are both narrow and intersected by the Fermi level (Wills and Eriksson 1992, Söderlind et al. 1995). The light actinides fulfill these two criteria.

The importance of the narrow bandwidth in producing low-symmetry structures is apparently independent of whether the electrons in the band originated from s, p, d, or f valence states. Figure 13 shows the calculated total energies of p-, d-, and f-bonded elements (aluminum, iron and niobium, and uranium, respectively) as a function of bandwidth for different crystal structures. The total energies for the fcc, bct, and α -uranium structures are plotted relative to the energy of the bcc structure. In these calculations, varying the input volume produces changes in bandwidth, and the total energy and the bandwidths are outputs. For all these elements, very low symmetry actinide-like structures are the most stable (lowest energy) configurations when the bands are narrow, and higher-symmetry structures are stable for broad bands. Note that in using the structure of α -uranium as an example of low symmetry, we do not imply that an α -structure is the most stable kind for all the other actinides.

DFT Calculations of the Charge-Density Wave.

An extremely intricate connection between electronic and structural properties is the charge-density wave. Because of specific interactions between the electrons and the lattice, the charge density abandons the

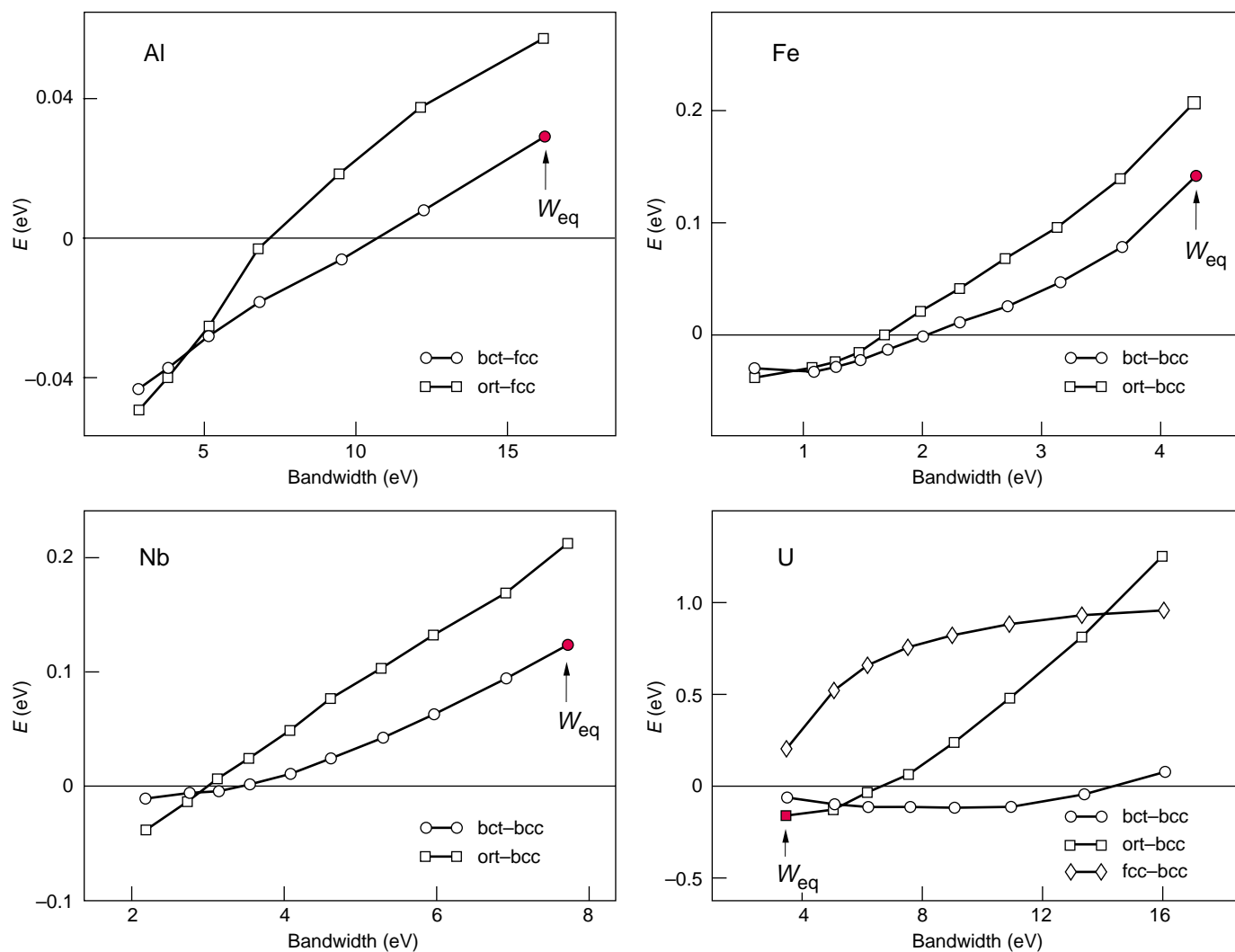


Figure 13. Calculated Total Energy of Different Crystal Structures as a Function of Calculated Bandwidth

In (a) through (d), we plot the DFT results for the total energies of aluminum (p-bonded), iron (d-bonded), niobium (d-bonded), and uranium (f-bonded) as a function of bandwidth for several different structures. We vary the bandwidth by varying the input volume. For all these elements, very low symmetry structures, similar to those of the actinides, are most stable configurations when the bands are narrow. High-symmetry structures, on the other hand, are stable for broad bands. The reference level (fcc for aluminum and bcc for the other metals) is set to zero. W_{eq} is the calculated bandwidth at the experimental equilibrium volume. Thus, if we use the observed equilibrium volumes, we predict that the transition metals will have broad bands and symmetric structures, whereas the light actinides will have narrow bands and low symmetry structures. (This figure was reproduced courtesy of *Nature*.)

perfect periodicity associated with the Bravais lattice and becomes a modulated function in space, with an oscillation period ranging, theoretically, over thousands of atoms. As a result, the atoms of the lattice move out of the position normally dictated by the Bravais lattice vectors and, instead, follow the periodicity of the charge-density wave.

The charge-density wave was originally proposed to occur in s-band met-

als such as sodium (Overhauser 1971), but as is often the case with interesting new physics, the only element that actually exhibits the new phenomenon is an actinide. After many decades of thorough experimental work, it was established that uranium metal goes through a sequence of distinct low-temperature phases and that those phases are different charge-density waves called α_1 , α_2 , and α_3

(Smith et al. 1980, Lander et al. 1994). The first transition takes place at 43 kelvins (α_1), and the last one stabilizes at 23 kelvins (α_3). After the completion of the last charge-density-wave transition, the approximate volume of the unit cell is a staggering 6000 cubic angstroms per primitive cell.

Smith et al. (1980) and Lander et al. (1994) have identified the charge-

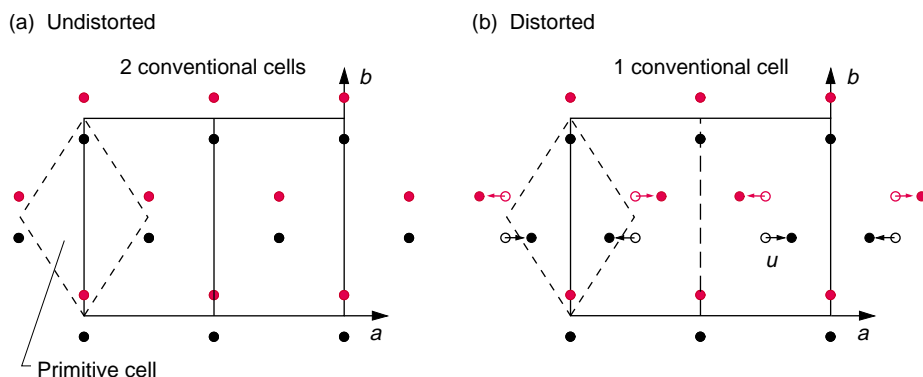


Figure 14. Structural Distortion Associated with the α_1 Charge-Density Wave of Uranium

Uranium metal goes through three distinct low-temperature phases, which are charge-density waves called α_1 , α_2 , and α_3 . We calculated the transition to the α_1 state.

The figure shows the crystal structure before and after the transition to the α_1 charge-density wave (the structures are projected onto the a - b plane). The conventional unit cell doubles as atoms are displaced by an amount u along the a -direction. In each structure, the black (red) circles mark atoms situated in the $c = 0$ ($c = 1/2$) layer, respectively.

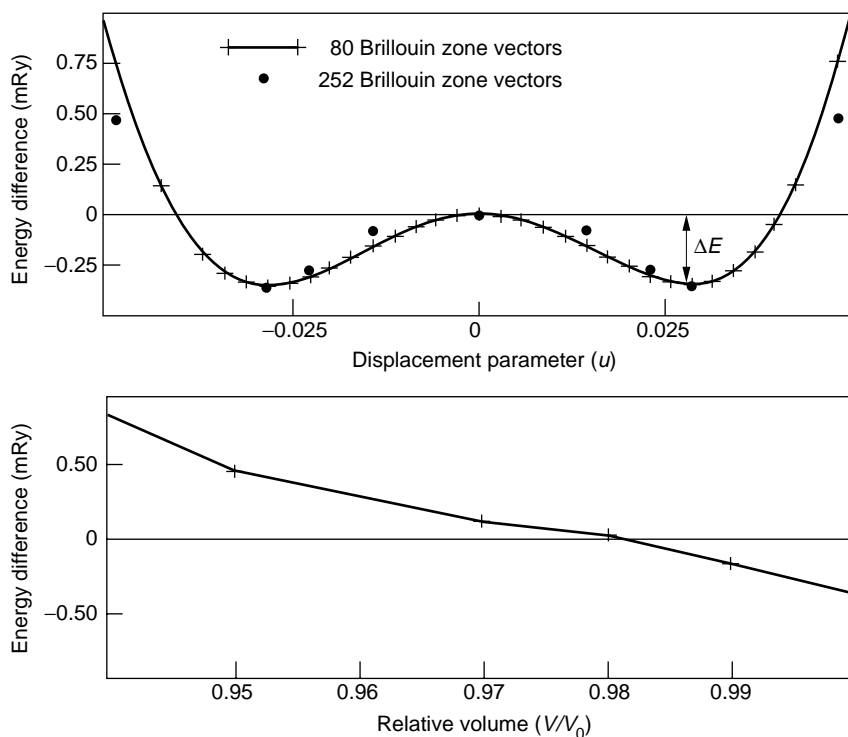


Figure 15. Calculated Energy Dependence of the α -Uranium Charge-Density-Wave Distortion

In both plots, the horizontal line represents the energy of α -uranium, and the energy of the α_1 -phase (charge-density wave) is plotted relative to it. (a) The calculated energy of the α_1 -phase at ambient conditions reaches a minimum for a displacement parameter (u) value of 0.028. This value agrees well with the experimental one of 0.027. (b) The calculated energy of the α_1 -phase increases as the volume is compressed, and at a compression of $V/V_0 = 0.98$, the α_1 -energy becomes higher. In other words, the α_1 -phase should disappear at this compression. This prediction agrees well with the observed transition at a compression of $V/V_0 = 0.99$.

density-wave state in uranium through structural changes. Transmission electron microscopy shows well-characterized twin/tweed patterns in the charge-density-wave state and reveals a most-pronounced shape memory effect. Neutron scattering experiments indicate that significant phonon softening occurs in the charge-density-wave state at 43 kelvins. Knowing this fact may be helpful in understanding this martensitic transition.

From a materials science point of view, the charge-density-wave state in uranium manifests itself by a small distortion, which has a drastic effect on several physical properties: lattice parameter, resistivity, elastic response, and thermal expansion (Smith et al. 1980, Lander et al. 1994). The physical mechanisms driving the different charge-density waves in uranium are similar, and for that reason, as well as for practical reasons, we focused on calculating the transition to the α_1 -state. In this transition, the conventional unit cell doubles as atoms are displaced by an amount u along the a -direction, according to the pattern shown in Figure 14. In Figure 15, the calculated total energy of uranium in the doubled unit cell is shown as a function of the displacement parameter u , which serves as the order parameter for the transition (Fast et al. 1998). Note that the total energy reaches a minimum at $u = 0.028$, which agrees almost perfectly with the experimental value of 0.027. Note also that, because the energy involved in this transition is minute, tremendous demands are placed on the theoretical method.

We have performed similar calculations for compressed volumes. At a compression of $V/V_0 = 0.98$, the total energy of the α_1 state becomes higher than the energy of the α -uranium structure, that is, the calculation predicts that the charge-density wave disappears. The calculated result agrees well with the observed transition at a compression of $V/V_0 = 0.99$. Here again, compressed volumes (and the resulting broadened bandwidths) destroy the more-complex less-symmetric structure in favor of

the more-symmetric one.

The specific mechanism driving the transition to the charge-density-wave state involves a feature of the energy bands and the Fermi surface called “nesting” (that is, many sheets of the Fermi surface are connected by vectors of similar length and direction). It is again a Peierls-like mechanism (Fast et al. 1998), but a much smaller part of the Brillouin zone is involved relative, for example, to the region that stabilizes plutonium in the low-symmetry α -plutonium structure.

In closing this section, we note that the fine details of the structural properties of the light actinides shown here reflect a very accurate treatment of the density, potential, and wave functions, in addition to all the relativistic effects. That accuracy was born from developments in theory and software over many years.⁵

Calculated Magnetic Susceptibilities of Uranium and Plutonium

Experiment has shown that all the light actinides are paramagnetic: Even at the very lowest temperatures, they do not spontaneously order in a magnetic configuration (they never become ferromagnets). Only when an external magnetic field is applied, does a small (positive) magnetic moment develop. This finding is consistent with the fact that the f electrons in the light actinides occupy band states rather than localized states.

To test the quality of the band picture further, we used the calculated set of bands to compute the field-induced magnetic moments of uranium and plutonium and compared our results with measured data for the magnetic susceptibilities and magnetic form factors (Hjelm et al. 1994). This is a sensitive test of our calculations. Good

⁵ J. M. Wills, software package FP-LMTO (Los Alamos National Laboratory, Los Alamos, New Mexico, unpublished).

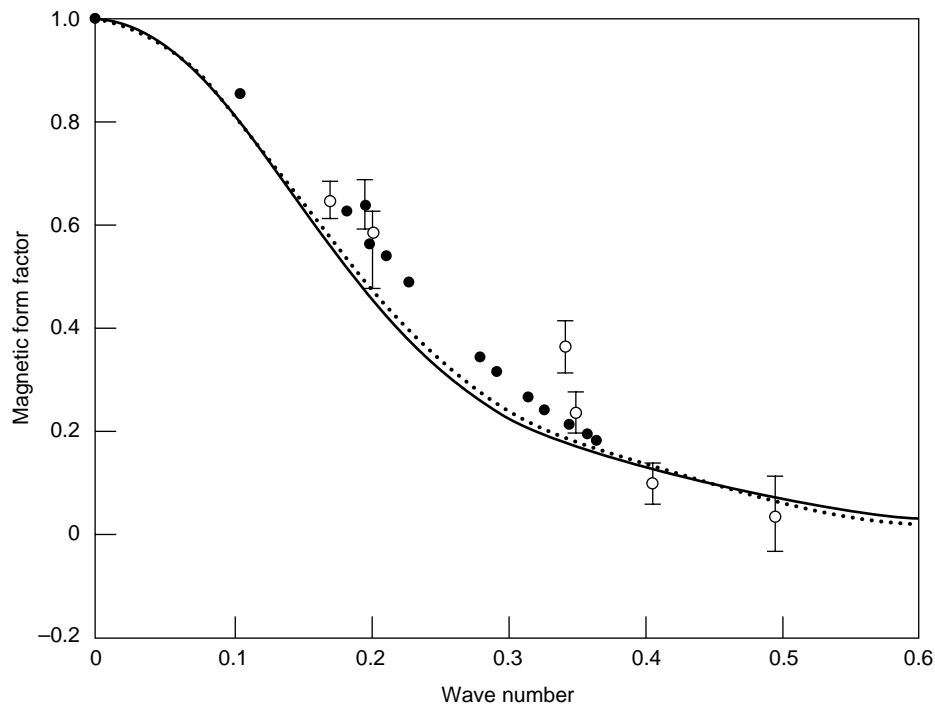


Figure 16. Calculated Field-Induced Form Factor of α -Uranium

We compare our DFT results for the field-induced magnetic form factor of α -uranium (full line) with experimental values (dotted line). The good agreement in both magnitude and shape of the spin density suggests that the DFT provides an accurate description of electronic structure in uranium.

agreement means that our band calculation is accurate and the whole concept of itinerant states in the light actinides is appropriate. In these calculations, we include the so-called “Zeeman term,” $B(2S + L)$, where B is the magnetic field in the Hamiltonian.

In an applied field of 7 tesla, the calculated field-induced moment in uranium is 4.7 milliboehr magnetons ($m\mu_B$), and the experimentally measured value is 4.9 $m\mu_B$. There are no measurements of induced moments in α -plutonium, so we infer them from measured magnetic susceptibilities. In an applied field of 10 tesla, the calculated field-induced moment of α -plutonium is 8.4 $m\mu_B$, whereas the induced moment inferred from measured susceptibilities is 9.8 $m\mu_B$. We have also calculated the field-induced magnetic form factor for α -uranium. The magnetic form factor is simply the Fourier transform of the field-induced magnetization density,

which we can calculate from spin DFT. Figure 16 compares the experimental and theoretical magnetic form factors and shows good agreement between them. Hence, DFT calculations reproduce the magnitude of the field-induced moment, as well as intricate details concerning the shape of the spin density for both α -uranium and α -plutonium, confirming that a band picture is appropriate for these two elements.

A Mott Transition in the Actinide Series

Because the question of electron localization and delocalization is central to actinide physics, we will note here that the variation of the energy levels with k , also called the energy dispersion, is a good measure of how localized the electrons are. Little dispersion, or a narrow energy band,

means that each conduction electron is close to being localized on an atomic site and, hence, spends a long time around this site before it jumps to the next site. The longer an electron is localized to a given nucleus, the more atomic-like its behavior, and the narrower the band. When the bandwidth becomes sufficiently narrow, the electrons localize and stop being itinerant. In practice, one expects localization to occur when the energy associated with the electron-electron interaction (correlation) is about the same size as the energy bandwidth.

To understand the effects of electron correlations, one traditionally turns to model Hamiltonians, such as the expression in Equation (1). That Hamiltonian can be augmented to incorporate electron-electron correlations. One such possibility would be

$$H = e \sum_{i\mu} \hat{n}_{i\mu} + h \sum_{i\mu} \sum_{j \neq i, \nu} \hat{c}_{j\nu}^\dagger \hat{c}_{i\mu} + U \sum_{i\mu\nu} \hat{n}_{i\mu} \hat{n}_{i\nu}, \quad (15)$$

where we now consider a degenerate atomic level with energy e and orbitals μ on lattice sites i . In contrast to the Hamiltonian in Equation (1), this Hamiltonian has two competing terms: the hopping term (proportional to h), which tends to lower the energy if electrons are shared between atoms, and the on-site Coulomb term (proportional to U), which raises the energy if electrons are shared between atoms. When the ratio h/U is small, the electronic states of such a Hamiltonian are substantially localized and may, in a good approximation, be considered to belong to one atom or another. This is the low-density limit of an elemental solid. When h/U is large, the electronic states of such a Hamiltonian are substantially itinerant, and the band picture, which was described in the earlier sections, is a good approximation. In the latter case, which is the high-density limit of a solid, exchange and correlation are included in an average way, as in the

LDA. At some point in the transition from low to high density, it becomes energetically favorable for electrons to hop between atoms, and the system undergoes a Mott transition.

The density at which it becomes energetically favorable to delocalize depends on the atomic number and the orbital character of the atomic valence states. States with a small angular-momentum barrier (s and p states) delocalize easily, whereas states with a larger angular-momentum barrier (d and particularly f states) retain their atomic character to higher densities. With the exception of the lanthanides past cerium and the actinides past plutonium, elements at zero pressure and low temperature have a delocalized, or itinerant, electronic character, and are well described by band theory.

Now, let us return to Figure 1 for a moment. As mentioned earlier, the volume and structure of americium (and of the elements following it) are drastically different from those of the light actinides. This finding was observed many years ago. Skriver et al. (1978), Skriver et al. (1980), and Brooks et al. (1984) explained it by assuming a Mott localization of the 5f shell. Therefore, the 5f states are localized and chemically inert in americium, just as they are in the rare-earth elements. As a result, the chemical bonding provided by the 5f electrons is lost, and the equilibrium volume is increased. In addition, the narrow 5f band pinned at E_F in the light actinides is absent in americium, and the mechanism for driving open and/or low-symmetry structures is lost. Thus, americium has a well-behaved double hexagonal close-packed (dhcp) structure, which is found frequently among the lanthanides.

We may explain the localization of the 5f electrons in americium by comparing the way in which the energy is lowered through band formation (itinerant electrons) and through multiplet formation (localized electrons). The idea is that the 5f electrons in americium form an atomic multiplet in a ‘‘Russell-Saunders coupling.’’ This strongly cou-

pled formation lowers the repulsive energy generated by the electron-electron interactions. At the same time, the strong coupling in the multiplet also lowers the total energy by an amount Δ_{coupling} . This lowering in energy should be compared with that stemming from band formation, E_{band} . It has been demonstrated that, for the light actinides, the energy is mainly lowered through band formation whereas for americium and the actinides after americium, it is lowered through multiplet formation (Skriver et al. 1978, Skriver et al. 1980, Brooks et al. 1984). The ground-state, localized 5f atomic multiplet of americium corresponds to a total angular momentum of zero, $J = 0$, which explains why no magnetic ordering occurs in this material. It was even observed (Smith and Haire 1978) that americium becomes superconducting at low temperatures. This observation agrees with predictions (Johansson and Rosengren 1975).

The δ -Phase of Plutonium

Thus far, we have outlined what may be viewed as a rather successful theoretical description and understanding of the ground-state physics of the light actinides. In the final section of this article, we outline an important problem of actinide physics and chemistry, which has escaped most researchers’ attention.

From Figure 1, we see that the actinide series naturally divides into two parts: an early part, in which the 5f states are delocalized and chemically active, and a later part, in which the 5f states are localized, atomic-like, and chemically inert, as are most rare-earth elements. However, one allotrope of plutonium, the δ -phase, does not categorize well into either of the groups (all plutonium allotropes other than α -plutonium may be hard to categorize in a simple way, but we will not address that issue here). One should note here that the δ -phase is observed at elevated temperatures, but it may be stabilized at low

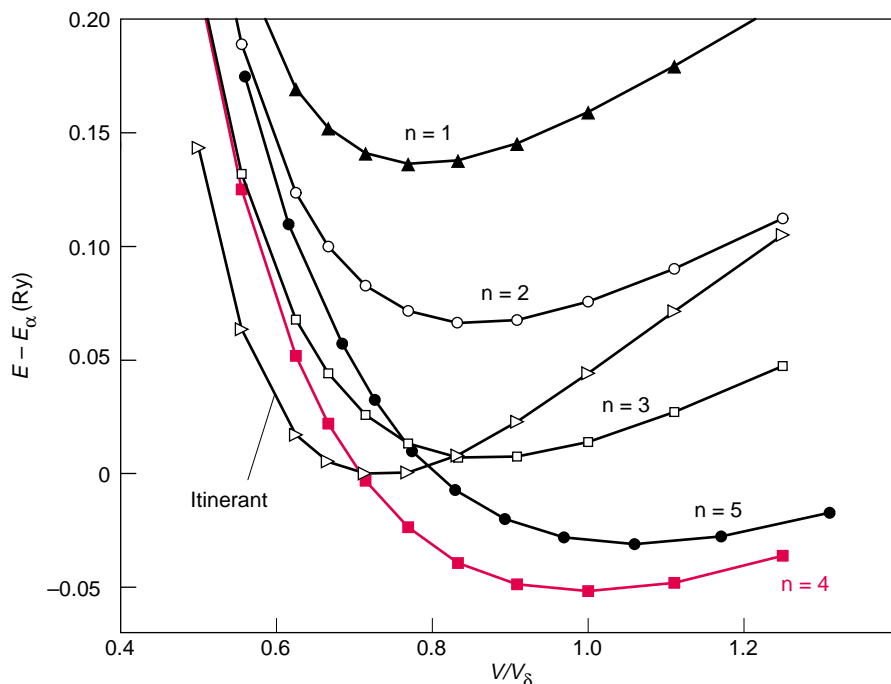


Figure 17. Energy of fcc Plutonium for Different Numbers of Localized 5f Electrons

Each curve shows our results for the total energy of δ -plutonium relative to that of α -plutonium as a function of V/V_δ . The curves are labeled by n , the number of localized 5f electrons assumed for those calculations. The curve that predicts the lowest energy at the correct δ -plutonium volume, $V/V_\delta = 1$, is the configuration with four of the 5f electrons localized and only one itinerant. Moreover, the energy of this state relative to the α -phase is about right.

temperatures when we add a few atomic percent of aluminum, gallium, or cerium.

As seen in Figure 1, the volume of δ -plutonium is between that of α -plutonium and americium. If the 5f electrons of δ -plutonium were localized, the equilibrium volume would be close to that of americium, and if the 5f electrons were delocalized, the equilibrium volume would be close to that of α -plutonium. Instead, δ -plutonium has an intermediate volume, indicating that the 5f electrons are in some unknown intermediate state. Thus, the traditional view that electrons localize between plutonium and americium needs to be modified and allow for an in-between phase represented by δ -plutonium.

In addition to its unusual equilibrium volume, δ -plutonium has an exotic negative thermal expansion—upon heating, the volume decreases. According to the conclusions drawn in the previous section, if the 5f states were delocalized in

δ -plutonium, the structure of this allotrope would be distorted. Therefore, the observed fcc structure of δ -plutonium suggests that the 5f states, like those in α -plutonium, are not delocalized. Moreover, if the 5f states were localized, as they are in americium, one would expect (from atomic theory) that they would couple to give a magnetic moment for each plutonium atom, and as a consequence, one would observe magnetic ordering in the crystal at low temperatures. Although experiments on this allotrope are quite sparse, the question of whether a temperature-dependent magnetic susceptibility has been observed in plutonium above the α -phase is currently controversial. If such a behavior could be confirmed, a conclusion about the existence of local moments (indicating the 5f localization) could be confirmed.

Our most-recent efforts have addressed this problem (Eriksson et al.

1999). We have modified the energy expression in Equation (7) to incorporate states that are a mixture of localized and delocalized states, a mixed-level approximation. With this expression, we calculated the total energy as a function not only of volume and structure but also of the fraction of the electron density that corresponds to localized electrons. By using the Russell-Saunders coupling, we calculated the total energy of any localized part of the 5f electron sea.

We achieve the mixed-level approximation by imposing a constraint on certain electrons so that they become localized. The constraint is that these electrons should not hop from site to site and should not mix (hybridize) with any other electron states. One can perform a constrained calculation using the method outlined in our discussion of Equation (4). However, because of the constraint, the total energy is now larger than that obtained from the unconstrained LDA calculation, $E = E_{\text{LDA}} + \Delta_{\text{constraint}}$. One may now associate the localized f configuration with an uncoupled (that is, in terms of the Russell-Saunders coupling) atomic configuration. This configuration is sometimes called the grand barycenter of an atomic configuration.

From atomic theory, one can calculate the energy difference between this configuration and the lowest atomic multiplet. Because such a description becomes quite lengthy, we simply refer to this energy as Δ_{coupling} . A true estimate of the total energy of a 5f localized configuration of an actinide material should therefore be $E = E_{\text{LDA}} + \Delta_{\text{constraint}} - \Delta_{\text{coupling}}$. In this expression, all terms can be calculated. If they are applied to americium metal, the localized f^6 configuration has the lowest total energy, in agreement with experiment. This approach is not phenomenological; it simply combines knowledge of DFT with knowledge of atomic theory (Russell-Saunders coupling). Some atomic-theory parameters are taken from experiments, but nothing prevents us from calculating these

parameters from, for example, configuration-interaction theories. A partitioning of the 5f manifold into localized and delocalized parts is physically reasonable, and one can investigate if the total energy is lowered by this procedure. In Figure 17, we show such a calculation for δ -plutonium, and we note that most of the ground-state properties (equilibrium volume and energy separation to the α -phase) of the δ -plutonium are reproduced with 4 localized electrons. The total energy is also lowest for this configuration. The good agreement between theory and experiment referred to here suggests that δ -plutonium is in a unique electronic configuration that has not been discussed before: The 5f manifold is partly delocalized and partly localized (Eriksson et al. 1999).

Summary and Outlook

We have outlined some of the more interesting aspects of the electronic structure of the actinides and especially how that structure relates to chemical bonding and structural properties. We argue that the presence of a narrow 5f band that is intersected by the Fermi level is the key ingredient for explaining the unusual structural aspects of the light actinides. From the research conducted in this past decade, a picture emerges of the physics of the unique actinide structures. From it, we can argue that most actinides should transform into high-symmetry structures (namely, bcc for uranium, neptunium, and plutonium) when they are compressed (Wills and Eriksson 1992, Söderlind et al. 1995). This prediction was recently verified for neptunium. A more extended discussion of these issues can be found in a recent overview article by Söderlind (1998).

The work on the low-temperature phases of the light actinides shows that the theoretical formalism of DFT, in the LDA or GGA, reproduces many of the ground-state properties, such as lattice constants, formation (cohesive) energy, structural properties, susceptibility, and

elastic properties. It is our view that this method can then form a basis for the theoretical modeling of other more-practical aspects of materials, such as alloy formation, segregation profiles, stacking fault energies, and energies of grain boundaries.

In addition, we have presented evidence that the electronic configuration of δ -plutonium is unique in the periodic table. Hence, it is not only the structural properties of plutonium (for instance the low-symmetry structure of the α -phase) that are unique, but also the electronic ones. Before theory can make much more progress in explaining the complex phase diagram of plutonium, there is a great need for accurate experimental work to be performed on high-purity single crystals. (Comparison with the first photoemission data on polycrystalline α - and δ -samples are encouraging but leave many unanswered questions, as discussed on page 152) A successful understanding of the plutonium phase diagram and especially δ -plutonium may help in answering questions about the stability of this allotrope. When considering stockpile stewardship, it is important to know if the impurity-stabilized δ -plutonium is a ground-state or a metastable phase. If it is a metastable phase, knowing its decay rate is very important. There are compelling reasons to expect that impurity-stabilized δ -plutonium has the same structure as temperature-stabilized δ -plutonium. There is also evidence that the same 5f bonding prevails in stoichiometric plutonium compounds as in δ -plutonium.

We have applied our theory to the plutonium-gallium compounds Pu_3Ga and PuGa and find good agreement between experimental and calculated volumes and energies—again with a partitioning of the 5f manifold into four localized states. In this paper, we have outlined a model for understanding the electronic properties of δ -plutonium. Although the proposed theory seems to work well, we need to see other, parallel attempts aimed at describing the correlated electronic properties of this allotrope of plutonium. As already indi-

cated, this effort could involve theories based on the GW approximation or dynamical mean-field theory.

In future work, it will become important to have theoretical models for calculating the free energy of the actinide elements as a function of temperature. The theory presented here only applies to zero temperature. To include temperature effects, however, is a formidable task, and we must create some simplifications. A possibility is to integrate the existing expertise in molecular dynamics simulations with the expertise in electronic-structure and total-energy calculations. Alternatively, accurate calculations of the phonon spectrum of different allotropes may enable reliable calculations of the free energy as a function of temperature. With either of these approaches, one could then gain understanding about the structural and electronic properties of the different allotropes in the pressure-temperature phase diagram of the actinide elements. Also important in future work will be the application of the present DFT formalism to much larger systems in order to study the effects of impurities and segregation profiles for impurities, grain boundaries and their effect on materials properties, and finally, structural disorder. This last application is most important to investigate because there is a possibility that, without recourse to a more complex correlation than presently exists in DFT functionals, local deviations from a global structure might induce at least partial localization in plutonium.

Some of the results presented here show a recent trend in solid-state physics: Total-energy calculations are approaching an accuracy that enables a reliable and robust reproduction of experimental data, providing new insight into mechanisms pertinent to a given physical or chemical question. In addition, the calculations sometimes have become predictive, as they have for the high-symmetry structures of uranium, neptunium, and plutonium under compression. One can envisage that, in the near future, first principles calcu-

lations will be used in testing certain chemical and physical concepts about the actinides before a more cumbersome and expensive experiment is made. As for the electronic configuration of δ -plutonium, it has been revealed as truly novel in our calculations. The time has now come for experimental work on this interesting material to take a step forward and confirm or refute present theories of this material. ■

Acknowledgments

Most of this work has been collaborative. Our thanks for the excitement we have enjoyed over the physics of the actinides go to A. Balatski, D. Becker, A. M. Boring, L. Fast, A. Hjelm, B. Johansson, L. Nordström, H. Roeder, G. Straub, P. Söderlind, and J. Trygg. Nikki Cooper's critical reading and many useful comments are gratefully acknowledged.

Further Reading

- Brooks, M. S. S., H. L. Skriver, and B. Johansson. 1984. In *Handbook on the Physics and Chemistry of the Actinides*. Edited by A. J. Freeman and G. H. Lander. Amsterdam: North Holland.
- Dreizler, R. M., and E. K. U. Gross. 1990. *Density Functional Theory*. Berlin: Springer.
- Eriksson, O. D., D. Becker, and A. S. Balatski. 1999. *J. Alloys and Compounds* **287**: 1.
- Fast, L., O. Eriksson, L. Nordstrom, B. Johansson, and J. M. Wills. 1998. *Phys. Rev. Lett.* **81**: 2978.
- Friedel, J. 1969. *The Physics of Metals*. J. M. Ziman, ed. New York: Cambridge Univ. Press.
- Georges, G., G. Kotliar, W. Krauth, and M. J. Rosenberg. 1996. *Rev. Mod. Phys.* **68**: 13.
- Hedin, L. 1965. *Phys. Rev. A* **139**: 796.
- Hill, H. H., and E. A. Kmetko. 1970. W. N. Miner, ed. *Nucl. Met.* **17**: 223.

- Hjelm, A., J. Trygg, O. Eriksson, and B. Johansson. 1994. *Phys. Rev. B* **50**: 4332.
- Hohenberg, P., and W. Kohn. 1964. *Phys. Rev.* **136**: 864.
- Johansson, B. 1974. *Phil. Mag.* **30**: 469.
- Johansson, B., and A. Rosengren. 1975. *Phys. Rev. B* **11**: 2836.
- Kmetko, E. A., and J. T. Waber. 1965. "Plutonium." In *Proc. 3rd Int. Conf.* London: Chapman and Hall Ltd.
- Koelling, D. D., A. J. Freeman, and G. Arberman. 1970. W. N. Miner, ed. *Nucl. Met.* **17**: 194.
- Kohn, W., and L. J. Sham. 1965. *Phys. Rev.* **140A**: 1133.
- Lander, G. H., E. S. Fisher, and S. D. Bader. 1994. *Adv. Phys.* **43**: 1
- Overhauser, A. W. 1971. *Phys. Rev. B* **3**: 3173.
- Pettifor, D. 1995. *Bonding and Structure of Molecules and Solids*. Oxford: Oxford Science Publications.
- Sandalov, I., O. Hjortstam, B. Johansson, and O. Eriksson. 1995. *Phys. Rev. B* **51**: 13987.
- Seaborg, G. T. 1945. *Chem. Eng. News* **23**: 2190.
- Skriver, H. L., O. K. Andersen, and B. Johansson. 1978. *Phys. Rev. Lett.* **41**: 42.
- . 1980. *Phys. Rev. Lett.* **44**: 1230.
- Smith, J. L., and R. J. Haire. 1978. *Science* **200**: 535.
- Smith, H. G., N. Wakabayashi, W. P. Crummett, R. M. Nicklow, G. H. Lander, and E. S. Fischer. 1980. *Phys. Rev. Lett.* **44**: 1612.
- Söderlind, P. 1998. *Advances in Physics* **47**: 959.
- Söderlind, P., O. Eriksson, B. Johansson, J. M. Wills, and A. M. Boring. 1995. *Nature* **374**: 524.
- Steiner, M. M., R. C. Albers, and L. J. Sham. 1992. *Phys. Rev. B* **45**: 3272.
- Wills, J. M., and O. Eriksson. 1992. *Phys. Rev. B* **45**: 13,879.



John Wills graduated from the University of Hawaii in 1979 with a Bachelor's degree in physics and received a Ph.D. in physics from Stanford University in 1983. John worked as a postdoctoral researcher at West Virginia University from 1983 to 1986, when he became staff member in the theoretical Division at Los Alamos, where he is currently employed. He is the author of a full-potential electronic-structure method, the first method to be used successfully on cerium and the light actinides. A significant fraction of his research has been on the theory of the magnetic and structural properties of the actinides, which he has studied for the past fifteen years.



Olle Eriksson received his Ph.D. in condensed matter physics at the University of Uppsala in Sweden. Between 1989 and 1997, he was a postdoc, consultant, and a long-term visiting staff member at Los Alamos. Olle holds several awards, including the 1994 Prize for Young Researchers given by the Swedish government annually to "the best research work of the year." His interests lie in magnetism, electronic structure, f electron materials, theories of electron correlations, optical and magneto optical properties, as well as structural and cohesive properties of matter and their pressure dependence. He is currently professor in the Department of Physics, at the University of Uppsala.

Basics of the Density Functional Theory (DFT) Approach

To calculate the ground-state electronic energy of an atomic system, one normally starts from the time-independent Schrödinger equation. In addition, the Born-Oppenheimer approximation is frequently used because it neglects the motion of the nuclei and allows calculating the total energy of the electrons in the potential created by the nuclei. Therefore, one could calculate the ground-state (lowest-energy configuration) total electronic energy from

$$H\Psi(r_1, r_2, \dots, r_n) = E\Psi(r_1, r_2, \dots, r_n) \quad (2)$$

where H is the Hamiltonian containing the kinetic energy and all the interactions of the system (electron-electron correlation and exchange and electron-nuclei interactions), $\Psi(r_1, r_2, \dots, r_n)$ is a many-electron wave function of the n -electron system, and E is the total electron energy of the ground state. The input parameters in Equation (2) are the atomic numbers of the atoms and the geometry of the crystal (the lattice constant, the crystal structure, and the atomic positions).

To determine the equilibrium volume theoretically, one could keep the crystal structure fixed and calculate the ground-state electronic energy for different input volumes (or lattice constants). The volume that produced the lowest energy would represent the theoretical equilibrium volume. Similarly, one could compare the total energy of different structures at different volumes and draw conclusions about structural stability and possible structural phase transitions that might occur when the volume is changed (experimentally, one can compress the volume by applying an external pressure). In addition, one could calculate the energy gain when free atoms condense to a solid (the cohesive energy). Unfortunately, there is no practical way to solve Equation (2) for a solid.

Nevertheless, we have been able to carry out this program of calculations because there is an alternative theoretical formulation for determining the electronic structure. In two important theorems (Hohenberg and Kohn 1964, Kohn and Sham 1965, Dreitzler and Gross 1990), it has been shown that the total energy of a solid (or atom) may be expressed uniquely as a functional of the electron density. We can therefore minimize this functional with respect to the density in order to determine the ground-state energy. Therefore, instead of working with a many-electron wave function, $\Psi(r_1, r_2, \dots, r_n)$, one can express the ground-state energy in terms of the electron density at a single point $n(r)$, where that density is due to all the electrons in the solid:

$$n(r) = \sum_{i=1}^n \int \Psi^*(r_1, r_2, \dots, r_n) \delta(r-r_i) \Psi(r_1, r_2, \dots, r_n) dr_1 dr_2 \dots dr_n \quad (3)$$

In addition, Hohenberg and Kohn (1964), Kohn and Sham (1965), and Dreitzler and Gross (1990) demonstrated that, instead of calculating the electron density from the many-electron wave function $\Psi(r_1, r_2, \dots, r_n)$, one may work with the solutions to an effective one-electron problem.

The trick is to use the form of the total-energy functional to identify an effective potential $V_{\text{eff}}(r)$ for one-electron states and then solve for the one-electron states to produce a density equal to the many-electron density. The equation for the one-electron states is

$$\left(\hat{T} + V_{\text{eff}}\right)\psi_i(r) = \epsilon_i \psi_i(r) \quad (4)$$

where \hat{T} is a kinetic energy operator (for example, $-\hbar^2\nabla^2/2m$ in a nonrelativistic approximation)

and the resulting total electron density is given by

$$n(r) = \sum_i |\psi_i(r)|^2 . \quad (5)$$

To include relativistic effects important in the actinides, one replaces the nonrelativistic, Schrödinger-like one-electron equation—see Equation (4)—by the relativistic Dirac equation. By finding the correct form for the effective potential, the electron density in Equation (5) will be the same as that in Equation (3).

As mentioned in the section “Density Functional Theory” in the main text, the one-electron problem defined by Equation (4) has the same form as the equations solved by band theorists before DFT was invented, and the eigenvalues of those equations as a function of crystal momentum are precisely the energy bands. The contribution of DFT is to provide a rigorous prescription for determining the effective potential and for calculating the total ground-state energy. The DFT prescription for the effective potential in Equation (4) is

$$V_{\text{eff}}(r) = \frac{\delta}{\delta n(r)} \left[E_H(n(r)) + E_{xc}(n(r)) + E_{eN}(n(r)) \right] , \quad (6)$$

where the different terms are derived from the total-energy functional $E(n(r))$:

$$E(n(r)) = T(n(r)) + E_H(n(r)) + E_{xc}(n(r)) + E_{eN}(n(r)) + E_{NN} . \quad (7)$$

In this equation, $T(n(r))$ represents the kinetic energy of the effective one-electron states and is calculated from

$$T(n(r)) = \sum_i \int \psi_i^\dagger(r) \hat{T} \psi_i(r) dr . \quad (8)$$

$E_H(n(r))$ is the classical Hartree interaction (the electrostatic interaction between two charge clouds):

$$E_H(n(r)) = \frac{1}{2} e^2 \int \frac{n(r_1)n(r_2)}{|r_1 - r_2|} dr_1 dr_2 . \quad (9)$$

$E_{eN}(n(r))$ is the electron-nuclei interaction:

$$E_{eN}(n(r)) = -e^2 \sum_R Z_R \int \frac{n(r)}{|r - R|} dr . \quad (10)$$

$E_{xc}(n(r))$ is the part of the interaction that goes beyond the classical Hartree term as well as the difference between the true kinetic energy and the one-electron kinetic energy. In the LDA, this term has the form

$$E_{xc}(n(r)) = \int n(r) \mathcal{E}_{xc}(n(r)) dr . \quad (11)$$

Finally, E_{NN} is the Coulomb interaction between the different atomic nuclei of the lattice:

$$E_{NN} = \frac{1}{2} e^2 \sum_R \sum_{R' \neq R} \frac{Z_R Z_{R'}}{|R - R'|} . \quad (12)$$

From these definitions, it becomes obvious that the effective potential in which the electron moves has contributions from the electron's interaction with the nuclei and the other electrons in the solid both by the classical Hartree term and by the quantum mechanical exchange and correlation term.

Because all electron-electron interactions that go beyond the classical Hartree term are found in $E_{XC}(n(r))$, it is crucial to have a good approximation for this term (unfortunately, there is no exact form of this term for a real solid). However, if one assumes the functional to be local, a numerical form may be obtained from many-body calculations (quantum Monte Carlo or perturbation series expansion), and very good values may be obtained for the ground-state energy for different values of the electron density. If the electron density of a real system varies only smoothly in space, one expects that a form of E_{XC} taken from a uniform electron gas should be applicable to the real system as well. This approximation is no other than the LDA. The good agreement, for many solids,* on cohesive energy, equilibrium volume, and structural properties between this approximate theoretical approach and experimental values suggests that the LDA form of E_{XC} works even if the electron density varies rapidly in space. As an example of how E_{XC} might look, we quote the full form of the exchange and correlation energy density in Equation (11), as given by Hedin and Lundqvist, with parameters calculated in the random-phase approximation:

$$\mathcal{E}_{XC}(n(r)) = \mathcal{E}_X(r_s) + \mathcal{E}_C(r_s) \quad ,$$

where

$$r_s = \left(\frac{3}{4\pi n(r)} \right)^{\frac{1}{3}}$$

$$\mathcal{E}_X(r_s) = \frac{-0.91633}{r_s}$$

$$\mathcal{E}_C(r_s) = -0.045 G\left(\frac{r_s}{21}\right)$$

$$G(x) = (1+x^3) \ln\left(1 + \frac{1}{x}\right) - x^2 + \frac{x}{2} - \frac{1}{3} \quad . \quad (13)$$

Thus, one can calculate the total ground-state energy by solving an effective one-electron equation. This tremendous simplification of replacing interacting electrons with effective one-electron states will work only if one can find the correct, effective one-electron potential. ■

* Among such solids are simple metals, transition metals, actinides, p electron elements, and thousands of compounds formed between these elements.

Electronic Structure of α - and δ -Plutonium

Theory vs experiment

Aloysius J. Arko, John J. Joyce, and John M. Wills

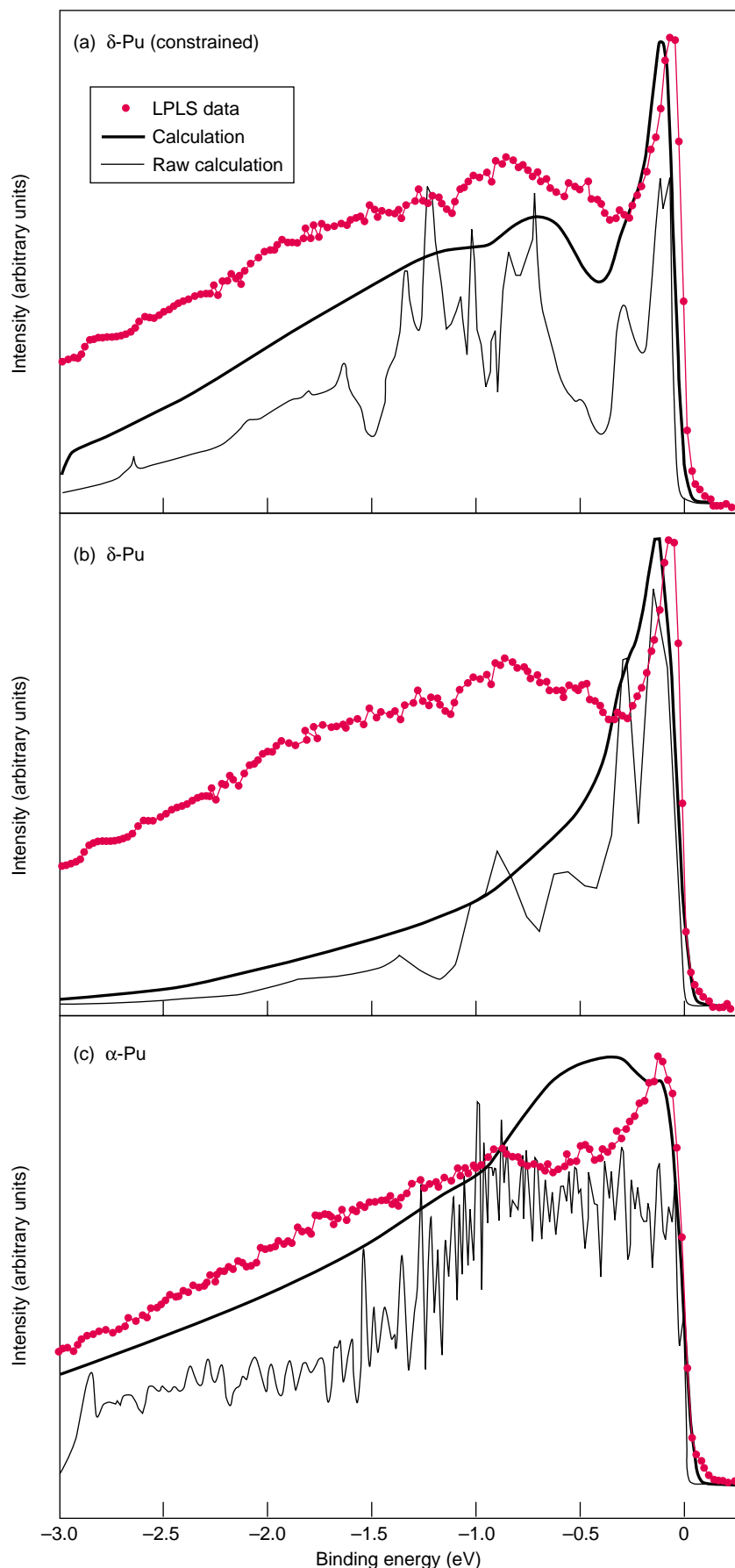
Photoelectron spectroscopy (PES) provides a direct means for comparing the calculated density of states with the measured electronic structure. Because the photoemission cross sections vary strongly with both photon energy and orbital symmetry, one must choose for comparison spectra at a photon energy at which the d and f cross sections are about equal. That value turns out to be near $h\nu = 40$ electron-volts (eV), which is conveniently near the helium II resonance line. For this reason, we compare the calculated results with the data from a spectrum obtained with helium II radiation at a temperature of 80 kelvins and with a resolution of about 75 milli-electron-volts (meV). (See the article “Photoelectron Spectroscopy of α - and δ -Plutonium” on page 168.)

Figures 1(a)–1(c) show this comparison for α - and δ -plutonium. In each frame, the experimental curves are the red data points, the unbroadened calculated density of states is shown by the thin black lines, and the broadened calculated density of states is represented by the thick black lines. Broadening of the calculated spectra is necessary for comparison with experiment. A photoemission spectrum is broadened by Gaussian instrument resolution cut by the Fermi energy, and more important, by Lorentzian lifetime broadening created by the hole produced in the photoemission process, typically called a photohole. Lifetime broadening occurs because, the farther below the Fermi energy a photohole is created, the faster it is refilled from higher-lying states. Thus, this broadening is energy dependent. The density of states in Figure 1 has thus been convoluted with a

Lorentzian whose full width at half maximum (FWHM) increases as $[E_0 + E_1 (E_B^{-2})]$, where E_B is the energy below the Fermi energy, E_0 is set to 20 meV, and E_1 is 1.1 eV^{-1} to simulate lifetime broadening of the photohole. The maximum allowed broadening is restricted to 1 eV. All calculations are broadened identically. The secondary electrons have been subtracted from the experimental data by a Shirley-type background subtraction. The constants E_0 and E_1 were chosen to fit the data in Figure 1(a). The same constants were used in all three frames.

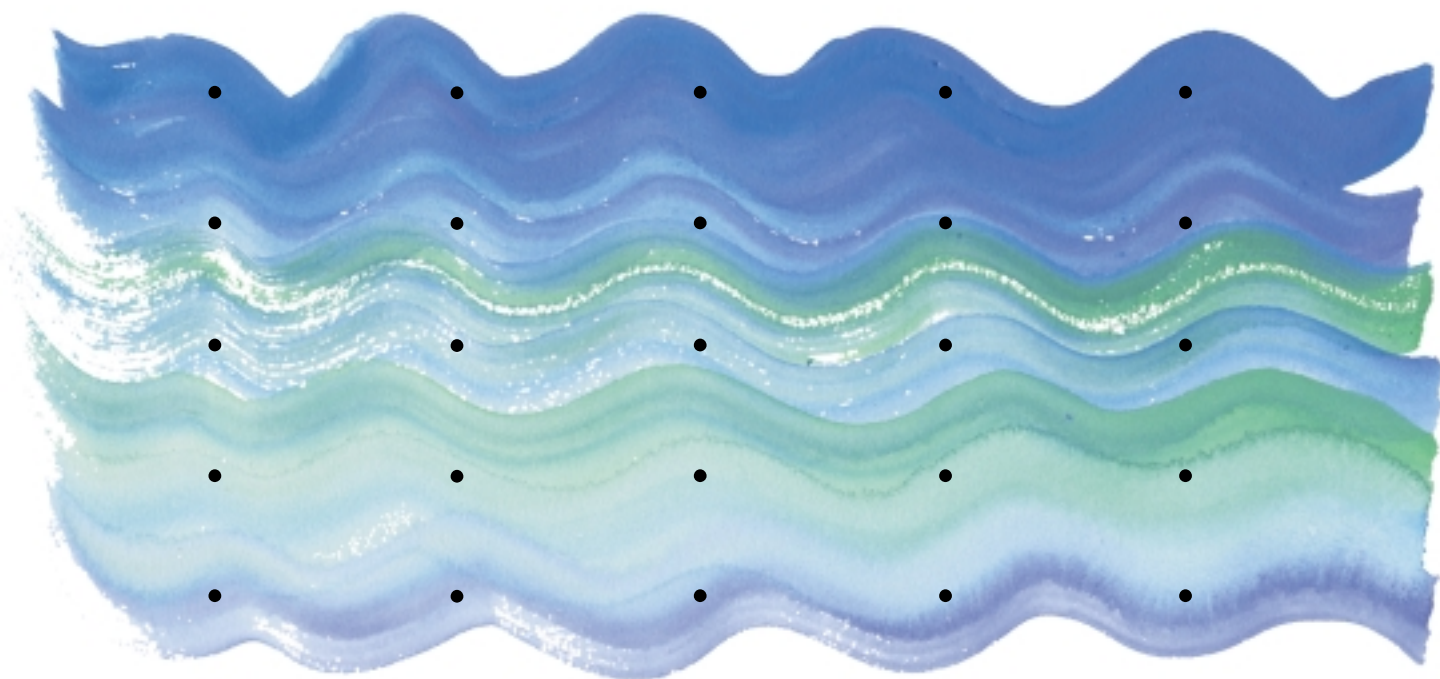
In Figure 1(a), we compare the δ -plutonium spectrum with results of a generalized-gradient approximation (GGA) calculation in which four of the five 5f electrons are constrained to localization. Globally, the experimental δ -plutonium spectrum is well reproduced by the calculated spectrum, suggesting that perhaps this is a good starting point for a basic understanding of plutonium. This notion is reinforced by the observation that the band calculations predict some admixture of 5f and 6d character for the narrow peak, the amount depending on the choice of constraint conditions as needed for interpreting the photon energy dependence. However, at present, the calculation would place the narrow feature 60 meV below E_F as opposed to exactly at E_F , where it is found experimentally. The exact nature of this discrepancy is not understood at this time.

Figure 1(b) compares the δ -plutonium spectrum with results of an unconstrained GGA calculation in which all 5f electrons are allowed to be itinerant. In this calculation, the bulk of the 5f density



of states is found to be contained in a narrow region within 0.5 eV of the Fermi energy (similar to uranium results). This result is clearly at odds with experiment and reinforces the notion that at least some of the 5f electrons are localized.

The α -plutonium calculation and measured spectrum are compared in Figure 1(c). Some puzzling problems become evident because the sharp structure near E_F , clearly observed experimentally, is not well reproduced in an unconstrained GGA calculation. Conventional wisdom states that α -plutonium is much like a transition metal with conventional bands. A sharp peak at the Fermi energy would suggest that even this transition-like material exhibits strong correlation effects. But the sharp feature in the α -plutonium spectrum occurs at 100 meV below E_F , and it therefore calls into question the correlation effects. Moreover, one would not anticipate electron-electron correlations in a system with a temperature-independent susceptibility as well as a densely packed crystal structure, in which direct f-f overlap is possible. Nonetheless, we must recall that α -plutonium 4f core levels show satellite behavior similar to, yet not as intense as, that in δ -plutonium. Perhaps correlation phenomena are important in spite of the 5f maximum occurring at 100 meV below E_F . A reasonable calculational approach for α -plutonium might be one of renormalized bands, in which the Hubbard Hamiltonian is introduced as a perturbation on GGA-derived bands. Variation of the Coulomb correlation energy interaction U controls the strength of the electron-electron correlations. This approach may solve the problem for α -plutonium but is more problematic for δ -plutonium, whose GGA-calculated bands are too narrow compared with experiment. The structure at 1 eV may not be reproduced by renormalization. ■



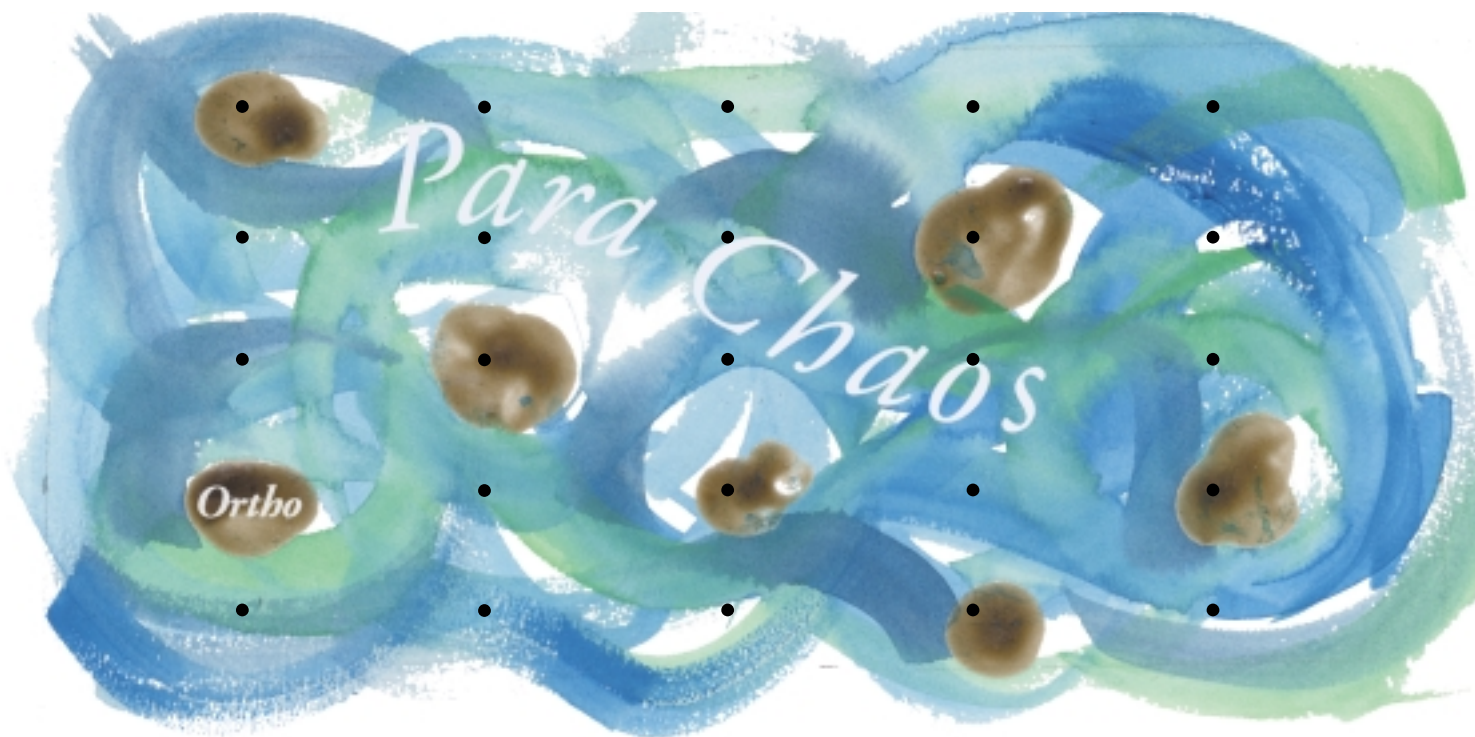
A Possible Model for δ -Plutonium

Self-induced Anderson localization, δ -phase stability,
and the melting temperature of plutonium

Bernard R. Cooper

It has been evident for some time that the unusual structural behavior of plutonium in the transition from the α - to the δ -phase is related to the localization mechanism for the 5f electrons. As shown by Donohue (1982), the atomic volume of plutonium expands as the metal goes through the structural sequence alpha (monoclinic at 300 kelvins), beta (monoclinic at 395 kelvins), gamma (orthorhombic at 479 kelvins), and delta (face-centered-cubic, fcc, at 592 kelvins). The δ -phase has a negative thermal expansion; the body-centered-tetragonal δ' -phase (at 724 kelvins) also has negative thermal expansion; and the body-centered-cubic (bcc) ϵ -phase (at 749 kelvins) expands until melting occurs at the anomalously low temperature of 913 kelvins. In this article, we explain this unusual behavior by a multistep, spatially nonuniform 5f localization process, which is a variant of the disorder-induced localization described by Anderson (1958).

Our localization process involves a disordered array of two types of plutonium on crystallographically equivalent fcc sites that breaks the translational symmetry of the crystal. The sites occupied by the plutonium are of two kinds: the fluctuating para (spin-singlet two-electron state) sites, whose localized f electrons fluctuate between f^4 and f^5 because they hybridize with non-f band electrons, and the localized ortho (spin-triplet two-electron state) sites, whose localized f electrons remain stable at f^5 . It is the entropy of mixing between these two types of sites that drives the thermal stepwise transition from plutonium's monoclinic α -phase (ground state) to its fcc δ -phase (Cooper et al. 1999c, Cooper and Lin 1999, Cooper 2000).



This mechanism for f electron localization emerges from the use of two-electron dynamics. The Coulomb exchange interaction (a consequence of electron permutation symmetry) requires that two-electron states have either para singlet or ortho triplet character. As a consequence, not only are there two kinds of 5f electron states (para and ortho), but depending on the relative dominance of exchange vs hybridization in the dynamics, there is a phase transition between a narrow correlated 5f-band-like state that is found in α -plutonium and a homogeneous spatially disordered mixture of the two types of 5f electron states. That is, the localized ortho and fluctuating para states occupy different sites. This is a unique prediction of the two-electron dynamics.

This type of Anderson localization can be self-induced when light-actinide atoms on some sites assume an occupied ortho state (the f electrons at these sites are almost fully localized) and thereby provide sufficiently strong scattering of the itinerant 5f electrons that originate from the para actinide sites. Those itinerant electrons lose their coherent-wave character and return to a localized state, thereby maintaining the para actinide sites in their fluctuating 5f configuration. This spatially disordered mixture of the para and ortho sites, therefore, has overall partial localization. We call this partially localized solid-solution-like phase the randomly localized fluctuating-site (RLFS) phase. In the absence of magnetic ordering, the RLFS phase becomes stable against total localization by maximizing the entropy gain and thereby lowering the free energy. Likewise, the RLFS phase replaces 5f bonding when its free energy is lower than that of the coherent 5f bonding that it destroys. In the absence of magnetic ordering, the entropy of the RLFS phase will be maximized if the sites are equally divided between para and ortho. Which sites are ortho and which are para presumably varies with time, but the mean lifetime of each state is sufficiently long to establish a configurational free energy and, hence, entropy. We show how such a division into two types of plutonium sites can explain the thermal stabilization of fcc plutonium. Figure 1 is an artist's rendition of the change from the f bonding phase of α -plutonium to the RLFS partially localized phase of δ -plutonium.

This partial localization mechanism becomes operative in the light actinides provided the hybridization between the f electrons and non-f band electrons is sufficiently weak (that is, the f band is sufficiently narrow). If magnetic ordering is present, this

Figure 1. Transition of α - into δ -Plutonium by Entropy-Generating Mechanism
(Left) In this rendition, the coherent bonding states of the f electrons in α -plutonium are likened to the serene flow of water in a cold winter stream. **(Right)** As the system is heated, the serene flow breaks up into a partially localized state as itinerant f electrons from the para sites crash against the localized ortho sites and therefore fluctuate between localization and itinerancy. This localization mechanism drives the stepwise transition with increasing temperature from the α -phase to the β -, γ -, and δ -phases of elemental plutonium.

localization mechanism is enhanced, and it therefore starts at a lower temperature.

A resonant scattering point of view (Coqblin and Schrieffer 1969) is pertinent in the weak hybridization regime. Working from that point of view, we studied the onset of magnetic ordering in certain uranium compounds—the uranium monochalcogenides—as hybridization decreases. Our calculations yielded remarkably accurate absolute *ab initio*-based predictions (Cooper and Lin 1998, Cooper et al. 1999a, Cooper et al. 1999b) of the Curie temperatures T_C (transition to ferromagnetism) and of the low-temperature ordered moments of these uranium monochalcogenides (Schoenes et al. 1996, Bourdarot et al. 1997, Bourdarot et al. 1999) as they are driven by alloying from ferromagnetic ordering to nonmagnetic behavior. Based on this success, we have since been able to recognize the role of a weakening hybridization and increasing entropy in driving that transition in reverse, that is, from a strongly correlated, extremely narrow band state (sometimes characterized as enhanced-mass or heavy-fermion behavior) to a state of spatially disordered localized magnetism (coupled magnetic ions). The latter ferromagnetic phase is an RLFS solid-solution-like phase with two types of sites, one of which (ortho) has large ordered moments and the other (para) is hybridizing and drives the magnetic coupling between the ortho sites.

In the absence of magnetic ordering, but at sufficiently high temperature, the same weakening hybridization and increasing entropy drive the phase transition between the correlated narrow-band 5f bonding state that stabilizes monoclinic α -plutonium and the RLFS solid-solution-like phase characterizing fcc δ -plutonium. We will discuss how this phase transition comes about and how the fcc δ -phase is stabilized at room temperature and below by the addition of trivalent additives such as gallium. In addition, we will discuss the relationship of this phase transition to the depression of melting temperature in plutonium.

Behavior of 5f Electrons in the Hybridizing Regime

To treat the 5f electron behavior of the light actinides, we focus on the regime in which the 5f electrons are not significantly influenced by direct overlap with 5f electrons from other sites. In this case, the role of the 5f electrons is determined by the hybridization of each such electron with band electrons of non-5f atomic origin, as constrained by the Coulomb exchange interaction with those band electrons and as diminished by the Coulomb repulsion with the other on-site 5f electrons. To treat such a situation, one can derive a model Hamiltonian describing 5f electrons that interact with non-5f band electrons (Sheng and Cooper 1994a). In this Hamiltonian, some of the quantities can be matched to the output of a standard band calculation that uses a linear muffin-tin orbitals (LMTO) method within the local density approximation (LDA). The other quantities can be calculated separately, using the information given by a combination of several LMTO band calculations. In Equations (1a)–(1c), H_0 is the Hamiltonian without interactions between non-f band and f electrons, and H_1 describes the interactions between non-f band and f electrons.

$$H = H_0 + H_1 , \quad (1a)$$

$$H_0 = \sum_k \varepsilon_k b_k^\dagger b_k + \sum_{Rm} E_f c_m^\dagger(R) c_m(R) + \frac{U}{2} \sum_{R, m \neq m'} n_m(R) n_{m'}(R) , \quad \text{and} \quad (1b)$$

$$H = H_0 + H_1 , \quad (1c)$$

In H_0 , Equation (1b), the first term is the non-f band energy and comes directly from the LDA calculation; the second term is the f state energy, which can be calculated indirectly from the LDA; and the third term is the intraatomic f-f Coulomb interaction, a two-electron correlation-energy interaction, which can also be calculated indirectly from the LDA. The first term in H_1 is the LDA hybridization between the non-f band and f electrons; and the second term is the Coulomb exchange interaction between the non-f band and f electrons. Refer to Sheng and Cooper (1994) for the treatment of this two-electron interaction in the almost-atomic-like limit.

Finding the ground state of this Hamiltonian is a truly formidable problem because we have included two two-electron terms—the f-f Coulomb interaction and the non-f band to f electron Coulomb exchange. The on-site f-f Coulomb interaction itself presents great difficulties, but those are increased manifold if we take into account the two-electron nature of the Coulomb exchange interaction.

Ortho/Para Fine Structure and the Cerium Analogue. To consider the relevance of this physics to the phase transitions of elemental plutonium, we first briefly review the most obvious analogue in the periodic table, the atomic volume collapse from the fcc γ - to the fcc α -phase of elemental cerium on cooling at moderate pressures. That isostructural transition in cerium entails an atomic volume decrease of about 17 percent (Koskenmaki and Gschneider 1978), similar to the atomic volume decrease of about 18.5 percent in the transition between δ - and α -plutonium (Donohue 1982).

In proposing their Kondo volume-collapse model of the cerium transition, Allen and Martin (1982) pointed out the difficulty of explaining the large atomic-volume change involved while at the same time accounting for the atomic-like form factors and other behavior observed experimentally for both cerium phases. In our model for the ground state of either cerium or plutonium, the correlated narrow 5f band in the α -phase has a fine structure of nonmagnetic (para) and magnetic (ortho) subbands imposed by the exchange symmetry of the correlated-electron dynamics. Local probes then see the para or ortho spectral densities (which are atomic-like, or very narrow in energy), but the atomic-volume changes are governed by the cohesive energy associated with the entire 5f spectral width. In both the Kondo model mentioned before and the lattice-periodic Mott transition (Georges et al. 1996), the entropy difference driving the α - to γ -transition in cerium depends on the difference in electronic entropy between an almost-localized and a fully localized lattice-periodic state. In our model, the transition is from a low-temperature coherent (bonding) state to a high-temperature RLFS state, and it is driven by the additional entropy of mixing in a solid-state solution of para and ortho f sites, that is, a perfect mixture with homogeneous lattice disorder. The sum of this entropy¹ of mixing plus the entropy from the individual ortho and para sites is significantly larger than the conventional electronic entropy difference between lattice-periodic states with almost-localized and fully localized behavior.²

The existence of the ortho/para fine structure implies a small energy scale associated with thermodynamics and a large energy scale associated with the primary electronic interactions (Fermi energy, occupied 5f spectral width, f-f correlation energy U , and one-electron hybridization potential). The correct small energy scale of the

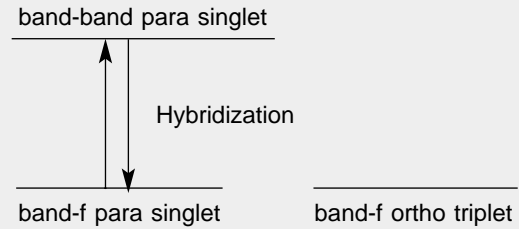
¹ As discussed below, the transition to this solid-solution-like state is driven by Anderson localization which is physically equivalent to Mott localization for a disordered system (Mott 1980, Mott 1990).

² Depending on the degree of f localization (for example, cerium versus plutonium vs uranium in the same chemical environment), exchange tends to homogenize the para and ortho behavior, and we anticipate there being considerable homogenization for elemental cerium. We will not discuss elemental cerium further but note that Laegsgaard and Svane (1999) have investigated the Kondo volume-collapse model very thoroughly by a combination of the self-interaction-corrected LDA and the Anderson impurity model. They could explain the α - to γ -transition only by assuming an ad hoc rescaling of the hybridization parameters and concluded that better understanding of the hybridization function is needed.

Hybridization in the RLFS Phase of the Weak Hybridization Regime

As defined in this diagram, the two-electron antisymmetrized states at each site in the lattice are the band-5f para singlet ground state, the band-5f ortho triplet ground state, and the band-band para singlet excited state. (Itinerancy quenches orbital moments, and so there is no band-band ortho state.) The band-f para singlet hybridizes with the band-band para singlet whereas the ortho triplet cannot hybridize with the band-band singlet because hybridization conserves (does not mix) spin. This lattice of two-electron antisymmetrized states is analogous to a lattice of helium atoms in which the atomic-helium ordering of the low-lying

Energy Levels of RLFS Phase



energy levels is inverted (the helium-like para ground-state singlet becomes an excited state). The situation shown is for the Hartree-Fock approximation corrected for two-electron correlations to lowest order in band-f hybridization. In this approximation, the hybridization interaction drives the singlet (para) component of the 5f contribution to the two-electron spectral density to fluctuate between configurations differing by one 5f electron. A large-scale calculational scheme, incorporating multiple-scattering effects, which has been designed to predict the Anderson localization will effectively include all orders of hybridization and will yield wave functions more complicated than the simple antisymmetrized products shown.

Properly Antisymmetrized Two-Electron States

$$\text{Band-f para singlet} = [\text{band}(\mathbf{r}_1) f(\mathbf{r}_2) + f(\mathbf{r}_1) \text{band}(\mathbf{r}_2)] [\uparrow(1)\downarrow(2) - \downarrow(1)\uparrow(2)]$$

$$\text{Band-band para singlet} = [\text{band}(\mathbf{r}_1) \text{band}(\mathbf{r}_2) + \text{band}(\mathbf{r}_1) \text{band}(\mathbf{r}_2)] [\uparrow(1)\downarrow(2) - \downarrow(1)\uparrow(2)]$$

$$\text{Band-f ortho triplet} = [\text{band}(\mathbf{r}_1) f(\mathbf{r}_2) - f(\mathbf{r}_1) \text{band}(\mathbf{r}_2)] \times \left\{ \begin{array}{l} \uparrow(1) \uparrow(2) \\ \uparrow(1) \downarrow(2) + \downarrow(1) \uparrow(2) \\ \downarrow(1) \downarrow(2) \end{array} \right\}$$

ortho/para fine structure has been obtained in previous calculations (Wills and Cooper 1987, Wills and Cooper 1990).

Ortho and Para States Defined. The f to non-f band electron hybridization term in Hamiltonian H_1 , the first term in Equation (1c), consists of a linear combination of terms that destroy one f electron and create one non-f band electron or vice versa. To treat the correlated dynamics between these two electrons (the exact, instantaneous effects on motion caused by coupling via the interelectronic Coulomb interaction), we must calculate two-electron matrix elements using exchange-symmetrized two-electron wave functions, as one does for the helium atom. Recall that these two-electron wave functions have two possible forms, which we call para and ortho. The first is a product of a symmetric (para) two-electron orbital state and a two-electron spin singlet (which is antisymmetric on exchange of electrons); the second is a product of an antisymmetric (ortho) two-electron orbital state and a two-electron spin triplet (which is symmetric on exchange of electrons). Refer to the box above for the form of such states.

As long as the hybridization is treated as acting between two-electron wave functions that are antisymmetric under exchange, the effects of exchange can be

incorporated adequately through the one-electron exchange-correlation potential provided the electrons in the system are not too close to being fully localized. This very substantial simplification allowed us both to develop a calculational technique for the magnetic ordering of a class of uranium compounds and to recognize the mechanisms controlling the phase-transition sequence in elemental plutonium. This development incorporates what was learned from the work of Wills and Cooper (1987) and Sheng and Cooper (1994) on the weakly hybridizing more-atomic-like cerium compounds. Our technique has been very successful in predicting the magnetic ordering behavior of the uranium monochalcogenides, which have sodium chloride crystal structure, under high pressures (to about 20 gigapascals) and under certain uranium-dilution-alloying changes, which are described later. This predictive power led us to apply the same theory and physical picture to elemental plutonium and its stabilization into the fcc structure.

In the weak hybridization regime, the hybridization process can be correctly and usefully pictured if one thinks of a lattice of helium (two-electron) atoms, in which the usual order of the low-lying atomic-energy levels is inverted (see the box on the opposite page). That is, the atomic ground states in this lattice have both s-5f para singlet and s-5f ortho triplet two-electron components, and the excited state is a doubly s-occupied para singlet. The s-like part of these two-electron wave functions comes from the virtual occupation of this state by p and d band electrons that have lost their p and d orbital character through itinerancy (Van Vleck 1932, Kittel 1996).

From Equation (1c), we can see that hybridization conserves spin (does not involve spin) and thus acts only between the excited s-s para singlet and the ground state s-5f para singlet. Thus, to the lowest order, the hybridization interaction drives the singlet (para) component of the 5f contribution to the two-electron spectral density to become itinerant, that is, to fluctuate between configurations differing by one 5f electron. The triplet (ortho) component remains localized—that is, it has a stable configuration (see the box on the opposite page). In fact, this description corresponds to the resonant scattering physics of the Coqblin-Schrieffer (1969) treatment of hybridization.

In the sufficiently weak hybridization regime, the 5f behavior viewed locally at a given site is one of two types: (1) totally localized (ortho) and therefore capable of having a large (free-ion-like) orbital contribution to an ordered magnetic moment (and because of strong spin-orbit coupling, a large spin contribution as well) or (2) fluctuating between f^4 and f^5 (para), and thereby providing an itinerant 5f component that can pass a hybridization-mediated message of orbital magnetic polarization between the localized 5f sites. Thus, magnetic ordering with a large orbital contribution can occur in the weak hybridization regime.

The localized sites are randomly distributed on the lattice, and this disorder supplies a source of entropy, which at sufficiently high temperature stabilizes this RLFS phase. That is, it sufficiently lowers the free energy, $F = U - TS$, to compensate for the loss of 5f bonding energy even in the absence of magnetic ordering. In the RLFS phase, the 5f electronic contribution to the entropy is analogous to the configurational entropy in a random alloy. As the hybridization strengthens or as the temperature drops (especially in the absence of magnetic ordering), the 5f electrons abruptly delocalize to a narrow correlated 5f-band phase because the increase in 5f bonding more than compensates for the loss of the electronic-entropy and possible magnetic-ordering contributions to the free energy.

The RLFS Phase in Uranium Monochalcogenides. This physical picture, which we apply to the structural phase transition and melting behavior of plutonium, was inspired by our remarkably successful predictions of magnetic ordering in a class of uranium compounds. For several years, we realized that there are two subregimes of hybridizing f electron behavior: a very weak regime associated with localized magnetic (ferromagnetic) ordering (Sheng and Cooper 1994, Sheng et al. 1994) and

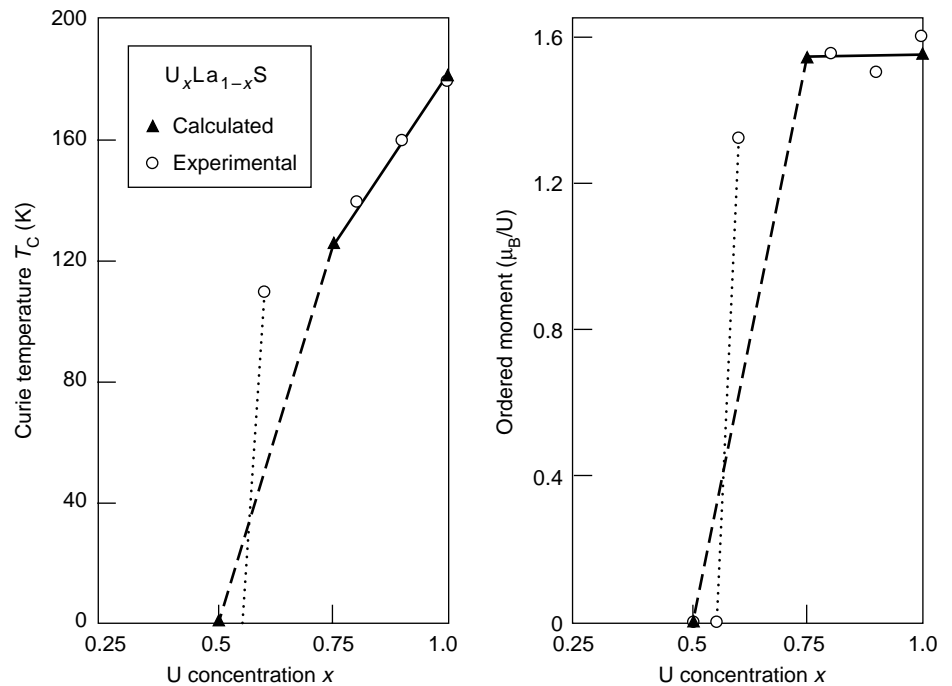


Figure 2. Calculated and Measured Ferromagnetic-Ordering Temperatures and Low-Temperature Ordered Moments of a Uranium Compound with f Dilution Alloying These plots illustrate the extraordinary absolute agreement between predictions and experiment for the magnetic behavior of the uranium monochalcogenides. In materials such as the uranium-sulfur compound US, both pressure and dilution alloying (substituting a lanthanum for a uranium atom) increase the hybridization of the 5f band with the p/d band, which drives the 5f electrons from the well-localized ortho (stable f configuration) to the itinerant (rapidly fluctuating f configuration) para two-electron states. Lanthanum and yttrium are chemically very similar and close in size to uranium but do not have partially filled f shells. Thus, their substitution for uranium in a system such as $U_xLa_{1-x}S$ increases the hybridization of each of the f electrons in the remaining uranium atoms. The analogy to dissolving a solute (the uranium 5f electrons) in a solvent (the band electrons of non-f atomic parentage) to form a solution may be useful in picturing this situation. In effect, one is decreasing the amount of solute while keeping the amount of solvent the same, and the mixing is provided by the hybridization. This increase of hybridization gives a decrease in the low-temperature ordered moment, and interestingly, we expect a correspondingly enhanced Pauli paramagnetism. That enhancement has been observed (see Figure 4). (Reproduced with permission from the American Physical Society, J. Schoenes, *Phys. Rev. B*, 53 (22), 1996.)

a weak regime (Sheng and Cooper 1995) associated with heavy-fermion, or enhanced-mass (narrow-band), behavior. In Figure 3(a), we show the calculated and measured decrease in T_C (the temperature for the transition to ferromagnetism) of the uranium compound $U_xLa_{1-x}S$, as lanthanum is added to the alloy. As explained in the caption, this dilution of uranium by lanthanum increases the f electron hybridization because the number of f electrons, “the solute,” decreases, while the number of non-f band electrons, “the solvent,” remains the same. Figure 3(b) shows the calculated and measured low-temperature ordered moment of $U_xLa_{1-x}S$. Only recently (Cooper et al. 1999) have we realized that, as the lanthanum content decreases below 45 percent, the weakening of f electron hybridization induces the type of Anderson localization described in this article. In this uranium compound, magnetic ordering enhances the localization process, and it drives the system from a narrow-f-band

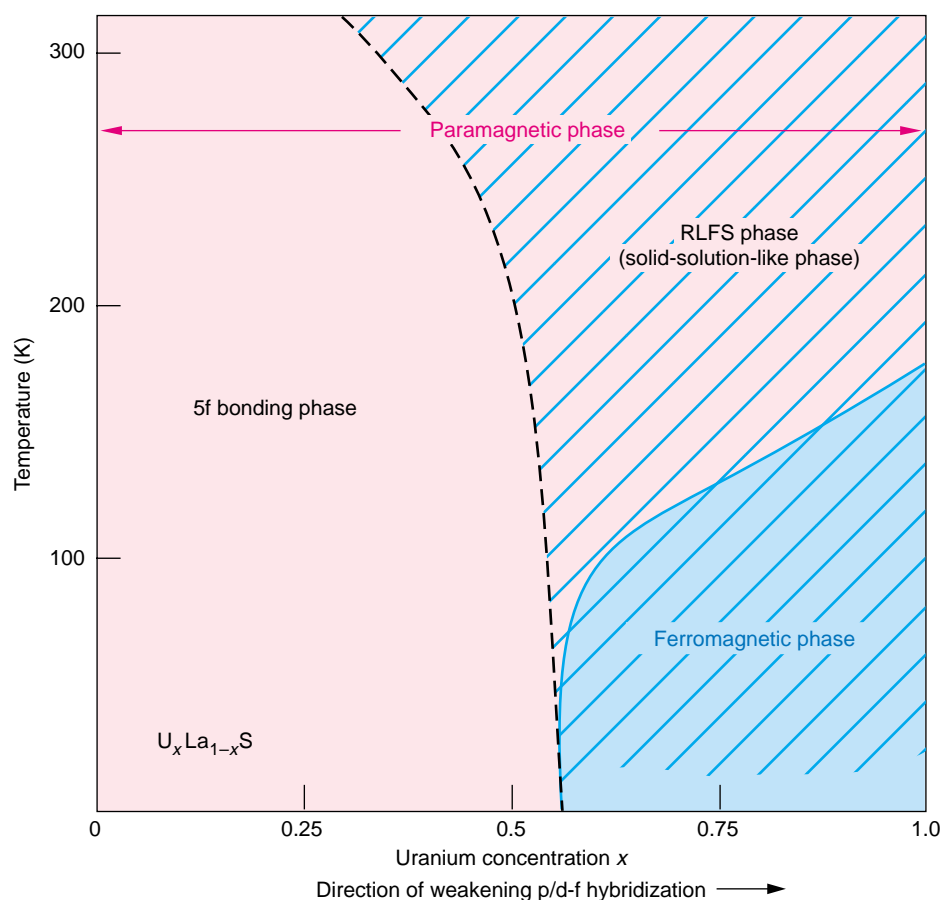


Figure 3. Schematic Representation of the Phase Diagram of $U_xLa_{1-x}S$
 The RLFS phase is the hatched area to the right of the dashed curve. The blue curve separates the ferromagnetic phase from the paramagnetic phase. As the uranium concentration increases from left to right, the hybridization of the f electrons decreases, and the system becomes partially localized in an RLFS phase.

paramagnetic bonding phase to a strongly ferromagnetic partially localized (RLFS) phase.

To clarify the analogy between this phase transition and that in plutonium, in Figure 3, we show a schematic representation of the $U_xLa_{1-x}S$ phase transition. We consider the behavior from left to right, that is, as hybridization between the f electrons and the p and/or d band electrons decreases (and uranium concentration increases). At the left, this material is in a 5f bonding phase. As hybridization decreases, this material goes through a magnetic-ordering-enhanced Anderson localization of the 5f electrons to the RLFS solid-solution-like phase. This process can be wholly self-induced, as described below for elemental plutonium.

Once an Anderson localization occurs, it is energetically favorable to develop the maximum entropy. Thus, to have a phase transition at a sufficiently high temperature in the absence of magnetic ordering, there is an abrupt localization at half the lattice sites occupied by the light actinide. If magnetic ordering occurs, this abrupt localization can occur at more than half of these randomly located lattice sites.

Magnetic Susceptibility in the RLFS Phase. The Curie temperature T_C and the ordered-moment behaviors of the uranium monochalcogenides shown in Figures 2(a) and 2(b) are appropriate for the RLFS phase. Those compounds, other magnetically ordered actinide materials, and δ -plutonium (which does not have magnetic ordering) share the experimental signature of the RLFS phase, namely, a high-temperature magnetic susceptibility (χ) that has both Curie-Weiss and enhanced Pauli contributions (Schoenes et al. 1996, Méot-Reymond and Fournier 1996).

$$\chi = \chi_{CW} + \chi_{\text{Pauli}} \quad (2a)$$

$$\chi_{CW} = \frac{C}{T - \theta_p} \quad , \text{ and} \quad (2b)$$

$$\chi_{\text{Pauli}} = \chi_0 \left\{ 1 - \frac{\pi^2}{12} \left(\frac{k_B T}{E_F} \right)^2 \right\} \quad (2c)$$

Equation (2b) gives the typical inverse temperature dependence of the Curie-Weiss susceptibility, which is due to localized moments. Equation (2c) consists of the typical temperature-independent Pauli susceptibility characteristic of itinerant electrons (delocalized moments) and a T^2 term that depends on the Fermi energy and represents departures from free-electron behavior. (This temperature-dependent Pauli term could arise in our model if the number of para sites increases with temperature.) Figure 4 (reproduced from Schoenes et al. 1996) shows the inverse of the magnetic susceptibility versus temperature for the behavior of $\text{U}_{0.15}\text{La}_{0.85}\text{S}$.

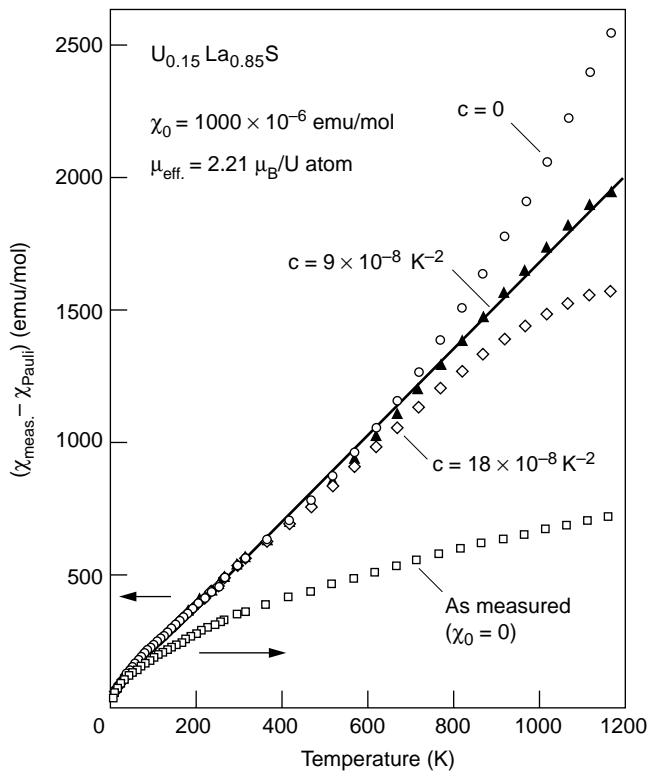


Figure 4. Inverse Susceptibility vs Temperature for $\text{U}_{0.15}\text{La}_{0.85}\text{S}$

A plot of the inverse of the measured susceptibility minus the Pauli susceptibility should yield the straight line characteristic of standard Curie-Weiss behavior. The plot for $\text{U}_{0.15}\text{La}_{0.85}\text{S}$ (reproduced with permission from *Physical Review B*) shows several fits obtained by varying the coefficient of the T^2 term in the Pauli susceptibility, Equation (2c). That coefficient is labeled c in the plot. A nonzero value of c yields the straight line (best) fit, implying an enhanced Pauli contribution to the susceptibility.

That behavior is typical of the susceptibility of magnetically ordered actinide materials, and the best fit to the data indicates an enhanced Pauli term. Figure 5 is a plot of the susceptibility (rather than its inverse) and is reproduced from Méot-Reymond and Fournier 1996. This plot shows a similar behavior for cerium-stabilized δ -plutonium.

For spatially disordered systems, the Anderson and Mott views of the localization process become equivalent. In the Anderson view, if the presence of impurities at random sites of an otherwise perfectly periodic lattice provides sufficiently strong scattering, the integrated intensity of a wave initiated at some starting point becomes localized within some finite distance. In the present context, we can regard the narrow correlated 5f band in the 5f bonding regime as such a wave. If we assume that the 5f electrons become localized on some actinide atoms randomly located on the lattice, the difference in the core (nucleus plus nonvalence electrons) potential caused by the presence of those localized 5f electrons can provide a scattering center for the wave composed of the itinerant 5f electrons. (That is, the departure from a charge density with lattice periodicity scatters the itinerant charge density.) The scattering strength for each such site is diminished by the screening provided by the band electrons of p and/or d atomic origin, and the hybridization of p and/or d band electrons with f electrons is a measure of that screening strength. As the hybridization weakens, the screening does too, and the scattering becomes stronger, favoring the localization, which in turn provides the scattering that causes the localization. In the Mott view of localization, one focuses on the events in the vicinity of one lattice point. As the hybridization and, hence, the screening of the site-centered potential weaken (in effect, the dielectric constant decreases), the site-centered potential becomes more binding. When the hybridization of p/d band electrons with f electrons weakens below a critical value, the 5f states become bound; that is, the 5f electrons localize. Thus, weakening hybridization, whether viewed as providing stronger random scattering of 5f band electrons or weaker

screening and hence stronger local binding, ultimately leads to 5f localization at random sites.

It is reasonable to expect that such a situation occurs fairly easily in a narrow-band situation. The banding comes from the hybridization-mediated overlap of orbitals that originate from the periodic array of atomic sites. As disorder develops, it causes the energy levels of the individual atoms to vary randomly from site to site. Atoms with energies near the average-band energy are more likely to have at least some neighbors of similar energy to overlap (bond) with, whereas atoms with energies more toward the band's edges are more likely to be isolated from their neighbors. Thus, the narrowing proceeds toward the band average more and more precipitously as the disorder (and hence the narrowing) increases. Hence, a phase transition occurs. Clearly, starting with a narrower band favors the ease with which localization occurs.

If we go in the opposite direction—from a very weak to a less weak 5f hybridizing subregime—we see that coherent behavior develops and leads to narrow correlated bands. By including two-electron correlations, one imposes a nonmagnetic (singlet) and magnetic (triplet) substructure on the already narrow 5f (or 4f for cerium) bands, but any ordered magnetism will be much weaker than in the RLFS solid-state-solution (“random-alloy”) phase. Numerous behaviors are possible, depending on the narrowness of the 5f bands and the singlet or triplet subbands. One extreme is the heavy-fermion regime. As shown in Sheng and Cooper (1995) and Cooper et al. (1997), the characteristic enhanced electronic-specific-heat and Pauli susceptibility behavior in our treatment of this regime occurs with the correct energy (temperature) scale. In addition, as shown in Sheng and Cooper (1995), the division into nonmagnetic and magnetic subbands, which may be overlapping or nonoverlapping, and their placement relative to the Fermi energy (chemical potential) provide a range of Wilson ratio behavior in agreement with experiment for a substantial number of heavy-fermion systems.

In treating thermodynamic behavior for heavy fermions, the extreme narrowness of the magnetic-nonmagnetic subbands means that one must take into account the temperature dependence of the Fermi energy. In elemental plutonium, the 5f band is sufficiently narrow to favor a very low symmetry structure such as the monoclinic α -structure (see the article “Actinide Ground-State Properties” page 128 for details), but the hybridization of the non-f band with the 5f band electrons is sufficiently strong to give a somewhat broader 5f band than is necessary for characteristic heavy-fermion phenomenology.

Entropy Generation and Self-Induced Anderson Localization

If $E_{f \text{ bond}}$ denotes the f electron contribution to the bonding energy per atom (measured in millirydbergs, where 1 millirydberg = 158 kelvins in temperature equivalent), then the temperature at which we would observe self-induced Anderson localization to the RLFS phase, considering only the entropy change from the site disorder, is given by

$$T_{A \text{ loc}} \approx \frac{158 E_{f \text{ bond}}}{\ln 2} \approx 228 E_{f \text{ bond}} . \quad (3)$$

In other words, at this temperature, the loss of bonding energy per atom would be balanced by the increase in entropy per atom (which is equal to $\ln 2$ for the transition to the RLFS phase because each atom now has two possible states—ortho or para). If magnetic ordering occurred at temperatures above the temperature given in Equation (3), then it would be favorable for localization to occur (the free energy

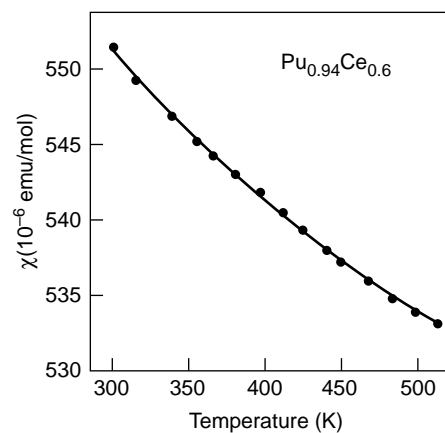


Figure 5. Susceptibility vs Temperature for the Plutonium-Cerium Alloy $\text{Pu}_{0.96}\text{Ce}_{0.6}$

The fit through the data points, which was calculated with Equation (2), suggests that this plutonium alloy also exhibits an enhanced Pauli paramagnetism.

(This graph is reproduced with permission from the *J. Alloys and Compounds* 123, S. Méot-Reymond, “Localization of 5f Electrons in Delta-Plutonium: Evidence for the Kondo Effect, page 122, Copyright 1996, Elsevier Science.)

would be minimized) at a lower temperature. That is, magnetic-ordering enhancement of the f electron localization will occur provided the f bonding energy is not too high. In the case of plutonium, it is apparently too high, and therefore the localization temperature will be too high for magnetic ordering and the consequent magnetic-ordering enhancement of the localization.

Stabilization of fcc Plutonium

We are saying that the transition of pure plutonium to the low-density δ -phase at 592 kelvins is due to a self-induced Anderson localization of the 5f electrons driven by the configurational entropy of a random distribution (solid solution) of ortho (stable) f^5 and para (fluctuating between f^5 and f^4) plutonium sites. Equation (3) predicts that this transition at 592 kelvins corresponds to a loss of 2.6 millirydbergs in 5f bonding energy per atom, which falls at the expected value. This value is about 1 percent of the total cohesive energy of 255 millirydbergs per atom of plutonium (Brooks et al. 1984).

It is well known that δ -plutonium becomes stable down to low temperatures by the addition of small amounts of a trivalent IIIB additive such as gallium. (See Figure 6 for a schematic drawing of the phase-transition behavior of plutonium on alloying with small percentages of gallium.) The randomly located additive species atoms presumably provide sufficiently strong scattering (and therefore decreased hybridization) to lower the transition into the RLFS phase to a temperature below room temperature.

A possible way to quantify the distribution between para and ortho plutonium as a function of gallium content is based on the prediction that an increase in hybridization (with a consequent increase in the number of para sites) would lead to a decrease in the low-temperature ordered moment for certain magnetically ordered compounds. That decrease would correspond to an increase in the Pauli paramagnetic component³ of the paramagnetic susceptibility above T_c (see Figures 4 and 5). This quantitative correspondence between the increase in Pauli susceptibility and the decrease in ordered moment is currently being experimentally validated for a number of magnetically ordered uranium compounds. If it is indeed validated, we will be justified in using measurements of the susceptibility of gallium-stabilized fcc plutonium with varying gallium contents as a way to quantify the distribution between the para and ortho configurations of plutonium. One would expect that the Curie-Weiss component of susceptibility (the number of ortho sites) would increase with gallium content because, as explained next, the hybridization weakens with increasing gallium content.

The effect of alloying in the uranium-sulfur compound US is quite different than that in plutonium because pure US is ferromagnetic. It already has an ortho-para mixture at low temperatures, and the disordered distribution of the ortho 5f sites provides the “imperfections” that prevent the overall propagation of banding 5f waves. Thus, the effect of substituting lanthanum for uranium in US is to dilute the 5f electrons of uranium and, as explained in the caption to Figure 2(a), thereby strengthen hybridization.

In elemental plutonium, the 5f bonding energy is sufficiently high for the transition to the RLFS phase to occur in the absence of magnetic ordering. At zero temperature, all plutonium sites are in the para configuration, and the ground state is the monoclinic α -structure stabilized by 5f bonding. The 5f banding, associated with the 5f bonding, is mediated by hybridization with the plutonium 6d band (valence) electrons originating from other plutonium sites. This process gives rise to a narrow

³ The Pauli component can be separated from the Curie-Weiss component by the kind of fitting shown in Figure 4.

5f band with a consequent high density of states at the Fermi energy. Almost invariably in such a narrow band (high density of states—“almost degeneracy” at the Fermi level), the lowering of the free energy will favor some sort of Jahn-Teller distortion in order to break the degeneracy. (In δ -plutonium, elastic forces stabilize the degeneracy inherent in the fcc structure.) However, at $T = 0$, the system still has to choose the most favorable distortion, and that, presumably, in the case of the low-symmetry monoclinic α -plutonium structure reflects the directionality of the weak 5f bonding (Söderlind et al. 1997).

Why Hybridization Decreases when Gallium Is Added to Plutonium.

The effect of gallium substituting for plutonium in elemental plutonium is quite different from that of lanthanum or yttrium substituting for uranium in the uranium monochalcogenides. When lanthanum or yttrium substitutes for uranium, the valence d electrons from the lanthanum (5d) or yttrium (4d) simply blend into the hybridizing d band formed from the uranium 6d valence electrons. Thus, one has an essentially unchanged band solvent containing less uranium 5f solute, and the effect is to increase the d band hybridization per 5f electron of uranium, giving 5f delocalization as the dominant effect. On the other hand, for gallium substituted in plutonium, the valence 4p electrons from the gallium compete with the plutonium 5f electrons to hybridize with the band electrons originating from the plutonium 6d electrons. This competition not only effectively decreases the 6d hybridization per 5f electron of plutonium, but it also provides a severe disordered disruption of the 6d-mediated 5f banding. In this way, the 5f electrons become localized. Indeed, the disruption of plutonium-to-plutonium 6d-mediated 5f bonding is sufficiently great for even the vestigial 5f bonding (5f contribution to the cohesive energy) preserved by magnetic ordering not to be present.

Because alloying has a highly nonlinear effect in driving the restructuring of the ground state, the nucleation of localized sites by the addition of gallium is likely to create an avalanche effect, in which stable f^5 (ortho) plutonium sites form at random locations and further break up the f bonding coherency between the fluctuating f^5/f^4 plutonium (para) sites. The extended x-ray absorption fine structure (EXAFS) and x-ray diffraction work of Faure et al. (1996) provides both gallium-plutonium and plutonium-plutonium interatomic distances as the gallium content varies between 1.89 and 10.43 atomic percent (at. %). The gallium-plutonium bond length is always shorter than the plutonium-plutonium bond length, but the difference between them has a minimum near or at 7.7 at. % gallium corresponding to one gallium atom for every 12 plutonium atoms (see Figure 7). Faure and coworkers state that they cannot understand why there is then a substantial increase in bond shortening (that is, a decrease in the gallium-plutonium bond length relative to that of plutonium-plutonium) in going from 7.7 to 10.4 at. % gallium. The avalanche effect might provide an explanation because it reinforces the effect of the gallium nucleation centers in breaking up the plutonium-plutonium bonding. The stabilizing effect per gallium atom depends both on diminishing the hybridization and on breaking up the coherency of the plutonium-plutonium bonding. Thus, as the increase in gallium concentration decreases the coherent hybridization per plutonium atom, a threshold for the spontaneous generation of stable localized f^5 plutonium sites is reached. (At this point, spontaneous, strong magnetic ordering would occur if the gallium sites were not interfering with the magnetic coupling between the plutonium sites.) We suggest that adding gallium beyond 7.7 at. % leads to the formation of the ortho sites and the further stabilization of the system.

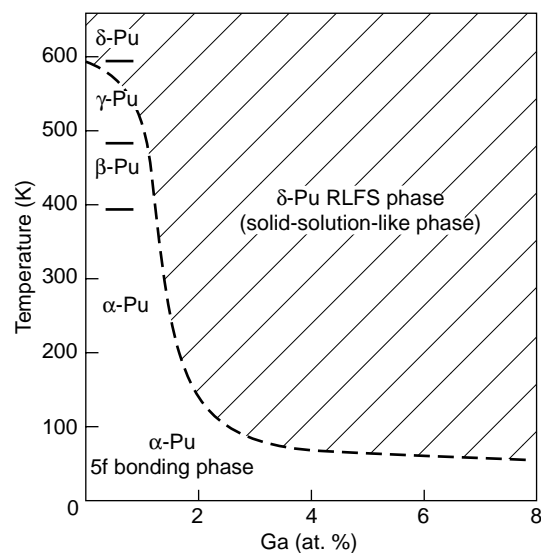


Figure 6. Schematic Representation of the Phase Diagram for Plutonium-Gallium Alloys

As the gallium concentration increases, the hybridization of the f electrons in the narrow f band of α -plutonium decreases. The result is self-induced Anderson localization, producing the partially localized RLFS phase (hatched area) in the higher-temperature phases of plutonium.

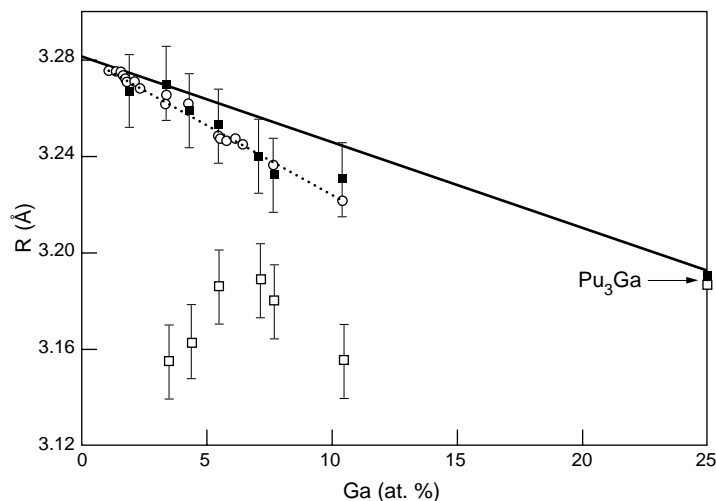


Figure 7. Interatomic Distances for Plutonium-Gallium Alloys in the δ -Phase

These data for plutonium-plutonium and plutonium-gallium bond lengths were obtained with two complementary techniques: x-ray absorption spectroscopy (EXAFS) and x-ray diffraction. The behavior of the ordered compound Pu_3Ga is also shown. A Vegard's law linear plot is shown for comparison. The shortening of the plutonium-gallium bond length at gallium concentrations beyond 7.7 at. % may be explained by the formation of ortho sites in an RLFS phase.

(This graph is reproduced with permission from the *Journal of Alloys and Compounds* 123, P. Faure et al., "Lattice Collapse around Gallium in PuGa Alloys as Revealed by X-Ray Absorption Spectroscopy," page 131, copyright 1996, Elsevier Science.)

The Depressed Melting Temperature of Plutonium.

How does this physics relate to the anomalous melting behavior of plutonium and neptunium? The melting temperature of plutonium is 913 kelvins and of neptunium, the element immediately preceding plutonium in the periodic table, is 912 kelvins. These temperatures are depressed by 500 to 600 kelvins relative to those of the immediately neighboring uranium and americium. And they are depressed by a significantly larger amount relative to the melting temperatures of the other actinides. Sublimation corresponds to a full debonding—that is, the coherent bonding (delocalization) of the valence and transition-shell electrons in the solid is destroyed. Thus, to the extent that the melting behavior reflects the behavior expected for sublimation, one could think of melting as the phase transition associated with Anderson localization

because the heating of a solid generates a sufficient number of imperfections to provide the critical strength of scattering. The RLFS phase transition corresponds to the part of the melting provided by the loss of 5f bonding. Because the temperature for the transition

to δ -plutonium corresponds to the configurational entropy gain necessary to counterbalance the 5f bonding, that temperature (592 kelvins) should also correspond rather closely to the depression of the melting temperature. (Having the disorder provided by the ortho-para solid solution means that correspondingly fewer additional thermally induced lattice defects are required for the overall-melting Anderson localization. The transitions to the monoclinic β -phase at 395 kelvins and to the orthorhombic γ -phase at 479 kelvins may be thought of as partial meltings of the 5f bonding.) If one adopts this picture for neptunium, one would have to view the transition from the orthorhombic α -phase to the tetragonal β -phase at 553 kelvins (in that transition, the collapse in the atomic volume is about 6 percent) as corresponding to the 5f melting. Presumably, the immediately neighboring uranium and americium have a much-smaller melting-temperature depression because they are sufficiently closer to full 5f delocalization and coherent 5f localization, respectively. Uranium would perhaps undergo a self-induced RLFS transition sufficiently close to the overall melting temperature so that one lowered phase-transition temperature occurs, rather than two distinctly different ones; and americium is probably in an RLFS phase over much of the temperature range below melting. ■

Acknowledgments

We have benefited from discussions of the data of F. Bourdarot, P. Burlet, and O. Vogt and appreciate their permission to quote their results. S. Beiden, L. Muratov, S. Mukherjee, O. Vogt, and H. A. Weldon provided valuable insights. Our association with Los Alamos through the Seaborg Institute and the Center for Materials Science provided invaluable support, especially through the contributions of A. C. Lawson, L. E. Cox, J. L. Smith, and M. F. Stevens. The U. S. Department of Energy (grant DE-FG07-97ER45671) supported the research on which this article is based.

Further Reading

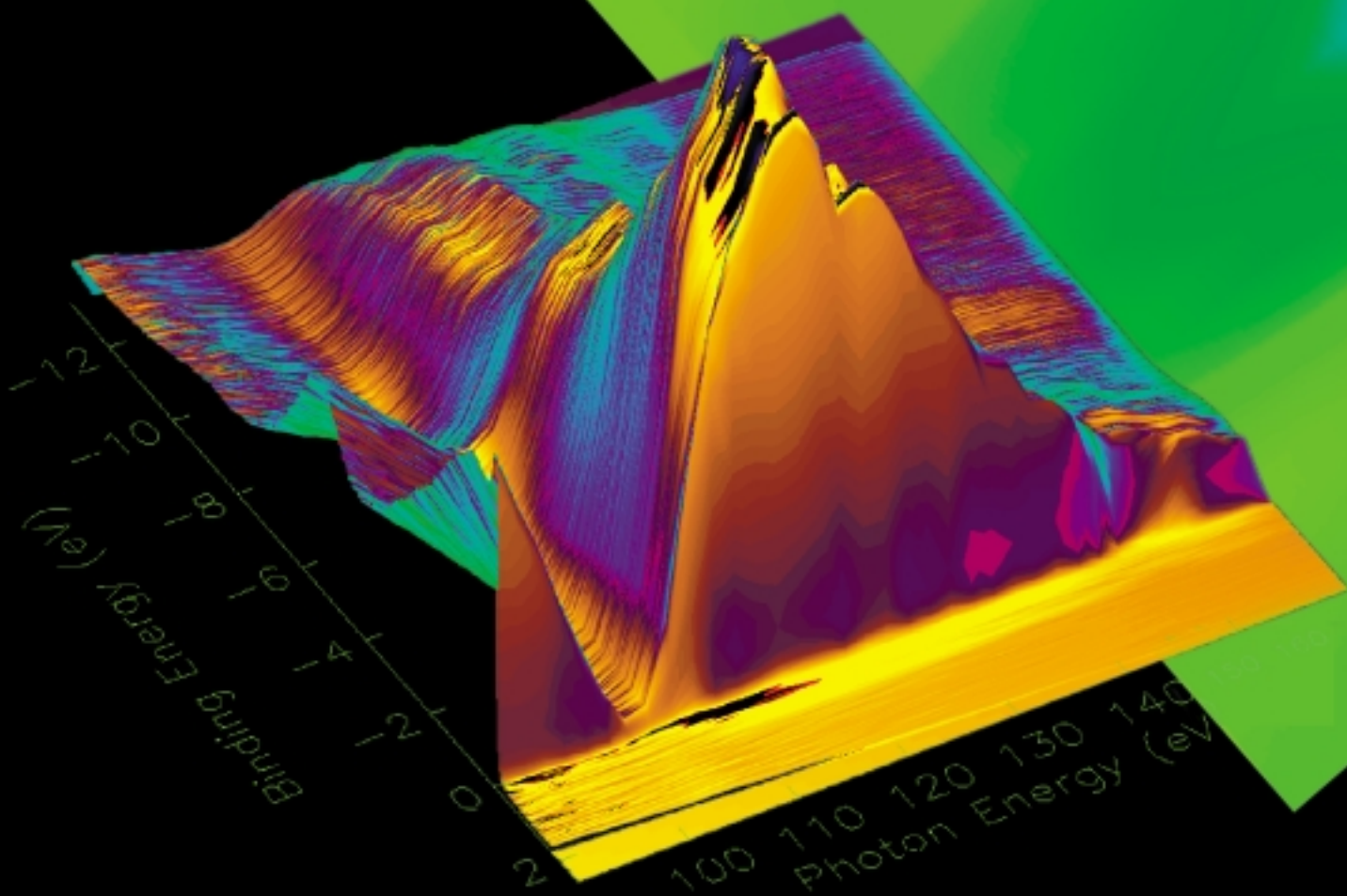
- Allen, J. W., and R. M. Martin. 1982. *Phys. Rev. Lett.* **49**: 1106.
- Anderson, P.W. 1958. *Phys. Rev.* **109**: 1492.
- Bourdarot, F., P. Bulet, R. Calemczuk, F. LaPierre, K. Mattenberger, and O. Vogt. 1997. *J. des Actinides*: 79.
- Bourdarot, F., A. Bombardi, P. Bulet, R. Calemczuk, G. H. Lander, F. LaPierre, J. P. Sanchez et al. 1999. *European Physical Journal B* **9**: 605.
- Brooks, M. S. S., B. Johansson, and H. L. Skriver. 1984. In *Handbook on the Physics and Chemistry of the Actinides*. Vol. I, p. 158. Edited by A. J. Freeman and G. H. Lander. Amsterdam: Elsevier Science Publishers.
- Cooper, B. R., and Y.-L. Lin. 1998. *J. Appl. Phys.* **83**: 6432.
- Cooper, B. R., Y.-L. Lin, and Q. G. Sheng. 1997. *J. Appl. Phys.* **81**: 3856.
- . 1999a. *J. Appl. Phys.* **85**: 5338.
- . 1999b. *Physica B* **176**: 259.
- Cooper, B. R., O. Vogt, Q.-G. Sheng, and Y. L. Lin. 1999c. *Phil. Mag. B* **79**: 683.
- Coqblin, B., and J. R. Schrieffer. 1969. *Phys. Rev.* **185**: 847.
- Donohue, J. 1982. In *The Structures of the Elements*. Malabar, FL: Robert E Krieger Publishing Co.
- Faure, Ph, B. Deslanders, D. Bazen, C. Tailland, R. Doukhan, J. M. Fournier, and A. Falanga. 1996. *J. Alloys and Compounds* **244**: 131.
- Georges, A., G. Kotliar, W. Krauth, and M. J. Rozenberg. 1996. *Rev. Mod. Phys.* **13**: 68.
- Kittel, C. 1996. *Introduction to Solid State Physics*. Seventh Edition. New York: John Wiley & Sons.
- Koskenmaki, D. C., and K. A. Gschneider, Jr. 1978. "Cerium", Chapter 4. In *Handbook on the Physics and Chemistry of the Rare Earths*. Edited by K. A. Gschneider, Jr., and J. Eyring. Amsterdam: North-Holland Publishing Co.
- Laegsgaard, J., and A. Svane. 1999. *Phys. Rev. B* **59**: 3450.
- Méot-Reymond, S., and J. M. Fournier. 1996. *J. Alloys and Compounds* **232**: 119.
- Mott, N. F. 1980. In *Encyclopedia of Physics*. Edited by R.G. Lerner and G.L. Trigg. Reading, MA: Addison-Wesley Publishing Co.
- . 1990. In *Encyclopedia of Physics*. 2nd Edition. Edited by R.G. Lerner and G.L. Trigg. New York: VCH Publishers.
- Schoenes, J., O. Vogt, J. Löhle, F. Hulliger, and K. Mattenberger. 1996. *Phys. Rev. B* **53**: 14,987.
- Sheng, Q. G., and B. R. Cooper 1994. *Phys. Rev. B* **50**: 965.
- . 1995. *Phil. Mag. Lett.* **72**: 123.
- Sheng, Q. G., B. R. Cooper, and S. P. Lim. 1994. *Phys. Rev. B* **50**: 9215.
- Söderlind, P., J. M. Wills, B. Johansson, and O. Eriksson. 1997. *Phys. Rev. B* **55**: 1997.
- Van Vleck, J. H. 1932. *The Theory of Electric and Magnetic Susceptibilities*. London: Oxford University Press.
- Wills, J. M., and B. R. Cooper. 1987. *Phys. Rev. B* **36**: 3809.
- . 1990. *Phys. Rev. B* **42**: 4682.

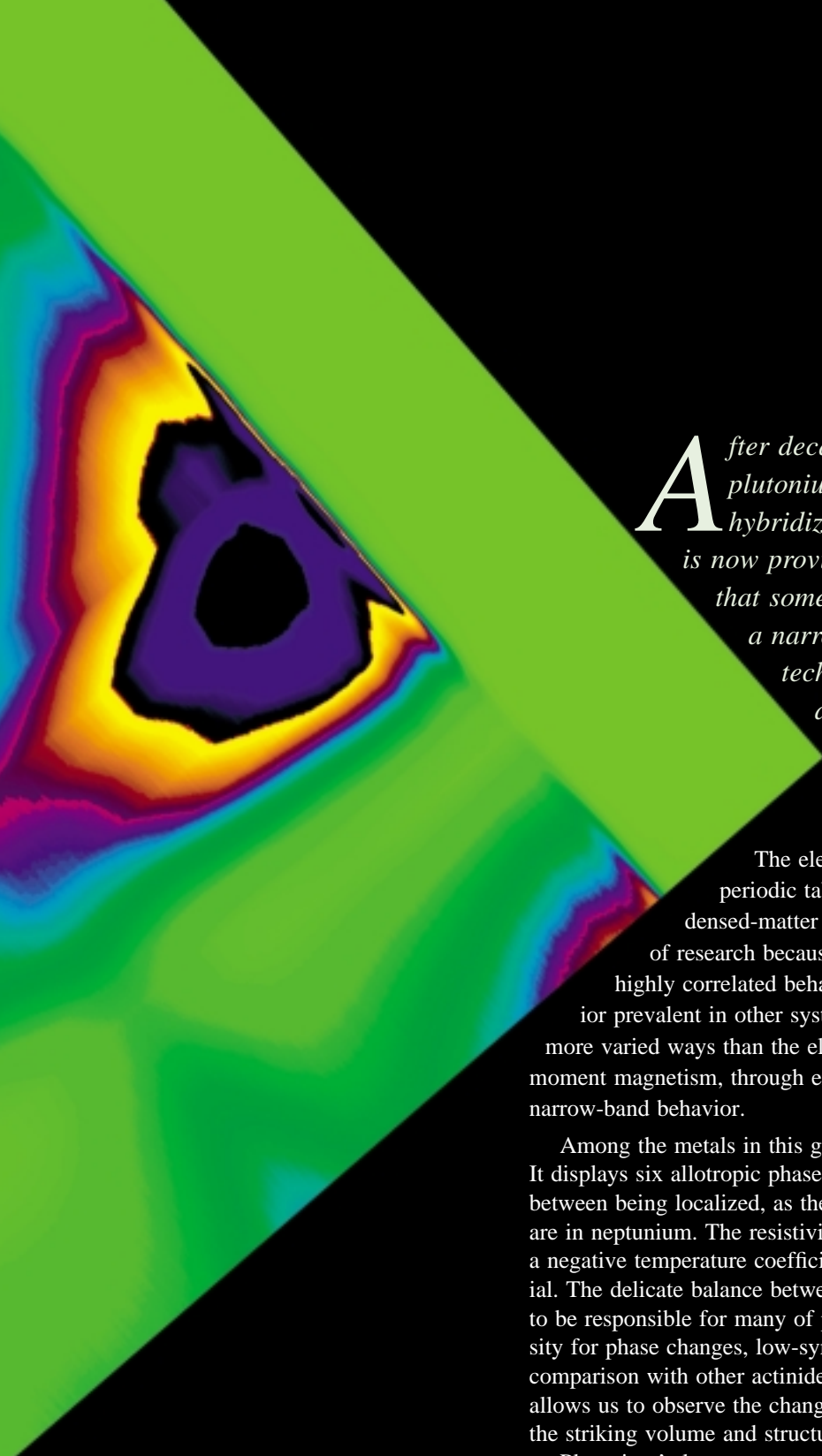


Bernard R. (Barry) Cooper received his B.S. and Ph.D. degrees in physics from the Massachusetts Institute of Technology (1957) and the University of California at Berkeley (1961), respectively. Cooper did postdoctoral studies at Harwell (John Hubbard's group) and Harvard. He started his collaboration with Los Alamos in 1982 and has been a consultant since then. Cooper is currently a Benedum Professor of Physics at West Virginia University. In 1976, he became the founding Chairman of the American Physical Society Committee on the International Freedom of Scientists. His research interests are in theoretical condensed-matter and materials physics, with special emphasis on magnetic behavior, electronic structure, surface and interface behavior, and diffusion and diffusion-controlled phenomena. Cooper authored and coauthored 250 or so publications, of which about 20 are on plutonium-based materials and many more on actinide or rare-earth systems. Cooper believes that δ -plutonium presents the most challenging problem in magnetic ordering. In his opinion, when one lowers the δ -phase stabilization temperature by alloying, chaos replaces the coherent wave propagation of the 5f component of the electronic structure occurring in the α -phase.

Photoelectron Spectroscopy of α - and δ -Plutonium

*Aloysius J. Arko, John J. Joyce, Luis A. Morales,
Jeffrey H. Terry, and Roland K. Schulze*





After decades of speculation about the role of plutonium's 5f electrons in bonding and hybridization, photoelectron spectroscopy (PES) is now providing the first detailed results indicating that some of the 5f electrons are itinerant and form a narrow conduction band. This measurement technique probes electronic structure directly and with great accuracy, defining a new path into the complex world of actinide behavior.

The electronic structure of the 5f series of metals in the periodic table represents a relatively unexplored area in condensed-matter physics. It is also one of the most interesting areas of research because the 5f electrons in all these elements tend toward highly correlated behavior as opposed to the independent-particle behavior prevalent in other systems. The 5f electrons in the actinides behave in more varied ways than the electrons in any other series of elements—from local-moment magnetism, through enhanced specific heat like heavy fermions, to narrow-band behavior.

Among the metals in this group, plutonium appears to be the most exotic. It displays six allotropic phases, and its 5f electrons are at the transition point between being localized, as they are in americium, and being delocalized, as they are in neptunium. The resistivities of both α - and δ -plutonium are large and have a negative temperature coefficient, which is highly unusual for an elemental material. The delicate balance between 5f electron bonding and localization is thought to be responsible for many of plutonium's unusual properties, including its propensity for phase changes, low-symmetry crystal structures, and low melting point by comparison with other actinides. Because of its many allotropic forms, plutonium allows us to observe the changes in electronic structure and their relationship to the striking volume and structural differences of those allotropes.

Plutonium's low-temperature phase (α -phase) has a simple monoclinic crystal structure and a high density—about 19 grams per cubic centimeter (g/cm^3). Typically, local-density approximation (LDA) band calculations suggest that the f-electron wave functions have direct overlap, yielding narrow but robust 5f bands. As a result, α -plutonium can be described as having transition-metal properties (see the article "Actinide Ground-State Properties" on page 128). By contrast, the high-temperature δ -phase is an fcc structure with a density of $16 \text{ g}/\text{cm}^3$. Direct f-f overlap is considered unlikely for most of the 5f electrons. Small residual hybridization with s and d band electrons, as proposed by the Periodic Anderson

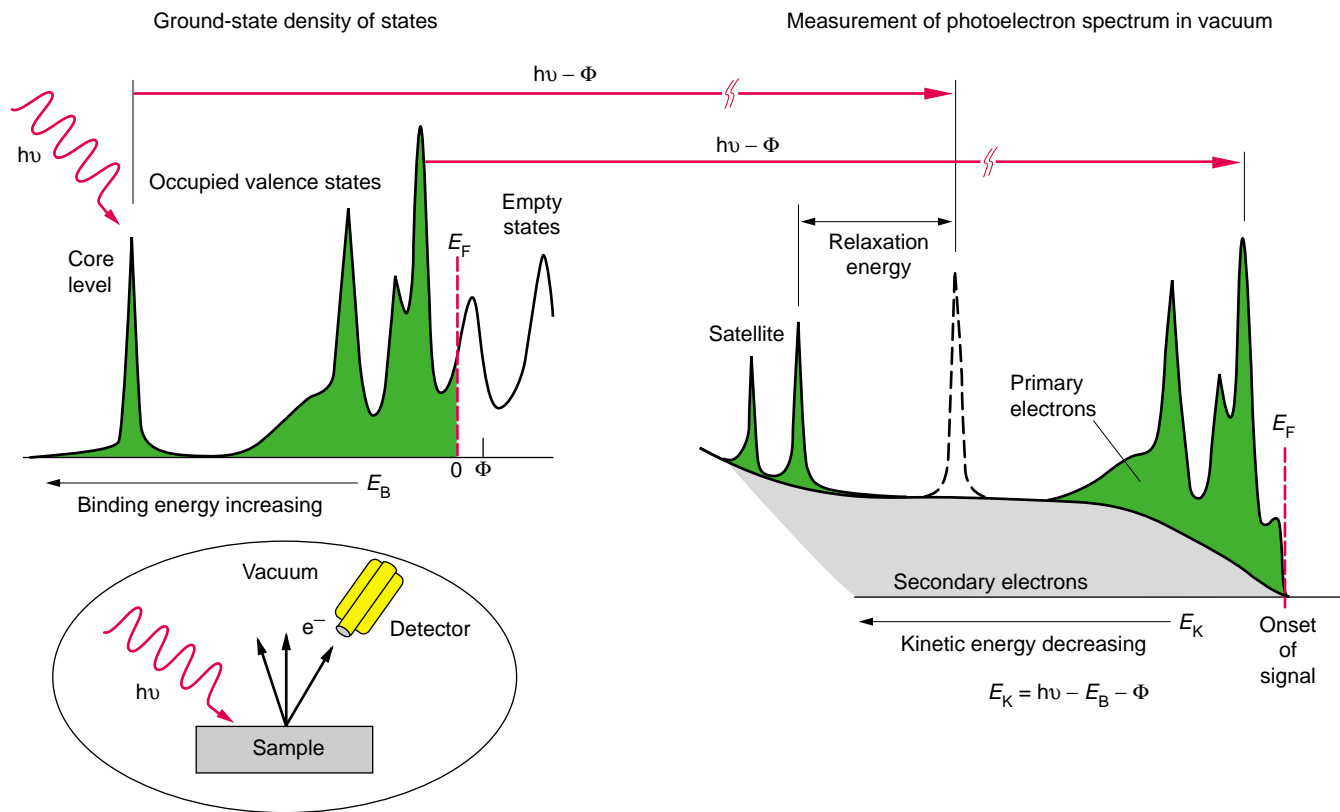


Figure 1. Schematic Representation of the Photoemission Process

The experimental setup for photoemission is shown in the inset at lower left. Monochromatic ultraviolet or soft x-ray light of energy $h\nu$ is focused onto a clean sample surface in high vacuum (typically, 10^{-10} torr), and a detector records the number of photoelectrons emitted from the surface as a function of their kinetic energy E_K . The ground-state electronic structure is shown by the schematic density of states on the upper left. The filled states are shown in green and labeled by E_B , where the binding energy E_B is defined to be positive. The higher the binding energy E_B , the farther is the electron below the Fermi level at $E_B = 0$. Empty states above the Fermi level are not colored. Electrons at E_B absorb a photon of energy $h\nu$ and are raised in energy by that same amount. If they are emitted into the vacuum, they lose not only the energy E_B needed to raise them to the Fermi level, but also the energy associated with the work function Φ due to an image charge at the surface. Thus, their kinetic energy in the vacuum is $E_K = h\nu - E_B - \Phi$, as shown on the right. The primary electrons are those at each E_K (this is what the spectrometer actually measures) transmitted into the vacuum without a scattering event. Their number is, to a first approximation, directly related to the number of electrons in the states E_B . Those electrons that are inelastically scattered before emission through the surface are called secondary electrons and contribute to a featureless background (indicated in gray). A core-level electron at ground-state energy E_{BC} may be emitted with energy $E_K = h\nu - E_{BC} - \Phi$ and produces the sharp dashed peak, provided the core hole left by the electron is well screened by the conduction electrons. Emission of core-level electrons may also lead to one or more satellites at lower E_K if the screening of the core hole is poor.

Model, or perhaps itinerancy from some fraction of the 5f electrons may yield some 5f density of states at the Fermi energy (see the articles “A Possible Model for δ -Plutonium” and “Actinide Ground-State Properties” on pages 154 and 128, respectively). Indeed, both resistivity data and recent magnetic-susceptibility measurements suggest that δ -plutonium has a narrow (very flat) conduction band pinned to the Fermi energy. Moreover, low-temperature specific-heat measurements indicate that the crystalline effective mass of conduction electrons at the Fermi energy is many times the rest mass of electrons, a property suggestive of heavy-fermion materials. Clearly, a detailed understanding of the plutonium 5f electronic structure is fundamentally important to the overall understanding of plutonium properties and to condensed matter physics as a whole.

In this article, we present measurements of the electronic structure of plutonium metal done by photoemission spectroscopy. Both α - and δ -plutonium were examined with several methods of surface preparation and in two independent photoelectron-spectrometer systems. The qualitative agreement between the two measurements is good. Spectra from both phases display a narrow 5f-related feature at the Fermi energy. That feature is narrower in δ - than in α -plutonium—a full width at half maximum (FWHM) of about 70 milli-electron-volts (meV) vs one of about 150 meV. The 70-meV FWHM is also typical of f electron peaks near the Fermi energy in heavy fermions. In both plutonium allotropes, the photon energy dependence of this feature suggests nonnegligible 6d admixture—albeit, somewhat less in δ -plutonium. These results were made possible by the design, development, and implementation of a unique laser-plasma light source at Los Alamos (by Arko, Joyce, and Morales) and by the first use of a synchrotron source to acquire photoemission data on plutonium metal (Terry and Schulze).

Basics of Photoelectron Spectroscopy (PES)

PES may be the most direct and detailed tool for measuring the electronic structure of metals. Photons of known energy (ultraviolet to soft x-ray) incident on a sample surface in vacuum are absorbed by the metal's electrons. The kinetic energy of these electrons increases by the amount of the photon energy. Electrons that are near the sample surface and that, prior to absorption, have a momentum component perpendicular to the surface¹ may escape from the material into the vacuum, where a detector records the number of electrons collected as a function of kinetic energy. As shown in the Figure 1 schematic, the measured photoelectron spectrum gives, to a first approximation, the shape of the occupied electron density of states in the sample (scaled by the orbital cross sections).

PES is especially effective when the photon source is tunable. We can then measure the photoelectron spectra at different incoming photon energies. Because the cross section for photoabsorption varies strongly with electron orbital symmetry at vacuum-ultraviolet (VUV) energies (Yeh and Lindau 1985), comparison of the different spectra at different photon energies allows identifying those spectral features that are due to electrons of a given orbital symmetry (s, p, d, or f). We can therefore compare such contributions as those of plutonium's 5f and 6d electrons.

In the very near future, when high-quality crystals with mirror surfaces become available, one could utilize precise sample-orientation devices to determine accurately the incoming photon direction, as well as the direction of the exiting electrons with respect to the sample surface. This angle-resolved PES technique, or ARPES, would allow development of a complete map of the energy bands—electron

energies as a function of crystal momentum. Certainly, the latter possibility represents the future for research into the electronic structure of plutonium. Below, however, we limit the discussion to the simpler angle-integrated PES.

The PES Spectrum. Figure 1 defines the essential parameters of PES. Monochromatic ultraviolet or soft x-ray light of energy $h\nu$ is focused onto a clean sample surface in high vacuum (typically, 10^{-10} torr). The electron energy in the material is specified by E_B , the binding energy, which is measured relative to the Fermi level, E_F . When an electron in the material absorbs a photon (the process may be described by dipole selection rules), its energy is raised by an amount $h\nu$. To escape the surface into the vacuum, the electron must have a momentum component normal to the sample surface, it must originate close enough to the surface—at the most, a few electron mean free paths (MFPs)—so that it should not be easily scattered, and it must gain sufficient energy from the photon in the normal component of momentum to overcome the electric dipole energy of the surface (usually referred to as the work function, or Φ). Once this photoelectron is in the vacuum chamber, its energy and momentum can be determined by an electron energy analyzer.

Because energy and, to some degree, momentum are conserved in the transmission through the surface, there is a simple relationship between the photoelectron's kinetic energy, E_K , in the vacuum and its binding energy, E_B , in the sample: $E_K = h\nu - E_B - \Phi$. (Actually, Φ is the work function of the analyzer because the measured kinetic energy of the electron is relative to the level of vacuum in the analyzer.) To measure a typical spectrum, we count the electrons detected at any given kinetic energy in the vacuum, and the number detected is directly related to the number (density) of electrons within a given energy interval in the sample.

¹Note that photoabsorption does not alter the electron momentum significantly.

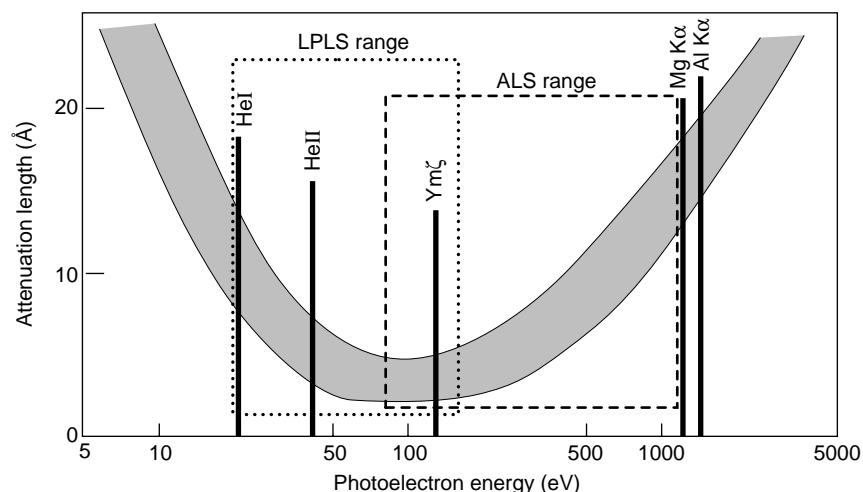


Figure 2. Universal Curve of the Probing Depth of PES

The photon energy range of the laser-plasma light source (LPLS) system is depicted by the dotted rectangle. The range of Beamline 7.0.1 at the Advanced Light Source (ALS) is shown by the dashed rectangle. Also shown are the energies of various line sources commonly used in PES. The attenuation length, or probing depth, is plotted as a function of the photoelectron energy. The probing depth is proportional to the MFP of the photoelectron, which has not yet exited the sample. Approximately 95% of the photoelectrons come from a probe depth within 3 MFPs of the surface.

The schematic view in Figure 1, however, greatly simplifies the true situation. In reality, many complications prevent the PES spectrum at a certain photon energy from being a replica of the occupied density of states, or the electronic band structure. Here, we consider two major complications: surface sensitivity and photoabsorption cross-section dependence on photon energy.

Surface Sensitivity. One limitation of PES is that it probes only the first few atomic layers of a material's surface. Although the surface and bulk electronic structures may differ, it has often been demonstrated that the bulk electronic structure of homogeneous solids is already well established at one or two monolayers below the surface. The universal curve in Figure 2 shows that the probing depth (related to the MFP of the outgoing electron) varies strongly with the kinetic energy of the outgoing electron, and the deepest probe (the greatest bulk sensitivity)

occurs at very low and again at very high kinetic energies. This continuous variation allows us to separate surface from bulk features. We can measure a set of PES spectra at photon energies spanning a significant portion of the electron kinetic-energy range and then, by comparing them directly, distinguish surface from bulk features.

The great sensitivity to the surface layer also implies that atomically clean surfaces prepared in vacuum are an absolute requirement if one is to measure true bulk properties.

Photoelectron Cross Sections. As Yeh and Lindau point out (1985), the probability of an electron absorbing a photon—that is, the photoelectron cross section—varies strongly with the incident photon energy ($h\nu$), the electronic orbital symmetry (s, p, d, or f), and the atomic configuration (for example, Z -number and occupied energy levels). These variations complicate interpretation of the measured PES

spectra and of the material's electronic structure. To obtain a complete picture of the density of states, one needs to take many spectra, using different photon energies, and then take into account the effects of the photoabsorption cross sections on the measured intensities of the photoelectron features.

Figure 3 shows photoabsorption cross sections for a plutonium atom calculated with the code of Yeh and Lindau (1985). At low photon energies—1 to about 30 electron-volts (eV)—the 6d states have the highest cross section and dominate the photoemission spectrum, whereas above about $h\nu = 40$ eV, the 5f states begin to dominate. In principle, one can therefore easily separate the 5f from the 6d contributions to the density of states by comparing several photoemission spectra taken at different energies in the range of 20 to 50 eV. Figure 4 shows such a set of spectra for the compound neptunium-arsenide (NpAs). The 6d emission predominates in the 21-eV spectrum. In Figure 4, we have overlaid copies of the 21-eV spectrum on the spectra taken at higher photon energies. Clearly, the 5f contribution grows dramatically with $h\nu$ and may be deconvolved from the 6d features. Such a separation is possible for plutonium and any of its compounds or alloys.

Resonant PES. Another method to identify specific orbital contributions to the spectrum is resonant PES (Fano 1961). In this technique (see Figure 5), one works at a photon energy near the 5d absorption edge (approximately 115 eV for plutonium) to promote a 5d core-level electron into an empty 5f state just above the Fermi energy. Because this is primarily an atomic process, it is the final-state electronic configuration $5d^9 5f^{n+1}$ that determines the exact photon energy (energies) at which resonance occurs (Lynch and Weaver 1987). As this electron decays to refill the core hole, it gives up its excess energy via an Auger-like process to a 5f (or, to a lesser extent, a 6d) electron near the Fermi energy. That

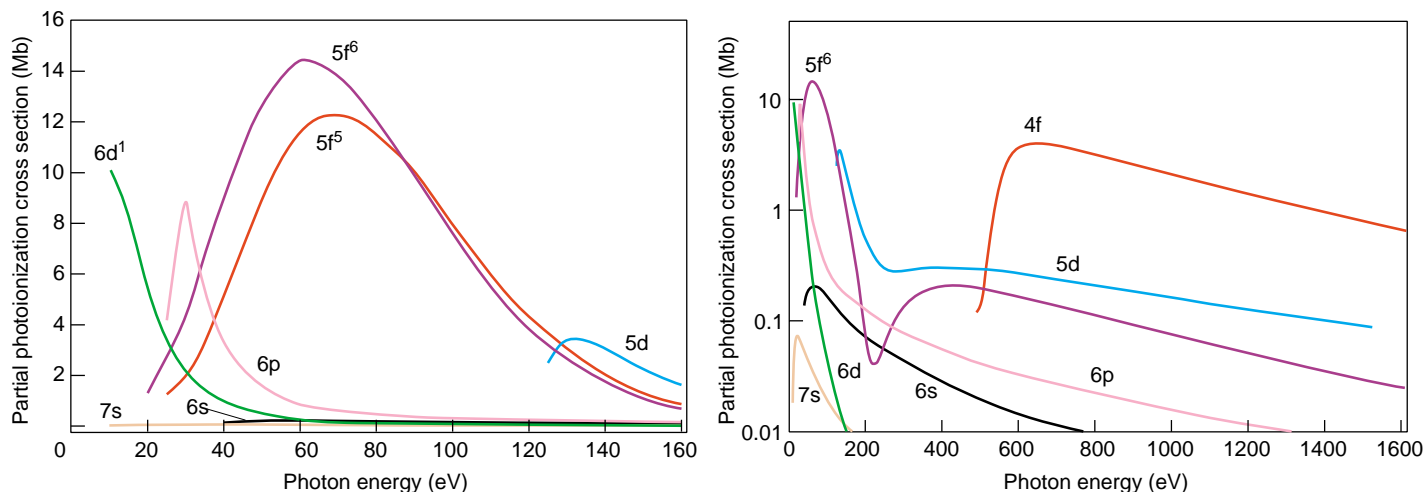


Figure 3. Calculated Photoabsorption Cross Sections for Plutonium

The photoabsorption cross sections for different atomic states in plutonium calculated using the methodology of Yeh and Lindau (1985) are shown here as representative of the cross sections in plutonium. (a) At low photon energies, the 6d cross section dominates over the 5f, but above approximately 30 eV, the opposite is true. The cross sections for the $5f^5 6d^1$ configurations are shown because they are more relevant to plutonium metal than the $5f^6 6d^0$ configuration of isolated atoms. (b) The cross sections for plutonium valence and core-level electrons down to the 4f state are plotted on a log scale up to 1600 eV.

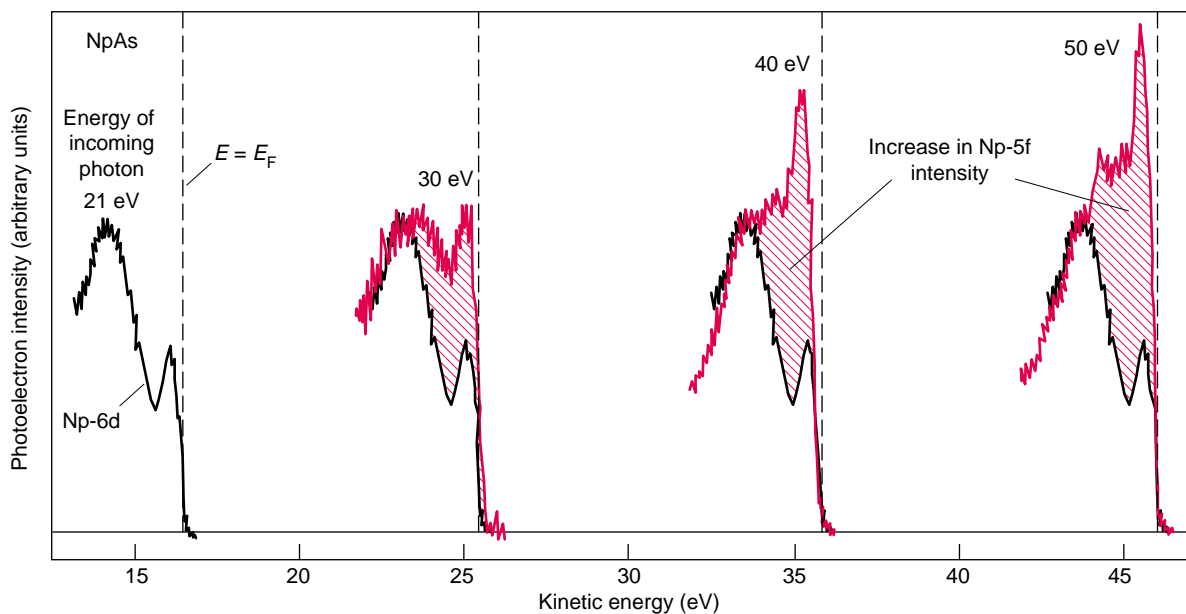


Figure 4. Photoemission Spectra of NpAs for Different Photon Energies

This plot shows several measurements of the d- and f-electron photoemission peaks as a function of photoelectron kinetic energy E_K . Because E_K increases with the incoming photon energy $h\nu$, the Fermi edges of the different spectra, indicated by the sharp and sudden onset of emission, are offset from each other by $h\nu$. The spectrum taken with $h\nu = 21$ eV, the lowest photon energy, has been superimposed on the spectra taken at higher photon energies. In each spectrum, the broad feature at -3 eV relative to the Fermi edge is due to the 6d electrons. The sharp peak at -0.5 eV relative to the Fermi edge increases in intensity as the photon energy increases. This increase, as well as the change in line shape, is due to increased 5f cross section and subsequent emission at higher $h\nu$. The increase in 5f intensity is represented by the hatched areas.

electron is ejected into the continuum of states above the vacuum level. (The refilling of the hole may produce a photon of commensurate energy instead of an Auger-electron, but the radiative process is much less favored.)

The Auger-like process yields a final state that is identical to that resulting from normal PES and therefore interferes either constructively or destructively with the normal PES photoabsorption. Because the resonant cross section (constructive interference) is very large (it is proportional to the cross section for the initial core-level process promoting a 5d electron into a 5f state), it greatly increases the 5f emission intensity in a narrow range of photon energies near the absorption edge. By contrast, destructive interference, or antiresonance, may yield almost zero 5f emission at the so-called antiresonance (approximately 104 eV for plutonium). Spectra of actinide compounds taken at resonance and antiresonance are particularly useful for separating the 5f and, to some extent, the 6d components from other electronic states.

Experimental Details

Powerful synchrotrons have been developed into intense tunable light sources for photoemission studies. The Advanced Light Source (ALS) at the Lawrence Berkeley National Laboratory represents the cutting edge of today's machines. Although potential hazards and political sensitivity surrounding plutonium have often precluded studying this material at synchrotron sources, the situation is being remedied, and as we will describe, Schulze and Terry have performed successful PES measurements of plutonium at the ALS. Arko and Joyce, on the other hand, designed, constructed, and currently operate a one-of-a-kind tunable laser-plasma light source (LPLS)², which mimics the output of a synchrotron. In addition, the LPLS system has an in situ capability for automatically produc-

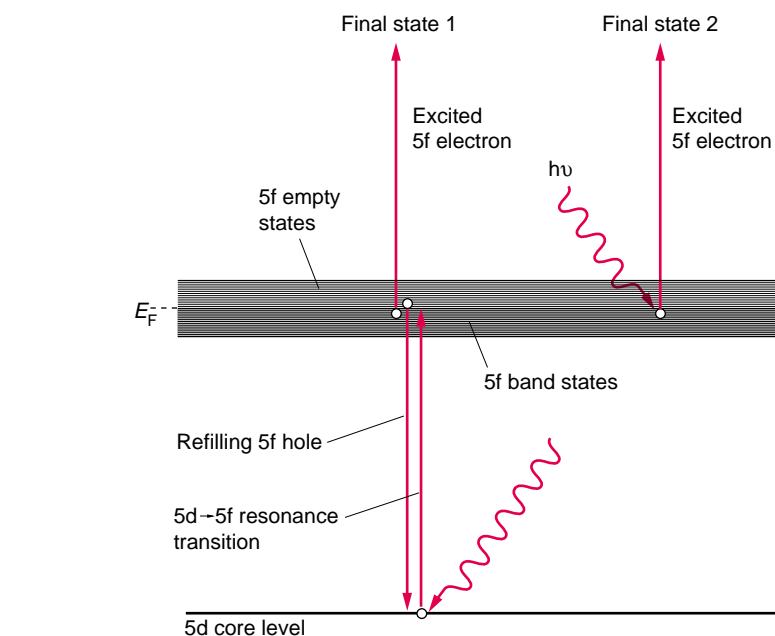


Figure 5. Schematic of Resonant Photoemission

In resonant photoemission in plutonium, a photon of energy $h\nu$ is sufficient to promote a core 5d electron into an empty state, just above the Fermi level. As this electron decays to refill the core hole, it gives up its energy to a 5f electron in the occupied states via an Auger process, and the resulting state is final state 1. However, the identical final state can also be reached by direct photoemission and is depicted as final state 2. The two final states can interfere with each other constructively (resonance) or destructively (antiresonance). In plutonium, the resonance and antiresonance are at 120 eV and 104 eV, respectively.

ing clean actinide surfaces, an essential feature for work at VUV photon energies. The LPLS and ALS are described in the short articles “Laser-Plasma Light Source” and “Actinide Photoemission Measurements at the Advanced Light Source” on pages 186 and 188.

Surface preparation is crucial to a PES experiment because, as shown in Figure 2, the probing depth of PES is only a few atomic layers (in most metals, about 1 to 5 atomic layers, or 5 to 25 angstroms). Atomically clean surfaces are thus essential to accurate PES results. In the synchrotron experiments, surfaces are cleaned by sputter anneal, and in the LPLS experiments, by laser

ablation—the laser beam is redirected into the vacuum chamber and cleans the sample. The latter technique is simple to use and allows cleaning the sample at low temperatures. Low temperatures are significant because they limit diffusion and reduce degradation reactions at the sample surface.

Figure 6 shows a sequence of PES spectra taken at five stages of in situ cleaning. The top spectrum is of the α -plutonium sample with a thick oxide overlayer, and it shows a broad oxide peak centered around an electron kinetic energy of 29 eV ($E_B = -6$ eV), which is due to the electrons in the oxygen 2p band states, and a second peak centered at 33.5 eV, which is due to the localized 5f electrons in the plutonium oxide. These LPLS data were taken at a photon energy of 40 eV to enhance the

²Since 1992, this project has been funded by the Office of Basic Energy Sciences, Division of Materials Sciences, of the Department of Energy.

PES intensity of the oxygen 2p electrons relative to that of the 5f electrons. We used only a few laser pulses to ablate the sample surface between taking each of the subsequent spectra. Note that, with each cleaning, the Fermi edge grows in intensity whereas the oxide peak at a binding energy of -6 eV decreases and changes in shape (residual surface oxygen is still present in cycle 5, but by comparison with the starting oxide, it is clearly different in shape and reduced in intensity). The final metallic spectrum is dramatically different from the starting spectrum, but it is similar to the final spectra obtained by the more-traditional sputter-anneal (or scraping) methods, thus demonstrating the effectiveness of laser ablation.

In preparation for the synchrotron experiments at the ALS, the samples were first passed through numerous sputter-anneal cycles in the Chemistry and Metallurgy Research (CMR) Facility at Los Alamos, and they were examined by traditional x-ray photoemission and Auger surface spectroscopies. The samples were then transferred under vacuum into vessels maintained at a pressure of 10^{-8} torr by a portable battery-powered ion pump system. Being isolated from oxygen and air in these vessels, the samples were shipped to the Lawrence Berkeley National Laboratory, where they were transferred under vacuum to a preparation system appended to the x-ray photoelectron-diffraction analysis chamber of the Spectromicroscopy Facility Beamline 7.0.1 (see the article "Actinide Photoemission Measurements at the Advanced Light Source" on page 188). In the preparation chamber, the samples underwent final sputter-anneal cleaning cycles before being transferred into the chamber for synchrotron PES measurements.

Using these techniques, we have obtained the world's first resonant-photoemission data on α - and δ -plutonium. The higher resolutions and cleaner surfaces made possible by laser ablation have yielded dramatic,

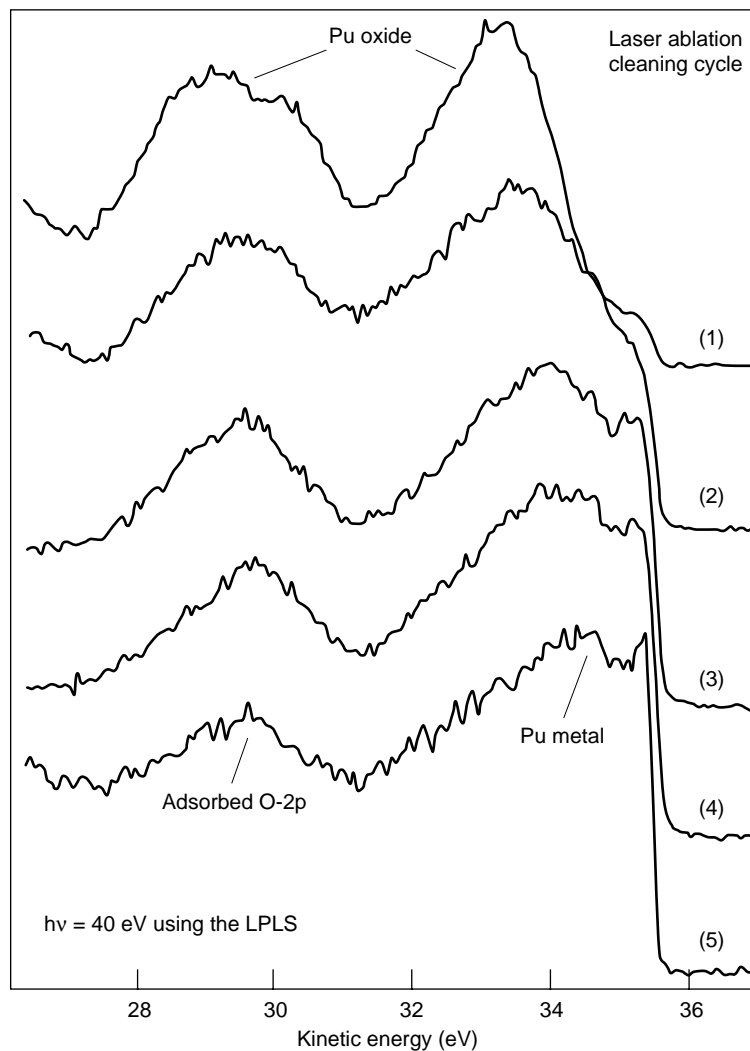


Figure 6. Cleaning of α -Plutonium by Laser Ablation

This sequence of spectra from an α -plutonium sample was taken at various stages of the laser-ablation cleaning cycle. At the start of the cycle shown in (1), the α -plutonium sample has an oxide surface, and the broad peaks are due to plutonium oxide molecular states. The features of the oxygen 2p electrons centered at $E_K = 29$ eV are a double peak due to oxygen band states. The large peak centered at 33.5 eV is associated with localized 5f states in plutonium oxide. As the ablation cycle proceeds, the line shape of the oxygen feature at $E_K = 29$ eV changes because the oxygen is no longer in a molecular state, and the density of states at the Fermi edge from the pure plutonium metal grows in intensity. By stage (5), the greatly reduced oxygen 2p signal is entirely due to adsorbed oxygen, while the localized 5f plutonium oxide state at 33.5 eV has been replaced by the metallic 5f band states. Only a few laser pulses were applied between each of the spectra shown.

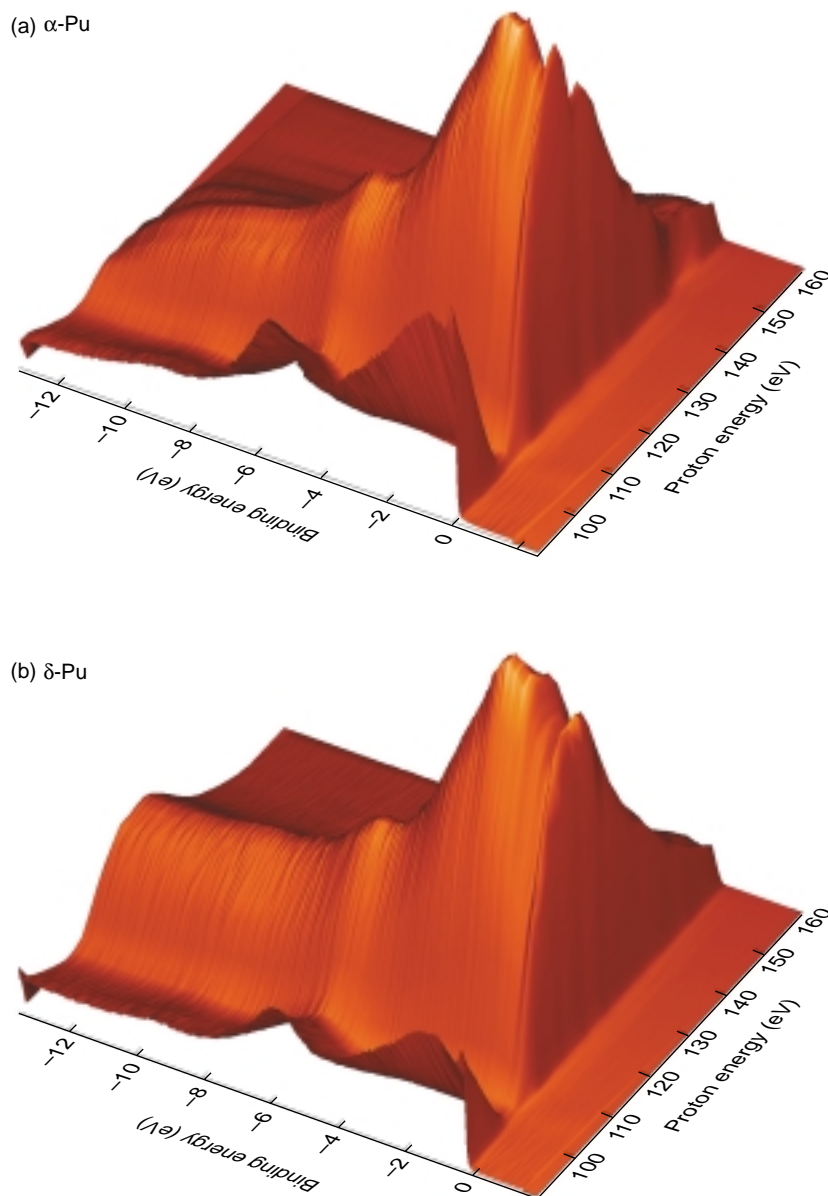


Figure 7. Valence-Band Resonant Photoemission Spectra for α - and δ -Plutonium

These three-dimensional plots of valence-band resonant photoemission spectra for (a) α -plutonium and (b) δ -plutonium were obtained at the ALS at the Lawrence Berkeley National Laboratory. The usual photoemission spectra showing intensity as a function of binding energy are plotted along a third axis, that of photon energy. The photon energy was scanned across the 5d absorption edge at about 120 eV so that one can follow intensity as a function of photon energy for a fixed binding energy (also called a CIS curve for constant initial state) through both the antiresonance and resonance energies. The spectra in both (a) and (b) show strong prominent resonance features.

unexpected results, as we show next. Lower-energy data were obtained with the LPLS system, whereas higher-energy data, including core levels, were obtained at the ALS.

PES Results for α - and δ -Plutonium

ALS Resonance Data at 300 Kelvins. Figures 7(a) and 7(b) show three-dimensional plots of resonant photoemission from α - and δ -plutonium, respectively. The α -plutonium sample was high-purity polycrystalline. The δ -plutonium sample was a small single-crystal grain (about 1 millimeter on a side) stabilized with nominally 1 weight percent (wt %) gallium and surrounded by a matrix of smaller crystallites—see Figure 5(b) in the article “Preparing Single Crystals of Gallium-Stabilized Plutonium” on page 226). Both surfaces had been cleaned to a level of oxygen on the order of 0.5 monolayer or less based on a simple calculation using peak intensities and the photoemission cross sections. The data were taken at a temperature of 300 kelvins.

The three-dimensional plots are a compilation of the standard valence-band photoemission spectra (intensity as a function of electron binding energy) for different photon energies around the primary resonance energy. Thus, at a fixed photon energy, the photoemission spectrum yields a measure of the valence-band density of states (convoluted with orbital cross sections). At a fixed electron binding energy (or fixed initial electronic state), the intensity as a function of photon energy is a measure of the photoemission cross section for that electronic state as a function of the photon energy, which is modulated by the resonant process.

From a cursory examination of the data, we can identify the salient features of the spectrum. Along the binding-energy axis, the huge intensity peak from E_F (where $E_F \equiv E_B = 0$) to about $E_B = -4$ eV constitutes the

contributions from the valence bands, specifically the 7s, 5f, and 6d states of plutonium. The feature at a binding energy of about -6 eV is probably caused by the residual oxygen at the sample surface. Along the photon energy axis, the intensity minimum (about 104 eV) and maximum (approximately 120 eV) correspond to the 5d \rightarrow 5f antiresonance and primary resonance, respectively. These general features are similar for the α - and δ -plutonium PES measurements.

A more detailed examination reveals subtle differences in resonant behavior between α - and δ -plutonium. These differences become most evident if one examines the intensity as a function of photon energy for a fixed binding energy (usually referred to as a constant initial state, or CIS, curve). To a rough first approximation (within the one-electron approximation), CIS spectra represent the empty-state density of states convoluted with the 5d photoelectron cross section, including final-state effects. Thus, to a limited degree (governed by dipole selection rules, $\Delta\ell = \pm 1$, where ℓ is the orbital angular momentum), they give a hint of the density of states and, particularly, the 5f multiplet structure for the (5d⁹5fⁿ⁺¹) configuration above the Fermi energy.

By examining the CIS spectra near the Fermi energy in Figure 7, we see that, although both the α - and the δ -allotrope show the antiresonance minimum at virtually the same point in photon energy (104 eV), the CIS curves for α -plutonium show much more structure than those for δ -plutonium. For example, the α -plutonium data have a shoulder at a photon energy of 110 eV, rising to a sharp peak at 117 eV followed by well-defined secondary features at photon energies of 123 eV, 135 eV, and 148 eV. In contrast, the δ -plutonium data show a much less pronounced shoulder at 110 eV, rising to a relatively broad, featureless peak at a 120-eV resonance energy followed by relatively less-pronounced secondary features.

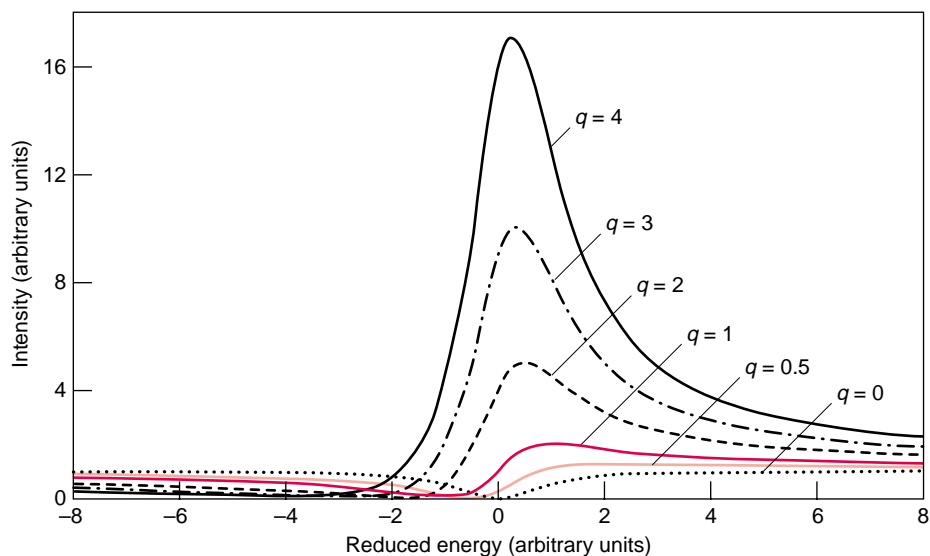


Figure 8. Calculated Fano-Line Shapes

This plot of standard Fano-line shapes as a function of the parameter q (basically, the intensity at resonance minus that at antiresonance) shows that the resonance peak gets sharper (the difference between the resonance and antiresonance) as the electrons involved become more localized. The shape with $q = 1$ is similar to the CIS curve for α -plutonium, and the shape with $q = 2$ is similar to the CIS curve for δ -plutonium. Thus, the resonance data suggest that the 5f electrons are more localized in δ - than in α -plutonium.

The interpretation of all the secondary features (for example, their relation to the density of states) will require supporting theoretical work, which is ongoing.

The CIS curves show a distinct Fano-line shape (see Figure 8), especially near antiresonance (104 eV). The symmetry of the curve and the magnitude of q (basically, the difference between the intensities at resonance and antiresonance) are highly dependent on the relative probabilities of resonance vs direct photoemission. The experimental CIS spectrum of δ -plutonium has a q value of 2, whereas that of α -plutonium has a q value of 1. The CIS spectrum of δ -plutonium has also a greater Fano-like symmetry. These features indicate that the relative probability for the resonant process is larger in δ - than in α -plutonium. This increase may be ascribed to an increase in electronic localization in the 5f states for the following reason. The photoabsorption

cross section for the resonant 5d \rightarrow 5f transition (D_a) is not likely to be significantly enhanced for itinerant versus localized 5f. However, the cross section for direct 5f photoemission (D_e) is increased for itinerant electrons relative to localized electrons. The q value is given by $q = D_a/(\pi V D_e)$, where D is the matrix element for the specified transition and V is the relaxation matrix element. Thus, the Fano symmetry (and the magnitude of q) of the CIS spectrum is very sensitive to the degree of 5f electron localization. Compared with α -plutonium, δ -plutonium exhibits a greater Fano symmetry with a larger value of q , consistent with a greater degree of f electron localization.

The valence-band photoemission spectra at fixed photon energies (which are reflective of the density of states in the material to within the limitations stated in the introduction) are surprisingly similar for the two plutonium allotropes. Again, however, the data show some subtle differences. Figure 9

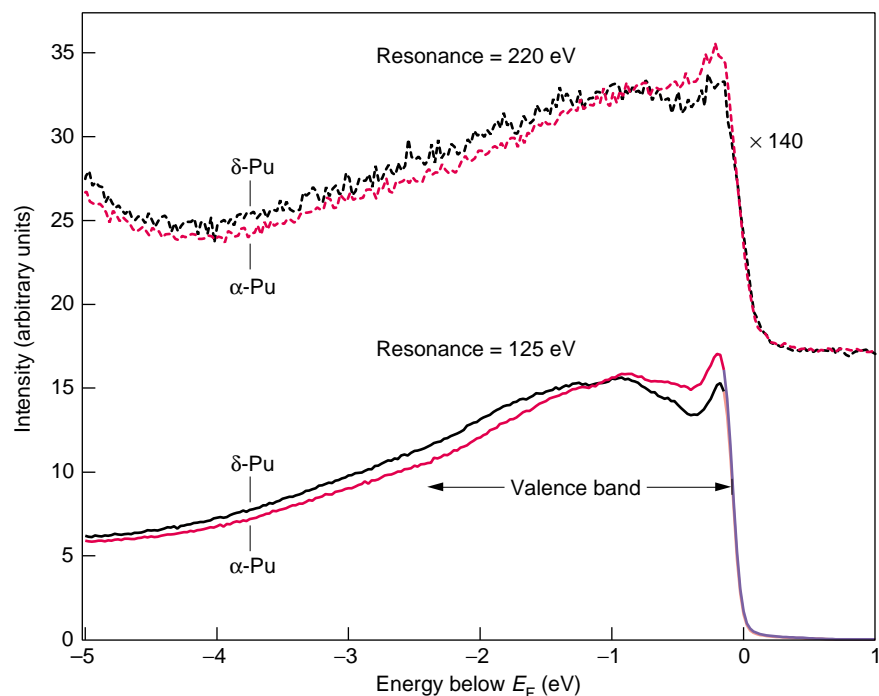


Figure 9. Spectra for α - and δ -Plutonium Near Resonance and Near the Cooper Minimum

These valence-band spectra for α - and δ -plutonium taken near resonance ($h\nu = 125$ eV) and at the Cooper minimum ($h\nu = 220$ eV) are remarkably similar. At both photon energies, the width of the emission band is about 200 meV wider in δ -plutonium than in α -plutonium, when normalized to the peak at a binding energy of ~ 1 eV. The increased intensity of δ -plutonium at the high binding-energy edge of the valence band may be a consequence of greater electron localization.

shows the plutonium valence-band spectra for the α - and δ -phase near resonance ($h\nu = 125$ eV) and at the Cooper minimum³ ($h\nu = 220$ eV).

At resonance (spectra at 125 eV), the δ -plutonium valence-band photoemission width extends about 200 milli-electronvolts (meV) farther below the Fermi level than the α -plutonium valence-band photoemission width.

The sharp feature near the Fermi level appears more intense in α - than in

δ -plutonium. At first glance, this difference seems inconsistent with the general trend of localization in δ -plutonium. The lower intensity of the δ -plutonium feature, however, is at least partially a consequence of its narrowness—its FWHM is on the order of 70 meV. At 300 kelvins, the Fermi function is about 110 meV wide (the resolution is 10 to 90 percent of the Fermi function value), and any spectral feature of approximately this width or less located within $k_B T$ of the Fermi energy will be affected by the Fermi function (truncated and broadened). The narrow feature in δ -plutonium falls into this category. However, temperature alone may not account for all the missing intensity relative to the data at 40 eV (see below). Some of the differences may be ascribed to different gallium concentrations in the two speci-

mens or, perhaps, to differences in 6d admixture.

LPLS Data at 80 Kelvins. To circumvent the issue of thermal broadening and aim for a more accurate approximation of the density of states in the PES spectrum, we have collected data at 80 kelvins and 60 meV in resolution by using the sharp discharge line of a helium arc lamp at a photon energy of 41 eV. At this photon energy, the calculated 6d and 5f photoabsorption cross sections per electron are approximately equal. The surfaces were prepared by laser ablation. Figures 10(a) and 10(b) show a wide scan and an expanded view, respectively, of the resulting PES spectra for both α - and δ -plutonium. Here, the secondary electron background has been subtracted, and the integrated intensities between E_F and -4 eV are set to be equal. For this normalization, there is another slight difference in bandwidth. Globally, the two phases of plutonium appear surprisingly similar except for the narrow feature near the Fermi level, which, unlike the data at resonance in Figure 9, is now much narrower in δ - than in α -plutonium. All features observed in δ -plutonium are also found in α -plutonium, but they are much better defined in δ -plutonium, perhaps reflecting greater localization. Note that the residual feature around -6 eV represents submonolayer surface-oxygen contamination, perhaps between 0.1 and 0.2 monolayer, and is therefore ignored. For the most part, the 41-eV data are similar to those presented in Figure 9, except for the sharp features near the Fermi level in the low-temperature data.

The expanded view in Figure 10(b) shows the only clearly understandable difference between α - and δ -plutonium in the valence band data. In particular, the sharp feature in gallium-stabilized δ -plutonium is clearly much narrower than that found in α -plutonium and, to within the resolution of our spectrometer (75 meV), it crosses E_F . This feature is consistent with the larger specific-

³The Cooper minimum provides a way for using a tunable light source when there is a node in the radial wave function of the initial state. By matching this node to a final-state wave function, which would give equal contributions to the positive and negative components of the transition probability, one obtains a minimum in the absorption cross section. This matching depends on the energy of the final state and thus on the incident photon energy.

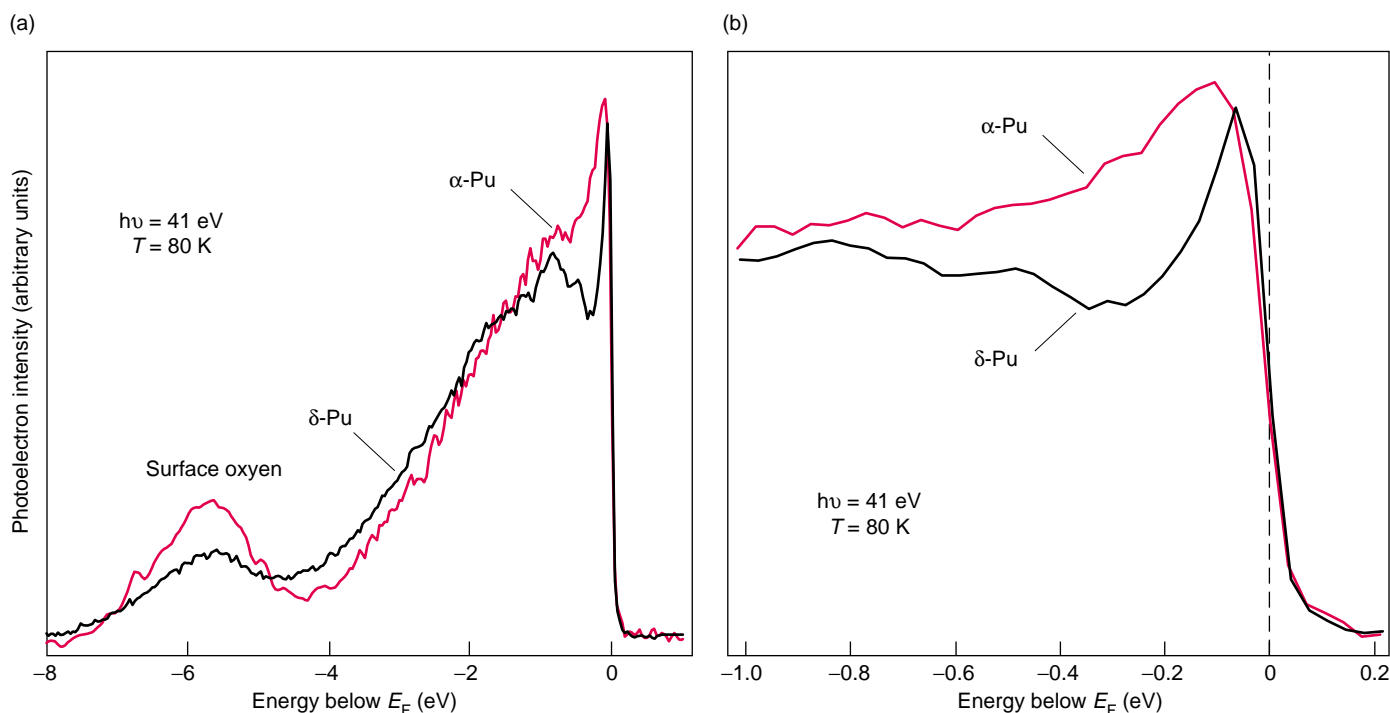


Figure 10. Spectra of α - and δ -Plutonium with Helium II Radiation

(a) In the wide-scan spectra of α - and δ -plutonium at 80 K using helium II radiation, the feature at -6 eV is due to about 0.1 monolayer of adsorbed oxygen. The secondary electron background has been removed from the spectra, and the normalization is such that the areas under the spectra, between E_F and -4 eV, are equal. (b) In the expanded view of spectra near the Fermi energy, the most significant difference between the spectra is the broader near- E_F feature in α -plutonium.

heat γ -value of δ -plutonium and is similar to the feature found in spectra of uranium compounds identified as heavy fermions.

Heavy-fermion materials are metals or compounds with an unfilled 4f or 5f shell, whose specific heat and other bulk properties suggest (Lee et al. 1986) that the f electrons at the Fermi energy have a crystal effective mass larger by orders of magnitude than the rest mass of the electron and, indeed, much larger than the calculated band mass for the material. A long-standing (though simplistic) model to explain this behavior is the so-called single-impurity model (SIM) (Gunnarsson and Schonhammer 1987), which postulates that the f electrons behave as noninteracting magnetic impurities at high temperatures. As the temperature is lowered, a cloud of conduction electrons aligns antiparallel to the f spin to form a singlet state, thus quenching the magnetic moment. Within the SIM, very weak residual f-electron

hybridization with this cloud produces a narrow resonance at the Fermi energy, sometimes called the Kondo resonance, which should manifest itself as a very narrow sharp feature in a photoemission spectrum. However, the applicability of the SIM to such periodic, crystalline systems is tenuous at best since the concept of an f electron “impurity” on every site (as would be required for δ -plutonium) is almost a contradiction in terms. Recent measurements in uranium heavy-fermion compounds suggest that LDA-derived bands are well reproduced experimentally, except at the Fermi energy, where the measured bands are flatter, or equivalently, narrower than the calculated bands. A comprehensive model that incorporates both lattice periodicity and electron correlations is yet to be quantified.

Temperature Dependence of the Data. One test for the applicability of the SIM to plutonium is a determina-

tion of the temperature dependence of the narrow 5f feature. In Figure 11, we show data taken at 21 eV at both 300 and 20 kelvins for α - and δ -plutonium. No change with temperature is evident in α -plutonium. On the other hand, a decrease in intensity occurs in δ -plutonium at 300 kelvins. Before interpreting this temperature dependence as evidence for the applicability of SIM, one must take into account the role of the Fermi function, which truncates this narrow feature as the temperature increases. One can approximate the effect of the 300-kelvin Fermi function by simply convoluting the data taken at 80 kelvins with a Gaussian whose FWHM is about 100 meV. This convolution broadens the narrow features at E_F but has no effect on features wider than 100 meV. With this convolution, we can fully account for the whole temperature dependence between the data at 20 and at 300 kelvins. Invoking the SIM or any other correla-

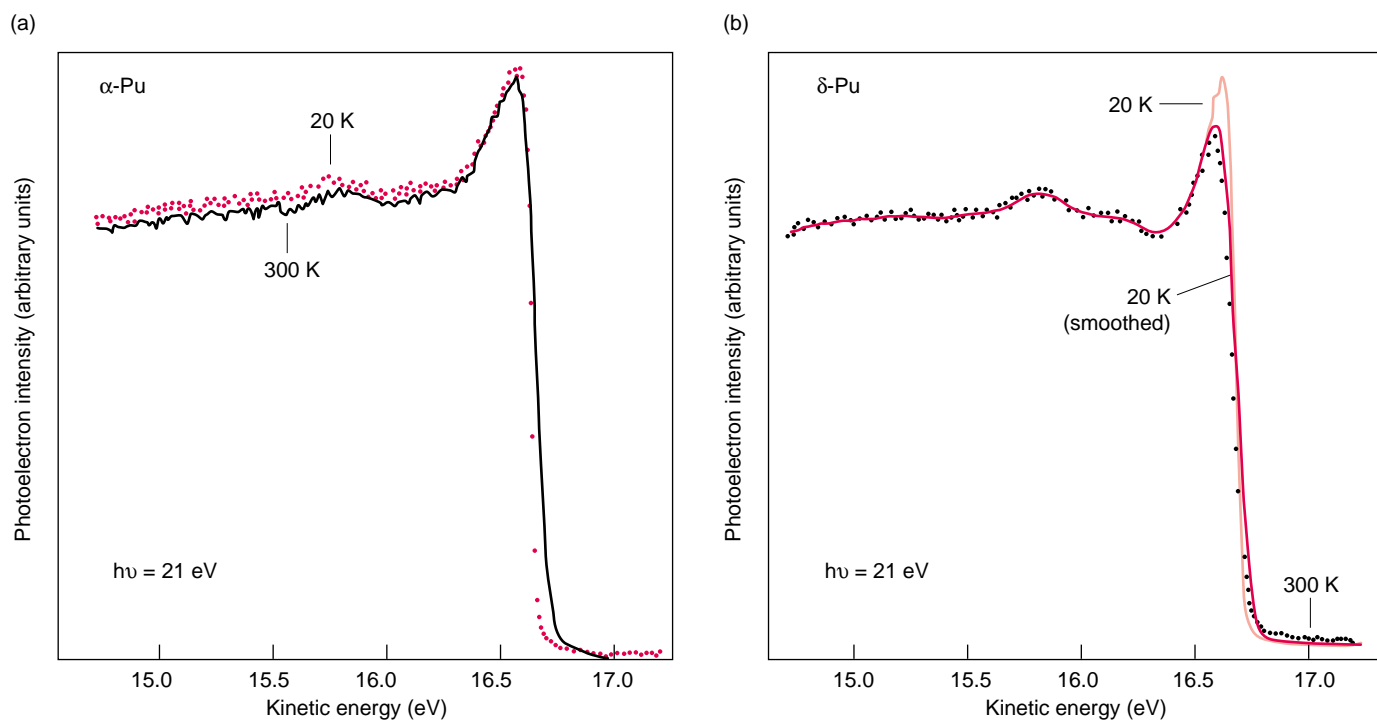


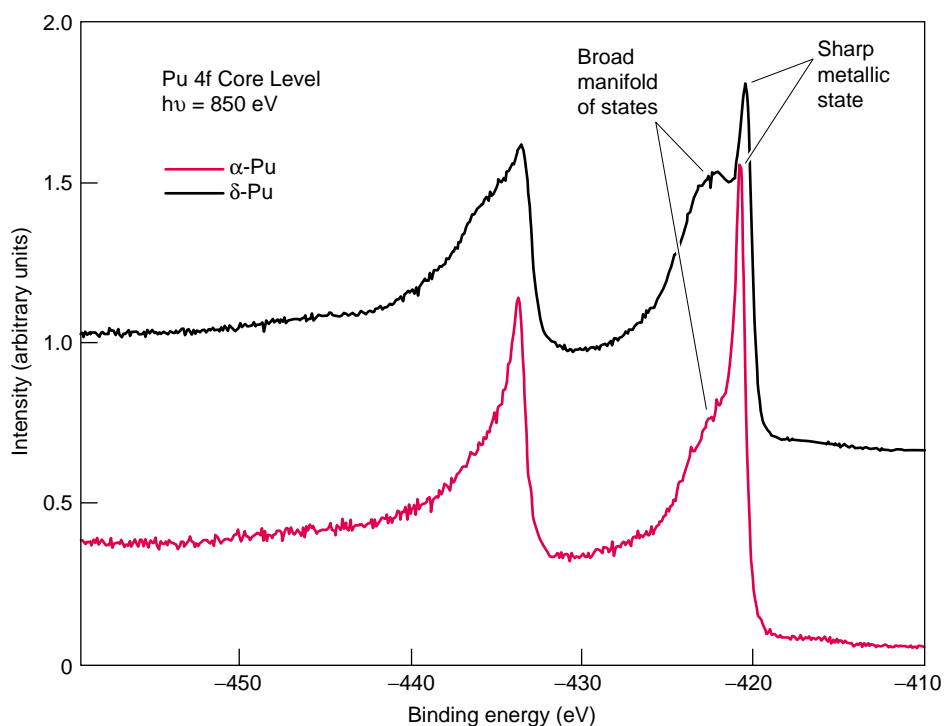
Figure 11. Spectra of α - and δ -Plutonium at 20 and 300 K

(a) Whereas α -plutonium is temperature independent, the temperature dependence of δ -plutonium (b) can be well accounted for by a convolution with an approximately 100-meV FWHM Gaussian, which approximates the Fermi function broadening at 300 K.

Figure 12. Plutonium 4f Core-Level Photoemission Spectra for α - and δ -Plutonium

The 4f core-level spectra suggest that electrons in δ -plutonium are more localized than electrons in α -plutonium.

These spectra were taken at high resolution at the ALS, and the photon energy was 850 eV. In both cases, the spectra show a sharp peak at a binding energy of about -421 eV, reflecting the 4f core-level state in the metal. The core hole produced in the photoemission process is well screened from the departing photoelectron. Thus, the photoelectron reflects its initial core-level energy state. The broad peak at higher binding energies (-422 to -424 eV), by contrast, reflects a manifold of final states produced when the departing electron is poorly screened by the surrounding conduction electrons.



tion effects to explain that dependence becomes therefore unnecessary. One must use some other model (perhaps the Periodic Anderson Model or a renormalized band calculation) to explain the correlations shown as the narrow peak at the Fermi energy.

Evidence for 5f Localization in δ -Plutonium. Satellites in a 4f core-electron spectrum can shed light on the nature of the 5f states. When a core electron is ejected from an atom, the final state of the system is an atom with a core hole (a positively charged atom) and a photoelectron in the continuum. If the core hole is fully screened from the departing electron (perhaps by a refilling of the core hole on the time scale of the photoemission process), there is no electrostatic interaction between the departing electron and the core hole (no loss of energy), and the electron carries information from the initial state of the system. If, however, the screening is incomplete (as, for example, in the case of screening by a reconfiguration of the density of states around the atom), the photoelectron loses energy because of the electrostatic interaction with the positive core hole and displays characteristics that are a convolution of initial and final states.

The 4f core-level spectra in Figure 12 suggest that electrons in δ -plutonium are more localized than those in α -plutonium. These spectra were taken at the ALS at high resolution. The photon energy was 850 eV. In both cases, the spectra show a sharp peak at a binding energy of about -421 eV, reflecting the 4f core-level state in the metal. The core hole produced in the photoemission process is well screened from the departing photoelectron, and thus the photoelectron reflects its initial core-level energy state. The broad peak at higher binding energies (-422 to -424 eV), by contrast, reflects a broad manifold of final states produced when the departing electron is poorly screened by the surrounding conduction electrons. Poor

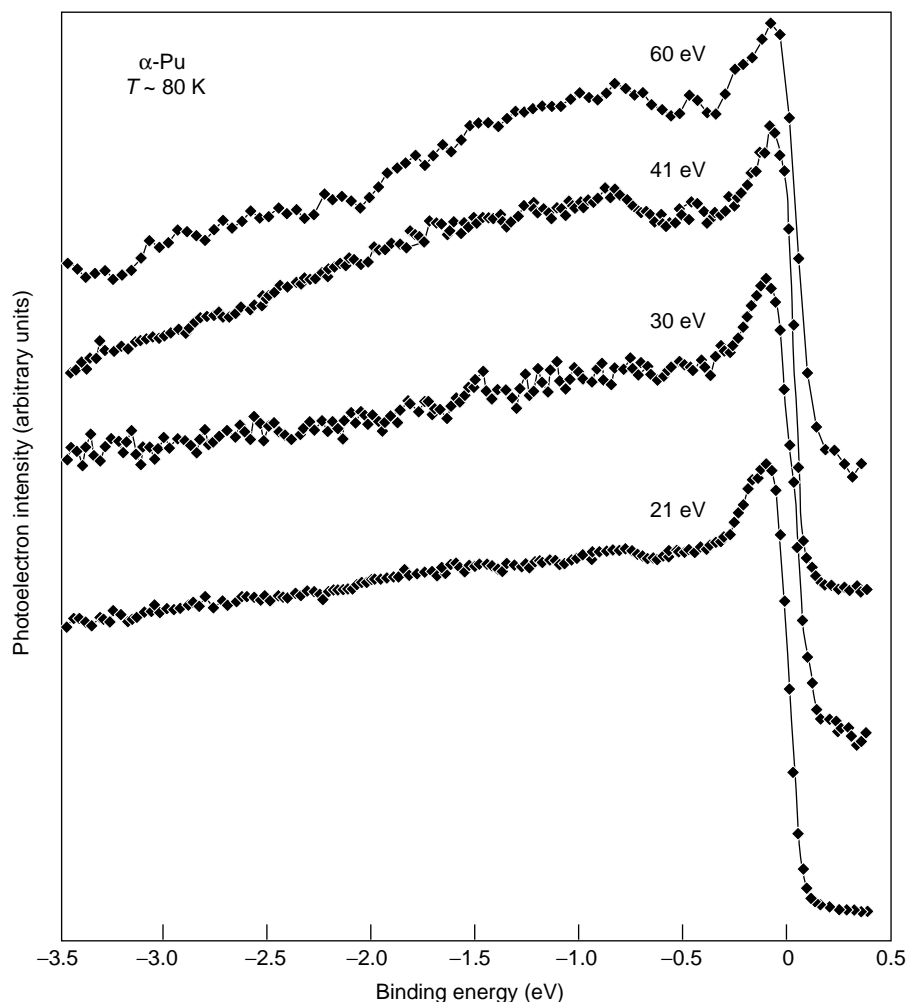


Figure 13. Spectra of α -Plutonium at 80 K and Several Photon Energies
The narrow feature near E_F is persistent at all photon energies and must thus contain substantial 6d admixture in its orbital symmetry. At 21 eV, the photoemission should be dominated by 6d emission (see Figure 4). Moreover, it is most likely bulk-derived based on the larger escape depth at 21 eV. The purer 5f states are in the region of -1 eV. That region clearly grows faster with photon energy than the near- E_F peak.

screening may result when the density of states of the electrons at the Fermi energy is low or when the electron mobility is poor because these electrons have a large effective mass (that is, they exhibit correlation behavior). By comparing the α - and δ -plutonium spectra, we find that δ -plutonium shows a greater percentage of poorly screened final-state events than α -plutonium. This result suggests that δ -plutonium has fewer mobile (delocalized) electrons available for screening of the core hole, which is consistent with δ -plutonium having a narrow f band and its f electrons having a larger effective mass

and hence being more localized. The core-level results are consistent with the valence-band PES data.

Ruling out Surface Effects. In the past, questions were raised about the possibility that α -plutonium may contain a δ -like surface structure. Indeed, the similarities of the PES spectra would seem to suggest such a possibility. However, the more-bulk-sensitive spectra at 220 eV appear similar to those at resonance (125 eV) and at 40 eV and would indicate that, in all cases, we are observing bulk features and that the small differences

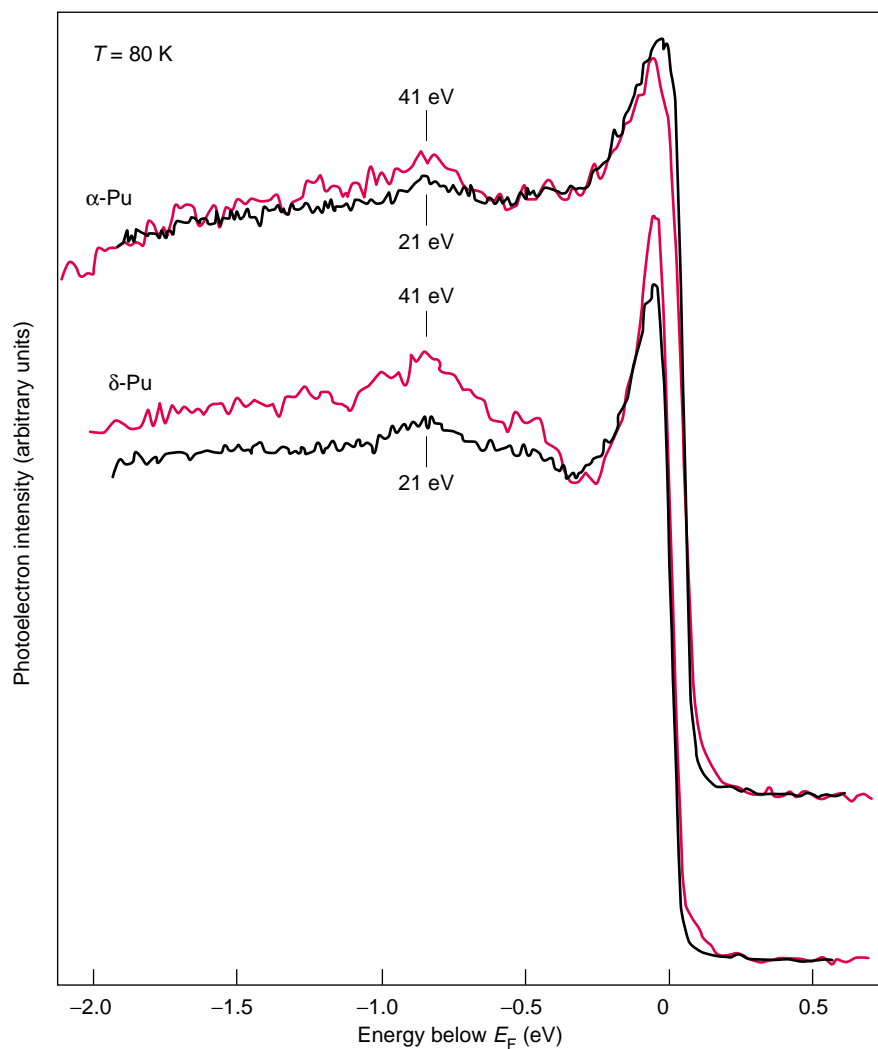


Figure 14. Spectra of α - and δ -Plutonium at 21 and 41 eV and at 80 K
 Data at 21 eV (black lines) and 41 eV (red lines) and a temperature of 80 K for α - and δ -plutonium are overlaid to show relative peak intensities of the near- E_F features. There is a noticeable increase in the 5f vs 6d character in δ -plutonium.

between α - and δ -plutonium are bulk derived. Further, this assumption suggests that α -plutonium does not exhibit a δ -like surface. This conclusion is additionally corroborated by spectra at lower photon energies. At these energies, PES measurements using 21-eV photons yield even greater bulk sensitivity than those using 220-eV photons (see Figure 2). In Figure 13, we show α -plutonium PES spectra taken at 80 kelvins with 21-, 30-, 41-, and 60-eV photons. The sharp feature at E_F is, in fact, somewhat more intense rela-

tive to the other features in the 21-eV spectrum than in the spectra at higher energies, which indicates not only that this peak derives from the bulk, but also that it contains more 6d admixture in its orbital character than the remaining features, which may be more 5f in character.

A similar plot for δ -plutonium (see Figure 14) reveals that we are again dealing with bulk phenomena because the 21-eV data are similar to the 41-eV data. In this case, however, the intensity of the sharp peak at E_F relative to other

features increases significantly from the 21-eV spectrum to the 41-eV spectrum. This result indicates that the near- E_F peak contains more 5f character in δ - than in α -plutonium. The near invariance of the relative intensities of the features with photon energy points to a relatively uniform admixture of 6d character throughout the valence band region (compare these data to the NpAs data illustrated in Figure 4). Irrespective of the amount of 6d admixture, the spectrum is consistent with the very narrow band behavior observed in bulk properties and with the conventional wisdom that the 5f states in α -plutonium are more hybridized and band-like than those in δ -plutonium.

Surface reconstruction is common for metals throughout the periodic table. In general, however, it is only observable in high-quality single crystals, and even then, one must distinguish between a reconstructed surface and simply a surface termination layer. Although interpretations of previous data suggested that the crystal structure on the surface of α -material would become δ -like, the dependence of normal emission spectra on photoelectron escape depth measured by varying the photon energy was not available. Our new measurements of the α -plutonium spectra as a function of escape depth yield nearly invariant spectra, strongly suggesting a lack of reconstruction (from α - to δ -material).

Current understanding would indicate that we have indeed measured the bulk electronic structure of α - and δ -plutonium. All data are consistent with the concept of much narrower itinerant states in the δ - than in the α -phase of plutonium. Indeed, bulk property data for δ -plutonium suggest behavior like that of heavy fermions. However, very narrow bands are already obtained within a constrained band calculation (see the article “Actinide Ground-State Properties” on page 128). An additional electric-field component acts on the 5f electrons within this generalized-gradient approximation (GGA), which is a refinement of

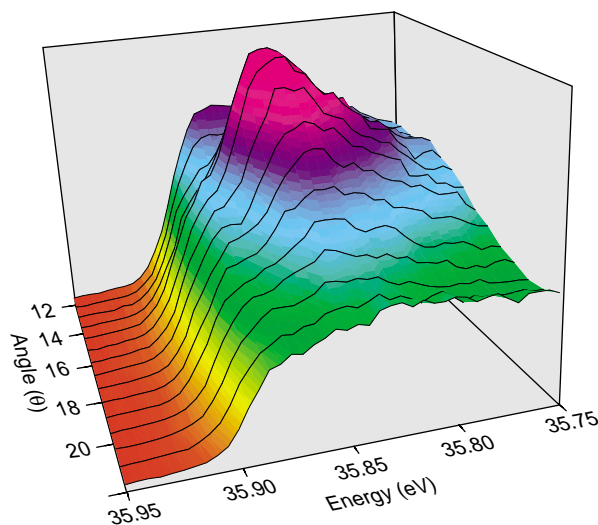
the traditional local-density approximation (LDA), the workhorse of density functional theory. These bandwidths in the constrained calculation agree, to some extent, with the experimental bandwidths in δ -plutonium. Thus, there may be no need for further band narrowing such as might result from additional correlation effects (see the comparison with calculations in the article “Electronic Structure of α - and δ -Plutonium” on page 152). Note that, by constraining some of the 5f electrons to be localized in the above-mentioned GGA calculation, one has already introduced substantial correlation effects.

The Need for Single Crystals.

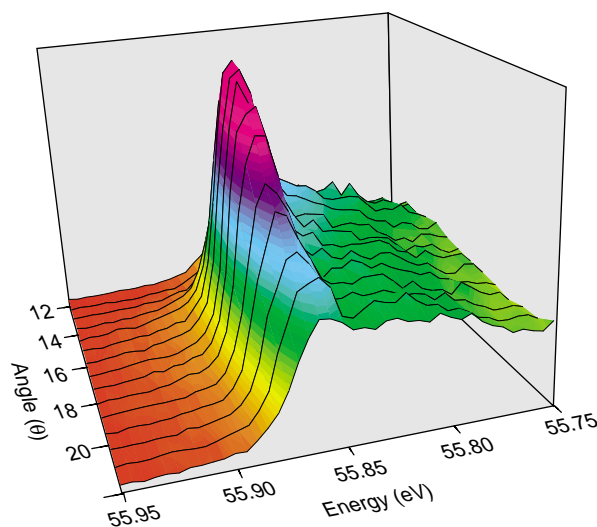
Many of the remaining questions on plutonium and its compounds or alloys will be resolved once data are obtained on high-quality single-crystal materials. For photoemission experiments, these crystals should have mirror surfaces and well-defined axes normal to the surface. A glimpse of this future can be observed in Figure 15, in which we show angle-resolved spectra on a high-quality single crystal of the uranium-antimony compound USb_2 grown⁴ by precipitation from a flux. In addition to reflecting the high quality of the crystal, the data in Figure 15 represent state-of-the-art resolution (15 meV) obtained with a state-of-the-art detector (the Scienta), which simultaneously preserves energy and angle information. Each scan of the Scienta simultaneously measures up to 100 electron emission angles (relative to the sample surface) and, hence, 100 spectra. Using this apparatus at a high-intensity undulator beamline (at the Synchrotron Radiation Center in Madison, Wisconsin) produces the dramatic spectra of Figure 15. The figure shows only the first 200 meV of the valence bands below the Fermi energy. The data at 40-eV photon energy in (a)

⁴ John Sarrao of Los Alamos grew this single crystal.

(a) $h\nu = 40$ eV



(b) $h\nu = 60$ eV



$T = 12$ K $T_N = 200$ K

Figure 15. Angle-Resolved PES Data for Antiferromagnetic USb_2

This is essentially E vs k dispersion, with k represented by the angle (1 degree = 0.07 \AA^{-1} for 60-eV data and 0.06 \AA^{-1} for 40-eV data). Only the first 200 meV within the Fermi energy are shown. The 40-eV data in (a) are primarily sensitive to 6d emission, whereas the 60-eV data in (b) represent primarily 5f emission. Note that both 6d and 5f bands show dispersion and that the 5f intensity disperses below the Fermi energy. The center of the Brillouin zone is near 18° .

contain contributions mainly from d states, whereas the data at 60-eV photon energy in (b) derive primarily from the 5f electrons. The three-dimensional plot in (b) clearly shows that the 5f intensity in antiferromagnetic USb_2 is confined to a narrow portion of the Brillouin zone. As the 5f band hybridizes

with the 6d electrons, it disperses away from the Fermi energy, and the quasiparticle peaks broaden and diminish to near zero. The center of the Brillouin zone is located near the 18° angle. One can see that there is no 5f intensity whatsoever at angles larger than about 23° . This constitutes a classic case of f-d

hybridization. Similar-quality single crystals of plutonium compounds have recently been grown with flux growth techniques.⁵ Data such as those in Figure 15 could therefore be obtained for plutonium compounds with a Scienta energy and angle analyzer. It should then be possible to view the band structure of these plutonium compounds directly.

Conclusions

The large photon fluxes now available from bright, low-emittance undulator beamlines have made it possible to perform some photoemission experiments on plutonium at synchrotron sources. This development will enhance our knowledge of the electronic structure of this material. We have also developed the LPLS as a viable source for conducting photoemission experiments within a conventional laboratory environment. With intensities rivaling those of second-generation synchrotrons, the LPLS is particularly useful for those experiments on hazardous materials that benefit from a highly controlled and contained environment. A combination of PES tools will be used to tackle the least studied, yet the most interesting, series in condensed matter physics—the transuranics.

Results on α - and δ -plutonium suggest that the electronic structure is characterized by an intense, sharp feature of mixed 5f and 6d character near the Fermi energy, as well as a manifold of broad 5f features centered at a binding energy of about -1 eV. The sharp feature near the Fermi energy is much broader in α - than in δ -plutonium, consistent with stronger hybridization. The intense, narrow 5f peak in δ -plutonium is reminiscent of the sharp features in cerium compounds referred to as a Kondo resonance, but this feature

appears to be reproduced in a GGA band calculation that constrains some of the 5f electrons to be localized. The use of periodic models based on the Anderson Hamiltonian may be eventually necessary for modeling the electronic structure of δ -plutonium, but the constrained GGA result for δ -plutonium provides a reasonable starting point. The similarity between α - and δ -plutonium spectra raises suspicion about a surface reconstruction in α -plutonium to a δ -like surface, particularly since the sharp feature in α -plutonium is not reproduced in a band calculation. However, measurements with varying escape depths do not support this notion. Future measurements on single crystals will open a whole new field of study for plutonium materials. ■

Further Reading

- Arko, A. J., J. J. Joyce, and L. Morales 1999. *J. Alloys and Comp.* **286**: 14.
- Arko, A. J., J. J. Joyce, L. E. Cox, L. Morales, J. Sarrao, J. L. Smith, et al. 1998. *J. Alloys and Comp.* **826**: 271.
- Blank, H., and R. Linder, eds. 1976. *Plutonium 1975 and Other Actinides*. 1976. North Holland: American Elsevier.
- Fano, U. 1961. *Phys. Rev.* **124**: 1886.
- Freeman, A. J., and J. B. Darby, eds. 1974. *The Actinides: Electronic Structure and Related Properties*. Vols. I and II. New York: Academic Press.
- Gunnarsson, O., and K. Schonhammer. 1987. In *Handbook of the Physics and Chemistry of Rare Earths*, Vol. 10, p. 103. Edited by K. A. Gschneidner, Jr., L. Eyring, and S. Huffner. Amsterdam: Elsevier Publishers.
- Lee, P. A., T. M. Rice, J. W. Serene, L. J. Sham, J. W. Wilkins. 1986. *Commun. Cond. Matter Phys.* **12**: 99.
- Lynch, D. W., and J. H. Weaver. 1987. In *Handbook of the Physics and Chemistry of Rare Earths*, Vol. 10. Edited by K. A. Gschneidner, Jr., L. Eyring, and S. Huffner. Amsterdam: Elsevier Publishers.
- Miner, W. N., ed. 1970. *Plutonium 1970 and Other Actinides*. Nuclear Metallurgy 17, Vols. I and II. New York: Metallurgical Society and American Mining, Metallurgical, and Petroleum Engineers.
- Shirley, D. A. 1978. In *Topics in Applied Physics: Photoemission in Solids*, Vol. 26, p. 192. Edited by M. Cardona and L. Ley. New York: Springer-Verlag.
- Yeh, J. J., and I. Lindau 1985. *At. Data Nucl. Data Tables* **32**: 1.

⁵ In April 2000, John Sarrao of Los Alamos has grown single crystals of the compounds PuIn₃, PuGa₃, and PuSn₃.

Aloysius J. Arko received his Ph.D. in condensed matter physics from Northwestern University. He is currently a staff member at the Los Alamos National Laboratory. His primary research interest has been photoelectron spectroscopy in narrow-band materials. Arko is a Fellow of the American Physical Society and of Los Alamos National Laboratory. In recognition of his contributions

to the Laboratory, Arko received the Los Alamos Fellows Prize and the Distinguished Performance Award. His recent interests are increasingly directed toward the study of plutonium and its compounds with the unique photoemission capabilities of the laser-plasma light source.



John J. Joyce received a B.A. in Physics *Summa Cum Laude* from St. Mary's University and a Ph.D. in Materials Science from the University of Wisconsin.

He has conducted photoemission research, the results of which have been published in over 80 articles and presented in 50 invited and contributed talks. John joined the Laboratory in 1990. His current research interests include electronic properties of rare earths and actinides with photoemission research conducted at the Synchrotron Radiation Center and the Laser Plasma Light Source (LPLS). He is a member of the Advisory Committee for the Synchrotron Radiation Center and one of the principal investigators on the LPLS project. For his work on the LPLS, John received the Los Alamos Distinguished Performance Award and the Los Alamos Achievement Award.



Luis A. Morales received his undergraduate degree in chemistry from Arkansas State University and his Ph.D. from the University of Kansas, where he was in the High-Temperature/Materials Science group. After a postdoctoral stint at Los Alamos National Laboratory, Luis became a staff member in the Nuclear Materials and Technology group. His research interests cover areas of solid state and solid-gas phase chemistry. In order to understand structure-property relationships, Luis applies aspects of thermodynamics, kinetics, and crystallography to actinide-containing chemical systems.



Jeffrey H. Terry received his B.S. in chemistry from The University of Chicago and his Ph.D. in chemical physics from Stanford University. After joining the Laboratory as a postdoctoral fellow, Jeff focussed on the application of vacuum ultraviolet synchrotrons to the study of plutonium metal and compounds. Currently a staff member at Los Alamos, Jeff has been working on expanding actinide research at the third-generation synchrotron radiation facilities in the United States. His research interests include the surface chemical behavior of actinide solids, mineral surface interactions with molecular actinides in environmental situations, and the electronic structure of actinide materials.



Roland K. Schulze received his B.S. in chemistry from the University of Minnesota, Duluth, and his Ph.D. in chemistry from the University of Minnesota, Minneapolis. Roland joined the Los Alamos Laboratory as a postdoctoral fellow in the Analytical Chemistry Group, where he conducted surface science research and developed and built a time-of-flight secondary ion mass spectrometer for surface and interface studies. Since becoming a technical staff member, Roland has been with the Materials Characterization Team in the Chemical and Metallurgical Research (CMR) Facility, first in the Materials Science and currently in the Nuclear Materials Division. In the past four years, he has built up an analytical surface-science facility in the CMR to study radiological materials and perform fundamental measurements on actinide solids. Roland's research interests include the surface chemical behavior of actinide solids, mineral surface interactions with molecular actinides in environmental situations, and the electronic structure of actinide materials.



Laser-Plasma Light Source

Design and operation

John J. Joyce, Aloysius J. Arko, and Luis A. Morales

The Laser-Plasma Light Source (LPLS) developed at Los Alamos is the world's only tunable light source dedicated to transuranic photoelectron spectroscopy (PES). Our compact LPLS simulates the continuum of photon energies available at a synchrotron source, and it costs much less. The large-scale public synchrotrons generate a wide range of photons from the infrared to hard x-rays—20 kilo-electron-volts (keV)—by bending the orbit of the relativistic stored particle beam in a magnetic field. By contrast, the LPLS generates photons throughout the ultraviolet (UV) region, including vacuum UV and extreme ultraviolet (25–140 eV), by laser ionization of a metal target. The extreme power densities that are generated create a plasma in a small volume of the metal target, which emits pseudo-continuum photons over the entire UV range as a result of the recombination process between multiple-ionized multivalent interactions. The photon energy range of 25 to 140 eV includes the regions of largest 5f cross sections, greatest cross-sectional variations, and the giant 6d-5f resonances. Our current version of the LPLS consists of a krypton fluoride (KrF) excimer laser, focusing optics, a metal liquid target chamber, an energy-dispersing diffrac-

tion-grating monochromator, as well as measurement and preparation chambers.

The excimer laser system produces 800 millijoules per pulse (mJ/pulse) at 200 hertz in 20-nanosecond pulses at a

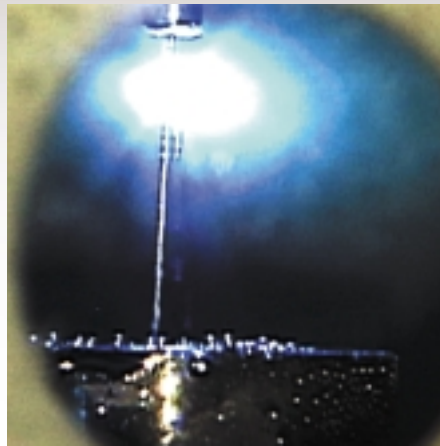


Figure 1. Mercury Stream Showing Light-Emitting Plasma

wavelength of 248 nanometers (5 eV). These 10- by 20-millimeter laser pulses are delivered to the target chamber (top photo) by turning mirrors. A two-lens assembly, which is 30 millimeters in focal length, then focuses these pulses on the target to a 50-micrometer spot size. This system generates a power density of about 1.6×10^{12} watts per centimeter squared (W/cm^2) and target temperatures on the order of 100,000 kelvins.

This power density is sufficient to generate a plasma at the target.

The target chamber system consists of a high-pressure mercury stream shown in Figure 1, a vacuum chamber, a mercury cold trap, a turbo pump, and magnesium fluoride (MgF_2) optics for laser input and output (for the beam portion not absorbed by the mercury stream). The plasma generated at the target produces photons with characteristic lines, as well as a broad-band spectrum covering energies from 25 to 140 eV (the entire UV region), which are used by the LPLS. The mercury target does not significantly deteriorate the input (laser) or collection (UV) optics and provides an infinite supply of plasma (source material) through the closed-cycle pumped system.

The plasma spectrum (indicated by a black line in Figure 2) is monochromatized by a variable line space, spherical-grating instrument with two diffraction gratings (nominally 450 and 900 lines per millimeter) and a resolving power of 1000 at 100 eV. We use rhodium-coated collection optics for excellent reflectivity over the UV range and inert characteristics with mercury. The monochromator portion of the LPLS (refer to Figure 2) consists of vacuum tanks and pumps that house

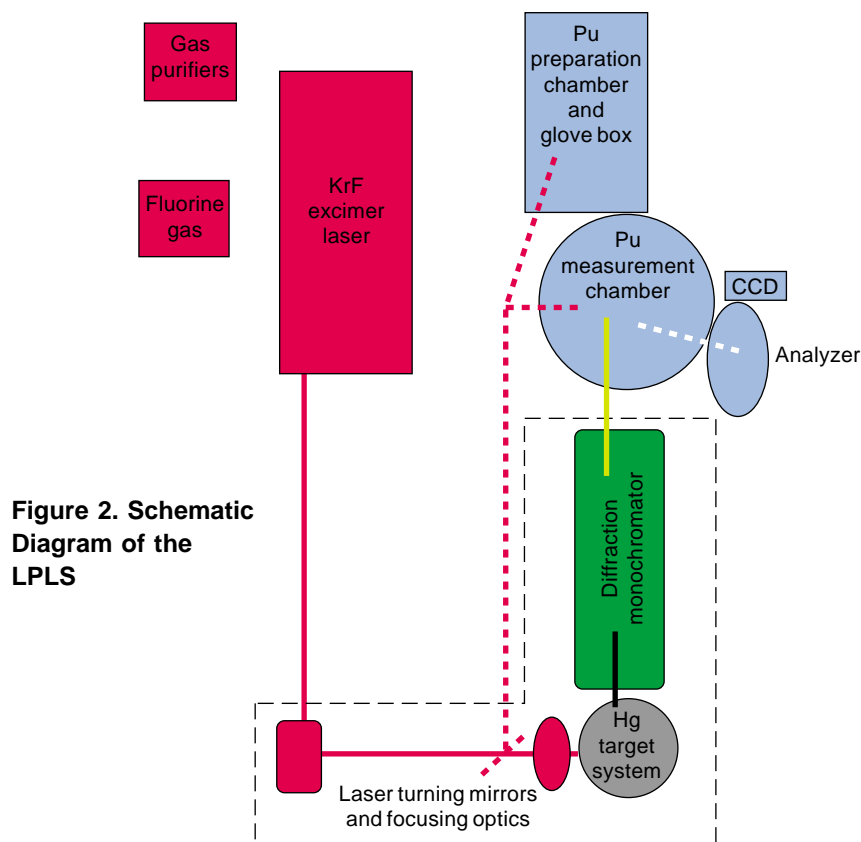


Figure 2. Schematic Diagram of the LPLS

the entrance slit (currently fixed at 75 micrometers), the plasma collection mirror, the diffraction gratings, the variable-width (35–400 micrometers) exit slit, and the refocusing mirror.

The plutonium-capable portion of the system (blue on Figure 2) consists of the measurement chamber, preparation chamber, magnetic transfer mechanisms and load locks, as well as a glove-box assembly. Samples are transported from a Los Alamos plutonium facility to the LPLS in a stainless steel magnetic-transfer arm, which is bolted onto the preparation chamber. The sample is placed behind a gate valve and is always kept under vacuum. After the load-lock region is evacuated, the plutonium samples are moved into the preparation chamber by the magnetic transport device. The preparation chamber is enclosed in a glove box.

Primary cleaning of the samples takes place in the preparation chamber to minimize contamination of the measurement system. Laser ablation, ion sputtering, and cleaving are the cleaning techniques available in the system. For laser ablation, the best method for

cleaning transuranic surfaces, the laser light is diverted with mirrors onto the plutonium sample through a quartz window (red dashed line in Figure 2). We control the power density by varying an aperture and the degree of focusing and the sample heating by varying the frequency of the laser pulses.

The cleaned sample is then transferred to the measurement chamber by three additional magnetic transfer arms. Once it is in the measurement chamber, the sample is attached to a low-temperature cryostat, which can vary the sample temperature from room temperature to 20 kelvins. Many of the interesting properties of transuranic materials are observed only at cryogenic temperatures. Cleaning the surface of these materials in situ at cryogenic temperatures is essential for determining their fundamental properties and is one of the success stories of the LPLS. The cleaned, cooled sample is placed at the intersection of the monochromator focus and the electron analyzer focus. The monochromatic photon beam (green line to measurement chamber) is placed on the sample, and photoelec-

trons are ejected. The photoelectrons (white dashed line) are measured by a hemispherical, electrostatic analyzer whose mean radius is 100 millimeters.

For multichannel electron detection, we modified the off-the-shelf analyzer by opening the exit plane of the deflection hemispheres to 10×50 millimeters and then mounting dual microchannel plates and a phosphorus screen behind the exit plane. A charge-coupled-device (CCD) camera detects the phosphorus screen. The channel plate, phosphorus screen, and CCD camera assembly measure the energy of the photoelectrons coming through the analyzer.

The multichannel detection assembly has the potential for simultaneously collecting several photoelectron energies and angular-dispersion information. The angular information may be used to determine the crystal momentum of photoelectrons in single-crystal samples thereby expanding the usefulness of the LPLS. Future improvements in the LPLS, including an angle-resolved capability and increased photon flux, provide a path for laser-plasma sources used for transuranic research to rival the large public synchrotron facilities in capability and productivity.

Recent advances in laser technology (improved capabilities for delivering a higher laser-photon density onto the target material) now allow an increase of an order of magnitude or more in UV photon flux. Commercial solid-state lasers (Nd:YAG) now cost less than large KrF lasers and deliver a 900 mJ/pulse in 2.5 nanoseconds at 1064 nanometers, which can be focused to 25 micrometers, giving rise to power densities of about 6×10^{13} W/cm². Equally impressive advances in plasma technology, including photon channeling with inert gases, show promise for additional order-of-magnitude increases in plasma photon fluxes. Indeed, it is possible that such technological advances will make laboratory-based light sources comparable to the very best synchrotron facilities. ■



Actinide Photoemission Measurements at the Advanced Light Source

Roland K. Schulze and Jeffrey H. Terry

The Advanced Light Source (ALS) at the Lawrence Berkeley National Laboratory is the nation's premier third-generation synchrotron light source for performing vacuum ultraviolet (VUV) and soft x-ray studies of materials. We have used Beamline 7.0.1 at the ALS to perform photoemission spectroscopy (PES) measurements of plutonium metal and compounds. The beamline operates over the energy range 80–1200 electronvolts (eV) using an undulator (shown in the top photo) with a 5-centimeter period and a spherical-grating monochromator. Spectral resolutions of up to 8000 ($E/\Delta E$) can be achieved with a

light flux (per 0.01 percent bandwidth) of approximately 10^{13} photons per second (photons/s) for energies less than 200 eV, 10^{12} photons/s for intermediate energies, and 10^{11} photons/s for energies greater than 500 eV. Shown in Figure 1 is a schematic of the beamline from the undulator insertion device in the synchrotron ring to the end stations (or analysis chambers), where the light is used for materials and surface measurements. To select the photon energy, we use one of three gratings. The adjustable beam-defining apertures and the refocusing mirrors set the size of the photon spot at the sample surface.

The UltraESCA photoemission analysis chamber was built around a 137-millimeter spherical-capacitor electron-energy analyzer (Physical Electronics Omni IV), which allows high-resolution photoemission measurements, as well as photoelectron imaging through adjustment of the input lenses. The schematic in Figure 2 shows the location of the UltraESCA analysis chamber on the beamline, past the last refocusing mirror, relative to the other instruments on the beamline. This location takes advantage of the small focus of the photon beam, which may be as small as 50 micrometers in diameter at

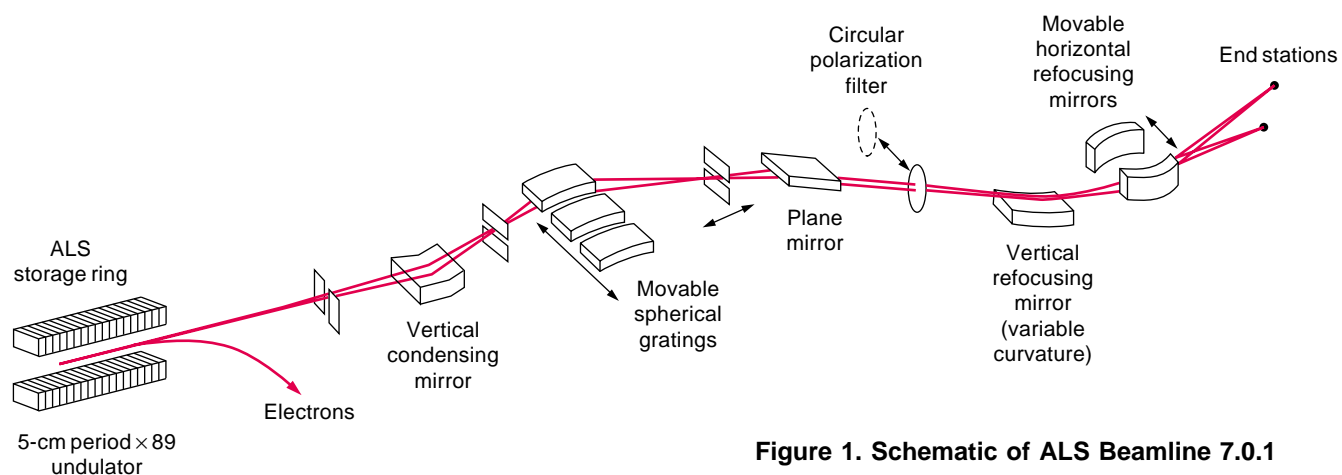


Figure 1. Schematic of ALS Beamline 7.0.1

the sample surface, while still maintaining the high flux. This feature was critical in our measurements, and it will also be so in future experiments because the samples we analyze are very small. In addition to dealing with limitations regarding the size of samples, we attempted to measure the photoemission spectrum from a single-crystallite surface, 500×1000 micrometers in size, which was surrounded by a matrix of other crystallites. The focused photon beam allowed us to measure exclusively from the surface of this single crystallite. Future work will include measurements for mapping the electronic structure bands of plutonium metal and x-ray photoelectron diffraction measurements to examine surface crystal structure. In addition, a dedicated actinide spectrometer is being assembled to allow final sample cleaning and preparation to take place within the analysis chamber. In this way, excessive

sample transfer operations are eliminated and sample purity is ensured. We will be able to move this spectrometer system to other ALS beamlines and thus use other specific light characteristics (such as photon energy range or polarization) in our measurements.

To make these measurements at the ALS, we designed and built a special vacuum system with which to handle the samples. We called it the Sample-Handling and Integrated-Transfer System for Plutonium Intense-Light Experiments. The system is a quad-chamber, wholly enclosed ultrahigh-vacuum ion-pumped system with sample-transfer devices. It also includes a differentially pumped ion gun and sample-heating stage used for sample cleaning (by argon-ion sputtering) and annealing. This system was temporarily connected to the UltraESCA analysis chamber during our experiments so that the plutonium metal samples could be

prepared and transferred under vacuum, with surfaces kept clean until the samples could be measured by photoemission. The initial sample preparation, cleaning, and analytical spectroscopy take place at Los Alamos. The samples are then placed under vacuum into transfer vessels, which are maintained at a pressure of 10^{-8} torr with a battery-powered ion pump system. These transfer vessels are then shipped to the ALS, where they are coupled to our sample-handling system. To maintain the cleanliness and integrity of the samples, we never allow them to see the atmosphere but transfer them under high vacuum. The sample-handling system then allows us to perform a final clean-and-anneal cycle before the samples are transferred into the UltraESCA analysis chamber for PES measurement. ■

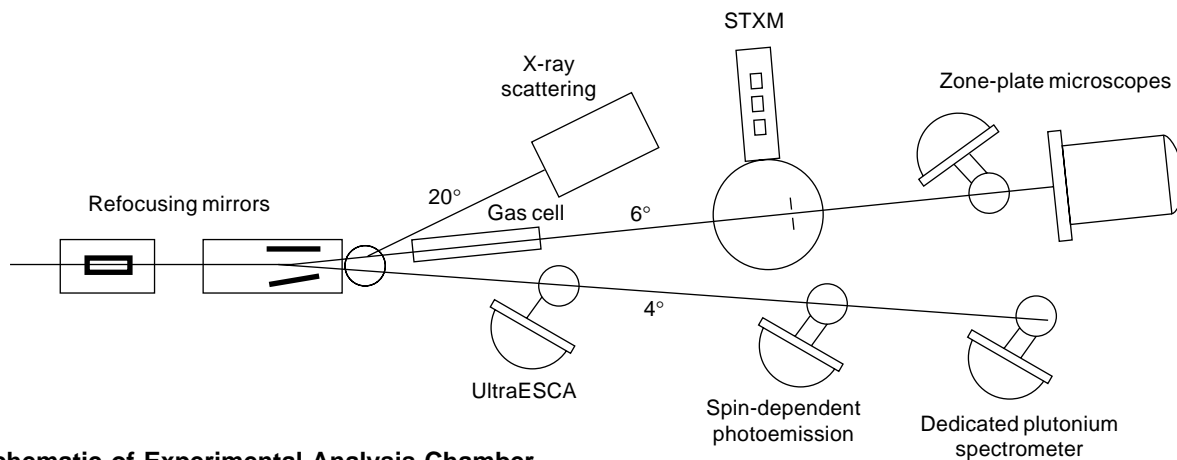
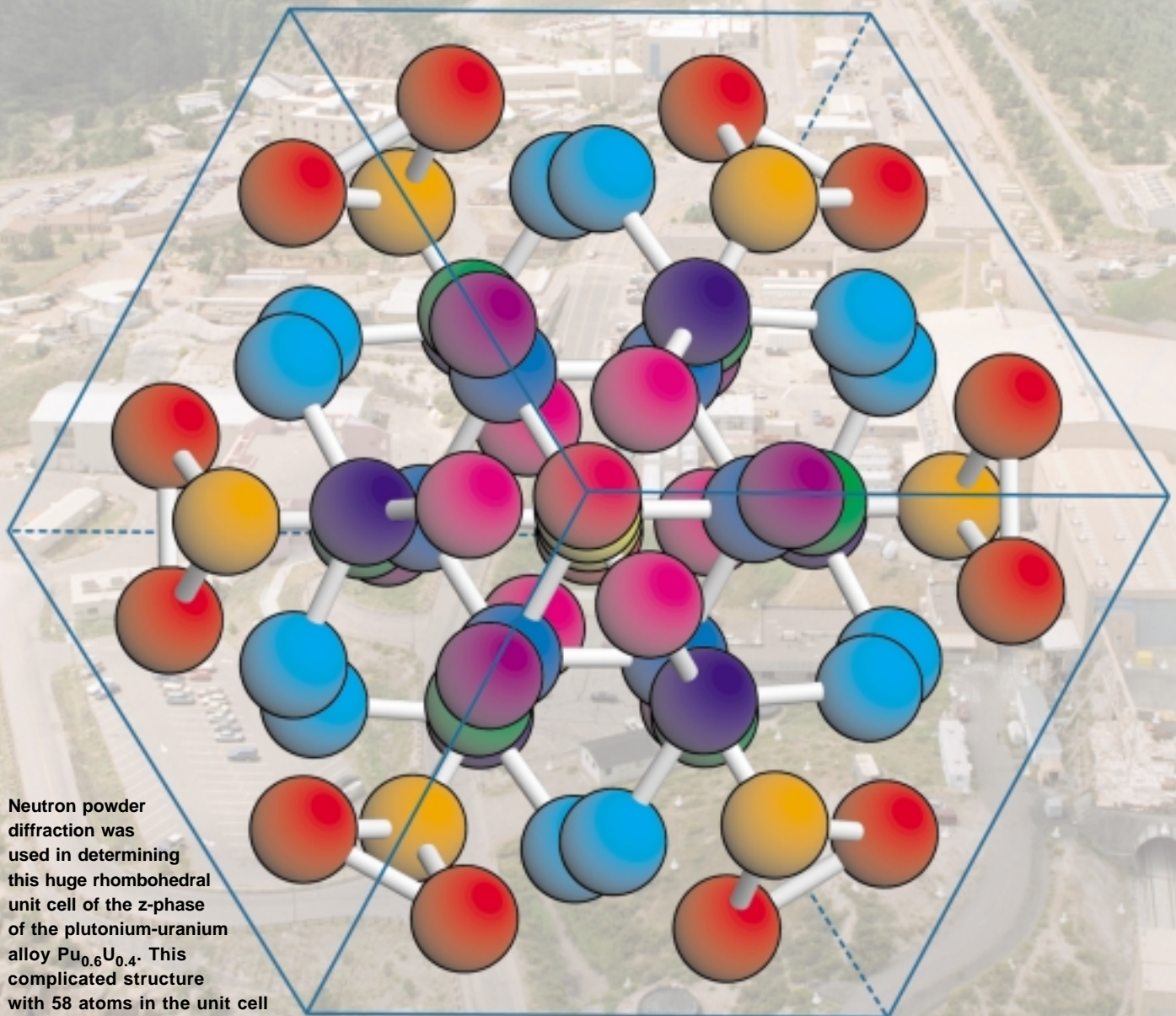


Figure 2. Schematic of Experimental Analysis Chamber

Atomic Vibrations and Melting in Plutonium

Andrew C. Lawson, Barbara Martinez, Joyce A. Roberts, James W. Richardson, Jr., and Bard I. Bennett



Neutron powder diffraction was used in determining this huge rhombohedral unit cell of the z-phase of the plutonium-uranium alloy $\text{Pu}_{0.6}\text{U}_{0.4}$. This complicated structure with 58 atoms in the unit cell and 10 crystallographically distinct atom types illustrates the general tendency for complex structures in plutonium and its alloys. The Los Alamos Neutron Scattering Center is shown in the background. (Crystal structure was reproduced with permission from *Acta Crystallographica* B52, 1996.)

At any temperature, the atoms in a crystalline solid are constantly vibrating about their equilibrium positions. Those positions define the crystal lattice and are ultimately determined by the electronic structure of the solid. As the material heats up, the atoms vibrate about their lattice sites with increasing amplitude until they shake loose and the material melts. The square of the vibrational amplitude is inversely proportional to the strength of the atomic forces that bind each atom to its lattice site. In some materials, including plutonium, the vibrational motion that accompanies heating can cause the electrons to rearrange around the atoms, changing the strength of the interatomic forces. Measuring the atomic vibrations therefore gives information about the strength of these interatomic forces and, ultimately, about the electronic structure and its variation with temperature and applied pressure.

The response of plutonium metal to thermal and mechanical perturbations is characterized by instability. Figure 1 shows plutonium's phase diagram at temperatures below its melting temperature (640°C) and at pressures below 10 kilobar. Under these relatively small changes in temperature and pressure, plutonium goes through seven distinct crystallographic phases. These solid-to-solid phase transitions arise from rearrangements of the electrons that cause the interatomic forces to weaken and the crystal structure to change.

The melting point of plutonium metal is another sign of instability, as it is very low when compared with the melting points of its neighbors in the periodic table (see Figure 2). These instabilities have been known since the forties, when Manhattan Project metallurgists struggled to fashion plutonium metal into the shape needed for the first atomic bomb, but they still baffle condensed matter physicists. Here, we report on some new measurements of atomic vibrations that shed light on both the

phase instability and the melting anomaly of plutonium.

Atomic Vibrations and the Equation of State

Understanding the instabilities of plutonium and other actinides is not only of fundamental interest, but also of great practical importance for the current nuclear missions of the Department of Energy. Among those missions are cleaning up the nuclear contamination and preventing further contamination, storing nuclear waste, and maintaining a safe and reliable nuclear weapons stockpile. Foremost among the missions of Los Alamos is stockpile stewardship, which requires the construction of a reliable equation of state (EOS) for plutonium to predict the performance of nuclear weapons in the absence of weapons testing. To ensure that the EOS provides this predictive capability, we must understand the vibrational excitations of plutonium at a fundamental level because they contribute directly to the EOS.

The EOS describes the internal pressure in plutonium metal as a function of temperature and density. Plutonium metal is, of course, a solid, and its internal pressure can be divided into several contributions, whose relative sizes vary with temperature and external pressure. At $T = 0$, there is only the zero-point vibrational energy, and the pressure comes mostly from the static attraction or repulsion between the atoms. Bare nuclei repel each other, and the material flies apart. Some of the electrons surround the nuclei, forming ion cores, and screen this repulsion. Other electrons (the conduction electrons) are shared with neighboring atoms, causing the atoms to bind together. The net balance between these competing forces determines the pressure the solid can exert on its surroundings.

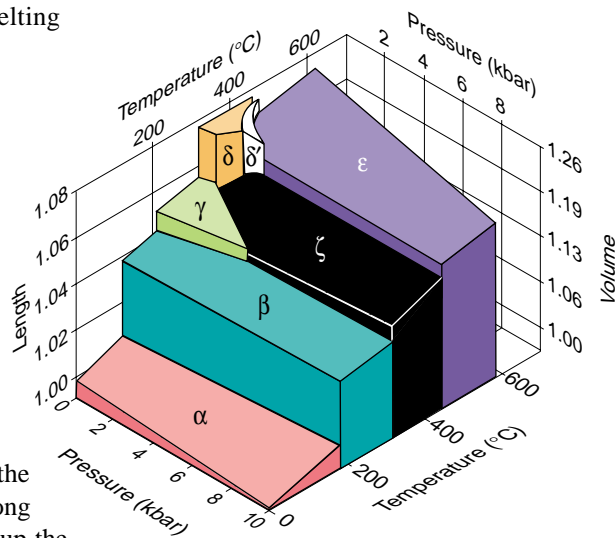


Figure 1. Pressure-Temperature Phase Diagram of Plutonium Metal

Plutonium has the most complex phase diagram of any element in the periodic table. Its seven distinct crystallographic phases arising from the rearrangements of the electrons can be stabilized with slight changes in temperature or pressure. (Reproduced with permission from the Metallurgical Society.)

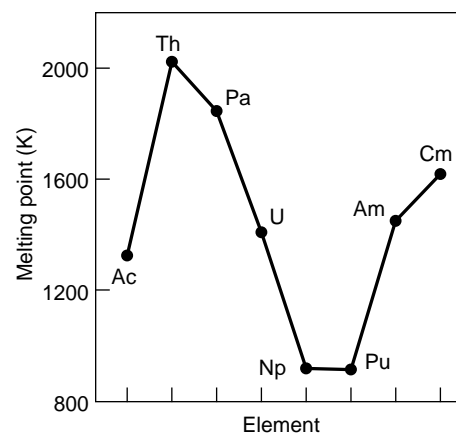


Figure 2. Melting Points of the Light Actinides

As illustrated here, the melting points of neptunium and plutonium are anomalously low by comparison with those of neighboring elements. The same is illustrated in a metallurgical context in Figure 13 in the article "Plutonium Condensed-Matter Physics" on page 61. (Reproduced with permission from *Philosophical Magazine B80*, 2000, page 53, Taylor & Francis.)

Equations of State—Theoretical Formalism

by Bard I. Bennett

Theoretical and experimental research in equations of state and material modeling is essential to ensuring a firm scientific footing for these disciplines. This type of research is necessary not only for assessing the nuclear weapons stockpile but also for developing a predictive computational capability. Here, I will outline the general theoretical formalism for calculating equations of state and then expand on the contribution from the vibrational (or thermal) excitations of solids to the equation of state (EOS). The temperature dependence of the Debye temperature reported in the main article has a direct bearing on our models for the vibrational contribution.

The EOS for any material is typically expressed as an equation for the pressure as a function of temperature and density. Generally speaking, at densities less than 100 grams per cubic centimeter (g/cm^3) and temperatures less than 100 kilo-electron-volt (keV), there are three distinct contributions to the pressure:

$$P(\rho, T) = P_c(\rho) + P_N(\rho, T) + P_e(\rho, T) \quad (1)$$

The pressure at $T = 0$, $P_c(\rho)$, is commonly called the “cold curve” and is due to the electronic forces that bind the individual atoms into a solid; $P_N(\rho, T)$ is the pressure due to the vibrational excitation of the nuclei in the solid, liquid, or gas states; and $P_e(\rho, T)$ is the pressure due to the electrons’ thermal excitation.

The cold curve is traditionally modeled by empirical formulae (Lennard-Jones and Morse potentials combined with Thomas-Fermi-Dirac theory). Modern calculations of electronic band structure include relativistic effects. Experimental measurements conducted in a diamond-anvil or tungsten carbide cell can provide data for pressures up to approximately 2 megabars.

The vibrational contribution for the solid state, $P_N(\rho, T)$, is traditionally modeled with the Debye theory. Models of the liquid state use an interpolation scheme between a Debye solid and an ideal gas. Modern theory for all these states uses molecular dynamics or Monte Carlo methods to obtain pressures as a function of density and temperature. No direct experimental data are available, but to infer a melting temperature, we use shock wave methods and laser-heated diamond-anvil cells.

The pressure for electron excitations, $P_e(\rho, T)$, is traditionally modeled by Saha or Thomas-Fermi-Dirac theories. Modern theory for this contribution to the pressure uses relativistic, quantum mechanical,

self-consistent field theory. No direct experimental data are available, but $P_e(\rho, T)$ can be inferred from data obtained from pressure waves generated by nuclear explosions.

We now add more detail to the vibrational contribution to pressure from the motion of the nuclei. The Mie-Grüneisen form is given by

$$P_N(\rho, T) = \rho \Gamma(\rho, T) E_N(\rho, T) \quad (2)$$

where the energy in the Debye model is given by

$$E_N(\rho, T) = \frac{3 N_0 k_B T}{A} \left\{ D_3 \left(\frac{\Theta_D}{T} \right) + \frac{3}{8} \frac{\Theta_D}{T} \right\} \left\{ 1 + \frac{\partial \ln \Theta_D(\rho, T)}{\partial \ln T} \right\} \quad (3)$$

and the Grüneisen parameter Γ is defined by the following equation:

$$\Gamma(\rho, T) = \frac{\int \ln \Theta_D(\rho, T)}{\int \ln \rho} \quad (4)$$

The Debye temperature $\Theta_D(\rho, T)$ is the effective atomic vibrational temperature, and it determines when a material melts or loses its strength. In Equation (3), $D_3(x)$ is the Debye integral of the third kind. In traditional EOS modeling, Θ_D is assumed to be independent of temperature—that is, $\Theta_D(\rho)$. Consequently, Γ would also be a simple function only of density. Modern theories suggest that Θ_D and Γ depend on a material’s density, temperature, and electronic structure.

The neutron diffraction measurements reported in the main article confirm these theoretical ideas. The data show that the Debye temperature and the Grüneisen parameter are, indeed, a function of temperature and electronic structure.

To verify the predictions from quantum mechanical theory, we need to further validate our current models. Measuring the Debye-Waller factor with a new, heated high-pressure cell shows great promise. By using the apparatus containing this cell, we have obtained interesting data for molybdenum. After validation, the theory will be used in modeling material melting and strength for applications in weapons physics (conventional and nuclear), metal casting, or explosively driven shape-forming.

The ground-state distribution of these electrons relative to the ion cores can be predicted by electronic-structure calculations (see the article “The Ground-State Properties of the Actinide Elements: A Theoretical Overview”).

As temperature increases, pressure from the vibrational motion of the ion cores increases as well. These excitations can be treated at several levels of approximation. The first two levels are the Einstein and Debye models. In both, we imagine that an external source of heat gives the ion cores an average kinetic energy, and the cores move away from their equilibrium positions, which are assumed to be fixed in space for the Einstein model and fixed to each other for the Debye model. At the same time, in both models, the electronic forces act like springs, pulling on the ions and causing them to oscillate back and forth. In the Einstein model, the ions oscillate independently of each other. Every atom vibrates at a single characteristic frequency, ω_E , and there are no propagating waves. Even though this model is unrealistically simple, it does give useful first approximations for the heat capacity and the thermal vibration amplitude. At high enough temperatures, the heat capacity is constant, and the vibration amplitude is proportional to the temperature.

Debye made the much more realistic assumption that the electronic springs attach each atom to its near neighbors in the lattice, and not to a lattice site fixed in space. Travelling waves are now allowed, and the vibrational modes (phonons), which are dictated by the crystal structure, obey different dispersion relations (frequency versus wavelength) along different crystal directions. The phonon spectrum (that is, the number of allowed vibrational frequencies per frequency interval) depends on the spacing between the crystal planes and on the atomic spring constants in those directions, but it will always be proportional to ω^2 at low frequencies. In calculating the contribution to pressure from the vibrational excitations, common practice is to use the

model from Debye’s theory as a starting point and extrapolate wherever necessary (see the box “Equations of State” on the opposite page).

The Debye model is a simplified description of the thermal excitations of a solid because it ignores most of the details of lattice dynamics, but it is very useful for interpreting experiments that measure the average elastic and thermal properties of a solid. (See the box “The Debye Model and the Actinides” on page 197.)

The characteristic vibrational energy of the lattice is given in temperature units by the Debye temperature. Defined as the maximum energy of any sound wave that will propagate in a periodic lattice, this energy is determined by the fact that the wavelength of sound must be greater than the lattice spacing (or lattice constant) a_0 defining the size of the crystallographic unit cell. The characteristic frequency in the Debye model is given in terms of an appropriate average sound velocity V_{sound} and the atomic volume Ω (a sphere of radius $a_0/2$):

$$\omega_D = \left(\frac{6\pi^2}{\Omega} \right)^{1/3} V_{\text{sound}} \quad (1)$$

The characteristic Debye temperature is

$$k_B \Theta_D = \hbar \omega_D \quad (2)$$

where k_B is the Boltzmann constant. The sound velocity is determined by a complicated average over the crystal direction and wave polarization:

$$V_{\text{sound}} = \Omega^{1/3} \left(\frac{\beta_{\text{spring}}}{m} \right)^{1/2} \quad (3)$$

where β_{spring} is an average atomic spring constant and m is the atomic mass. The spring constant tells how much force is required to extend the spring per unit length of extension.

The Debye theory predicts that the phonon spectrum has a simple quadratic dependence on frequency up to ω_D and then drops off discontinuously to zero.

The phonon spectrum of a real crystal is more complicated but retains a quadratic behavior at low frequencies.

Therefore, the Debye spectrum, characterized by Θ_D , is a reasonable improvement over the Einstein model, which has only one vibrational frequency. The point of our work is to use neutron diffraction measurements to measure Θ_D , which is essentially the same as the Debye-Waller temperature Θ_{DW} .

The Debye-Waller temperature Θ_{DW} is an average in two ways. First, it is an ω^2 -weighted average over all possible frequencies in the phonon spectrum, so that a measurement of the Debye-Waller temperature Θ_{DW} is equivalent to a measurement of the average elastic constant, which is equivalent to the bulk modulus B . Note that B and the average elastic constant are proportional to $\beta_{\text{spring}}/a_0$ or $\Omega^{-1/3}\beta_{\text{spring}}$. Second, Θ_{DW} is an average over all possible directions in the crystal. The Debye theory is essentially exact at low temperatures because only the low-frequency quadratic part of the phonon spectrum is excited at those temperatures. At higher temperatures, the theory is only approximate, but that approximation can be improved if Θ_D is allowed to be temperature dependent. Ultimately, we would like to measure the actual phonon spectrum rather than predict it from theory, but this is a project for the future.

At present, the question of how accurate the plutonium equation of state (EOS) is over a range of temperatures, pressures, and shock-induced conditions relevant to nuclear weapons is central to the Stockpile Stewardship Program. And our goal is to gather enough information—both experimental and theoretical—to derive the EOS from measurements of microscopic properties and first principles calculations, thereby reducing the uncertainties to a minimum. The most complete characterization of the vibrational properties could be obtained through measurements of inelastic neutron scattering on single crystals. Those measurements would determine the dispersion relations (the

dependence of vibrational frequency on wavelength) for different crystal directions. And this knowledge would provide a powerful check on the microscopic basis for the vibrational contribution to the EOS regardless of whether that contribution is calculated in the Debye or another model.

Although large single crystals (about 1 cubic centimeter) needed for neutron-scattering measurements are not currently available, a significant effort is under way at Los Alamos to grow suitable crystals (see the articles “Preparing Single Crystals of Gallium-Stabilized Plutonium” and “A Single-Crystal Saga” on pages 226 and 233, respectively). In the meantime, however, ultrasonic measurements of the elastic constants will provide the directional dependence of the long-wavelength elastic constants (see the article “Elasticity, Entropy, and the Phase Stability of Plutonium on page 208).

Neutron Diffraction Studies of Atomic Vibrations

Until the large crystals required for inelastic neutron scattering become available, we are measuring polycrystalline materials. Here, we report on our neutron-powder-diffraction studies of polycrystalline samples. We measured powder diffraction patterns over a range of temperatures and fitted each measured pattern to a model of the diffraction pattern through a process known as Rietveld refinement. From the pattern of positions and intensities of the Bragg diffraction peaks at each temperature, we were able to deduce the average vibrational displacement of the nuclei from their lattice positions at that temperature and, in turn, the material’s Debye-Waller temperature, Θ_{DW} . Our measurements demonstrate that Θ_{DW} varies with temperature. Indeed, by incorporating that temperature dependence into the Lindemann melting rule, we were able to predict melting temperatures for the light actinides. The theoretical and experimental values are in good agreement.

Experiments and Data Analysis

The neutron diffraction data presented in this paper were collected at the pulsed-neutron sources at Argonne National Laboratory and Los Alamos National Laboratory. We used polycrystalline samples of lead, thorium, neptunium, and plutonium encapsulated in vanadium and of uranium encapsulated in fused silica. Encapsulation is required for radiological safety. Vanadium is used for two reasons: Its coherent neutron cross-section is tiny, so its Bragg peaks are negligible, and metallurgically, vanadium is compatible with plutonium at high temperatures. The plutonium sample was highly enriched in plutonium-242 because this isotope has a very low probability of absorbing neutrons compared with the more abundant plutonium-239. Our measurements covered as much of the stability range of each phase as possible without leaving any chance for the containment to fail.

Powder diffraction is the simplest technique for obtaining crystal structures because single crystals of the material are not required. For all but the simplest structures, however, the analysis of these complex patterns can be ambiguous. Hugo Rietveld developed a method for data refinement in the late 1960s to extract precise estimates of all crystallographic parameters from x-ray and neutron-powder-diffraction patterns. In this method, the experimental data are fitted to a detailed model of the positions, intensities, and shapes of the diffraction peaks. The model accounts for the effects of the crystal symmetry, the lattice constants, the atom positions in the unit cell, and the broadening of the diffraction peaks from local crystal strain and size effects. The model also accounts for the effects of the mean-square thermal (or vibrational) displacement of the atom, $\langle u^2 \rangle$, from its equilibrium position in the crystal. The Rietveld refinement thus enables us to infer the average vibrational displacement $\langle u^2 \rangle$ from powder diffraction data. We implemented the method using the

code developed by Allen Larson and Robert Von Dreele of the Los Alamos Neutron Scattering Center (LANSCE). At present, this is the most widely used computer code for Rietveld refinement in the world (Von Dreele 1990).

Figure 3 illustrates the effects of vibrational motion on the appearance of the diffraction pattern. The figure shows portions of two neutron-diffraction patterns of an aluminum-stabilized δ -phase plutonium alloy ($\text{Pu}_{0.95}\text{Al}_{0.05}$) taken at temperatures of 13 and 260 kelvins, respectively. The data are plotted as a function of d , the spacing between the crystallographic planes, and only the diffraction peaks at short d -spacings are shown. In both data sets, the Bragg diffraction peaks have the characteristic pattern produced by the face-centered-cubic structure of δ -phase plutonium. There are, however, two features that derive directly from the vibrational motion of the atoms. First, the intensities of the Bragg peaks in both data sets decrease rapidly as the d -spacing decreases. Second, the attenuation is noticeably stronger in the 260-kelvin diffraction pattern than in the 13-kelvin pattern.

Interpreting Diffraction Data with the Debye Theory

In 1914, Debye worked out the effect of the vibrational motion on the diffraction patterns of crystals. He showed that the intensity of a diffraction peak is proportional to an exponentially decreasing factor, now known as the Debye-Waller factor, which is given by

$$I \propto e^{-\frac{8\pi^2\langle u^2 \rangle}{d^2}} \quad (4)$$

The negative exponent is proportional to $\langle u^2 \rangle$, implying that the intensities decrease with increasing temperature as seen in the powder diffraction data illustrated in Figure 3. Moreover, the exponent is inversely proportional to d^2 , which means that the attenuation due to vibrational motion is very

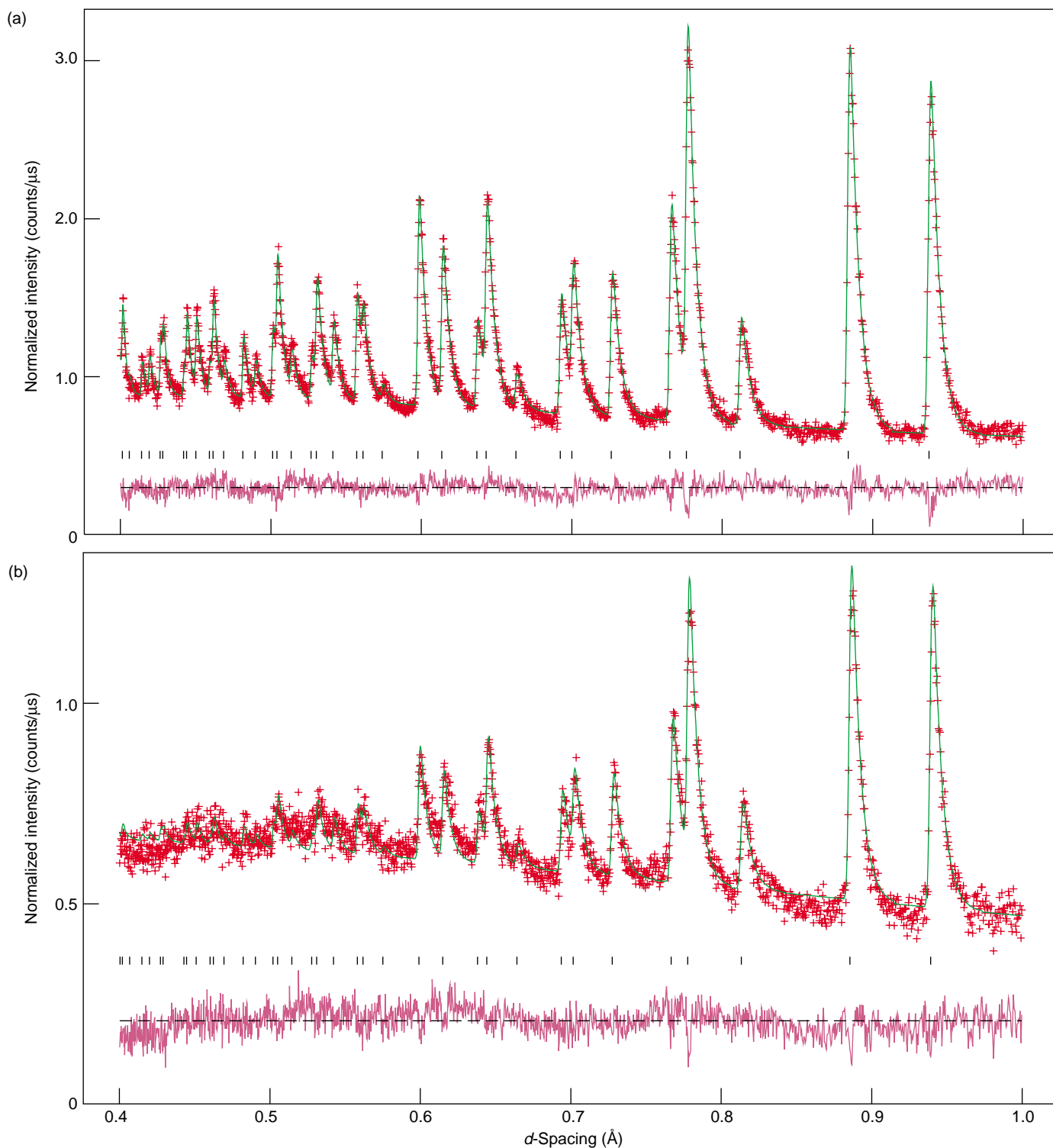


Figure 3. Neutron Diffraction Patterns for $\text{Pu}_{0.95}\text{Al}_{0.05}$

The diffraction data of the aluminum-stabilized δ -phase plutonium alloy have been fitted by Rietveld refinement. In (a), the experiment was conducted at 13 K and in (b) at 260 K. The red crosses are the observed scattered neutron intensity plotted versus crystallographic d -spacing, the green line through them is the Rietveld fit, and the purple curve below the data is the error of the fit. Only the short d -spacing portions of the patterns are shown. Notice that the Bragg peak intensities decrease from right to left as the d -spacing decreases. The attenuation is noticeably stronger in the 260 K than in the 13 K diffraction pattern, in keeping with the trend predicted by the Debye-Waller factor. The article describes how we deduce the Debye-Waller temperature Θ_{DW} from the Bragg peak intensities. (Reproduced with permission from *Kluwer Academic*, A. C. Lawson et al., Edited by A. Gonis et al., "Light Actinides" in *Electron Correlation and Materials Properties*, 1999, page 75.)

strongly enhanced at short d -spacings, also seen in Figure 3. In fact, pulsed-neutron sources such as the one at LANSCE are best suited for these powder-diffraction measurements because the neutron spectrum contains many neutrons with wavelengths at these short d -spacings, at which neutron diffraction scattering is most affected by the vibrational motion.

If the interatomic forces behave like harmonic springs, as they do in the Debye model, the very general equipartition law requires that each vibrational mode have $(k_B T)/2$ of energy, which means that $\langle u^2 \rangle$ increases linearly with temperature at high enough temperatures:

$$\langle u^2 \rangle = \frac{k_B T}{\beta_{\text{spring}}} \quad (5)$$

The Debye theory for $\langle u^2 \rangle$ at low temperatures shows that the temperature dependence for $\langle u^2 \rangle$ is given by

$$\langle u^2 \rangle = \frac{3\hbar^2 T}{mk_B \Theta_{\text{DW}}^2} \times \left\{ \frac{\Theta_{\text{DW}}}{4T} + \frac{T}{\Theta_{\text{DW}}} \int_0^{\Theta_{\text{DW}}/T} \frac{udu}{e^u - 1} \right\} \quad (6)$$

A materials constant that appears in this equation is Θ_{DW} , which as mentioned earlier, is a direct measure of the atomic spring constant β_{spring} of the material. The relationship between Θ_{DW} and β_{spring} is given by the following equation:

$$\beta_{\text{spring}} = \frac{mk_B^2 \Theta_{\text{DW}}^2}{3\hbar^2} \quad (7)$$

Temperature-Dependent Results for Plutonium's Elastic Properties

We now describe how Θ_{DW} can be experimentally determined from measurements of $\langle u^2 \rangle$. As mentioned before, we obtain diffraction patterns over an appropriate temperature range and then

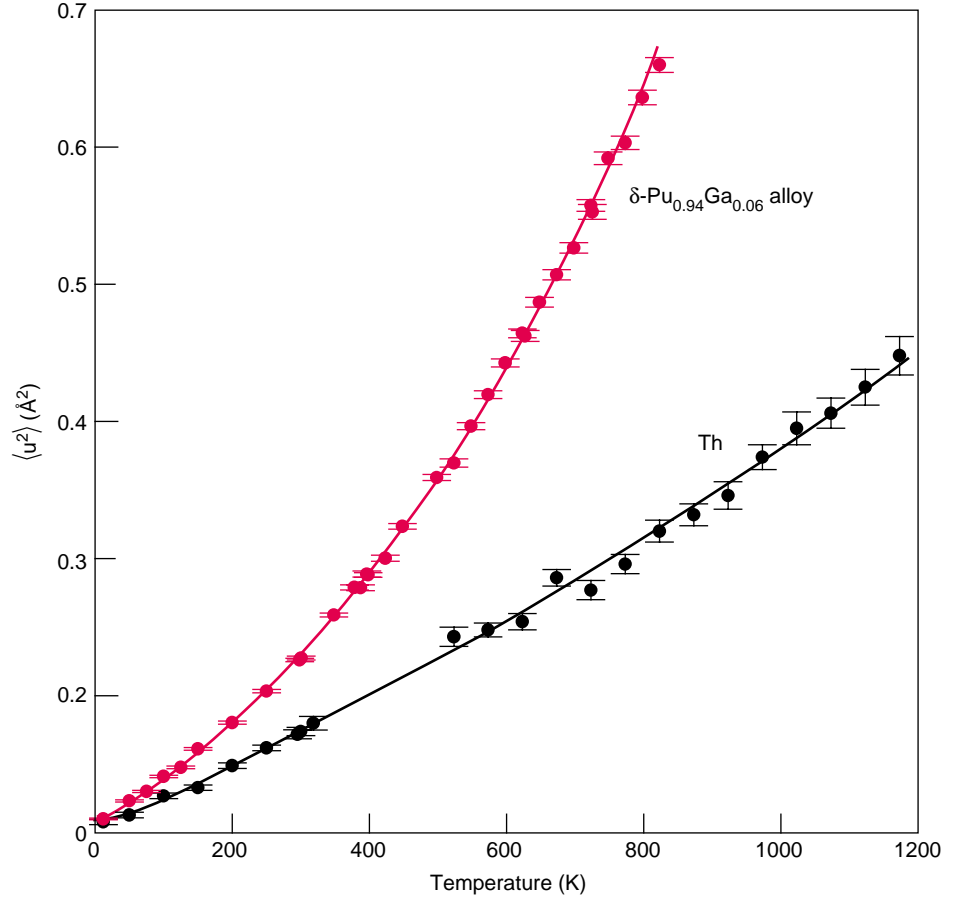


Figure 4. Mean-Square Thermal Vibration Amplitudes for δ -Phase Pu_{0.94}Ga_{0.06} and Thorium Metal

Although thorium and gallium-stabilized δ -plutonium are face-centered-cubic metals, their vibrational amplitudes behave very differently as a function of temperature. As illustrated here, the linear portion of the plutonium curve is steeper than that of thorium, indicating that plutonium is more compressible (that is, its spring constant β_{spring} , which is inversely proportional to the amplitudes squared, is lower than that of thorium). At the same time, the plutonium curve displays a larger upward curvature, indicating that, at high temperature, the springs in plutonium are softening more rapidly than those in thorium.

(Reproduced with permission from *Philosophical Magazine* B80, 2000, page 53, Taylor & Francis.)

apply the Rietveld refinement method to determine $\langle u^2 \rangle$ at each temperature.

According to Equations (5) and (7) of the Debye model, if Θ_{DW} were a temperature-independent constant, $\langle u^2 \rangle$ should increase linearly with temperature at high temperatures, with a slope inversely proportional to Θ_{DW}^2 . It should thus be easy to extract Θ_{DW} from a fit of $\langle u^2 \rangle$ versus temperature. Indeed, we have measured and analyzed many different metallic elements in this way and found that Debye's theory explains the data very well. Moreover, the measured values of Θ_{DW} are in good agreement

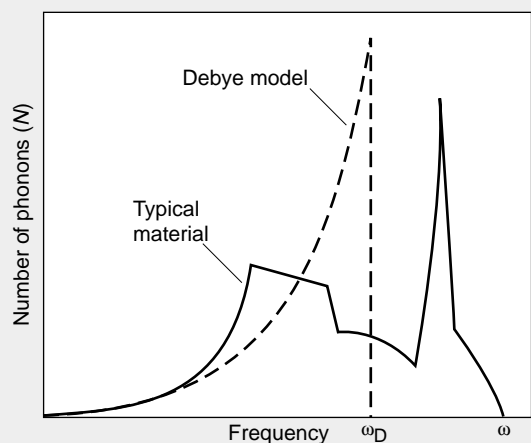
with those determined by heat capacity measurements.

It is expected, however, that Θ_{DW} should have a slight temperature dependence, reflecting changes in the crystal's elastic properties as its volume is changed by ordinary thermal expansion. For the actinides, the thermal expansion is far from ordinary: Depending on the material, the coefficient of thermal expansion spans a wide range of values. In fact, the negative thermal expansion of unalloyed δ -phase plutonium at high temperatures is one of the unexpected properties of plutonium.

The Debye Model and the Actinides

Mechanical Assumptions of the Debye Model

- The atoms (mass m) are separated by the lattice constant (a_0) and are connected by harmonic springs, whose strengths are described by the atomic spring constant β_{spring} .
- Excitations are sound waves of wavelength λ , velocity $V_{\text{sound}} = \Omega^{1/3}(\beta_{\text{spring}}/m)^{1/2}$, where Ω is the atomic volume, and frequency $\omega = V_{\text{sound}}/\lambda$.
- Velocities are the same for longitudinal and transverse waves, and they are the same in all crystal directions.
- Sound waves cannot propagate if $\lambda < a_0$.
- The low-frequency sound wave (phonon) spectrum is proportional to ω^2 .



A comparison of the phonon spectra $N(\omega)$ for the Debye model (dashed line) and a typical material (solid line) shows that, whereas at low frequencies both spectra are proportional to ω^2 , at high frequencies the actual spectrum of a material deviates significantly from the Debye spectrum.

Thermal Consequences of the Debye Model

If the solid has ideal, harmonic springs,

- the characteristic Debye temperature Θ_D is given by $k_B \Theta_D = \hbar(6\pi^2/\Omega)^{1/3} V_{\text{sound}}$;
- the low-temperature heat capacity is $Nk_B(T/\Theta_D)^3$, where N is the number of atoms in the solid;
- the high-temperature heat capacity is $3Nk_B$;
- the Debye temperature Θ_D is independent of temperature;
- there is no thermal expansion; and
- the solid never melts!

If the solid has weakly anharmonic springs,

- there is measurable thermal expansion;
- the spring constants depend on volume;
- the Debye temperature Θ_D depends on temperature via thermal expansion and the Grüneisen constant; and
- the melting point is approximately determined by the Lindemann criterion.

Observed Properties of the Actinides

- Thermal expansion is anomalous.
- The Debye temperature Θ_D depends strongly on temperature through an explicit temperature variation of the elastic constants.
- The melting point is anomalously low.

And yet, our measurements of Θ_{DW} held an even bigger surprise. They showed that Θ_{DW} has a very large temperature dependence. The Debye-Waller temperature decreases at a higher temperature in an approximately linear fashion. That is, Θ_{DW} obeys an equation of the approximate form

$$\Theta_{\text{DW}} = \Theta_0 + cT \quad (8)$$

where Θ_0 is the low-temperature value of the Debye-Waller temperature and c is a small negative constant. This result

means that the spring constants are effectively temperature dependent and that the springs become weaker at high temperatures. This behavior is known as elastic softening, and its effect is shown in Figure 4. In that figure, we compare our measurements of $\langle u^2 \rangle$ for δ -phase $\text{Pu}_{0.94}\text{Ga}_{0.06}$ with those for thorium metal. The two metals have the same crystal structure, but the data indicate that thorium's spring constants are stronger and much less dependent on temperature.

The curves for plutonium and thorium differ in two ways. First, the

linear part of the plutonium curve is much steeper than that of thorium. The increase in slope means that plutonium is more compressible than thorium—that is, it has a lower Θ_{DW} , or atomic spring constant. Second, whereas the thorium curve is nearly linear, the plutonium curve shows a considerably upward curvature, which indicates that the atomic springs in plutonium are softening at high temperature. The experiments demonstrate directly that plutonium is more unstable than thorium, in agreement with the instabil-

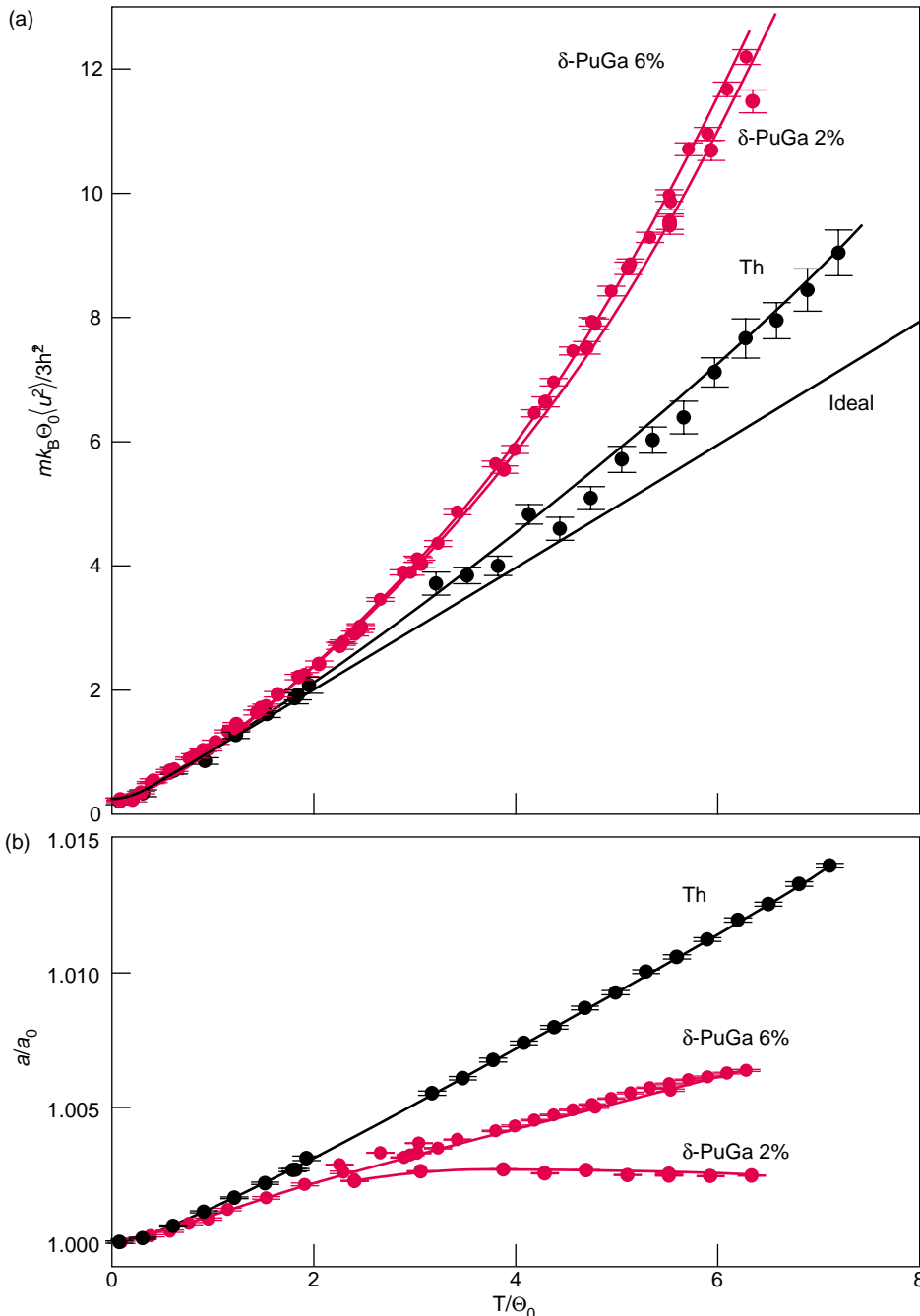


Figure 5. Dimensionless Plots of the Vibrational Displacement and Lattice Constants as a Function of Temperature

These plots are for δ -phase $\text{Pu}_{0.94}\text{Ga}_{0.06}$ and thorium metal. (a) Shown here are dimensionless displacement versus dimensionless temperature, $mk_B\Theta_0\langle u^2\rangle/3\hbar^2$ vs T/Θ_0 . The ideal curve is computed from Equation (6), and it shows the universal Debye behavior for a temperature-independent Θ_{DW} , that is, $c = 0$ in Equation (8). (b) Shown here is the reduced lattice constant, a/a_0 vs T/Θ_0 . The curves indicate that the thermal expansion of plutonium-gallium alloys is less than that of thorium and depends strongly on gallium concentration. The thermal expansion of the 2% sample is different from that of the 6% sample, but the corresponding vibrational-displacement course is nearly identical for these two samples. We deduce that the temperature dependence of Θ_{DW} is not a simple Grüneisen effect. (Reproduced with permission from *Philosophical Magazine* B80, 2000, page 53, Taylor & Francis.)

ities shown in Figure 1. To display these trends more clearly, we replotted the results in Figure 5 by using the dimensionless mean-square vibrational displacement, $mk_B\Theta_0\langle u^2\rangle/3\hbar^2$, versus the dimensionless temperature, T/Θ_0 . Figure 5(a) shows that the temperature-induced softening of the elastic constants is quite large, and Figure 5(b) that the softening is independent of thermal expansion.

The $\langle u^2 \rangle$ measurements can be used for quantifying this instability in elastic properties, and the results can be applied to modeling stockpile materials. We have observed similar softening in the other light actinides— α -uranium, α -neptunium, and α -plutonium—but not in any nonactinide material we have studied so far. From neutron diffraction measurements, we deduced the temperature dependence of Θ_{DW} for the light actinides (see Figure 6). Measurements of $\langle u^2 \rangle$ are more sensitive to the behavior of the phonon spectrum at lower frequencies than are other thermal measurements, so that they reflect the portion of the phonon spectrum that is truly Debye-like. As a result, Θ_{DW} is a robust characteristic of a given material. Our findings on the temperature dependence of Θ_{DW} for δ -phase plutonium are in fair agreement with the much earlier ultrasonic measurements of Taylor et al. (1965). The observed elastic softening appears to be an intrinsic property of the light actinides.

The Melting Temperatures of the Actinides

One consequence of the measured lattice softening is that the light actinides have higher vibrational amplitudes at high temperatures than would be predicted from the low-temperature value of Θ_{DW} , that is, from a temperature-independent Θ_{DW} . That is why, we decided to reexamine the melting points of the actinides in terms of the old Lindemann melting rule.

In 1910, even before the Debye theory was proposed, Lindemann suggested that a material would melt when

the vibrational amplitude exceeds a fixed fraction f of the interatomic distance. According to Lindemann's rule, the melting point is determined by

$$T_{\text{melt}} = \frac{f^2 \Omega^{2/3} m k_B \Theta_{\text{DW}}^2}{3 \hbar^2} \quad (9)$$

where Ω is the atomic volume and f is the fractional value of the interatomic distance at which materials are supposed to melt. The melting point will appear on both sides of this equation when we substitute $\langle u^2 \rangle$ with the temperature-dependent expression for Θ_{DW} in Equation (8). For the actinides, experiment shows that $f = 8.3$ percent, and this value is not much different in other regions of the periodic system.

Figure 7 shows the melting points predicted from Lindemann's rule when we use the value for c deduced from experiment—see Equation (8). For melting temperatures, the agreement with experimental values is quite good. But when the temperature dependence of Θ_{DW} is ignored, the Lindemann criterion does not work at all. Thus, we should no longer consider anomalous the trend in the melting point of the actinides shown in Figure 2. Instead, we need to understand the microscopic reasons for the peculiar temperature dependence of Θ_{DW} .

We also found that, whether α -phase or stabilized δ -phase plutonium data are used in the Lindemann criterion, the predicted melting point of plutonium is almost the same. This remarkable result suggests that the melting point is an essentially atomic property.

Future Directions

Since the Debye-Waller work was completed, we have used the analysis of diffuse scattering to establish that plutonium-gallium alloys are really good Debye solids. Diffuse scattering is an oscillatory feature that appears in the background of the diffraction patterns when the motions of neighboring atoms are correlated, and these features are

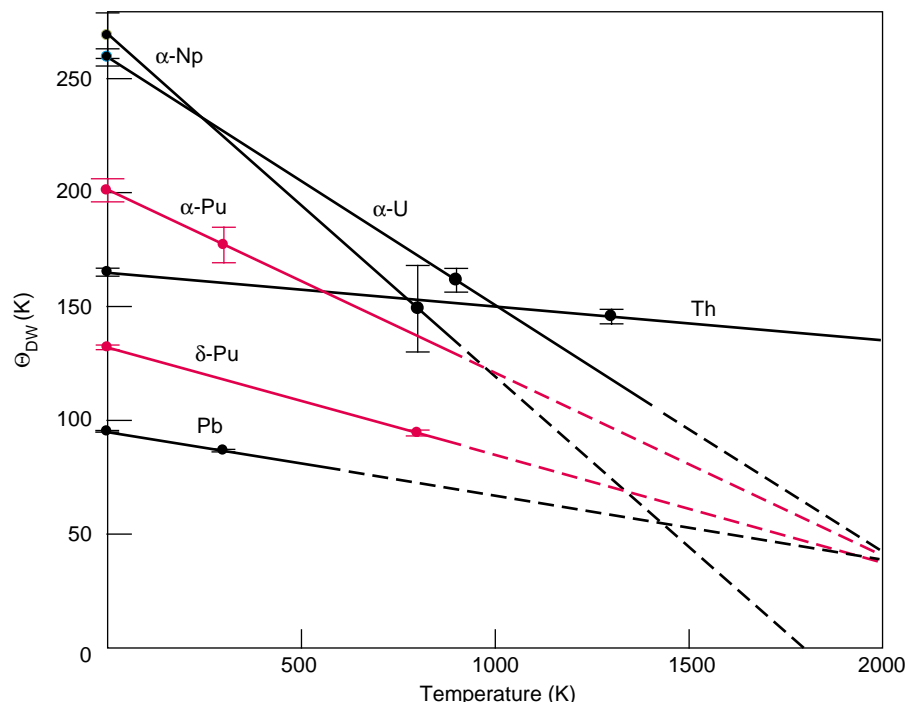


Figure 6. Temperature Dependencies of Θ_{DW} for the Light Actinides
Results from our neutron-diffraction measurements show the temperature dependence of Θ_{DW} for the light actinides. The lines span the temperature range of the solid phases. The intercept of each line shows Θ_{DW} at $T = 0$, and the slope shows the elastic softening observed for each material. This elastic softening is an intrinsic property of the light actinides. (Reproduced with permission from *Kluwer Academic*, A. C. Lawson et al., Edited by A. Gonis et al., "Light Actinides" in *Electron Correlation and Materials Properties*, 1999, page 75.)

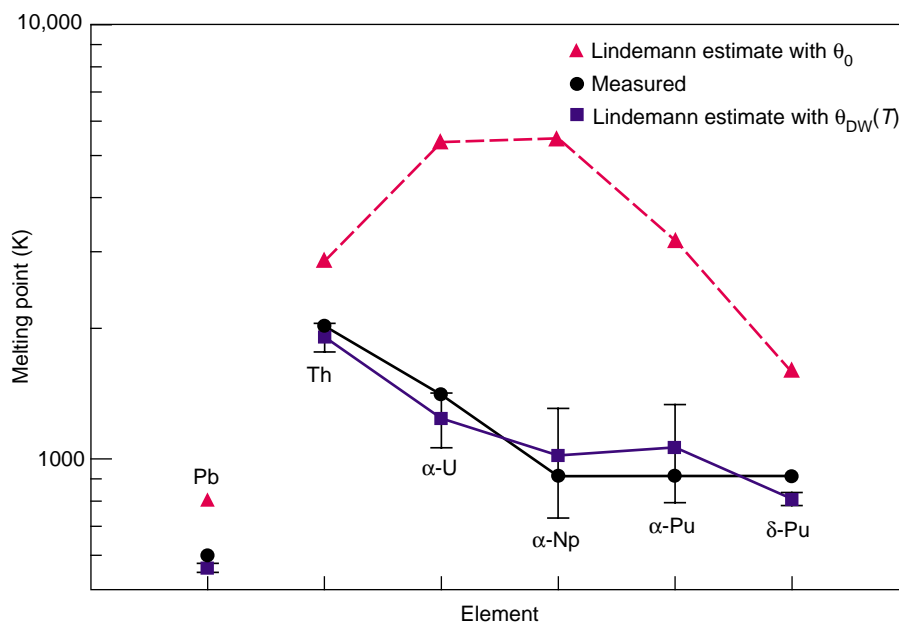


Figure 7. Melting Points of the Light Actinides
The melting points of the light actinides were determined in three ways: from experiment (black dots), from the Lindemann estimate of the melting point based on Θ_0 , the low-temperature value of Θ_{DW} (red triangles), and from the Lindemann estimate based on the temperature-dependent Θ_{DW} (blue rectangles). Experimental data and the estimate based on the temperature-dependent Θ_{DW} are in good agreement.

actually visible in the data of Figure 3 (see error curve). The analysis shows that diffuse scattering is in good agreement with the Debye model and that the measured correlations are exactly as expected when the atoms are coupled to each other (the Debye model) rather than to fixed lattice sites (the Einstein model).

The next stage of this work is the difficult task of extending the measurements to high pressure. In effect, we will be using neutrons to make high-pressure elasticity measurements. Also in future years, single crystals will become available, and very detailed phonon-dispersion measurements will be completed. Those measurements will supersede the ones we have reported here by mapping out the dependence of vibrational energy on wavelength and crystal direction. They will enable us to relate important properties of stockpile materials, such as melting, to their fundamental origins in the properties of the 5f electrons present in the actinides. ■

Further Reading

Debye, P. 1914. *Annalen der Physik* **43**: 49. Reprinted in Peter J. W. Debye. 1988. *The Collected Works*. Woodbridge, CT: Oxbow Press. 3.

Lawson, A. C., J. A. Goldstone, B. Cort, R. Sheldon, and E. Foltyn. 1994. Debye-Waller Factors of the Light Actinide Elements. In *Actinide Processing: Methods and Materials. Proceedings of an International Symposium Held at the 123rd Annual Meeting of the Minerals, Metal, and Materials Society*. Edited by B. Mishra and W. A. Averill. Warrendale, PA: TMS. 31.

Lawson, A. C., B. Martinez, J. A. Roberts, B. I. Bennett, and J. W. Richardson, Jr. 2000. *Phil. Mag.* **B80**: 53.

Lindemann, F. A. 1910. *Phys. Z.* **11**: 609.

Stephens, P. W. 1999. *J. Appl. Crystallogr.* **32**: 281.

Taylor, J. C., R. G. Loasby, J. D. Dean, and P. F. Linford. 1967. Some Physical Properties of Plutonium at Low Temperatures. In *Plutonium 1965. Proceedings of the Third International Conference on Plutonium*. Edited by A. E. Kay M. B. Waldron. London: Chapman and Hall Ltd.

Von Dreele, R. B. 1990. *Los Alamos Science* **19**: 132.

Bard I. Bennett received his Ph.D. in theoretical solid-state physics from the University of California at Irvine. Currently, he is the Program Manager for Nuclear Emergency and Proliferation. Bard has over 23 years of experience in equation of state and opacity theories with particular emphasis on the application of these theories to the design of nuclear weapons. As codeveloper of the SESAME equation of state and Opacity Data Library, he has been involved in the design of many Los Alamos nuclear tests.



Andrew C. Lawson received his undergraduate degree in physics from Pomona College and his Ph.D. from the University of California (U.C.) at San Diego, where he was in Bernd Matthias's superconductivity group. After a postdoctoral stint at UC San Diego, Lawson taught physics at Pomona College and mechanical engineering at California State University at Long Beach. Lawson then joined the Physical Metallurgy Group at Los Alamos and now works in the Structure and Properties Group of the Materials Science and Technology Division. His research interests cover the study of actinide materials with neutron and x-ray diffraction.



Barbara Martinez received her B. S. and M. S. degrees in physics from Stephen F. Austin State University. She received her Ph. D. in physics from Texas A&M University, where she studied phase transitions in low-dimensional organic metals at low temperatures. She joined the Los Alamos National Laboratory as a Director-funded postdoctoral fellow in 1980 and is now a technical staff member in the Chemistry, Metallurgy, and Materials Group. Her research interests include transport and magnetic properties, phase transitions, and aging effects in plutonium and other actinide materials.



James W. Richardson, Jr. received his B.S. degree from Purdue University and his Ph.D. degree from Iowa State University. Richardson is a materials scientist in the Intense Pulsed Neutron Source Division at Argonne National Laboratory and has over 15 years of experience in neutron and x-ray diffraction. He is recognized for his work in structure solutions of microporous zeolites and molecular sieves from neutron powder diffraction. Richardson developed novel analysis techniques for mixed crystalline/amorphous systems and has conducted in situ diffraction studies of industrial materials and processes, as well as nonambient (neutron irradiation) structural studies of transuranic intermetallics. He has more than 70 publications and is a corecipient of a 1992 Federal Laboratory Consortium Special Award for Excellence in Technology Transfer for determining strain by neutron diffraction.



Joyce A. Roberts received her undergraduate degree in physics from Syracuse University and her Ph.D. on radiation damage in materials at the State University of New York at Stony Brook. She joined Los Alamos as a postdoctoral fellow in 1981. In 1990, she was appointed Deputy Leader of the Manuel Lujan Jr. Neutron Scattering Center. She has been responsible for the construction of the Neutron Powder Diffractometer at the Manuel Lujan Jr. Neutron Scattering Center. Roberts's research interests include the structure of actinide materials, actinide and other metal hydrides, superconductors, binary alloys, and strain in composite materials measured by neutron and x-ray diffraction techniques.



Microstrain in δ' -Plutonium

Andrew C. Lawson

In addition to giving information on crystal structure, the shapes of the diffraction peaks also give valuable information on other aspects of the state of the material. In particular, if the lattice "constant" is not really constant but actually fluctuates throughout the bulk material, then the diffraction lines will be broadened. One mechanism for fluctuation is the strain caused by the forces exerted by the grains on one another in the course of a crystallographic transformation.

Thanks to the analysis developed recently by Peter Stephens, it is now possible to include anisotropic microstrain broadening in the Rietveld analysis. This means that one allows for the strain in individual grains to depend on crystal direction. The observed microstrain, which is an average over many grains, is a distribution that must be consistent with the crystal symmetry. The observed microstrain in δ' -plutonium is shown in Figure 1. The figure indicates that the spread in the distribution of lattice spacings is much greater in the crystallographic c -direction of the tetragonal crystals of δ' -plutonium than in the a -direction.

Why is the microstrain so high for δ' -plutonium? We do not know in detail, but it would seem that the tetragonal δ' -structure is a rather unhappy compromise between the two cubic structures, δ and ϵ (Figure 2).

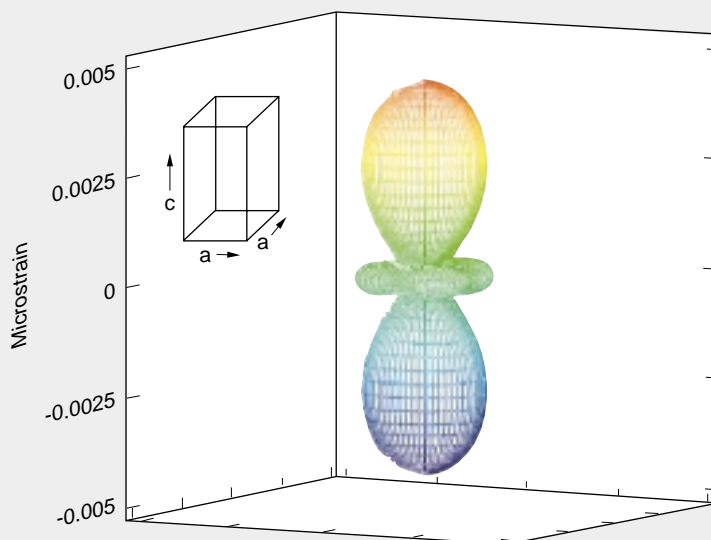
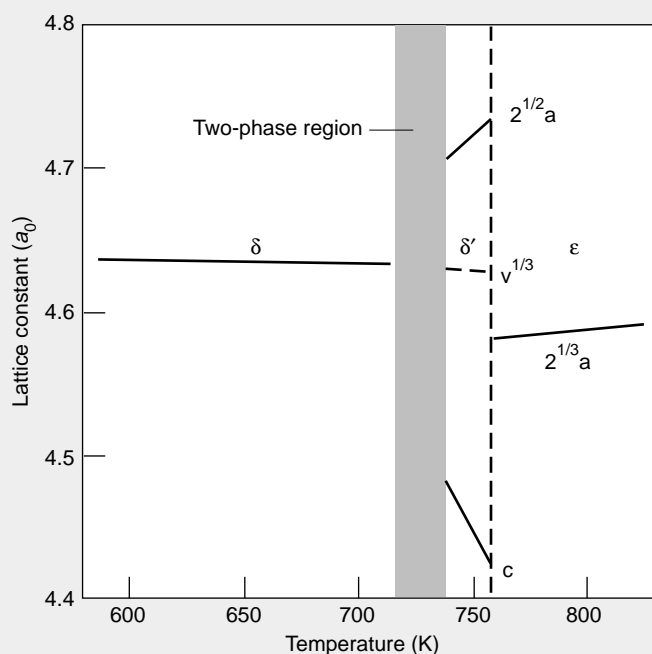


Figure 1. Anisotropic Microstrain for δ' -Plutonium at 740 K

This plot shows the root-mean-square average deviation of the crystal d -spacings in δ' -Pu plotted versus crystal direction. This quantity is called the microstrain, and it is determined by intergranular stresses. In the tetragonal crystal shown here, the microstrain is much larger in the crystallographic c -direction. The microstrains are caused by intergranular stresses.

Figure 2. Temperature Dependence of the Normalized Lattice Constants of Pure Plutonium Between 600 and 800 K, plutonium transforms from face-centered-cubic δ' -phase to face-centered-tetragonal δ' -phase and then to body-centered-cubic ϵ -phase. Even though they are both cubic, the structures of the δ' - and ϵ -phases are not closely related to each other, and the atomic volumes are very different. The interatomic distances have to change considerably during the transformation, and this change leads to a large microstrain for the tetragonal δ' -phase. (Reproduced with permission from *Kluwer Academic*, A. C. Lawson et al., Edited by A. Gonis et al., "Light Actinides" in *Electron Correlation and Materials Properties*, 1999, page 75.)

Equations of State—Theoretical Formalism

by Bard I. Bennett

Theoretical and experimental research in equations of state and material modeling is essential to ensuring a firm scientific footing for these disciplines. This type of research is necessary not only for assessing the nuclear weapons stockpile but also for developing a predictive computational capability. Here, I will outline the general theoretical formalism for calculating equations of state and then expand on the contribution from the vibrational (or thermal) excitations of solids to the equation of state (EOS). The temperature dependence of the Debye temperature reported in the main article has a direct bearing on our models for the vibrational contribution.

The EOS for any material is typically expressed as an equation for the pressure as a function of temperature and density. Generally speaking, at densities less than 100 grams per cubic centimeter (g/cm^3) and temperatures less than 100 kilo-electron-volt (keV), there are three distinct contributions to the pressure:

$$P(\rho, T) = P_c(\rho) + P_N(\rho, T) + P_e(\rho, T) \quad (1)$$

The pressure at $T = 0$, $P_c(\rho)$, is commonly called the “cold curve” and is due to the electronic forces that bind the individual atoms into a solid; $P_N(\rho, T)$ is the pressure due to the vibrational excitation of the nuclei in the solid, liquid, or gas states; and $P_e(\rho, T)$ is the pressure due to the electrons’ thermal excitation.

The cold curve is traditionally modeled by empirical formulae (Lennard-Jones and Morse potentials combined with Thomas-Fermi-Dirac theory). Modern calculations of electronic band structure include relativistic effects. Experimental measurements conducted in a diamond-anvil or tungsten carbide cell can provide data for pressures up to approximately 2 megabars.

The vibrational contribution for the solid state, $P_N(\rho, T)$, is traditionally modeled with the Debye theory. Models of the liquid state use an interpolation scheme between a Debye solid and an ideal gas. Modern theory for all these states uses molecular dynamics or Monte Carlo methods to obtain pressures as a function of density and temperature. No direct experimental data are available, but to infer a melting temperature, we use shock wave methods and laser-heated diamond-anvil cells.

The pressure for electron excitations, $P_e(\rho, T)$, is traditionally modeled by Saha or Thomas-Fermi-Dirac theories. Modern theory for this contribution to the pressure uses relativistic, quantum mechanical,

self-consistent field theory. No direct experimental data are available, but $P_e(\rho, T)$ can be inferred from data obtained from pressure waves generated by nuclear explosions.

We now add more detail to the vibrational contribution to pressure from the motion of the nuclei. The Mie-Grüneisen form is given by

$$P_N(\rho, T) = \rho \Gamma(\rho, T) E_N(\rho, T) \quad (2)$$

where the energy in the Debye model is given by

$$E_N(\rho, T) = \frac{3 N_0 k_B T}{A} \left\{ D_3 \left(\frac{\Theta_D}{T} \right) + \frac{3}{8} \frac{\Theta_D}{T} \right\} \left\{ 1 + \frac{\partial \ln \Theta_D(\rho, T)}{\partial \ln T} \right\} \quad (3)$$

and the Grüneisen parameter Γ is defined by the following equation:

$$\Gamma(\rho, T) = \frac{\int \ln \Theta_D(\rho, T)}{\int \ln \rho} \quad (4)$$

The Debye temperature $\Theta_D(\rho, T)$ is the effective atomic vibrational temperature, and it determines when a material melts or loses its strength. In Equation (3), $D_3(x)$ is the Debye integral of the third kind. In traditional EOS modeling, Θ_D is assumed to be independent of temperature—that is, $\Theta_D(\rho)$. Consequently, Γ would also be a simple function only of density. Modern theories suggest that Θ_D and Γ depend on a material’s density, temperature, and electronic structure.

The neutron diffraction measurements reported in the main article confirm these theoretical ideas. The data show that the Debye temperature and the Grüneisen parameter are, indeed, a function of temperature and electronic structure.

To verify the predictions from quantum mechanical theory, we need to further validate our current models. Measuring the Debye-Waller factor with a new, heated high-pressure cell shows great promise. By using the apparatus containing this cell, we have obtained interesting data for molybdenum. After validation, the theory will be used in modeling material melting and strength for applications in weapons physics (conventional and nuclear), metal casting, or explosively driven shape-forming.

Microstrain in δ' -Plutonium

Andrew C. Lawson

In addition to giving information on crystal structure, the shapes of the diffraction peaks also give valuable information on other aspects of the state of the material. In particular, if the lattice "constant" is not really constant but actually fluctuates throughout the bulk material, then the diffraction lines will be broadened. One mechanism for fluctuation is the strain caused by the forces exerted by the grains on one another in the course of a crystallographic transformation.

Thanks to the analysis developed recently by Peter Stephens, it is now possible to include anisotropic microstrain broadening in the Rietveld analysis. This means that one allows for the strain in individual grains to depend on crystal direction. The observed microstrain, which is an average over many grains, is a distribution that must be consistent with the crystal symmetry. The observed microstrain in δ' -plutonium is shown in Figure 1. The figure indicates that the spread in the distribution of lattice spacings is much greater in the crystallographic c -direction of the tetragonal crystals of δ' -plutonium than in the a -direction.

Why is the microstrain so high for δ' -plutonium? We do not know in detail, but it would seem that the tetragonal δ' -structure is a rather unhappy compromise between the two cubic structures, δ and ϵ (Figure 2).

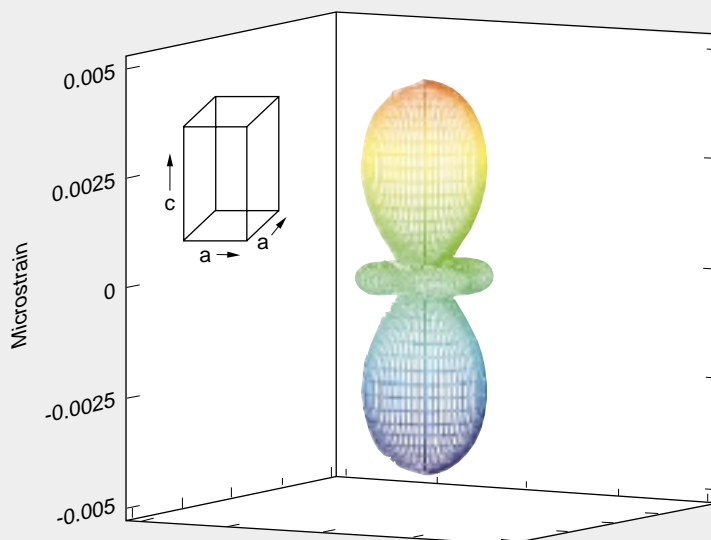
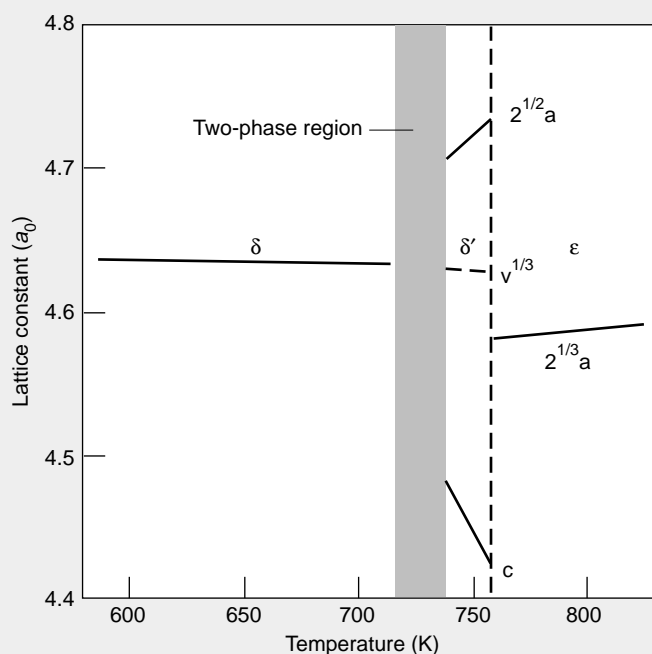


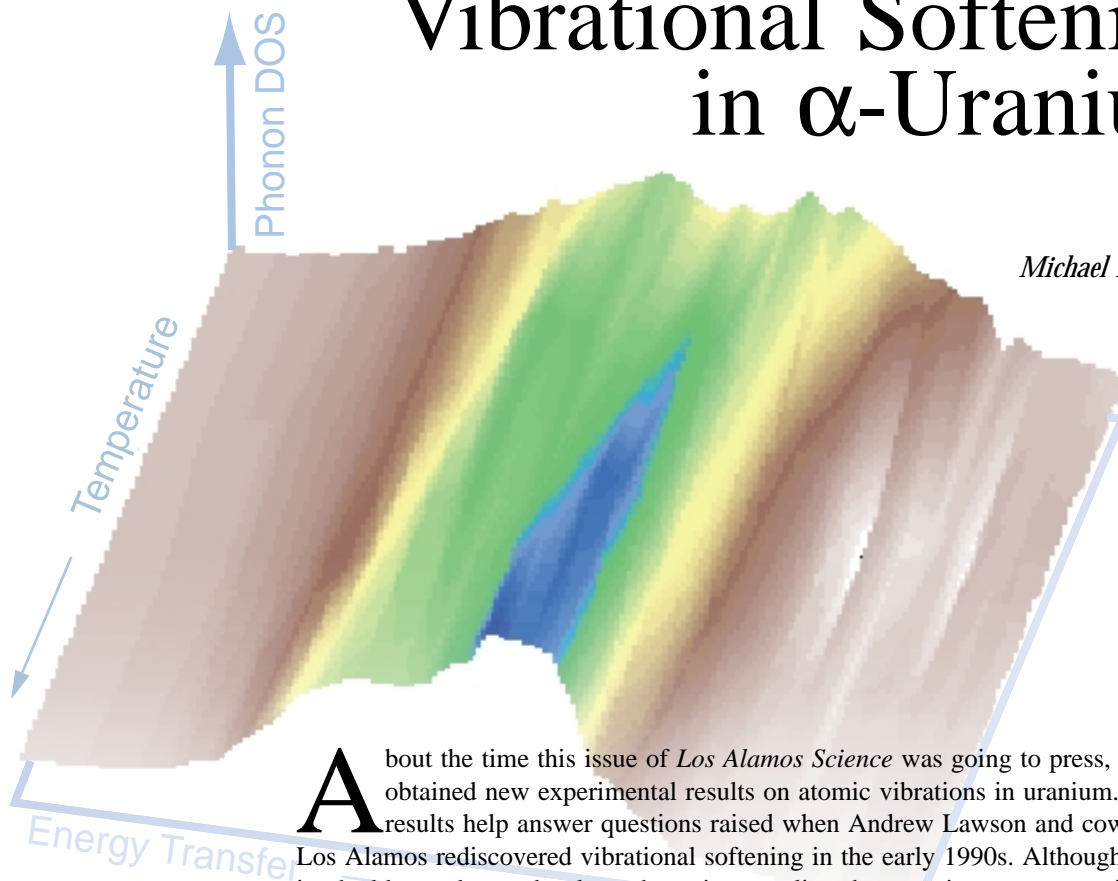
Figure 1. Anisotropic Microstrain for δ' -Plutonium at 740 K

This plot shows the root-mean-square average deviation of the crystal d -spacings in δ' -Pu plotted versus crystal direction. This quantity is called the microstrain, and it is determined by intergranular stresses. In the tetragonal crystal shown here, the microstrain is much larger in the crystallographic c -direction. The microstrains are caused by intergranular stresses.

Figure 2. Temperature Dependence of the Normalized Lattice Constants of Pure Plutonium Between 600 and 800 K, plutonium transforms from face-centered-cubic δ' -phase to face-centered-tetragonal δ' -phase and then to body-centered-cubic ϵ -phase. Even though they are both cubic, the structures of the δ' - and ϵ -phases are not closely related to each other, and the atomic volumes are very different. The interatomic distances have to change considerably during the transformation, and this change leads to a large microstrain for the tetragonal δ' -phase. (Reproduced with permission from *Kluwer Academic*, A. C. Lawson et al., Edited by A. Gonis et al., "Light Actinides" in *Electron Correlation and Materials Properties*, 1999, page 75.)

Vibrational Softening in α -Uranium

Michael E. Manley



About the time this issue of *Los Alamos Science* was going to press, we obtained new experimental results on atomic vibrations in uranium. These results help answer questions raised when Andrew Lawson and coworkers of Los Alamos rediscovered vibrational softening in the early 1990s. Although softening had been observed at least three times earlier, the most important questions about the phenomenon were never addressed experimentally: What is the nature of vibrational softening? Is it an anharmonic or electronic effect? This article summarizes preliminary inelastic neutron-scattering results that address both questions. Our full results will be published in a journal article (Manley et al. 2000a).

Lawson's measurements of Debye-Waller factors—mean-square atomic displacement, $\langle u^2 \rangle$ —suggest that the average phonon frequency decreases by about 40 percent as the temperature is raised from room temperature (300 kelvins) to uranium's β -phase transition temperature (940 kelvins), a much larger decrease than the quasi-harmonic theory of anharmonicity would normally predict (see the article "Atomic Vibrations and Melting in Plutonium" on page 190). In the quasi-harmonic approximation, anharmonic vibrations are assumed to be independent harmonic modes whose frequencies are not fixed but, instead, depend on volume (V). In this approximation, the vibrational entropy S of a collection of vibrational modes can be written as

$$S(V, T) = \sum_j -3k_B \ln \left(\frac{\hbar \omega_j(V)}{k_B T} \right), \quad (1)$$

where ω is the frequency of the quasi-harmonic mode. Using this expression, we can determine the entropy difference between a constant-pressure (changing ω) and a constant-volume (fixed ω) experiment. Specifically, for the 40 percent decrease in frequency implied by the results of Lawson, Equation (1) would predict that $(S_p - S_V)_{940 \text{ K}} - (S_p - S_V)_{300 \text{ K}} = -3k_B \ln(0.6) = 1.5k_B/\text{atom}$, which is about 5 times larger than the total entropy change of the α - β transition.

On the other hand, if we neglect the electronic entropy, we can also determine this vibrational-entropy difference directly from classical thermodynamics. Using the

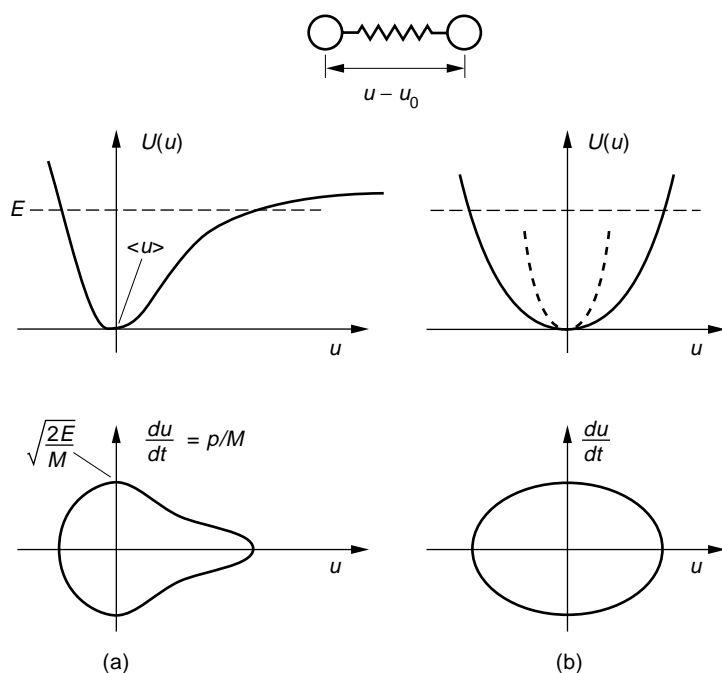


Figure 1. Anharmonic vs Harmonic Oscillators
 Potentials (top) and phase space (bottom) are shown for (a) anharmonic and (b) harmonic oscillators with the same mean square displacement $\langle u^2 \rangle$ and energy E . The dashed lines in (b) represent the effective potentials seen at low energy. The anharmonic phase space contains a smaller area and hence has a lower vibrational entropy.

classical expression relating the specific heats at constant volume and constant pressure, $C_p - C_v = 9B_T v \alpha^2 T$, and the well-known values for bulk modulus B_T , molar volume v , and thermal expansion coefficient α , we obtain

$$(S_p - S_v)_{940\text{K}} - (S_p - S_v)_{300\text{K}} = \int_{300\text{K}}^{940\text{K}} \frac{C_p - C_v}{T} dT = 9B_T v \alpha^2 (640\text{K}) = \frac{0.16 k_B}{\text{atom}}, \quad (2)$$

which is nearly an order of magnitude smaller than the quasi-harmonic value derived from Equation (1). Clearly, a greater understanding of vibrational softening is needed.

Equation (1) is based on the usual assumption that phonon softening comes from anharmonicity. That is to say, the softening is assumed to come from higher-order terms (higher than quadratic) in a temperature-independent interatomic potential. A simple analog of this potential is the pair potential shown in Figure 1(a). In this case, the increase in the average interatomic separation $\langle u \rangle$ with increasing temperature can be related directly to the softening (or flattening) of the potential. In other words, as the masses, or atoms, are pulled farther apart by thermal motion, the potential has less restoring force than is expected from a linear spring (hence, the term softening). But what if the potential is not fixed? Could the interatomic potential remain harmonic and soften because the electronic contribution to the potential changes with temperature? If true, this fact would have profound implications on the way we think about the electronic structure and equation of state for uranium.

Figure 1 shows the potentials and phase-space trajectories for an anharmonic (a) and a harmonic (b) oscillator, both having the same energy E and mean-square displacement $\langle u^2 \rangle$. Note that the phase-space trajectory of the anharmonic oscillator has a smaller area than that of the harmonic oscillator. In the classical limit ($k_B T \gg$ the energy spacing of quantum states), a unit of phase-space area of size $\Delta p \Delta u \sim \hbar$ (set by the uncertainty principle) contains one quantum state. So, a smaller area accesses fewer quantum states. Because entropy is proportional to the log of the number of accessible quantum states, the anharmonic oscillator with its smaller

phase-space area must have less vibrational entropy. A similar argument can be made for harmonic and anharmonic oscillators at equal temperatures, but in that case they would have equal entropies, and the energy of the anharmonic oscillator would be larger. Either way, the vibrational free energy ($F = E - TS$) is larger for the anharmonic oscillator. Thus, determining whether anharmonic or harmonic models describe the vibrational modes of uranium is essential to understanding the equation of state for uranium.

Most standard measurements of vibrations in solids are immediately interpreted in terms of harmonic models. However, it is possible to take a more general view. In particular, for inelastic neutron scattering, the dynamic-structure factor can be interpreted in terms of the mean-square power spectrum. The dynamic-structure factor $S(Q, \omega)$ gives the scattering intensity as a function of momentum transfer Q and energy transfer $\hbar\omega$. The limiting case of zero-energy transfer (elastic scattering), $S(Q, \omega = 0)$, gives the usual diffraction pattern used for structural determination. The limiting case of $Q = 0$ can be measured by various vibrational spectroscopies such as infrared. But neutrons are unique in their ability to accurately probe both the dynamics and positions of atoms in solids simultaneously. This is because, as if by some lucky twist of fate, neutrons with energies on the order of the vibrational energies also have wavelengths similar to the spacing between atoms.

For a Bravais lattice, the polycrystalline averaged incoherent dynamic scattering function is given by

$$S_i(Q, \omega) = \frac{1}{2\pi\hbar} \int_{-\infty}^{\infty} \langle e^{-iQr(0)} e^{iQr(t)} \rangle e^{-i\omega t} dt \quad , \quad (3)$$

where the brackets imply a thermal and powder average. Expanding Equation (3) in powers of Q gives the following:

$$\langle e^{-iQr(0)} e^{iQr(t)} \rangle \cong 1 + iQ(\langle r(t) \rangle - \langle r(0) \rangle) - \frac{1}{2}Q^2(\langle r^2(t) \rangle + \langle r^2(0) \rangle) + Q^2\langle r(0)r(t) \rangle + \dots \quad .$$

Substituting this expansion into Equation (2) and simplifying in the classical approximation gives

$$S_i(Q, \omega) \cong \frac{\delta(\omega)}{\hbar} \left(1 - Q^2 \langle r^2(0) \rangle\right) + \frac{Q^2}{2\hbar} |R(\omega)|^2 + \dots \quad , \quad (4)$$

where $R(\omega)$ is the Fourier transform of the atomic motion given by

$$R(\omega) = \int_{-\infty}^{\infty} r(t) e^{-i\omega t} dt \quad . \quad (5)$$

The first term in Equation (4) gives the elastic line, and the second gives the modulus-square power spectrum. The average potential energy per oscillator can then be determined from

$$\langle U \rangle = \frac{1}{2} M \int \omega^2 |R(\omega)|^2 d\omega \quad , \quad (6)$$

where M is the mass of the vibrating atom.

In the case of harmonic phonons in the high-temperature limit, the power spectrum can be related to the phonon density of states $Z(\omega)$ by the relation

$$\frac{1}{2} M \omega^2 |R(\omega)|^2 = \frac{1}{2} k_B T Z(\omega) . \quad (7)$$

Integrating both sides with respect to ω gives the expected classical result, $\langle U \rangle_h = k_B T/2$. Note that this result holds true even if the harmonic potential is temperature dependent. On the other hand, if the potential is fixed and the softening comes from anharmonicity, the potential energy is given by

$$\langle U \rangle_{\text{anh}} \cong \frac{1}{2} k_B T + A(k_B T)^2 + B(k_B T)^3 + \dots , \quad (8)$$

where the A and B coefficients can be related to true anharmonic terms in the interatomic potential.

In recent experiments, we took inelastic neutron-scattering spectra of uranium at several temperatures from 50 to 913 kelvins. Measurements at room temperature and below were taken on the Low-Resolution Medium-Energy Chopper Spectrometer (LRMECS) at the Intense Pulsed Neutron Source at Argonne National Laboratory. Spectra at room temperature and above were taken on the Fermi-Chopper Spectrometer (FCS) at the Center for Neutron Research at the National Institute of Standards and Technology. Both spectrometers are time-of-flight instruments. We used these instruments with polycrystals to obtain the best average over the phonon spectrum. Because uranium scatters coherently, interference modulates the inelastic scattering intensity as a function of momentum transfer Q . Thus, to determine a phonon density of states, we must sum over all Q in the Brillouin zone.

We extracted the phonon density of states from data taken over a wide range of momentum transfers using a procedure described in Manley et al. 2000b. The results, shown in Figure 2, do indeed indicate the phonon softening with increasing temperature predicted by Angus Lawson and coworkers. That is, the average phonon frequency decreases as the temperature is increased. But the data show another surprise. The phonon density-of-state features sharpen with increasing temperature. Normally, the features broaden with increasing temperature if the potential is anharmonic. The reason is that the anharmonicity becomes more pronounced at high temperatures, causing phonon-phonon scattering and thereby reducing the lifetimes of the phonons. Because of the wave nature of neutrons, shortened phonon lifetimes result in broadened phonon energy line widths according to the time-energy relationship $\Delta E \Delta t > \hbar$. Thus, the sharpening of the phonon density-of-state features with increasing temperature does not indicate anharmonicity. More likely, the low temperature broadening is a result of increased electron-phonon coupling associated with the charge density wave that occurs at ~ 43 kelvins.

A result that contradicts the fixed anharmonic potential model is the linear increase with temperature of the average potential energy

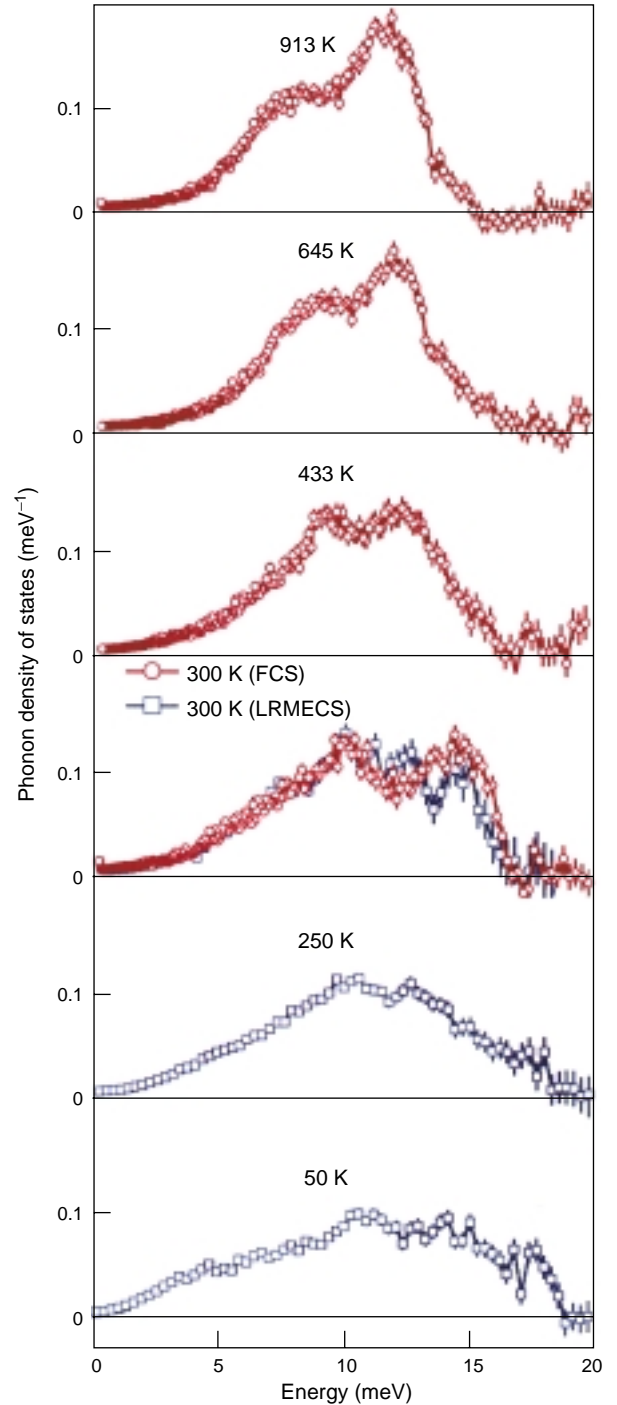
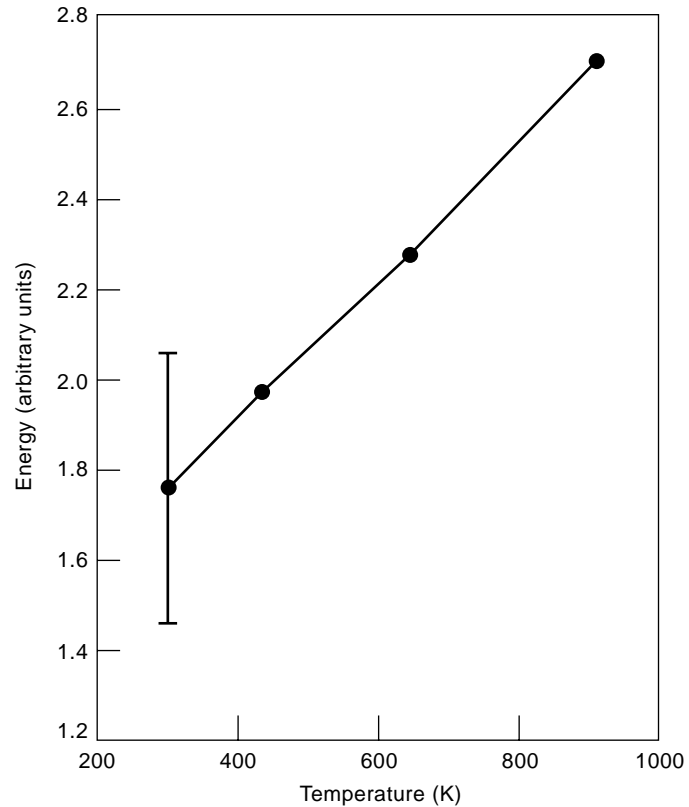


Figure 2. Phonon Density of States for α -Uranium Our data from the Fermi-Chopper Spectrometer (FCS) at the National Institute of Standards and Technology are shown in red and those from the Low-Resolution Medium-Energy Chopper Spectrometer (LRMECS) at Argonne National Laboratory are shown in blue. They both indicate phonon softening.

Figure 3. Vibrational Potential Energy of α -Uranium

The average vibrational potential energy calculated from the mean-square power spectrum increases linearly with temperature. The linear increase implies that the thermal vibrations obey harmonic statistics.



(see Figure 3), which we calculated by substituting our measurements of the mean-square power spectrum into Equation (6). The linear increase implies that the motion obeys harmonic statistics and that the higher-order terms in Equation (8) are zero. Therefore, although the phonon density of states is softening, the underlying potential must be harmonic in this temperature range (consistent with the sharper features). Evidently, the potential is temperature dependent, and the simple model given in Figure 1(b) best describes the nature of the phonon softening. Because the potential originates with the sensitivity of the electronic energy to atom displacements, it follows that thermal excitations of the electronic states are altering the potential.

Although uranium has temperature-dependent phonon frequencies, the vibrational part of the equation of state of uranium can be treated with the well-understood harmonic statistics. Therefore, preliminary phonon density-of-states data measured near the α - β transition and the β - γ transition in uranium, shown in Figure 4, were used to estimate the vibrational entropies of these transitions. The change in phonon density of states at each phase transition accounted for vibrational entropy changes of $(S^\beta - S^\alpha)_{\text{vib}} = +(0.15 \pm 0.01)k_B/\text{atom}$ and $(S^\gamma - S^\beta)_{\text{vib}} = +(0.36 \pm 0.01)k_B/\text{atom}$. Both these values are significantly smaller than the total entropy obtained from latent heat measurements: $(S^\beta - S^\alpha)_{\text{tot}} = 0.37k_B/\text{atom}$ and $(S^\gamma - S^\beta)_{\text{tot}} = 0.55k_B/\text{atom}$. The remaining entropy increases of the phase transitions must be electronic in origin. This is quite a surprise because vibrations by far make up the largest contribution to the total entropy (see the article “Elasticity, Entropy, and the Phase Stability of Plutonium” on page 208). The total electronic entropy is smaller because the Pauli exclusion principle restricts the number of countable electronic states. Another important observation is that the large thermal softening observed in α -uranium did not occur in the high-temperature γ -uranium (bcc) phase.

These results are most interesting because they challenge the way we think about the strength of bonding. With very few exceptions, changes in the stiffness of a bond between two atoms or a collection of atoms in a crystal are related to atomic

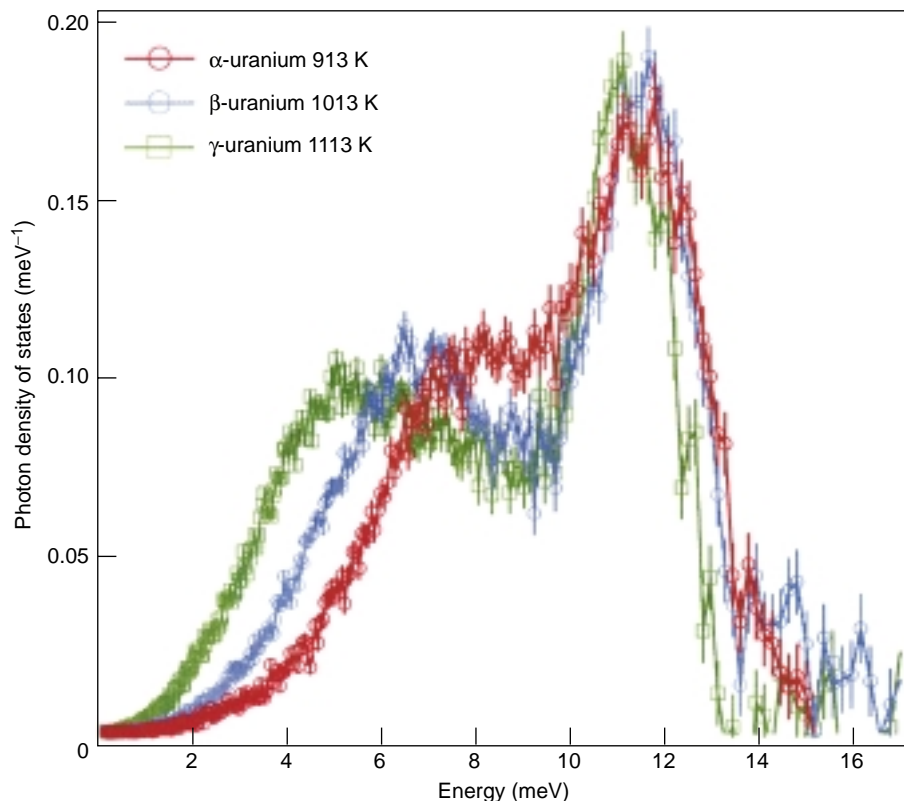


Figure 4. Phonon Density of States of the Three Solid-State Phases

The plot shows our results for the phonon density of states of the three solid-state phases of uranium: α -uranium (orthorhombic), β -uranium (tetragonal), and γ -uranium (bcc). The shifting of the peaks to lower energies for the higher-temperature phases implies an increase in vibrational entropy with each phase transition.

distances and/or the symmetry of the arrangement in the case of a crystal, and the effects of electronic thermal excitations are usually ignored. The results presented here suggest the opposite and therefore should be of considerable interest to those studying electronic structures and related issues, such as the equation of state. Quantifying and understanding the vibrational and electronic parts of the equation of state of uranium as well as the other actinides are our primary objectives in the near future.

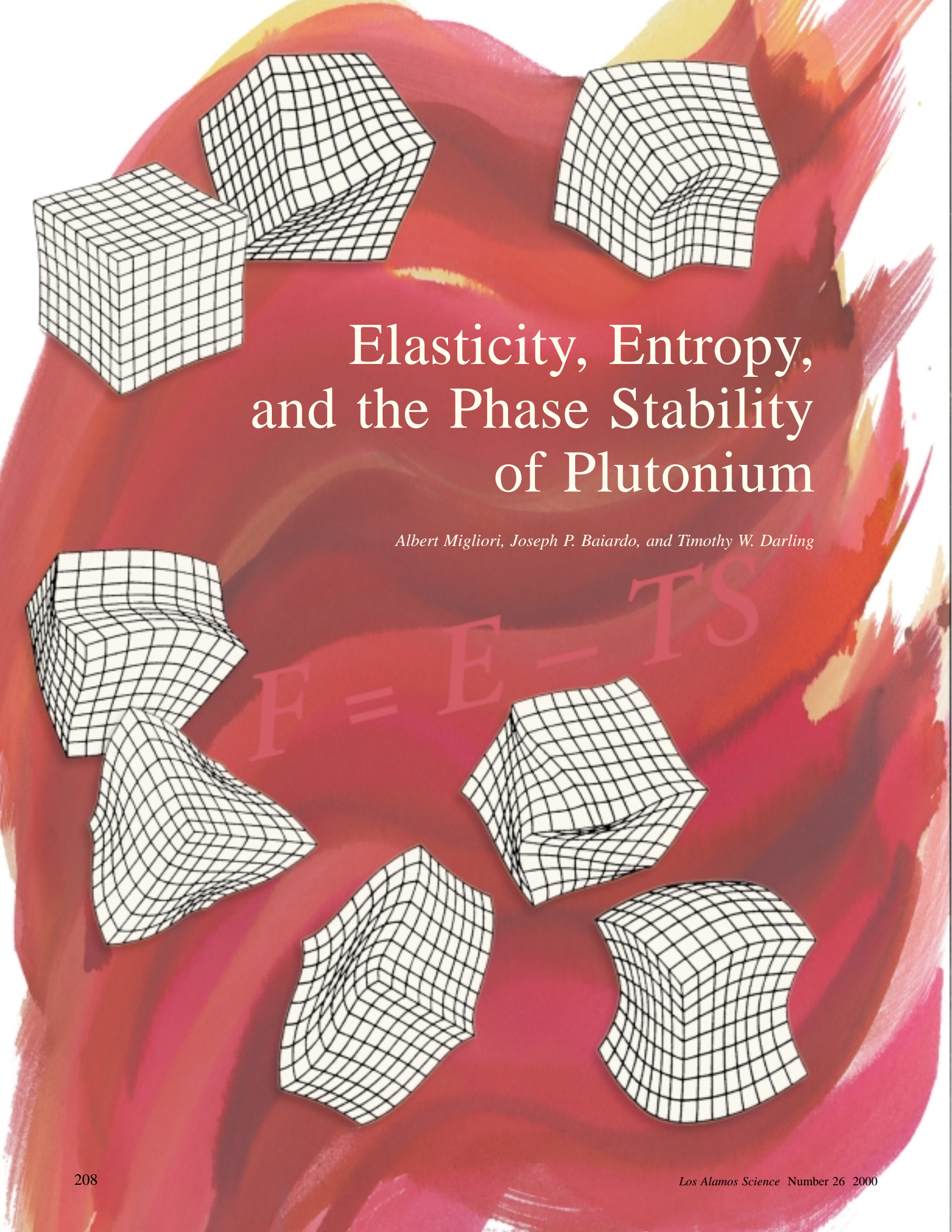
Further Reading

- Lawson, A. C., B. Martinez, J. A. Roberts, B. I. Bennet, and J. W. Richardson. 2000. *Phil. Mag. B* **80**: 53.
- Manley, M. E., B. Fultz, R. J. McQueeney, C. Brown, W. L. Hults, J. L. Smith, D. J. Thoma, et al. 2000a. Temperature Dependence of the Phonon Density of States of α -Uranium. Los Alamos National Laboratory document LA-UR 00-2720. Submitted to *Phys. Rev. Lett.*
- Manley, M. E., R. J. McQueeney, J. L. Robertson, B. Fultz, and D. A. Neumann. 2000b. *Phil. Mag. Lett.* **80**: 591.
- Squires, G. L. 1978. *Introduction to the Theory of Thermal Neutron Scattering*. Mineola, NY: Dover Publications.

Michael E. Manley is currently pursuing a Ph.D. in materials science at the California Institute of Technology, but he spends a large



part of his time working at the Los Alamos Neutron Science Center (LANSCE). His research focuses on the entropies of elementary excitations in metals and alloys. He is also studying how mechanical properties and microstructure affect the thermodynamics of metals and alloys. He is a member of the LANSCE User Group Executive Committee for 2000.



Elasticity, Entropy, and the Phase Stability of Plutonium

Albert Migliori, Joseph P. Baiardo, and Timothy W. Darling

$$F = E - TS$$

Elastic moduli are the material constants that connect stress with strain and are therefore crucial to engineering applications. They also determine the long wavelength vibrational modes, or sound waves, in a solid and therefore play a leading role in determining how thermal energy is distributed among internal vibrations. Because at ambient temperatures and above vibrational excitations contribute most of the entropy (which is determined by the total number of possible configurations), accurate measurement of elastic moduli as a function of temperature can help us compute much of the energy and entropy, and therefore the free energy, in systems at finite temperature, including plutonium. In fact, a considerable effort at Los Alamos over the last decade has led to the development of resonant ultrasound spectroscopy (RUS) for accurate measurements of elastic moduli in polycrystalline and millimeter-sized single crystal samples. We have recently begun to apply that novel technique to the study of plutonium.

In this article, we explain how this empirical approach to determining the free energy provides an important new avenue for understanding the phase stability of plutonium. First principles electronic-structure calculations have given an impressive description of α -plutonium, the lowest-temperature phase of plutonium, but no one has developed the tools to calculate the higher-temperature phases from first principles. To do so, one needs to include the effects of temperature and entropy. Theorists cannot do that yet. Instead, many of them point to changes in electronic structure as the key to understanding phase changes. They argue that the gradual localization of the itinerant f electrons causes the transition from one solid phase to the next. In contrast, we emphasize that both energy and the number of configurations (entropy) contribute to the free energy and are of comparable importance in determining the most probable states and, therefore, the observed phase of a

system. This point of view leads us to attempt answering the following question: What controls the most probable and, therefore, the only observable phases of plutonium? We show that we can estimate large parts of the free energy at temperatures above ambient by measuring elastic moduli and that those data will also enable us to catalog the missing parts. In particular, this approach may enable us to figure out whether or not the localization of the f electrons is a main ingredient in determining phase instability.

Because plutonium is very soft and has a relatively high melting point, we expect its elastic behavior and entropy to play a big role in explaining its nature. The combination of softness and high melting point alone could lead to some very odd behavior and, in fact, may explain the phase changes of plutonium without requiring the dramatic changes in electronic structure now being invoked by theorists.

Given the fundamental importance of elastic properties, it might seem strange that we have little accurate and reliable elasticity information on plutonium. Moreover, the data we have are decidedly unusual. When Moment and Ledbetter (1975) made the first, and so far the only, measurement on a single crystal of gallium-stabilized δ -plutonium—1 weight percent (1 wt %) gallium—they showed that the elastic properties were amazingly anisotropic. The very large shear anisotropy in plutonium means that elastic measurements on polycrystalline samples will produce averages of strongly varying quantities, masking the underlying physics. To get at these details, it is important to make as many measurements as possible on single crystals. However, because powerful regulatory and safety issues come to bear when working with plutonium, only very small (a few millimeters in each dimension) gallium-stabilized δ -plutonium crystals will likely be grown in the next several years. Fortunately, RUS is perfectly suited to measuring these small crystals. In this

very simple technique, an analysis of the mechanical resonances of a solid object whose shape is known provides the complete elastic tensor. In the last section of this article, we will describe how RUS is being used to remeasure the elastic moduli of plutonium, both in single-crystal and in polycrystalline materials. We also summarize our latest results.

Statistics, Free Energy, and Phase Stability

The following rapid review of statistics, the laws of large numbers, and the concepts of temperature, entropy, and free energy is designed to explain how a phase with a higher, and therefore less likely, energy can become stable. Because a higher-energy phase has many more configurations than a lower-energy phase—that is, it has more entropy—the higher-energy phase may be the more probable of the two. The climactic point of this section shows that minimizing the free energy is equivalent to finding the most probable phase.

The configuration of a large group of atoms is called a phase, and the study of what happens to large groups of atoms and what phases they exhibit as temperature or pressure is varied has fascinated scientists for many years. It is, of course, a subject strongly pursued today. One key to understanding phase stability relates to the properties of systems composed of very large numbers of identical objects. When the numbers are really large, there is no hope of computing anything exactly. But one can make approximations, and the accuracy of the approximations becomes outstanding. In fact, very precise predictions arise strictly out of the large numbers.

Statistics. Let us take a collection of 8 coins, each with a different date. We put the coins in a sack and then remove them, one by one, and place them in a row. The first coin in the row can be

any one of 8; the second, any one of 7, and so on. Thus the total number of possible arrangements, or states, is $8 \times 7 \times 6 \times 5 \times 4 \times 3 \times 2 \times 1$, which is called 8! (eight factorial), and its value is 40,320. But because we were careless in placing the coins in a row, some are heads and some are tails. For the 40,320 ways of placing the coins on the table, there are also 40,320 ways of placing all the coins heads up because each coin has a distinct date. However, if we could not read the date (the coins become indistinguishable from each other), things change.

There are far fewer distinguishable states if the objects are indistinguishable ($256 = 2^8$, to be exact, heads or tails for each of 8 objects). Of those 256 states, only one is all heads, and only one is all tails. There is also only one state in which the first coin is heads and the rest of the coins are tails. There is only one state in which the first, second, and fifth coins are heads and all the rest are tails, and so on. Each distinguishable state has the same probability of appearing, namely, 1 in 256. But how many states have 1 head and 7 tails? The answer is 8. That is, the head can be in any one of 8 different positions. How about 3 heads and 5 tails? We have 8 choices for the first head, 7 for the second, and 6 for the third. But when we put the first head in position 1 and the second in position 2, we get the same number of heads as when we put the first head in position 2 and the second in position 1. In fact, there are 6 ways of arranging the order of placing 3 coins heads up. Thus, the total number of states with 3 heads is $(8 \times 7 \times 6)/(3 \times 2 \times 1) = 56$. From the above reasoning, we construct the bar graph in Figure 1. The most likely occurrence is equal numbers of heads and tails, and the probability of other outcomes slowly drops as we move to either side of the peak probability of 70/256. In general, we see that the number of states $\Omega(n)$ of a system of N objects, n of which are of one equally probable type and $N - n$ of which are of the other equally probable type, for

which the exact arrangement of the n objects is unimportant, is

$$\Omega(n) = \frac{N!}{n!(N-n)!} \quad (1)$$

Recalling the binomial expansion, we can also see that

$$\begin{aligned} (a+b)^N &= a^N + Na^{N-1}b \\ &\quad + \frac{N(N-1)a^{N-2}b^2}{2!} + \dots \\ &= \sum_{m=0}^N \frac{a^{(N-m)}b^m N!}{m!(N-m)!} \end{aligned} \quad (2)$$

If $a = b = 1$, then

$$(1+1)^N = 2^N = \sum_{m=0}^N \frac{N!}{m!(N-m)!} \quad (3)$$

which is exactly the sum of all the states. For our example in Figure 1, we knew that the sum was 256, a value we reasoned out by knowing that each object had two possible states and that there were 8 objects.

The Effect of Large Numbers. If instead of 8 random flips, we took $N = 10^{22}$ flips, about the number of atoms in a small chunk of matter, then there are $2^{10^{22}}$ distinguishable states. The most probable result is equal numbers of heads and tails. If we compute the probability of obtaining equal numbers of heads and tails and call it P , then what outcome has a probability of $P/2$? Using Equation (3), we find that we get about 10^{11} more heads than tails (or vice versa) with a probability of $P/2$. In other words, in 10^{22} flips, it would be reasonably likely to get 10^{11} more heads than tails—the error in getting exactly equal numbers of heads and tails is only a hundred billionth of the total number of flips (that is, about $1/N^{1/2}$ of the total). We also know there is only one state, far from the maximum probability, in which we get 10^{22} heads. Thus, the width of the peak in the probability distribution is $N^{1/2}$, and there is not much left outside the peak.

What we learn from all this is that, as the numbers become large, the peak becomes extremely narrow and that all practically useful information is in the peak. It will be very accurate, later on, to approximate the real peak with a very tall rectangular distribution with constant probability over the width of the peak and zero probability elsewhere. These arguments lead to some important rules for systems (visible pieces of matter) in which the number of identical particles is of the order of Avogadro's number (6.02×10^{23}).

The first rule for these macroscopic systems is that we can count on all the numbers to be very large. For that reason, what may seem wildly inaccurate approximations will be nearly exact ones. The errors will be of the order of either the square root of a large number (for example, the square root of 10^{22} is 10^{11} , a much smaller number than the original one) or the logarithm of a large number (for example, $\ln(10^{22}) = 51$, which is pretty small compared to 10^{22}).

The next rule is that any accessible state of the system is equally likely, but we see only the most probable ones. Accessible states are those that do not violate any constraints, such as fixed volume, or physical laws, such as conservation of energy, momentum, or charge. As time passes, a system composed of a large number of objects with a “reasonably large” total energy (we will beg off on the definition of reasonably large for now) explores all the possible arrangements of those objects (each arrangement is a state) near that energy.¹ That is, if we were to take suitably fast snapshots of the system, each picture would be of an accessible state. In more concrete terms, we take our sack of coins, empty it on the floor, count the number of heads, and then repeat the process. But our sack has 10^{22} coins, and we perform the experiment, say, 10^{11} times per second (that is about the number of times per second that a gas molecule undergoes a collision).

¹There are, however, some systems that violate this ergodicity hypothesis.

sion with another gas molecule).

Because each state is equally likely, we only see very few of the approximately $2^{10^{22}}$ total possible states. Let us say that the universe will last 10^{110} seconds. Then, in the life of the universe, we will perform the experiment $10^{121} = 2^{402}$ times. If the experiment is really done on a container of gas instead of a sack of coins, then one possible observable to use instead of the number of heads is the fraction of gas molecules in, say, the left half of the container. The probability of any one atom of gas to be in the left half is $1/2$. The probability that all of them are in the left half is $2^{-10^{22}}$. The number of times that we observe this configuration to happen in the entire life of the universe is $2^{-10^{22}} \times 2^{402} \approx 2^{-10^{22}}$. Therefore, we will not see it happen! What we do see in the time we have to observe it is that the gas mostly accesses the states near the most probable one. That is, the states we see most often are the ones with nearly exactly half the mass in the left side of the container, and the typical variation in that value is $1/(10^{22})^{1/2}$, or about 1 part in 10^{11} . In more practical terms, we would expect the measured value of pressure, energy, or other macroscopic physical quantity to be within about 1 part in 10^{11} of its most likely value. The statistical properties of systems of very large numbers come round again to behaving like those of systems of only one or two particles. That is, even though we can only take a probabilistic view of a system that is way too complicated to compute exactly, the results are, for all practical purposes, exact!

The last rule is that the total number of states of a system is a very strongly increasing function of the total energy. We use a simple quantum harmonic oscillator to illustrate this property. Unlike most other physics problems, the statistical mechanics of quantum systems is easier to work with than that of classical systems because the quantum numbers make the counting of states easy. A quantum oscillator might be composed of a mass and spring or

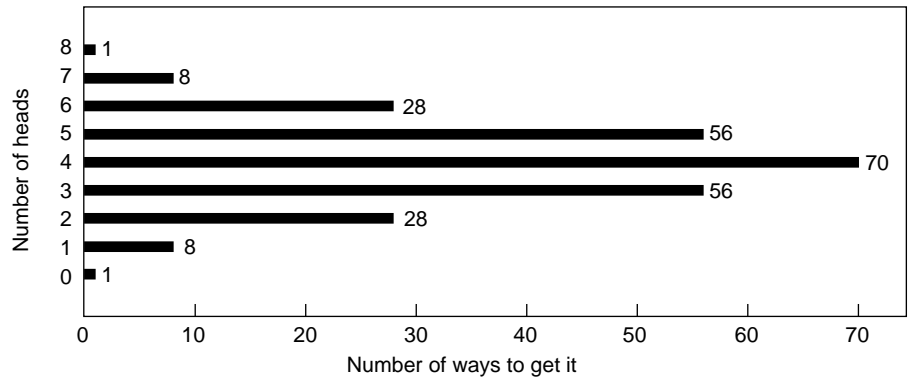


Figure 1. Number of Heads vs Ways to Get That Number

This graph shows the number of states of a system of 8 coins in which the only quantity of interest is the number of heads. That is, the 8 coins are indistinguishable, and the order in which a given number of heads is obtained is irrelevant. If we keep track of which toss produced what value, the total number of distinguishable states is 256, the most probable state has 4 heads (and 4 tails), the total number of ways to make that state is 70, and therefore the probability of that state is $70/256$.

an atom and a chemical bond. In either case, the energy of the quantum oscillator increases in proportion to the square of the amplitude of vibration. No matter what the amplitude might be, the frequency remains $f = \omega/2\pi$, just like the frequency of a tuning fork. The total energy of the oscillator is always $E = (n + 1/2)\hbar\omega$, where n is any positive integer, \hbar is Planck's constant, and each quantum of vibrational energy is $\hbar\omega$. We now consider a set of three harmonic oscillators, as shown in Figure 2. If the total energy of the three oscillators is $E = (2 + 1/2)\hbar\omega$, then the system contains two quanta, and it can be in one of six equally probable states (110 means the first oscillator has one quantum, the second has one, and the third has none). The six states are the following:

200 020 002 110 101 011.

If there are three quanta in the system, $E = (3 + 1/2)\hbar\omega$. The 10 available states are

300 030 003 210 201
120 102 012 021 111.

If we increase the energy of the

system, the number of available states increases, as does the average energy of each oscillator, and the increase per oscillator is roughly proportional to the fractional energy increase. Therefore, if we have 10^{22} oscillators, or vibrational modes, as in a solid of 10^{22} atoms, and the total energy of the system is increased by 10 percent, then so is the average energy of each oscillator. Therefore, the total number of states in the systems increases by a factor of $(1.1)^{10^{22}}$, or approximately $2^{1.4 \times 10^{21}}$, which is an enormous increase. It is now apparent that a reasonably large amount of energy in a system with a large number of objects is enough energy so that roughly every object in that system has more than its ground-state energy.

Entropy and Temperature. We will use simple properties of probabilities to generate a universal definition of temperature. Consider a very small chunk of matter that is touching or is part of a very much larger chunk. We assume the total energy of the whole system is fixed at E ; the smaller piece has an energy E_1 , and the larger has an energy $E - E_1$. What is the probability that we observe this configuration? If the number of states of the smaller

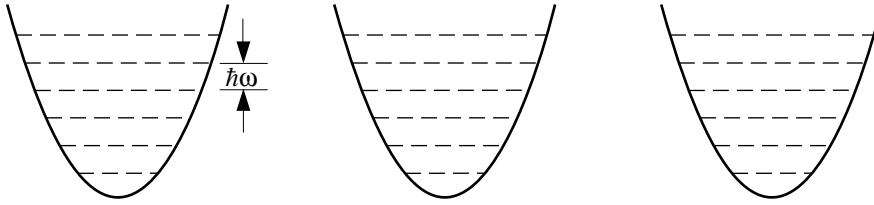


Figure 2. A System of Three Independent Quantum Harmonic Oscillators
 The figure shows the parabolic potential wells and the energy levels (dashed lines) for a system of three independent quantum harmonic oscillators. The energy levels are equally spaced at intervals of $\hbar\omega$, where ω is the angular frequency of oscillation. That is, we excite the system by adding vibrational energy in quantized units called phonons, and the energy of each phonon is $\hbar\omega$. Because the oscillators are indistinguishable, any state of n quanta is equally likely—no matter how those phonons are distributed among the oscillators. As a result, the average energy per oscillator will be $n/3$. Also, the larger the number of quanta, the larger the number of ways to distribute them, and therefore, the larger the entropy of the system.

system is $\Omega_1(E_1)$ and of the larger system, $\Omega_2(E - E_1)$, then the probability of observing this configuration is the product of the probabilities of observing each system separately, and

$$P(E_1) \propto \Omega_1(E_1) \Omega_2(E - E_1) \quad (4)$$

Note that we have also used the property that the probability of a state of energy E_1 is proportional to the total number of states with energy E_1 . To convert Equation (4) to an equality, we must divide it by the total number of states Ω_{total} . To find this constant, we must first compute the total number of states for each value of E_1 , where E_1 ranges from zero to E , and then add up those numbers.

Equation (4) is a very important result. Let us therefore review what it means. Things in each system are whizzing and banging around all the time. Considered individually, the systems do not have fixed energy, and therefore the number of states of each system will vary as energy is exchanged between them. Every time we look at the whole system, we will see it in one of its equally likely configurations. We have shown that, as energy increases, the number of states increases very rapidly. Conversely, if energy

decreases, the number of states drops very rapidly. Because the large and small subsystems are in thermal contact, they trade probabilities. Equation (4) is a very sharply peaked function that is the product of a rapidly increasing function of E_1 and a rapidly decreasing function of E_1 . For large numbers, the maximum is extremely sharp—in fact, so sharp that it is unlikely that anything but the most probable configurations will ever be observed. Thus, after a while, no matter what the initial states were, the system is observed near its most likely configurations (those that are near the maximum in the probability distribution). Those configurations divide the energy between the two subsystems in a very special way: The fractional increase in the number of configurations of the smaller system, as energy is added to it, is exactly matched by the fractional decrease in the number of configurations of the larger system, as energy is removed from it. That is, for small fluctuations in the energy of either part of the system, the overall probability stays about the same, or

$$\frac{dP(E_1)}{dE_1} = 0 = \Omega_2 \frac{d\Omega_1}{dE_1} - \Omega_1 \frac{d\Omega_2}{dE_1} \quad (5a)$$

Using the properties of the natural logarithm, this expression becomes

$$\frac{d \ln \Omega_1}{dE_1} = \frac{d \ln \Omega_2}{d(E - E_1)} \quad (5b)$$

Equation (5b) expresses one property common to both systems once they have reached thermal equilibrium, something we already know about. What we know is that, after a while, the temperature of both systems is the same. The definition of the temperature is

$$T = \left(k_B \frac{d \ln \Omega}{dE} \right)^{-1} \quad (6)$$

where k_B is Boltzmann's constant. We also define entropy to be

$$S = k_B \ln \Omega \quad (7)$$

The definition of entropy is particularly important because it represents a general way for constructing an additive quantity from multiplied probabilities. From Equations (4)–(7), we see that thermal equilibrium occurs when the temperatures of the subsystems are the same, which is equivalent to saying that the system is very near a maximum probable configuration. We also see that, because the logarithms of products add, entropy is a good extrinsic quantity (2 pounds of butter have twice the entropy of 1 pound).

The system will, however, also exhibit a strange property relating to entropy. We already mentioned the intuitively attractive property that no matter in what state we start the system, after a while, it will be observed in one of its very probable accessible configurations (mathematically equivalent to maximum entropy). All the physical laws apparently governing this system are time reversal invariant. Therefore, if we go either forward or backward in time, entropy should increase. Whenever we observe this system, its entropy must be a mini-

num—something the universe does not, in fact, provide for. If the system was in a very probable configuration in the past, it will continue to be in a very probable configuration in the future.

But if it was in a very improbable configuration in the past, the system will rapidly adjust itself to a probable configuration. The behavior of entropy is not time reversal invariant (we cannot tell the state of the system in the past by observing it in the present). To quote the English translation of “Statistical Physics” by L. D. Landau and E. M. Lifshitz (1980),

“The question of the physical foundations of the law of monotonic increase in entropy thus remains open: it may be of cosmological origin and related to the general problem of initial conditions in cosmology; the violation of symmetry under time reversal in some weak interactions between elementary particles may play some part. The answers to such questions may be achieved only in the course of further synthesis of physical theories.”

Free Energy. To make the connection between statistics and quantities we can measure, we need to study how to calculate the values of measurables if we know the probabilities of possible states. Consider a small system in exactly one definite state i of energy E_i (there are many states with energy E_i) connected to a much larger system of energy $E - E_i$. Then a simple Taylor expansion yields

$$\ln \Omega(E - E_i) \cong \ln \Omega(E) - \frac{d \ln \Omega}{dE} E_i, \quad (8)$$

or

$$\frac{\Omega(E - E_i)}{\Omega(E)} = e^{-\frac{E_i}{k_B T}}, \quad (8)$$

where we used the definition of temperature and relied on E_i to be small. We can easily compute probabilities from

Equation (8) by remembering that the sum of all the probabilities is 1. The correct normalized probability, where the sum is over each distinct state i , is

$$P_i = \frac{e^{-\frac{E_i}{k_B T}}}{\sum_i e^{-\frac{E_i}{k_B T}}}, \quad (9)$$

which describes the probability of observing a state i with energy E_i . The numerator of Equation (9) is the famous Boltzmann factor. The equally famous partition function is the normalization factor in Equation (9), with one term for each allowed state of energy E_i such that

$$Z = \sum_i e^{-\frac{E_i}{k_B T}}. \quad (10)$$

There are, however, many states $\Omega(E_i)$ with energy near E_i . Equation (10) can therefore be rewritten as a sum over each distinct energy E_i , and we will find that

$$Z = \sum_{E_i} \Omega(E_i) e^{-\frac{E_i}{k_B T}}. \quad (11)$$

Because numbers are large and probability distributions sharply peaked, we can accurately approximate the real shape of $\Omega(E_i)$ by a rectangular distribution that is constant over the approximate width of the real distribution and zero everywhere else. The width and height are adjusted so that the area of the rectangle is the correct total number of states near the energy. “Near” in this case can be very crude, and errors in it and this process will only affect the answers to the order of $\ln \Omega$, which is an extremely small error. With these approximations, we perform the sum in Equation (11) to obtain

$$Z \cong \Omega(\bar{E}) e^{-\frac{\bar{E}}{k_B T}} = e^{-\frac{F}{k_B T}}, \quad (12a)$$

where $\Omega(\bar{E})$ is the total number of states near the most probable energy and F is the free energy. Because

$$\ln Z = \ln \Omega(\bar{E}) - \frac{\bar{E}}{k_B T}, \quad (12b)$$

we can express the partition function solely in terms of the free energy and temperature:

$$-k_B T \ln Z = \bar{E} - TS = F. \quad (12c)$$

The significance of writing the partition function in this way is as follows. If the system can be in two phases at once (ice in water), somehow, the fantastically large numbers and wildly swinging probabilities must conspire to make both phases equally likely, even though their energies are obviously different. In addition, the partition function Z must now have two pieces, one for ice and one for water. For the two phases to be observable simultaneously, keeping in mind the monstrous numbers, the two pieces of the partition function must be equal. Therefore, we see that, when the free energy of ice per molecule equals the free energy of water per molecule, the partition functions for equal numbers of molecules are equal, or

$$\begin{aligned} Z_{\text{water}} &= \Omega_{\text{water}}(\bar{E}_{\text{water}}) e^{-\frac{\bar{E}_{\text{water}}}{k_B T}} \\ &= Z_{\text{ice}} = \Omega_{\text{ice}}(\bar{E}_{\text{ice}}) e^{-\frac{\bar{E}_{\text{ice}}}{k_B T}}. \end{aligned} \quad (13)$$

The number of molecules and, therefore, the number of accessible states are typically so large that, if the free energies of the two phases differ, only the phase with the lowest free energy is sufficiently probable to be observed. This is the primary concept that determines the observed phase.

Note that the likelihood of observing a state with a particular energy is equal to the product of (1) the number of states with that energy and (2) the probability of observing any one of them.

Thus, both the energy and the entropy control the phase stability. In the example of ice and water, the increase in energy per molecule associated with stretching and breaking the bonds that lock water into a frozen state makes water less probable by itself because of the Boltzmann factor. But because there are many more ways to arrange the molecules in the liquid than in the solid, this reduction in probability is offset by the increase in the number of states of water. When the energy is just right, the overall probabilities (free energies) of each phase are equal, and ice begins to melt.

Phase Stability and Plutonium

We have seen how both the energy and entropy contribute to determining the free energy and therefore the most probable states (phases) of a system. We will now consider the various contributions to the phase stability of plutonium.

At low temperature and pressure, the monoclinic α -phase of plutonium is stable. This phase is predicted by minimizing the internal energy associated with the electronic structure. In fact, modern electronic-structure calculations by John Wills and coworkers appear to describe completely and astonishingly accurately the behavior of the low-temperature phase of plutonium, essentially from first principles. These calculations are performed for the system at zero temperature, and thus entropy, or the number of states available, is neglected because the entropy contribution to the free energy is zero at zero temperature. It is interesting that plutonium retains the zero-temperature phase to about 400 kelvins, and the electronic-structure calculations predict well the behavior throughout this temperature range.

As temperature rises, the theorist must decide how to include the effects of temperature in determining the free energy. In addition to the internal electronic energy, the contributions to the free energy include a harmonic vibra-

tional (phonon) piece, a thermally activated conduction electron piece, and as Duane C. Wallace writes (1998), an aggregate piece associated with anharmonic phonons and electron-phonon coupling. Of these, the harmonic phonon contribution to the entropy is by far the largest, whereas the aggregate and electronic pieces are less than 6–12 percent of the total. Still, the anharmonic terms give rise to important effects, including thermal expansion, and cause the phonon frequencies (which, in turn, affect the entropy and specific heat) to be temperature dependent. It is attractive, therefore, to use all the available data to attempt to understand the harmonic phonons as perhaps the largest contributor to the root causes of the unusual set of structures that plutonium exhibits.

We will consider first the electronic structure. Remember that isolated atoms in a vacuum have completely localized unmovable electrons with no overlap between the electronic wave functions of different atoms. As the atoms move closer together, the wave functions of their valence electrons overlap weakly at first. The electrons are now shared among the atoms and contribute to the bonding that holds the solid together, but they are hard to move (effectively heavy) from one atom to the next. As the overlap increases, the electrons in a metal become more and more mobile and finally may behave as a gas of nearly free electrons as they do in sodium. For metals such as plutonium, in which the 5f electrons have little overlap, it is not surprising that the crystal structure is very open (otherwise more overlap would occur) and that the overlap and hence the degree of localization are extremely sensitive to interatomic spacing and therefore to pressure. Such a system is expected to be very compressible. As a result, vibrational motion should increase more than usual with increasing temperature as should anharmonic effects so that the average atomic separation should also increase, producing a greater variety of phases than in a system in which overlap is

already strong. Note that the thermal-expansion coefficient of iron is about 13 parts per million per kelvin (ppm/K) whereas that for α -plutonium is near 42 ppm/K.

To get an idea of the extreme compressibility of plutonium, the bulk modulus (an elastic constant describing the stiffness against hydrostatic compression) of α -plutonium that we have measured on high-quality research samples is about 55 gigapascals. In contrast, the bulk modulus of ordinary steel is about 170 gigapascals. The stiffest phase of plutonium is therefore three times easier to compress than steel!

Increasing the temperature does not only cause thermal expansion, but it also increases the entropy. Associated with this increase is the selection of high-entropy/high-energy phases that become more and more favorable as temperature rises. Wallace (1998) provides a very careful computation of the total entropy of plutonium as a function of temperature (and phase) by using the best currently available specific-heat data. He finds that by far the largest contribution to the entropy of plutonium at temperatures above ambient is that from the harmonic vibrations. To get an idea of the energy scales, TS for δ -plutonium at the δ - ϵ phase boundary is about 735 milli-electron-volt (meV) per atom, whereas the enthalpy change (ΔTS) between the δ - and ϵ -phase is on the order of 20 meV per atom. Thus, the δ -phase differs from the ϵ -phase by only 20 meV per atom, which is a very small fraction of the free energy and is tough for the theorist to compute accurately.

Vibrational Entropy and Elastic Constants. Here we show how the vibrational entropy of plutonium can be estimated from measurements of elastic constants, or sound speeds. We begin by approximating plutonium as a collection of masses and springs. This mass/spring, or harmonic, picture connects directly to such mechanical properties as the Young's and shear

moduli, compressibility, and speed of sound, all critical quantities for the best-known practical application of plutonium-239. Consider a long, thin bar of plutonium of length L (we will keep it under a kilogram or so, just to be safe). If we set the bar to vibrating, the lowest tone, or normal mode, is the one whose half-wavelength just fits in the bar, $\lambda/2 = L$. (That wavelength is very much longer than the springs connecting the atoms—therefore, the system behaves as if it were continuous). For the next higher tone, two half-wavelengths fit in the bar; for the next, three fit; and in general, $n\lambda/2 = L$, where n is an integer. In a perfect simple cubic crystal of N atoms, there are N allowed tones, or wavelengths, for a given type of vibrational mode, and there are three types of modes—one compressional and two shear. We have a total of $3N$ normal modes. Each tone (mode) has a fixed frequency but can have any amplitude (careful there, with plutonium, anyway). Thus, each mode is just like the simple harmonic oscillator discussed above. For the lower-frequency normal modes, the frequency f is $f = nv_S/(2L)$. In this expression, v_S is a sound speed (compressional or different types of shear speeds), and n is an integer less than about $N^{1/3}$, which is about the number of atoms in a row along the length L of the bar. From all this, it is apparent that the sound speeds control the lower frequencies of the vibrations in plutonium.

To compute the vibrational contribution to the entropy at temperatures above 300 kelvins, we need to find all the vibrational modes, even those higher-frequency modes whose wavelengths are comparable to the atomic spacing. Neutron scattering measurements can, in principle, measure them all (rather imprecisely and with great difficulty), but we can make very good guesses if we know the sound speeds to high accuracy, and even better guesses if we can use sound speed data to constrain approximate data from neutron scattering methods. Ultrasonic techniques, even the ones we employ, determine

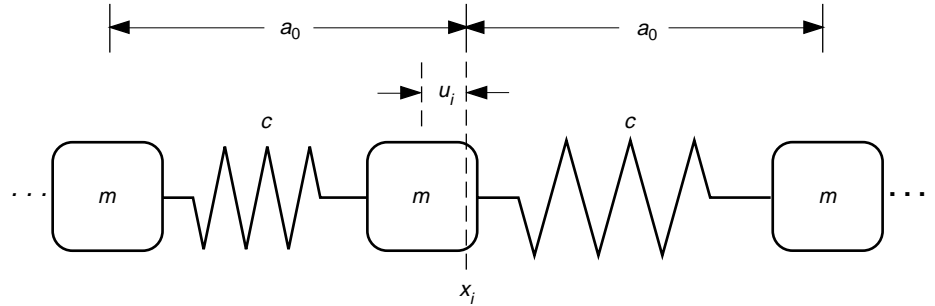


Figure 3. Elastic Forces in the Harmonic Picture of a Solid

In the harmonic picture of a solid, a very long string of atoms connected by chemical bonds and separated by a_0 , the lattice constant, or interatomic distance, is represented as a very long string of masses m connected by springs. The strength of those springs is measured by the elastic constant c . The distance u_i is the displacement of each mass from its rest position x_i , and Equation (14) in the text describes the elastic forces that result from displacements that stretch and compress the springs. The wavelike solutions to Equation (14) describe the longitudinal sound waves that will propagate in this idealized harmonic solid.

the sound speeds only at very long wavelengths, but once we measure the long wavelength modes, with a little help, we can make a pretty good estimate of the variation of frequency with wavelength from our harmonic picture of the solid.

We imagine a very long string of N masses (atoms), each at a distance a from its nearest neighbors, and each connected to those neighbors by springs (bonds) as shown in Figure 3. Looking at one of the masses at position u_i , we find that the stretching of springs to the left and right of that mass produces an acceleration (Newton's famous $F = ma$) such that

$$m \frac{d^2 u_i}{dt^2} = -c(u_i - u_{i-1}) + c(u_{i+1} - u_i). \quad (14)$$

We can solve Equation (14) to find the relationship between the allowed wavelengths and the vibrational frequencies. For each allowed wave vector $k = 2\pi/\lambda$, there is a solution with angular frequency $\omega = 2\pi f$,

$$u_i(t) = u_{i0} e^{i(kx_i - \omega t)}, \quad (15a)$$

where the relationship between k and ω (also called the dispersion relation) is given by

$$\omega = \sqrt{\frac{2c}{m}} \sin ka. \quad (15b)$$

The shortest wavelength λ must be greater than twice the interatomic spacing, or $2a_0$ (if any shorter, we could describe the wave as if it had a longer wavelength and get exactly the same motions), and an integral number of half wavelengths must fit along the string, $n\lambda/2 = L$. In other words, $k = n\pi/Na_0$, and the largest value of k is π/a_0 . Thus, there is a discrete set of allowed wave vectors, and the frequencies given by Equation (15b) define a discrete set of vibrational modes.

The plot of these discrete vibrational modes versus wave vector in Figure 4 looks continuous because the number of modes is very large. The slope of the straight line, which is the slope of the curve at the origin, is typically the sound velocity and is given by $d\omega/dk = v_S = a_0(2c/m)^{1/2}$, where c is the elastic constant in Equation (14). It is important to note that this simple picture is for nearest-neighbor springs only. As is also shown in the figure, second-nearest neighbors change things, but still the curves are tightly constrained. Our measurements of sound speeds (or elastic constants) are essentially within only a few parts per million away from zero in Figure 4. The flattening of the curve

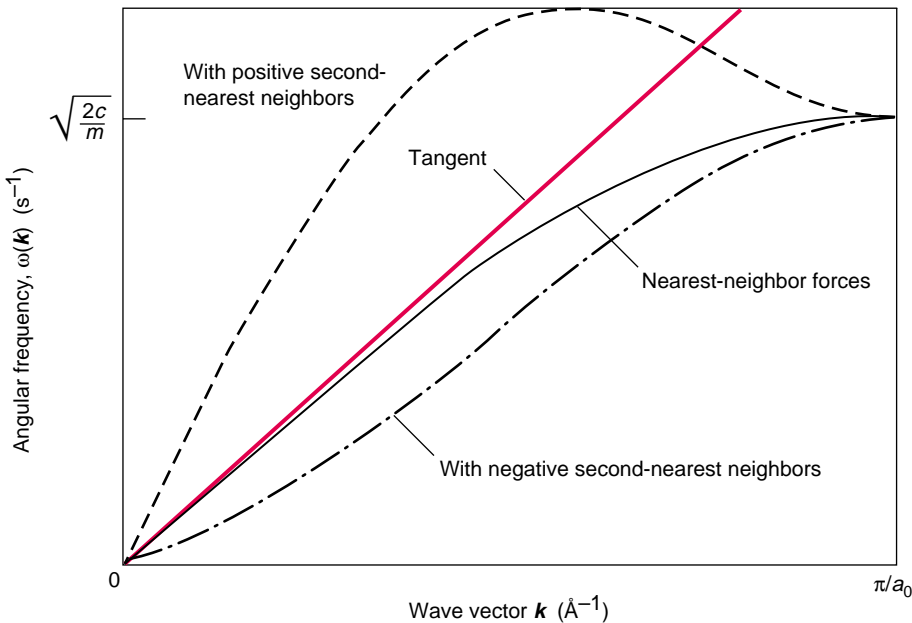


Figure 4. Vibrational Modes vs Wave Vector

The black solid curve is a plot of Equation (15b), the dispersion relation (or frequency versus wave vector) for the longitudinal sound-wave solutions to Equation (14). That equation describes forces (springs) between nearest neighbors only. The slope of that curve at $k = 0$, marked by the red straight-line tangent, is the sound velocity, $v_s = a_0 (2cm)^{1/2}$. The dispersion curves for systems that have either positive or negative second-nearest neighbor forces (in addition to nearest-neighbor forces) are also shown.

at high wave vectors (short wavelengths) is the effect of the discrete system over the continuous one.

For the real solid, the plot is four-dimensional, with three dimensions for the directions of the wave vector and one dimension for frequency. The end-point of the plot in any direction depends on details of the crystal symmetry. In addition, there are three branches in each direction, two for the shearlike waves and one for the longitudinal wave (see Figure 5). The shear-wave speeds are usually about two-thirds of the longitudinal-wave speed. For plutonium and body-centered-cubic (bcc) metals, some shear-wave speeds are much lower. Therefore, the shear modes have lower frequencies of vibration and contribute more to the entropy as we shall see next. Note that in a real solid, the elastic constant c generalizes to a fourth-rank elastic-modulus tensor with as many as 21 independent elements.

But because most plutonium samples currently available are isotropic polycrystalline samples, much of the directional information is lost, and we can measure only two elastic moduli: c_{11} , the compressional modulus, and c_{44} , the shear modulus. In general, each elastic constant is the ratio of a particular type of stress to a particular strain.

Interestingly, if we knew all the sound speeds (or elastic moduli), we could have a good guess at the full four-dimensional plot of the vibrational modes (the phonon dispersion curve) because the frequency dependence is always expected to be very close to that given by Equation (15b) or one of its next-nearest-neighbor analogues. Even in systems with more than nearest-neighbor forces, the general forms of the dispersion curves are tightly constrained, with only a few parameters needed to describe them.

Once the frequency of an oscillator is known, it is very easy to compute its

entropy directly from the partition function—Equation (10). We mentioned earlier that the energy levels of each harmonic oscillator or normal vibrational mode i are equally spaced, that is, $E_i = (n+1/2)\hbar\omega_i$. The average number of quanta (phonons) thermally populating that mode can be written as

$$\begin{aligned} \bar{n}_i &= \frac{1}{Z} \sum_{n=0}^{\infty} n e^{-(n+1/2) \frac{\hbar\omega_i}{k_B T}} \\ &= \frac{1}{\frac{\hbar\omega_i}{k_B T} - 1}, \end{aligned} \quad (16a)$$

where we have used the partition function to compute the expectation value of the number of phonons in that mode. Note that, if the temperature (or $k_B T$) is high relative to the energy of each phonon, there is a simple expression for the average number of phonons in that mode:

$$\bar{n}_i \approx \frac{k_B T}{\hbar\omega_i} \quad \text{for } k_B T \gg \hbar\omega_i. \quad (16b)$$

Based on the result for the average occupation number of mode i , we can obtain expressions for the average energy in that mode, \bar{E}_i , and the free energy F_i :

$$\bar{E}_i = \hbar\omega_i \left(\bar{n}_i + \frac{1}{2} \right) = k_B T, \quad (17)$$

$$F_i = -k_B T \ln Z, \quad (18)$$

where

$$Z = \frac{1}{e^{\frac{\hbar\omega_i}{2k_B T}} - e^{-\frac{\hbar\omega_i}{2k_B T}}}.$$

The entropic contribution to the free energy for a single mode TS_i is

$$TS_i = \bar{E}_i - F_i. \quad (19a)$$

If the temperature is relatively high, that is, $k_B T$ is much greater than the energy per phonon, the entropic

contribution in (19a) becomes

$$TS_i \approx k_B T (1 + \ln \bar{n}_i). \quad (19b)$$

We want to know the vibrational entropy of the entire system, and so we need to compute an average over all modes i of the $\ln \bar{n}_i$, or, at relatively high temperatures, an average of $\ln \hbar \omega_i$. The Debye temperature, or more exactly, $k_B \Theta_D$ is a special low-temperature average of $\hbar \omega_i$ rather than an average of the $\ln \hbar \omega_i$. A better characteristic temperature in the high-temperature limit could be computed by taking an average over Equation (19b) for all the modes along all the dispersion curves in a four-dimensional plot. If we define this temperature in the high-temperature limit to be Θ_0 , then the total vibrational contribution to the entropic term in the free energy is

$$TS \approx 3Nk_B T \left(1 + \ln \left(\frac{T}{\Theta_0}\right)\right). \quad (20)$$

With Equation (20), we have arrived at a description of the total vibrational entropy of a solid of N atoms, and we have shown that it can be calculated from a measurement of the speed of sound at all wavelengths and in all directions. Measured sound speeds can also be compared with those computed directly from theoretical models of plutonium energy. Therefore, sound speeds or, equivalently, elastic moduli are important for determining both the entropy and energy contributions to the free energy. It is for this reason that measurements of the elastic modulus tensor, dependent on the type of strain and its direction, provide so much stronger feedback to the theorist than simple scalar thermodynamic measurements such as heat capacity or bulk modulus. Surprisingly, only a few sound speeds are known for plutonium, and these are mostly averages obtained from measurements on polycrystalline samples. At present, there is only one measurement at ambient temperature of the full elastic-modulus tensor on a gallium-stabilized δ -plutonium single crystal.

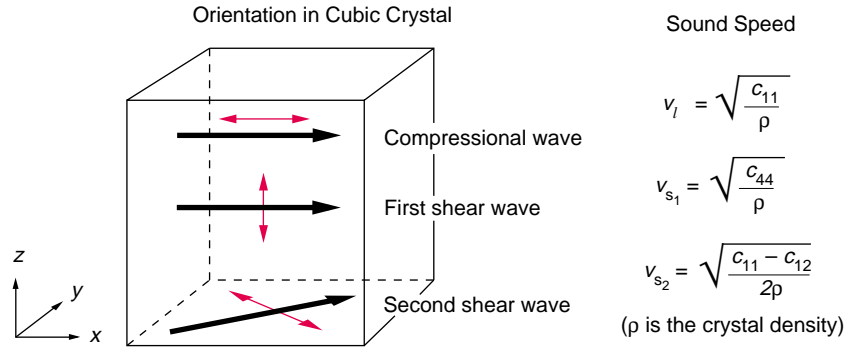


Figure 5. Vibrational Modes and Sound Speeds in a Cubic Crystal

There are three types of sound waves. One is a longitudinal wave in which atoms vibrate (red arrow) along the direction of propagation (black arrow), and two are shear waves in which the atoms vibrate perpendicular to the direction of propagation. In a cubic crystal, these waves are associated with three independent elastic moduli— c_{11} , c_{12} , and c_{44} . As shown in the figure, c_{11} determines the speed of the longitudinal wave, c_{44} determines the speed of the first shear wave, and c_{11} and c_{12} determine the speed of the second shear wave.

Estimated Free-Energy Changes and the Role of Entropy in Stabilizing Plutonium

Because the elastic constants in plutonium are very low, we expect the average number of quanta in each mode, and therefore the vibrational entropy, to be high in the high-temperature phases of plutonium. We would even guess that vibrational entropy could be the primary ingredient in stabilizing all the phases of plutonium with the exception of the α -phase. It would be nice if the changes in entropy and electronic energy in going from phase to phase could be computed from first principles, but it is extremely difficult to compute the electronic energy with the atoms vibrating. Instead, we suggest that one can estimate large parts of the free energy on either side of a phase boundary by measuring elastic moduli and that those data will also enable identification of the missing contributions—especially any changes in the zero-temperature internal electronic energy in going from the α -phase to the higher-temperature phases. In particular, this approach may enable us to figure out the magnitude of the contribution played by

f-electron localization in determining phase stability in plutonium.

The δ - to ϵ -Phase Transition. We will estimate changes in contributions to the free energy across plutonium's δ - to ϵ -phase transition at 753 kelvins. This face-centered-cubic (fcc) to bcc transition follows a Bain's path (discussed later) and is most likely to be explained by vibrational- and/or elastic-entropy arguments. There is no net change in free energy across a phase boundary, so any change in internal vibrational (elastic) and electronic energy must be balanced by a change in entropy. One obvious change in the internal energy in going from the δ - to ϵ -phase is triggered by volume changes. A crude guess for this contribution can be based on the measured bulk modulus B of δ -plutonium (measured, of course, by the sound speeds as well as by x-ray diffraction). Suppose we precompress plutonium isothermally just below this phase boundary by 3.58 percent, the measured volume decrease across the boundary (plutonium shrinks in volume on warming throughout the range of existence of the δ -phase and also upon transition to the ϵ -phase). We will wind up with a state at the correct volume

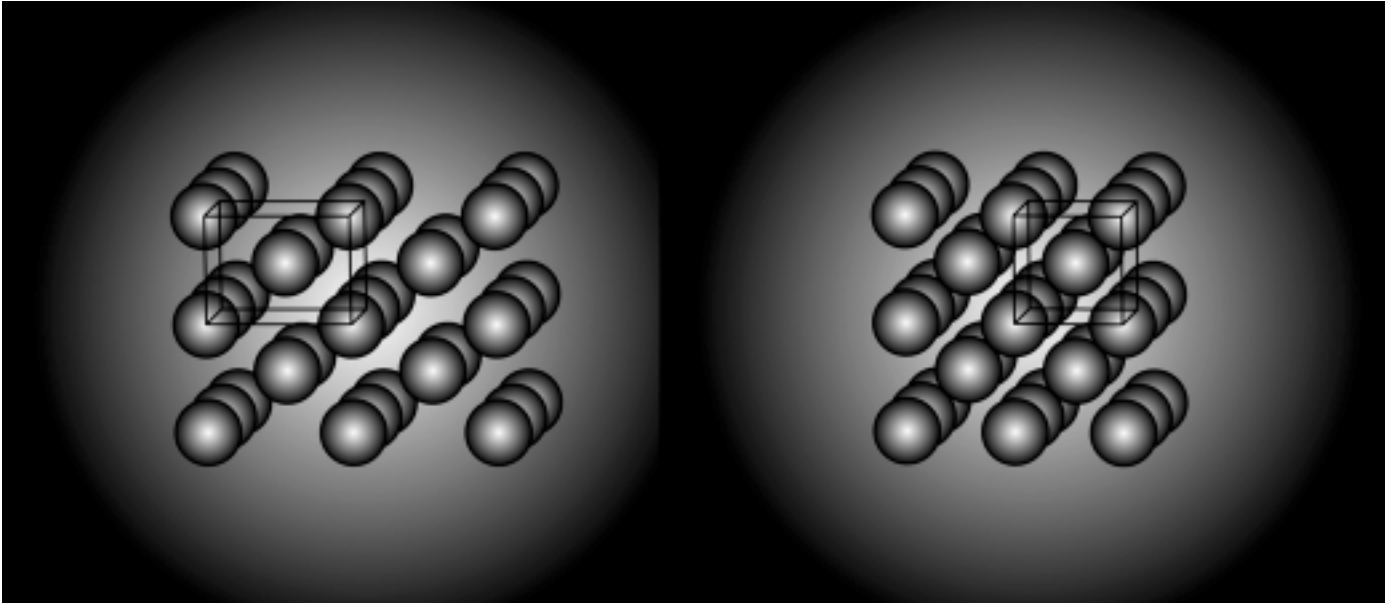


Figure 6. The Bain's Path for the δ - to ϵ -Phase Transition in Plutonium

The figure on the left shows the fcc structure of δ -Pu, and the one on the right the bcc structure of ϵ -Pu. The particular viewing angle and the unit cell outlined on the left show that the fcc phase is equivalent to a bcc phase in which the long edge is $2^{1/2}$ times the short edges of the unit cell. From this view of the fcc phase, it is clear how the system can shrink continuously from the fcc to the bcc structure. That path is called a Bain's path.

for the ϵ -phase but at a temperature infinitesimally too low for it to be stable and having the wrong structure. The compressional energy to make this state is

$$\Delta\bar{E} = \frac{1}{2} B \left(\frac{\Delta V}{V} \right)^2. \quad (21)$$

Using the unit cell size of δ -plutonium, four atoms in 4.64 cubic angstroms, and the bulk modulus $B = 29$ gigapascals,² we find that the energy required to compress is 3 meV per atom. The measured latent heat for the δ - to ϵ -phase transition is about 20 meV per atom. So, simply changing the volume of plutonium cannot account for the internal-energy change. We also learn that elastic moduli other than the bulk modulus must be controlling this transition, and therefore,

²This value comes from our recent very accurate RUS measurements on polycrystals, and it agrees well with the only single-crystal elastic-modulus measurements of gallium-stabilized δ -plutonium.

simple scalar quantities such as specific heat will not provide all the information we need.

If the volume change does not explain the 20 meV per atom of latent heat, where should we look? We note that, at 753 kelvins, the thermal energy per atom is $3k_B T = 192$ meV per atom, an enormous energy. It is therefore very attractive to see if much of the latent heat goes into vibrational entropy, which is then balanced by increases in vibrational (elastic) energy, thereby ensuring a zero change in free energy across the transition.

$$\Delta E = T\Delta S. \quad (22)$$

If we can get most of the latent heat with vibrational entropy alone via sound speed changes across the phase boundary, perhaps only small changes in electronic structure are needed.

Figure 6 suggests the type of strain or distortion that could eat up 20 meV per atom. On the left is the fcc δ -plutonium structure, shown as the

exactly equivalent bcc structure with the long edge $2^{1/2}$ times larger than the short edges. If we are at a temperature just below the δ - ϵ phase boundary and we uniaxially and isothermally stress δ -plutonium so that it shrinks from fcc to bcc (it shrinks along the stress direction and expands perpendicular to it), we produce a bcc structure at just below the temperature at which it is stable. This is a Bain's path. On raising the temperature a tiny amount, absolutely nothing happens except that the bcc structure becomes stable. There is no latent heat for this final step. Therefore, the measured latent heat without a Bain's strain must be equal to the energy required to strain the fcc phase into a bcc shape along the Bain's path. A small volume adjustment might be needed, but we have shown this to be a small effect. What strains are involved in this process?

Measured elastic properties of δ -plutonium show an unusually large shear anisotropy. The shear stiffness in

one direction (110, or an angle $\pi/4$ from an edge) is very low compared to the shear stiffness parallel to an edge. For that reason, Young's modulus, exactly the modulus encountered along the Bain's path, is also very low. Also, Poisson's ratio, which describes how much a material bulges when uniaxially compressed, is very large (0.424, a value close to Poisson's ratio for a liquid). Hence, the Bain's path is traversed with little volume change, and the energy required goes mostly into shear strain energy. We have now connected a change in shear strain energy to the measured latent heat, and we learn that shearlike rearrangement of the plutonium atoms must be the important process at this phase transition! Can we get a handle on this argument via sound speeds as well?

In general, bcc materials have a very large shear anisotropy, typically even larger than for δ -plutonium. We expect, then, that the generally low shear stiffness in one direction of bcc structures should provide those modes with lots of entropy, thereby making the bcc structure favorable as the temperature rises. From standard ultrasound measurements by Ledbetter and Moment (1975) and Kmetko and Hill (1976), we obtain the low-temperature average phonon frequencies, or Debye temperatures (not the right average, but at least related to what we want), for both δ - and ϵ -plutonium. Those characteristic temperatures are 106 kelvins for δ -plutonium and 89 kelvins for ϵ -plutonium. Using those not-quite-right characteristic temperatures to compute the entropic contribution to the free energy at 750 kelvins—Equation (20)—we find that the measured latent heat Q balances the change in vibrational entropy perhaps to within 10 percent. In other words,

$$\begin{aligned} 3k_{\text{B}}T \left(1 + \ln \left(\frac{T}{\Theta_{\delta}} \right) \right) + Q \\ = 3k_{\text{B}}T \left(1 + \ln \left(\frac{T}{\Theta_{\epsilon}} \right) \right). \end{aligned} \quad (23)$$

Thus, we can account for essentially all the energy and entropy changes in the δ - to ϵ -phase transition from sound speed (elastic constant) changes. Do these changes in elastic moduli come strictly from the typical changes that occur when a material goes from fcc, a phase expected to have low shear anisotropy, to bcc, a phase expected to have high shear anisotropy, or are the modulus changes a result of changes in electronic structure? Although much more work must be done to establish the relevance of these arguments for the lower-temperature phases, for which the entropy is less, an approach based on ultrasound studies appears the right route to understanding the higher-temperature phases.

The Bain's path may account for the negative volume thermal-expansion coefficient of δ -plutonium as well. The very large strains that accompany the Bain's route ensure that, using the latent heat and the starting and ending moduli, we can only roughly construct the elastic moduli along the route. There is also no constraint that the end-point volume be larger or smaller than the starting volume. For plutonium, the end-point bcc volume just happens to be smaller, and the route is very soft—that is, the value of Young's modulus is low along the Bain's path. Therefore, an attractive argument for the negative thermal expansion coefficient of the volume is that, at temperatures below the boundary between the δ - and ϵ -phase, plutonium thermally "samples" the bcc volume along the very soft Bain's path. Thus, part of the time, it has a volume closer to bcc, which is smaller than the fcc volume. The negative thermal-expansion coefficient of the volume may be a direct consequence of the lower bcc volume and the existence of a Bain's path.

The size of these entropy-driven effects is very large in plutonium. For example, in nickel, which has a melting point almost twice that of plutonium, the bulk modulus is about five times higher, and the Debye tem-

perature (related to the sound speeds and therefore the bulk modulus) is four times higher than in plutonium. Therefore in nickel, compressional energies are larger than in plutonium, and entropy effects are smaller. Nickel has far fewer options in its search for stable high-temperature phases. It also exhibits far fewer structures than plutonium over the range of existence of the solid and always has a positive thermal-expansion coefficient. We might guess then that the root of plutonium's odd behavior may be the localized electrons with weak overlap that force plutonium to have an easily compressed open structure.

Elastic Moduli Measurements

By now we have probably convinced the reader that knowing the elastic modulus tensor as a function of temperature and pressure for each of the phases of plutonium would be required for a complete experimental understanding of its thermodynamics. Although such data exist for many elements, we have only sparse data for plutonium. To determine the complete elastic tensor using ultrasonic techniques, we must have single crystals of each phase. The phase changes plutonium undergoes as it cools from the melt hinder us from growing single crystals of α -plutonium unless the metal is under extreme pressure. All the other phases exist only at high temperature. Thus, a single crystal of pure δ -plutonium would have to be kept at above 550 kelvins for the entire measurement process. Moreover, because plutonium-239 absorbs neutrons, neutron scattering studies must use pure plutonium-242, and that is a rare isotope. Finally, measuring the moduli in such a dangerous system requires extreme environmental and safety overhead. All these factors combined result in little accurate and reliable elasticity and thermodynamic information on plutonium.

Implications of Previous Data. The few data we have, as stated above, are decidedly unusual. Table I shows a summary of the only existing elastic data measured from a plutonium single crystal. These measurements were made by Moment and Ledbetter (1975) at ambient temperature on a 7-millimeter-long δ -plutonium grain stabilized with 3.3 atomic percent (at. %) gallium. It took them over a decade to find suitable methods for growing measurable single crystals of plutonium. Their results show that δ -plutonium is amazingly anisotropic. Note that c^* is the shear modulus at an angle of $\pi/4$ to the cubic axis, c_{11} controls the longitudinal sound speed, and c^* and c_{44} control shear speeds.

Several points must be made about this measurement. First, at a radioactive heating rate of 50 milliwatts per cubic centimeter (mW/cm^3), larger crystals cannot be measured accurately because they heat internally as a result of their larger surface-to-volume ratio. Second, gallium-stabilized δ -plutonium is different from pure δ -plutonium. That is, in a crystal of plutonium stabilized with 3.3 at. % gallium, there are only about two plutonium atoms between each gallium atom along any of the principal crystallographic directions. Thus, the presence of gallium thoroughly distorts the structure, the phase transitions, the temperature at which the transitions occur, and even the sign of the thermal-expansion coefficient. Although the atomic volume of the plutonium-gallium (PuGa) alloy varies very smoothly with decreasing gallium concentration and intercepts the atomic volume of pure δ -plutonium as the gallium content goes to zero, the elastic properties are often more than an order of magnitude more sensitive to atomic volume than other physical quantities. Thus, it is possible that the elastic moduli of pure δ -plutonium are different from those of gallium-stabilized δ -plutonium. Third, the elastic anisotropy c_{44}/c^* is the largest for any fcc metal. (An isotropic system, such as glass, has $c^* = c_{44}$.) This strong variation of mod-

Table I. The Elastic Moduli of δ -Pu (1 wt % Ga) at Ambient Temperature^a

Modulus	Measured Value (GPa)
c_{11}	36.28 ± 0.36
c_{44}	33.59 ± 0.11
$1/2(c_{11} - c_{12}) = c^*$	4.78 ± 0.38

^aResults are from measurements by Moment and Ledbetter.

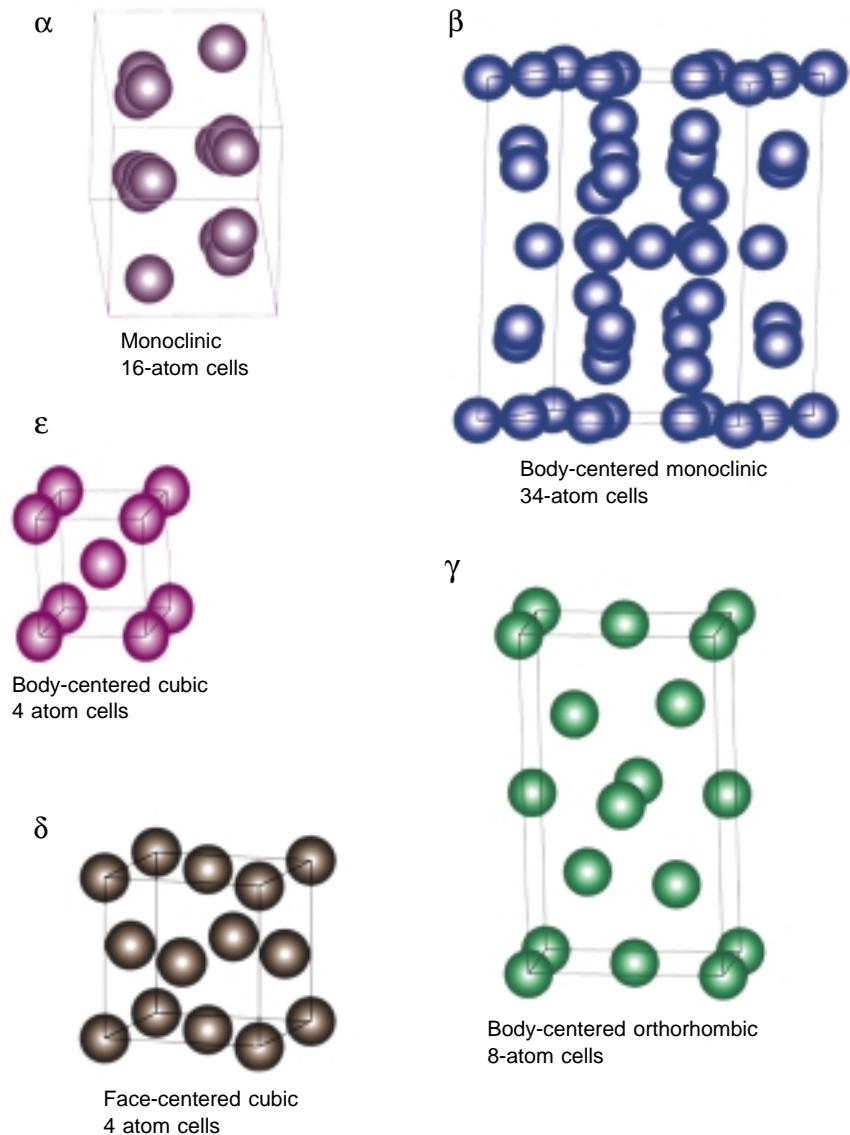


Figure 7. The Six Crystal Structures of Plutonium

Starting from α -Pu and proceeding clockwise are five of the six crystal structures of plutonium in the order in which they appear as the metal is heated. The sixth structure, δ' (which occurs between δ - and ϵ -phase), is not shown because δ' and δ look about the same.

uli with direction means that we must take more care when computing averages, especially because the soft directions contribute more strongly to entropy. Fourth, c_{44} nearly equals c_{11} , and therefore the material does not change volume much when compressed along a cubic axis; in other words, it acts a lot like a liquid. Fifth, radiation damage changes the properties of plutonium. Taken together, these comments suggest that modulus data derived from PuGa alloys are not necessarily applicable to pure δ -plutonium and that elasticity measurements must be made to determine the effect of gallium. Nevertheless, we can work with the gallium-stabilized phases, which are crucial for engineering applications. As a result, our initial measurements were focused on those materials.

Finally, we note that, because of the very large shear anisotropy in plutonium, elastic measurements on polycrystalline samples will produce averages of strongly varying quantities, masking the underlying physics. To get at these details, we must make as many measurements as possible on single crystals. That information is necessary to check electronic-structure calculations and develop a fundamental understanding of plutonium. Figure 7 shows the crystal structures of five of plutonium's six solid phases (the δ' -phase, which looks like a slightly compressed version of the fcc δ -phase, is not shown). The cubic phases have only three independent elastic moduli whereas the monoclinic phases have 13 such moduli.

Resonant Ultrasound Spectroscopy.

The powerful regulatory and safety issues that come to bear will likely allow only gallium-stabilized δ -plutonium crystals of a few millimeters to be grown in the next several years. But small samples are difficult to study with conventional pulsed ultrasound because of both size and attenuation effects. Fortunately, RUS³ is perfectly suited for remeasuring plutonium's elastic moduli in both single-crystal

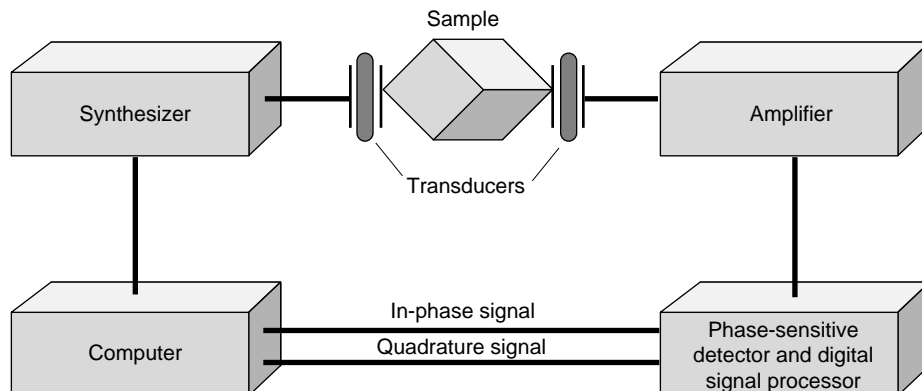


Figure 8. Block Diagram and Photo of a Resonant Ultrasound Spectrometer

The resonant ultrasound spectrometer measures a sample (shaped as a rectangular parallelepiped), which is placed between two transducers, one of which drives the sample over a continuous range of frequencies in the megahertz range. While the temperature is held fixed, an electronic-signal generator (or synthesizer) changes the frequency of the driver gradually and automatically. The applied signal is amplified when it passes through regions where the sample resonates. The amplified signal is picked up by the second transducer and recorded automatically by a specially designed electronic phase-sensitive detector. The requisite resonance spectrum at a given temperature is measured in several seconds and is displayed on the computer. Most important, the computer calculates the elastic constants.

and polycrystalline samples.

RUS is a very simple technique, in which the mechanical resonances of a solid object of known shape are induced, measured, and analyzed to provide the complete elastic tensor. This technique is usually implemented on a sample with all faces either parallel or perpendicular to each other (a rectangular parallelepiped resonator, or RPR). Because weak, dry point contact

is made between transducers and very small samples (a few millimeters or less on one side), this system is both extremely accurate and well suited for glove-box operations. The weak contact requires that extreme care be taken with the electronics. Figure 8 shows a block diagram of the current state-of-the-art system.⁴ Figure 9 shows the very sharp resonances observed with this system when a typical sample is measured.

³Resonant ultrasound spectroscopy (RUS) was developed into a practical tool by Albert Migliori at Los Alamos over the last several years.

⁴The current system was designed by Albert Migliori and is manufactured by Dynamic Resonance Systems, Inc.

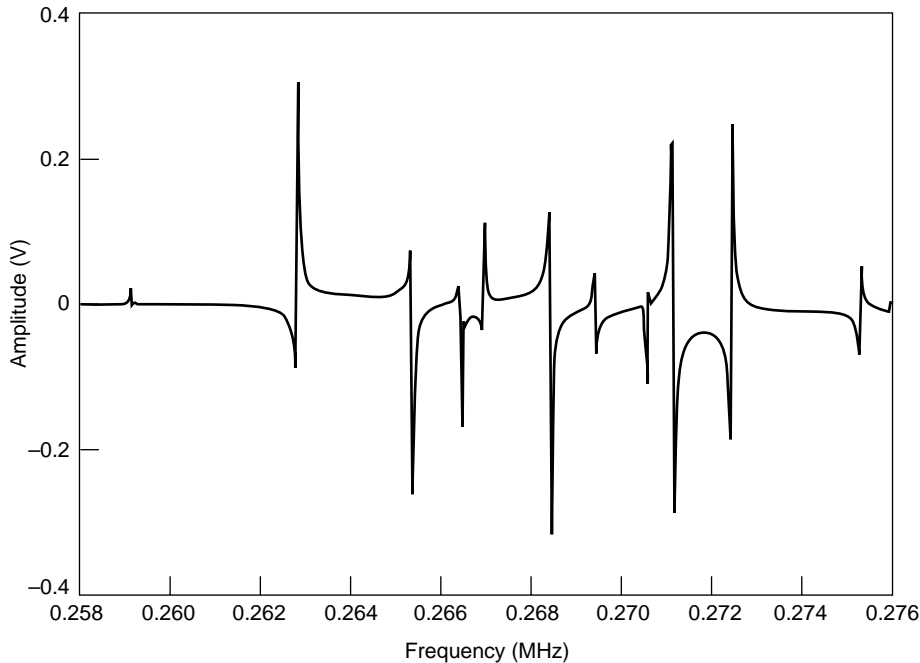


Figure 9. RUS-Measured Resonances of a High-Purity Plutonium Sample
 This spectrum of resonant vibrational frequencies of a high-purity polycrystalline sample of Pu 3.3 at. % Ga was recently measured by our resonant ultrasound spectrometer, which was adapted for use in a glove box environment. Because the resonant ultrasound measurement is phase sensitive, some peaks are negative.

These data were obtained from a high-purity chill-cast new polycrystalline sample of plutonium with 3.3 at. % gallium supplied by Jason Lashley. (See the article “Preparing Single Crystals of Gallium-Stabilized Plutonium” on page 226.) The measure of sharpness of a resonance, or Q , is $f/\Delta f$, where f is the frequency of a resonance and Δf is the full width at half maximum of the resonance. For our plutonium samples, f is about 0.2 megahertz. If Q , which is a direct measure of the intrinsic dissipation, is greater than 1000, we expect very high accuracy for elastic-modulus measurements. For plutonium, we observe Q s greater than 10,000.

Although acquiring extremely accurate resonances on carefully prepared plutonium samples is straightforward, analysis of those resonances is computationally intensive. To put this statement in perspective, a computation

took 1 second of CPU time on the first Cray, 12 hours on a PC-AT, and now 1.3 seconds on a 600-megahertz Pentium III. In Figure 10, we show the complex deformations corresponding to several particular mode types. These deformations need to be calculated. The RUS algorithm must iteratively compute the deformations and then adjust the elastic moduli of the model RPR to match the measured ones. A typical result is illustrated in Figure 11, showing the deviation between fitted and measured resonances. The actual accuracy of the measurement is not quite the root-mean-square error in the fit because the best fit has different curvatures in the different directions of elastic-modulus space. Typically, we obtain shear moduli on plutonium to better than 0.1 percent and compressional moduli to better than 0.7 percent. Because there are no corrections to such results, RUS typically provides the

highest absolute accuracy for any routine modulus-measurement technique. For the measurement of Figure 11, we used a sample weighing 1.33 grams, with a geometrically determined density of 15.968 grams per cubic centimeter (g/cm^3). The sample was rather large for RUS measurements, $0.3081 \times 0.4928 \times 0.5603$ centimeters. The errors for this measurement were about 0.9 percent for c_{11} , which determines the compressional-wave speed, and 0.1 percent for c_{44} , which determines the shear wave speed.

In Table II, we provide a summary of both our recent measurements and previous measurements by others. Of particular interest is the almost exact correspondence between the very careful measurements of Moment and Ledbetter on a single crystal of new plutonium (3.3 at. % gallium) and our measurement on a nominally identical polycrystal sample. Other measurements, however, unexpectedly disagree. For example, the data for the 3.2 at. % gallium sample are very different. The reason may be an uncontrolled variable (age) or the data may simply be wrong. Moreover, our modern measurement of pure polycrystalline plutonium (α -phase) at room temperature agrees with one older measurement but not with the other. Finally, the variation in the results of pure plutonium in the δ -phase at higher temperatures is so extreme that those results beg for corroboration. We hope to address all these points and others in the next few years.

For all the measurements we have made on plutonium, the Q s were greater than 3000 and as much as 12,000 for the sample whose data are illustrated in Figure 11. With a Q of 10,000 and signal-to-noise ratios typified by Figure 9, we are able to track frequency changes smaller than 1 ppm. This extraordinary sensitivity to changes makes possible two unique measurements. The first is done in real time and is a measurement of the effect of radioactive decay on the elastic properties of plutonium. For example,

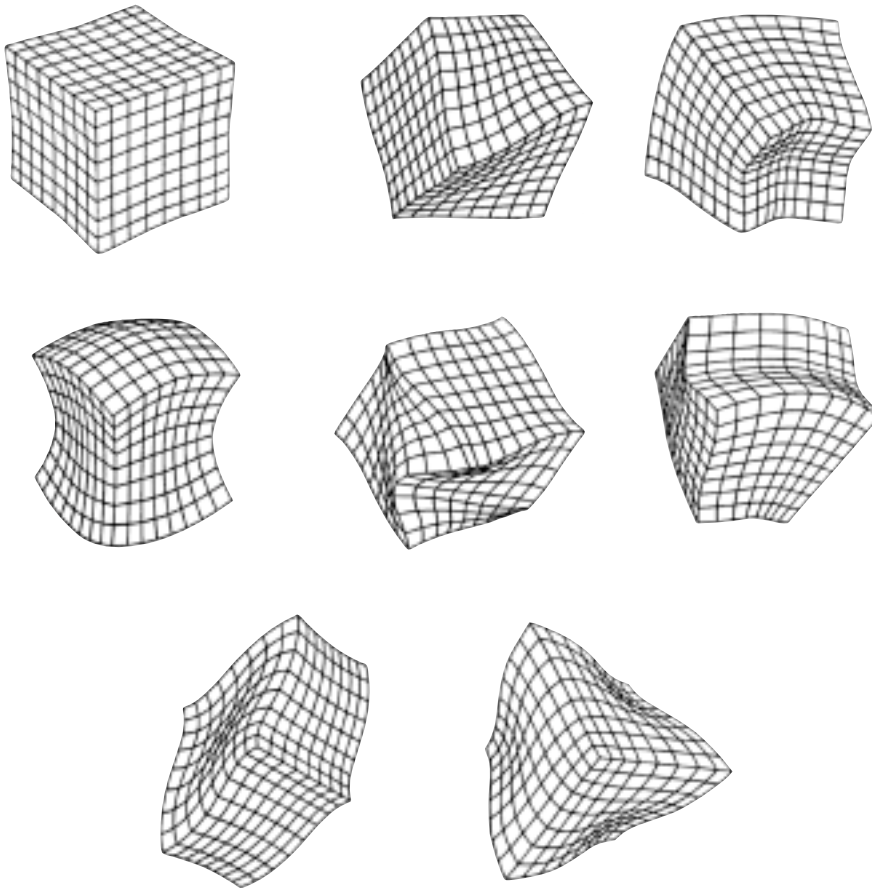


Figure 10. Vibrational Modes of a Rectangular Parallelepiped

There are eight types of normal vibrational modes for a crystalline sample of orthorhombic or higher symmetry shaped as a rectangular parallelepiped. The modes are either symmetric or anti-symmetric about three perpendicular planes. The lowest of each mode type is shown here.

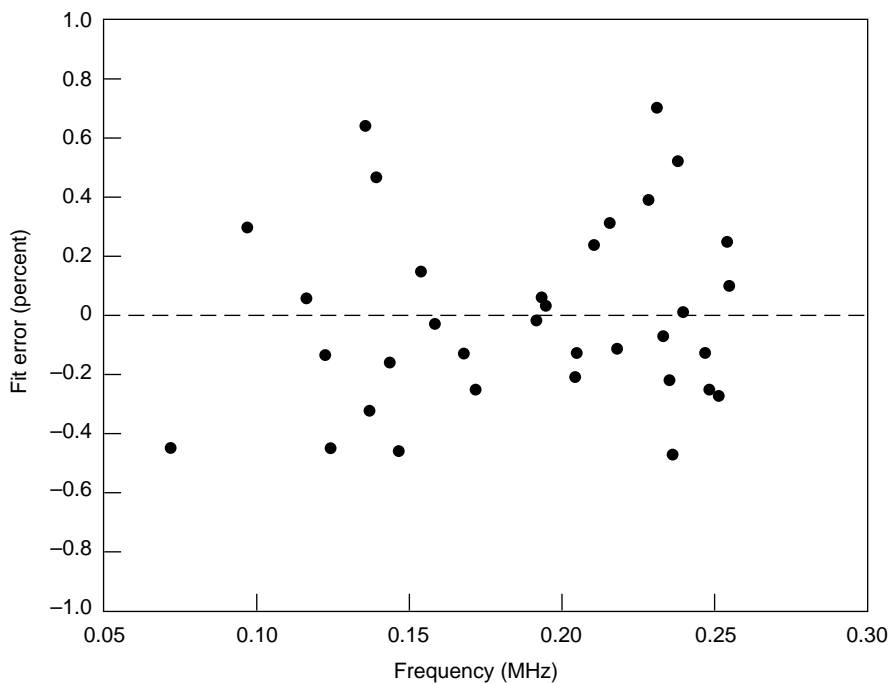


Figure 11. Accuracy of RUS Measurements

Shown here is the deviation between fitted and measured resonances on a typical polycrystalline plutonium sample. The experimental data are fed into a computer program that tries to find a set of elastic moduli consistent with the measured resonances, the sample dimensions, and the symmetry of the sample's crystal lattice. Each circle represents the difference between the observed and calculated resonances.

Table II. Summary of Elastic-Moduli Measurements of Plutonium^a

Sample	C_{11} (GPa)	Bulk (GPa)	Shear (GPa)
Polycrystal pure δ -Pu (703 K)	41.3	33.9	5.59
Polycrystal pure δ -Pu (655 K)	63.6	55.9	5.79
Single crystal δ -Pu 3.3 at. % Ga	51.4	29.9	16.1
Polycrystal δ -Pu 5.9 at. % Al	54.9	30.9	18.0
Polycrystal δ -Pu 2.1 at. % Al	40.3	19.1	15.9
Polycrystal δ -Pu 5.8 at. % Ga	65.1	37.1	21.0
Polycrystal δ -Pu 3.2 at. % Ga	64.4	37.7	20.0
Polycrystal δ -Pu 5.4 at. % Ga (aged)	50.0	27.0	17.2
Polycrystal δ -Pu 4.0 at. % Ga (aged)	58.4	34.3	18.1
Polycrystal δ -Pu 3.3 at. % Ga (new)	51.8	29.6	16.7
Polycrystal δ -Pu 3.3 at. % Ga (aged)	47.5	26.7	15.6
Polycrystal δ -Pu 2.2 at. % Ga (new)		30.3	
Cast α -Pu (laquer)	104.6	46.6	43.5
Cast α -Pu*	109.1	55.8	40.0
Cast α -Pu (DeCadenet)	109.0	54.5	40.9

^a The measurements conducted by the authors of this article are in red. All measurements took place at ambient temperature except where noted.

a Q of 10,000 would enable us to see a change of about 1 ppm in stiffness, something we might expect to see in a few days if the temperature can be held stable to 0.005 kelvin, a perfectly feasible task. The second is a measurement that enables us to study the effects of aging on phase stability in real time. For example, if gallium-stabilized δ -plutonium is cooled, it may become increasingly and measurably (by the RUS method) unstable, a feature exhibited by a very slow change in elastic moduli versus time. Such metastability is observed in many systems, including steel and precipitation-hardened aluminum (known as aircraft aluminum). To observe both radioactivity-induced changes and metastability will require a precisely temperature-controlled environment for the measurement. Such a system will leverage another critical set of measurements—the variation of mod-

uli with temperature.

One source of variation in the elastic properties of plutonium with temperature comes from changes in the phonon frequencies with vibrational amplitude—an important nonlinear effect, as is thermal expansion. Noting that plutonium has a very large thermal-expansion coefficient, other nonlinear effects are also expected to be unusually large. Their study will therefore be particularly revealing. Few temperature-dependent modulus measurements have been made so far, and there are no single-crystal data. The polycrystal work has been done on large samples that self-heat, and only one set of data appears on the gallium-stabilized alloy. The elastic moduli results of those measurements are substantially different from our recent results (the value for the 3.2 at. % gallium sample in Table II was taken from the temperature-dependence

study). Understanding the cause for those differences will be difficult and time-consuming but is badly needed. Our approach, especially considering the safety concerns, is to begin with measurements of the temperature variation of the elastic moduli around ambient temperature by using thermoelectrically cooled stages to vary temperature by 30 kelvins or so. Such a variation will enable us to determine the slope of the temperature dependence at ambient temperature to about 0.3 percent. This work is well under way, as we are tackling the much more difficult task of introducing furnaces and cryogenics into the RUS experimental area so that other phases can be studied. The results of this latter aspect of our work will be well worth our effort. ■

Further Reading

- Eriksson, O. D., J. N. Becker, A. V. Balatsky, and J. M. Wills. 1999. *J. Alloys and Compounds* **287**: 1.
- Kmetko, E. A., and H. H. Hill. 1976. *J. Phys. F* **6** (6): 1025.
- Landau, L. D., and E. M. Lifshitz. 1980. *Statistical Physics*. Translated from Russian by J. B. Sykes and M. J. Kearsley. Oxford: Butterworth-Heinemann.
- Ledbetter, H. M., and R. L. Moment. 1975. *Acta Metall.* **24**: 891.
- Söderlind, P. 1998. *Adv. Phys.* **47**: 959.
- Wallace, D. C. 1998. *Phys. Rev. B* **58** (23): 890.



Joe Baiardo received his undergraduate degree in chemistry from Loyola University, Chicago, and his Ph.D. in chemical physics from the University of Florida. After completing postdoctoral work at the University of Florida and at Monsanto Corporate Research Laboratories, Joe became a staff member at Los Alamos. At first, he first worked on the Plutonium Molecular Laser Isotope Separation Project, primarily to develop methods for in situ time-resolved Fourier-transform optical spectroscopy of transient photochemical species. Subsequently, his efforts focused on development of an integrated spectroscopy system with unique capabilities for actinide surface science, applications of in situ Fourier-transform infrared surface characterization of actinide materials and acoustic-resonance spectroscopy of components, as well as resonant ultrasound measurements of elastic constants of plutonium alloys.



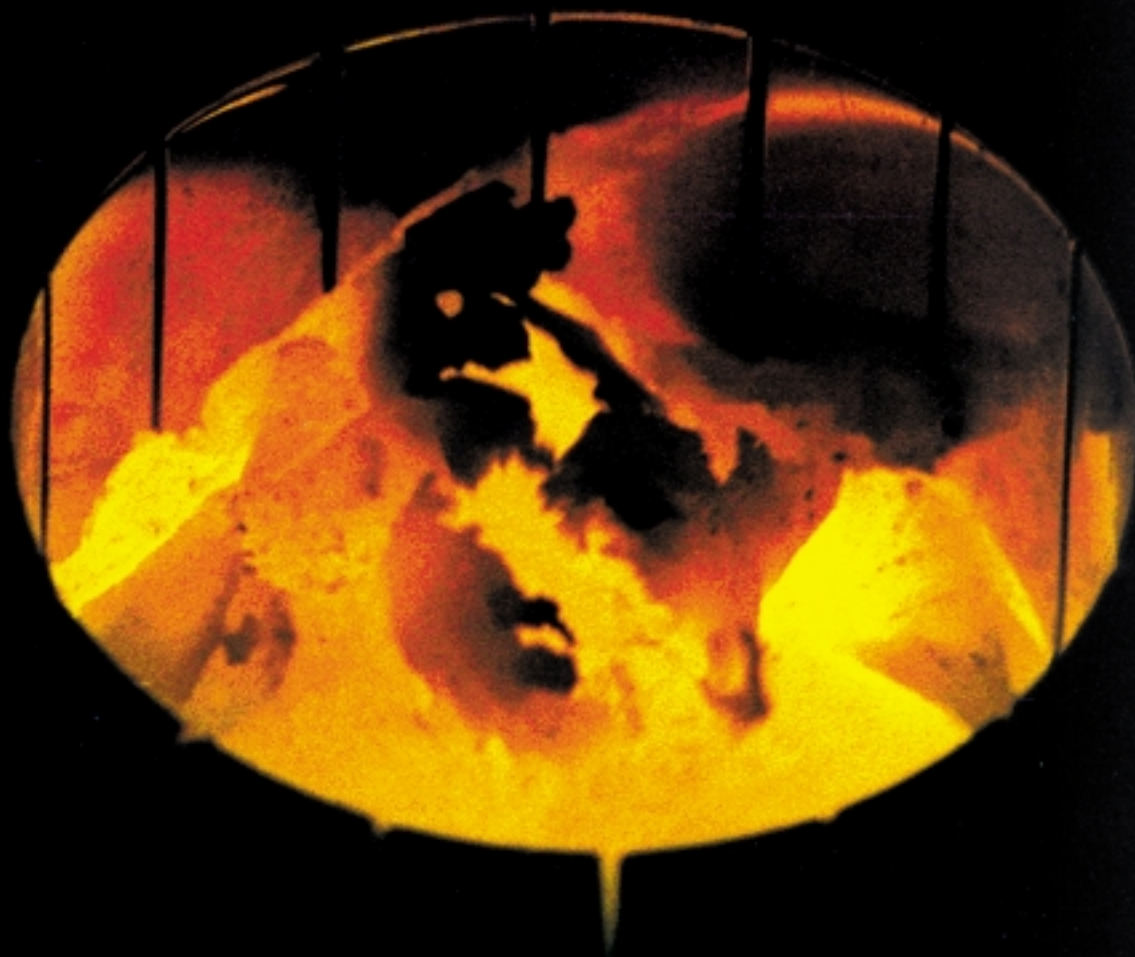
Tim Darling received his undergraduate degree and his Ph.D. from the University of Melbourne, Australia. Tim began his postdoctoral work in 1989 at the Los Alamos National Laboratory and is presently working as staff member on resonant ultrasound spectroscopy and electronic transport. For his work, Tim received a 1993 Distinguished Performance Award, the highest award granted by the Director of Los Alamos. His current interests are the fundamental connections between elastic moduli temperature variations and stability in solid-state systems and the role and sources of internal friction at low temperatures and high frequencies. Current experiments involve phase transformations in cubic systems, particularly on the formation and dynamics of martensitic phases.



Albert Migliori received his B.S. in physics from Carnegie-Mellon University and his Ph.D. in physics from the University of Illinois. He joined the Los Alamos National Laboratory as a Laboratory Director postdoctoral fellow and later became a staff member. He is codiscoverer of acoustic heat engines and a leading expert in the use of resonant ultrasound spectroscopy as a solid-state physics tool. For his work, Albert won R&D 100 awards in 1991 and 1994; a Federal Laboratory Consortium Award for Excellence in Technology Transfer in 1993; and a Los Alamos National Laboratory Distinguished Performance Award in 1994. Albert is a Fellow of the American Physical Society and the Los Alamos National Laboratory.

Preparing Single Crystals of Gallium-Stabilized Plutonium

*Jason C. Lashley, Michael S. Blau, and
Roger L. Moment*



Americium and gaseous impurities bubble from the surface of molten plutonium. The sample remains levitated within the vertical crucible of a vacuum distillation furnace. Such preparations are used to create ultrapure samples from which are grown single crystals of gallium-stabilized δ -phase plutonium.

Scientists need large single crystals of plutonium to determine many of the fundamental properties of this metal, such as its electronic structure and atomic vibrational modes. In general, the electronic structure of a crystalline solid governs bonding, magnetism, and elasticity. The vibrational properties become increasingly important as the temperature of the material increases.

Because the electronic structure and vibrational modes of metals reflect the underlying symmetries of the lattice, which is never spherically symmetric, those properties always have a directional dependence. But measurements on polycrystalline samples cannot reveal that directionality because probing a polycrystal is akin to averaging over all crystal directions. Only a single crystal, as an extended, regular array of unit cells, can yield directional information. But single crystals of plutonium do not currently exist.

A program was recently initiated at Los Alamos to prepare plutonium and then grow large single crystals of gallium-stabilized δ -phase plutonium. Our samples must be prepared from metal of the highest purity, because the electronic structure and vibrational modes of plutonium are highly affected by the presence of trace elemental impurities and alloy compositions. The required crystal size depends on the measurement techniques. For example, photoemission spectroscopy measurements of the density of electronic states require crystals on the order of 1 cubic millimeter. Resonant ultrasound spectroscopy measurements of the elastic constants need crystals a few cubic millimeters in size. Finally, inelastic-neutron-scattering experiments, which probe the phonon spectra, require single crystals of plutonium-242 that are

as large as 1 cubic centimeter. (Plutonium-242 has a smaller neutron-absorption cross section than plutonium-239 and is the favored isotope for the scattering measurements.)

In this article, we review solidification and solid-state methods for growing plutonium crystals and explain why it is difficult to grow single crystals of the required size. We then

to each other in an orderly fashion because an equilibrium position is reached between attractive and repulsive forces.

It is very difficult, however, to grow single crystals of pure plutonium by simply letting the melt solidify. The pure metal passes through six allotropic phases (ϵ , δ' , δ , γ , β , and α) as it solidifies from the melt and cools to room temperature. In each new phase, the plutonium atoms shift positions to form a new crystalline structure with a different density. Any large crystal grains that develop early in the cooling process become disrupted with each subsequent phase transformation. The result is invariably a polycrystalline solid. (See Figure 1.)

In the 1960s, scientists at Argonne National Laboratory grew single crystals of α -phase plutonium by allowing the molten material to cool under 55 kilobar of pressure. Under those conditions, plutonium solidifies directly into the β -phase and transforms to the room-temperature stable α -phase at 420°C, rather than at 112°C, as it does at ambient pressure. (The higher temperature means that the atoms are relatively mobile as they begin to form α -phase grains.)

Furthermore, the metal does not change volume in going from the β - to the α -phase at 55 kilobar. The combination of those advantageous properties allowed researchers to grow large grains, which were then cut from the surrounding matrix and polished into single crystals. Al Arko, who is now at Los Alamos, measured the resistivity and magnetic susceptibility of some of those α -phase single crystals.

Also during the 1960s, Roger Moment of Rocky Flats tried to grow large grains of gallium-stabilized δ -phase plutonium. At gallium concentrations between 1 and 2 weight percent (wt %), the plutonium-gallium alloy exhibits

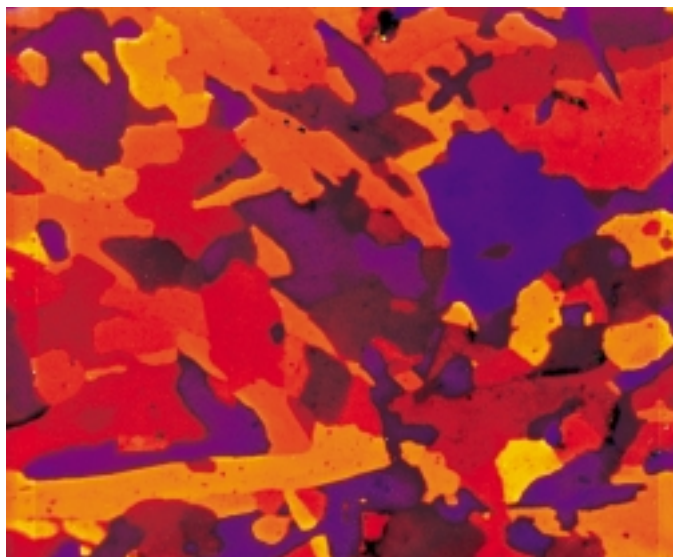


Figure 1. Polycrystalline Plutonium
Gallium-stabilized, δ -phase plutonium invariably solidifies into a multigrain structure. This sample of δ -plutonium (1 wt % Ga) was photographed under polarized light in order to make that structure visible. Each grain reflects light differently because the atoms in each grain are aligned in different directions. Efforts are under way to grow grains of plutonium with linear dimensions on the order of 1–10 mm.
(Photo by Ramiro Pereyra)

discuss our purification techniques and crystal-growth program. We have already grown a plutonium grain that was large enough to be measured by photoemission spectroscopy.

Techniques for Growing Plutonium Crystals

Growing Crystals from Molten Plutonium. The easiest way to obtain single crystals of a material is to grow them from the liquid phase (also called the melt). As the molten metal cools and solidifies, the atoms begin bonding

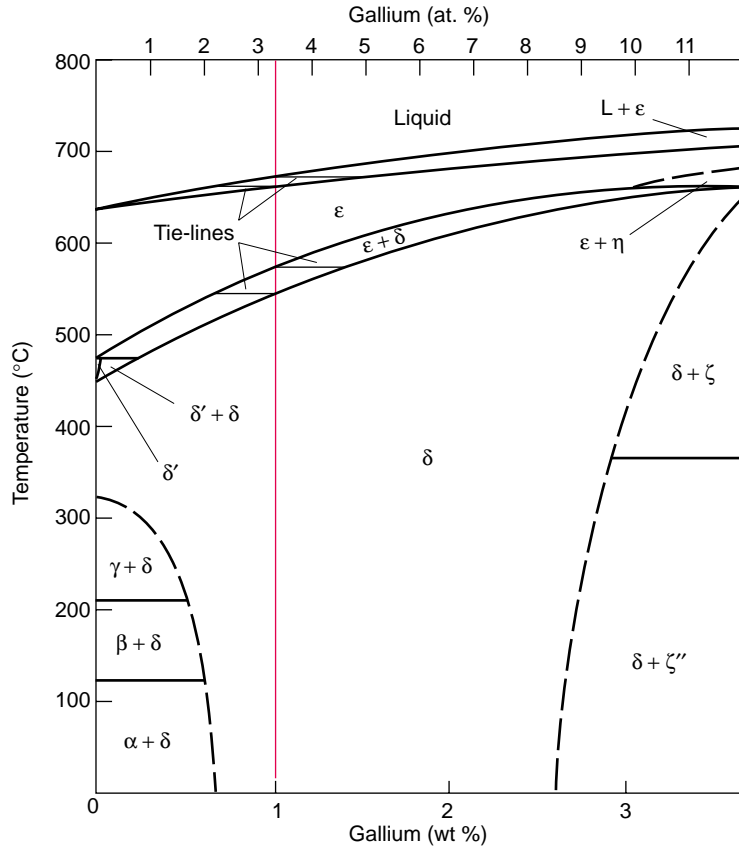


Figure 2. The Low-Gallium Composition of the Plutonium-Gallium Binary Phase Diagram

Pure plutonium has the most allotropes of any element. Following its phase transformations down the leftmost axis, we notice that liquid plutonium (L) solidifies into the ϵ -phase below 640°C and then assumes five more structural phases (δ' , δ , γ , β , and α) as it cools to room temperature. Alloying plutonium with small amounts of gallium (less than about 2.5 wt % gallium) reduces the number of allotropes from six to two. For example, at 1 wt % gallium (red line), the molten alloy cools by passing through a mixed (L + ϵ)-phase, then a pure ϵ -phase, then a mixed (ϵ + δ)-phase before reaching the δ -phase, which is stable down to room temperature. The first bits of ϵ -phase material to solidify from the (L + ϵ)-phase have a higher gallium concentration than the melt. We determine the exact composition by following the first horizontal tie-line in the (L+ ϵ)-region to the right. Newly solidifying material has less gallium, and thus there are composition gradients within each grain (coring). Coring reoccurs when the alloy passes through the (ϵ + δ)-phase.

only two allotropes (ϵ and δ), and the δ -phase forms at approximately 500°C. This phase is then thermodynamically stable down to room temperature.

Moment produced several large grains by the Bridgeman technique: the melt froze and slowly transformed to the δ -phase as it passed through a decreasing temperature gradient. (Moment recalls his work in the accompanying article beginning on page 233.) As revealed by x-ray pictures taken with a

back-reflection Laue camera, however, all those large grains contained substructure. They were therefore unsuitable for high-quality measurements of physical properties.

One reason for the low grain quality might have been the internal conditions resulting from coring. As discussed in Figure 2, when the alloy freezes from the melt or passes through a mixed phase, such as liquid and ϵ , (L + ϵ), the grains that form have a higher concen-

tration of gallium at the center. The uneven distribution of alloying material introduces strain into the crystal lattice that could detrimentally affect grain growth.

Primarily to avoid coring and other potential problems associated with the ϵ - to δ -phase transition, Moment abandoned the Bridgeman technique and focused his attention on growing plutonium grains by strain-anneal methods. Those methods ultimately proved to be successful, and his measurements of the elastic constant are still the only ones made on a single crystal of δ -phase plutonium. Our current program has been guided by Moment's experiences.

Growing Plutonium Crystals in the Solid State. Strain-anneal techniques allow crystals to grow entirely within the solid state. During the strain-anneal process, the metal is plastically deformed so that dislocations form within it. The dislocations are disruptions to the minimum-energy state of the perfect lattice and are consequently a form of stored energy. At small plastic strain values (less than 10 percent), approximately 1 to 4 percent of the strain energy is stored within the lattice from dislocations, and the rest is dissipated as heat.

The stored energy is released when the metal is heated during the first step in the annealing process. The energy drives the formation of new grains in a process called recrystallization. Keeping the metal at constant high temperatures (the next step in the annealing process) then allows the recrystallized grains to grow larger through the migration of grain boundaries.

A grain boundary has a surface energy. Smaller grains have proportionally more surface energy than larger ones, so it is energetically favorable to merge smaller grains into larger ones. The boundary migrates as the atoms from one grain shift and become integrated into another. One grain is "consumed" while the other grows. In principle, one grain can dominate, growing steadily larger until the system reaches equilib-

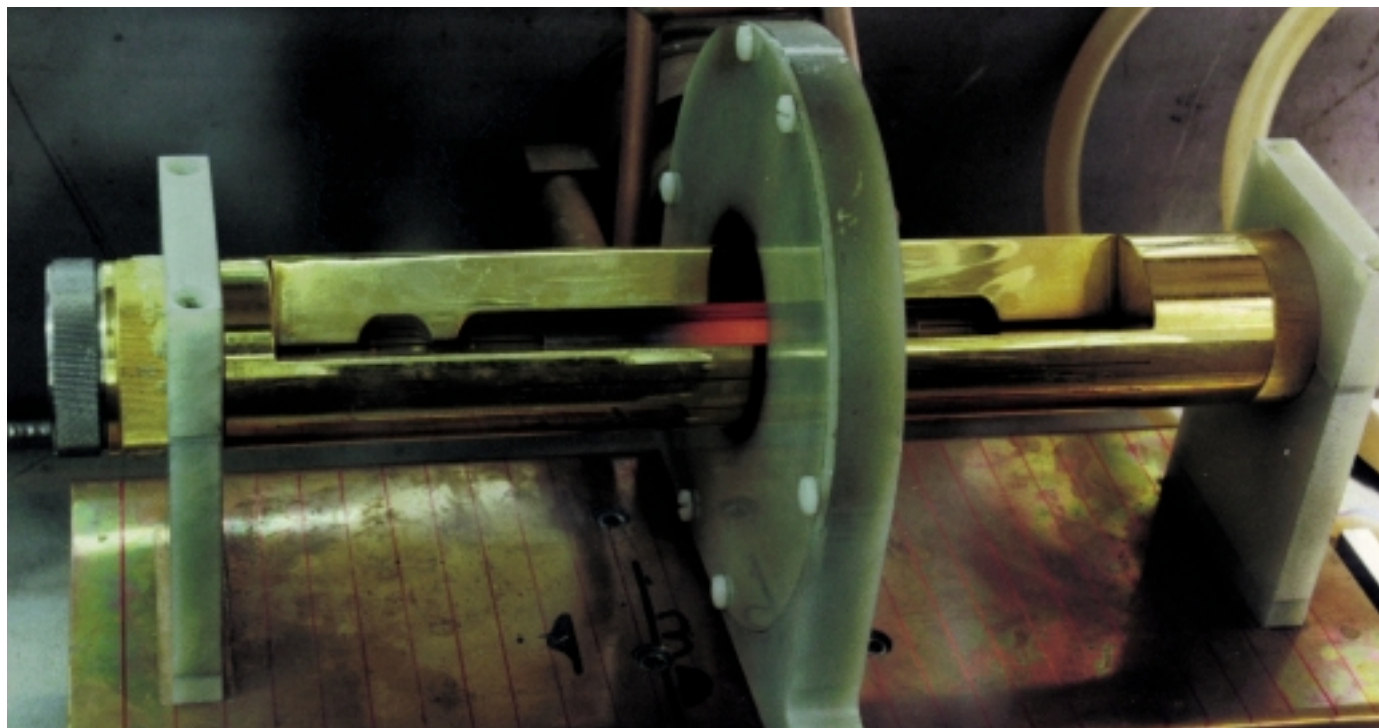
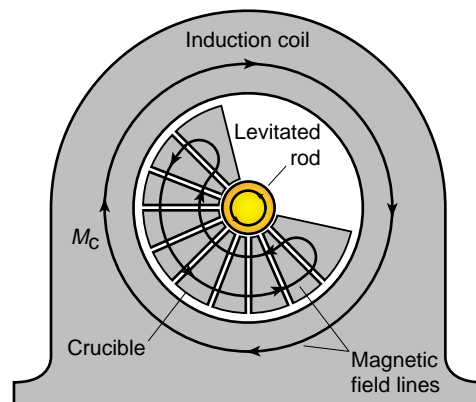


Figure 3. Levitation Zone-Refining Furnace

An electromagnetic-levitation furnace consists of a crucible that holds the sample and an induction coil. As shown in the schematic on the right, radio-frequency power running through the coil induces currents to flow in the crucible. The current generates a magnetic field M_c that induces eddy currents to flow in the sample, which heats up and melts. But the eddy currents generate a secondary magnetic field in the direction opposite to M_c . Magnetic repulsion causes a zone of liquefied metal to levitate a small distance from the crucible walls. The photo shows a stainless steel rod loaded in the horizontal crucible. The glowing region under the induction coil is the levitated molten zone, and moving the crucible causes the zone to sweep through the rod. Elements that lower the melting point of the material travel with the zone, while those that raise the melting point diffuse into the solid. In either case, impurities are swept to the end of the rod, which are then cut off. For our program, we purify rods of α -phase plutonium, rather than δ -phase, to avoid complications stemming from the addition of gallium.



rium. Grain-boundary migration is enhanced at high temperature because the heat increases the mobility of the atoms. As mentioned earlier, specimens containing 1 wt % gallium can be annealed at temperatures as high as 500°C and still remain in the δ -phase (refer to Figure 2.)

The strain-anneal technique is clearly advantageous for alloy systems and multiphase materials such as plutonium. Because the temperature is kept within the room-temperature stable phase, there are no phase transformations and no coring effects. Once a

large grain forms, its structure can be preserved down to room temperature.

Los Alamos Program for Growing Plutonium Crystals

Purification. Because impurities hamper the mobility of grain boundaries, any crystal-growth methodology hinges on starting with plutonium metal that is free of elemental impurities. Consequently, the first step in our program is to purify the plutonium starting material.

Purification must be done on molten

plutonium, but the strong affinity that the liquid exhibits for almost all elements severely complicates the process. The elements that make up the container holding the liquid inevitably contaminate the melt.

We have solved this problem by using electromagnetic levitation furnaces. These devices, consisting of an induction coil and a crucible, are designed to levitate molten material. Any interactions between the crucible and the liquid metal are therefore eliminated. A levitation furnace is described in more detail in Figure 3. No other



Figure 4. Vacuum Distillation of Plutonium Metal

In the photo on the left, molten plutonium metal held suspended in the middle of a vertically-oriented crucible by an electromagnetic field. Americium and gas impurities boil off. Enough gallium has been added to stabilize the δ -phase plutonium upon solidification. The photo on the right shows a half sphere of gallium-stabilized δ -phase plutonium that was produced by vacuum distillation in a levitation furnace. The lines on the surface reveal where the plutonium solidified to the shape of the mold. Samples for growing crystals were fabricated from this specimen.

laboratory in the world uses such advanced equipment to purify plutonium.

Our purification technique starts with plutonium metal that has already been purified twice by electrorefining and has then been cast into a rod. We clean the rod's surface to get rid of any oxides and hydrides that may have formed. At this point, the metal typically contains impurity levels in

the range of 500 to 600 parts per million (ppm). Iron, uranium, magnesium, calcium, nickel, aluminum, potassium, and silicon are among the impurities.

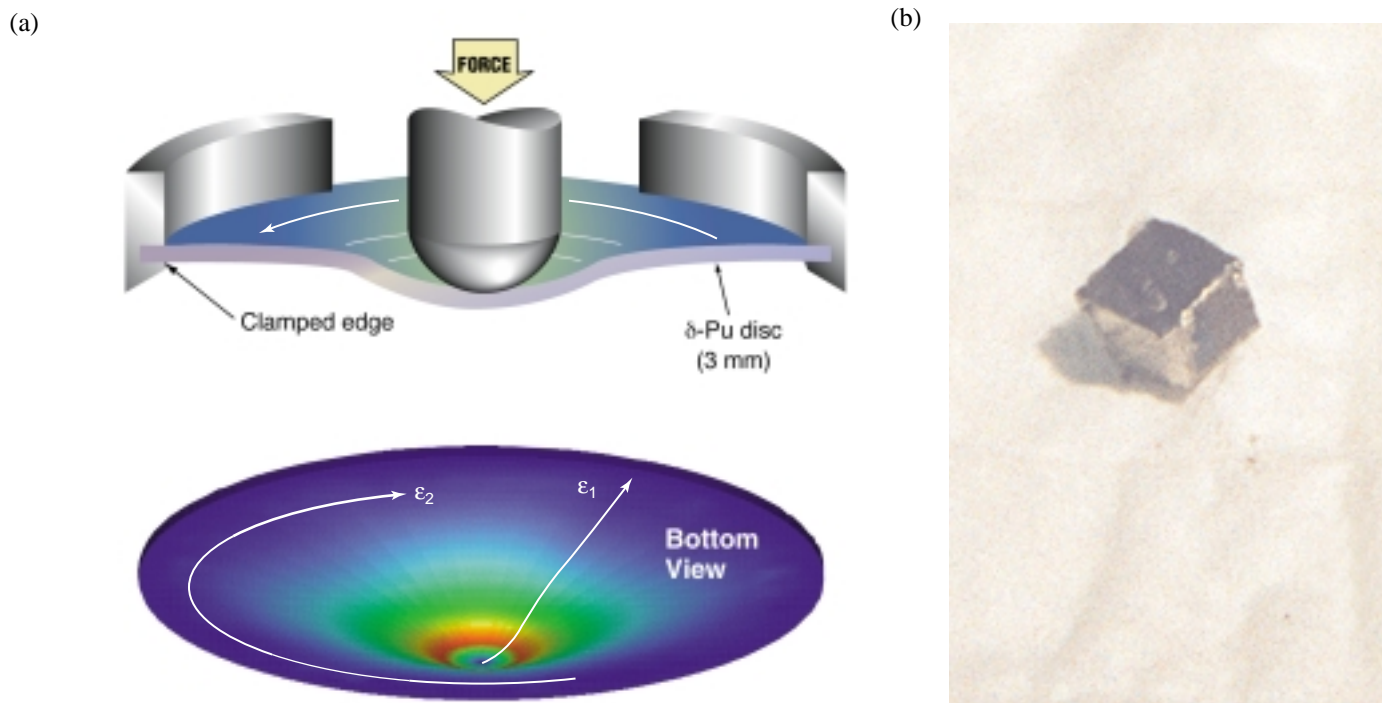
The rod is placed in the horizontal crucible of the levitation furnace, as shown in Figure 3. The induction coil of this furnace is the large disk in the middle of the photo. Only the small section of the rod directly under the induction coil is liquefied and levitated. When we move the crucible, the molten zone passes slowly through the rod in one direction. Impurities that lower the melting point of the metal remain in the liquid zone, whereas those that raise it are driven into the solid material. Because impurities either move with the zone or are pushed in front of it, both kinds are eventually swept to the end of the rod. Repeating this procedure several times leaves the central portion of the rod highly purified.

We use a mass spectrometer with very low detection limits to measure the impurity levels of 78 trace elements. Results to date indicate that zone refining in a levitation furnace reduces impurities from 523 to 174 ppm; uranium accounts for about

70 percent of that remainder.¹ Also, we have not detected any crucible material in our sample, which indicates a complete lack of plutonium-crucible interactions.

The purified rod then undergoes vacuum distillation in a vertical levitation furnace, a process that purges the rod of americium and interstitial gas impurities. The zone-refined plutonium is placed under reduced pressure (10^{-7} torr) in a cylindrical, vertical crucible. An induced high current circulates through the entire metal rod, which melts and levitates. Because americium and other impurities have a high vapor pressure, they distill away. We also add enough gallium during this stage to produce the plutonium-gallium alloy. Sudden removal of furnace power lets the molten alloy drop into a chilled copper crucible, where it quickly solidifies. (See Figure 4.) Because the solidification is so rapid, coring is

¹Previously, researchers could only report on the impurity levels of 20 to 40 trace elements because their measurement techniques had higher detection limits. Although our material is likely the purest that has ever been produced, our total impurity levels are often higher than the levels reported in the early literature.



minimized, and we obtain an as-cast density of 15.938 grams per cubic centimeter (g/cm^3), which is only slightly higher than the theoretical δ -phase density of 15.810 g/cm^3 . (A small amount of coring creates some high-density α -phase plutonium that increases the overall density.)

Recent results obtained from vacuum distillation show that the americium could be removed almost entirely. Several weeks after distillation, the measured impurity level was 1.5 ± 0.3 ppm. During that time, however, some of the plutonium-241 that was present in the starting material decayed to americium-241. What we detected was simply the newly created americium.

The ability to make plutonium samples that are essentially free of americium is critically important to the Laboratory. Such a sample is needed for an experiment to measure the $(n,2n)$ cross section of plutonium-239. The cross section can be used to infer the neutron spectrum in an exploding weapon and is therefore a central concern of the Science-Based Stockpile Stewardship program.

Using ultrapurified material, we set up a series of experiments to grow

large grains of δ -phase plutonium. Our starting material was a set of 3-milli-meter-thick polycrystalline disks (1 wt % gallium) that had been cut from a homogenized ingot (average grain size of 30 micrometers). After rigidly fixing each disk's circumference into a die, we deformed the disks over a hemispherical punch at room temperature, as in Figure 5(a).

This setup made it easy to strain the material uniformly in both the radial and circumferential directions (balanced-biaxial strain). The total, true strain on the surface is described by the three diagonal components of the true strain tensor: the radial component (ϵ_1), a circumferential component (ϵ_2), and a through-thickness component (ϵ_3). Only two of those components are independent. The strain peaks at the pole and goes to zero at the periphery. Because the volume of the material is conserved, the disk also becomes thinner. At small plastic deformations, a uniform through-thickness compressive strain is also achieved that varies with the radius.

With the strain-anneal technique, the largest grains are produced if the metal is strained a "critical" amount and then annealed. (See Figure 2 on page 235 in

Figure 5. Biaxial Strain in a Plutonium Disk

(a) A 3-mm-thick disk of gallium-stabilized δ -phase plutonium is stretched in two dimensions with a hemispherical punch. The magnitude of the strain decreases in the radial direction, from the pole to the edge. A strain gradient, described by ϵ_1 is therefore generated and is shown here by different bands of color. A second strain gradient is produced as the disk becomes thinner. (b) After having been annealed isothermally at 480°C for 90 hours, the disk contained several newly grown, large (1 mm) plutonium grains. The cube shown above contains one of those grains. Some of its electronic-structure properties were later measured by photo-emission spectroscopy.

the article "A Single-Crystal Saga.") If strained too little, the metal does not acquire enough dislocations (that is, stored energy) to promote recrystallization, but if strained too much, it acquires so many dislocations that grain refinement occurs. We wanted to achieve this critical strain at the center of the disk so that the grain would then

grow out uniformly in all directions. Unfortunately, the critical strain depends on many factors, including the initial sizes and orientations of the grains and the manner in which the load is applied to the bulk material. That is why the critical strain can be determined only empirically for each type of sample.

After a 90-hour isothermal anneal at 480°C and reduced pressure, grains of 1-2 millimeters in length were produced. The largest grain was located about 6 mm from the center of the disk. We estimated a critical strain of about 3 percent. Analysis of the disc surface at the location of the largest grain yielded components of the strain tensor (corresponding to the critical strain for this material) of $\epsilon_1 = 0.022$ and $\epsilon_2 = 0.018$.

Having some sufficiently large grains available to us, we extracted from the disk a small section containing one such grain—see Figure 5(b). That crystallite was measured by photoemission spectroscopy, as discussed in the article “Photoelectron Spectroscopy of α - and δ -Plutonium” on page 168.

We have also experimented with a second method for growing crystals. Liquid plutonium-gallium alloy is dropped out of the magnetic field of a levitation furnace and is chill-cast in a mold shaped like a long, thin cone. The microstructure of this chill-cast plutonium consists of very fine, small acicular (or needlelike) grains 10×25 micrometers in size.

We anticipate that the conical geometry of this chill-cast sample and the fine grain size will help promote grain growth. Because the tip of the cone is so small, the number of grains competing to grow there is reduced. Hopefully, a single grain will grow at the expense of the others once we begin a strain-anneal process. Because the grain size in the rest of the sample is so small, there is a lot of surface energy available to help drive that grain growth, and the growing “seed” grain could continue to expand into the cone. Ideally, the large volume at

the top of the cone would consist of a single grain from which precisely oriented samples could readily be cut.

The lack of large single crystals is currently the only obstacle that prevents researchers from obtaining high-quality data on the fundamental solid-state properties of δ -phase plutonium. By applying several variations of the strain-anneal technique to δ -phase plutonium, we have enjoyed some success in growing millimeter-sized grains. Our future work is aimed at developing crystal-growing methods with repeatable results. ■

Acknowledgments

The authors thank Michael Stout, David Embury, Manuel Lovato, Ramiro Pereyra, Jim Smith, Larry Thulen, Jason Cooley, and Karl Staudhammer of the Materials Science Division. Special thanks to Floyd Rodriguez, Fred Hampel, and Kenny Vigil for laboratory assistance, and to Mick Greenback and Larry Vaughn for photography and induction support, respectively.

Further Reading

- Goss, A. J. 1963. In *The Art and Science of Growing Crystals*. J. L. Gilman, ed. New York: John Wiley and Sons.
- Hecker S. S. 1976. *Scientific American*, November issue.
- Hecker, S. S. 1976. Los Alamos National Laboratory document LA-UR-76-1413.
- Lander G. H., E. S. Fisher, and S. D. Bader. 1994. *Adv. Phys.* **43**: 1.
- Lashley, J. C., M. S. Blau, K. P. Staudhammer, and R. A. Pereyra. 1999. *J. Nucl. Mater.* **274**: 315.
- Liptai, R. G., L. T. Lloyd, and R. J. Friddle. 1967. *J. Phys. Chem. Solids* **1**: 573.
- Wallace, D. C. 1972. *Thermodynamics of Crystals*. New York: Dover Publications, Inc.

Jason Lashley received a B. S. in Chemistry in 1994 from the College of the Ozarks in Point Lookout, Missouri. He joined Los Alamos National Laboratory full time in January 1996 and is now a staff member in the Structure/Properties Relations Group of the Materials Science Division. His research interests are the total synthesis and thermodynamic properties of exotic materials. He will graduate in August 2000 with a Ph.D. in Physical Chemistry.



Roger Moment received his B. S. in Physics in 1959 from Reed College, and his Ph.D. in Metallurgy from Yale University in 1964.



He worked at Rocky Flats from 1963 to 1995, first in the Plutonium Metallurgy group and subsequently in Non-Destructive Testing. He worked on the Small Wind Energy Conversion Systems program

and went on to managed the Process Development Program. Later in his long career, he was involved in Complex 21 manufacturing planning and the disposition of radioactive wastes and residues. His hobbies include skiing, music, and restoring old sports cars.

Michael Blau received a B.S. in Chemical Engineering in 1983 and a B. S. in Physical Metallurgy in 1984 from Washington State University. He received his Ph.D. in Metallurgical Engineering from University of Idaho in 1998. He worked at the Los Alamos National Laboratory from 1986 to 1999 as a Staff Member in the Nuclear



Material Technology Division. Michael was a supervisor for the Special Recovery Line and Plutonium Foundry, and a principal investigator of the Plutonium Crystal and the Declass Projects. He was also the principal researcher on the Plutonium Foundry levitation melting systems. He is currently a metallurgist in the Nuclear Materials Technology Program at the Lawrence Livermore National Laboratory (LLNL), doing research and development on components of nuclear weapons at the Plutonium Facility.

A Single-Crystal Saga

Roger L. Moment

From 1963 to about 1976, Roger Moment of Rocky Flats attempted to grow single crystals of gallium-stabilized, δ -phase plutonium that were suitable for measurements. He finally succeeded and was able to make what are still the only measurements of the elastic constants of a single crystal of δ -phase plutonium. The staff of Los Alamos Science are pleased to present his story.

The early 1960s were truly a “golden era” in metallurgy within the weapons complex. While many research programs were being conducted at Los Alamos Scientific Laboratory and Lawrence Livermore Scientific Laboratory, limited research efforts were also taking place at other “production” sites such as Rocky Flats. Weapons budgets during those years were generous, and Rocky Flats staffed its metallurgy and chemistry groups with many new members holding doctorate degrees. Although their primary responsibility was to support the main objective of pit production, the staff members were also encouraged to spend a portion of their time pursuing any scientific research they thought would be of value. I had spent my graduate years growing and measuring properties of single crystals, and when I showed up at Rocky Flats in September

1963, it was only natural that I would try and see whether similar work might be done with plutonium.

During that same period, Roland Fisher, who was also at Rocky Flats, was attempting to grow a single crystal of α -phase plutonium by allowing the liquid metal to solidify while being kept under high pressure. Not wanting to duplicate effort, I turned my attention to growing single crystals of the gallium-stabilized δ -phase.

Conducting plutonium research experiments was quite easy in those days, compared with now. We set up our furnaces in a small glove box and did the encapsulation in an open-faced hood. My experimental operator¹, Jim Parker, was skilled at working with small items, using the standard 0.76-millimeter-thick, lead-lined gloves, and he handled all the delicate operations without incident. We were most con-

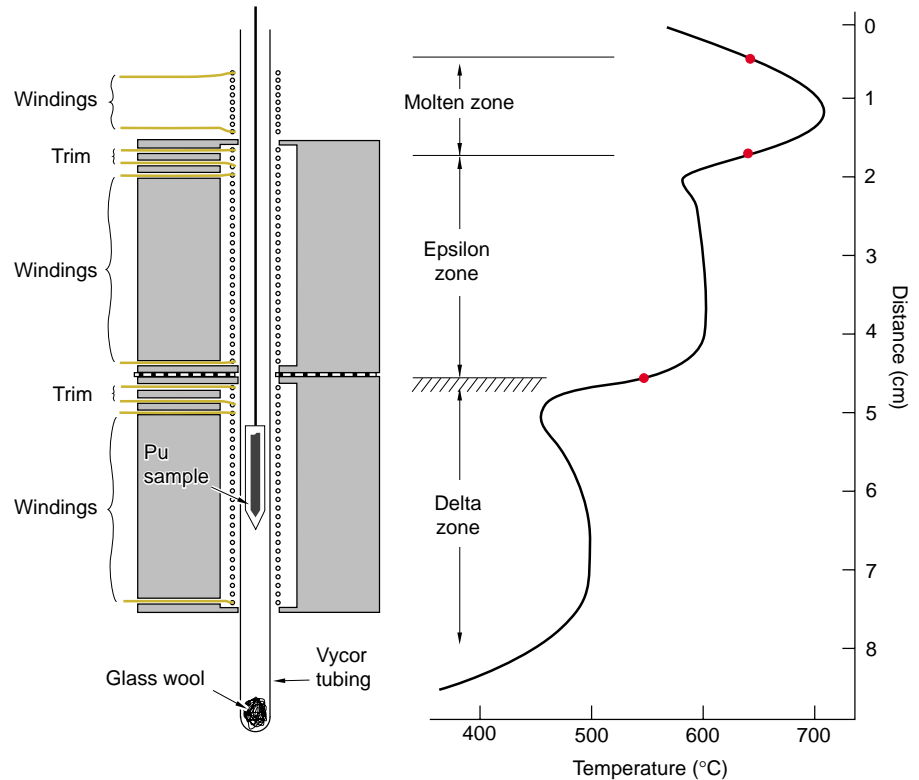
cerned about potential breakage of the sealed, evacuated glass tubes that held the plutonium and designed our equipment with containment layers—just in case. When the furnaces were finally dismantled after approximately 10 years of use, they were still uncontaminated.

My experience had been in growing crystals from the melt, and I thought that approach would be worth an initial try. If a large ϵ -phase crystal could be formed upon solidification, then slow, directional transformation into δ -phase might still result in retention of large grains. Although I had expected some difficulties with this approach, I did not fully appreciate all the problems created by the solid-state

¹Much of the workforce at Rocky Flats was unionized. The Experimental Operator classification was used for support personnel who worked in R&D and performed most of the hands-on operations with plutonium and our test equipment.

Figure 1. Schematic of Multistage Furnace

We used multistage furnaces to melt and then recrystallize gallium-stabilized, δ -phase plutonium. The furnaces were constructed from stainless steel cylindrical blocks. Nichrome wire, used for heating, was wrapped around a Vycor™ tube running through the middle of the blocks. Trim windings created a smooth yet steep temperature gradient through the phase-transition zones, as seen in the temperature profile on the right. The plutonium sample was enclosed in a pointed Vycor™ capsule and slowly lowered through the tube. The plutonium would melt, solidify in the ϵ -phase, and then transform to the δ -phase. The glass wool pad was inserted to prevent the inner capsule from breaking should its suspending wire break.



transformation from ϵ - to δ -phase.

A fairly simple, multistage furnace was constructed, which consisted of a series of ovens, each oven cooler than the one preceding it. Gallium-stabilized δ -phase plutonium (1 wt % gallium) was placed in a Vycor™ capsule that was drawn to a fine point at one end. The capsule was then lowered point first through the furnace by a primitive clock motor system, as seen in Figure 1. The drop rate was usually 0.76 to 3.3 millimeters per hour.

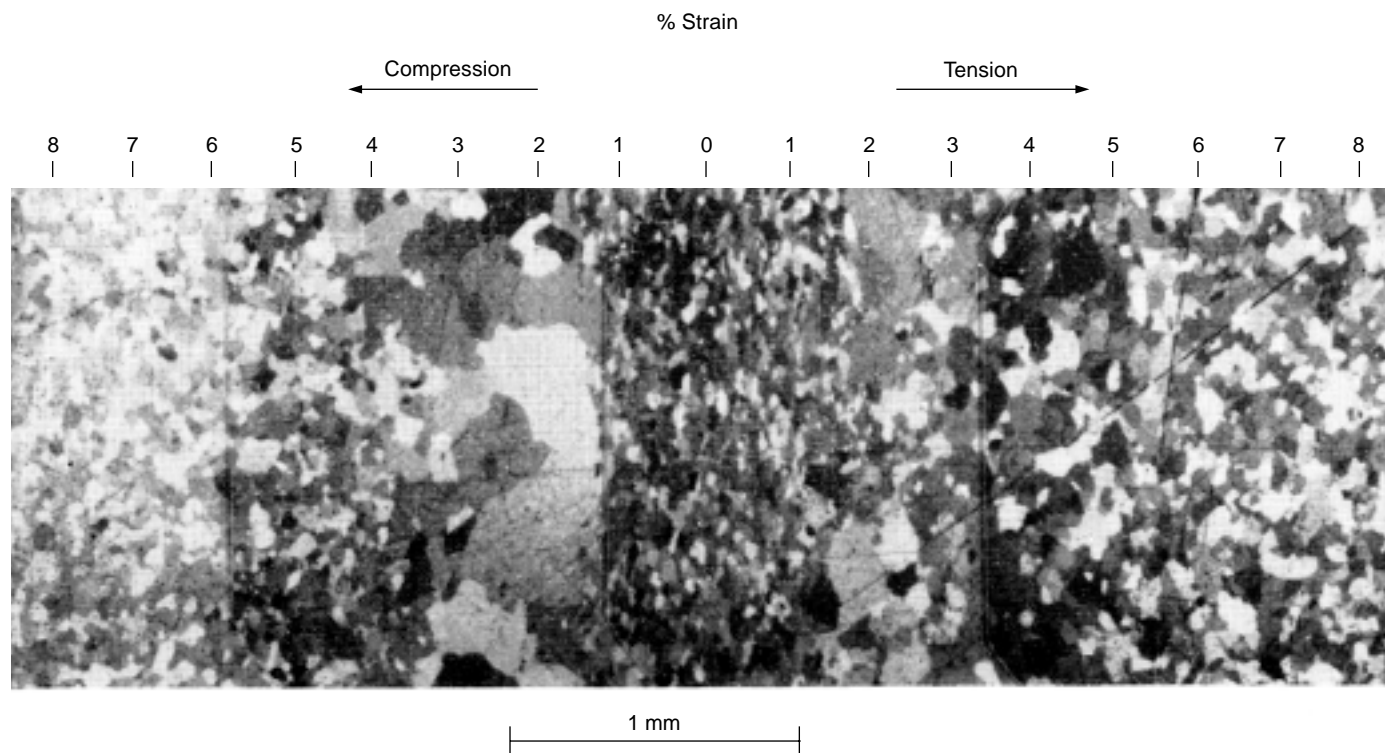
The metal liquefied in the top furnace and transformed into ϵ -phase as it entered the middle furnace. Solidification first occurred in the capsule's point, but only a few grains could grow within that small volume. We hoped that one of those grains would grow larger at the expense of others as the rest of the melt solidified and transformed into ϵ -phase. As the capsule entered the lower oven, we hoped that the ϵ -phase grain would smoothly transform into one or a few large δ -phase grains.

We tried this solidification tech-

nique for years and grew many large grains ranging from 3–4 millimeters in their largest dimension, but in the end, we could not use those grains to make any measurements. Back-reflection-Laue x-ray diffraction, which gives detailed information about the crystallographic quality of grains, showed that most of the large grains were polygonized; that is, they were composed of several subgrains that were slightly misaligned to each other. As such, the grains were not suitable for high-quality physical-property measurements. Furthermore, a 4-millimeter-long grain imbedded in a plutonium rod was simply not usable. The measurements required the grain to be isolated, but typically one-third to one-half of the sample volume was polished away during metallography (that is, the polishing and subsequent etching of a metal surface that helps to visualize the grain structure). By the time we extracted the grain, too little of it was left, and using it in physical-property measurements became almost impossible.

We were never able to determine why the solidification technique was unsuccessful. One reason might have been the internal conditions resulting from coring, or alloy segregation within a grain. When an alloy freezes from the melt, the composition of the solid that forms varies, depending on how the alloying element partitions itself between the liquid and solid states. In the case of the plutonium-gallium alloy, the first bit of ϵ -phase grains to solidify from a nominally 1.0 wt % plutonium-gallium alloy have a composition of about 1.5 percent by weight gallium. As the temperature drops, new material accretes onto the grain, but the percentage of gallium in the next material to solidify is less.

Coring due to the liquid to ϵ -phase transformation was probably negligible, since the diffusion rate for gallium in the ϵ -phase is very high and there would have been ample time during that transition for homogenization to occur throughout each grain. But similar coring takes place during the ϵ - to δ -phase transformation, and the



diffusion rate for gallium in the δ -phase is substantially slower. Even though I did not know what effect all this would have on grain growth, I anticipated there might be some problems. Additionally, the crystallographic substructure in those large grains that had been grown may well have been a consequence of both coring and the solid-state transformation. I therefore wanted to try crystal-growing techniques that would avoid these complications.

A method that takes place entirely within the room-temperature phase is strain anneal. A minimum amount of strain is introduced into a specimen, just enough to cause new crystals to form and then grow when the specimen is heated to an elevated temperature. This process relieves internal stresses through a number of mechanisms and lowers the total-energy state through grain-boundary migration.

If the number of growing grains can be kept to a minimum, they will consume the surrounding matrix and produce a material composed of only a

few large grains. At the “critical” strain, relatively few grains become “active,” and those that do are able to grow into the surrounding matrix with minimal competition from others. During this grain growth, a structure of high crystallographic perfection is formed, and some grains can become large, their dimensions being often limited only by the size of the specimen. To succeed in obtaining these large grains, however, one needs to anneal at fairly high temperatures. In the case of plutonium 1.0 wt % gallium, we could heat specimens to 500°C and still be well within the alloy’s room-temperature stable δ -phase.

I first needed to determine the critical strain that would be required to initiate limited recrystallization and grain growth. I did this by bending a small plutonium strip around a curved mandrel, thereby introducing strains that ranged from compressive at the inner diameter, through zero, to tensile at the outer diameter (see Figure 2). A high-temperature anneal caused recrystallization to occur in high-strain regions

Figure 2. Critical Strain
Bending a plutonium (1 wt % Ga) alloy strip around a mandrel created a range of strains, both tensile and compressive, about a central neutral axis. Annealing the strip at 500°C for three days allowed those grains in the region of critical strain to grow the most. As seen in this photomicrograph, the critical strain appears to be around 2–3 percent.

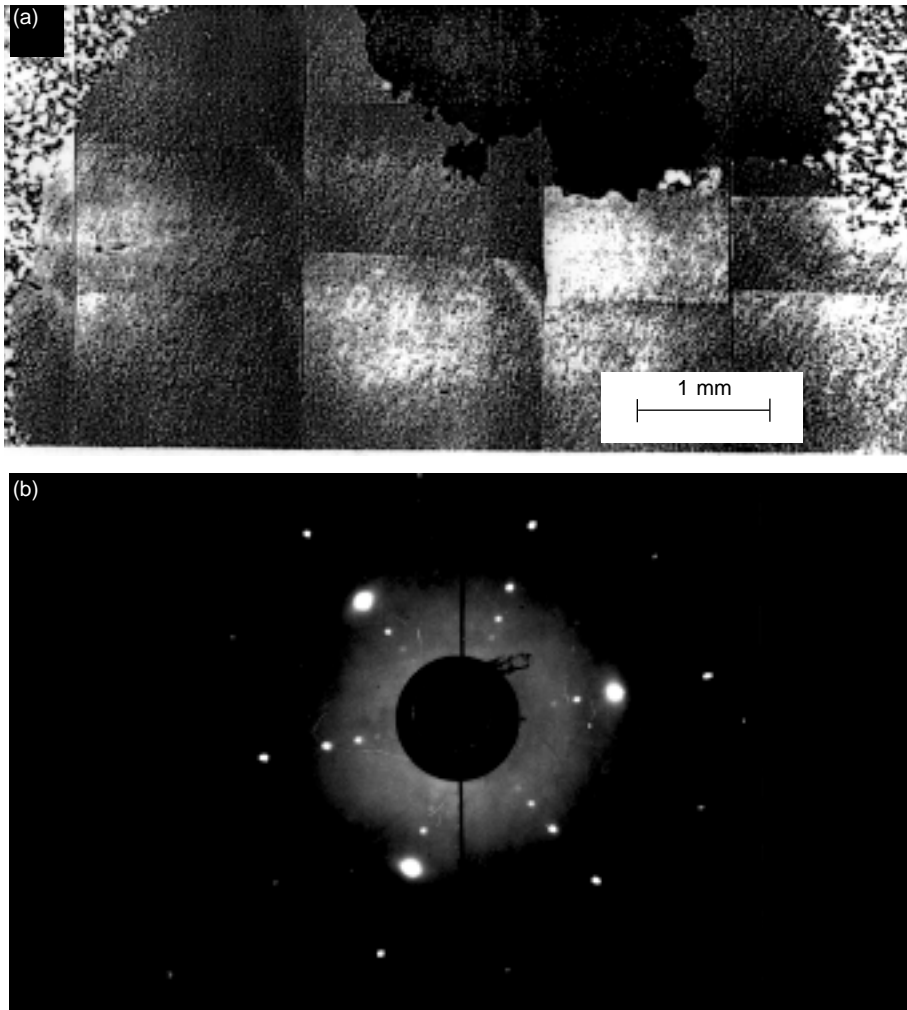


Figure 3. Single Crystals of Plutonium

(a) The grain shown here, grown by a strain-anneal technique, was more than 7 mm across. It lengthened to nearly 9 mm after a second anneal. Unfortunately, much of it was polished away in the course of performing metallography. The remaining grain had no more than 2 mm in depth and was not suitable for elasticity measurements. (b) Many of the crystals grown by strain anneal displayed a high degree of perfection, as indicated by sharp points in the back reflection Laue x-ray films. The crystal used for this Laue photograph was oriented normal to a $[111]$ axis.

and extensive grain growth in others. The largest grains that resulted were located in the specimen in which approximately 2 to 3 percent of the strain had occurred.

We therefore took a bar of δ -phase plutonium that was about 5 millimeters squared in cross section—total impurity level less than 150 parts per million (ppm) excluding oxygen²—and strained it about 2 percent in tension. A point was shaped on one end that was then

electropolished to remove any surface contamination. We placed the specimen in a Vycor™ capsule and lowered it slowly into a furnace, where it was annealed for three days at 500°C. One very large grain (7.5 × 3.5 millimeters) was found although it was not located at the sample tip, as had been expected. (See Figure 3.) This grain grew further to a maximum length of 9 millimeters after an additional 7-day anneal. However, its maximum thickness was only 2

millimeters, and it would have been impossible for us to isolate it and still preserve a crystal suitably large for the elasticity experiments we had planned. Back reflection Laue x-ray diffraction showed it to be quite perfect, as one would expect.

This crystal-growth approach was repeated many times, but we could not achieve consistent or repeatable results. Partly out of frustration, we also tried cycling through the solid-state ϵ - to δ -phase transformation. Instead of applying an external stress, we would have plutonium metal transform between those two phases several times. I reasoned that there might be some transformation-induced stress that could initiate grain growth in the δ -phase.

A rod 4.3 millimeters in diameter was pointed at one end and slowly lowered through two ovens with steep temperature gradients, first to transform it into ϵ -phase and then to transform it back into δ -phase. This double transformation cycle was repeated three times, followed by a 5-day anneal at 500°C to encourage grain growth. Metallographically polishing one side of the rod revealed a fine grain structure but also two large grains filling the diameter. One of the grains was 7 millimeters long. A 3-millimeter-thick section of this larger grain was cut from the rod, and its opposite faces were polished flat and parallel. Back reflection Laue x-ray diffraction showed a high degree of crystallographic perfection and the polished surface to be oriented 4° from a $[110]$ direction in a $\{001\}$ plane. These features made the sample extremely suitable for measurements of its elastic properties. The result of that work (see Figure 4) was published in 1976 (Moment and Ledbetter).

Because plutonium is radioactive, any crystal quickly becomes radiation-

²The presence of significant levels of impurities can limit grain growth because precipitates will arrest and pin the movement of grain boundaries as they sweep through the matrix. Our starting material was the purest available at the time; it typically contained about 120 ppm of impurities, excluding oxygen.

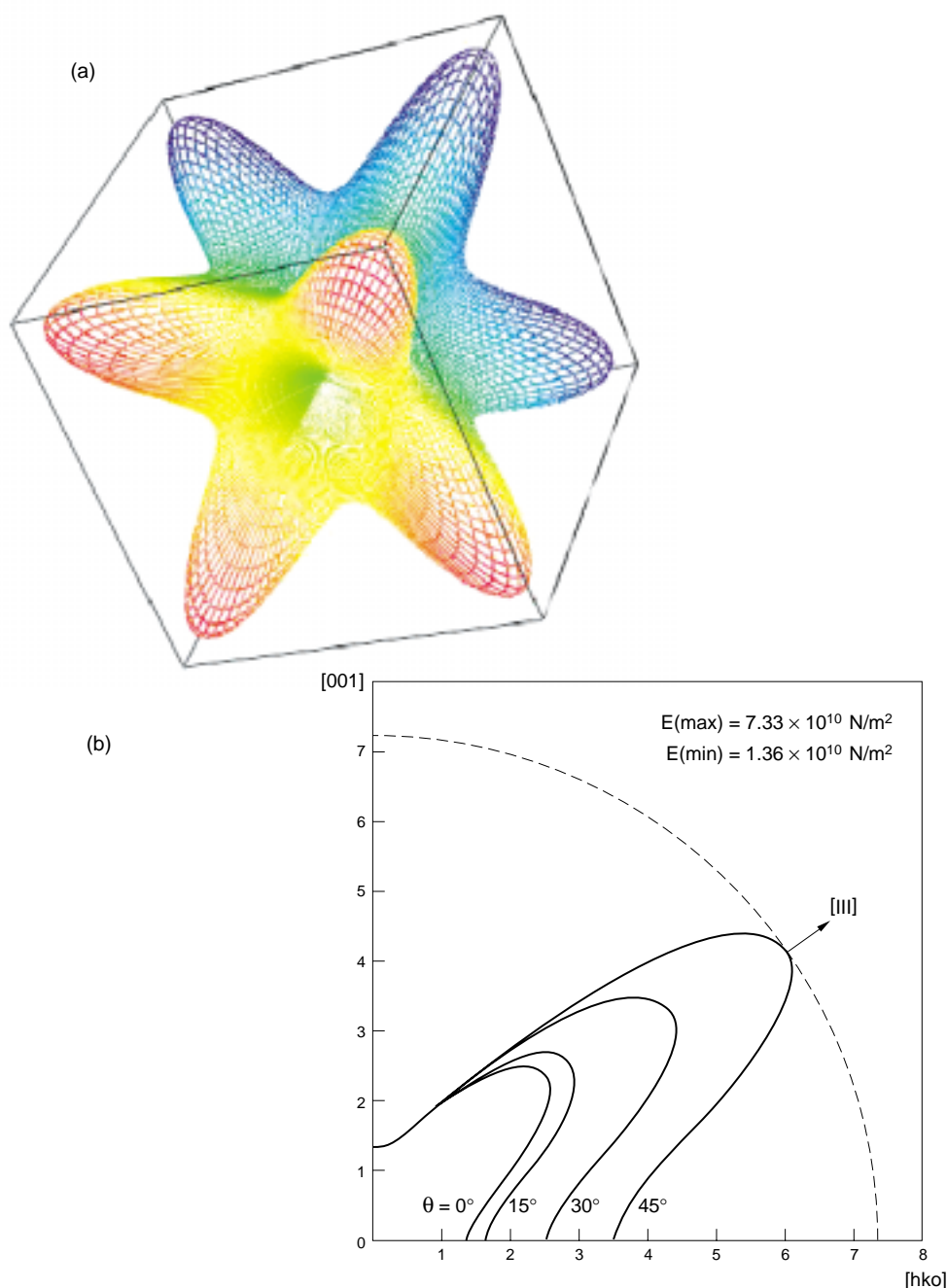


Figure 4. Young's Modulus in δ -Phase Plutonium

Single-crystal elastic constants were measured on the one large grain that was finally grown and isolated. (a) This graphic depicts the variation of Young's modulus (the ratio of applied tension to deformation in a direction parallel to the tension) in δ -phase plutonium as a function of direction in the face-centered-cubic crystal. The response of a single crystal to stress is highly anisotropic. As seen in the graph in (b), the ratio of maximum to minimum values is approximately 5.5, that is, δ -phase plutonium is more than five times stiffer in the [111] than in the [001] direction.

damaged and ceases to be useful for measurements of fundamental parameters. There is a constant need for new samples. But none of our efforts ever resulted in a technique that could be used to reliably provide crystals large enough for measurements of physical properties. The one successful experiment showed that some proper combination of parameters would work, but we did not know what all of these might be. Metal purity was probably an issue, as the best material we had to work with contained about 120 ppm, not including oxygen.

As I look back on this work, I can see many questionable decisions that we made and numerous areas for improvement. Today, we certainly have a much better understanding of the various metallurgical processes taking place. In addition, new technologies present opportunities to exercise greater control over the experimental technique. For example, levitation furnaces are now available for chill-casting high-purity samples with a very fine grain size. Zone-refining techniques are also available for consistently producing metal with an impurity content around or below 100 ppm. All these achievements provide an opportunity to revisit the growing of plutonium alloy grains under conditions that are greatly improved by comparison with those available 20 to 30 years ago. Hopefully, we will find a way to produce single crystals of plutonium in a repeatable fashion. ■

Further Reading

- Moment, R. L., and H. M. Ledbetter. 1976. *Acta Metall.* **24**: 891.
- Moment, R. L. 1968. *J. Cryst. Growth* **2**: 15.
- Moment, R. L. 1966. *J. Nucl. Mater.* **20**: 341.

Aging of Plutonium and Its Alloys

Siegfried S. Hecker and Joseph C. Martz

Like other reactive materials, plutonium ages with time. In moist air, it “rusts” much more profusely than iron, and when exposed to other atmospheric environments, it will react to form several surface-corrosion products. In other words, plutonium ages from the outside in. What makes plutonium really special, however, is that it also ages from the inside out. As a result of its radioactive nature, it relentlessly undergoes self-irradiation damage throughout its volume. Consequently, nature’s most unusual element becomes even more complex as it ages.

In the past, we were resigned to keeping plutonium from self-destructing—at least for two or three decades. Today, we are intensely interested in extending its storage life for many more decades, preferably as much as a century. The three articles that follow this introduction highlight the challenges we face in understanding aging phenomena in plutonium with the hope of achieving that goal.

In “A Tale of Two Diagrams” (page 244) Hecker and Timofeeva shed new light on the question of δ -phase stability. Since there is no clear understanding of the face-centered-cubic (fcc) δ -phase of plutonium, questions continue to persist about the long-term stability of this phase when it is retained to room temperature by the addition of a few atomic percent (at. %) gallium. In “Surface and Corrosion Chemistry of Plutonium” (page 252), Haschke, Allen, and Morales discuss the outside-in problem. Their article highlights the enormous importance of storing plutonium under controlled atmospheres in order to avoid potentially catastrophic events. Finally, Wolfer describes the inside-out problem in “Radiation Effects in Plutonium” (page 274) and develops the case for the most plausible scenario of damage induced by self-irradiation.

After briefly introducing the paper on phase stability and summarizing the paper on surface and corrosion chemistry, we will outline more broadly the potential microstructural effects of self-irradiation damage in plutonium.

Phase Stability

During aging, thermally activated kinetic processes are at work that constantly try to drive the solid toward equilibrium (its lowest energy state). Hence, any nonequilibrium structures are subject to change during aging. One of the greatest concerns about the structural integrity of plutonium and its alloys is phase stability because of the large volume changes that accompany phase changes. Hence, much work has been done over the years to determine the equilibrium phase diagrams of plutonium with most other elements in the periodic table.

However, the plutonium-gallium (Pu-Ga) phase diagram as measured by researchers in the West and in Russia showed a critical difference. The western dia-

gram shows the fcc δ -phase as the equilibrium phase at room temperature, whereas the Russian diagram shows the δ -phase decomposing to $\alpha + \text{Pu}_3\text{Ga}$ below 100°C.

The lack of agreement stemmed from the fact that kinetic processes in materials near room temperature are immeasurably slow, and so it is extremely difficult to achieve true phase equilibrium. In an effort to speed up the low-temperature kinetics, the Russians “preconditioned” their Pu-Ga alloys by transforming some of the δ -plutonium to the α' -phase. They then annealed the samples for up to 10,000 hours. The results of the experiments indicated the decomposition to $\alpha + \text{Pu}_3\text{Ga}$.

Unfortunately, the Russian work was not accepted in the West because the precise nature of the experiments was not presented in sufficient detail. The article “A Tale of Two Diagrams” provides enough detail to give the Russian work proper credibility and to make experiments that were exacting and careful known to a wide audience.

Atmospheric Surface Reactions

Although plutonium is a very reactive metal, its oxidation rate in very dry air is a minuscule 20 picometers per hour (pm/h), or less than 0.2 micrometer per year. The reason is that, much like aluminum, the plutonium metal rapidly forms, and is passivated by, a protective layer of dioxide (PuO_2) over its entire surface. However, corrosion of plutonium metal in moist air occurs at a rate 200 times greater than in dry air at room temperature and is, astonishingly, 100,000 greater at 100°C. The mechanisms of water-catalyzed corrosion of plutonium have only recently been elucidated by Haschke and coworkers. They demonstrated for the first time that hyperstoichiometric plutonium oxide (PuO_{2+x} , where x can be as large as 0.26) forms in the presence of either gaseous or liquid water. Rapid oxidation by adsorbed water produces hydrogen at the gas-solid interface and forms the higher oxide, catalyzing oxidation.

Hydrogen reacts with plutonium metal at unprecedented rates. It gains access to the metal surface by penetrating the ever-present dioxide layer at cracks or at sites where the oxide spalls, making the nucleation of the hydride reaction very heterogeneous. The hydriding rate increases exponentially as nucleation sites grow. Once the entire metal surface is covered with hydride, the reaction occurs very rapidly, and the hydride layer can grow at a rate as much as 20 cm/h linear penetration for hydrogen at atmospheric pressure. This rate is 10^{10} times faster than that of the oxidation reaction in dry air. This incredibly rapid reaction is catalyzed either by the formation of PuH or by a cubic form of the sesquioxide, Pu_2O_3 . The reaction of oxygen with hydride-coated plutonium is also greatly catalyzed by PuH_x , resulting in reaction rates 10^{13} times faster than in dry air.

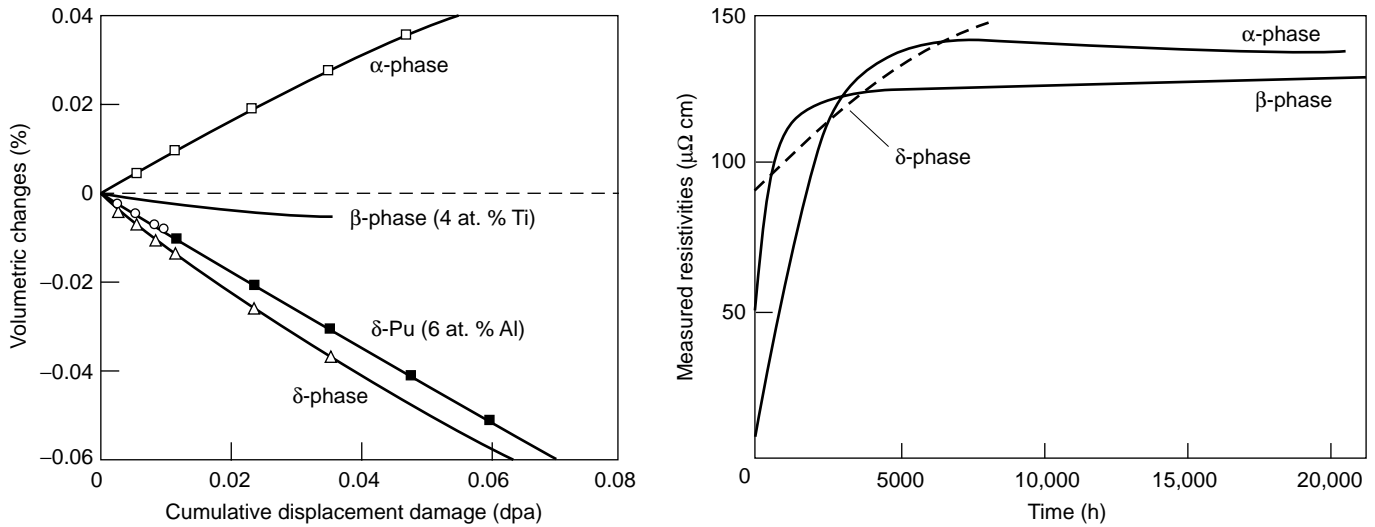


Figure 1. Volume Changes in Plutonium Resulting from Self-Irradiation at Cryogenic Temperatures

(a) The α -phase expands substantially at 4 K because Frenkel pairs are created. Whereas the β -phase shows only a slight contraction, the δ -phase shows a substantial contraction. Self-irradiation exposures were less than 0.1 dpa, which is equivalent to the damage received in 1 year. The volume changes eventually saturated at approximately 10% for the α -phase and 15% for the δ -phase. Interestingly, at saturation, the densities of all three phases appear to converge to approximately 18.4 g/cm³, indicating that all have reached a very disordered state. (b) The damage was also monitored with electrical-resistance measurements. The electrical resistance increases for all plutonium phases of some of the same samples shown in (a). The δ -phase results are averages from several experiments.

At this time, the dramatic enhancements in corrosion rate have not been fully understood. Haschke has speculated that, under the above conditions, it is possible to get superionic transport of anions in complex crystal structures such as Pu₂O₃. Moreover, we have little fundamental knowledge, either theoretical or experimental, about how oxygen or hydrogen adsorbs on plutonium surfaces, nor do we understand the effects of alloying or defect structure in the plutonium substrate. The potential influence of electronic effects is also poorly understood. It is therefore time to turn the new surface techniques developed by the surface science community over the past 20 years to the study of interfacial reactions in plutonium.

One additional peculiarity of plutonium metal deserves mention, namely, its pyrophoricity. Plutonium ignites spontaneously in air at 500°C, but plutonium particulates, such as powder or machining chips, are known to ignite at temperatures as low as 150°C to 200°C. Martz and Haschke have shown that low-temperature pyrophoricity is caused by the formation of Pu₂O₃ followed by a rapid oxidation to PuO₂, which causes a thermal spike to the self-ignition temperature.

The above-mentioned surface reactions greatly impact plutonium handling and storage procedures. As a result, it is imperative that plutonium be protected in sealed containers without the presence of hydrogenous materials. The reason for excluding such materials is that their radiolysis, resulting from the α -decay of plutonium, will make hydrogen available, which can have catastrophic consequences.

Self-Irradiation Effects

The radioactive nature of plutonium presents an interesting interplay between nuclear and electronic processes. The unstable plutonium nucleus decays principally by α -decay¹. The decay event produces two energetic nuclear particles—an α -particle and a recoil uranium nucleus. These particles are created in much less than a femtosecond (10^{-15} second). They share the energy released by the decay and are propelled through the crystal lattice.

The α -particle has an energy above 5 million electron-volts (MeV) and a range of approximately 10 micrometers in the plutonium lattice. It captures two electrons from the plutonium metal and comes to rest in the lattice as a helium atom. The light

¹The isotope plutonium-241 decays by β -decay (with a half-life of 12.3 years) to americium-241, which decays to neptunium-237 by α -decay (with a half-life of 433 years).

α -particle loses nearly 99.9 percent of its energy to electrons, heating the plutonium lattice. Some atomic displacements occur near the end of the range, producing “self-interstitial” plutonium atoms that come to rest in the interstices of the plutonium lattice and vacancies (the holes in the lattice left behind by the displaced plutonium atoms). These defects—the vacancies and the self-interstitials—are called Frenkel pairs.

The heavier uranium nucleus carries approximately 85 kilo-electron-volts (keV) of the decay energy, and it converts nearly three-quarters of its energy into atomic displacements. Its recoil triggers a complicated “ballistic”-collision cascade, which causes most of the initial damage to the plutonium lattice. The range of the uranium recoil atom in the plutonium lattice is approximately 12 nanometers. In the article “Radiation Effects in Plutonium” (page 274), Wolfer calculates the expected damage for the isotopic mix of plutonium typical of weapons stockpiles. Each uranium/helium damage cascade interacts with approximately 20,000 plutonium atoms. Most of these atoms (90 percent) are thermally excited at their lattice position, and only a small fraction (10 percent) are displaced, resulting in the generation of roughly 2500 Frenkel-pair defects per decay event. The large displacement and relaxation of plutonium atoms results in every plutonium atom being displaced, on the average, once every 10 years (or, in the units commonly used, 0.1 displacements per atom/year (dpa/yr)).

The violent events of the primary nuclear-particle decay and the resulting collision cascade are followed by a local thermal spike persisting for at least picoseconds, during which additional reconfiguration of the defect structure (recombination, migration, and agglomeration) takes place. The interactions of these surviving defects with the microstructure and their evolution as a function of time and temperature determine the extent of self-irradiation effects on the properties of plutonium. Theoretical modeling using a special form of the Monte Carlo method (called kinetic Monte Carlo) provides us with insight into these important atomistic processes.

General Lattice Damage. Vacancies and interstitials affect material properties because they perturb the atomic interactions in solids. Vacancies induce lattice softening because of the missing atomic interaction at the vacancy site. Self-interstitials cause very large lattice perturbations and local stress fields. Both types of damage lead to changes in the effective atomic volumes of the lattice. In most metals, such defects affect macroscopic properties such as elastic constants, density, lattice parameters, electrical resistivity, strength, and ductility. In plutonium, we expect these to be large because the 5f electrons sit on the knife-edge between bonding and localization. It is easy to imagine that changes in atomic volume or internal stresses resulting from irradiation-induced defects could affect the delicate balance of phase stability in plutonium.

Surprisingly little research has been done into plutonium self-irradiation at ambient temperature. So far, electronic-structure calculations have been unable to deal with defect structures adequately. There are also very few systematic experimental observations. At ambient temperature, there is a very complex interplay between damage and annealing (or healing). The residual damage depends greatly on the mobility of the defects, their interactions with each other, and their interactions with other defects and solutes.

Most experiments on self-irradiation damage in plutonium have been conducted at cryogenic temperatures, at which little annealing occurs. But subsequent annealing studies looked into defect mobilities and recovery of lattice damage. As shown in Figure 1(a), the α -phase expands significantly at 4 kelvins during self-irradiation. The δ -phase (retained by alloying with several atomic percent aluminum) contracts substantially, whereas the β -phase (retained by alloying with titanium) contracts slightly. In all three cases, the electrical resistivity increased markedly during

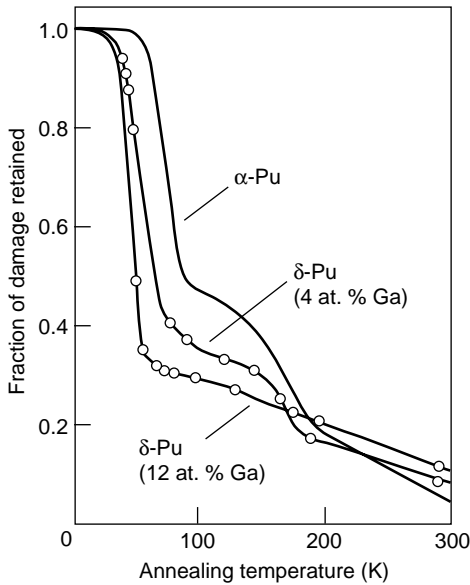


Figure 2. Recovery of Self-Irradiation Damage

Self-irradiated α - and δ -plutonium recover most of the lattice damage introduced at 4.5 K. The fraction of damage retained is measured by the fractional change in electrical resistance recovered when the samples are annealed isochronally (for short periods) as the temperature is warmed back up from 4.5 K. Most of the damage is recovered by room temperature. The α -phase sample was held at 4.5 K for 640 hours, the Pu-Ga alloy (12 at. % gallium) for 665 hours, and the Pu-Ga alloy (4 at. % gallium) for 920 hours.

self-irradiation (reflecting the generation of lattice defects) as seen in Figure 1(b). If self-irradiation is allowed to proceed long enough, all three phases appear increasingly disordered, perhaps approaching an amorphous state, converging at a density of 18.4 grams per cubic centimeter (g/cm^3).

Data from a typical annealing study (Figure 2) show that much of the damage is annealed out by 100 kelvins and most of it is annealed out at room temperature. Because of insufficient data, key parameters such as the mobility of self-interstitials and vacancies cannot be determined. However, we know that these mobilities scale with the homologous temperature (the temperature divided by the melting temperature of the material), so a comparison with other metals irradiated inside accelerators or reactors provides us with useful insight. Specifically, we estimate that self-interstitials are mobile at temperatures above 20 kelvins. Vacancies begin to migrate and annihilate near 200 kelvins, and both interstitial and vacancy clusters dissociate thermally above 400 kelvins, resulting in the complete recovery of lattice damage.

Based on our current rudimentary understanding of these processes, we cannot preclude the possibility of the continued accumulation of radiation damage in plutonium under typical storage temperatures. However, general observations of self-irradiation damage show no major macroscopic changes for at least 40 years—in other words, plutonium does not “crumble”. There also appear to be no gross microstructural changes, such as phase changes or segregation. Early studies found a slight volume expansion in δ -phase alloys, on the order of 0.3 percent in 10 years. However, detailed microstructural examinations are needed to provide a better understanding. In particular, the power of x-ray absorption fine structure (XAFS) spectroscopy to probe the local structure in the vicinity of the plutonium and gallium atoms as the plutonium ages should be explored thoroughly.

Transmutation, Helium Bubbles, and Voids. The transmutation products resulting from α -decay—radiogenic helium and other actinide atoms—can also affect bulk properties. After 50 years of storage, weapons-grade plutonium will have grown in the following amounts of transmutation products: approximately 2000 atomic parts per million (ppm) helium, 3700 ppm americium, 1700 ppm uranium, and 300 ppm neptunium. After that length of time, a piece weighing 1 kilogram will contain nearly two-tenths of a liter of helium measured at standard conditions. Said differently, after 50 years of decay, the accumulated helium in plutonium would generate a pressure of 3 atmospheres in an equivalent empty volume!

The most important concern about the in-growth of actinide transmutation products in plutonium is their potential effect on the delicate balance of phase stability. Under equilibrium conditions, the addition of americium makes fcc δ -plutonium more thermodynamically stable, so several thousand parts per million of americium should help to further stabilize δ -phase alloys. Uranium and neptunium, on the other hand, reduce δ -phase stability. In both cases, however, the conditions present after the α -decay events are far from equilibrium and, hence, may not have the expected effects at ambient temperature.

The accumulation of radiogenic helium could affect the properties of plutonium substantially. Helium has extremely low solubility in metals because it does not bind. It diffuses rather easily through the lattice (as easily as vacancies) until it becomes trapped in one of the vacancies. The helium-vacancy clusters can migrate and coalesce, potentially forming into helium bubbles, which cause swelling. It is well known that less than 100 ppm of helium in fcc stainless steel can cause swelling or dramatic embrittlement. Wolfer concludes, however, that macroscopic swelling in plutonium as a result of helium bubbles is very unlikely at ambient temperature.

The combination of irradiation-induced lattice damage and the presence of helium atoms can cause void growth and bulk swelling without the presence of helium

bubbles. Void growth is an obvious potential consequence of vacancy migration and clustering. Void swelling has been found to be a serious problem for materials in the irradiation environment of reactors.

Reliable predictions of void swelling in plutonium are not currently possible because of a lack of fundamental knowledge of intrinsic properties such as the relaxation volumes for vacancies and interstitials. Wolfer's best estimate is that void swelling is expected to begin for δ -phase plutonium alloys in the temperature range of -30°C to 150°C after 10 to 100 years (for typical plutonium-239). Once void swelling begins, he estimates that the swelling rate will be approximately 1–2 percent per 10-year lifetime for plutonium-239. This value is similar to that found for other fcc metals. Compared with the range of swelling resulting from helium bubble formation, void swelling is the more important concern.

But more experiments are needed to pin down pertinent metallurgical variables. Experiments are also needed to determine whether plutonium is subject to other potential problems that arise within irradiated metals and alloys, such as irradiation-induced segregation, which can preferentially transport solute atoms into and out of local regions (impacting phase stability), and mechanical deformation. Because we are attempting to measure the effects of decades, methods must be developed to accelerate the damage process. The best method proposed to date is the doping of plutonium with small fractions of plutonium-238 (note that plutonium-238 generates almost 300 times greater α -decay activity than plutonium-239). This accelerated-aging experiment is just beginning in a joint effort between the Los Alamos and Lawrence Livermore National Laboratories.

We present these possible effects of self-irradiation as a caution. A scientific comparison with other materials subjected to external radiation fields tells us that self-irradiation of plutonium near ambient temperature has all the requisites for potentially catastrophic damage. Yet, our experience with plutonium over several decades shows no evidence for such damage. However, we know that, even if lattice defect structures induced by self-irradiation are insufficient to cause some of the catastrophic effects discussed, they may affect diffusion and transport properties, which could accelerate the kinetics of phase instability. With the new emphasis on extended lifetimes for plutonium and long-term storage, it behooves us to better understand the fundamental processes behind irradiation damage and the concurrent healing processes. ■

Siegfried S. Hecker received his B.S., M.S., and Ph.D. in metallurgy from Case Western Reserve University. After being a postdoctoral fellow at Los Alamos, he became a senior research metallurgist with the General Motors Research Laboratories. He joined Los Alamos as a technical staff member in the Physical Metallurgy Group and served as Chairman of the Center for Materials



Science and Leader of the Materials Science and Technology Division before becoming Director. Sig was Director of Los Alamos National Laboratory from 1986 to 1997. He is currently a Senior Fellow at Los Alamos. In addition to his current research activities, Sig is a member of the Council on Foreign Relations and the Pacific Council on International Policy. He also serves on the National Academy of Engineering Committee on Membership (chairman), Nominating Committee, and Draper Prize Committee, and on the Fellows Awards Committee of The Metallurgical Society. Over the years, Sig received numerous awards in recognition of his achievements. In 1998, he was named Laboratory Director of the Year by the Federal Laboratory Consortium, and in 1984, he received the Department of Energy's E. O. Lawrence Award.

Joseph C. Martz received his B.S. in chemical engineering from Texas Tech University and his Ph.D. in chemical engineering from the University of California at Berkeley. He is currently program manager for Enhanced Surveillance and Weapon Materials in the Nuclear Weapons Stockpile Systems program office at Los Alamos. His current research interests include analysis and assessment of aging effects in weapon materials, development of techniques for nuclear warhead dismantlement, technical issues related to plutonium storage, and advanced chemical-processing methods for environmental restoration and recovery of nuclear materials from contaminated waste. He is recognized as a leading authority on the issues of plutonium aging and the impact of aging effects on nuclear warhead function.



A Tale of Two Diagrams

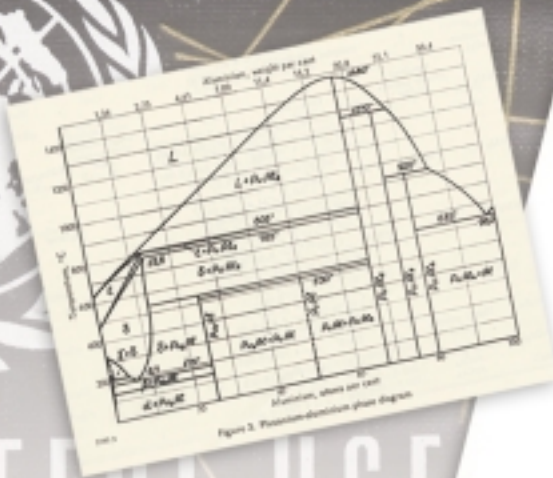


Figure 3. Plutonium-gallium phase diagram.

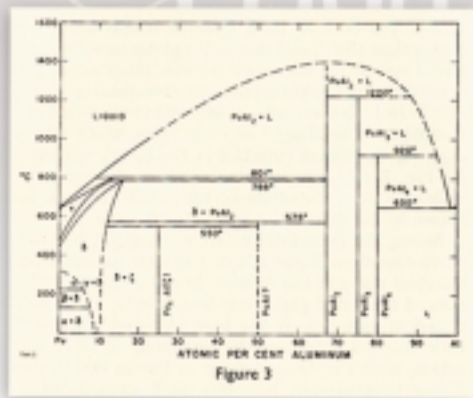
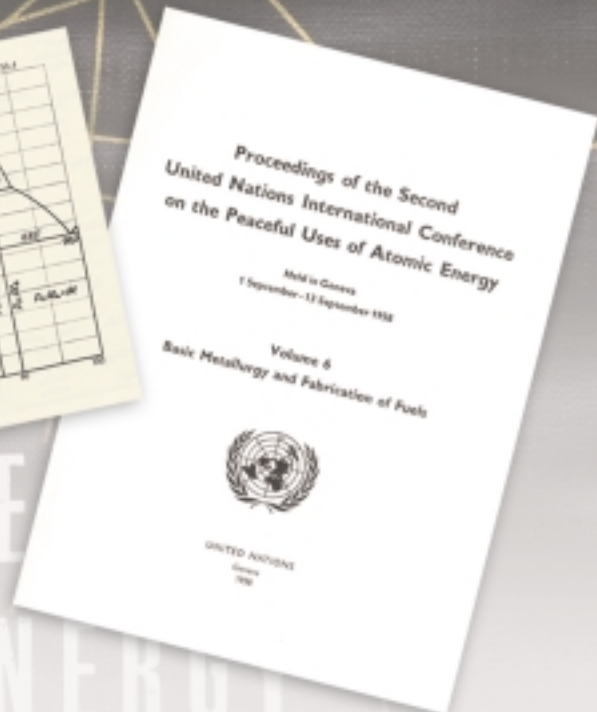


Figure 3

КРИТИЧЕСКИЕ ТЕМПЕРАТУРЫ И ДАВЛЕНИЯ НА РАВНОВЕСИИ В СИСТЕМАХ ПЛУТОНИЙ-АЛЮМИНИЙ, ПЛУТОНИЙ-ГАЛЛИЙ
 С.Т. Конобеевский, С.С. Кузнецов, Л.Ф. Тимофеева,
 В.А. Абрамзон, В.С. Селев

Получены экспериментальные данные равновесия в системах плутоний-алюминий и плутоний-галлий в области от стоек до стоек плутония при атмосферном давлении и в области высокого давления. Значение угла δ -фазы при равновесии определено, состав сплава экспериментальной системы. Значения параметров критического давления δ -фазы в системах плутоний-алюминий.

Siegfried S. Hecker and Lidia F. Timofeeva

It is difficult to believe that in 1999, more than 50 years after the Manhattan Project, the authors as well as other scientists from Russia and the United States still disagreed about the stability of the δ -phase plutonium-gallium (Pu-Ga) alloys used in nuclear weapons. Typically, the face-centered-cubic (fcc) δ -phase of plutonium, which is malleable and easily shaped, is retained down to ambient temperatures by the addition of gallium or aluminum. But do those δ -phase alloys remain stable for decades or do they decompose into the denser, brittle α -phase and something else at ambient temperature? A crucial part of the answer lies in the equilibrium binary phase diagrams for the Pu-Ga and plutonium-aluminum (Pu-Al) systems.

Unfortunately, two very different versions of those phase diagrams have existed for several decades—one measured in the laboratories of the United States, the United Kingdom, and France and the other in the laboratories of the former Soviet Union (now Russia).

During the first 10 years following World War II, Soviet, American, and British scientists worked in secret to develop a wide range of technologically important phase diagrams for plutonium alloyed with other elements. In 1953, the door for scientific collaboration opened. That year, President Eisenhower spoke to the United Nations, proposing an international effort to promote the peaceful uses of atomic energy. Encouraged by conferences on this topic sponsored by the

United Nations, Soviet researchers (Academician A. A. Bochvar, member of the Soviet Academy of Sciences, and S. T. Konobeevsky, a corresponding member) presented their work on plutonium phase diagrams in Moscow (Konobeevsky 1955) and then in Geneva (Bochvar et al. 1958). After the 1955 conference, American and British researchers followed suit at various national and international conferences (Coffinberry et al. 1958).

F. W. Schonfeld of Los Alamos reviewed the early work (1961a, 1961b) and noted that the predictions of δ -phase stability differed significantly in the Soviet and U.S. Pu-Al equilibrium diagrams: "...although it is to be expected that these differences will soon be

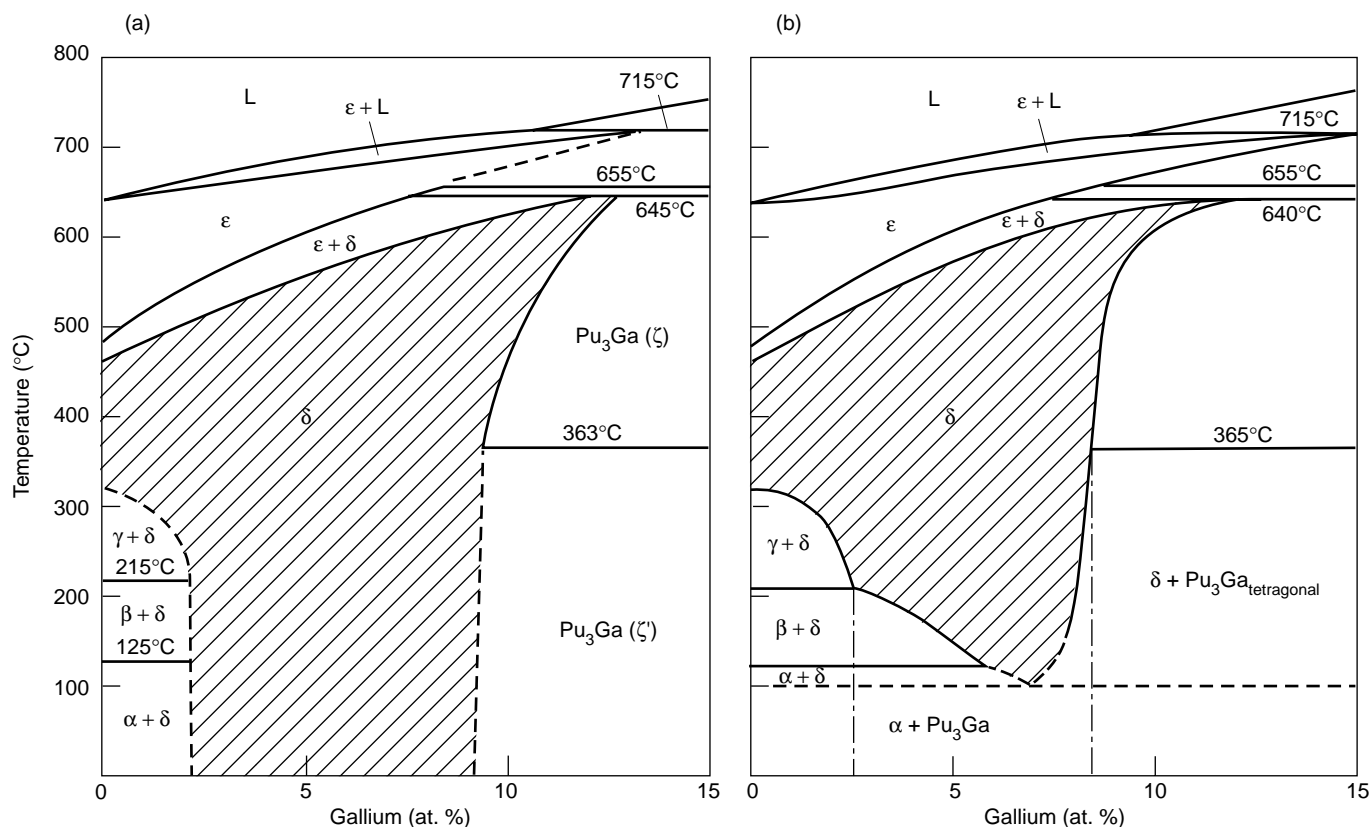


Figure 1. U.S. and Russian Equilibrium Pu-Ga Phase Diagrams

The U.S. equilibrium Pu-Ga phase diagram in (a) was reported by Peterson and Kassner (1988) and is based on the work of Ellinger et al. (1964). The Russian phase diagram in (b) was reported by Chebotarev et al. (1975). The principal difference is that Ellinger et al. found the fcc δ -phase to be retained at room temperature by gallium concentrations greater than approximately 2 at. % and less than approximately 9 at. %, whereas Chebotarev et al. reported a eutectoid decomposition of the δ - to the α -phase plus Pu_3Ga below 100°C. Both diagrams have dashed lines at the lower end of the temperature spectrum because diffusion processes become so slow that it is very difficult to determine what the real “equilibrium” structure is. So, both diagrams represent extrapolations to equilibrium—but with very different conclusions. The dash-dotted lines in (b) represent the metastable phase boundaries.

(Reproduced courtesy of ASM International.)

resolved through the performance of further experimental work in both countries, it is difficult at this stage to speculate in any particular case regarding the probable outcome of such further work.” What Schonfeld thought would be resolved “soon” took almost another 40 years. The tale of two diagrams is fascinating from both a scientific and a social perspective.

Why Is It Important to Know if δ -Plutonium Decomposes?

During aging, thermally activated kinetic processes are at work, constantly trying to drive the solid toward equilibrium (its lowest-energy configuration). Hence, any nonequilibrium

structures are subject to change during aging. One of the greatest concerns about plutonium and its alloys is phase stability because the large volume changes that accompany phase changes can compromise structural integrity. During the Manhattan Project (and later in the corresponding project in the Soviet Union), gallium was purposely added to plutonium to retain the fcc δ -phase down to ambient temperatures, making it possible to shape plutonium into requisite shapes. The monoclinic α -phase of pure plutonium was brittle and totally unwieldy from a metallurgist’s viewpoint. Because of its relevance to nuclear weapons, the Pu-Ga diagram was not reported by either country until both sides realized that

the omission itself signaled its appeal to their nuclear weapons programs.

By 1964, U.S. researchers published the Pu-Ga phase diagram in the open literature (Ellinger et al. 1964), showing that gallium, just like aluminum, retains the fcc δ -phase to room temperature. French researchers published very similar results (Hocheid et al. 1967). In 1975, S. Hecker heard Professor N. T. Chebotarev of the Bochvar Institute present the Soviet version of the Pu-Ga diagram at the Plutonium 1975 Conference in Baden-Baden, Germany. Soviet researchers had reached conclusions that were strikingly different from those of researchers in the West. As illustrated in Figure 1, the U.S. equilibrium diagram shows that alloys with gallium

concentrations between 2 and 9 atomic percent (at. %) are in the δ -phase at ambient temperatures, whereas the Russian equilibrium diagram shows that those alloys decompose at ambient temperatures into a eutectoid, or mixture of phases, consisting of α -plutonium and Pu_3Ga . Both diagrams show dotted lines at these temperatures, indicating that diffusion processes are very slow and that the phases shown represent an extrapolation to equilibrium.

It is important to know whether a thermodynamic driving force is pushing the fcc δ -phase to decompose into a eutectoid mixture because such a transformation would produce volume changes, dimensional distortions, and potentially undesirable property changes. If slow kinetics is the only obstacle to the transformation, we must fully understand all the factors that could speed up the kinetics. Atomic diffusion, the rate-limiting step, could speed up over decades if, for example, lattice damage from self-irradiation were to accumulate as plutonium ages.

At the Baden-Baden conference, Hecker mentioned that U.S. researchers had found no such decomposition and asked Professor Chebotarev if Soviet researchers had enhanced the kinetics. The reply was that they had annealed at high pressure to speed up the eutectoid transformation. In the published proceedings, Chebotarev et al. (1975) wrote that the decomposition was achieved by the “long-term annealing [of] alloys at high pressure.” Hecker’s attempts to get clarification from Professor Chebotarev after the presentation were unsuccessful.

Back in Los Alamos, Hecker and his colleagues attempted to duplicate the Soviet results in the late 1970s and early 1980s. They found that new phases and different microstructural features can be readily found if Pu-Ga alloys are annealed under pressure. However, they were unable to duplicate the Soviet phase diagram. The Soviet work was considered a temperature-composition diagram valid only at high pressures. It was not accepted as valid at atmospheric

pressure because pressure was viewed as an additional thermodynamic parameter.

Lack of Scientific Contacts Prolongs the Mystery

Until 1998, the tales of the two diagrams remained very separate—not because either country considered them secret but because the Cold War prohibited scientific peer review and discussions of this work. The United States (as well as the United Kingdom and France) believed that the fcc δ -phase was stable at room temperature and above. It was well known in both the Soviet Union and the West that, for low concentrations of aluminum or gallium and below room temperature, the fcc δ -phase can transform martensitically to an α -like phase known as α' . This phase has the monoclinic structure of the α -phase but contains dissolved gallium (the equilibrium α -phase has absolutely no solubility for gallium). Martensitic transformations are sudden, displacive, and diffusionless. Therefore, they trap the gallium within the monoclinic lattice. In contrast, the eutectoid decomposition to the α -phase plus Pu_3Ga is a diffusional transformation.

Until 1990, Soviet scientists continued to study the approach to equilibrium at temperatures just above room temperature for additions of gallium and other Group IIIB elements in the periodic table. The results of their studies confirmed the eutectoid decomposition. At an international conference on the actinides held in Tashkent, Timofeeva presented a brief summary, which was then published in a Russian journal not well known in the West (Chebotarev et al. 1990).

Without being aware of that summary, Paul Adler of Lawrence Livermore National Laboratory published (1991) a thermodynamic analysis in which he concluded that the Russian diagram most likely was correct. Adler suggested that, if a δ -phase alloy were transformed martensitically to the α' -phase and then annealed, it would decompose to the

eutectoid seen in the Russian diagram. But such experiments were not performed mainly because programmatic interest in plutonium research had waned before the advent of the Stockpile Stewardship Program. The official western Pu-Ga phase diagram as published in the American Society for Metals International compilation of phase diagrams (Peterson and Kassner 1988) is an update of the diagram of Ellinger et al. (1964).

In 1998, the authors of this article met for the first time through the continuing scientific exchange between U.S. and Russian researchers that has developed since the end of the Cold War and the dissolution of the Soviet Union. Academician Boris Litvinov from the All-Russian Research Institute of Theoretical Physics (VNIITF), who had worked with Hecker during the past six years on cooperative nuclear-security programs, introduced the authors at the Bochvar Institute in Moscow. Timofeeva presented her work on plutonium phase diagrams at the International Conference on Ageing of Materials held in Oxford in July 1999 (both authors were invited to that conference). She had conducted that work under the leadership of Academician A. A. Bochvar almost 30 years before the Oxford conference.

At that meeting and during subsequent discussions, one of the greatest pieces of the puzzle was resolved. As it turned out, the Russian work had not involved annealing under pressure. Instead, the samples were subjected to pressure and plastic deformation and were subsequently annealed for very long times at atmospheric pressure. The role of pressure and plastic deformation was to “precondition” plutonium alloys and thus enhance the kinetics of the δ -phase decomposition. This approach is similar to that suggested by Adler in 1991, but the Russian work had already been carried out 20 years before.

The proper determination of equilibrium diagrams at low temperatures has long been a point of disagreement in the metallurgical community because slow diffusion rates at low temperatures make it very difficult to achieve equilibrium.

Timofeeva's preconditioning treatments introduced slight amounts of the α -phase and initial densities far above and below the equilibrium density, enabling her to study the approach to equilibrium from both sides of the equilibrium density. She had to convince Soviet scientists that this unconventional approach was valid. Fortunately, Academician Bochvar supported her. Nevertheless, confusion about the exact nature of the treatments continued in the Soviet scientific community and apparently resulted in the statements made in 1975 that long-term annealing was performed under pressure. We will describe Timofeeva's experiments to clear up the confusion surrounding the Russian phase diagram.

The Russian Approach to Equilibrium at Low Temperatures

In initial studies, Timofeeva prepared Pu-Ga and Pu-Al alloys ranging in composition from 0 to 25 at. %. Samples with less than 10 at. % gallium or aluminum were prepared in a conventional manner. It is well known that such alloys must be homogenized at high temperature for long times to minimize microsegregation of gallium or aluminum and to ensure that the fcc δ -phase is retained to room temperature. As expected, when those δ -phase samples were annealed from room temperature to 300°C for long periods, they showed no decomposition reactions. These initial results were identical to those produced in the West. If the equilibrium state below 100°C was not the fcc δ -phase, then diffusion under normal conditions was too slow to bring it about.

To speed up diffusion and encourage the eutectoid decomposition transformation shown in Figure 1(b), Timofeeva applied two preconditioning treatments (I and II), which partially transformed the δ -phase to the α -phase. Long-term annealing experiments followed. We show the results for Pu-Al alloys because those alloys had been studied in depth before the Pu-Ga system was investigat-

Preconditioning Treatments

(a)

Treatment I Features

Pressure: 1–3 GPa at 200°C–300°C for periods up to several hours. Room temperature density: 19.4 g/cm³. Structure: fine dispersion of α -phase + PuAl.

Treatment II Features

Compressive plastic deformation at room temperature to transform δ -phase partially. Room temperature density: 16.7 g/cm³. Structure: α' -phase in a δ -phase matrix.

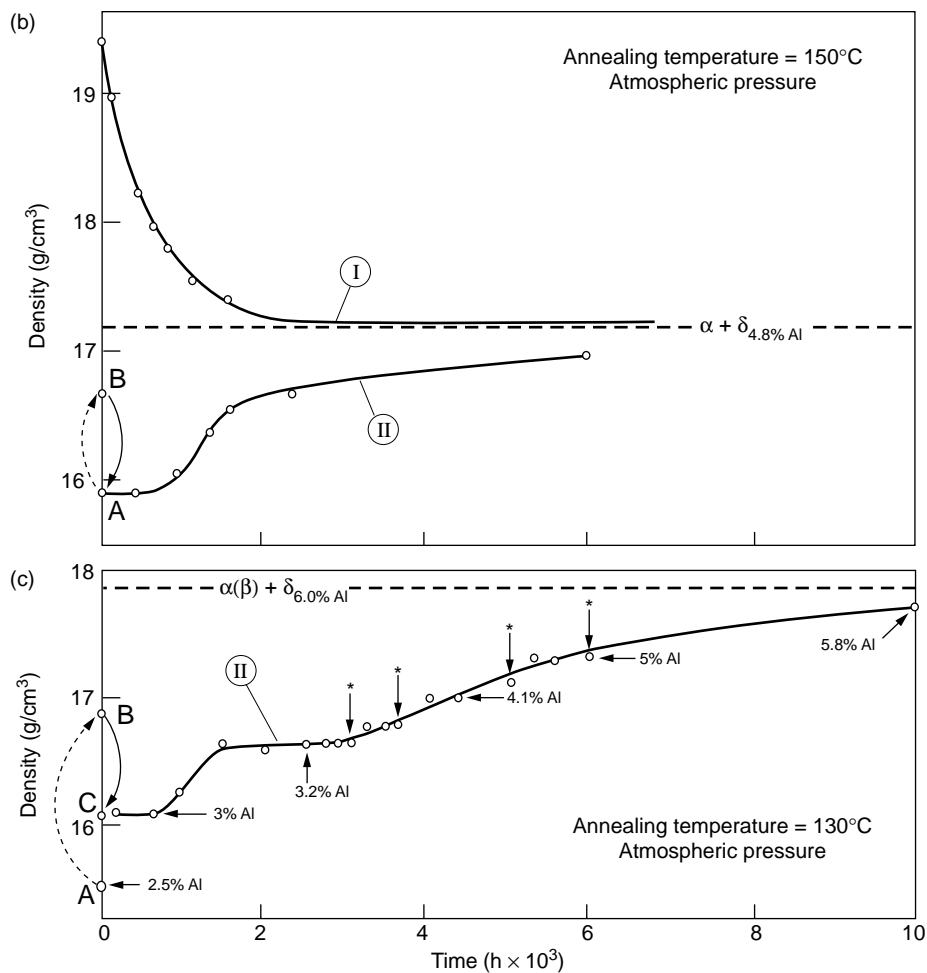


Figure 2. Long-Term Annealing Experiments with Pretreated Samples Samples of well-homogenized fcc δ -phase Pu-Al alloys (2.5 at. % aluminum) with a starting density of ~ 15.8 g/cm³ were preconditioned with treatment I or II as outlined in (a). Group I and II samples, labeled according to the type of preconditioning treatment they received, were annealed for thousands of hours at atmospheric pressure. Density changes with time for annealing at 150°C and at 130°C are shown in (b) and (c), respectively. The starting density for the all- δ -phase samples in (c) was somewhat low, most likely because of the presence of microcracks. The designation $\alpha(\beta)$ indicates that, at the annealing temperature, the β -phase is present, which then transforms to the α -phase during cooling to room temperature (all measurements are made at room temperature). The subscript of various percent aluminum in the δ -phase designation refers to the atomic percent of aluminum dissolved in the δ -phase. For group II samples, we show the starting density (point A), the initial density following treatment II (point B), and the change in density (see arrows) upon heating to the annealing temperature.

ed. For considerations discussed here, aluminum and gallium are virtually interchangeable. Figure 2(a) outlines treatments I and II, and Figures 2(b) and 2(c) show the results of long-term annealing experiments conducted at atmospheric pressure for a Pu-Al alloy (2.5 at. % aluminum) with a starting density of about 15.8 grams per cubic centimeter (g/cm^3).

We refer to the samples preconditioned with treatment I and treatment II as group I and II samples, respectively. Figure 2(b) shows the changes in density and phase as a function of time for group I and II samples annealed at 150°C . Immediately after treatment, group I samples have an initial density of about $19 \text{ g}/\text{cm}^3$. Their density drops rapidly with time and approaches a value of $17.1 \text{ g}/\text{cm}^3$. Group II samples have an initial density of $16.7 \text{ g}/\text{cm}^3$ (point B), but their density drops back to the starting density (point A) upon heating to 150°C . That density remains constant for the first 500 hours of annealing and then gradually increases. After 6000 hours, the densities of group I and II samples approach the same value. The open circles indicate the times at which the samples were returned to room temperature for detailed examination, including density measurements, metallographic examination, x-ray diffraction lattice-parameter measurements, and microhardness measurements. Those examinations revealed unequivocally the phases present at each stage of the annealing.

Figure 2(c) shows the results for annealing group II samples at 130°C . Upon heating to that temperature, the initial density of group II samples (point B) drops to point C rather than to the starting density (point A), as was the case for annealing group II samples at 150°C —see Figure 2(b). Again, there is an incubation period before the group II sample density starts to increase, in this case toward $17.8 \text{ g}/\text{cm}^3$ (although not shown in the figure, group I samples approached this density from the high-density side). During various periods of

annealing group II samples, the density changes ceased. It appeared that transformation from the δ - to the β -phase at 130°C had stalled because of very slow diffusion. Therefore, at the points marked by arrows, samples had been returned to room temperature and plastically deformed before the annealing treatments were continued. No additional δ to α' transformation was induced during deformation, but the rate of transformation did increase, as shown, following the deformation treatments. Figure 2(c) also shows that the concentration of aluminum in the δ -phase increased with annealing times. Those concentrations were inferred from the x-ray diffraction measurements of the δ -phase lattice parameter taken at those times.

Similar experiments were run at several annealing temperatures and for alloys of varying aluminum concentrations. The combined results were used to deduce the Pu-Al equilibrium phase diagram shown in Figure 3(a). Similar experiments involving treatments I and II and extended annealing times were performed on Pu-Ga alloys and led to the Pu-Ga phase diagram shown in Figure 3(b).

Several differences were observed between the gallium and aluminum alloys. First, the intermetallic compound formed in the aluminum alloys is PuAl, whereas that in the gallium alloys is Pu_3Ga . Second, in the aluminum system, the δ -phase transforms to the α' -phase during the plastic deformation of treatment II, whereas in the gallium system, some γ -phase forms in addition to the α' -phase. Third, the gallium alloys pretreated according to treatment II required even longer times to come to equilibrium—up to 16,000 hours at 130°C .

Is Decomposition the Equilibrium State?

The eutectoid decomposition shown in Figure 3 was never seen directly, but convincing evidence for that endpoint

is inherent in Figures 2 and 3. These figures show that annealing at temperatures from 130°C to 200°C causes plutonium alloys with a few atomic percent aluminum or gallium to transform to a pure α -phase plus a δ -phase enriched in aluminum or gallium (for temperatures above the α to β transformation, the alloys transform to a pure β -phase plus a δ -phase enriched in aluminum or gallium). Figure 2 shows the gradual progress of the transformation in Pu-Al samples preconditioned with treatment II. Detailed examination showed that the structure of group II samples consists of the α' -phase interspersed in a δ -phase matrix. At the initial point of the 150°C anneal, most of the α' -phase in group II samples has transformed directly back to the δ -phase alloy, as indicated by the drop in density to point A in Figure 2(b). At the initial point of the 130°C anneal, more of the α' -phase remains in group II samples—the density drops only to point C in Figure 2(b). During the first few hundred hours, nothing else happens, but then the density begins to increase.

At the temperature of the anneals, the density increase is associated with the formation of pure β -plutonium and the rejection of gallium into the remaining δ -phase. (Pure β -plutonium reverts to pure α -plutonium as the temperature is cooled below the β to α transformation.) These conclusions were confirmed by room-temperature examinations conducted periodically during the annealing treatments. In spite of the very different starting structures for samples in groups I and II, both structures converged to pure β -plutonium plus δ -plutonium enriched in aluminum or gallium following an annealing period of several thousand hours. We note that, in the case of the Pu-Al alloy, small amounts of aluminum may be soluble in β - and γ -plutonium as shown in Figure 3(a). Because the samples in groups I and II converged to the same density on a common structure from above and below the limiting density, Timofeeva

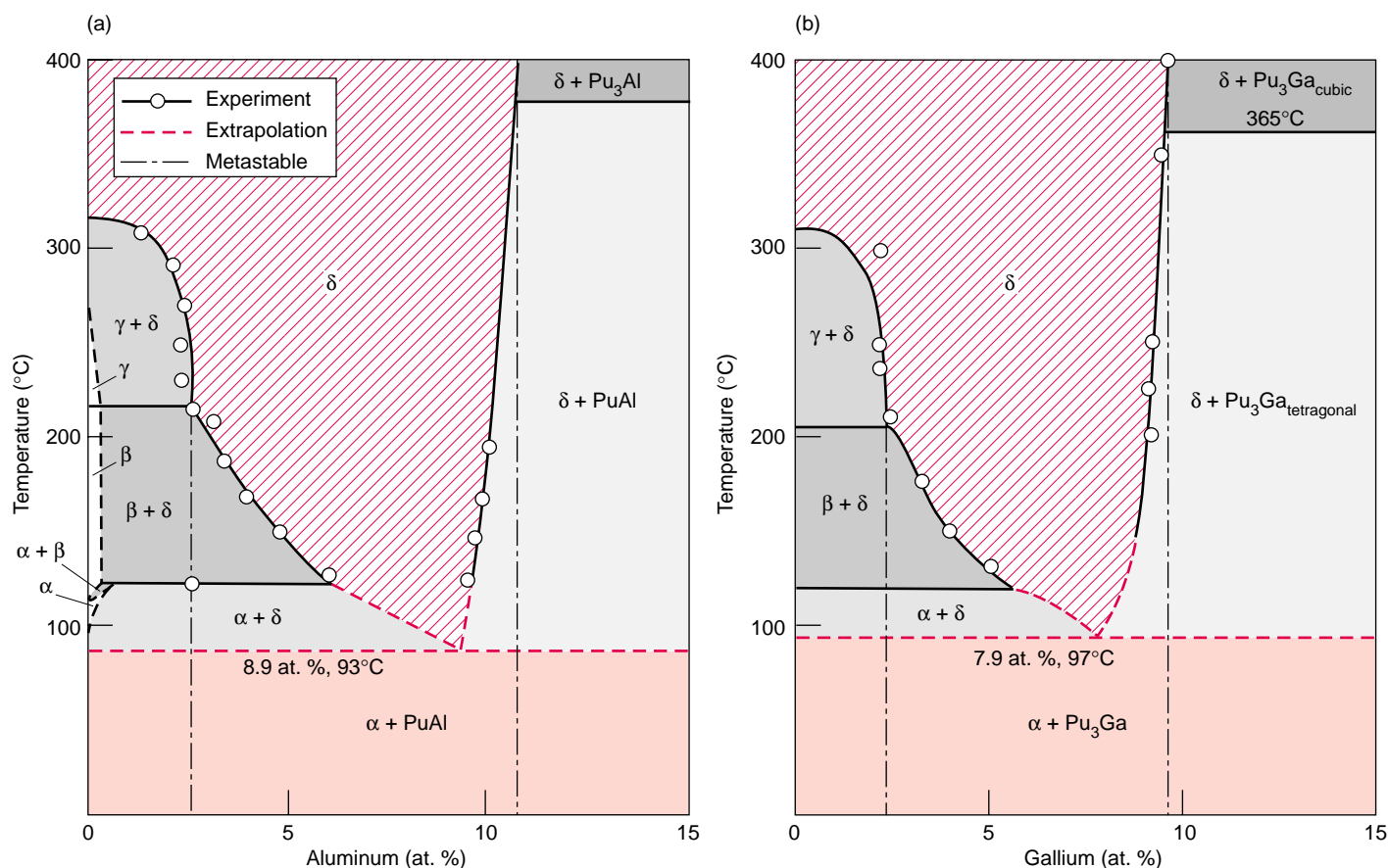


Figure 3. Pu-Al and Pu-Ga Equilibrium Phase Diagrams

This figure shows the plutonium-rich part of the Pu-Al equilibrium phase diagram (a) and the Pu-Ga diagram (b) as reported by Chebotarev et al. (1990) and Timofeeva (2000). Each solid circle represents an experiment of the type depicted in Figure 2. The dashed lines represent the extrapolation of the experimental points to temperatures below which diffusion was too slow to allow the transformation to proceed in a reasonable time. The dash-dotted lines are the metastable phase boundaries determined without preconditioning treatments.

was confident that equilibrium had been achieved. She found that inducing the presence of the α -phase (by preconditioning) was essential to promoting the transformations observed. The residual α - or β -phase structures served as nucleation sites for the transformation occurring at elevated temperatures and long times.

Below 130°C, no long-term phase decomposition from the δ - to the α -phase plus enriched δ -phase was observed for group I and II samples. Diffusion was simply too slow. Hence, the phase boundaries in Figure 3 had to be extrapolated (dashed lines) to a eutectoid point. Chebotarev et al. (1990) and Timofeeva (2000) showed that the logarithm of the aluminum (or

gallium) concentration of the phase boundary is a linear logarithmic function of $1/T$. Because the relationship between concentration and temperature was linear on a log-log plot, L. Timofeeva was able to extrapolate the annealing data in the range 130°C–200°C to the eutectoid points for aluminum (8.9 at. %, 93°C) and gallium (7.9 at. %, 97°C).

The western phase diagrams lead one to expect very different results for the same pretreatments and annealing conditions. The Pu-Al and Pu-Ga samples should have transformed back entirely to δ -plutonium or to δ - with very small amounts of α -plutonium. In no case would one expect significant amounts of β -plutonium forming

at the annealing temperatures, nor would one expect to find δ -plutonium with the enriched concentrations of aluminum or gallium as in Figures 2 and 3. Because of the different expectations, no attempts at pretreatments followed by elevated-temperature annealing were pursued in the West. Moreover, because the incubation periods are on the order of 500 hours even with the pretreatment, it is unlikely that the experiments would have been continued for the extended times necessary to detect the evidence for phase decomposition. Most of the focus in the West was on the martensitic transformation of the δ - to the α' -phase at temperatures below room temperature.

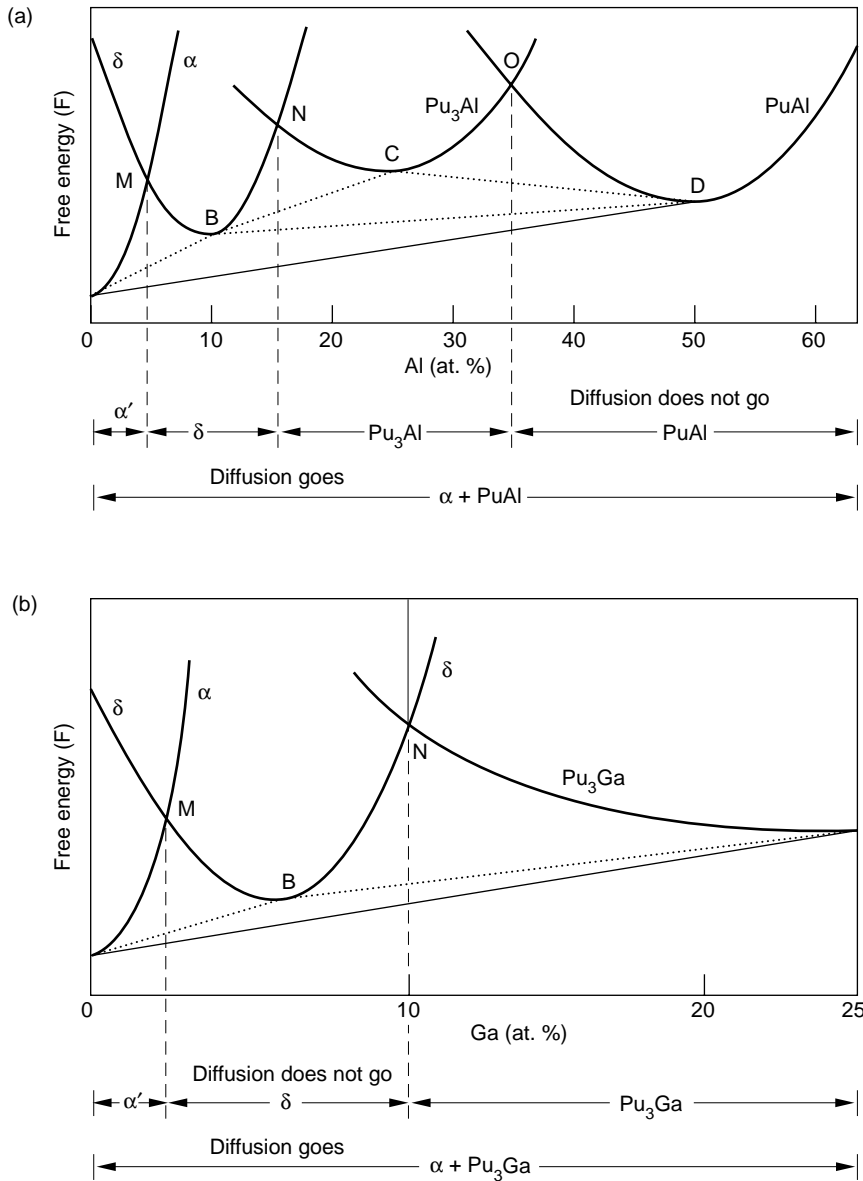


Figure 4. Free-Energy Diagrams for Pu-Al and Pu-Ga Alloys

These schematic free-energy diagrams for Pu-Al (a) and Pu-Ga (b) alloys were developed by Russian scientists (Chebotarev et al. 1990, Timofeeva 2000). Under equilibrium conditions, the straight tie line between the free-energy curves for the α -phase and the intermetallic compound (PuAl or Pu₃Ga) represents the lowest energy as long as diffusion is sufficiently rapid to allow the decomposition to occur. If diffusion is not rapid enough, then other tie lines can be drawn as shown, and the δ -phase would persist over some range of aluminum or gallium concentrations.

Decomposition of the δ -Phase: Practical Consequences

The Russian equilibrium phase diagram shows convincingly that all δ -phase alloys stabilized by additions

of aluminum or gallium are metastable at ambient temperature. The situation is best depicted by the free-energy diagrams shown in Figure 4.

Both Russian and western experiences have shown that diffusion is too slow to allow the decomposition trans-

formation to occur. So, although the “equilibrium” diagram shows decomposition occurring below 100°C, that phenomenon has never been observed. We have not observed any decomposition in δ -phase alloys that are 20 to 30 years old. Therefore, for practical purposes, the U.S. diagram shown in Figure 1(b) is adequate—it represents the metastable condition. In fact, the same metastable boundaries are shown in the Russian diagrams in Figure 3. Timofeeva estimated that even a pre-conditioned Pu-Al alloy at room temperature would take on the order of 11,000 years to decompose based on room-temperature data on self-diffusion in δ -phase plutonium. The Pu-Ga alloys are expected to take even longer to decompose. The situation in plutonium alloys is similar to that in steel. Note that, in steel, equilibrium favors carbon to be present as graphite; however, because diffusion at ambient temperature is also limited in steels, carbon is either tied up in the intermetallic compound Fe₃C or stuck in the iron lattice. Our highway bridges do not decompose into iron plus graphite.

So, why be concerned? One must always respect the power of a thermodynamic driving force because the system (in this case, the plutonium alloy) will always tend to lower its energy. If only kinetics protects the system from changing to a lower-energy configuration, then it is important to understand fully the factors controlling the kinetics. Regarding plutonium, we must develop a better understanding of how the relentless process of self-irradiation (that displaces every plutonium atom once every 10 years) affects diffusion and consequently phase stability. In addition, the effects of impurities (either adsorbed on the surface or transmuted from self-irradiation during aging) on phase stability must be better understood. These problems will be not only an important area of research, but also a scientifically fascinating one. ■

Further Reading

Adler, P. H. 1991. *Met. Trans.* **22A**: 2237.

Bochvar, A. A., S. T. Konobeevsky, V. I. Kutaisev, T. S. Menshikova, and N. T. Chebotarev. 1958. The Interaction between Plutonium and Other Metals in Connection with their Arrangement in Mendeleev's Periodic Table. In *Proceedings of the Second United Nations International Conference on the Peaceful Uses of Atomic Energy* **6**: 184. Geneva: United Nations.

Chebotarev, N. T., E. S. Smotriskaya, M. A. Andrianov, and O. E. Kostyuk. 1975. Some Results of a Study of the Pu-Al-Ga Phase Diagram. In *Proceedings of the 5th International Conference on Plutonium and Other Actinides*. Edited by H. Blank and R. Lindner, 37. New York: North Holland Publishing Co.

Chebotarev, N. T., V. S. Kurilo, L. F. Timofeeva, M. A. Andrianov, and V. V. Sipin. 1990. *VANT, Ser. Materialovedenie i noviiie materialii* **3** (37): 20.

Coffinberry, A. S., F. W. Schonfeld, E. M. Cramer, W. N. Miner, F. H. Ellinger, R. O. Elliott, and V. O. Struebing 1958. The Physical Metallurgy of Plutonium and Its Alloys. In *Proceedings of the Second United Nations International Conference on the Peaceful Uses of Atomic Energy* **6**: 681. Geneva: United Nations.

Ellinger, F. H., C. C. Land, and V. O. Struebing. 1964. *J. Nucl. Mater.* **12**: 226.

Hocheid, B., A. Tanon, S. Bedere, J. Despres, S. Hay, and F. Miari. 1967. Studies of the Binary Systems Plutonium-Gold, Plutonium-Gallium, and Plutonium-Indium. In *Proceedings of 3rd International Conference on Plutonium 1965*. Edited by A. I. Kay and M. B. Waldron, 321. London: Chapman and Hall.

Konobeevsky, S. T. 1955. Phase Diagrams of Some Plutonium Systems. In *Session of the Division of Chemical Science of the U.S.S.R. Academy of Sciences (Conference on the Peaceful Use of Atomic Energy)*, 362. Moscow: Soviet Academy of Sciences.



Left to right: Academician Boris Litvinov, Lidia Timofeeva, Evgeny Kozlov, and Sig Hecker at the Bochvar Institute in Moscow, in 1998. Academician Litvinov and Evgeny Kozlov are with the All-Russian Research Institute of Theoretical Physics.

Lidia Fedorovna Timofeeva was born in Moscow. She attended the Faculty of Metal Sciences headed by Academician A. A. Bochvar at the Moscow Institute of Steel and Alloys. Timofeeva earned her Ph.D. with distinction in engineering science. She is currently a lead plutonium scientist at A. A. Bochvar's All-Russian Scientific Research Institute of Inorganic Materials in Moscow.

Peterson, D. E., and M. E. Kassner. 1988. *Bull. Alloy Phase Diagr.* **9**: 261.

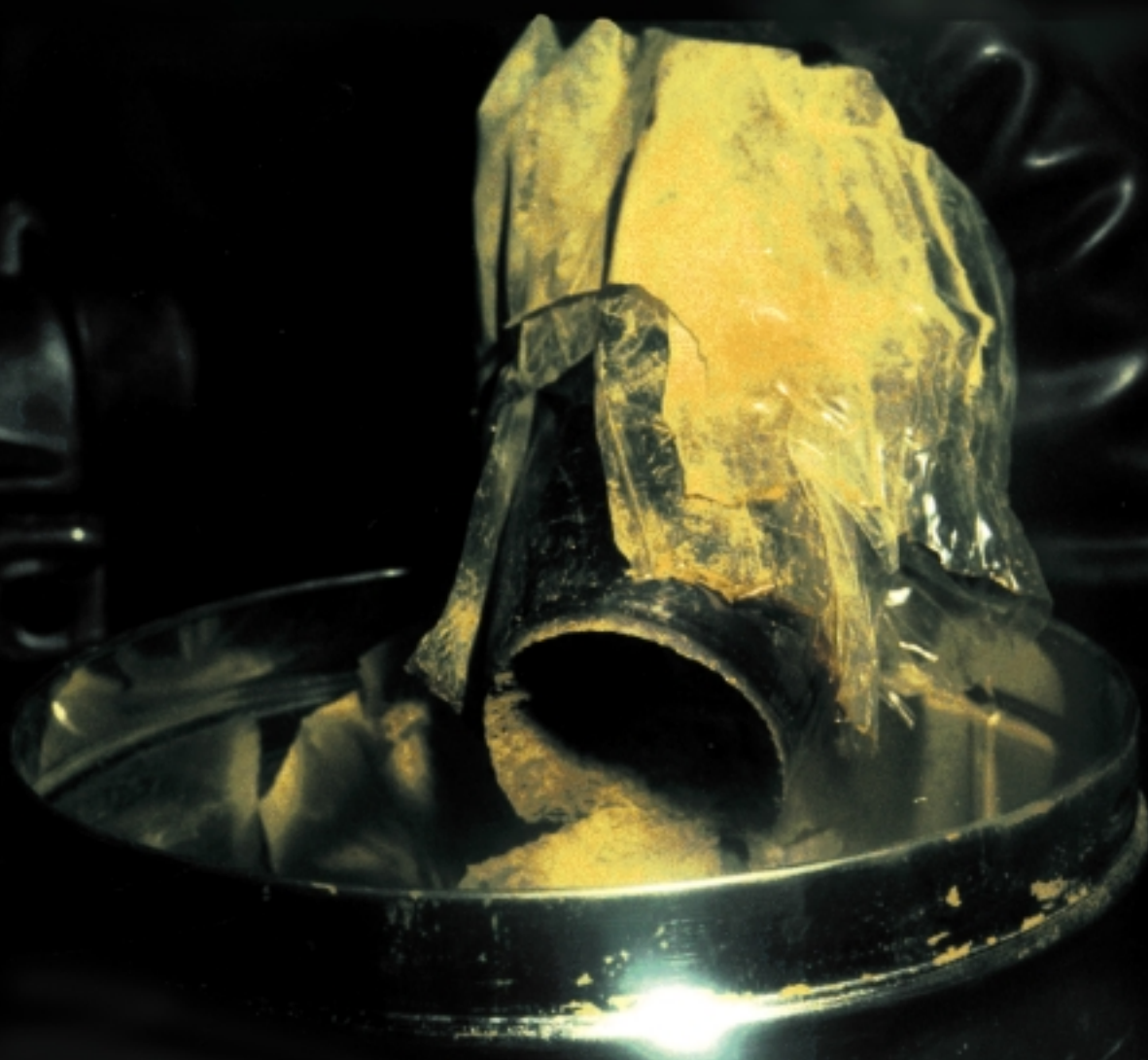
Schonfeld, F. W. 1961a. Phase Diagrams Published by the Russians. In *The Metal Plutonium*, 255. Chicago: The University of Chicago Press.

———. 1961b. Plutonium Phase Diagrams Studied at Los Alamos. In *The Metal Plutonium*, 240. Chicago: The University of Chicago Press.

Timofeeva, L. F. 2000 (to be published). Low-Temperature Equilibrium Aging under Self-Irradiation in Binary Alloys of Pu with Elements of the IIIB Group. In *Proceedings of the International Conference on Ageing Studies and Lifetime Extension of Materials*. Edited by L. G. Mallinson, 191. Dordrecht: Kluwer Academic Publisher.

Surface and Corrosion Chemistry *of* PLUTONIUM

John M. Haschke, Thomas H. Allen, and Luis A. Morales



Elemental plutonium, the form in which most of the weapons-grade material exists, is a reactive metal. When exposed to air, moisture, and common elements such as oxygen and hydrogen, the metal surface readily corrodes and forms a powder of small plutonium-containing particles. Being easily airborne and inhaled, these particles pose a much greater risk of dispersal during an accident than the original metal. The present emphasis on enhancing nuclear security through safe maintenance of the nuclear stockpile and safe recovery, handling, and storage of surplus plutonium makes it more imperative than ever that the corrosion of plutonium be understood in all its manifestations.

Metallic plutonium was first prepared at Los Alamos in 1944, during the Manhattan Project. After samples became available, scientists studied the properties of the metal, including its reactions with air, moisture, oxygen, and hydrogen. Extensive investigation of plutonium continued into the early 1970s, and the results of those studies are documented in the handbooks of chemistry, physics, and metallurgy.

In dry air—less than 0.5 part per million (ppm) of water—at room temperature, plutonium behaves much like other active metals, forming a protective layer of dioxide (PuO_2) on the surface. The PuO_2 layer limits corrosion of unalloyed plutonium to the almost imperceptible rate of 20 picometers per hour. The corrosion chemistry of plutonium is therefore assumed to be relatively simple and well understood, but that assumption is far from true. Unexplained phenomena, such as plutonium pyrophoricity (spontaneous ignition in air) and moisture-accelerated corrosion, in air were observed in the earliest plutonium studies (Cleveland 1979, Wick 1980, Katz et al. 1986). Recent Los Alamos studies confirm and add to these examples of unexpectedly rapid corrosion. Moreover, our analysis suggests that J. T. Waber,

a Los Alamos pioneer in plutonium corrosion, was prescient when he wrote, “Most investigators are inclined to concentrate their attention on PuO_2 , which can be well characterized, and to ignore other compounds that may contribute to the overall corrosion behavior” (Wick 1980). Indeed, we believe that plutonium oxides other than PuO_2 and compounds other than oxides play a potent role in plutonium corrosion. These compounds appear to be catalysts, causing anomalous corrosion reactions to proceed at enormous rates.

“Runaway” reactions can occur under fairly routine conditions. In one case, a failed storage package containing a plutonium casting was examined in a glove box, which had a nitrogen-rich atmosphere (less than 3 percent oxygen) normally used for handling plutonium metal. The package remained there for 3 hours after disassembly and initial inspection. When the workers returned to continue their evaluation, they found that the inner container was hot to the touch and its diameter had increased by 50 percent in the region surrounding the casting (Haschke and Martz 1998b). Our subsequent investigation showed that a corrosion reaction involving both oxygen and nitrogen

initiated spontaneously at room temperature and advanced into the plutonium metal at a rate of more than 1 centimeter per hour (cm/h), or a factor of 10^{10} faster than the corrosion rate in dry air. The reaction generated excessive temperatures and started under conditions that are considered safe for the routine handling of plutonium.

Further studies suggest that the course of corrosion depends very heavily on the chemical condition of the plutonium surface. A surface layer of sesquioxide (Pu_2O_3), which forms in the absence of oxygen, promotes corrosion of the metal by hydrogen. Conversely, a surface layer of hydride (PuH_x , where $1.9 < x < 3$) increases the plutonium oxidation rate in oxygen by a factor of 10^{13} to a value near 3 meters per hour (m/h). Finally, a surface layer of the previously unknown higher oxide PuO_{2+x} , which forms on the PuO_2 layer in the presence of moisture, apparently enhances the bulk corrosion of plutonium metal in moist air. The fact that PuO_2 reacts with water demonstrates that it is thermodynamically unstable in air and environmental media. Evidently, its reaction with water is responsible for both the implosion and the pressurization of sealed containers of plutonium oxide during their extended storage.

In this article, we present our observations and analysis of the chemistry and kinetic behavior of important corrosion reactions involving oxygen, nitrogen, and hydrogen. We observe that PuH_x , Pu_2O_3 , and PuO_{2+x} on the metal surface catalyze anomalous corrosion reactions and that the Pu(III) and Pu(VI) oxidation states are important in addition to the predominant Pu(IV) state. We also outline the kinetics that relates specific surface compounds and conditions to anomalous reactions. Our analysis provides explanations for many puzzling phenomena, but it also leaves a multitude of unanswered questions. We conclude that the present understanding of plutonium chemistry is inadequate and that the new evidence presents an immediate technical challenge to the scientific community.

Plutonium Oxides and Atmospheric Oxidation

Plutonium corrosion and oxidation are often treated as equivalent topics because plutonium oxides are the only products normally observed during atmospheric corrosion. The metal does not react appreciably with elemental nitrogen even at elevated temperatures, although plutonium mononitride (PuN) is a stable compound. Therefore, we begin with a review of oxide chemistry and oxidation kinetics.

Diffusion-Controlled Oxidation in Dry Air. Like aluminum and other reactive metals, plutonium is passivated, or rendered unreactive, upon exposure to air because a coherent (continuous, uncracked) oxide layer rapidly forms over the entire surface. Although oxidation continues despite the protective oxide coating, its rate in dry air at room temperature is extremely low. Evidence from kinetic data demonstrates that the oxidation rate is limited by the rate at which oxygen can diffuse through the oxide surface to the oxide-metal interface.

Figures 1(a)–1(c) show the oxidation

process broken down into a sequence of steps. A freshly burnished surface of plutonium is exposed to oxygen gas. Oxygen molecules (O_2) adsorb on the oxide surface at a concentration determined by temperature and the partial pressure of oxygen in the gas phase. The adsorbed molecules then dissociate on the oxide surface to form atomic oxygen, a species that either recombines or associates with electrons to form oxide ions (O^{2-}). Both adsorption and dissociation depend strongly on the electronic properties of the oxide layer and its ability to transport electrons from the metal to the gas-solid interface. After entering the oxide lattice, O^{2-} diffuses through the oxide layer and ultimately reacts with plutonium to produce oxide, electrons, and heat at the oxide-metal interface. The slowest step in this sequence is called rate limiting because the overall reaction can proceed no faster.

Kinetic data on the thickness τ of the adherent oxide layer as a function of time t demonstrate that classic oxygen diffusion is the rate-limiting step in the $\text{Pu} + \text{O}_2$ reaction. On a freshly burnished plutonium surface, the thickness τ reflects the extent of the reaction. This thickness exhibits parabolic growth, increasing linearly with the square root of t at a fixed temperature T . The rate of reaction, which is the time derivative of the thickness, must therefore be inversely proportional to the thickness, exactly the behavior expected if the rate of reaction is con-

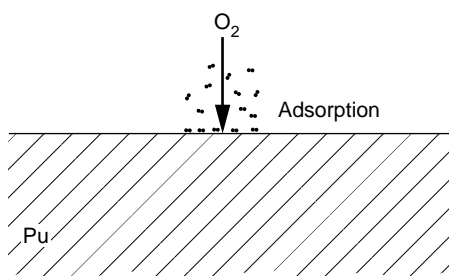
trolled by the rate at which oxygen diffuses through the oxide layer.¹ As the oxide layer gets thicker, the time to diffuse through the layer becomes longer, and thus the oxidation rate decreases with time. Figure 1(d) shows the decreasing slope of the curve describing thickness versus time during parabolic growth.

Parabolic growth tapers off to a steady-state regime when the low-density oxide—11.45 grams per cubic centimeter (g/cm^3)—on high-density plutonium ($19.86 \text{ g}/\text{cm}^3$) begins to induce stresses that lead to the localized spallation of oxide particles from the surface. The thickness of the oxide layer then varies from point to point with regions of thin oxide in recently spalled areas, regions of thick oxide in unspalled areas, and regions of intermediate oxide thickness in between, as illustrated in Figure 1(c). During this stage, the average thickness of the oxide layer and the isothermal oxidation rate reach constant values as diffusion-controlled oxidation continues. The corrosion rate becomes constant because the continuous spallation of oxide particles and the reoxidation of the surface maintain a steady-state diffusion barrier of constant average thickness. As shown in Haschke et al. (1996), the corrosion rate of unalloyed plutonium in dry air at 25°C is approximately 0.5 nanogram of plutonium per centimeter squared a minute ($\text{ng Pu}/\text{cm}^2 \text{ min}$), and the steady-state oxide thickness is 4 to 5 micrometers (Martz et al. 1994).

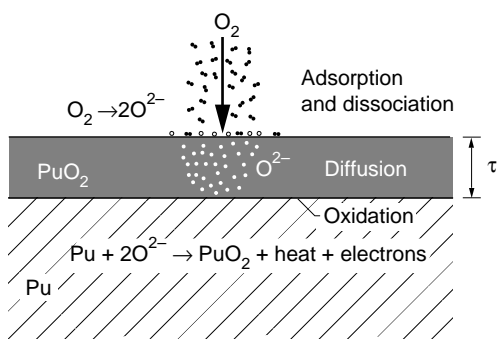
As expected, the diffusion rate through the oxide layer increases strongly with increasing temperature and produces a corresponding increase in the oxidation rate of plutonium. During both the parabolic and constant-rate stages of oxidation, the reaction rate R obeys the classical Arrhenius relationship $R = \exp(-E_a/R^*T)$, where E_a is the activation energy for the reaction and R^* is the gas constant. Activation energies for the parabolic and constant-rate stages are typically derived from the slopes of experimental curves for $\ln R$

¹ For a diffusion-controlled reaction, the rate at which the thickness of the product layer increases is inversely proportional to that thickness, as described by the differential equation $d\tau/dt = k/\tau$. The proportionality constant k is characteristic of the reaction. We derive the parabolic rate law by rewriting this equation as $\tau d\tau = k dt$, integrating it, and applying the boundary condition $\tau = 0$ at $t = 0$. In the resulting expression of the parabolic rate law, $\tau^2 = k_p t$, k_p is the parabolic rate constant that includes the temperature-dependent coefficient for diffusion of the reactant through the product. Diffusion control of the rate is implied if a linear relationship is obtained upon graphing τ or any other experimental measure of the extent of reaction against the square root of t .

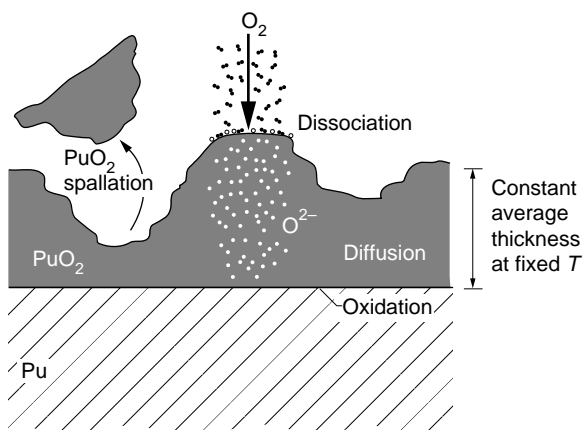
(a) Freshly Burnished Surface



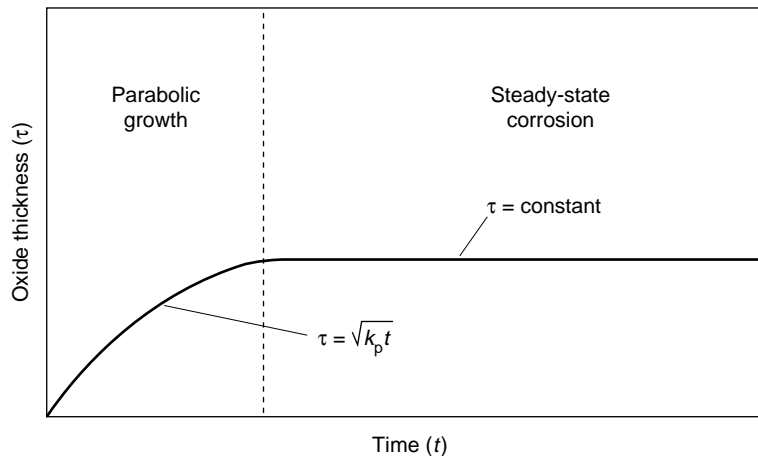
(b) Parabolic Growth



(c) Steady-State Corrosion



(d) Oxide Thickness versus Time

**Figure 1. Standard Chemical Picture of Plutonium Oxidation in Dry Air**

(a) A freshly burnished plutonium surface is exposed to molecular oxygen that readily adsorbs onto the metal surface. (b) The oxygen dissociates into atomic oxygen, and combines with plutonium to form a layer of oxide. Oxidation continues, but now the oxygen on the surface must diffuse through the oxide layer before it can react with plutonium and produce more oxide at the oxide/metal interface. The thickness of the oxide layer increases parabolically with time because its growth is limited by the rate of oxygen diffusion through the oxide layer. (c) At a certain oxide thickness (typically, 4–5 μm), at room temperature, surface stresses cause oxide particles to spall from the surface. The oxide layer reaches a steady-state thickness as further oxidation is counterbalanced by spallation. If the reaction is to occur as outlined in steps (a)–(c), the electrons must be transported from the metal to the oxide surface so that O^{2-} ions should form. (d) The plot of oxide layer thickness (τ) versus time (t) shows the two distinct oxidation stages. During parabolic growth, the reaction extent and τ grow as the square root of t , and the oxidation rate (slope of the curve) continually decreases, indicating that diffusion through the oxide layer is the rate-limiting step in the oxidation process. Later on, the extent of the reaction grows linearly with time, and the corrosion rate becomes constant as continuous spallation of oxide particles and reoxidation of the surface maintain a steady-state diffusion barrier of constant average thickness. Diffusion remains the rate-limiting step.

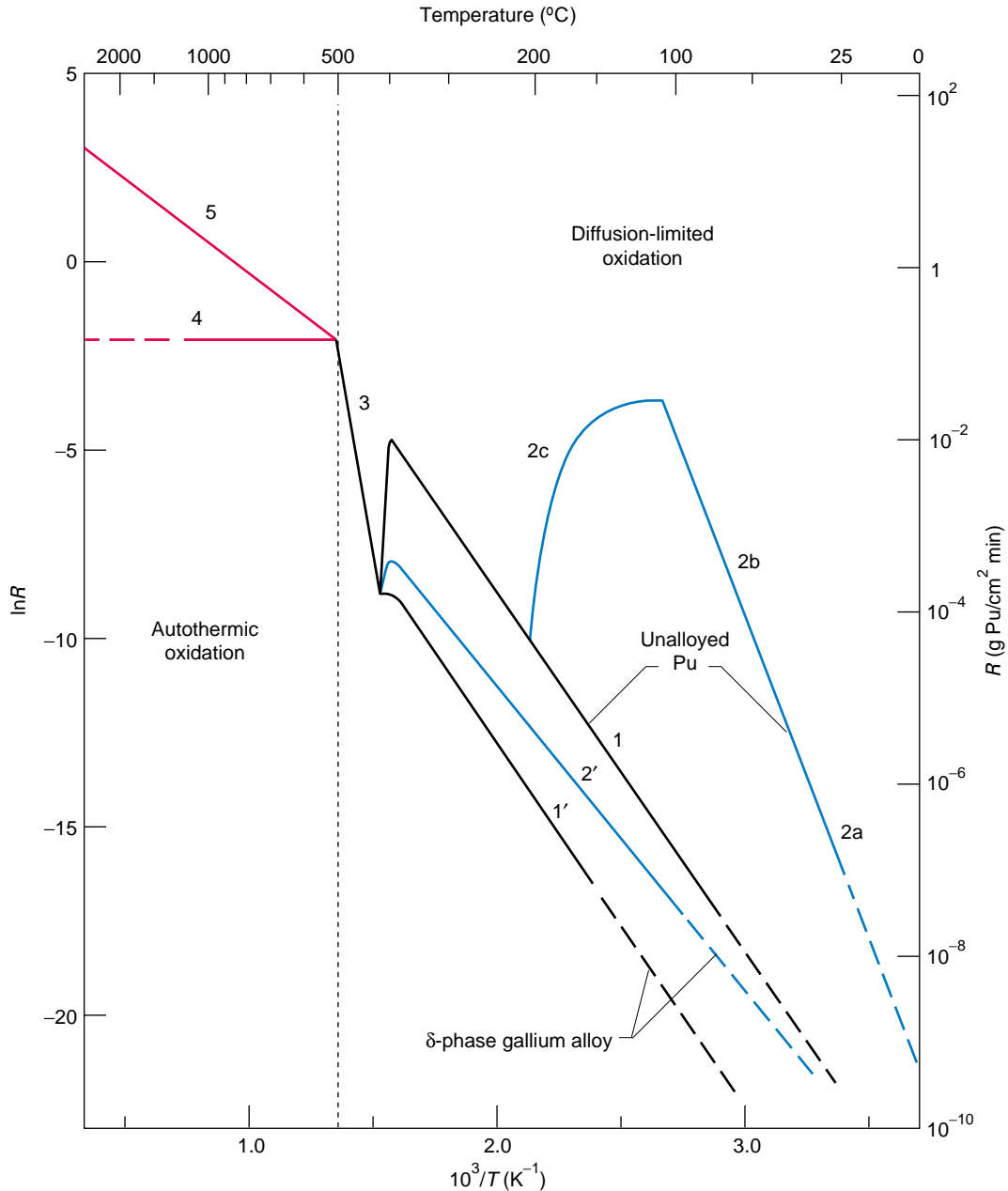


Figure 2. Arrhenius Curves for Oxidation of Unalloyed and Alloyed Plutonium in Dry Air and Water Vapor

Data on the steady-state oxidation rates of alloyed and unalloyed plutonium are summarized for a wide temperature range. Each labeled curve is an Arrhenius plot, showing the natural logarithm (ln) of the reaction rate R versus $1/T$ for a metal or alloy in a specific atmosphere or under a specific condition. The slope of each curve is proportional to the activation energy for the corrosion reaction. Curve 1 plots the well-known oxidation rate of unalloyed plutonium in dry air or dry O_2 at a pressure of 0.21 bar. Curve 2a shows the increase in the oxidation rate when unalloyed metal is exposed to water vapor at equilibrium pressures up to 0.21 bar (160 torr), a concentration equal to the partial pressure of oxygen in air. Curves 2b and 2c show the moisture-enhanced oxidation rate at a water vapor pressure of 0.21 bar (160 torr) in the temperature ranges of 61°C–110°C and 110°C–200°C, respectively. Curves 1' and 2' give the oxidation rates for the δ -phase gallium-stabilized alloy in dry air and moist air (water vapor pressure 0.21 bar), respectively. Curve 3 indicates behavior in the transition region between the convergence of rates at 400°C and the onset of the autothermic reaction at 500°C. Curve 4 defines the temperature-independent reaction rate of ignited metal or alloy under static conditions. The rate is fixed by diffusion through an O_2 -depleted boundary layer of N_2 at the gas-solid interface. Curve 5 shows the temperature-dependent oxidation rate of ignited droplets of metal or alloy during free fall in air.

versus $1/T$ (see Figure 2). Curve 1 shows the oxidation rate of unalloyed plutonium in dry air during the constant-rate stage of the reaction, and its slope yields an E_a of 17.4 kilocalories per mole (kcal/mol).

Variations from the Standard

Diffusion Picture. To get a comprehensive picture of the kinetics of plutonium oxidation, we have reviewed published data and prepared a single graph (Figure 2) of Arrhenius curves for corrosion of unalloyed metal and delta-phase gallium alloy in dry air and water vapor during the constant-rate stage of oxidation. The data are normalized to an oxidant pressure of 0.21 bar, the partial pressure of O_2 in air at 1 atmosphere.

Curve 1, the oxidation rate of unalloyed plutonium in dry air, spans a temperature range in which the metal exists in four allotropic forms: the alpha, beta, gamma, and delta phases. The variations among curves 1, 2a–2c, 1', and 2' reflect the complex effects of temperature, humidity, and alloying on the oxidation rate. The convergence of these curves near 400°C marks the onset of a region (curve 3) in which the oxidation rate depends only on temperature and oxidant pressure. The research we describe below shows that all the curves below 500°C in Figure 2 are consistent with control by classic oxygen diffusion through an oxide layer, even those enhanced by the presence of moisture.²

For completeness, we also include Arrhenius data for the very high temperature range—from the 500°C ignition point of plutonium to the boiling point of the liquid metal at 3230°C . (Haschke and Martz 1998a, Martz and Haschke 1998). Activation energies in this region are difficult to measure because the reaction temperature is

² This enhancement apparently results from an unanticipated increase in the oxygen gradient rather than from a proposed mechanistic change involving diffusion of hydroxide (OH^-) ions, but that story is the most surprising, and we save it for last.

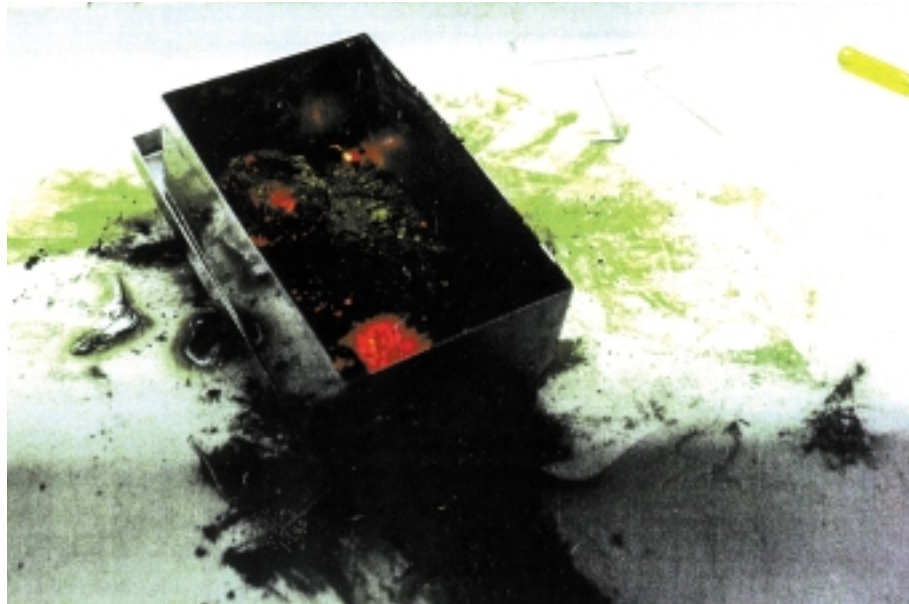


Figure 3. Plutonium Pyrophoricity

Plutonium is shown here spontaneously burning in air under static conditions. The burning metal is glowing like embers as oxidation occurs at the constant rate defined by curve 4 in Figure 2.

determined by the rate of reaction and the accumulation of heat by the reacting metal, not by experimental control. The oxidation rate— $0.14 \text{ gram (g) Pu/cm}^2 \text{ min}$ —for ignited metal droplets in static air (curve 4) is independent of temperature and fixed by the rate of O_2 transport across a boundary layer of oxygen-depleted nitrogen formed at the gas-solid interface of the burning particle. An example of this behavior is illustrated in Figure 3, in which plutonium is shown spontaneously burning in air under static conditions. The oxidation rate ($E_a = 9.6 \text{ kcal/mol}$) for ignited metal droplets in air during free fall (curve 5) is temperature dependent because there is no longer a static nitrogen-rich boundary layer limiting the diffusion of oxygen. Self-heating by the oxidation reaction drives droplet temperatures above the boiling point of plutonium and causes an “explosion” in which unreacted metal vaporizes and burns in a flash.

Although the standard picture of diffusion-controlled oxidation given in Figure 1 seems to apply below 500°C , this model does not account either for

the spontaneous ignition of metal chips and powder in air at 150°C – 200°C or for the large effect of moisture on the oxidation rate (compare curves 2a and 2b with curve 1 in Figure 2). Involvement of compounds other than the dioxide and transport processes other than diffusion must be considered in addressing pyrophoricity, moisture-enhanced oxidation, and other anomalous kinetic behaviors described in subsequent sections of this article.

Pu_2O_3 and the Oxide Layer. The presence of oxide is an unavoidable feature of plutonium metal surfaces. Even if one tries to create a perfectly clean surface through repeated cycles of heating and bombardment by an energetic ion beam in ultrahigh vacuum, several atomic percent of oxygen remains on the surface, as measured by x-ray photoelectron spectroscopy (XPS). Such measurements also show that exposure of a cleaned surface to O_2 at low pressure (about 1 nanobar) immediately produces a surface layer of Pu_2O_3 (Larson and Haschke 1981). Over time, this sesquioxide oxidizes to

PuO_2 even at these low oxygen pressures. If the surface is exposed to air at atmospheric pressure, a coherent layer of PuO_2 quickly forms over the entire metal surface. Thus, a dioxide layer is present on all plutonium metal surfaces after exposure to air unless extreme measures are exercised.

A surprising feature of the oxide layer at room temperature is the apparent absence of Pu_2O_3 . Studies of the plutonium-oxygen system have shown that both Pu_2O_3 and PuO_2 are stable in the solid phase at room temperature. Moreover, above 700°C , the two oxides coexist as a solid solution in which the average composition varies between these oxides as the oxygen-to-plutonium ratio in the system increases from 1.5 to 2. (The mechanism for forming a solid compound with a continuously varying composition is described in the box “Fluorite and Fluorite-Related Structures in Plutonium Corrosion” on page 260.)

Thermodynamic data presented in the box “Thermodynamics, Kinetics, Catalysis, and the Equilibrium State in the Plutonium-Oxygen System” (page 261) verify that Pu_2O_3 is a stable oxide in the presence of plutonium metal. Thus, a thin layer of Pu_2O_3 must be present at the oxide-metal interface of the oxide layer. Because this layer is undetectable at room temperature, we deduce that Pu_2O_3 is readily oxidized to PuO_2 by oxygen and that the observed composition of the oxide layer is determined by the rapid kinetics of PuO_2 formation, not by thermodynamics. This conclusion is supported by our observations that a change in conditions, such as an increase in temperature or a decrease in the availability of oxygen, leads to an increase in the fraction of Pu_2O_3 . Indeed, our recent results (Haschke et al. 1998) strongly suggest both the presence and participation of Pu_2O_3 in the corrosion chemistry of plutonium, possibilities that have not been examined by previous investigators.

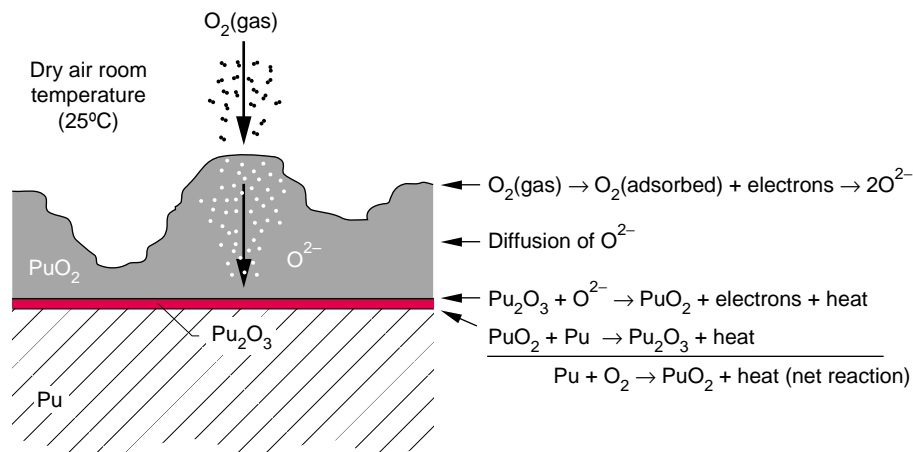


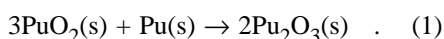
Figure 4. Kinetics of the Steady-State Oxide Layer in Dry Air at Room Temperature

In contrast to the standard picture shown in Figure 1, the oxide layer on plutonium metal in dry air at room temperature must contain a steady-state layer of Pu_2O_3 at the oxide-metal interface (red). Its thickness, however, is small compared with the constant average oxide thickness (4–5 μm) maintained by spallation. The processes producing the slow constant-rate oxidation are shown in the figure. Molecular oxygen adsorbs onto the oxide surface, it dissociates to form oxygen ions, and the ions diffuse through the oxide layer. Autoreduction of the dioxide by the metal at the oxide-metal interface continually produces Pu_2O_3 . This lower oxide then reacts with the diffusing oxygen ions to produce the dioxide. The steady-state oxide layer on plutonium in dry air at room temperature (25°C) is essentially PuO_2 , indicating that oxidation of Pu_2O_3 is the predominant surface reaction.

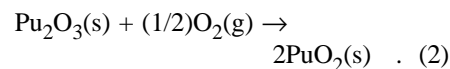
The Pyrophoricity of Plutonium.

The first example of Pu_2O_3 participation is our quantitative model for the pyrophoricity of plutonium chips and powder at 150°C – 200°C (Martz et al. 1994). This model grew from understanding the role of Pu_2O_3 in the kinetics of plutonium oxidation.

Figure 4 shows the revised view of the PuO_2 diffusion barrier in the presence of oxygen. By separating a region with excess oxygen from one with excess plutonium, this barrier creates a nonequilibrium condition on the metal surface, in which Pu_2O_3 is simultaneously consumed and formed by competing reactions. The dioxide is reduced to Pu_2O_3 by plutonium at the oxide-metal interface.



Concurrently, Pu_2O_3 is consumed by reaction with the oxygen that diffuses through the oxide layer:



The ultimate equilibrium state of a reaction depends on the molar ratio of oxygen to plutonium in the product. During corrosion in air, excess O_2 is present, and equilibrium is reached when all the metal is converted to dioxide. In contrast, when placed in a vacuum, an inert atmosphere, or a sealed container, plutonium consumes any residual O_2 and continues to react with the PuO_2 surface until only Pu_2O_3 is present. In the absence of excess oxygen, equilibrium is reached when the PuO_2 layer is completely reduced to Pu_2O_3 by the reaction described by

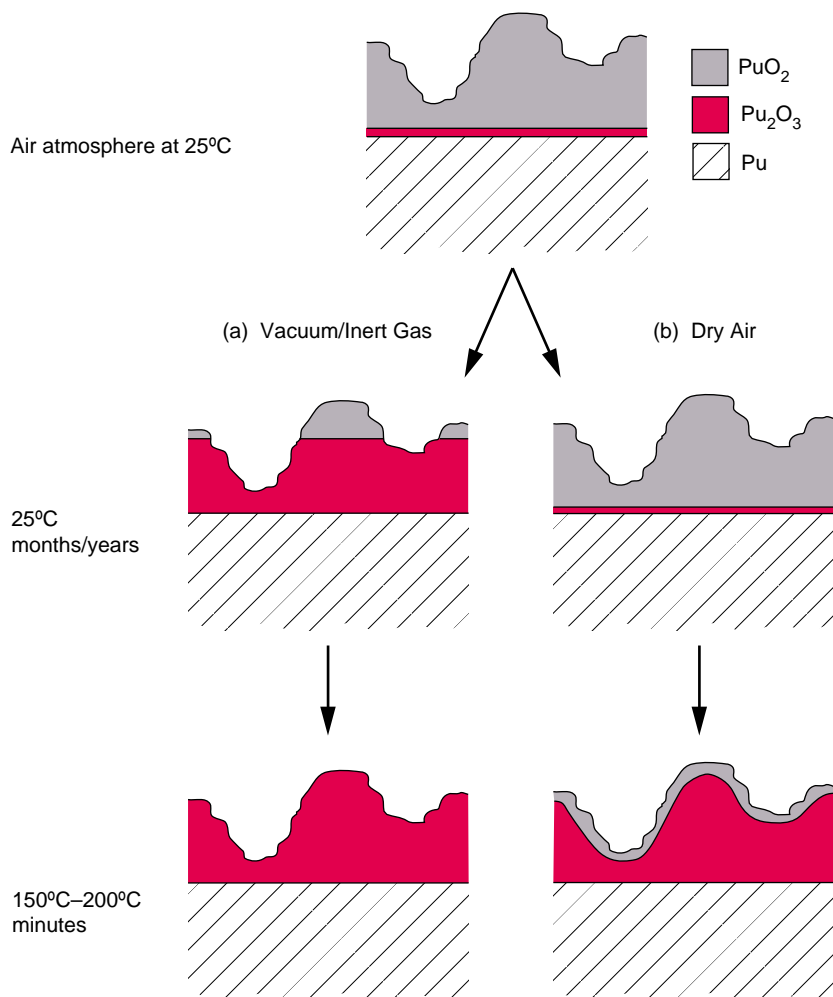


Figure 5. The Oxide Layer on Plutonium Metal under Varying Conditions

These highly idealized sketches indicate how changes in atmosphere, temperature, and time alter the surface chemistry of the oxide layer. The corrosion rate is strongly dependent on the metal temperature and varies significantly with the isotopic composition, quantity, geometry, and storage configuration of the metal. Serving as reference, the steady-state oxide layer on plutonium in dry air at room temperature (25°C) is shown at the top. (a) Over time, isolating PuO₂-coated metal from oxygen in a vacuum or an inert environment turns the surface oxide into Pu₂O₃ by the autoreduction reaction described by Equation (1). At 25°C, the transformation is slow. The time required for the complete reduction of PuO₂ depends on the initial thickness of the PuO₂ layer and is highly uncertain because the reaction kinetics is not quantified. At temperatures above 150°C, rapid autoreduction transforms a several-micrometer-thick PuO₂ layer to Pu₂O₃ within minutes. (b) Exposure of the steady-state oxide layer to air results in continued oxidation of the metal. At 25°C in dry air, the layer is essentially unaltered over time. Kinetic data indicate that a one-year exposure to dry air (<0.5 ppm H₂O at 1 bar of total pressure) at room temperature increases the oxide thickness by about 0.1 μm. At a metal temperature of 50°C in moist air (50% relative humidity), the corrosion rate increases by a factor of approximately 10⁴, and the corrosion front advances into unalloyed metal at a rate of 2 mm per year. At 150°C–200°C in dry air, the rate of the autoreduction reaction increases relative to that of the oxidation reaction, and the steady-state condition in the oxide shifts toward Pu₂O₃, a phase that is simultaneously formed by Equation (1) and consumed by Equation (2).

Equation (1). Indeed, data from x-ray diffraction (XRD) and XPS measurements show that, although the surface layer of PuO₂ on a plutonium sample is not detectably altered when the sample is placed in vacuum at room temperature, the dioxide layer is immediately transformed to Pu₂O₃ when that same sample is heated to 150°C in vacuum. Evidently, the rate of Pu₂O₃ formation according to Equation (1) increases sharply with temperature as shown in Figure 5(a).

Data from XRD and XPS measurements also demonstrate that the oxide layer formed in air at 350°C is predominantly Pu₂O₃ beneath a thin layer of PuO₂ and a higher oxide. (The nature of this higher oxide is discussed later.) In other words, the ratio of Pu₂O₃ to PuO₂ at 350°C is essentially the reverse of that observed at room temperature. This observation and the rapid rate of Pu₂O₃ formation at 150°C suggest that the temperature dependence for oxide reduction, Equation (1), is stronger than for the subsequent oxidation of Pu₂O₃, Equation (2). Therefore, we conclude that the fraction of Pu₂O₃ in the oxide layer during oxidation in dry air increases significantly at elevated temperatures as illustrated in Figure 5(b). This dynamic picture of the oxide layer suggests that plutonium pyrophoricity at 150°C–200°C results from an increased fraction of Pu₂O₃ in the oxide layer at those temperatures.

With this picture in mind, we consider details of plutonium ignition studies performed earlier by numerous investigators, who determined ignition points by heating a metal specimen at a constant rate in flowing air while measuring the metal's temperature. The ignition temperature was marked by the onset of a self-sustained reaction, indicated by a sharp and sustained increase in specimen temperature above the programmed value. Temperature curves for relatively massive (greater than 0.2 millimeter in thickness) pieces of metal with low specific surface areas—less than 5 centimeters squared per gram (cm²/g)—show small thermal spikes at 150°C–200°C, but those samples do not spontaneously

Fluorite and Fluorite-Related Structures in Plutonium Corrosion

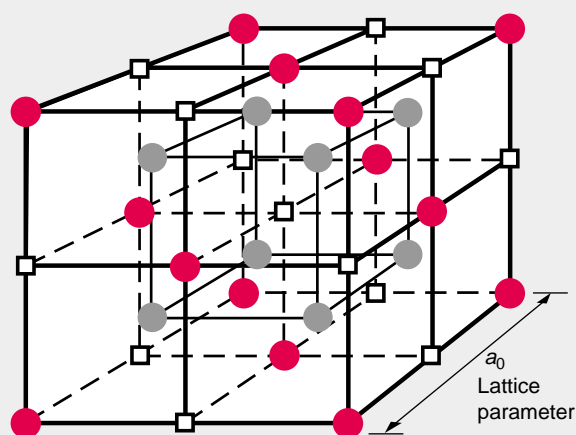
Plutonium-oxygen compounds and many other products of plutonium corrosion form in the classic calcium fluoride (CaF_2) structure or one of its variations (see figure). As discussed below and in the main text, these particular structures seem to facilitate the remarkable catalytic properties of plutonium compounds.

Within the fluorite-type structure, plutonium cations (the red circles in the figure to the right) form a face-centered-cubic (fcc) lattice; that is, they occupy sites at the corners and centers of all the faces of a cube, where a_0 is the length of the cubic cell in angstroms. Atoms at corner sites are shared by eight cubes, and those in faces are shared by two cubes. Thus, four atoms reside within a single unit cell.

Anions such as O^{2-} and H^- occupy interstitial sites within the fcc cation lattice. The figure shows two types of interstitial sites: eight tetrahedral sites (gray circles), each surrounded by four cations, and four octahedral sites (white squares), each surrounded by six cations. The CaF_2 structure has an fcc lattice of cations with even-integer charge ($2n^+$); all tetrahedral sites are occupied by anions with charge n^- . If octahedral sites are also occupied, the resulting structure is identified as a bismuth trifluoride (BiF_3) or tri-iron aluminum (Fe_3Al) type. If anions and cations have the same charge, an ordered occupancy of all octahedral sites or half of the tetrahedral sites forms sodium chloride (NaCl) and zinc sulfide (ZnS) structures, respectively. The CaF_2 -type structure is most frequently observed for hydrides, fluorides, and oxides of such electropositive metals as plutonium.

In the plutonium-oxygen system, Pu(IV) is a stable oxidation state and forms a CaF_2 -type structure at the PuO_2 composition. The trivalent Pu(III) ion is also a relatively stable oxidation state. A cubic form of the oxide ($\alpha\text{-Pu}_2\text{O}_3$) forms at temperatures below 1500°C . The $\alpha\text{-Pu}_2\text{O}_3$ structure is obtained

by ordered removal of 25 percent of the oxide ions from PuO_2 . Above 700°C , a continuous solid solution (PuO_{2-x} , where $0 < x < 0.5$) forms between the two oxide compositions. Each decrease of x in the oxide composition of this solid solution results from the formation of anion vacancies and is accompanied by a $2x$ increase in the fraction of cation sites occupied by Pu(III). A homologous series ($\text{Pu}_n\text{O}_{2n-2}$) of oxide compositions ($n = 7, 9, 10,$ and 12) apparently forms at low temperatures and fixed



The Fluorite (CaF_2) Structure

Cationic positions occupied by plutonium are in an fcc configuration indicated by red circles. Tetrahedral and octahedral sites in the lattice are shown by gray circles and white squares, respectively. The cubic-lattice parameter is defined by a_0 .

ratios of Pu(III) to Pu(IV). A hyperstoichiometric oxide, PuO_{2+x} , forms from PuO_2 by accommodating additional O^{2-} anions at octahedral sites. Charge balance is maintained because Pu(VI) cations replace the usual Pu(IV) cations in the metal lattice.

The fluorite structure also dominates the plutonium-hydrogen system. Plutonium hydride (PuH) crystallizes in a fluorite structure in the plutonium dihydride (PuH_2) composition and forms a solid solution phase, PuH_x , over the range $1.9 < x < 3.0$. Although formation of PuH_2 seems to imply that plutonium is present as Pu(II), a plutonium oxidation state known to be unstable, measurements show that plutonium

is present as Pu(III) and that PuH_2 is metallic. These results suggest that PuH_2 may be formulated as $\text{Pu(III)(H}^-\text{)}_2(\text{e}^-)$, a phase in which charge balance is achieved by two hydride ions plus an electron in a conduction band. This description is consistent with electrical conductivity measurements showing that PuH_x progressively changes from a metallic material to a semiconductor, as x increases from 2 to 3. Electrons are apparently removed from the conduction band and bound as H^- on octahedral sites as the hydride composition increases.

Another example of a fluorite-related structure is provided by plutonium monoxide monohydride (PuOH), which is formed by the reaction of plutonium metal with liquid water at 25°C . Charge balance in this ternary compound of Pu(III) is achieved because O^{2-} and H^- occupy tetrahedral sites equally.

These fluorite and fluorite-related structures provide a stable fcc matrix of invariant, immobile plutonium cations, in which anions are surprisingly mobile. Anions move in and out of the stationary metal as chemical reactions occur and the plutonium oxidation state changes. The NaCl type of plutonium mononitride (PuN) forms from PuH_2 of the CaF_2 type because H^- is displaced from tetrahedral sites and N^{3-} is allowed to occupy all octahedral sites. The rapid rates of ionic transport and exchange are remarkably similar to those of superionic conduction, a phenomenon frequently observed in fluorite materials. Superionic conductors are solids characterized by a very rigid host lattice, light mobile ions, and high direct-current ionic conductivities. Transport in anion-deficient fluorite materials may also be enhanced because both tetrahedral and octahedral sites are vacant and able to participate in the concerted movement of anions. The impact of such factors on the surface and corrosion chemistry of plutonium has not yet been investigated.

Thermodynamics, Kinetics, Catalysis, and the Equilibrium State in the Plutonium-Oxygen System

Plutonium corrosion chemistry involves the complex interplay of thermodynamic, kinetic, and catalytic factors. Although often misunderstood and incorrectly applied, these concepts are the foundation of all chemistry and chemical processing. It is worthwhile to review those concepts and see how their careful application to the plutonium-oxygen system under varying conditions leads to some surprising results.

Thermodynamic properties quantify the fundamental driving force of chemical reactions. In particular, the drive toward thermodynamic equilibrium is due to the energy differences between atoms in different chemical configurations (or states). Energy differences between initial (reactant) and final (product) states are defined by the free energy change (ΔG°) for the reaction. If a reaction releases energy (ΔG° is negative), it is thermodynamically favorable and can occur spontaneously. Conversely, if ΔG° is positive, the reaction is not spontaneous and cannot occur unless sufficient energy is added to the system.

The reaction that occurs in a given system is not necessarily the energetically most favorable one, even though the latter would lead to the equilibrium state of that system. For example, when several reactions with negative free energies are possible, kinetics determines the reaction rate and pathway. In certain systems, energetically favorable reactions never occur at room temperature because their rates are immeasurably slow. Although such systems are not thermodynamically stable, they are kinetically stable, or "metastable." The reaction observed initially is always the one with the highest rate. If that reaction did not have the most negative ΔG° , it would lead to different metastable states and to the possibility of subsequent reactions that progressively move the system toward equilibrium. A system remains in kinetic control until it reaches the equilibrium state.

Catalysts are substances that change reaction rates but not equilibrium states. By altering a reaction pathway, a catalyst increases the rate of the observed reaction or changes the chemistry of the system by enhancing the rate of a competing reaction. Typical catalysts for the reaction of gases are solids with active surfaces that promote the adsorption and dissociation of reactants and their recombination as products.

Applying these principles to the plutonium-oxygen system requires some care. Table I shows that the free energy for oxidizing 1 mole of plutonium into plutonium dioxide (PuO_2) is more negative than that for forming a half mole of plutonium sesquioxide (Pu_2O_3). However, contrary to a widely accepted view, coexistence of a PuO_2 layer and plutonium metal is not always the equilibrium configuration. If oxygen is present in

inherently nonequilibrium condition.

The oxide layer on the metal surface is a diffusion barrier separating an oxygen-rich region and a metal-rich region. Thus, pseudo-equilibrium conditions exist on opposite sides of that barrier. The presence of excess O_2 in the gas phase produces PuO_2 near the gas-oxide interface; the reaction of excess plutonium with the dioxide at the oxide-metal interface yields Pu_2O_3 . At room temperature, the rapid formation of PuO_2 compresses the metal-rich region to the point that Pu_2O_3 is not observed, but increasing temperature promotes the formation of Pu_2O_3 , which becomes dominant above 150°C – 200°C .

Although thermodynamic properties define possible reactions and equilibrium states of chemical systems, they fail to predict the strong metastable behavior of the plutonium-

oxygen system. A system cannot reach equilibrium if slow kinetics prevents the most stable product from forming. Such is the case for the higher oxide, PuO_{2+x} . After early workers had failed to prepare oxides with compositions greater than PuO_2 , they

concluded that the dioxide is the equilibrium oxide in air. Their use of strong oxidants such as ozone (O_3) and nitrogen dioxide (NO_2) increased the free energy for reaction, making the thermodynamics favorable, but slow kinetics prevented further oxidation. Although water is energetically a less favorable oxidant than O_2 , our research has shown that it both participates in and catalyzes the formation of PuO_{2+x} by altering the chemical pathway.

The need to characterize fundamental behavior in a plutonium-oxygen system and in other chemical systems is evident. We are trying not only to understand how water promotes oxidation, but also to define the phase equilibria and thermodynamic properties of PuO_{2+x} .

Table I. Free-Energy Data for the Formation of Plutonium Oxides

Reaction	ΔG° of Reaction	
	(kcal/mol Pu)	(kcal/mol O_2)
$\text{Pu(s)} + \text{O}_2(\text{g}) \rightarrow \text{PuO}_2(\text{s})$	-239	-239
$\text{Pu(s)} + 3/4 \text{O}_2(\text{g}) \rightarrow 1/2 \text{Pu}_2\text{O}_3(\text{s})$	-189	-252

excess, the most stable configuration is, indeed, achieved by reaction of the available metal with the maximum amount of oxygen. The relevant measure of stability is the energy released per mole of plutonium reactant, and PuO_2 is the equilibrium oxide. Conversely, if plutonium is present in excess, the most stable configuration is achieved by reacting the available oxygen with the maximum amount of plutonium. The relevant measure is the energy released per mole of atomic oxygen (O_2), and Pu_2O_3 is the equilibrium oxide on plutonium at room temperature. Thus, the predominance of dioxide on the metal surface at room temperature is clearly controlled by kinetic factors, not by product stability.

Figure 5 in the main text illustrates that exposure of plutonium to the abundant supply of oxygen in the atmosphere creates an

ignite until they reach 500°C ($\pm 25^\circ\text{C}$) during continued heating. In contrast, small pieces—turnings, chips, and powder—with maximum dimensions less than 0.07 millimeter and specific areas greater than 15 cm²/g are pyrophoric when heated to 150°C–200°C in air. The thermal spikes observed at 150°C–200°C decrease in size with increasing specimen thickness, suggesting that pyrophoricity is driven by a surface reaction involving oxides. A surface reaction would produce a fixed amount of heat per unit of surface area, resulting in small thermal spikes for massive pieces of metal and large thermal excursions for material forms with high ratios of specific surface area to volume, exactly the pattern observed.

Our model of pyrophoricity applies the idea of surface reaction to our kinetic picture of the oxide layer. According to the model, heating the metal to 150°C–200°C in dry air transforms a large fraction of the steady-state dioxide layer (4–5 micrometers thick) to Pu₂O₃, as indicated by the lower sketch in Figure 5(b). Rapid oxidation of the Pu₂O₃ layer back to PuO₂ produces 54 kilocalories of heat per mole of dioxide, and a constant oxide thickness fixes the amount of heat produced per unit of surface area. The size of the resulting thermal spike is determined by the rate of reoxidation, the metal's ratio of surface area to volume, and the heat capacities of the oxides and metal.

We have used this model to calculate the thermal excursion of specimens with different dimensions and with geometries having the smallest (spheres) and largest (sheets) ratios of surface area to volume. We assume that the entire oxide layer is Pu₂O₃, reoxidation of Pu₂O₃ is rapid, and all heat from the reaction is instantaneously deposited in the reacting particle. If the excursion for a given metal dimension and geometry exceeds 350°C, we expect the metal temperature to reach or exceed 500°C and predict self-sustained reaction. Results show that pyrophoric behavior is not expected

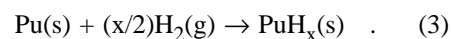
for metal spheres with diameters greater than 0.25 millimeter but is predicted for metal sheets with thicknesses less than 0.09 millimeter. Excellent agreement with experimental observation suggests the validity of our model.

We also propose that a likely mechanism for initiating pyrophoric reaction is exposure of the Pu₂O₃ layer to air by spallation of an oxide particle. A protective PuO₂ layer is not reestablished after ignition because rapid diffusion of oxygen and rapid reduction of PuO₂ to Pu₂O₃ are favored at the elevated temperatures reached during a self-sustained reaction. We also note that diffusion cannot account for the rapid transport of oxygen needed to initiate a self-sustained reaction at 150°C and conclude that Pu₂O₃ promotes transport of oxygen to the oxide-metal interface.

Conjecture on Oxygen Transport in Plutonium Oxide. Of the many kinetic factors introduced in this overview of corrosion in air, the mobility of the oxygen in the product layer is especially important and intriguing. One must wonder why diffusion of oxygen in PuO₂ is slow and rate limiting, whereas transport of oxygen in Pu₂O₃ is apparently very rapid. This behavior and other key properties of solid reaction products are strongly influenced by their crystal structures. All corrosion products formed by reaction with oxygen, hydrogen, and water have structures whose plutonium atoms are arranged in face-centered-cubic (fcc) configurations (see the box “Fluorite and Fluorite-Related Structures in Plutonium Corrosion” on page 260). And the chemical and kinetic behaviors described in this article suggest that the fcc plutonium lattice remains stationary whereas anions such as O²⁻ and H⁻ move in and out of the interstitial sites in that lattice with apparent ease. The facile transport of anions in Pu₂O₃ is neither quantified nor understood but is consistent with enhanced anionic mobility in structures with vacant lattice sites.

Reaction of Oxide-Coated Plutonium with Hydrogen

We now turn to the reaction of plutonium with hydrogen (hydriding), in which surface compounds are, once again, a determining factor. Plutonium hydride (PuH_x) is an fcc phase that forms a continuous solid solution for 1.9 < x < 3.0 (Haschke 1991, Ward and Haschke 1994).



The observed value of x depends on hydrogen pressure and temperature. The hydride is readily oxidized by air, and it decomposes back to its component elements when heated in dynamic (continuously pumped) vacuum.

Hydriding occurs only after the ubiquitous dioxide layer on the metal is penetrated. Unlike oxidation, which proceeds evenly over the entire dioxide surface, the reaction of hydrogen initiates at a limited number of nucleation sites, and a single nucleation site typically appears only after a lengthy, but unpredictable, induction period. Once formed, these sites are the most reactive areas of the surface. They grow like bacterial colonies; that is, the hydriding rate is proportional to the active area covered by the hydride, and it increases exponentially over time to a maximum value as sites grow and ultimately cover the surface. At that point, the rate is enormous and constant because the surface is fully active. For temperatures between -55°C and 350°C and a molecular hydrogen (H₂) pressure of 1 bar, the reaction at a fully active surface consumes plutonium at a constant rate of 6–7 g/cm² min and advances into the metal or alloy at about 20 cm/h.

Curve b in Figure 6 shows that hydriding is 10¹¹ times faster than oxidation of unalloyed metal in dry O₂ at 25°C. Moreover, the hydriding rate is independent of temperature and proportional to the square root of hydrogen pressure, indicating that the rate-controlling step involves dissociation of H₂ at the gas-hydride interface rather

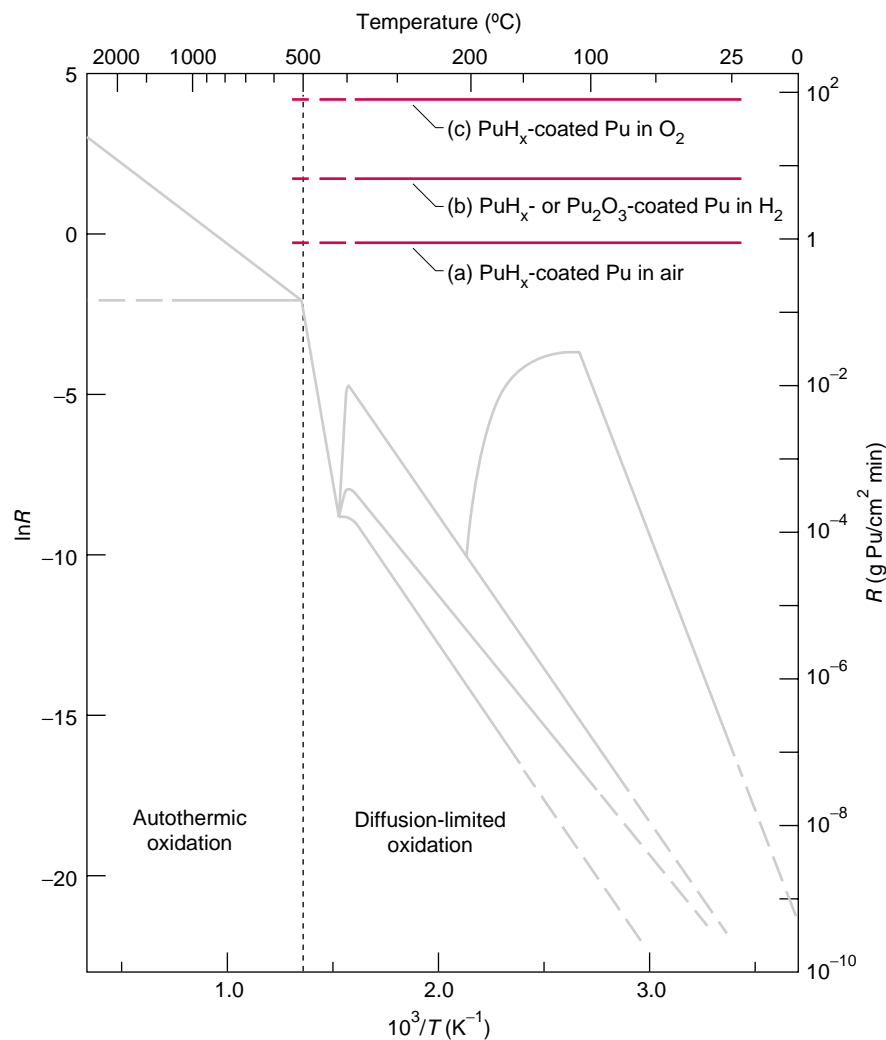


Figure 6. Rates for Catalyzed Reactions of Plutonium with Hydrogen, Oxygen, and Air

The diffusion-limited oxidation data from Figure 2 (shown here in gray) are compared with data for the rates of reactions catalyzed by surface compounds. Curves a, b, and c show the oxidation rates of PuH_x -coated metal or alloy in air, the hydriding rates of PuH_x - or Pu_2O_3 -coated metal or alloy at 1 bar of pressure, and the oxidation rates of PuH_x -coated metal or alloy in oxygen, respectively, all given as a function of temperature. Notice that the rates are extremely rapid, and their values are constant regardless of the change in temperature, indicating that the surface compounds act as catalysts in promoting corrosion.

than diffusion of hydrogen through the surface layer of the hydride product. On the basis of this extremely rapid rate, we conclude that PuH_x catalyzes the dissociation of adsorbed H_2 and promotes the transport of atomic hydrogen to the hydride-metal interface.

A dramatically different kinetic behavior occurs if Pu_2O_3 replaces PuO_2 on the surface layer. Instead of forming

and growing isolated nucleation sites, hydriding of Pu_2O_3 -coated metal proceeds over the entire surface at once. In our studies, we heated PuO_2 -coated metal to 150°C – 200°C in vacuum to transform the surface to Pu_2O_3 —see bottom sketch in Figure 5(a)—then cooled the sample to 25°C , and finally exposed it to H_2 at 1 bar of pressure. We found that the initial (zero time)

hydriding rate equals that attained after the dioxide-coated metal is fully activated by the growth and coalescence of PuH_x sites. These results show that Pu_2O_3 is equivalent to PuH_x as a catalyst for the dissociation of H_2 and as a medium for hydrogen transport to the product-metal interface. Hydriding may nucleate at specific sites on the surface of the dioxide-coated plutonium metal because Pu_2O_3 is exposed at those locations by the autoreduction of the dioxide layer in thin areas or by the spallation of an oxide particle.

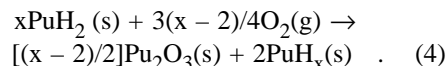
In summary, two independent surface processes catalyze the corrosion rate of oxide-coated plutonium metal by hydrogen. The surface self-activates by the nucleation and growth of PuH_x sites on the dioxide-coated metal or, before it is exposed to H_2 , by the autoreduction of PuO_2 to Pu_2O_3 . In both cases, the catalytic enhancements of the dissociation and transport of H_2 increase the initial corrosion rate at 25°C by a factor of 10^5 .

Reaction of Hydride-Coated Plutonium with Oxygen

Suppose now that the plutonium has been coated with hydride before being exposed to O_2 . We find that PuH_x and Pu_2O_3 are simultaneously involved in promoting an extreme pyrophoricity of both pure hydride particles and hydride-coated metal. We also relate the pyrophoricity of PuH_x to its variable stoichiometry, which allows the hydride to absorb additional hydrogen until x approaches 3. The stoichiometry of PuH_x varies, depending on conditions. Values of x near 2 are favored for surface layers formed on the metal at high temperatures and low H_2 pressures; higher values of x are found on isolated hydride particles at low temperatures and high pressures.

Earlier studies (Haschke 1991) show that particles of PuH_2 react spontaneously and rapidly upon controlled exposure to O_2 at 25°C , and the reaction produces an oxide layer on the

exterior of the particles. The hydrogen produced by this reaction does not appear as H_2 . Instead, it accumulates within the reacting particle, increasing the value of x in the residual PuH_x . Our recent work (Haschke et al. 1998) shows that self-heating from the reaction raises the temperature of the particle so that the oxide product is Pu_2O_3 instead of PuO_2 . The net reaction is given by



Pyrophoricity and rapid oxidation of the hydride are promoted by the absence of gaseous reaction products that would restrict access of O_2 to the surface. As the value of x within a hydride particle approaches 3, the particle ruptures while the equilibrium H_2 pressure rises. The particle's extent of oxidation and ratio of surface area to volume determine the point of rupture.

In recent studies (Haschke et al. 1998), we also focused on hydride-coated metal and alloys and found that they react violently when rapidly exposed to oxygen. We prepared specimens with PuH_2 surface layers (100 micrometers thick) by first heating dioxide-coated plutonium (1–2 millimeters thick) above $150^\circ C$ in vacuum to form Pu_2O_3 on the surface and then exposing that lower oxide layer to the requisite quantity of H_2 . After exposure to excess O_2 , the metal in the hydride-coated specimens was completely consumed in less than 1 second, and the resulting gas-phase temperatures exceeded $1000^\circ C$. Hydrogen was not released as H_2 even though excess O_2 was present. Instead, the hydrogen appeared as a small PuH_3 core inside an expanded product shell of Pu_2O_3 that retained the shape of the starting specimen. The reaction ended so quickly, and the thermal effect was so large that the rate could not be accurately determined by pressure-time data. Based on a reaction time of 1 second, the rate is about $80 \text{ g Pu/cm}^2 \text{ min}$, corresponding to a corrosion rate of 3 m/h.

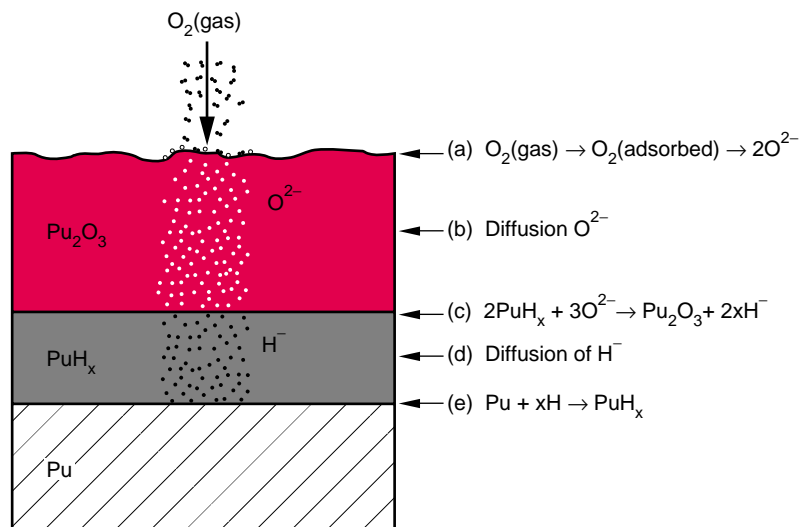
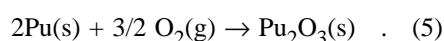


Figure 7. Hydride-Catalyzed Oxidation of Plutonium

After the hydride-coated metal or alloy is exposed to O_2 , oxidation of the pyrophoric PuH_x forms a surface layer of oxide and heat. Hydrogen formed by the reaction moves into and through the hydride layer to reform PuH_x at the hydride-metal interface. In the catalyzed reaction, there are five sequential processes. (a) Under the concentration gradient created by O_2 pressure, oxygen adsorbs at the gas-solid interface as O_2 , dissociates, and enters the oxide lattice as an anionic species. A thin steady-state layer of PuO_2 may exist at the surface. (b) Under the oxygen concentration gradient created by the reaction of O_2 at the surface, oxide ions are transported across the oxide layer to the oxide-hydride interface. We identified the oxide as Pu_2O_3 , but it might also be PuO_{2-x} ($0 < x < 0.5$), the continuous solid-solution phase formed between Pu_2O_3 and PuO_2 above $700^\circ C$. (c) Oxygen reacts with PuH_x to form heat ($\sim 160 \text{ kcal/mol}$ of plutonium) and hydrogen. (d) The hydrogen produced at the oxide-hydride interface moves through the PuH_x layer to the hydride-metal interface under the gradient in hydrogen concentration created by oxidation. (e) The reaction of hydrogen with plutonium produces PuH_x and heat ($\sim 40 \text{ kcal/mol}$ of plutonium).

We attribute the extraordinarily rapid oxidation of hydride-coated plutonium to catalysis by PuH_x . For both the pure hydride and hydride-coated metal, the reaction of O_2 with the hydride initiates spontaneously, produces oxide, and increases the stoichiometry of the hydride by driving the product hydrogen into the solid phase as described by Equation (4). Excess hydrogen in the hydride is continuously produced at the oxide-hydride interface and consumed at the hydride-metal interface. The reaction generates a large amount of heat (approximately 200 kcal/mol of plutonium). At elevated temperatures, the net reaction is accurately described by Equation (5).



This hydride-catalyzed oxidation of plutonium continues until all the metal is consumed and the composition of the residual hydride reaches PuH_3 . Oxidation of that hydride is expected but not observed because the hydride is encased in the thick shell of the silver gray oxide.

The rate of oxidation is definitely much higher than anticipated for a gas-solid reaction. Plutonium hydride is an effective catalyst for the oxidation of plutonium because it forms at a rapid rate via the $Pu + H_2$ reaction and also oxidizes rapidly via the $PuH_x + O_2$ reaction. Thus, the relatively slow $Pu + O_2$ reaction is promoted by participation of the hydride as a reactive intermediate. As detailed in Figure 7, five major processes are

involved in a hydride-catalyzed oxidation: reaction of O_2 at the gas-solid interface, transport of oxygen across the layer of product oxide, oxidation of the pyrophoric hydride at the oxide-hydride interface, transport of product hydrogen across the hydride layer, and reformation of the hydride at the hydride-metal interface. The slowest of these processes apparently determines the corrosion rate, but it has not been identified.

Other compounds also promote rapid corrosion. For example, diplutonium monoxide monocarbide (Pu_2OC), a surface phase incorrectly identified as plutonium monoxide (PuO) in early literature, forms at elevated temperatures and promotes hydriding. We have recently shown (Allen and Haschke 1998) that plutonium monoxide monohydride ($PuOH$) formed by the rapid corrosion of plutonium in salt water also catalyzes the $Pu + O_2$ reaction.

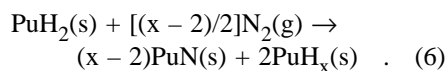
The unusual transport properties of Pu_2O_3 and PuH_x discussed in earlier examples are implied here as well. Based on the observed rate of catalyzed oxidation, the hydride advances into the metal at the rate expected for the reaction of plutonium with H_2 at a pressure of 150 bar. If transport across the hydride layer (approximately 100 micrometers thick) is rate limiting, the coefficient for the diffusion of hydrogen in PuH_x is temperature independent and on the order of 10^{-4} centimeter squared per second (cm^2/s). The corresponding value for the transport of oxygen in Pu_2O_3 must be of equal magnitude or larger. By comparison, coefficients determined for the self-diffusion of oxygen in PuO_2 at $250^\circ C$ – $500^\circ C$ are in the range of 10^{-15} to 10^{-12} cm^2/s (Stakebake 1988). The very rapid temperature-independent transport of both oxygen in Pu_2O_3 and hydrogen in PuH_x suggests that these compounds may be superionic conductors—solids with ionic mobilities and conductivities typically observed in molten salts.

We have shown that plutonium hydride on the metal activates the surface for the catalyzed corrosion with

plutonium. Often the hydride forms from unanticipated sources of hydrogen, such as α -particle radiolysis of organic materials or chemical reactions of water. Regardless of the hydrogen source, the potential consequences are enormous. A comparison of curves c and l in Figure 6 shows that hydride-catalyzed corrosion of δ -phase plutonium alloy by O_2 at $25^\circ C$ is more than 10^{13} faster than oxidation of plutonium in dry oxygen or air.

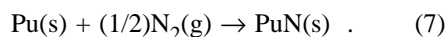
Reaction of Hydride-Coated Plutonium with Air

When exposed to air as opposed to oxygen, plutonium hydride reacts with both oxygen and nitrogen. The $PuH_x + N_2$ reaction is slow at room temperature but occurs readily at temperatures above $200^\circ C$ – $250^\circ C$. According to Equation (4), the reaction of O_2 with pyrophoric hydride produces sufficient heat to promote rapid formation of PuN .



Again, the hydrogen (produced by the oxidation and nitriding reactions) remains in the solid and increases the stoichiometry of residual hydride. Thus, the pyrophoricity of PuH_x is promoted because neither product H_2 nor residual N_2 accumulates and blocks the flow of oxygen to the gas-solid interface.

Plutonium metal coated with hydride also corrodes rapidly when exposed to air, and as in the previous example, the hydride coating catalyzes the reaction. The net reactions for the corrosion of the metal by oxygen and nitrogen in air are defined by Equations (5) and (7), respectively.



Both reactions occur simultaneously at the gas-solid interface and indiscriminately consume nitrogen and oxygen at the molar ratio (3.71 $N_2:1 O_2$) of the elements in air. Hydrogen produced by these reactions is transported across the

PuH_x layer and reacts at the hydride-metal interface. Each mole of air consumes 1.86 moles of plutonium and generates approximately 170 kilocalories of heat. The corrosion rate is independent of temperature and alloying, is proportional to the square of air pressure, and equals 0.7 ± 0.1 g Pu/cm^2 min in air at 1 bar of pressure. If air gains unrestricted access to surfaces of hydride-coated plutonium, a metal specimen with a thickness of 1 millimeter is completely corroded in about 1.5 minutes. We must further characterize the gray corrosion product to determine if it is an oxide-nitride mixture or a single-phase oxide nitride, but we know it reacts slowly in air at room temperature to form PuO_2 .

The presence of hydride on the plutonium surface not only alters the kinetics of corrosion in air, but also changes the chemistry of corrosion. Elemental plutonium and molecular nitrogen (N_2) do not react directly to any significant extent even during their prolonged heating at temperatures above $1000^\circ C$. By contrast, nitrogen is the primary reactant during the hydride-catalyzed corrosion of plutonium in air. As a result, a nitrogen boundary layer does not form at the gas-solid interface as it does during the rapid oxidation of ignited plutonium. Thus, the observed rate for hydride-catalyzed corrosion in air is a factor of 5 faster than the rate for the self-sustained oxidation of ignited plutonium in air.

Compared with the rate for hydride-catalyzed corrosion in O_2 , the rate in air is 100 times slower. This finding suggests that one or more steps involving reaction or transport of nitrogen limit the rate for air. The data in Figure 6 show that the hydride-catalyzed corrosion rate is 10^8 times faster than the oxidation rate of unalloyed metal in saturated water-vapor or moisture-saturated air at room temperature. Occurrence of this hydride-catalyzed reaction in a storage container at Los Alamos is described in the box "Catalyzed Corrosion of Plutonium: Hazards and Applications."

Catalyzed Corrosion of Plutonium: Hazards and Applications

John M. Haschke and Joseph C. Martz

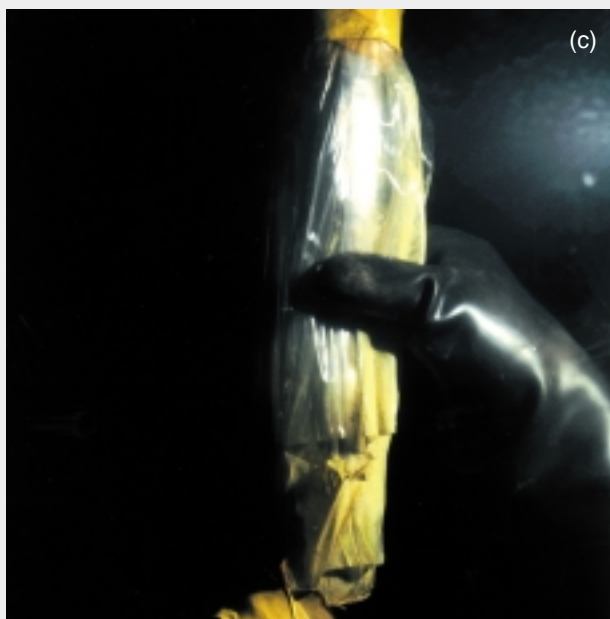
Catalyzed corrosion reactions of plutonium metal are not laboratory curiosities produced by careful manipulation of chemical reactants. Several incidents involving the corrosion of plutonium metal, failure of storage containers, and localized release of plutonium-containing particles into the work environment were attributed to catalyzed corrosion reactions (Haschke and Martz 1998b) and led to redesigning the storage package. In addition, catalyzed corrosion reactions have become the basis of efficient methods for converting plutonium metal from classified weapons configurations into simple ingots.

In 1993, a worker at the Los Alamos Plutonium Facility became contaminated with plutonium-containing particles while handling a standard storage package containing a 2.5-kilogram plutonium casting. The packaging configuration was similar to that used worldwide. It consisted of an inner cylindrical steel container to hold the casting, two layers of sealed "bag-out" plastic to contain radioactive contamination, and an outer slip-lid can. The incident occurred after the package had been stored for 11 years. As the outer can was flexed during handling, a puff of air carrying plutonium-containing particles

escaped through a break in the taped seal of the can and contaminated the worker. The package was placed in a reduced-oxygen (less than 3 percent O₂) glove box, and the inner cylinder was left there for 3 hours after having been removed from the package. The accompanying photographs were taken during the disassembly. As the plastic-wrapped inner

container was lifted out, its end ruptured because of pressure from the continuing rapid formation of plutonium oxides and other low-density corrosion products. A typical plutonium casting would form about 10 grams of PuO₂ per year from normal oxidation in air. Instead, the observed extent of the reaction was many orders of magnitude greater. Also, the inner vessel, which still contained unreacted metal, had become hot, and its diameter had increased by about 50 percent. The vessel was transferred to an argon-filled glove box, where the reaction ceased at once.

Evaluation of this incident shows that hydride catalysis caused by a complex set of physico-chemical processes led to rapid corrosion of



the metal casting during storage and to very rapid corrosion during the 3-hour waiting period in the reduced-oxygen glove box. The weld at the ruptured end of the inner vessel had evidently been defective from the start, allowing gases to be continually pumped in and out of that vessel, as atmospheric pressure changes compressed and expanded the sealed plastic bagging. Plutonium oxide particles were entrained by thermal currents in the vessel, transported through openings in the weld, and deposited on the plastic over several years. During that period, the bagging isolated the metal casting from any external oxygen source, and the normal surface PuO_2 was apparently autoreduced to Pu_2O_3 . Over time, the plastic bagging became discolored near the weld, as well as embrittled from the radiolytic decomposition induced by α -particles emitted from the deposited plutonium oxide particles. The molecular hydrogen produced during the radiolysis of the plastic entered the inner vessel and formed hydride on the Pu_2O_3 -activated surface of the casting. During these processes, the storage package did not change its mass, and therefore the problem was not detected. When the embrittled plastic failed during storage, air reached the inner vessel, and a hydride-catalyzed reaction of the oxygen and nitrogen with the hydride-coated plutonium ensued at a throttled rate determined by access of air to the reaction zone. The resulting expansion of the solid led to the complete failure of the defective weld.

The corrosion rate became rapid during exposure to the glove box atmosphere and was estimated from the dramatic increase in the the vessel's volume during the 3-hour period, the bulk density of the corrosion product, and the approximate surface area of the metal. The result ($0.3 \text{ g Pu/cm}^2 \text{ min}$) is in excellent agreement with the value measured during studies of hydride-catalyzed corrosion ($0.7 \pm 0.1 \text{ g Pu/cm}^2 \text{ min}$).

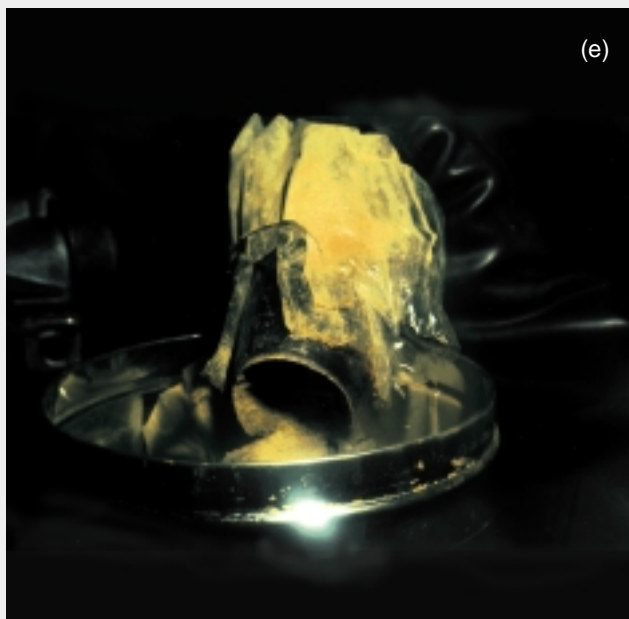
The experience and knowledge we gained from evaluating this incident and from studying catalyzed corrosion reactions find broad application in reducing the nuclear danger. The safe storage of plutonium requires using two metal containers with certified seals and ensuring that organic materials are excluded from the package. These two safety criteria are incorporated in the plutonium storage standards adopted by the U.S. Department of Energy and the International Atomic Energy Agency.

Knowledge of plutonium corrosion kinetics and particle-size distributions for a whole range of conditions enables realistic hazard assessments of plutonium dispersal during accidents. Catalyzed hydriding is also the key reaction in the hydride-dehydride recycle process for destroying weapon configurations and recovering plutonium metal—both done in a single step. Hydride-dehydride recycling generates no mixed or liquid waste of any

kind. The recovered plutonium is a storage-ready ingot, and the hydrogen gas, which is both created and recycled in a uranium hydride storage system, is never released and does not present an explosion hazard. This process was recognized by the *R&D Magazine* as one of the best 100 technical innovations of the year and is the foundation technology of the Automated Retirement and Integrated Extraction System (ARIES) for separating plutonium from weapon components. The hydride-catalyzed oxidation of plutonium holds potential for development as a parallel single-step process in the rapid recovery of plutonium as oxide rather than metal.

Failed Storage Container for Plutonium Metal

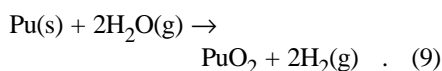
Each photo shows a step in the disassembly of the container for a 2.5-kg casting of plutonium metal. (a) The outer container is placed in a glove box; (b) when the lid is removed, the plastic bagging shows; (c) when the plastic bagging and inner cylinder are lifted out of the container, discolored, embrittled plastic decomposed by radiolysis is revealed; (d) a rupture in the inner container is visible; (e) the corrosion product pours out of the ruptured end; and (f) an increase in the inner vessel's diameter near the ruptured end shows the extent of hydride-catalyzed corrosion during a 3-hour period.



Moisture-Enhanced Oxidation and the Role of Higher Oxides

The moisture-enhanced corrosion of plutonium in air was first observed during the Manhattan Project, but the mechanism of this process remained a mystery until very recently (Haschke et al. 1996, Haschke and Martz 1998b). We shall first outline that mystery.

At room temperature, the corrosion rate of plutonium by water vapor at its equilibrium vapor pressure is more than 100 times faster than the corrosion rate in dry air. At 100°C, the two rates differ by almost 10^5 . Early work showed that exposure of plutonium to both molecular oxygen and water vapor results in the formation of PuO_2 .



Moreover, corrosion rates for moisture-saturated air and moisture-saturated oxygen are equal to those for equilibrium water vapor, suggesting that the oxidation of plutonium metal in the presence of moisture is described by Equation (9). The situation is perplexing because O_2 , not H_2O , disappears from the gas phase during corrosion, and H_2 is not observed as a gaseous product if oxygen is present. Similarly, uranium metal oxidizes faster in moist oxygen than in dry oxygen, but again O_2 disappears, the concentration of H_2O remains constant, and H_2 is not released (Baker et al. 1966). However, after O_2 is depleted from the gas phase, the H_2O concentration decreases at a rate matched by the formation of H_2 .

Early attempts to explain the moisture-enhanced oxidation of plutonium metal involved changes in the mechanism of that reaction: The usual O^{2-} diffusion was eliminated as the rate-limiting step of the oxidation process. Most proposed models assumed that the increased rate was

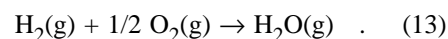
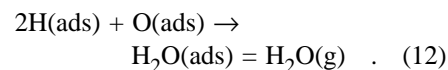
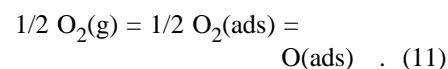
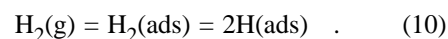
due to the relatively fast diffusion of a hydroxide ion (OH^-) through the oxide layer. Those models suggested a possible explanation for the enhanced rate but did not account for the disappearance of O_2 at the rapid rate characteristic of the $\text{Pu} + \text{H}_2\text{O}$ reaction nor for the formation of oxide as the only corrosion product in moist air. If OH^- were the diffusing species, an equimolar mixture of PuO_2 and PuH_2 would form at the product-metal interface.

We solved the mystery by a number of discoveries. Studying the plutonium-water reaction, we observed a previously unknown product and realized it was an oxide higher than PuO_2 (Stakebake et al. 1993). In separate studies of PuO_2 (Allen and Haschke 1999, Morales et al. 1999), we defined the chemistry of the $\text{PuO}_2 + \text{H}_2\text{O}$ reaction, in which the higher oxide PuO_{2+x} is formed. We also identified the role of this higher oxide in catalyzing the formation of H_2O from H_2 and O_2 . We then realized that PuO_{2+x} would always be found on the surface of plutonium metal in the presence of moisture, increasing the oxygen gradient across the steady-state oxide layer. It then became apparent that O^{2-} is indeed the diffusing species and that the rate of plutonium oxidation increases because a higher oxygen gradient increases the flux of O^{2-} transport through the layer.

Plutonium Dioxide and Water Vapor. We gleaned the key elements of this solution while trying to define safe conditions for the extended storage of surplus plutonium oxide in sealed containers (Haschke and Allen 1995). Our initial concern was the possible radiolysis of water adsorbed on the dioxide surface. Alpha radiation produced in plutonium decay might dissociate water into hydrogen and oxygen and thereby generate unacceptably high gas pressures within the containers. In one test for radiolysis, we exposed PuO_2 to saturated water vapor (0.032 bar) at 25°C. In another test, we exposed the oxide to an $\text{O}_2 + \text{H}_2$ mixture in a 1:2 molar ratio at 25°C and 0.2 bar of total pressure.

We measured kinetic data and identified products by chemical analysis.

These measurements demonstrated that the dioxide surface is an active template for equilibration of the oxygen-hydrogen system. When the dioxide was exposed to the $\text{O}_2 + \text{H}_2$ mixture, both H_2 and O_2 were consumed, and H_2O was formed as the reaction product. The reaction pathway apparently involves adsorption and dissociation of the diatomic gases on the oxide surface—Equations (10) and (11)—followed by association of the atomic species as water—Equation (12).

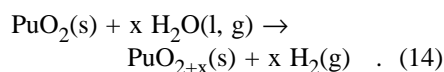


We recently measured the rate of the net reaction defined by Equation (13). At 25°C, the production of water vapor in the presence of the oxide surface is approximately 6 micromoles per meter squared of oxide surface per day (Allen and Haschke 1999).

Molecular hydrogen appears when the dioxide is exposed to water vapor, but O_2 is not observed during these tests. Evidence for the radiolysis of water is absent. If, in fact, water is dissociated by alpha radiation, the O_2 and H_2 products are transient and immediately recombine on the catalytic oxide surface.

Our detection of hydrogen, but not oxygen, during exposure of the dioxide to water vapor is consistent with results of the earlier study (Stakebake et al. 1993), showing that an oxide with compositions substantially greater than PuO_2 forms at the gas-oxide interface during the reaction of plutonium with water vapor. The existence of the higher oxide was surprising and controversial because extensive studies by earlier workers

(Cleveland 1979, Wick 1980, Katz et al. 1986) had shown that PuO_2 does not react with oxygen, ozone, or nitrogen dioxide. The earlier workers concluded that PuO_2 is the highest oxide composition for plutonium. In contrast, our studies with the dioxide and water vapor at 25°C – 350°C and a water vapor pressure of 0.025 ± 0.007 bar (20 ± 5 torr) demonstrate that water reacts with the dioxide to form a higher oxide (PuO_{2+x}) and hydrogen (Haschke and Allen 1999, Morales et al. 1999).



We readily determined the reaction rate and oxide composition by quantifying the production of hydrogen over time.

On the basis of this work, we conclude that the $\text{PuO}_2 + \text{H}_2\text{O}$ reaction in Equation (14) is a normal chemical process and is not promoted by radiolysis. The release of hydrogen from the oxide surface implies that the plutonium oxidation state in the product oxide is higher than Pu(IV). It also implies that mass increases observed by earlier workers during studies under humid conditions cannot be attributed solely to adsorption of water on the oxide surface. We measured a constant reaction rate of $6 \text{ nmol H}_2/\text{m}^2$ of oxide per day at room temperature and found that the rate of hydrogen production increases systematically with temperature. An Arrhenius analysis of the data yields an activation energy of 9.4 kcal/mol . Compositions in excess of $\text{PuO}_{2.25}$ are formed, but the maximum value of x is unknown. In the box “ PuO_{2+x} : The Stable Oxide of Plutonium in Air and the Environment,” we describe additional properties of PuO_{2+x} .

Plutonium Dioxide and Moist Air.

The studies of PuO_2 in moist air unequivocally demonstrate that, relative to PuO_{2+x} , PuO_2 is thermodynamically unstable in moist air over a substantial

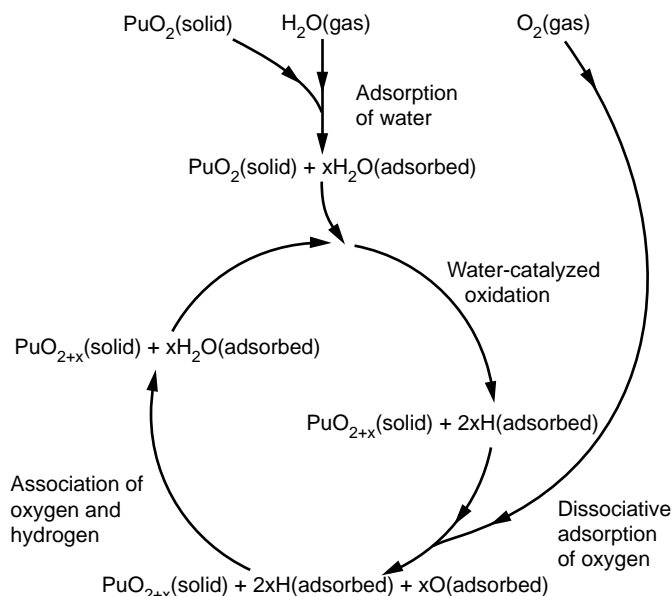


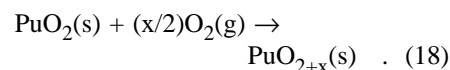
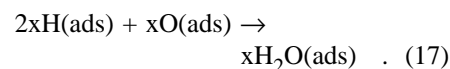
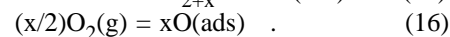
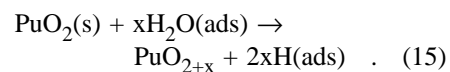
Figure 8. Moisture-Enhanced Oxidation of Plutonium Dioxide

When PuO_2 is exposed to moist air, a cyclical reaction begins, in which a higher oxide of plutonium is formed. The cycle initiates by adsorption of water on the dioxide and its subsequent reaction to form a higher oxide and adsorbed hydrogen. The cycle continues as oxygen, adsorbed and dissociated on the oxide surface, is consumed either by reacting with the adsorbed hydrogen to reform water or by reacting with the oxide to increase its oxygen content. The amount of water remains constant until all the oxygen is consumed. The reaction of water with the oxide continues in the absence of oxygen until all the water is consumed. Hydrogen formed in this reaction is released as gas.

range of temperatures. Therefore, PuO_2 must be unstable in an atmosphere of oxygen, ozone, or nitrogen dioxide. The failure of early workers to obtain PuO_{2+x} by exposing the dioxide to strong oxidants is undoubtedly a consequence of the very slow kinetics for the oxidation reaction. In contrast, according to Equation (14), the reaction of PuO_2 with H_2O occurs at a significant rate and is relatively easy to observe. Although we did not detect the formation of the higher oxide during exposure of the dioxide to dry oxygen, we did observe it when we added moisture to the system. Moreover, the behavior of the system was parallel to that encountered during the moisture-enhanced corrosion of plutonium metal: O_2 was consumed at the rate observed for the $\text{PuO}_2 + \text{H}_2\text{O}$ reaction, but H_2 was not produced until oxygen was depleted.

Defining the steps in the net reaction

between PuO_2 and moist air is essential for understanding the moisture-enhanced corrosion of plutonium metal. The observed interactions of PuO_2 with water and oxygen-hydrogen mixtures in air suggest that the reaction of PuO_2 with moist air proceeds via a catalytic cycle at the gas-solid interface described below and shown in Figure 8.

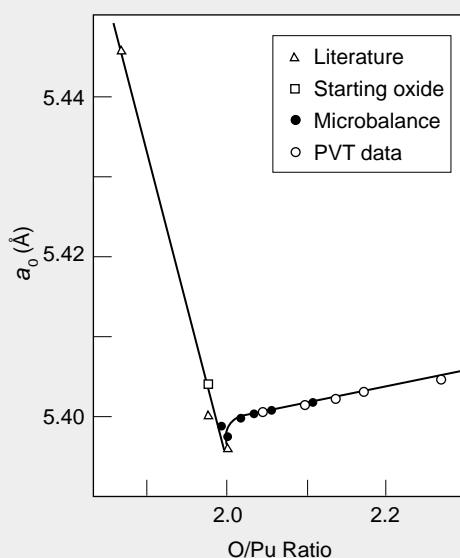


The reaction of adsorbed water with PuO_2 to form PuO_{2+x} described by Equation (15) is faster than the

PuO_{2+x}: The Stable Oxide of Plutonium in Air and the Environment

Thermochemical predictions and results of extensive experiments between the 1940s and 1970s led researchers to conclude that plutonium oxides with compositions greater than PuO₂ are unstable and cannot be prepared. Recent results discussed in the main article show, however, that a hyperstoichiometric oxide (PuO_{2+x}) is the thermodynamically stable plutonium phase in air at temperatures between 25°C and 350°C. The PuO₂ + H₂O reaction produces the higher oxide and hydrogen, and the standard enthalpy and free energy for the formation of PuO_{2.25}(s) at 298 K are more negative than -270 and -253 kilocalories per mole (kcal/mol), respectively. Corresponding values for the formation of PuO₂(s) are -252.4 and -238.5 kcal/mol. Although favored thermodynamically, the reactions of O₂ and other strong oxidants with PuO₂ are not observed because they occur extremely slowly. In contrast, the reaction of the dioxide with liquid or gaseous water is kinetically favorable at low temperatures and is easily monitored by measurement of the extent to which H₂ forms. Pressure-volume-temperature methods are used for those measurements.

Data from the x-ray diffraction of PuO_{2+x} products obtained from kinetic studies reveal a fluorite-related face-centered-cubic (fcc) structure with lattice parameters near those of PuO₂. The graph plots the variation of the lattice parameter a_0 versus oxide composition. Below the dioxide stoichiometry (O/Pu = 2), a_0 decreases steeply with increasing oxygen content. Above the dioxide stoichiometry, the lattice parameter is surprisingly insensitive to composition. Evidently, the two simultaneous changes tend to have opposite effects on the lattice parameter. The proposed replacement of Pu(IV) by Pu(VI) at the cationic sites of PuO₂ tends to shrink the lattice, whereas the occupation of octahedral sites by the additional oxygen atoms tends to expand the lattice. Note that x-ray photoelectron spectroscopy data



The Dependence of a_0 for PuO_{2±x} on Composition

The lattice parameter a_0 is plotted as a function of increasing oxygen content. Below the dioxide stoichiometry, the lattice parameter decreases sharply with increasing oxygen content. Above the dioxide stoichiometry, the lattice parameter increases very slowly. The open triangles indicate reference data from literature sources. The open squares show data from the high-purity weapons-grade oxide used in our study. Filled and open circles show lattice parameters for products obtained during microbalance and pressure-volume-temperature (PVT) experiments with water vapor at 0.025 bar of pressure and temperatures in the range of 25°C to 350°C. The data point for the highest reported composition (O/Pu = 2.265) is from a literature source (Haschke 1992) describing PVT experiments of plutonium corrosion in aqueous salt solutions at 25°C. Molecular hydrogen was generated beyond the PuO₂ stoichiometry, but the experiment had been terminated before the maximum oxide composition was reached. An appropriate mass loss was observed when the PuO_{2.265} product was heated at 500°C in dynamic vacuum until its mass became constant. The lattice parameter of the fired product (5.395 Å) corresponds to that of PuO₂.

verify that Pu(VI) is present in PuO_{2+x}, and preliminary neutron-diffraction results for ²⁴²PuO_{2+x} indicate that the additional oxygen anions in PuO_{2+x} occupy the vacant octahedral sites of the fluorite structure. The net result is that a_0 changes very slowly above the dioxide stoichiometry (an increase of 0.0018 angstrom for each increase of x by 0.10). It is also interesting that the presence of the higher oxide is easily detected by a color change. The PuO₂ and PuO_{2-x} phases are a dull yellow to khaki color, whereas PuO_{2+x} is green.

The formation of PuO_{2+x} may have far-reaching consequences. In addition to promoting the corrosion rate of plutonium in moist air, the reaction of H₂O with the oxide generates hydrogen pressures capable of rupturing sealed containers during extended storage of the oxide. For this reason, plutonium oxide must be fired before it is packaged in sealed containers for extended storage. This process removes water and makes the oxide less soluble. Firing eliminates the higher oxide and thus Pu(VI). The presence of U(VI) increases the solubility of the higher uranium oxide UO_{2+x}, and the absence of Pu(VI) is expected to reduce the dissolution rate.

The PuO_{2+x} phase forms in conditions present in natural systems, implying that the higher oxide is the stable phase in the environment. Failure of x-ray diffraction measurements to identify a higher oxide is consistent with the insensitivity of a_0 to oxide composition. Recent x-ray absorption fine-structure, or XAFS, results indicate that only PuO₂ is present in the environment. Additional work is needed to resolve this discrepancy.

$\text{PuO}_2 + \text{O}_2$ reaction and determines the rate at which the higher oxide is formed. Atomic hydrogen produced by this reaction is not released as H_2 but remains on the oxide surface and recombines with O_2 to form water. According to Equation (16), adsorption and dissociation of O_2 on the dioxide surface, which we first identified in the oxygen-hydrogen-dioxide system, appear here as integral steps of the oxide-catalyzed reaction of H_2 with O_2 to form water. A water-catalyzed cycle is entered as H_2O from Equation (17) reacts with PuO_{2+x} from Equation (15) to progressively increase the x of the higher oxide. Equation (18) gives the net reaction for the process.

The catalytic cycle defined by Equations (15)–(17) accounts for the unusual behavior encountered during the reaction of PuO_2 with moist air or moist oxygen. In water vapor, the rate at which PuO_{2+x} forms is determined by the rate of Equation (14). In moist O_2 , the higher oxide forms at the same rate but by following Equation (15). However, the hydrogen atoms formed by the reaction of H_2O molecules immediately recombine with oxygen atoms from O_2 . Oxygen is consumed according to Equation (18) at the same rate as in the $\text{PuO}_2 + \text{H}_2\text{O}$ reaction, but H_2 is not observed. The net reaction involves two catalytic processes acting in concert: first, H_2O acts as a reactive intermediate (or catalyst) in promoting the oxidation of PuO_2 by O_2 , and second, the oxide surface acts as a catalyst in promoting the regeneration of H_2O .

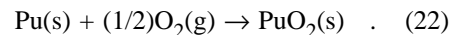
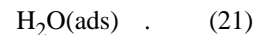
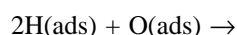
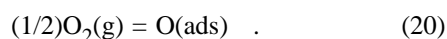
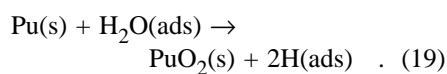
We can now explain the unanticipated implosion of storage vessels containing plutonium oxide. Although the reaction of the oxide with residual water shown in Equation (14) is expected to pressurize containers with H_2 , negative pressures are observed in cans containing unfired oxide that was originally packaged in air. As demonstrated in laboratory tests, the pressure decreases because of the moisture-catalyzed reaction of the oxide with oxygen according to Equations (15) to (17). However, reduced pressure is a

transient condition. After the O_2 in the storage atmosphere has been depleted, the pressure rises as the reaction of the residual H_2O produces H_2 .

Plutonium Metal and Moist Air.

Likewise, the catalytic cycle in Figure 8 can explain the moisture-enhanced corrosion of plutonium metal because that cycle creates PuO_{2+x} on the surface of the oxide-coated metal. The result is a gradient in the oxygen concentration across the oxide layer—from a higher concentration at the gas-oxide interface to a lower concentration at the oxide-metal interface. Earlier in this article, we described how the transport of oxygen from the surface to the oxide-metal interface determines the oxidation rate of plutonium in dry air. That rate of transport depends on three factors: the thickness of the coherent oxide layer, the temperature-dependent coefficient of oxygen diffusion in the oxide, and the gradient in oxygen concentration across the oxide layer. In the steady-state situation, when the temperature is fixed and the thickness of the oxide layer is constant because of continual spallation from the surface, the increase in the oxygen gradient produced by the formation of the higher oxide should increase the rate of oxygen transport to the oxide-metal interface and thereby the oxidation rate. In contrast, the higher oxide is not readily formed by dry air, and the lower rate of oxygen transport leads to a lower corrosion rate.

Thus, we find that the chemistry of plutonium corrosion in moist air or moist oxygen is consistent with a catalytic cycle similar to that proposed for the reaction of the dioxide with moist oxygen. The process is driven by the kinetically favored reaction of the metal with water as defined by Equation (19).



Instead of forming H_2 by Equation (9), as shown for water vapor, the product hydrogen from the $\text{Pu} + \text{H}_2\text{O}$ reaction combines with oxygen to regenerate water on the oxide surface. As described by the net reaction in Equation (22), O_2 and plutonium are consumed at the rapid rate characteristic of the $\text{Pu} + \text{H}_2\text{O}$ reaction. Retention of hydrogen at the surface implies that O^{2-} is the diffusing species in the oxide layer and that the rate is controlled by oxygen diffusion through the oxide layer, as it is in the reaction of plutonium with dry air.

In summary, the moisture-enhanced corrosion of plutonium in air apparently proceeds via a complex catalytic cycle in which plutonium oxide with a high stoichiometry is formed. Enhanced corrosion of plutonium would also occur if both H_2 and O_2 were present because the oxide surface would catalyze the formation of H_2O . Note that hydrogen often forms gradually through the thermal or radiolytic decomposition of organic materials. As shown in Figure 2, the effects of moisture on plutonium corrosion are evident at temperatures of up to 400°C .

Conclusions and Future Directions

Almost 60 years after it was first made in the laboratory, plutonium is still yielding surprises. We have observed unanticipated reactions and new compounds in various binary and ternary combinations of plutonium, oxygen, and hydrogen. We have also found that the reaction kinetics of those systems is extremely important in determining the reaction products. Our understanding of the chemistry of those systems seems surprisingly inadequate.

Although not reported in this article, we have also observed that the salt-

catalyzed corrosion of plutonium metal by liquid water forms a rich variety of products including oxide hydrides, Pu_2O_3 , mixed-valence oxides of Pu(III) and Pu(IV), and PuO_2 . The higher oxide PuO_{2+x} forms as well, but it was identified only recently. Like the catalytic compounds Pu_2O_3 , PuH_x , and PuO_{2+x} discussed in this article, the products obtained in aqueous media apparently have fluorite-related structures. We wonder about the importance of such materials in determining the solid-state chemistry of plutonium. More work is needed to define corrosion processes and products. We must investigate structures, thermodynamics, conductivities, transport processes, and other fundamental properties of plutonium compounds to understand how they influence the corrosion chemistry of plutonium.

We are intrigued by the consistent appearance of catalytic activity during plutonium corrosion. Although we have demonstrated the effects of surface chemistry and catalytic materials on bulk corrosion kinetics for several systems, studies are far from exhaustive. We must investigate catalytic behavior at the atomic level to augment our understanding and interpretation of kinetic results and other macroscopic observations. The following are some important research efforts in this regard: characterization of adsorption processes and adsorbates, definition of surface reactions at the atomic level, and determination of relationships between a solid's catalytic activity and electronic structure.

Of particular relevance are our continuing efforts to explore moisture-enhanced plutonium oxidation and to define the phase equilibria and thermodynamic properties of PuO_{2+x} , the higher plutonium oxide. By measuring the dissolution rates and solubilities of PuO_{2+x} in aqueous media, we hope to understand the role of PuO_{2+x} in plutonium transport. Formation of PuO_{2+x} and leaching of the hexavalent ion are consistent with the appearance of Pu(V) and Pu(VI) in aqueous media.

Another area in which the new findings on plutonium corrosion are indispensable is estimating dispersal hazards during accidents involving nuclear weapons or surplus nuclear material. Metallic plutonium is essentially nondispersible; it therefore presents very little risk of being released into the environment during an accident. In contrast, fine plutonium-containing particles (less than 10 micrometers in diameter) produced by corrosion are at much greater risk of being dispersed. When the solid expands or when gas forms during corrosion, pressures are generated that are known to rupture storage containers and release radioactive materials (Haschke and Martz 1998b). Moreover, mixtures containing hydrogen can form and explode, thus posing additional hazards. To a large extent, this potential hazard depends on the corrosion rate, size distribution of product particles, and time of corrosion, a period that may be as short as hours for accidents or as long as decades for storage.

We conclude that surface compounds are extremely important in determining the course and kinetics of plutonium corrosion and that both the chemical history and external conditions determine the chemical nature of the metal surface. We have been able to identify and characterize surface compounds and determine their effects on the reaction kinetics of plutonium metal and plutonium compounds. But the implications of our recent findings on plutonium technology have yet to be assessed. Certainly, our results are relevant to plutonium recovery, reprocessing, storage, accident assessment, and environmental migration. Continued investigation is therefore a must. ■

Further Reading

- Allen, T. H., and J. M. Haschke. 1998. "Hydride-Catalyzed Corrosion of Plutonium: Initiation by Plutonium Monoxide Monohydride" (June). Los Alamos National Laboratory report LA-13462-MS.
- Allen, T. H., and J. M. Haschke. 1999. "Interaction of Plutonium Dioxide with Water and Oxygen-Hydrogen Mixtures" (January). Los Alamos National Laboratory report LA-13537-M.
- Baker, M. McD., L. N. Ness, and S. Orman. 1966. *Transactions Faraday Society* **62**: 2525.
- Cleveland, J. M. 1979. *The Chemistry of Plutonium*. Chap. 9. La Grange Park, IL: American Nuclear Society.
- Haschke, J. M. 1991. Actinide Hydrides. In *Topics in f-Element Chemistry: Synthesis of Lanthanide and Actinide Compounds*. Chap. 1, p. 1. Dordrecht, The Netherlands: Kluwer Academic Publishers.
- Haschke, J. M. 1992. Hydrolysis of Plutonium: The Plutonium-Oxygen Phase Diagram. In *Transuranium Elements: A Half Century*. Edited by L. R. Morss and J. Fuger. Chap. 4. Washington, DC: American Chemical Society.
- Haschke, J. M., and J. C. Martz. 1998a. *Journal of Alloys and Compounds* **266**: 81.
- Haschke, J. M., and J. C. Martz. 1998b. Plutonium Storage. In *Encyclopedia of Environmental Analysis and Remediation*. Vol. 6, p. 3740. New York: John Wiley and Sons.
- Haschke, J. M., T. H. Allen, and Luis A. Morales. 2000. Reaction of PuO_2 with Water: Formation and Properties of PuO_{2+x} . *Science* **287**: 285.
- Haschke, J. M., T. H. Allen, and J. C. Martz. 1998. *Journal of Alloys and Compounds* **271**: 211.
- Haschke, J. M., T. H. Allen, and J. L. Stakebake. 1996. *Journal of Alloys and Compounds* **243**: 23.
- Katz, J. J., G. T. Seaborg, and L. R. Morss, eds. 1986. *The Chemistry of the Actinide Elements*. Vol. 1, Chap 7. New York: Chapman and Hall Ltd.
- Larson, D. T., and J. M. Haschke. 1981. *Inorganic Chemistry* **20**: 1945.
- Martz, J. C., and J. M. Haschke. 1998. *Journal of Alloys and Compounds* **266**: 90.

Martz, J. C., J. M. Haschke, and J. L. Stakebake. 1994. *Journal of Nuclear Materials*. **210**: 130.

Morales, L. A., J. M. Haschke, and T. H. Allen. 1999. "Kinetics of Reaction between Plutonium Dioxide and Water at 25°C to 350°C: Formation and Properties of the PuO_{2+x} Phase" (May). Los Alamos National Laboratory report LA-13597-MS.

Stakebake, J. L. 1988. "Calculation of Oxygen Diffusion in Plutonium Oxide Films during Oxidation of Plutonium 1 Weight Percent Gallium in 500 Torr Air" (May). Rocky Flats report RFP-3790.

Stakebake, J. L., D. T. Larson, and J. M. Haschke. 1993. *Journal of Alloys and Compounds* **202**: 251.

Ward, J. W., and J. M. Haschke. 1994. Comparison of 4f and 5f Element Hydride Properties. In *Handbook on the Physics and Chemistry of Rare Earths*. Vol. 18, p. 293. New York: Elsevier Science.

Wick, O. J., ed. 1980. *Plutonium Handbook*. Chaps. 6, 8, 11, and 12. La Grange Park, IL: American Nuclear Society.



John M. Haschke received his undergraduate degree from Texas Tech University, did post-graduate work as a Fulbright Fellow at Johannes Gutenberg University in Mainz, Germany, and obtained his Ph.D. degree from Michigan State University. His thesis was on the equilibrium and thermodynamic properties of lanthanide compounds at high temperatures. After working as a postdoctoral fellow at Arizona State University, Haschke joined the faculty in the Department of Chemistry at the University of Michigan. Haschke began his career in actinide chemistry as a research scientist for Rockwell International at the Rocky Flats Plant and developed his skills as a visiting scientist at the Institute for Transuranium Elements at Karlsruhe, Germany, before becoming a staff member at Los Alamos National Laboratory. His research interests have focused on fundamental aspects of plutonium corrosion chemistry and on their application to enhancing plutonium process operations, ensuring safe storage of surplus nuclear material, assessing hazards, and maintaining the nuclear stockpile. Haschke has published more than 150 technical papers and has authored several review chapters on lanthanide and actinide chemistry. He is currently working as an independent consultant on plutonium chemistry.

Catalyzed Corrosion of Plutonium: Hazards and Applications

John M. Haschke and Joseph C. Martz

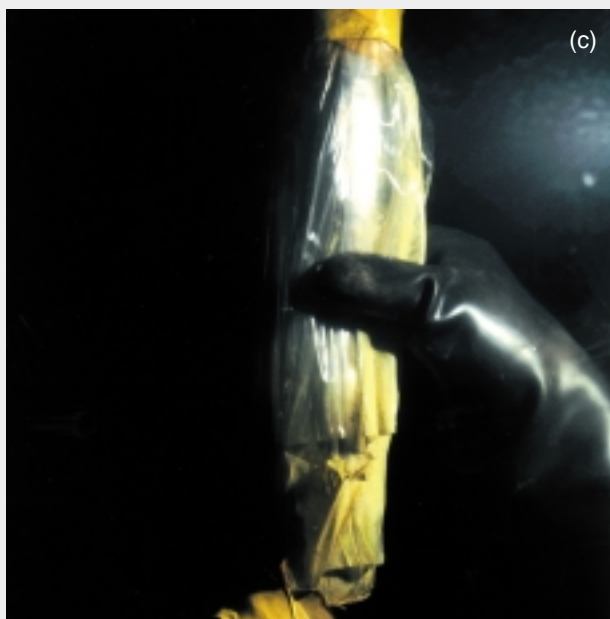
Catalyzed corrosion reactions of plutonium metal are not laboratory curiosities produced by careful manipulation of chemical reactants. Several incidents involving the corrosion of plutonium metal, failure of storage containers, and localized release of plutonium-containing particles into the work environment were attributed to catalyzed corrosion reactions (Haschke and Martz 1998b) and led to redesigning the storage package. In addition, catalyzed corrosion reactions have become the basis of efficient methods for converting plutonium metal from classified weapons configurations into simple ingots.

In 1993, a worker at the Los Alamos Plutonium Facility became contaminated with plutonium-containing particles while handling a standard storage package containing a 2.5-kilogram plutonium casting. The packaging configuration was similar to that used worldwide. It consisted of an inner cylindrical steel container to hold the casting, two layers of sealed "bag-out" plastic to contain radioactive contamination, and an outer slip-lid can. The incident occurred after the package had been stored for 11 years. As the outer can was flexed during handling, a puff of air carrying plutonium-containing particles

escaped through a break in the taped seal of the can and contaminated the worker. The package was placed in a reduced-oxygen (less than 3 percent O₂) glove box, and the inner cylinder was left there for 3 hours after having been removed from the package. The accompanying photographs were taken during the disassembly. As the plastic-wrapped inner

container was lifted out, its end ruptured because of pressure from the continuing rapid formation of plutonium oxides and other low-density corrosion products. A typical plutonium casting would form about 10 grams of PuO₂ per year from normal oxidation in air. Instead, the observed extent of the reaction was many orders of magnitude greater. Also, the inner vessel, which still contained unreacted metal, had become hot, and its diameter had increased by about 50 percent. The vessel was transferred to an argon-filled glove box, where the reaction ceased at once.

Evaluation of this incident shows that hydride catalysis caused by a complex set of physicochemical processes led to rapid corrosion of



the metal casting during storage and to very rapid corrosion during the 3-hour waiting period in the reduced-oxygen glove box. The weld at the ruptured end of the inner vessel had evidently been defective from the start, allowing gases to be continually pumped in and out of that vessel, as atmospheric pressure changes compressed and expanded the sealed plastic bagging. Plutonium oxide particles were entrained by thermal currents in the vessel, transported through openings in the weld, and deposited on the plastic over several years. During that period, the bagging isolated the metal casting from any external oxygen source, and the normal surface PuO_2 was apparently autoreduced to Pu_2O_3 . Over time, the plastic bagging became discolored near the weld, as well as embrittled from the radiolytic decomposition induced by α -particles emitted from the deposited plutonium oxide particles. The molecular hydrogen produced during the radiolysis of the plastic entered the inner vessel and formed hydride on the Pu_2O_3 -activated surface of the casting. During these processes, the storage package did not change its mass, and therefore the problem was not detected. When the embrittled plastic failed during storage, air reached the inner vessel, and a hydride-catalyzed reaction of the oxygen and nitrogen with the hydride-coated plutonium ensued at a throttled rate determined by access of air to the reaction zone. The resulting expansion of the solid led to the complete failure of the defective weld.

The corrosion rate became rapid during exposure to the glove box atmosphere and was estimated from the dramatic increase in the the vessel's volume during the 3-hour period, the bulk density of the corrosion product, and the approximate surface area of the metal. The result ($0.3 \text{ g Pu/cm}^2 \text{ min}$) is in excellent agreement with the value measured during studies of hydride-catalyzed corrosion ($0.7 \pm 0.1 \text{ g Pu/cm}^2 \text{ min}$).

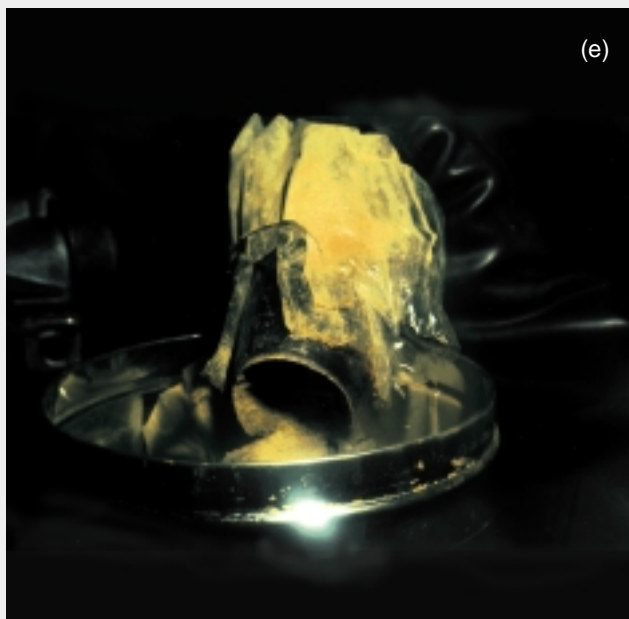
The experience and knowledge we gained from evaluating this incident and from studying catalyzed corrosion reactions find broad application in reducing the nuclear danger. The safe storage of plutonium requires using two metal containers with certified seals and ensuring that organic materials are excluded from the package. These two safety criteria are incorporated in the plutonium storage standards adopted by the U.S. Department of Energy and the International Atomic Energy Agency.

Knowledge of plutonium corrosion kinetics and particle-size distributions for a whole range of conditions enables realistic hazard assessments of plutonium dispersal during accidents. Catalyzed hydriding is also the key reaction in the hydride-dehydride recycle process for destroying weapon configurations and recovering plutonium metal—both done in a single step. Hydride-dehydride recycling generates no mixed or liquid waste of any

kind. The recovered plutonium is a storage-ready ingot, and the hydrogen gas, which is both created and recycled in a uranium hydride storage system, is never released and does not present an explosion hazard. This process was recognized by the *R&D Magazine* as one of the best 100 technical innovations of the year and is the foundation technology of the Automated Retirement and Integrated Extraction System (ARIES) for separating plutonium from weapon components. The hydride-catalyzed oxidation of plutonium holds potential for development as a parallel single-step process in the rapid recovery of plutonium as oxide rather than metal.

Failed Storage Container for Plutonium Metal

Each photo shows a step in the disassembly of the container for a 2.5-kg casting of plutonium metal. (a) The outer container is placed in a glove box; (b) when the lid is removed, the plastic bagging shows; (c) when the plastic bagging and inner cylinder are lifted out of the container, discolored, embrittled plastic decomposed by radiolysis is revealed; (d) a rupture in the inner container is visible; (e) the corrosion product pours out of the ruptured end; and (f) an increase in the inner vessel's diameter near the ruptured end shows the extent of hydride-catalyzed corrosion during a 3-hour period.

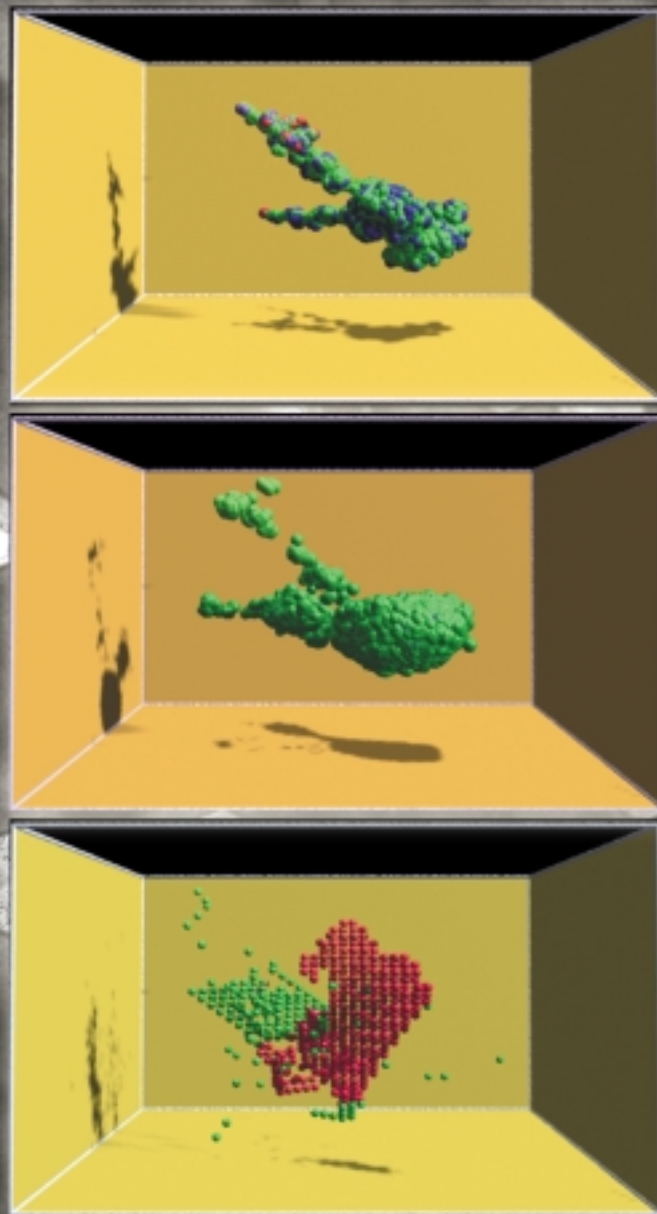


Radiation Effects in Plutonium

What is known?

Where should we go from here?

Wilhelm G. Wolfer



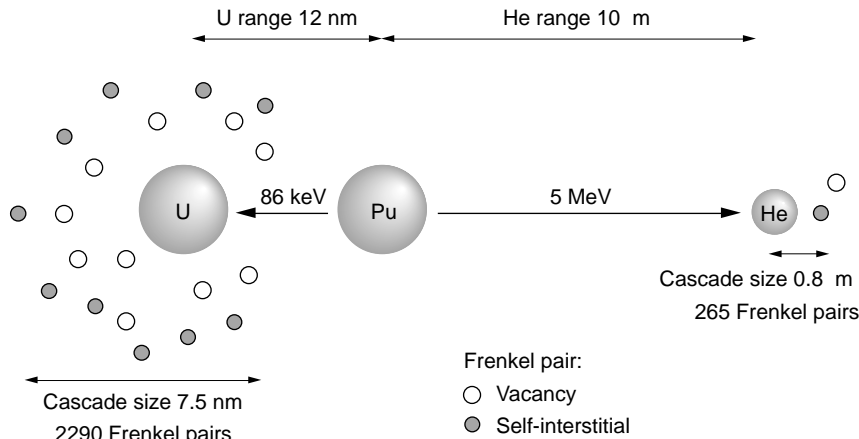


Figure 2. Plutonium Decay and the Generation of Defects

Plutonium decays to uranium by α emission. The α particle (a helium nucleus) takes away most of the energy and has a range of about 10 μm through the plutonium crystal. The heavy uranium nucleus recoils as a result of the α emission. It receives far less energy, and its range is only about 12 nm. Both particles produce displacement damage in the form of Frenkel pairs, namely vacancies and interstitial atoms, predominantly at the end of their ranges. Most of the damage results from the uranium nucleus and is confined to the collision cascade region of the size indicated.

238. Because the α -decay rate of plutonium-238 is nearly 300 times faster than that of plutonium-239, it is possible to accumulate helium nuclei and radiation damage within a sample at an accelerated rate. This acceleration of the processes will help us to obtain data on plutonium aging in just a few years.

Primary Radiation Effects in Plutonium

Radiation damage accumulates in metals after a complicated sequence of events that evolve over various time and distance scales. Figure 2 gives a schematic overview of the initial processes as they occur in plutonium. The plutonium nucleus decays to a uranium nucleus and a helium nucleus. Those daughter nuclei fly off through the lattice in opposite directions. Along their paths, and particularly toward the end of their range, they initiate a collision cascade wherein they transfer energy and momentum to the electrons and atoms of the material. Plutonium

atoms can become displaced, or knocked from their lattice positions, thus creating numerous vacancies. A displaced plutonium atom will eventually come to rest at an interstitial site (between the normal lattice sites), becoming a “self-interstitial.” Each displacement therefore creates a so-called Frenkel pair consisting of a vacancy and a self-interstitial, and each decay event creates many Frenkel pairs.

Many of the processes involved in this sequence have not been studied in plutonium, but the initial accumulation of helium atoms and Frenkel pairs can be estimated fairly reliably. Those estimates change depending on the plutonium isotope.

A typical isotopic composition of weapon-grade material is listed in Table I, which among other things lists the contribution of each isotope to the rate of helium generation per year. The cumulative rate of helium production is moderate—about 41.1 atomic parts per million (appm) per year. For example, during 10 years, 411 helium atoms will accumulate for every million plutonium

atoms, making a helium concentration of about 0.04 atomic percent.

The last column in Table I lists our estimates for the rate at which the decay products displace plutonium atoms from their normal lattice sites, in units of displacements per atom (dpa) per year. To obtain the rate, we first estimate the number of displacements per decay event (normalized to the number of plutonium atoms in the material), and then divide by the number of decay events per year. The latter is obtained from the half-life of plutonium.

The Linhard-Scharff-Schiott theory of energy dissipation, combined with a procedure outlined by Robinson (1994), enables us to evaluate the number of displaced atoms per plutonium decay. Table II summarizes this evaluation for the isotope plutonium-239. In principle, both the helium and uranium decay products can damage the crystal lattice through collisions with plutonium atoms and with the bound and free electrons. However, the highly energetic helium nucleus loses all but 0.1 percent of its 5-million-electron-volt (MeV) energy through collisions with electrons. Only when it moves with low energy at the end of its range will it produce displacements. In contrast, nearly 75 percent of the uranium nucleus’ 85 kilo-electron-volt (keV) kinetic energy results in the displacement of plutonium atoms.

To calculate the number of displacements, we need to know the so-called displacement energy, E_d , which is the minimum kinetic energy an atom must receive to be dislocated from its stable lattice site. The E_d for plutonium has not yet been measured, but an empirical rule provides the basis for a reasonable estimate:

$$E_d \cong 175 k_B T_m \quad , \quad (1)$$

where k_B is the Boltzmann constant and T_m is the melting point of the metal. Using the melting temperature of plutonium, $T_m = 913$ K, gives the value $E_d \cong 14$ electron volts. The recoil nucleus needs to impart at least this

Table II. Radioactive Decay Characteristics of Plutonium Isotopes

Isotope Mass	Half-life (yr)	Abundance (at. %)	Decay Energy (MeV)	He Energy (MeV)	Recoil Energy (keV)	Helium Rate (appm/yr)*	Displacement (dpa/yr)
238	86.4	0.02	5.50	5.39	92.2	1.6	0.0043
239	24,390	93.6	5.15	5.04	85.8	26.6	0.0679
240	6580	5.9	5.16	5.07	85.9	6.2	0.0159
241	14.98	0.44	4.89	4.84	82.0	6.7	0.0152
242	388,000	0.04	4.90	4.85	81.9	0	0
Total:						41.1	0.1033

*Determined by the half-life.

Table II. Electronic and Nuclear Energy Losses and Displacements for the Decay Products of ^{239}Pu

Product	Kinetic Energy (keV)	Fraction of energy Lost to Electrons	Available Energy (keV)	Number of Displacements
^4He	5040	0.9985	7.56	265
^{235}U	85.8	0.253	64.1	2290
Total number of displacements per decay:				2555

amount of energy to dislodge a plutonium atom. That occurs in about half of all collisions, since often the two nuclei only graze each other (Robinson 1994). Dividing the available collision energy by approximately $2 \times E_d$ yields the total number of displaced plutonium atoms per plutonium decay, which is given in Table II as 2555.

Referring back to Table I, the displacement rate is then calculated to be about 0.068 dpa per year for plutonium-239, leading to a total rate of 0.1033 dpa per year for all isotopes in weapon-grade material. Each atom in the crystal lattice of plutonium is displaced from its stable site once every decade. During this same period, about 400 appm of helium is produced and retained within the material.

To summarize, the immediate result of self-irradiation in plutonium is the buildup of helium and uranium decay products, and the accumulation of

vacancy and self-interstitial lattice defects. These primary defects, which are on the atomic scale, eventually diffuse and create a new microstructure of defect clusters, which ultimately control the macroscopic properties (Kiritani 1994). In the sections that follow, we estimate the ultimate effects of these initial atomic-scale defects.

Helium Bubble Formation

Following a radioactive decay event in a host material, the energetic helium nucleus races through the metal lattice and loses energy through collisions with electrons. It captures two electrons and eventually comes to rest as a helium atom.

What is the likely fate of the helium that accumulates in plutonium? Helium has an extremely low solubility in condensed matter because it does not bind.

If the helium atom comes to rest at an interstitial site, it can easily diffuse through the lattice until it becomes trapped in one of the vacancies it created as it came to rest. The helium atom is only about half the size of a metal atom, however, so the vacancy it occupies is not eliminated.

Helium diffusion, both by association with vacancies and by dissociation from vacancies, has been studied in several metals, particularly in nickel (Adams and Wolfer 1988). These studies suggest that short-range diffusion of helium will certainly occur in plutonium at ambient temperatures and that the helium mobility is on the order of the vacancy mobility. The helium atoms/vacancies will likely cluster together, and these clusters can act as precursors to helium bubbles. We suggest therefore that helium bubble formation will take place in plutonium.

But how fast and to what extent?

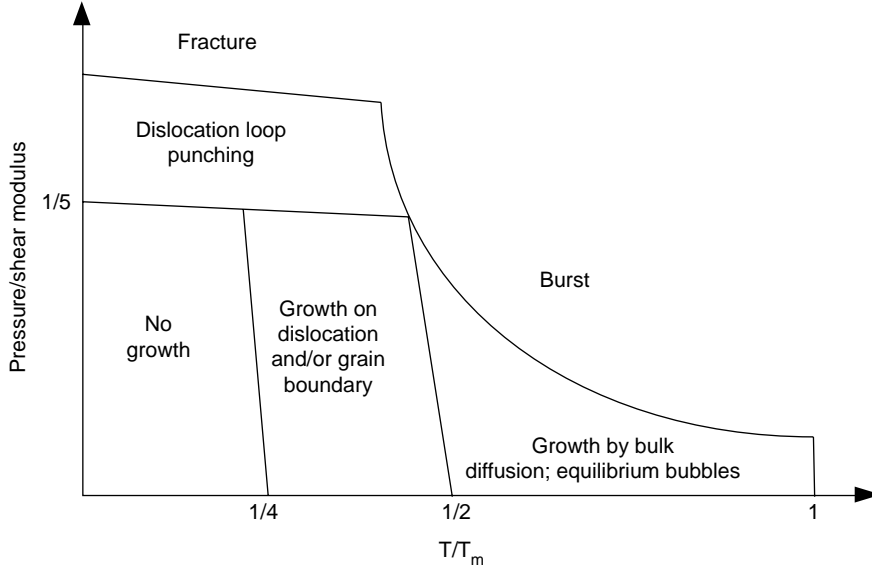


Figure 3. Helium Bubble “Growth Map” for Metals

The operative mechanism depends on the temperature of the material relative to the melting temperature, T/T_m (the homologous temperature). The helium pressure required to activate the growth depends on the mechanism and on the metal. However, the dependence on the metal is eliminated when the pressure for growth is scaled with the shear modulus. At low temperatures, bubble growth occurs by dislocation loop punching when the helium pressure exceeds one-fifth of the shear modulus. At temperatures at or above one-half the melting point, bubble pressure remains close to the value determined by the surface tension of the host material, and growth occurs by the absorption of thermal vacancies. In the intermediate temperature range, growth can also take place for bubbles on dislocations and grain boundaries.

In the absence of direct studies on plutonium, we turn to models we have developed from studies of other materials.

Helium bubble formation and growth in the absence of radiation damage can be studied in metal tritides, that is, metal–tritium compounds. In this case, helium accumulates in the material from tritium decay, and the recoil energy from the decay is so small that no displacements are produced.

Several mechanisms for bubble growth, including bulk diffusion and the formation of dislocation loops, were identified in those studies. We found that bubble growth depends on the temperature of the metal relative to its melting temperature (the homologous temperature) and on the helium pressure. Usually, one growth mechanism dominated over the others within a given temperature/pressure regime, as

seen in the schematic bubble-“growth map” of Figure 3. We also developed quantitative models for the various growth mechanisms and compared our predictions with the experimental swelling results for metal tritides. We can apply those models to derive lower and upper bounds on helium-induced swelling in plutonium.

The lower bound is given by the dislocation-loop-punching mechanism, which requires no thermal activation but a very high helium pressure inside the bubble. The studies on metal tritides show that helium bubbles produced by this mechanism have a density of roughly two helium atoms per host atom, that is, every two helium atoms take up the volume, V , of one vacancy. Therefore, the minimum volume expansion induced by the formation of the helium bubbles is given by (Wolfer 1989)

$$\left(\frac{\Delta V}{V}\right)_{\min} \cong 0.5 [\text{He}] , \quad (2)$$

where the helium concentration $[\text{He}]$ is given in atomic parts per million. This model predicts that as helium accumulates, the swelling will increase linearly in proportion to the helium concentration.

To develop an upper bound for helium-induced swelling, we consider the growth of equilibrium bubbles by bulk diffusion, which occurs when the temperature is greater than or equal to one-half the melting temperature. Bubbles are in equilibrium when the helium pressure inside the bubble equals the surface tension of the host material, that is,

$$p = \frac{2\gamma}{r} , \quad (3)$$

where p is the helium pressure, γ is the surface energy of the host metal, and r is the bubble radius. If the density of bubbles per unit volume is N_B and we assume an ideal gas law, then the helium-induced swelling is given by

$$\begin{aligned} \left(\frac{\Delta V}{V}\right)_{\max} &= N_B \left(\frac{4\pi}{3}\right) r^3 \\ &= \sqrt{\frac{3}{4\pi N_B}} \left(\frac{[\text{He}] k_B T}{2\gamma}\right)^{\frac{3}{2}} . \end{aligned} \quad (4)$$

We can evaluate helium-induced swelling from equilibrium bubbles using Equation (4), but first we need to know the bubble density, as well as the surface energy in the host material. The latter can be estimated from the value for liquid plutonium at the melting point, $\gamma_{\text{lm}} = 0.55$ joule per square meter, which is the only value of the surface energy for plutonium reported in the literature. We use an empirical formula given by Murr (1975),

$$\gamma \cong 1.2\gamma_{\text{lm}} + 0.45(T_m - T) . \quad (5)$$

The bubble density N_B depends mainly on the temperature, or more precisely on the helium mobility. At

temperatures at which vacancy migration is possible, small helium–vacancy clusters form at very low helium concentrations of about 10 appm or less. After nucleation, the existing clusters or bubbles capture any newly generated helium atoms. Thus the bubbles grow.

At one-half the melting point of a metal with helium concentrations of 100 to 1000 appm, the observed bubble densities range from 10^{12} to 10^{14} bubbles per cubic centimeter (bubbles/cm³). The density, however, increases sharply with decreasing temperature as the mobility of vacancies declines. At one-fourth the melting point, bubble densities increase by about four orders of magnitude and range from 10^{16} to 10^{18} bubbles/cm³. Noting that lower bubble densities give higher bubble swelling according to Equation (4), we conservatively estimate bubble densities in plutonium to be about 2×10^{14} bubbles/cm³ at an ambient temperature of 70°C. (See Figure 4.)

We are now in a position to compute the swelling caused by helium bubbles using Equations (3) and (4) for a lower and upper estimate, respectively. The results are shown in Figure 5 for a temperature of 70°C. Helium bubble swelling for lower aging temperatures falls within the range limited by the upper and lower bounds. Even though these estimates are crude, the volume changes caused by helium bubbles alone are small. Even after 60 years, the swelling is substantially less than 1 percent. It is therefore important to look into other mechanisms for density changes, such as void swelling.

Radiation-Induced Void Swelling in Metals

Void swelling is a byproduct of processes that occur during the recovery of the damaged crystal lattice. We have already mentioned that a decay event causes the heavy daughter nucleus to recoil through the material, and the subsequent displacement damage creates

thousands of Frenkel pairs consisting of vacancies and self-interstitials. In fcc materials, the self-interstitials are mobile even at cryogenic temperatures and, during their random migration, become absorbed at dislocations and grain boundaries. But the self-interstitials will also recombine with vacancies, thus annihilating a Frenkel pair and restoring the perfect crystal structure. About 100 picoseconds after the decay of a plutonium atom, up to 70 percent of the Frenkel pairs have recombined.

As seen in Figure 6, the remaining defects have rearranged in the form of defect clusters, mainly small dislocation loops. A few isolated vacancies also remain. The vacancy clusters eventually lead to the nucleation and subsequent growth of voids.

The macroscopic swelling of the metal that is due to the growth of voids—void swelling—has been studied extensively. It became clear that the phenomenon occurs in all metals within a well-defined temperature range and as the result of any irradiation process that produces displacement damage,

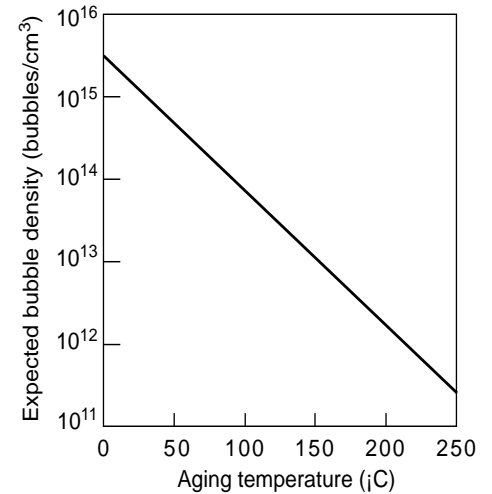


Figure 4. Estimate of the Helium Bubble Density

The helium bubble density is needed to predict an upper limit to the extent of helium swelling. The curve shows the expected density for plutonium as a function of temperature. At 70°C, the helium bubble density is approximately 2×10^{14} bubbles/cm³.

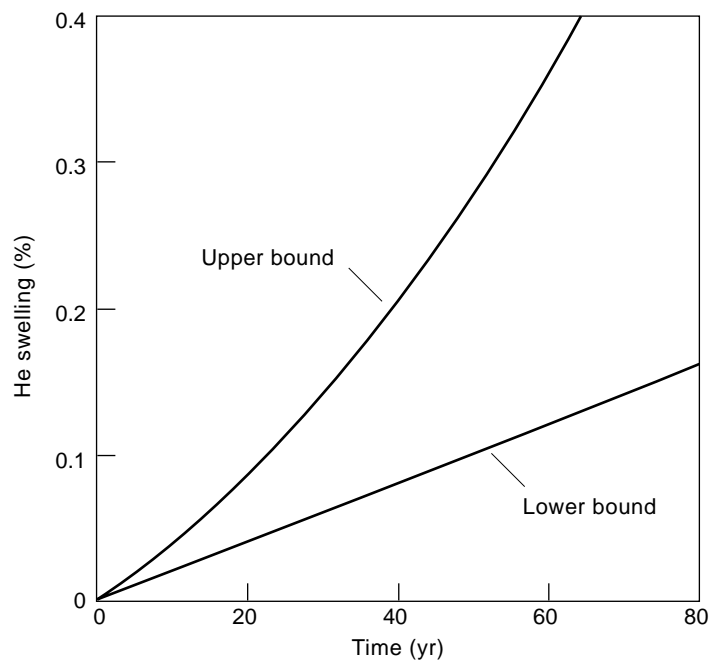


Figure 5. Helium Bubble Swelling in Plutonium at 70°C

The lower bound assumes the loop-punching mechanism for bubble growth; the upper bound, the mechanism of equilibrium bubble growth. At 70°C, helium bubble swelling is expected to fall between the two bounds.

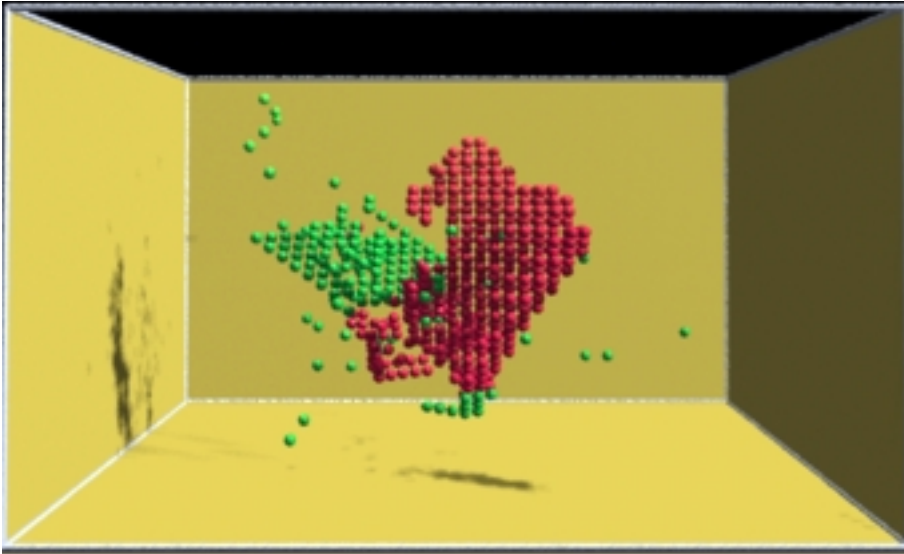


Figure 6. Cluster Formation in Lead

This output from a simulation shows the final damage in one part of a collision cascade in lead. Red balls are interstitial atoms and green balls are missing atoms, or vacancies. In this frame, 183 ps after one atom received a recoil energy of 80 keV, two large clusters have formed, one made of dislocation loops, or planar arrangements of interstitials (red cluster), and the other made of vacancies (green cluster). Note that very few of the vacancies or interstitials are not in clusters.

(Unpublished results by M. J. Caturia and T. Diaz de la Rubia, Lawrence Livermore National Laboratory, January 2000.)

including electron irradiation. (Electron irradiation does not generate collision cascades, but only isolated Frenkel pairs.)

Given the general occurrence of void swelling, there is no reason to believe that it will not happen in plutonium. In order to assess the temperature range and the magnitude of the swelling for plutonium, it will be useful to review the fundamental aspects of this phenomenon.

Void formation requires favorable conditions for nucleation and subsequent growth. Vacancies must be mobile, and a minimum amount of helium has to have accumulated. The minimum temperature necessary to initiate vacancy mobility determines the lower temperature limit for void formation. The upper temperature limit results from a supersaturation of the irradiation-induced vacancy concentration. As opposed to thermally induced vacancies, the clusters formed from

the collision cascade are not thermodynamically stable. They slowly dissolve over time. Once the concentration of thermal vacancies exceeds the irradiation-induced vacancy concentration, void swelling ceases. Both temperature limits are weakly (that is, logarithmically) dependent on the displacement rate.

Table III contains a list of parameters that characterize different radiation environments where void swelling has been observed. The estimates for plutonium (last column) were obtained from scaling relationships that were derived from the theoretical models of void swelling.

The two irradiation methods, accelerators and reactors, often lead to very similar results, but there are differences. Accelerators implant metal ions (self-ion implantation) or helium ions (helium implantation) into the samples. The displacement damage occurs in a very thin (a few micrometers) layer,

close to the surface and confined by the surrounded material. Reactors irradiate the sample with neutrons and the damage is uniformly spread over much larger dimensions. As a result, the two methods produce a different ratio for the void and dislocation densities, resulting in a different swelling rate. Neutron irradiation more closely resembles the self-irradiation damage in plutonium.

A typical swelling curve, derived from neutron irradiation studies (Wolfer 1984), is shown in Figure 7. There are three stages: the first stage is an incubation period during which void nucleation takes place; the second stage is a transient period during which an optimum ratio is established for the densities of voids and dislocations; and the third stage is a steady-state swelling period, which will eventually terminate at a saturation swelling value. The saturation value is usually too large to be of any practical concern.

Although these general features are observed in many metals and alloys (Garner 1994), large variations exist, particularly in the length of the transient period, which can range from a few to 100 dpa. Metals of high purity and fcc structure swell almost immediately. In well-annealed materials with an initially low dislocation density, large grain size, and low precipitate density, swelling commences immediately after the incubation period. The latter has been found to be roughly the time needed to accumulate 5 to 10 appm of helium (Wiedersich and Hall 1977) from nuclear transmutations. However, oxygen impurities in excess of the solubility limit can also shorten the incubation time (Zinkle et al. 1987).

Cold-worked materials with initially high dislocation densities have, in general, long transient periods. However, the initial dislocation density does not remain constant. It evolves during irradiation and reaches a new steady-state density determined by the irradiation conditions (Wolfer and Glasgow 1985). When this steady-state density is reached, void swelling can proceed at its steady-state rate.

Table III. Comparison of Radiation Environments

Irradiation Parameter	Accelerator		Breeder Reactor	Thermal Reactor	Plutonium
	Self-Ion Implantation	Helium Implantation			
Dose rate (dpa/sec)	10 ⁻³	10 ⁻³	10 ⁻⁶	10 ⁻⁷	10 ⁻⁹
He accumulation rate (appm/dpa)	sequential ^a	1000	1	15	400
Homologous temperature range	0.45–0.65	0.45–0.65	0.35–0.55	0.3–0.4	0.25–0.45

^aHe ions are implanted in the material prior to heavy ion bombardment.

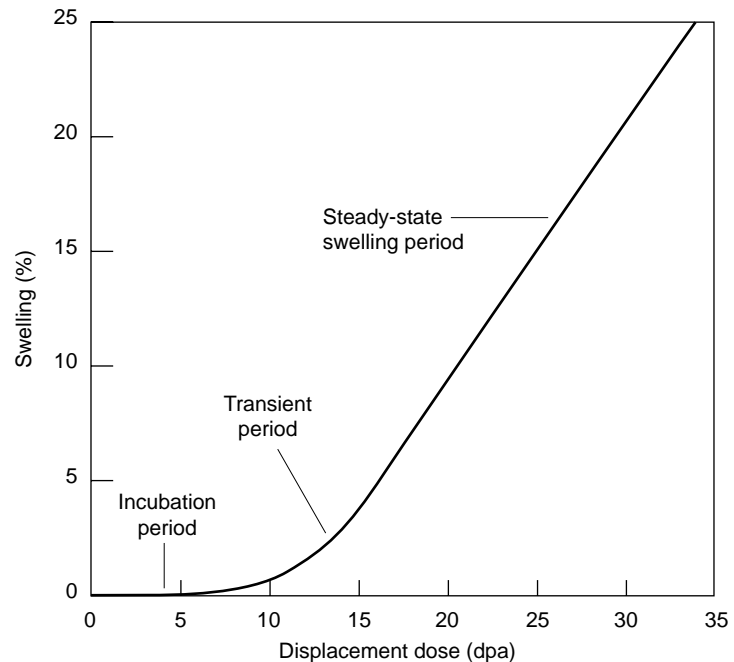
A characteristic feature of this steady state is that parity exists between the dislocation density and the void density. The dislocations are in fact the primary cause of void swelling. They attract self-interstitials slightly more than vacancies and therefore possess a “bias” for preferential absorption of self-interstitials. In contrast, voids, which also absorb self-interstitials, are more neutral or less biased.

The difference in these biases, the net bias B , is the fundamental driving force for void swelling. The maximum possible separation of vacancies and self-interstitials—as determined by net bias—is realized only when voids and dislocations are of equal abundance. This state is referred to as the state of sink parity. During the initial stages of void swelling, the dislocations are more abundant and the swelling rate is less than what it could be. For very large values of swelling, and hence void sizes, the voids are the most abundant sink, and the swelling rate diminishes again.

It has been shown by Garner and Wolfer (1984) that an upper bound to the void swelling rate can be derived when sink parity exists. As a result,

$$\frac{d}{d\tau} \left(\frac{\Delta V}{V} \right) \leq 1.25 \Delta B, \quad (6)$$

where τ is the time measured in units

**Figure 7. The Different Stages for Radiation-Induced Void Swelling**

The fractional volume increase due to void swelling is plotted as a function of irradiation exposure time measured in displacements per atom. The incubation period is, in general, determined by the time required to accumulate about 5 to 10 appm of helium by nuclear transmutation reactions. The transient period can extend from a few to 100 dpa, depending on the crystal structure, alloy composition, initial dislocation density, precipitate evolution, and irradiation temperature. The steady-state rate is mainly determined by the fundamental properties of the crystal lattice and of the vacancy and self-interstitial.

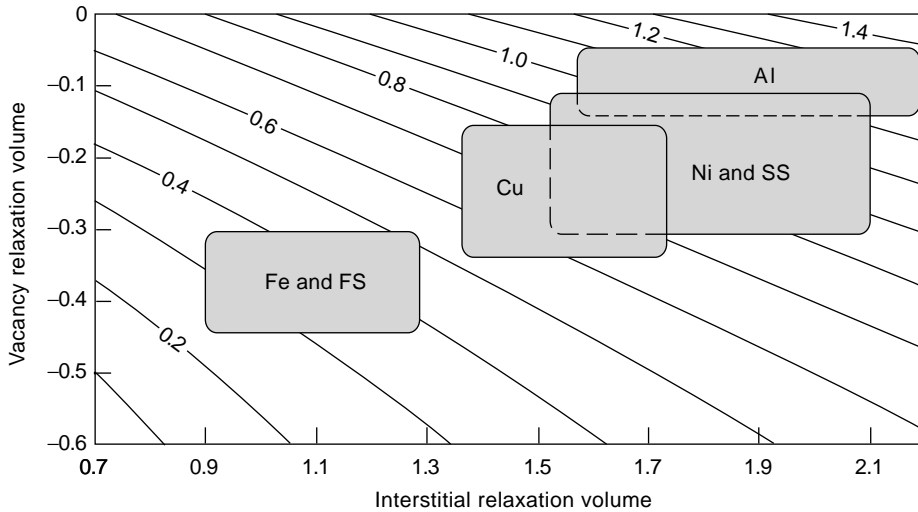


Figure 8. Net Bias for Radiation-Induced Void Swelling
 Dislocations attract and absorb self-interstitials slightly more than vacancies. The different rate of absorption is known as the net bias, B , and is the fundamental driving force for void swelling. The contour lines are lines of constant net bias value as indicated. The boxes circumscribe the range of predicted values for the net bias using measured relaxation volumes and their uncertainties. The materials are aluminum (Al), nickel and austenitic stainless steels (Ni and SS), copper and copper-nickel alloys (Cu), and body-centered-cubic iron and ferritic steels (Fe and FS).

Table IV. Swelling Rates of Some Metals and Alloys

Metal	Measured Steady-State Swelling Rate ^a	Estimated Upper Bound ^a
Al	1.0	1.1–1.7
Ni and SS	1.0	0.8–1.5
Cu	0.5	0.7–1.2
Fe and FS	0.2	0.35–0.6

^aMeasured in units of percent volume change per dpa, %/dpa

of dpa. (In a reactor, the neutron flux produces damage at a rate that is expressed in dpa/sec. For a constant flux, dpa is therefore proportional to the time.)

Sniegowski and Wolfer (1984) have developed a theory to derive the net bias from the fundamental properties of the crystal lattice and the defects. The two most influential parameters are the so-called relaxation volumes of the self-

interstitial and of the vacancy, which can either be measured or determined from atomistic defect calculations. Figure 8 shows the theoretical results of Sniegowski and Wolfer for the net bias.

The comparison shown in Table IV of measured steady-state swelling rates with the estimates of the upper bounds indicates that both exhibit the same trends, that the steady-state swelling rate is close to the maximum possible,

and that metals with the more open body-centered-cubic (bcc) structure swell less than fcc metals do.

The fcc phase of plutonium, δ -phase plutonium, exhibits some unusual properties, including a negative thermal expansion coefficient. This behavior could be indicative of a very soft interatomic repulsive force between plutonium atoms in the δ phase. If so, the relaxation volumes of both vacancies and interstitials would be low, resulting in a small net bias.

However, the addition of an alloying element such as gallium to stabilize the δ phase may change the net bias in two ways. First, the electronic band structure could be affected sufficiently to alter the interatomic forces and hence the relaxation volumes. Second, radiation-induced segregation of the alloying element can significantly alter the net bias (Wolfer 1983). If this segregation occurs, microscopic regions in the crystal could possibly become sufficiently depleted of the stabilizing element and be converted to the denser α phase. This would result in a negative volume change of $\Delta V/V = -0.14f$, where f is the volume fraction of the transformed material.

Void Swelling in δ -Stabilized Plutonium

Figure 9 compares the predictions for helium bubble swelling and void swelling in δ -phase plutonium. A reliable prediction of void swelling is not possible at the present time without knowledge of the relaxation volumes for vacancies and interstitials. A conservative assumption is to adopt the typical values for fcc metals, and hence, the steady-state swelling rate of 1 percent volume change per dpa. With regard to the incubation dose for void nucleation, the required amount of helium is available after about 4 months or a dose of about 0.025 dpa. The temperature range for swelling is expected to be from -30°C to 150°C .

There is a large uncertainty, howev-

er, in the length of the transient period. To obtain an accurate prediction, it would be necessary to perform extensive model calculations, both of the dislocation evolution and of the void evolution. Theoretical predictions, performed by Wolfer and Glasgow and by Wehner and Wolfer (1985), and experimentally observed transient periods seem to indicate that a minimum dose of at least 1 to 2 dpa is needed before steady-state swelling is approached. Based on these assumptions, void swelling in stabilized δ -phase plutonium could in principle begin as early as 10 years after pit fabrication. However, there is no evidence for void swelling even after 30 years; it is entirely possible that the transient period is much longer, and void swelling may not occur within the next 100 years.

Nevertheless, the swelling predictions shown in Figure 9 already provide an important result: Swelling due to displacement damage is potentially a more serious problem than swelling due to helium.

Radiation-Induced Creep and Stress Relaxation

Radiation-induced creep has been recognized as a phenomenon even before the discovery of void swelling. First reported as a deformation process accompanying fission in uranium fuel (Roberts and Cottrell 1956), it has been found to occur in graphite, ceramic nuclear fuel, steels, and zirconium alloys, as well as in glass. The primary cause is again the displacement damage and the diffusion of the self-interstitial and, at higher temperature, the diffusion of the radiation-produced vacancies. Radiation-induced creep is distinct from thermal creep in that it exhibits a rather weak temperature dependence and an (approximately) linear dependence on stress and displacement damage rate. It occurs below the homologous temperature, which defines the upper temperature limit for void swelling. In the case of plutonium, this means

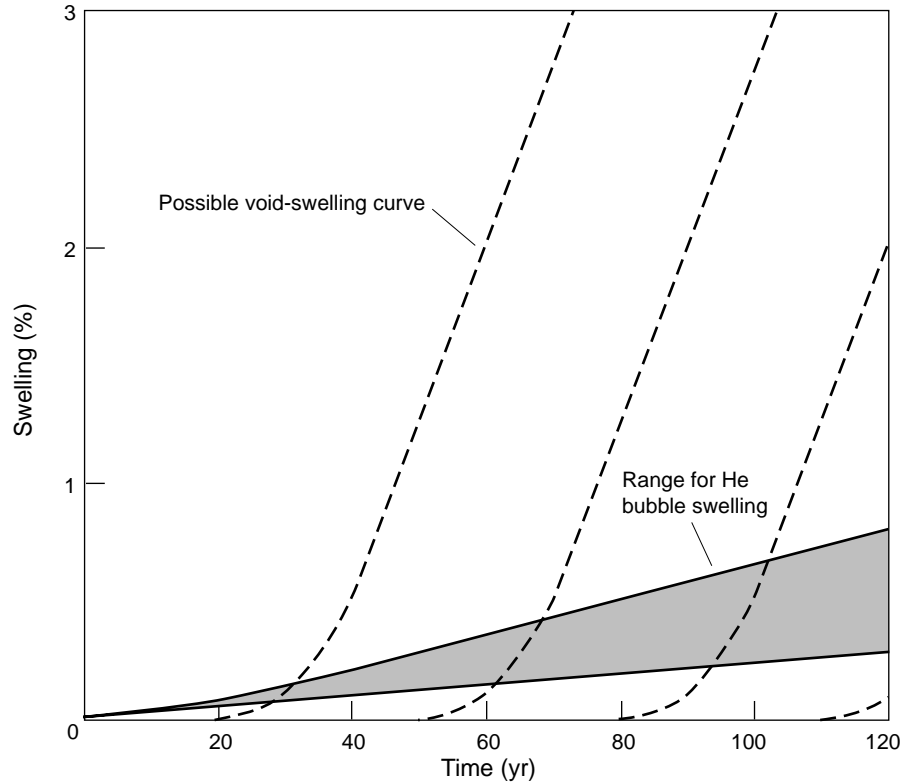


Figure 9. Predictions for Radiation-Induced Damage in Plutonium

The figure shows the predicted contributions to volume distortion in stabilized plutonium (aged at 70°C). Distortions due to void swelling are likely to be much larger than those due to helium-bubble formation. However, the large uncertainty in the transient period prevents us from estimating when the void swelling should begin its linear growth rate. The figure shows several possible swelling curves.

below a temperature of 150°C.

Radiation-induced creep will plastically deform a material and so is capable of relaxing stresses. It is therefore a beneficial mechanism in conjunction with void swelling because it limits the amount of stress that can be generated. For example, when swelling takes place in a thin layer of material attached to a rigid substrate, stresses build up in this layer according to the equation

$$\frac{1}{M} \frac{d\sigma}{dt} + \frac{d}{dt} \left(\frac{\Delta V}{V} \right) + \psi \sigma = 0, \quad (7)$$

where σ is the lateral stress component in the swelling layer, $M = E/[3(1 - \nu)]$ with E the Young's modulus and ν the Poisson ratio, and ψ is the compliance coefficient for radiation-induced creep. It is seen from Equation (7) that a

saturation stress is reached that is given by

$$\sigma_{\text{sat}} = -\frac{1}{\psi} \frac{d}{dt} \left(\frac{\Delta V}{V} \right). \quad (8)$$

This saturation stress is found to be about half the initial yield strength of the annealed material. However, as mentioned above, secondary processes lead to an increase in the dislocation density of annealed materials, and their yield strength increases rapidly with the irradiation dose and reaches values two to three times higher after about 5 dpa. The increase in yield strength is accompanied by a reduction in ductility, and it is therefore all the more important to have an additional stress relaxation mechanism such as radiation-induced creep.

The prediction of the radiation-in-

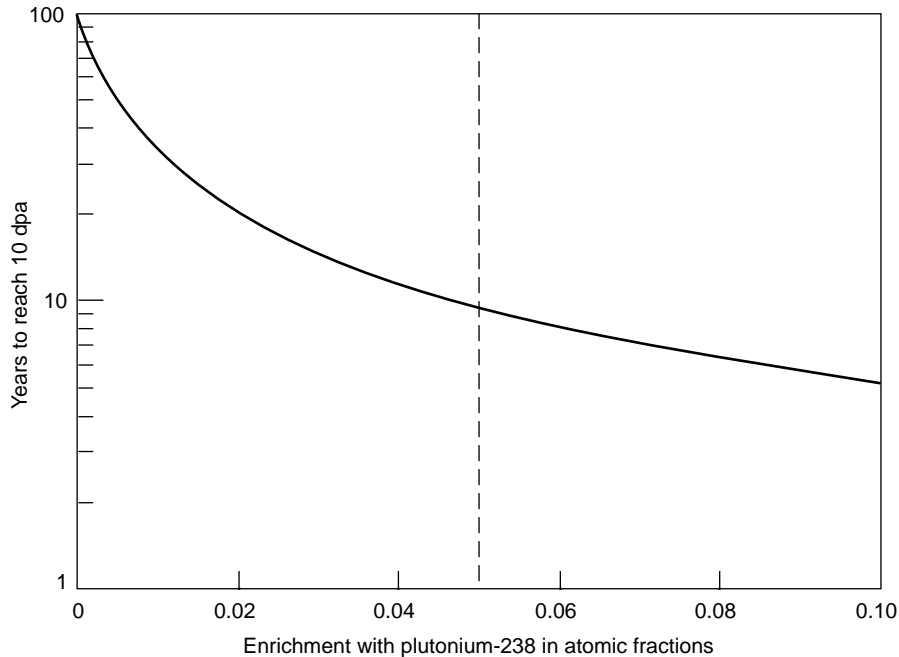


Figure 10. Accelerating Aging

By enriching a sample of weapon-grade plutonium with ^{238}Pu , the time to accumulate a radiation damage dose of 10 dpa can be significantly reduced. Without enrichment, it takes 100 years to acquire such a dose. Upping the ^{238}Pu fraction by as little as 5 percent will reduce the time to ten years. However, the effects of radiation dose rate on aging are not known. It is not clear how to translate the data from accelerated aging experiments to the study of aging in pits.

duced creep rate, or more precisely of the creep compliance ψ , is in principle possible, as demonstrated by Wolfer (1980) and by Matthews and Finnis (1988). However, in addition to the defect parameters and microstructural data required for void swelling predictions, other defect parameters are needed that are more difficult to determine experimentally or by computer simulations. These are the so-called elastic polarizabilities for both the vacancy and the self-interstitial.

Summary and Recommendations for Further Research

The analysis presented here of self-irradiation damage effects in plutonium reveals that both helium accumulation and displacement damage must be considered. Although helium accumulation

alone is unlikely to pose a serious plutonium aging problem, the displacement damage effects can lead to significant dimensional changes as a result of the following two phenomena.

First, void swelling is expected to occur in the temperature range from -30°C to 150°C and may reach a rate of about 0.1 percent per year. However, the transient period, or the time it takes to reach this steady-state swelling rate, may be anywhere from 10 to 100 years after pit fabrication. The length of the transient period depends on many variables, including alloy composition, dislocation and grain structure, and the evolution of the latter two with time. It is unlikely that these metallurgical variables can be specified with sufficient accuracy to predict the transient period in δ -phase plutonium.

Second, radiation-induced phase transformation from δ to α in marginally stabilized plutonium alloys can result

in significant shrinkage. (The α phase has a specific volume that is 20 percent less than the δ phase.) This phenomenon is closely coupled to the processes that occur in void swelling, and the two mechanisms for dimensional changes may in fact take place simultaneously. Experimental x-ray diffraction studies on phase compositions in aged plutonium can easily reveal the occurrence of this process.

The analysis presented in this article relies to a large extent on the assumption that δ -phase plutonium can be viewed as a typical fcc metal with regard to radiation and helium effects. Clearly, this assumption must be replaced with actual data on radiation-induced dimensional changes and with measurements and theoretical calculations of critical defect properties for stabilized δ -phase plutonium.

To accomplish these two goals, an accelerated-plutonium-aging research program has been initiated using material with a higher content of the isotope plutonium-238. This isotope decays at a much faster rate than plutonium-239 (refer to Table I), and by its addition, the rate of radiation damage can be accelerated.

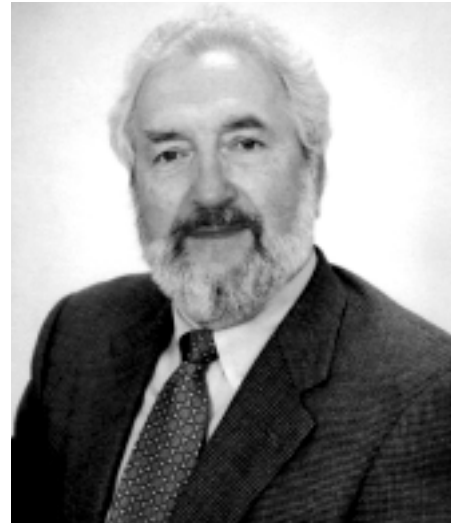
For example, suppose one wants to study radiation effects up to a total dose of 10 dpa. For plutonium metal with an isotope composition as listed in Table I, it would take 100 years to accumulate such a dose. But as seen in Figure 10, that time is reduced to 10 years with a 5 percent enrichment of plutonium-238.

Accelerating the rate of radiation damage, however, raises several other issues. One is the dissipation of the thermal energy and the temperature control of the irradiation experiments. The other is the effect of dose rate on the evolution of the defect morphology, on void nucleation, and on the transient period. The void-swelling results from neutron and ion irradiations give a clear indication that the steady-state swelling rate is independent of the rate of damage production, but the incubation and transient periods do depend on dose rate.

It is therefore necessary to develop detailed models for all the important processes involved in the damage production, including the evolution of the microscopic defect structure and the nucleation and growth voids, together with the evolution of the dislocation structure. With these models in hand and verified with experimental data, we can translate the results obtained from the accelerated-aging experiments to the lower dose rates in stockpile materials. ■

Further Reading

- Adams, J. B., and W. G. Wolfer. 1988. *J. Nucl. Mater.* **158**: 25.
- Aging Arsenal Poses Dilemma. 1995. *Aviation Week & Space Technology* July 17 issue: 24.
- Brailsford, A. D., and R. Bullough. 1972. *J. Nucl. Mater.* **44**: 121.
- Garner, F. A. 1994. *Irradiation Performance of Cladding and Structural Steels in Liquid Metal Reactors*. Chapter 6 in *Nuclear Material, Part I*. B. R. T. Frost, ed. Volume 10A of *Materials Science and Technology: A Comprehensive Treatment*. R. W. Cahn, P. Haasen, and E. J. Kramer, eds. Weinheim, Germany: VCH Verlagsgesellschaft.
- Garner, F. A., and W. G. Wolfer. 1984. *J. Nucl. Mater.* **122**: 201.
- Kiritani, M. 1994. *J. Nucl. Mater.* **216**: 220.
- Matthews, J. R., and M. W. Finnis. 1988. *J. Nucl. Mater.* **159**: 257.
- Murr, L. E. 1975. *Interfacial Phenomena in Metals and Alloys*. Reading, Massachusetts: Addison-Wesley.
- Roberts, A. C., and A. H. Cottrell. 1956. *Philos. Mag.* Series 8 **1**(8): 711.
- Robinson, M. T. 1994. *J. Nucl. Mater.* **216**: 1.
- Sniegowski, J. J., and W. G. Wolfer. 1984. In *Proceedings of Topical Conference on Ferritic Alloys for Use in Nuclear Energy Technologies* (Snowbird, Utah, June 19–23, 1983). J. W. Davis and D. J. Michel, eds. Warrendale, Pennsylvania: The Metallurgical Society of AIME.
- Wehner, W. M., and W. G. Wolfer. 1985. *Philos. Mag.* A **52**: 189.
- Wiedersich, H., and B. O. Hall. 1977. *J. Nucl. Mater.* **66**: 187.
- Wolfer, W. G. 1980. *J. Nucl. Mater.* **90**: 175.
- Wolfer, W. G. 1983. *J. Nucl. Mater.* **114**: 292.
- Wolfer, W. G. 1984. *J. Nucl. Mater.* **122**: 367.
- Wolfer, W. G. 1989. *Philos. Mag.* A **59**: 87.
- Wolfer, W. G., and B. B. Glasgow. 1985. *Acta Metall.* **33**: 1997.
- Zinkle, S. J., et al. 1987. *Philos. Mag.* A **55**: 127.



Wilhelm Wolfer received his B. S. in Engineering Physics from the Technical University, Vienna, Austria, 1961, his Diplom-Physiker (M. S.), in Physics from the University of Stuttgart and the Max Planck Institute for Metal Physics, Stuttgart, Germany, 1965, and his Ph.D. in Nuclear Engineering Sciences from the University of Florida, 1969. Dr. Wolfer is currently Program Leader for the Materials Science and Technology Division at Lawrence Livermore National Laboratory. His research interests are in computational materials science, plutonium aging, and high-level nuclear waste materials. He has published over 100 scientific papers and technical reports and is a Member of the Materials Research Society, former co-editor of *Nuclear Engineering and Design*, member of the Editorial Advisory Board for *Radiation Effects*, member of a National Research Council Committee on Computer Simulation and Analysis of Complex Material Phenomena, and a member of the International Advisory Committee for EURO-CRYST, a planned European Centre of Excellence for Crystal Growth Research and Technology.

Transmission Electron Microscopy of Plutonium Alloys

Thomas G. Zocco

Until the 1950s, direct observation of microstructures was limited by the wavelength of light to resolutions of some fraction of a micrometer, even under the best of circumstances. With the advent of transmission electron microscopy (TEM), in which electrons rather than light are used to image microstructural features, the resolution reached a nanometer. Today, we can image those features with near-atomic-scale resolution. These developments have revolutionized the study of defects and microstructures, which has led to a better understanding of material properties.

Plutonium Proves to Be Most Difficult for TEM

TEM samples must be thin enough to allow the electron beam to penetrate and probe the structure. For most materials, the samples can be made into foils only a few thousand angstroms thick by chemical thinning or ion milling. Because of its high atomic number, however, plutonium foils must be thinner than those of most other metals or alloys. In addition, because of the radioactive and hazardous nature of plutonium, samples must be prepared in glove boxes, and the sample loading must be carefully carried out so as to minimize contamination of the electron-microscope chamber and its surroundings during examination.

However, the most difficult aspect of preparing plutonium for TEM measurements is its extremely reactive nature. Even in very dry air, the plutonium surface will immediately oxidize to plutonium dioxide. Clearly, the key to successful preparation of TEM specimens of plutonium metal is to minimize the surface oxidation. Plutonium samples have been successfully prepared with standard TEM electropolishing techniques, although preparing the thin foil is typically a struggle. We prepared suitable foils by rapidly transferring the prepared samples into an inert environment such as a liquid medium or vacuum (Zocco and Rohr 1988), thus minimizing the time the samples were exposed to the atmosphere.

For our plutonium observations, we used a JEOL 2000EX microscope. An accelerating voltage of 200,000 volts produces a highly penetrating electron beam that enables us to examine plutonium samples. I will briefly describe results of the few TEM examinations conducted at Los Alamos. Ours was the only work of this kind until very recently, when Adam Schwartz and Mark Wall began TEM studies of plutonium at Lawrence Livermore National Laboratory (private communication).

Direct Observation of Martensite in Pu-Ga Alloy

TEM has become an indispensable tool to study mechanisms of phase transformations, especially the crystallographic relationship between the parent and

product phases. For the first time, Zocco et al. (1990) were able to confirm the martensitic nature of the transformation from δ -stabilized Pu-Ga alloys to monoclinic α' (for a discussion of phase transformations in plutonium, see the article "Plutonium and Its Alloys" on page 290). The α' -martensite platelets in δ -grains are shown in Figure 1(a). During the transformation, the change in shape must be accommodated in the product and the parent phases. Indeed, we were able to demonstrate that the α' -martensite platelets twin internally along the

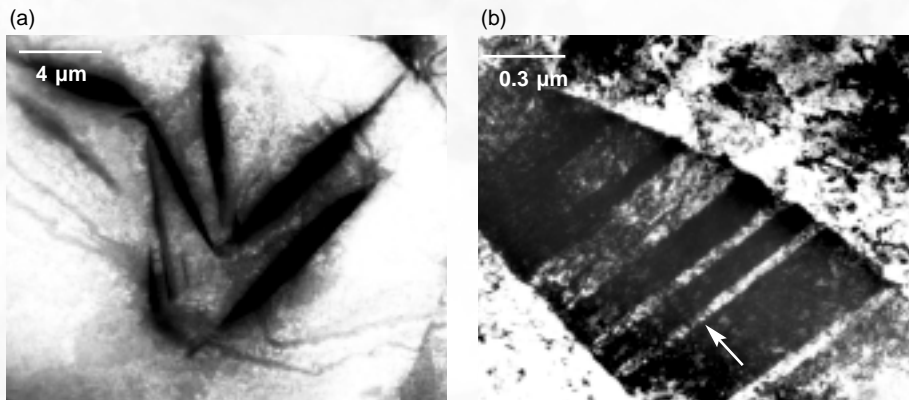


Figure 1. Direct Observation of Martensites in Pu-Ga Alloy
 (a) A TEM image shows α' -plates (dark phase) inside the δ -phase of a Pu-3.4 at. % Ga alloy. The sample was cooled to low temperature to transform martensitically to the monoclinic α' -phase. Note the crystallographically distinct orientations of the martensite plates. (b) At higher magnification, twin boundaries (one perpendicular to arrow) can be seen within an individual plate.
 (This figure was reproduced courtesy of *Acta Metall. Mater.*)

(205) planes to make this accommodation, as shown in Figure 1(b).

With the aid of selected-area electron diffraction, we were also able to identify the crystallographic relationship between the α' - and the δ -phase. The close-packed $(111)_\delta$ planes were nearly parallel to the closest-packed $(020)_\alpha$ planes in the α' -phase. The habit plane was found to be near the $(132)_\alpha$ plane. These results were consistent with the predictions based on crystallographic theories of martensite formation (Adler et al. 1986). As Hecker pointed out (page 328), to solve some of the remaining mysteries surrounding phase transformations in plutonium alloys, we should be able to apply TEM routinely in the study of those transformations.

Helium Bubbles in Plutonium

The need to extend the lifetime of plutonium pits and concerns over the long-term storage of excess plutonium have refocused attention on self-irradiation damage of plutonium and its alloys. One of the most intriguing puzzles about aged plutonium is what happens to the 40 parts per million by weight per year of helium that are grown into the plutonium lattice as a result of α -particle radioactive decay. Specifically, will helium bubbles form during long-term plutonium storage or will the helium help to initiate void swelling as plutonium ages? (For a full discussion, see the article "Radiation Effects in Plutonium" on page 274.)

Helium is not expected to be very mobile at room temperature. To allow it to move, we intentionally annealed a 21-year Pu-Ga alloy sample at 400°C for one hour. Under those conditions, the helium did indeed move and agglomerate, as first shown at Los Alamos by Rohr et al. (1984). We subsequently showed that very fine bubbles formed in the grain interiors and larger bubbles formed in the grain boundaries, as shown in Figure 2. These techniques must now be applied to the study of all facets of self-irradiation damage—helium generation, void swelling, and lattice damage.

Nanoscale Structures in Plutonium

Like many other metals, plutonium can be deposited onto substrates by vapor-deposition processes (for example, magnetron sputtering). Such deposition processes are often used to synthesize very fine grained microstructures or to retain metastable phases. Structures at the nanoscale level are of great interest because they offer new avenues for tailoring materials according to very special properties that are needed. They also provide new avenues for studying the fundamental properties of materials.

We have examined thin foils of triode sputter-deposited Pu-Ga alloys fabricated by Harry Rizzo at Lawrence Livermore National Laboratory. These foils exhibited an extremely fine grain structure, as shown in Figure 3. Some grains were as small as 100 nanometers. In addition, sputter deposition often produced multiphase structures, including α - + β -phase mixtures. We used electron diffraction analysis to identify the (201) plane, a twin plane in the α -phase (Zocco et al. 1989), in contrast to the (205) plane found in the α' -martensite. TEM is an indispensable tool for characterizing such materials.

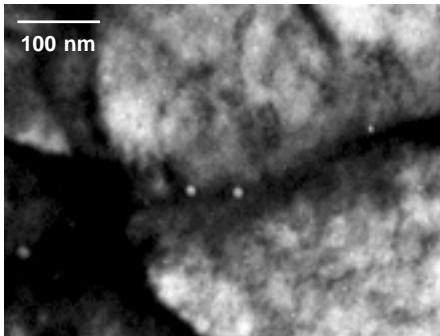


Figure 2. Helium Bubbles in Plutonium

After heating a 21-year Pu-Ga alloy sample at 400°C for one hour, we observed helium bubbles along the grain boundaries. A significant number of bubbles were seen inside grains as well.

(This figure was reproduced courtesy of the Materials Research Society.)

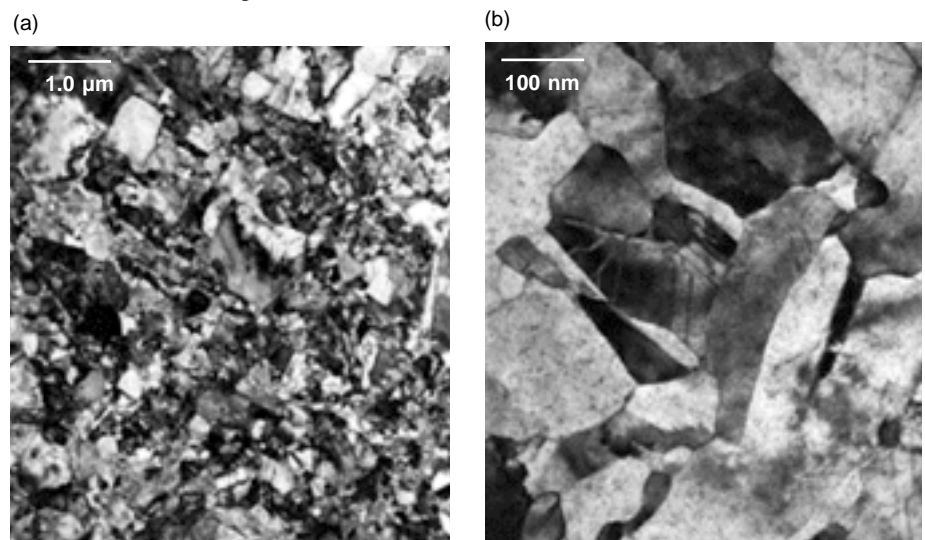


Figure 3. Nanoscale Structures in Plutonium

(a) A sample showing the fine-grained, two-phase α + β Pu-Ga alloy made by sputter deposition. (b) At higher magnification, the sample is seen to have extremely fine grains and some substructure—twin boundaries, stacking faults, and dislocations.

Summary

TEM has helped us understand the unusual properties of and physical phenomena in plutonium and its alloys. Los Alamos paved the way for the use of this technique many years ago. Unfortunately, however, further development of TEM stopped during the 1990s. Only now are we reviving this capability at Los Alamos and Lawrence Livermore National Laboratories. Indeed, it is imperative that we turn TEM into a routine investigative tool for the study of plutonium metallurgy and interfaces. We must investigate the latest TEM capabilities that yield resolution near the atomic level, which would allow us to do analytical electron microscopy (for chemical analysis at the microlevel) to help us in deciphering the mysteries of plutonium. ■

Further Reading

- Adler, P. H., G. B. Olson, and D. S. Margolies. 1986. *Acta Metall.* **34**: 2053.
- Rohr, D. L., K. P. Staudhammer, and K. A. Johnson. 1984. "Development of Plutonium Transmission Electron Microscopy." Los Alamos National Laboratory report LA-9965-MS.
- Zocco, T. G., and D. L. Rohr. 1988. *Mater. Res. Soc. Symp. Proc.* **115**: 259.
- Zocco, T. G., R. I. Sheldon, M. F. Stevens, and H. F. Rizzo. 1989. *J. Nucl. Mater.* **165**. (3): 238.
- Zocco, T. G., M. F. Stevens, P. Adler, R. I. Sheldon, and G. Olsen. 1990. *Acta Metall. Mater.* **38**: 2275.



Thomas Zocco received his B.S. (1982) and M.S. (1984) degrees in materials science and engineering from the University of Utah. In 1984, Tom joined the Laboratory as a technical staff member in the Plutonium Metallurgy Group of the Materials Science and Technology Division. He was originally tasked to provide transmission electron microscopy analyses to several programs, including irradiated materials for fusion reactors and optical coatings for laser mirror applications. Over the last 16 years, Tom investigated the microstructural and crystallographic characteristics of many materials—from fossilized dinosaur bones to plutonium metal and alloys. Tom is an active member of the Science Leadership Council of the Nuclear Materials Technology Division and has authored and coauthored over 60 scientific journal and Laboratory publications.

Plutonium and Its Alloys

From atoms to microstructure

Siegfried S. Hecker



Plutonium is an element at odds with itself—with little provocation, it can change its density by as much as 25 percent; it can be as brittle as glass or as malleable as aluminum; it expands when it solidifies; and its freshly-machined silvery surface will tarnish in minutes, producing nearly every color in the rainbow. To make matters even more complex, plutonium ages from the outside in and from the inside out. It reacts vigorously with its environment—particularly with oxygen, hydrogen, and water—thereby, degrading its properties from the surface to the interior over time. In addition, plutonium's continuous radioactive decay causes self-irradiation damage that can fundamentally change its properties over time. Only physicists would think of using such a material.

In the periodic table, plutonium is element 94, and it fits near the middle of the actinide series (ranging from thorium to lawrencium, atomic numbers 90 to 103). Plutonium is of practical interest principally because the 239 isotope has attractive nuclear properties for energy production and nuclear explosives. Manhattan Project physicists managed to extract the more than millionfold advantage of plutonium over conventional explosives. It was the chemists and metallurgists who learned how to extract plutonium, fabricate it, and keep it sound until the time of detonation. The Manhattan Project history of plutonium metallurgy recently published by Edward Hammel (1998) is a remarkable tale of scientific and engineering achievement. These pioneers were working with a metal whose electronic structure and consequent engineering properties were even more puzzling than its nuclear properties. In a remarkably short period, they learned enough to accomplish their goal and left the rest for us to decipher.

The end of the Cold War has signaled a dramatic change in the nuclear weapons programs of the nuclear powers. The challenge now is to help reduce the size of the nuclear arsenals while ensuring that the nuclear weapons are safe and reliable into the indefinite future—without nuclear testing and without a continuous cycle of new nuclear weapons development and deployment. Therefore, extending the lifetimes of plutonium components is more important now than in the past. Similarly, remanufacturing plutonium components for existing weapons systems has become a greater challenge because no new plutonium components have been fabricated for almost 12 years. Moreover, the manufacturing facilities no longer exist, and most of the technical experts have now retired. The long-term behavior of plutonium is also important at the back end of the nuclear weapons cycle—the dismantlement and disposition phases. Because many thousands of nuclear weapons are being withdrawn from the nuclear arsenals of Russia and the United States, we must deal with excess plutonium recovered from these warheads. But the reactive and continuously changing nature of plutonium makes this task a serious challenge. Compounding this challenge is the fact that excess weapons plutonium must be carefully secured against diversion or theft. Burning as fuel in nuclear reactors and geologic disposition are the most likely methods for its eventual disposal. In either case, plutonium must be stored for decades or longer. It has therefore become imperative that we understand the aging of plutonium and of its alloys or compounds. And if we are to accomplish this goal, the next generation of scientists and engineers must become deeply involved in deciphering the complexities of plutonium.



Both this article and “Mechanical Behavior of Plutonium and Its Alloys” (page 336) describe the fascinating mysteries of plutonium metallurgy in a forum open to the research community with the hope of attracting those young men and women into plutonium research. At Los Alamos, we are trying to move from an empirical approach to one based on fundamental principles. At the moment, however, our knowledge rests with the practitioners—and most of our experienced plutonium practitioners have retired or are nearing retirement. To develop a solid fundamental understanding of plutonium, we need the most modern ideas and tools from the international scientific research community. We can then apply this understanding to our practical problems, many of which must naturally remain secret to the public.

The Unusual Properties of Plutonium

Here, I will describe how plutonium is unusual before tackling the question of why it is so.

Manhattan Project pioneers were puzzled by plutonium’s unusual behavior right from the beginning. As soon as they received sufficient amounts of the new element to measure its density, they found unexplained variations ranging from 8 to 24 grams per cubic centimeter (g/cm^3)—see the article “The Taming of ‘49’” on page 48. Also, some tiny samples were as malleable as aluminum, whereas others were as brittle as glass. The list of remarkable properties is quite long (see the box “The Unusual Properties of Plutonium” on page 294), but it was only after the war that those properties were studied systematically.

The most exasperating property from an engineering standpoint is the extraordinary thermal instability of plutonium—that is, the large length (or volume) changes during heating or cooling shown in Figure 1. These volume (or phase) changes are accompanied by

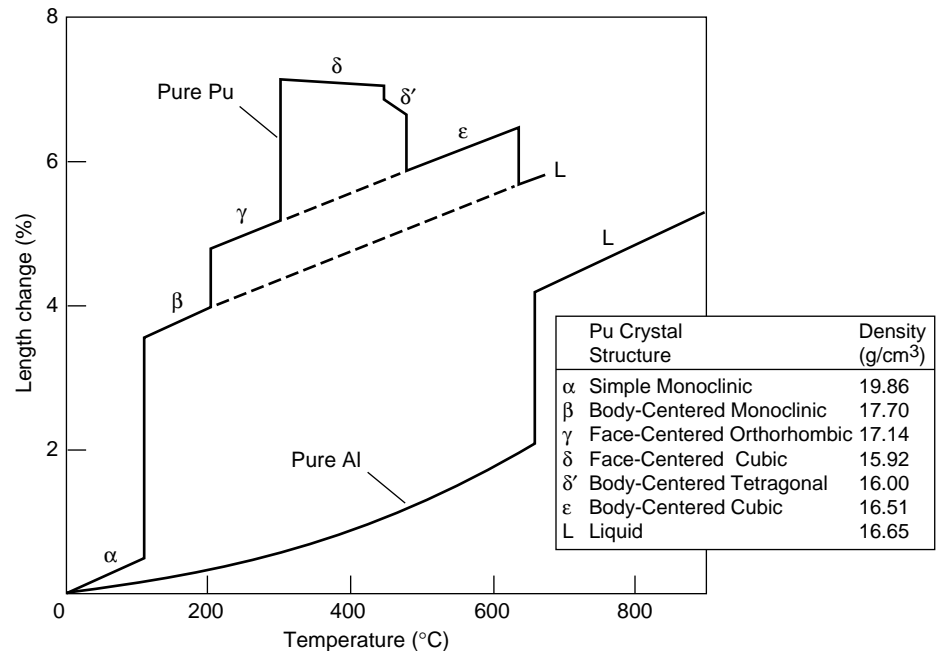


Figure 1. Anomalous Length Changes in Plutonium

Plutonium is a unique element in exhibiting six different crystallographic phases at ambient pressure (it has a seventh phase under pressure). In addition, unlike most metals, plutonium contracts on melting. Transformations to different crystal structures occur readily and are accompanied by very large volume changes. By comparison, aluminum’s behavior is predictable and uneventful. It expands monotonically on heating in the solid phase, and it also expands on melting. The dashed lines show that thermal contraction on cooling the liquid (L) phase of plutonium extrapolates to that of the β -phase; the thermal contraction on cooling the ϵ -phase extrapolates to that of the γ -phase.

significant changes in other properties (see Table I). In particular, the δ -phase, which is stable at high temperatures, is desirable because its highly symmetric face-centered-cubic (fcc) structure makes it very malleable (ductile) and easily formed into desired shapes. In contrast, the room temperature α -phase is an engineering nightmare—its simple monoclinic, low-symmetry structure makes it very brittle. (It has been the metallurgists’ tradition to designate polymorphic phases of elements and alloys with symbols from the Greek alphabet, beginning with α for the lowest-temperature phase.)

The Manhattan Project pioneers soon discovered that they could prevent transformation to the three low-temperature phases by intentionally adding chemical

elements such as aluminum or gallium. The benefits of adding gallium, and thereby retaining plutonium in the δ -phase, are easily derived from Figure 2.

All alloying elements are “impurities” in a nuclear chain reaction because they reduce the number of plutonium-239 atoms per unit volume, but metallurgical considerations strongly favor using the δ -phase alloys for weapons applications. The amount of alloying elements, however, must be kept to a minimum, so plutonium-rich alloys are of greatest interest. Because requirements for a controlled chain reaction in a nuclear reactor are very different, reactor alloys or compounds span a much broader range of plutonium concentrations.

The mysteries of plutonium metallurgy have been studied over the

years within the metallurgical and condensed-matter physics communities—unfortunately, with rather little collaboration between the two. These communities do not even share a common language. For example, they cannot agree on what to call a phase change—whereas physicists prefer transition, metallurgists prefer transformation. Yet, the behavior of plutonium defies conventional metallurgical wisdom. Understanding plutonium involves a close collaboration between physicists, metallurgists, and chemists. Metallurgists must learn to appreciate the intricacies of electronic bonding, especially the role of 5f electrons. Physicists must develop an appreciation for the role of microstructure and crystal defects in determining the engineering properties of plutonium. My intention in writing this article and the companion one on mechanical properties was to bridge the gap between the two communities and complement the very informative articles on plutonium condensed-matter physics found in Volume I of this issue of *Los Alamos Science*.

5f Electrons for Metallurgists

On a fundamental level, the properties of solids are determined by their electronic structure, and thanks to the painstaking work of the electronic-structure physics community, we have a fairly good picture of the simple alkali metals all the way through to the more-complex transition metals and rare earths (lanthanides). Today, the actinides are at the frontier of electronic-structure theory. The current status for actinide atoms and molecules is reviewed in the articles “The Complex Chemistry of Plutonium” (page 364) and “Computational Studies of Actinide Chemistry” (page 382); for metals, it is covered in the articles “Plutonium Condensed-Matter Physics” (page 90), “Actinide Ground-State Properties” (page 128), and “A Possible Model for δ -Plutonium” (page 154). In this section, I summarize those ideas—both old

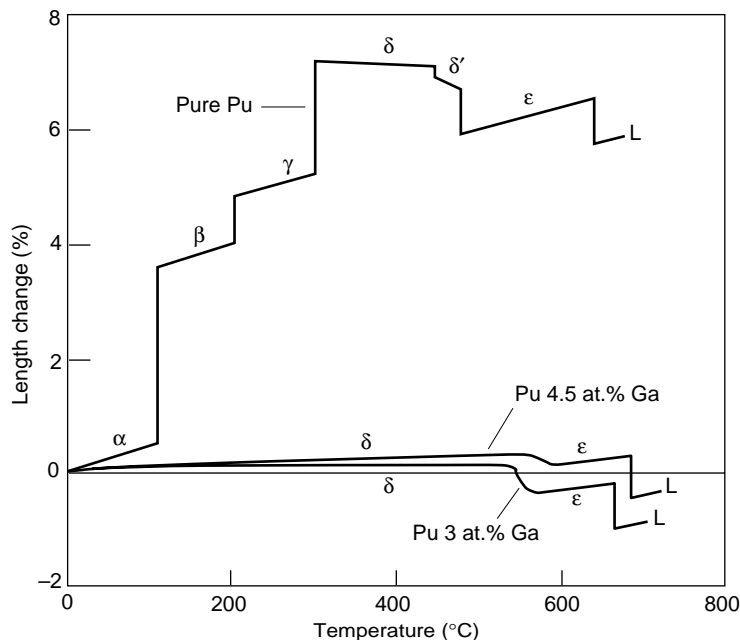


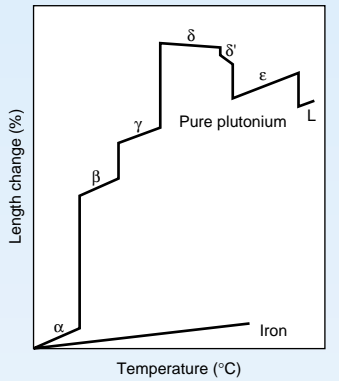
Figure 2. The Benefits of Alloying Plutonium

Both unalloyed plutonium and Pu-Ga alloys expand upon solidification to the bcc ϵ -phase, which expands when it transforms to the fcc δ -phase. Upon cooling, however, plutonium alloys do not exhibit the enormous shrinkage of unalloyed plutonium. They contract only slightly as they cool to room temperature because they remain in the δ -phase, avoiding the transformation to γ , β , and α . Increases in gallium concentration shift the melting temperature and the δ to ϵ transformation to slightly higher temperatures.

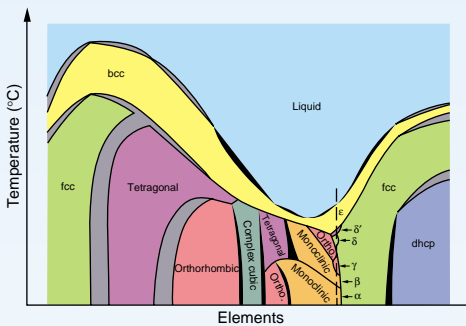
Table I. Comparison of Some Properties of α - and δ -Phase Plutonium

Property	α -Plutonium (unalloyed)	δ -Plutonium (1.8 at. % Ga)
Crystal Structure	Simple monoclinic	fcc
Density (g/cm ³)	19.86	15.8
Thermal Expansion Coefficient (10 ⁻⁶ K ⁻¹)	53	3
Thermal Stability		
Upon heating	To β at 123°C	To $\delta + \epsilon$ at ~500°C
Upon cooling	Stable	To α' at -75°C
Pressure Stability		
Hydrostatic compression	Stable to >50 kbar	To α' at 2.7 kbar
Hydrostatic tension	To δ at ~3.5 kbar	Stable
Young's Modulus (GPa)	100	~40
Poisson's Ratio	0.15	0.26
Compressibility (GPa ⁻¹)	0.020	0.033
Yield Strength (MPa)	—	68
Ultimate Tensile Strength (MPa)	425	100
Total Elongation	<0.1%	~35%
Electrical Resistivity (Ω cm $\times 10^{-6}$)	145	100
Thermal Conductivity [cal/(cm-s-K)]	0.010	~0.026 (3.4 at. % Ga)

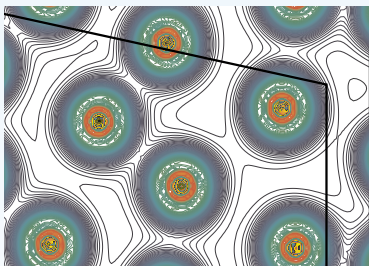
The Unusual Properties of Plutonium



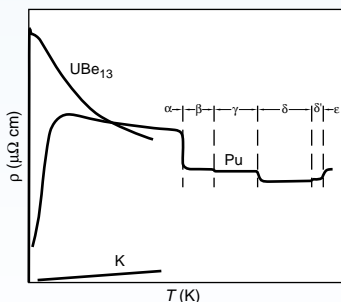
Thermal expansion of plutonium



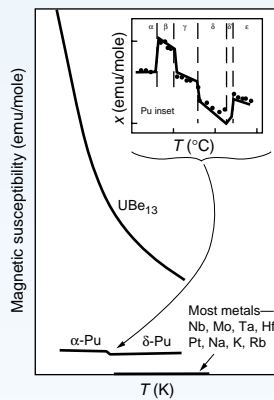
Low melting temperature



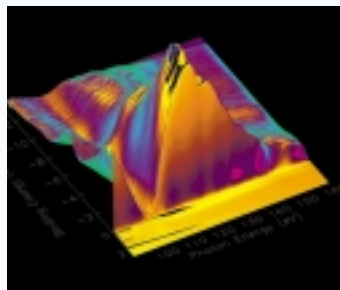
Charge-density contours in α -plutonium



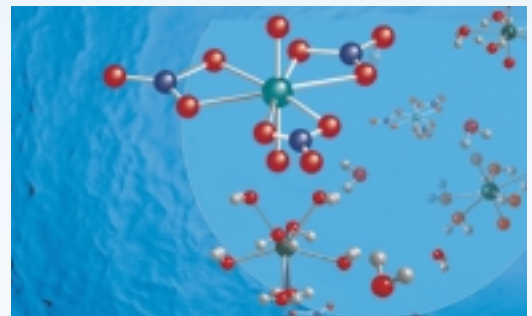
Resistivity



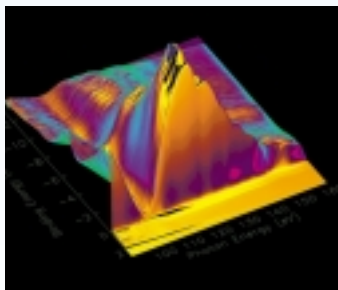
High magnetic susceptibility



Photoelectron spectroscopy data



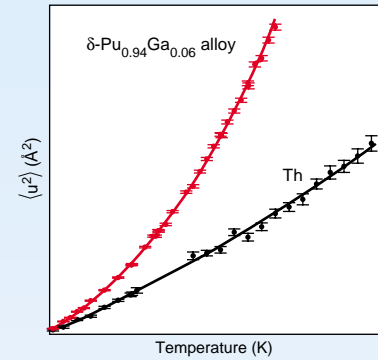
Complex chemistry of plutonium



Self-irradiation

1. Plutonium has six allotropes—that is, six different crystal structures—and a seventh under pressure.
2. The energy levels of these allotropic phases are very close to each other, making plutonium extremely sensitive to changes in temperature, pressure, or chemistry.
3. The densities of the allotropes vary significantly, resulting in dramatic volume changes accompanying phase transitions.
4. The crystal structure of the allotropes closest to room temperature are of low symmetry, more typical of minerals than metals.
5. Among the six allotropes, the face-center-cubic phase (a close-packed atomic arrangement) is the least dense.
6. Plutonium expands when it solidifies from the melt—like ice freezing from water.
7. Its melting point is low.
8. Liquid plutonium has a very large surface tension and the highest viscosity known near the melting point.
9. Diffusion in the highest-temperature solid phase, body-centered-cubic ϵ -phase is anomalously high.
10. The plutonium lattice is very soft vibrationally and very nonlinear.

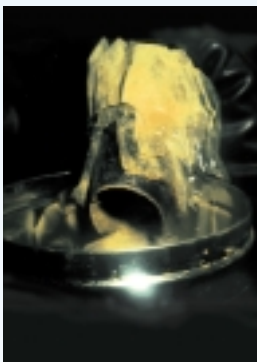
11. The low-symmetry allotropes have very high, positive thermal-expansion coefficients.
12. The fcc and tetragonal allotropes exhibit negative thermal-expansion coefficients—that is, they shrink when heated.
13. There are numerous anomalies in the low-temperature properties of plutonium—such as an increase in electrical resistivity down to 100 kelvins.
14. Plutonium allotropes exhibit dramatic variation in mechanical properties—they range from completely brittle to extremely ductile (malleable).
15. The fcc phase displays the greatest directionality in elastic properties known in fcc metals.
16. Plutonium undergoes self-irradiation because of the radioactive decay of its nucleus—resulting in both lattice damage and transmutation products, including other actinides and helium.
17. Plutonium has great affinity for oxygen and hydrogen.
18. Plutonium exhibits enormous, reversible reaction rates with pure hydrogen.
19. At elevated temperatures, plutonium is pyrophoric in certain atmospheres.
20. In solution, plutonium can appear in five different valence states—four of them have very similar reduction potentials.



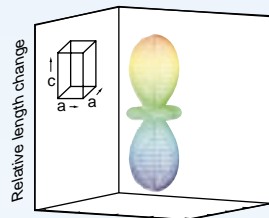
Lattice softening



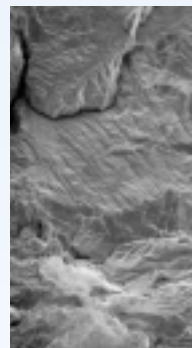
Polycrystalline δ -phase plutonium alloy



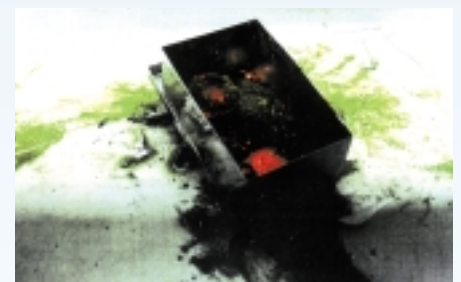
Plutonium corrosion product



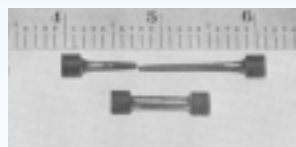
Anisotropic microstrain for δ' -plutonium



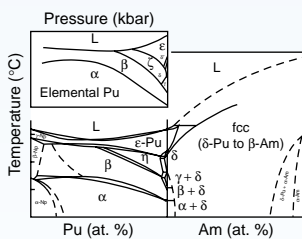
Brittle fracture



Pyrophoricity



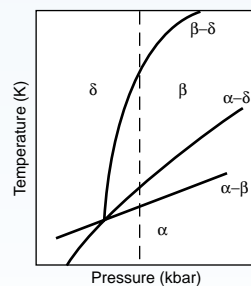
Ductile fracture



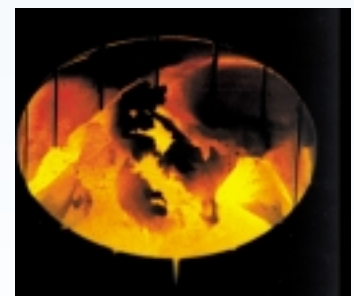
Pressure-temperature diagram and Np-Pu-Am phase diagram



Half sphere of as-cast δ -plutonium alloy



Phase change under hydrostatic tension



Molten plutonium metal

H																	He
Li	Be											B	C	N	O	F	Ne
Na	Mg											Al	Si	P	S	Cl	Ar
K	Ca	Sc	Ti	V	Cr	Mn	Fe	Co	Ni	Cu	Zn	Ga	Ge	As	Se	Br	Kr
Rb	Sr	Y	Zr	Nb	Mo	Tc	Ru	Rh	Pd	Ag	Cd	In	Sn	Sb	Te	I	Xe
Cs	Ba	La	Hf	Ta	W	Re	Os	Ir	Pt	Au	Hg	Tl	Pb	Bi	Po	At	Rn
Fr	Ra																
		Ce	Pr	Nd	Pm	Sm	Eu	Gd	Tb	Dy	Ho	Er	Tm	Yb	Lu		
Ac ⁸⁹	Th ⁹⁰	Pa ⁹¹	U ⁹²	Np ⁹³		Am ⁹⁵	Cm ⁹⁶	Bk ⁹⁷	Cf ⁹⁸	Es ⁹⁹	Fm ¹⁰⁰	Md ¹⁰¹	No ¹⁰²	Lr ¹⁰³			
–	–	5f ²	5f ³	5f ⁴		5f ⁷	5f ⁷	5f ⁹	5f ¹⁰	5f ¹¹	5f ¹²	5f ¹³	5f ¹⁴	5f ¹⁴			
6d	6d ²	6d	6d	6d		–	6d	–	–	–	–	–	–	–			
7s ²	7s ²	7s ²	7s ²	7s ²		7s ²	7s ²	7s ²	7s ²	7s ²	7s ²	7s ²	7s ²	7s ²			
						Pu ⁹⁴											
						5f ⁶											
						–											
						7s ²											

Figure 3. The Actinides and Their Outermost Configuration of Electrons

The actinides are the 14 elements (thorium through lawrencium) following actinium in the periodic table. With a few exceptions, an additional 5f electron is added to the outermost (valence) electron shell of each successive element. Early in the series, the 6d electrons are lower in energy than the 5f electrons. All the ground-state configurations of the first four actinides have a 6d electron in their valence shell. (Having two 6d electrons, thorium is irregular.) The energy of the 5f electrons decreases with atomic number, however, and starting with plutonium, all the actinides have only 5f electrons in the valence shell (with the exception of curium and lawrencium).

and new—that are crucial for metallurgists to understand as they ponder over the unusual behavior of plutonium and its alloys.

The actinide series marks the emergence of the 5f electrons in the valence shells of the elements. The actinide valence-shell configurations (beyond the filled atomic shells of the inert gas radon-86) are highlighted in Figure 3 because it is only valence electrons that form chemical bonds in molecules. This good fortune relieves us of the burden of accounting rigorously for all the other electrons, and it is, of course, the basis for the systematic correlations among chemical properties found in the periodic table. In metals, those valence electrons that overlap electrons from neighboring sites become conduction electrons and form the chemical bonds holding the solid together. The bonding between the conduction electrons and the ion cores is responsible in whole or in part for such properties as crystal

structure, elasticity, phase stability, and melting temperature. It turns out that much of plutonium metal's extreme sensitivity and variability of properties can be traced to the unique behavior of plutonium's 5f valence electrons.

I will explain how the following three specific features of plutonium's electronic structure combine to set this metal apart from other metals in the periodic table: (1) the spatial extent of its 5f electrons is just enough to allow them to bond, (2) multiple low-energy electronic configurations have nearly equal energy levels, and (3) the 5f electrons sit on the knife-edge between bonding and localized behavior.

Spatial Extent of 5f Electron—Just Enough for Bonding. The atomic orbitals in Figure 4 provide the foundation for understanding bonding in molecules and metals. Isolated plutonium atoms have eight valence electrons with a configuration of $7s^25f^6$.

The difference in energy between the 6d and 5f orbitals is very small and results in competing $5f^n7s^2$ and $5f^{n-1}7s^26d^1$ configurations in molecular bonding. That competition accounts for some of the complex chemistry of the actinides as related in the article “The Chemical Complexities of Plutonium” (page 364). The highly directional nature of the f electron orbitals (with three units of angular momentum) promotes very directional, covalent bonding in certain actinide molecules and molecular complexes.

In the metallic state, plutonium has the electronic configuration $7s^26d^15f^5$, and the most-important new result from modern electronic-structure calculations is that, in its α -phase, all eight valence electrons are in the conduction band, which means that the 5f electrons in α -plutonium behave like the 5d electrons of the transition metals: participating in bonding and holding the metal together.

Figure 5 illustrates what is meant by a conduction electron and how a conduction energy band forms in a simple metal. The figure first shows that, in order for two sodium atoms to bind as a diatomic molecule, the 3s valence electron orbitals from the two atoms must be close enough to overlap. In that configuration, the 3s energy level of a single sodium atom splits into two levels—one bonding, the other anti-bonding. Similarly, when 10^{23} sodium atoms condense so that the electron orbitals of neighboring atoms overlap, the atoms bind together in a crystalline array, and the 3s valence level splits into a band of approximately 10^{23} very closely spaced levels. The figure also shows that, as the atoms condense to form a crystal lattice, the electrostatic potential well seen by an electron in an isolated atom becomes a periodic array of potential wells. The core-level electrons (1s, 2s, and 2p) remain bound in individual potential wells at lattice sites, but the energies of the 3s valence electrons are above the wells. They feel the pull of many atoms in the periodic array and become itinerant, traveling

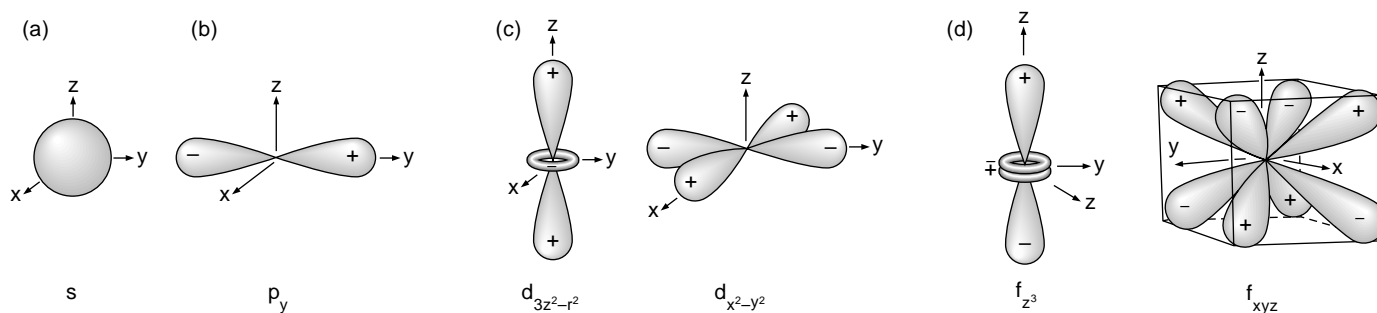
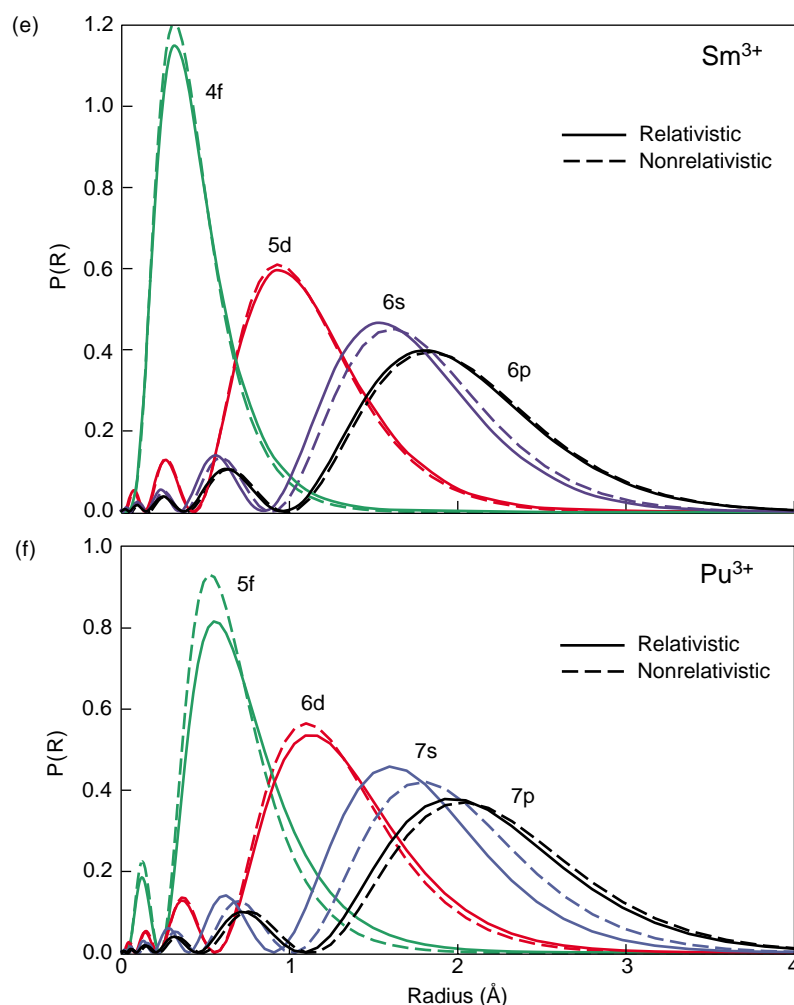


Figure 4. Angular Properties of s, p, d, and f Orbitals and Radial Extent for Samarium and Plutonium Atoms

The shape and orientation of an atomic orbital are characterized by a pair of quantum numbers (ℓ, m_ℓ) . The azimuthal number ℓ is a positive integer that also has letter designations (s for $\ell = 0$, p for $\ell = 1$, d for $\ell = 2$, and f for $\ell = 3$). An electron in an orbital specified by ℓ has \hbar units of orbital-angular momentum. The magnetic number, m_ℓ , is an integer that ranges from $-\ell$ to ℓ . Thus, for every ℓ value, there is a set of $2(\ell + 1)$ orbitals. (a) This is the spherically symmetric s orbital. (b) One of the three p orbitals is illustrated here. The other two are found by rotating the orbital by 90° about the x- and y-axis, respectively. (c) Shown here are two of the five d orbitals. Another orbital is found by rotating $d_{x^2-y^2}$ by 45° about the z-axis, and the remaining two by rotating $d_{x^2-y^2}$ by 90° about the x- and y-axis, respectively. (d) There is no unique polynomial description of the f orbitals. Two orbitals are shown in the cubic representation with simplified polynomial designations. Two more orbitals are found by rotating f_{z^3} by 90° about the x- or y-axis, and three more by rotating f_{xyz} by 45° about the x-, y-, or z-axis—for a total of seven orbitals.



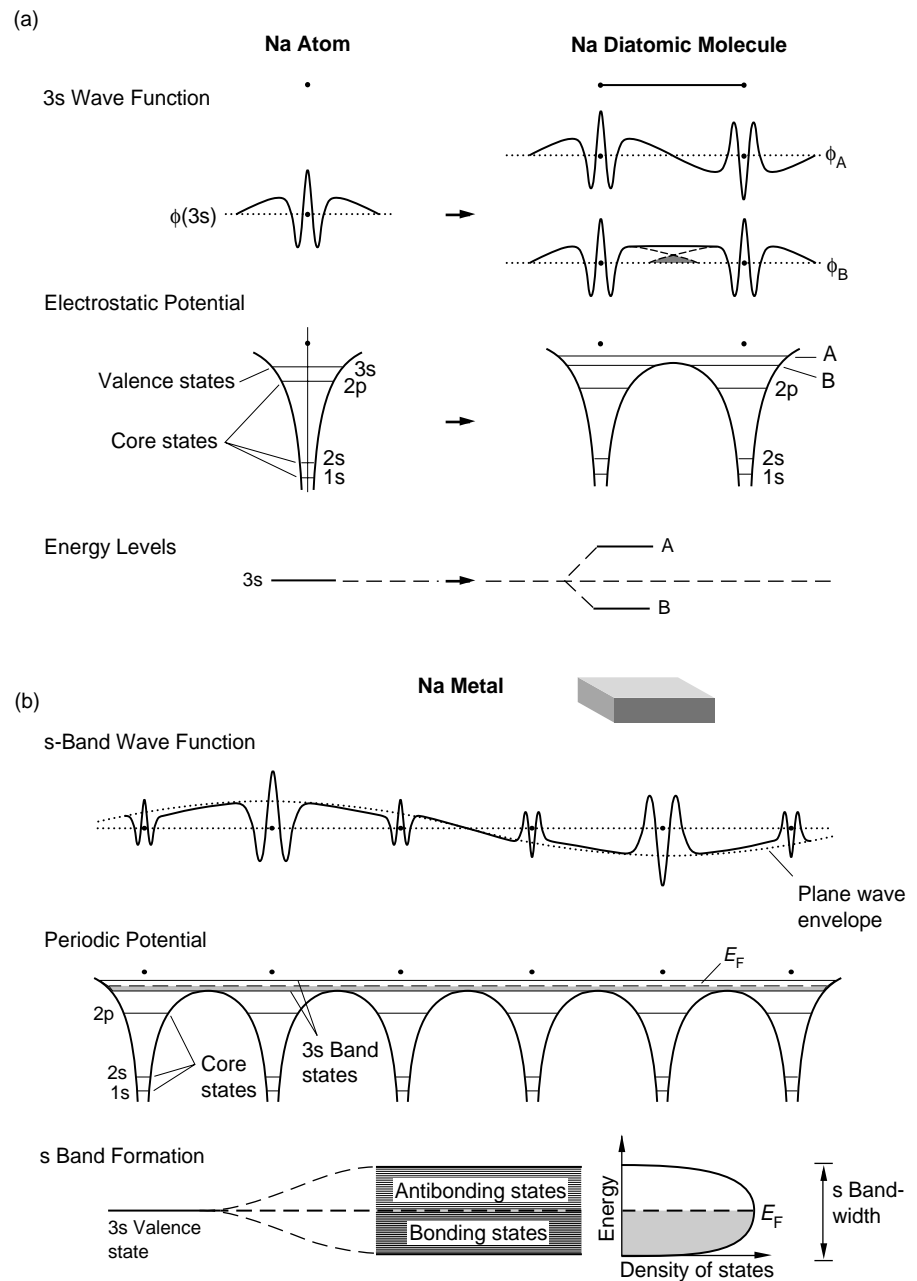
The probability density of finding an electron at a certain distance from the nucleus is shown for the valence electrons of isolated samarium and plutonium ions.

(The peak in the distribution indicates only the most likely distance from the nucleus of that electron.) Using density functional theory, Jeffrey Hay and Richard Martin of Los Alamos calculated these results from first principles. (e) The 4f electrons in Sm^{3+} are localized close to the nucleus and have only a marginal influence on molecular bonding. They do not bond in the solid. (f) The 5f electrons in Pu^{3+} extend relatively far from the nucleus compared to the 4f electrons of Sm^{3+} . (Compare, for example, the probability at 1 Å). For this reason, the 5f electrons participate in the chemical bonding of molecules and also contribute to the chemical bonding of the solid.

Also noteworthy is the much-greater radial extent of the probability densities for the 7s and 7p valence states in Pu^{3+} compared with those of the 5f valence states. The fully relativistic calculations show that the 5f and 6d radial distributions extend farther than shown by nonrelativistic calculations and the 7s and 7p distributions are pulled closer to the ionic cores.

Figure 5. Band Formation, Bloch States, and the Density of States for the Simple Metal Sodium

(a) Two sodium atoms bond to form a diatomic molecule. (b) This bonding process is generalized to the metallic state. For the two sodium atoms, the sum and difference of the 3s valence wave functions of each atom form the bonding (B) and antibonding (A) molecular orbitals of the diatomic molecule, and the 3s atomic-energy level splits into energy levels A and B. Note the double well of the diatomic molecule and the bonding level, just below the top of the well. When many atoms are brought together, they crystallize in a periodic potential array of ion cores and conduction electrons that are shared among the atoms. The core-level electrons (1s, 2s, and 2p) remain localized at lattice sites. The 3s valence electrons form Bloch states consisting of a 3s wave function at each atomic site modulated by a plane wave. The original 3s levels of $\sim 10^{23}$ atoms becomes a band of very closely spaced energy levels with a width related to the amount of overlap between atomic wave functions from neighboring sites. In sodium metal, the 3s conduction band is only half filled, and the highest occupied state at absolute zero temperature is denoted by E_F , the Fermi energy. The number of states at different energy levels is shown as the density-of-states curve.



through the entire crystal. Looking at it another way, we can say that the atoms in the solid are so close together that the individual 3s electron orbitals overlap those of neighboring atoms. As a result, a single electron has the probability of hopping from neighbor to neighbor throughout the crystal lattice.

Figure 5 also shows that for two atoms, the sum and difference of two overlapping 3s atomic orbitals form the bonding and antibonding molecular orbitals, respectively, of the diatomic

molecule. In the solid, a 3s orbital from each lattice site combines with all the others in all possible linear combinations to form a set of Bloch states, the solid-state equivalent of molecular orbitals. Each Bloch state extends over the entire crystal, and just like a molecular orbital, it can be occupied by two electrons at the most—one with spin up, the other with spin down. Figure 5 shows a one-dimensional version of a Bloch state. It is made up of the 3s wave functions at each atomic site

modulated by a plane wave. Because an electron in a Bloch state has a probability to be anywhere in the crystal, it has the potential to conduct electricity when an electric field is applied and is called a conduction electron.

Although each of the 10^{23} Bloch states has a slightly different energy (thus satisfying the exclusion principle for fermions), the levels are so close to each other that we treat them as a continuum and talk about the number of energy levels per unit energy, or

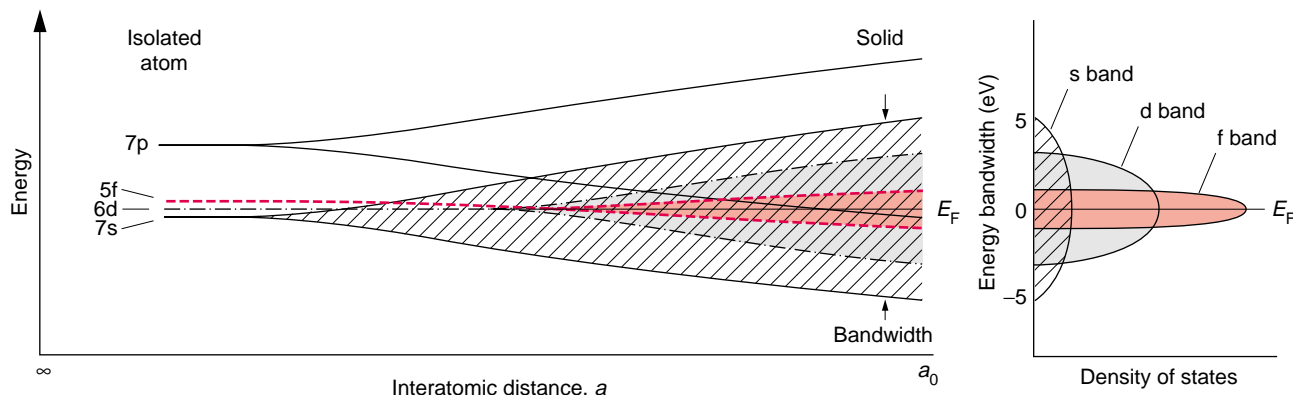


Figure 6. Overlapping Energy Bands in the Actinides

The 7s, 6d, 5f, and 7p valence levels of isolated actinide atoms are relatively close in energy and form overlapping energy bands when the atoms condense into solids. The width of each band is proportional to the overlap between the wave functions of neighboring atoms. The overlap goes in decreasing order from the s and p orbitals to the d and then to the f orbitals, and therefore the sp band is wider than the d band, which is wider than the f band. The f band compresses the energy levels for all the f-electron Bloch states into a very narrow energy range of about 2 to 4 eV, yielding a high density of states. For uranium, neptunium, and plutonium, there are enough 5f electrons per atom that the f band dominates the bonding. Bloch states of the same wave vector but different orbital character can hybridize, or mix, forming states of mixed orbital character.

the density of states, in the conduction band. The Fermi energy E_F is the energy of the highest occupied level for a given element at absolute zero temperature. In a metal, the Fermi level is toward the middle of the energy band—so, there are many empty states available at energies close to those of the occupied levels.

One of the important properties of an energy band is its width. Figure 5 shows that this bandwidth is approximately equal to the difference between the bonding and antibonding energy levels of the diatomic molecule, which is proportional to the amount of orbital overlap between neighboring atoms. Thus, the energy band becomes broader as the atoms get closer together. The fact that the bottom and top boundaries (defining the bandwidth) of each band represent the most-bonding and least-bonding Bloch states is not obvious from the figure but can be determined from the radial extents of the Bloch wave functions. These radial extents are greatest for states at the bottom of the band and least for those at the top.

The energy band structure becomes more complicated in the light actinides

(see Figure 6). The sharp 7s, 6d, and 5f valence levels of the isolated actinide atom are so close in energy that they broaden into overlapping conduction bands in the metal. (At the same time, the Bloch states of the same energy but different orbital origin can combine or hybridize to yield states of mixed orbital character.) Figure 6 indicates that the bandwidth narrows with increasing orbital angular momentum (from s, p, d to f electrons). That narrowing reflects the decreasing radial extent of orbitals with higher angular momentum, or equivalently, the decrease in overlap between neighboring atoms.

Figure 4(b), which was calculated from first principles by Hay and Martin of Los Alamos, shows very clearly that the radial extents are much less for 6d and 5f valence electrons than for 7s and 7p valence electrons. Figure 7 demonstrates that the

7s orbitals of neighboring plutonium atoms overlap substantially. This overlap leads to a broad energy band, whereas the 5f orbitals barely overlap and produce a relatively narrow band. It is also significant that the 5f orbitals are very steep in the overlap region, so a small increase in interatomic distance leads to a rapid decrease in overlap and a narrowing of the band. Wills and Eriksson obtained the same qualitative results for energy bands in actinide solids.¹

Large overlap, or broad bandwidth, of s and p electrons results in those electrons having a large probability of hopping from site to site, spending little time orbiting around a single ion core, and traveling quite freely throughout the crystal. In contrast, 6d and 5f electrons, with their smaller spatial extent and progressively narrow bandwidths, spend more time circling around the ion cores and interacting with other elec-

¹Note that this confinement of states of higher angular momentum is familiar from classical mechanics. Conservation of angular momentum in an attractive central potential leads to an effective force (or potential barrier) that keeps a bound particle in a well-defined range of radial distances. As angular momentum increases but energy remains constant, the range of allowed radial distances decreases, and the potential barrier at the largest radius gets steeper. In quantum mechanics, electrons can tunnel through the barrier, but because the barrier is higher for particles of higher angular momentum, the probability of tunneling decreases, and the probability density outside the barrier is much smaller than that for states of lower angular momentum.

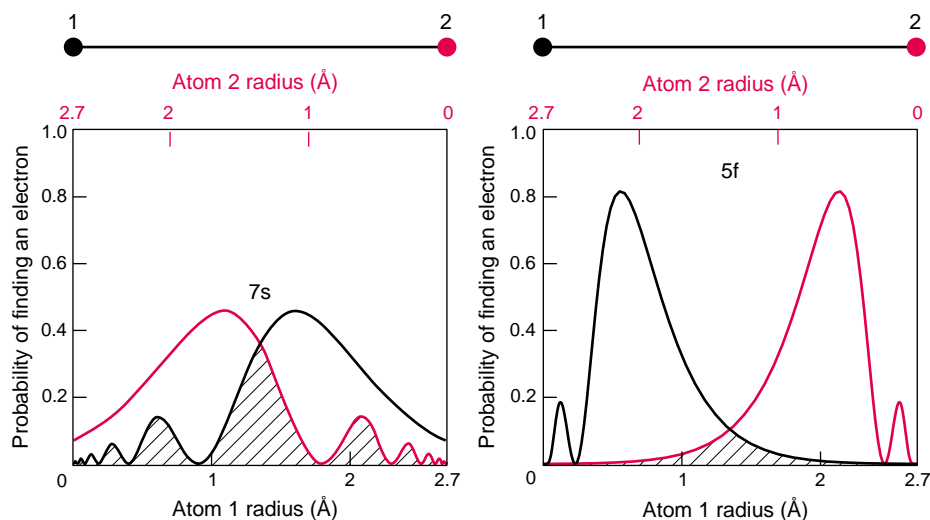


Figure 7. Schematic of Overlapping Wave Functions

The atomic orbitals for plutonium illustrated in Figure 4 are redrawn to show the overlap that occurs when two plutonium atoms are placed at a distance of 2.7 Å (which is the average distance of the short bonds in α -plutonium). The 7s wave functions overlap substantially; the 5f wave functions, only slightly. In plutonium metal, the orbitals become modified, but the 5f overlap is still sufficient for bonding. In the rare earths and heavy actinides starting with americium, the overlap is insufficient for bonding. As a result, 5f electrons remain localized, or bound, in the potential wells at each lattice site.

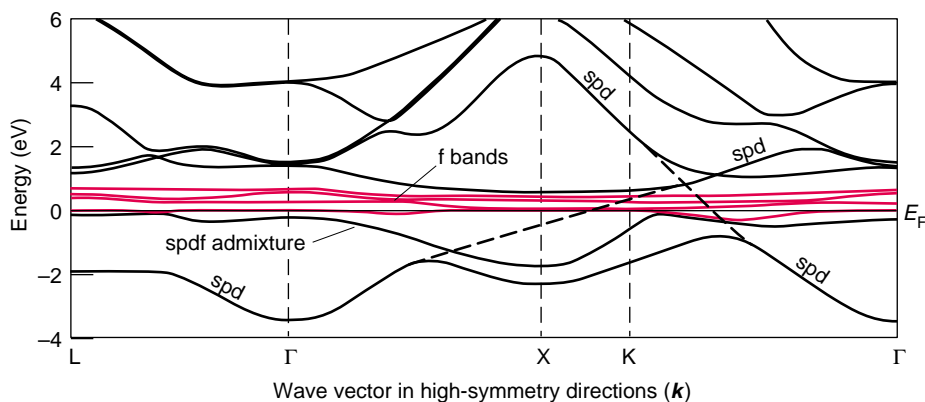


Figure 8. Narrow f Band in Cerium

Here, the one-electron energies in α -cerium are plotted as a function of the electron wave vector, or crystal momentum. Notice that the bands with substantial f character (red) are very flat—that is, the energy range (bandwidth) is very narrow. For a material with many f electrons, a crystal distortion will lower the energy of many of the occupied levels and create a structure that is more stable.

trons at lattice sites. They are thus more likely to depart from the free or nearly free electron behavior seen in the s and p bands of simple metals. In the language of physicists, the narrow-band d and f electrons are highly correlated and are responsible for the unusual behavior of so-called correlated-electron materials. The exact nature of

those correlations in plutonium and other narrow-band materials is now under intense study in the condensed-matter physics community.

One last feature in Figure 6 is the very high density of states for f electrons—that is, a large number of Bloch states are confined to a very narrow band—on the order of 2 to 4 electron-

volts (eV). Because in a band there are always approximately 10^{23} states (one per atom), narrow bandwidths automatically yield a high density of states. Figure 8 shows a plot of the narrow conduction band (energy vs crystal momentum k) for the 4f electrons in α -cerium. The narrow bandwidth means the plot is very flat—that is, as the crystal momentum of the Bloch state varies, the energy of the state remains very close to the Fermi energy.

Narrow f Bands and Low-Symmetry Structures in the Light Actinides.

Having glibly stated that the 5f electrons in α -plutonium occupy a narrow conduction band (2–4 eV in width), I need to point out that the nature of the 5f electrons and their role in determining properties have been a source of speculation for nearly half a century. Only recently has there been a breakthrough: Electronic-structure calculations yielded believable predictions for α -plutonium (see the article “Actinide Ground-State Properties” on page 128) and photoemission experiments confirmed them (see the article “Photoelectron Spectroscopy of α - and δ -Plutonium” on page 168).

In general, electronic-structure calculations predict the energy bands and the total binding energy from an assumed crystal structure and atomic density (or volume) of a metal. Today, these calculations are so fast and accurate that one can try out various crystal structures and atomic volumes as inputs and solve for the energy bands and total energy for many different combinations. Invariably, the lowest energy solutions have the right crystal structures and atomic volumes. But this approach has been very difficult to apply to the actinides, and to plutonium in particular, because the differences in total binding energy between different crystal structures are very small and relativistic effects are a significant factor in determining which structure and atomic volume yield the lowest energy. In the past decade, however, the elegant work by Söderlind et al. (1995), which

incorporates most of the physics that is difficult to calculate (for example, low-symmetry structures and the relativistic motion of core electrons), demonstrates convincingly that the 5f electrons are bonding in α -plutonium.

It is still true, however, that early pioneers such as Willie Zachariasen and Jacques Friedel led the way, predicting that the 5f electrons in the light actinides are bonding. They based their conjecture on a comparison of the atomic radii (or volumes) of the light actinides with those of the d-electron transition metals. Atomic volumes provide one of the best guides to what the electrons are doing.

As shown in Figure 9, the nearly parabolic decrease in atomic radii of the light actinides is very similar to that of the 5d transition metals, providing convincing evidence that, as 5f valence electrons are added across the early part of the actinide series, they increase cohesion and thus cause the atomic volume to decrease. This decrease in atomic volume due to 5f bonding was not anticipated for the 5f series. The 5f electrons were supposed to behave like the 4f valence electrons in the rare earths, which are localized in the ionic cores and are therefore chemically inert, or nonbonding. For that reason, the atomic volume remains relatively constant across the rare-earth series.

Another sign of electron localization vs itinerancy is the presence or absence, respectively, of local magnetic moments. The 4f electrons in the rare earths produce local moments (except for those elements with half-filled or filled 4f shells), whereas the 5f electrons in the light actinides, up to α -plutonium, do not.

Why do 5f electrons bond in the light actinides? Why do 4f electrons not bond in the rare earths? In other words, why are the 5f electrons spatially more extended than the 4f electrons? The Pauli exclusion principle requires that the 5f wave functions be orthogonal to the 4f core-level wave functions in the actinides. This requirement pushes the

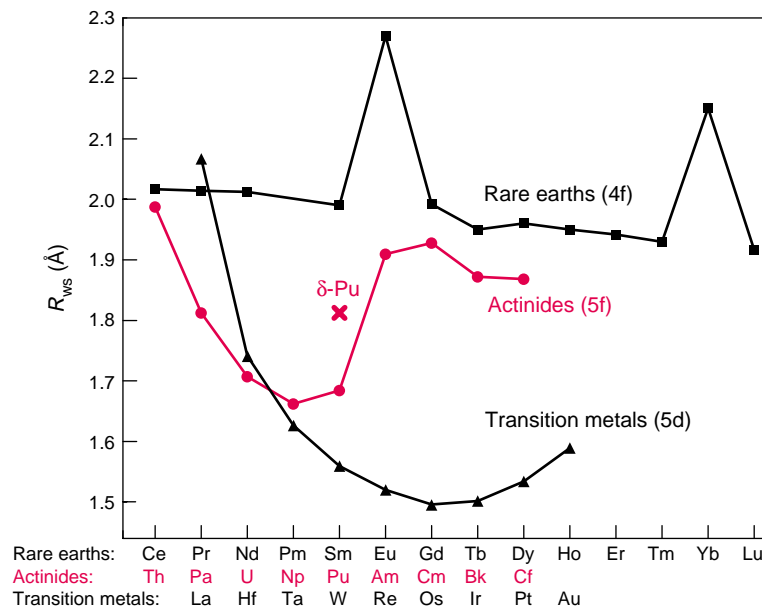


Figure 9. Experimental Atomic Radii of the Actinides, Rare Earths, and 5d Transition Metals

The atomic radius displayed is the Wigner-Seitz radius, defined as $4\pi/3 R_{WS} = V$, where V is the equilibrium volume per atom of the primitive unit cell. The rare-earth elements show only a slight lattice contraction, indicating that the 4f electrons are added to the core (that is, they are localized) as the nuclear charge is increased across the series. The exceptions are europium and ytterbium for which one electron is removed from the conduction band to fill up half of the f shell and the entire f shell, respectively. Fewer conduction electrons (or lower valence) result in weaker bonding and an expanded volume. The actinides follow the transition-metal trend up to plutonium. Past americium, they behave more like the rare earths.

5f wave functions somewhat farther from the ion cores. In addition, the greater nuclear charge of the actinides compared with that of the rare earths causes larger relativistic effects, increasing the radial extent of the 5f wave functions somewhat, while drawing the 7s and 7p orbitals closer to the cores, as shown in Figure 3. One implication is that the relative radial separation of the 5f, 6d, and 7s orbitals in the actinides is less than the corresponding radial separation of the 4f, 5d, and 6s orbitals in the rare earths. So, in the rare earths, the 5d and 6s orbitals of neighboring atoms overlap, whereas the 4f electrons remain nonbonding. In the actinides, on the other hand, as the 6d and 7s orbitals of neighboring atoms overlap and become bonding, so do the 5f orbitals.

Boring and Smith emphasize (see the article on page 90) that the 5f conduction band determines the bonding properties and crystal structure of α -plutonium, which has five 5f electrons and only one d and two s electrons. They also emphasize the interplay of the different bands in determining the equilibrium crystal volume. Their simplified band calculations (for fcc structures with spherical potentials) show that occupation of the s states in plutonium provides a repulsive force, expanding the equilibrium crystal volume and making the f bands narrower than they would be otherwise. This general picture is borne out by the more-sophisticated full-potential band structure calculations performed by Wills and Eriksson. Those calculations demonstrate clearly that the 5f electrons

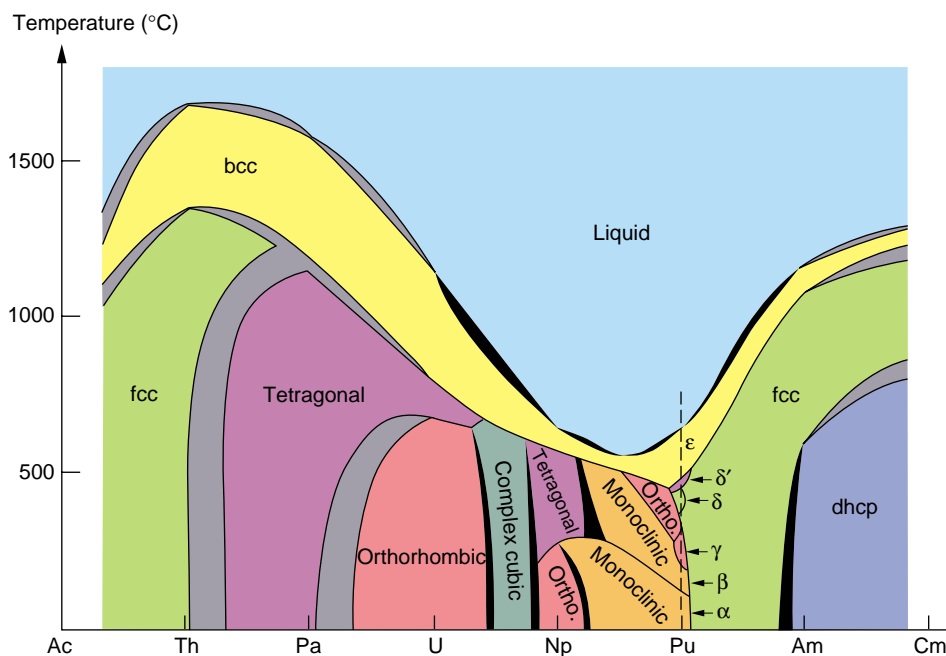


Figure 10. Connected Binary-Phase Diagram of the Actinides

The binary-phase diagrams (temperature vs composition) for adjacent actinide elements are connected across the entire series to demonstrate the transition from typical metallic behavior at thorium to the enormous complexity at plutonium and back to typical metallic behavior past americium. Two-phase regions are in black; uncertain regions are in gray.

in the light actinides extend just far enough to overlap and form narrow conduction bands, whereas the 4f electrons in the rare earths do not.

The calculations of Söderlind et al. (1995) also demonstrate how those narrow 5f bands stabilize low-symmetry structures. Until recently, the low-symmetry ground-state crystal structures and many other peculiar properties in the light actinides up to α -plutonium were attributed to the highly directional nature of the f-electron orbitals (see Figure 3). That orbital directionality was believed to cause covalent-like directional bonding (that is, electron charge buildup between the ion cores) in the solid. But band structure calculations show no charge buildup between the ion cores, refuting the original assumption.

Instead, Söderlind et al. show that it is the narrowness of the 5f conduction band that favors the stability of low-symmetry structures. As shown in Figure 8, a narrow energy band has a very large number of occupied states (high density of states) right below the Fermi energy. If the crystal structure is

highly symmetric, the conduction bands are degenerate in high-symmetry directions—that is, there are two (or more) states of equal energy for each value of the crystal momentum. However, a distortion to a tetragonal, orthorhombic, or monoclinic lattice will split the degenerate portion of the band into two (or more) bands—one lower and the other higher in energy. If the band is narrow, the distortion will lower the energy of billions of occupied states (there are about a billion states within 10^{-14} eV of the Fermi energy), thereby tending to lower the total binding energy of the sample. This effect is demonstrated in Figure 11 on page 143 of the article “Actinide Ground-State Properties.”

A competing influence is the electrostatic, or Madelung, energy (the result of conduction electrons not completely shielding the ion cores on the lattice sites). The Madelung energy is lowest for high-symmetry crystal structures, and it increases if the lattice is distorted. Thus, for moderate and wide bands (moderate to low density of states near the Fermi level), the Madelung energy,

which favors high symmetry, wins out, and no distortion occurs. In narrow-band materials, the opposite is true.

Peierls (1955) was the first to suggest that lowering the symmetry of a one-dimensional lattice could lower the energy and increase stability, and Heine (1969) made a similar suggestion for s-p electron metals such as mercury, gallium, and indium, which also exhibit lattice distortions that favor low-symmetry structures. Söderlind et al. (1995) showed that, by forcing transition metals or p-bonded metals to have narrow bands (that is, by assuming an unnaturally large separation between atoms), the low-symmetry structure becomes the lowest-energy structure although no f electrons are involved.

One might argue that cerium provides a counter example to the rule that narrow bands favor low-symmetry structures. Cerium transforms from the fcc γ -phase to the much denser fcc α -phase when the temperature is lowered or the pressure is increased. Johansson (1974) suggested that this transition occurs because localized f states in the fcc γ -phase become itinerant (Bloch) states in the fcc α -phase, forming a narrow f band and increasing the bonding. (This transition is similar to the Mott insulator-to-metal transition, except only the f electrons are involved.) Thus, the existence of a narrow f band in the highly symmetric fcc α -phase of cerium seems to contradict the rule that narrow bands produce low-symmetry structures. However, in cerium, there is less than one full f electron per atom that can bond, compared with two s electrons and one d electron per atom. Hence, the s and d electrons, which favor high-symmetry structures, play a dominant role in determining crystal structure.

We can now begin to interpret the systematic changes in crystal structure that occur across the actinide series. Smith and Kmetko (1983) devised a clever graphic way to view these trends, a “connected” phase diagram (see Figure 10). Calculations show that f electron bonding begins at thorium with a

fraction of an *f* electron per atom in the conduction band. That contribution to bonding is insufficient to swing the energy balance toward a low-symmetry distortion, and cubic crystal structures are observed. From left to right across the actinide series down to plutonium, the number of *f* electrons in the conduction band increases, the *f* electrons play a larger role in bonding, and the ground-state crystal structures have increasingly lower-symmetry—plutonium is the least symmetric with a monoclinic structure. Beyond plutonium, the *f* electrons become localized (as in the rare earths), the *s* and *d* bands determine the crystal structure, and high-symmetry ground-state structures become prevalent.

Multiple Electronic Configurations of Nearly Equal Energy. The second fundamental feature leading to the unusual properties of plutonium was already mentioned in connection with Figure 5: The energy levels of the 7*s*, 6*d*, and 5*f* electrons in the isolated atom are very close to each other, resulting in overlapping energy bands and hybridized Bloch states. Wills and Eriksson have shown (in the article on page 128) that, under high pressure, the 6*p* core states may overlap and form Bloch states, producing an energy band that overlaps the *s*, *d*, and *f* bands.

Because the energy levels are so close, very little change in temperature, pressure, or chemical additions is required to prompt a change in crystal structure. Increasing temperature, for example, introduces entropy effects through lattice vibrations. The higher the temperature, the more important the entropy term becomes in determining the free energy of the system. So, it is easy to see why the crystal structures in plutonium are so unstable with respect to temperature. Unfortunately, it is very difficult to add the effects of vibrating (thermally excited) atoms to electronic-structure calculations because density functional theory, the basis for all modern calculations, only applies to the ground state ($T = 0$).

By varying the atomic volume, we

can, however, model pressure. Increasing the pressure (assuming smaller atomic volumes) shifts the relative stability of the bands and broadens the bands. As I discuss later, we know empirically that increased pressure quickly squeezes out the high-volume, high-symmetry phases of the light actinides in favor of the low-symmetry structures. However, as the pressure is increased further, the bands will eventually broaden sufficiently for crystal distortions not to be energetically favorable, and high-symmetry structures are predicted to return. For the heavy actinides, increased pressure will cause a delocalization similar to that in cerium, yielding low-symmetry structures initially. Such calculations can be done at absolute zero for ground-state predictions. The predictions of Wills and Eriksson for pressure-induced phase transformations are highly accurate.

Changing chemistry by alloying can affect electronic structure. Moreover, alloying can affect vibrational and configurational entropy contributions. So, one would expect phase stability in the actinides to be very sensitive to chemical additions. Band structure calculations cannot yet deal with alloying effects to the level of required accuracy.

Brewer (1983) adopts the chemist's viewpoint to predict the effect of multiple, closely spaced energy levels in plutonium on crystal stability. On the basis of spectroscopic evidence, he claims that at least four different atomic configurations are of nearly equal energy in plutonium metal. Different atomic configurations result in atoms of different sizes, and those atoms account for increased liquid stability. Stability is increased when compared with that for cubic structures that have equivalent lattice sites. He also points out that atoms of different sizes can pack more efficiently in a complex structure. Whereas close-packed structures are most efficient at filling space when the atoms are of equal size, mixing atoms of different sizes can result in higher densities and larger coordination numbers.

For example, the Laves phases, the most-common intermetallic compounds, can be packed to a coordination number of 13.3 by A and B atoms with a radius ratio of 1.225 being arranged in either the cubic structure of MgCu_2 or the hexagonal structure of MgZn_2 or MgNi_2 (Haasen 1992). The α -phase monoclinic structure of plutonium is a slightly distorted hexagonal structure. Lawson et al. (1996) point out that its nature can be viewed as "self-intermetallic" because it contains 16 atoms per unit cell and 8 distinct positions for those atoms. They compare the α -plutonium structure with the very complex structure of α -manganese, which has 58 atoms per unit cell and 4 distinct atomic positions. In addition, short bonds are prevalent on one side of the α -plutonium atom, and long bonds are prevalent on the other side, suggesting that the atoms are also nonspherical, a feature that further complicates the crystal packing. Therefore, it seems intuitively correct to say that α -plutonium packs more closely than do single-sized hard spheres.

Sitting on the Knife-Edge between Bonding and Localized Behavior. Plutonium has one more feature that sets it apart from uranium, neptunium, and americium, its neighboring elements. That feature derives from its position in the actinide series. Plutonium sits right at the transition point at which the 5*f* electrons change from being bonding to being localized (chemically inert). As the nuclear charge increases across the actinides, the increase causes the atomic volume to contract slightly because the electron wave functions are pulled slightly closer to the ion cores (in the rare earths this same phenomenon is called the lanthanide contraction). The much larger effect is that, much like each additional *d* electron in transition metals, each additional 5*f* electron produces a relatively large decrease in atomic volume because the 5*f* electrons go into the conduction band and add to the bonding (see Figure 9).

The atomic volume of the transition

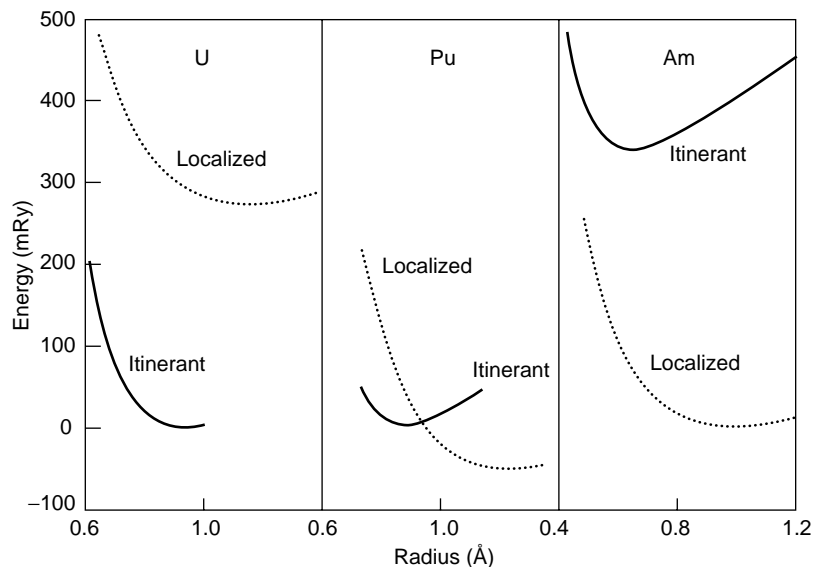


Figure 11. Bonding of 5f Electrons in Plutonium vs Adjacent Elements These plots of total energy vs normalized lattice based on Eriksson et al. (1999) demonstrate the effects of shifting the 5f electrons from bonding states (solid line) to localized states (dotted line). At uranium, there is little question that 5f bonding produces the lowest energy state, and at americium, 5f localization produces the lowest energy state. At plutonium, the balance clearly shifts from bonding to localization. Experimental error in the estimated energy gain on localization—about 50 mRy—precludes a clear prediction of the nature of the plutonium ground state from these calculations. (This figure was adapted with permission from Elsevier Science.)

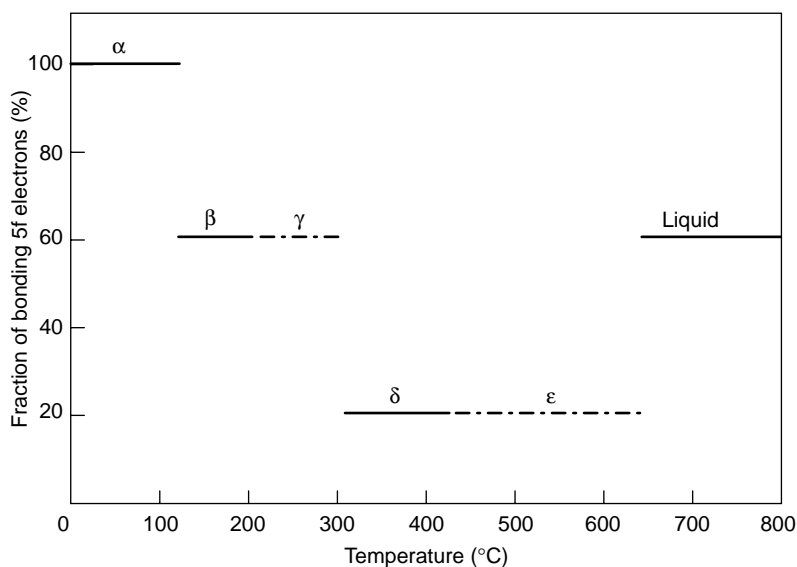


Figure 12. Notional Diagram for 5f Electron Bonding in Plutonium Phases Söderlind et al. (1997) have shown that all five 5f electrons bond in the α -phase. To get the correct volume for the δ -phase, Eriksson et al. (1999) must allow four 5f electrons to localize and only one to bond. In the β -phase, γ -phase, ϵ -phase, and the liquid phase, the number of bonding 5f electrons is expected to be between five and one. In this diagram, the estimates for the β -, γ -, and ϵ -phase are based on the atomic volumes. The estimate for the liquid phase is based on the fact that, from these calculations, the thermal-expansion curve for the β -phase extrapolates to that of the liquid state.

metals reaches a minimum when the d shell, which holds 10 electrons, is half full. Past that point, cohesion begins to decrease and atomic volume begins to increase because the antibonding states of the d band start to be filled. The 5f shell holds 14 electrons, and one might expect the atomic volumes of the actinides to decrease in moving toward curium whose f shell is half full. Instead, the atomic volume of plutonium is slightly greater than that of neptunium. Total energy calculations of Eriksson et al. reproduce this upturn when the low-symmetry monoclinic structure of plutonium's α -phase serves as input. These scientists attribute the upturn to the openness of that structure. In any case, the increase in nuclear charge finally causes the 5f electrons to localize at americium, and the atomic volume expands dramatically because now none of the 5f electrons bond.

The transition from bonding (itinerant) 5f electrons in uranium to localized 5f electrons in americium is graphically illustrated by the plots of total energy vs relative lattice constant in Figure 11. Perhaps even more intriguing, the transition appears to occur right at plutonium, not between plutonium and americium. Eriksson et al. have tried to match the atomic volume of the fcc δ -phase in plutonium. They find that they have to let four of the 5f electrons localize but keep one of them bonding. (I will return to the puzzle of the δ -phase later). On the basis of discussions with Wills, I show a notional sketch of how localization may proceed in the plutonium allotropes (Figure 12). The value for the liquid is only a guess guided by comments made by Hill and Kmetko (1976) that the liquid accommodates 5f bonding better than the cubic solid phases. Based on the extensive work on liquid plutonium by Wittenberg et al. (1970) that showed that the molar volume of the liquid is the same as that of the β -phase, Hill and Kmetko called the β -phase the "solid-state" analogue of the liquid. Hence, I estimated the degree of 5f electron localization to be the same for the liquid as for the β -phase.

Having to describe different allotropes of the same element at room temperature and above by such different electronic states (mixtures of Bloch states and localized states) is unprecedented. Plutonium is truly unique among the elements in the periodic table. And more important for the metallurgists who must work with this material, the transition from Bloch states to localized states causes both the atomic volume and the crystal structure to change dramatically.

What Basic Properties Really Matter to Metallurgists?

The electronic structure at absolute zero is a starting point for understanding plutonium, but it is far removed from typical interests in the practical world of metallurgy. Metallurgists must relate the basic properties of metals and alloys to their microstructures and then tailor those microstructures to produce desired engineering properties for specific applications. As Peter Haasen pointed out (1992), microstructure begins where condensed matter physics typically leaves off. Crystal structure—the perfect periodic array of atoms in a single crystal—forms the foundation of condensed matter physics. Metallurgy is directly affected by those perfect crystalline arrays (see the box “Atomic Packing and Slip Systems in Metals” on page 308), but it also takes into account that they are mostly confined to very small, microscopic regions. In other words, between the macroscopic scale of continuum mechanics and the atomic scale of perfect crystal lattices, there is another scale, that of microstructure, which is governed by the properties of individual grains, their crystalline defects, and the interactions among them all. Examples of microstructures and their defect substructures are shown in Figure 13.

For most technologically important materials, especially structural materials, microstructure determines engineering properties. Therefore, the basic properties that really matter to the

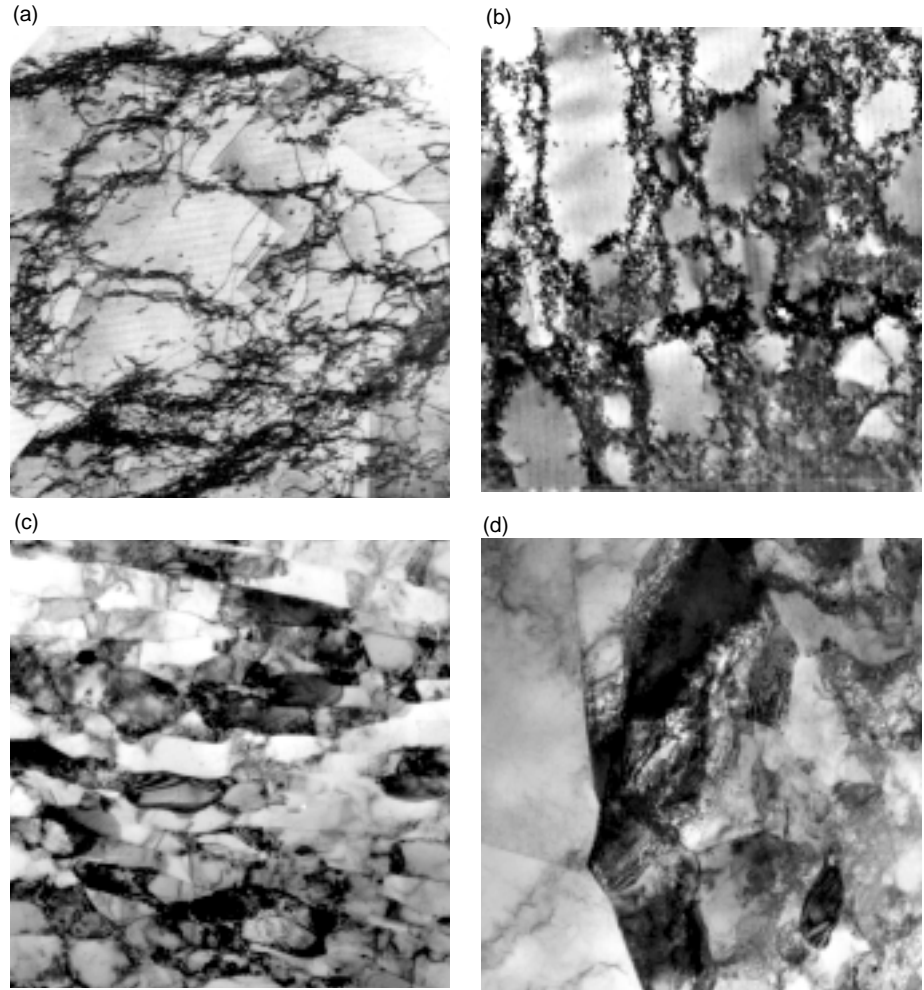


Figure 13. Dislocation Microstructures in fcc Metals

Dislocations are key microstructural features in solids. These line defects typically range in concentration from 10^6 to 10^{12} dislocations/cm². Readily formed during solidification or deformation, they easily arrange themselves to lower the overall energy of the system, leaving a substructure within a crystal or within the grains of a polycrystal. The examples here show that dislocations form and rearrange during cold-working and subsequent annealing. Dislocations are best imaged by their contrast in an electron beam. They can be observed as dark lines in a transmission-electron-microscope image. (a) Individual dislocations and dislocation tangles in the form of “braids” appear in copper deformed at 77 K. (b) Dislocations organize into cell walls during heavier deformation of copper at room temperature. (c) Commercially pure aluminum undergoes even greater organization of dislocations during heavy deformation at room temperature, forming clean cell walls (sample was cold-rolled 83% at room temperature—cells are stretched out in the direction of principal elongation). (d) During annealing at 440°C, commercially pure aluminum recrystallizes, or forms new, nearly-strain-free grains as indicated by the high-angle grain boundaries. Some of the dislocation cells, or subgrains, are still visible in the right-hand grain.

Figures 13(a) and 13(b) were reprinted from *Physical Metallurgy*, edited by R. W. Cahn and P. Haasen, copyright 1996, page 3, with permission from Elsevier Science. Figures 13(c) and 13(d) are courtesy of M. G. Stout of Los Alamos National Laboratory.

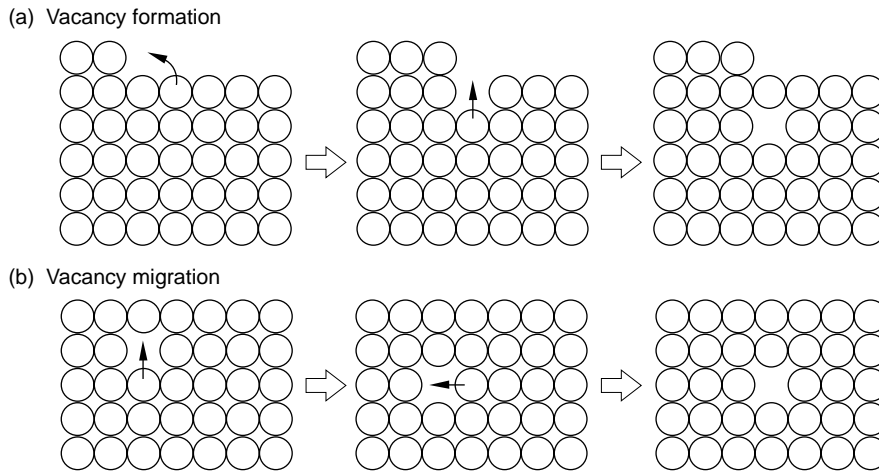


Figure 14. Vacancy Mechanism for Diffusion and the Strong Dependence of Metallurgical Properties on Homologous Temperature

(a) A lattice vacancy is created when an atom at an interior lattice site jumps to a site on the surface. The equilibrium ratio of vacancies to atoms is $n_v/n_0 = \exp(-Q_f/k_B T)$, where Q_f is the activation energy for vacancy formation. (b) Vacancies migrate in a crystal as atoms jump to vacant lattice sites. The number of jumps per atom is $r_a = n_v/n_0 A \exp(-Q_m/k_B T)$, where Q_m is the activation energy for vacancy migration. Note that both vacancy formation and migration are highly dependent on the homologous temperature rather than the absolute temperature. For example, in copper at 1350 K (6 K below the melting point of copper, or $T/T_m = \sim 1.0$), the equilibrium vacancy concentration is 10^{-3} , the jump rate is $10^9/s$, and the vacancies are ~ 10 atoms apart on average, whereas at room temperature ($T/T_m < 0.25$), the vacancy concentration decreases to 4.5×10^{-15} , the jump rate decreases to $10^{-6}/s$, and the vacancies are $\sim 10^5$ atoms apart. At room temperature ($T/T_m = \sim 0.5$), the jump rate in lead is 22/s, and the vacancies are ~ 100 atoms apart.

plutonium metallurgists are those that have the greatest influence on microstructure: crystal structure, melting point, and phase stability.

Crystal Structure. The internal energy of metals depends primarily on their atomic volumes. Energy differences resulting from different structural arrangements are typically very small. For example, in sodium the heat of transformation from a body-centered-cubic (bcc) to hexagonal close-packed (hcp) structure at 36 kelvins is only one-thousandths of the total binding energy. Yet, crystal structure has a dominant effect on metallic properties.

Metallic bonding exhibits little directionality because the conduction electrons that hold the atoms together are shared throughout the crystal lattice. Therefore, atoms in metals tend to pack

uniformly, leaving the minimum amount of void space. Indeed, metals solidify preferentially into close-packed fcc and hcp structures and into the nearly close-packed bcc structure (see the box “Atomic Packing and Slip Systems in Metals” on page 308). In fact, in their ground states, 53 of the elements up to plutonium (element 94) have fcc or hcp structures and 23 have bcc structures. If the tetragonal structure is also considered nearly close-packed, all but four of the metals in the periodic table exist in one of these four simple crystal structures.

The host crystal structure determines macroscopic structural properties of metals in many ways. For example, as shown on pages 308 and 309, crystal structure determines the operative slip planes, as well as the nature of crystalline defects, and those defects control

the strength of the material and most other structural properties. For example, plastic deformation by slip does not occur homogeneously when entire lattice planes are slipped over each other. Instead, it is made significantly easier by the motion of line defects known as dislocations (see Figure 4 in “Mechanical Behavior of Plutonium and Its Alloys” on page 341).

The formation and motion of point defects such as lattice vacancies are also influenced by crystal structure. We will show later that migration of vacancies is the primary mechanism for bulk diffusion in metals. Interestingly, because relaxation of atoms surrounding a vacancy is controlled by atomic coordination and the strength of the bonding, vacancy migration is easier in the bcc structure than in close-packed structures, and therefore diffusion is significantly faster in the bcc structure. On the other hand, vacancies are formed more easily in the close-packed structures.

Crystal structure also has a direct effect on the nature of thermal lattice vibrations and, therefore, on the vibrational entropy of crystals. At high temperatures, the entropy contribution to the free energy can become very large and therefore have a dominating influence on phase stability. For example, because it has fewer nearest neighbors than close-packed metals, the bcc lattice exhibits lower vibrational frequencies and therefore higher vibrational entropy (or a high uncertainty of position in the lattice) than other crystal structures. Indeed, the bcc lattice is the structure with the lowest free energy at high temperatures. Consequently, most metals melt from the bcc structure.

It should now be apparent that the phase changes in plutonium are more than an annoyance because the accompanying changes in crystal structure have a dramatic influence on structural properties. In particular, at low and slightly elevated temperatures, the low-symmetry α -, β -, and γ -phase become stable as opposed to the high-symmetry, ductile structures found in most metals.

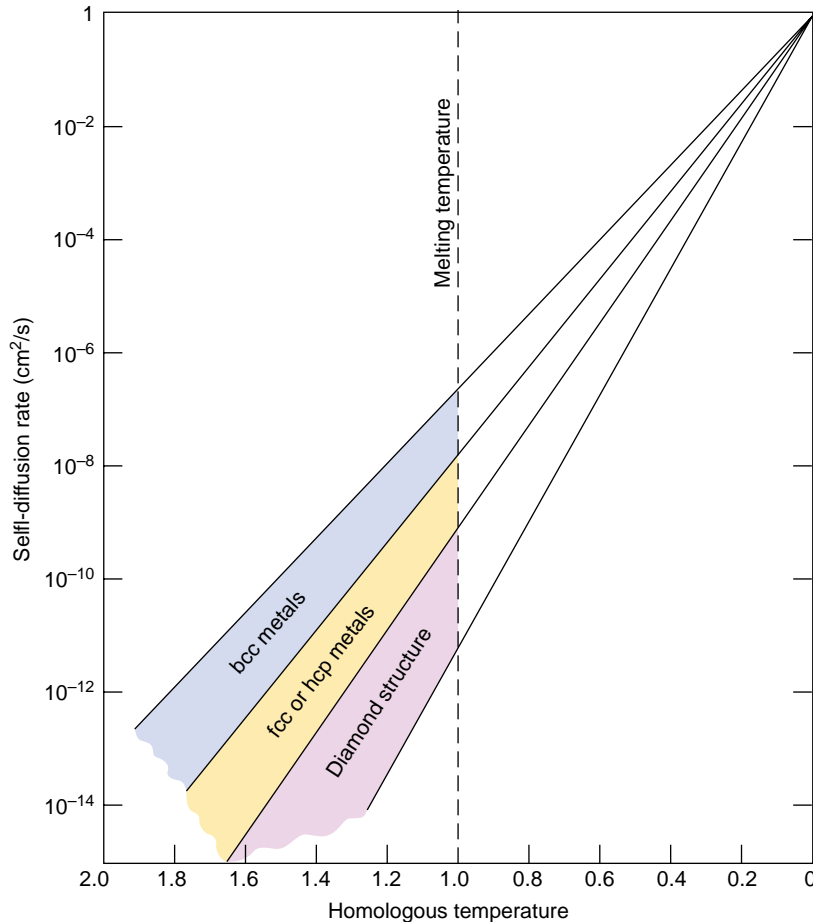


Figure 15. Self-Diffusion Rate, Melting Point, and Crystal Structure

Sherby and Simnad (1961) demonstrated that rates of self-diffusion in metals fit a common form, $D = D_0 \exp(-K/(TT_m))$, scaling with the homologous temperature TT_m . There is also a crystal-structure dependence with the open bcc structure exhibiting faster diffusion than the close-packed and diamond-cubic structures. Only the trends are indicated here. You can refer to the above-mentioned reference for specific data on the following: bcc metals— γ -uranium, sodium, α -iron, lithium, niobium, β -titanium, chromium, tantalum, and β -zirconium; hcp metals—magnesium, zinc, cadmium, α -titanium, α -zirconium, complex hexagonal β -uranium, and graphite; fcc metals—platinum, gold, silver, copper, β -cobalt, γ -iron, nickel, lead, and face-centered-tetragonal (fct) indium; and diamond structures—germanium, complex bct β -tin. At high temperatures, several bcc elements, such as β -zirconium and ϵ -plutonium, have anomalously high self-diffusion rates that do not fit the trends.

Melting Point. The melting point marks the end of solid-phase stability—the temperature at which the free energy of the liquid drops below that of the solid phase (or solid allotropes). Although liquid metals have a finite bulk modulus and many other properties common to metals, they have no shear strength. (They do, however, have internal friction, otherwise known as viscosity). Some theories of melting, such as that of Lindemann (Lawson et al. 1996), predict that melting occurs when the amplitude of atomic vibration reaches a critical fraction of the separation between atoms. That critical fraction is typically found to be approximately one-tenth. Other theories relate melting to a critical density of mobile vacancies.

The melting point is of interest to metallurgists not only because it marks the end of solid stability, but also because it indirectly affects most processes of engineering interest. For

example, most processes that affect formation and evolution of microstructures depend on temperature through an Arrhenius-type rate equation, $R = R_0 \exp(-Q/k_B T)$, where Q is the activation energy for the process and R_0 is a constant. At moderate temperatures, those processes tend to be thermally activated, meaning that thermal vibrations help to overcome activation barriers, but as the temperature is increased (typically to nearly half of the melting point), diffusional processes begin to dominate microstructural evolution.

The most prevalent mechanism for bulk diffusion is the vacancy mechanism shown schematically in Figure 14. As suggested above, formation and migration of vacancies obey an Arrhenius relationship. As metals approach their melting points, vacancies form and move easily because thermal lattice vibrations become large enough to overcome activation barriers. Conse-

quently, diffusion rates in solids increase rapidly near the melting point. It seems reasonable then that atomic mobility should depend not on the absolute temperature, but on the homologous temperature (T/T_m); that is, on how close the temperature is to the melting point of the material.

Sherby and Simnad (1961) demonstrated the importance of homologous temperature on the rate of diffusion in solids (Figure 15). They found that the Arrhenius-like rate equation for self-diffusion, $D = D_0 \exp(-Q/k_B T)$, where D_0 is a constant and Q is the activation energy for self-diffusion (vacancy formation and migration), provided a good fit to most of the measured diffusion data in solids when it was rewritten as a function of homologous temperature: $D = D_0 \exp(-K/(TT_m))$. In addition to the dependence on homologous temperature, they also found that the diffusion rate—in particular, the activation para-

Atomic Packing and Slip Systems in Metals

The details of atomic packing (space filling, coordination number, and symmetry) govern most physical and mechanical properties of metals. In particular, the slip planes and slip directions of each structure determine the response to shear stresses. Here we focus on the atomic packing and slip systems of the most-common crystal structures of metals: face-centered cubic (fcc), hexagonal close-packed (hcp), and body-centered cubic (bcc). These three have direct relevance to plutonium: the fcc δ -phase Pu-Ga alloys are the most important from an engineering standpoint, monoclinic α -plutonium can be thought of as a slightly distorted hcp structure, and plutonium and its alloys melt out of the bcc ϵ -phase—see Figures (a)–(c) below.

The fcc and hcp crystal lattices (with a c/a ratio of 1.633) are close-packed, filling space most efficiently. If one assumes spherical atoms, 74 percent of the volume is filled, and each atom has 12 nearest neighbors (or a coordination number of 12). By comparison, simple cubic packing of atoms

at the cube corners fills only 52 percent of the volume. The nearest neighbors in the close-packed lattices are very close at $0.707a_0$, where a_0 is the lattice parameter and the 6 next-nearest neighbors are at a_0 . Higher coordination numbers are possible if the atoms have different sizes.

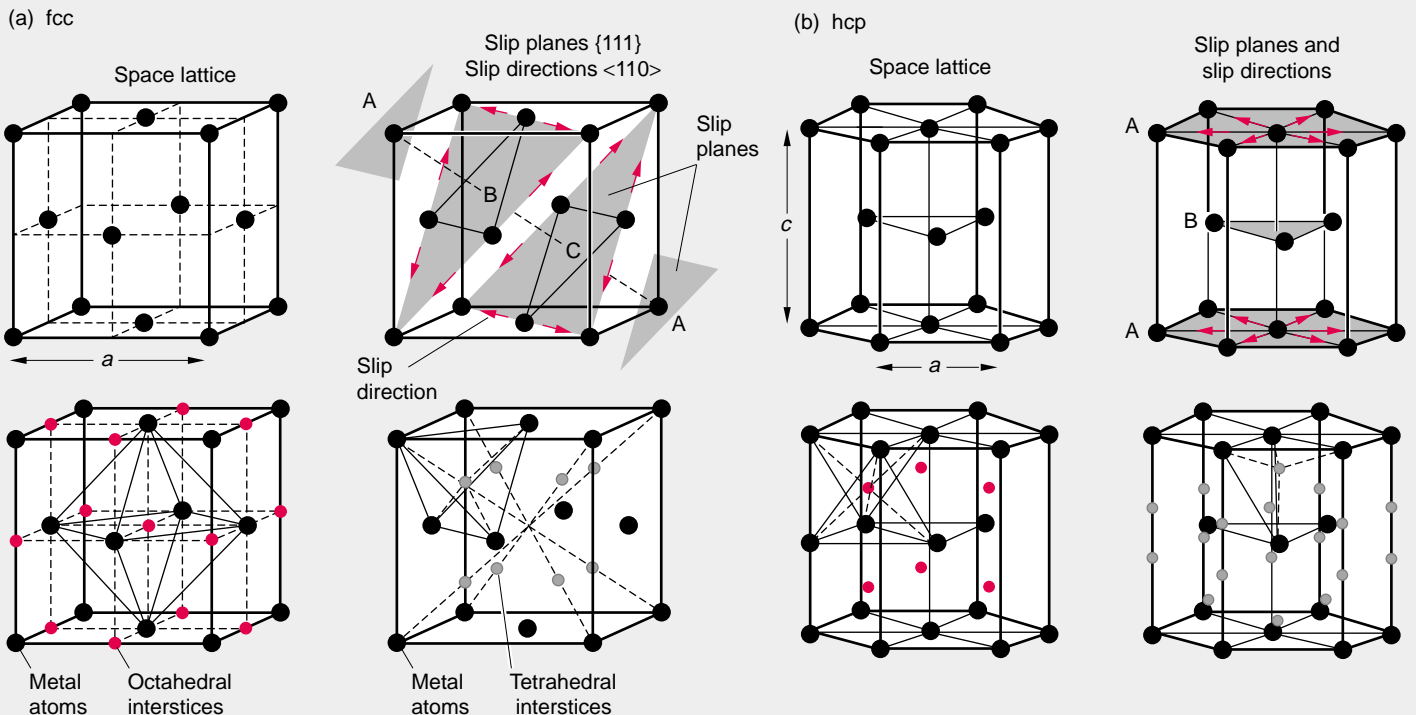
The bcc structure (c) has only 8 nearest neighbors at a distance of $0.866a_0$, but it has 6 next-nearest neighbors at a_0 . The more open bcc structure results in significantly different properties as well. The directionality (or anisotropy) of properties depends on the symmetry of the crystal lattice.

Stacking of Close-Packed Planes. The fcc and hcp lattices have identical close-packed planes (shaded), but as shown in the figure, the relative placement of those planes differs as they are stacked on top of each other—ABCABC for fcc and ABABAB for hcp. In other words, the placement repeats every third layer for fcc and every second layer for

hcp. Note that the close-packed planes in the fcc structure are perpendicular to the fcc body diagonal, or $[111]$ direction. The difference in stacking between hcp and fcc, although seemingly small, has profound effects on metallic properties because the fcc structure has many more equivalent slip systems than the hcp.

The figure also shows the close-packed directions in each close-packed plane. For example, the face diagonals of the fcc structure are close-packed. The atoms can be considered as touching in this direction, and it is easy to imagine that the elastic response (the reversible stretching of the atomic bonds) in a close-packed direction may be much stiffer than in other directions in which the atoms do not touch. The number of close-packed directions depends on crystal symmetry.

Slip Planes and Slip Directions. Plastic deformation leading to a permanent shape change (at constant volume) occurs by shear.



From a simple hard-sphere model, it is apparent that it is easiest to shear (or slip) rows of atoms over close-packed planes and along close-packed directions because close-packed planes have the largest separation and sliding them along close-packed directions offers the least geometrical resistance to shear.

Slip occurs when the critical resolved shear stress (shear stress in a slip plane at which dislocations begin to move, and plastic flow is initiated) is reached on one of the close-packed slip systems (combination of slip plane and slip direction). The greater the number of crystallographically equivalent slip systems that exist, the easier it will be to reach the critical resolved shear stress on one of the slip systems. The fcc structure has 4 equivalent close-packed planes—the octahedral or {111} Miller indices planes—and each of these planes has 3 equivalent close-packed directions (the face-diagonals or $\langle 110 \rangle$ directions) for a total of 12 equivalent slip systems. This redundancy of slip systems makes fcc metals typically very malleable (or ductile).

In the hcp structure, on the other hand, the basal plane is the only close-packed plane. It has three equivalent close-packed directions (same as the fcc lattice) and, hence, only three equivalent slip systems. However, some properly oriented hcp single crystals (for example, of magnesium) can still exhibit large amounts of slip. In addition, at higher stresses or elevated temperatures, other slip systems can be activated. Also, an entirely different deformation mode, twinning, is readily activated in hcp metals in which slip does not occur readily. An additional serious complication in hcp metals is that the structure is close packed only if the c/a ratio is 1.633, the ideal ratio for spherical atoms. Most hcp metals deviate from this ratio, indicating that the atoms are not ideally spherical. The ductility of most polycrystalline hcp metals is limited because of their inability to operate a sufficient number of multiple slip systems simultaneously.

The bcc structure has no close-packed planes similar to the {111} planes in the fcc

structure. The most-closely-packed planes are the six {110} planes, which contain two close-packed $\langle 111 \rangle$ directions along which hard spheres would be in contact. Many bcc crystals slip along almost any plane that contains a close-packed direction. The {112} slip planes are the most common ones for bcc crystals at ambient temperature. At low temperatures, the {110} planes are more prevalent. In fact, one generally finds that, in any of the structures, the rule that slip occurs in close-packed directions is almost never violated, whereas the close-packed plane rule is less stringent. The multiplane slip character of bcc crystals is decidedly different from slip in fcc and hcp crystals. Another peculiarity of bcc crystals is that they are essentially unstable when subjected to a shear on the {110} planes in the $\langle 110 \rangle$ direction. This instability plays an important role in the collapse of most bcc lattices to close-packed lattices by martensitic phase transformations.

Interstitial Lattice Sites. The size, shape, and coordination of interstices (or holes) in the different lattices control how easily foreign atoms can be accommodated in interstitial positions. The close-packed structures (a) and (b) have two types of interstices—octahedral and tetrahedral (the interstices are arranged differently in the two lattices). The octahedral holes will accommodate a sphere of maximum radius equal to $0.41r$ (where r is the spherical radius of the close-packed atoms) and the tetrahedral holes will accommodate spheres of $0.225r$. In the bcc structure (c), the interstices are smaller in spite of the fact that it is considered the more-open structure. The tetrahedral holes will accommodate spheres of $0.291r$ and the octahedral holes, $0.154r$. However, the shape of the interstices is also important. For example, a carbon atom ($r = 0.8$ angstrom) in bcc iron prefers the smaller octahedral sites (0.19 angstrom) to the tetrahedral sites of 0.36 angstrom because the different shape and coordination of the interstices require the carbon atom squeeze in between four iron atoms in the tetrahedral sites and only in between two atoms in the octahedral sites.

(c) bcc

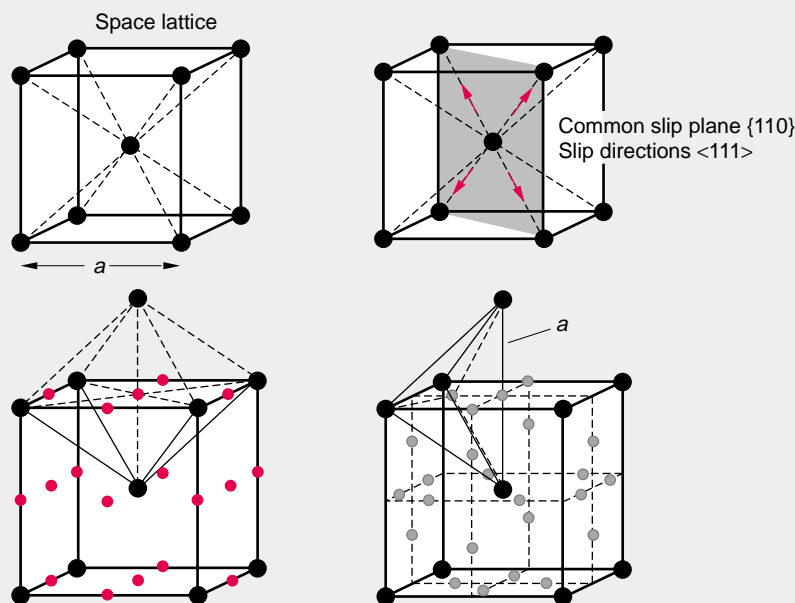


Table II. Dependence of Several Metallurgical Processes on Temperature

Process	Temperature Range
Thermal recovery of nonequilibrium point defects	
Interstitials	$\sim 0.02 T_m$
Limited vacancy migration	$\sim 0.2 T_m$
Bulk vacancy migration	$> 0.45 T_m$
Thermal recovery of dislocation structures ^a	$\sim 0.3 T_m$
Recrystallization of highly strained microstructure	$0.3\text{--}0.5 T_m$
Homogenization of segregated microstructures	$> 0.5 T_m$
Grain growth	$> 0.5 T_m$

^aMetals with high stacking fault energies, such as aluminum, show significant recovery of dislocation structures below $0.33 T_m$, whereas metals such as copper with lower stacking fault energies show little recovery before recrystallization.

meter K —depended on crystal structure. It is intuitively reasonable that the activation energies for the formation and migration of vacancies should depend on both homologous temperature and atomic packing (crystal structure). They also claimed a correlation with valence, but this idea was less convincing.

Many metallurgical processes that control microstructure depend strongly on the homologous temperature as summarized in Table II. For metals and alloys with multiple allotropes, Ardell (1963) pointed out that the homologous temperature depends on the effective or hypothetical melting point of the lower-temperature allotropes, not the melting point for the highest-temperature allotrope. The effective melting point is determined by constructing metastable free-energy diagrams that extend the free-energy curve of the low-temperature allotrope to higher temperatures and that of the liquid downward to lower temperatures. The effective melting point of the allotrope is the temperature at which the free energies are equal. This correction is especially important for metals that have low-temperature allotropes, far removed in temperature from the actual melting point. For example, for α -uranium, α -titanium, and α -zirconium, this correction lowers the effective melting point by ~ 200 kelvins. Nelson, Bierlein, and Bowman (1965) used Ardell's method to show that the effective melt-

ing point for δ -plutonium is lowered only by 52 kelvins, whereas that for α -plutonium is lowered by 360 kelvins. Hence, whereas room temperature is 0.33 of the absolute melting point of plutonium calculated by conventional methods, it is effectively 0.35 for δ -plutonium and 0.53 for α -plutonium. I will examine the ramifications of these corrections later.

Phase Stability. The most immediate impact of a phase change is the change in crystal structure and the accompanying volume change. In metals such as pure aluminum, this is not a problem since aluminum cannot be coaxed, either by changing pressure or temperature, to crystallize in any other structure but the fcc. Iron, on the other hand, exhibits both fcc and bcc lattices at ambient pressure, and a hexagonal version under increased pressure. For thousands of years, metallurgists and artisans have taken advantage of transformations in iron to craft iron and steels to exhibit useful properties. However, for both aluminum and iron, several phases can be retained at room temperature by alloying—that is, intentional chemical additions. Additions of copper, magnesium, silicon, zinc, lithium, and other elements to aluminum can help stabilize phases with different crystal structures. If these phases are created as microscopic precipitates, they can effectively strengthen pure alu-

minum. Strengthening metals and alloys by controlling the fraction, size, and shape of second-phase constituents lies at the heart of metallurgy. The aircraft, auto, and sporting goods industries depend on such treatments. Similarly, iron has been alloyed with carbon and other elements to process steels with desirable structural properties.

Having reviewed the most important material properties of direct metallurgical interest, I will now discuss what we know about those properties in plutonium and its alloys. I will focus on the high phase instability in plutonium as well as the unusual phase transformations and their effect on microstructure. The article “Mechanical Behavior of Plutonium and Its Alloys” on page 336 reviews the effect of those strange properties on mechanical behavior, including the unusual interaction between stress (or deformation) and phase transformation in plutonium.

Phase Instability in Plutonium and Its Alloys

For plutonium and its alloys, understanding phase stability is most important. Plutonium is notoriously unstable to almost any external disturbance. In this section, I will outline how small changes in temperature, pressure, or chemistry transform plutonium easily from one crystal structure to another, and I will also summarize our level of understanding in each case.

Temperature Instability. As it is heated, plutonium transforms from its ground-state monoclinic structure, indicating that the relative levels of the total free energies (F) of the different phases are shifting with temperature. As discussed previously, several electronic configurations in plutonium have nearly identical potential energy. Therefore, small changes in any of the four terms that compose F (see the box on the facing page) can give rise to a phase change. The static lattice potential ϕ_0 typically changes very little with

Predicting Temperature Effects

Electronic-structure calculations are performed at absolute zero, at which temperature the only contribution to the total free energy of a solid is the internal energy due to the electrostatic interaction among the ions and electrons of the crystal lattice. However, to predict the stability of crystalline phases and their bonding properties at finite temperatures, it is necessary to compute all contributions to the total free energy of a solid.

Wallace (1998) developed a rigorous lattice-dynamics treatment that requires four terms to describe the crystal Helmholtz free energy:

$$F = \phi_0 + F_H + F_A + F_E ,$$

where ϕ_0 is the static lattice potential (the energy of the crystal with ions located at the lattice sites and the electrons in their ground state—that is, the energy calculated in electronic-structure calculations); F_H , the quasiharmonic free energy due to lattice vibrations, or phonons; F_A , the anharmonic free energy due to phonon-phonon interactions; and F_E , the thermal excitation of electrons, which includes electron-phonon interactions.

In general, the temperature dependence of F is dominated by lattice vibrations (F_H), except at very low temperatures, where the T^2 internal electronic-energy term dominates the T^4 internal-energy term of lattice vibrations. Each temperature-dependent term of the free energy (F_H , F_A , and F_E) is composed of both an internal energy term and an entropy term. The differential form of the Helmholtz free energy shows that the preferred independent variables for F are T and V :

$$dF = -SdT - PdV ,$$

where S is the entropy, T is the absolute temperature, P is the pressure, and V is the volume. In most applications involving condensed phases, the convenient control parameters are the temperature and the pressure. While changing the temperature, it is easier to keep a solid at constant pressure and more difficult to keep it at constant volume. For systems controlled by T and P , the Gibbs free energy, $G = F + PV$, is the appropriate thermodynamic function to describe equilibrium and phase transformations. The differential is now $dG = -SdT + VdP$. In transformations between condensed phases, the PV term is negligible compared with F . Then, the difference between the Gibbs and Helmholtz free energies becomes insignificant. In metallurgy and chemistry, it is customary to express the Gibbs free energy as $G = H - TS$, where H is the enthalpy, and accept the change in the Gibbs free energy, $\Delta G = \Delta H - T\Delta S$, as the driving force for a phase change.

First-principles calculations of total free energy at finite temperatures are still beyond our reach. However, one can determine the quasiharmonic phonon density of states and dispersion curves by calculating potential energies of configurations in which the nuclei are displaced from crystal lattice sites. Successful calculations based on electronic-structure theories have been greatly aided by inelastic-neutron-scattering measurements of phonon dispersion curves. The power of inelastic neutron scattering is demonstrated in the article "Vibrational Softening in α -Uranium" (page 202). Unfortunately, information for plutonium is scarce because appropriate samples of plutonium-242 are unavailable (the large neutron-absorption cross section of the more-abundant plutonium-239 isotope makes the latter unsuitable for neutron-scattering experiments). Another approach to estimating the various contributions to the free energy is to determine the vibrational entropy terms semi-empirically. For a more detailed discussion, see the article "Elasticity, Entropy, and the Phase Stability of Plutonium" on page 208.

temperature. However, we suspect that the degree of 5f-electron localization in plutonium varies considerably from one phase to another (Figure 12), so we cannot rule out that significant changes in the static lattice potential occur with temperature.

In addition, as the temperature is increased, the other three terms of the total free energy can easily change crystal structure stability. Although plutonium is considered to be very anharmonic—that is, its lattice vibrations increase abnormally with increased temperature (indicating that the bonding, or spring stiffness, between atoms decreases substantially with temperature because of the thermal expansion of the lattice)—Wallace (1998) concluded that the temperature-dependent contribution to the free energy is dominated by the lattice vibration (quasiharmonic) contribution rather than the anharmonic effects. He also concluded that the dominant source of entropy in plutonium, as in other crystals, is represented by the phonons, or thermally induced lattice vibrations. However, lack of thermodynamic data and incomplete theoretical understanding do not allow us to pin down which terms in F are mainly responsible for the temperature instability of plutonium. In other words, we do not know whether the instability is caused by electron localization or just by entropy.

Low Melting Point. Another puzzling aspect of temperature instability in plutonium is its low melting point. Plutonium melts at a temperature much lower than one would expect from the trends observed in the transition metals. In fact, at first glance, one would expect the volume contraction of the light actinides (Figure 9) to signal increasing cohesive energies as the atomic number increases and, therefore, also higher melting points. This trend is generally observed in the transition metals. In the light actinides, as shown in Figure 10, the melting point decreases rapidly with increasing

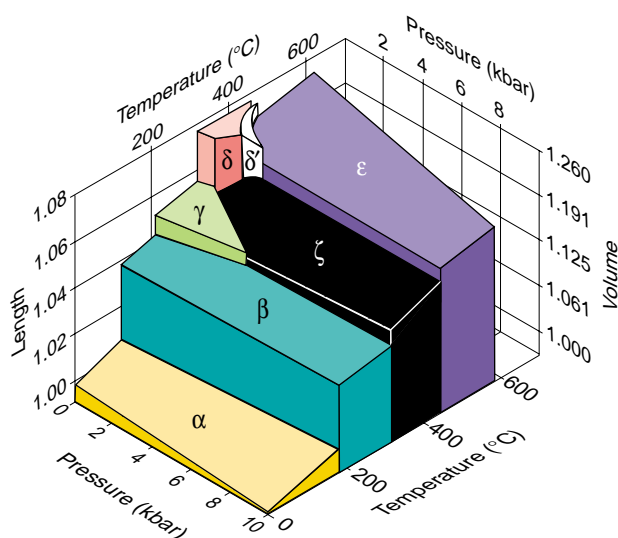


Figure 16. Plutonium Instability with Temperature and Pressure

Plutonium is notoriously unstable under almost any external disturbance. Over a span of only 600°, it exhibits six different allotropic phases with large accompanying volume changes before it melts. Pressures on the order of kilobar (100 megapascals) are sufficient to squeeze out the high-volume allotropes (Morgan 1970). Small chemical additions can stabilize these high-volume phases.

(Reproduced with permission from The Metallurgical Society.)

atomic number. The cohesive energies, however, decrease only slightly across the light actinides. In addition, the liquid phase is denser than three of the high-temperature solid phases of plutonium, it has a very large viscosity, and the highest known surface tension of any liquid metal. What makes the liquid so stable?

Lawson et al. (2000) relate the low melting point to the large thermal atomic vibrations associated with the strongly reduced elastic constants at high temperature. They incorporated a temperature-dependent Debye temperature into Lindemann's rule for melting. Lawson et al. demonstrated reasonable agreement with the melting points of the actinides by making the temperature-dependence correction for the Debye temperatures of the light actinides.

Hill and Kmetko (1976) made the intuitive argument that 5f electrons bond quite readily in the liquid phase because the atoms have greater spatial

and rotational freedom. Brewer (1983) offers a very appealing explanation from a chemist's point of view. Since several electronic configurations of comparable stability exist in plutonium (he has used thermodynamic data to show that four or more electronic configurations exist in elements such as uranium, neptunium, and plutonium), there is a natural tendency for plutonium atoms to exist in different sizes (to match the different electronic configurations). When there are size differences, structures with equivalent lattice sites such as bcc, fcc, and hcp are destabilized by the resulting strain energy of accommodating such atoms. The liquid state, on the other hand, is actually stabilized by a mixture of sizes because it can use space better. Hence, the stability of the liquid is enhanced as one cools the melt, and metals such as uranium, neptunium, and plutonium exhibit a low melting point compared with what is expected based on their cohesive energies. Similarly, manganese

and cerium favor multiple electronic configurations, and they also exhibit abnormally low melting points. It is also interesting to note that the thermal contraction upon cooling in liquid plutonium extrapolates to the β -phase contraction curve. As shown earlier, I set the degree of 5f bonding in the liquid to the same level as that in the β -phase in the notional diagram of Figure 12.

Pressure Instability. The electronic structure calculations of Wills and Eriksson demonstrate that pressure increases the 5f-electron orbital overlap, thereby initially stabilizing the high-density α - and β -phase in plutonium. The experimentally determined pressure-temperature-volume phase diagram in Figure 16 and the diagram shown in Figure 17 (Liptai and Friddle 1967) confirm the increased stability of these phases and the rapid "squeezing out" of the high atomic volume of the δ - and ϵ -phase. The γ -phase also gives way to a seventh plutonium allotrope, ζ , whose precise crystal structure has yet to be determined. The melting point of plutonium is initially lowered as pressure is applied, which is consistent with the fact that the liquid favors 5f bonding and is denser than the high-temperature solid phases. With continued pressure, however, the solid phases compress to a greater density than the liquid, and the melting point rises.

The calculations of Wills and Eriksson show that continued increased pressure broadens the f band, making it energetically unfavorable to lower the crystal energy through a Peierls-like distortion—thereby, eventually stabilizing the high-symmetry cubic or hcp structures. Pressure also increases 5f overlap in americium and the heavier actinides, leading to low-symmetry crystal structures followed by high-symmetry structures as pressure is increased. One can also conjecture that applying a negative pressure (hydrostatic tension) to the monoclinic α -phase should decrease the 5f electron overlap, thereby increasing

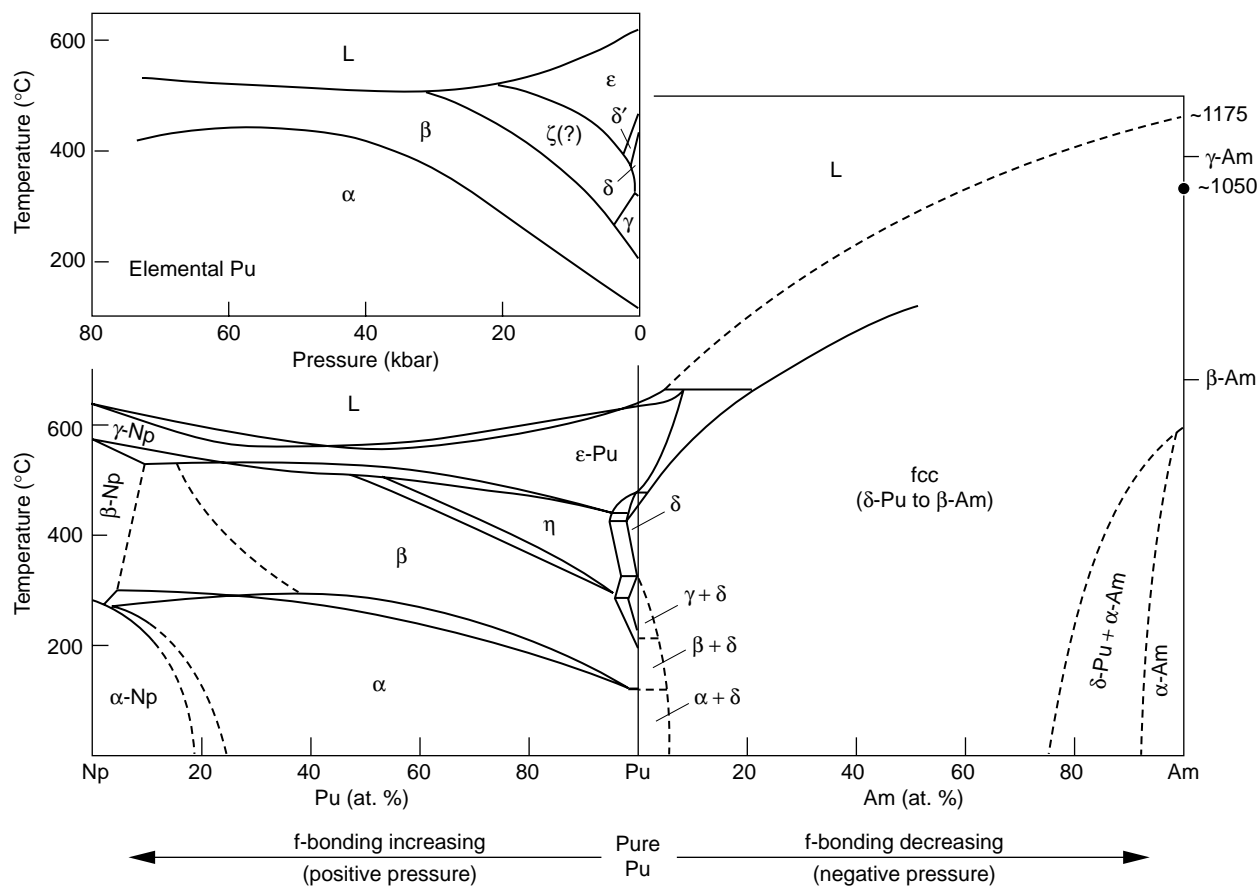


Figure 17. Pressure-Temperature Diagram of Pure Plutonium vs Np-Pu-Am Phase Diagram

The pressure-temperature phase diagram for unalloyed plutonium (Liptai and Friddle 1967) is drawn above the Np-Pu phase diagram (Ellinger et al. 1968) to show the striking similarities. It appears that adding neptunium to plutonium acts like increasing pressure. In both cases, the melting point drops initially, the α - and β -field expand, and a new phase (designated as either ζ or η) appears. By analogy, the addition of americium may mimic the application of hydrostatic tension (that is, negative pressure). As shown, americium additions cause the retention of the fcc δ -phase across the entire phase diagram.

the volume and favoring the high-temperature δ - or ϵ -phase cubic structures. Of course, applying negative pressure is not an easy feat.

A very informative way of looking at potential pressure effects was devised by Reed Elliott at Los Alamos in the 1980s (unpublished work). He compared the pressure-temperature phase diagram of plutonium to the phase diagrams of Pu-Np and Pu-Am as shown in Figure 17. Elliott pointed out that adding neptunium to plutonium acts just like increasing pressure in unalloyed plutonium. The melting point decreases initially; the low-temperature, dense phases are stabilized; and the high-temperature, high-volume phases

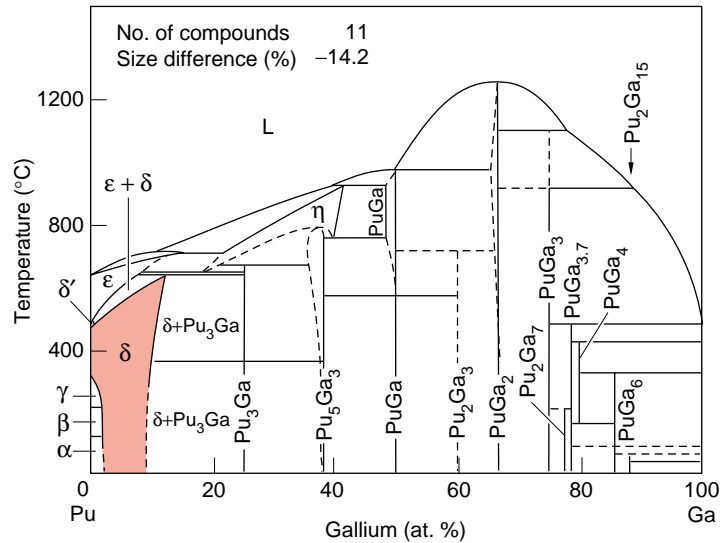
become less stable. A new phase appears, which looks very much like the new high-pressure ζ -phase in unalloyed plutonium. In fact, the plutonium-rich side of the diagram looks almost identical to the pressure-temperature diagram for unalloyed plutonium. On the other side, adding americium simulates applying negative pressure (hydrostatic tension). The high-volume phases are stabilized; the low-symmetry, high-density phases disappear rapidly; and the melting point increases. This view is consistent with the fact that, as one moves from plutonium to neptunium, the f bonding increases whereas from plutonium to americium, f bonding decreases.

Alloying and Current Efforts to Understand the δ -Phase. Adding other elements to plutonium leads to dramatic changes in its phase stability, as demonstrated in Figure 17 (neptunium and americium additions) and Figure 18 (gallium additions). These effects are even more difficult to predict than temperature effects (see the box “Predicting Alloying Effects” on page 315).

Because the δ -phase alloys of plutonium are of particular interest, I will review our current understanding of the fcc δ -phase in unalloyed plutonium (between 583 and 725 kelvins). The δ -phase most closely resembles the structure of typical metals such as aluminum. However, both the δ -phase

Figure 18. Alloying Effects on Plutonium Stability

Small chemical additions can stabilize the high-volume phases of plutonium. The Pu-Ga phase diagram shows how gallium additions of a few atomic percent form a solid solution (gallium atoms are incorporated into the plutonium fcc δ -phase) that is retained to room temperature. The rest of the diagram shows the enormous complexity and richness of alloying behavior. The Pu-Ga system exhibits 11 different intermetallic compounds and several new phases that are different from those of elemental plutonium or gallium (Peterson and Kassner 1988).



and the δ' -phase appear to be aberrations in the lineup of plutonium phases (the ϵ -phase thermal expansion line extrapolates almost exactly to that of the γ -phase in Figure 1). Of all plutonium phases, the δ -phase has the largest atomic volume in spite of its close-packed structure. Its volume falls between that of α -plutonium and americium (Figure 9). These properties are yet to be explained, and δ -phase stability and electronic structure remain the topics of hot debates.

Although the electronic-band-structure calculations of Wills and Eriksson based on local-density approximation (LDA) do a very impressive job of predicting pressure effects in the actinides, they cannot predict the existence of the high-temperature phases. They do, however, predict the correct atomic volume of the δ -phase (calculated at 0 kelvins) by constraining four of the five 5f electrons to localize (collapse into the ionic core). These constrained calculations capture the essential features of the electronic structure of the δ -phase as measured for the first time on gallium-stabilized δ -phase polycrystals. However, their unconstrained band calculations (all five 5f electrons are bonding) do not agree with either the α - or δ -plutonium photoelectron spectroscopy (PES) results of Arko and his colleagues. (See the article “Photoelectron Spectroscopy of

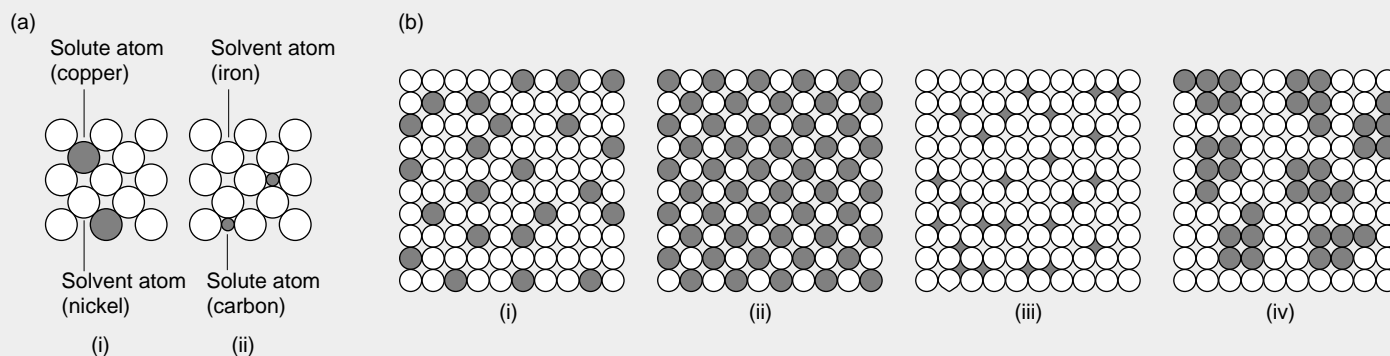
α - and δ -Plutonium” on page 168.) Boring and Smith (see page 90) point out that there is no obvious mechanism that allows for partial localization of the 5f electrons. They also show, however, that if only one of five 5f electrons bonds in the δ -phase, the repulsive sp band contributions will expand the lattice and the symmetry of the crystal structure will be determined by the three spd electrons—that is, cubic structures will be favored.

Instead of partially localizing 5f electrons, Arko and Albers of Los Alamos (unpublished work) now suggest that all 5f electrons participate in bonding, but at reduced bond strengths. They link reduced bond strengths to strong electron-electron correlations. Such correlations effectively narrow the 5f band and enhance the density of states at the Fermi energy. Arko and Albers argue that reducing the bandwidth weakens the bonding because the average bond strength is directly proportional to the bandwidth. They also suggest that correlation effects may be at work even in α -plutonium, causing the 5f electrons to be more localized than LDA calculations predict. According to them, understanding α - and δ -plutonium requires that calculations use a perturbation theory extension to the first-principles LDA band-structure calculations.

In the article “A Possible Model for δ -Plutonium” (page 154), Cooper also goes beyond the LDA band-structure models to a two-electron, impurity-like model to explain the δ -phase. He proposes that the δ -phase is the result of a self-induced Anderson localization of the 5f electrons. According to Cooper, in Anderson localization, the electrons are driven from coherent-wave bonding in the α -phase to localized behavior by strong impurity scattering. To create an “impurity” in unalloyed plutonium, Cooper envisions two types of plutonium atoms—one in which the 5f electrons are localized and the other in which they oscillate between being localized and bonding. The fcc δ -phase becomes the lowest free-energy phase over a certain temperature interval because of the gain in configurational entropy (an additional contribution to entropy when more than one type of atom is incorporated into a crystalline array) of a solid solution of the two types of plutonium atoms occupying crystallographically equivalent sites in a disordered array. Unfortunately, the calculations necessary to deal with two-electron models for such complex systems are several years from fruition.

The bottom line is that we do not have a satisfactory explanation of the δ -phase in unalloyed plutonium today. It remains as one of the unsolved challenges in condensed-matter physics.

Predicting Alloying Effects



Substitutional and Interstitial Solid Solutions

(a) There are two types of solid solutions: (i) solute atom substitutes for the parent (solvent) atom, and (ii) solute atom fits into the interstices of the solvent atom lattice. (b) Four schematic models of solid solutions are illustrated: (i) substitutional random; (ii) substitutional ordered; (iii) interstitial random; and (iv) solute clusters in solid solution.

Alloying effects are even more difficult to predict from first principles than temperature effects. Alloying changes both the internal energy and the entropy—the latter, by changing both the vibrational spectrum and the configurational entropy. Metallurgists are keenly interested in the elusive goal of predicting what structures form when solute element B is added to solvent element A. The alloy is called a solid solution if the solute atoms are incorporated into the lattice of A without changing its basic structure. Solutes can substitute for solvent atoms or fit into the interstices of the solvent lattice as shown in the accompanying figure. The maximum amount that can be accommodated varies significantly from one alloy system to another. In addition, if there is limited solubility, the amount of A that can be dissolved in B is typically not the same as the amount of B that can be dissolved in A. For metals with multiple allotropes (such as plutonium), it is important to know how little solute it takes to expand a high-temperature phase regime to low temperatures. Alloying can also produce new compounds or new phases. Intermetallic compounds with specific ratios of A to B are very common in metallic systems. Such compounds typically form if there is a strong chemical affinity of element A for B. Another possibility is for A and B to be immiscible—that is, solvent A rejects element B altogether.

Whereas first-principles treatments have not been very helpful in predicting alloying behavior, the Hume-Rothery rules, developed in the 1920s, reformulated 30 years ago, and reviewed recently by Massalski (1996), are still used by metallurgical practitioners today. These rules relate the limits of solid solubility as well as the stability and extent of intermediate phases to three factors: (1) If the atomic size difference between A and B is greater than 15 percent, solid solubility will be restricted. Significant experimental data support this essentially “negative” rule, which makes intuitive sense because large size differences produce very large elastic-strain energies and should therefore be unfavorable. Within favorable size ranges, the exact size differences have only secondary importance and the following two factors become important. (2) High chemical affinity of A for B (usually denoted by large differences in electronegativity) helps promote the formation of intermetallic compounds and therefore limits solid solubility. (3) The relative valence rule stresses the importance of electron concentrations, or e/a ratios, in determining alloying behavior. (Typically, e/a is the number of valence electrons per atom, or equivalently, the group number in the periodic table.) Meaningful and useful correlations exist between crystal structure types and the e/a ratios of alloys. However, the physics behind those correlations remains elusive. Moreover, the success of the relative valence rules in metals with d or f electrons is limited because the values of the valence and the e/a ratio are by no means straightforward to assign.

It is now time to extend the very successful first-principles electronic-structure predictions of Wills and Eriksson for the actinide elements (including their excellent predictions of pressure effects) to alloys. It would also be very useful to extend to plutonium alloys the semi-empirical methods developed by Kaufman and Bernstein (1970) to predict phase diagrams (binary and higher order) based on thermodynamic measurements (heat capacities and enthalpies of transformation) and predictions that involve the construction of free-energy curves as a function of concentration and temperature. Such methods would provide near-term guidance on what to expect if more than one element is alloyed with plutonium or to predict the effects of multiple impurity elements.

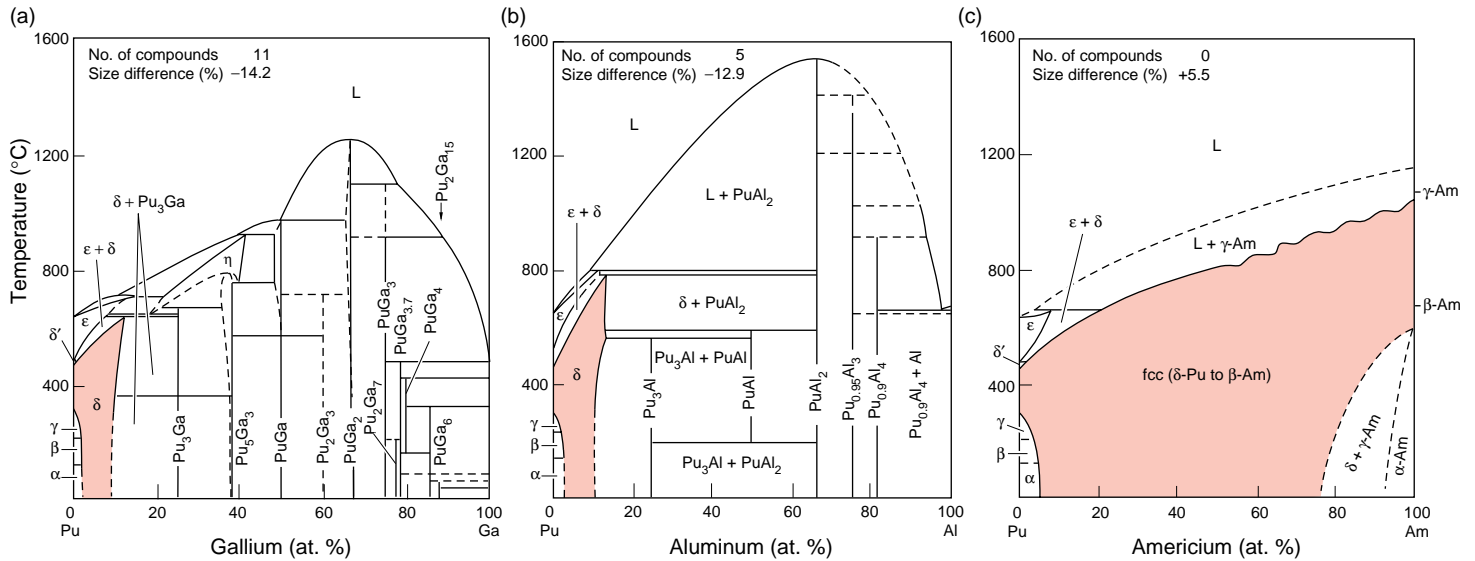


Figure 19. Binary-Phase Diagrams and Their Significance for Plutonium Metallurgy

The binary diagrams (a)–(c) are of δ -phase stabilizers. Gallium, aluminum, americium, scandium, and cerium retain the fcc δ -phase to room temperature, and all, except cerium, increase plutonium’s melting point. For Pu-Ga alloys (a), gallium concentrations from approximately 2 to 9 at. % stabilize the δ -phase to room temperature. This phase is a solid solution of gallium atoms in an fcc plutonium lattice. Gallium atoms are 14.2% smaller than plutonium atoms, their electronegativity is greater, and they crystallize into a face-centered orthorhombic crystal structure. According to most empirical alloying rules, gallium barely fits the class of δ -phase stabilizers for plutonium. The Pu-Al (b) and Pu-Ga phase diagrams are controversial with Russian researchers who claim that the δ -phase is metastable at room temperature and will decompose, albeit over a period of thousands of years, to the monoclinic α -phase plus the intermetallic compound Pu₃Ga (see the article “A Tale of Two Diagrams” on page 244). (c) In the Pu-Am diagram, the δ -phase solid solution extends across the entire concentration range.

A second group of elements (silicon, indium, zinc, and zirconium) retains the δ -phase in a metastable state under rapid cooling from high temperatures (in either the ϵ - or δ -phase fields), but those elements do not stabilize the δ -phase at room temperature as shown in (d) for Pu-Si. In addition, alloying with substantial amounts of hafnium, holmium, and thallium will also retain some of the δ -phase to room temperature. (Interestingly, Pu-Zr, Pu-Al, and Pu-Ga alloys were once considered as potential metallic fuel elements for fast reactors).

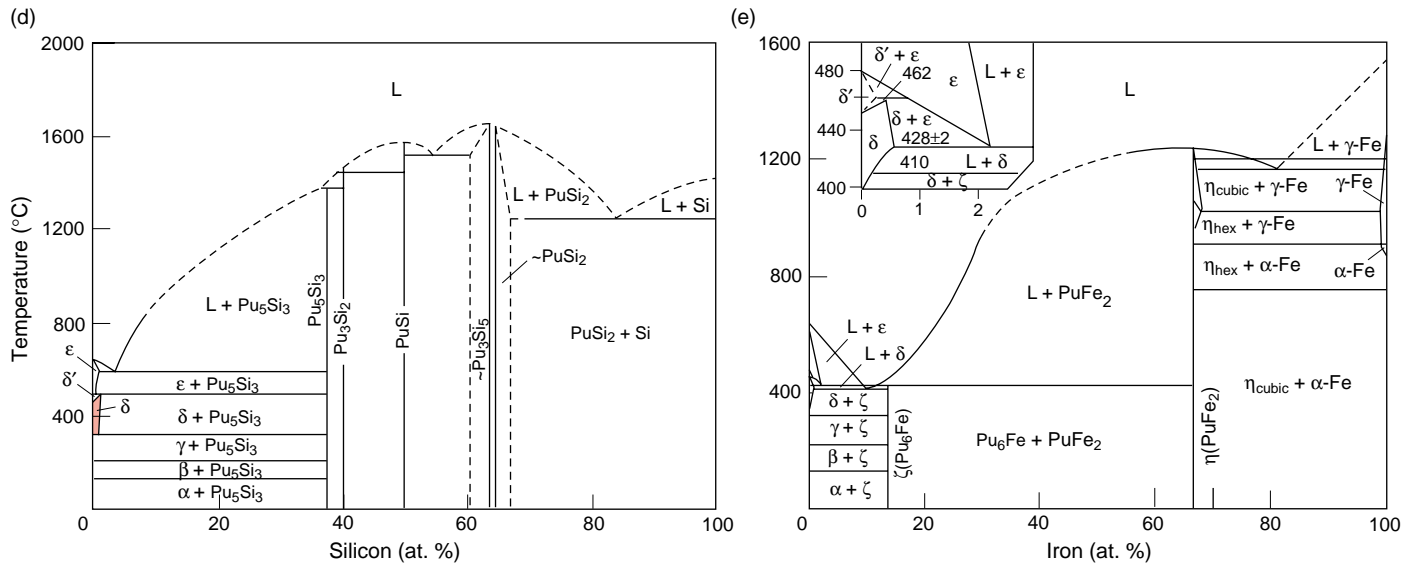
Neptunium is an α -phase stabilizer, and it does an exceptional job (see Figure 18). No other element has been shown to have any equilibrium solubility in the very dense, monoclinic α -phase. Neptunium is also the only element that significantly expands the β -phase region. However, uranium, hafnium, and zirconium have limited solubility in the β -phase. Titanium, hafnium, and zirconium retain the β -phase to room temperature and below by rapid quenching. Neptunium and uranium lower the melting point of plutonium slightly; hafnium, zirconium, and titanium raise it significantly, even when added in small amounts.

Although based on the thermal expansion curve of Figure 1, the δ -phase appears to be an aberration, it is clearly the harbinger of what is to come as the atomic number is increased, as shown in the connected phase diagram of Figure 10. As Boring and Smith (page 90) point out, the δ -phase in plutonium is only the “tip of the iceberg.” It is the transitional phase from the unusual properties of the light actinides to the rather well-behaved properties of the heavy actinides. Alloying plutonium

with gallium or americium (as shown in Figures 17 and 18) helps retain the δ -phase to room temperature, thereby making it an alloy of great engineering significance.

Unfortunately, electronic-band-structure calculations cannot yet predict the effects of alloying in such complex systems. Clearly, electronic and stress effects arise when atoms of different electronic structure and size are added to the parent plutonium lattice. We would like to explain how and why

some elements extend the stability of the fcc δ -phase to room temperature as plutonium solidifies and cools from the melt. But the key experimental data (such as phonon dispersion curves) that could help guide theorists are very scarce. No realistic interatomic potentials are available to allow approximate treatments of temperature and alloying effects. It will be important to understand entropy contributions because alloying may affect entropy both configurationally and through a change



Iron, nickel, or cobalt lowers the melting point of plutonium dramatically, forming a low-melting eutectic, much as the addition of lead to tin makes solder. (e) The eutectic point for the Pu-Fe alloy (~10 at. % iron) is at 410°C. (This eutectic alloy was used in the first metallic plutonium fuel elements of the Los Alamos Molten Plutonium Reactor in the late 1940s). Silicon, magnesium, osmium, ruthenium, rhodium, and thorium form eutectics at somewhat higher temperatures. Eutectic-forming elements limit the useful temperature range of plutonium and its alloys. For example, plutonium metal heated above 410°C in steel will melt through the steel by forming the eutectic. Even when present in small amounts in plutonium, the alloying elements can segregate to grain boundaries, enriching the local alloying concentration and causing local melting or embrittlement at temperatures close to the eutectic temperature.

When nonmetallic elements with very small radii are alloyed with metals, they tend to form interstitial solid solutions. A general rule is that, if the radius of the nonmetallic element is <0.59 that of element A, an intermetallic compound with a simple structure (often fcc or hcp) forms. If the ratio is greater than that, then compounds with complex structures form. The important nonmetallic elements for plutonium are oxygen, carbon, nitrogen, and hydrogen. The first three form several high-melting (refractory) intermetallic compounds. For example, PuO_2 is a refractory oxide that melts at 2400°C and is used in radioisotopic heat sources and as reactor fuel (mixed with UO_2). Similarly, the carbides and nitrides of plutonium were once of considerable interest as reactor fuel for breeder reactors. Hydrogen also has a tendency to form compounds, but these decompose readily.

Almost all the rest of the elements in the periodic table show only limited solubility in the δ -phase. Many of them (for example, barium, strontium, and calcium) are immiscible. Most of these elements increase the melting point. Some have very shallow eutectics before the melting point increases. More than half of the elements in this group show solubility in the ϵ -phase (for example, thorium, neptunium, uranium, titanium, ruthenium, rhodium, platinum, osmium, and most rare earths).

in lattice vibrations. We pointed out earlier that the semi-empirical alloying theories have not been very successful in predicting alloying effects in plutonium. Cooper (page 154) suggests that gallium atoms located randomly in the plutonium lattice provide sufficiently strong scattering to lower the temperature for self-induced Anderson localization to below room temperature, thereby accounting for δ -phase retention. However, rigorous calculations to provide quantitative guidance

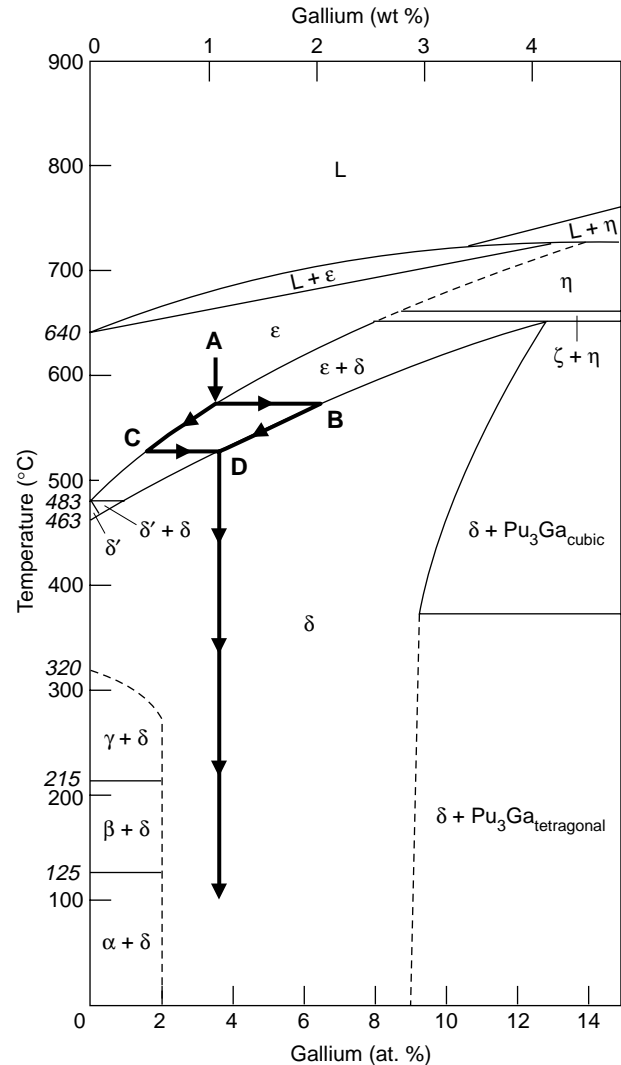
appear to be a long way off.

Fortunately, metallurgists and chemists learned how to measure phase diagrams experimentally long before the advent of electronic-structure theory. Phase diagrams such as those shown in Figures 17 and 18 were measured painstakingly by thermal analysis, dilatometry (length-change measurements), calorimetry, x-ray diffraction, and metallography (optical microscopy of the grain and phase structures). For

the actinides, Finley Ellinger and his colleagues at Los Alamos spent their professional careers determining the binary-phase diagrams of plutonium with many other elements in the periodic table. They also published a few ternary-phase diagrams (that is, two elements added to plutonium), but the number is limited because of the enormous effort required. We must develop better theories to help us understand alloying (and impurity) behavior.

Figure 20. Plutonium-Rich Pu-Ga Phase Diagram

(a) The phase diagram of Ellinger et al. (1968) as modified by Peterson and Kassner (1988) shows that the fcc δ -phase regime in plutonium is extended by alloying with gallium. Nearly 13 at. % gallium can be dissolved in the fcc δ -phase at high temperature. (Note that 1 wt % gallium is roughly 3.4 at. % because of the disparity in the atomic mass of the elements.) At ambient temperature, the limit is closer to 9 at. %. During solidification and cooling, alloys within this gallium range must cool through the liquid plus the ϵ -phase region and the ϵ - plus the δ -phase region. In a two-phase region, the composition of each phase is given by the phase boundaries at that temperature. Therefore, at point A, the first δ -phase to form has the gallium concentration shown at point B. As the temperature is lowered, the gallium concentration in the δ -phase moves along the BD line whereas the gallium concentration in the ϵ -phase moves along the AC line provided that diffusion is sufficiently rapid to allow migration of gallium consistent with the imposed cooling rate. (The average gallium concentration in the alloy, of course, has to be the initial concentration.) Because the gallium diffusion rate in the open bcc structure of the ϵ -phase is approximately 10^4 times faster than that in the δ -phase, gallium concentrations in the δ -phase remain above their equilibrium values for most cooling rates, whereas those in the ϵ -phase are pushed farther and farther below equilibrium values as cooling proceeds. The net result is increased gallium segregation, or coring, within a δ -phase grain over that expected from equilibrium conditions.



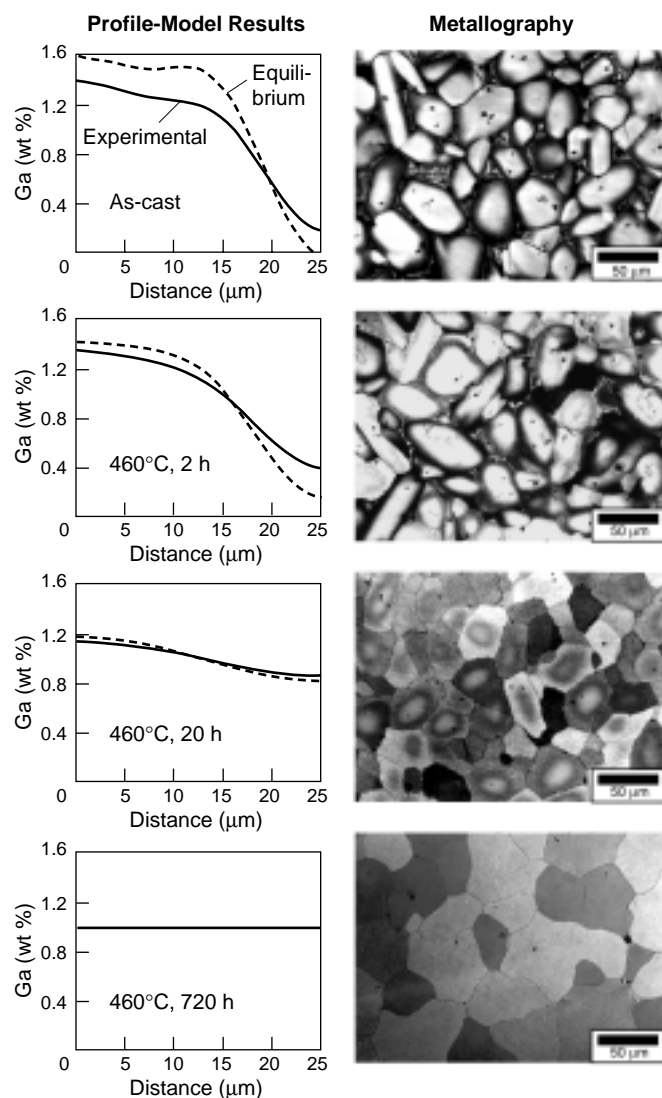
I have tried to capture the principal features of the phase diagram compendium of Ellinger et al. (1968) in Figure 19, hoping that this knowledge will provide guidance for theorists and experimentalists. This compendium has served as the most valuable document for plutonium metallurgists. Little has been added to it since the time it was published. It demonstrates that when alloyed with plutonium, the elements in the periodic table fall into the following groups: (1) δ -phase stabilizers and δ -phase retainers, (2) α -phase stabilizers, (3) eutectic-forming elements, (4) interstitial compounds, and (5) all the remaining elements, most of which either show little solubility in the δ -phase or form very shallow eutectics before raising the melting point.

Metallurgical Considerations for δ -Phase Pu-Ga Alloys

It should be quite apparent by now that more than chemical analysis is required to describe the properties of alloys. Microstructure is important, and it is determined by chemical composition and processing—namely, thermal and mechanical treatments. For example, thermal and mechanical treatments will affect the homogeneity of the chemical composition, the presence of second phases or inclusions (as well as their volume fraction, morphology, and distribution), and the types and distributions of defects. Typical mechanical processes include rolling and forging, which introduce stored energy into the system in the form of increased defect concentrations

(mostly increased dislocation density). This stored energy, in turn, can be reduced or eliminated by subsequent thermal annealing treatments that lead to recovery (rearrangement and elimination of many dislocations) or recrystallization (formation of new, relatively strain-free grains) of the deformed structure. Moreover, there are other external conditions such as irradiation (or in the case of plutonium, self-irradiation) that create new defects and store energy. All these effects must be considered if one is to understand the properties of plutonium alloys.

I will begin a brief examination of thermal treatments by discussing the plutonium-rich portion of the Pu-Ga phase diagram shown in Figure 20. The minimum amount of gallium



(b) The microstructure of a typical as-cast δ -phase alloy exhibits a range of gallium concentrations between points B and C in (a). The interior of the δ -phase grains reflects the gallium concentration at point B, and the grain boundaries may have very little gallium, reflecting the last ϵ -phase to transform with gallium at or below point C. As shown, the resulting microstructure appears heavily “cored” or segregated. It consists of a gallium-rich δ -phase in the center, a gallium-lean δ -phase shell (dark areas) at the core boundaries, and an intercore region very lean in gallium that transformed to the α -phase during cooling because of insufficient gallium content. The measured and calculated gallium-concentration profiles from the center to the edge of a grain (Mitchell et al. 2000) are also shown. This type of microsegregation typically occurs during cooling through the liquid plus solid region of most alloys because diffusion in the liquid is typically so much faster. The anomalously high diffusion rate in ϵ -plutonium avoids the problem in the liquid- plus ϵ -phase region, only to have it appear in the ϵ - plus δ -phase region. To equilibrate the gallium concentration, it is necessary to return to very high temperatures in the δ -phase region and hold those temperatures for long times. The progression of gallium homogenization and consequent change in microstructure are also shown for a temperature of 460°C.

required to stabilize the δ -phase at ambient temperature is 2 at. % according to Ellinger et al. (1968). In reality, this phase boundary is very uncertain (shown by a dashed line) because it is difficult to achieve equilibrium. Over 30 years ago, Elliott and others reported that as little as 1 at. % gallium or aluminum effectively retains the δ -phase to room temperature if samples are cooled rapidly enough from elevated temperature. It is quite remarkable that only one gallium atom in one hundred plutonium atoms causes such a dramatic change in crystal structure. On the other hand, as discussed by Hecker and Timofeeva (page 244), carefully performed Russian work showed that all δ -phase Pu-Ga alloys are metastable at room temperature.

One of the principal differences between δ -phase alloys and unalloyed plutonium is the solidification behavior important in casting. As shown in Figure 2, unalloyed plutonium exhibits a large expansion upon solidification, followed by very large contractions in the solid state. Cracking and distortion are the rule. Consequently, it is very difficult to make a full-density (19.86 g/cm^3), sound α -phase casting. The Pu-Ga alloys, on the other hand, show a smaller expansion upon solidification followed by a small, quite uniform contraction. However, for reasons demonstrated in Figure 20, it is quite common for alloy castings to exhibit two phases—the gallium-rich δ -phase and the gallium-lean monoclinic α -phase. The exact amount of each phase depends primarily on the average gallium concentration and

on the cooling rate. To minimize gallium microsegregation and “homogenize” the gallium distribution, it is necessary to anneal at the highest possible temperature in the δ -phase region. The time required for homogenization decreases with decreasing grain size and increasing temperature (as long as the temperature remains in the δ -phase region).

Density and x-ray diffraction measurements have demonstrated conclusively that the crystal structure of the δ -phase alloy is the same as the high-temperature δ -phase of unalloyed plutonium except that gallium solute atoms substitute for plutonium atoms in the fcc lattice. Results of x-ray diffraction typically show well-defined Bragg peaks of the single fcc phase. The lattice parameters of the alloys shrink with the addition of gallium. The con-

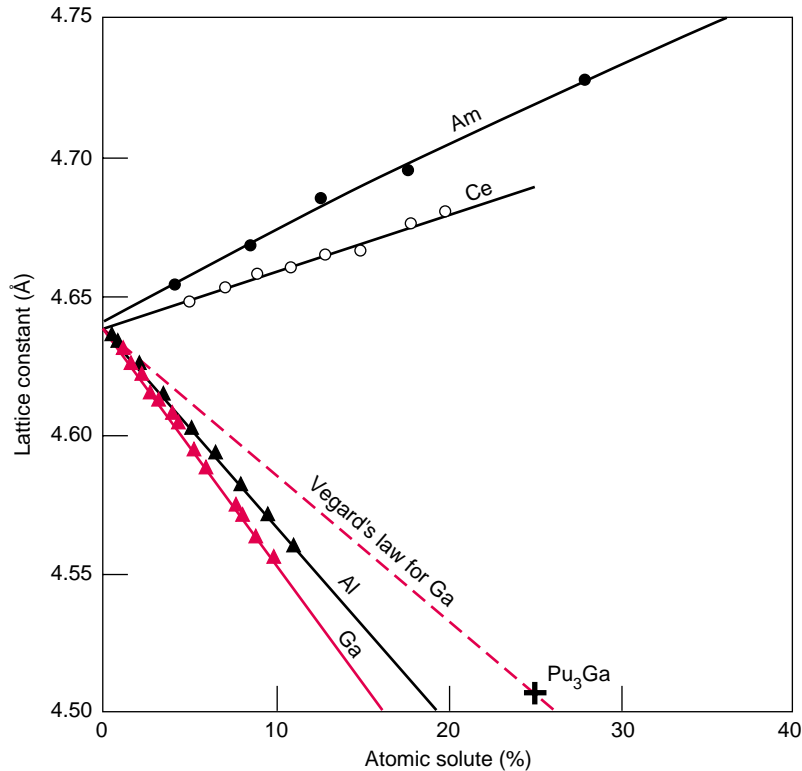


Figure 21. Lattice Parameters and Vegard's Law for fcc Plutonium Alloys When gallium, aluminum, scandium, cerium, and americium are added to plutonium, they substitute for plutonium in the fcc δ -lattice, causing the retention of the δ -phase to room temperature. Additions of gallium, aluminum, and scandium contract the lattice, whereas those of cerium and americium expand it. The contractions for gallium and aluminum are greater than the contraction predicted by a rule of mixtures based on atomic radii (known as Vegard's law). The figure compares Vegard's law and experimental results for gallium additions.

traction is greater than expected from a rule of mixtures (called Vegard's law) as shown in Figure 21. The only two elements that increase the lattice parameter of the δ -phase are cerium and americium.

We do not know if gallium atoms are present at random in the fcc plutonium lattice or in an ordered array. In the past few years, Steve Conradson of Los Alamos and researchers in France have used x-ray absorption fine structure (XAFS) spectroscopy techniques at synchrotrons to probe the local environment around both plutonium and gallium atoms in the alloys. They confirmed the substitutional nature of the gallium atoms. The Pu-Pu atom spacing is considerably larger than the Pu-Ga spacing.

For gallium-lean alloys, Conradson's data suggest a short-range, local order in addition to the long-range structure characterized by the usual fcc lattice parameters. We do not fully understand these finer details at this time. However, these features may be very important to the aging of plutonium alloys.

The role of impurities, or unintentional chemical additions, on phase stability in δ -phase fcc alloys is also not well understood. Impurities typically result from solidification or other processing operations, and the levels in plutonium metal are typically 1000 to 2000 parts per million (ppm) total by weight. Purification by electrorefining drops this level easily to <500 ppm, and levels of tens of parts per million have

been achieved with great care (see the article "Preparing Single Crystals of Gallium-Stabilized Plutonium" on page 226). At the higher levels, impurities can influence phase stability, transformation behavior, mechanical properties, and a whole array of other physical properties. In recent work, Dan Thoma and coworkers at Los Alamos have convincingly demonstrated these effects for uranium. No theory or modeling is currently available to help us understand the role of impurities in plutonium.

From a practical standpoint, the effect of impurities on phase stability is best assessed if impurities are classified according to the scheme used for alloying elements in Figure 19. Hence, common impurities such as aluminum, silicon, and americium that retain the δ -phase are simply added to the gallium concentration (on an atomic percentage basis) to give an equivalent content for Pu-Ga alloys. Since these impurity elements are present on the plutonium lattice sites, they are not distinguishable by typical metallographic or x-ray diffraction techniques. XAFS offers some hope for distinguishing the impurity atoms if they are present in sufficiently large concentrations. However, even small amounts of impurities can cause serious degradation of properties because impurities typically concentrate in the melt during casting. Solute atoms are usually rejected during the early stages of solidification because atoms of different size are more easily accommodated in the liquid. This tendency to segregate impurity elements leads to inclusions (second-phase particles) in the microstructure of plutonium or its alloys. Typical eutectic-forming impurities and refractory-compound forming inclusions are shown in Figure 22. There is also the tendency for impurities to form complex compounds such as oxycarbides and carbo-nitrides, or for them to scavenge some of the intentional alloying elements or other impurities. We understand very little about these effects in plutonium.

To conclude this section, let me reiterate the importance of metallurgical processing in understanding the behavior

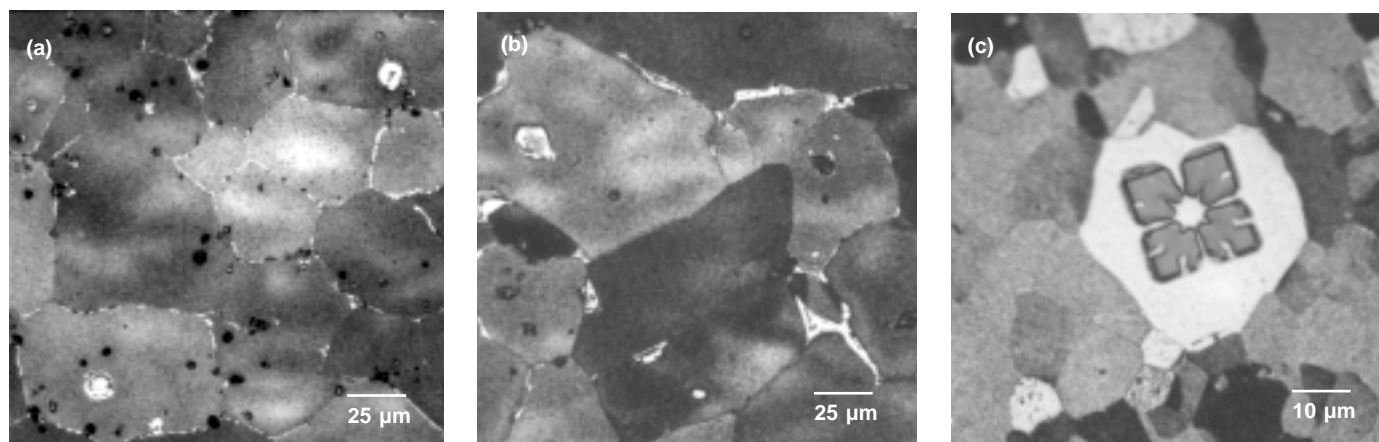


Figure 22. Iron and Nitrogen Impurities in Plutonium

Impurities typically segregate in the melt and form microscopic inclusions in the δ -phase structure. Even reasonably small concentrations of impurities, on the order of a few hundred parts per million by weight, can give rise to micrometer-size inclusions as shown in (a) and (b), which are representative of Pu-Ga alloys with 300 to 500 ppm iron concentrations. In (a), the processing conditions favored inclusions of the low-melting eutectic compound Pu_6Fe strung out along the grain boundaries, whereas in (b) processing conditions favored the conglomeration of Pu_6Fe at the grain-boundary triple points in particular. The reasons for the different morphology of inclusions for different processing conditions are not understood. In (c), an isolated plutonium nitride inclusion is shown in Pu-Ga alloy containing several hundred parts per million by weight nitrogen in the bulk alloy.

of plutonium alloys. An accurate chemical analysis is necessary, but not sufficient. Knowing the processing parameters is crucial to ascertain the level of segregation of the alloying element and the state of the impurity atoms. In addition, mechanical treatments will change the microstructure. These effects are discussed by Hecker and Stevens (page 336). So, even if a plutonium alloy is retained in the fcc δ -phase at room temperature, it is at best metastable and very sensitive to external conditions, such as temperature, pressure, or other applied stresses. The phase diagrams provide us with an overall guide to phase stability, but they do not tell us much about just how stable these alloys will be to all possible external changes.

We know from experience, for example, that plutonium alloys with <2 at. % gallium transform readily to the monoclinic α -phase just below room temperature. And I mentioned above that the δ -phase is squeezed out easily by the application of pressure at room temperature. In addition, under the stresses induced during cutting, machining, or

polishing, the lean alloys readily transform to the α -phase on the surface (sometimes in combination with the γ -phase). As the gallium concentration is increased, stability with respect to these external forces increases steadily. Predictions of phase stability as a function of solute concentration and external stresses may be helped significantly by electronic-structure calculations, especially if these calculations were to include temperature effects. It would also be very helpful if theorists could develop other physics-based models that incorporate realistic interatomic potentials capable of calculating the influence of defects and microstructure on phase stability.

Phase Transformation in Plutonium and Its Alloy

The Ellinger compendium of plutonium alloy phase diagrams provides structural maps of possible phases and crystal structures at thermodynamic equilibrium (or, at least, the best one can do in a practical sense given kinetic limita-

tions). Phase transformations provide the vehicle to get from one phase region to another. And, more important, the nature of the phase transformations governs resulting microstructures, which control the properties. In plutonium, phase transformations are triggered easily by changes in temperature, pressure, stress, or chemistry. Plutonium and its alloys exhibit virtually every phase transformation found in all other elements combined. To understand phase transformations, we must first understand the thermodynamic driving forces, the crystallographic mechanisms at the atomic level, and the kinetics of the transformation processes. (see the box “Phase Transformation Basics” on page 322). Direct observations of transformations in plutonium—either in situ or after they have occurred—are very difficult because of the metal’s reactive and radioactive nature. Moreover, the large number of allotropes and large surface distortions also make such observations difficult. Consequently, most information about transformation mechanisms in plutonium and its alloys is based on

Continued on page 328

Phase Transformation Basics

All phase transformations are driven by a reduction in the Gibbs free energy from the original to the final structure. Although the driving force for a phase change may exist, thermal activation is typically necessary to overcome the existing activation barriers. As a result of the random thermal motion of atoms, the energy of any particular atom or small collection of atoms will be just sufficient to initiate the phase change. Kinetics will determine how fast the transformation proceeds, and the transformation mechanism will help shape the resulting microstructure.

Diffusional Transformations. Phase transformations can be divided into two predominant types—diffusional and diffusionless. Most transformations occur by diffusional processes—that is, they occur at sufficiently high homologous temperatures to allow diffusion to play a role in the nucleation and growth processes of the transformation itself. In single-component systems (such as the high-temperature allotropes of plutonium), the only atomic process that occurs is the random, short-range (on the order of an atomic spacing) thermally activated atom-by-atom jumps across the interface from the parent to the product crystal structure. In transformations in which the product and parent phases have different compositions, two successive processes occur: (1) long-range transport by diffusion of, say, the solute atoms over distances of many atomic spacings and (2) short-range atomic transport across the parent-product interface. The atoms make thermally activated random jumps across the interface to create a product nucleus, or a new small region that has a completely different composition and/or structure from the parent phase. The product nucleus is separated from the parent matrix by an interface with an interfacial energy. Most of the matrix remains untransformed until the product nucleus grows to consume it. Figure A shows an example of a diffusional transformation in steel, in which both structure and composition are changed.

Diffusional transformations can proceed isothermally to completion, being limited only by adequate diffusion rates. They may or may not display specific crystallographic orientation relationships, and the product-parent interface may be coherent, semicoherent, or incoherent (Figure B), involving the nucleation and growth of the product phase from the parent phase. In all of them, an activation barrier must be overcome to reach a critical nucleus size. Because of the diffusional nature of the atomic movements required, the activation energy and the critical embryo size vary exponentially with temperature and scale with the melting point. The kinetics is described by an Arrhenius rate equation. The rate is proportional to $\exp(-\Delta G/k_{\text{B}}T)$, where G is the Gibbs free energy.

The principal barriers that must be overcome to nucleate the product phase are the interfacial free energy of the product-parent phase and the misfit strain energy. For homogeneous (uniform) nucleation, the interfacial energy represents an almost insurmountable obstacle. So, most diffusional transformations in solids are nucleated heterogeneously at defects such as excess vacancies, dislocations, grain boundaries, stacking faults, inclusions, and free surfaces. Defects can greatly reduce the size of the activation barrier required to nucleate the new phase in response to the thermodynamic driving force to lower the Gibbs free energy. The optimal shape of the new product phase typically minimizes the total interfa-

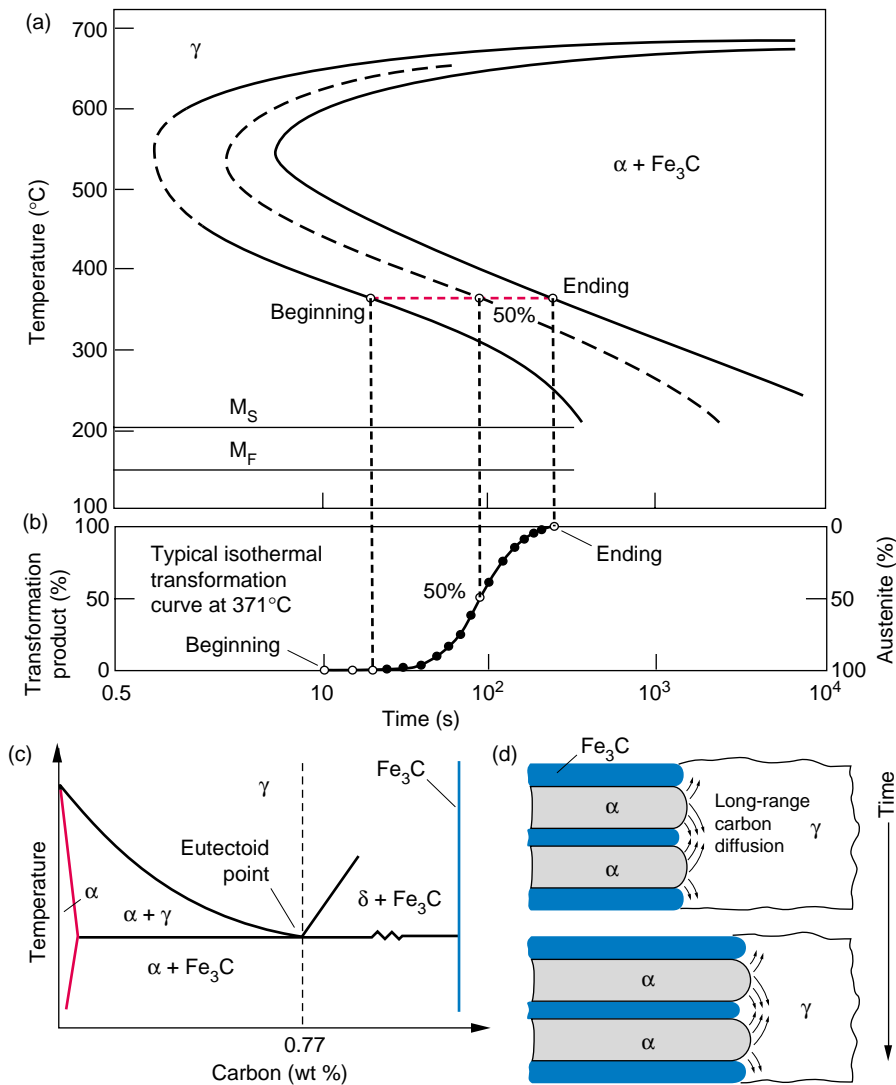


Figure A. Schematic Temperature-Time-Transformation (TTT) Diagram for Steel

The high-temperature γ -phase of steel (called austenite) is fcc. At lower temperatures, this phase transforms to a bcc ferrite (α -phase) and Fe_3C (an orthorhombic intermetallic compound). (a) The results of isothermal-transformation experiments are shown on a temperature vs time plot (TTT diagram), in which C-shape curves mark the start and finish of each isothermal experiment. That shape results from a tradeoff between the thermodynamic driving force and diffusion. At high temperature, diffusion is fast, but the driving force is too low to trigger the transformation. At low temperature, the driving force is high, but diffusion is too slow for the transformation to proceed. (b) The lower diagram shows how the transformation products increase with time if the γ -phase is quenched to miss the nose of the C-curve and then is held isothermally at 371°C (dashed red line). If the γ -phase is cooled quickly enough to avoid the C-curve altogether, then it will begin to transform martensitically (diffusionless and displacive) at the M_S temperature. Typically, the amount of transformation product depends on temperature only—not on the length of time the γ -phase is held at that temperature. The M_F temperature marks the point below which no additional martensite forms. (c) If the γ -phase has the eutectoid composition (0.77 wt % carbon), carbon must diffuse so as to create the α -phase with very little carbon (given by the red phase boundary of the α -region) and Fe_3C with 25 at. % carbon. (d) This schematic illustrates that long-range diffusion is required in austenite (γ -phase) to allow the transformation to α -phase plus Fe_3C to proceed.

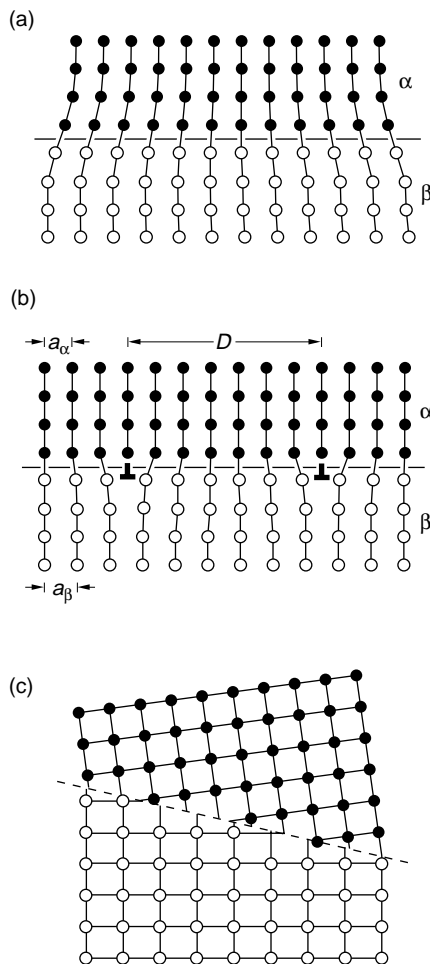
cial free energy. Grain boundaries are very effective sites for transformations with incoherent interfaces. Grain edges or corners (called triple points in two-dimensional micrographs) are even more effective. Likewise, impurities and inclusions are very effective nucleation sites. Dislocations are not very effective at lowering the interfacial energy, but the lattice distortions in the vicinity of dislocations can reduce the total strain energy of the nucleus. Dislocations can also expedite diffusion of solute atoms as can grain boundaries and excess vacancies trapped during rapid cooling.

For the nucleus to grow, the interfaces—typically a combination of semicoherent and incoherent ones—must migrate. Incoherent interfaces typically move rapidly, whereas semicoherent interfaces do so with difficulty. Consequently, precipitates in many systems take on a disc- or plate-like shape. Growth of nuclei, like nucleation itself, requires diffusion; hence, it is also controlled by an Arrhenius-type rate equation. Transformation kinetics is typically displayed in TTT diagrams, named for showing the progression of the transformation with time and temperature (Figure A) and provide valuable engineering insight into the expected evolution of microstructures expected for various heat treatments.

Figure B. Parent-Product Interfaces

The interfaces between parent and product phases can be coherent, semicoherent, or incoherent. Many transformation products contain a combination of the interface types shown here.

(a) Coherent interface between two phases with slight lattice mismatch leading to elastic coherency strains in both lattices. (b) Semicoherent interface with the misfit parallel to the interface being accommodated by a series of edge dislocations. (c) Incoherent interface with complete lack of atomic registry at the interface.



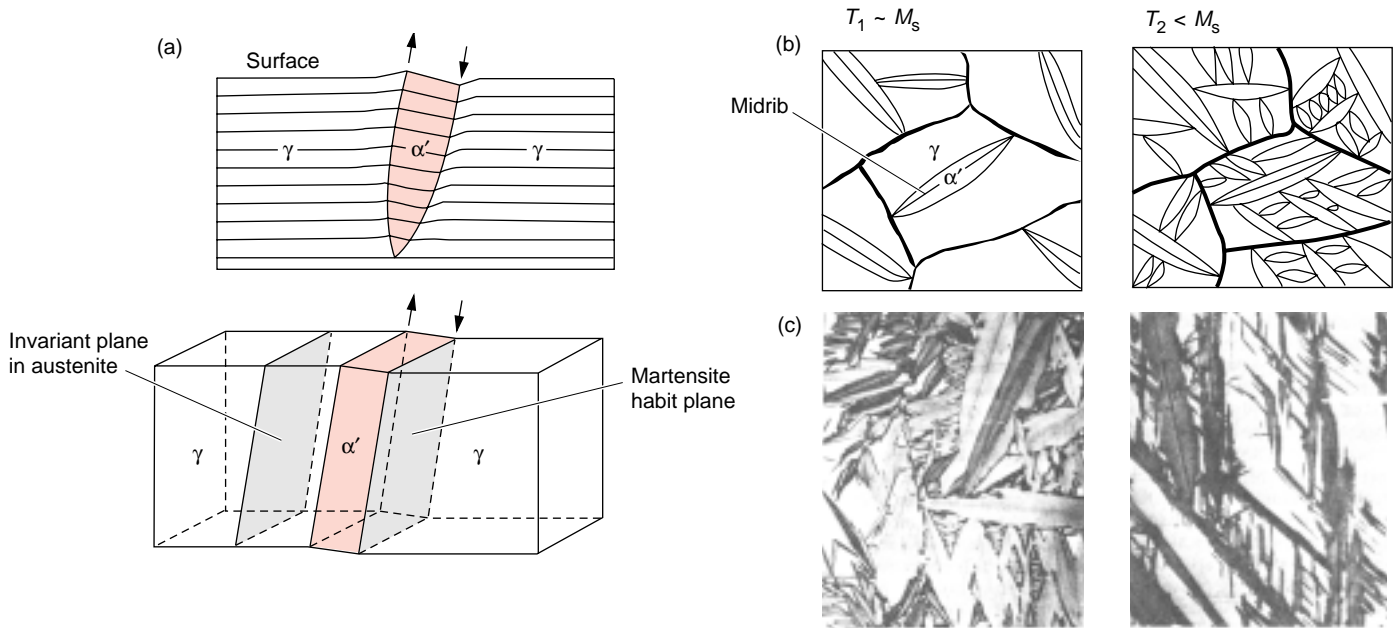
Martensitic Transformations. Diffusional transformations can be very sensitive to cooling rate. In many systems, these transformations can be avoided by a sufficiently fast quench to temperatures too low for diffusion to take place during the transformation (as shown in Figure A). In such cases, the transformations occur in a diffusionless manner. Martensitic transformations are the most important class of diffusionless transformations. They are displacive and dominated by the strain energy that arises from shear-like displacements. Diffusionless in this context means no random-walk mixing of atoms, or atom-by-atom jumping across the interface, during the structural change. Consequently, the product phase inherits the same composition, atomic order, and lattice defects that are present in the parent phase. Since solute or interstitial atoms are trapped in the martensite product, such products are always metastable—meaning that the system is not in its lowest free-energy state, and a driving force exists for decomposition to the equilibrium phases. Displacive signifies that atoms move in an organized manner by a coordinated shift of atoms—a combination of a homogeneous lattice shear and shuffle. (These are often called military transformations because they require a coordinated and regimented motion of atoms). In such transformations, the atoms move less than an interatomic spacing relative to a habit plane and a line in the product that remains undistorted and unrotated from its original form in the parent phase. In other words, it is an invariant plane relative to the parent phase. Such habit planes generally do not have simple crystallographic (Miller) indices.

During most martensitic transformations, the amount of transformation product depends on the temperature at transformation, but not the length of time at that temperature. The transformation is therefore called athermal. The overall kinetics of the martensitic transformation depends on both nucleation and growth processes, with the slower of the two largely dominating. For example, slow, thermally activated nucleation can dominate in some cases and lead to time-dependent martensitic transformations called isothermal.

A definite crystallographic relationship—lattice correspondence—exists between the product and the parent phases. The lattice correspondence for most martensitic transformations typically consists of the close-packed planes and close-packed directions in the product and parent phases being approximately parallel. The plate-like or lens-like product phase (called martensite) forms in only a limited number of orientations in the parent phase, and therefore the habit planes, which are approximately parallel to the large-area cross sections of the martensite, have those same orientations (Figure C). The martensite shape develops to minimize the sum of the strain and interfacial energies.

The lattice deformation required to produce the product phase involves (1) the coordinated shift or shear of atoms that homogeneously converts one crystallographic lattice to another—illustrated in Figure D and called the Bain strain because it was originally proposed by E. Bain (1924) to explain the face-centered-cubic (fcc) to body-centered-cubic (bcc)—actually, body-centered-tetragonal—martensitic transformation in ferrous alloys—and (2) any lattice rotation required to couple the transforming region and the adjacent parent matrix.

Many displacive transformations also involve a shuffle—that is, a coordinated shift of atoms within the unit cell that changes the structure but does not constitute a homogeneous lattice-distortive strain. In martensitic transformations, lattice deformations dominate, not shuffles. As mentioned above, the shear component of deformation must play the prominent role in the kinetics and morphology of the transformation. That is why, for example, the diffusionless fcc γ to α transformation in cerium at low temperatures is not classified as a martensitic transformation. Instead, it involves a large hydrostatic volume collapse but no shear component. On the other hand, the γ to γ' to α'' transformation in U-6 wt % Nb is classified as martensitic although it involves an



atomic shuffle because the overall transformation is dominated by shear.

The lattice-distortive nature of the martensitic transformation generates strain energy that must be relieved by additional displacements that may occur inhomogeneously as an integral part of the transformation. These displacements take place by slip or twinning in the product and are called lattice invariant because they do not change the crystal structure of the product phase—see Figure D(b–c). Hence, the lattice deformation produces a distortion of the transforming region, whereas the lattice-invariant deformation acts to reduce the magnitude of that distortion. The inhomogeneous lattice-invariant shear allows the habit plane to remain macroscopically undistorted.

The free energy required to nucleate martensite homogeneously by thermal fluctuations alone is prohibitively high, and therefore defects play a critical role in nucleation. However, unlike diffusional transformations, which tend to begin at grain boundaries and inclusions, martensitic transformations are nucleated predominantly by arrays of dislocations because their elastic strain fields help to lower the misfit strain energies of the product. Olson and Cohen (1981) demonstrated that pre-existing arrays of lattice dislocations provide the necessary embryos for nucleation. If properly arranged, and driven by the thermodynamic driving force for a phase change, these dislocations can dissociate to carry out the nucleation process. Alternatively, Clapp (1973) proposed that nucleation is triggered by a strain-induced elastic instability in special regions of the parent lattice, and that the inclusion of anharmonic terms in the elastic free energy will considerably reduce the nucleation barrier—meaning that thermal vibrations (phonons) in these anomalous regions play an important role in the nucleation process. Such nucleation processes should be accompanied by a “premartensitic” phonon softening of the lattice. Soft modes have been seen in several systems such as Ti-Ni, Au-Cd, and Au-Cu, but not in ferrous alloys. Mechanisms of martensite nucleation are not fully resolved and remain an active area of research today.

Once the activation barrier is overcome, martensite plates will grow rapidly until they hit a barrier such as a grain boundary or another martensite plate. Because martensites grow at low temperature and high velocities, the transformation interface must be very mobile. In steels, martensite plates have been measured to form in 10^{-7} second with speeds approaching the speed of sound. The marten-

Figure C. Martensitic Transformations

(a) In the 2-D schematic, the parent fcc γ -phase has transformed to a bcc α' -martensite platelet that has coherent interfaces with the parent phase and creates a distortion, or tilt, where it intersects the surface. The corresponding 3-D drawing shows the invariant plane in the parent phase that corresponds to (is parallel to) the habit plane in the α' -martensite platelet. (b) Schematic shows α' -platelets in the parent γ -grains at M_s , and the subsequent growth of new platelets between existing ones at a lower temperature. The black line in the α' -platelets is called a midrib and results from the martensite growth process. The α' -platelets are visible in a metallographic cross section polished before transformation because of their surface tilt, as shown in (a). They are also visible in a sample polished after transformation because the different crystal structures and orientations etch preferentially, thereby providing contrast. (c) Actual micrographs of martensite platelets in a medium-carbon steel and a Fe-Ni alloy.

(Figure adapted from D. A. Porter and K. E. Easterling, 1981. *Phase Transformations in Metals and Alloys*. New York: Van Nostrand Reinhold.)

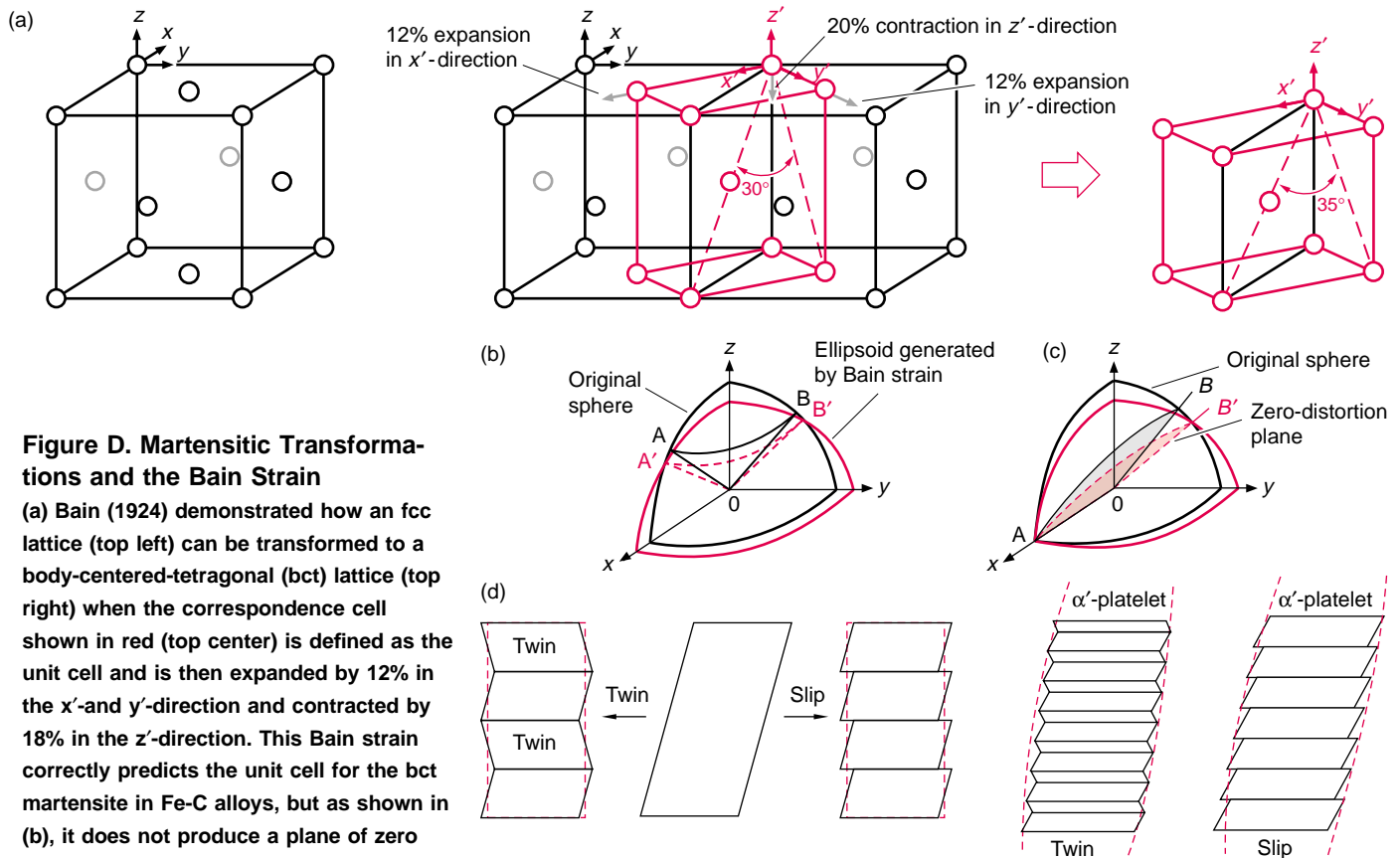


Figure D. Martensitic Transformations and the Bain Strain

(a) Bain (1924) demonstrated how an fcc lattice (top left) can be transformed to a body-centered-tetragonal (bct) lattice (top right) when the correspondence cell shown in red (top center) is defined as the unit cell and is then expanded by 12% in the x' - and y' -direction and contracted by 18% in the z' -direction. This Bain strain correctly predicts the unit cell for the bct martensite in Fe-C alloys, but as shown in (b), it does not produce a plane of zero distortion as is required in martensitic transformations. The Bain strain generates an ellipsoid from an original sphere present in the parent with no plane of zero distortion. To obtain a plane of zero distortion following the Bain strain, one must collapse the lattice back to its original position along one axis, for example, along the x -axis as in (c). Now a plane of zero distortion exists, but it has rotated in direction from OAB to OAB' . Hence, a martensitic transformation can be described by three formal operations: (1) Allow the Bain strain to generate the new lattice. (2) Introduce a shear to collapse the lattice back in one direction. (3) Rotate the martensite matrix so that the zero-distortion plane has its original position. (d) The shear introduced in (c) must be a lattice-invariant deformation so as not to change the bct structure produced by the Bain strain. The deformation can be accomplished by either slip or twinning in the martensite product. Hence, the martensite phase is required to have an internal substructure of twin stacks or to be severely slipped along parallel planes. Indeed, these substructures are found in martensite laths and plates.

site nuclei thicken by slip or twinning. Transformation dislocations are essential for the interface motion required during nucleation and growth (Olson and Cohen 1981). Specific models have been developed for some of the most studied martensites in ferrous alloys. Twinning is also critical in accommodating the overall shape and volume changes of the transformation—as shown in Figure D (c).

In most martensites, the transformation interface appears to become immobilized after a martensite plate has thickened. Since the interface is pinned by its damaged surroundings, it will be unable to reverse its motion during reverse transformation upon heating. Instead, the reverse transformation will have to be nucleated anew inside the martensite plates. Damage in the form of dislocations is typically introduced if the stress fields in the parent phase during the initial nucleation and growth of martensite plates cause the parent phase to yield plastically. On the other hand, if the martensite plates are accommodated elastically in the parent, the interface may remain mobile and the transformation can reverse itself by the shrinkage of the interface. Such transformations, called thermoelastic martensitic transformations, are fully reversible as in some Ti-Ni alloys.

As mentioned earlier, most martensitic transformations are athermal and depend principally on the temperature, not on the length of time at that temperature. The temperature for the start of the transformation is called the M_s temperature as shown in Figure 23. Although diffusion plays no direct role in the martensitic transformation itself, thermal activation is important during the nucleation stage in isothermal martensitic transformations, and diffusion is important in the post-transformation “tempering” stage. In isothermal martensitic transformations, the nucleation stage is thermally activated, followed by rapid propagation of the martensite plates or laths (morphology depends on many factors, especially the misfit strain energy). During the time-dependent nucleation stage thermally assisted motion of interfacial dislocations is necessary to reach the critical embryo

configuration and size. Since dislocations play such a prominent role in the nucleation and growth of martensites, it is easy to see that these transformations will be greatly influenced by the microstructure of the parent phase. For example, the presence of solute atoms may “pin” the dislocations necessary for nucleation. Likewise, since accommodation is necessary in the parent and product, the properties of both have a profound effect on the transformation.

In alloy systems, more solute (substitutional or interstitial) can typically be dissolved in the parent phase at high temperature than in the product at the transformation temperature. Since the composition in martensitic transformations is invariant (that is, it does not change because there is no diffusion), the product is then supersaturated (beyond its equilibrium solubility) and metastable. Depending on temperature and time (and the stresses associated with the supersaturated solute atoms), the solute atoms will begin to migrate and achieve a lower energy state. In steels, this process is called tempering and is used to beneficially control the properties of the martensite product.

Martensitic transformations can also be triggered by mechanical stresses. For most metallic systems, shear stresses are most effective in triggering martensitic transformations. Olson and Cohen (1981) have shown how one can divide such transformations into stress-assisted and strain-induced transformations. In the former, the applied stress adds to the thermodynamic driving force and has the effect of increasing the temperature for the start of the martensite transformation (the stress-assisted M_s temperature is now called M_d , where “d” designates 30 percent deformation). In strain-induced martensite transformations, plastic flow introduces new and more potent nucleation sites. Although martensitic transformations under dynamic loading have been studied little, it is well documented that they occur readily under shock-loading conditions.

Another interesting purely electronic effect that can trigger phase transformations is the charge density wave (CDW)—a static modulation of the conduction electrons typically associated with a periodic distortion of the lattice. As pointed out earlier, Peierls (1955) first suggested that periodic lattice distortions can lower the total energy of a system for a one-dimensional solid. One- or two-dimensional solids can form CDWs relatively easily because energy gaps can be created at the Fermi surfaces that will allow the system’s energy to be lowered more than it is increased by the strain associated with the periodic lattice distortion. A phase (structural) change will occur when the CDW formation is accompanied by ion displacements that stabilize the charge perturbation. Often, a precursor phenomenon such as soft phonon modes occurs above the transition temperature to assist the CDW instability (Wayman and Bhadeshia 1996).

Although CDWs should be rare in solids because favorable Fermi-surface geometry is unlikely, they have been observed in conjunction with “premartensitic” effects in Ti-Ni martensites. For example, Ti-Ni alloys containing a few percent iron show a two-stage evolution of three-dimensional CDWs. First, there is a gradual, second-order transition to a structure with distorted cubic symmetry, then a first-order transformation to a lower-symmetry rhombohedral structure. Typically, phonon softening accompanies the first stage. Although these premartensitic effects are scientifically interesting and exhibit numerous nanoscale structures, it has not been demonstrated that they influence martensitic transformations in structural alloys in a substantial manner.

I present this extensive tutorial on phase transformation basics because these concepts are necessary for understanding phase transformations in plutonium discussed in the main text. For a more complete description of phase transformations, you can refer to the cited references. ■

Continued from page 321

indirect information from dilatometry (length changes), differential thermal analysis, and other methods to measure the reaction kinetics.

Much of the early work on phase transformations in plutonium focused on understanding the polymorphic transformations from one phase of pure plutonium to another. The β to α transformation during cooling and the reverse transformation during heating received the most attention. Under equilibrium conditions, these transformations take place at 123°C, a sufficiently low temperature for diffusional transformations to proceed with great difficulty. Indeed, various transformation behaviors and resulting microstructures have been observed (Goldberg and Massalski 1970). The β to α transformation temperature is depressed substantially by high cooling rates and by the presence of impurities. Goldberg and Massalski concluded that both the β to α and reverse transformations may proceed by diffusional or diffusionless mechanisms. The conditions that govern the operative mechanisms have never been fully understood, and very little work has been done in this area over the past three decades.

Interest in the α to β and reverse transformations has now been revived because of concerns over long-term storage of plutonium, especially plutonium that has been declared excess to the weapons programs of the United States and Russia. One potential concern is the stability of the α -phase and potential volume changes and distortions associated with changes in storage temperatures should they accidentally reach the α to β transformation temperature. In addition, the ϵ to δ transformation is of interest because it holds the key to the nucleation of the δ -phase. We know that this transformation is diffusional, but very little work has been done to understand it.

However, the most interesting transformations in plutonium are those in δ -phase alloys retained to room temperature by the addition of a few atomic

percent aluminum or gallium. Cooling such alloys below room temperature triggers a diffusionless transformation to the α -phase. Similarly, the application of external stresses at room temperature can transform δ - to α -phase alloys. The transformation product in both cases is referred to as α' because it has aluminum or gallium atoms trapped in the monoclinic α -lattice, which has no solubility for these solutes under equilibrium conditions. The other intermediate phases, β and γ , are often “skipped” in the δ to α' or reverse transformations. I will highlight only some of the most interesting features and challenges of martensitic transformations in δ -phase plutonium alloys.

At first glance, we expect martensitic transformations in δ -phase plutonium alloys to resemble those studied extensively in steel and illustrated in Figure 23. The transformation from the fcc δ -phase to the monoclinic α' -phase is expected to be diffusionless during cooling because it takes place below room temperature, below which diffusion rates are too slow. Similarly, either pressure- or stress-induced transformations at room temperature are also expected to be diffusionless. However, we know that the δ to α' transformation involves not only a change in crystal structure but also a significant change in electronic structure accompanied by a large volume decrease (on the order of 20 percent). Volume changes of this magnitude have been observed in only a few other metallic systems, such as cerium and tin, but they are much larger than the few percent typical of most martensitic transformations in steel. Only recently has it been established that the δ to α' transformation can be classified as martensitic because it was believed unlikely that an undistorted habit plane (necessary for a martensitic mechanism) can be retained if such a large volume change has to be accommodated. A martensitic transformation must be displacive and dominated by the strain energy that arises from the shear-like displacements of the atoms

(as explained in the box “Phase Transformation Basics” on page 322) rather than by volume changes.

I will present some experimental results. In Figure 23, both temperature-induced and stress-induced (by the application of hydrostatic pressure) transformations are illustrated for a Pu-2 at. % Al alloy (Hecker et al. 1982, Zukas et al. 1982). The samples were homogenized at 450°C for 200 hours. In this way, the fcc δ -phase was retained to room temperature. Both cooling and isostatic pressing resulted in a slight contraction followed by an abrupt length change (or volume collapse), marking the onset of the δ to α' transformation. The transformation continued upon cooling or pressing but at decreased rates. Holding at liquid nitrogen temperature or at 1 gigapascal pressure yields very little additional transformation product. Only minor reversion of α' to δ occurred during warming back to room temperature or during pressure release. However, a small amount of additional transformation occurs initially while warming up to room temperature (because transformation stresses are relieved in the δ -phase matrix). A significant fraction of the α' transformation product is retained at room temperature or ambient pressure in the original δ -phase matrix (as confirmed by x-ray diffraction measurements) because the transformation is not fully reversed.

The α' transformation product (the light-etching platelets in Figure 23 and at higher magnification in Figure 24) present at room temperature after a cooling cycle resembles conventional martensite platelets in steels. It is lenticular in shape, has specific crystallographic orientations, and terminates at grain boundaries or at intersections with other platelets (it even exhibits a midrib centerline seen in many steels as shown schematically in Figure C in the box “Phase Transformation Basics”). The transformation sequence for the isostatic pressure experiment was δ to β' to α' , with α' and β' coexisting over most of the transformation range. Results of

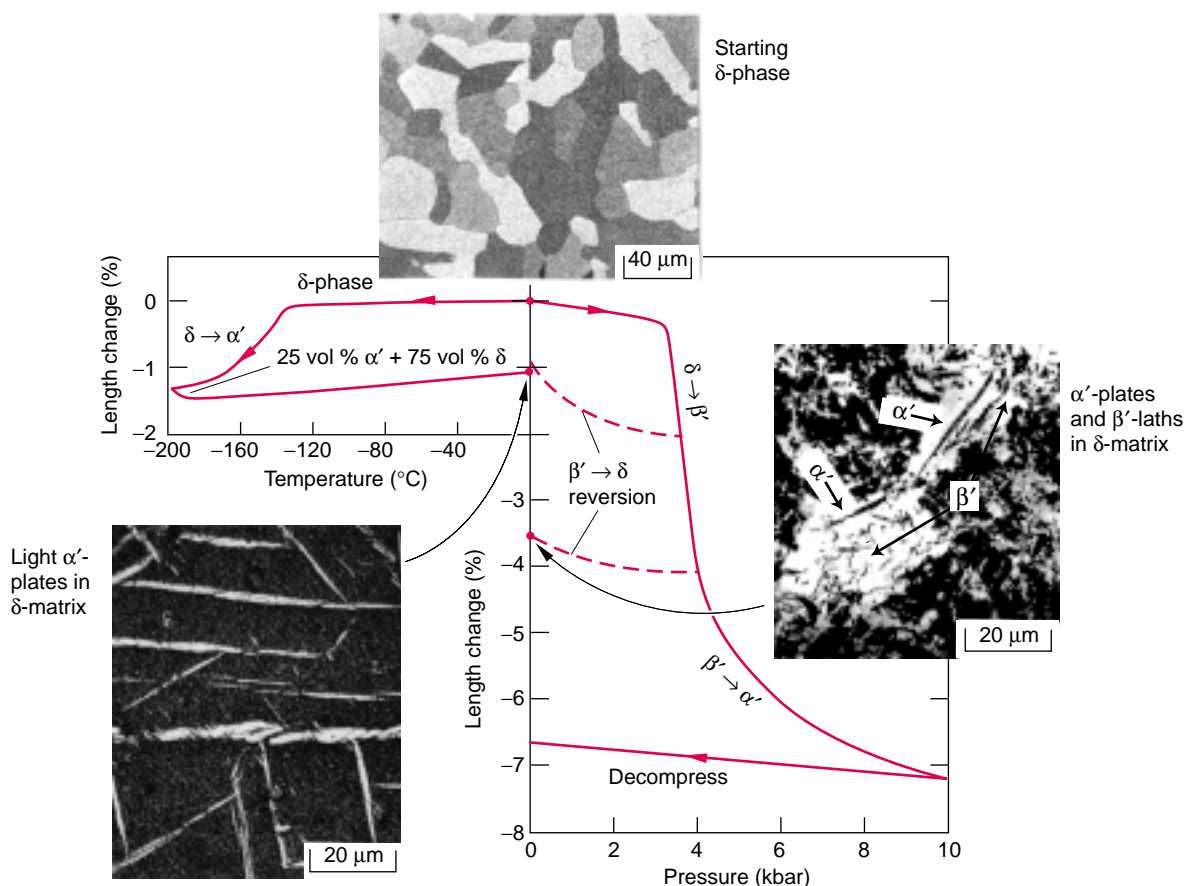


Figure 23. Temperature and Pressure Transformations in a δ -Phase Plutonium Alloy

A high-purity Pu-2 at. % Al alloy was homogenized for several hundred hours at 450°C to produce an all-fcc δ -phase microstructure as shown in the top micrograph. The red curve on the left-hand side illustrates the transformation from δ to α' during cooling at a relatively slow rate of 1.5°C/min. Approximately 25 vol % of α' is retained when the sample is returned to room temperature.

The micrograph on the left shows the white α' -platelets in the dark-etching δ -phase parent grains. The curve on the right-hand side illustrates the transformation behavior under hydrostatic compression (isostatic pressing) conducted in a Bridgman press to allow length changes to be measured during pressing. A larger amount of α' is retained when the sample is returned to ambient pressure. The entire experiment takes about 2 hours. The α' transformation product is shown in the micrograph on the right. (More detailed descriptions are provided in Hecker et al. 1982, Zukas et al. 1982).

x-ray diffraction measurements of the sample returned to ambient pressure after isopressing to 1 gigapascal showed most of the δ -phase had transformed to a combination of 90 percent α' plus 10 percent β' . The morphologies of the transformation products for the isostatically transformed products were lath-like martensite for β' and lenticular martensite for α' . The lattice parameters of the α' -phase are expanded compared with those of unalloyed α -plutonium. Analysis of crystallographic relationships for the δ to α' transformation is complicated by the low symmetry of the monoclinic α -structure and the large volume

changes. The lattice parameters of β' were indistinguishable from those of unalloyed β -plutonium. Crystallographic relationships between δ and β' and α' were not determined.

Lomer (1963) postulated specific crystallographic relationships for the δ to α' transformation by viewing the α -monoclinic structure as a distorted hexagonal structure (Figure 25). Choudry and Crocker (1985) reported preliminary theoretical results, and then Adler et al. (1986) and Adler et al. (1992) made rigorous predictions of the likely crystallographic relationships and resulting lattice strains and demonstrated that these are consistent with a

martensitic transformation. Adler et al. had to examine as many as three possible lattice correspondences and 53 possible lattice-invariant shear systems to determine the most likely crystallographic parameters because of the complex monoclinic lattice.

Experimental confirmation of their results proved difficult because the tools typically used for studying transformation crystallography, namely, transmission electron microscopy (TEM) and electron diffraction, proved elusive for plutonium. As described by Zocco in the article "Transmission Electron Microscopy of Plutonium Alloys" on page 286, plutonium is very

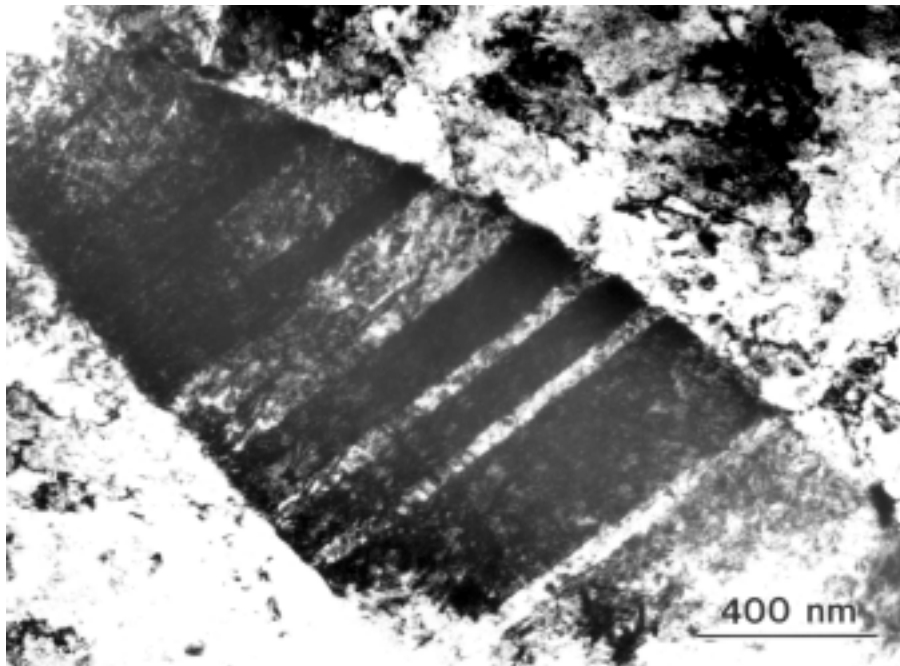


Figure 24. Transmission Electron Micrograph of α' -Martensite in δ -Phase Pu-Ga Alloy

This TEM photomicrograph is one of the few ever captured of an α' -platelet in a transformed Pu-1 wt % Ga alloy (Zocco et al. 1990). Note that the twins in the α' -platelet resemble the schematic shown in Figure D on page 326. The photomicrograph is for the $[11-0]$ α -zone. The orientation relationships for the twin and the matrix are $(001)_{\text{matrix}}$ parallel to $(2-01)_{\text{twin}}$ and $(225)_{\text{matrix}}$ parallel to $(2-25)_{\text{twin}}$.

difficult to prepare in sufficiently thin and clean sections for such an examination (the radioactive nature of plutonium is additionally complicated by its very reactive nature, making the preparation of clean surfaces difficult). However, Zocco et al. (1990) for the first time successfully examined and interpreted the transformed microstructure of plutonium by TEM (Figure 24).

Direct TEM examination of the transformed product revealed a lattice correspondence of nearly parallel close-packed planes and directions in the product α' -phase and parent δ -phase— $(111)_{\delta}$ and $(020)_{\alpha}$ planes and $[\bar{1}10]_{\delta}$ and $[100]_{\alpha}$ directions. The α' -phase habit plane was found to be near $(1\bar{3}2)_{\alpha}$. The lattice-invariant deformation mode in the product α -phase was determined to be $(205)_{\alpha}$ twinning. These experimental results are consistent with the

theoretical predictions of Adler et al. (1986) and confirm that the δ to α' transformations in Pu-Al and Pu-Ga alloys under these conditions are diffusionless and martensitic, in spite of the unusually large volume change. Unfortunately, TEM has not become a routine experimental tool for plutonium. The results shown in Figure 24 remain essentially the only examples of transformation studies using TEM in plutonium alloys. Hence, we have very little detailed understanding of temperature and stress-induced transformations in plutonium today.

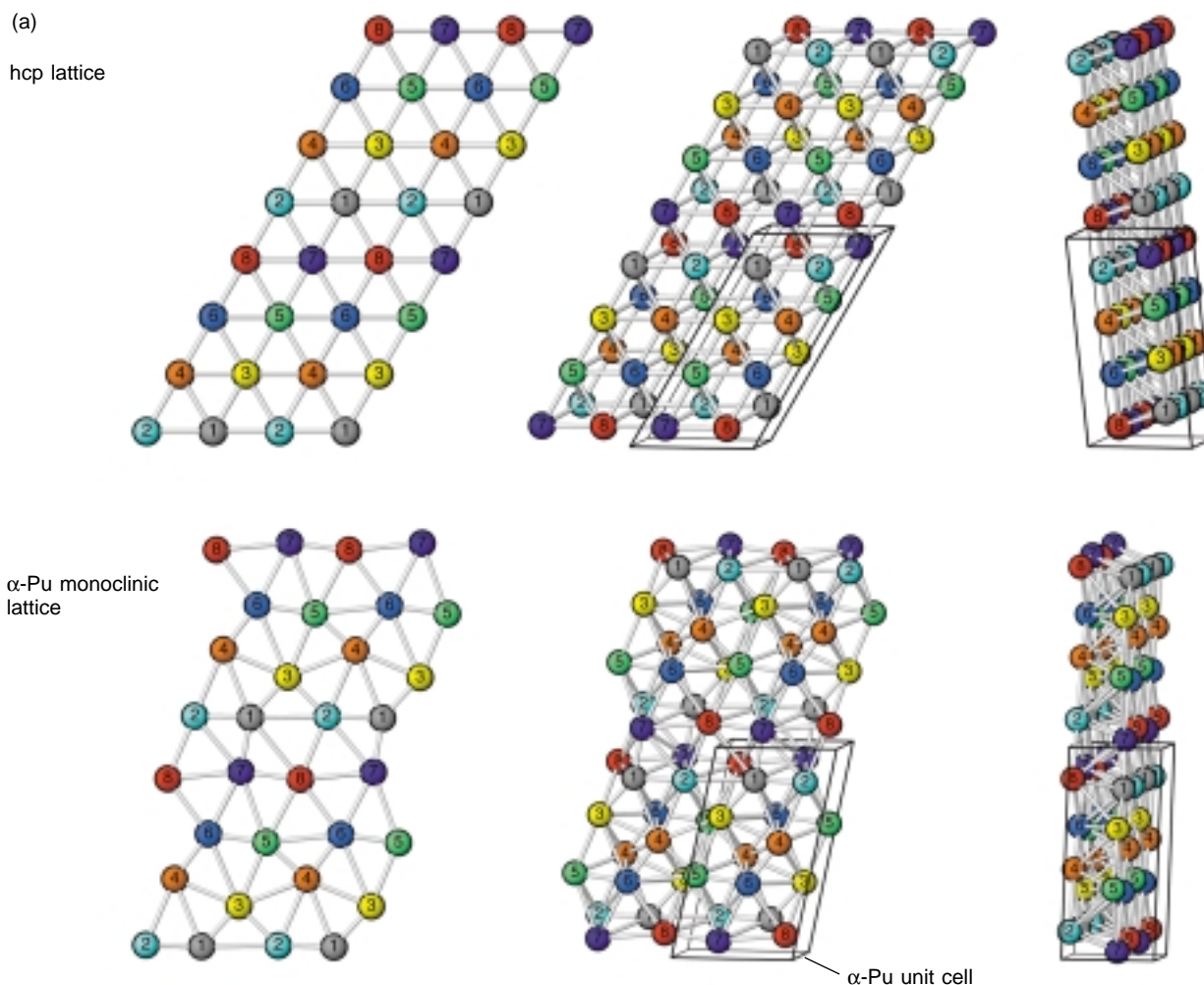
Although the martensitic nature of the δ to α' transformation is now well established, we must explain the rate (or time) dependence of the transformation. As shown in Figure A on page 323, the onset and extent of martensitic transformations are typically determined

by temperature, independent of cooling rate. The transformation behavior during cooling illustrated in Figure 23 is that observed at a constant cooling rate. However, Orme et al. (1975) found the δ to α' transformation in Pu-Ga alloys followed a C-curve behavior similar to that shown schematically in Figure A on page 323 for diffusional transformations. In fact, they found the “double C” curves shown in Figure 26.

The times and temperatures for the onset of transformation depend strongly on gallium concentration. Hecker et al. (1982) found similar time dependence for Pu-Al alloys. They concluded that the transformation occurs by an ‘isothermal’ martensitic transformation. As explained in the box on page 322, such transformations proceed by a thermally activated nucleation stage (hence the time dependence) followed by a rapid martensitic growth stage.

Recent work by Deloffre et al. (1998) has shed some light on the double-C-curve nature shown in Figure 26. They claim that the crystallographic mechanisms of the martensitic transformations differ for the upper and lower C-curves and for different gallium concentrations. Low gallium concentrations and higher transformation temperatures (upper C curve) favor the transformation to proceed from δ to γ' to α' , whereas higher gallium concentrations and lower temperatures (lower C curve) favor transformation directly from the δ - to the α' -phase. They also showed that the morphologies of the martensite products differ accordingly. As in the isostatic pressing case, this two-step transformation (but in this case δ to γ' to α' instead of δ to β' to α') produces a product phase of thin plates or laths, whereas the direct transformation produces lenticular martensite as shown in Figure 24.

They also found that products for the two different paths transformed very differently when heated, as shown in Figure 27. The two-step transformation products (upper C curve) showed evidence of α' to δ , as well as α' to β and β to γ transformations. The one-step product, on the other hand, appeared to



(b)

Table III. Bonds in α -Plutonium

Atom	Number of Short Bonds ^a	Average Length (Å)
1	5	2.57
2-7	4	2.54
8	3	2.77

^aShort bond 2.57–2.78
Long bond 3.19–3.71

(c)

Table IV. Monoclinic α -Lattices

Structure	a (Å)	b (Å)	c (Å)	β (deg)	Atomic Volume (Å ³)
α	6.183	4.822	10.963	101.79	319.96
α'	6.217	4.859	11.019	101.84	325.79
Change (%)	0.56	0.77	0.51		1.82

Figure 25. α -Plutonium Compared to an hcp Structure and Parameters for α - and α' -Plutonium

(a) The figure contrasts the hcp structure with the monoclinic structure of α -plutonium, demonstrating that the latter resembles a distorted hcp. The bonds shown are between nearest neighbors. Each of the eight numbered sites in α -plutonium is crystallographically unique, and the second plane is a 180° rotation of the first plane. (b) Table III shows that the eight nearest-neighbor bonds fall into two groups. (c) Table IV shows the lattice parameters for the normal α -lattice (unalloyed plutonium) and for the α' -lattice transformed from the δ -phase of the Pu-2 at. % Al alloy shown in Figure 23. The lattice parameters along all three axes are expanded slightly, and the monoclinic angle is increased slightly. Overall, forcing 2 at. % Al into the α' -lattice expands the lattice volume by approximately 2%.

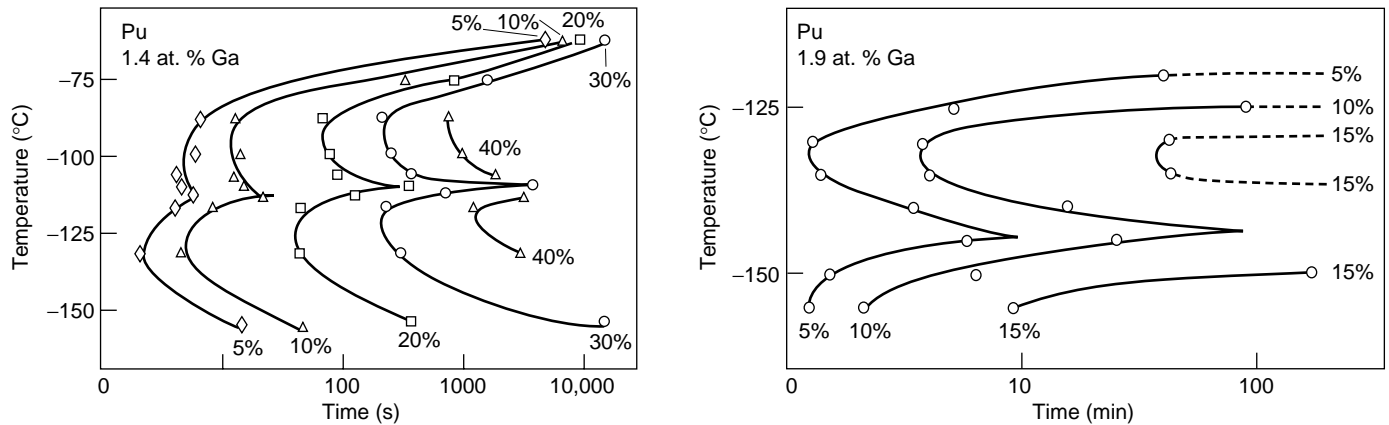


Figure 26. Temperature-Time-Transformation Curves for Two High-Purity Pu-Ga Alloys

High-purity alloys with two gallium concentrations had been homogenized to retain the fcc δ -phase to room temperature before isothermal transformation experiments were conducted at low temperatures. The transformation behavior follows a double-C-curve behavior (Orme et al. 1975). Each curve of the nested set represents a different level of transformation from δ to α' . Note that time in the Pu-1.4 at. % Ga diagram is given in seconds whereas that in the Pu-1.9 at. % Ga diagram is in minutes, indicating how much more unstable and ready to transform the lower gallium alloy is.

revert from α' directly back to δ in one step. All these results are inferred indirectly from the dilatometry experiments shown in Figure 27. Unfortunately, because no TEM studies were performed, it is not possible to draw definitive conclusions about the exact nature of the transformation mechanisms for either C-curve or the reverse transformations upon heating. Likewise, we do not know the exact transformation mechanism or crystallography of the pressure-transformed alloys. For example, the Pu-Ga alloys do not show the β' -phase as an intermediate step as do the Pu-Al alloys. In addition, we have no insight into the isothermal nature of the martensitic transformations upon cooling—that is, how the nucleation sites are thermally activated for either of the two mechanisms. By comparison with other alloy systems, we can only surmise that the pre-existing nuclei are insufficient to trigger the transformation at these temperatures and that a thermally activated rearrangement of dislocations must occur to successfully nucleate the transformation. Once nucleated, the transformation proceeds rapidly by the combination of lattice deformations and lattice-invariant deformations.

One additional complication, similar to the tempering of martensite products in steels, is worth noting. The α -phase has virtually no solubility for any alloying element except neptunium. Yet, the diffusionless martensitic transformation of δ to α' is composition invariant—that is, the gallium or aluminum atoms that substitute for plutonium atoms in the δ -phase are now stuck unhappily in the α' -phase. Consequently, these solute atoms expand the monoclinic α -phase as shown by the change in lattice parameters for a Pu-Al alloy in Figure 25. The properties of the α' -phase (supersaturated in aluminum or gallium) can differ substantially from that of the normal monoclinic α -phase. For example, when heated above room temperature, α' transforms directly to δ just above room temperature—much like the transformation product derived from the lower C-curve in Figure 26(b)—and essentially completes that transformation by 150°C. The α -phase of unalloyed plutonium, by contrast, transforms to β , γ , and δ sequentially at the temperatures shown in Figure 1.

Holding the α' -phase at slightly elevated temperatures (from 50°C to 100°C) will cause the gallium or aluminum atoms to migrate away from

those lattice sites that cause expansion of the α' -phase. Unfortunately, we have no microstructural information on where the solute atoms are trapped during the transformation, nor about how they migrate and to what locations they migrate. We suspect that the migration occurs in stages—first to crystallographically different sites in the plutonium lattice, next to defects such as dislocations and lattice vacancies, then to grain boundaries, and eventually, given sufficiently long times and elevated temperatures, out of the α' -platelets altogether.

A Program of Future Studies on Phase Stability and Transformation.

To summarize phase stability and phase transformations in plutonium and its alloys, we have a large body of experimental phase diagram information and a limited number of transformation curves such as the TTT curves for a few Pu-Ga alloys. Unfortunately, we have very little fundamental understanding of the transformation mechanisms and essentially no theoretical understanding of the effect of alloying on phase stability or on transformation mechanisms. Consequently, we are not able to

extrapolate phase stability or transformation behavior outside our limited data base. For example, we have little understanding of the effects of multiple alloying elements or impurities on phase stability and transformation behavior. We do not understand the effects of transformation rate—either during cooling or during pressurization. We have insufficient knowledge of the effect of the stress state on transformations. Unlike most other martensitic transformations that depend primarily on the shear stress, those in plutonium are governed primarily by the hydrostatic stress component. We do not understand the role of the electronic transition from the δ - to the α -phase or the reverse transformation.

XAFS measurements provide hints that a local structure may be superposed on the long-range fcc δ -structure. Yet, we do not understand what controls this local structure and what role it plays in phase transformations. We do not know if premartensitic phenomena, such as phonon softening, play a role in the transformation behavior of δ -phase alloys, or if CDWs play a role at low temperatures as they do in uranium—see Lander et al. (1994). We have little information about the role of surfaces. If a free surface is present, it may change the stress state sufficiently to affect transformation mechanisms. Moreover, we do not even know the sign of the effects of self-irradiation on δ -phase stability. In other words, do the defects generated by the radioactive decay stabilize or destabilize the δ -phase during aging? Unfortunately, the list of what we don't know about phase stability and transformations goes on and on.

On the other hand, this seemingly endless list also presents us with exciting scientific challenges. Electron-electron correlations play an important role in determining the structure and properties of the fcc δ -phase, and correlated-electron materials are currently at the forefront of the challenges in condensed-matter physics. For the δ -phase, we have the additional

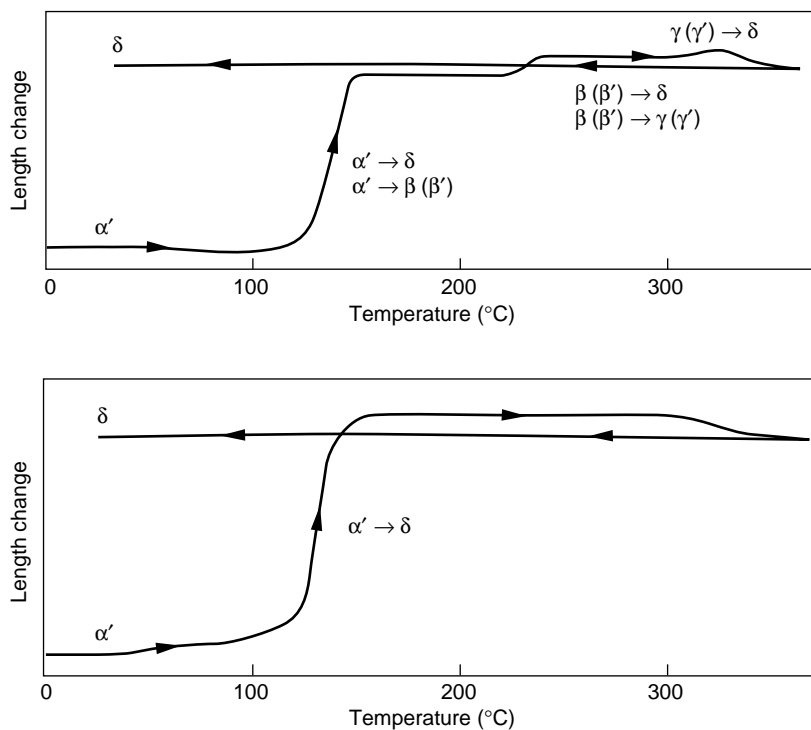


Figure 27. Reverse Transformation Behavior during Heating

Deloffre et al (1998) conducted experiments similar to those of Orme et al. (1975) shown in Figure 26. They transformed a well-homogenized Pu-1.2 at. % Ga alloy to establish the double-C-curve. They subsequently heated samples transformed at low temperature and measured the resulting length changes (indicative of reverse transformations). (a) Shows the results for a sample previously transformed in the upper C-curve and (b) a sample transformed in the lower C-curve. The likely transformation path during the reverse transformation of α' is indicated in each diagram.

challenge of trying to understand its transformation behavior to α' , both the electronic transition from partially localized to itinerant 5f electrons and the crystallographic transformation from an fcc to a monoclinic lattice. We must now bring to bear not only the tools used routinely in other alloy systems (for example, TEM and in situ x-ray diffraction), but also such powerful tools as XAFS, neutron scattering, and PES that can provide us with additional electronic and structural information. For example, neither the local atomic structure nor the electronic structure of the α' -phase has ever been measured experimentally. PES experiments, such as those conducted by Arko and coworkers (see the article on page 168), are particularly important

for the α' -phase to see if this phase sits between the electronic structures of the α - and δ -phase. Likewise, XAFS experiments on α' may identify where in the α' -lattice the gallium or aluminum atoms are trapped and how they migrate with time and temperature. Neutron diffraction offers the possibility of following the transformation in bulk samples (unlike x-ray diffraction which is limited to the near-surface region) in situ during cooling or pressurization.

Theoretically, we must now extend the band-structure calculations to include alloying effects. Moreover, we must attempt to include the effects of electron correlations in first-principles calculations. Neutron-scattering experiments to determine the phonon dispersion curves will be crucial to help

guide theoretical prediction of temperature effects. Likewise, careful ultrasonic measurements of elastic moduli will be important to understand temperature effects and phonons. To understand the role of defects and microstructure, we must develop an accurate interatomic potential that would allow modeling such effects.

Experimentally, we need high-purity, high-quality single crystals and polycrystals of α - and δ -phase plutonium alloys to study fundamental properties. As we have pointed out, knowing the precise nature of the metallurgical processing is paramount to ensuring that we understand the starting material. Moreover, surface preparation is crucial because most processing steps alter the surface crystal structure. In addition, we absolutely need plutonium-242 to conduct neutron scattering experiments.

Summary of Challenges in Plutonium Metallurgy

The properties of plutonium depend on its crystal structure, which depends critically on temperature, pressure, chemistry, and microstructure. Finally, the microstructure depends on all of the previous variables plus the details of thermal and mechanical processing. We demonstrated that plutonium is truly unique because of its position in the periodic table and that its unusual properties are derived from the nature of the 5f electrons. Specifically, it is the narrow band and the high density-of-states of the 5f electrons at the Fermi energy that make plutonium unique. Although these features favor an unusual low-symmetry monoclinic structure at room temperature, it takes only a slight change in temperature or the addition of a few atomic percent of elements such as aluminum or gallium to approach a structure that is closer to that of americium, with a much larger atomic volume than the monoclinic α -phase and a high-symmetry crystal structure. The uniqueness of plutonium can only be appreciated and

understood by studying its neighbors in the actinide series, and I am convinced that it will be understood only through the close collaboration between the condensed-matter physics and metallurgical communities.

All the peculiarities of plutonium have a profound effect on its physical and mechanical properties. Many physical properties such as electrical resistivity and magnetic susceptibility are expected to reflect directly the peculiarities of the 5f electrons in plutonium (see the article by Boring and Smith on page 90). The low-temperature behavior of plutonium is highly anomalous—for example, the electrical resistivity for α -plutonium (which is already very high at room temperature) climbs as the temperature is lowered to approximately 100 kelvins before it falls as it is cooled toward absolute zero. Some of the other transport properties such as diffusion depend primarily on the bonding properties of the electrons, hence they scale with the homologous melting point as mentioned earlier. The mechanical properties of plutonium depend to first order on the crystal and defect structure—varying dramatically from those of the soft, ductile δ -phase to that of the strong, brittle α -phase. Other peculiarities of the mechanical behavior of plutonium and its alloys are discussed by Hecker and Stevens (page 336).

Finally, the complexities of plutonium are further exacerbated by the continuous lattice damage inflicted during its self-irradiation as discussed by Wolfer (page 274) and Hecker and Martz (page 238). From a practical point of view, we know that plutonium does not destroy itself over a period of a few decades. All indications are that significant self-annealing heals much of the damage of self-irradiation. Yet, by comparison with other metals and alloys that suffer similar irradiation from external sources, the conditions in plutonium are ripe for substantial property changes to happen as plutonium ages. ■

Further Reading

- Adler, P. H., G. B. Olson, and D. S. Margolies. 1986. *Acta Metall.* **34**: 2053.
- Adler, P. H., G. B. Olson, M. F. Stevens, and G. F. Gallegos. 1992. *Acta Metall. Mater.* **40**: 1073.
- Ardell, A. J. 1963. *Acta Metall.* **11**: 591.
- Bain, E. C. 1924. *Trans. AIME.* **70**: 25.
- Brewer, L. 1983. *Systematics and the Properties of the Lanthanides*. Edited by S.P. Sinha, 17. Dordrecht: D. Reidel Publishing Company.
- Choudry, M.A. and A. G. Crocker, 1985. *J. Nucl. Mater.* **127**: 119.
- Clapp, P. C. 1973. *Phys. Stat. Sol.* **57**: 561.
- Deloffre, P., J. L. Truffier, and A. Falanga. 1998. *J. Alloys Compounds* **271-273**: 370.
- Ellinger, F. H., W. N. Miner, D. R O'Boyle, and F. W. Schonfeld. 1968. "Constitution of Plutonium Alloys" (Dec.). Los Alamos National Laboratory report LA-3870-MS.
- Eriksson, E., J. D. Becker, A. V. Balatsky, and J. M. Wills. 1999. *J. Alloys and Compounds* **287**: 1.
- Goldberg, A., and T. B. Massalski. 1970. In *Proc. of 4th Int. Conf. on Plutonium and Other Actinides 1970*. Edited by W. N. Miner, 875. New York: The Metallurgical Society of AIME.
- Haasen, P. 1992. *Physical Metallurgy*. Cambridge: Cambridge University Press. Cambridge.
- Hammel, E. F. 1998. *Plutonium Metallurgy at Los Alamos, 1943-1945*. Los Alamos, NM: Los Alamos Historical Society.
- Hecker, S. S. 2000 (to be published). *Plutonium Aging: From Mystery to Enigma*. In *Proceedings of the International Conference on Aging Studies and Lifetime Extension of Materials*. Edited by L. G. Mallinson, 191. Dordrecht: Kluwer Academic Publisher.
- Hecker, S. S., J. R. Morgan, and R. A. Pereyra. 1982. In *Proc. Int. Conf. Solid-Solid Phase Transf.* Edited by H. I. Aaronson, 1339. New York: Am. Inst. Min. Engrs.
- Heine, V. 1969. *The Physics of Metals: 1. Electrons*. Edited by J. M. Ziman, 1. Cambridge: Cambridge University Press.
- Hill, H. H., and E. A. Kmetko. 1976. *J. Phys. F* **6**: 1025.
- Johansson, B. 1974. *Phil. Mag.* **30**: 469.

- Kaufman, L., and H. Bernstein. 1970. *Computer Calculation of Phase Diagrams*. New York: Academic Press.
- Lander, G. H., E. S. Fisher, and S. D. Bader. 1994. *Adv. Phys.* **43**: 1.
- Lawson, A. C., J. A. Goldstone, B. Cort, R. J. Martinez, F. A. Vigil, T. G. Zocco, J. W. Richardson, and M. H. Mueller. 1996. *Acta Crystall.* **B52**: 32.
- Lawson, A. C., B. Martinez, J. A. Roberts, and B. I. Bennett. 2000. *Phil Mag.* **80**: 53.
- Liptai, R. G., and R. J. Friddle. 1967. *J. Nucl. Mater.* **21**: 114.
- Lomer, W. M. 1963. *Solid State Commun.* **1**: 63.
- Massalski, T. B. 1996. *Physical Metallurgy*. Edited by R. W. Cahn and P. Haasen, 136.
- Mitchell, J. N., F. E. Gibbs, T. G. Zocco, and R. A. Pereyra. 2000 (to be published). *Met. Trans.*
- Morgan, J. R. 1970. In *Proc. of 4th Int. Conf. on Plutonium and other Actinides 1970*. Edited by W. N. Miner, 669. New York: The Metallurgical Society of AIME.
- Nelson, R. D., T. K. Bierlein, and F. E. Bowman. 1965. Battelle, Pacific Northwest National Laboratory report BNWL-32.
- Olson, G. B. and M. Cohen. 1981. *Ann. Rev. Mater. Sci.* **11**: 1.
- Orme, J. T., M. E. Faiers, and B. J. Ward. 1976. In *Proc. of 5th Int. Conf. on Plutonium and Other Actinides*. Edited by H. Blank and R. Lindner, 761. New York: North Holland Publishing Co.
- Peierls, R. E. 1955. *Quantum Theory of Solids*. Oxford: Oxford University Press.
- Peterson, D. E., and M. E. Kassner. 1988. *Bull. Alloy Phase Diagr.* **9**: 261.
- Porter, D. A., and K. E. Easterling. 1981. *Phase Transformations in Metals and Alloys*. New York: Van Nostrand Reinhold Company.
- Sherby, O. D., and M. T. Simnad. 1961. *Trans. ASM* **54**: 227.
- Smith, J. L., and E. A. Kmetko. 1983. *J. Less Common Met.* **90**: 83.
- Söderlind, P., O. Eriksson, B. Johansson, J. M. Wills, A. M. Boring. 1995. *Nature* April 6 issue: 6522.
- Söderlind, P., J. M. Wills, B. Johansson, O. Eriksson. 1997. *Phys. Rev. B.* **55**: 1997.
- Wallace, D. C. 1998. *Phys. Rev. B* **58**: 15433.
- Wayman, C. M. and H. K. Bhadeshia. 1996. In *Physical Metallurgy*. Edited by R. W. Cahn and P. Haasen, 1507. North-Holland: Elsevier.
- Wittenberg, L. J., G. A. Vaughn, and R. DeWitt. 1970. In *Proc. of 4th Int. Conf. on Plutonium and other Actinides 1970*. Edited by W. N. Miner, 659. New York: The Metallurgical Society of AIME.
- Zocco, T. G., M. F. Stevens, P. H. Adler, R. I. Sheldon, and G. B. Olson. 1990. *Acta Metall. Mater.* **38**: 2275.
- Zukas, E. G., S. S. Hecker, J. R. Morgan, and R. A. Pereyra. 1982. In *Proc. Int. Conf. Solid-Solid Phase Tranf.* Edited by H. I. Aaronson, 1333. New York: Am. Inst. Min. Engrs.

Acknowledgments

I acknowledge all those who helped with this article: for technical discussions on electronic structure, Mike Boring, Nikki Cooper, Jim Smith, and John Wills; on metallurgy, Frank Gibbs, Del Harbur, Mike Stevens, and Tom Zocco; on crystallography, Steve Conradson, Angus Lawson, and Luis Morales; on thermodynamics, Marius Stan and Duane Wallace. I thank Jeremy Mitchell and Ramiro Pereyra for allowing me to use their plutonium segregation data and micrographs. The critical reading of the manuscript by Mike Baskes, Bob Field, and Dan Thoma is appreciated. I also thank my scientific collaborators in plutonium metallurgy over the years: Dave Eash, Reed Elliott, Del Harbur, Jim Morgan, and Gene Zukas. The motivation for writing a metallurgical article directed at a broader audience came from many discussions with Mike Boring, Nikki Cooper, and Jim Smith. I also thank the entire *Los Alamos Science* staff for their wonderful and very professional support.

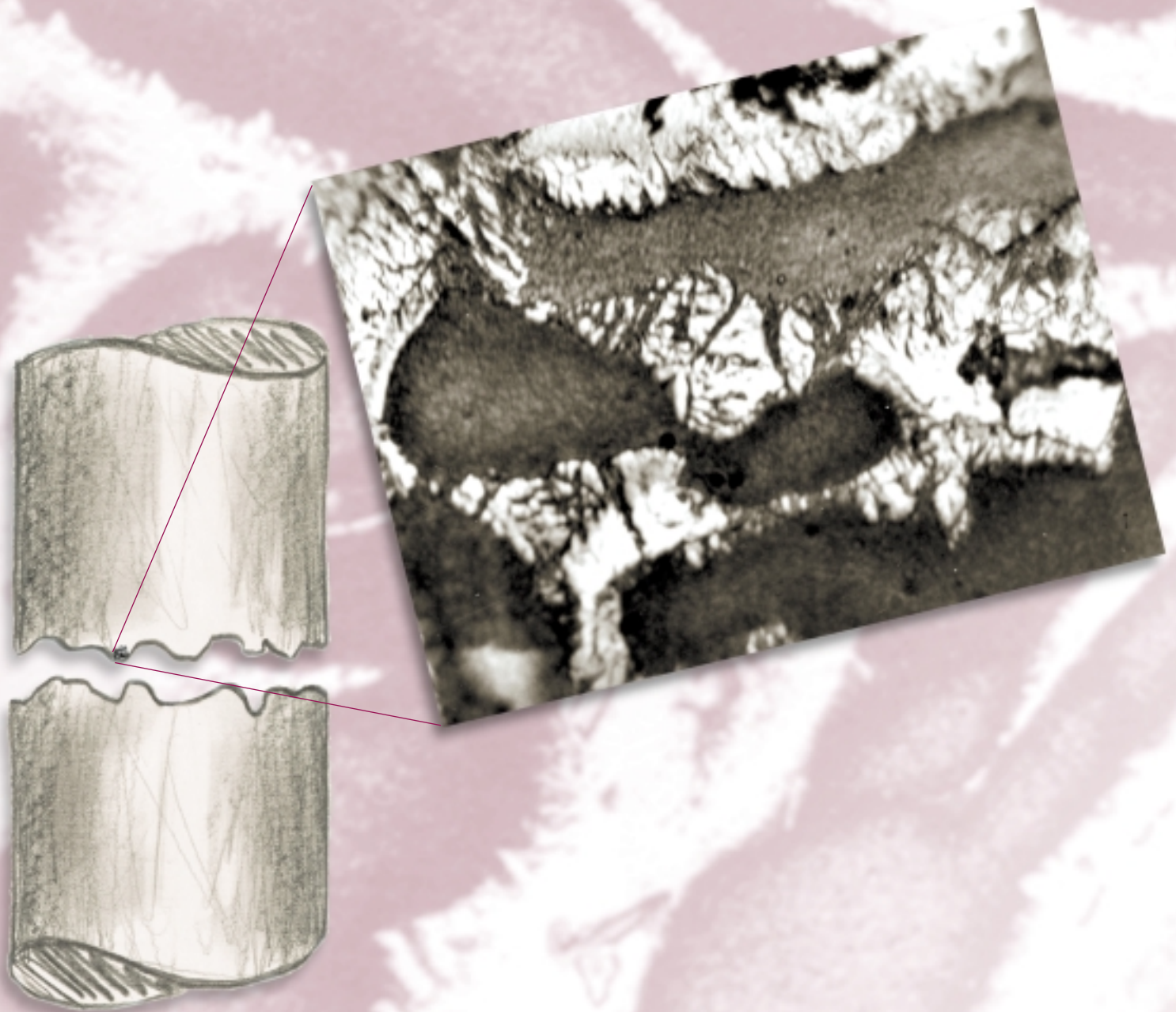
Siegfried S. Hecker received his B.S., M.S., and Ph.D. in metallurgy from Case Western Reserve University. After two years as a post-doctoral appointee at Los Alamos, he became a senior research metallurgist with the General Motors Research Laboratories. He joined the Laboratory as a technical staff member in the Physical Metallurgy Group, and served as Chairman of the Center for Materials Science and Leader of the Materials



Science and Technology Division before becoming Director. Sig was Director of Los Alamos National Laboratory from 1986 to 1997. He is currently a Senior Fellow at Los Alamos. Sig is a member of the National Academy of Engineering, Fellow of the TMS (Minerals, Metallurgy and Materials Society), Fellow of the American Society for Metals, and Honorary Member of the American Ceramics Society. In recognition of his achievements, Sig was named Laboratory Director of the Year by the Federal Laboratory Consortium, (1998). In 1998, he also received the honorary Doctor of Science degree (Honoris Causa) from Case Western University. Sig received the Department of Energy's Distinguished Associate Award, (1997), the University of California's President's Medal, (1997), the ASM Distinguished Life Membership Award, (1997), an Honorary Degree of Scientiae Doctoris, Ripon College (1997), the Navy League New York Council Roosevelt Gold Medal for Science (1996), the Aviation Week Group Laurels Award for National Security (1995), the James O. Douglas Gold Medal Award (1990), the ASM International's Distinguished Lectureship in Materials Society (1989), the Kent Van Horn Distinguished Alumnus Award, Case Western Reserve University (1989), an Honorary Degree of Scientiae Doctoris, College of Santa Fe (1988), the Year's Top 100 Innovations Award from Science Digest (1985), and the Department of Energy's E. O. Lawrence Award (1984). In addition to his current research activities, Sig is a member of the Council on Foreign Relations and the Pacific Council on International Policy. He also serves on the National Academy of Engineering Committee on Membership (chairman), Nominating Committee, and Draper Prize Committee, and on the Fellows Awards Committee of The Metallurgical Society.

Mechanical Behavior of Plutonium and Its Alloys

Siegfried S. Hecker and Michael F. Stevens



The current renaissance in plutonium research derives in large part from our need to predict the mechanical, or load-bearing, response of this material under different conditions. The Manhattan Project chemists and metallurgists learned enough in a very short time to make this fickle metal behave in an acceptable way during casting, pressing, machining, and assembly. Their achievement was all the more remarkable because only very small quantities of plutonium were available for study during most of the project (see the article “The Taming of ‘49’” on page 48). Stockpile certification in the absence of nuclear testing, as it is done today, requires that we have a much more thorough understanding of plutonium’s structural and mechanical properties.

Plutonium exists in six different crystallographic phases before it melts at the relatively low temperature of 640°C. The two phases of greatest interest are the monoclinic α -phase, the stable form of unalloyed plutonium at room temperature, and the face-centered-cubic (fcc) δ -phase, which can be retained down to room temperature by the addition of a few atomic percent (at. %) of aluminum or gallium. The mechanical properties of these two forms of plutonium are as different as night and day. Although metallurgists have little experience with monoclinic structures (plutonium is the only metallic element that exists in this form), conventional wisdom and comparison with minerals that have monoclinic structures suggest that α -plutonium should be very brittle at room temperature. And indeed, this appears to be the case. Similarly, metallurgists’ experience with fcc metals and alloys suggests that fcc δ -plutonium alloys should be very ductile and tolerant of flaws, and should have low strength. Again, such is the case for the δ -phase alloys.

Yet, plutonium and its alloys are full of surprises. In this article, we focus on some of their exotic mechanical behaviors in the hope that we can generate renewed scientific interest in this unusual metal. We also touch on the fundamental dichotomy in all structural materials—the inverse relationship between strength and ductility. How to make strong materials more ductile

(and tougher) and ductile materials stronger is a real challenge for all structural materials. For a thorough review of the conventional mechanical properties of plutonium, you can refer to the compendium of mechanical properties of engineering interest presented by Gardner (1980).

Renewed Interest in Fundamental Mechanical Properties

Mechanical properties are relevant to all aspects of manufacturing—from shaping to machining—as well as to the engineering and dynamic performance of nuclear weapons. Plutonium is the heart of the “nuclear trigger” of modern nuclear weapons. For decades, we could compensate for the gaps in our understanding of plutonium’s complexities by testing nuclear devices underground at the Nevada Test Site. Today, we must be able to certify without nuclear testing that the nuclear weapons remaining in the United States stockpile are safe and reliable. We must also remanufacture plutonium components or extend their design lifetimes in the absence of testing.

Today’s manufacturing engineer must know how all processing steps affect the evolution of microstructure in order to ensure that the final plutonium product may be substituted for original, certified, or “diamond-stamped,” com-

ponents now in the stockpile. Variability in the manufacturing process and in the factors that cause such changes, such as impurity streams, must be reduced to previously unattained levels if we are to establish a quality-assured scheme for the manufacture of small numbers of units. In the past, plutonium components in weapons systems were specified simply on the basis of the chemical assay of the plutonium, the average component density, and adherence to required dimensions. Today, we must understand how microstructure affects mechanical properties in order to predict acceptable performance.

In the present nontesting environment, nuclear weapons physicists and engineers are using sophisticated computer models and calculations to assess performance. These computer models require realistic models of materials behavior, backed up by rigorous experimental data. Both engineering and dynamic performance, however, involve loading conditions that are not easily achieved in the laboratory. Hence, materials models must be guided not only by experiment but also by a fundamental understanding of the atomic processes governing the mechanical behavior of plutonium.

In light of those needs, we present some of the unusual mechanical properties that require study. Specifically, we will discuss anomalous plastic flow in α -plutonium and the role of stress-induced transformations in the fracture of

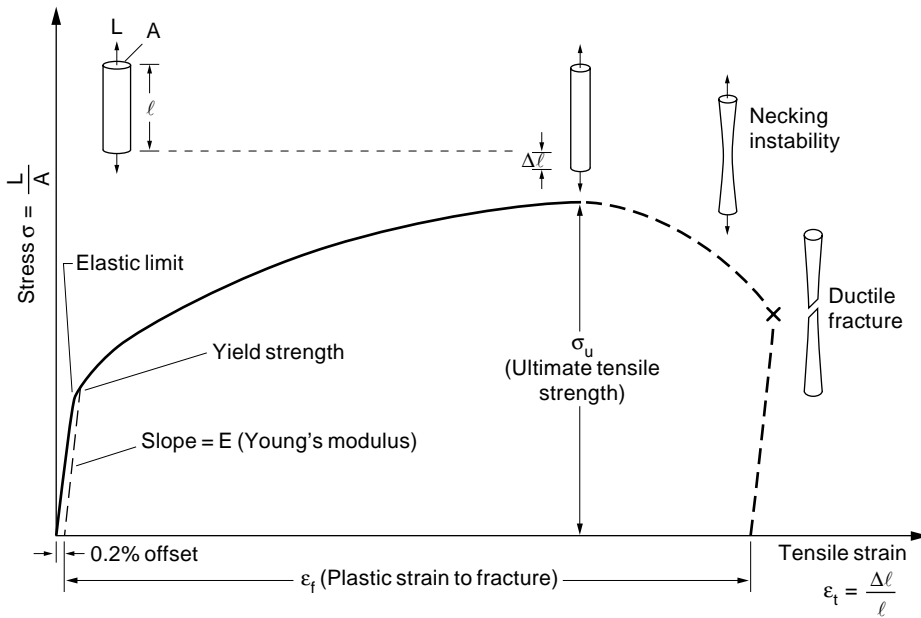


Figure 1. Tensile Stress-Strain Curve for a Typical Ductile Metal

The tensile test is the most common test used to measure mechanical properties. Round-bar or sheet samples are gripped at their ends and pulled at constant velocity (nominally, at constant strain rate) until they fail. Load and displacement of the sample are measured and plotted as stress σ (load/cross-sectional area) vs strain ϵ (sample elongation/original length). The elastic region, represented by Hooke's law ($\sigma = E\epsilon$, where E is the elastic modulus known as Young's modulus), is linear and reversible. The point of deviation from linearity is called the elastic limit and marks the onset of permanent deformation, or plastic flow. Because the onset of deviation is often very gradual, the "yield strength" of a metal is defined as the stress at 0.2% permanent (or plastic) strain. Continued plastic flow beyond the elastic limit produces increasing stress levels—a process called work hardening. During this stage, the sample deforms uniformly, elongating and thinning while the volume remains constant, until work hardening can no longer keep up with the continuing increase in stress caused by the reduction in the sample's cross-sectional area. At this point, the stress goes through a maximum, called the ultimate tensile strength, and the sample begins to deform nonuniformly, or neck, before it fractures in a ductile manner. In soft, annealed fcc metals, the typical total plastic (or permanent) strain immediately prior to fracture is 20% to 50%.

α -plutonium and in the plastic flow of δ -phase plutonium alloys. However, we will first introduce both macroscopic engineering and microscopic concepts as a necessary background for the plutonium discussions.

Engineering Response

Structural materials are designed and fabricated based on their response to external loads, or stresses. The design

engineer usually specifies high-strength materials that will strain, or deform, in an elastic manner under anticipated loads, meaning that the material will revert to its original dimensions when the load is released. When stressed beyond their elastic limit, many structural materials fail abruptly, absorbing little energy. Among these materials are concrete, many ceramics, and many thermosetting plastics. In contrast, most metals and thermoplastics (for example, polyethylene) are ductile, or malleable.

They deform extensively, beyond the elastic limit, as they absorb large amounts of energy. Consequently, these materials are much more tolerant of flaws, and they can be worked, or formed, into different shapes through a variety of processing techniques, such as injection molding, extrusion, rolling, and forging. The microstructural processes that allow these materials to deform plastically differ appreciably from one type of material to the next. In the thermoplastic polymer, especially during high-temperature processing, molecules flow over or move past each other much as they do in a liquid. In metals, as we will see, plastic deformation occurs by the motion of line defects known as dislocations.¹

A material's mechanical strength, or the stress it can withstand before it deforms or fractures, is typically measured by a standard uniaxial tensile test. Round or sheet samples are pulled along one axis at constant velocity while the deformation, or strain, incurred is measured. Ductile materials show limited elastic response (low yield strength) followed by extensive plastic deformation and ductile fracture, as shown schematically in Figure 1. In Figure 2(a) we show that the plutonium-gallium (Pu-Ga) δ -phase alloys follow this pattern, whereas unalloyed α -plutonium is strong and brittle like cast iron: It has an elastic response with very little plastic flow until the stresses become so high that the metal fails by brittle fracture. We note for later reference that the strength of the unalloyed α -phase decreases dramatically with increasing temperature—see Figure 2(b)—much like the strengths of many body-centered-cubic (bcc) and hexagonal-close-packed (hcp) metals. In contrast, the yield strength of the

¹Many times, ductility and malleability are confused with toughness. Strictly speaking, toughness, or fracture toughness, refers to the metal's ability to resist crack or flaw growth. Stresses are extremely high in the region just ahead of the tip of a crack, and it is thus the stress-dissipating capacity of the microstructure, or the material's toughness, that becomes important when catastrophic crack growth is a concern.

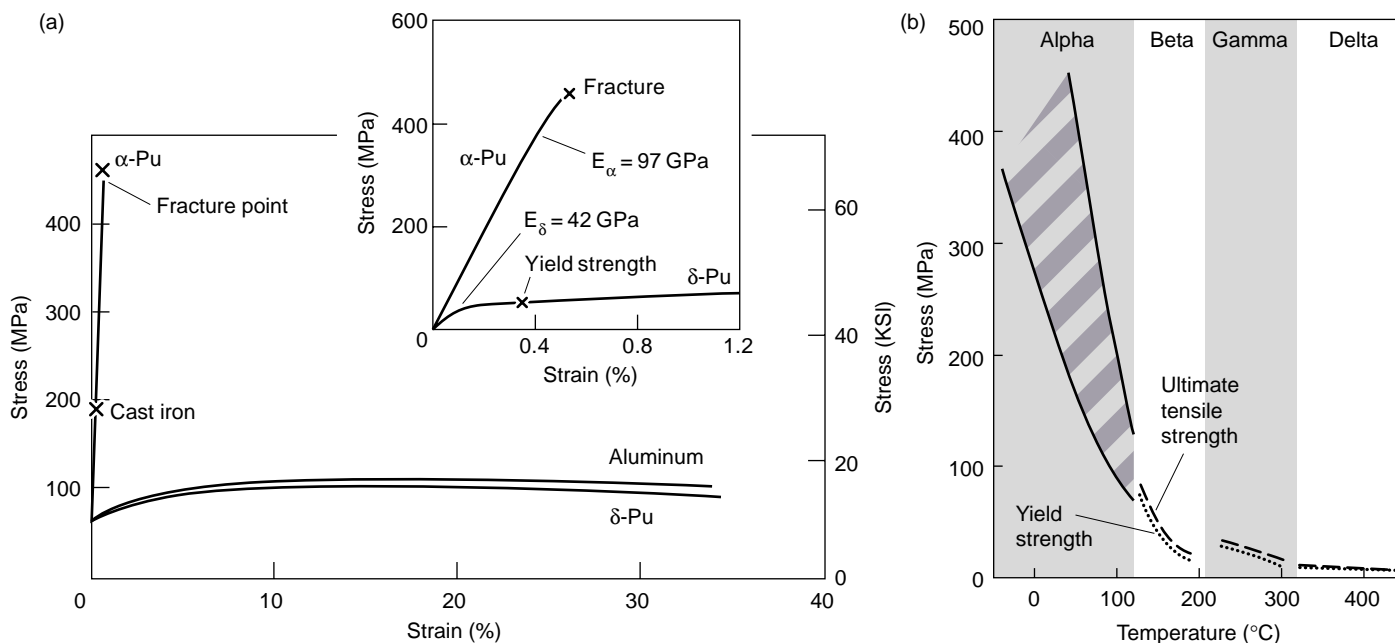


Figure 2. Tensile Stress-Strain Response for Plutonium at Ambient and Higher Temperatures

(a) Typical uniaxial stress-strain responses at room temperature for unalloyed monoclinic α -plutonium and fcc δ -phase Pu-1.7 at. % Ga alloy are compared with the response for aluminum. For α -plutonium, the elastic limit essentially coincides with the fracture strength. Very much like aluminum, the ductile Pu-1.7 at. % Ga alloy work-hardens before failing by ductile fracture. (b) The typical tensile-test results for unalloyed polycrystalline plutonium shown here are based on those reported by Gardner (1980). They indicate overall trends in the dependence of strength on temperature for the different plutonium phases. The strengths of the α - and β -phase are very sensitive to temperature, those of the γ -phase less so, and the δ -phase has little strength over its entire range of stability. The strength of the ϵ -phase is very low and time dependent because its more-open bcc structure exhibits very high diffusion rates. These data represent the work of several investigators, different purity materials, and different testing speeds. Except for α -plutonium, the upper curves designate the ultimate tensile strength and the lower the yield strength. For α -plutonium, the yield and ultimate strengths show tremendous scatter and are not easily discernable. Hence, we simply show a band of strength values. (Reproduced with permission from H. R. Gardner and the American Nuclear Society, *Plutonium Handbook*, page 68, 1980.)

unalloyed δ -phase behaves like most other fcc metals, showing little temperature dependence.

The electronic structure and the resulting cohesive forces holding the metal together are directly responsible for the metal's elastic response. Generally, metallic bonding produces high cohesive forces and high elastic constants (stiffness). Metallic bonding is not very directional because the bonding (or valence) electrons are shared throughout the crystal lattice (see the article "Plutonium and its Alloys" on page 290). Consequently, metal atoms tend to surround themselves with as many neighbors as possible, forming close-packed, relatively simple crystal structures. In plutonium, however,

the narrow conduction bands and high density-of-states of the 5f electrons make it energetically favorable for the ground-state crystal structure to distort to a low-symmetry monoclinic lattice at room temperature. Plutonium adopts the more typical symmetric structures only if the temperature is raised or if the metal is suitably alloyed.

The variation of elastic moduli with direction in a crystal lattice provides important information about the cohesive electrostatic forces—the balance between attractive forces that act at long range vs the repulsive forces that dominate at short range. The directionality of the elastic moduli is partially averaged out in polycrystalline samples if the polycrystalline aggregates are sufficiently

random. For that reason, measurements of elastic moduli must be done on high-quality single crystals. Unfortunately, the multiple phase transformations in plutonium make crystal growth immensely difficult, and only very few studies have been conducted on single crystals of either α -plutonium or δ -phase plutonium alloys (see the article "Preparing Single Crystals of Gallium-Stabilized Plutonium" on page 226).

Although a few single crystals of α -plutonium were grown in the 1960s (Liptai and Friddle 1970), elastic constants have not been studied systematically. Limited elastic-modulus measurements performed as part of Liptai and Friddle's deformation studies, which will be reported next,

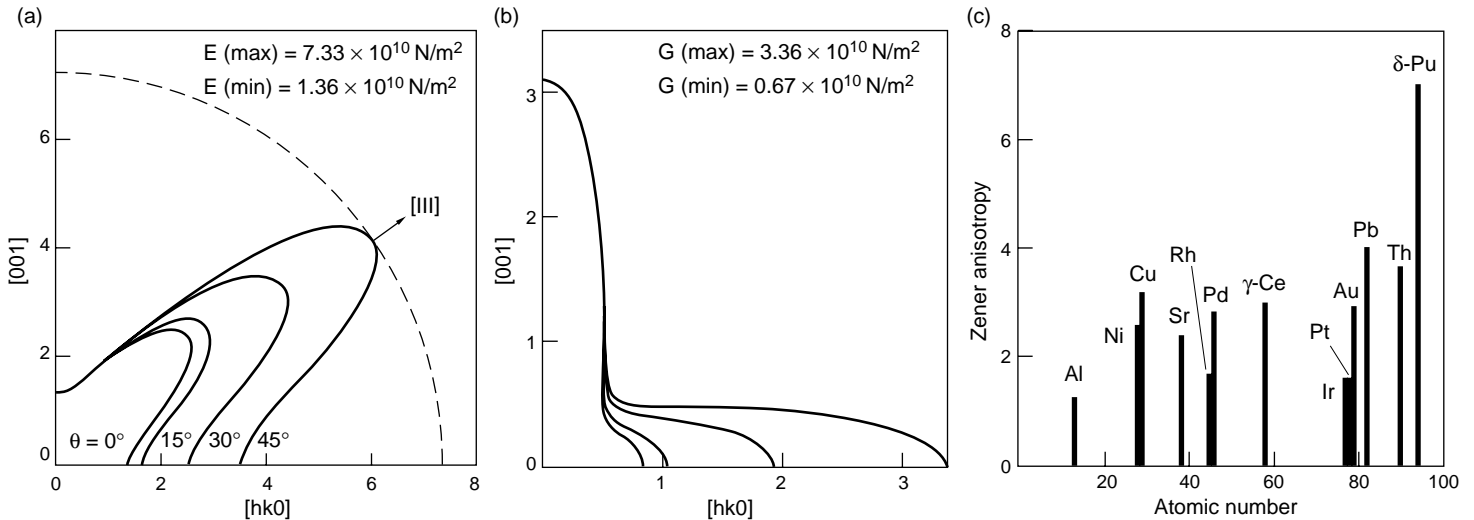


Figure 3. Single-Crystal Results for Elastic Moduli of δ -Plutonium

The ultrasonic velocity measurements reported by Moment and Ledbetter (1976) on δ -phase Pu-3.4 at. % Ga single crystals show surprising anisotropy—the crystals are very stiff in tension and compression and soft in shear in the [111] direction and vice versa in the [100] direction. In this case, the Zener anisotropy, $A = 2C_{44}/(C_{11} - C_{12})$, is very large when compared with that of other fcc metals, but it is about equal to that of the alkali metals (sodium, potassium, and lithium). A polar plot of Young's modulus with crystal direction is shown in (a). Each curve lies in a plane containing [001] at an angle θ from [100]. The polar plot shown in (b) is of the shear modulus with crystal direction. Plot (c) shows the Zener anisotropy for fcc metals.

showed variations of greater than a factor of 2 in the elastic modulus with crystal orientation. Young's modulus (the average elastic constant for uniaxial tension) for polycrystalline α -plutonium is almost twice that of the δ -phase alloy (see Figure 2). However, even polycrystalline α -plutonium is not considered very stiff; its Young's modulus is approximately equal to that of titanium, but only half of that of steels. Even by comparison with other fcc metals, δ -phase plutonium alloys are very soft. For example, Young's modulus of δ -phase plutonium alloys is 40 percent lower than that of pure aluminum. Elastic-constant measurements on textured polycrystalline materials could also provide us with some indication of the directionality of single-crystal properties. Unfortunately, no such studies have been reported for textured polycrystalline α -plutonium.

The elastic constants of single-crystal δ -phase plutonium alloys show surprising anisotropy. Only one set of such measurements has been made at

room temperature (Moment and Ledbetter 1976) on a small single crystal of Pu-3.4 at. % Ga alloy. As shown in Figure 3, the elastic moduli in the "soft" and "stiff" directions differ by more than a factor of 5—the largest variation for any fcc metal. Fortunately, much of this anisotropy of elastic moduli is averaged out in δ -phase plutonium polycrystals.

Unlike elastic constants, which vary directly with the strength of the cohesive forces between the atoms, the mechanical strength and plastic properties of metals depend on cohesive forces in a subtle manner. Metals yield, or flow plastically, at stress levels as low as 0.01 percent of the theoretical stresses required to pull the atoms apart or cause entire rows of atoms to slip over each other. This enormous reduction in strength compared to the theoretically predicted value results from the influence of defects, principally dislocations. On the other hand, the interactions of dislocations with each other and with other

microstructural defects increase the strength of ductile metals considerably by a process called work hardening. In brittle materials, plastic flow (that is, the ability of dislocations to move) is severely limited. Therefore, the strength of those materials is reduced dramatically by the presence of microscopic cracks or other flaws. Before discussing some of the anomalous plastic-flow properties of plutonium, we provide a brief description of dislocations and twinning as background for understanding plastic flow and work hardening in plutonium.

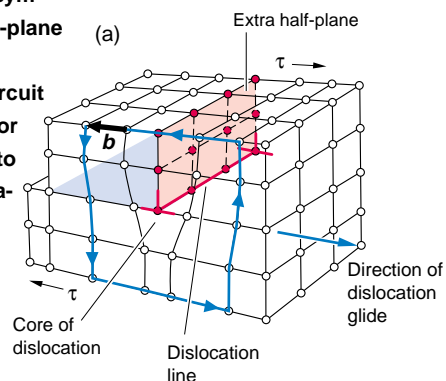
Dislocations and Twinning

More than 20 years before dislocations were actually observed in a transmission electron microscope, their existence was postulated to explain why the observed yield strengths of metals are so much lower than their theoretical values. A dislocation is a line defect formed by the presence of an extra half

Figure 4. Dislocations and Their Role in Facilitating Slip

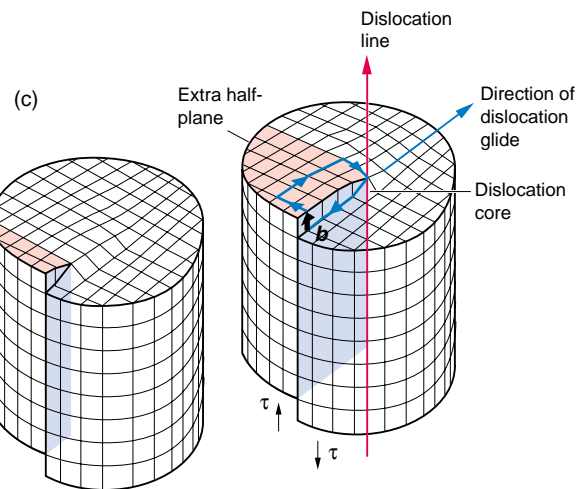
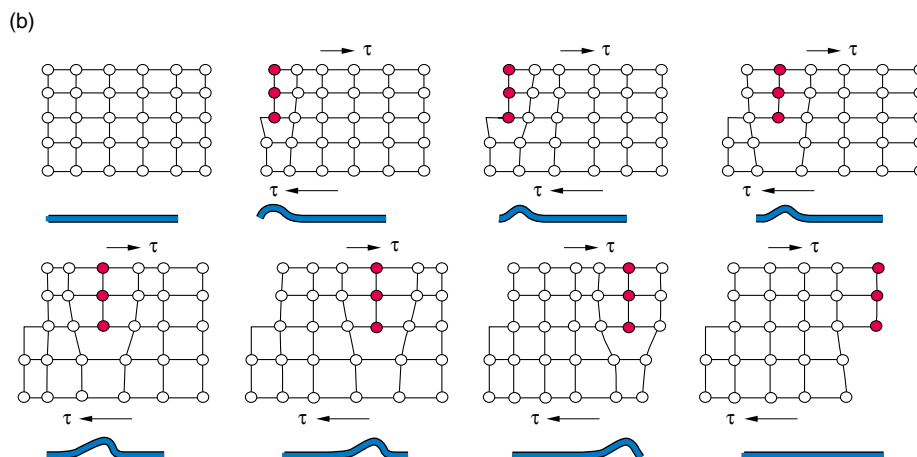
A dislocation is a crystalline line defect that enables one crystal plane to slide over another at much-smaller applied shear stresses than would be required in a perfect crystal. There are two basic orientations, edge and screw. Most dislocations are actually curved or wavy, with mixed character (varying from pure edge to pure screw orientation).

(a) An edge dislocation can be simply imagined as an extra half plane of atoms (shaded red) inserted into a crystal. The dislocation line created by the edge of this extra half plane is symbolized with a perpendicular sign, \perp , shown in red. When the sign points up, the extra half-plane is up and vice versa. The distortion in the periodic lattice caused by the dislocation is represented by the Burgers vector b , which is defined by lack of closure of the Burgers circuit drawn around the dislocation. The dislocation is completely described by its Burgers vector b and the orientation of the dislocation line. Because the Burgers vector is perpendicular to the dislocation line, a given edge dislocation can move only on one slip plane. The dislocation line also marks the boundary between the deformed region of the slip plane (shaded in blue) and the undeformed region.



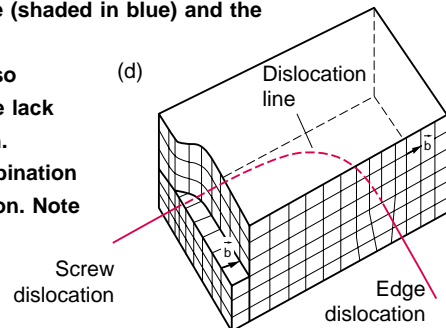
(b) This series of cross-sectional views of the edge dislocation shows how it moves one atomic distance at a time through an entire crystal and thereby produces a step of one Burgers vector on the crystal surface.

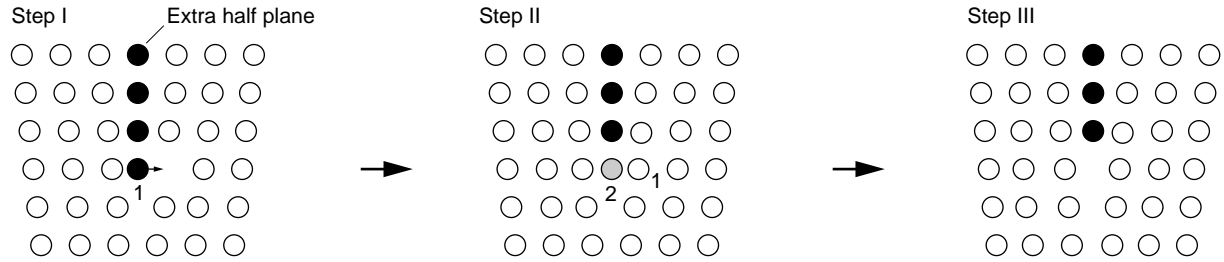
As illustrated at the bottom of each view, the edge dislocation acts like a wrinkle in a rug, reducing the interatomic forces in its vicinity and allowing an entire plane of atoms to slip over another at a reduced stress. Continued application of shear stress (τ) will move these dislocations by repeated steps along the slip planes of the crystal, a process called dislocation glide. The dislocation slip planes and slip directions are the same as those for shear of entire atomic planes in perfect crystals.



(c) A screw dislocation can be imagined as a tear that propagates through the crystal, creating an extra half plane (shaded in red) perpendicular to the dislocation line (red). The resulting distortion resembles the levels of a spiral staircase, or the thread on a screw. The screw dislocation itself is the pole about which the spiral ramp circles. In a screw dislocation, the Burgers vector b is parallel to the dislocation line. Hence, any plane that contains a screw dislocation can act as its slip plane. Again, the dislocation line marks the boundary between the deformed region of the slip plane (shaded in blue) and the undeformed region. The Burgers circuit for a screw dislocation also defines the Burgers vector as the lack of closure around the dislocation.

(d) A mixed dislocation is a combination of a screw and an edge orientation. Note that the dislocation line for a mixed dislocation is curved.





(b) Twinning

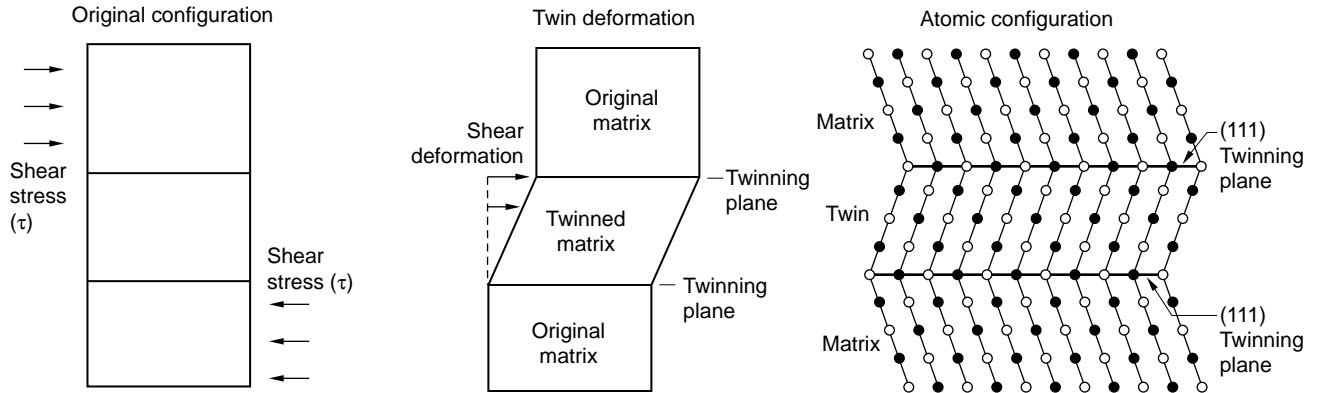


Figure 5. Climb and Twinning

(a) The positive climb of an edge dislocation is illustrated here. The extra half plane is perpendicular to the plane of the diagram and is indicated by filled circles. For the dislocation to climb, a vacancy has moved up (Step I) to a position just to the right of atom 1, one of the atoms forming the edge of the extra plane. If atom 1 jumps into the vacancy (Step II), the edge of the dislocation loses one atom, and atom 2 (shaded circle) becomes the next atom of the edge (lying just below the plane of the paper). If all other atoms that formed the original edge of the extra planes move off through interaction with vacancies, the edge dislocation will climb one atomic distance in a direction perpendicular to the slip plane (Step III). (b) At left, the shear stress applied to the original configuration produces a twin deformation. The atomic arrangement at the twinning planes in an fcc crystal is shown at right. The solid and open circles represent atoms above and below the plane of the paper, respectively. The interface between the original matrix and its mirror image is exactly parallel to the twinning plane. In this case, the twin and parent lattices match perfectly at the interface (called a coherent twin boundary).

plane of atoms in a crystal. The two basic types of dislocations, edge and screw, are defined in Figure 4. The figure also shows schematically how dislocations move, or glide, along slip planes in response to applied shear stresses (τ). Each step of the motion requires only a slight rearrangement of the atoms in the vicinity of the extra half plane, thereby reducing the enormous shear stresses that would otherwise be required to move one entire plane of atoms over another. The movement of a dislocation through a crystal produces conservative displacement of the crystal in much the same way that a rug can be incrementally

moved across a floor when one pushes a wrinkle, or “ruck,” in the rug across its length. Moreover, as it moves along the slip plane, the dislocation defines a moving boundary between plastically deformed and undeformed material on that slip plane.

Dislocation Glide. Slip, also called dislocation glide, can occur in metals because the metallic bond is not very directional, and atoms can slide past one another relatively easily for long distances without breaking bonds. In high-symmetry metallic crystals, dislocations can adopt a configuration in which cohesive forces offer very little

resistance to their glide motion along the close-packed planes, allowing most metals to undergo large plastic deformations before fracture. However, many hundreds of thousands of dislocations must move across a slip plane to produce a visible slip line on the surface. Passage of a dislocation leaves the crystal in the same atomic configuration in which it was before. Hence, the lattice is unchanged, and volume is conserved. In other words, plastic deformation—whether caused in tension, compression, in a rolling mill to make thin sheet, or in a forging to make a complex shape—produces the desired change of shape without a change in volume.

Dislocations tend to form at sites of imperfection either during solidification and subsequent cooling or during plastic deformation. The density of dislocations equals the number of dislocations passing through a unit area. Unlike lattice vacancies, dislocations do not lower the Gibbs free energy of a crystal, but they are unavoidable because tiny stresses cause them to form. Even with the greatest care, it is virtually impossible to solidify or anneal a typical material with a dislocation density below 10^4 dislocations per centimeter squared (dislocations/cm²).

Dislocations are also a natural consequence of metallic-crystal growth from the liquid, or supersaturated vapor, because the transfer of atoms to the growing crystal occurs more readily along a step or ledge, than on a perfect surface. Typical annealed metals and alloys contain 10^7 dislocations/cm². Heavily deformed (cold-worked) metals and alloys contain on the order of 10^{11} dislocations/cm² because dislocations are created during cold working. Paradoxically, metals can be made to approach their theoretical strength by either of two opposite methods: removing virtually all dislocations, as in the growth of very fine metal whiskers, or generating excessively large numbers of dislocations that will impede each other's motion to increase strength.

Dislocation Climb. During dislocation glide at low temperatures, edge dislocations are confined to their slip plane, whereas screw dislocations may “cross-slip” from one slip plane to another. At temperatures on the order of half the melting temperature of a material, edge dislocations begin to move by a mechanism known as dislocation climb. In this process, the inherent stress field surrounding the edge dislocation line induces vacancies to migrate sequentially to positions along that line. Each time a vacancy attaches to the edge dislocation, that small segment has climbed one atom spacing out of its previous glide plane—see Figure 5(a). As the process continues through many

repetitions, the affected dislocations move appreciable distances and cause the bulk material to exhibit macroscopic “creep,” that is, elongation and thinning on a macroscopic scale. Climb is fundamentally different from glide in several ways: Climb is sensitive to normal stress (tensile or compressive for positive and negative climb, respectively), whereas glide results from a shear stress. Also, climb requires enough energy to create or annihilate vacancies (for negative and positive climb, respectively). Climb thus requires temperatures at which vacancies migrate easily—typically above half of the absolute melting point.

Twinning. Metals sometimes respond to shear by a process called mechanical (or deformation) twinning. In this organized transformation, shear stresses cause a portion of a crystal to become the mirror image of its original crystal structure. The plane of symmetry between the two portions of a twinned crystal is called the twinning plane—see Figure 5(b). In the simple lattice shown, a homogeneous shear has caused each atom in the twinned region to move a distance proportional to its distance from the twinning plane. The atoms move less than one atomic spacing and produce an orientation difference across the twinning plane. In contrast, dislocation glide produces no orientation difference across a slip plane, and it occurs in discrete multiples of atomic spacing. Twinning can, however, be considered a variant of dislocation glide, involving the motion of partial, rather than complete, dislocations. Nucleation, not propagation, appears to be the typical rate-limiting step for twinning.

The lattice strains required for twinning are very small, making the total deformation achieved quite small. However, if the orientation of the crystal is changed, twinning may enable new slip systems to activate new slip modes. This process is therefore especially important in metals with a limited number of slip systems, such as the hcp metals.

Deformation twinning is not prevalent in fcc crystals, occurring only in some fcc metals and alloys at very low temperature. It does, however, occur more readily in bcc and hcp metals, especially at low temperatures or under shock-loading conditions. Twins can also form during annealing, especially in fcc metals after they have been deformed.

We have provided only a brief introduction to dislocation basics. For a comprehensive treatment of dislocations in materials, refer to Hirth and Lothe (1982). We now return to the discussion of plutonium's mechanical behavior.

Anomalous Plastic Flow in α -Plutonium

Manifestations of Low Crystal Symmetry in Single-Crystal Experiments

Figure 6(a-c) shows the monoclinic structure of α -plutonium in three views that emphasize its similarity to a distorted hexagonal lattice. Metallurgists have very little experience with monoclinic structures—these are typically in the domain of geologists. In geologic minerals, one finds that plastic deformation by dislocation glide occurs on a single plane of the {001} family. Similarly, metal crystals of lower symmetry slip relatively easily on a single slip plane. For example, hcp metals that are perfectly packed (that is, the ratio of lattice constants $c/a = 1.633$) slip on the basal, or close-packed plane in the three close-packed directions (refer to the box “Atomic Packing and Slip Systems in Metals” on page 308 in the article “Plutonium and Its Alloys”). Crystals of hcp magnesium, zinc, and cadmium with $c/a > 1.633$ are also observed to slip easily on the basal planes. On the other hand, hcp titanium, zirconium, and hafnium with $c/a < 1.633$ slip more easily on the family of prism planes.

Carefully controlled experiments on single crystals deformed at different orientations are required to sort out the

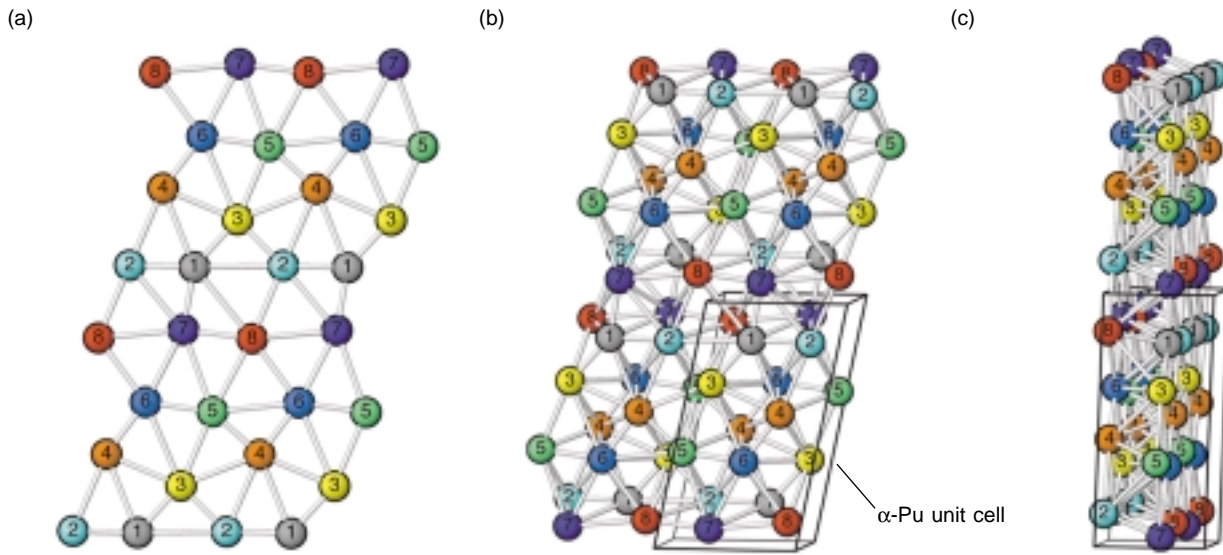
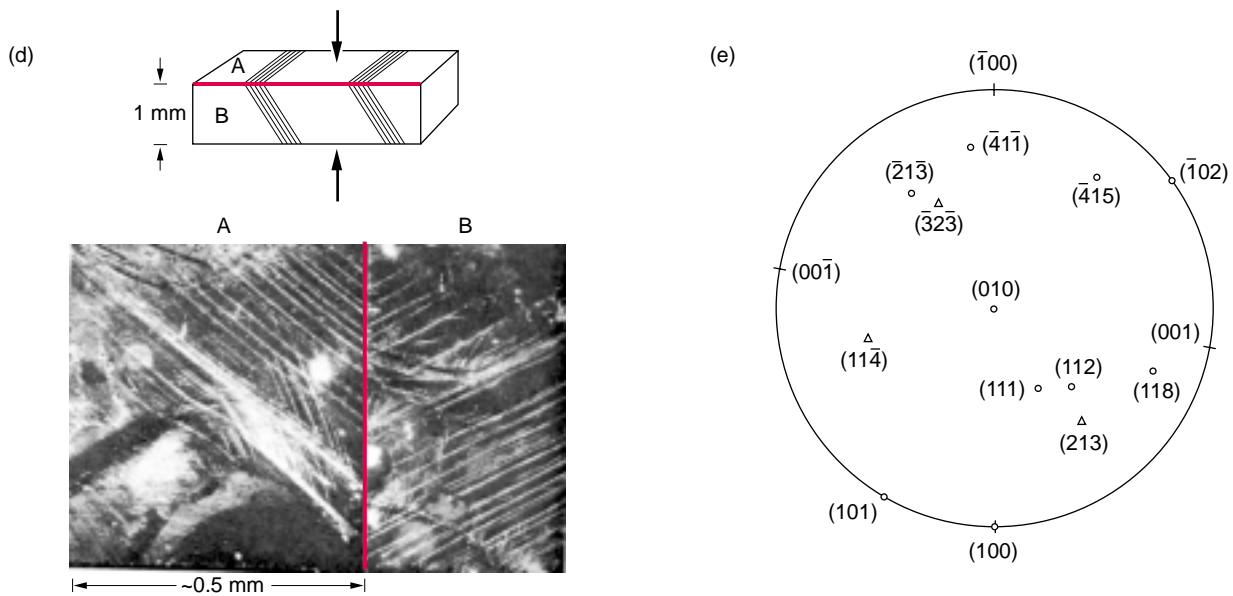


Figure 6. Slip Systems in α -Plutonium Single Crystals

(a) The (020) plane of the α -plutonium monoclinic crystal resembles an hcp plane. (b) Two stacked (020) planes of the crystal contain four unit cells. Although the bonds fall into two groups (long bonds between ~ 3.19 and 3.71 and short bonds between ~ 2.57 and 2.78), each of the eight numbered sites is crystallographically unique. Lawson et al. (1996) refer to α -plutonium, which has 16 atoms per unit cell with eight distinct lattice positions, as a self-intermetallic material. (c) Here is a 90° rotation of (b), showing that (020) plane layers in α -plutonium lie in almost flat close-packed planes, as in an hcp structure. For more details on the structure, see Figure 25 on page 331 of the article “Plutonium and Its Alloys.” (Reproduced with permission from the Metallurgical Society.)



(d) A room-temperature deformation is illustrated, which resulted from compression of a high-purity single-crystal bar of α -plutonium grown under pressure at Argonne National Laboratory (Argonne). Slip traces are seen on polished surfaces. The micrographs are placed to match traces from surface A and B (see the boundary between these surfaces). (e) Shown here is a stereographic projection of poles of planes along which slip was observed during experiments on single-crystal and polycrystal α -plutonium at Argonne (Liptai and Friddle 1970) and Los Alamos (Bronisz and Tate 1965). For this projection, a cube face is parallel to the projection plane, the x- and y-axis lie in the projection plane so that the poles of planes (100) and (001) are on the basic circle, and the z-axis is normal to the projection plane so that the pole of plane (010) is at the circle’s center.

fundamental behavior of dislocations in a material. But the difficulty of growing single crystals of α - or δ -plutonium has precluded all but the few experiments conducted on α -plutonium single crystals and polycrystals by Bronisz and Tate (1967) and Liptai and Friddle (1970). The results of those experiments, shown in Figure 6(e), were very unexpected. Because the α -plutonium structure is like a distorted hexagonal lattice, α -plutonium was expected to behave like hcp metals and low-symmetry ceramics and minerals. Specifically, it was expected to slip on a single family of slip planes, namely, the (020) planes, which are the closest-packed and the only atomically flat planes in the monoclinic α -structure—see Figure 6(a–c).

Quite surprisingly, a single crystal of α -plutonium placed at different orientations and deformed in compression at room temperature (single-crystal samples were too small to test in tension) exhibited slip on many different slip planes although, predominantly, on one plane for a given orientation. Some evidence of wavy slip traces was also found, suggesting that slip occurred on several planes in a single direction (as it does often in bcc metals).

In many metals, twinning becomes a predominant deformation mode when slip is difficult. Consequently, our assumption that slip was difficult on planes other than the (020) planes led us to expect twinning to be a predominant deformation mode in α -plutonium. Instead, twinning occurred only sporadically at room temperature, and was judged not to be an important deformation mechanism. Most α -plutonium single crystals were also found to be quite brittle (< 1 percent plastic strain) in compression, whereas a few samples stretched a respectable 13 to 16 percent. For comparison at both extremes, a properly oriented hcp magnesium single crystal can stretch out to a ribbon of four or five times its original length at room temperature and at shear stresses as low as 0.7 megapascal, whereas single crystals of hcp beryllium or

titanium exhibit only limited slip at very high resolved shear stresses (35 to 110 megapascals).

Clearly, we need more experiments on single crystals to understand slip and the fundamental behavior of dislocations in monoclinic α -plutonium. Likewise, modeling with realistic interatomic potentials would help guide critical experiments. We would like to understand, for example, if the “self-intermetallic” nature of α -plutonium described by Lawson et al. (1996), that is, the fact that the unit cell has eight distinctly different atoms of different sizes—refer to Figure 6(a–c)—influences the operation of different slip planes, as documented in Figure 6(e).

Effects of Low Crystal Symmetry in Polycrystalline Samples. The number of active slip systems and the relative lattice resistance of different slip systems are very important in determining the mechanical response of polycrystalline metals. An individual grain in a stressed polycrystal feels a strong restraining effect from the surrounding grains of different orientations because the net cohesive forces holding the grains together tend to prevent the opening up of voids or cracks. Consequently, stress concentrations build up near grain boundaries and grain triple points. Only very complex modes of deformation involving multiple slip systems within the grains can relieve those stresses. G. I. Taylor (1934) showed that no less than five independent slip systems (or other modes of shear deformation) must operate to maintain continuity in polycrystalline materials. Since the very high symmetry of fcc crystals leads to 12 equivalent slip systems (four equivalent close-packed planes and three close-packed directions in each plane), fcc materials such as δ -phase plutonium alloys easily meet those constraints and therefore exhibit extensive ductility.

Polycrystalline materials of lower symmetry do not have the requisite number of equivalent slip systems for easy dislocation glide. Instead, other

slip systems (with higher lattice resistance) or other deformation modes, such as twinning, become operative, raising the stress required for deformation and making these materials more prone to fracture. Despite having many different planes, α -plutonium is unlikely to have five slip systems operate at once at room temperature. Furthermore, the extent of slip in α -plutonium single crystals is typically very limited. Consequently, we understand why polycrystalline α -plutonium is macroscopically brittle at room temperature in tension, typically exhibiting less than 0.1 percent plastic strain to failure, as shown in Figure 1.

Although α -plutonium is relatively strong at room temperature (typical tensile strength of 350 to 500 megapascals), its limited number of slip systems means it has little resistance to brittle crack propagation under tensile loads. The lack of plastic accommodation by slip also makes α -plutonium particularly prone to forming microcracks (which are virtually impossible to avoid during solidification because of large volume changes caused by phase transformations during cooling). Strength measurements in α -plutonium show scatter of ± 30 percent—see Figure 2(b)—because of the variation in number and propagation of microcracks. In addition, large grains lead to greater stress concentrations and more microcracks, which reduce the strength, as does the presence of second-phase inclusions.

Finally, polycrystalline materials with a limited number of slip systems tend to develop strong preferred orientation (or texture) when they are plastically deformed. In contrast to the anisotropy of elastic constants, which has little effect on macroscopic mechanical properties, texture, or plastic anisotropy, can have large mechanical effects because the different slip planes in aligned grains will present strongly varying lattice resistance to dislocation glide. Plastic anisotropy is prevalent in hcp polycrystals, for example, and strong textures can be developed in

deformed polycrystalline α -plutonium as long as it is deformed with sufficient confinement (as during compression or extrusion) to avoid microcracking and fracture. Very strong textures have also been created in polycrystalline α -plutonium by the application of stress during the β to α transformation, as reviewed by Nelson (1980).

Although no detailed experiments on texture formation in polycrystalline δ -phase alloys have been conducted, preliminary information suggests that these fcc alloys behave much like most other fcc alloys and do not develop strong textures. The very large elastic anisotropy in these alloys (see Figure 3) does not play a strong role in plastic deformation—most likely because the lattice resistance for dislocation glide is very low and there are 12 equivalent slip systems in fcc crystals.

Before discussing anomalous time-dependent plastic flow in plutonium, we introduce the deformation mechanisms that are expected at different temperatures. Our discussion focuses on how the collective motion of dislocations determines those deformation mechanisms.

Basic Kinetics of Plastic Flow in Polycrystalline Materials

The strength of a solid, or the stress at which it yields and begins to flow plastically, is not fixed. Instead, it depends on strain, strain rate, and temperature. On the atomic scale, plastic flow is a kinetic process in which crystal defects, such as lattice vacancies and dislocations, move in response to shear forces. In turn, those movements produce macroscopic changes in shape. Dislocation glide and climb were already discussed. Other atomic-scale processes by which defects move through the material and cause deformation include the diffusive flow of individual atoms, diffusion and defect motion in grain boundaries producing grain-boundary sliding, mechanical twinning, and others. Which

process is dominant changes, depending on the homologous temperature, T/T_m .

In their theoretical treatment of plastic flow, Frost and Ashby (1982) refer to defects as the “carriers” of deformation, much as an electron or an ion is the carrier of charge. And just as an electric current is proportional to the density and velocity of the electrons, the deformation rate, or shear strain rate, $\dot{\gamma}$, is proportional to the density of deformation carriers (mainly dislocations) and the velocity at which those defects move through the crystalline grains.

Each atomic-scale mechanism for the motion of defects leads to a different model equation for the strain rate as a function of stress, temperature, and material structure at that time (including dislocation densities and other microstructural properties, as well as material properties). The parameters in these rate equations are determined from experiments such as tensile tests at constant strain rate, an example of which is illustrated in Figure 1. Another common test is the creep test, in which materials are subject to constant load while the sample’s change in length is measured as a function of time.

Based on these model-derived equations and measured strain rates, Frost and Ashby developed deformation-mechanism maps for metals, ceramics, and some minerals that show the regions of stress and temperature over which each deformation mechanism is dominant. (A map of pure aluminum is shown in Figure 7, and the dominant mechanisms at low and high homologous temperatures are illustrated in Figures 8 and 9, respectively.) The maps illustrate steady-state deformation behavior over a large range of stress levels and temperatures. They show calculated contours of constant strain rate produced by the appropriate superposition of all the deformation mechanisms at work at a given temperature and stress.

We do not have sufficient experimental information or theoretical understanding to construct such maps

for plutonium and its alloys. Instead, we present a brief review of the deformation mechanisms that lead to both the steady-state behavior represented on those maps and the transient behavior measured, for example, in a tensile test.

At the upper end of the applied shear-stress region in Figure 7 is the ideal, or theoretical, shear strength. Above that stress level, a perfect crystal, or one in which all the defects were pinned, would cease to be elastic and would fail catastrophically. Ideal strengths are calculated from a suitable interatomic potential. Some of the estimates using a Lennard-Jones potential place the ideal strengths of metals (at 0 kelvins) at values of 0.05 to 0.1 of the shear modulus (μ)—very high stress levels that are essentially never reached in practice.

Below that stress level and at low homologous temperatures (typically $T/T_m < 1/3$), the dominant deformation mechanism is dislocation glide. On the atomic scale, the motion of dislocations is limited by the inherent periodic resistance posed by the atomic structure of the lattice (known as the Peierls stress) and by discrete obstacles such as other dislocations, solutes or precipitates, and grain boundaries (see Figure 8). We have already discussed the limited capacity of polycrystalline α -plutonium for dislocation glide. On the other hand, in fcc aluminum and δ -phase plutonium alloys, dislocation glide is easy because 12 equivalent slip systems are operative, all with extremely low lattice resistance at all temperatures. Those systems therefore exhibit low strength and high ductility. Also, on the steady-state map for aluminum (Figure 7), the stress required for steady-state deformation through dislocation glide shows very little temperature or strain-rate dependence, again because the slip systems are numerous and have low lattice resistance.

However, during transient deformation, such as in a tensile test at room temperature, the atomic-scale behavior of these metals changes dramatically. Instead of exhibiting steady-state glide,

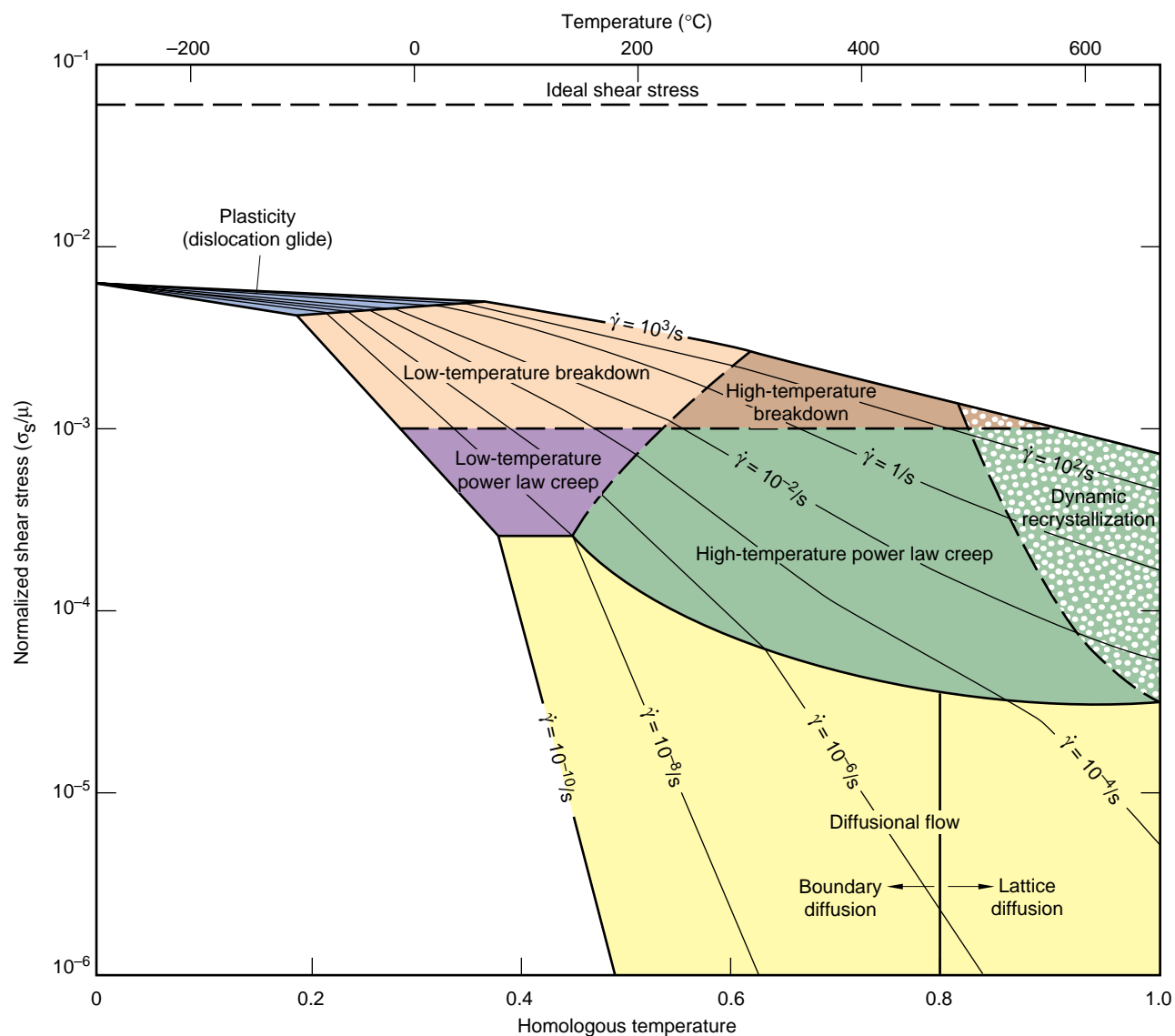


Figure 7. Map of Deformation Mechanisms for Pure Aluminum

The deformation-mechanism map for pure aluminum (10- μm grain size) was created by Frost and Ashby (1982). The different regions of flow (plasticity by dislocation glide, breakdown creep, power-law creep, and diffusional flow) correspond to the mechanisms shown in Figures 8 and 9. The region for dynamic recrystallization is indicated by the mottled area. The fine black lines represent the shear strain rate expected in these regions for a given normalized shear stress level and homologous temperature. For example, at $T/T_m = 0.4$ and a normalized stress of 3×10^{-3} , aluminum would deform in the low-temperature breakdown creep regime with a shear strain rate $\dot{\gamma}$ of 1/s. Note that there is very little rate sensitivity in the dislocation glide regime. For example, at $T/T_m = 0.2$, the normalized shear stress varies by as little as $\sim 25\%$ over 13 orders of magnitude of shear strain rate. Frost and Ashby also showed that there is only a mild dependence of dislocation glide on grain size. However, the other deformation regimes are a strong function of grain size. (This figure was adapted with permission from Michael F. Ashby.)

the dislocations multiply during slip, presenting increasing obstacles to the plastic flow and thereby increasing the flow strength, or instantaneous resistance to dislocation glide. This process, known as work hardening, can increase the yield strength of fcc metals several-

fold before the metals fail in a ductile manner (see Figure 1). Both δ -phase plutonium alloys and aluminum respond in this way during a tensile test—see Figure 2(a).

Alloying with solutes such as aluminum or gallium also introduces a

friction-like resistance to dislocation glide. These solute atoms represent weak obstacles for moving dislocations and therefore strengthen the fcc crystal only moderately. However, increased solute concentrations of aluminum or gallium do produce additional harden-

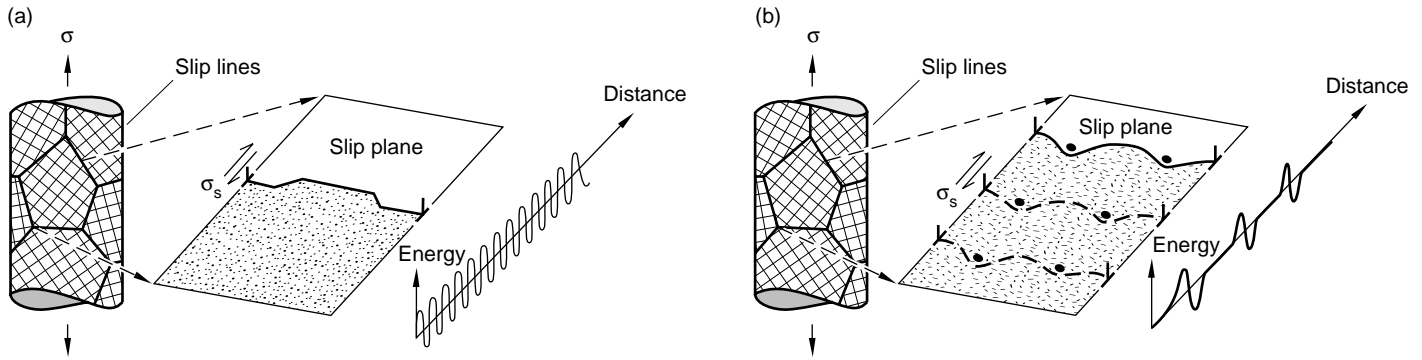


Figure 8. Plastic Flow at Low Homologous Temperatures

Plastic flow at low temperatures ($T/T_m < 0.3$) is controlled predominantly by dislocation glide in response to a shear stress (σ_s) on close-packed planes. Glide can be limited by the intrinsic lattice resistance (Peierls' stress) as shown in (a). This resistance is extremely low ($<10^{-5}$ of the shear modulus) for most fcc metals at all temperatures and quite low for bcc and hcp metals at higher temperatures. The dislocation velocity is determined by the ability of the dislocation to nucleate and

propagate kinks—the bends in the dislocation line shown in (a). This process becomes very difficult in bcc metals at temperatures less than a T/T_m of 0.15. Consequently, the yield stress of bcc metals rises sharply below these temperatures. Typically, the lattice resistance of lower-symmetry crystals varies substantially for different slip planes. (b) Plastic flow in fcc metals is controlled predominantly by the interaction of dislocations with discrete obstacles (other disla-

tions, point defects, solute atoms, grain boundaries, second-phase particles, and precipitates). For bcc and hcp metals, strengthening by discrete obstacles begins to overshadow strengthening resulting from the intrinsic lattice resistance as the temperature is increased. The slip lines shown schematically are surface offsets caused by the glide motion of hundreds of thousands of individual dislocations. (Reproduced courtesy of Michael F. Ashby.)

ing, as is observed in experiments. By introducing dispersed particles or second-phase precipitates, one can also strengthen fcc metals substantially. The amount of strengthening depends on the strength of the particle, its size, and the spacing—which will govern whether a dislocation can cut through the particle or has to bow around the particle. Generally, the stronger the particle and the finer the dispersion, the greater the strengthening. For example, large second-phase inclusions do very little to strengthen fcc metals since the dislocations do not develop an effective interference with such particles.

The low homologous temperature regime also favors deformation twinning, especially when the lattice resistance for dislocation glide becomes substantial as in bcc and hcp crystals at low temperatures. Twinning is sensitive to the sign of the shear stress whereas dislocation glide is not. Although little twinning was observed in α -plutonium at room temperature, we expect twinning to be a more-domi-

nant deformation mode below room temperature.

As the homologous temperature is increased, atomistic processes other than dislocation glide and twinning begin to dominate—in particular, the coupled glide and climb of dislocations, the diffusive motion of individual atoms, and the sliding of grain boundaries to produce relative displacements of grains (involving diffusion and defect motion in the boundaries). Figure 9 illustrates several of these mechanisms as well as the process of dynamic recrystallization.

Under conditions of explosive or shock loading (typically at strain rates $>10^6$ /second) dislocations can enter the “dislocation drag” regime, in which their velocity is limited by interaction with phonons or electrons. The drag-controlled regime is poorly understood for most metals, including plutonium and its alloys.

This very brief overview of the kinetics of plastic flow demonstrates that atomistic processes control the macroscopic shear-strain rate and that

microstructure plays a predominant role. For more complete treatments, refer to the extensive work of Frost and Ashby (1982) and Kocks et al. (1975).

Anomalous Rate-Dependent Deformation in α -Plutonium

The mechanical strength of polycrystalline unalloyed plutonium in the α - and β -phase depends strongly on temperature, as shown in Figure 2(b). Merz and Nelson (1970) showed that polycrystalline α -plutonium is also much more sensitive to strain rate close to room temperature than first expected (see Figure 10a). Their results provided the first definitive evidence that deformation mechanisms, in addition to slip by dislocation glide, come into play at the higher end of the α -phase temperature range and in the β -phase range, that is, at apparently low homologous temperatures.

Grain-boundary sliding, for example, was shown to play a prominent role in the deformation of fine-grained α - and

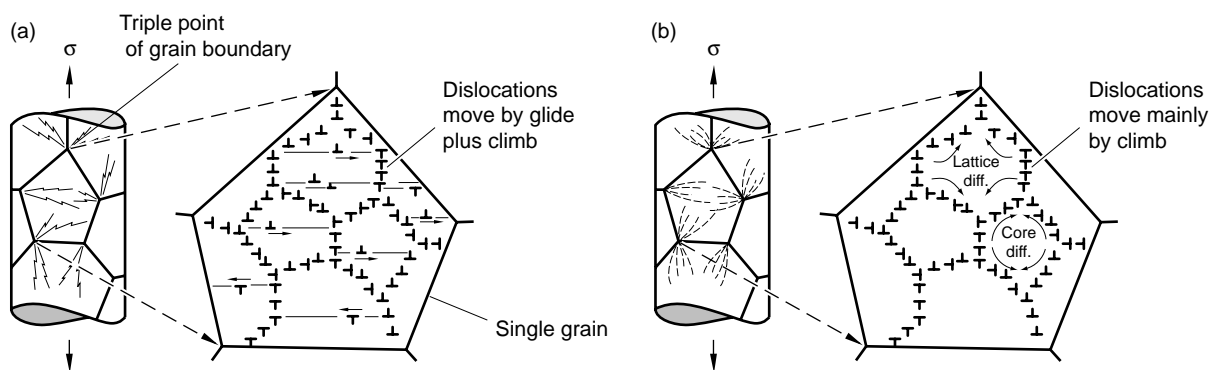
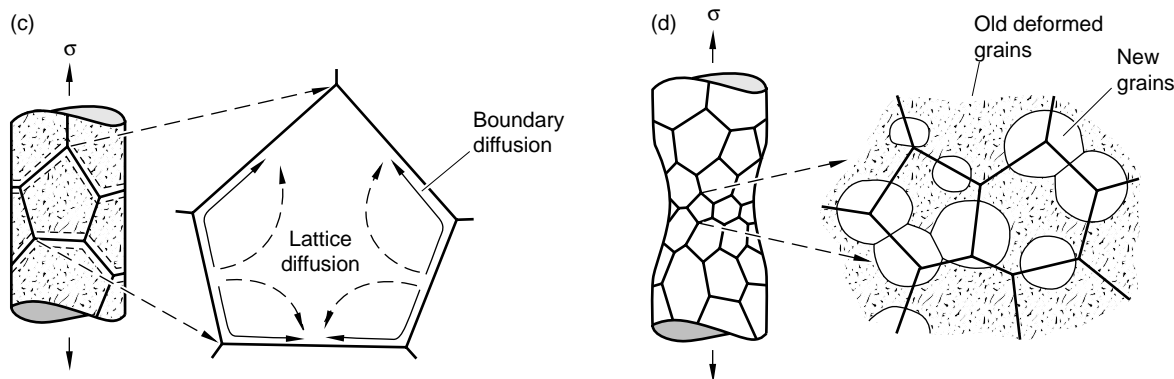


Figure 9. Plastic Flow at High Homologous Temperatures

Plastic flow at elevated temperatures ($T/T_m > 0.3$) is very much rate-dependent and is typically referred to as creep. (a) The regime in which dislocation glide plus climb dominates is prevalent at relatively high stresses—a region known as power-law breakdown. The overall strain rate is controlled primarily by dislocation glide. Cells or subgrains begin to form within the grains because the temperature is high enough that the stored energy resulting from dislocation buildup can be reduced if the dislocations organize themselves into cell or subgrain boundaries. Climb of edge

dislocations helps to organize and align the dislocations within these boundaries. The bundles of slip lines at the triple points of grain boundaries here and in (b) suggest strongly inhomogeneous deformation. (b) At lower stresses (the power-law regime), creep is controlled mainly by climb. If a gliding dislocation is held up at an obstacle, a little climb may release it, allowing it to move on to the next obstacle. Although the glide step is responsible for most of the accumulated deformation, the climb step determines the average velocity. Since climb is more

prevalent than in (a), the dislocations within the cells or subgrains are more aligned. Also, the strongly inhomogeneous deformation at the triple points is accommodated by slip and climb, so slip traces would appear more rounded. At $T/T_m > 0.6$, climb is generally controlled by lattice diffusion. At lower temperatures, experimental results show that accelerated diffusion at the dislocation core appears to be rate controlling. The arrows in the right-hand sketch of (b) indicate the directions of atom movement resulting from lattice and core diffusion.



(c) Deformation by atomic diffusional flow is illustrated. Shear stresses can induce a change in the chemical potential of atoms at the grain surfaces in polycrystals, giving rise to the diffusional flow illustrated. The chemical potentials on some grain surfaces are affected more than others, depending on grain orientation to the stress axis. The left-hand sketch is shaded to accent those areas of the grain surface that are favorably oriented to trigger diffusional transport of atoms. Such flow by diffusional transport through and around grains, coupled with sliding displacements in the plane of the

boundaries, leads to strain. The clear areas near grain boundaries are meant to denote those surfaces at which the diffused atoms accumulate. As in (b), strain rates are controlled by lattice diffusion at higher temperatures and by grain-boundary diffusion (instead of dislocation core diffusion) at lower temperatures. This deformation mechanism becomes more important for very fine grained polycrystals, whose grain-boundary surface areas are very large. (d) At $T/T_m > 0.6$, creep deformation may also be accompanied by repeated waves of recrystallization, a process called dynamic recrystallization,

which is shown here. This process occurs first by enough accumulation of lattice damage from primary creep (the mottled areas in the right-hand sketch represent stored energy resulting from dislocation interaction and multiplication). The next step is recrystallization (generation of new, relatively strain-free grains with a greatly reduced dislocation density) to relieve the buildup in strain energy during deformation. This cycle is then repeated numerous times, depending on temperature and deformation strain rate. (This figure was reproduced courtesy of Michael F. Ashby.)

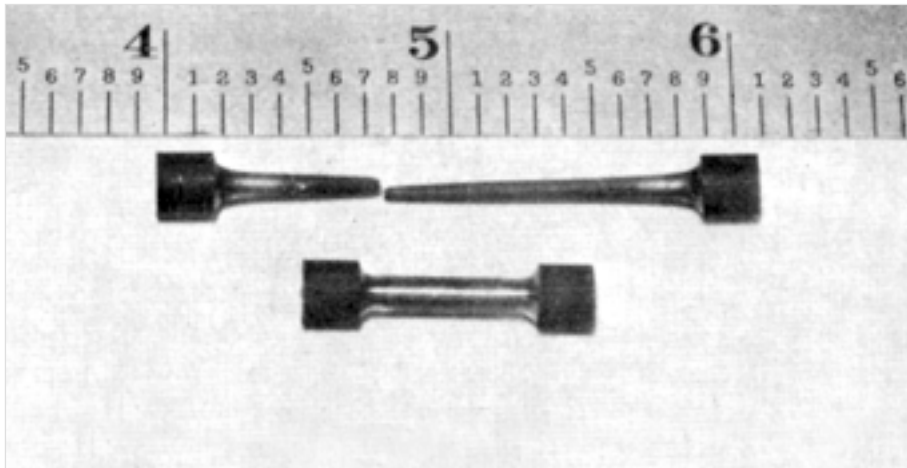
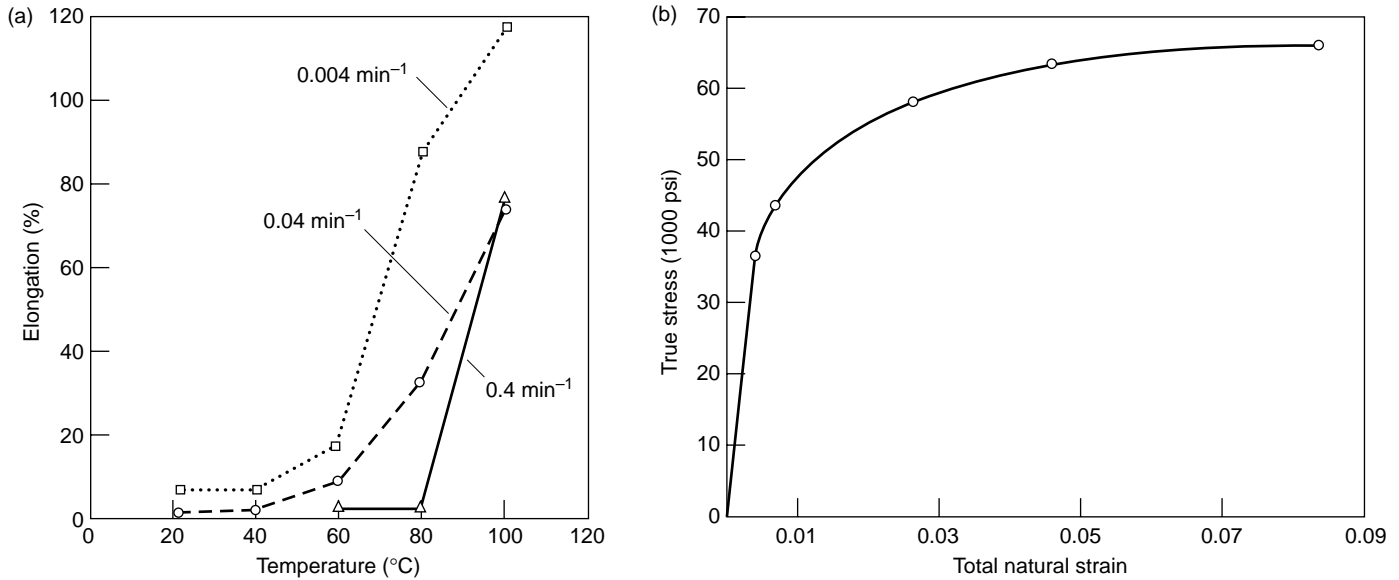


Figure 10. Tensile Test Results for Extruded Polycrystalline α -Plutonium (a) Tensile test results (Merz 1973) for extruded polycrystalline α -plutonium show how ductility (as measured by percent elongation in tension) changes with temperature and testing speed (strain rate). (b) Tensile stress-strain curve for fine-grained extruded α -plutonium tested at a strain rate of $0.7 \times 10^{-4}/s$ at room temperature shows substantial ductility. (c) A sample of the same α -plutonium was subjected (Merz 1971) to a tensile stress-strain test at 108°C , during which it was strained to 218% its original length.

β -plutonium. Such sliding involves shear at the grain boundaries, translation of grains, some dislocation glide and climb, and diffusional flow (shown schematically in Figure 8) so that grains can accomplish a shape change. In most metals and alloys, grain-boundary sliding and diffusional flow become predominant deformation modes if strain rates are low, grains are very small, and temperatures are above half the melting point. These mechanisms mostly rearrange the grains while causing very little work-hardening or change in grain shape. Such mechanisms can lead to “superplastic” behavior, that is, elongations by several hundred percent. This behavior has been observed in fine-grained (micrometer-size) lead-

thallium alloys at room temperature and aluminum alloys tested above half their melting points.

Merz (1971, 1973) prepared polycrystalline α -plutonium extruded and recrystallized to yield very fine grains of 1 to 3 micrometers in diameter compared to typical grain sizes of 20 to 50 micrometers. Pulled in tension at room temperature, these samples produced a surprising elongation of 8 percent before the material failed in a ductile manner—see Figure 10(b). At higher temperature (108°C), this material showed amazing ductility, extending over twice its original length before failing. We should note here that, once grain-boundary sliding replaces dislocation glide as the dominant mechanism

of deformation, the relationship between strength and grain size reverses. For slip by dislocation glide, smaller grains increase the strength because the grain boundaries are discrete obstacles to dislocation glide, whereas for grain boundary sliding, small grains make sliding easier (because there is more grain-boundary surface area) and lower the strength. However, at high strain rates, small grains strengthen because there is insufficient time for the diffusional processes involved in grain-boundary sliding to take place.

Merz and Nelson (1970) also showed that dynamic recrystallization—shown schematically in Figure 9(d)—can occur in α -plutonium concurrently with grain-boundary sliding.

Recrystallization allows a deformed material to lower its energy by rearranging its defects (developed during deformation) so as to create entirely new grains. In α -plutonium, the deformation leading to dynamic recrystallization must be introduced in a very confined manner (for example, by extrusion) so as not to fracture the material in tension. Merz and Nelson extruded α -plutonium in the upper temperature region of stability and found that as little as 3 to 14 percent strain will cause dynamic recrystallization. Merz's deformation map (Figure 11) shows that both slip (dislocation glide) and grain-boundary sliding (accompanied by diffusional flow) play prominent roles in the deformation of α -plutonium. In addition, dynamic recrystallization was found to occur even at room temperature if very large deformation was applied. The map shown in Figure 11 is not based on the same rigorous framework developed by Frost and Ashby (Figure 9). Nevertheless, it is useful in helping us examine the deformation of α -plutonium.

In the β -phase, the conditions that favor grain-boundary sliding (low strain rate, high temperatures, and small grain size) have even more dramatic effects. Merz showed that, if the β -phase is formed from the α -phase (that is, by cooling first to the α -phase and then reheating into the β -field), it has a fine grain size of 5 micrometers and is superplastic, extending up to seven times its original length. In contrast, β -plutonium formed from γ -plutonium has a grain size of 50 to 500 micrometers and elongates by only 5 percent before it fails.

The experimental results we have shown demonstrate that, under the right conditions of temperature, strain rate, and microstructure, the α - and β -phase of plutonium can be remarkably ductile whereas monoclinic structures are typically brittle. In fact, one can achieve superplastic behavior. Finding these surprising rate effects and large plastic deformations in plutonium near room temperature is surprising until one real-

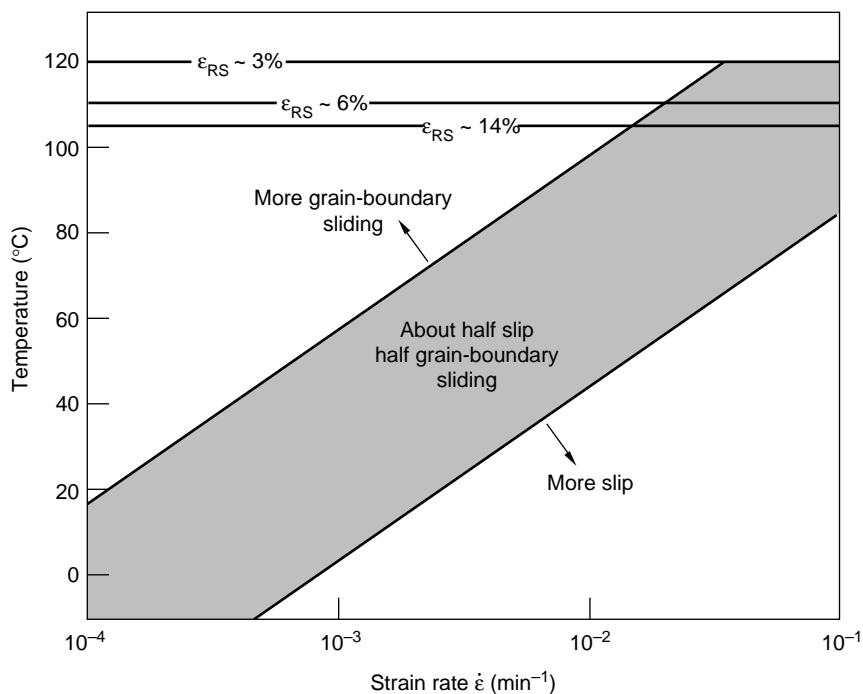


Figure 11. A Simplified Deformation Map for α -Plutonium

A simplified deformation map for α -plutonium within the α -phase temperature range and at moderate strain rates was proposed by Merz (unpublished research at Pacific Northwest Laboratory). Both slip by dislocation glide and grain-boundary sliding are prevalent. Higher temperature, lower strain rates, and smaller grain sizes favor grain-boundary sliding. The strain required for dynamic recrystallization (ϵ_{RS}) is shown for three temperatures.

izes that the value of the effective homologous temperature for α -plutonium at room temperature is actually 0.53, not 0.32 as calculated on the basis of the actual melting point of 913 kelvins (see the article "Plutonium and Its Alloys" on page 290). Therefore, the α -plutonium results are consistent with the results for other metals that show grain-boundary sliding, diffusional flow, and dynamic recrystallization to occur only above half the melting point.

Stress-Assisted or Deformation-Induced Transformation. Another fascinating aspect of mechanical behavior in plutonium and its alloys is the strong interplay between stress (or deformation) and transformation. Let's look first where we would least expect it—in α -plutonium. Under increased pressure, the α -phase maintains its well-known

room-temperature stability within a wide range of temperatures. However, we found a hint of a new instability when we examined the fracture surface of typical polycrystalline α -plutonium (50-micrometer grain size). The sample had exhibited very little plastic strain (< 0.1 percent) when fractured in tension at room temperature. The tensile fracture looked macroscopically brittle, and the sample failed in a perpendicular direction relative to the applied stress, as expected. We were astonished (so much so that we thought we had mixed up the samples) when an examination of the fracture surface by electron microscopy showed ductile dimples—Figure 12(a). Although the dimples were very shallow, thereby indicating limited plastic flow, they were unmistakably ductile.

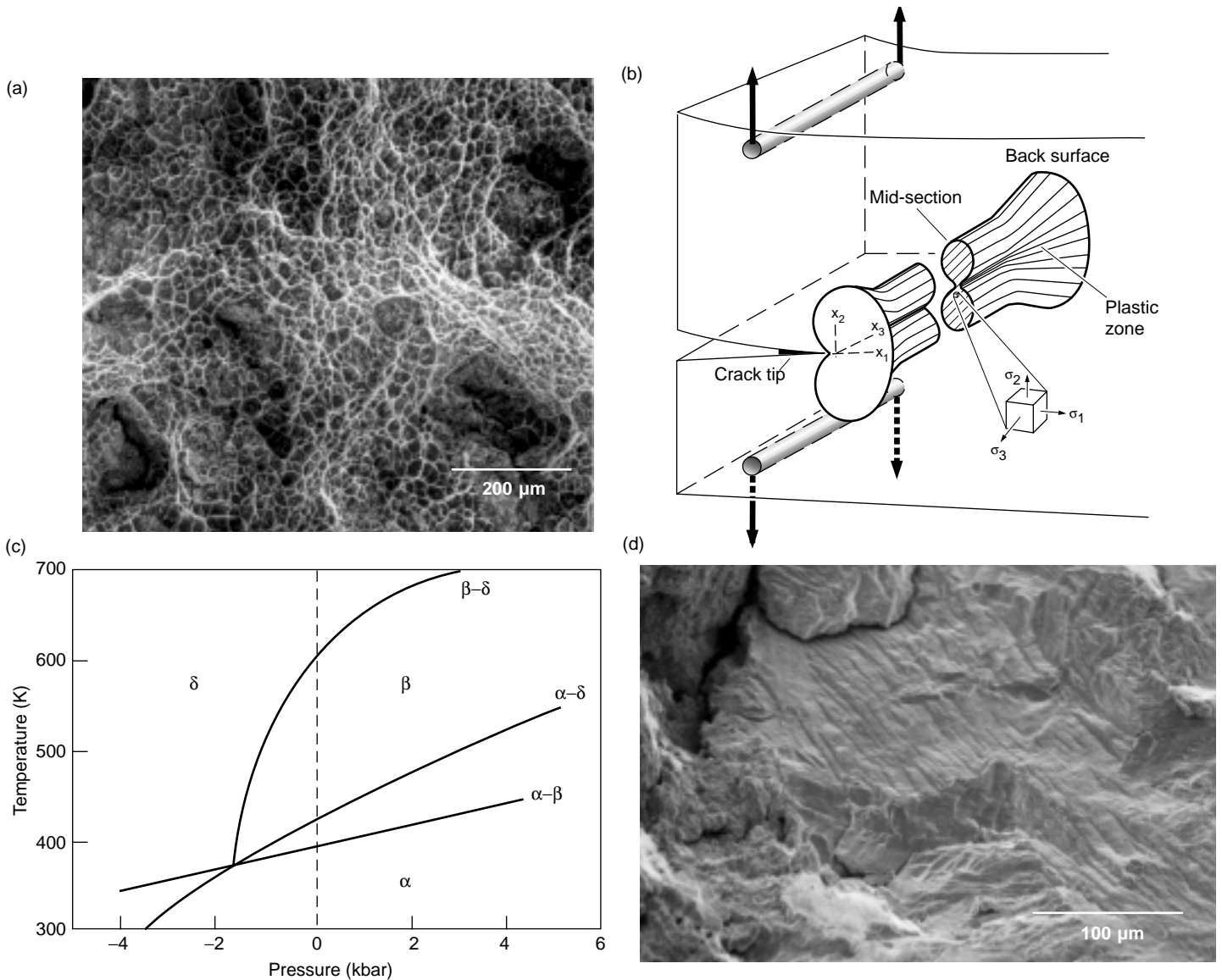


Figure 12. Evidence for α to δ Transformation during Hydrostatic Tension

(a) Typical polycrystalline α -plutonium tested in tension at room temperature fails in a macroscopically brittle manner with little energy absorption but with evidence of microscopic ductility. The “ductile-dimple” fracture surface in the micrograph looks very much like that of a peanut butter sandwich that has been pulled apart. This image was taken with a scanning electron microscope. (b) This schematic shows how the stress field at the tip of an advancing crack creates a state of triaxial tension that can reach levels as high as three times the applied uniaxial stress. (c) Robert Mulford of Los Alamos extended the metastable phase boundaries of the δ - to α -phase field to hydrostatic tension (negative pressure) and showed (unpublished work) that, at room temperature, the α -phase becomes unstable and transforms to the δ -phase at ~ -3.6 kbar (or 365 MPa). (d) The surface of a macroscopically brittle α -plutonium sample fractured in torsion (shear) shows cleavage facets indicative of microscopically brittle fracture. There is no hydrostatic tension in shear fracture, and we find a typical brittle-fracture surface with no evidence of the α to δ transformation found in (a).

The connected neptunium-plutonium-amerium phase diagram (see Figure 18 in the article “Plutonium and Its Alloys” on page 290) provides a clue for solving this puzzle. The addition of neptunium increases the stability of the α -phase, whereas americium expands the δ -phase field and makes the

α -phase unstable. Therefore, adding neptunium to plutonium mimics the application of hydrostatic pressure, and it is reasonable to assume that adding americium resembles applying “negative” pressure (hydrostatic tension). Therefore, applying hydrostatic tension may promote the transformation from

α to δ , but hydrostatic tension is difficult to achieve—except at the stress field near a crack tip, as shown in Figure 12(b). Our initial suggestion that the α -phase transforms to the δ -phase just ahead of the crack tip, as the brittle crack propagates, was found to be quite plausible in the more rigorous

analysis reported by Adler et al. (1992). Little energy is absorbed in the δ -layer as it fails by ductile fracture because the δ -layer is very shallow, resulting in a macroscopically brittle-looking fracture. Moreover, once the crack tip passes, the hydrostatic tension disappears, and the surface transforms back to α -plutonium, destroying the evidence. Indeed, examination of the fractured surface showed only α -plutonium. One indirect check of this hypothesis is to fracture α -plutonium in torsion, which produces no hydrostatic tension. The brittle cleavage features of the scanning electron micrograph of a torsion sample shown in Figure 12(c) support our hypothesis.

We also examined the likelihood of hydrostatic-tension-induced α to δ transformation by extrapolating the plutonium allotropic phase boundaries of the pressure-temperature diagram backward to negative pressure. In unpublished work, Robert Mulford of Los Alamos estimated that, at room temperature, α -plutonium would transform to the δ -phase at 3.6 kilobar (365 megapascals), as shown in Figure 12(d). The component of hydrostatic tensile stress at a crack tip can reach three times the applied tensile stress. Because the applied stress is limited by the tensile strength of the material (350 to 500 megapascals for α -plutonium), it is quite likely that the hydrostatic-tension component at the crack tip exceeds the projected 365 megapascals required to transform α - to δ -plutonium. Interestingly, the band structure calculations of Wills and Eriksson (see the article "Actinide Ground-State Properties" on page 128) predict that, in the absence of applied stress, the free surface of α -plutonium also transforms to δ -plutonium over a very thin surface layer.

We have also seen deformation-induced transformation of α to δ in as-cast plutonium-aluminum (Pu-Al) and Pu-Ga δ -phase alloys that contained significant amounts of retained α -phase because of their cored (segregated) microstructures. When the composite of

α - and δ -phase was fractured in tension, regions of the α -phase transformed, creating thin spikes of δ -phase (shown in Figure 13). The transformation and the accompanying plastic deformation blunted the crack tip and provided additional fracture resistance. Taken together, these results provide undisputable evidence that, given sufficient hydrostatic tension, the α -phase will transform to the δ -phase and greatly influence the resulting mechanical behavior.

Conversely, it is well known that δ -plutonium alloys collapse easily to an α -phase under hydrostatic pressure via a martensitic phase transformation (refer to the article "Plutonium and Its Alloys"). In most materials, shear stresses and plastic deformation, as opposed to hydrostatic pressure, are most effective in promoting martensitic transformations, but the δ to α transformation in plutonium alloys is governed primarily by the hydrostatic-stress component. For example, when Pu-2 at. % Al is deformed at room temperature in uniaxial compression, it does not transform to α even at strains as large as 0.7. The strength of the δ -phase, or the maximum hydrostatic pressure (1/3 of the uniaxial compressive stress), at these large strains is only ~50 megapascals, whereas the hydrostatic pressure required to transform this alloy at room temperature is closer to 250 megapascals. Robbins and coworkers at Lawrence Livermore National Laboratory and we, at Los Alamos, have also deformed Pu-Ga alloys to very large strains (on the order of 10—that is, by 1000 percent) in torsion (pure shear and no compressive component) without finding any deformation-induced transformation from δ to α . On the other hand, during cold-rolling plutonium billets into thin sheet, it is possible to partially transform the δ - to the α -phase because a significant hydrostatic-pressure component exists during rolling and the strength of the δ -phase is elevated significantly by work hardening. The δ to α transformation is facilitated by lowering the temperature or by lowering

the solute concentration of alloys. For example, δ -phase Pu-3.4 at. % Ga alloys will not transform to α in uniaxial compression at room temperature, but will do so readily at 77 kelvins.

It appears that hydrostatic pressure is the most effective agent of a stress-assisted martensitic transformation from δ to α , and plastic deformation has, at most, a minimal role in providing more favorable nucleation sites for that transformation. Hence, instead of shear stress or deformation dominating the transformation behavior, as it does in most ferrous alloys, hydrostatic stress dominates in plutonium. If the hydrostatic stress is tensile, the α to δ transformation is favored; if it is compressive, the reverse is favored.

To conclude, we comment just briefly on the strengthening of weak δ -phase plutonium alloys. In this case, the stress-induced δ to α transformation provides an even more effective strengthening mechanism than work hardening because it distributes a network of hard α -phase platelets throughout the parent δ -phase. Also, alloying additions—such as aluminum, gallium, silicon, scandium, cerium, and americium—strengthen the δ -phase moderately. Other elements that do not dissolve in the δ -phase are quite ineffective. Elements such as carbon, oxygen, nitrogen, and hydrogen form relatively large (micrometer-size) inclusions that do not interfere with dislocation glide. Likewise, the eutectic-forming elements—iron, nickel, and manganese—form very large inclusions (often tens of micrometers in size) and also tend to be ineffective strengtheners. Carbide, oxide, and nitride inclusions are very brittle and will act as nucleation sites for fracture. Low-melting eutectic inclusions—for example, of the plutonium-iron compound Pu₆Fe—bond poorly with the δ -phase and will therefore also nucleate fracture. Fortunately, δ -phase alloys are sufficiently ductile that a moderate concentration of such impurities does not seriously limit their fracture resistance.

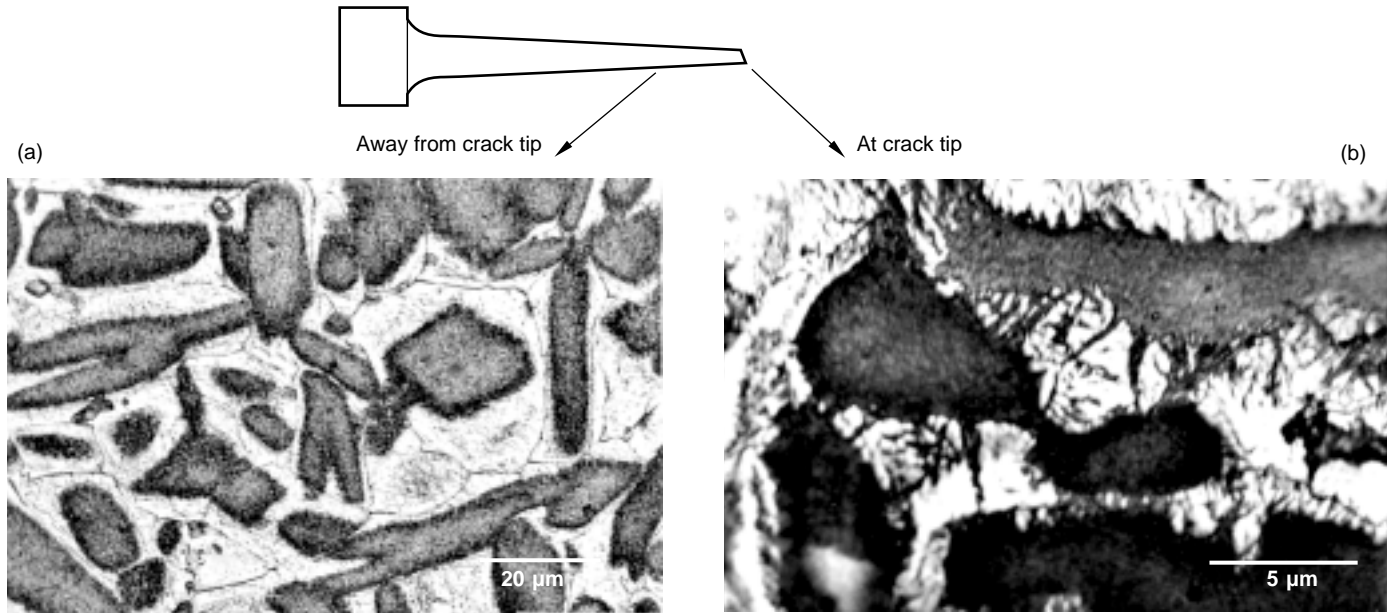


Figure 13. Further Evidence for α to δ Transformation during Hydrostatic Tension

(a) The metallographic cross-section of an as-cast Pu-Ga alloy consists of two phases because of gallium segregation during cooling: a continuous α -phase that etches light (the thin, dark lines inside the light areas are remnants of high-temperature ϵ -grains) and islands of δ -phase that etch dark. This structure represents the starting material and is representative of the tested sample away from the tensile-fracture area. (b) The cross section very near the fracture shows dark bands extending through the light α -phase regions. These bands are δ -spikes transformed from α near the crack tip. The areas of the sample more than a few millimeters from the fracture showed no transformation product.

Concluding Remarks

The fascinating examples discussed in this article are intended to demonstrate the richness and complexity of mechanical behavior in plutonium and its alloys and to whet the appetites of future researchers. The Frost-Ashby map introduced in Figure 7 provides an excellent tool for identifying the crucial ingredients necessary for a fundamental understanding of the mechanical behavior of α -plutonium and δ -phase plutonium alloys. We know very little about the fundamental properties of dislocations in the monoclinic crystal structure. For example, does the unusual electronic structure of α -plutonium, which manifests itself in eight distinct atomic positions in the lattice, affect the nature of the lattice resistance or other characteristics of dislocations? Does the yield strength at absolute zero temperature approach an appreciable fraction of the

theoretical shear strength because of increased lattice resistance at low temperatures? Does twinning play a dominant role in the deformation of polycrystalline α -plutonium at low temperatures or high strain rates? What is the role of crystallographic texture in the deformation of α -plutonium, and why is it so easy to induce significant texture through the β to α transformation?

A detailed construction of a deformation-mechanisms map would help to quantitatively determine the interplay between dislocation glide and grain-boundary sliding found by Merz and Nelson (1970). And a better understanding of the stress-induced α to δ transformation in α -plutonium or in $\alpha + \delta$ alloys would determine if such transformations absorb sufficient energy to greatly improve fracture resistance. We should emphasize that single crystals are very important for most of these fundamental studies, including determining elastic constants over a

wide range of temperatures (see the article “Elasticity, Entropy, and Phase Stability of Plutonium” on page 208).

For δ -phase alloys, we need a quantitative description of the deformation-mechanisms map, which would determine, for example, whether the Mechanical Threshold Strength Model developed at Los Alamos by Follansbee and Kocks (1988) describes the behavior of these alloys in the dislocation-glide regime. Whereas the map for pure aluminum (Figure 7) shows that steady-state strain rates change very little with stress and temperature in this regime, we expect the stress-induced δ to α transformation in plutonium alloys at low temperature and high strain rates to cause significant strengthening under transient loading conditions. In fact, the transformation behavior will introduce new variables into the deformation-mechanisms map, namely, the sign of the applied stress and the effect of the hydrostatic-stress

component. These are typically neglected for dislocation glide because glide results from the shear stress—that is, it depends very little on the hydrostatic stress and not at all on the sign of the shear stress. These effects will also be important in the shock-loading regime, in which the applied stress produces large hydrostatic stresses. Consequently, pressure-induced transformations may dominate the mechanical response. In addition, dislocation drag, which results from the interactions of dislocations with phonons or electrons (these interactions are expected to dominate in the shock-loading regime), remains virtually unexplored for plutonium. These are areas in which the mechanical behavior of δ -phase plutonium alloys may differ greatly from that of their more stable fcc cousins.

We must also develop a much better fundamental understanding of the effects of self-irradiation damage on the mechanical behavior of α -plutonium and δ -phase plutonium alloys. At low temperatures, both materials undergo substantial lattice damage, resulting in loss of crystallinity, or amorphization (see the article “Aging of Plutonium and Its Alloys” on page 238). At ambient temperature, most lattice damage is annealed out. We do not know how the residual damage affects phase stability, diffusion, and dislocation dynamics. In addition, we know that, as little as 100 atomic parts per million (ppm) of helium in stainless steel cause dramatic embrittlement. In plutonium, roughly 40 atomic ppm of helium per year are generated internally. Although we have not observed plutonium or its alloys “crumble” even after decades of storage, we do not know if helium degrades any of the mechanical properties. In other words, we have very little understanding of the effects of aging on mechanical behavior. In all cases, better materials models with realistic interatomic potentials are required to help guide much-needed experimental work.

The fundamental work we have outlined in this article will provide a much better foundation for understand-

ing the engineering response of plutonium and its alloys and will allow us to deal with the difficult job of predicting or extending the lifetime of plutonium in weapons or in storage. ■

Acknowledgments

We acknowledge technical contributions from Angus Lawson, Ramiro Pereyra, José Archuleta, Michael Stout, George Kaschner, Carlos Tomé, Thomas Zocco, and Ray Martinez. We thank Michael Ashby and Harold Frost for allowing us to adapt their drawings for our article. The motivation provided by Mike Boring and Jim Smith is greatly appreciated.

Further Reading

- Adler, P. H., G. B. Olson, M. F. Stevens, and G. F. Gallegos. 1992. *Acta Metall. Mater.* **40**: 1073.
- Bronisz, S. E., and R. E. Tate. 1967. In *Proc. of 3rd International Conference on Plutonium 1965*. Edited by A. I. Kay and M. B. Waldron, p. 558. London: Chapman and Hall.
- Eriksson, O., L. E. Cox, B. R. Cooper, J. M. Wills, G. W. Fernando, Y. G. Hao, and A. M. Boring. 1992. *Phys. Rev. B* **46**: 13,576.
- Follansbee, P. S., and U. F. Kocks. 1988. *Acta Metall.* **36**: 81.
- Frost, H. J., and M. F. Ashby. 1982. *Deformation Mechanism Maps: The Plasticity and Creep of Metals and Ceramics*. Oxford: Pergamon Press.
- Gardner, H. R. 1980. In *The Plutonium Handbook*. Edited by O. J. Wick, p. 59. La Grange Park, IL: The American Nuclear Society.
- Hecker, S. S., and J. R. Morgan. 1975. In *Proc. of 5th International Conference on Plutonium and Other Actinides 1975*. Edited by H. Blank and R. Lindner, p. 697. New York: North Holland Publishing Co.
- Hirth, J. P. and J. Lothe. 1982. *Theory of Dislocations*. New York: John Wiley & Sons.
- Kocks, U. F., A. S. Argon, and M. F. Ashby. 1975. *Prog. Mat. Sci.* **19**: 1.
- Lawson, A. C., J. A. Goldstone, B. Cort, R. J. Martinez, F. A. Vigil, T. G. Zocco et al. 1996. *Acta Crystall.* **B52**: 32.
- Liptai, R. G., and R. J. Friddle. 1970. In *Proc. of 4th International Conference on Plutonium and other Actinides 1970*. Edited by W. N. Miner, p. 406. New York: The Metallurgical Society of AIME.
- Merz, M. D. 1971. *J. Nucl. Mater.* **41**: 348.
- Merz, M. D., and R. P. Allen. 1973. *J. Nucl. Mater.* **46**: 110.
- Merz, M. D., and R. D. Nelson. 1970. In *Proc. of 4th International Conference on Plutonium and other Actinides 1970*. Edited by W. N. Miner, p. 387. New York: The Metallurgical Society of AIME.
- Moment, R. L., and H. M. Ledbetter. 1976. *Acta Metall.* **24**: 891.
- Nelson, R. D. 1980. In *The Plutonium Handbook*. Edited by O. J. Wick, p. 101. La Grange Park, IL: The American Nuclear Society.
- Taylor, G. I. 1934. *Proc. Royal Soc.* **A145**: 362.

Mike Stevens holds a Bachelor's of Chemical Engineering degree from the University of Delaware and Master's and Ph.D. degrees in



Metallurgical Engineering and Materials Science from Carnegie-Mellon University. Mike joined the Los Alamos National Laboratory in 1984 as a staff member in the Physical Metallurgy Group, where he studied the metallurgical properties of plutonium and

other actinide metals, as well as the microstructural response of materials to high-rate deformation. His work includes studies of the phase transformations in plutonium, the mechanical and fracture properties of plutonium alloys, and detailed examinations of actinide microstructures by transmission electron microscopy.



Where Is the Gallium?

Searching the plutonium lattice with XAFS

Steven D. Conradson

The high-temperature face-centered-cubic (fcc) δ -phase of plutonium can be retained to room temperature by the addition of a few atomic percent gallium. Through processing, metallurgists can even control the overall distribution of the gallium within the parent plutonium metal to create alloys with desirable properties.

Undoubtedly, the local distribution of the gallium, that is, the specific location of the gallium within the plutonium lattice, affects the delicate stability of the δ -phase as well as its transformation behavior to the low temperature monoclinic phase. However, we do not know where the gallium is located in the fcc lattice, nor do we know how it moves within the lattice as the material ages or as

it is subjected to other external influences. Moreover, we do not know where the gallium is trapped when the fcc lattice transforms into the monoclinic lattice or how it subsequently migrates.

Because it provides a picture of the average structure of the coherent portions of crystalline materials, x-ray diffraction (XRD) has been the principal tool for studying plutonium solids. The extent of atomic displacements from ideal lattice sites is contained in the diffuse background, however, and is more difficult to analyze quantitatively. Thus, conventional laboratory-based XRD analysis cannot provide a detailed picture of local structure. With the availability of x-rays from synchrotron light sources, however, it is possible to study

the local structure surrounding atoms using x-ray absorption fine structure (XAFS) spectroscopy.

For XAFS, the sample is probed with x-rays that are tuned to measure the absorption spectrum of the sample, typically from the energy of a core electron shell in the element of interest to approximately 1000 electron volts (eV) above it. A core electron in a target atom can absorb the x-ray energy and get liberated, but the probability that it does so depends on several factors, including the position, type, and number of nearby atoms, as well as the energy of the incoming x-rays. Thus, the x-ray absorption spectrum contains encoded information about the local environment, and precise measurement of the spectrum allows us to extract the distances between

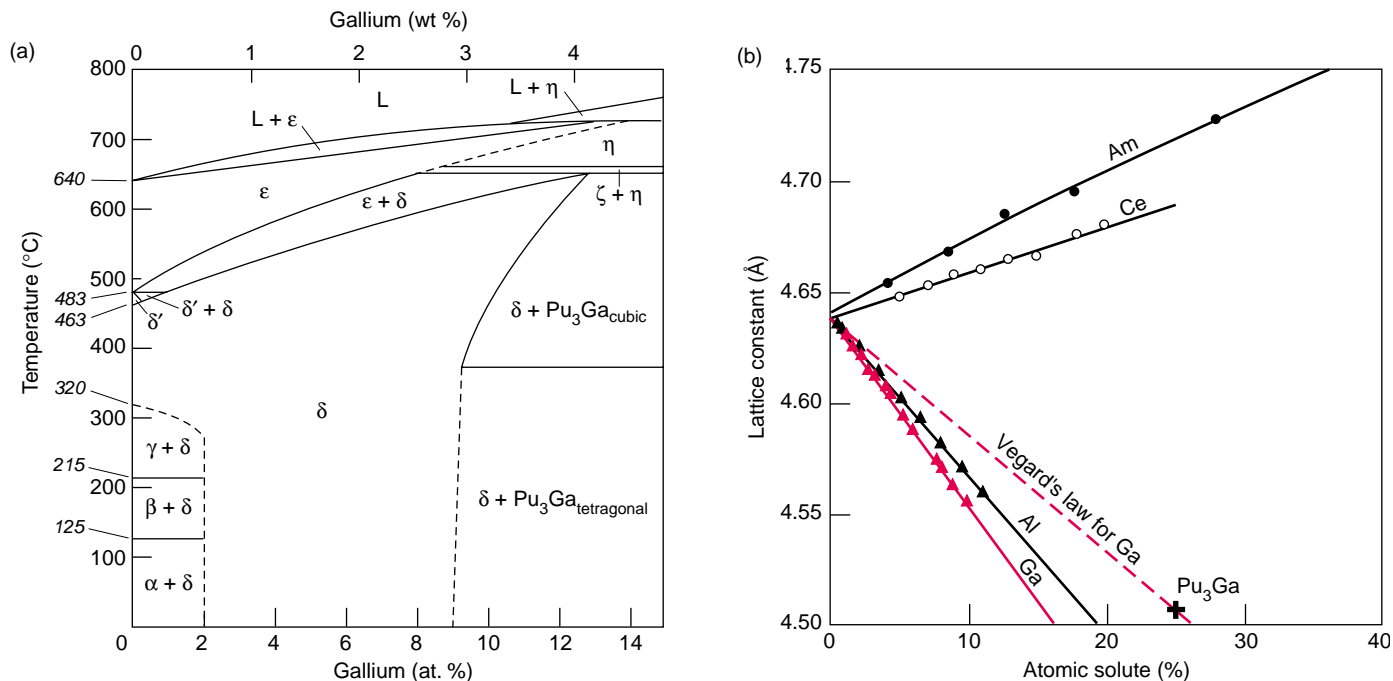


Figure 1. Plutonium-Gallium Alloys

(a) Additions of very small amounts of gallium (between about 2 and 9 at. %) to plutonium metal stabilize the fcc δ -phase to room temperature. (b) The additions alter the size of the fcc-lattice. Gallium is smaller than plutonium, and the lattice parameter decreases with gallium concentration. The scaling is at odds with Vegard's law, which assumes that solute atoms substitute in an ideal manner within the metal lattice. Aluminum additions also shrink the fcc δ -phase lattice, whereas additions of americium or cerium cause it to expand.

the absorber and its near-neighbor atoms. By tuning the x-ray energy, we can obtain this information for any element in the sample.

In contrast to the difficulties of analyzing the diffuse x-ray scattering component of XRD, XAFS is well suited for the characterization of local atomic distortions present in solids. The information it provides is therefore complementary to the information obtained by x-ray diffraction. XAFS can also be used to probe molecular species in liquids or amorphous solids such as glass.

For the past eight years, we have led a large, international, multicollaborator program at the Stanford Synchrotron Radiation Laboratory (SSRL) to apply XAFS to actinide chemistry and materials science. All our experiments were conducted with synchrotron radiation from the SPEAR ring at SSRL. Some of our results are presented in other articles in this volume, including "XAFS" on page 422.

Recent Evidence for Local Structure in δ -Phase Plutonium Alloys

The commonly accepted Pu-Ga phase diagram indicates that the fcc δ -phase can be retained with additions of 2 to 9 atomic percent (at. %) gallium to room temperature, as shown in Figure 1(a). In fact, if great care is taken to ensure a microscopically uniform gallium concentration, the fcc δ -phase can be retained with as little as 1 at. % gallium and up to as much as 10 at. % gallium (see the article "Plutonium and Its Alloys" on page 290). However, the work of Timofeeva shows convincingly that the fcc phase is metastable even at room temperature and over all gallium concentrations. Only the very low diffusion rates of gallium through the plutonium lattice prevent the decomposition of the δ - to the α -phase plus Pu_3Ga .

Classical x-ray diffraction studies over the years indicate that the crystal

structure of the gallium-stabilized δ -phase is that of a single fcc lattice. From a combination of density measurements and x-ray determinations of the lattice parameter, it was concluded that the gallium atoms form a "substitutional solid solution" in plutonium, that is, the gallium atoms substitute for the plutonium atoms in the fcc lattice. As stated earlier, however, it is not possible to determine how the smaller gallium atoms fit into the plutonium lattice. We know that the gallium atoms do not arrange themselves with systematic long-range order because superlattice reflections (indicative of long-range order) have not been observed. As shown in Figure 1(b), the average lattice parameter of the δ -phase solid solution decreases linearly with increasing gallium concentration. The decrease is greater than that predicted by the linear rule of mixtures, called Vegard's law, indicating that the δ -phase is not an ideal solid solution.

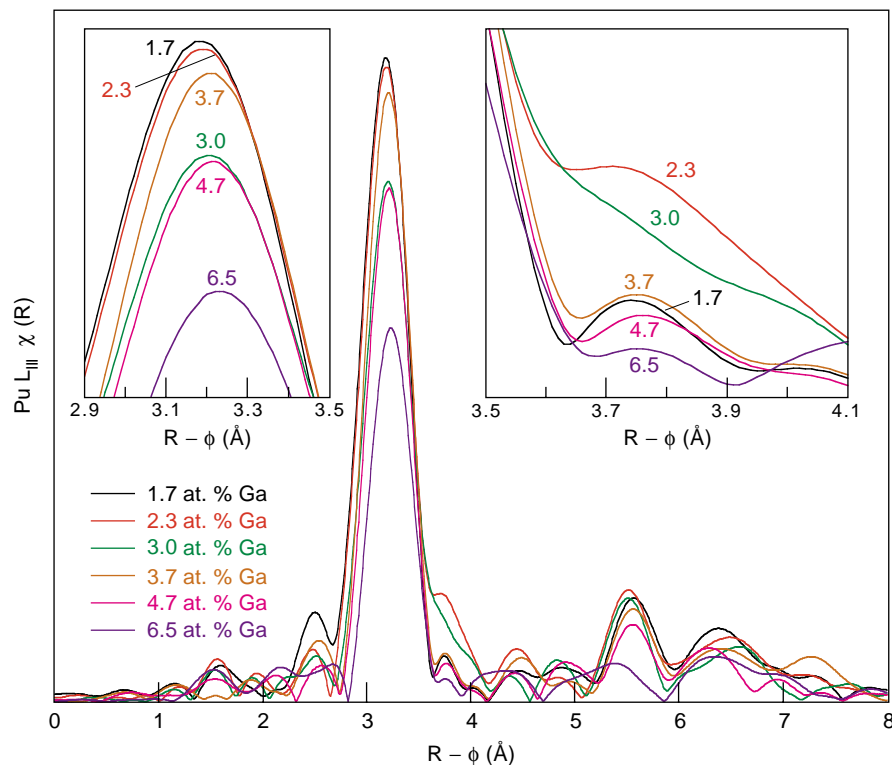


Figure 2. Fourier Transform Moduli of Pu-Ga δ -Phase Alloys

The principal peaks of the Fourier transform moduli $\chi(R)$ correspond to shells of atoms surrounding a target atom. The height of a peak is proportional to the number of atoms in the shell but inversely proportional to the square of the distance away from the target atom. The height is also reduced by thermal and static disorder within the local structure. The raw XAFS data contain phase as well as amplitude information, so $\chi(R)$ is not a direct representation of the actual structure. Because of the phase shift ϕ , for example, the peak position in $\chi(R)$ is typically 0.1–0.5 Å below the true interatomic distance. (Main graph) The large peak near $R - \phi = 3.1$ Å represents the first shell of plutonium atoms that surrounds each plutonium atom in the fcc δ -phase lattice. (The shell contains 12 atoms at 3.28 Å) The relatively small peak near $R - \phi = 4.4$ Å corresponds to 6 atoms at 4.64 Å—the second shell of the fcc lattice. The peak at $R - \phi = 5.5$ Å is due to 24 atoms in the third shell at 5.68 Å. The amplitude of this peak is typically the best figure of merit for the degree of extended local order. Peaks at $R - \phi = 6.4$ and 7.2 Å correspond to the fourth and fifth shells, respectively. (Inset left) Detail of the first peak shows the variation with gallium concentration. (Inset right) Detail of the 3.8-Å region shows the height of this peak as indicative of the σ -structure.

The XAFS technique is suited precisely for this type of local-structure study. Unfortunately, for several years, we were not able to obtain well-controlled and well-characterized δ -phase plutonium alloy samples. Instead, we used what samples were available as we refined the XAFS technique for crystalline plutonium.

By analyzing dozens of alloys and hundreds of XAFS spectra (including plutonium alloyed with various amounts of gallium, cerium, indium, lead, and combinations thereof), we were able to make two overarching observations: (1) A definite local structure was apparent in solute-lean alloys. This local structure, which we will call

the σ -structure, is extraneous to the fcc structure of the δ -phase. (2) This superposed σ -structure tended to disappear with age over a decade or more. Regrettably, the great variability in sample chemistry and processing did not allow for unambiguous characterization of the σ -structure or an understanding of its stability.

We recently completed the first systematic examination of carefully processed Pu-Ga alloys with gallium concentrations varying from 1.7 to 6.7 at. %. These samples were arc-melted from high-purity, zone-refined plutonium with appropriate amounts of high-purity gallium. The resulting purity was approximately 120 parts per million (ppm) by weight of uranium, with all other metallic impurities being less than 100 ppm total. The samples were rolled into thin sections (with intermediate annealing treatments), homogenized at 450°C for 48 hours, and electropolished to remove any surface oxides. X-ray diffraction measurements of the thin sections used for XAFS studies confirmed the lack of any discernible phases besides the fcc δ -phase. We have yet to confirm the microscopic uniformity of gallium but expect it to be reasonably uniform on a micrometer scale.

Some of the measurements were made at 300 kelvins, although it is very difficult to get high-quality data at those temperatures because the high thermal softness of both α - and δ -phase plutonium gives rise to large lattice vibrations (see the article “Atomic Vibrations and Melting in Plutonium” on page 190). Most of the measurements were made at 90 and 35 kelvins to reduce the thermal vibrations and hence the diffuse thermal scattering. The low temperature also makes it easier to quantify the diffuse scattering that results from the structural arrangements of the plutonium and gallium atoms (rather than from thermal vibrations). The principal concern about making the measurements at low temperatures is that the δ -phase alloys may transform to the monoclinic α' -phase.

Figure 2 shows the Fourier transform modulus of some of our plutonium L_{III} edge spectra. (The Fourier transform modulus is an approximate representation of the average local structure around the absorbing atom. The steps involved in analyzing an XAFS spectrum are discussed more thoroughly in the article "XAFS" on page 422.) The most notable difference between the sample's Fourier transform modulus and that of a calculated fcc δ -structure is the peak or resolved shoulder at $R-\phi \sim 3.75$ angstroms. This peak is well fit by assuming a plutonium shell at about 3.8 angstroms, which is quite outside the range of any of the standard fcc neighbors. This feature was the first and best indication of the presence of the local σ -structure. Another feature is the Pu-Pu shell at 5.0 angstroms, which is similarly not found in the fcc structure of δ -plutonium.

Interpretation of the 3.8 angstroms Pu-Pu distance has been a point of contention because it is very close to that in PuO_2 , a possible surface contaminant. However, searches of the XAFS data failed to find oxygen atoms at 2.35 angstroms, which must be present if the probed structure is PuO_2 . We also couldn't find any of the more distant oxygen and plutonium shells indicative of PuO_2 . Lastly, the other features associated with the σ -structure are not associated with this oxide.

The rightmost inset in Figure 2 shows that the amplitude of the feature around 3.75 angstroms (and presumably the fraction of plutonium atoms in this local structure) generally decreases with increasing gallium concentration, diminishing to near zero between 3.7 and 4.7 at. % Ga. These results are generally consistent with our earlier experiments, which indicated that the amount of local structure significantly decreased near or slightly above 3.3 at. % Ga. We were surprised, however, that the 1.7 at. % gallium sample exhibited very little local structure. Previous experiments had showed that this gallium concentration range exhibited the largest amount of the σ -structure. However, we also note that

this 1.7 at. % gallium sample showed some evidence of transforming to the α' -phase upon cooling to 35 kelvins.

The amplitude of the first large peak in the data set shown in Figure 2 (corresponding to the first shell of atoms around a plutonium atom) also reveals the influence of gallium concentration on the fcc structure. Because the gallium is smaller than the plutonium, the Ga-Pu bond length is reduced. The gallium thus displaces nearby plutonium atoms from their lattice sites and disorders the Pu-Pu pair distribution in the material, with increasing disorder associated with increasing gallium concentration. This effect is observed in the spectra, with the height of the peak decreasing as the gallium concentration increases from 1.7 to 2.3 to 3.0 at. % gallium, and also from 3.7 to 4.7 to 6.5 at. % gallium. In fact, at the highest measured concentration (6.5 at. % gallium), the average number of gallium neighbors approaches unity, and the disrupting effect can even be seen to disorder the extended local structure involving the more distant shells.

Interestingly, the peak height jumps higher as the gallium concentration increases from 3.0 to 3.7 at. %. This is also the concentration at which the σ -structure undergoes a rapid decrease to near zero. The transformation from a heterogeneous structure to a homogeneous fcc arrangement of atoms should be accompanied by an overall increase in the plutonium order and, hence, an increase in the height of the first peak. Thus, the behavior of the first peak generally corroborates the trend observed in the 3.75-angstrom region.

We believe that our most recent XAFS results demonstrate that the uniform fcc structure deduced from x-ray diffraction measurements is not strictly all δ -phase. Instead, plutonium microstructures harbor an additional structure on the nanometer scale. The nature and amount of this local σ -structure appears to vary in a complex manner with increased gallium concentration. We must still reconcile the appearance of the σ -structure with

the fact that lattice parameters and densities (as well as other properties such as mechanical strength and resistivity) are consistent with the existence of a single fcc δ -phase structure. Clearly, our observations must be confirmed with additional experiments on well-characterized samples. But these recent experiments, combined with data from earlier experiments and from x-ray diffraction and transmission electron microscopy, may hold the key to understanding the nature of phase stability in plutonium alloys.

Gallium XAFS

By changing the x-ray energy, we were also able to probe the environment surrounding the gallium atoms to determine how the Ga-Pu distances compare with the Pu-Pu distances. Faure et al. (1996) reported that the Ga-Pu nearest-neighbor distance was as much as 0.1 angstrom shorter than the nearest-neighbor Pu-Pu distance. Moreover, the Ga-Pu distance lengthens with increasing gallium concentration, but begins to shorten above 7.5 at. %. The Pu-Pu distance was very close to that expected from the XRD lattice parameter measurements and decreased with increasing gallium concentration. These results, if correct, would provide valuable insight into the effect of gallium on the stabilization of the δ -phase.

However, we are very concerned that Faure et al. fit the nearest-neighbor contribution with a single plutonium shell, even when the average number of gallium nearest-neighbors is one. Under those circumstances, the plutonium distribution should be highly disordered.

We investigated the interatomic distances using a very sensitive phase-difference method that is not subject to the same assumptions used by Faure et al. The gallium XAFS results from samples spanning the range of gallium concentrations presented before are shown in Figure 3. To compare the Pu-Pu and Ga-Pu distances to each other, we used phase differences.

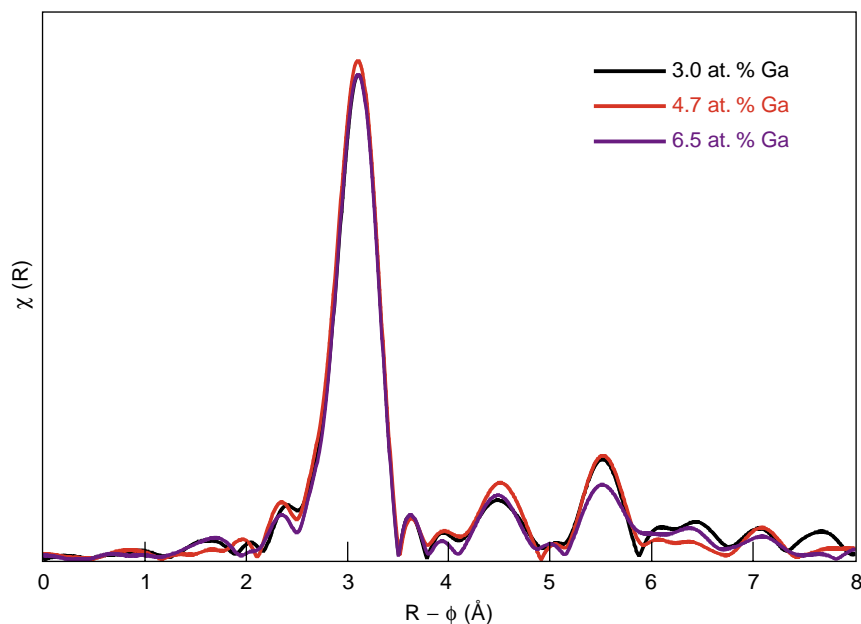


Figure 3. Fourier Transform Moduli of Gallium XAFS

Comparison of the gallium XAFS for three alloys reveals little change in the Ga-Pu bond length with gallium concentration. All samples were probed at 35 K. The amplitudes of the Fourier Transform moduli are scaled identically.

In contrast to Faure et al., we found that the Pu-Pu distances varied by less than 0.008 angstrom over the range of gallium concentrations. The changes for the Ga-Pu distance were somewhat larger: We measured a contraction around the gallium atoms of 0.13 angstrom in the first shell, 0.05 angstrom around the second shell, and 0.01 angstrom around the third shell (this latter contraction is within our experimental uncertainties).

Although we found that the average Pu-Pu distance was approximately 0.13 angstrom larger than the Ga-Pu distance, the plutonium and gallium XAFS measurements show that the nearest-neighbor distances are relatively unchanged with gallium concentration. The decrease in the lattice parameter reflects the fact that, as the gallium concentration is increased, the fraction of shorter Ga-Pu bonds increases. These results are very similar to those found by Mikkelsen and Boyce (1983) for GaInAs solid solutions.

Tracking Gallium and Other Solutes during Aging

Plutonium is radioactive—hence, the metal continually irradiates itself. As discussed in the article “Aging of Plutonium and Its Alloys” on page 238, the relentless deposition of energy in the material because of self-irradiation potentially alters the phase stability and behavior of plutonium alloys. For example, self-irradiation studies at cryogenic temperatures show a significant contraction (on the order of 15 percent over many thousands of hours) of the lattice parameter of δ -phase plutonium alloys at 4.2 kelvins. On the other hand, these alloys expand slightly (between 0.01 to 0.1 percent per year, at least for the first few years) at ambient temperature. We do not understand this behavior.

We know that self-irradiation creates copious Frenkel pairs (plutonium self-interstitials and vacancies), and the lattice damage, in turn, may influence

the distribution of δ -phase stabilizing elements such as gallium. Self-irradiation also creates transmutation products (such as helium, americium, neptunium, and uranium), which by themselves can potentially affect the thermodynamic long-term stability of the alloys. For example, it is well known that americium is a δ -phase stabilizer, whereas uranium destabilizes the δ -phase, and neptunium is the only known α -phase stabilizer. Moreover, the creation of vacancies and helium may affect the diffusion rates of plutonium and solutes in δ -phase alloys.

We have examined a limited number of α - and δ -phase plutonium alloys aged at ambient temperature for up to 36 years. Figure 4(a) shows the XRD results from our synchrotron experiments for two of these samples. The aged Pu–3.3 at. % Ga δ -phase alloy exhibits only the expected fcc phase with sharp diffraction peaks, indicating very little disturbance to the crystalline lattice. The α -phase pure plutonium samples exhibit the expected monoclinic phase, also with excellent crystallinity. These results indicate that most of the self-irradiation damage in both α - and δ -phase plutonium is annealed out (or healed) at ambient temperature. There is no indication of the samples becoming amorphous. However, from XRD we cannot tell if any rearrangement of alloying elements takes place. Neither can we tell the location of the transmutation products in the crystal lattice.

XAFS measurements comparing fresh and aged samples may provide a clue to changes in local structure with aging. We would particularly like to track the gallium as the plutonium ages. We have examined a limited number of aged plutonium alloys to date and compared them with newly prepared samples. Because some of the aged samples are decades old, we were not able to reproduce their processing histories. The new samples could only roughly match the chemical makeup of the aged alloys. However, the initial impurity content of these alloys was typically in excess of 1000 ppm by weight com-

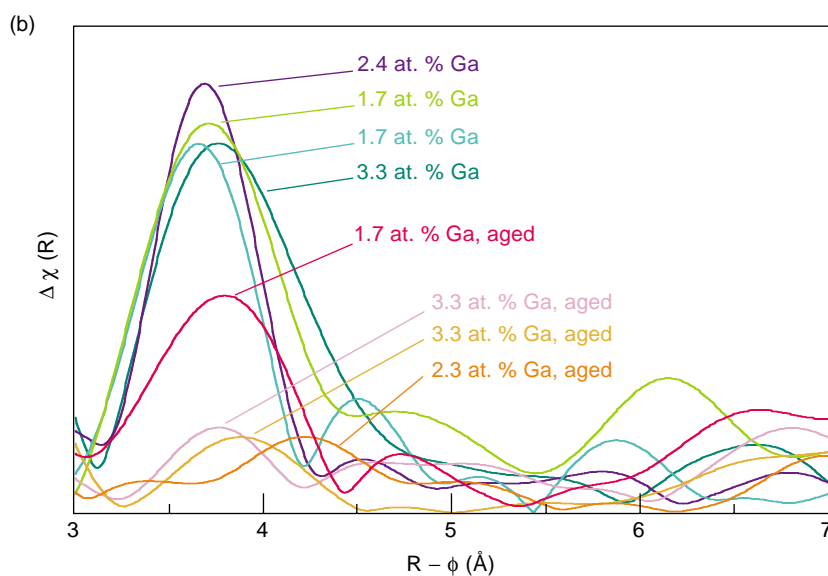
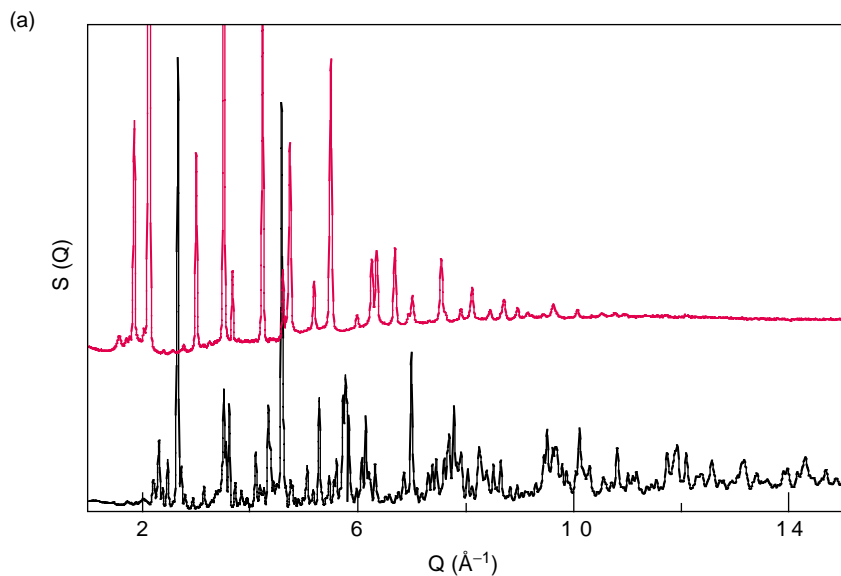


Figure 4. Probing Aged Plutonium Alloys

(a) XRD experiments conducted at the SSRL achieve a very high momentum transfer Q , defined as $Q = 4\pi\sin(\Theta)/\lambda$, where Θ is the diffraction angle and λ is the x-ray wavelength. The top curve in red (y-axis zero offset for clarity) represents a δ -phase Pu–3.3 at. % Ga alloy aged at ambient temperature for 36 years. The bottom curve is an α -phase sample aged at ambient temperature for 32 years. The sharp diffraction peaks maintained out to very high Q indicate that excellent crystallinity is maintained during aging. Note that classical XRD run in the laboratory with a copper anode would be limited to $Q \sim 8 \text{ \AA}^{-1}$.

(b) XAFS measurements reveal the σ -structure's dependence with sample age. Several samples with the same composition were probed to check reproducibility. The graph shows the difference between the Fourier transform modulus of the data and a calculated fcc δ -phase alloy. The largest difference is in the region of $R - \phi = 3.75 \text{ \AA}$, indicating the presence of the local σ -structure. Newly prepared alloys with Ga concentrations less than 3.3 at. % have a large amount of this structure. Decade-old alloys with Ga concentrations between 2.3 and 3.3 at. % show only negligible amounts. A low-purity Pu–1.7 at. % Ga alloy aged for 15 years displays an intermediate quantity.

pared with the few hundred parts per million impurity levels of the new samples. (Additional impurities are also introduced during aging by transmutation of the plutonium atoms). We wish to share our preliminary observations.

First, we find that the local σ -structure tends to disappear with age, as seen in Figure 4(b). We found no local structure in new or aged samples of the low-purity alloys for gallium concentrations in excess of 3.3 at. %. Second, while samples of low-purity, Pu–1.7 at. % Ga clearly exhibited substantial amounts of the local structure,

newer samples of higher purity showed far less structure.

Our results lead to the tempting observation that aging may alter the local structure and have a stabilizing effect on the fcc δ -phase. However, these results are very preliminary. Los Alamos and Lawrence Livermore National Laboratories are planning a program to accelerate the aging process in plutonium samples. (The more radioactive plutonium-238 will be blended with plutonium-239 to accelerate the self-irradiation.) We hope that future XAFS studies using these samples will allow a direct comparison

of aging effects.

It would also be very informative to track the transmutation products helium, americium, uranium, and neptunium. Most likely, these elements are present at random in the plutonium lattice at the end of the collision cascade, but XAFS studies would allow us to determine how these elements rearrange with time and temperature. Unfortunately, helium is simply too light to track with x-rays, and it was not possible to observe americium because of interference from the strong signal of plutonium. We have not yet

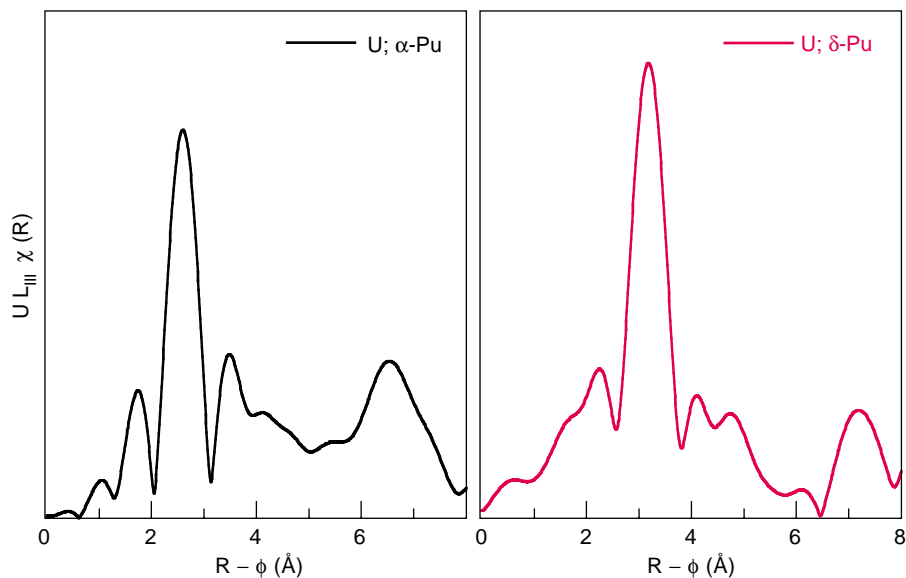


Figure 5. Uranium L_{III} Edge Fourier Transform Modulus

The two graphs show the XAFS for uranium atoms in different plutonium lattices (taken at -80 K). The graph on the left shows an α -phase plutonium sample aged for 32 years at ambient temperature. The graph on the right represents a δ -phase Pu–3.3 at. % Ga alloy aged at ambient temperature for 36 years. The results show that the uranium atom substitutes for the plutonium atoms in both lattices—a surprising result considering that uranium has no equilibrium solid solubility in either phase of plutonium.

looked for neptunium because its small concentration would make the experiments extremely time-consuming. We were, however, able to make preliminary observations on the location of the uranium transmutation product in the aged samples.

The uranium XAFS spectrum of aged samples is shown in Figure 5. The uranium was most likely introduced via the decay of the plutonium. The spectrum shows that the nearest neighbor U–Pu distance is only about 0.07 angstrom shorter than the average Pu–Pu length in the δ -phase alloy. Additional samples of aged α -plutonium show that, within the experimental uncertainty, the distance between uranium and plutonium atoms is nearly identical to that between plutonium atoms in the α -phase. This is a surprising result, given uranium’s low solubility in both of these plutonium phases and its propensity to form high-

density structures with small atomic volumes. It is possible that its immersion in the plutonium lattice modifies its electronic structure to match that of the plutonium host in both phases.

Gallium Migration in Transformed Structures

Below room temperature or under high pressure, the low-gallium alloys readily transform by a martensitic transformation to a monoclinic α' -phase. (See the article “Plutonium and Its Alloys” on page 290.) The gallium atoms are trapped in the monoclinic α -lattice and result in a slight expansion to the α' -phase. Since there is no equilibrium solubility for gallium in the α -phase, there is a strong driving force to reject the gallium atoms from the lattice.

As stated earlier, our XAFS samples

are typically cooled to cryogenic temperatures to yield the best measurements. Based on the transformation characteristics of δ -phase Pu–Ga alloys, we expect the Pu–1.7 at. % Ga samples to transform to approximately 25 to 30 percent α' -phase upon cooling. However, we have rarely seen any evidence of the α' -phase in our previously examined samples.

We have recently examined a Pu–1.7 at. % Ga sample that was cooled in the laboratory to transform it to a mixture of δ - plus α' -phase. We then carefully examined the sample by XRD to confirm the mixture and then probed it by XAFS. The plutonium XAFS, seen in Figure 6(a), clearly shows the set of short Pu–Pu distances indicative of the α' -structure, as well as the prominent peak at the longer distance from the δ -component. This was the first time that XAFS had unambiguously seen the α' -phase in a sample.

Figure 6(b) shows the gallium XAFS. Only the prominent peak of the δ -phase is apparent for the mixed δ - plus α' -phase sample. The height of the peak is reduced, however, because both phases are present. The figure also shows the newly prepared Pu–1.7 at. % Ga alloy that showed a small amount of σ -structure. Its peak height indicates some disordering of the δ -phase, most likely by the local strains resulting from the partial transformation to the α' -phase.

The gallium XAFS results for the mixed-phase sample confirm that gallium atoms are initially trapped at random in the α' -lattice. This random trapping is expected because martensitic transformations allow no compositional changes from the parent phase during transformation. However, as these samples are returned to room temperature or above, there is a strong driving force to move the gallium out of the plutonium lattice. XAFS measurements offer the promise of allowing the tracking of the gallium atom motion in the transformed product as a function of time and temperature.

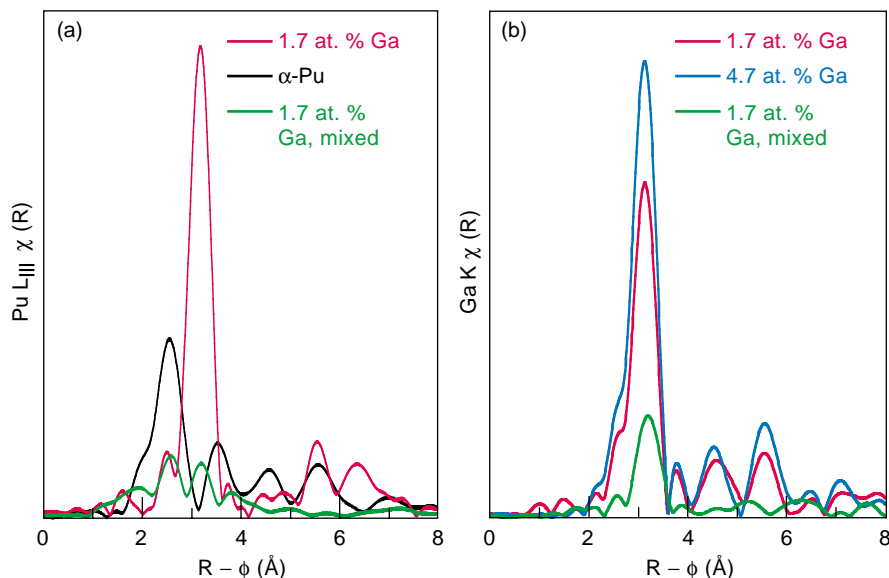


Figure 6. Evidence for the α' -phase in XAFS Spectra

(a) The green curve is the plutonium XAFS of a Pu–1.7 at. % Ga sample that was partially transformed (on purpose) to the α' -phase at low temperatures. In contrast to either the α - or δ -phase sample, the mixed $\delta + \alpha'$ sample shows two peaks. The peak on the left is consistent with the short Pu–Pu bonds of the α' -phase, whereas the peak on the right is consistent with the fcc δ -phase structure. (b) Gallium XAFS (from the gallium K edge) at 35 K from three samples: δ -phase samples of high-purity newly prepared Pu–1.7 at. % Ga and Pu–4.7 at. % Ga alloys and the mixed $\delta + \alpha'$ sample shown in (a). The reduced peak height for the mixed sample indicates the δ -phase is disordered as a result of transformation to the α' -phase. The absence of a distinct gallium peak at the shorter Pu–Pu distance characteristic of the α' -phase confirms that gallium atoms are trapped at random in the α' -lattice. The newly prepared Pu–1.7 at. % Ga sample shows features similar to the mixed sample, suggesting that it too partially transformed upon cooling.

Conclusions

We have demonstrated the utility of XAFS for studying the local structure of plutonium alloys. The complexity of phase stability and phase transformations, particularly as they are affected by alloy chemistry and processing, has made it difficult to unambiguously interpret our results to date. Preliminary observations using XAFS to track solutes in plutonium during aging and as a result of phase transformations are very encouraging. We are convinced that additional studies of well-characterized plutonium alloy samples will help solve some of the long-standing puzzles of phase stability and phase transformations in plutonium, as well as provide new insight into the

mechanisms by which plutonium and its alloys age with time. ■

Acknowledgments

My thanks go to P. Villella, L. Cox, B. Martinez, R. Martinez, J. Lashley, L. Morales, A. Lawson, R. Pereyra, J. Terry and F. J. Espinosa for sample preparation, experimental assistance, and essential discussions. I would especially like to thank S. S. Hecker for discussions and assistance with this manuscript. XRD and EXAFS experiments were performed at the Stanford Synchrotron Radiation Laboratory, which is operated by the U.S. Department of Energy, Office of Basic Energy Sciences.

Further Reading

- Conradson, S. D. 1999. *Appl. Spec.* **52**: 252.
- Faure, P., B. Deslandes, D. Bazin, C. Tailland, R. Doukhan, J. M. Fournier, and A. Falanga. 1996. *J. All. Compounds* **244**: 131.
- Hecker, S. S. 2000 (to be published). Plutonium Aging: From Mystery to Enigma. In *Proceedings of the International Conference on Ageing Studies and Lifetime Extension Materials*. Edited by L. G. Mallinson, 191. Dordrecht: Kluwer Academic Publisher.
- Mikkelsen, J. C., and J. B. Boyce. 1983. *Phys. Rev. B* **28**(12): 7130.
- Zachariasen, W. 1963. *Acta Cryst.* **16**: 777.

For a biography of Steven D. Conradson, see page 435.

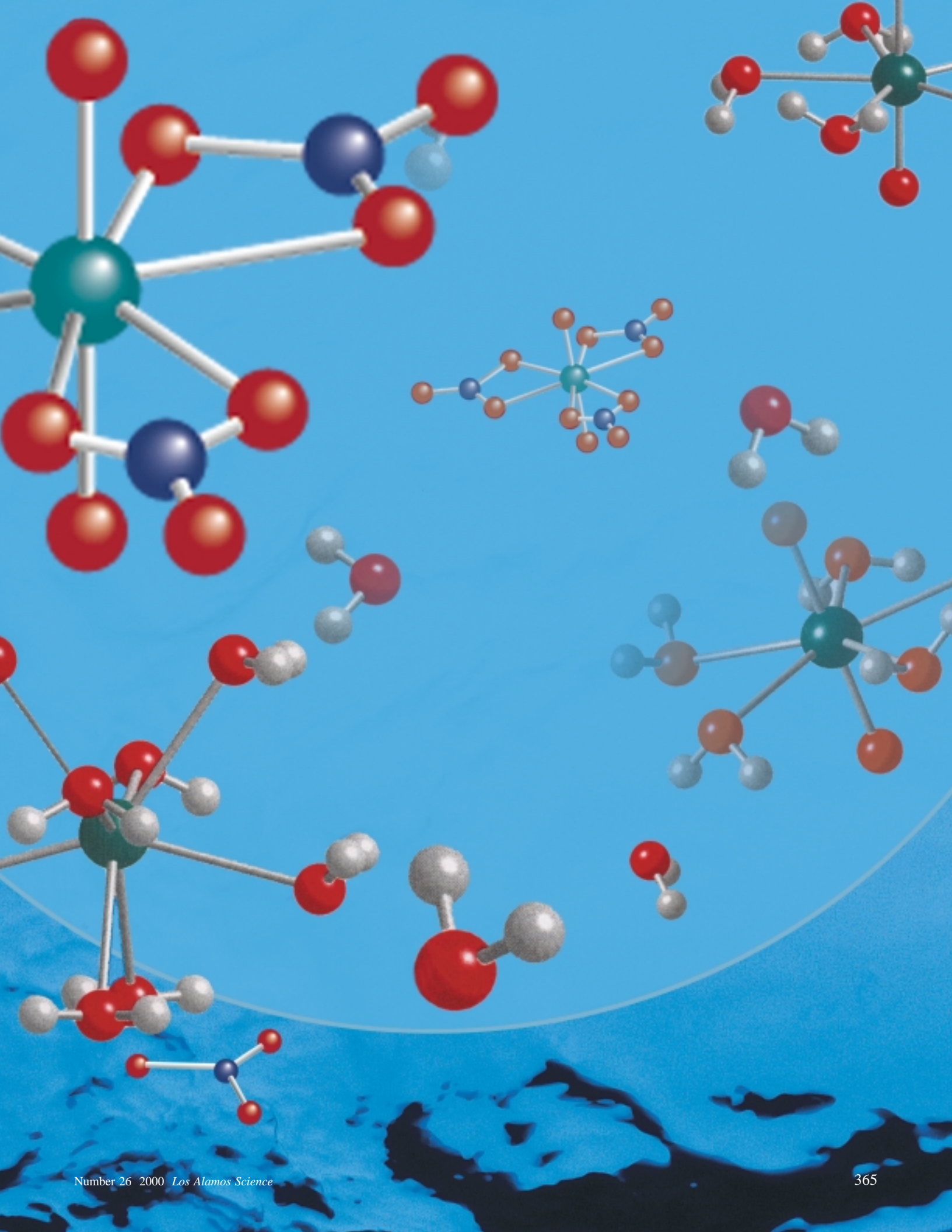


The Chemical Complexities of Plutonium

David L. Clark

Few people have ever seen plutonium, and far fewer have actually handled or manipulated it. Yet this manmade element has arguably altered the course of civilization as much as copper, bronze, iron, or steel. Within five years of its synthesis, the primary use of plutonium was for the release of nuclear energy in weapons of mass destruction, and it seemed that the new element might lead the human race to the brink of self-annihilation. But instead, plutonium has become a stabilizing agent in global politics, forcing the human race to govern itself without resorting to nuclear war. Never before has a simple chemical element had such a profound impact on the consciousness of mankind.

Plutonium has had a similarly humbling impact in the more circumscribed arena of science. Incredibly, it displays physicochemical behaviors that are among the most complex of any element in the periodic table. The pure element exhibits seven distinct crystal phases, is highly reactive, and is known to form compounds, complexes, or alloys with virtually every other element. Molten plutonium is highly corrosive and will slowly react with its container, causing difficulties for handling. When elemental plutonium reacts to give up its valence electrons, it can form a wide variety of positively charged ions with the ability to form up to twelve chemical bonds to other ions or molecules in solution. The element can exhibit five oxidation states, and under certain chemical conditions, four different oxidation states can be present in appreciable amounts simultaneously! No other element displays such a complex chemistry.



s		d										p																							
1	2											13	14	15	16	17	18																		
1	H											5	B	6	C	7	N	8	O	9	F	10	He												
3	Li	4	Be											11	Na	12	Mg																		
19	K	20	Ca	21	Sc	22	Ti	23	V	24	Cr	25	Mn	26	Fe	27	Co	28	Ni	29	Cu	30	Zn	31	Ga	32	Ge	33	As	34	Se	35	Br	36	Kr
37	Rb	38	Sr	39	Y	40	Zr	41	Nb	42	Mo	43	Tc	44	Ru	45	Rh	46	Pd	47	Ag	48	Cd	49	In	50	Sn	51	Sb	52	Te	53	I	54	Xe
55	Cs	56	Ba	57	La	72	Hf	73	Ta	74	W	75	Re	76	Os	77	Ir	78	Pt	79	Au	80	Hg	81	Tl	82	Pb	83	Bi	84	Po	85	At	86	Rn
87	Fr	88	Ra	89	Ac	104	Rf	105	Ha	106	Sg	107	Ns	108	Hs	109	Mt	110	111	112															
		f																																	
Lanthanides		58	Ce	59	Pr	60	Nd	61	Pm	62	Sm	63	Eu	64	Gd	65	Tb	66	Dy	67	Ho	68	Er	69	Tm	70	Yb	71	Lu						
Actinides		90	Th	91	Pa	92	U	93	Np	94	Pu	95	Am	96	Cm	97	Bk	98	Cf	99	Es	100	Fm	101	Md	102	No	103	Lr						

Figure 1. Chemical Periodicity and the Periodic Table

The modern periodic table derives principally from the work of Dimitri Mendeleev, who in 1869 enunciated a “periodic law” that the properties of the elements are a periodic function of their atomic weights and arranged the 65 known elements in a “periodic table.” Fundamentally, every column in the main body of the table is a group of elements that display similar chemical and physical behavior. Similar properties are therefore exhibited by elements with widely different masses. Chemical periodicity is central to the study of chemistry, and no other generalization comes close to its ability to systematize and rationalize known chemical facts. With the development of atomic theory and an understanding of the electronic structure of atoms, chemical periodicity and the periodic table now find their natural explanation in the electronic structure of atoms. Moving from left to right along any row, the elements are arranged sequentially according to nuclear charge (the atomic number). Electrons balance that charge, hence each successive element has one more electron in its configuration. The electron configuration, or distribution of electrons among atomic orbitals, may be determined by application of the Pauli principle (paired spin in the same orbital) and the Aufbau principle (which outlines the order of filling electrons into shells of orbitals s, p, d, f, etc.) such that in a given atom, no two electrons may have all four quantum numbers identical.

The chemical complexity is a double-edged sword. Plutonium chemistry is rich, varied, and fascinating, but it can also be difficult to control. Its behavior is in great contrast to the chemistry of light elements of the periodic table, where our understanding of molecular transformations and the theory of chemical bonding between light atoms is such that we can undertake complex, multistep processes to synthesize new pharmaceuticals, polymers, ceramics, and other materials that are expertly tailored to our specific needs. We can exercise such control over the

chemistry because we have a detailed understanding of the electronic structure and chemical reactivity of the light elements in the periodic table. Presently, we have no such comprehension of plutonium. Only recently have we at Los Alamos been able to gain new insight into the molecular- or atomic-scale properties of the element. It is obvious, however, that a fundamental grasp of plutonium chemistry will have clear implications for modern improvements in process and separations chemistry, the storage and disposition of legacy materials, the fate and transport of

plutonium in the environment, and the long-term predictions of nuclear weapons aging and safety. Understanding and predicting the chemistry of plutonium will be the key to solving plutonium-related problems that have resulted from 50 years of nuclear weapons production.

This article will therefore present plutonium chemistry from a basic, molecular-level perspective. It will start with a discussion of 5f electrons, which define the actinide series and are responsible for the chemical properties of the series. It will end with a summary

Table I. Ground-State Valence Shell Configurations of Lanthanum, the Lanthanides, Actinium, and the Actinides

Lanthanide		Configuration		Actinide		Configuration	
La	lanthanum	5d ¹	6s ²	Ac	actinium	6d ¹	7s ²
Ce	cerium	4f ¹ 5d ¹	6s ²	Th	thorium	6d	7s ²
Pr	praseodymium	4f ³	6s ²	Pa	protactinium	5f ² 6d ¹	7s ²
Nd	neodymium	4f ⁴	6s ²	U	uranium	5f ³ 6d ¹	7s ²
Pm	promethium	4f ⁵	6s ²	Np	neptunium	5f ⁴ 6d ¹	7s ²
Sm	samarium	4f ⁶	6s ²	Pu	plutonium	5f ⁶	7s ²
Eu	europium	4f ⁷	6s ²	Am	americium	5f ⁷	7s ²
Gd	gadolinium	4f ⁷ 5d ¹	6s ²	Cm	curium	5f ⁷ 6d ¹	7s ²
Tb	terbium	4f ⁹	6s ²	Bk	berkelium	5f ⁹	7s ²
Dy	dysprosium	4f ¹⁰	6s ²	Cf	californium	5f ¹⁰	7s ²
Ho	holmium	4f ¹¹	6s ²	Es	einsteinium	5f ¹¹	7s ²
Er	erbium	4f ¹²	6s ²	Fm	fermium	5f ¹²	7s ²
Tm	thulium	4f ¹³	6s ²	Md	mendelevium	5f ¹³	7s ²
Yb	ytterbium	4f ¹⁴	6s ²	No	nobelium	5f ¹⁴	7s ²
Lu	lutetium	4f ¹⁴ 5d ¹	6s ²	Lr	lawrencium	5f ¹⁴ 6d ¹	7s ²

of some of our most recent structural studies of plutonium carbonate complexes, studies that are relevant for understanding the behavior of plutonium ions in natural groundwaters. Along the way, it will also bring to light some fundamental chemistry of the most fascinating element known.

The Actinide Elements

Plutonium is one of the actinide elements, those fourteen elements with atomic numbers 90 to 103 that follow actinium in the periodic table. The table itself is shown in Figure 1. The figure caption also provides some background material on chemical periodicity and electronic structure. The actinide elements occupy their unique position at the bottom of the periodic table because they contain 5f electrons in their valence shell. Because the valence electrons are the ones that ultimately dictate chemical behavior, we would expect the actinides to be chemically similar to the only other elements that have f electrons in their valence shell—the lanthanides. Those are the fourteen elements with atomic numbers 58

through 71, which sit directly above the actinides in the periodic table and have 4f valence electrons.

Chemically, the lanthanides are characterized by relatively homogeneous behavior (especially in aqueous solution). All members tend to form trivalent ions and form similar chemical compounds. In general, the chemical and physical differences between adjacent elements in the series are small. If placed in the main body of the periodic table (which is organized according to similarities in chemical traits), all fourteen would occupy the single position set aside for the element lanthanum (number 57).

The chemical homogeneity of the lanthanides results from the relatively small radial extension of the 4f valence orbitals, which are buried beneath the spatially more extended 5d and 6s orbitals. Since 4f electrons are buried so deep within the atom, they have little opportunity to participate in chemical bonding, hence the addition of another f electron to the valence shell has little effect on the overall bonding character or reactivity of the element. Thus, all of the lanthanides tend to behave chemically the same.

To a large degree, the actinides exhibit this same tendency toward homogeneous chemical behavior. The chemistry of plutonium, for example, is similar to the chemistry of uranium and neptunium. Lanthanide-like behavior, in fact, was the main prediction of Glenn Seaborg's "actinide concept" (Seaborg 1984). Seaborg asserted that the 5f subshell begins to fill after actinium, and so the electron configurations of the actinides and lanthanides should be completely analogous, and the two series should behave in a chemically homologous manner. (See the box "The Actinide Concept" on page 368.)

The 5f orbitals are very close in energy to the 6d's. In the early part of the actinide series, electrons find it relatively easy to switch between 5f and 6d configurations, and some of the "light" actinides—actinium through americium—exhibit traits that are reminiscent of elements that have at least one unpaired d electron in their valence shell—namely the transition elements.

The transition elements, also called the transition metals, comprise the d-block elements in columns 3 through 11 of the periodic table. They are the classical hard metals, such as iron,

elements with atomic numbers 95 and 96 based on assumed similarities to uranium were unsuccessful. Both Wahl and Zachariasen had proposed a thoride series that started with protactinium.

In 1944, Seaborg proposed that the series started with thorium and that all of the elements heavier than actinium constituted an “actinide” series similar to the lanthanides (see the 1945 table). Because the 5f shell began filling in the same relative position as the 4f shell, the electronic configuration of elements in the two series would be similar. Guided by the hypothesis that elements 95 and 96 were homologues of europium and gadolinium, new experiments were designed, and the elements were uniquely separated from all others. The new elements were subsequently named americium and curium.

Seaborg’s “actinide concept” thus played a major role in the discovery of the transplutonium elements. It provided the framework that supported synthesis, isolation, and identification of the succeeding actinide elements berkelium through lawrencium and beyond to the element with atomic number 118! But as research has progressed in the study of the actinide elements, it has become clear that the 5f series has a unique chemistry that is distinct from that of the 4f series. One of the focal points of study in actinide research has been to better define the scope and limitations of the actinide concept.

1																	2																				
3	4											5	6	7	8	9	10																				
11	12											13	14	15	16	17	18																				
19	20	21	22	23	24	25	26	27	28	29	30	31	32	33	34	35	36																				
37	38	39	40	41	42	43	44	45	46	47	48	49	50	51	52	53	54																				
55	56	57	72	73	74	75	76	77	78	79	80	81	82	83	84	85	86																				
87	88	89											94	95	96	97	98	99	100	101	102	103	104	105	106	107	108	109	110	111	112	113	114	115	116	117	118
		Lanthanides																																			
		Actinides																																			

In 1945, the actinide elements from thorium through curium were correctly placed under the 4f elements in the periodic table. The table reflects the now famous “actinide concept.”

where $n = 6$ to 14. This is exactly analogous to the standard $4f^m 6s^2$ configuration of the lanthanides, and like the lanthanides, the chemistry of the heavy actinides exhibits fewer oxidation states and simpler behavior. The reason for the differences in the light actinide elements relative to the light lanthanide elements has to do with the greater radial extension of 5f orbitals compared with 4f orbitals, and with relativistic effects that are increasingly important for heavy elements.

¹An exception is curium, which has electronic configuration $5f^7 6d^1 7s^2$, owing to the enhanced stability of a partially filled 5f shell. The f subshell can accommodate seven unpaired electrons, and it is energetically favorable to place the eighth in the d orbital rather than create an electron pair.

Shape and Radial Extension of f Orbitals

The spatial distribution of the electron density in an atom is often described by means of hydrogen-like atomic orbitals, which are obtained by solving the one-electron Schrödinger equation in a spherically symmetric Coulomb potential. The assumption of spherical symmetry allows the electron wave function to be mathematically separated into radial and angular parts.

The angular part of the wave function is independent of distance from the nucleus, and it determines the shape of the electron cloud. The shape varies depending on the type of orbital (s, p, d, f) and hence the orbital’s orientation

in space. The orbital shapes of the s, p, and d atomic orbitals are well known and can be found in most undergraduate textbooks, but the shapes of the f orbitals are not commonly discussed. These are illustrated qualitatively in Figure 2. It is seen that the individual f orbitals are nonspherical and lie within specific planes and along specific axes. Thus, bonding to f electrons is often considered to be highly directional.

The radial part of the wave function depends only on the distance of an electron from the nucleus, often displayed as a probability distribution. A radial probability distribution is a plot of the statistical probability that a particular electron could be found as a function of distance from the center of

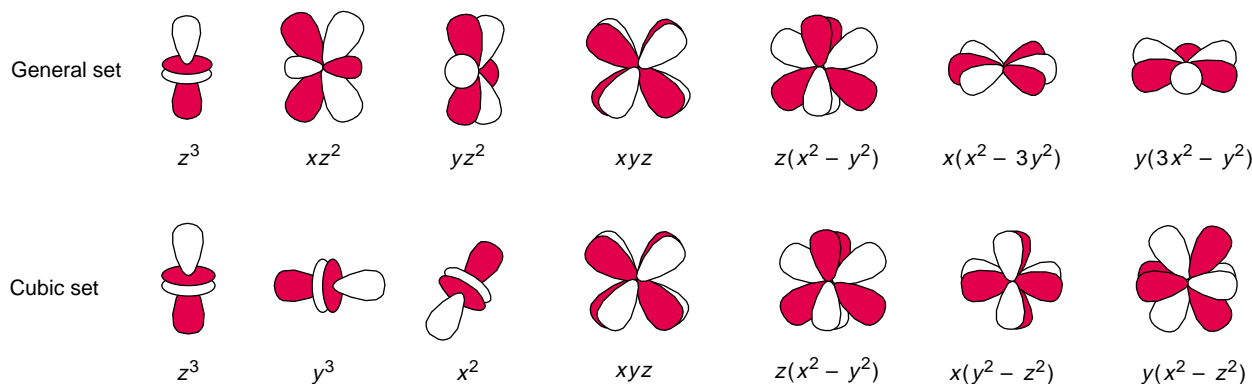


Figure 2. Angular Properties of f Orbitals

The seven f orbitals that arise from solving the Schrödinger equation for a hydrogen-like atom have specific shapes, shown above along with their simplified polynomial designations. The general set of orbitals (top) is useful for understanding molecular complexes or solid structures that contain a single high-order axis of symmetry (where one often finds doubly degenerate orbitals). However, this set is not very useful for solving problems in cubic symmetry because it is not easy to see how these orbitals can be combined to give triply degenerate sets that span the space of cubic point groups. Instead, a cubic set (bottom) can be derived from linear combinations of the general set of orbitals.

the nucleus. In Figure 3, the radial probability distributions of the outer valence electrons for the samarium ion Sm^{3+} (the most common charge of samarium in solution) are plotted and compared with the corresponding radial distributions of Pu^{3+} . These distributions were derived from rigorous, state-of-the-art relativistic calculations performed by Los Alamos researchers (P. Jeffery Hay, unpublished results).

For the samarium ion, the region of space occupied by the 4f electrons is buried deep within the atom. The calculations illustrate in a very qualitative fashion why the 4f electrons of lanthanide elements do not participate in chemical bonding to any great extent; they simply do not extend out far enough from the nucleus to participate in bonding interactions.

The 5f electron density of the plutonium ion, although also concentrated within the principal parts of the valence electron distributions, shows a significant tail. The broad extent of this tail is due in part to relativistic effects. The root-mean-square speed of an orbiting electron scales with the nuclear charge, and electrons in heavy elements (especially the inner s and p electrons in the

core of the atom) can have speeds that approach an appreciable fraction of the speed of light. According to the theory of relativity, such electrons have an effective mass that is heavier than that of a nonrelativistic electron. As a result, the core s and p electrons in heavier elements contract closer to the nucleus compared with those in lighter elements. These contracted s and p electrons are now more effective at shielding some of the nuclear charge from electrons in outer d and f orbitals. Those electrons move farther out from the nucleus. This contraction/expansion influences even the valence electrons.

When relativistic effects are taken into account for Pu^{3+} (the solid curves in Figure 3), we see that the 5f electron density extends well into the region occupied by the 6d electrons. This greater extension from the nucleus is perhaps the major difference between the light actinides and the light lanthanides, for it allows the 5f electrons to participate (in some cases) in covalent bonding interactions.

We can also infer what happens to the f orbitals as more nuclear charge is added, that is, as we move from left to right in the periodic table across a 4f or

5f subshell. Because the 5f orbitals are not spherically symmetric, the nuclear charge is not completely screened by the additional electron. Each successive element, in effect, exhibits a slightly greater charge, with the result that the outer valence orbitals contract. Thus, the ionic radius should gradually decrease as one moves through the actinide series. Such a contraction is observed for the lanthanides and is known as the lanthanide contraction. It amounts to approximately 0.2 angstrom over the entire series, or on average about 0.014 angstrom between elements.

Following the development of Seaborg's actinide concept, it was long thought that the actinides should exhibit a similar contraction. Up until a few years ago, only indirect evidence supported this conjecture (Seth et al. 1995), but we have recently been able to measure the actinide contraction directly. It is approximately 0.04 angstrom from uranium to plutonium, or about 0.02 angstrom between elements. This observation of the actinide contraction is perhaps the most famous example of the actinide concept.

Chemistry of Plutonium in Aqueous Solution

The chemistry of plutonium is important for many reasons, including the processing and purification of plutonium for preparation of the pure metal, for managing our nation's nuclear wastes, for predicting its behavior in the environment, and for predicting the effects of aging on and the safety of nuclear weapons. For example, as discussed in the article "The Chemical Interactions of Actinides in the Environment" beginning on page 392, if plutonium is accidentally released into the environment, its chemical properties will determine to a large extent whether its transport will be retarded by precipitation from solution or sorption to a mineral surface or whether it will migrate freely as a soluble molecular species. During process chemical operations, we control the chemistry in concentrated nitric acid solutions or molten halide salts to obtain the desired oxidation state for further chemical manipulation or the desired chemical purity for manufacturing purposes. (See the article "A Vision for Environmentally Conscious Plutonium Processing" on page 436.) These rather "forced" chemical conditions were historically required for chemical processing because of the complexity of plutonium chemistry.

Because of its electropositive nature, a plutonium atom in aqueous solution will readily lose between three and seven of its outer electrons to form positively charged cations in five formal oxidation states, Pu(III), Pu(IV), Pu(V), Pu(VI), and Pu(VII). (The roman numeral in parentheses refers to the "formal" charge exhibited by the central positive ion.²) Much of the solution chemical behavior of plutonium

²Formal charges can be assigned to each element or ion in a compound. For example, both oxygen, O^{2-} , and the carbonate ion, CO_3^{2-} , are assigned a formal charge of -2 in any compound. Thus, $Pu(CO_3)_5^{6-}$ is a Pu(IV) species, since the plutonium ion has a formal charge of $+4$, and PuO_2^+ is a Pu(V) species, since the plutonium ion has a formal charge of $+5$.

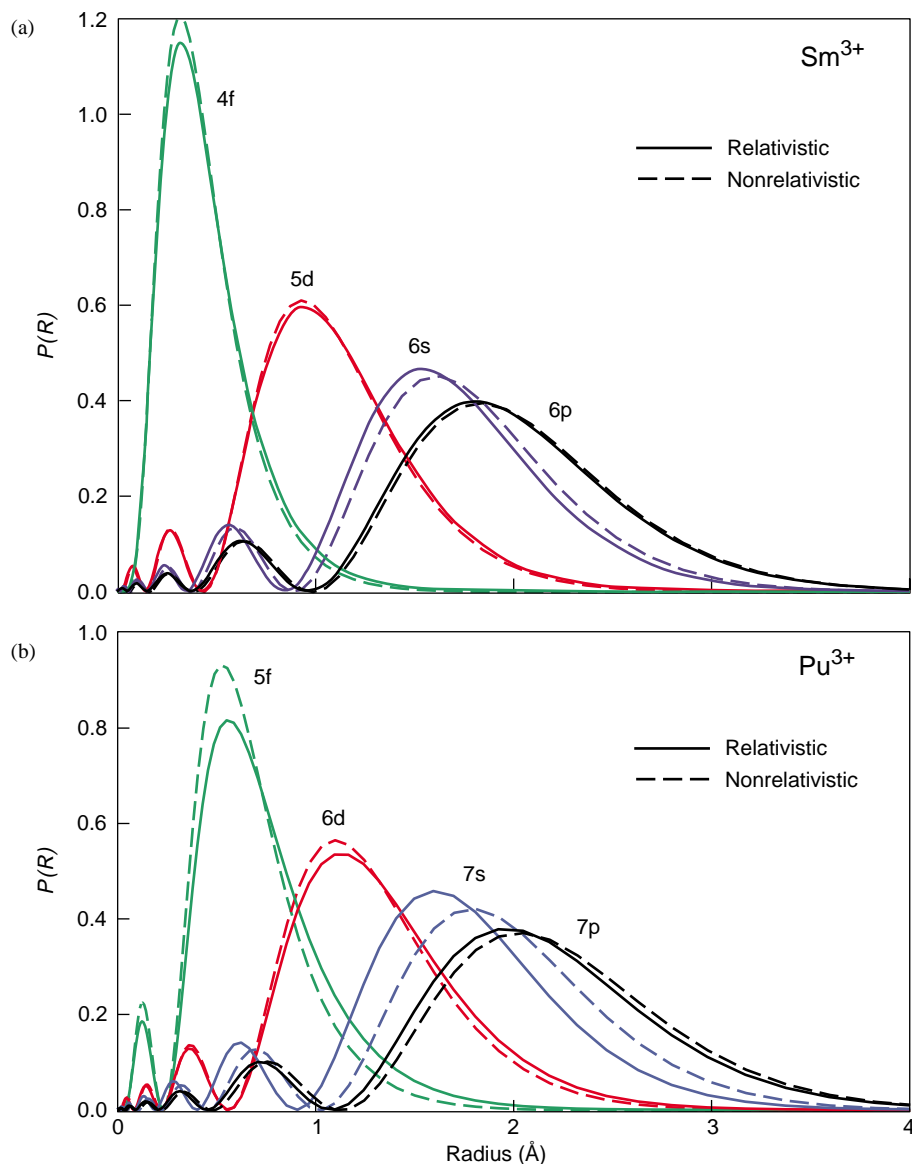


Figure 3. Radial Extent of 4f and 5f Valence Electrons

(a) The radial probability $P(R) = 4\pi r^2 R_n^2$ of finding an electron at a distance r from the nucleus is shown for the valence 4f, 5d, 6s, and 6p orbitals of Sm^{3+} . The solid lines show the probabilities after the inclusion of relativistic effects. The relativistic corrections are of minor importance for 4f elements, and most of the 4f electron density lies close to the nucleus. Bonding to the Sm^{3+} ion takes place by means of electrons occupying the 5d, 6s, or 6p orbitals, and so 4f electrons only marginally influence the chemistry. (b) The analogous figure for Pu^{3+} shows that the tail of the relativistically correct 5f electron distribution extends out much farther from the nucleus than a 4f electron does. In addition, the valence 7s and 7p electrons contract closer to the nucleus when relativistic effects are taken into account. The net effect is that the 5f electrons of the actinides can much more readily participate in bonding than the 4f electrons of the lanthanides. (Calculations courtesy of P. Jeffrey Hay.)

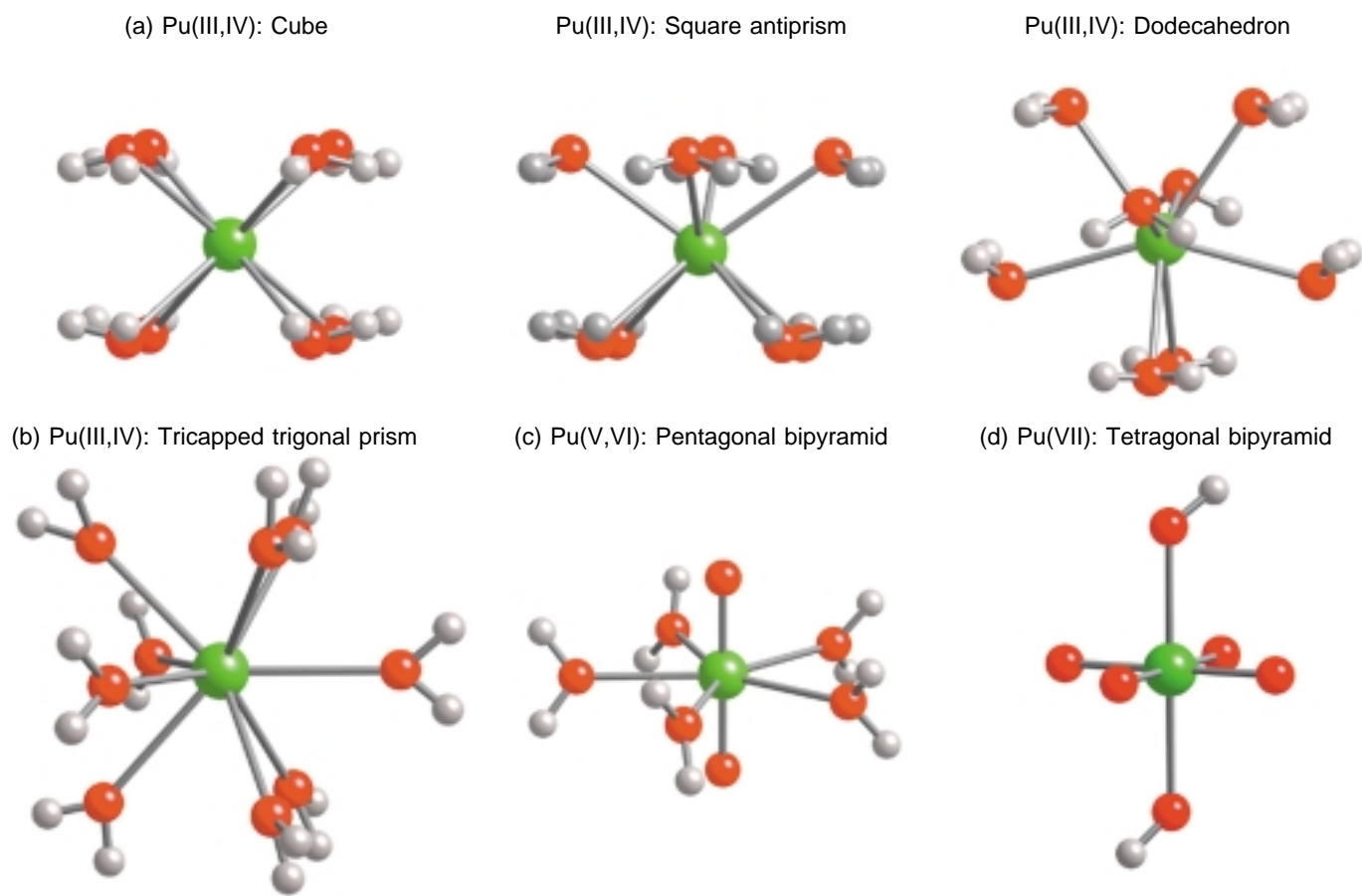


Figure 4. Possible Molecular Geometries for the Plutonium Aquo Ions

(a) Three common geometric arrangements are possible for eight water ligands around a central Pu(III) or Pu(IV) ion: a cube, a square antiprism, and a dodecahedron. A cubic arrangement of ligands is rather rare in molecular chemistry because a simple twist of one square face by 45 degrees gives the square antiprism, which is known to minimize ligand–ligand repulsive forces. The dodecahedron can be viewed as two interpenetrating tetrahedra, one flattened and one elongated with respect to the cube. (b) With nine water ligands, Pu(III,IV) can form the tricapped trigonal prism. Six water molecules are arranged on the top and bottom planes of the vertically oriented right prism. Each of the three molecules in the equatorial plane are centered about one face of the prism. (c) Both the Pu(V) and Pu(VI) aquo ions exist as actinyl ions. Two oxygen atoms form strong covalent bonds with the plutonium to form a linear plutonyl unit, O=Pu=O. All the water molecules bond in the equatorial plane. The actinyl aquo ions typically have five water ligands, and the common geometry is a pentagonal bipyramid. (d) Plutonium VII can form under extreme oxidizing conditions. The $\text{PuO}_4(\text{OH})_2^{3-}$ molecule shown here has a tetragonal bipyramid arrangement; four oxygen atoms form double bonds in the equatorial plane, while the two OH ligands bond along the axis of the bipyramid.

depends on the nature of its oxidation state. The metal ion in each of those states can form a variety of molecular complexes, each with a characteristic solubility and chemical reactivity. In addition, we shall see later that plutonium is the only element in the periodic table that can have appreciable amounts of four different oxidation states existing in aqueous acidic solutions simultaneously.

Under noncomplexing acid conditions (such as perchloric or triflic acid), both Pu(III) and Pu(IV) exist as the simple hydrated (or aquo) ions. Water molecules are coordinated around the metal ion, resulting in the molecular cations $\text{Pu}(\text{H}_2\text{O})_n^{3+}$ and $\text{Pu}(\text{H}_2\text{O})_n^{4+}$, where n can vary depending on the concentration of other ions (the ionic strength). Common values for n are 8, 9, and 10. Aquo ions with eight ligands

are shown in Figure 4(a), while a structure with nine ligands is shown in Figure 4(b).

Both Pu(V) and Pu(VI), have such large positive charges that in aqueous solution they readily strip oxygen atoms from water molecules to form a unique class of *trans*-dioxo cations, PuO_2^+ or PuO_2^{2+} . The plutonium atom is aligned between the two oxygen atoms in a linear structure, O=Pu=O, known as an

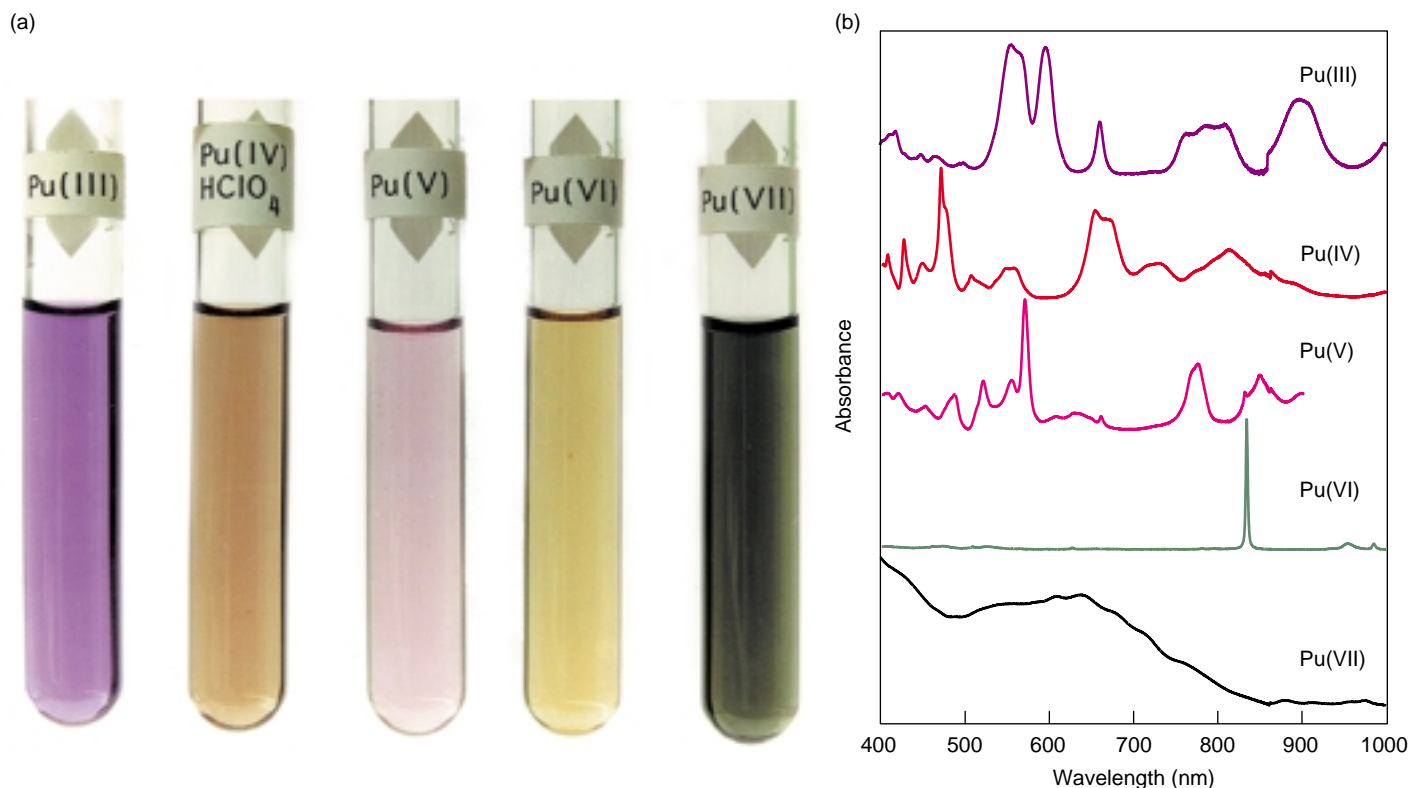


Figure 5. The Color of Plutonium

(a) Each of the plutonium oxidation states has a characteristic color in solution. The colors are specific and depend on the type and number of ligands. The photograph shows the aquo ions in 1 M perchlorate (HClO_4) solution. (Pu(V) is in NaClO_4 at pH = 7, Pu(VII) is in 2.5 M NaOH .) (b) The electronic absorption spectra of the plutonium aquo ions are compared here. (The relative absorbance values are not to scale.) The solution conditions are the same as in (a). Pu(VII) is a relatively rare oxidation state, but it can be formed under alkaline solution conditions. Each oxidation state can be identified by its characteristic absorption fingerprint.

actinyl³, and all ligands (molecules or ions that donate at least one electron pair to a central metal ion) bond in the equatorial plane of this structure. The actinyl geometry is ubiquitous for the V or VI complexes of uranium, neptunium, plutonium, and americium. As discussed later, this geometry is known to be a result of a balance between valence 5f, 6d, and “shallow core” 6p electron interactions within the framework of the linear actinyl ion ($\text{O}=\text{An}=\text{O}$) bonds, where An represents either U, Np, Pu, or Am.

The Pu(V) and Pu(VI) aquo ions $\text{PuO}_2(\text{H}_2\text{O})_n^+$ and $\text{PuO}_2(\text{H}_2\text{O})_n^{2+}$ commonly have five water molecules in the

equatorial plane, as seen in Figure 4(c). Determining the structures of the plutonium aquo ions required a significant, multidisciplinary effort by many Los Alamos researchers. (See the articles “Characterizing the Plutonium Aquo Ions by XAFS Spectroscopy” on page 418 and “Computational Studies of Actinide Chemistry” on page 382.)

The oxidation state of plutonium affects its chemical behavior in solution. For example, Pu(III) and Pu(IV) are, in general, relatively insoluble, whereas Pu(V) and Pu(VI) are, in general, more soluble. These different properties are why knowledge of the oxidation state under environmental conditions is critically important for the long-term performance of underground nuclear waste repositories such as the Waste Isolation Pilot Plant (WIPP) in

New Mexico and the Yucca Mountain Site in Nevada (Hobart 1990). In oxidation state IV, plutonium strongly hydrolyzes (reacts with water), often to form light green “sols,” or colloidal solids that behave much like a solution. These intrinsic colloids eventually age, and the solubility decreases over time. These intrinsic colloids can also attach themselves to natural mineral colloids that have important consequences for the migration of plutonium in the natural environment. The importance of colloid-facilitated transport of plutonium in groundwater at the Nevada Test Site in Nevada was recently underscored when plutonium from underground weapons testing were shown to have migrated just over a mile from the location of an underground test performed over 20 years ago (Kersting et al.

³Actinyl is a general term that can refer to the linear *trans*-dioxo cations $\text{O}=\text{U}=\text{O}$ (also called uranyl), $\text{O}=\text{Np}=\text{O}$ (neptunyl), $\text{O}=\text{Pu}=\text{O}$ (plutonyl), or $\text{O}=\text{Am}=\text{O}$ (americyl).

1999). Colloid-facilitated migration is discussed in the article by McGraw. In contrast, Pu(V) hydrolyses the least of all the oxidation states. At trace (nanomolar) concentrations in near-neutral pH solutions, Pu(V) is both reasonably stable and is the dominant oxidation state under many natural environmental conditions, such as in seawater or many groundwaters (Hobart 1990).

Each of the various plutonium oxidation states has a characteristic color in solution and exhibits a distinctive spectral “fingerprint” in its electronic absorption spectrum, as seen in Figure 5. The electronic spectra are the result of the absorption of visible and near-infrared light by the plutonium molecules in the different solutions. The exact frequency of the photons absorbed by a particular plutonium ion corresponds to the energy required to promote an electron from one f electron energy state to another in that particular oxidation state. Thus, the electronic absorption spectrum is a unique diagnostic research tool for identification of the plutonium oxidation state.

The energy required to add or subtract electrons from an ion (and therefore change from one oxidation state to another) is known as the reduction/oxidation (redox) potential. It is normally expressed in volts. For most elements in the periodic table, the redox potentials between oxidation states are sufficiently different that one state is usually favored over all the others. Plutonium is unique among all elements in that the redox potentials that couple the four common oxidation states in acid solution (III, IV, V, and VI) are all remarkably similar, and approximately equal to 1.0 volt (Katz et al. 1986), as seen in Figure 6(a). The plutonium cations therefore have a marked tendency to react with ions of their own kind by means of a *disproportionation* reaction, in which two interacting ions in the same oxidation state are simultaneously oxidized and reduced to higher and lower states. Conversely, under some conditions, two plutonium ions of

different oxidation states can react by means of a *reproportionation* reaction. The two ions are simultaneously oxidized and reduced to form two ions of the same oxidation state. This redistribution of oxidation states is a messy situation, and one that makes aqueous plutonium solution chemistry particularly complex and fascinating.

To further complicate matters, all plutonium isotopes are radioactive. One milligram of plutonium-239 (radioactive half-life of 2.4×10^4 years) emits about 10^6 alpha particles per second, and the radioactive decay is constantly adding energy to any plutonium solution. The radiolytic decomposition of water can generate some rather potent redox agents, including short-lived radicals $\bullet\text{H}$, $\bullet\text{OH}$, and $\bullet\text{O}$, and radical recombination products such as H_2 , O_2 , and H_2O_2 . The result is that radiolysis tends to reduce Pu(VI) and Pu(V) to the Pu(IV) and Pu(III) states.

Interestingly, the reactions involving the making and breaking of Pu=O bonds in the *trans*-dioxo cations of Pu(V) and Pu(VI) are kinetically slow processes. Therefore, it is possible for four oxidation states (III through VI) to coexist with one another in appreciable concentrations in the same solution under certain chemical conditions.

At present, we understand enough about the kinetics of those reactions to predict how rapidly the redox equilibria are reached (Newton 1975). The rate constants and H^+ dependencies for the equilibrium reactions are all known, and if one considers the forward and reverse rates, the rates of disproportionation and reproportionation reactions can be calculated. Figure 6(b) outlines the calculations, Figure 6(c) plots the equilibrium rate constants, and Figure 6(d) shows graphs of the disproportionation of Pu(IV) in a solution of 1 M NaClO_4 . Appreciable concentrations of the other oxidation states appear after relatively short periods of time, and the rates depend on the total plutonium concentration. At equilibrium, a plutonium solution of approximately pH 1 contains signifi-

cant concentrations of Pu(III), Pu(IV), Pu(V), and Pu(VI).

Clearly, part of the experimental problem faced by plutonium chemists is in obtaining stable, oxidation-state-pure solutions. Years of experience have enabled plutonium scientists to develop electrochemical techniques to prepare such plutonium solutions, which are then used in the synthesis and characterization of molecular complexes (Newton et al. 1986).

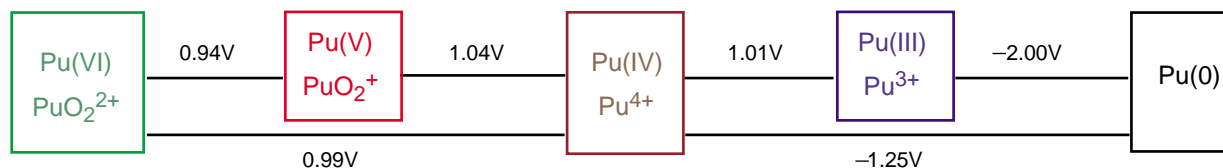
The Complexation and Coordination Chemistry

The molecular science of plutonium is critical to the Laboratory and the Department of Energy (DOE) missions because it provides the technical basis for process and separations chemistry, the fate and transport of plutonium in the environment, the remediation of contaminated soils, and the long-term disposition of legacy materials. The behavior of plutonium under these conditions ultimately depends on the nature of the molecular complexes formed and their resulting electronic and molecular structure. For process chemistry, we care about the chemical behavior of plutonium in strong acids with abundant nitrate, chloride, fluoride, or water ligands. For environmental behavior, we care about the interaction of plutonium with the ligands found in natural waters—carbonate, phosphate, sulfate, and silicate—and with natural organic matter such as humic and fulvic acids. For legacy wastes such as those in the aging waste tanks at the DOE Hanford Site in Washington or Savannah River Site in South Carolina, we care about how plutonium interacts with hydroxides, aluminates, organics, and a myriad other chemical agents formed under the highly alkaline conditions of the tanks.

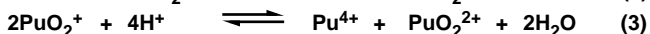
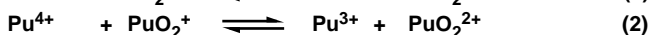
As an example, consider that the molecular behavior of plutonium in nitric acid allows for its chemical purification. In 7 molar nitric acid solution, Pu(IV) exists as a complex

Figure 6. Complications of Plutonium Chemistry

(a) Each of the redox potential differences that separate the primary oxidation states is approximately 1 V. Thus, it is easy for plutonium to change its oxidation state. The figure shows the redox potential differences for the plutonium aquo ions in 1-M perchloric acid, as well as the potential difference between the plutonium aquo ions and the pure metal, Pu(0).



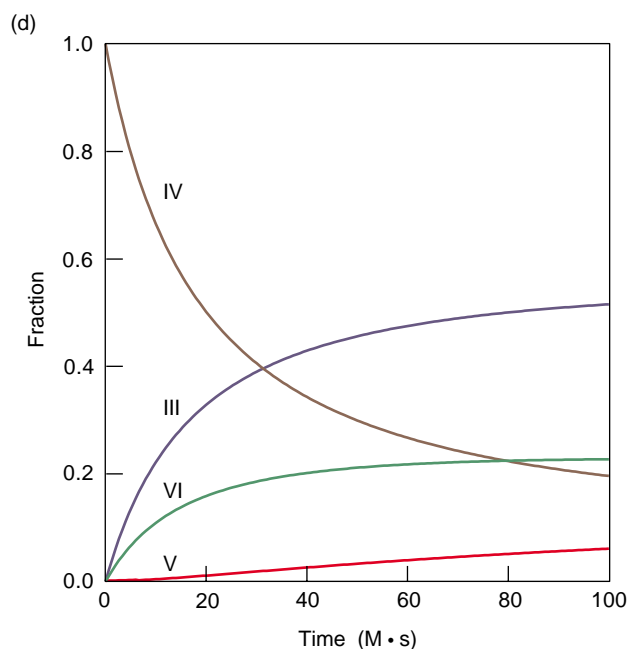
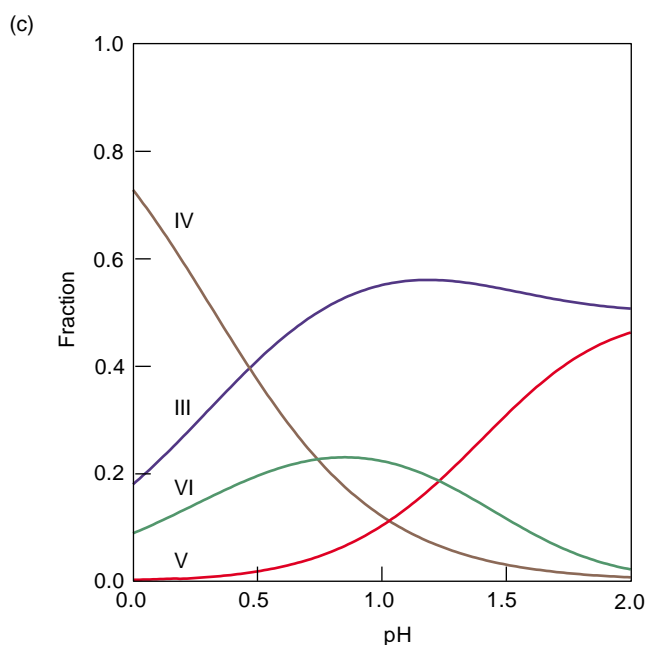
(b) The equations governing the redox reactions for plutonium ions under acidic conditions are



Note that only two of these reactions are independent, as Equation (3) can be derived from Equations (1) and (2). The redox potentials in 1 M perchlorate solutions have been determined with high precision, and they can be used in calculating the equilibrium constants of these reactions as a function of pH if hydrolysis of Pu(IV) is taken into account. Because the hydrogen ion appears in Equations (1) and (3), the equilibrium constants for these reactions are highly dependent on pH.

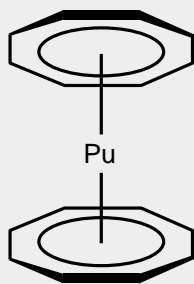
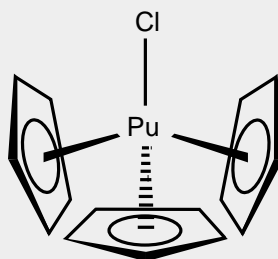
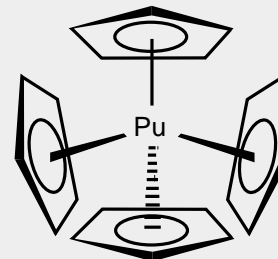
(c) The equilibrium constants, corrected for hydrolysis, were used to calculate the equilibrium distribution curves for plutonium ions in 1 M NaClO₄ solution (assuming an average oxidation state of IV). In the region between pH 1 and 2, the values of the curves are less certain because the second hydrolysis constant for Pu(IV) has been omitted. (Calculations courtesy of T.W. Newton.)

(d) The graph shows the disproportionation of Pu(IV) in 1 M NaClO₄, pH = 1, at 25°C as a function of time (units of molar-seconds). Dividing by the total concentration gives the time required to reach any particular distribution. For an initial Pu(IV) concentration of 0.002 M, half of the IV species will be gone in 10,000 s, or about 3 h.



Organoplutonium Complexes

In nonaqueous solutions, where organoplutonium complexes can be stabilized against reaction with air and moisture, other unique kinds of stereochemistry have been observed. Of historical significance is the Pu(IV) "sandwich" compound, $\text{Pu}(\eta\text{-C}_8\text{H}_8)_2$, known as "plutonocene." The molecular structure has been determined for the uranium analog, and spectroscopic data indicate that a similar structure is present for plutonium. The molecule has rigorous D_{8h} symmetry where the eight-member cyclooctatetraenyl (COT) rings are arranged in an eclipsed conformation. Research at Los Alamos is underway to determine the crystal structure of plutonocene, as part of our "Actinide Molecular Science" competency development project. Other organoplutonium compounds of interest include complexes of the cyclopentadienyl ligand ($\eta\text{-C}_5\text{H}_5$), abbreviated Cp. The COT and Cp ligands are considered to occupy three coordination sites on the Pu(IV) metal center, and as such, $\text{Pu}(\eta\text{-C}_8\text{H}_8)_2$, $\text{Pu}(\eta\text{-C}_5\text{H}_5)_3\text{Cl}$, and $\text{Pu}(\eta\text{-C}_5\text{H}_5)_4$ can be considered as having coordination numbers of 6, 10, and 12, respectively. The Cp ligands are very large indeed, and actinides are among the few elements in the periodic table large enough to accommodate four Cp rings in a multi-hapto (η) bonding arrangement.

 $\text{Pu}(\eta\text{-C}_8\text{H}_8)_2$  $\text{Pu}(\eta\text{-C}_5\text{H}_5)_3\text{Cl}$  $\text{Pu}(\eta\text{-C}_5\text{H}_5)_4$

equilibrium mixture of plutonium molecules containing two, four, and six nitrate ligands: $\text{Pu}(\text{NO}_3)_2^{2+}$, $\text{Pu}(\text{NO}_3)_4$, and $\text{Pu}(\text{NO}_3)_6^{2-}$ (Allen et al. 1996).

The hexanitrate anionic species $\text{Pu}(\text{NO}_3)_6^{2-}$ sorbs strongly to an anion-exchange column, and anion exchange is used to purify large quantities of plutonium every year.

Once the molecular structure of the hexanitrate species was determined, however, Los Alamos researchers were able to molecularly engineer a revolutionary new anion-exchange resin tailored to its molecular properties (Marsh et al. 1997). The sorption of plutonium to this new resin increased by about an order of magnitude. The new resin allows for a more efficient purification process, with significantly less waste and with a smaller facility footprint (see the article "Molecularly Engineered Resins for Plutonium Recovery" on page 454). This technological advance has been critical to the Laboratory's ability to meet future pit production goals. Obviously, our

continued expertise in the molecular science of plutonium will be critical to our future.

The complexation strength is a measure of how effectively a ligand can compete with water in the coordination shell of the aquo ion. In most cases, complex formation involves an exchange of the water molecules with complexing ligands to form *inner-sphere* complexes. Both the ligand and any remaining water molecules are bound directly to the central metal atom. Those kinds of interactions can form very stable complexes. Weaker complexes result when a ligand is bound to the central metal atom by the waters of hydration. Those are called *outer-sphere* complexes.

Plutonium ions are "hard" acids and consequently form strong, inner-sphere complexes with ligands containing oxygen donor atoms and with highly ionic ligands, such as fluorides, chlorides, etc. They also form an extensive series of compounds with oxo anions of nearly every type (CO_3^{2-} , NO_3^- , PO_4^{3-} ,

etc.), many of which are common in natural waters. Furthermore, plutonium ions form complexes of moderate strength with nitrogen donors and weak, outer-sphere complexes with sulfur donor ligands. They also show a special stability for chelating ligands with oxygen and nitrogen donor atoms.

The relative tendency of plutonium to form complexes is dependent on its charge-to-ionic-radius ratio. Because the ionic radii of the four common oxidation states are of similar magnitude, the stability of the complex parallels the overall charge of the central plutonium ion or of the actinyl ion:



Pu^{4+} forms the strongest complexes and PuO_2^+ forms the weakest. It should be noted that the actinyl cations, PuO_2^+ and PuO_2^{2+} , form complexes that are stronger than would be expected when compared with monovalent and divalent cations of lighter elements.

Plutonium ions have relatively large

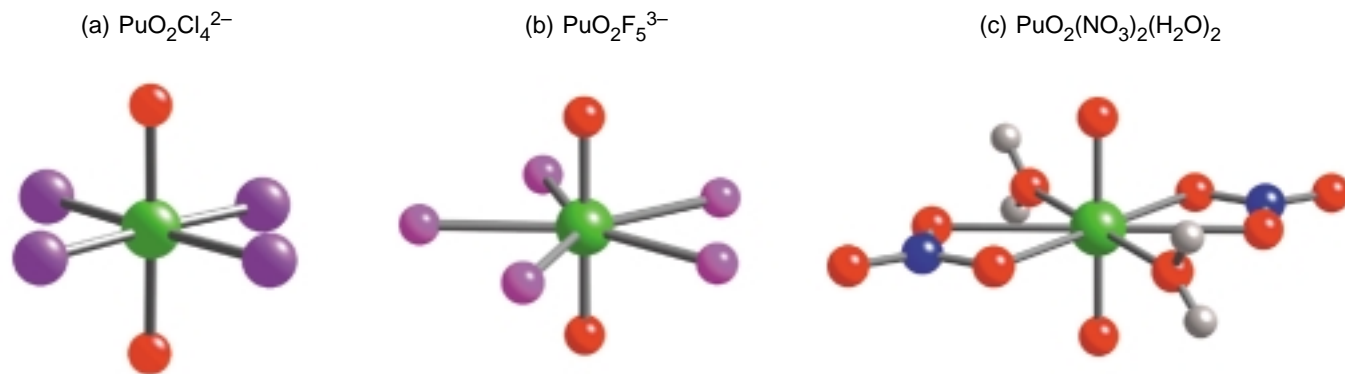


Figure 7. Structural Motifs of Pu(V) and Pu(VI)

In aqueous solution, Pu(V) and Pu(VI) complexes are nearly always actinyl ions. The linear O=Pu=O unit forms the axis of a tetragonal, pentagonal, or hexagonal bipyramid. (a) The tetragonal bipyramid structure is usually seen for large, monodentate ligands such as Cl^- . The $\text{PuO}_2\text{Cl}_4^{2-}$ ion has a coordination number of 6. (b) Smaller monodentate ligands such as F^- and OH_2 favor the pentagonal bipyramid. The $\text{PuO}_2\text{F}_5^{3-}$ ion has a coordination number of 7. (c) Hexagonal coordination in an equatorial plane is usually only seen for bidentate ligands. The two nitrate ligands bond in a bidentate fashion in $\text{PuO}_2(\text{NO}_3)_2(\text{H}_2\text{O})_2$, while the two water ligands are monodentate. The complex has a coordination number of 8.

ionic radii, so that many ligands can fit around them. They also can exhibit high oxidation states and have a large number of valence shell orbitals available for bonding. As a result, many donor atoms will bond to the central plutonium ion, and so coordination numbers of 8 and 9 appear to be very common in plutonium complexes. However, the actual number of molecular structures that have been determined for plutonium compounds is quite small. Due to the technological importance of water-based solvent extraction, ion-exchange, and precipitation processes needed to prepare plutonium for reduction to the metallic state, almost all of the structures have been deduced in aqueous solution. Some studies, however, have been performed on plutonium complexes in nonaqueous solutions. (See the box “Organoplutonium Complexes.”)

Perhaps the most work to date has been performed on V and VI oxidation states, where the actinyl ions are nearly always observed. The overall pattern is always one in which the linear unit O=Pu=O forms the axis of a tetragonal, pentagonal, or hexagonal bipyramid, as indicated schematically in Figure 7. The tetragonal bipyramid is seen for

large monodentate (single donor) ligands such as Cl^- , while smaller monodentate ligands such as F^- and OH_2 favor the pentagonal bipyramid. Hexagonal coordination in an equatorial plane is usually seen only for bidentate (two-donor) ligands such as NO_3^- , CO_3^{2-} , RCO_2^- , etc., or where a combination of monodentate and bidentate ligands are used, such as $\text{PuO}_2(\text{NO}_3)_2(\text{OH}_2)_2$.

Historically, the molecular structures of plutonium compounds have been inferred based on analogy with uranium, and only a handful of plutonium molecular structures have actually been determined. To help illustrate this point, we bring to your attention that at the time of this writing, the two major international crystal structure databases (The Cambridge Structural Database and the Inorganic Crystal Structure Database) combined contained 1072 molecular structures for uranium and only 81 for plutonium, many of which were duplicates. The structures shown in Figure 7 were only deduced within the past several years.

Advances in our understanding of plutonium molecular science over the last decade can be attributed, in part, to the development and application of

many new techniques that can characterize chemical species, including photoacoustic spectroscopy (PAS), photothermal lensing (PTL), laser-induced fluorescence (LIF) spectroscopy, x-ray absorption fine structure (XAFS) spectroscopy, x-ray and neutron diffraction, laser resonance ionization mass spectroscopy, improved trace analyses, combined extraction methods, and nuclear magnetic resonance (NMR) spectroscopy. Some of these tools will be highlighted in the next section, which discusses an example of our most recent molecular-level structural studies of anionic carbonate complexes of plutonium ions.

Modern Studies in Plutonium Chemistry

To better illustrate how the various chemical properties, modern structural tools, and present understanding of the nature of chemical bonding come into play, I will discuss a current example of molecular studies on carbonate complexes of Pu(VI) and the motivation for the work. Carbonate and bicarbonate are common anions present in significant concentrations in many

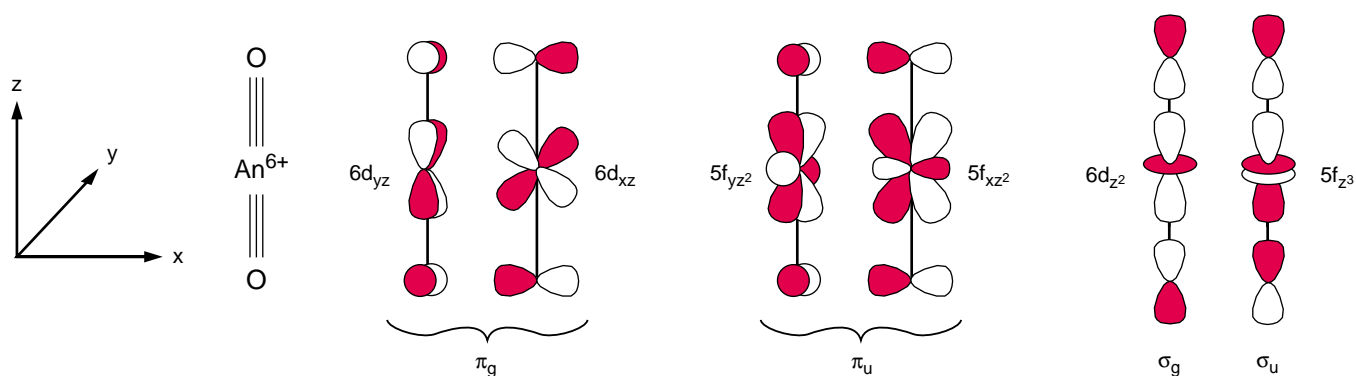


Figure 8. Bonding within the AnO_2^{2+} Cation

Twelve valence electrons participate in bonding the central actinide ion to the two oxygen atoms within the actinyl unit. Those electrons occupy six molecular orbitals so that, formally, a triple bond exists between the actinide and each oxygen. Each molecular orbital is a linear combination of either 6d or 5f atomic orbitals of the actinide and the 2p atomic orbitals of the oxygen atoms. The two π_g molecular orbitals, for example use the $6d_{yz}$ and $6d_{xz}$ atomic orbitals, respectively, whereas the π_u molecular orbitals use the $5f_{yz^2}$ and $5f_{xz^2}$. The designations of the molecular orbitals indicate the electron distribution and parity. The electron density in the orbitals is concentrated on either side of an imaginary line connecting the three nuclei. The subscript g refers to inversion symmetry (positive parity) about the origin, whereas u refers to an antisymmetric (negative parity) state. The electron density in the σ orbitals is concentrated along the line connecting the nuclei.

natural water environments (Clark et al. 1995). They are exceptionally strong complexing agents for plutonium and the actinide ions in general. Ions that normally exhibit quite low solubilities in near-neutral solutions can be complexed by carbonate ligands and (through the formation of anionic complexes) become much more soluble. Therefore, carbonate complexes may play an important role in the migration of plutonium ions from a nuclear waste repository or an accidental site contamination. The environmental behavior of plutonium carbonate complexes will ultimately depend on their molecular scale structure and properties, and as such, it is of intrinsic interest to determine the coordination chemistry and molecular behaviors of these complexes.

As mentioned earlier, Pu(VI) will exist in aqueous solution as an actinyl ion. These cations are remarkably stable. They show a high degree of covalency and chemical inertness with respect to the axial $\text{An}=\text{O}$ bonds, yet a relatively low degree of covalency with respect to the ligands in the equatorial plane. Recent developments in both theory and spectroscopy have helped to elucidate the nature of the chemical bond in the linear actinyl ions. Several

fundamental differences exist between the spatial extent, orbital energetics, and diffuse nature of valence and nonvalence atomic orbitals of the light actinides relative to transition metals that give rise to this unusual chemical bonding.

For a transition metal ion in an octahedral ligand field, the metal center can use one valence s (a_{1g}), three p (t_{1u}), and two d (e_g) atomic orbitals to form six metal–ligand σ bonds, and the remaining three d (t_{2g}) orbitals can be used for π interactions. In contrast, we now recognize that the valence 7s and 7p orbitals of the light actinides are far too diffuse for formation of chemical bonds, and this fact accounts for many of the differences in bonding between actinide and transition-metal ions.

The linear actinyl ions, AnO_2^{2+} , have a nominal $\sigma_g^2\pi_g^4\sigma_u^2\pi_u^4$ electronic configuration and a formal $\text{An}\equiv\text{O}$ triple bond (Denning 1992). In the linear configuration, strong, covalent interactions are observed through the formation of $\text{An } 6d-\text{O } 2p$ and $\text{An } 5f-\text{O } 2p$ π bonds, and the underlying 6s and 6p closed shells are semiactive in σ bonding. The $\text{An}-\text{O } \pi_g$ and π_u multiple bonding orbitals derived from 6d and 5f atomic orbitals are shown in Figure 8. The use

of 5f orbitals in π bonding only takes place at the very short bond distances seen in $\text{An}=\text{O}$ bonds, which span 1.74 to 1.80 angstroms. Because the virtual 7s and 7p orbitals are essentially unavailable for bonding, equatorial metal–ligand σ bonding can only take place through the use of the few remaining 6d or 5f orbitals in the equatorial plane. Hence, equatorial bonding is quite weak. This picture of the electronic structure explains the strong, multiple, covalent bonds in the axial direction and the weak, relatively ionic bonds in the equatorial plane.

The plutonyl(VI) carbonate system can also be quite complicated in that it consists of several different complex ions in equilibrium with one another and with the aquo ion or hydrolyzed species, depending on solution conditions. Under dilute solution conditions, compounds of composition $\text{PuO}_2(\text{CO}_3)$, $\text{PuO}_2(\text{CO}_3)_2^{2-}$, and $\text{PuO}_2(\text{CO}_3)_3^{4-}$ have all been reported (Clark et al. 1995). Our approach toward understanding this problem was to focus our initial attention on the identity of the limiting complexes formed in this system. Understanding the limiting structure can then provide a starting point for identifying the other complexes formed in

the equilibrium. Hence, efforts were focused on solution conditions that favor the limiting anionic $\text{PuO}_2(\text{CO}_3)_3^{4-}$ complex (Clark, et al. unpublished results).

We used our knowledge of plutonium redox behavior and kinetics to prepare oxidation-state-pure solutions of Pu(VI), and the oxidation state purity was monitored using electronic absorption spectroscopy, by monitoring the intensity of the 830-nanometer absorption band (as seen in Figure 5). Complexation of Pu(VI) by carbonate subsequently stabilizes Pu(VI) against redox disproportionation. Electronic absorption and carbon-13 NMR spectroscopy were used to follow the chemistry and to confirm that our chemical conditions favored a single species in solution. Next, we employed the guanidinium counter cation $\text{C}(\text{NH}_2)_3^+$ to form hydrogen bonds to the carbonate ligand in solution and thereby grow single crystals of $[\text{C}(\text{NH}_2)_3]_4[\text{PuO}_2(\text{CO}_3)_3]$ suitable for x-ray diffraction analysis. One of these single crystals was carefully selected, triply contained for radiological safety, and mounted on the goniometer of an x-ray diffractometer where it was studied by x-ray diffraction. We used a state-of-the-art charge-coupled-device area detector capable of acquiring a full hemisphere of data in only a few hours. This rapid data collection is very helpful for determining the structures of plutonium compounds because the alpha radiolysis of the crystal can damage crystallinity over time, leaving us with an amorphous, nondiffracting solid. The atom positions were determined by routine computational procedures.

A thermal ellipsoid drawing that shows the molecular structure of the $\text{PuO}_2(\text{CO}_3)_3^{4-}$ ion is shown in Figure 9(a). The central $\text{PuO}_2(\text{CO}_3)_3^{4-}$ ion displays a hexagonal bipyramidal coordination geometry where three bidentate carbonate ligands lie approximately in a hexagonal plane and two oxo ligands occupy coordination sites above and below the plane. Guanidinium cations (not shown) form outer-sphere hydrogen bonds with the CO_3^{2-} ligands and

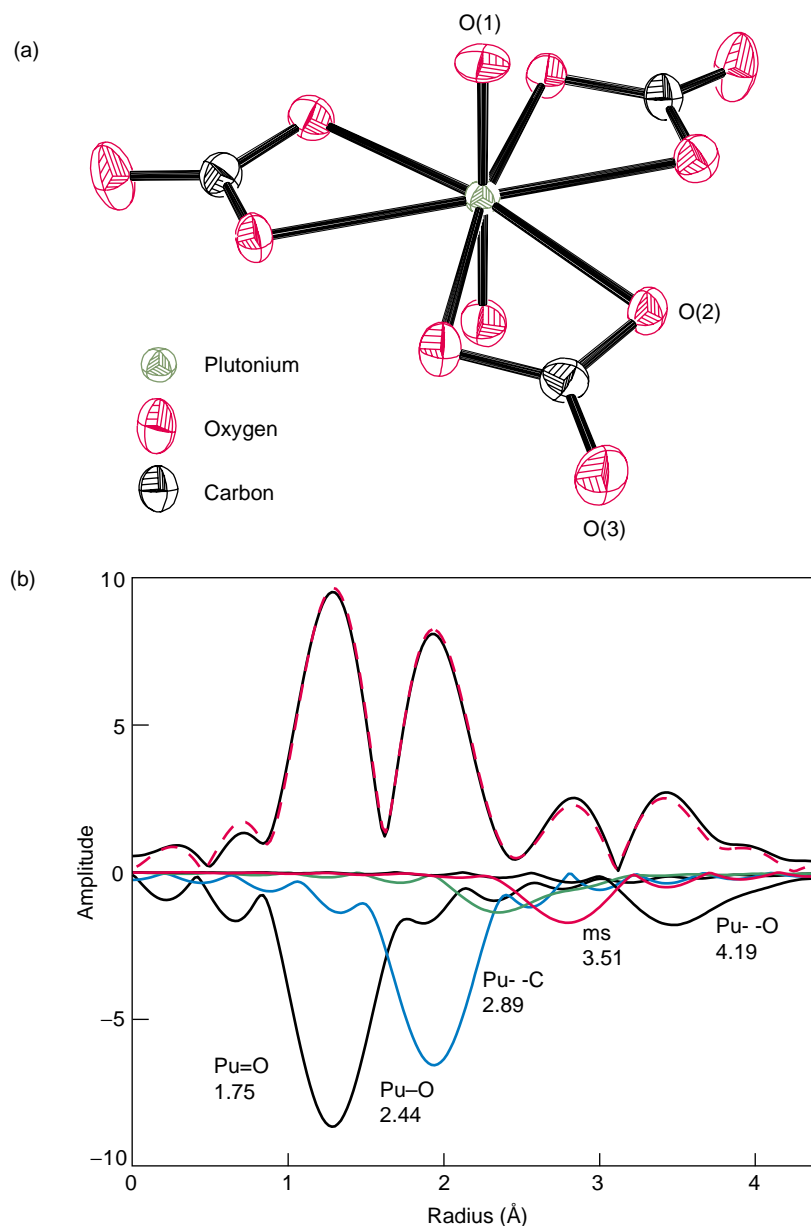


Figure 9. Limiting Structure of Pu(VI) in Carbonate Solution

(a) The structure of the $\text{PuO}_2(\text{CO}_3)_3^{4-}$ anion in the solid state was determined by x-ray crystallography. This thermal ellipsoid drawing emphasizes the pseudo-hexagonal-bipyramidal coordination geometry about the central plutonium metal ion. (The ellipsoids are indicative of the excursions of the atoms due to thermal motion.) A bond length of 1.75(1) Å was measured to the “-yl” oxygen O(1) and 2.44 Å to the nearest-neighbor oxygen atoms O(2) of the carbonate ligand. (b) The structural parameters of the limiting Pu(VI) complex in 2.5 M Na_2CO_3 solution was determined by XAFS spectroscopy. The figure shows the Fourier transform of the XAFS spectrum (solid black line) and the theoretical fit (dashed red line). The components of the fit, shown beneath the spectrum with negative amplitudes, correspond to individual shells of atoms. (There are no atoms at 3.51 Å [twice the Pu=O distance]. The peak labeled “ms,” which is routinely observed in the XAFS data of actinyl ions, is due to multiple scattering of a photoelectron off the oxygen atoms in the linear actinyl unit.) The radii of the coordination shells of the limiting structure in solution match the solid-state structure, and we conclude that the $\text{PuO}_2(\text{CO}_3)_3^{4-}$ anion is the limiting Pu(VI) species in carbonate solution.

form an extensive hydrogen-bonding network that links the molecules together in a three-dimensional array.

We also determined the structures of the uranium and neptunium analogs. For the axial An=O bonds in isostructural compounds, one can observe a relatively smooth decrease in bond distance from 1.79(1) to 1.77(1) to 1.75(1) angstroms for uranium, neptunium, and plutonium compounds, respectively. This bond length shortening is an experimental manifestation of the actinide contraction. For the equatorial An–O distances to the carbonate ligand, the distances are essentially identical at 2.45(1) angstroms for uranium and 2.44(1) angstroms for neptunium and plutonium.

We then employed solution x-ray absorption fine structure (XAFS) spectroscopy to determine the structural details of the limiting Pu(VI) complex in solution. Samples were synthesized and characterized as before to confirm the sample composition before XAFS analysis. Plutonium solutions were packaged in specially designed sample cells with three layers of radiological containment, then shipped to the Stanford Synchrotron Radiation Laboratory (SSRL). Electronic absorption spectra of the solution examined both before and after XAFS analysis indicated that the same limiting Pu(VI) species was present in excess of 99 percent. The XAFS Fourier transforms show four well-resolved peaks whose qualitative assignment based on the monomeric structure observed in the solid state is straightforward. A representative solution Fourier transform spectrum of $\text{PuO}_2(\text{CO}_3)_3^{4-}$ is shown in Figure 9(b). Curve fitting revealed peaks at 1.75(1), 2.44(1), 2.89(1), and 4.19(3) angstroms, which may be identified as distances from the plutonium to the plutonyl oxygens, the six carbonate oxygens in the equatorial plane, and the carbonate carbon and distal oxygen atoms, respectively. A well-established O=Pu=O multiple-scattering peak is seen at 3.51 angstroms in both spectra. The close spacing of Pu–O and Pu–C

shells generates the appearance of a single peak in the XAFS Fourier transform.

These studies prove the identity of the $\text{PuO}_2(\text{CO}_3)_3^{4-}$ ion as the limiting complex in the system and provide structural data for comparison of structural trends across the series uranium, neptunium, and plutonium. Additional studies at more near-neutral pH values indicate that both uranium and neptunium can form monomeric $\text{AnO}_2(\text{CO}_3)_2^{2-}$ or trimeric $(\text{AnO}_2)_3(\text{CO}_3)_6^{6-}$ complexes (Clark et al. 1995, Allen et al. 1995). Plutonium, however, does not appear to form the trimeric complex (Mary P. Neu and Sean D. Reilly, unpublished results). That result indicates that there are some fundamental differences between uranium, neptunium, and plutonium chemistry.

Concluding Remarks— Plutonium Chemistry in the New Millennium

In the above discussions I have tried to provide a fairly general overview on the complexities of plutonium chemistry in aqueous solutions. Its radioactivity and redox instabilities give solutions that are constantly changing and evolving. The nature of the oxidation state is crucial for understanding and predicting the behavior of plutonium, with implications for behavior in the environment, in waste matrices, in aging storage tanks, and in our daily process chemical operations. Over the years, we have learned to control these redox states by complexation with a variety of ligands. Some of these ligands, such as the nitrate anion, have played a historically significant role in the processing and purification of plutonium over the last 50 years. Other ligands, such as the carbonate anion, are omnipresent in natural groundwaters and play a dominant role in the fate and transport of plutonium in the natural environment. In more recent times, we have begun to recognize that ligands such as hydroxide and aluminate will

play a significant role in the behavior of plutonium under the conditions present in aging waste tanks. Hence, a fundamental understanding of the molecular behavior of plutonium in its various oxidation states is critical to understanding, predicting, and manipulating plutonium in groundwaters, contaminated soils, nuclear waste repositories, spent nuclear fuels, aging waste tanks, and the large-scale process streams used in reprocessing and purification. Many of our advances in plutonium molecular science were made through the application of new research tools to probe all aspects of the molecular and electronic structure of these complexes. Indeed, in some cases, the development of new tools (such as PAS) was driven by the need to study plutonium under the extremely low concentrations anticipated in the natural environment.

Now that we have obtained this new knowledge about fundamental molecular-level plutonium behavior, we can look forward to a future in which we can apply our improved molecular understanding toward more efficient chemical processes. Imagine a “zero effluent” nuclear facility in the future, based on new, molecularly engineered plutonium compounds and total recycle of environmentally benign designer solvents. This concept is closer to becoming reality than one might think. For example, the French already have a “zero effluent” nuclear facility at Valduc based on molecular waste polishing processes. I imagine that changing regulatory requirements will force the United States to modify its current processes in the near future. Historically, we developed a nitrate anion-exchange process for plutonium purification, then spent decades working out the fundamental understanding of how the process actually worked. Another decade of effort focused on optimizing the process through molecularly engineered ion-exchange processes and through nitric acid recycle or destruction. Is molecular science important for the future of Los Alamos? The answer is a very clear and undeniable

yes! Faced with constantly changing regulatory requirements, I predict that we will be forced to identify better, more efficient, and more environmentally friendly processes as we enter the new millennium.

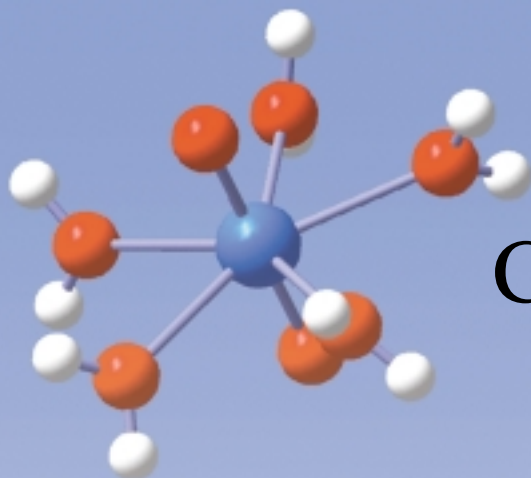
At this stage, I would like to share my own vision of a futuristic plutonium facility at Los Alamos in the next millennium. My personal view is that we could use our molecular-level understanding of carbonate complexation as the scientific foundation for a brand-new plutonium flowsheet. Imagine a process in which a highly stable anionic carbonate complex is purified on a molecularly engineered ion-exchange resin tailored for the unique molecular structure of the *trans*-dioxo ion. After recovery of the plutonium, the complex can be gently destroyed to release carbon dioxide and water as the only effluent. The carbon dioxide and water can be readily recycled to regenerate the carbonate ligand, thereby eliminating altogether the regulatory issues concerning high-nitrate waste streams leaving the Laboratory. In a subsequent process, I can envision the reduction of purified plutonium to the metallic state, not in a high-temperature molten-salt flux with its associated quantities of radioactive salt waste, but rather at an electrode surface at room temperature using a molecularly engineered room-temperature ionic liquid. I truly believe that such revolutionary approaches in the way we accomplish our mission are coming soon and are limited only by our courage and imagination. ■

Further Reading

- Allen, P. G., J. J. Bucher, D. L. Clark, N. M. Edelstein, S. A. Ekberg, J. W. Ghodes, and E. A. Hudson et al. 1995. *Inorg. Chem.* **34**: 4797.
- Allen, P. G., D. K. Veirs, S. D. Conradson, C. A. Smith, and S. F. Marsh. 1996. *Inorg. Chem.* **35**: 2841.
- Clark, D. L., D. E. Hobart, and M. P. Neu. 1995. *Chem. Rev.* **95**: 25.
- Clark, D. L., S. D. Conradson, M. P. Neu, P. D. Palmer, B. L. Scott, and C. D. Tait. Unpublished results.
- Cleveland, J. M. 1979. *The Chemistry of Plutonium*. LaGrange Park, IL: American Nuclear Society.
- Denning, R. G. 1992. *Structure and Bonding.* **79**: 215.
- Hobart, D. E. 1990. *Proc. Robert A. Welch Found. Conf. Chem. Res.* **34**: 379.
- Katz, J. J., G. T. Seaborg, and L. R. Morss, eds. 1986. *The Chemistry of the Actinide Elements*. London: Chapman and Hall.
- Kersting, A. B., D. W. Efurud, D. L. Finnegan, D. J. Rokop, D. K. Smith, and J. L. Thompson. 1999. *Nature*. January issue. **397**: 56.
- Marsh, S. F. 1997. *React. Funct. Polym.* **35**: 75.
- Newton, T. W. 1975. *The Kinetics of Oxidation-Reduction Reactions of Uranium, Neptunium, Plutonium, and Americium in Aqueous Solutions*. ERDA Critical Review Series. ERDA Technical Information Center. Oak Ridge, TN.
- Newton, T. W., D. E. Hobart, and P. D. Palmer. 1986. *The Preparation and Stability of Pure Oxidation States of Neptunium, Plutonium and Americium*. Los Alamos National Laboratory document LA-UR-86-967.
- Seaborg, G. T. 1994. In *Handbook on the Physics and Chemistry of Rare Earths*. Vol. 18. *Lanthanides/ Actinides: Chemistry*. K. A. Gschneidner, Jr., L. Eyring, G. R. Choppin, G. H. Lander, eds. Amsterdam: Elsevier Science.
- Seaborg, G. T. 1978. ed. *The Transuranium Elements—Products of Modern Alchemy*. Stroudsburg, PA: Hutchinson Ross Publishing.
- Seaborg, G. T. and W. D. Loveland. 1990. *The Elements Beyond Uranium*. New York: John Wiley & Sons.
- Seth, M., M. Dolg, P. Fulde, and P. Schwerdtfeger. 1995. *J. Am. Chem. Soc.* **117**: 6597.



David Clark received a B.S. in chemistry in 1982 from the University of Washington, and a Ph.D. in inorganic chemistry in 1986 from Indiana University. His thesis work garnered the American Chemical Society's Nobel Laureate Signature Award for the best Ph.D. thesis in the United States. Clark spent a year as a Science and Engineering Research Council (SERC) post-doctoral fellow at the University of Oxford before coming to Los Alamos as a J. Robert Oppenheimer Fellow in 1988. He became a Laboratory staff member in 1989. He is currently director of the Glenn T. Seaborg Institute for Transactinium Science, where he coordinates actinide science across the Laboratory; adjunct professor of chemistry at the University of Alabama; adjunct research professor at the University of New Mexico; and a consulting faculty member at Stanford Synchrotron Radiation Laboratory. He has authored over 90 publications in refereed journals in addition to encyclopedia chapters and review articles on a wide variety of topics including metal alkoxides, organoactinide chemistry, actinide coordination chemistry, behavior of actinides in the environment, and electronic structure and bonding in inorganic compounds.



Computational Studies of Actinide Chemistry

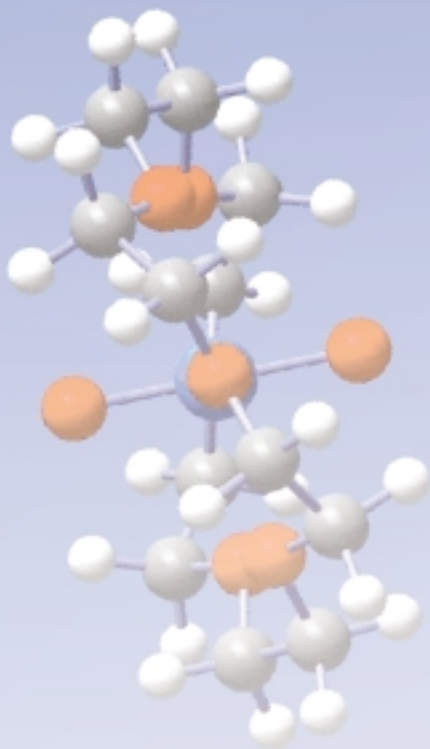
P. Jeffrey Hay and Richard L. Martin

The electronic properties of organic and inorganic molecules can now be calculated from first principles with far greater reliability than has ever been possible. Recent advances in both theory and computation are at the heart of this change. Our Los Alamos group and scientists at other institutions as well have applied the methodology for calculating electronic structure to molecules containing actinide elements. From electronic-structure calculations, one can also compute other molecular properties that can be compared with experimental observations or that can provide information whenever experimental data are absent.

These molecular properties and the corresponding techniques used in determining them experimentally are listed in Table I. For more information on molecular properties, see the articles “The Chemical Complexities of Plutonium” and “XAFS” on pages 364 and 422, respectively.

The ability to perform quantum mechanical calculations on actinide molecules of reasonable size is the result of several factors: steady progress in techniques for solving the molecular Schrödinger equation, tractable approximations to treat relativistic effects, and new approaches in density functional theory (DFT) for calculating properties of chemical interest. We will discuss these issues in greater detail in the next section, but here we will note that the 1998 Nobel Prize in Chemistry recognized the convergence of traditional quantum chemical methodology and DFT. The recipients were John Pople, a pioneer in the development of quantum chemical techniques embodied in the Gaussian electronic-structure codes, and Walter Kohn, one of the founders of DFT.

In the section “Application to Actinyl Species,” we illustrate the use of molecular electronic structure calculations on actinide species by examining the series of molecules $\text{AnO}_2(\text{H}_2\text{O})_5^{2+}$ for the actinide elements (An) uranium, neptunium, and plutonium. Finally, we give an example of an actinide complex, $\text{NpO}_2(18\text{-crown-6})^+$, involving an organic ligand to show how DFT enables the study of large molecules containing actinides.



Theoretical and Computational Developments

The first approximation made in treating the quantum mechanics of a set of electrons interacting with a set of nuclei is to “decouple” the electronic motion from the nuclear motion. This is usually a very good approximation because the electrons are much lighter than the nuclei and nearly “immediately” adjust their motion to a

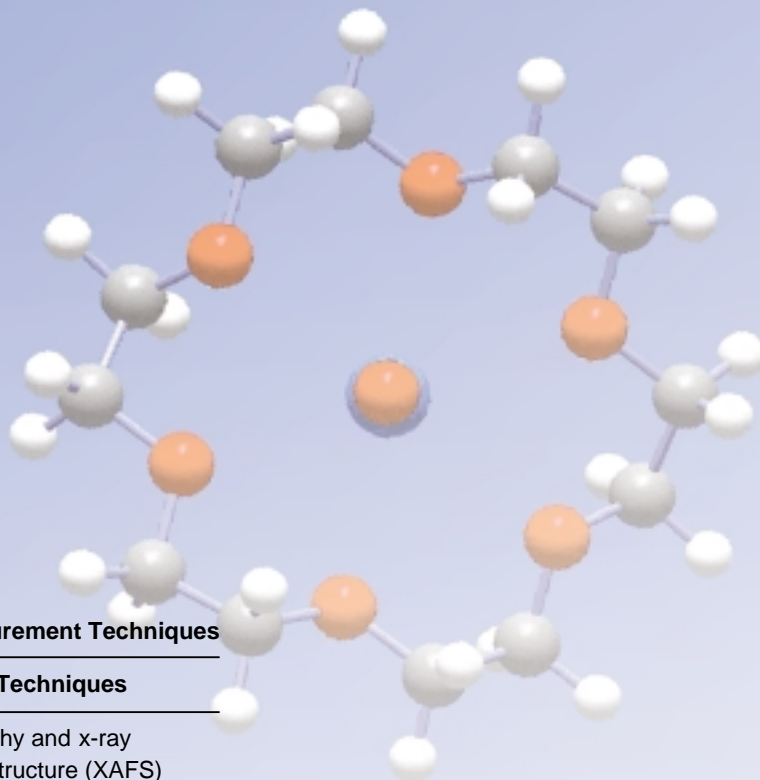


Table I. Molecular Properties and Corresponding Measurement Techniques

Molecular Properties	Measurement Techniques
Bond lengths and angles	X-ray crystallography and x-ray absorption fine-structure (XAFS) spectroscopy
Molecular vibrations	Infrared and Raman spectroscopy
Bond energies and reaction energies	Thermochemical measurements
Activation barriers	Kinetic measurements
Nuclear chemical shifts	Nuclear magnetic resonance (NMR) spectroscopy
Excited electronic states	Visible and ultraviolet spectroscopy

change in the position of the nuclei. We can then write an expression for the electronic energy of the electrons in the fixed electrostatic field of the nuclei:

$$E_e(\mathbf{R}) = E_{\text{kin}} + E_{\text{elec-nuc}} + E_{\text{elec-elec}} \quad (1)$$

The energy $E_e(\mathbf{R})$ is written as a function of the fixed nuclear coordinates \mathbf{R} , where $\mathbf{R} = (\mathbf{R}_1, \mathbf{R}_2, \dots, \mathbf{R}_N)$ represents the coordinates of all the nuclei in the molecule. The succeeding terms in Equation (1) represent the kinetic energy of the electrons, the attractive interaction between the electrons and the nuclei, and the electron-electron repulsion energy. It is interesting to note that the decoupling of the electronic motion from the nuclear motion is known as the Born-Oppenheimer approximation. It was first introduced by J. Robert Oppenheimer, later to become the first director of Los Alamos, and Max Born, the German physicist and Oppenheimer's postdoctoral advisor (Born and Oppenheimer 1927).

Wave Function Approaches. There are two conceptually distinct approaches to determining the electronic energy in Equation (1): the wave function method and DFT.

In the wave function approach, the electronic Hamiltonian corresponding to the set of electrons and fixed nuclei is written down, and one attempts to solve the Schrödinger equation. The solution, the many-electron wave function, describes the motion of the electrons. It is a function of $3n$ -variables— x , y , and z —for each of the n electrons in the molecule. Given the many-electron wave function, evaluating the energy and other molecular properties is a straightforward but not a simple process.

The most-basic wave function approximation is to assume that the many-electron wave function is a simple product of one-electron wave functions. This approximation is equivalent to assuming that the motion of each electron is independent of the motion of all the other electrons. As a consequence, an electron feels only the average Coulomb repulsion energy associated with the electron-electron repulsion. The electrons are said to be “uncorrelated” because each is unaware of the detailed positions of the other electrons at any time. Only their average position is felt.

Things are actually a little more complicated because the quantum mechanical requirement that electrons obey Fermi statistics dictates certain symmetry properties when the positions of two electrons are exchanged. This symmetry is satisfied when the simple, independent particle product is generalized to a Slater determinant:

$$\Psi_{\text{tot}}(\mathbf{r}_1, \mathbf{r}_2, \dots, \mathbf{r}_n) = |\Psi_1(\mathbf{r}_1)\Psi_2(\mathbf{r}_2)\dots\Psi_n(\mathbf{r}_n)| \quad , \quad (2)$$

where $\Psi_i(\mathbf{r})$ are the one-electron molecular orbitals, and Ψ_{tot} is the total n -electron wave function. Enforcing this exchange symmetry introduces some correlation in the motion of the electrons—in particular, no two electrons can occupy the same position in space—and leads to a decrease in the electronic energy known as the “exchange” energy. This approach is known as the Hartree-Fock approximation.

Because the Hartree-Fock approximation assumes that the particles are independent, we can write down a separate Schrödinger equation for each electron

$$h_i^{\text{HF}}\Psi_i(\mathbf{r}) = \varepsilon_i\Psi_i(\mathbf{r}) \quad , \quad (3)$$

using the same one-electron Hamiltonian h^{HF} for each electron. The eigenvectors, or molecular orbitals, $\Psi_i(\mathbf{r})$ will each have a characteristic orbital energy ε_i . To evaluate the one-electron Hamiltonian h^{HF} , as well as the expressions in the total energy, one needs the total electronic density ρ obtained by adding the densities of the individual orbitals:

$$\rho(\mathbf{r}) = \sum_i |\Psi_i(\mathbf{r})|^2 \quad . \quad (4)$$

The procedure for obtaining self-consistent solutions to the Schrödinger equation is to guess an initial total density and solve for the molecular orbitals $\Psi_i(\mathbf{r})$. We then use these orbitals to determine a new guess for the density and effective Hamiltonian and carry on the calculation until the input density agrees with the output density. The molecular orbitals themselves are usually expanded in a finite Gaussian basis set on each atomic center composed of a radial part, a Gaussian function of the distance from the nucleus, and an angular part, corresponding to various angular momenta (s , p , d , f). The solution to the self-consistent equations involves calculating the one- and two-electron operators over the Gaussian basis set to evaluate the expressions in Equations (1) and (2).

Whereas bond lengths obtained from Hartree-Fock calculations are generally reasonable, bond energies calculated with this method are not accurate enough for the requirements of chemistry. The exchange interaction introduces some correlation in the motion of the electrons, but for reliable bond energies, one must account in a much more detailed way for the explicit correlation between the motion of one and another electron. Several approaches have been developed for including the electron

correlation and for generating increasingly accurate molecular wave functions and electronic energies. Among them are many-body perturbation theory, coupled-cluster theory, and configuration interaction techniques, which typically use the Hartree-Fock wave function as a starting point. These techniques give more accurate results but are computationally even more demanding than Hartree-Fock calculations. As a result, it is difficult to obtain accurate theoretical predictions for moderate to large molecules of interest to experimental chemists.

Developments in Density Functional Theory (DFT). The DFT approach dramatically simplifies the computational demands by replacing the search for an accurate many-electron wave function, which is a function of the coordinates of all the electrons in the molecule, with that for an accurate electronic density, which depends on the coordinates of just a single point in space.

The conceptual foundation of DFT is the Hohenberg-Kohn theorem (Hohenberg and Kohn 1964), which states that knowing the ground-state electronic density suffices in determining all the properties of a many-body system. In the Kohn-Sham electronic-structure formulation of DFT, the electronic energy is partitioned into three terms which are analogous to those in the Hartree-Fock method—the kinetic energy, the electron-nuclei attraction, and the average electron-electron repulsion $\langle E_{\text{elec-elec}} \rangle$. Everything else is lumped into an exchange-correlation energy term:

$$E^{\text{DFT}}(\mathbf{R}) = E_{\text{kin}} + E_{\text{elec-nuc}} + \langle E_{\text{elec-elec}} \rangle + E_{\text{exch-corr}} \quad (5)$$

Given an expression for $E_{\text{exch-corr}}$, one can formulate one-electron Schrödinger equations analogous to the Hartree-Fock equation, Equation (3), discussed in the previous section. In fact, the Hartree-Fock approximation may be thought of as a specific form of DFT, in which $E_{\text{exch-corr}}$ is approximated by the Hartree-Fock exchange energy. (See the article “Ground-State Properties of the Actinide Elements: A Theoretical Overview” for further details.)

The earliest approximations to the exchange-correlation potential in $E_{\text{exch-corr}}$ were extracted from the properties of the homogeneous electron gas (Kohn and Sham 1965), an approach that worked quite well for describing electrons in metals and was therefore immediately adopted by the physics community. This approach led to an exchange-correlation potential for an electron at some point r , which depended only upon the electronic density at point r , $\rho(r)$. It became known as the local density approximation (LDA). But LDA significantly overestimates bond energies. In the past few years, however, functionals called generalized gradient approximations, or GGA, have been developed (Perdew 1986, Becke 1988), in which the exchange-correlation energy $E_{\text{exch-corr}}$ depends on the local density and its gradient, thereby introducing some inhomogeneity and nonlocality. Even more recently, additional improvements in bond energies have been obtained with hybrid density functionals (Becke 1993), which contain a portion of the full, nonlocal Hartree-Fock exchange interaction discussed earlier in the context of the wave function approaches.

The tremendous simplification afforded by DFT arises from the fact that all the expressions depend only on an accurate knowledge of the density in three spatial dimensions. It is this feature that allows DFT to be applied to much larger molecules than is possible with approaches based on Hartree-Fock, which were described earlier. This simplification is especially important when one considers the $E_{\text{exch-corr}}$ term described before, which incorporates the electron correlation effects. By contrast, Hartree-Fock-based methods for treating electron correlation typically include expressions involving all the occupied and unoccupied orbitals. The combination of improved functionals and computational advances has now enabled chemists to routinely apply DFT methods to the electronic structure of molecules of ever-increasing complexity.

Relativistic Effective Core Potentials (RECPs). The final ingredient for our specific approach to actinide chemistry is the use of RECPs. In molecules containing heavy atoms, such as the actinides, the motion of the electrons must be treated relativistically because the effective velocity of the electrons (especially the inner core electrons that penetrate closer to the nucleus) is nonnegligible relative to the speed of light. In the Schrödinger equation for a valence orbital, Equation (3), the one-electron Hamiltonian h ,

$$h = T + V_{\text{core}} + V_{\text{nuc}} + V_{\text{rel}} + V_{\text{val}} \quad (6)$$

includes the kinetic energy of the electron (T), the interactions with the nucleus and the core electrons ($V_{\text{core}} + V_{\text{nuc}}$), the interactions with the other valence electrons (V_{val}), and the relativistic operator (V_{rel}), which contains the so-called “mass-velocity” and “Darwin” operators. With the RECP, the Schrödinger equation becomes

$$h = T + V_{\text{RECP}} + V_{\text{val}} \quad (7)$$

The RECP in Equation (7) serves to replace the Coulomb effects of the inner core electrons on the valence electrons, as well as the direct relativistic effects on the valence electrons. RECPs can be used in either Hartree-Fock or DFT approaches to studies of molecules containing heavier elements. As a rule, relativity has a noticeable effect on the electronic levels and, in turn, on calculated molecular bond lengths and bond energies for elements beyond krypton ($Z > 36$). This range includes the second and third transition-metal series, as well as the lanthanides and actinides. The effects of spin-orbit coupling, which also arises from relativistic interactions, must be included directly in any calculation.

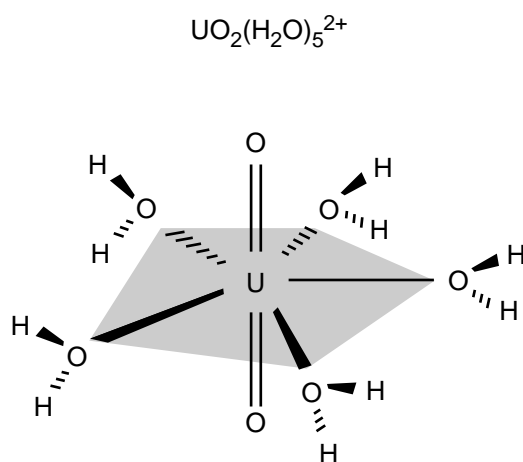
The procedures for generating RECPs for heavy atoms were developed by Jeffrey Hay and Willard Wadt (1985). The initial impetus for these developments came from the programmatic effort at Los Alamos to study actinide molecules for laser isotope separation. We calculated the electronic structure of uranium hexafluoride (UF_6), plutonium hexafluoride (PuF_6), and related molecules, using “first-generation” RECPs for uranium and plutonium (Hay et al. 1979, Hay 1983, Wadt 1987). A set of RECPs for 56 main-group and transition-metal elements of the periodic table was published (Hay and Wadt 1985) and disseminated to the quantum-chemistry community. The methodology for manipulating RECPs developed by Richard Martin, Larry McMurchie, and Ernest Davidson has been incorporated into the Gaussian codes for performing quantum-chemistry calculations developed by John Pople and his collaborators over the past twenty years. Following these developments, investigators throughout the world have been using both Hartree-Fock and DFT approaches to treat heavy-atom chemistry by using RECPs. More recently, we have developed a set of “second-generation” RECPs (Hay and Martin 1998) and have employed them in our studies of actinide molecules (Hay and Martin 1998, Schreckenbach et al. 1998) by using the DFT approaches described in this article.

Application to Actinyl Species

Electronic Structure of Actinyl Complexes. In this section, we present DFT results for the structures and properties of a typical actinyl species in solution denoted generically as $\text{AnO}_2(\text{H}_2\text{O})_5^{2+}$, where An is uranium, neptunium, or plutonium. These molecules, all of which contain the common AnO_2^{2+} unit surrounded by five water molecules, are the commonly observed species involving the An(VI) oxidation

Table II. Analysis of the Electronic Structure of $\text{UO}_2(\text{H}_2\text{O})_5^{2+}$ from a Simplistic “Ionic” Picture and from DFT Calculations

Occupied Orbitals in Neutral Atoms	Charge on Each Entity				Occupation of Atomic Orbitals	
	Ionic Model	DFT Results	Ionic Model	DFT Results	Ionic Model	DFT Results
U $6s^2 6p^6 5f^3 6d^1 7s^2 7p^0$	U +6.0	U +1.66	U $6s^2 6p^6 5f^0 6d^0 7s^0 7p^0$	U $6s^2 6p^6 5f^{2.71} 6d^{1.26} 7s^{0.21} 7p^{0.16}$		
O $2s^2 2p^4$	O -2	O -0.26	O $2s^2 2p^6$	O $2s^{1.94} 2p^{4.32}$		
	H_2O 0.0	H_2O +0.18				

**Figure 1. Schematic of the Geometric Structure of $\text{UO}_2(\text{H}_2\text{O})_5^{2+}$**
The linear $\text{O}=\text{U}=\text{O}$ uranyl is oriented vertically, and the five water molecules are coordinated to the uranium atom in the equatorial plane. The hydrogen atoms of the equatorial water molecules are oriented in such a way as to lie roughly perpendicular to the equatorial plane.

state in solution at low pH. Shown in Figure 1 is a schematic representation of the uranyl complex.

The electronic properties of the molecule are determined primarily by the AnO_2^{2+} actinyl unit because the water molecules act essentially as neutral ligands coordinated to the metal. The electronic structure of AnO_2^{2+} , in turn, is closely tied to the orbitals of the actinide atom. For the case of UO_2^{2+} , it is useful to consider an extreme “ionic” picture as a starting point for thinking about the electronic structure although this picture turns out to be somewhat unrealistic for describing the true electronic density of the molecule, as we will discuss shortly. In this picture, the oxygen atoms are treated as O^{2-} , and the uranium atom is treated as U^{6+} . Each atom has adopted a closed-shell configuration. As shown in Table II, the O^{2-} ions adopt the inert gas $2s^2 2p^6$ configuration, and all the atomic levels in the U^{6+} ion are filled up through the 6s and 6p shells. (The radial functions of the actinide atoms are shown in the article “The Chemical Complexities of Plutonium” on page 364.) The 5f, 6d, and higher levels are formally empty in this picture. Based upon this picture, one would also anticipate a $\text{UO}_2(\text{H}_2\text{O})_5^{2+}$ molecule with no unpaired electrons, as is indeed found to be the case in the ground-state solution of the electronic structure.

For the neptunium and plutonium counterparts of this species, we recall that the atomic state of Np^{6+} has a filled $6s^2 6p^6$ core as does U^{6+} , but it also has one unpaired electron in the 5f orbital. Similarly, the atomic state of Pu^{6+} has a $5f^2$ configuration with two unpaired electrons. The same is true of the molecular calculations, in which the ground states have one unpaired electron with spin = 1/2 for $\text{NpO}_2(\text{H}_2\text{O})_5^{2+}$ and two unpaired electrons with spin = 1 for $\text{PuO}_2(\text{H}_2\text{O})_5^{2+}$.

When the molecular orbitals are calculated self-consistently, a picture of the bonding emerges that is much more covalent when compared with the ionic model for the uranyl UO_2^{2+} entity, which has +6 and -2 charges on the uranium and oxygen,

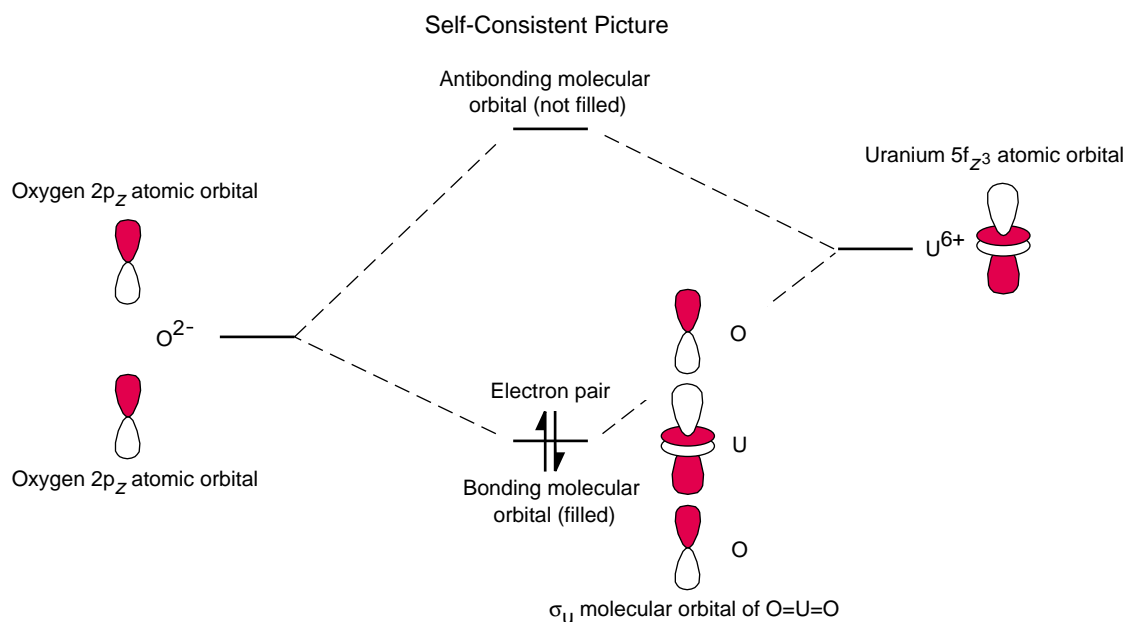


Figure 2. Formation of a Bonding σ_u Molecular Orbital
The figure shows the interaction of two oxygen $2p_z$ orbitals (left) in the uranyl unit with the uranium $5f_{z^3}$ orbital (right) to form a bonding σ_u molecular orbital (center) in the O=U=O bond. The figure also suggests the energy levels (solid lines) of the atomic orbitals relative to the energy levels of the molecular orbitals in the self-consistent picture.

respectively. An analysis of the DFT results for $\text{UO}_2(\text{H}_2\text{O})_5^{2+}$ shows that the resultant charge distribution is closer to +1.66 for uranium and -0.26 for each oxygen in the uranyl group (see Table II). Some residual charge (+0.18) remains on each of the equatorial water molecules. This change is evident in the six molecular orbitals describing the uranyl bond. In the ionic picture, these orbitals would be strictly atomic in character and would involve the $2p_x$, $2p_y$, and $2p_z$ orbitals on each of the oxygen atoms. Using the symmetry designations of O=U=O, we denote these orbitals σ_g , σ_u , π_{ux} , π_{uy} , π_{gx} , and π_{gy} . One of the most important contributions arises from the σ_u orbital, which involves not only the $2p_z$ atomic orbitals of the oxygen atoms but also the $5f_{z^3}$ orbital of the uranium atom. In Figure 2, the atomic orbitals of each atom are shown before they interact, as we assumed in the ionic model. In the middle of Figure 2, the molecular orbital is shown schematically in order to illustrate bonding interactions of the oxygen $2p_z$ orbitals with the uranium $5f_{z^3}$ orbital.

We now turn to another aquo complex, $\text{PuO}_2(\text{H}_2\text{O})_5^{2+}$, which is qualitatively similar to $\text{UO}_2(\text{H}_2\text{O})_5^{2+}$. As mentioned before, unlike its uranium counterpart, the plutonium complex has two unpaired electrons in the $5f_{xyz}$ and $5f_{x(x^2-y^2)}$ molecular orbitals. These molecular orbitals are essentially identical to the atomic $5f_{xyz}$ and $5f_{x(x^2-y^2)}$ orbitals of plutonium. The calculated optimum structure from DFT results is shown in Figure 3(a), which closely resembles the schematic drawing of aquo complexes in Figure 1. A contour plot in Figure 3(b) shows the positive and negative amplitudes of the self-consistent molecular orbital most closely corresponding to the σ_u molecular orbital of the isolated O=Pu=O group. The constructive interference of the bonding interaction between the oxygen $2p_z$ orbitals and the plutonium $5f_{z^3}$ orbital, which was sketched in Figure 2, now actually appears as a single contour in the figure. As already mentioned, there are five other molecular orbitals representing the 12 electrons in the O=An=O bonds, in which the $5f$ and $6d$ orbitals on the actinide can participate, but we will not discuss these other orbitals in detail here.

Properties of Aquo and Crown Complexes of Actinyl Species. In this section, we discuss the geometries and other properties of actinyl complexes obtained from DFT calculations. To obtain the optimized structure, we vary the total molecular energy $E^{\text{DFT}}(\mathbf{R})$, which was discussed in the section “Theoretical and Computational Developments,” as a function of all the nuclear coordinates until a stable, or minimum-energy, solution is found. Table III compares the calculated bond lengths

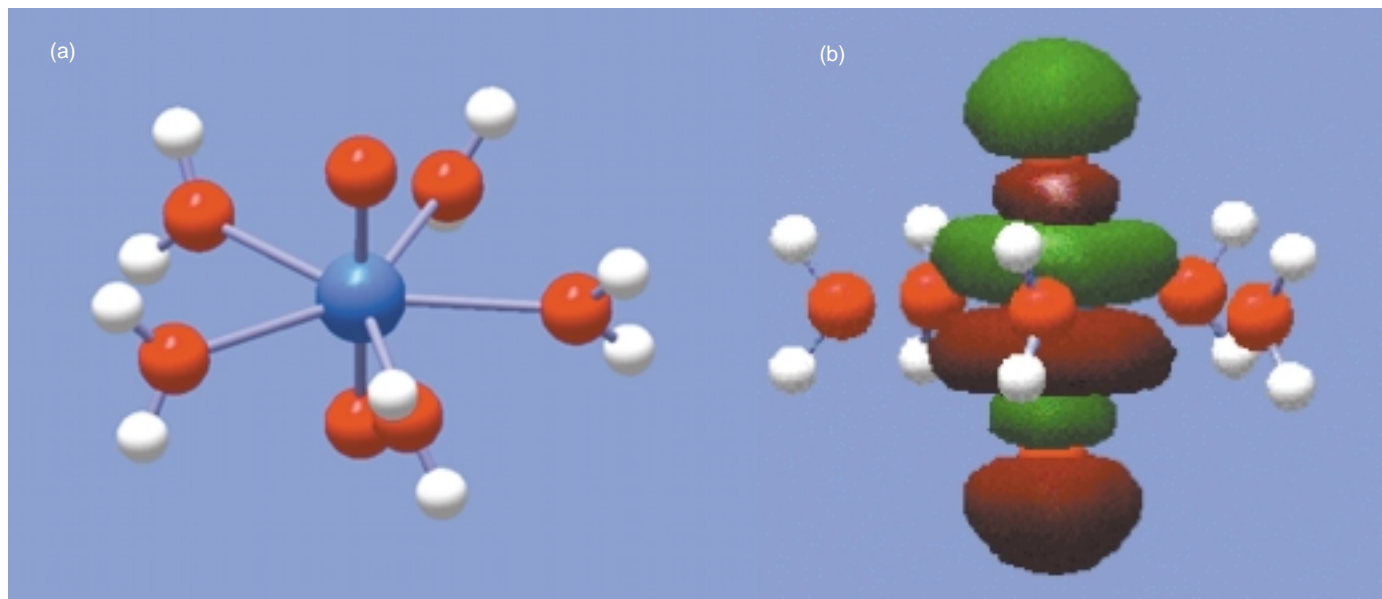


Figure 3. Structure of $\text{PuO}_2(\text{H}_2\text{O})_5^{2+}$ and a Bonding Molecular Orbital of PuO_2
 (a) The structure of $\text{PuO}_2(\text{H}_2\text{O})_5^{2+}$, as determined from quantum chemical DFT calculations, is shown on the left, where the colored spheres indicate plutonium (blue), oxygen (red), and hydrogen (white). (b) Shown here is a contour plot of one of the occupied bonding molecular orbitals of the $\text{O}=\text{Pu}=\text{O}$ unit, where positive and negative amplitudes are depicted as green and brown, respectively. The plotted orbital resembles most closely the σ_{U} orbital of PuO_2^{2+} . The plot shows the participation of the $5f_{z^2}$ atomic orbital on the plutonium atom and of the $2p_z$ atomic orbital on the oxygen atoms. Relatively little participation is evident from the atomic orbitals of the equatorial atoms.

from DFT with experimentally measured quantities from XAFS spectroscopy in solution. As shown in the table, there is good agreement between the theoretical calculations and the measured values for the actinyl bond: both find a bond length of 1.76 angstroms for $\text{U}=\text{O}$, 1.75 angstroms for $\text{Np}=\text{O}$, and 1.74 angstroms for $\text{Pu}=\text{O}$. By contrast, the Hartree-Fock results predict that the $\text{U}=\text{O}$ bond length is substantially shorter (1.69 angstroms). In the case of the uranyl complex, for the longer equatorial bonds to the water molecules, DFT predicts a slightly longer bond length (2.51 angstroms) compared with experiment (2.42 angstroms).

The vibrational frequencies are calculated from the curvature (second derivatives) of $E^{\text{DFT}}(\mathbf{R})$ about the minimum-energy geometry with respect to the nuclear coordinates. The two modes corresponding to the symmetric and antisymmetric motion (denoted ν_s and ν_{as} , respectively, in Table III) of the $\text{O}=\text{U}=\text{O}$ atoms are the most characteristic vibrational fingerprint of the molecule. These two modes can be detected by Raman and infrared vibrational spectroscopy, respectively. The symmetric stretch is predicted to lie at lower energy than the antisymmetric stretch (908 cm^{-1} versus 1001 cm^{-1}), and this prediction agrees with the experimental data.

The structural comparisons (Table III) show a slight contraction (namely, by 0.01 angstrom) of the actinyl bond as one goes down the actinide series from uranium to neptunium and then to plutonium. This trend is fairly typical in actinide compounds and is often called the actinide “contraction,” analogous to the lanthanide contraction found in the 4f series. Similarly, one also finds a slight progressive decrease in the neptunium-water and plutonium-water bond lengths.

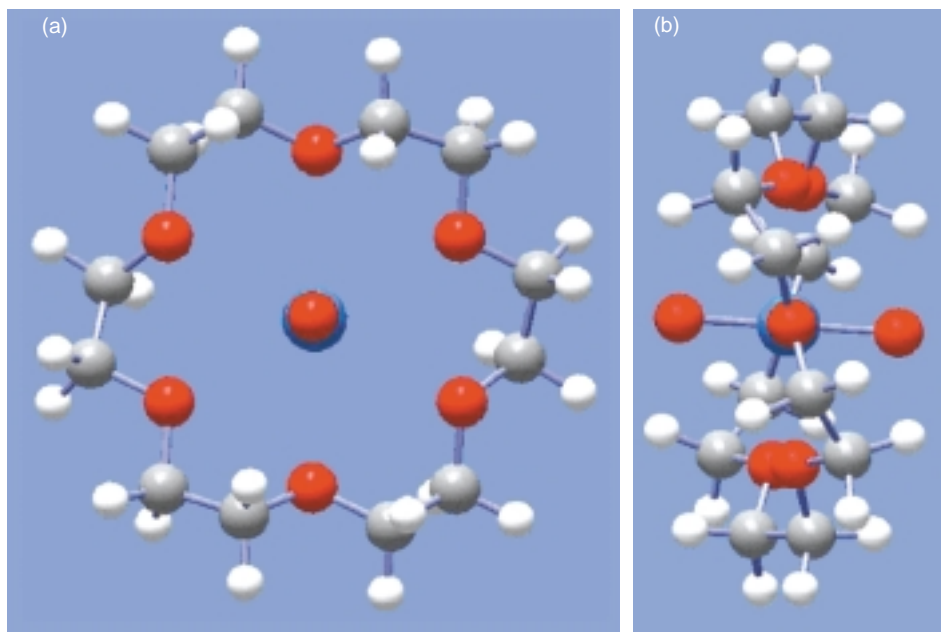
Although we have focused on just a few features of the results of electronic-structure calculations—those that allow comparisons with experiment—the calculations provide other useful information, which can be difficult to measure. For example, the calculations automatically give the frequencies of all 48 vibrations. Using these theoretical techniques, one can also look at questions in solution chemistry that can be difficult or too ambiguous to measure experimentally. Such issues include how much energy is involved in binding additional water molecules to the central actinyl species, the relative energies in binding water compared with other ligands, such as hydroxide (OH^-) or halide (Cl^-), and the activation barriers that must be surmounted in chemical reactions. In fact, calculations by Schreckenbach et al. (1998) have shown that the uranyl bond can exist under the right circumstances in a bent form, with $\text{O}=\text{U}=\text{O}$ bond angles ranging from 115° to 130° , whereas all known forms of

Table III. Bond Lengths and Vibrational Frequencies from DFT and Hartree-Fock (HF) Calculations and from Experimental Results for $AnO_2(H_2O)_5^{2+}$ Complexes

	$UO_2(H_2O)_5^{2+}$			$NpO_2(H_2O)_5^{2+}$		$PuO_2(H_2O)_5^{2+}$	
	Spin = 0			Spin = 1/2		Spin = 1	
	Methodology						
	HF	DFT	XAFS	DFT	XAFS	DFT	XAFS
Bond Length							
R(An=O) (Å)	1.69	1.76	1.76	1.752	1.75	1.742	1.74
R(An-OH ₂) (Å)	2.54	2.51	2.42	2.50	2.42	2.485	2.41
Stretch Frequency	HF	DFT	Raman, IR	DFT	Raman, IR	DFT	Raman, IR
ν_s (cm ⁻¹)	1091	908	872	854	863	805	835
ν_{as} (cm ⁻¹)	1149	1001	965	983	969	951	962

Figure 4. Predicted Atomic Positions in the $NpO_2(18\text{-crown-6})^+$ Complex

Shown here are the top (a) and side (b) views of the calculated atomic positions in the complex $NpO_2(18\text{-crown-6})^+$ as determined from quantum chemical DFT calculations. The spheres indicate neptunium (blue), oxygen (red), carbon (gray), and hydrogen (white).



uranyl complexes have linear O=U=O bonds (180°). It remains to be seen if such species can actually be isolated as stable compounds.

All the previous results have been obtained while ignoring the interactions of the actinide species with the surrounding aqueous solution. In order to compare these results with those from experimental measurements in solution, we must include solvent effects on the molecular energies obtained by DFT or other techniques. A discussion of these techniques, however, would take us beyond the scope of this article. We will mention briefly that we have been investigating solvent effects in collaboration with Lawrence Pratt of Los Alamos (Martin et al. 1998). These interactions can often be successfully incorporated when we treat the interaction of the molecular wave functions with a classical “dielectric” model for the surrounding medium. Depending on the overall charge of the actinide species, these solvent effects can be very large (100–200 kilocalories per mole) for energies of reaction in solution,

and they must be included for complete comparisons with experiment.

These theoretical capabilities, together with the experimental characterization techniques described in the main article, now offer a powerful combination for unraveling the complexities of actinide chemistry. Figure 4 is an illustration of the results of our recent DFT calculation on a much larger neptunyl(V) complex with an organic ether, 18-crown-6, that contains six oxygen atoms. The crown ether molecule has been observed (Clark et al. 1998) experimentally to bind to the neptunium along the equator of the neptunyl bond in a manner similar to that of the water molecules in our previous case. The predicted Np=O bond length of 1.814 angstroms agrees well with the measured value of 1.800 angstroms. The same good agreement is true of the predicted frequency value (776 cm^{-1}) and the results obtained by Raman spectroscopy (780 cm^{-1}). Calculations have now predicted the structural and vibrational properties of crown ether complexes of uranium, neptunium, and plutonium in both +6 and +5 oxidation states, as well as ligand binding energies in solution. All these findings illustrate how the new DFT methodologies, coupled with constantly improving computational capabilities, enable theory to make predictions on large actinide molecules of experimental interest. ■

Further Reading

- Becke, A. D. 1988. *Physical Review A* **37**: 3098.
- Becke, A. D. 1993. *Journal of Chemical Physics* **98**: 5648.
- Born, M., and J. R. Oppenheimer. 1927. *Annalen Physik* **84**: 457.
- Clark, D. L., D. W. Keogh, P. D. Palmer, B. L. Scott, and C. D. Tait. 1998. *Angewandte Chemie—International Edition* **37**: 164.
- Hay, P. J. 1983. *Journal of Chemical Physics* **79**: 5469.
- Hay, P. J., and R. L. Martin. 1998. *Journal of Chemical Physics* **109**: 3875.
- Hay, P. J., and W. R. Wadt. 1985. *Journal of Chemical Physics* **82**: 270.
- Hay, P. J., 1979. *Journal of Chemical Physics* **70**: 1767.
- Hohenberg, P., and W. Kohn. 1964. *Physical Review B* **136**: 864.
- Kohn, W., and L. J. Sham. 1965. *Physical Review A* **140**: 113.
- Martin, R. L., L. R. Pratt, and P. J. Hay. 1998. *Journal of Physical Chemistry A* **102**: 3565.
- Perdew, J. P. 1986. *Physical Review B* **33**: 8922.
- Schreckenbach, G., P. J. Hay, and R. L. Martin. 1998. *Inorganic Chemistry* **37**: 4442.
- Wadt, W. R. 1987. *Journal of Chemical Physics* **86**: 339.

Jeffrey Hay received a B.A. in chemistry from Franklin and Marshall College in 1967 and a Ph.D. in chemistry from the California Institute of Technology in 1972. He has been a staff member in the Theoretical Division at Los Alamos since 1974 and was named a Laboratory Fellow in 1992. Hay is the author of more than 100 articles in refereed journals. His research interests include the electronic structure and chemistry of transition-metal and actinide compounds and applications of quantum chemistry and cluster approaches to problems in heterogeneous catalysis and materials chemistry.



Richard Martin received his B.S. in chemistry (magna cum laude) from Kansas State University and a Ph.D. in chemistry from the University of California, Berkeley. He spent two years as a Chaim Weizmann fellow with Ernest Davidson at the University of Washington before joining the theoretical chemistry and molecular physics group at Los Alamos in 1978. His research interests are in the general area of electronic-structure theory, particularly as applied to the description of transition-metal and actinide systems.





The Chemical Interactions of Actinides in the Environment

Wolfgang Runde

From a chemist's perspective, the environment is a complex, particularly elaborate system. Hundreds of chemically active compounds and minerals reside within the earth's formations, and every patch of rock and soil is composed of its own particular mix. The waters that flow upon and through these formations harbor a variety of organic and inorganic ligands. Where the water meets the rock is a poorly understood interfacial region that exhibits its own chemical processes.

Likewise, from a chemist's point of view, the actinides are complex elements. Interrupting the 6d transition elements in the last row of the periodic table, the actinides result as electrons fill the 5f orbitals. Compared with the 4f electrons in the lanthanide series, the 5f electrons extend farther from the nucleus and are relatively exposed. Consequently, many actinides exhibit multiple oxidation states and form dozens of behaviorally distinct molecular species. To confound matters, the light actinides are likely to undergo reduction/oxidation (redox) reactions and thus may change their oxidation states under even the mildest of conditions. Uranium, neptunium, and especially plutonium often display two or

more oxidation states simultaneously in the same solution. Accordingly, the light actinides exhibit some of the richest and most involved chemistry in the periodic table.

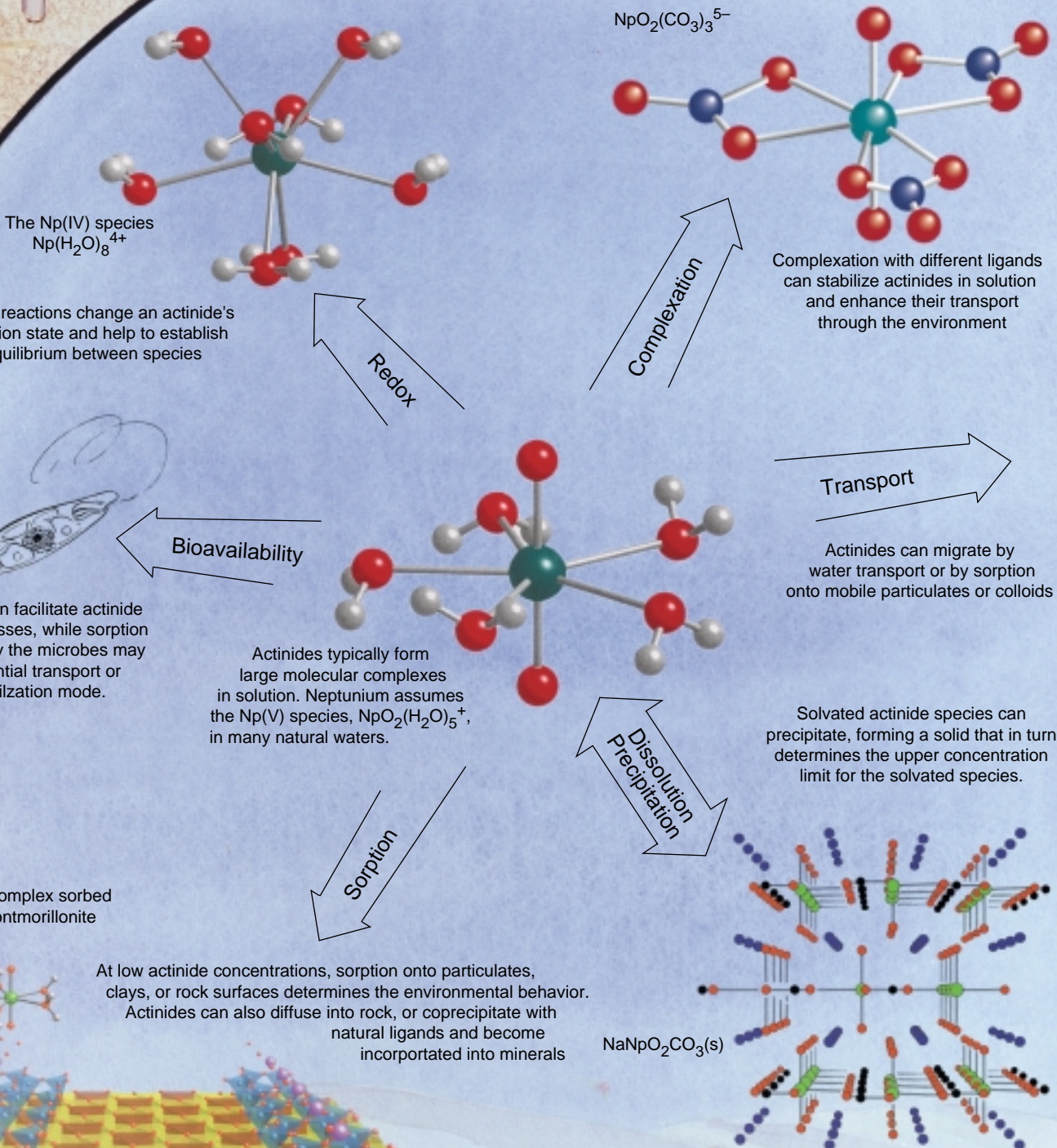
As a result, the chemical interactions of actinides in the environment are inordinately complex. To predict how an actinide might spread through the environment and how fast that transport might occur, we need to characterize all local conditions, including the nature of site-specific minerals, temperature and pressure profiles, and the local waters' pH, redox potential (Eh), and ligand concentrations. We also need a quantitative knowledge of the competing geochemical processes that affect the actinide's behavior, most of which are illustrated in Figure 1. Precipitation and dissolution of actinide-bearing solids limit the upper actinide concentration in solution, while complexation and redox reactions determine the species' distribution and stability. The interaction of a dissolved species with mineral and rock surfaces and/or colloids determines if and how it will migrate through the environment.

Understanding this dynamic interplay between the actinides and the environment is critical for accurately as-

sessing the feasibility of storing nuclear waste in geologic repositories. The actinides¹ are radioactive, long-lived, and highly toxic. Over the last few decades, vast quantities of transuranic actinides (those with atomic numbers greater than that of uranium) have been produced inside the fuel rods of commercial nuclear reactors. Currently, most spent fuel rods are stored above-ground in interim storage facilities, but the plan in the United States and some European countries is to deposit this nuclear waste in repositories buried hundreds of meters underground. The Department of Energy (DOE) is studying the feasibility of building a repository for high-level waste in Yucca Mountain (Nevada) and has already licensed the Waste Isolation Pilot Plant (WIPP) in New Mexico as a repository for defense-related transuranic waste. Given the actinides' long half-lives, these repositories must isolate nuclear waste for tens of thousands of years.

¹Although "actinides" refers to the fourteen elements with atomic numbers 90 through 103 (thorium through lawrencium), in this article we limit the term to refer only to uranium, neptunium, plutonium, americium, and curium, unless stated otherwise. These five actinides are the only ones that pose significant environmental concerns.

Figure I. Overview of Actinide Behavior in the Environment



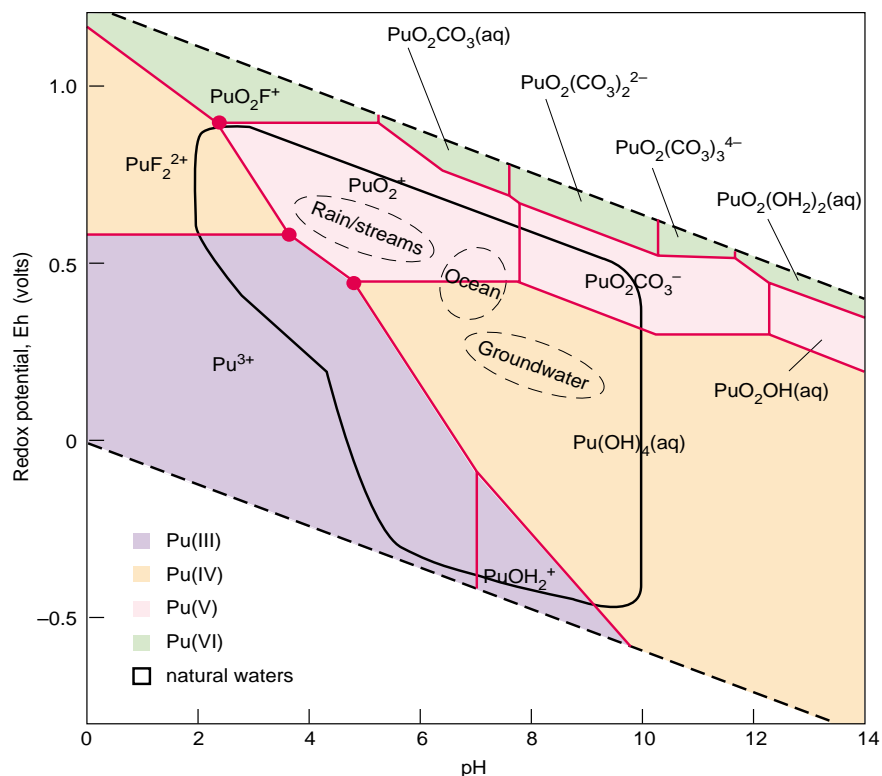


Figure 2. Pourbaix Diagram for Plutonium

This Eh-vs-pH diagram is calculated for plutonium in water containing hydroxide, carbonate, and fluoride ions. (The ligand concentrations are comparable to those found in water from well J-13 at Yucca Mountain, Nevada, while the plutonium concentration is fixed at 10^{-5} M). Specific complexes form within defined Eh/pH regions, while the stable oxidation states (colors) follow broader trends. For example, more-oxidizing conditions (higher Eh values) stabilize redox-sensitive actinides like plutonium in the higher oxidation states V and VI. The red dots are triple points, where plutonium can exist in three different oxidation states. The range of Eh/pH values found in natural waters is bounded by the solid black outline. In ocean water or in groundwater, plutonium is likely to be found as Pu(IV), while in rainwater or streams, plutonium can assume the V state. Other natural environments will favor Pu(III) or Pu(VI) complexes. The dashed lines define the area of water stability. Above the upper line, water is thermodynamically unstable and is oxidized to oxygen; below the lower line, water is reduced to hydrogen.

Over the course of millennia, however, it is possible that water seeping into a repository will eventually corrode the waste containers. The actinides will then have access to the environment.

Research at Los Alamos has focused on characterizing the behavior of actinides in the environments surrounding those repository sites. (Only small amounts of transuranic elements are generally found in other environments, as discussed in the box “Actinides in Today’s Environment” on page 396.)

Our solubility studies, for example, confirm that neptunium is more than a thousand times more soluble in Yucca Mountain waters than plutonium. That is because plutonium in those waters favors the IV oxidation state while neptunium favors the far more soluble V state. Thus, for Yucca Mountain, neptunium is the actinide of primary concern. WIPP, however, is built within in a geologically deep salt formation. In the extremely salty brines found there, the focus shifts to plutonium, since

reactions with chloride ions are known to stabilize plutonium in the VI oxidation state. Plutonium(VI) species are much more soluble than Pu(IV) species, and plutonium mobility would be enhanced at WIPP unless a reducing environment can be maintained within or around the waste containers.

Unfortunately, very few studies of actinide geochemistry can be conducted *in situ*, so that we are forced to simulate environmental conditions in the laboratory. The concentrations of the actinides in natural waters are typically on the order of 10^{-6} molar (M) or lower. While those concentrations are high enough to be of environmental concern, they are too low to allow direct study with conventional spectroscopies. We have thus had to adapt advanced spectroscopic techniques, such as x-ray absorption fine structure (XAFS) and laser-induced fluorescence spectroscopies, to study these toxic, radioactive elements.

As an example, recent XAFS investigations of Pu(IV) colloids have yielded significant insights into the colloids’ structure, which for years has complicated the determination of Pu(IV) solubility. Scanning electron microscopy (SEM) has helped us elucidate the confusing sorption behavior of U(VI) onto phosphate mineral surfaces. The box on page 412 highlights a few examples of these spectroscopic studies.

The scope of actinide interactions in the environment is too broad to cover in a single article. We will concentrate therefore on the solubility and speciation of actinides in the presence of hydroxide and carbonate ions, which are the two most environmentally relevant ligands. We will then briefly discuss some aspects of actinide sorption and actinide interactions with microorganisms. The solubility and sorption of actinides pose two key natural barriers to actinide transport away from a geologic repository, while microorganisms pose a less-studied but potential third barrier. While we are fully aware of additional geochemical reactions in

Table I. Oxidation States of Light Actinides^a

Th	Pa	U	Np	Pu	Am	Cm
III	III	III	III	III	III	III
IV	IV	IV	IV	IV	IV	IV
	V	V	V	V	V	
		VI	VI	VI	VI	
			VII	VII		

^aThe environmentally most important oxidation states are bolded.

the environment, such as coprecipitation, mineralization, and diffusion processes (and have thus included them in Figure 1), we will not discuss their roles here.

Oxidation States and Redox Behavior

Water is the dominant transport medium for most elements in the environment. Compared with the pH values and ionic strengths that can be obtained in the laboratory, most natural waters are relatively mild. Typically, they are nearly neutral (pH 5 to 9), with a wide range of redox potentials (from -300 to +500 millivolts) and low salinities (ionic strengths < 1 molal). The water conditions determine which actinide oxidation states predominate and which actinide species are stable.

For example, Figure 2 shows the Pourbaix diagram (Eh vs pH) for plutonium in water containing the two most environmentally relevant ligands, the hydroxide (OH⁻) and carbonate (CO₃²⁻) ions. Even in this simple aqueous system, plutonium can exist in four oxidation states: III, IV, V, and VI. (Plutonium is unique in this regard. The Pourbaix diagrams for the other actinides are simpler.) The normal range of natural waters is outlined in the figure and overlaps with the stability fields of plutonium in the III, IV, and V oxidation states. Within this range, plutonium exhibits two triple points,

where species in three different oxidation states are in equilibrium.

Because of intrinsic differences in redox potentials, each actinide will exhibit a different set of oxidation states for a given set of solution conditions. In contrast to plutonium, U(III) is unstable under most conditions and oxidizes easily to U(IV), while U(V) disproportionates easily to U(IV) and U(VI). Neptunium(III) and Np(VI) are on the edges of the water stability region and can exist only under strongly reducing or oxidizing conditions, respectively. Americium and curium will only be found in the III oxidation state under most conditions. Similarly, all actinides beyond curium are dominated by the lanthanide-like trivalent oxidation state.

As a rule of thumb, we expect to find U(VI), Np(V), Pu(IV), Am(III), and Cm(III) as the prevalent oxidation states in most ocean or groundwater environments. But in other aqueous environments, including streams, brines, or bogs, U(IV), Np(IV), and Pu(III,V,VI) are also common and likely to be stable. Table I summarizes the oxidation states of the actinides and highlights the environmentally most relevant ones. Some of the states listed in the table, such as Pa(III) or Pu(VII), can be synthesized only under extreme conditions, far from those found in natural systems.

Additional chemical processes occurring in solution are likely to influence the actinide's oxidation state stability.

The stability of Pu(V) in natural waters containing carbonate is an example. The plutonium will complex with the carbonate ligands, and if the plutonium concentration is low (less than about 10⁻⁶ M), radiolytically induced redox reactions are minimized. Consequently, the stability of Pu(V) is enhanced and its disproportionation to Pu(IV) and Pu(VI) is reduced. As discussed later, the solubilities of solids formed from Pu(V) complexes are orders of magnitude greater than those of Pu(IV) solids, so the enhanced stability of Pu(V) would serve to increase the total plutonium concentration in solution.

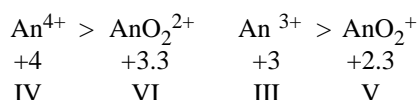
Another example for the stabilization of actinides in solution is the oxidation of Am(III) and Pu(IV) through radiolytic formation of oxidizing species, such as peroxide (H₂O₂) or hypochlorite (ClO⁻). At high actinide concentrations and hence under the influence of (its own) alpha radiation, those normally stable oxidation states are oxidized to form Am(V) and Pu(VI), respectively, especially in concentrated chloride brines.

Despite the complexity of actinide redox behavior, however, we should emphasize that within a given oxidation state, actinides tend to behave similarly. For example, we can study a U(IV) complex and from it infer the behavior of the analogous Np(IV) and Pu(IV) complexes. In the following discussions, therefore, we often refer to "generic" actinides—e.g., An(IV) complexes—where An is shorthand for actinide.

Effective Charge. It has been known for many years that An(IV) forms the strongest, most stable complexes and An(V) the weakest. This behavior follows directly from the effective charges of the ion.

In the III and IV states, the actinides form hydrated An³⁺ and An⁴⁺ ions in solution, respectively. In contrast, the highly charged ions in the V and VI states are unstable in aqueous solution and hydrolyze instantly to form linear *trans*-dioxo cations, AnO₂⁺ and

AnO_2^{2+} , with overall charges of +1 and +2, respectively. These cations are often referred to as the actinyl ions. The covalent bonding between the actinide and the two oxygen atoms in the actinyl ion $(\text{O}=\text{An}=\text{O})^{n+}$, where $n = 1$ or 2 , enhances the effective charge of the central actinide ion to 2.3 ± 0.2 for AnO_2^+ and 3.3 ± 0.1 for AnO_2^{2+} (Choppin 1983). A ligand approaching the actinyl ion sees this enhanced effective charge and bonds directly to the actinide in the equatorial plane of the linear actinyl ion. Thus, the preference for actinides to form complexes generally follows their effective ion charges, as shown below:



The second and third lines show the ion's effective charge and formal oxidation states.

Recent measurements of bond lengths in the actinyl ions of V and VI complexes reflect the above sequence. A higher effective charge correlates with a stronger, hence shorter, bond to the coordinated ligands. Accordingly, the bond length of the actinyl bonds increases from about 1.75 angstroms (\AA) in the VI oxidation state ($\text{U}=\text{O}$ is 1.76 \AA ; $\text{Pu}=\text{O}$ is 1.74 \AA) to about 1.83 \AA in the V oxidation state ($\text{Np}=\text{O}$ is 1.85 \AA ; $\text{Pu}=\text{O}$ is 1.81 \AA).

Because $\text{An}(\text{IV})$ has the highest effective charge, it forms the most stable complexes in solution and also forms the most stable precipitates with the lowest solubility. Conversely, $\text{An}(\text{V})$ complexes are the weakest, and its solubility-controlling solids are the most soluble. $\text{An}(\text{V})$ species are therefore the most likely to migrate through the environment. Table 1 shows that the only transuranics that favor the V state are neptunium and plutonium. But in the environments surrounding repository sites, as well as in most groundwaters and ocean environments, plutonium will most likely assume the IV state. Thus neptunium is predicted to be the most

Actinides in Today's Environment

In 1942, Enrico Fermi built mankind's first fission reactor, and nuclear reactions within that nuclear pile created the transuranic elements neptunium, plutonium, americium, and curium. With the subsequent development of nuclear power, the inventory of transuranics has increased dramatically. As of 1990, the estimated accumulations in spent nuclear fuel were approximately 472 tons of plutonium, 28 tons of neptunium, 6 tons americium, and 1.6 tons of curium.

Fortunately, the amount of radioactive material accidentally released from nuclear power plants has been relatively small. Environmental contamination is severe in only a few locations. Major releases were due to a fire in a reactor at Windscale (now Sellafield) in the United Kingdom in 1957, an explosion at the Kyshtym nuclear waste storage facility in the former USSR in 1957, and an explosion and fire at the Chernobyl reactor in Russia in 1986. In addition, a number of DOE sites in the United States, including the Hanford Site in Washington, Rocky Flats Environmental Technology Site in Colorado, and Idaho National Engineering and Environmental Laboratory in Idaho, contain high local concentrations of actinides.

The main source of transuranics in the environment has been nuclear weapons testing. Since the first detonation of a nuclear device in 1945 at Trinity Site in Alamogordo, New Mexico, more than 4 tonnes of plutonium have been released worldwide (accounting only for announced nuclear tests). Atmospheric and underground tests have also injected about 95 kilograms of americium into the environment, along with tiny amounts of the still heavier element curium.

Until they were banned by international treaty in 1963, aboveground nuclear tests propelled the actinides directly into the atmosphere. There they dispersed and migrated around the globe before settling back to earth. Little can be done to isolate or retrieve this material. It is a permanent, albeit negligible, component of the earth's soils and oceans and poses little health risk to the general public.

Underground nuclear tests injected transuranics into highly localized regions surrounding the detonation sites. These concentrated actinide sources became mineralized and integrated into the rock matrix once their areas cooled and solidified. For the most part, the nuclear material is fixed in place. However, plutonium from a test conducted at the Nevada Test Site in 1968 has been detected in a well more than a kilometer away. Its remarkably fast migration rate (at least 40 meters per year) is likely due to colloidal transport through the highly fractured, water-saturated rock surrounding the detonation site.

soluble and easily transported actinide and is the actinide of major concern in assessing the performance of Yucca Mountain.

Coordination Number and Ionic Radii. Another fundamental aspect about the actinide cations is that they tend to act as hard Pearson "acids," which means that they form strong

complexes with highly anionic ligands by electrostatic interactions. Because the actinide-ligand bond is substantially ionic, the number of bound ligands (the coordination number) and the relative positions of the ligands around the cation are determined primarily by steric and electrostatic principles. Consequently, for a given oxidation state, a range of coordination numbers

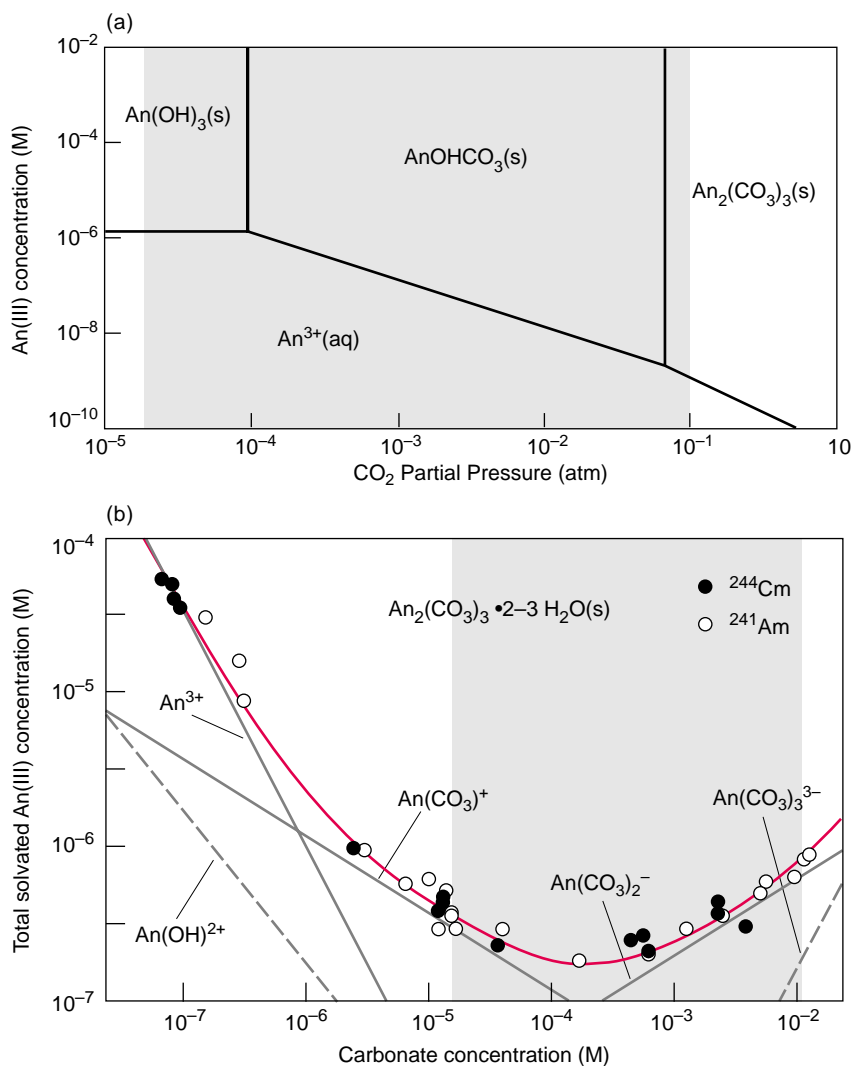


Figure 3. Total An(III) Concentration Versus Carbonate Concentration

(a) The partial pressure of CO_2 in natural waters spans about three orders of magnitude (gray area). The stability diagram for An(III) solid phases (at pH 7) shows that the An(III) hydroxocarbonate is favored in most natural waters. Lower partial pressures or soluble carbonate concentration translate to increased stability of the An(III) hydroxide; higher pressures mean increased stability for the normal carbonate solids. (b) The red curve is the total concentration of An(III) in solution when the solubility-controlling solid is $\text{An}_2(\text{CO}_3)_3 \cdot 2-3\text{H}_2\text{O}(\text{s})$. Calculated concentrations for individual solution species are indicated by the gray lines that run tangent to the solubility curve, or by the gray dashed lines. At low carbonate concentrations, the An^{3+} ion dominates the solution species. The total An(III) concentration drops rapidly with higher carbonate concentrations as more of the solid phase precipitates. But carbonate complexation begins to stabilize the amount of actinide in solution. By the time the anionic bis- and triscarbonate complexes dominate, the solution concentration increases.

is allowed. Coordination numbers between 6 and 12 have been reported for complexes of An(III) and An(IV) and between 2 and 8 for the actinyl ions.

For example, the aquo ions of the actinides, which have only water molecules in the first coordination sphere surrounding the ion, exhibit coordination numbers that vary with oxidation state: 8–10 for An^{3+} , 9–12 for An^{4+} , 4–5 for AnO_2^+ and 5–6 for AnO_2^{2+} . These coordination numbers have been determined from nuclear magnetic resonance (NMR) and XAFS spectroscopy studies (see the article by Conradson et al. on page 422).

Generally, the stabilities of actinide complexes at a given oxidation state increase with atomic number. This increase in stability follows the trend of the actinide contraction, wherein the

ionic radii decrease with atomic number. The ionic radii for An(IV) ions with coordination numbers of 8 are reported to be 1.00, 0.98, 0.96, 0.95, and 0.95 Å for uranium, neptunium, plutonium, americium, and curium, respectively (Shannon 1976).

Solubility and Speciation

The solubility of an actinide is limited primarily by two properties: the stability of the actinide-bearing solid (the solubility-controlling solid) and the stability of the complexed species in solution. An actinide species will precipitate when its dissolved concentration is above the thermodynamic (equilibrium) solubility of its solubility-controlling solid, or if the kinetics

favors the formation of a solid of higher solubility. Formation of the solid sets an upper concentration limit for the actinide in solution.

Figure 3 illustrates these concepts for An(III), where An is either americium or curium. The data points in the lower graph show the measured total concentration of An(III) in solution. At low pH with increasing carbonate concentration, the hydrated carbonated solid $\text{An}_2(\text{CO}_3)_3 \cdot 2-3\text{H}_2\text{O}(\text{s})$, where (s) indicates the solid phase, readily precipitates and hence lowers the concentration of An^{3+} in solution. But complexation of An^{3+} with carbonate stabilizes the solution species and increases the overall An(III) solubility. As the carbonate concentration increases and the different carbonate species form, the total actinide concentration in solution first

reaches a minimum and then increases due to the formation of anionic An(III) complexes. The solubility would change if conditions favored the formation of a new solubility-controlling solid.

We obtain solubility data by performing experiments in the laboratory under well-controlled conditions in which the actinide concentration is measured while varying the ligand concentration. Such experiments enable us to measure the solubility product K_{sp} and the stability constant β . These thermodynamic parameters are the basis for modeling the solubility boundaries for actinides in natural waters, as discussed in the box on "Solubility and Speciation Parameters."

We should note, however, that meaningful interpretation of solubility data requires a detailed knowledge of the composition, crystallinity, and solubility of the solubility-controlling solid, along with the steady-state concentration and composition of the solution species. Steady state is assumed to be established when the actinide concentration remains stable for several weeks or longer. But the solubility-controlling solids of the actinides generally precipitate as an amorphous phase because radiolysis affects their crystallization. Actinide solids may become less soluble with time as they transform from their initially formed, disordered structures into ordered crystalline solids, thereby lowering their free energy. Such a change, however, may not appear for several years. Thus, the solids formed in laboratory experiments may not represent the most thermodynamically stable solids with the lowest solubility. Laboratory-based solubility studies therefore provide an *upper limit* to actinide concentrations in a potential release scenario from a nuclear waste repository.

Because of their omnipresence, hydroxide ions (OH^-) and carbonate ions (CO_3^{2-}) are the most important ligands that complex to actinides in the environment. While other ligands, such as phosphate, sulfate, and fluoride, can lower the actinide concentration

Solubility and Speciation Parameters

Solubility products (K_{sp}) of actinide-bearing solid phases are indispensable primary data for predicting the concentration limits of actinides in the environment. The solubility product describes the dissolution reaction of the solid into its ionic components. For example, the solubility product of $\text{AmOHCO}_3(\text{s})$, where (s) refers to the solid phase, is given by the product of the concentration of the dissolved ions Am^{3+} , OH^- , and CO_3^{2-} according to the following reaction:



The solubility product is then given by

$$K_{sp} = [\text{Am}^{3+}][\text{OH}^-][\text{CO}_3^{2-}] \quad (2)$$

where the brackets indicate ion concentration. The formation of an actinide complex in solution, for example,



is described by the complex's formation constant, β_n . For the forward reaction in Equation (3), the formation constant is

$$\beta_n = \frac{[\text{Am}(\text{CO}_3)_n^{3-2n}]}{[\text{Am}^{3+}][\text{CO}_3^{2-}]^n} \quad (4)$$

where n refers to the number of ligands. For the reverse reaction, β_n changes sign and is known as the stability constant. The concentration of an actinide solution complex can be calculated by using the known solubility product of the solubility-limiting solid and the formation constant of the species of interest as follows:

$$[\text{Am}(\text{CO}_3)_n^{3-2n}] = \beta_n [\text{Am}^{3+}][\text{CO}_3^{2-}]^n = \beta_n K_{sp} \frac{[\text{CO}_3^{2-}]^{n-1}}{[\text{OH}^-]} \quad (5)$$

Accordingly, the total actinide concentration in solution is given by the sum of the concentrations of species present in solution as follows:

$$\begin{aligned} [\text{Am(III)}] &= [\text{Am}^{3+}] + [\text{Am}(\text{CO}_3)_n^{3-2n}] + [\text{Am}(\text{OH})_m^{3-m}] \\ &= \frac{K_{sp}}{[\text{CO}_3^{2-}][\text{OH}^-]} \times \left(1 + \sum_n \beta_n [\text{CO}_3^{2-}]^n + \sum_m \beta_m [\text{OH}^-]^m \right) \quad (6) \end{aligned}$$

Complexation of the dissolved actinide ion with ligands in solution (large β_n values) generally increases the total actinide concentration in solution.

(because of the low solubility of the corresponding solid phase), their concentrations in natural waters are generally low. Consequently, they cannot compete successfully with hydroxide or carbonate complexation. However, organic biodegradation products, such as humates or fulvates, are generally present in natural aquifers and can potentially play a role in actinide solubility and migration.

Hydrolysis. The interaction of actinide and hydroxide ions produces monomeric and—particularly for Pu(IV)—polymeric solution species. The solid-phase structures are oxides, oxyhydroxides, or hydroxides of low solubility.

In the absence of carbonate or other strong ligands (or with very low concentrations of them), trivalent actinides form the positively charged or neutral hydroxo complexes of general formula $An(OH)_m^{3-m}$, where $m = 1, 2, \text{ or } 3$, that is $An(OH)^{2+}$, $An(OH)_2^+$, and $An(OH)_3(aq)$. Similarly, An(IV) forms complexes in solution of general formula $An(OH)_n^{4-n}$, where $n = 1, 2, 3, \text{ or } 4$. The solid hydroxide $An(OH)_n(s)$, where $n = 3$ for An(III) and 4 for An(IV) or the hydrated oxide $AnO_2 \cdot nH_2O$ for An(IV) are expected to control the solubility of actinides in both oxidation states.

Understanding the An(IV) solution chemistry is still a formidable challenge. The high charge allows the An^{4+} ions to easily hydrolyze and form multiple species simultaneously, even at low pH. Plutonium(IV) is known to hydrolyze even in dilute acidic solutions and, at concentrations greater than 10^{-6} M, will undergo oligomerization and polymerization to form very stable intrinsic colloids.

Recent x-ray absorption fine-structure (XAFS) studies, discussed on page 432 in the article by Conradson, have given more insight into the structural details of Pu(IV) colloids. The sub-micron-scale colloid particles are nominally composed of Pu(IV) hydroxo polymers and contain structural characteristics of

plutonium oxide, PuO_2 . However, the XAFS data reveal that these particles possess multiple functional groups, such as terminal hydroxo and bridging oxo and hydroxo groups. Each colloid particle can be considered an amorphous oxyhydroxide compound. The functional groups originate from the polymerization of monomeric species formed through hydrolysis, and the number of functional groups depends on the history of the solution preparation and aging process. While the chemical “structure” of every Pu(IV) colloid may be similar, each colloid can have a unique distribution of functional groups depending on solution preparation, particle size, and water content. Once they form, however, the colloids are inordinately stable in near-neutral solution, presumably because over time, the hydroxo groups that join the plutonium atoms together in the polymer are converted into chemically resistant oxygen bridges.

The generation of Pu(IV) colloids is one of the main processes that complicate determining thermodynamic constants and accurately predicting soluble plutonium concentrations in natural waters. Both the colloids and other amorphous Pu(IV) hydroxide solids span a wide range of structural features, crystallinities, and stabilities, and hence exhibit a wide range of solubilities. The presence of Pu(IV) colloids will therefore complicate any calculation of plutonium solubility, as will be evident when we review plutonium solubility and speciation in Yucca Mountain waters.

Solid hydroxides and oxides are also expected to limit the solubility of An(V) and An(VI) complexes. For example, $Np_2O_5(s)$ has been determined to be the solubility-controlling solid in waters from Yucca Mountain, while schoepite, $UO_2(OH)_2 \cdot nH_2O(s)$ is most stable for U(VI). Interestingly, these solids exhibit both acidic and basic characteristics. With increasing pH, their solubilities tend to decrease in acidic media and increase in alkaline (basic) solutions because of the forma-

tion of anionic hydroxo complexes: $AnO_2(OH)_2^-$ for An(V) and $AnO_2(OH)_n^{2-n}$ ($n = 3$ and 4) for An(VI). The hydrolysis of U(VI) is complicated even more by the formation of polymeric hydroxide species at high U(VI) concentration ($>10^{-5}$ M), i.e., $(UO_2)_3(OH)_5^+$ or $(UO_2)_4(OH)_7^+$. We are currently conducting experiments to see if Pu(VI) undergoes a similar polymerization.

Carbonate Complexation. Carbonate is ubiquitous in nature. In surface waters, such as oceans, lakes, or streams, its concentration ranges generally between 10^{-5} and 10^{-3} M. In groundwaters, its concentration is enhanced (up to 10^{-2} M) because of the increased CO_2 partial pressure, which is about 10^{-2} atm deep underground compared with the atmospheric partial pressure of about 3×10^{-4} atm. These relatively high carbonate concentrations influence the environmental chemistry of actinides in all oxidation states.

Carbonate generally bonds to actinides in a bidentate fashion, that is, two of the three oxygen atoms in the complex bond to the actinide. Thus, actinide carbonate complexes are very strong and highly stable both in solution and in the solid state.

We have investigated the structure of carbonate complexes involving the actinyl ions AnO_2^+ and AnO_2^{2+} . (These complexes are more soluble and thus more easily studied.) As shown in Figure 4, three monomeric solution complexes form. Depending on the solution conditions, these complexes may coexist with each other and with hydroxo complexes. It is therefore difficult to obtain clean, unambiguous structural data about a single species.

We can make inroads into that problem by investigating the stability and structure of the triscarbonato species, $AnO_2(CO_3)_3^{m-6}$, shown in Figure 4(c). This is the limiting (fully coordinated) An(V,VI) carbonate complex in solution. At carbonated concentrations above 10^{-3} M, this complex forms at the exclusion of the others. Using a

battery of spectroscopic techniques, including multinuclear NMR spectroscopy, x-ray diffraction, and XAFS, we have obtained formation constants, bond lengths, and other structural parameters for the An(V) and (VI) carbonate complexes (Clark et al. 1999). This information has helped us understand various aspects of the An(V,VI) carbonate system. (The article by Clark that begins on page 310 describes structural investigations of the Pu(VI) tris-carbonate.)

Carbonate Solids. In many natural waters, carbonate effectively competes with hydrolysis reactions, and mixed hydroxocarbonate solids are likely to form. These solids have general formulas $\text{An}(\text{OH})(\text{CO}_3)(\text{s})$ for An(III) and $\text{An}(\text{OH})_{2m}(\text{CO}_3)_n(\text{s})$ for An(IV), where An stands for uranium, neptunium, plutonium, or americium. (The equilibria in these systems are quite complicated, and neither the structure nor the values for n has been determined accurately for An(IV) compounds.)

In the laboratory, however, we can study actinide solids of different compositions by increasing the carbonate concentration. This increase reduces the extent of hydrolysis and allows the formation, for example, of pure An(III) carbonate solids, such as $\text{Am}_2(\text{CO}_3)_3 \cdot n\text{H}_2\text{O}(\text{s})$ or $\text{NaAm}(\text{CO}_3)_2 \cdot n\text{H}_2\text{O}(\text{s})$, which are the solubility-controlling solids in solutions containing high concentrations of sodium and carbonate. These solids are analogous to the ones formed by the trivalent lanthanides Nd(III) and Eu(III).

Similarly, we have observed the formation of solid An(VI) and An(V) compounds in solutions containing high concentrations of alkali metals and carbonate. These An(V,VI) carbonate solids are inherently interesting. Together, they can be viewed as a structural series, as evident in Figure 5. Binary An(VI) solids have a general composition $\text{AnO}_2\text{CO}_3(\text{s})$ and are made from highly ordered actinyl carbonate layers. However, An(V) solids need to

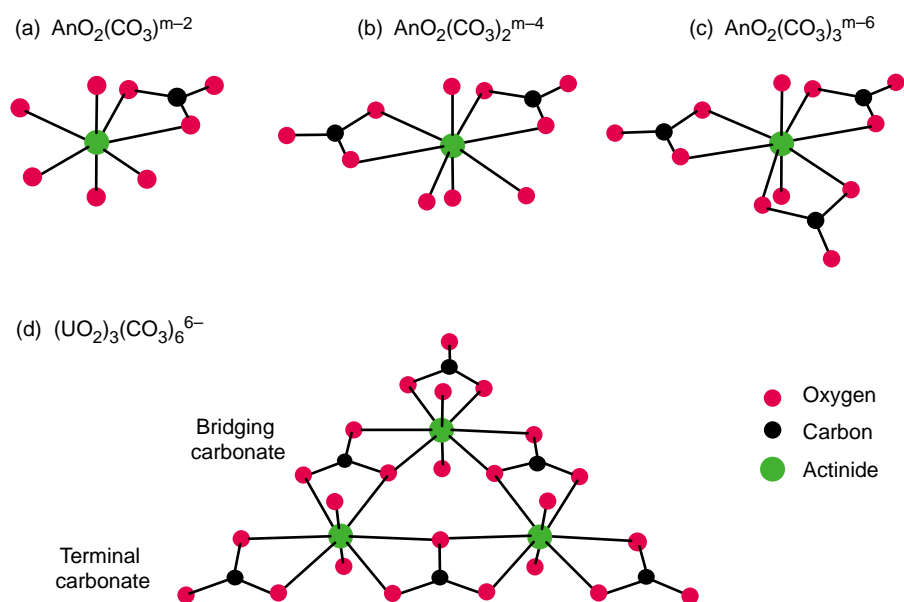


Figure 4. Carbonate Complexes of the Actinyl Ions

Actinides in the V and VI state form similar carbonate complexes in solution, although the charge of the species depends on the oxidation state. Thus, in the three monomeric complexes shown in (a)–(c), $m = 1$ for An(V) and $m = 2$ for An(VI). Actinides in the V state have the lowest effective charge and form the weakest complexes. In these complexes, Np(V) has the longest actinyl bond ($\text{An}=\text{O}$) length (1.86 Å). We have also determined only slight changes in the equatorial An–O distances to the carbonate ligands: they vary between 2.42 and 2.44 Å for An(VI) and between 2.48 and 2.53 Å for Np(V). (d) Uranium(VI) may also polymerize at high carbonate and uranium concentrations to form the polynuclear actinyl carbonate complex $(\text{UO}_2)_3(\text{CO}_3)_6^{6-}$. If present, this polynuclear complex stabilizes U(VI) in solution and increases the overall U(VI) solubility in comparison with the solubility of its monomeric counterpart, $\text{AnO}_2(\text{CO}_3)_2^{2-}$.

incorporate a monovalent cation, such as Na^+ , K^+ , or NH_4^+ , into their structure (otherwise they would have an overall charge). Thus, we observe only ternary An(V) solids with general compositions $\text{M}_{(2n-1)}\text{AnO}_2(\text{CO}_3)_n \cdot m\text{H}_2\text{O}(\text{s})$, where $n = 1$ or 2, M is the monovalent cation, and An stands for neptunium, plutonium, or americium.

As the number of cations incorporated into the An(V,VI) carbonate solids increases (stoichiometrically from 0 to 1 to 3), the structures become increasingly open, and the solids generally become more soluble under conditions in which the uncomplexed actinide ion dominates solution speciation. Replacement of the cations with larger ones

enhances the solubility of the actinide by several orders of magnitude. We exploited that fact when we studied the neptunyl “double carbonate” solids $\text{M}_3\text{NpO}_2(\text{CO}_3)_2$. These solids exhibit such low solubilities in near neutral solutions (10^{-4} to 10^{-7} M) that the solution species cannot be studied by many spectroscopic methods. To modify the solubility and obtain more-concentrated neptunyl solutions, we examined the use of large, bulky cations in an attempt to generate an unfavorable fit of the complex into the stable lattices shown in Figures 5(b) and 5(c). We found that tetrabutylammonium provided stable solutions of $\text{NpO}_2\text{CO}_3^-$ and $\text{NpO}_2(\text{CO}_3)_2^{3-}$ in

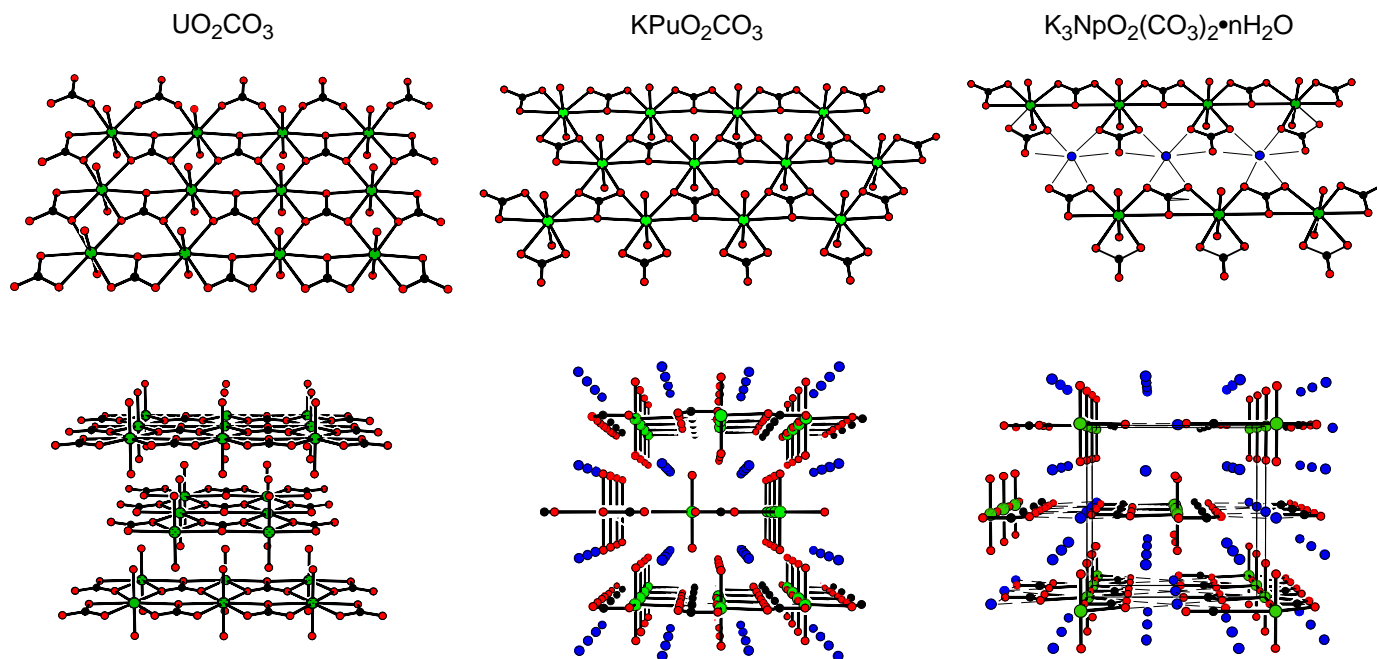


Figure 5. Actinide(V,VI) Alkali Metal/Carbonate Solids

Actinide(V,VI) carbonate solids form a “structural series” that progresses from dense, highly ordered layered structures to more open structures. A single layer is shown above a perspective drawing of each solid. (a) An(VI) will combine with carbonate to form binary solids, such as $\text{UO}_2\text{CO}_3(\text{s})$ or $\text{PuO}_2\text{CO}_3(\text{s})$. Within a layer, each actinide is bonded to two carbonates in a bidentate fashion and to two others in a monodentate fashion. (This is in contrast to solution species, in which carbonate always bonds to an An(VI) in a bidentate fashion.) (b) Actinide(V) ions cannot form binary carbonate solids, since the structural unit would have an overall charge. Solid An(V) carbonates therefore form ternary complexes in conjunction with monovalent metal cations (M), such as Na^+ , K^+ , or NH_4^+ . Within a layer, each actinyl ion binds to three carbonate ligands in a bidentate fashion. The metal ions sit between the layers and form the ternary complex $\text{MAnO}_2\text{CO}_3(\text{s})$. This opens the structure, in comparison with the An(VI) binary structure, and increases solubility. (c) At higher metal ion concentrations, metal ions will be incorporated into each layer to form very open structures of general formula $\text{M}_3\text{AnO}_2(\text{CO}_3)_2(\text{s})$.

millimolar concentrations over a wide pH range. The enhanced solubility allowed us to study the temperature dependence of the carbonate complexation reactions with near-infrared (NIR) absorption spectroscopy and to obtain additional structural information about the Np(V) solution carbonate complexes with XAFS spectroscopy.

The compositions and stabilities of these actinyl carbonate solids depend on the ionic strength and carbonate concentration and are controlled by the actinide, carbonate, and sodium concentrations in solution. For example, the stability of the Np(V) solids $\text{Na}_{(2n-1)}\text{NpO}_2(\text{CO}_3)_n \cdot m\text{H}_2\text{O}(\text{s})$ is given by the solubility product K_{sp} :

$$K_{\text{sp}} = [\text{Na}^+]^{2n-1} [\text{NpO}_2^+] [\text{CO}_3^{2-}]^n .$$

For the An(VI) solid $\text{AnO}_2\text{CO}_3(\text{s})$, n is equal to 1 and its solubility is nominally independent from the sodium concentration in solution. At the low ionic strengths of most natural waters, an unrealistically high NpO_2^+ concentration would be needed to precipitate a ternary Np(V) carbonate solid. Thus, solid An(V) or An(VI) carbonates are in general not observed in natural waters. However, because the ternary compounds of Np(V) have been observed to form in concentrated electrolyte solutions, these solids are important for solubility predictions in brines found at WIPP.

Solubility and Speciation in Yucca Mountain Waters

As a way of tying together many of the concepts presented in the previous sections, we can consider the solubility and speciation of neptunium and plutonium in Yucca Mountain waters. (The article by Eckhardt, starting on page 410, discusses more of the research conducted for Yucca Mountain.) As mentioned earlier, neptunium tends to exist in the V oxidation state in natural waters and because of the lower effective charge of the AnO_2^+ ion, forms weak complexes. Thus, neptunium has the distinction of being the most soluble and transportable actinide and is the

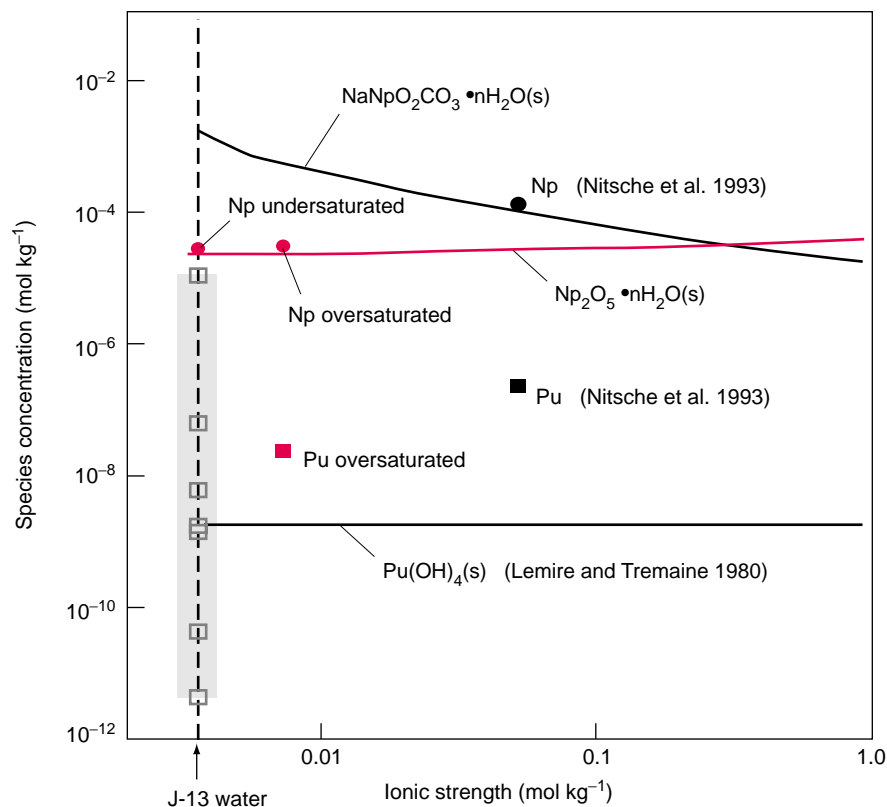


Figure 6. Solubility of Neptunium(V) and Pu(IV) J-13 Water

The figure shows our measured total soluble concentrations of neptunium (red circles) and plutonium (red square) in J-13 water at a fixed carbonate concentration of 2.8 mM (indicated by the dashed line), as well as earlier measurements conducted at a higher ionic strength (black circle and square). The lines are theoretical predictions for different solubility-controlling solids. The Np(V) concentration is about 100 times greater than that of Pu(IV). Our measurements confirm that the controlling Np(V) solid is the oxide $\text{Np}_2\text{O}_5(\text{s})$, rather than the previously postulated sodium carbonate solid $\text{NaNpO}_2\text{CO}_3(\text{s})$. The solubility of plutonium in J-13 water presumably is controlled by amorphous oxides/hydroxides or colloidal forms of Pu(IV), since the measured Pu(IV) solubilities are nearly an order of magnitude higher than predicted by Lemire and Tremaine for the solubility product of $\text{Pu}(\text{OH})_4(\text{s})$. Our data are consistent with the range of Pu(IV) solubilities as calculated from K_{sp} data of Pu(IV) hydroxide or hydrous oxide reported in the open literature (gray area).

one of greatest concern when assessing the environmental safety of the potential underground storage site at Yucca Mountain. Plutonium is considered the most toxic actinide and is always of environmental concern.

Our studies were conducted in water from a particular borehole in Yucca Mountain (J-13 water). The sodium and carbonate concentrations are low (both around 2 to 3 mM), as is the ionic strength of J-13 water (0.003 molal).

However, groundwater conditions within and around Yucca Mountain vary. The carbonate concentration changes (because the CO_2 partial pressure changes with depth), as does the pH, Eh, and temperature. We mimicked this variation in the natural waters by conducting our studies at various pH values while maintaining a constant ionic strength. We also conducted our studies at different temperatures (25°C, 60°C, and 90°C) to approximate the range of

temperatures expected at the repository. Not surprisingly, changing these basic parameters greatly affected the actinide behavior (Efurud et al. 1998). Figure 6 summarizes the results of our studies.

The controlling solids for the actinides in J-13 water—in all oxidation states—were mainly oxides and hydroxides. We observed only the formation of greenish brown Np(V) crystalline solids of general formula $\text{Np}_2\text{O}_5 \cdot n\text{H}_2\text{O}(\text{s})$, green Pu(IV) solids of general formula $\text{PuO}_2 \cdot n\text{H}_2\text{O}$ and/or amorphous Pu(IV) hydroxide/colloids. The solubility of neptunium was about 10^{-3} M at pH 6, but dropped to about 5×10^{-6} M at pH 8.5. The neptunium species distribution similarly changed with conditions. At pH 8.5, about 31 percent of Np(V) was present as the neptunyl ion NpO_2^+ . The remaining soluble Np(V) was complexed with either carbonate or hydroxide, with about 58 percent $\text{NpO}_2\text{CO}_3^-$ and 11 percent $\text{NpO}_2\text{OH}(\text{aq})$. At pH 6, however, Np(V) hydrolysis and carbonate complexation reactions were minimized, and all of the neptunium was present as NpO_2^+ .

By comparison, at all pH values examined in our study, 99 percent of the soluble plutonium was calculated to be in the IV state as $\text{Pu}(\text{OH})_4(\text{aq})$. When using $\text{Pu}(\text{OH})_4(\text{s})$ as the solubility-limiting solid in our geochemical models, the plutonium concentration in solution was predicted to be about 10^{-9} M (using the thermodynamic data available in the open literature). As seen in Figure 6, experimental data are about one to two orders of magnitude higher. The discrepancy presumably arises because plutonium solubility is instead controlled by amorphous oxides/hydroxides or colloidal forms of Pu(IV). (Note that if crystalline $\text{PuO}_2(\text{s})$ were the solubility-controlling solid, Pu(IV) solubility would be about 10^{-17} M, well below the Pu(IV) hydroxide solubility range.)

The J-13 water is almost neutral (pH ~7) and has a redox potential of about +430 millivolts. But different water conditions would dramatically affect neptunium solubility, as illustrated

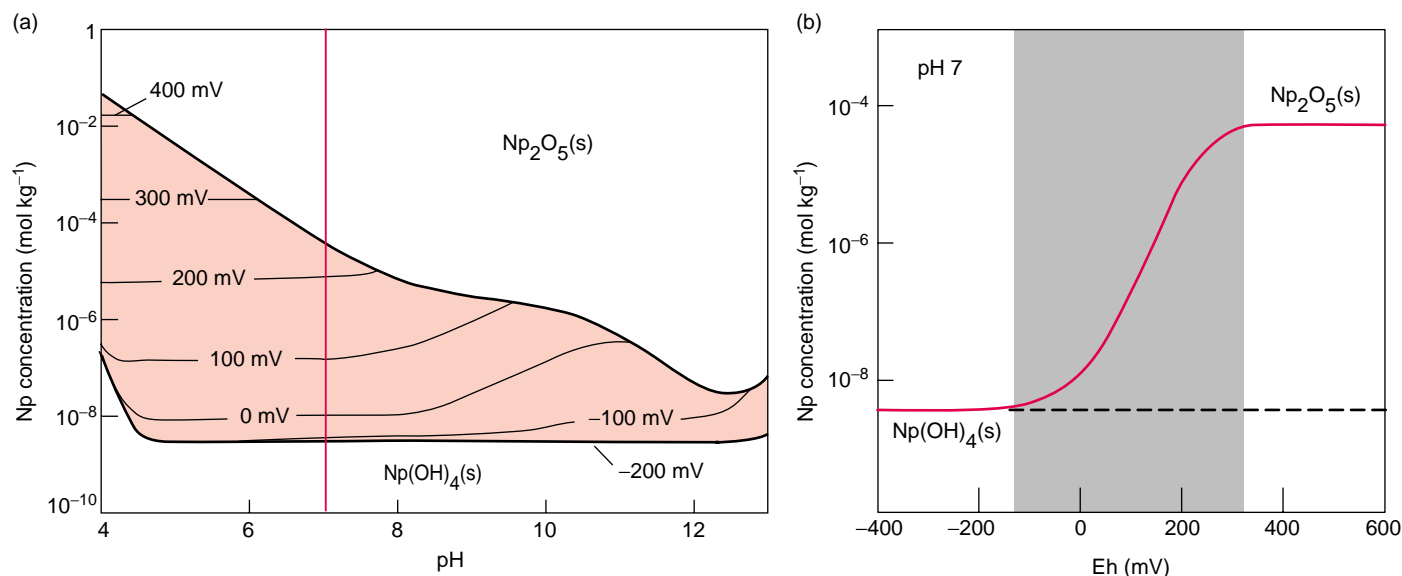


Figure 7. Neptunium Solubility in Yucca Mountain J-13 Water

Neptunium solubility varies tremendously depending on the Eh and pH of the water. (a) The graph shows the neptunium concentration as a function of pH. Calculated solubility boundaries at various Eh values are superimposed on the graph. The colored region contains mainly Np(V) in solution, while the upper and lower bold lines are the solubility boundaries of the Np(V) solid phase, $\text{Np}_2\text{O}_5(\text{s})$, and the Np(IV) solid phase, $\text{Np}(\text{OH})_4(\text{s})$, respectively. Solutions with neptunium concentrations above these boundaries are oversaturated and will precipitate the respective solid. The total neptunium concentration in solution may vary by more than six orders of magnitude over the entire pH range under oxidizing conditions. (b) This graph shows the solubility as a function of Eh at a fixed pH of 7, and corresponds to the Np solubility as one moves along the red line in the previous graph. Under reducing conditions (below -120 mV), Np(IV) dominates the solution speciation. Its concentration in solution is limited to less than 10^{-8} molal by the solubility of $\text{Np}(\text{OH})_4(\text{s})$. As conditions become more oxidizing, Np(V) becomes the redox-stable oxidation state and begins to dominate the speciation. [The Eh determines the Np(IV)/Np(V) ratio in solution, while the overall Np(IV) concentration is maintained by the solubility of $\text{Np}(\text{OH})_4(\text{s})$.] The neptunium concentration rises with redox potential until it reaches approximately 10^{-4} molal at an Eh of ~ 250 mV. Solutions containing a higher neptunium concentration are oversaturated, and the Np(V) solid phase $\text{Np}_2\text{O}_5(\text{s})$ precipitates. The soluble neptunium concentration remains constant from then on. The shaded area spans the region where Eh and solubility of the Np(IV) solid control the neptunium concentration in solution. Outside this area, the solubilities of the Np(IV) and Np(V) solids govern neptunium solution concentration, independent of Eh.

in Figure 7 (Kaszuba and Runde 1999). Under strong reducing conditions (below about -120 millivolts), the total soluble neptunium concentration is limited by a Np(IV) solid phase, $\text{Np}(\text{OH})_4(\text{s})$, and is conservatively assumed to be about 10^{-8} M. Similar to plutonium, the presence of a more ordered solid oxyhydroxide or oxide, such as $\text{NpO}_2(\text{s})$, would reduce that conservative boundary by several orders of magnitude. Under these reducing conditions, Np(IV) also dominates the solution speciation in the form of the neutral complex $\text{Np}(\text{OH})_4(\text{aq})$. The total neptunium concentration will rise as the water conditions become more oxidiz-

ing and Np(V) becomes more stable in solution. Eventually, the Np(V) concentration is great enough to allow a Np(V) solid phase, $\text{Np}_2\text{O}_5(\text{s})$, to precipitate. Formation of this solid sets an upper limit to the soluble neptunium concentration. Within the pH and Eh ranges of most natural aquifers (between 4 and 9 and between -200 and $+700$ millivolts, respectively), that concentration may vary by more than four orders of magnitude.

When modeling actinide release from a radioactive waste repository, we must anticipate the conditions at the source (e.g., close to a spent nuclear fuel container) as well as those in the

far-field environment. Spent nuclear fuel contains mainly UO_2 and actinides in low oxidation states (III and IV). If conditions at the disposal site are reducing—for example, because of microbial activities or the reduction capacity of corroding iron from storage containers—the actinides will be maintained in their lower oxidation states and soluble actinide concentrations may be low. If local reducing conditions change because oxidizing waters infiltrate from the surroundings, actinides will enter their more-soluble oxidation states and begin to migrate into the environment. Once far from the repository, conditions may change drastically,

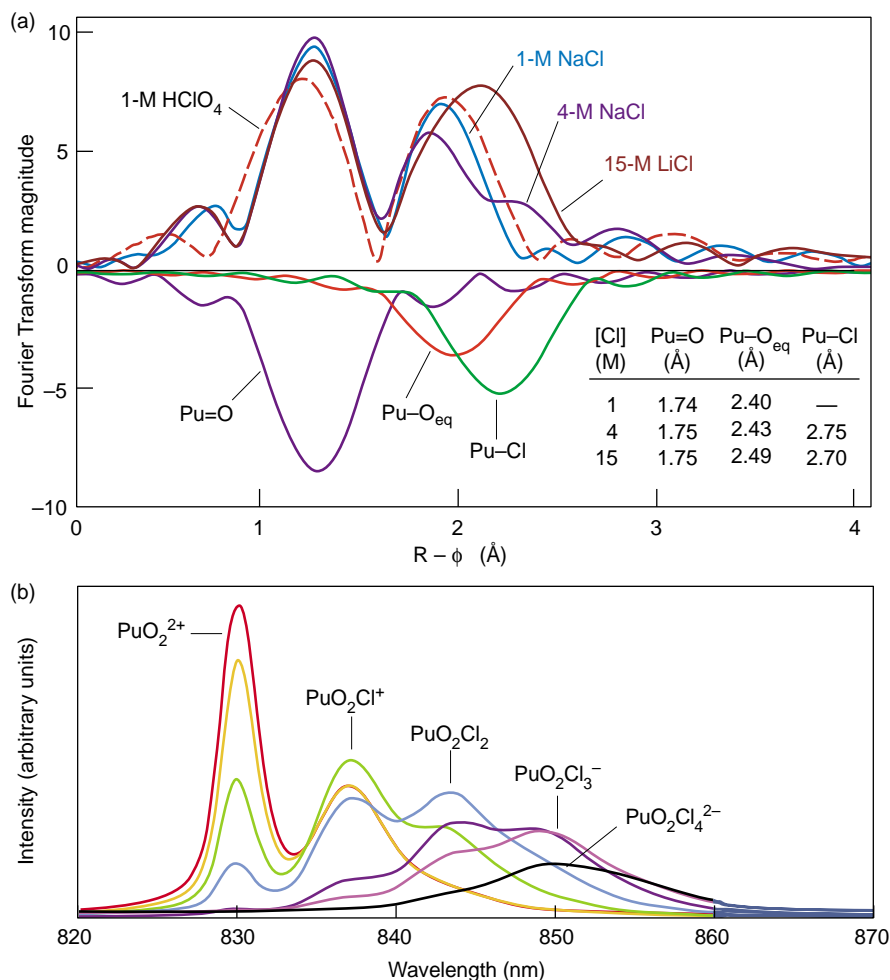


Figure 8. XAFS Data and NIR Spectra of Pu(VI) in NaCl Solutions

(a) By comparing XAFS data for Pu(VI) in 1-M NaCl, 4-M NaCl, and 15-M LiCl, and non-complexing 1-M HClO₄, we have obtained condition-specific structural information about the solution species. Chloride appears to bond above 1-M chloride in solution. Bonding is clearly evident by 4-M chloride. As seen in the table (inset), the plutonyl bond length (Pu=O) increases slightly after the chlorine bonds and replaces water molecules (indicated by the Pu-O_{eq} bond) in the equatorial plane of the O=Pu=O moiety. (b) The absorption bands at 838, 843, 849, and about 855 nm, plus the characteristic band at 830 nm for the PuO₂²⁺ ion, indicate the formation of inner-sphere Pu(VI) chloride complexes. These bands allowed us to determine the formation constant, β , of the most important Pu(VI) chloride complexes in NaCl solutions, PuO₂Cl⁺ and PuO₂Cl₂(aq).

and the transport behavior of redox-sensitive elements such as plutonium or neptunium may change. Clearly, evaluation of actinide mobility in the geochemical environment around nuclear waste repositories must account for soluble actinide concentrations that are controlled by the redox potential of the transport medium and as well by the solubility of the actinides' solid phases.

Complexation with Chloride and Implications for WIPP

In most natural waters, actinides are usually associated with hydroxide or carbonate ligands. However, WIPP, which is designed to hold defense-related transuranic waste, is carved out of a salt formation. Water at the WIPP site thus consists of concentrated brines

that are saturated with chloride salts and exhibit very high ionic strengths (between 4 and 8 molal). With increasing distance from the repository, the brines' ionic strength decreases and may ultimately reach the lower values of most natural surface and groundwaters. This variation complicates our transport models, since the species that form within the WIPP site will not be those that control actinide behavior far from the site.

Chloride has been shown to affect the solubility and speciation of actinide compounds significantly. As mentioned earlier, in most natural waters plutonium favors the IV and V oxidation states, but radiolytic hypochlorite formation in concentrated chloride solution may result in the formation of Pu(VI). Furthermore, complexation by chloride may enhance stabilization of Pu(VI) with respect to reduction to Pu(V) and Pu(IV).

We have studied the complexation reactions of U(VI) and Pu(VI) with chloride using a variety of spectroscopic techniques, including ultraviolet, visible, and NIR absorption and XAFS spectroscopies (Runde et al. 1999). We could determine when U(VI) and Pu(VI) chloride species, such as PuO₂Cl⁺ and PuO₂Cl₂, formed as a function of chloride concentrations (see Figure 8). Interestingly, the tris- and tetrachloro complexes are not formed in significant concentrations in NaCl solutions (up to the point of NaCl saturation). However, we have observed spectroscopically UO₂Cl₄²⁻ and PuO₂Cl₄²⁻ at very high LiCl concentrations and obtained structural data from single crystals synthesized from concentrated chloride solutions.

The interaction of actinides with chloride and other weak anionic ligands significantly affects solubility predictions and must be considered in risk assessments of WIPP and other nuclear waste repositories in salt formations. With regard to neptunium, chloride enhances the Np(V) solubility because of a strong ion interaction between the Np(V) compounds and chloride ions

(see Figure 9). Runde et al. (1996) simulated this interaction using the Pitzer ion-interaction model and developed a Pitzer parameter set to predict the Np(V) solubility at different NaCl concentrations and in artificial brine solutions (Runde et al. 1999). Neglecting the chloride interaction leads to a predicted Np(V) solubility about an order of magnitude too low at a neutral pH. The change of water activity with ionic strength affects the chemical potential of the solid phase because of hydration water molecules in the solid.

Np(V) solubilities were measured from oversaturation in two artificial WIPP brines, AISinR and H-17. The solutions reached a steady state after 241 days. The measured Np(V) solubilities reported in the literature are 2×10^{-6} molal and 1×10^{-6} molal in AISinR and H-17, respectively, while our model predicts Np(V) solubilities of 1×10^{-5} and 3×10^{-6} molal, respectively. The prediction is acceptable for the H-17 brine but lacks accuracy for the AISinR brine. This is because the model accounts only for interactions between Np(V) and Na^+ and Cl^- ions, while the Pitzer parameters for electrolyte ions such as K^+ , Mg^{2+} , Ca^{2+} , and SO_4^{2-} (other constituents in the brines) are unknown. Additional data in various electrolyte solutions are required to develop a more accurate model for the Np(V) solution chemistry in complex brines.

Sorption

The solubility of an actinide species provides an upper limit to the actinide concentration in solution and may be considered as the first barrier to actinide transport. Once an actinide has dissolved in water, its sorption onto the surrounding rock or mineral surfaces is expected to act as a secondary barrier. When the actinide concentrations are far below the solubility limits, as is likely in most surface and groundwater systems, water/rock interfacial processes are

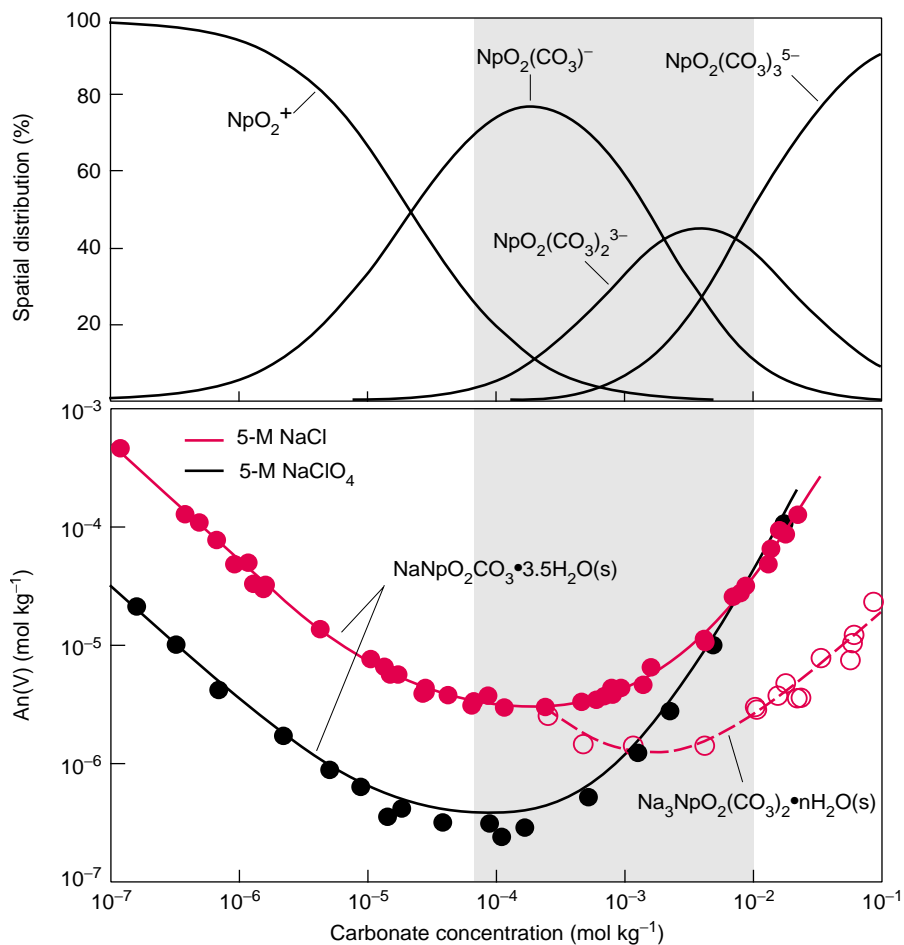


Figure 9. Solubility of Np(V) in Concentrated Electrolyte Solutions

The upper graph shows the distribution of predominant Np(V) solution species as a function of carbonate concentrations, with environmentally relevant concentrations shown in gray. The lower graph shows the soluble Np(V) concentrations in 5-M NaCl solution—conditions that are relevant for WIPP—and noncomplexing 5-M NaClO_4 solution over the same range. Similar data are obtained for Am(V). The neptunium solubility is about an order of magnitude higher in NaCl because of the stabilizing effect of actinide-chloride complexation reactions. The solubility-controlling solid for both curves at low carbonate is the hydrated ternary Np(V) carbonate, $\text{NaNpO}_2\text{CO}_3 \cdot 3.5\text{H}_2\text{O}(\text{s})$. Interestingly, this solid initially forms at high carbonate concentrations. While it is kinetically favored to precipitate, it is thermodynamically unstable. Over time, it transforms to the thermodynamically stable equilibrium phase $\text{Na}_3\text{NpO}_2(\text{CO}_3)_2 \cdot n\text{H}_2\text{O}(\text{s})$ (dashed curve).

expected to dominate actinide transport through the environment. (Simple dilution will lower the actinide concentration, typically to trace concentrations, once the actinide migrates away from the contaminant or waste source.)

Actinide sorption onto mineral surfaces depends on many factors, such as the actinide's speciation and concen-

tration, the flow rate and chemistry of the water, and the composition of the surrounding rocks. In addition, different mechanisms, such as physical adsorption, ion exchange, chemisorption, or even surface precipitation, can fix the actinide to a mineral/rock surface or in general inhibit its transport. Furthermore, redox processes complicate the

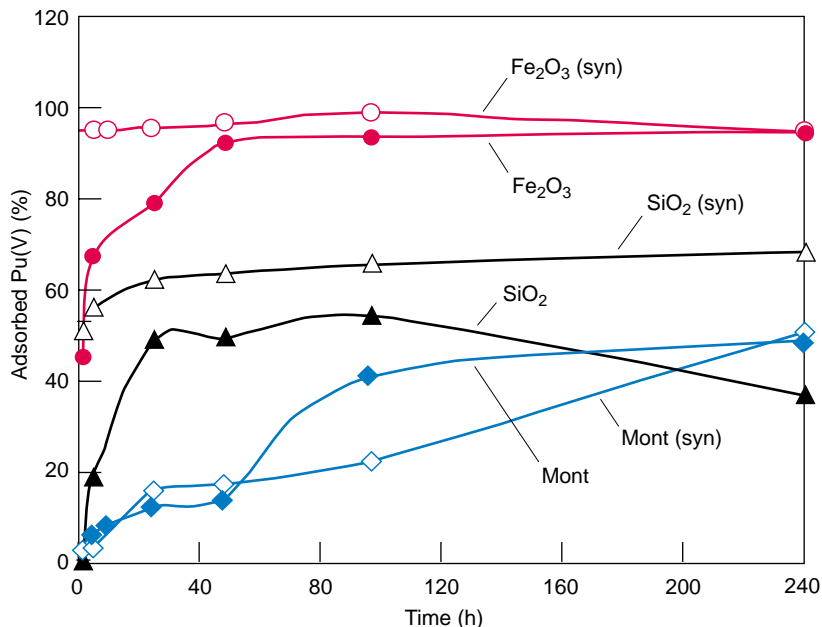


Figure 10. Uptake of Pu(V) by Colloids

Lu et al. (1998) obtained data for Pu(V) adsorption onto colloids, including hematite (Fe_2O_3), silica (SiO_2), and montmorillonite (Mont), in natural J-13 water and in a synthetic (syn) J-13 water. The colloid concentration was maintained at 200 mg/L, with the colloids being about 100 nm in size. The sorption clearly depends on the type of mineral, but the sorption mechanism remains unknown. The time-dependence of the sorption onto montmorillonite suggests a more complicated interaction than occurs with oxide minerals.

Table II. Desorption of Plutonium from Colloids in J-13 Water after 150 Days

Colloid Material	Amount Desorbed	
	Pu(IV) (%)	Pu(V) (%)
Hematite ($\alpha\text{-Fe}_2\text{O}_3$)	0.0	0.01
Goethite ($\alpha\text{-FeOOH}$)	0.57	0.77
Montmorillonite	8.23	0.48
Silica (SiO_2)	19.93	1.04

sorption behavior of neptunium and plutonium. Unfortunately, we are only beginning to understand such actinide sorption and transport mechanisms.

Generally, batch-sorption experiments are performed to investigate how actinides will be retained in the environment. An actinide-containing solution is allowed to come in contact with the geomaterial of interest, and we measure the amount of actinide that

remains in solution. The difference between the remaining and initial actinide concentrations equals the amount that sorbed to the sample. This difference allows us to calculate the batch-sorption distribution coefficient K_d , defined as the moles of radionuclide per gram of solid phase divided by the moles of radionuclide per milliliter of solution and reported as milliliters per gram (mL/g). Low K_d values mean low sorption, and

high values imply effective immobilization due to sorption onto rock surfaces.

Batch-sorption experiments provide helpful information about the sorption capacity of a mineral or soil. But while they are easy to perform, they have some drawbacks. The experiments are fundamentally static and provide only partial information about the dynamic, nonequilibrium processes that occur in nature.² Additionally, the results of batch-sorption experiments are very sample specific and difficult to extrapolate to the different conditions found throughout a repository.

To apply sorption data accurately, we must obtain sorption coefficients from both individual, well-characterized minerals, such as zeolites, manganese oxides, or iron oxyhydroxides, and from mineral mixtures with varying but known compositions. Sorption coefficients from these studies can serve as input data into a transport model that will estimate the actinide retention along water flow paths of known mineral content. The model predictions can then be compared with experimental results obtained from dynamic experiments that use complex soils and rocks.

Studies using minerals (hematite, calcite, gibbsite, albite, and quartz), clays (montmorillonite), and zeolites (clinoptilolite) have shown that Am(III) and Pu(IV) sorb very rapidly to these solids in the following descending order: hematite, montmorillonite, clinoptilolite, and calcite, followed to a much lesser extent by gibbsite, albite, and quartz. But other factors, such as the concentration, solution speciation, and oxidation-state distribution of the actinide species, significantly affect the extent of surface sorption. As an example, K_d values for neptunium sorption onto hematite range from 100 to

²Flow-through, or dynamic, column experiments, wherein the actinide solution is allowed to migrate through a short column of packed geomaterial, provide information about dynamic transport properties. Dynamic column experiments are difficult to perform and interpret, and most of the sorption studies on the actinides are still performed as batch experiments.

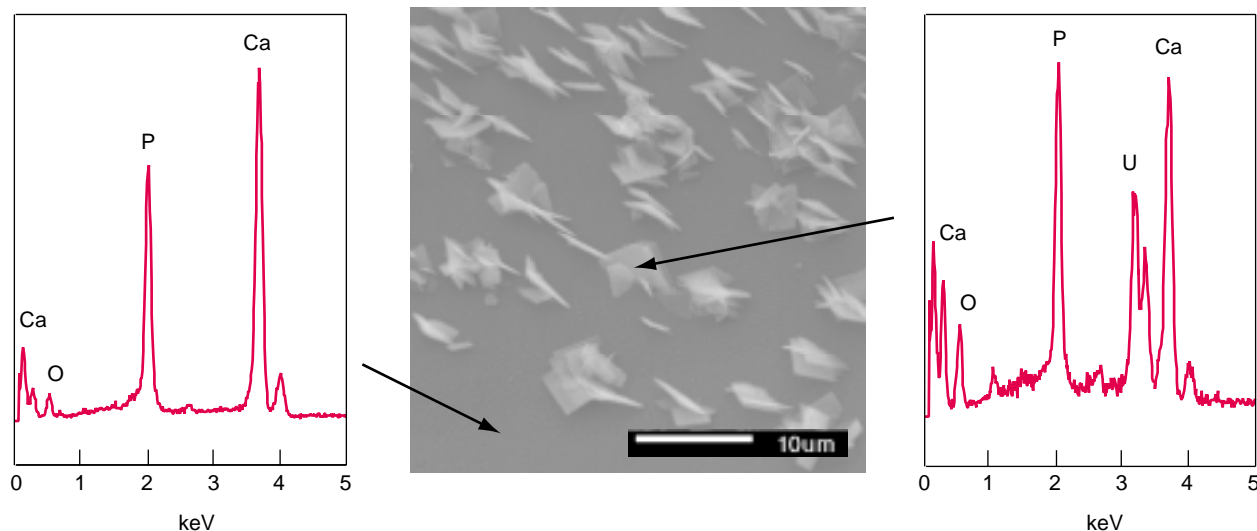


Figure 11. SEM Micrograph of Uranium Precipitate on Apatite

A solution containing U(VI) at 10^{-4} M was kept in contact with apatite for 48 hours. The central SEM micrograph ($1100\times$ magnification) shows crystalline plates on the smooth apatite mineral surface. Analysis of these plates by energy-dispersive spectroscopy (right graph) indicated the presence of calcium, oxygen, uranium, and phosphorus, consistent with crystalline uranium phosphate. Similar analysis of the bare regions of apatite (left graph) showed signals corresponding to only calcium, oxygen, and phosphorus. The precipitates were observed at uranium concentrations above 10^{-5} M. Studies show that at lower concentrations, uranium sorbs, rather than precipitates, to the mineral surface.

2000 mL/g, while plutonium sorption onto hematite results in K_d values above 10,000 mL/g. This difference is mainly caused by the different stabilities of the actinide oxidation states and their complexation strengths. The low charge of the NpO_2^+ ion results in a low sorption of neptunium, while Pu(IV) dominates the complexation and sorption processes of plutonium. Plutonium(V) is expected to follow the low sorption affinity of Np(V).

Lu et al. (1998) determined the sorption of Pu(V) onto oxide and clay colloids (Figure 10). Sorption onto iron oxides, such as hematite, is strong and irreversible, but only 50 percent of the Pu(V) is sorbed on the montmorillonite (clay). However, the sorption mechanisms are largely unknown. The time-dependence of the sorption onto the clay suggests a more complicated interaction than occurs with oxide minerals.

Interestingly, the *desorption* of Pu(V) does not follow this general pattern. Lu et al. (1998) also discussed the desorption of Pu(IV) and Pu(V) from various colloids. Table II summarizes

their findings: Surprisingly, Pu(IV) exhibits a greater tendency to desorb than Pu(V). Particularly striking is the relatively high desorption of Pu(IV) from silica, which indicates a different sorption mechanism or different binding to the silica functional groups than to the Fe(III) minerals, including possible changes in plutonium oxidation states.

These investigations indicate the importance of understanding the oxidation-state stability of the actinide sorbed on a mineral surface. Redox-active minerals, such as manganese or iron oxide/hydroxides, are present in subsurface environments and may alter the redox states of uranium, neptunium, and plutonium. At the Rocky Flats Environmental Technology Site, seasonal variations of plutonium concentrations in settling ponds correlate astonishingly well with soluble manganese concentrations, indicating a potential release of plutonium by way of seasonal redox cycling.

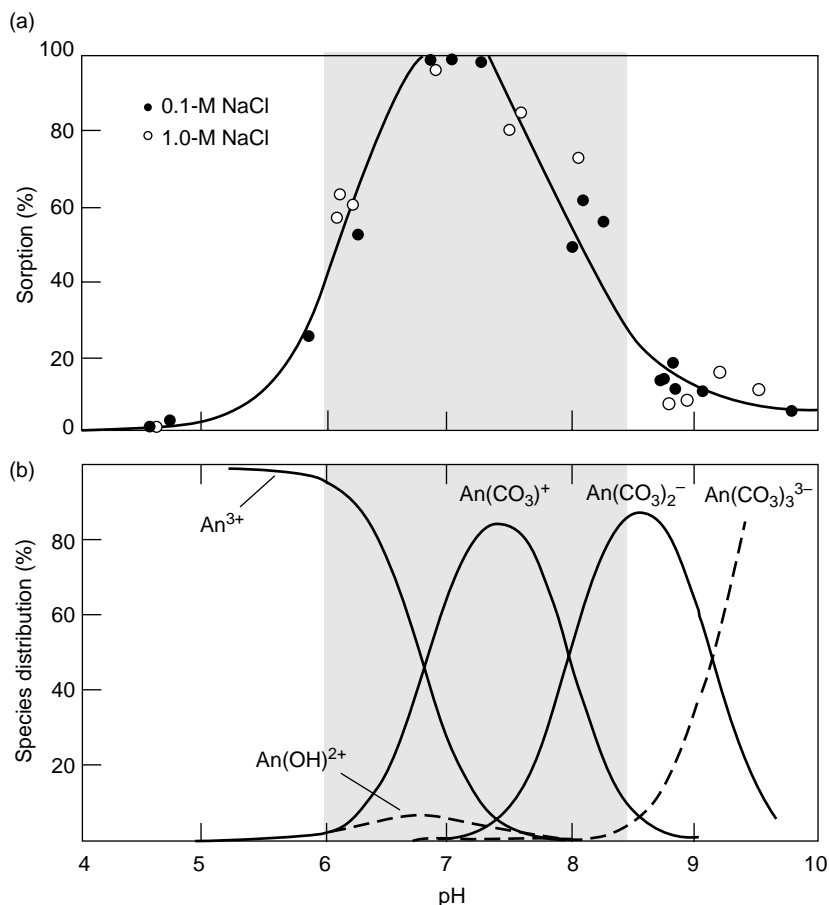
It has been generally hypothesized that the environmentally mobile Pu(V)

is reduced to Pu(IV) through the formation of strong mineral-surface complexes. Quite surprisingly, Neu et al. (2000) showed that Pu(V) is not reduced when sorbed on MnO_2 . X-ray absorption near-edge structure indicated the presence of Pu(V) on MnO_2 , even though the starting material of the batch-sorption experiment was colloidal Pu(IV) hydroxide. Their data also indicated that the plutonium was oxidized to Pu(VI). The only time they did not observe the higher-oxidation-state surface species was when Pu(IV) was complexed with a strong ligand, such as nitrilo triacetic acid (NTA). These observations strongly support the hypothesis that plutonium undergoes a redox cycling that is enhanced by surface interactions. We need more data about the surface species, however, to model such interactions.

Obviously, batch experiments alone cannot elucidate sorption mechanisms. Specifically, we have to distinguish between surface precipitation and interfacial molecular reactions in order to model sorption behavior. In the event

Figure 12. Correlation between An(III) Solution Speciation and Sorption onto Montmorillonite

(a) Even with an order-of-magnitude difference in NaCl concentration, sorption of the trivalent actinides Am(III) and Cm(III) peaks in near-neutral waters. At lower pH, the An^{3+} ion is stable and does not participate in complexation reactions with the most common ligands, hydroxide or carbonate, no matter if the ligands are in solution or on a surface. At higher pH, negatively charged An(III) species are formed that increase the species' solubility and reduce their sorption because they are repelled from the negatively charged functional groups on the mineral surface. (b) Calculations for a weak sodium chloride solution (0.1-M NaCl and CO_2 partial pressure of 0.01 atm) suggest that sorption is mainly correlated with the presence of cationic solution species. The gray area denotes the pH range of natural waters.



of a surface precipitation, the K_d value may represent the solubility product of the surface precipitate but will not reflect the sorption behavior of an actinide species.

For example, phosphate-containing minerals, such as apatite, are known to reduce thorium and uranium concentrations in contaminated solutions. Sorption distribution coefficients for U(VI) and Th(IV) have been reported in the literature, but there are also reports of U(VI) and Th(IV) precipitates. Our SEM studies have identified microcrystalline precipitates on the apatite when the initial U(VI) concentrations were above 10^{-5} M (see Figure 11). At lower U(VI) concentrations, no surface precipitation was observed. Thus, at the higher concentrations, the K_d values actually reflect a solubility product, while at the lower concentrations, the decrease of U(VI) in solution results from sorption of the actinide onto the mineral surface.

Complexation reactions can influ-

ence the actinide sorption processes that also depend strongly on pH (Figure 12). For the trivalent actinides Am(III) and Cm(III), the sorption reaches a peak under conditions of near-neutral waters. There, the cationic An(III) solution species predominate solution speciation. At lower pH, the An^{3+} ion is stable and does not participate in bonding with hydroxide or carbonate ligands. At higher pH, negatively charged An(III) species are formed that exhibit reduced interactions with chemically active groups at the mineral surface. Mineral or rock surfaces at high pH are generally negatively charged, and apparently the negatively charged actinide species are repelled from the anionic surface groups. As such, anionic actinide species behave as simple anionic ligands, such as SO_4^{2-} , CrO_4^{2-} or AsO_4^{3-} . In addition to An(III) species, the same trend of enhanced stability and low surface retention has been observed for the An(VI) complex $UO_2(CO_3)_3^{4-}$.

Enhanced modeling efforts have

begun to address the fundamental mechanism of actinide adsorption onto mineral surfaces. Janecky and Sattelberger (unpublished results) modeled the adsorption behavior of Np(V) on calcite by minimizing the free energy of the coordination. The structural parameters of $NpO_2CO_3^-$, which is the main solution complex in neutral and low-carbonate waters (such as J-13 water), were used to mimic the adsorption. The resulting surface-complex modeling indicates a distance of about 4 Å between the neptunium center and the nearest calcium ions in the calcite structure. Data from preliminary XAFS studies support this distance. Although this agreement between experiment and theory is encouraging, more detailed studies have to be performed to develop much more accurate transport models, including this surface complexation model.

We are also trying to better understand the sorption/desorption reactions of actinides with colloids and the

actinides' resulting transport characteristics. This area of environmental migration received heightened attention with the discovery of plutonium in a borehole at the Nevada Test Site (Kersting et al. 1999). The plutonium had evidently migrated 1.3 kilometers in only 30 years. (Each nuclear test is characterized by a unique $^{239}\text{Pu}/^{240}\text{Pu}$ isotope ratio, and that ratio can be used to identify the plutonium source.) As discussed in the article by Maureen McGraw, we now believe that colloidal transport was responsible for this remarkably fast movement of plutonium through the water-saturated rock. It is not clear, however, whether the transport was facilitated by intrinsic plutonium colloids or natural (clay or zeolite) colloids. What is clear is that transport models to date have underestimated the extent of colloidal transport on plutonium mobility.

Microbial Interactions

We have discussed the most prominent chemical processes involving actinides in the environment: dissolution and precipitation of solids, complexation in solution, and sorption onto surfaces. But there is growing attention to the importance of actinide interactions with microorganisms. Great varieties of microorganisms exist in all aquifers and soils, and many survive under the most extreme conditions, such as around hydrothermal vents at the bottom of the ocean, within deep subterranean aquifers, or within the hypersalinity of geologic salt beds.

Microorganisms can accumulate on solid surfaces often via formation of biofilms, or they may be suspended in the aquifer. As such they act as mobile or even self-propelled colloids. The concern is that the actinides can be associated with microbes, either through surface binding or through metabolic uptake, and be transported by them through the environment. However, the microorganisms' role in environmental transport behavior of radioactive

contaminants is still virtually unknown.

Microorganisms, especially bacteria, are also known to mediate redox processes. They may reduce elements from higher oxidation states and use the enthalpy of the redox reaction to grow and reproduce. Through metabolic activity, microbes can also establish reducing conditions by changing the pH and Eh of the local waters. While direct experimental evidence is still lacking, it is almost certain that some microbes can catalyze the transformation of uranium, neptunium, and plutonium into less-soluble forms. Several bacteria species have been reported in the literature to effectively reduce the highly mobile U(VI) into the far less soluble and mobile U(IV).

Given these characteristics, microbes could pose a third natural barrier to actinide transport from geologic repositories and could also help remediate actinide-contaminated soil, groundwater, and waste streams. The ultimate goal is to use microorganisms as "living" backfill to immobilize actinides through processes such as bioreduction, biosorption, or bioprecipitation and mineralization. At this time, however, actual applications of bacteria in remediation strategies and field demonstrations are rare.

Recent WIPP-related studies at Los Alamos have focused on the interaction of uranium and plutonium with the bacteria's cell walls or byproducts, such as extracellular biopolymers, and the toxicity and viability of microorganisms in the presence of the actinides. Francis et al. (1998) have shown that actinides are associated only at low levels with the halophilic bacteria isolated from muck pile salts around the WIPP site. The extent of association varied with bacterial culture, actinide species, pH, and the presence of organic or inorganic complexants. The radiolytic effects on the microbial viability were found to be negligible.

However, other microorganisms can concentrate metal ions to a great extent. Hersman et al. (1993) observed a strong uptake of plutonium by *pseudomonas*

sp. Within the first week of the experiment, the bacteria concentrated plutonium to levels that were nearly 10,000 times greater than a sterile control organism. Lower uptake was observed for contact times of two weeks or longer. Another strain of this bacteria, *pseudomonas mendocina*, is known to remove lead from Fe(III) hydroxide/oxides and was investigated for its potential to remove radionuclides from those environmentally abundant minerals. In fact, Kraemer et al. (2000) found that 20 percent of the sorbed plutonium was removed by this aerobically growing bacteria after about four days. The experimental conditions are presently optimized to remove the majority of the sorbed plutonium and to maximize its potential application in soil remediation strategies.

Leonard et al. (1999) also studied the inhibitory and toxic effects of magnesium oxide, MgO, on these WIPP-derived bacterial cultures. Magnesium oxide is of specific interest because it was chosen as backfill material at the WIPP repository to maintain the pH between 9 and 10, to reduce the amount of infiltrating water, and to limit the amount of CO₂ that can accumulate through degradation of cellulose and other organic compounds in the wastes. Initial studies indicated an inhibited cell growth as the amount of MgO increased, as well as a decrease in microbially generated gas (N₂O) by active halophilic bacteria. Ultimately, the toxic effect of MgO inhibits microbial growth, and consequently microorganisms may be unable to create a reducing environment at the repository that would stabilize actinides.

A more detailed study on the microbial association mechanism included analysis of the uptake of uranium and plutonium by sequestering agents and extracellular polymers (exopolymers). As an example, some exopolymers produced by *bacillus licheniformis* consist of repeating γ -polyglutamic acid (γ -PGA). Neu et al. (manuscript in preparation) observed actinide hydroxide precipitation at metal-to-glutamate ratios

higher than 1:20, but both U(VI) and Pu(IV) ions formed soluble complexes at ratios 1:100 and 1:200, respectively. Presumably at the higher PGA concentrations, the actinide ion is encapsulated and isolated from hydroxo-colloid formation. The binding strength for U(VI) and Pu(IV) is lower than for other strong ligands and chelators, such as Tiron or NTA, but on the same order as for other exopolymers or humic acids.

An upper binding boundary for the polyglutamate exopolymer was determined to be about 0.5 micromoles Pu(IV) per milligram of γ -PGA. Active cells of *Bacillus licheniformis* bonded to more than 90 percent of the introduced Pu(IV)—up to 8.4 micromoles of Pu(IV) were added. As expected, other functional groups on the exterior cell surface (in addition to the PGA exopolymer) increase the number of binding sites and enhance metal binding.

This research clearly shows that actinides bind with microorganisms and their metabolic byproducts. Depending on the static or dynamic nature of the microorganism, the interaction of plutonium and other actinides with extracellular ligands may affect the actinides' mobility both away from storage containers and within the environment. Future studies will focus on understanding the mechanisms of actinide/microbial interactions and exploiting their potential for remediation and immobilization efforts. Uptake studies of plutonium by means of sequestering agents are highlighted in the box on "Siderophore-Mediated Microbial Uptake of Plutonium" on page 416.

Concluding Remarks

From this overview of actinide interactions in the environment, it should be clear that such interactions are complex. Each local environment is unique, and the site-specific conditions determine which actinide species predominate as well as each species' overall transport and migration characteristics.

In general, actinide solubilities are low in most natural waters—below micromolar concentrations. Actinides in the V oxidation state will have the highest solubilities; those in the IV oxidation state, the lowest. Conversely, An(V) species show low sorption onto mineral and rock surfaces, and An(IV) species tend to sorb strongly. Typically, neptunium is the only actinide that favors the V oxidation state, and as such it is the most soluble and most easily transportable actinide under environmental conditions. Plutonium favors the IV oxidation state in many natural waters, and normally its solubility is quite low. Once plutonium is in solution, its migration is dominated by a variety of processes, including redox reactions in solution or on mineral surfaces, sorption, colloidal transport, simple diffusion into rock interfaces, coprecipitation, and mineralization. Furthermore, increasing research activities indicated that microbes can affect actinide migration, either through direct association or by helping to maintain a reducing environment.

To understand this complex set of interacting processes requires that we have a strong, multidisciplinary foundation in environmental chemistry, molecular science, and interfacial science and the requisite spectroscopies, subsurface testing, and laboratory experiments. But we also need to interpret experimental results within the context of the multi-component natural system.

A case in point is the recent identification of a higher oxide of plutonium of general formula $\text{PuO}_{2+x}(\text{s})$, which is formed by water-catalyzed oxidation of $\text{PuO}_2(\text{s})$. As discussed by Haschke in the article beginning on page 204, this Pu(IV) "superoxide" may also contain Pu(VI), which would increase plutonium solubility. In a recently published paper (Haschke et al. 2000), the authors speculated that the Pu(VI) could dissolve and be transported more easily from a nuclear waste storage site than previously estimated. Further, they conjectured that Pu(VI) might have caused the rapid migration of plutonium

at the Nevada Test Site. In these speculations, however, they failed to include influential environmental factors.

While we acknowledge that the potential presence of Pu(VI) in a $\text{PuO}_2(\text{s})$ matrix may increase the dissolution kinetics, the chemical conditions of the local environment (water and rock compositions) determine the stability of plutonium oxidation states in the aqueous phase and the overall plutonium mobility. Under ambient conditions and in most aqueous environments, Pu(VI) is unlikely to be stable. Once in solution, it is typically reduced to lower oxidation states and, depending on the water redox potential, may eventually precipitate as $\text{Pu}(\text{OH})_4(\text{s})$ or $\text{PuO}_2(\text{s})$. Consequently, the fact that the superoxide $\text{PuO}_{2+x}(\text{s})$ may include Pu(VI) does not automatically imply enhanced plutonium solubility or mobility in the natural environment. Furthermore, given the results on colloidal transport, it is improbable that Pu(VI) is responsible for the plutonium migration at the Nevada Test Site.

As the inventory of actinides in interim storage facilities grows and storage containers age, increasing the risk of accidental releases, and as the safety of permanently storing nuclear waste in geologic repositories must be evaluated, it becomes increasingly important to understand how actinides will interact with the environment. More sophisticated models are needed to account for all the potential migration paths away from an actinide source. Theoretical and experimental scientists will be challenged for years by the demands of developing those models. ■

Further Reading

- Brown, G. E., V. E. Heinrich, W. H. Casey, D. L. Clark, C. Eggleston, A. Felmy, D. W. Goodman, et al. 1999. *Chem. Rev.* **99**: 77–174.
- Clark, D. L., S. D. Conradson, D. W. Keogh, M. P. Neu, P. D. Palmer, W. Runde, et al. 1999. X-Ray Absorption and Diffraction Studies of Monomeric Actinide Tetra-, Penta-, and Hexavalent Carbonato Complexes. In *Speciation, Techniques and Facilities for Radioactive Materials at Synchrotron Light Sources*, OECD Nucl. Energy Agency. 121.
- Choppin, G. R., and E. N. Rizkalla. 1994. Solution Chemistry of Actinides and Lanthanides. In *Handbook on the Physics and Chemistry of Rare Earths*. Edited by K. A. Gschneidner Jr. and L. Eyring. New York: North-Holland Publishing Co.
- Choppin, G. R., J.-O. Liljenzin, and J. Rydberg. 1995. Behavior of Radionuclides in the Environment. In *Radiochemistry and Nuclear Chemistry*. Oxford: Butterworth-Heinemann.
- Choppin, G. R., 1983. *Radiochim. Acta* **32**: 43.
- Dozol, M., R. Hagemann, D. C. Hoffman, J. P. Adloff, H. R. Vongunten, J. Foos, et al. 1993. *Pure and Appl. Chem.* **65**: 1081.
- Efurd, D. W., W. Runde, J. C. Banar, D. R. Janecky, J. P. Kaszuba, P. D. Palmer, et al. 1998. *Environ. Sci. Tech.* **32**: 3893.
- Francis, A. J., J. B. Gillow, C. J. Dodge, M. Dunn, K. Mantione, B. A. Strietelmeier, et al. 1998. *Radiochim. Acta* **82**: 347.
- Hascke, J., T. Allen, and L. Morales. 2000. *Science* **287**: 285.
- Hersman, L.E., P. D. Palmer, and D. E. Hobart. 1993. *Mater. Res. Soc. Proc.* **294**: 765.
- Kraemer, S. M., S. F. Cheah, R. Zapf, J. Xu, K. N. Raymond, and G. Sposito. 2000. *Geochim. Cosmochim. Acta* (accepted).
- Kazuba, J. P., and Runde, W. 1999. *Environ. Sci. Tech.* **33**: 4427.
- Kersting, A. B., D. W. Efurd, D. L. Finnegan, D. J. Rokop, D. K. Smith, J. L. Thompson. 1999 *Nature* **397**: 56.
- Kim, J. I. 1986. Chemical Behavior of Transuranic Elements in Natural Aquatic Systems. In *Handbook on the Physics and Chemistry of the Actinides*. Edited by A. J. Freeman and G. H. Lander. New York: North-Holland Publishing Co.
- Langmuir, D. 1997. Chap. 13. In *Aqueous Environmental Geochemistry*. Upper Saddle River, NJ: Prentice Hall.
- Leonard, P. A., B. A. Strietelmeier, L. Pansoy-Hjelvik, R. Villarreal. 1999. Microbial Characterization for the Source-Term Waste Test Program (STTP) at Los Alamos. Conference on Waste Management 99, Tucson, AZ.
- Lemire, R. J. and P. R. Tremaine. 1980. *J. Chem. Eng. Data.* **25**: 361.
- Lu, N., I. R. Triay, C. R. Cotter, H. D. Kitten, and J. Bentley. 1998. "Reversibility of sorption of plutonium-239 onto colloids of iron oxides, clay and silica." Abstract of Agronomy, p.31 ASA, CAA, SSSA Annual Meetings, Baltimore, MD.
- Neu, M. P., W. Runde, D. M. Smith, S. D. Conradson, M. R. Liu, D. R. Janecky, and D. W. Efurd. 2000. EMSP Workshop, Atlanta, GA.
- Nitsche, H., A. Muller, E. M. Standifer, R. S. Deinhammer, K. Becraft, T. Prussin, R. C. Gatti. 1993. *Radiochim. Acta.* **62**: 105.
- Runde, W., S. D. Reilly, M. P. Neu. 1999. *Geochim. Cosmochim. Acta.* : 3443.
- Runde, W., M. P. Neu, D. L. Clark. 1996. *Geochim. Cosmochim. Acta* **60**: 2065.
- Shannon, R. D. 1976. *Acta Cryst.* **32A**: 751.

Wolfgang Runde earned B.S. and Ph.D. degrees in chemistry from the Technical University of Munich, Germany, in 1990 and 1993, under the direction of Professor Dr. J. I. Kim. He then worked for two years as a scientific staff



member at the Institute for Radiochemistry, TU Munich. During this time, he was invited to work as a guest scientist at Sandia National Laboratories on technical aspects of the actinide source term

model for WIPP. Wolfgang then spent a year as postdoctoral fellow at the G. T. Seaborg Institute for Transactinium Science at the Lawrence Livermore National Laboratory before joining the Chemical Science and Technology Division at Los Alamos National Laboratory in 1996. He is presently a staff member and leader of the Actinide Environmental Chemistry team in the Environmental Science and Waste Technology Division with a joint appointment in the Nuclear and Radiochemistry group in the Chemical Science and Technology Division. His research interests are in the areas of inorganic, environmental, and radiochemistry of f elements, including the actinides, with the focus on nuclear waste isolation and the environment. His research activities have been closely affiliated with the national nuclear waste programs in the US (WIPP and Yucca Mountain) and Germany (Gorleben).

Spectroscopies for Environmental Studies of Actinide Species

Wolfgang Runde

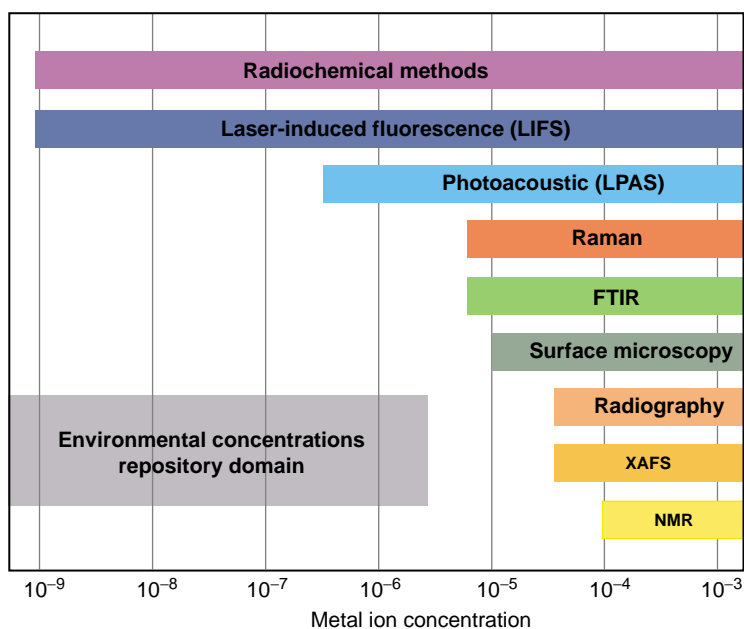


Figure 1. Spectroscopic Sensitivities

In order to understand the complex chemistry of actinides in the environment, we need to have detailed information about its chemical speciation in natural waters in association with natural mineral phases. Chemical speciation identifies not only the molecular formula, charge, and structure of an element's compounds, but also the isotopic composition of the molecule and the oxidation states of its constituents. This information is a prerequisite for making accurate assessments of the compound's thermodynamic and kinetic stability.

Unfortunately, actinide solubilities in natural waters are expected to be generally below micromolar (10^{-6}) concentrations, and these low concentrations complicate a direct non-destructive investigation. A number of spectroscopic methods have been developed to optimize understanding and quantification of actinides' reactions on the molecular scale (see Figure 1). Because of differences in the physical properties among the actinides, no single spectroscopy can adequately probe all actinides. We have had to apply a range of spectroscopic techniques in order to gain maximum insight into the environmental chemistry of the actinides. Some examples of our multifaceted approach to studying solid-state and solution speciation are given below. Other examples are given in the main text.

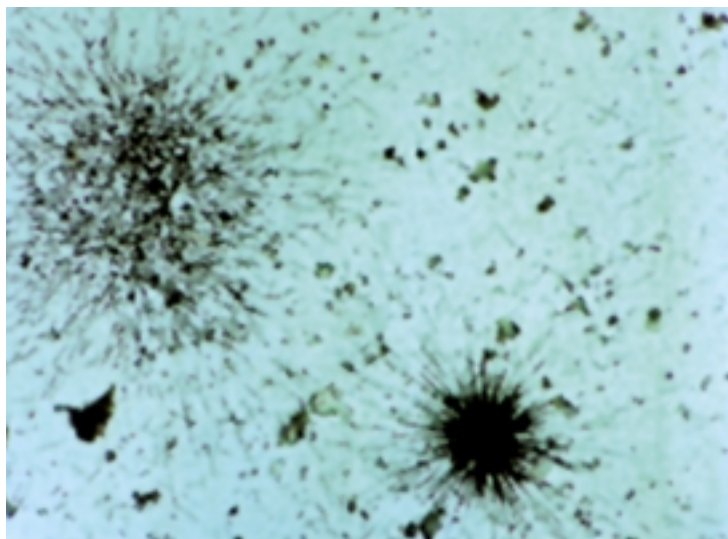


Figure 2. Autoradiograph of Plutonium in Rocky Flats Soil

Autoradiography. Autoradiography is one of the oldest techniques in radiochemistry, having been pioneered by Becquerel in 1896. It uses photographic emulsions to detect and determine the distribution of radioactive material in media and on surfaces. While used extensively for medical and biological research, the technique can also provide qualitative visual information on the distribution and density of radioactive material in soil. The photo seen in Figure 2 is a microautoradiograph of a $3.5 \text{ mm} \times 4.5 \text{ mm}$ soil sample from the Rocky Flats Environmental Technology Site. The sample is contaminated with plutonium and americium, and alpha particles emitted by either of those radioactive elements leave omni-directional tracks in the emulsion. We used this visualization technique to separate and concentrate 'hot' soil particles for further spectroscopic analysis. XAFS spectroscopy and SEM/EDS (see below) identified plutonium as the major contaminant in the soil, which contained only minor amounts of americium.

Scanning Electron Microscopy (SEM) and X-Ray Photoelectron Spectroscopy (XPS)

The interaction of actinides with mineral surfaces have been studied by radiochemical techniques (isotherm tracer experiments) or spectroscopic techniques. SEM and XPS are two surface analysis techniques that are widely used to investigate speciation at a solid-liquid interface. We use SEM to examine the crystallinity of micron-scale actinide and lanthanide solid phases.

As an example, the SEM picture seen in Figure 3(a) shows particles of $\text{NaNpO}_2\text{CO}_3 \cdot 3.5\text{H}_2\text{O}$ that precipitated from a Np(V) solution oversaturated with carbonate. The image clearly shows the crystalline nature of the solid and the lack of amorphous material. An energy-dispersed spectrometer was used to evaluate the chemical composition of those solids, which showed that only sodium, neptunium, and carbon are present in the solid. XPS is sensitive to an element's electronic state and can be used to examine the oxidation state of a metal ion. The oxidation state is revealed by a shift in the binding energy in the XPS photoemission spectra. Figure 3(b) shows that when Pu(IV) compounds sorb onto SiO_2 (one of the simplest metal oxide surfaces), the characteristic $4f_{7/2}$ photoemission peak shifts by several electron volts away from the peak position of metallic plutonium.

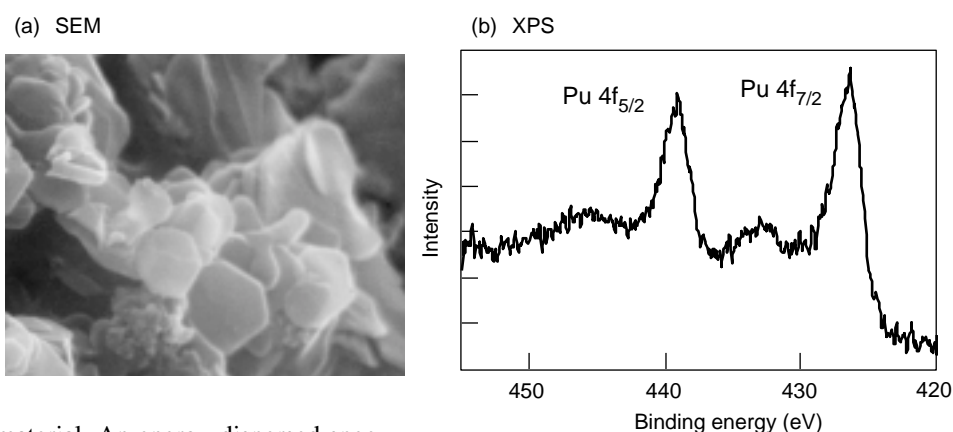


Figure 3. Surface Analysis of Np and Pu Compounds

Figure 3(b) is courtesy of R. Schulze and M. Neu.

X-Ray Absorption Fine Structure (XAFS) Spectroscopy.

The use of XAFS to gather information about the actinides has increased dramatically in the last five years. XAFS is element specific and allows us to deduce speciation without perturbing the sample's original distribution. The spectroscopy can yield information on the actinide's oxidation state, coordination number, bond length, and nearest-neighbor atoms. We have used XAFS to determine those features for solid (amorphous and crystalline) and solvated actinide compounds. Samples typically must have actinide concentrations in the lower millimolar range. More information about XAFS spectroscopy is found in the Conradson's article on page 422.

As discussed above, we used XAFS to identify the predominant plutonium species in contaminated soil at Rocky Flats. This was the first definitive spectroscopic data on plutonium in an environmental sample. The x-ray absorption near-edge structure data (XANES) of the L_2 absorption edge, seen in the graph in Figure 4(a), indicate that the plutonium in the most concentrated samples is in the highly stable and immobile form of plutonium dioxide, PuO_2 . The extended x-ray absorption fine structure (EXAFS)—Figure 4(b)—shows eight oxygen neighbors at a Pu–O distance of 2.33 Å, consistent with the fluorite structure PuO_2 . The data also show that plutonium is most concentrated in soil layers that are about 0.25–0.5 millimeters below the surface, is dispersed on both macro- and microscopic scales, and is not highly associated with any other particular element. These results help Rocky Flats personnel who must address potential plutonium migration paths from the site and remediate the area.

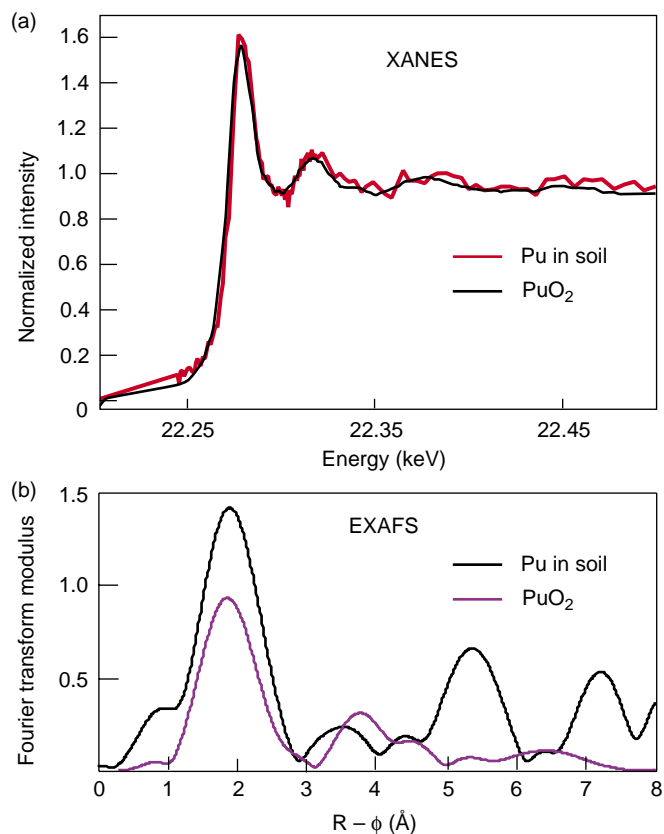


Figure 4. XAFS of Plutonium-Contaminated Soil Sample

Nuclear Magnetic Resonance (NMR) Spectroscopy. NMR is a standard analytical method in organic and inorganic chemistry. It is used for probing the electric quadrupole moments or magnetic dipole of some elements, which provides information about the structure and conformation of chemical species. Modern

high-field superconducting magnets allow us to investigate the speciation down to millimolar concentrations.

At Los Alamos, we have used ^{13}C and ^{17}O NMR to study the stability of the highly soluble triscarbonato complex, $\text{UO}_2(\text{CO}_3)_3^{4-}$, in NaCl solutions. This U(VI) anion is stable at relatively high carbonate concentrations, but with decreasing pH, the complex protonates and forms the trimer, $(\text{UO}_2)_3(\text{CO}_3)_6^{6-}$. The trimer's structure was determined previously by single-crystal x-ray diffraction and by XAFS spectroscopy. As illustrated in Figure 5, we have used the chemical shifts to characterize and quantify the U(VI) species involved in the chemical equilibrium. The $\text{UO}_2(\text{CO}_3)_3^{4-}$ complex has three equivalent terminal carbonate ligands (see Figure 4(c) in the main text) and thus it produces a single ^{13}C NMR frequency shift at $\delta = 165.6$ parts per million (ppm). The trimer has two different carbonate ligand environments—the outside of the complex (terminal) and between the uranyl ions (bridging)—that give rise to two signals:

$\delta = 165.2$ ppm for the three terminal ligands and at $\delta = 166.5$ ppm for the three bridging ligands. By integrating the signal, we obtain the stability constants. These indicate that increasing the ionic strength favors and stabilizes the more soluble triscarbonato complex. Our studies are relevant for the transport behavior of An(VI) in geologic salt formations, such as those at the WIPP site.

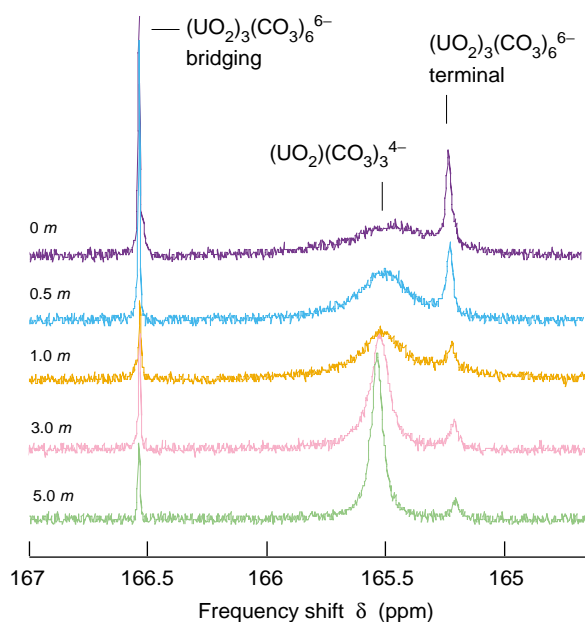


Figure 5. NMR Spectra of U(VI) Complexes

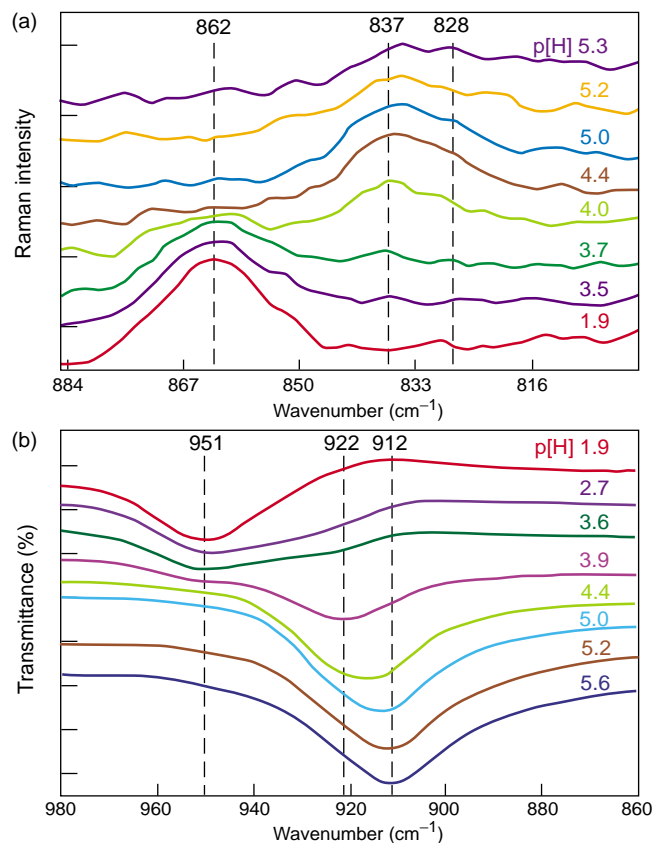


Figure 6. NMR Spectra of U(VI) Complexes

Fourier Transform Infrared (FTIR) and Raman Spectroscopies. These two techniques measure the vibrational spectrum of molecules and provide information on the molecular structure and the characterization of functional groups. We have used them to study the relationship between bond strength and length in An(V,VI) compounds, including U(VI) complexes with hydroxide, chloride, phosphate, or chloride ligands.

As seen in Figure 6(a), the Raman-active symmetric (ν_1) stretch of the UO_2^{2+} ion in solution, normally at 873 cm^{-1} , is shifted to 862 cm^{-1} as coordinated water molecules are replaced with chloride ions in 5-M NaCl. With increasing pH, hydrolysis species can be observed at different frequencies. Interestingly, solution speciation in chloride brines depart significantly from predictions based on previous investigations of U(VI) in non-complexing sodium perchlorate (NaClO_4) solutions. For example, the vibrational frequency of the first polynuclear hydrolysis product $(\text{UO}_2)_2(\text{OH})_2^+$, normally seen at 852 cm^{-1} in NaClO_4 , is not observed in chloride brines because of its lower stability. Instead, the signal for $(\text{UO}_2)_3\text{O}(\text{OH})_3^+$ is observed at 837 cm^{-1} while the tetramer $(\text{UO}_2)_4(\text{OH})_7^+$ appears at 828 cm^{-1} . Analogous shifts of the vibrational frequencies for the $(\text{UO}_2)_2(\text{OH})_2^+$ can be observed in the corresponding FTIR spectra seen in Figure 6(b). The IR frequency of the ion in 5-M NaCl shifts in NaClO_4 solution from 951 cm^{-1} to 961 cm^{-1} , the trimer shifts from 922 cm^{-1} to 924 cm^{-1} and the tetramer shifts to 912 cm^{-1} .

Ultraviolet, Visible, and Near-Infrared (UV-vis-NIR) Spectroscopy.

Absorption studies employing UV-vis-NIR spectroscopy have been widely used to study the complexation reactions of actinides in solution. The technique has a sensitivity down to micromolar concentrations, and actinide species in all oxidation states can be characterized because the actinides exhibit characteristic Laporte forbidden f-f transitions. (See Table I.) Complexation reactions of the non-complexed ion can be tracked because the absorption band is shifted significantly with the addition of ligands. For example, the non-complexed Np(V) aquo ion, $\text{NpO}_2(\text{H}_2\text{O})_5^+$, exhibits a strong absorbance at 980 nm.

As seen in Figure 7, the monocarbonato species $\text{NpO}_2(\text{H}_2\text{O})_3(\text{CO}_3)^-$ absorbs at 991 nm, the bicarbonato complex absorbs at 997 nm, and the tricarbonato complex absorbs at 974 nm. Combining these spectroscopic results with those from XAFS experiments has given us insight into the molecular structures of environmentally relevant Np(V) complexes.

Table I. Characteristic Absorption Wavelengths

Species	Wavelength (nm)
U(IV)	650
U(VI)	414
Np(IV)	960
Np(V)	980
Pu(IV)	470
Pu(V)	569
Pu(VI)	830
Am(III)	503
Cm(III)	400

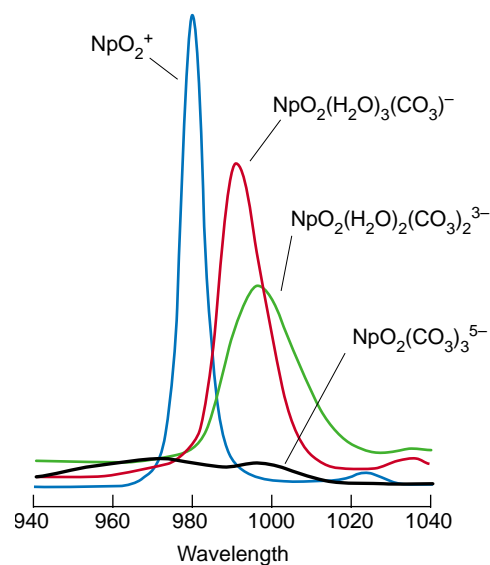


Figure 7. UV-vis-NIR Spectra

Laser-Induced Fluorescence (LIF) Spectroscopy (LIF).

Fluorescence spectroscopy can be used to probe the excited and ground states of only a few actinides species—for example U(VI), Am(III), and Cm(III). The fluorescence decay rate of the emission spectra depends on the nature of ligands that are present in an actinide's inner coordination sphere. When combined with information about the lifetime of non-radiative relaxation processes, LIFS is sufficiently sensitive to probe chemical speciation at nanomolar concentrations.

We have used this method to characterize the environmentally relevant solid and solution compounds of U(VI) and Am(III). As inner-sphere water molecules are replaced with carbonate ligands, the emission wavelength changes. One of the strongest absorption transitions for Am(III) compounds is the $^5\text{D}_1 \rightarrow ^7\text{F}_1$ band at 685 nm, and as seen in Figure 8, the peak emission for $\text{Am}^{3+}(\text{aq})$ (at 685 nm) shifts towards higher wavelengths with carbonate complexation. The fluorescent lifetime of the ion's excited state also increases, for example, from 20.4 nanoseconds for $\text{Am}^{3+}(\text{aq})$ to 34.5 nanoseconds for $\text{Am}(\text{CO}_3)_3^{3-}$. The increase follows the known trend for Eu(III) and Cm(III) complexes. From the measured lifetime of the excited state we determine that there are 11.1 ± 0.5 water molecules around the Am^{3+} ion and 6.0 ± 0.5 water molecules for $\text{Am}(\text{CO}_3)_3^{3-}$. Since the three carbonate ligands bond in a bidentate fashion, our results agree with a coordination number of 12 for the latter complex. Thus far, we have been unable to obtain fluorescence data on the mono- and bicarbonato complex due to the low solubility of Am(III) at lower carbonate concentration.

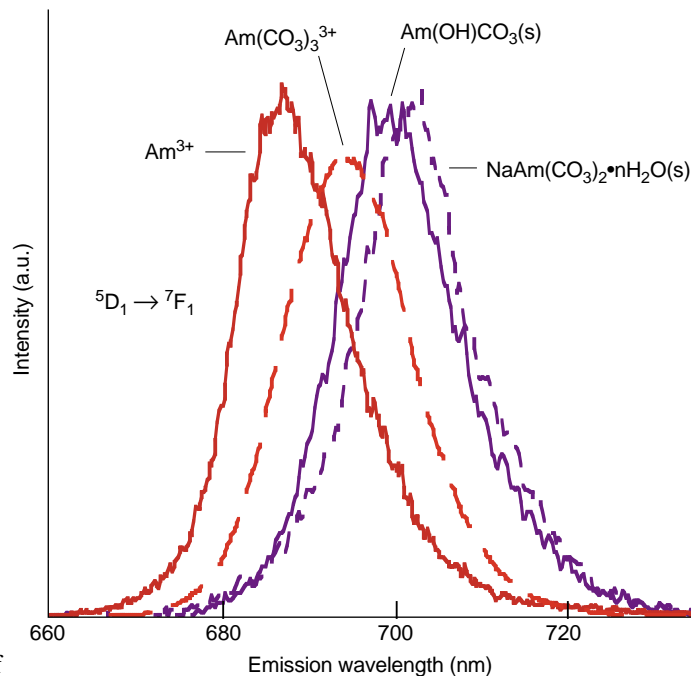


Figure 8. LIF Spectra

Siderophore-Mediated Chemistry and Microbial Uptake of Plutonium

Mary P. Neu

Metal ions can interact with microorganisms via a range of mechanisms. For example, metals can sorb directly to an organisms' cell wall, or can react with microbial byproducts, such as extracellular polymers. A classic system of microbial-metal interaction involves low molecular weight organic ligands (siderophores) which are excreted and used by plants and microbes to acquire iron.

All microorganisms, except the *Lactobacilli*, have nutritional requirements for Fe(III) that are not met in aqueous aerobic environments. Under those conditions, Fe(III) has a low solubility (at neutral pH, typical concentrations are about 10^{-18} molar) so that its bioavailability is limited. In order to acquire sufficient iron, bacteria synthesize and secrete siderophores that can chelate Fe(III) and carry it into the cell via specific high-affinity uptake receptors. The siderophores are typically multidentate, oxygen-donor ligands that usually have hydroxamate, catecholate, or carboxylate moieties. Although they are designed to have an extremely high affinity for Fe^{+3} , siderophores can bind other "hard" ions, such as Al(III), Zn(II), Ga(III), Cr(III), and, Pu(III,IV). (Hard metal ions have high charge to ionic radius ratios and form strong inner sphere complexes with ligands containing "hard" donor atoms, such as oxygen.)

We are examining the redox and coordination chemistry of plutonium with siderophores in order to understand how they could affect actinide biogeochemistry. We have investigated the ability of hydroxamate siderophores to coordinate Pu(IV) and solubilize the Pu(IV) solid, Pu(OH)₄(s), at neutral pH, and have studied the potential for common soil aerobes to interact with

plutonium by siderophore uptake mechanisms. We have focused on two trihydroxamate desferrioxamine (DFO) siderophores—desferrioxamine E (DFE) and desferrioxamine B (DFB)—because they are the most well studied and are readily available.

We have prepared and structurally characterized the first plutonium-siderophore complex, Al(H₂O)₆[Pu(DFE)(H₂O)₃]₂(CF₃SO₃)₅ • 14H₂O (Neu et al. 2000). In fact, our work is the first structural characterization of any plutonium biomolecule. (This complex also contains the first verified nine-coordinate Pu⁴⁺ ion.) X-ray crystallographic data reveal that the

crystal structures of the free ligand, the Fe(III) complex, and the Pu(IV)-DFO complex have interesting similarities. As seen in Figure 2, the DFE occupies approximately one-half of the plutonium coordination sphere. Three water molecules bind to the plutonium in the remaining space. The polytopal geometry of the plutonium coordination sphere is a slightly distorted tricapped trigonal prism; the three bound waters and three oximate oxygens form trigonal planes while the three carbonyl oxygens cap the prismatic faces.

Ruggerio et al. (2000) found that Pu(IV)-DFO is thermodynamically the most stable complex among all the possible Pu-DFO complexes: regardless of the initial state of the plutonium, eventually the Pu(IV)-DFO complex forms. If Pu(III) is present initially, it is rapidly oxidized by DFO to Pu(IV). Plutonium(V) and Pu(VI) are reduced to Pu(IV). At neutral pH and higher, the reduction to Pu(IV) is instantaneous. Under acidic conditions, Pu(VI) is rapidly reduced to Pu(V), followed by a slow reduction to Pu(IV), with the rate dependent on the pH and the DFO concentration. Stoichiometric titration of Pu(VI) into a DFO solution showed that up to 12 equivalents of plutonium could be reduced per DFO, showing that DFO is a powerful reductant for Pu(VI). In contrast, U(VI)-DFO is inert to reduction.

The formation constant, β , for the Pu(IV)-DFO complex formed at neutral pH has been estimated to be extremely high, $\log \beta = 30.8$, for DFB (Jarvis, et al., 1991). That constant is higher than those known for many organic chelators, such as EDTA, citrate, and tiron. High complex-formation constants are generally equated with effective solubilization of the metal ion by the ligand.

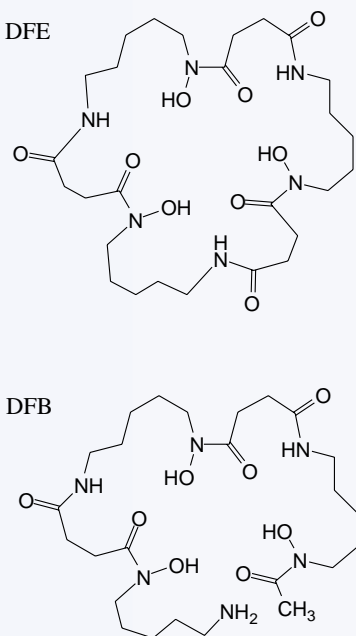
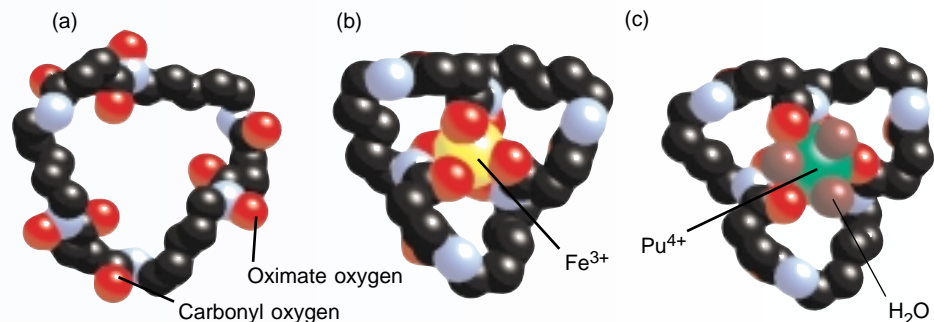


Figure 1. Hydroxamate Siderophores The chemical structures of two desferrioxamine siderophores are shown above; the linear trihydroxamate produced by *S. pilosus*, Desferrioxamine B (DFB), and the cyclic trihydroxamate produced by *P. stutzeri*, Desferrioxamine E (DFE).

Figure 2. Sidereophore Complexation
 (a) A space filling model of DFE.* (b) Fe-DFE complex.** A twist of the carbon backbone allows the three oximate oxygens and the three carbonyl oxygens to form a "cavity" that securely holds the Fe³⁺ ion. (c) The Pu-DFE complex is structurally similar to Fe-DFE. The large Pu⁴⁺ ion protudes slightly from the cavity. Three water molecules remain bound to the ion.



*Van der Helm, D., and M. Poling. 1976. *J. Am. Chem. Soc.* **98**: 82.

Hossain, M. B., D. van der Helm, and M. Poling. 1983. *Acta Cryst. B* **39: 258.

However, the DFO siderophores are far less effective at solubilizing Pu(OH)₄(s) in buffered neutral solution compared to the organic chelators, even though the latter have lower Pu(IV) complex-formation constants (Cleveland, 1991). Pu(IV) hydroxide can be slowly solubilized by EDTA at a rate of approximately 1.1 μmoles per day (μmol/day), and by citrate and iron at rates of 0.2 μmol/day, and 0.1 μmol/day, respectively. In contrast, the rates of solubilization by DFE and DFB are 50 to 500 times slower than EDTA. Additionally, EDTA solubilization of Pu(OH)₄(s) was 10 times slower after pre-treating the plutonium with DFB. These surprising results suggest that the DFO siderophores are passivating the surface of the Pu(IV) solid and inhibiting solubilization.

We also found that DFB can mediate plutonium association with bacteria (John et al. 2000). As an example, the soil isolate *Aureobacterium flavescens* (JG-9) is a siderophore auxotroph, producing no siderophore of its own but requiring one to obtain iron. We verified that all iron and plutonium uptake by *A. flavescens* is strictly associated with the added siderophore DFB, that is, no uptake occurs without its addition. Uptake of Fe-DFB or Pu-DFB also needed living, metabolically active bacteria; heat-killed or metabolically inhibited cells showed little association with the Fe-DFB or Pu-DFB complex. These results point to similar energy-dependant uptake processes by which the iron and plutonium are transported to the cell interior. Interestingly, DFB-mediated uptake of plutonium is about

two orders of magnitude lower than with iron and exhibits a different time dependence. Whereas iron uptake is fastest at the beginning, generally slowing and leveling out to approximately 100 nanomoles per milligram of bacteria after 1 hr, plutonium uptake increases linearly until it reaches a peak rate of 25 nanomoles per milligram of bacteria after 10 hours.

We have examined competition between Fe-DFB and Pu-DFB uptake by adding different quantities of the metal complexes at varying times. We are currently determining the location of iron and plutonium on and within the cell by using various chemical treatments of the cells. Our results indicate differences in recognition, uptake, and final location of the iron and plutonium. The Fe-DFB complex is rapidly recognized by the uptake channel receptors and is translocated into the cell interior. While the Pu-DFB complex appears to be recognized by the same binding site(s) with approximately the same affinity, it is only slowly transported across the cell membrane into the interior.

Hydroxamate siderophores are naturally present in the environment (Powell et al. 1980). They have a high binding affinity for Pu(IV), a large reducing capacity for Pu(VI) and Pu(V), and they inhibit the solubilization of plutonium solids. Our recent work shows that Pu-DFO complexes are recognized by microbial metal-siderophore binding sites and may be taken into cells. These varied and dynamic interactions suggest that these strong metal chelators will significantly affect plutonium biogeochemistry.

Further Reading

- Cleveland, J. M. 1979. *The Chemistry of Plutonium*, La Grange Park, Illinois: American Nuclear Society.
- Jarvis, N. V. and R. D. Hancock, 1991: *Inorg. Chim. Acta*, **182**: 229.
- John, S. G., C. E. Ruggiero, M. P. Neu, et al. Submitted to *J. Am. Chem. Soc.* Los Alamos National Laboratory document LA-UR 00-1879.
- Neu M. P., J. H. Matonic, C. E. Ruggiero, and B. L. Scott. 2000: *Angew. Chem. Int. Ed.* **39**: 1442.
- Powell, P. E., G. R. Cline, C. P. P. Reid, and P. J. Szanisló, 1980: *Nature* **287**: 833.
- Ruggiero, C. E., M. P. Neu, et al. Submitted to *Inorg. Chem.* Los Alamos National Laboratory document LA-UR 00-1878

Mary Neu earned B.S. degrees in math and chemistry and graduated *magna cum laude* from the University of Alaska, where she was named the Outstanding Student in the Physical Sciences in 1986. She received a Ph. D. in inorganic and nuclear chemistry from the University of California at Berkeley in 1993 under the direction of Professors Darleane Hoffman and Ken Raymond. After a year as a University of California post-doctoral research fellow at Los Alamos, she joined the technical staff in 1995. Mary currently directs and performs research in the Actinide, Catalysis and Separations Chemistry group in the Chemistry, Science, and Technology Division. Her areas of interest include inorganic, environmental, bioinorganic and radiochemistry, with an emphasis on plutonium and other actinides.



Characterizing the Plutonium Aquo Ions by XAFS Spectroscopy

Steven D. Conradson, David L. Clark, Mary P. Neu, Wolfgang Runde, and C. Drew Tait

Plutonium is one of only a handful of elements to exhibit four common oxidation states: Pu(III), Pu(IV), Pu(V), and Pu(VI). In addition, plutonium complexes in aqueous solution can change their oxidation state by undergoing disproportionation or re disproportionation reactions, or through radiolytic reactions. Because so many plutonium species can form and interact in solution, aqueous plutonium chemistry can be remarkably complex.

In environments where different ligands abound, such as the ground waters of Yucca Mountain or the waste materials (residues) produced during the manufacturing of nuclear weapons, the plutonium species need to be understood beyond simple elemental analysis. We need to have information about the possible oxidation states of the numerous species, along with information about their atomic compositions and molecular structures.

The plutonium aquo ions are the “baseline” plutonium species in aqueous solution because they only have water molecules attached to a central plutonium ion. Other species form as different ligands replace one or more of the water molecules in the coordination sphere of the plutonium ion. Understanding the aquo ions in detail can therefore provide a starting point for understanding other plutonium complexes.

The aquo ions of plutonium in the III and IV oxidation states have the general formula $\text{Pu}(\text{H}_2\text{O})_n^{3+}$ and $\text{Pu}(\text{H}_2\text{O})_n^{4+}$, respectively, which are often designated as $\text{Pu}^{3+}(\text{aq})$ and

$\text{Pu}^{4+}(\text{aq})$. But plutonium in the V or VI oxidation state has such a large positive charge that, in aqueous solution, it reacts with water to form the trans-dioxo (plutonyl) cations PuO_2^+ or PuO_2^{2+} . The corresponding aquo ions therefore have the general formulas $\text{PuO}_2(\text{H}_2\text{O})_n^+$ and $\text{PuO}_2(\text{H}_2\text{O})_n^{2+}$, which are conveniently designated as $\text{PuO}_2^+(\text{aq})$ and $\text{PuO}_2^{2+}(\text{aq})$. Before we conducted our research, the number of water molecules, n , surrounding the plutonium ions was still open to debate.

Several years ago, Los Alamos scientists from three Laboratory divisions began working together to apply x-ray absorption fine-structure (XAFS) spectroscopy to characterize the plutonium aquo ions. (More information about XAFS spectroscopy is found in the article “XAFS” on page 422.) All the measurements were performed at the SPEAR synchrotron x-ray source, which is owned and operated by the Stanford Synchrotron Radiation Laboratory (SSRL).

Solutions containing ions in a single oxidation state were prepared by electrochemical synthesis. These samples allowed us to study each aquo ion independently. We verified the oxidation state integrity of the samples before and after x-ray absorption analysis by measuring the electronic absorption spectra. Because the chemical environment surrounding the plutonium ion in each solution was very consistent (the only ligands were water molecules), we could also look for behavioral or structural trends among the four oxidation states.

Identifying the Plutonium Oxidation States

The x-ray absorption near-edge structure (XANES) of an XAFS spectrum can be used to determine the oxidation state of the target (x-ray absorbing) element in solution or the solid state. The energy at which an absorption edge appears depends on the ionization potential of the ion. This ionization potential increases with the ion’s valence, so in general the absorption edge shifts toward higher energy with increasing oxidation state. This known effect has been observed in some of the actinides, for example, in uranium and neptunium. We have recently observed this shift in the plutonium aquo ions.

Figure 1(a) shows a detailed view of the XANES spectra for the aquo ions of Pu(III), Pu(IV), Pu(V), and Pu(VI). The shift between successive oxidation states is clearly visible, although there is almost no difference in the absorption-edge energy (within experimental error) between Pu(IV) and Pu(V) complexes. Other parts of the XANES, however, can be used to help correlate a spectrum with an oxidation state. For example, the shoulder that appears just after the main absorption peak in the spectra of Pu(V) or Pu(VI) complexes in solution—the “-yl” shoulder—can be used to distinguish those oxidation states from Pu(IV). (Refer to the box “XANES” on page 432 in the article “XAFS”.)

A graph of the edge energy versus oxidation state for the plutonium aquo

ions is shown in Figure 1(b). We have obtained nearly identical graphs for other plutonium species—including plutonium nitrates, carbonates, carboxylates, and oxides—in solution and the solid state. (In fact, other than an overall shift in the edge energy, we obtained nearly identical graphs for uranium and neptunium.) Because the edge energies are independent of the chemical form of the plutonium, they can be used to identify the oxidation state of plutonium complexes in unknown chemical matrices.

There is still speculation about the underlying reason behind the small shift between the IV and V oxidation states. The shift toward higher energies depends on the actual charge of the ion, rather than its “formal” charge, and evidently, the actual charge does not vary much between the two states. One possible explanation is linked to the formation of the plutonyl cations.

The plutonyl cations have a linear structure, $\text{O}=\text{Pu}=\text{O}$. Recent calculations have shown that bonding between the plutonium and oxygen atoms in the plutonyl has a substantial covalent character, so that the actual charge of the central plutonium ion is reduced. (See the article “Computational Studies of Actinide Chemistry” on page 382.) The actual charge of the plutonium ion in the Pu(V) complex $\text{PuO}_2^+(\text{aq})$ may therefore be very similar to the actual charge of the plutonium ion in $\text{Pu}^{4+}(\text{aq})$.

The Structure of the Plutonium Aquo Ions

Data from the high-energy side of the x-ray absorption spectrum (the EXAFS region) provides information about the local atomic-scale environment. A Fourier transform of the data results in a radial distribution function that can be interpreted as shells of near-neighbor atoms surrounding the central ion. The position and intensity of the peaks in the Fourier transform are related to the atomic identity, distance, and number of atoms in each shell.

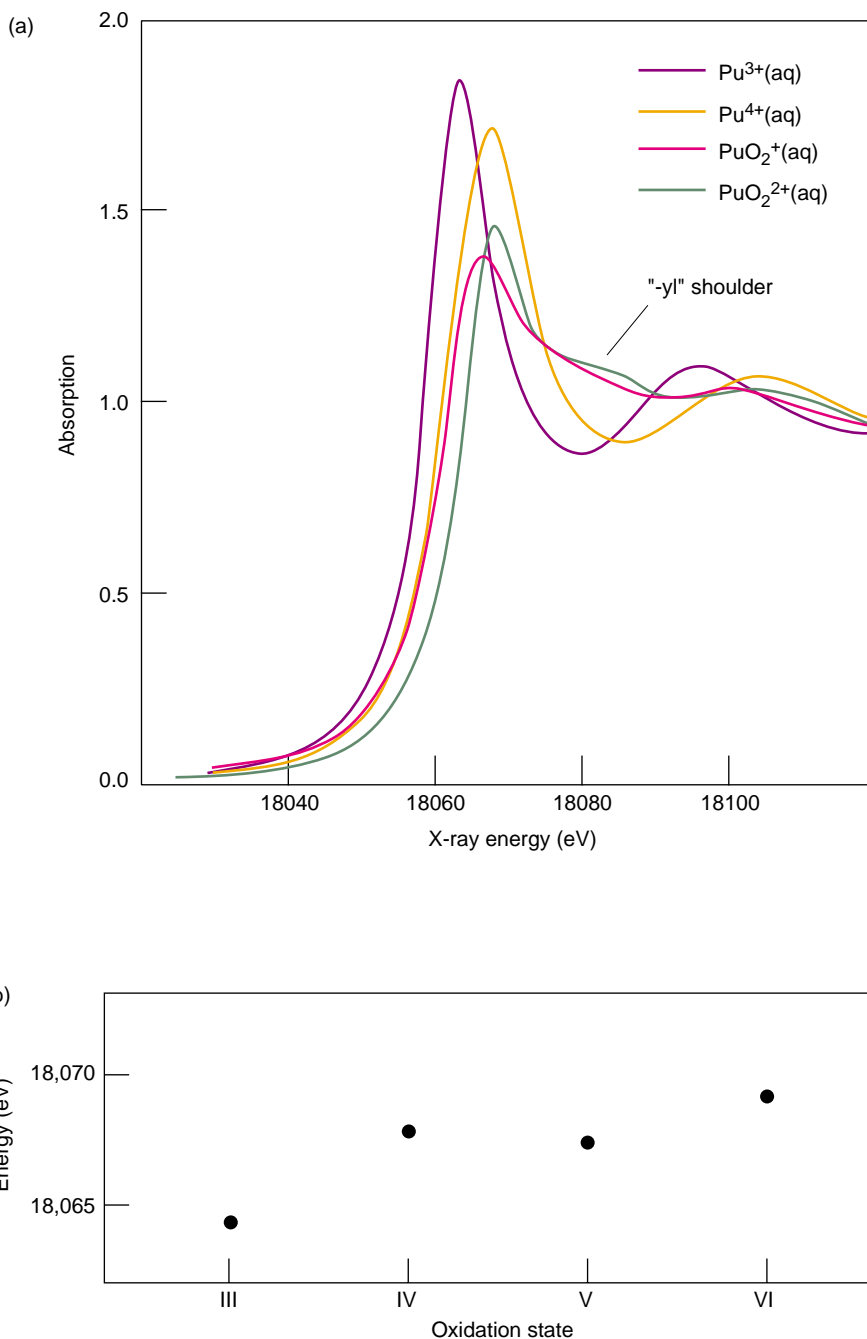
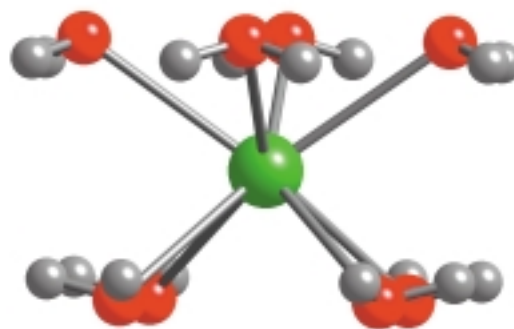
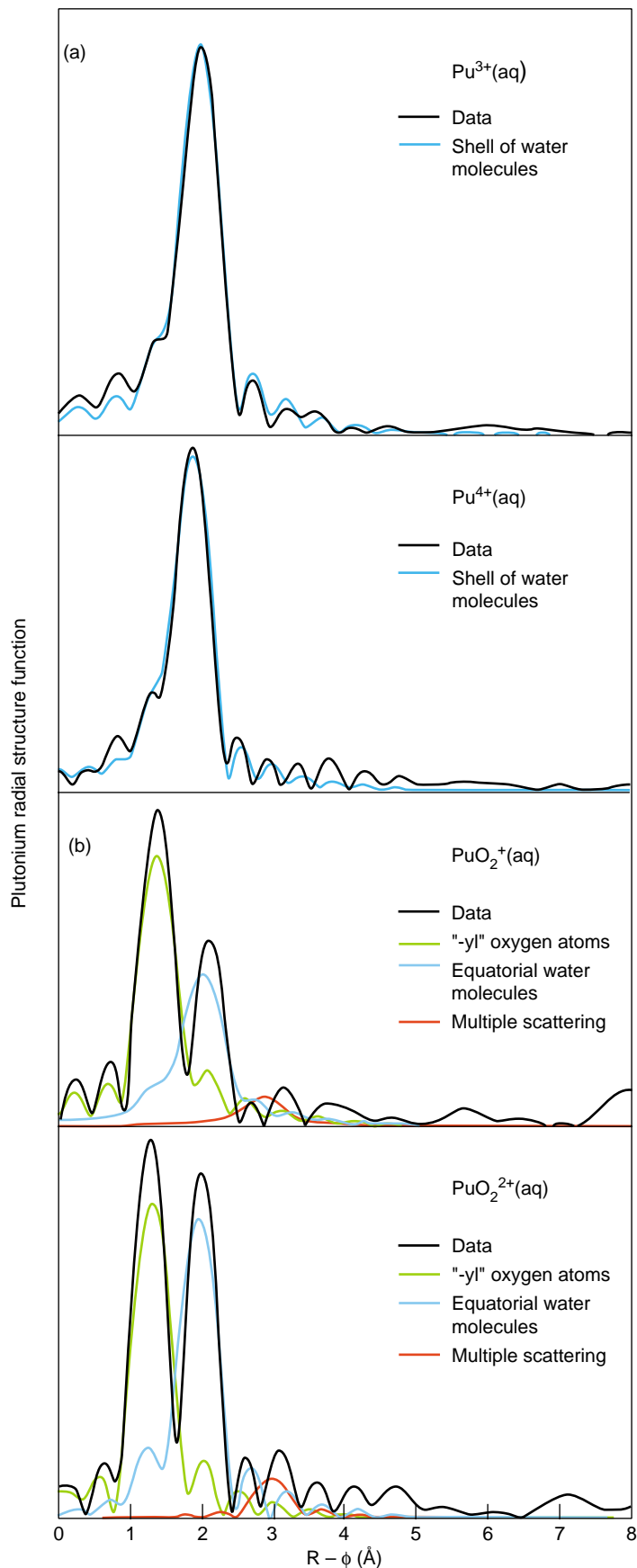


Figure 1. XANES Spectra of the Aquo Species of Pu(III) to Pu(VI)

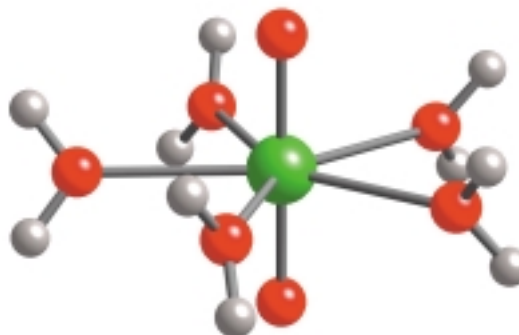
(a) The absorption edge shifts toward higher energy and increases almost linearly as a function of oxidation state. The change in energy between $\text{Pu}^{4+}(\text{aq})$ and $\text{PuO}_2^+(\text{aq})$ is quite small, but the two oxidation states can be distinguished by other features, such as the “-yl” shoulder in the XANES spectrum. (b) The edge energy is plotted as a function of oxidation state, which helps to illustrate the point that the IV and V oxidation states are in fact indistinguishable based on absorption-edge energy alone.



Square antiprism

Figure 2. EXAFS of the Plutonium Aquo Ions

(a) The Fourier transforms of the EXAFS of $\text{Pu}^{3+}(\text{aq})$ and $\text{Pu}^{4+}(\text{aq})$ show only one major peak, which indicates that all the oxygen atoms of the water ligands lie in the same coordination shell. The amplitude of the peak indicates between 8 and 9 oxygen atoms per shell. The bond length between III and IV complexes contracts by 4% with the increase in charge, whereas the number of ligands stays roughly the same. The graphic in the upper right shows a possible structure for $n = 8$, the square antiprism. (b) The Fourier transforms of the EXAFS of $\text{PuO}_2^+(\text{aq})$ and $\text{PuO}_2^{2+}(\text{aq})$ show two large peaks, which indicate two well-defined coordination shells. The first peak corresponds to the two oxygen atoms of the plutonyl moiety, which are located at 1.74 Å from the central plutonium ion. The second peak corresponds to the oxygen atoms of the water ligands, which are located about 2.4 Å from the central plutonium ion. The equatorial coordination of the Pu(V) complex compared with the Pu(VI) complex shows a significantly smaller number of water ligands, which are located at a longer distance. This observation is not fully understood. The graphic below shows a possible structure for $n = 5$ water ligands, the pentagonal bipyramid.



Pentagonal bipyramid

Figure 2(a) shows the Fourier transform of the EXAFS data¹. For $\text{Pu}^{3+}(\text{aq})$ and $\text{Pu}^{4+}(\text{aq})$, the data show only a single large peak, which indicates that all the nearest-neighbor atoms (the oxygen atoms of the water ligands) lie at the same distance from the plutonium ion. We obtained a Pu–O distance of approximately 2.49 angstroms for the III state and 2.39 angstroms for the IV state. The number of water molecules bound to the plutonium is similar for both species, with $n = 8$ or 9.

The transform of $\text{PuO}_2^+(\text{aq})$ and $\text{PuO}_2^{2+}(\text{aq})$ data shows two peaks, as seen in Figure 2(b). The first corresponds to the two oxygen atoms in the plutonyl ion. Analysis of the data indicates a Pu=O distance of 1.74 angstroms. The second peak in the Fourier transform corresponds to the oxygen atoms of the water ligands. It is known from other studies that all these oxygen atoms bond in the equatorial plane of the plutonyl moiety, and we deduce Pu–O distances that range from 2.39 to 2.49 angstroms.

The Fourier transform also shows a small peak at about 3 angstroms. This peak is an artifact of the EXAFS technique that results when an electron scatters more than once within the linear geometry of the plutonyl moiety. Thus we include a multiple-scattering peak in our fit to the data.

A significant result of our research is the finding that the $\text{PuO}_2^+(\text{aq})$ has a lower number of water ligands ($n = 4$ to 5), all at a longer distance, than $\text{PuO}_2^{2+}(\text{aq})$, where $n = 5$ to 6. This finding confirms a trend that was seen in studies of the actinyl ions of uranium and neptunium, namely, that actinide(V) species appeared to coordinate fewer ligands than actinide(VI) species. Because plutonium exhibits aquo ions in four oxidation states (and is the only actinide to do so),



Authors (from left to right): C. Drew Tait, Steven D. Conradson, David C. Clark, Mary Neu, and Wolfgang Runde.

our experiments are the first to observe this trend directly.

When other information is taken into account, the XAFS data are consistent with a bipyramidal coordination geometry for $\text{PuO}_2^+(\text{aq})$ and $\text{PuO}_2^{2+}(\text{aq})$. The plutonyl moiety forms the axis of the bipyramid, and depending on conditions, the geometry may be a tetragonal bipyramid (four ligands in the equatorial plane), a pentagonal bipyramid (five ligands), or a hexagonal bipyramid (six ligands).

We have used the plutonium aquo ions to establish the baseline data and oxidation state trends necessary to determine the oxidation states of plutonium complexes in matrices of unknown composition. With this background data in hand, we are in a position to apply

XAFS spectroscopy to help characterize plutonium or other actinide species in the environment or in the waste that remain after 50 years of nuclear weapons production. ■

¹An EXAFS spectrum is a function of energy, and we take a Fourier transform (FT) of the spectrum to produce a radial structure function that is a function of distance, R . But the transform actually produces a function $\chi(R+\phi)$, where ϕ is a phase shift. In the FT shown in Figure 2, the phase shift causes the peaks to be about -0.5 \AA from the true shell radii. The radial structure function is plotted versus $(R-\phi)$ to emphasize this fact.



XAFS

A Technique to Probe Local Structure

Steven D. Conradson as told to Jay Schecker

From the instant of their creation inside a nuclear fuel rod and forever thereafter, plutonium atoms are found in association with other atoms. In a solid, for example, plutonium becomes part of the lattice or matrix that makes up the condensed matter, while in solution, the element typically forms large molecular complexes in which many ligands bond to the central plutonium ion. To a large degree, the number, type, and arrangement of atoms or molecules that surround a plutonium atom determine its behavior. Thus if we are to understand and control plutonium's behavior in chemical processes, in the natural environment, or in stockpiled nuclear weapons, we need insight into the "local" structure of the atoms that surround it.

X-ray absorption fine structure (XAFS) spectroscopy is one of the most powerful tools we have for mapping local structure. In this technique, we probe a sample with x-rays that are tuned to the energy of a core electron shell in the element we wish to study. We monitor how many x-rays are absorbed as a function of their energy. If taken with sufficient accuracy, the spectrum exhibits small oscillations that are the result of the local environment's influence on the target element's basic absorption probability. From the spectrum, we can extract the distances between the absorber and its near-neighbor atoms, the number and type of those atoms, and the oxidation state of the absorbing element—all parameters that determine local structure. By selecting a different x-ray energy, we can obtain this information for any element in the sample.

A fundamental aspect of XAFS spectroscopy is that it is a "short-range" technique—the target element does not have to be part of a large, coherent domain of atoms. In fact, the sample need not have a periodic structure. XAFS spectroscopy is one of the few techniques that can probe the molecular structure of chemical species in solution or in amorphous solids such as a glass. For crystalline solids, XAFS provides information that is complementary to long-range techniques such as x-ray diffraction, which derives its signal by summing the contributions of millions of atoms arrayed

over hundreds or thousands of angstroms. Whereas x-ray diffraction provides a picture of the average structure of coherent portions of the solid, XAFS yields insight into the average structure surrounding each absorption site.

XAFS spectroscopy began to emerge as a practical experimental tool in the early 1970s, after Dale Sayer, Edward Stern, and Farrel Lytle demonstrated that a Fourier transform could be used to analyze the absorption spectra. Their work coincided with the development of synchrotron x-ray sources that emit enough x-ray photons in the right spectral range to enable rapid, highly accurate absorption measurements. With the subsequent availability of inexpensive computing power to analyze the data and implement the increasingly accurate theoretical models, XAFS flourished.

Only a few isolated XAFS studies, however, were done on the transuranics (elements with atomic numbers greater than that of uranium). In 1993, Los Alamos National Laboratory established the first systematic XAFS program for studying the transuranics and other highly radioactive samples. One of our goals for the first set of experiments was to determine the structure of plutonium complexes in concentrated nitric acid solution. That information was needed to improve our nitric acid recovery process for plutonium (see the article "Molecularly Engineered Resins for Plutonium

Recovery" on page 454). Our program involved developing the containment technology and safety procedures that would allow us to mount hazardous samples at the Stanford Positron-Electron Asymmetric Ring (SPEAR) synchrotron at Stanford University. It also involved assembling the teams of dedicated people who would carry out the work.

We have since used XAFS spectroscopy to study the local structure of plutonium alloys and to deduce the structure of hundreds of plutonium complexes in solutions, solids, slurries, soils, and sludges. In collaboration with scientists from many different institutions, we have also examined thorium, uranium, neptunium, americium, and curium complexes as part of our general program to advance the molecular science of the actinides. In this article,¹ we will delve into the theory and practice of XAFS and describe a few applications of the technique in probing uranium speciation and the structure of plutonium colloids. Other applications are discussed within several articles in this volume of *Los Alamos Science* (for example, see "Characterizing the Plutonium Aquo Ions by XAFS Spectroscopy" on page 418.)

¹Portions of this article were adapted from a 1998 article by S. D. Conradson, "Applications of XAFS to Materials and Environmental Science" (*Applied Spectroscopy* 52: 252A), with permission from the publisher, the Society for Applied Spectroscopy.

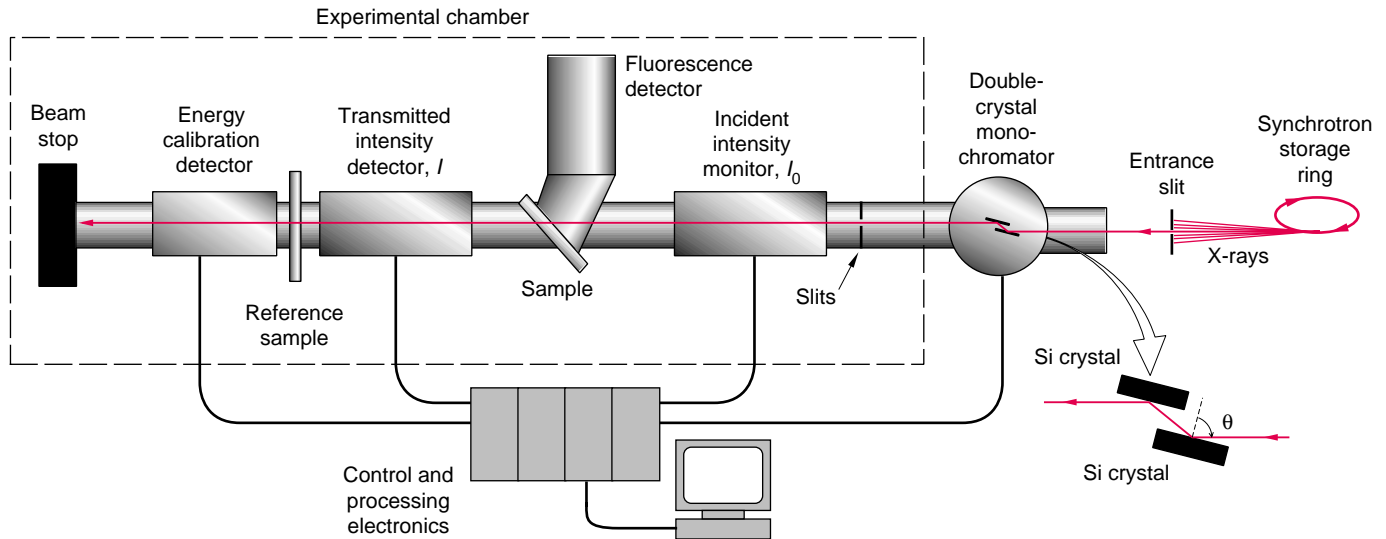


Figure 1. Typical Experimental Setup for XAFS

The full spectrum of x-rays emitted from a synchrotron pass through an entrance slit (which helps collimate the x-rays) before entering a double-crystal monochromator. The x-rays diffract off the crystals' lattice planes, which are aligned at an angle θ with respect to the incoming beam. Because of the Bragg scattering condition $n\lambda_i = 2d\sin\theta$, only x-rays of energy $E_n = nhc/\lambda_i$ can reflect off the crystals. Any of several techniques can eliminate the higher harmonics, so that only the fundamental ($n = 1$) makes it through the exit slits. Different x-ray energies can be selected by changing the angle θ of the crystals. The monochromatic beam passes through an ion chamber that monitors the beam intensity I_0 by absorbing part of it. The beam then passes through the sample, and the intensity of the transmitted x-ray I is measured by a second ion chamber. Taking the log of the ratio of I/I_0 yields the absorption. We can also determine the sample's absorption by measuring the intensity of its x-ray fluorescence with a detector that is out of the beam path. Finally, the beam passes through a reference sample whose absorption edge is used to help correct for uncertainties in the beam's energy.

XAFS Spectroscopy

Figure 1 shows a schematic diagram of a typical XAFS experiment. The broadband x-ray spectrum from a synchrotron is directed into a double-crystal monochromator. This instrument houses two parallel silicon crystals that are aligned at an angle θ with respect to the incoming beam. Only specific x-ray wavelengths (a fundamental plus its harmonics) can satisfy the Bragg scattering condition for constructive interference from the crystals' lattice planes and therefore be passed. After the higher harmonics are rejected, a "single" x-ray wavelength emerges from the instrument: because the relative bandwidth of the emerging beam is about 10^{-4} , that is, 10-kilo-electron-volt (keV) x-rays emerge with an energy spread of only 1 eV, the beam is deemed

monochromatic. By changing the orientation of the two crystals, we can select different energies; thus the monochromator allows us to probe a sample with a set of monochromatic x-rays that span a wide energy range.

The intensity I_0 of the x-ray beam is monitored with a detector (usually a gas ionization chamber) before the beam impinges on a sample. For an ideal sample, between 50 and 90 percent of the x-ray beam intensity is absorbed, while the remainder of the beam passes through. In a transmission-mode experiment, a second detector placed behind the sample monitors the intensity I of the transmitted beam. The latter will follow Beer's Law:

$$I = I_0 e^{-\mu(E)L}, \quad (1)$$

where $\mu(E)$ is the energy-dependent

absorption coefficient of the sample, L is the sample thickness, and E is the energy of the incident x-ray.

In general, $\mu(E)$ decreases approximately as E^{-3} with increasing x-ray energy. At certain energies, however, it abruptly jumps to a higher value, as indicated in Figure 2. These "jumps" in the absorption profile are called absorption edges. They occur whenever E equals the binding energy of an electron in one of the elements in the sample, and thus the energies at which edges appear are unique for each element. During an experiment, the x-rays are scanned with high accuracy over an absorption edge of the target element, and by comparing I with I_0 , we measure $\mu(E)$ versus E for that element.

During the absorption process, an electron moves from its initial bound state to a final unbound state that lies

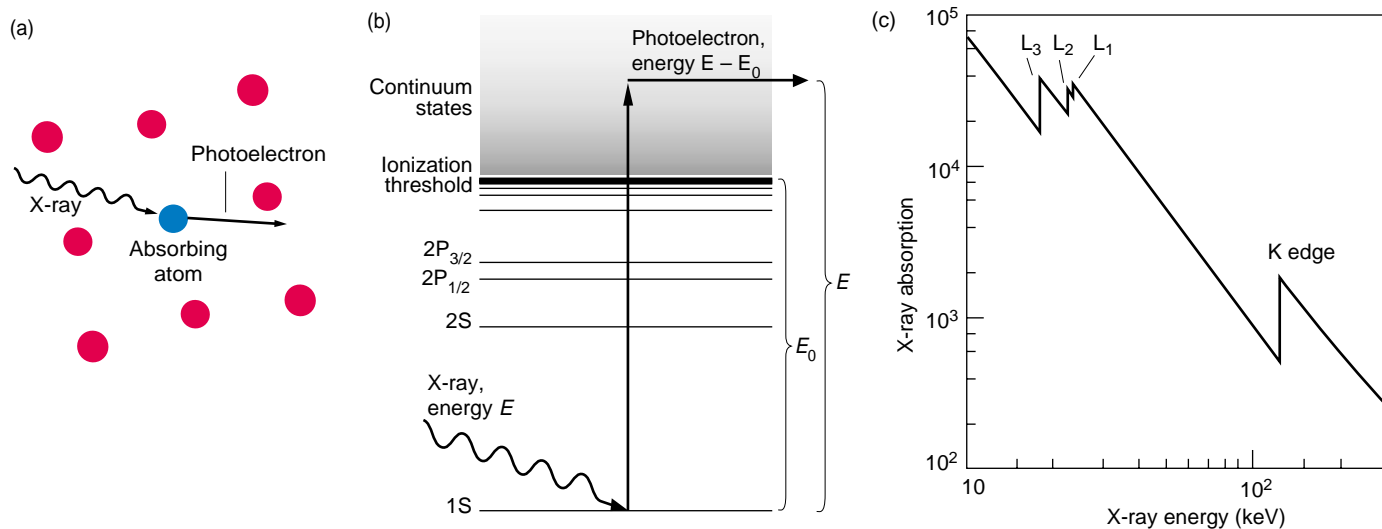


Figure 2. X-Ray Absorption

(a) An absorbing atom (blue) is shown here surrounded by several other atoms (red). Whenever the energy of an x-ray is greater than the binding energy of one of the absorbing atom's core electrons, the electron is liberated. (b) This schematic energy-level diagram of an absorbing atom shows the atom's first few core-electron orbitals: 1S, 2S, 2P_{1/2}, and 2P_{3/2}. The ionization potential energy is denoted by E_0 . With the absorption of a photon of energy E , the electron undergoes a transition to an unbound state in the continuum and, by conservation of energy, acquires a kinetic energy ($E - E_0$). (c) The abrupt jumps in this simplified absorption spectrum are the absorption edges, which correspond to the excitation of an electron from a specific orbital. The absorption edge due to excitation of the 1S electron is called the K edge, while excitations from the less strongly bound 2S, 2P_{1/2}, and 2P_{3/2} electrons are called the L₁, L₂, and L₃ edges, respectively.

above the ionization potential E_0 of the atom. (This electron is often referred to as a photoelectron since it is liberated in a photoabsorption process.) If we assume that a single electron absorbs all of the photon energy, then by conservation of energy, the photoelectron is kicked free with a kinetic energy ($E - E_0$).

At the x-ray energies available from today's synchrotrons—extending past 10 keV—the electron is ejected from one of the low-lying orbitals of the atom (the 1S, 2S, 2P_{1/2}, or 2P_{3/2} orbitals). The absorption edge due to excitation of the 1S electron is called the K edge, while excitations from the less strongly bound 2S, 2P_{1/2}, and 2P_{3/2} electrons are called the L₁, L₂, and L₃ edges, respectively.

The K-edge energies of plutonium and the other actinides are well above 100 keV, which is difficult to access experimentally. Also, K-shell electrons have a lower absorption cross section than L-shell electrons. Thus our XAFS

studies of the actinides are typically done on the L₂ and L₃ edges. The energy of the L₃ edge of plutonium varies between 18.056 and 18.061 keV, depending on the oxidation state of the plutonium ion.

Figure 3 shows the L₃ edge of platinum, obtained from a thin platinum foil. The spectrum has numerous small oscillations on the high-energy side of the edge. As explained in the next section, those oscillations result because the local atomic environment affects the probability that the target atom absorbs the x-ray photon. The effect is small: just 500 eV from the edge, the difference between the absorption coefficient μ of an element in the sample and the absorption coefficient μ_0 of the free atom may be only a few tenths of a percent. While it is difficult to measure such small changes, the synchrotron's stable high flux of photons allows us to do so with accuracy and precision.

The oscillations that start about 30 eV beyond the peak of the absorp-

tion edge and that persist for another 1000 eV are known as the extended x-ray absorption fine structure (EXAFS). In this region, the kinetic energy of the photoelectron is large compared with its interaction energy with nearby atoms, which is on the order of 3 eV. The local environment, therefore, only slightly perturbs the final state of most of the photoelectrons, and we can use perturbation theory to construct a theory of the physics underlying the EXAFS. Such work began in the 1930s, and a fairly complete theory was in place by the early 1960s. The EXAFS encodes most of the local structure parameters, such as the distance R to nearby atoms and both the number N and atomic number Z of those atoms.

The narrow region that starts slightly before the absorption edge and extends about 30 eV beyond the peak also shows structure—the x-ray absorption near-edge structure (XANES). In this region, the photoelectron has less kinetic energy, and its interactions with the

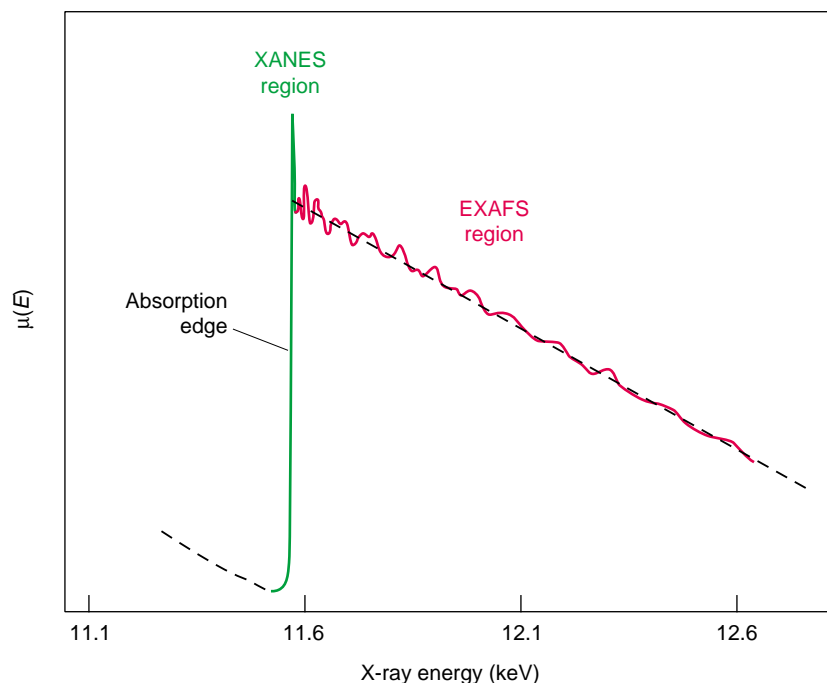


Figure 3. Typical XAFS Spectrum
In this XAFS spectrum of a platinum foil, small oscillations modify the basic absorption coefficient of the free atom μ_0 (represented by the dashed line). The small peaks and shoulders that modify the absorption edge and extend about 30 eV beyond it are known as the x-ray absorption near-edge structure (XANES). The XANES region contains information about the ionization potential and oxidation state of a chemical species and often exhibits features that are characteristic of specific molecular structures. The oscillations that begin approximately 30 eV beyond the absorption edge are called the extended x-ray absorption fine structure (EXAFS). The EXAFS region encodes structural information, such as the distance, type, and number of neighboring atoms.

local environment are more difficult to interpret. However, researchers have long realized that the oxidation state of the absorbing atom can be extracted from the XANES spectrum. (More information about this region is given in the XANES box on page 432.)

Originally, the XANES and EXAFS regions were thought to reflect different physical processes. But increasingly accurate calculations have indicated that with few exceptions, all of the peaks and valleys in the XANES spectra, including the maximum of the absorption edge, can be explained by the same physics that leads to the EXAFS. Today, both regions are jointly referred to as the XAFS. Because it is easier to describe, we will focus on the EXAFS in the discussion that follows.

EXAFS Theory

The extended fine structure fundamentally derives from the wave nature of photoelectrons. When an electron is ejected from an isolated atom, the photoelectron's final state can be represented by an expanding spherical wave. But when the absorbing atom is not isolated,

the photoelectron can scatter from the nearby atoms. At the "large" kinetic energies in the EXAFS region, it is reasonable to assume that the photoelectron scatters only once as it leaves (single-scattering approximation). The final electron state is then a superposition of the outgoing and scattered waves.

Interference between those two wave components affects the probability $P(E)$ that the target atom absorbs the incoming x-ray photon. To see this, recall that in quantum mechanics the absorption probability is proportional to the square of the transition matrix element that connects the initial and final states of the electron:

$$P(E) \sim |\langle \psi_f | H_{\text{int}} | \psi_i \rangle|^2, \quad (2)$$

where ψ_i and ψ_f are the initial- and final-state wave functions, respectively, and H_{int} is the part of the Hamiltonian that describes the interaction between the electron and the x-ray radiation field. The matrix element is evaluated over all space, but its value is nonzero only where the initial- and final-state wave functions overlap. Since the initial state ψ_i is one of the low-lying core orbitals and is highly localized, the ma-

trix element (which involves integrating ψ_i and the complex conjugate of ψ_f over space) depends only on the part of the final-state wave function that exists near the center of absorber. Only those portions of the outgoing wave that scatter back to the absorber (backscatter) affect the probability of x-ray absorption.

If (in the particle picture) the photoelectron elastically scatters from a nearby atom, then (in the wave picture) the backscattered wave will remain coherent with the outgoing wave. As seen in Figure 4, the two waves will interfere at the absorbing atom, either increasing or decreasing the amplitude of the final-state wave function. The amount of interference naturally depends on the amplitude and phase of the backscattered wave. The phase in turn depends on the distance between the absorbing and scattering atoms and on the photoelectron wavelength λ . This wavelength is related to the photoelectron momentum p through the de Broglie relation,

$$\lambda = \frac{h}{p}, \quad (3)$$

where h is Planck's constant. The momentum is a function of the

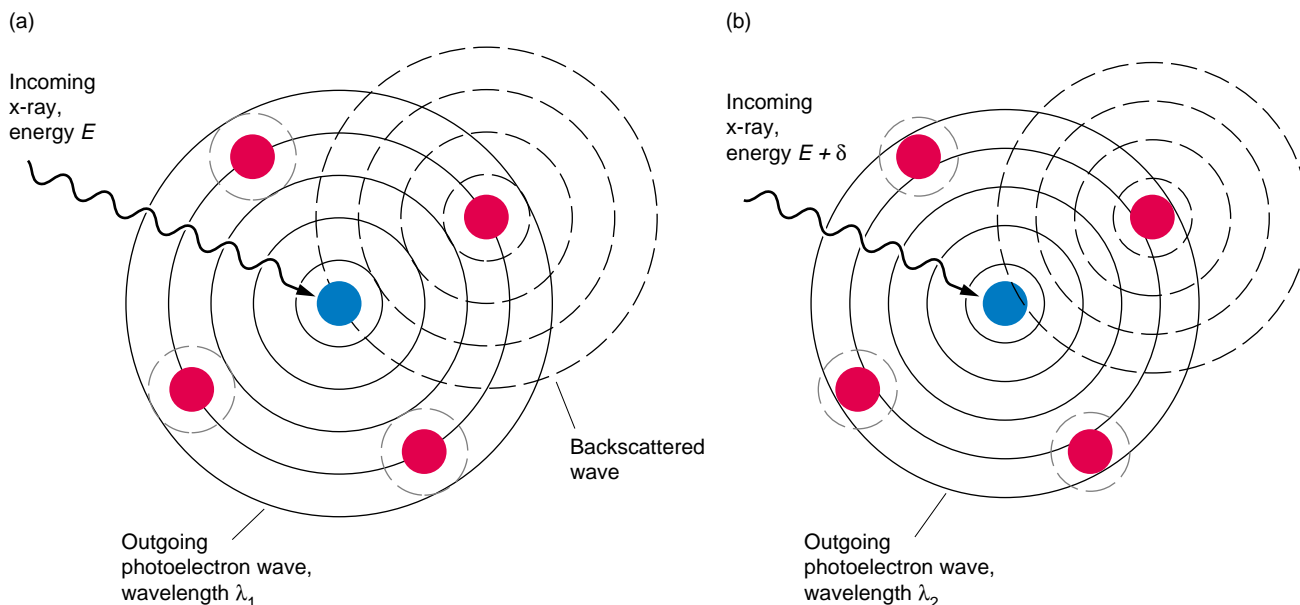


Figure 4. Interference in the Final-State Wave Function

The wave function of a photoelectron liberated from an absorbing atom (blue) is described by an outward-propagating spherical wave. This wave can backscatter from a nearby atom (red) and interfere with itself back at the absorber. (a) In constructive interference, wave crests (solid and dashed lines) meet in the center of the absorbing atom and increase the amplitude of the final-state wave function. Maximum constructive interference is shown here. (b) When an x-ray of a different energy is absorbed, the photoelectron wavelength and the interference change. Shown here is maximum destructive interference, when the waves are 180 degrees out of phase at the atom. The amplitude is decreased. Over a range of energies, the final-state wave function will increase or decrease many times, resulting in energy-dependent oscillations in the atom's absorption probability.

electron's kinetic energy,

$$p = \sqrt{2m(E - E_0)} \quad , \quad (4)$$

where m is the electron mass, and thus the wavelength of the photoelectron depends on its kinetic energy:

$$\lambda = \frac{h}{\sqrt{2m(E - E_0)}} \quad . \quad (5)$$

As the x-ray energy E increases, the photoelectron wavelength λ decreases. The relative phase between the outgoing and backscattered waves changes and alters the amplitude of the final-state wave function. Hence, the atom's photoabsorption cross section becomes modified as a function of x-ray energy.

Because the amplitude of the backscattered wave will vary depending on the position R of the backscattering atom (as R^{-2}) and on the type of atom

(since the scattering function depends on the atomic number Z of the scatterer), every atom in the local environment will uniquely modify the free-atom absorption. But crystal lattices and molecules are often highly symmetric; a number of identical atoms will typically surround the target atom at a common radius. These atoms are said to occupy a spherical shell of radius R . In a complex molecule or solid-state structure, numerous shells will be nested around the target atom, and we can construct a model in which the photoelectron scatters not from individual atoms, but from individual shells (see Figure 5).

Standard EXAFS Equation. In deriving a model for the EXAFS, we assume that the local environment perturbs the absorption coefficient μ_0 of the free atom. The measured absorption

coefficient is μ :

$$\mu = \mu_0 [1 + \chi(k)] \quad , \quad (6)$$

where $\chi(k)$ describes the EXAFS, and $k = 2\pi/\lambda$ and is the magnitude of the photoelectron wave vector. By incorporating the assumptions discussed above (that is, photoelectron kinetic energies of ~ 30 eV or higher and only single scattering,² we can derive the standard expression for EXAFS:

$$\chi(k) = \sum_j A_j(k) e^{-\beta_j(k)} \times \sin(2kR_j + \Phi_j(k)) \quad . \quad (7)$$

This equation is a sum over expo-

²Other assumptions include neglecting the x-ray's polarization and assuming only dipole interactions between the absorber and the radiation field.

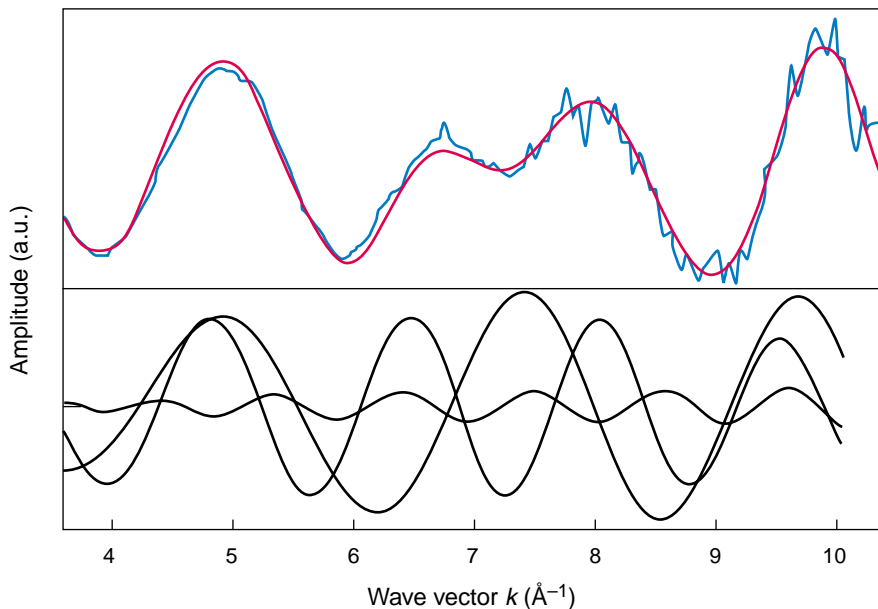


Figure 5. An EXAFS Spectrum

The local structure surrounding a target atom can be modeled as a series of spherical shells, where each shell has a unique radius and contains a finite number of identical atoms. A photoelectron that backscatters from a particular shell acquires a unique energy-dependent phase and amplitude, so its contribution to the EXAFS can be discerned. The upper graph shows part of a measured EXAFS spectrum (blue line) and its theoretical fit (red line). The lower graph shows the three waves that compose the fit. Each wave corresponds to backscattering from a different shell. The waves are plotted as a function of wave vector $k = 2\pi/\lambda$.

nentially damped sine waves, where each wave accounts for the backscattering of an electron from a shell of atoms (the index j references a shell).

The term $2kR_j$ in the argument of the sine function results from the phase shift of the photoelectron as it leaves the absorbing atom, backscatters from an atom at position R_j , and returns. The additional phase shift $\Phi_j(k)$ arises because the photoelectron travels through the spatially varying potentials of the absorbing and backscattering atoms.

The amplitude $A_j(k)$ of each wave is given by

$$A_j(k) = \frac{N_j}{kR_j^2} f_j(k) S_0^2 \quad (8)$$

where N_j is the number of atoms in each shell and $f_j(k)$ is the magnitude of

the complex function describing the scattering. The last term, S_0^2 , is a loss term that accounts for multielectron excitations and inelastic scattering.

We see that the amplitude of each wave is a function of the parameters N_j and R_j . In addition $f_j(k)$, as well as the phase shift $\Phi_j(k)$, is a function of the atomic number Z_j . Thus, we can extract those three primary pieces of information for each shell in the EXAFS data. But the amplitude decreases as R_j^{-2} , so the contributions from more-distant scattering shells decrease rapidly. The EXAFS is often not useful for obtaining information from shells that are more than 4 or 5 angstroms from the target.

The exponential damping term in Equation (7) accounts for additional processes that modify the final-state wave function. This term is also a product:

$$e^{-\beta_j(k)} = e^{-\frac{2R_j}{\lambda_e}} e^{-2k^2\sigma_j^2} \quad (9)$$

The first exponential takes into account the finite lifetime of the final state. The photoelectron leaves behind a hole in the absorbing atom's core configuration, and filling the hole with a new electron represents the end of the final state. The hole lifetime is typically about 1 femtosecond. The photoelectron also has a "lifetime," since it can scatter out of the system. Both processes can destroy the coherence between the components of the final-state wave function and hence wipe out the interference. The form of this damping term is phenomenological; it is parameterized in terms of the mean free path λ_e of the photoelectron.

The second exponential accounts for the fact that atoms are in constant thermal motion; hence the positions of the atoms within a shell are distributed about an average radius R_j . Photoelectrons scatter from each atom with a slightly different phase, with a subsequent "smearing" of the EXAFS. Localized strains (static disorder) will similarly affect atomic positions. By assuming that the positions vary according to a Gaussian distribution, we can derive the exponential form of the correction term, where the parameter σ_j acts like a pairwise Debye-Waller factor between the absorber and a scattering atom. Both thermal and static disorders are modeled by the second exponential.

In 1971, Stern, Sayers, and Lytle showed that Equation (7) could be analyzed by a Fourier transform. The EXAFS, $\chi(k)$, which is parameterized in terms of the wave vector k , could be transformed into a radial structure function $\chi(R)$ that represents the data in terms of distances from the absorber. Peak positions in this radial structure function roughly correspond to the radii of the scattering shells.³

Thus, atomic parameters such as N , R , and Z could be extracted directly from the EXAFS data. Before this time,

EXAFS data were compared with a theory function that used calculated values of these parameters. Because the values were often inaccurate, the data rarely correlated with theory. This lack of correlation had the net effect of calling into question the theoretical foundation of EXAFS. Introduction of the Fourier transform turned EXAFS into a viable experimental tool.

Since 1971, computer advances have allowed us to do away with many of the simplifying assumptions underlying the theory presented above. For example, Equation (7) assumes that the electron scatters as a plane wave from small, pointlike atoms. The effects of spherical wave scattering from more realistic atomic potentials can now be included. In addition, the scattering amplitude $f(k)$ can be replaced with an effective amplitude $f_{\text{eff}}(k, r)$ that has a weak radial dependence. This improvement to the theory has been incorporated into modern data analysis packages, such as the FEFF computer programs. (The name FEFF derives from f_{eff} .)

These programs also take multiple scattering into account, thus doing away with the single-scattering approximation. The effects of multiple scattering can sometimes make unexpectedly large contributions to the EXAFS. For example, in a face-centered cubic (fcc) solid such as δ -phase plutonium, the linear alignment of the absorber with atoms in the second and fourth shells creates a focusing effect that enhances the overall forward-scattering amplitude of the photoelectron by about a factor of 6 (at 0 kelvins). The phase shift is also enhanced, since a photoelectron is influenced by three or more atomic potentials as it journeys from the absorber to the second shell to the fourth shell and then back. The result is a “multiple-scattering” peak that overlaps with the location of the fourth shell. Analysis of

the higher shells in the EXAFS would be difficult without the ability to handle these multiple-scattering peaks.

Extracting and Interpreting the Parameters. As outlined in Figure 6, the EXAFS is extracted from $\mu(E)$ based on an estimate of the free-atom absorption μ_0 . The data are extrapolated to k -space, and amplitudes and phases can be either determined empirically or calculated. FEFF is used to fit $\chi(k)$ to a modern theory function through some variation of nonlinear least-squares curve fitting. Fitting the data before doing the Fourier transform avoids some issues of Fourier filtering (which can introduce errors into the data), but it is nonetheless difficult to evaluate the fit in k -space. Thus, as seen in Figure 6(c), both the data and the fit are transformed through a Fourier transform to a radial structure function. Inspection of the structure function provides the first insights into local structure. Information from other sources or from the EXAFS of a reference compound is then used to evaluate this initial model and to suggest ways to alter the fit criteria. These steps may be repeated numerous times, with the model being refined each time.

This iterative procedure is necessary because alone, EXAFS data is often too imprecise and the uncertainties in the fit parameters too large to support a definitive interpretation of the local structure. For example, the nominal uncertainty in determining the atomic number for each shell is $Z \pm 4$, and the uncertainty in the number of atoms in a shell can be as high as 30 percent. It is also impossible to calculate S_0^2 [see Equation (8)] to better than 20 percent. In addition, because all sites of an element contribute equally to the EXAFS, the data represent a population-weighted average of all the chemical species of

an element that are present in the sample. The EXAFS cannot *a priori* distinguish between a sample containing one chemical species and another containing many species.

Furthermore, Equation (7) assumes that the radial positions of atoms in a shell are randomized according to a Gaussian distribution (through the parameter σ). Any non-Gaussian distribution, such as might result from a local strain or from the presence of different chemical species, is very difficult to handle analytically. An odd-shaped hump in the radial distribution function can be interpreted in terms of a chemical species that has several closely spaced shells, several chemical species coexisting in the same sample, or a sample that has a severe amount of disorder.

The imprecision can be partially resolved by simultaneously measuring the EXAFS from a reference sample. The reference is well characterized and will ideally contain only a single chemical species. We can then do a comparative analysis of the data and are limited only by the relative errors. Along those same lines, XAFS is best used to determine the differences between an unknown compound and a closely related, well-characterized compound, or to follow changes in a sample that is subjected to temperature, pressure, or chemical variations. With a well-planned set of experiments, XAFS is usually sufficient to detect changes in the local environment surrounding the central atom involving as few as one of its nearby neighbors.

Still, we often need to have a pretty good idea of what the local structure is before beginning an analysis. XAFS spectroscopy is therefore a tool that is most powerful when used in conjunction with other structure-determining methods, such as x-ray diffraction, Raman spectroscopy, or nuclear magnetic resonance spectroscopy. Ultimately, however, the ability to understand the local structure surrounding an element in an unknown environment depends on the skill of the experimenters and their analytical prowess.

³Peaks in the radial structure function do not correspond directly with shell positions. The phase shift $\Phi(k)$ in Equation (7) always contains a part that is linear in k —that is, $\Phi(k) = \phi k + \varepsilon(k)$, where ϕ is a constant and $\varepsilon(k)$ is a nonlinear function of k . The sine terms can therefore be written as $\sin((R+\phi)k + \varepsilon(k))$, and the Fourier transform of $\chi(k)$ actually produces a function $\chi(R+\phi)$. A detailed knowledge of the phase shift (either theoretical or empirical) is necessary to extract the shell radii. The radial structure function $\chi(R)$ is often plotted versus $(R-\phi)$ to emphasize this fact.

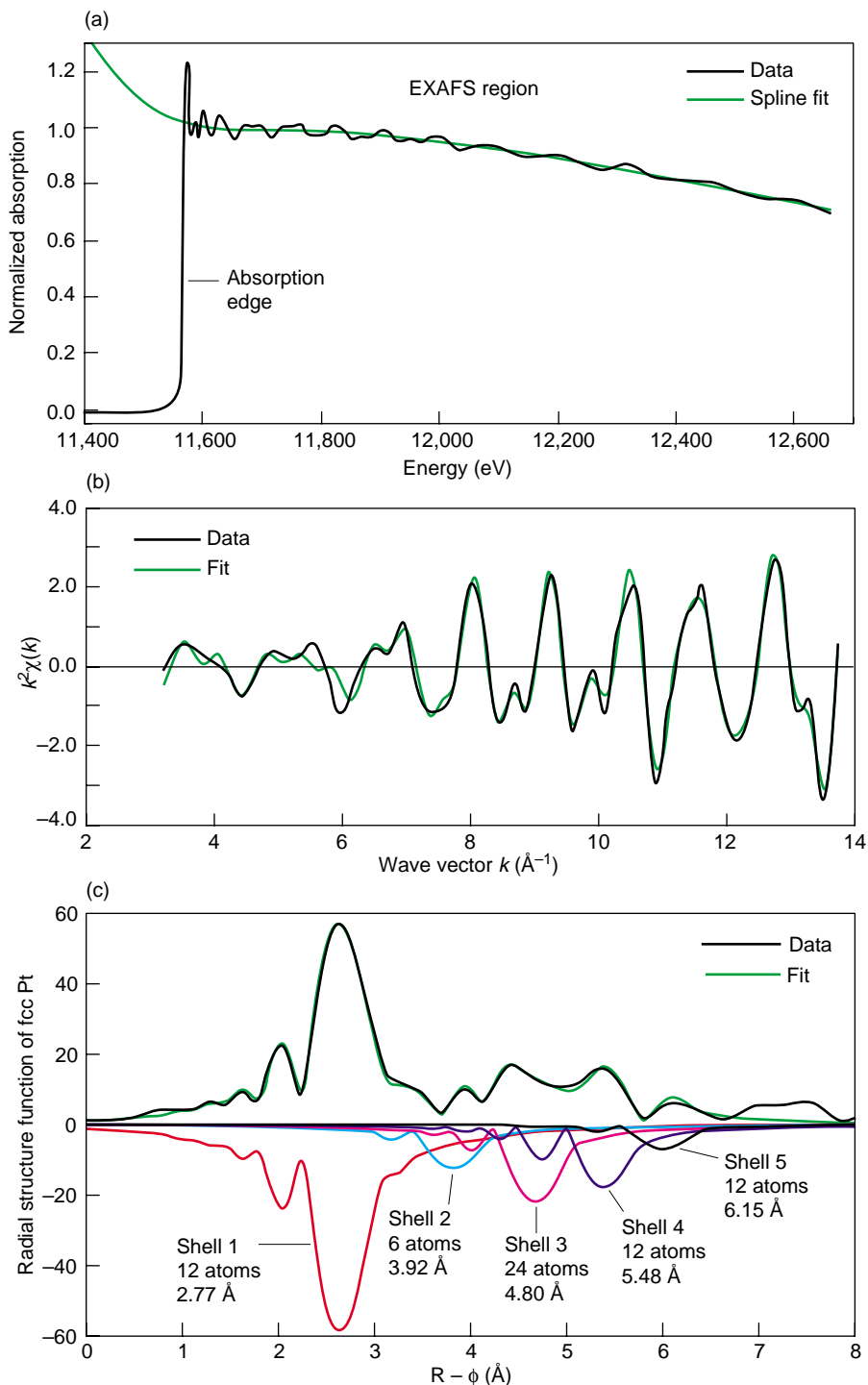


Figure 6. Analysis of a Platinum Foil

(a) The absorption coefficient $\mu(E)$ is obtained from the raw data (after correcting for the effects of various instrument defects or nonlinearities) by plotting $\ln(I/I_0)$ vs the x-ray energy, subtracting the background, and normalizing the edge jump to unity. The ionization potential energy E_0 is chosen, and the free-atom absorption coefficient μ_0 is approximated by a polynomial spline. (b) The EXAFS $\chi(k)$ is obtained by taking the difference between the data and the spline and converting the energy E to a wave vector k . As shown here, $\chi(k)$ is weighted by an arbitrary factor of k^2 to equalize the amplitude fluctuations at large k values and help avoid introducing errors in going from $\chi(k)$ to a radial structure function. Parameters are obtained by curve-fitting the data to a theory function such as Equation (7). (c) Taking the Fourier transform of $\chi(k)$ creates a radial structure function $\chi(R)$ that helps to illuminate shell positions. Platinum has an fcc crystal structure, and the positions of the first through fifth nearest-neighbor shells are at 2.772, 3.92, 4.801, 5.544, and 6.198 \AA , respectively. The fit to $\chi(R)$ is shown by the green curve. Beneath $\chi(R)$ are the components of the fit that correspond to each shell. Note that the x-axis does not indicate radial distances in the structure that $\chi(R)$ represents. Because of the phase shift in the sine term in Equation (7), distances to nearby atoms are only approximated by peak positions in $\chi(R)$. The correct shell radii are obtained from the curve-fitting analysis.

Probing Chemical Speciation with XAFS

Chemical speciation (the individual compounds and complexes exhibited by an element that determine its reactivity) is particularly important in environmental science, because different compounds of a hazardous element can

have greatly differing solubility and transport properties and differing effects on a biological system.

XAFS spectroscopy determines exactly those parameters needed to define chemical speciation: the valence of the central (absorbing) atom and the atom's radial structure function in terms of the atomic numbers of its neighbors, their

distances from it, and the number of each type of atom at each distance. In addition, the elemental specificity of XAFS precludes interference from other compounds. This means that little or no sample preparation is required, and thus there is no need for a separations process that could inadvertently alter the speciation. Even intensely radioac-

tive sludge from a Hanford waste-storage tank (containing dozens of elements in a dense, complicated matrix) relinquishes speciation information on its elements when small samples are placed in the XAFS beam.

Speciation of Uranium in Soils.

During the Cold War, the Feed Materials Production Center in Fernald, Ohio, was a DOE plant that processed uranium. When the plant closed after nearly 40 years of operation, some of the soil around it was contaminated with up to several thousand parts per million of uranium. A number of DOE-sponsored research and development projects were begun to develop a cost-effective method for washing the uranium out of the soil.

Even if accurate records of individual spills had been maintained, decades of weathering had ensured that the uranium species in the soil were substantially altered from their original forms. Various techniques, including ultraviolet-induced fluorescence and electron microscopy, showed that the uranium was present as discrete particles adhering to the soil's mineral grains. Those detection methods, however, could not identify the exact uranium species, and the efficiency of proposed extraction methods depended on such information. Thus, XAFS was selected as one of the primary characterization techniques. This marked its first use as a routine analytical tool for a project of this magnitude.

XAFS quickly proved itself. Even with the most rudimentary sample preparations—simply removing pebbles and grass stems and then lightly grinding the remaining soil with a mortar and pestle—XANES spectra revealed the presence of the characteristic “-yl” shoulder of the uranyl $O=U=O$ unit. (Refer to the XANES box on page 432.) Although XAFS probes all uranium species simultaneously, observation of this feature in all samples demonstrated that the soils contained a significant fraction of standard U(VI) species. At four site locations, the fraction of U(VI) was greater than 80 percent.

Analysis of the EXAFS confirmed

that initial identification, for it found a U–O distance corresponding to the uranyl bond length of about 1.74 angstroms. It also found other U–O distances between 2.3 and 2.4 angstroms that are typical of oxygen-containing ligands such as O^{2-} or OR^- (where R is a chemical group) that bond in the equatorial plane of U(VI) complexes. The remainder of the uranium in the soil appeared to be a non- UO_2 species of U(IV).

Our finding that the uranium existed mostly as U(VI) species was important. It immediately eliminated from consideration proposed separation methods targeted at the chemical or physical properties of U(IV), which had been promoted as the most stable oxidation state of uranium under site conditions.

Elucidating the particular species of U(VI) or U(IV) proved to be difficult, however. For the most part, identifiable features could be culled from the data for only the first shell of neighboring atoms, which were nearly always oxygen. But the analysis was too uncertain to indicate specifically which ligands were present. One interesting conclusion could be drawn, however. Because samples were taken from different soil layers, we could observe the evolution (by equating soil depth with time) of chemical structures. The solids seemed to become more crystalline with age.

Following this initial characterization, XAFS was used to help develop soil-washing methods. We tested one method that used citrate as a complexing agent (a method commonly used in mining). We also explored a more selective soil-washing method that used Tiron as a complexant in conjunction with a mobilizer, dithionite. The washing methods readily removed the bulk of the uranium but left behind an intractable fraction. In the XAFS spectra, soil washing reduced the “-yl” shoulder in the XANES and reduced the amplitude of the actinyl contribution in the EXAFS. Taken together, those two changes indicated a selective loss of U(VI) and an increase in the U(IV):U(VI) ratio.

To quantify this effect, we first needed to devise a method to analyze the XANES. For this series of experiments, performed around 1990, we could not use the energy of the absorption edge to identify the oxidation state of the species in the sample because we could not obtain a reliable edge energy. During the course of an experiment, the drifts in the monochromator and the beam location are irreproducible. Typically, the spectrum of a thin metal foil is taken simultaneously with one of the sample, and the known characteristics of the foil spectrum are used to correct for instrument drifts. However, uranium metal could not be used as a calibration standard because it oxidizes too rapidly when exposed to air, even when protected by a film of acrylic resin. Furthermore, we could not use UO_2 or some other reference oxide for this calibration since it would suffer from a change in the incident beam intensity when the uranium oxide in the sample absorbed the x-rays. Finally, the absorption edge of another, more stable element was too far away to be a good calibration standard.

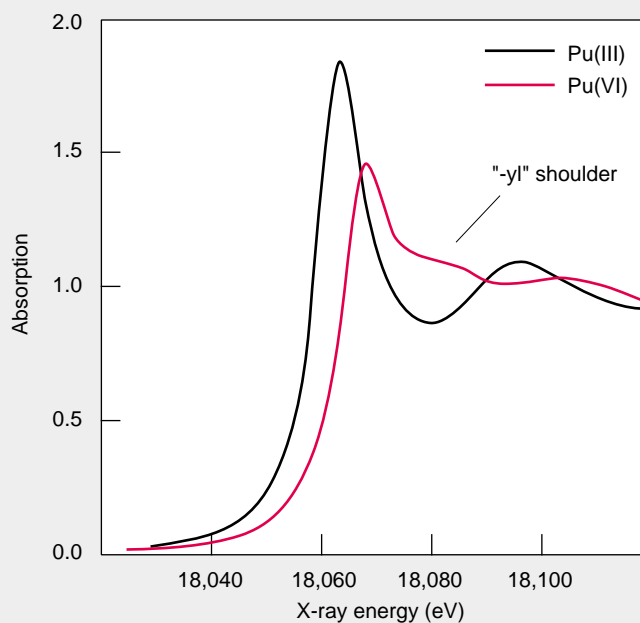
The problem of getting a reliable edge energy was solved by always assigning the inflection point in the absorption edge to the same energy. The edge was then fit with a particular combination of Gaussians and an arc-tangent. This method had the advantage that the position of the Gaussian corresponding to the “-yl” shoulder could be found with high accuracy even in relatively noisy data. The difference in energy between the U(VI) absorption edge and the shoulder is relatively invariant since the former depends largely on the ionization potential energy of the U(VI) species and the latter on the U=O bond length in the actinyl moiety, which does not change between different U(VI) complexes. As the percentage of U(IV) increased, the energy of the sample's absorption edge decreased since it is the average of the U(IV) and U(VI) edge energies. Hence the energy difference between the inflection point and the Gaussian increased, and this

XANES

The x-ray absorption near-edge structure (XANES) refers to the secondary peaks and shoulders that modify the appearance of the absorption edge and the 20- to 30-eV region beyond it. The XANES can reveal the oxidation state of an element in the sample, as well as serve as a “fingerprint” to identify certain structural motifs of a chemical species.

The energy at which an absorption edge appears depends on the ionization potential E_0 of the absorbing atom, but in general E_0 increases when the absorber is in a higher oxidation state. The accompanying figure shows XANES spectra of the Pu(III) and Pu(VI) aquo ions, $\text{Pu}(\text{H}_2\text{O})_n^{3+}$ and $\text{PuO}_2(\text{H}_2\text{O})_m^{2+}$, respectively. The absorption edge shifts toward higher energies with higher oxidation states. After gathering XANES data from several oxidation-state-pure samples, we can construct a curve of oxidation state versus edge energy. This calibration curve can then be used to identify the oxidation state of the various plutonium species in unknown samples.

The presence of certain molecular structures can also be inferred from features in the XANES. For example, in an aqueous solution, uranium, neptunium, and plutonium ions in the V and VI oxidation states nearly always exist as actinyl ions. The actinyl is a *trans*-dioxo cation with a linear structure: two oxygen atoms form strong, covalent bonds to the central actinide, $\text{O}=\text{An}=\text{O}$, where An can be uranium, neptunium, plutonium, or americium. The actinyl generates a distinctive “-yl” shoulder in the XANES at energies just above the absorption edge. The presence of this shoulder can be used to confirm the presence of the An(V) or An(VI) oxidation state in complex chemical matrices.



difference was used to track the U(IV):U(VI) ratio. We were able to confirm the presence of an easily removed U(VI) fraction and a much more inert U(IV) compound that was not UO_2 (see Figure 7).

Over two and a half years, we obtained and analyzed spectra from almost 60 samples, demonstrating the feasibility of using XAFS as a routine, albeit complicated and high-powered, analytical tool for determining average chemical speciation in complex environmental samples. Although our XAFS information could have been used to optimize cleanup operations, ultimately none of the soil-washing methods was used at Fernald. Because of the anticipated cost of all proposed schemes, the immediate problem was solved by loading the more heavily

contaminated soils into drums and trucking them to a chemical waste dump for indefinite storage.

Pu(IV) Colloid. In many natural water systems, such as aquifers or oceans, plutonium is in the IV oxidation state. However, measurements of the total Pu(IV) concentrations in synthetic waters that mimic natural conditions vary wildly—by many orders of magnitude. The huge variations are likely due to the presence of Pu(IV) oxyhydroxide, more commonly known as Pu(IV) colloid.

Colloids consist of tiny, 1- to 1000-nanometer-sized particles that remain suspended in solution. Laboratory-based x-ray diffraction patterns of aged Pu(IV) colloids display Bragg peaks that are similar to the fcc structure of plutonium

oxide, PuO_2 . This similarity led to the assumption that the colloids are tiny crystallites of plutonium oxide, perhaps with a water-saturated, or hydrated, surface. But our XAFS studies of Pu(IV) colloids demonstrated that this average fcc structure is overly simplistic and that additional chemical moieties are present that could substantially affect the colloids' solubility. Thus the variations in measured Pu(IV) concentrations may in fact be related to the local structure of the colloid particles.

Instead of the displaying the single Pu–O distance of the oxide (2.34 angstroms), the colloid displays many discrete Pu–O distances that are easily and unequivocally identified, ranging from 2.25 angstroms—characteristic of Pu–OH moieties—up to about 3.5 angstroms (see Figure 8). Also, relative

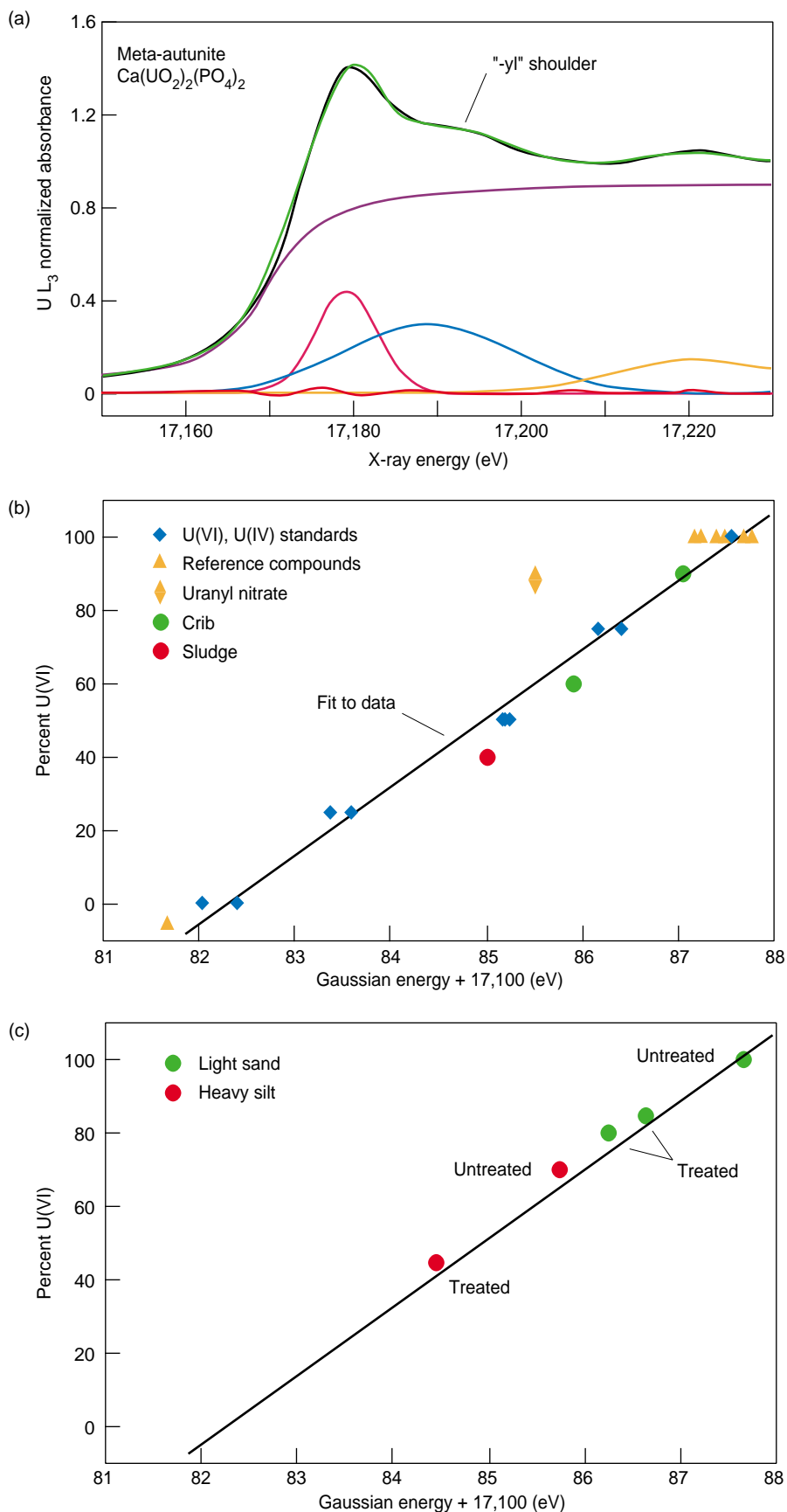


Figure 7. Determination of the U(IV):U(VI) Ratio for Washed Fernald Soils

(a) We used XANES spectra to identify the oxidation state of uranium complexes in soils around the Fernald plant. The XANES data were fit with a combination of Gaussian functions and an arctangent. The “-yl” shoulder at energies just above the main peak is indicative of U(VI). The position of the Gaussian corresponding to this feature could be found with high accuracy and could be used to track the U(IV):U(VI) ratio. (b) We used various mixtures of UO_2 , a U(IV) species, and meta-autunite, a U(VI) species, to obtain a ratio-vs-energy calibration line. Significant uncertainties were observed only at the lowest U(VI) concentrations, when the intensity of the “-yl” shoulder was very small. We deduced that our technique was accurate to within $\pm 10\%$ when tested with a number of standards possessing a range of local structures. Soil (crib) and tank-sludge samples taken from the Hanford site also fell reasonably close to the curve. (c) Many of the Fernald soils had high quantities of U(VI) species, although there was a significant variation between samples. The application of our Gaussian technique to the analysis of washed Fernald soils showed that, in general, washing removed U(VI) but left the less soluble U(IV) in the soil.

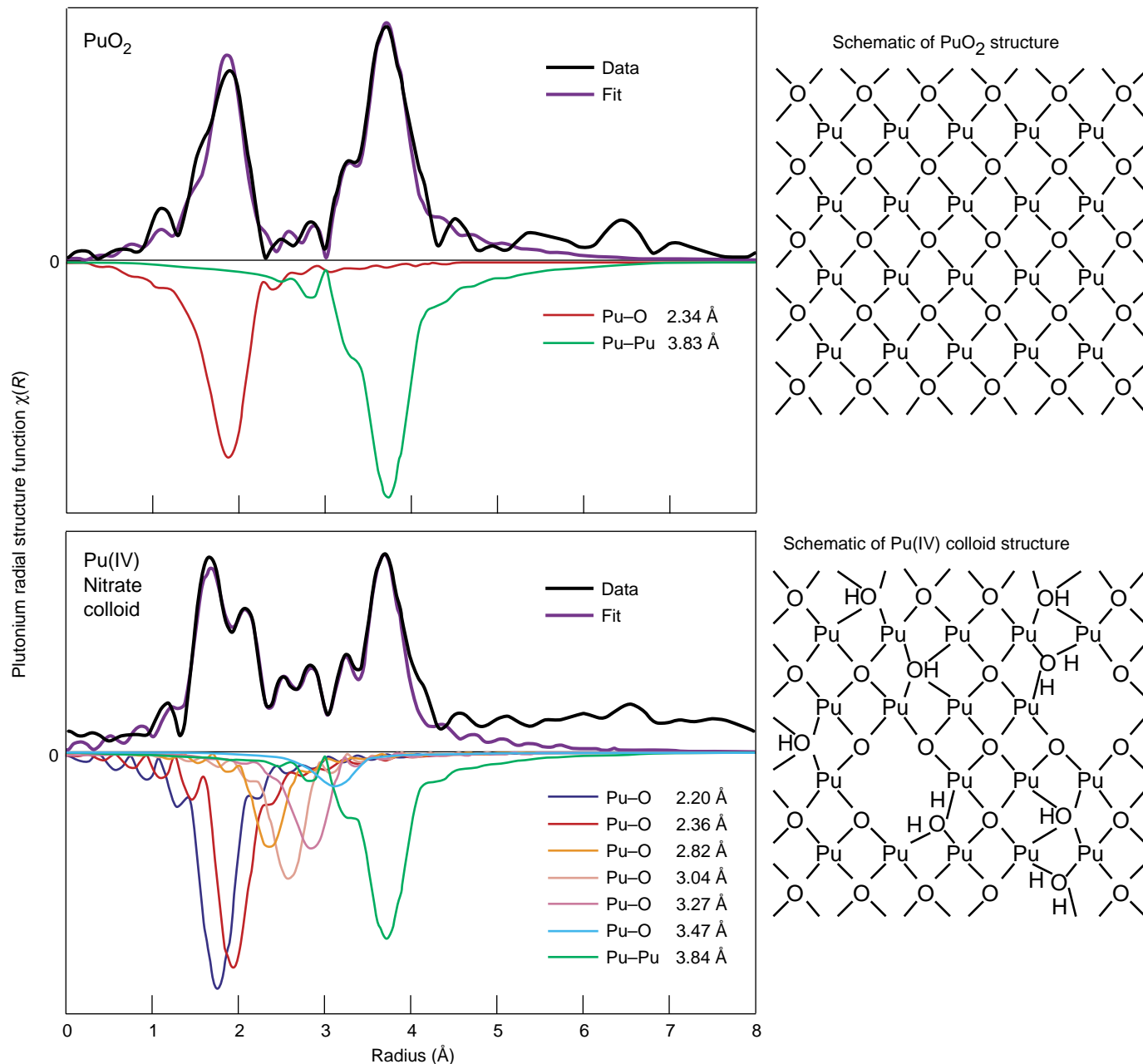


Figure 8. Plutonium(IV) Colloid

The Fourier transform for the EXAFS of PuO₂ (lower figure) shows some deviations from a highly ordered fcc crystal structure, but no shells other than the Pu-Pu and Pu-O. The Pu-Pu peak has a relatively large amplitude. The EXAFS of the Pu(IV) colloid (top figure) shows a reduced Pu-Pu amplitude and a plethora of Pu-O distances, including the one native to PuO₂. The Pu-O distance of 2.20 Å is indicative of a hydroxide ligand. These results suggest a model for the colloid: every four protons incorporated into the structure produce a plutonium vacancy. The different types of oxygen ligands will form different types of bonds with the plutonium, resulting in the series of well-defined bond lengths observed in the EXAFS. We expect that the plutonium atoms will also undergo displacements but that the average long-range order will be conserved. Portions of the material with plutonium vacancies, hydroxides, and water concentrations could be expected to form unique domains, as indicated in the two-dimensional diagram on the right. Different domains may have different structures and properties.

to the oxide's EXAFS, the amplitude of the Pu–Pu peak in the colloid's EXAFS is considerably reduced. By a simple charge-balancing argument, four hydrogen atoms incorporated into the Pu(IV) colloid structure could result in one plutonium-ion vacancy. Thus the reduced amplitude may indicate an actual decrease in the average number of plutonium nearest neighbors.

The fact that the Pu(IV) colloid displays a diffraction pattern tells us that the plutonium sublattice of the PuO₂ crystallite is retained on average. However, the EXAFS reveals that many atoms in the colloid structure are distributed in a non-Gaussian way when compared with their placement in the Pu(IV) oxide. This distribution again suggests that several different oxygen-containing groups are present in the colloid. In addition to the original O²⁻, there may be OH⁻ and possibly OH₂. This variety would further imply that the Pu–Pu distance distribution would have to display concerted excursions from the average unit cell.

Defects in the average structure of the Pu(IV) colloid could create chemically distinct domains within the colloid particle. If the Pu(IV) colloid has domains that are more properly described by, for example, Pu₅O₈(OH)₄, then the colloid's behavior in a natural system would be altered in comparison with a suspension of PuO₂ crystallites. Depending on the specific domain structure, the colloid could even exhibit a range of solubilities, and its behavior in a natural waters could be quite variable. By extension, defects in the local structure of other plutonium precipitates could to a large degree determine the behavior of those plutonium complexes in the environment.

Summary

Although not yet mature in the sense of being a routine spectroscopy, XAFS is already contributing to our understanding of environmental science and the nature of atomic structure in solids.

Its contribution will only increase as the field expands and the technique becomes standardized. Furthermore, the increased brightness of the next-generation light sources should enable x-ray beams of submicrometer dimensions within the next few years. Such a source will allow us to identify individual domains within a target sample, with significant applications to geochemistry, materials science, and bioremediation.

As discussed in numerous articles within this volume, our XAFS studies have helped us deduce the basic structure of plutonium complexes in matrices that are relevant to many areas of plutonium science. For example, our studies of plutonium in carbonate solutions have contributed to a basic understanding of the long-term viability of a nuclear-waste repository at Yucca Mountain, where carbonate waters abound. We have also studied actinide species in Hanford waste tanks and in the vitrified glass logs that are being considered for storage within Yucca Mountain. Our XAFS studies of plutonium in nitric acid solutions are important for improving our plutonium waste-treatment processes, and our investigations into the local structure of δ -phase plutonium have provided some insight into the aging of weapons-grade plutonium and the behavior of complex materials. We expect that our XAFS work will also contribute to a broader, more fundamental understanding of plutonium and the other actinides. ■

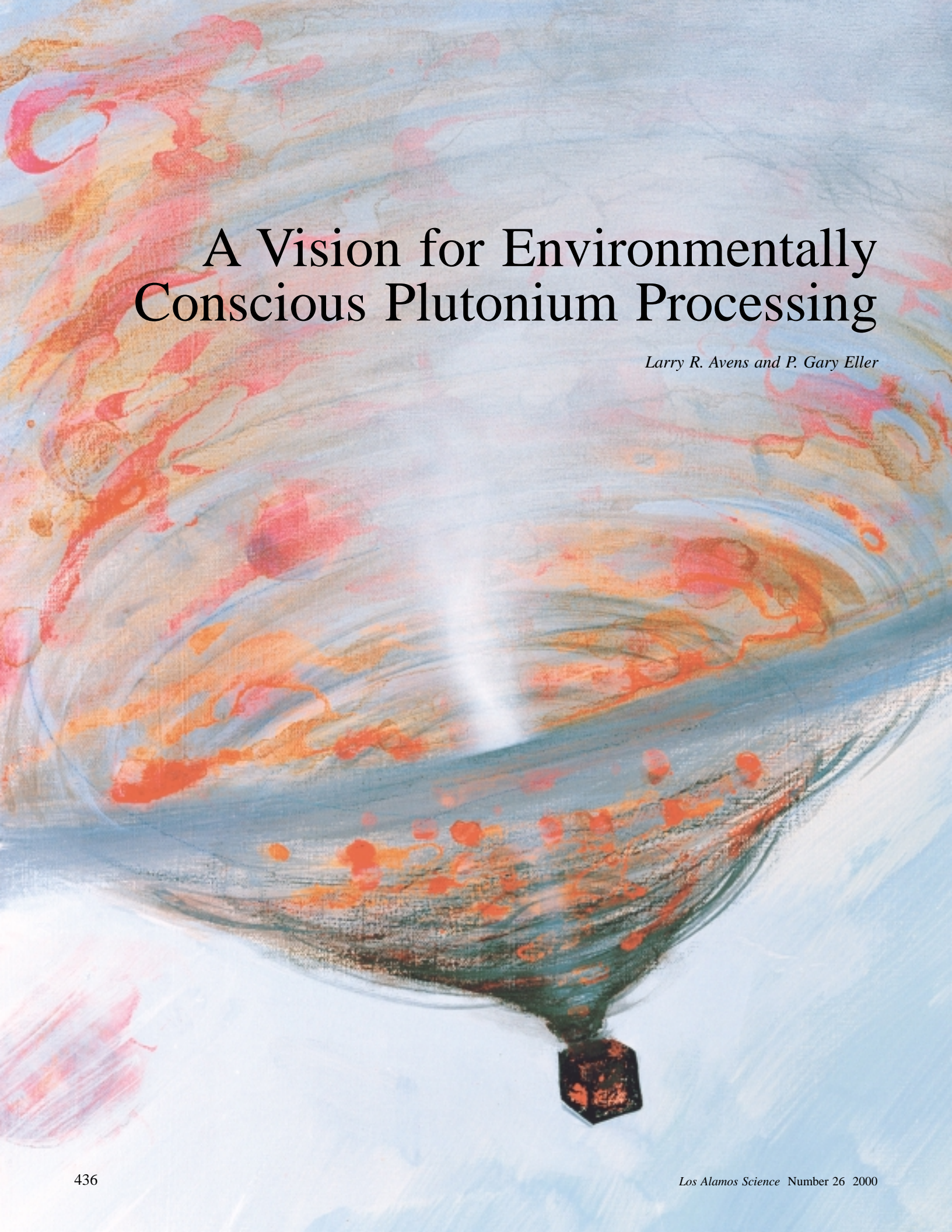
Further Reading

Conradson, S. D. 1998. *Applied Spectroscopy* **52**: 252A.

Stern, E. A. 1988. Theory of EXAFS. In *X-Ray Absorption: Principles, Applications, Techniques of EXAFS, SEXAFS and XANES*. New York: John Wiley and Sons.




Steven Conradson obtained his B.S. in chemistry from San Jose State University and his Ph.D. in physical chemistry from Stanford University, where he used XAFS spectroscopy to determine structural information about the molybdenum site in nitrogenase. He spent two years at Harvard University on a National Institutes of Health postdoctoral fellowship, performing XAFS and nuclear magnetic resonance measurements on the nitrogenase iron-molybdenum cofactor. Coming to Los Alamos as a postdoctoral fellow, he was subsequently hired as a technical staff member and is now the XAFS project leader in the Structure/Property Relations Group of the Materials Science & Technology Division. He initiated the ongoing program at the Stanford Synchrotron Radiation Laboratory for applying synchrotron x-ray methods to determine local structure and chemical speciation in radioactive samples. In collaboration with various national laboratory and university groups, he has participated in many projects involving environmental, separations, and fundamental actinide chemistry. His recent interests involve investigating nanoscale heterogeneity in both amorphous and crystalline systems as the origin of complex behavior.

An abstract watercolor painting of a hot air balloon. The balloon's envelope is filled with swirling patterns of light blue, orange, and red, suggesting a colorful sky or internal structure. The balloon is tethered to a dark, textured basket at the bottom. The background is a soft, light blue wash with some red and orange splatters, creating a dreamlike atmosphere.

A Vision for Environmentally Conscious Plutonium Processing

Larry R. Avens and P. Gary Eller



Regardless of popular or political opinions about the uses of plutonium, plutonium processing will continue globally for many decades. In the United States, plutonium plays a central role in national defense: it is routinely formed into samples for experiments, cast or machined into nuclear weapon pits, and extracted from retired nuclear weapons or weapon components and prepared for disposal. All these activities require that plutonium be chemically or mechanically processed.

An unavoidable consequence of plutonium processing is that it generates radioactively contaminated gas, liquid, and solid waste streams. Although these streams are currently handled in a manner that fully complies with today's laws, future laws will likely impose more-stringent requirements. Tellingly, President Clinton signed on Earth Day 2000 an executive order that directs federal facilities to reduce releases of

toxic compounds by 40 percent and to develop or update pollution prevention plans. Similar "green" regulations that deal explicitly with radioactive waste are not far behind.

Recent advances in actinide science and technology, however, now make it possible to drastically reduce, or even eliminate, the problematic waste streams from plutonium processing operations. Waste minimization will not only keep actinides out of the environment but also limit the amount of retrievable fissile material that must be shipped to a nuclear-waste repository (thus reducing proliferation risks). Waste minimization will also reduce the cost of current plutonium operations and ensure the viability of future ones. But most important, minimization is the morally correct waste-management action. With it, the nation can avoid saddling future generations with costly environmental and economic legacies from plutonium processing.

This article discusses the processing operations conducted at the Los Alamos Plutonium Facility and describes a number of advanced technologies that could radically reduce the operations' radioactive waste streams. Incorporating such technologies into an integrated waste-management program at Los Alamos promises to provide a "90 percent solution" to the facility's waste problem: it could reduce solid waste volume and liquid waste radioactivity by 90 percent. This program could be implemented within five years at Los Alamos and could also be implemented at other DOE sites that conduct plutonium operations. In addition, the advanced technologies could be used to treat and dispose of legacy wastes at DOE sites that must now be cleaned up, such as the Hanford Site in Washington and the Rocky Flats Environmental Technology Site in Colorado. Several of these technologies are elaborated upon in boxes that follow this article.

Plutonium Processes at TA-55

Virtually all plutonium operations at Los Alamos occur within the Plutonium Facility at Technical Area 55. It is the nation's most modern plutonium facility, consisting of a 75,000-square-foot building that is built to withstand 200-mile-per-hour tornadic winds and any credible seismic event. The facility has a back-up generator to power critical systems in case of power outages. TA-55, as the facility is commonly called, opened in 1978.

The work at TA-55 supports a wide range of national programs, such as stockpile stewardship, nuclear materials stabilization, materials disposition, and nuclear energy. Each of these programs, which are discussed briefly in the box that begins on this page, revolves around plutonium. In stockpile stewardship, for example, pure plutonium metal is used to manufacture nuclear-weapon pits or to conduct experiments related to maintenance of the nation's nuclear stockpile. The materials disposition program recovers plutonium from decommissioned weapons and processes it for eventual disposal or for burning as mixed oxide (MOX) fuel.

Almost all the plutonium at TA-55 has been recycled, having been recovered from previous TA-55 operations or from operations at other sites. But plutonium continually undergoes radioactive decay, and trace amounts of uranium, neptunium, and americium impurities accumulate in aged metal. These impurities must be removed before the material can be reused. In addition, the plutonium used for an experiment may have been alloyed, become oxidized, or been formed into a chemical compound; it too must be purified before reuse.

Thus a significant portion of the work done at TA-55 involves chemical processing to produce pure plutonium metal. Nitric acid anion exchange, or nitric acid processing, and pyrochemical processing are the two production-scale techniques that are used

Major Programs at TA-55

Stockpile Stewardship. The primary mission at TA-55 is to service the United States' nuclear stockpile. The largest task in the 21st century will be to fabricate nuclear



weapon pits for the stockpile. (The pit is a weapon's core and contains the plutonium.) We have already prepared a few pits for testing, and many operations at TA-55 are being upgraded and modified to build pits on a routine basis. In addition, under the Office of Defense Programs sponsorship, TA-55 performs surveillance activities on pits; they are dissected on a

prescribed schedule to ensure that all materials and parts will perform as intended. If a problem is identified, a remedy is developed and implemented. Furthermore, TA-55 also prepares alloys and other actinide-containing materials for many defense-related experiments. These experiments require plutonium samples that meet demanding chemical and physical specifications.



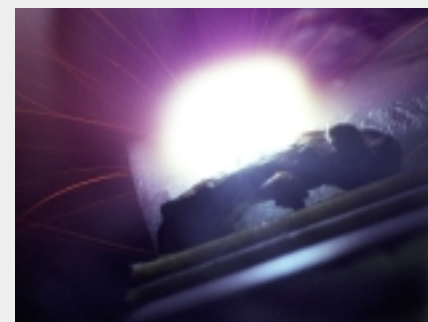
An induction furnace melts plutonium, which is then cast into pits.



A plutonium rod is being machined on a lathe.



The pressurized inert-gas metal arc welder is used for welding pits.



A laser ablates the surface of a plutonium sample. The vapor is spectroscopically analyzed to determine the chemical purity of the plutonium.

Materials Disposition. In 1993, President Clinton mandated the removal of 50 tonnes of plutonium from the defense stockpile. The plutonium, some of which is in storage, comes from retired nuclear weapons and weapon-production processing streams and is never to be used again in weapons. To support this mandate, the DOE formed the Office of Fissile Materials Disposition, whose mission is to define the path and final disposition of this excess plutonium.

As part of the disposition program, Los Alamos has developed the Advanced Recovery and Integrated Extraction System (ARIES), which will extract plutonium from pits and convert it to either a metal puck or plutonium oxide powder. In either form, the plutonium can be internationally monitored because the pits' original, classified shapes or sizes cannot be discerned. (The mass of the final product is also altered.) An outstanding attribute of ARIES is the minimal waste that is generated. Neither liquids nor solid chemicals are involved in any processing steps. A full-scale pit disassembly and conversion facility using ARIES technology is planned for construction and operation at the Savannah River Site within 10 years.

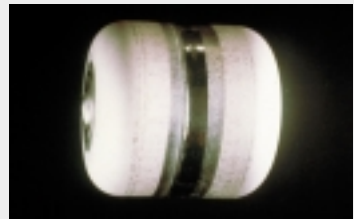
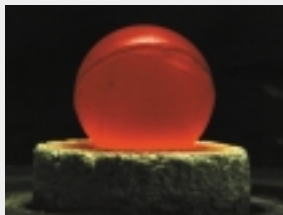
Ultimately, the excess plutonium will be either incorporated into MOX fuel for use in nuclear power reactors or immobilized in glass (vitrified) and stored in a high-level-waste repository. TA-55 prepared the first MOX fuel made from weapons plutonium. That fuel will be "burned" in Canada's Chalk River Reactor, along with equivalent fuel made from Russian weapons. Facilities to produce MOX fuel and glass waste are also planned for the Savannah River Site.

Nuclear Energy. TA-55 is also where the nation's plutonium-238 heat sources are fabricated. A 150-gram pellet of plutonium-238 dioxide has a thermal output of approximately 62 watts, and radioisotope thermoelectric generators can convert that heat energy to electrical energy. The United States has used radioisotope power and heater units in its space program for nearly 40 years, beginning with the Transit navigational satellites that were launched in 1961. Since then, plutonium-238 has provided power or heat for meteorological satellites, the Apollo Lunar Surface Experiment Packages (ALSEP), the Viking Mars lander, the Galileo deep-space probe to Jupiter, the Ulysses solar pole mission, and the Mars Pathfinder. A recent use of plutonium-238 in space is to power the Cassini probe, which was launched late in 1997 and is now on its way to Saturn. Components for these power sources undergo extensive safety testing to ensure their safe and reliable use in space.

Los Alamos is developing an aqueous recovery process to purify plutonium-238 from old heat sources and scrap oxide that are currently stored in the DOE complex. In addition, we are developing a molten-salt oxidation process to recover plutonium-238 from combustible process residues. Implementation of these technologies will reduce waste volume and enable us to recycle plutonium-238 for use in future space missions.



(Clockwise from upper left): The hydride/dehydride module in ARIES; the glove-box train for moving material between ARIES process steps; a plutonium metal puck; a decontaminated package for storing the plutonium.



(Clockwise from upper left): A 250-gram sphere of ^{238}Pu oxide with a thermal output of 100 watts; a general-purpose heat source that holds about 110 grams of ^{238}Pu and is used to fuel a radioisotope thermoelectric generator; ^{238}Pu supplies energy for the Cassini satellite.

Nuclear Materials Stabilization. A significant amount of America's excess defense plutonium is contained in chemical processing residues, metals, and oxides that were left when DOE ended weapons production in 1989. Much of this material is in a form that is inappropriate for storage or ultimate disposition. More than 65,000 items at 13 DOE sites—containing some 26 tonnes of plutonium—have been identified as posing potential hazards to workers and the environment.



In 1994, the Defense Nuclear Facilities Safety Board delivered Recommendation 94-1 to the Secretary of Energy, recommending that DOE establish a program to resolve this problem. The DOE response included establishing a research program to develop methods to safely stabilize and store plutonium metal, oxides, solutions, and residues from the Rocky Flats, Hanford, and Savannah River sites and from the Los Alamos and Livermore laboratories. A major program goal has been to minimize the creation of any further wastes.

The research program has been managed by the Laboratory's Nuclear Materials Technology Division on behalf of the DOE complex. Much of the required stabilization is now either completed or the required technologies are close to being implemented. The current objective is to ensure safe storage of the stabilized materials at Savannah River for up to 50 years, pending their ultimate disposition. Recent research demonstrated that up to four times as much material as was previously allowed can now be stored safely for 50 years.

Legacy wastes (from the top): scrap plutonium metal, a corroded plutonium-contaminated can, pieces of a magnesium oxide crucible once used for plutonium processing, and impure plutonium oxide powder inside a ceramic pestle.



Transuranic waste in interim storage at the Idaho National Environmental Engineering Laboratory. These barrels are to be shipped to WIPP.



Barrels often contain a potpourri of ordinary items, such as gloves, jars, rags, and tape, that are contaminated with plutonium and other actinides.

extensively. Nitric acid processing produces purified plutonium dioxide, which is then further processed by pyrochemical operations to produce very pure plutonium metal.

Nitric acid processing is the workhorse at TA-55, having been used over the last 20 years to process literally tons of plutonium. Pyrochemical processing was used extensively at Rocky Flats and is still used to purify plutonium at TA-55. While both processes are efficient and robust, they produce a prodigious stream of low-level and transuranic (TRU) waste.¹ There are various repositories around the country for low-level waste, including one at Los Alamos. The Waste Isolation Pilot Project (WIPP) in New Mexico is the nation's repository for defense-related TRU waste.

Several recent R&D successes at Los Alamos, however, have dramatically reduced the waste volume that results from these processes.

Nitric Acid Processing. Nitric acid is used both as a dissolution agent and a processing medium. Impure scrap plutonium or plutonium-contaminated items, such as glass, graphite casting molds, magnesium oxide crucibles, and incinerator ash, can be dissolved in or leached with nitric acid, while impure plutonium oxide can be dissolved in the acid. (Dissolving plutonium metal in nitric acid produces an unstable residue that is pyrophoric and susceptible to shock-induced explosions. Thus for processing, if the plutonium is not already an oxide, it is converted to one by burning the metal.)

During processing, the plutonium-containing nitric acid solution is passed

¹Low-level waste has less than 100 nanocuries of radioactive material per gram of waste material (nCi/g). TRU waste is contaminated with transuranic elements (elements whose atomic numbers are greater than that of uranium) at more than 100 nCi/g. (For ²³⁹Pu, this is equivalent to 1.6 µg/g.) TRU waste comes primarily from defense- and space-related programs. Other waste categories include remotely handled TRU waste, mixed wastes, and high-level waste. TA-55 produces only low-level, TRU, and mixed wastes.

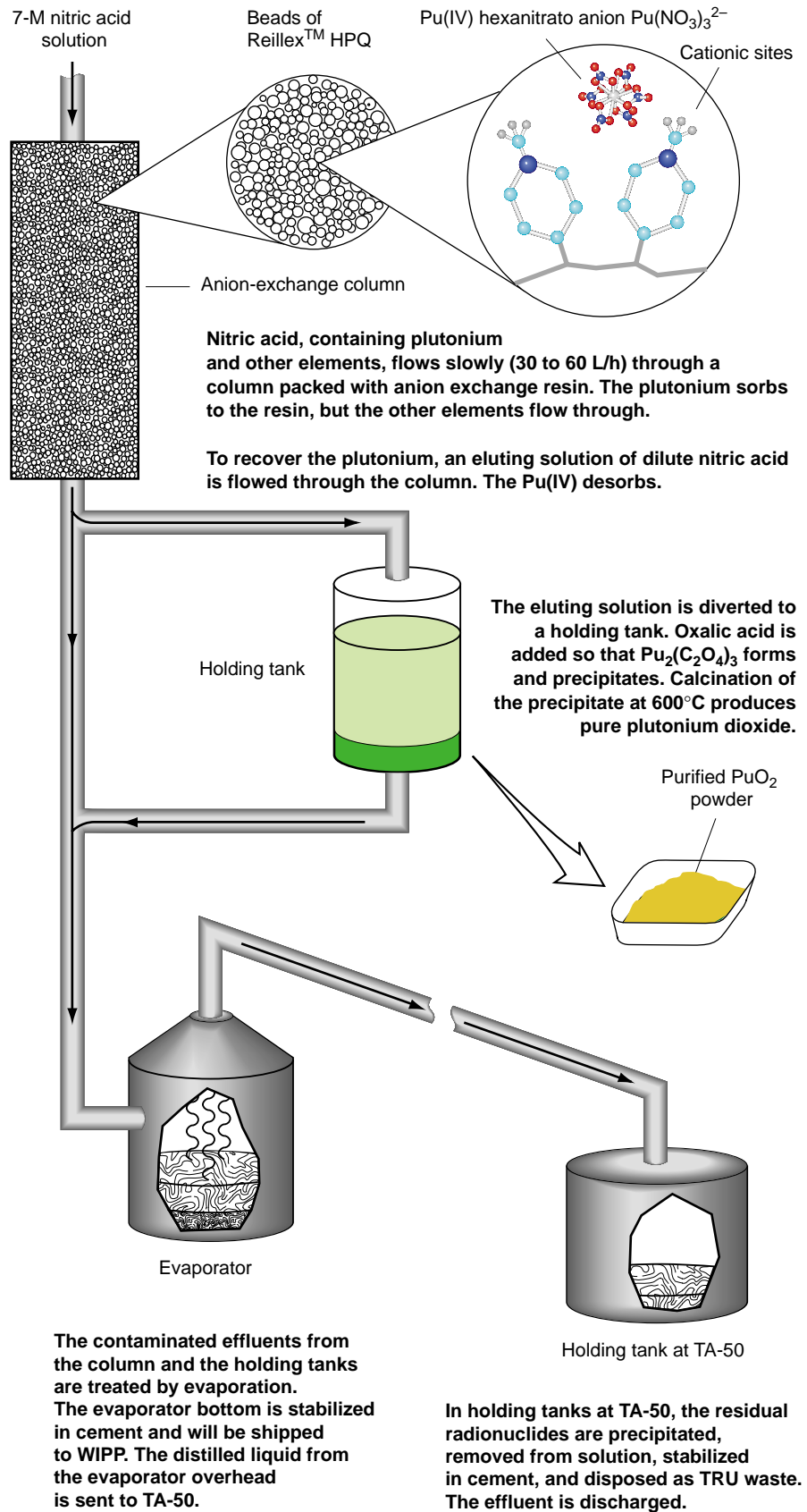
through a column packed with thousands of beads made from anion-exchange resin (Figure 1). The resin is an organic polymer that contains cationic (positively charged) sites. Anionic (negatively charged) complexes in solution bind these cationic sites and hence sorb to the resin. As it turns out, plutonium is one of only a handful of elements that can form stable anionic complexes in nitric acid; it forms plutonium hexanitrate $\text{Pu}(\text{NO}_3)_6^{2-}$. This Pu(IV) complex has the highest sorption coefficient of any metal ion to certain resins, particularly at nitric acid concentrations of about 7 molar (M). Plutonium is preferentially sorbed, while most other elements simply flow through the column and are flushed from the system.

Once the resin has been “loaded,” the plutonium is recovered by sending an eluting solution (0.5 M nitric acid plus a small amount of hydroxylamine nitrate) through the column. The Pu(IV) has little affinity for the resin in the dilute nitric acid, so it desorbs and flows with the solution into holding tanks.

Pure plutonium dioxide is recovered after precipitation and calcination steps. As with all plutonium processes, anion exchange produces contaminated waste. The resin does not remove all the plutonium from solution, and thus the nitric acid solutions always contain low levels of plutonium after they have passed through the anion-exchange process. The contaminated effluents from the column and the holding tanks are therefore sent to an evaporator. The evaporator bottoms, which contain most of the residual plutonium, other actinides, and impurity elements are stabilized in cement and disposed of as TRU waste.

The condensed vapor from the evaporator, however, is *still* radioactive, with an activity of about 6×10^{-5} curies per liter (Ci/L). This distilled liquid is piped to holding tanks at TA-50, where it is treated with a flocculating agent to precipitate all remaining actinides. With a miniscule activity of less than 3×10^{-11} Ci/L, the effluent is discharged to the environment.

Figure 1. Nitric Acid Processing System



For decades, Los Alamos has sought ways to improve the nitric acid process and reduce the hazardous components in the waste stream. For example, because some plutonium always remains sorbed to the anion-exchange resin, ultimately the resin must also be disposed of as TRU waste. In the late 1980s, Los Alamos collaborated with Reilly Industries, Inc., to develop Reillex™ HPQ resin. Compared with earlier resins, HPQ has an improved sorption for plutonium. It is less prone to radiolytic or chemical degradation in the harsh, radioactive nitric acid environment. Its enhanced stability allows the resin to be used for hundreds of plutonium recovery cycles before being replaced.

During the early 1990s, we began to use advanced spectroscopic techniques to obtain a molecular-level understanding of plutonium in nitric acid solutions. That research and a fruitful collaboration with Texas Tech University have led to the development of bifunctional exchange resins that promise to further improve the plutonium anion-exchange process. This R&D story is told by Marsh et al. on page 454.

We can do more, however, to treat the liquid-waste stream that is generated by the nitric acid process. The discharged effluent from TA-50, for example, is relatively high in nitrates. In general, these act as fertilizers in the environment and may adversely influence the local ecology. Equally disturbing is the fact that high nitrate concentrations in drinking water can lead to a health condition, methoglobinemia, in some infants younger than six months. The nitrates will be removed from the discharged liquid by a recycle evaporator, as discussed in a later section.

Pyrochemical Salt Processing.

Pyrochemical processes involving molten calcium, potassium, and sodium chlorides are used at TA-55 to prepare and purify plutonium metal. Two advantages of these methods are the compactness of their equipment and their rapid reaction kinetics.

The plutonium dioxide from nitric acid processing is converted to plutonium metal in a pyrochemical process called direct oxide reduction (DOR). As shown in Figure 2(a), plutonium dioxide and calcium metal are reacted in molten calcium chloride within a magnesium oxide crucible. The plutonium dioxide is reduced to plutonium metal, while the calcium oxide byproduct remains dissolved in the calcium chloride. The calcium oxide is then converted back to calcium chloride *in situ* by bubbling chlorine gas through the molten salt. Once the salt is regenerated, more plutonium dioxide and calcium metal can be added to the crucible to produce more plutonium metal. The DOR process can be run several times before the plutonium metal is recovered and the salt and crucible discarded as TRU waste.

The plutonium metal recovered from DOR is not very pure, however, because calcium chloride always contains trace amounts of impurities that are readily absorbed by the plutonium. The metal can be made very pure by electrorefining, which is described in Figure 2(b). Unfortunately, this pyrochemical process has a low product yield. Only about 80 percent of the original plutonium metal is purified. The remaining 20 percent—containing nearly all of the impurities—is fed back into the nitric acid and pyrochemical processing streams.

A third pyrochemical process, molten salt extraction (MSE), removes americium from aged plutonium metal. No plutonium sample is isotopically pure, but always contains a mix of isotopes, including plutonium-241. This isotope has a half-life of 13.2 years and decays by beta decay to americium-241. For many years, MSE was used at Rocky Flats to extract this ingrown americium. The aged plutonium metal was purified using liquefied sodium chloride/potassium chloride in a magnesium oxide crucible. The waste stream consisted primarily of the crucible and voluminous salt residue.

At TA-55, we have made several

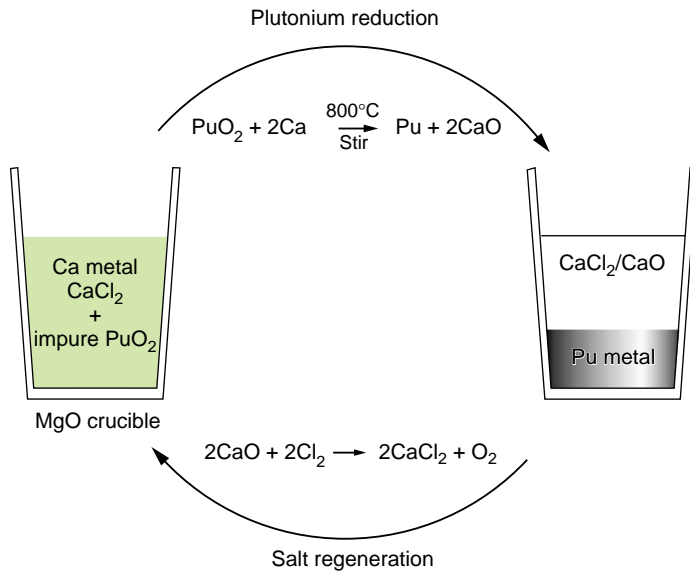
improvements to the MSE process that substantially reduce this waste stream. In our process, shown in Figure 2(c), the plutonium is reacted with chlorine gas at high temperature in a reusable tantalum crucible. This produces plutonium chloride, PuCl₃, *in situ*, which then reacts with the americium in the metal to produce americium chloride, AmCl₃. The AmCl₃ and some PuCl₃ form an easily removed salt crust on top of the purified plutonium metal.

The salt mixtures that are used in DOR and electrorefining, and that were used in the old MSE operations, become contaminated with residual plutonium and other actinides. Recovering this plutonium by nitric acid processing was problematic; the large concentration of chloride ions would combine with nitrate ions to form aqua regia, which is a volatile, highly corrosive liquid. Thus in the past, these residues were discarded as TRU waste if the plutonium content was low enough.

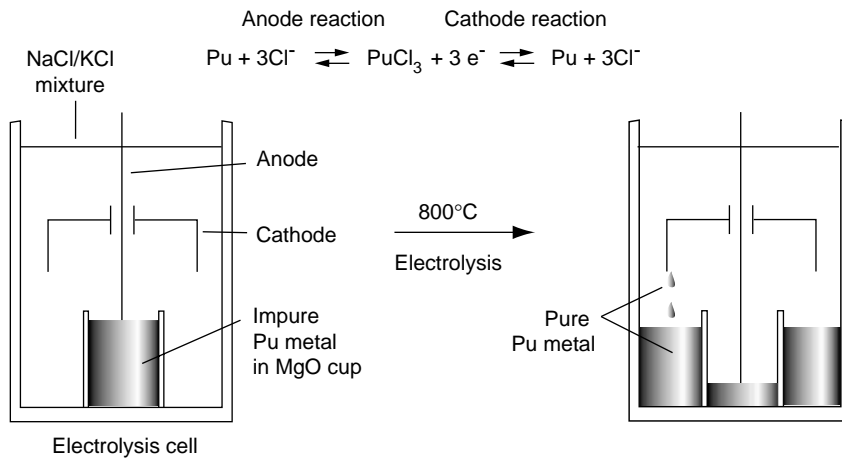
At TA-55, even this plutonium is recovered and removed from the waste stream. Instead of nitric acid, the salt or crucible residues are dissolved in hydrochloric acid (HCl). The plutonium is purified by solvent extraction, and the purified plutonium converted to plutonium dioxide powder through oxalate precipitation and calcination, similar to what is done during nitric acid processing. To treat the HCl waste solution, the effluent is made caustic, that is, it is made basic with a pH of 10 or higher. Under these conditions, the actinides precipitate and can be removed by simple filtration. At this point, the caustic liquid waste has an activity of about 10⁻³ Ci/L and is sent to TA-50 for further treatment. However, an extraction chromatography process is being developed to replace the caustic precipitation/filtration processes.

As a result of recent R&D work, the technology is now available to vacuum distill sodium and potassium chloride salts at elevated temperature. Distillation directly separates the plutonium residue from the bulk salt without the use of an aqueous process. (Given its

(a) Direct Oxide Reduction (DOR)



(b) Electrorefining (ER)



(c) Molten Salt Extraction (MSE)

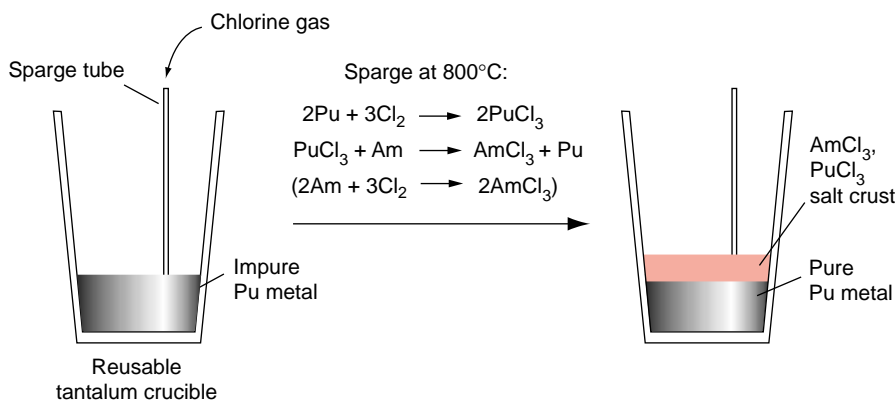


Figure 2. Current Pyrochemical Salt Processes

(a) DOR reduces plutonium dioxide (often obtained from nitric acid processing) to plutonium metal. The plutonium dioxide is combined with calcium metal and calcium chloride, and the mixture is liquefied. The plutonium dioxide is reduced to plutonium metal, producing calcium oxide. The calcium oxide is then converted back to calcium chloride by bubbling chlorine gas through the liquefied salt product. This conversion step allows us to reuse the salt and the crucible. More plutonium dioxide and calcium metal are added to the crucible, and the process can be run several times before the plutonium metal is recovered and the salt and crucible are discarded.

(b) Metal from DOR is purified by electrorefining. The impure plutonium metal is placed in a MgO cup inside an electrolysis cell, which is filled with a NaCl/KCl salt mixture. The cell is heated to 800°C to melt the contents and to begin electrolysis. The plutonium metal is oxidized to plutonium chloride, PuCl₃, which dissolves in the molten salt. The PuCl₃ migrates to the cathode, where it is reduced to pure plutonium metal. This drips from the cathode and collects in the annular region outside the cup. A ring of pure plutonium is produced within a few days. About 20% of the original plutonium stays in the cup and contains essentially all of the initial impurities.

(c) MSE is used to remove americium from aged plutonium. The plutonium metal is liquefied in a reusable tantalum crucible and then chlorine gas is bubbled (sparged) through the liquid. Plutonium chloride forms, which is reduced to plutonium metal as the americium oxidizes to americium chloride. (The americium is also oxidized directly to americium chloride, but at a much slower rate than the corresponding plutonium reaction.) Upon cooling, americium chloride and some plutonium chloride form a thin crust on top of the plutonium metal.

Table I. Approximate Annual Solid Waste at TA-55

Category	Volume (m ³)	Mass (kg)	55-Gallon Drums
TRU Waste			
Combustible	22	2600	100
Metal	31	14600	84
Cement	13	18000	65
Filters, glass, graphite	5	1000	24
Leaded gloves	3	2500	13
Low-level Waste	200 to 500		

Table II. Approximate Annual Liquid Waste at TA-55

Category	Volume (L)	Activity Limit (Ci/L)	Total Activity (Ci)
Caustic	10,000	4.5×10^{-3}	< 45
Acid	50,000	6×10^{-5}	< 3
Industrial	730,000	5×10^{-7}	< 0.4

low volatility, the calcium chloride used to reduce plutonium in DOR is not amenable to distillation.) As described in the box on “Salt Distillation” on page 449, salt distillate with contamination levels below low-level-waste thresholds has been achieved in small-scale tests. When this process is deployed for full-scale use at TA-55, the salt will be either discarded as low-level waste (at a fraction of its current disposal cost as TRU waste) or will be recycled into pyrochemical operations.

Waste Generation at TA-55

Nitric acid and pyrochemical processing produce radioactive waste in the form of contaminated reagents and processing equipment. But routine execution of the programs discussed on pages 438–440 also produces low-level and TRU waste because nearly everything associated with manipulating plutonium becomes contaminated. The air that passes through the stainless

steel glove boxes, for example, must be filtered through high-efficiency particulate air (HEPA) filters, which then become contaminated with plutonium. Any tools used within a glove box become contaminated, as do the glove boxes themselves and their lead-lined gloves. The towels used to wipe down equipment, the plastic containers used to hold parts or tools, the bottles, tubing, and tape—all become contaminated through use.

Table I lists the approximate annual quantities of solid waste generated at TA-55 during the 1990s. Over this period, nearly 40,000 kilograms of solid TRU waste was generated each year. Metal items and cement (which stabilizes evaporator bottoms) account for all but a fraction of the waste mass, and in terms of volume, represent about 60 percent of the waste. Combustibles, such as plastics, rags, rubber, and organic liquids, account for nearly 30 percent of the volume. The solid TRU and low-level wastes are stored at Los Alamos’ TA-54. The low-level wastes

are buried on-site, while the TRU wastes are stored until they can be shipped to WIPP in southern New Mexico.

Table II lists the approximate annual output of liquid waste. While the volume is dominated by industrial liquid waste, the total amount of radioactive material in this category is substantially less than a curie. Rather, the small volume of caustic liquid waste from hydrochloric processing contains about 90 percent of the radionuclides in the liquid-waste stream.

The 90 Percent Solution: Integrated Waste Management

We have already developed or are currently investigating new technologies, such as hydrothermal processing, enhanced pyrolysis, and electrochemical decontamination, that can drastically reduce our combustible and metallic waste volumes. These technologies are robust, can treat a variety of waste matrices, and produce minimal secondary wastes. In most cases, the equipment used by these technologies is compact enough to fit into existing glove-box systems or facilities without major modifications. We are looking to Polymer FiltrationTM and nitric acid recycle to clean up our radioactive liquid-waste streams.

By integrating these new technologies into a comprehensive waste-management program, we expect to achieve three near-term goals. The first is to decontaminate more than 90 percent of all metallic TRU waste to low-level waste by 2002. Second, we want to reduce the radionuclide content of all liquid effluent produced at TA-55 to the industrial waste limit by 2003. This would reduce by nearly 90 percent the activity of the liquid waste leaving the facility. Third, by 2004, we want to reduce the volume of combustible and noncombustible waste by more than 90 percent. In addition, we plan to vitrify, or encase in glass, the TRU-waste evaporator bottoms rather than stabilize them in cement. Because the glass can

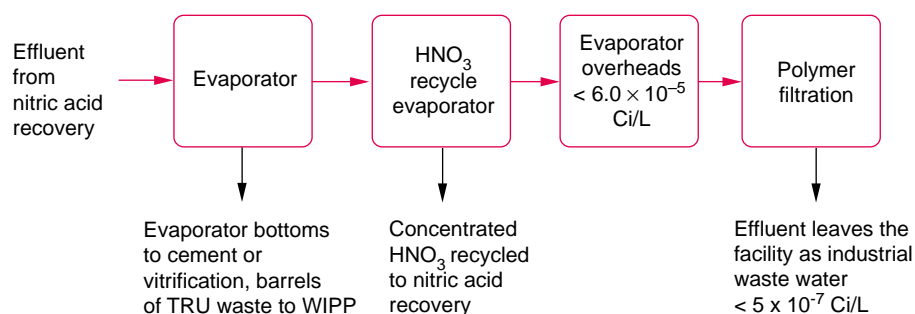


Figure 4. Flow Chart for Advanced Treatment of Liquid Wastes

Two technologies will be employed to clean up the liquid waste stream from nitric acid processing. A second evaporator will recycle the nitric acid and prevent nitrates from leaving the facility. Polymer Filtration™ will capture residual plutonium and other actinides from the recycle evaporator’s condensed vapor, so that the radioactive content of the filtration effluent will be reduced to discharge limits for industrial waste water before the effluent is sent to TA-50.

agent. Under hydrothermal conditions, reactions are extremely fast, almost completely destroying the organic matrices in seconds. The box on “Hydrothermal Processing” on page 450 provides more information about this technology.

Enhanced pyrolysis substantially decomposes solid polymeric materials (e.g., polystyrene, polyethylene, and polypropylene). A fully engineered system consists of a pyrolysis step, in which the materials are decomposed into a variety of liquid- and gas-phase constituents, followed by a catalytic conversion step that treats the off gases and liquids by oxidizing them to simple products. The integrated system provides greater than 99 percent conversion of the polystyrene to carbon, water, carbon dioxide, and a small amount of stabilized actinide material. Tests have shown that polyethylene, cellulose, and other organic polymers are equally amenable to this treatment. A fully engineered unit for processing small quantities of polystyrene and cellulose is already installed in a TA-55 glove box. More information on this technology is given in the box on “Enhanced Pyrolysis” on page 451.

In molten salt oxidation, the contaminated waste is oxidized by air in a molten sodium/potassium carbonate

bath. The residual actinides can be recovered from the sodium/potassium carbonate mixture, or the carbonate salt containing the plutonium can be discarded. At TA-55, we plan to use this technology to recover plutonium-238 from combustible process residues. Its implementation will reduce waste volumes and enable us to recycle plutonium-238 for use as a heat or power source in future space missions.

Although not shown in Figure 3, another technology being developed is mediated electrochemical oxidation, which can quickly decompose certain combustible mixed waste, including cation exchange resins, solvents, and plastic bottles. In contrast to hydrothermal processing, this oxidation process operates at low temperature and ambient pressure. In the process, a powerful oxidizing agent, such as Ag(II), is generated electrochemically at the anode of a divided electrochemical cell. When the anolyte solution comes into contact with the waste, its radioactive component is dissolved through reaction with the oxidizing agent. (The insoluble plutonium dioxide is oxidized to the soluble plutonyl ion PuO_2^{2+} .) The organic matrix components can also be oxidized to carbon dioxide by reaction with the oxidizing agent. With water serving as an oxygen donor to

complete the reaction, the oxidizing agent is reduced to its original state. The solution is then recycled to the electrochemical cell to regenerate the oxidizing agent, and the process is continued. Because of the cyclic nature of the process, only a small amount of oxidizing agent is required to treat a large amount of combustible waste.

Treatment of Liquid Wastes. Research into plutonium complexes in nitric acid has allowed us to design water-soluble molecules that are being deployed in TA-55 for ultrapurifying liquid waste streams. The polymers capture plutonium and other actinides and then are removed from solution by filtration. This technology, developed at Los Alamos and licensed by Polyionics Separation Technologies, Inc., is known as Polymer Filtration™. It is described in the box on page 452.

All liquid that emerges from the treatment of combustible wastes will be treated by Polymer Filtration™, as will the effluent from nitric acid processing. (See Figure 4.) The aqueous liquids that emerge from Polymer Filtration™ will be discharged as industrial waste water. The small volume of polymer that is filtered from solution will be disposed as TRU waste.

Figure 4 also shows that nitric acid recycle technology will be added to the evaporator system at the tail end of the nitric acid processing. Essentially all of the nitric acid will be recycled back to plutonium-recovery processing, and nitrates will no longer leave TA-50.

Treatment of Metallic Wastes.

Table I reveals that metal constitutes a substantial fraction of the solid waste generated annually at TA-55. This waste consists primarily of discarded stainless steel glove boxes, but it also includes other items such as storage cans and tools. These TRU-waste items can be decontaminated to low-level waste by a process known as electrochemical decontamination. This process uses electrolysis to remove a microscopic layer from metallic surfaces that contains most

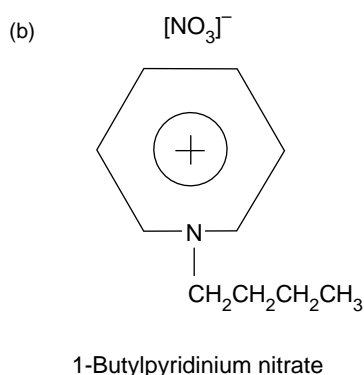
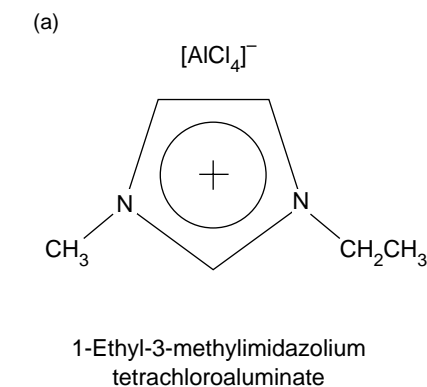
of the contamination. A filter then removes actinides from the electrolyte solution so that the latter can be recycled or discarded. The small volume of recovered contaminants is added to processing streams for further treatment or discarded as TRU waste. More information about electrochemical decontamination is given in the box about it on page 453.

Beyond the 90 Percent Solution

Almost all of the advanced waste treatment and minimization technologies discussed above can or will be implemented at TA-55 over the next three to four years. Integration of those technologies will enable the facility to reduce solid waste volumes and liquid waste activity by 90 percent. However, we will achieve an even higher level of environmental and operational excellence if we can reduce both solid and liquid radioactive waste discharges to near zero.

We can never eliminate TRU waste totally because the very function of much of TA-55's plutonium processing is to remove unavoidable TRU impurities (such as the americium that results from the radioactive decay of plutonium-241). However, the prospects are excellent for eliminating the largest remaining waste stream—the huge volume of industrial waste water that is discharged following Polymer Filtration™—by recycling it into plutonium recovery operations. All process-water discharges from plutonium operations could be eliminated in any next-generation plutonium facility.

Obviously, the most effective strategy for reducing radioactive waste is to avoid its generation. Achieving such a goal will require breakthrough, not incremental, technologies. One possibility is the use of room-temperature ionic liquids (RTILs), which are a new class of solvents. The unique chemical and physical properties of these liquids can augment traditional plutonium pyrochemical processes and possibly



eliminate their waste streams.

RTILs are composed of bulky, low-valent organic cations and inorganic anions (Figure 5). Because the ions are very large and have low charge, they interact only weakly and thus remain liquid at room temperature rather than condensing into well-ordered crystalline solids. Some desirable physical properties of these ionic liquids are high conductivity, low vapor pressure, and the ability to dissolve both organic and inorganic compounds. In addition, the ionic liquids' acidity can be adjusted.

The capabilities of RTILs, coupled with the lack of interference from hydrolysis reactions, create a unique opportunity to obtain detailed information on the fundamental chemical behavior of actinide compounds under conditions far less demanding than those found in pyrochemical processes. Thus, their use could lead to a greater understanding of actinide chemistry that would allow creation of next-generation

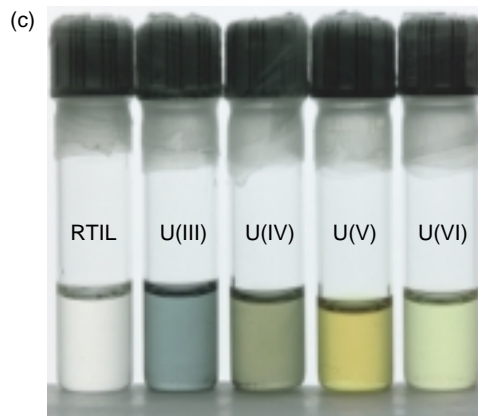


Figure 5. Room-Temperature Ionic Liquids

Room-temperature ionic liquids (RTILs) are being investigated as a novel processing medium for actinides. The molecular structure of an RTIL consists of a relatively large cation and anion, as seen in (a) and (b) for two prototypical systems. The leftmost vial in (c) contains the RTIL diagramed in (a). The remaining four vials contain uranium ions that were prepared electrochemically in different oxidation states. The colors arise because of the different oxidation states.

separation and purification processes.

The chemistry of plutonium in RTIL systems is currently being examined. This work has already demonstrated the stability of the Pu(III) and Pu(IV) oxidation states in chloride-rich RTIL solutions. We believe that continued RTIL work will yield valuable thermodynamic data that will help improve high-temperature pyrochemical processes. Further, the ability to fine-tune the properties of RTIL solvents holds the promise of room-temperature electrochemical techniques for purifying and recovering plutonium.

Another promising advance lies in the organometallic chemistry of the actinides. This area of research stems from the discovery that certain actinides (An)—uranium, neptunium, and plutonium—dissolve in ether/iodine mixtures. The resulting $AnI_3(THF)$ complexes, where THF is tetrahydrofuran, can be used to prepare myriad new compounds and complexes.

For example, one organometallic compound of interest is $\text{Pu}(\text{C}_8\text{H}_8)_2$, because it is reported to be diamagnetic. If this claim is confirmed, then we should be able to observe plutonium-239 by analyzing the compound with nuclear magnetic resonance (NMR). (To date, the plutonium-239 nucleus has not been observed by NMR.) If we can use NMR to analyze $\text{Pu}(\text{C}_8\text{H}_8)_2$, we will have a new opportunity to study covalent bonding in plutonium.

Another new compound—one that is potentially more relevant for process operations—is $\text{Pu}[\text{N}(\text{SiMe}_3)_2]_3$, where Me is a methyl group. This compound sublimates at approximately 50°C. Because of its high vapor pressure, we could use it to develop a chemical processing scheme based on organometallic chemistry. For example, we could dissolve impure plutonium metal in an iodine/THF mixture, use the $\text{PuI}_3(\text{THF})$ to prepare the volatile $\text{Pu}[\text{N}(\text{SiMe}_3)_2]_3$ complex, and then purify the $\text{Pu}[\text{N}(\text{SiMe}_3)_2]_3$ by sublimation. One advantage of such a process is that the plutonium would be dissolved without releasing potentially explosive hydrogen gas. Another is that because the plutonium is purified by sublimation—a physical separation process—all reagents could be recycled or destroyed. However, the most exciting use of $\text{Pu}[\text{N}(\text{SiMe}_3)_2]_3$ would be in a chemical vapor deposition (CVD) process that could deposit plutonium metal in any shape or thickness. Deposition could potentially eliminate waste-intensive plutonium casting and machining operations.

While we can prepare batches of $\text{Pu}[\text{N}(\text{SiMe}_3)_2]_3$, there are many challenges that must be resolved before we can use this compound in a processing scheme. Phase stability in plutonium metal is very sensitive to the amount of carbon present. During the deposition process, carbon from the methyl groups in $\text{Pu}[\text{N}(\text{SiMe}_3)_2]_3$ could be absorbed by the plutonium metal. One of the challenges of plutonium CVD will be to develop the process to the point that the final plutonium product contains lit-

tle carbon. Furthermore, plutonium for most uses is normally alloyed, and preparing a plutonium alloy with CVD could be difficult. But the rewards of using novel organometallic compounds for processing—safer procedures, minimal residual waste, and minimal need for purification—are sufficient to accept such challenges.

Summary

When integrated into a unified waste minimization program at TA-55, the advanced technologies we have described promise to radically reduce the radioactivity of our liquid waste streams and reduce the volume of our TRU solid wastes by 90 percent or more. Our ultimate goal, however, is to exceed even this 90 percent solution by engineering a next-generation plutonium facility that discharges close to zero radioactive waste. Such a feat would require that we eliminate the huge volume of industrial waste-water from leaving the building. A new plutonium facility may be built at Los Alamos as early as 2008 and its construction would present an ideal opportunity to implement the new technologies that should help us reach our near-zero-discharge goal. To reduce the TRU-solid waste from plutonium processes to near zero is a more daunting challenge, but we continue to conduct the R&D that we hope will one day produce the needed breakthrough technologies. ■

Further Reading

- Cleveland, J. M. 1979. *The Chemistry of Plutonium*. La Grange Park, IL: American Nuclear Society.
- Katz, J. J., G. T. Seaborg, and L. R. Morss, eds. 1986. *The Chemistry of the Actinide Elements*. Vol. I and II, London: Chapman and Hall.

Larry Avens received his B.S. degree in chemistry from Tennessee Tech University and his Ph.D. in inorganic chemistry from Texas Tech University.



After graduate school he moved directly to the Los Alamos National Laboratory. Plutonium chemical processing and separation science R&D have been Avens' areas of interest. He has four patents and numerous publications in the area. He

has also served on review teams associated with all areas of actinide science.

Gary Eller received an B.S. in chemistry from West Virginia University and a Ph. D. in inorganic chemistry from Ohio State University.



After a postdoctoral appointment at Georgia Tech, he moved to Los Alamos and has held positions as post doctoral fellow, staff member, line manager, and project leader. From 1994–1996 he served as a technical advisor to DOE-Hanford in the

high-level waste tanks program and since then has had a leadership role in the national program to stabilize and safely store excess plutonium-bearing materials for up to 50 years. His current technical interests are in the area of actinide, environmental, and fluorine chemistry and the development of scientific information through deployment to solve practical problems in the field.

Salt Distillation

Eduardo Garcia, Vonda R. Dole, James A. McNeese, and Walter J. Griego

The basis for a vacuum distillation separation is the large difference in vapor pressure between chloride salts and actinide oxides. Contaminated salts are heated in a furnace under high vacuum. The salts vaporize and leave the furnace, while the non-volatile plutonium compounds remain behind. The salt is recovered by allowing the vapor to strike a cold plate, where it condenses.

Because the vapor pressures of the various residue components are known, we can calculate the rate of deposition and the remaining plutonium concentration in distilled salts. The results are shown in Table I for a distillation process carried out at 850°C. Measured deposition rates have been found to be slower than these calculated values—sometimes by orders of magnitude. Nevertheless, experiments have shown that below 900°C, all of the chloride salts except calcium chloride can be distilled at acceptable completeness and rates. Column 2 in the table reveals that the best separation can be achieved between plutonium dioxide and the chloride salts. Efficient separation will not be obtained if plutonium trichloride, PuCl₃, is present in the system. But the residual salts can be pretreated by an oxidation process that will convert all plutonium species to plutonium dioxide, thereby eliminating this separation problem.

The calculated plutonium concentrations in the distilled salts (column 3) represent low theoretical limits. In practice, it has been found that plutonium contamination levels of distilled salts are determined by contamination in the glove-box environment in which the process is carried out. The product contamination levels are on the order of several parts per million (ppm).

Table I. Calculated Deposition Rates and Distillate Plutonium Concentrations for Salt Residue Constituents at 850°C

Compound	Log of Vapor Pressure (torr)	Calculated Deposition Rate (g hr ⁻¹ × 100 cm ²)	Calculated Pu Concentration (ppm)
NaCl	-0.063	4100	5.3 × 10 ⁻¹⁰
KCl	0.23	9100	2.4 × 10 ⁻¹⁰
MgCl ₂	0.27	11000	1.9 × 10 ⁻¹⁰
CaCl ₂	-2.9	9	2.4 × 10 ⁻⁷
Pu	-8	1 × 10 ^{-3.7}	
PuO ₂	-15.7	1 × 10 ⁻¹²	
PuCl ₃	-1.8	178	
PuOCl	-8	1 × 10 ^{-3.7}	



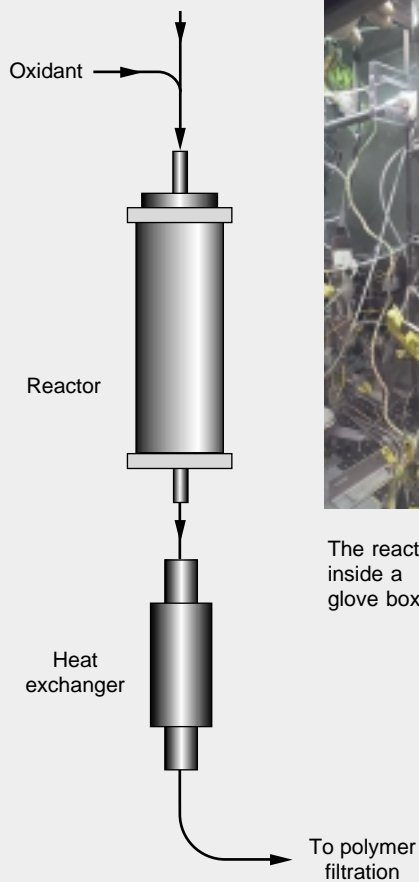
The salt distillation process will separate residual plutonium from pyrochemical chloride salt residues. The products from a test run are shown in the photograph. The large volume of recyclable chloride salt distillate stands next to the tray containing the small volume of nonvolatile actinides. The TRU waste volume reduction is greater than 95 percent.

Hydrothermal Processing

Laura A. Worl, Steven J. Buelow, and Dennis D. Padilla



Organic mixture



The reactor inside a glove box

Hydrothermal processing (reactions in hot water) offers the ability to destroy radioactive combustible wastes and is a viable alternative to incineration or costly storage options. For aqueous/organic mixtures, pure organic liquids, or contaminated combustible solids such as ion exchange resins, plastics, and rags, hydrothermal processing destroys more than 99.9 percent of the organic and nitrate components and facilitates the collection and separation of the actinides. The volume of TRU and mixed waste can be reduced by a factor of 100. The actual volume reduction depends on the type of waste being destroyed.

A schematic of a laboratory-scale process unit is shown in the Figure. The combustible waste is mixed with an oxidant (oxygen, air, or hydrogen peroxide) in water at pressures and temperatures above the critical point of water (374°C and 22.1 MPa). Under these conditions, water is a fluid with density high enough that reasonable process throughput can be achieved, but with transport properties like those of a gas, allowing rapid chemical reactions. Supercritical water is a unique solvent medium in which oxidation can take place at lower temperatures than those of incineration, thus limiting the production of NO_x and ash. Organic components are essentially completely oxidized to carbon dioxide and water by reaction with the supercritical water and oxidant. Chlorine-, sulfur-, and phosphorus-containing constituents are oxidized and converted to acids or salts, depending on the final pH of the product solution. At temperatures above 500°C, reactions are rapid and greater than 99 percent conversion is achieved in seconds.

The reaction is carried out entirely in an enclosed pressure vessel (the reactor) containing dilute reactants, so that the heat of reaction is absorbed by the solvent. The temperature within the reactor can be maintained at any desired level, typically in the range of 400 to 650°C. After about one minute of reaction, the mixture is cooled in a heat exchanger and depressurized. Any insoluble particles can be readily separated by a simple filtration step from the aqueous effluent. The effluent itself is further treated by polymer filtration for reuse or discharged as industrial waste.

We have conducted several experiment series using different waste matrices. In one series, actinide-contaminated organic mixtures reacted in 30 wt % H₂O₂. The total organic concentrations at the inlet of the pressure vessel were between 1800 and 25000 mg/L, depending on the organic mixture. Under these conditions, the residual organic content was below 20 mg/L and in most cases below 5 mg/L. From these tests, the organic destruction efficiencies were greater than 99.9%. Experiments also were conducted with ion-exchange resins, including Reillex HPQ resin. For these experiments, the resin was mixed with water and a small amount of sodium salt of carboxymethyl cellulose, which is a viscosity enhancing agent that improves the pumping characteristics of the mixtures. The viscosity of the mixture is high and the resin beads do not settle out in a 24-hour period. After one minute, the reaction produced carbon dioxide, water, nitrogen, and hydrochloric acid. The levels of the total organic carbon were reduced to near our detection limits of about 6 mg/L.

A "hot" unit and a "cold" pilot unit have provided operational data for a full-scale unit that is expected to be in operation in 2001.

Hydrothermal processing will decompose plutonium-contaminated organic waste, such as contained in the bottle, into simple organic products such as CO₂ and water. Any insoluble actinide-containing material is removed by filtration, while actinides in solution are removed by polymer filtration.

Enhanced Pyrolysis for Converting Polystyrene or Cellulose Polymers

Daniel J. Kathios

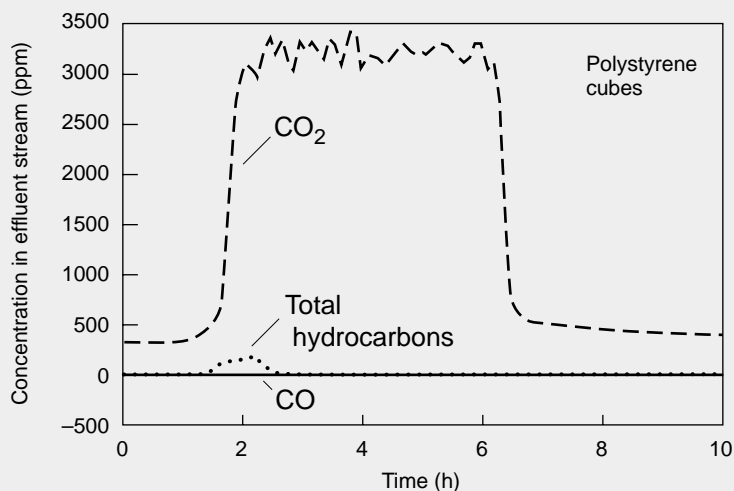
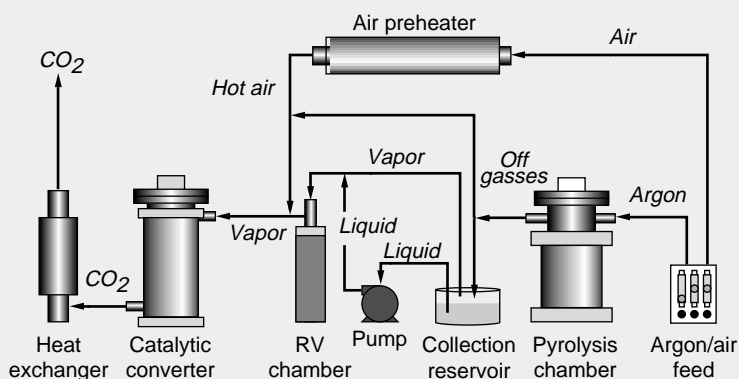
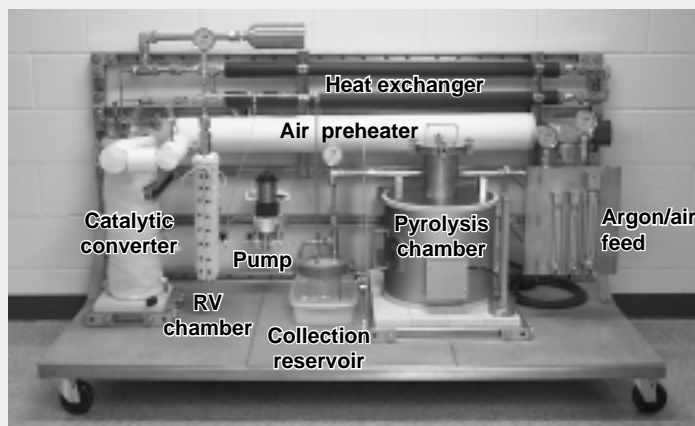
Enhanced pyrolysis results in substantial decomposition of solid polymeric materials. This technology was a direct outgrowth of 94-1 Research and Development, a part of which tasked TA-55 researchers to develop a non-incineration method for stabilizing almost two thousand plutonium- and uranium-impregnated polystyrene cubes ("polycubes") that are stored at the Hanford Site. The polycubes were manufactured during the early part of the Cold War for criticality studies. They now represent a legacy material that must be processed.

TA-55 personnel developed a system that converted more than 99 percent of the polycubes to carbon, carbon dioxide, and water, leaving behind a small mass of stable actinide material. Success of the pyrolysis system with polycubes made the potential application to TA-55 combustibles readily apparent.

As seen in the photo, the prototype system consists of a pyrolysis (burning) chamber, a revaporization (RV) chamber, and a catalytic converter. The pyrolysis chamber is charged with polystyrene or cellulose combustible material and heated to 750°C in a flowing atmosphere of argon. The high temperature decomposes organic polymers into numerous liquid and gaseous constituents. A collection reservoir accumulates the liquid byproducts while volatile gases proceed directly to the RV chamber. A pump injects the collected liquids at a controlled rate into the gas stream in the RV chamber. The liquid constituents enter the gas phase, and the combined gas fractions are injected into the catalytic converter, where they are oxidized primarily to CO₂.

The totality of the polystyrene or cellulose conversion process is evident from the graph, which shows the composition of the effluent stream that leaves the catalytic converter. Actinide-impregnated polystyrene cubes are converted to carbon, CO₂, water, and a small amount of actinide-containing residue with greater than 99 percent efficiency. The process efficiency is greater than 93 percent for cellulose materials.

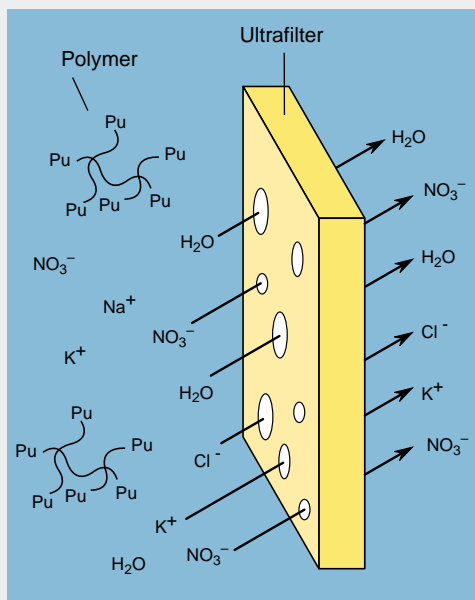
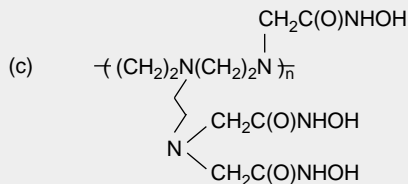
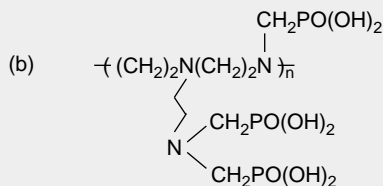
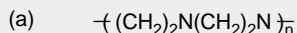
The system is controlled and monitored by computer, which improves the safety envelope of the process. The complete unit is also ergonomically friendly and requires minimal maintenance, so workers are at a reduced risk for exposure to radiation or caustic byproducts. Two identical systems are to be shipped to Hanford Site, while a third system is already installed in a glove box at TA-55.



An enhanced pyrolysis (burning) system, shown above, can convert polystyrene waste matrices to carbon, carbon dioxide, and water with greater than 99% efficiency. The graph shows the constituents of the effluent stream for polystyrene cubes. A system designed for cellulose has a process efficiency greater than 93%.

Treatment of Liquid Wastes

Gordon D. Jarvinen, Geraldine M. Purdy, Barbara F. Smith, and Thomas C. Robinson



The Polymer Filtration™ process uses water-soluble polymers to separate and concentrate tiny amounts of actinides from the bulk of the solution. The structural formula of the polyethyleneimine polymer is shown in (a), while (b) and (c) show the polymer functionalized with three phosphonic acid groups and three hydroxamic acid groups, respectively. The diagram illustrates a water-soluble polymer with bound plutonium ions that is too large to pass through an ultrafiltration membrane. Water and small ions, driven by a modest pressure gradient of 10–50 psi, pass through the membrane.

Polymer Filtration™ is a technology that can remove essentially all of the residual plutonium, americium, and other regulated metal ions from various liquid process and waste streams, including TA-55's liquid effluent.

The technology uses water-soluble polymers that selectively bind with target metal ions in aqueous solutions. Interactions between the metal ions and the binding groups on the polymer occurs homogeneously in solution. Reactions usually are faster compared to those that take place between ions and solid polymeric materials such as anion-exchange resins. In addition, water-soluble polymers can have much higher binding capacity for metal ions relative to the solid polymers because nearly all of the metal-binding groups are available in soluble polymers. (In the solid resins, some of the binding sites cannot contact the solution because they are "buried" in the solid structure.)

The water-soluble polymers have a sufficiently large molecular weight that they can be separated and concentrated from the bulk of the solution with an ultrafilter. (The ultrafiltration range is generally considered to include molecular weights from several thousand to several million daltons and particle sizes of about 2 to 1000 nanometers.) Water and the smaller unbound components of the solution pass freely through the ultrafiltration membrane (see figure). In the process, contaminants are highly concentrated in a small volume from a much larger bulk volume. The small volume of contaminated solution containing the polymer/metal ion complexes can be solidified for disposal. Alternatively, the polymer can be recycled for further metal-ion recovery. When polymer recycle is required, the uncomplexed polymers are regenerated by changing the solution conditions to release the bound metal ions. A small volume of rinse water is used in another ultrafiltration step to recover the released metal ions in concentrated form for reuse or disposal.

In many of the liquid waste streams to be addressed, the target actinide ion is present in very low concentration relative to innocuous metal ions such as sodium, potassium, calcium, and magnesium. Phosphonic acid, acylpyrazolone, hydroxamic acid, and iminocarboxylic acid groups have a demonstrated affinity for higher-valence actinide ions relative to lower-valent metal ions. Therefore, our water-soluble polymers have employed these functional groups in our investigations. In testing to date, phosphonic acid derivatives have shown the best properties for removing plutonium and americium from process and waste solutions. The pilot-scale tests yield reductions in target metal-ion concentration of 10^4 to 10^6 .

A Polymer Filtration™ unit will be installed in the new plutonium-238 Scrap Recovery glove-box line that will be operational in 2001. Demonstration runs also are underway to use Polymer Filtration™ to remove soluble actinides from aqueous chloride process streams at TA-55.

Polymer Filtration™ is a trademark of Polyionics Separation Technologies, Inc.

Electrochemical Decontamination of Metallic Wastes

Douglas E. Wedman and Jerry L. Lugo

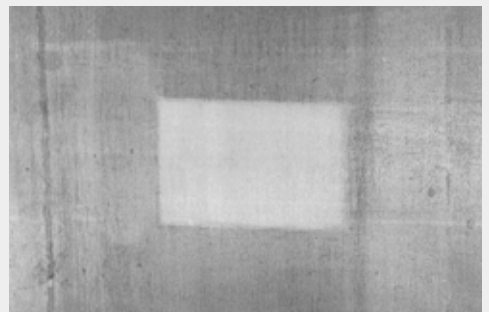
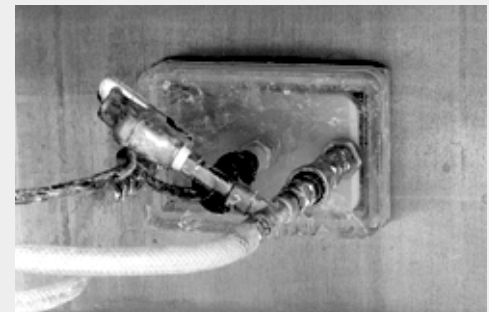
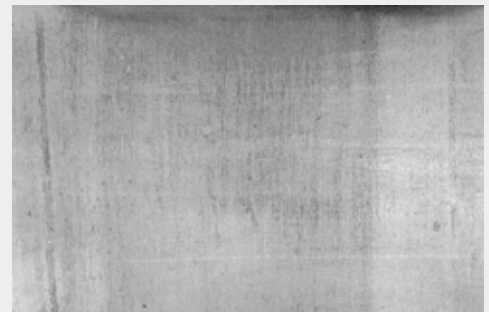
Currently, metal items such as glove boxes, tools, special nuclear material storage containers, etc. make up a significant fraction of TA-55's TRU solid waste volume. Research and development at TA-55 has led to a technique that decontaminates metal surfaces by electrochemically etching away atomic layers of the base metal. The cleaned metal can then be disposed as low-level waste.

In concept, the technique is similar to the industrial techniques of electropolishing and electrolytic cleaning. In electropolishing, the metal to be polished is made the anode (positive electrode) of an electrolytic cell. As current flows through this cell, a relatively thick viscous layer of reaction products from dissolution of the metal surface is generated. Diffusion of the dissolved metal ions through this film becomes rate limited, resulting in a microscopic smoothing of surface features. In contrast to electropolishing, electrolytic cleaning makes the surface the cathode (negative electrode) of an electrolytic cell. When current is passed through the cell, copious volumes of hydrogen gas are evolved and a highly caustic environment is created at the metal-solution interface. The caustic interface weakens the interaction between the metal surface and surface grime. The evolving gas that nucleates beneath and around surface dirt and grime aids to break it free of the surface, cleaning but without otherwise changing the surface of the metal.

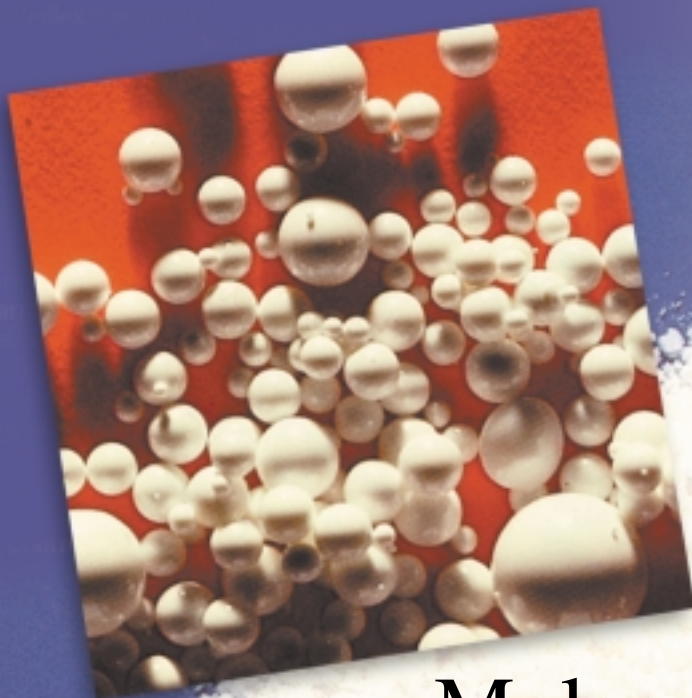
The methodology developed at TA-55 for decontaminating stainless steel surfaces has features of both electropolishing and electrolytic cleaning. The electrolyte contains a moderate concentration of a sulfate salt at an elevated pH of 10 to 12. The metallic object to be cleaned is made the anode. Current sent through the cell results in water oxidation, and the evolution of oxygen gas serves to lift particulates from the surface. The generation of hydronium ions lowers the local solution pH, allowing the metallic cations to remain soluble near the interfacial region and improving the uniformity of the metal surface dissolution. Stainless steel surfaces treated in this manner are uniformly etched.

To recycle the electrolyte solution, the radioactive and other metal cations must be removed. Because both iron and nickel cations are insoluble in alkaline sodium sulfate solution, the electrolyte is maintained at a high pH through the continuous addition of small quantities of a base like sodium hydroxide. The formation of metal hydroxide precipitates is key to the electrolytic decontamination process. Not only does the precipitation facilitate the removal of these elements from solution, but the precipitate also entrains or "captures" the actinide particles that have been released from the metal surface. In a succeeding step, mechanical filtration of the electrolyte solution decontaminates the electrolyte.

Chromium is a constituent of stainless steel alloys, but unlike divalent and trivalent iron and nickel, the hexavalent chromate does not precipitate in basic solution. Chromate is removed from solution by a secondary process in which the hexavalent chromium is reduced by addition of ferrous sulfate to a trivalent oxidation state, which in turn precipitates as chromium hydroxide $\text{Cr}(\text{OH})_3$. Filtration of the electrolyte solution then provides a compact metal hydroxide residue for discard while the filtrate is returned to the process for reuse.



Electrochemical decontamination (top photo) can be used to remove actinides from metal surfaces such as glove boxes. The series of three photographs shows a contaminated metal surface before cleaning, with the portable electrolysis head attached, and after cleaning.



Beads of anion-exchange resin are used in the nitric acid plutonium recovery process. The background shows a powder of Reillex™ 402 polymer, which was modified to produce new, highly sorbtive anion-exchange resins.

Photos courtesy of Reilley Industries, Inc.

Molecularly Engineered Resins for Plutonium Recovery

S. Fredric Marsh, D. Kirk Veirs, Gordon D. Jarvinen, Mary E. Barr, and Eddie W. Moody

For several decades, Los Alamos National Laboratory has played a key role in developing ways to reduce the radioactive waste produced in plutonium processing. Recent work has focused on developing molecular-engineered resins to improve the efficiency for removing plutonium from the nitric acid processing streams at the Los Alamos Plutonium Facility and at other plutonium facilities in the Department of Energy (DOE) complex.

Nitric acid processing is used to recover plutonium in a purified form. Plutonium-contaminated residues and waste items such as glass containers, graphite casting molds, and magnesium oxide crucibles can be leached with nitric acid to dissolve the contaminants, and impure scraps of plutonium (typically converted to plutonium oxide) can be dissolved in fluoride-catalyzed nitric

acid. The plutonium can then be selectively removed from the nitric acid by an organic polymer known as an anion-exchange resin.

Each polymer unit of the resin contains a cationic site that can retain an anionic complex. In nitric acid, the omnipresent nitrate anions, NO_3^- , will initially sorb to the resin. But plutonium is one of the few metals that form stable anions in nitric acid solutions, forming the Pu(IV) complex $\text{Pu}(\text{NO}_3)_6^{2-}$. Most metals form cationic or neutral nitrate complexes under such conditions. At an acid concentration of about 7 molar (M), the Pu(IV) anion will preferentially sorb to the resin by displacing, or exchanging with, nitrate anions. All other elements effectively stay in solution.

In the nitric acid process, porous beads made from resin are packed into a column through which the 7-M nitric

acid solution is flowed. The plutonium sorbs to the resin while impurity elements wash away. Once the resin has been sufficiently loaded with plutonium, the solution conditions are changed. The plutonium releases from the resin and goes back into solution and is eventually recovered as purified plutonium dioxide. (More information about the recovery process is given in the article "A Vision for Environmentally Conscious Plutonium Processing" on page 436.) Over the last 20 years, the nitric acid process has been used to purify and recover tonnes of plutonium at Los Alamos alone.

Increasing the efficiency of the nitric acid process is key to enhancing plutonium recovery and minimizing radioactive wastes. Such improvements have been the goal of our efforts to engineer new anion-exchange resins.

Improving the Efficiencies of Anion-Exchange Resins

As early as 1959, Jack Ryan, a researcher at Pacific Northwest Laboratory, recognized that the sorption of Pu(IV) on gel-type anion-exchange resins was very slow (Ryan and Wheelwright 1959). Little was done, however, to alter those sorption characteristics. A 1984 report stated that more than three weeks would be required for Pu(IV) to reach equilibrium with a single 1-millimeter-diameter, gel-type resin bead in 7.5-M nitric acid. In the Lab's plutonium facility, the contact time between the solution and the resin in an exchange column was only about 5 to 10 minutes. The slow sorption meant that excessive amounts of resin were needed to recover relatively small amounts plutonium from the nitric acid.

In about 1985, Los Alamos researchers began to address this shortcoming. From their initial studies, they concluded that resin porosity and bead size had the largest effects on the rate of plutonium sorption. Small beads of macroporous resin were found to dramatically increase Pu(IV) sorption kinetics. (Beads made of macroporous materials have extra-large pores that greatly increase the effective surface area of each bead as solutions flow through it.) As a result, the Los Alamos Plutonium Facility switched to a macroporous resin made from a polystyrene-divinylbenzene polymer. Positive results here also led the Rocky Flats Plant to adopt the improved anion-exchange resin.

This improvement, however, was quickly superseded by another one. In the 1960s, Ryan had reported that a polyvinylpyridine resin offered superior sorption and desorption kinetics. In addition, the resin offered a greater capacity for plutonium and greater resistance to nitric acid and radiation damage than polystyrene-divinylbenzene polymers. Although the resin Ryan championed was not commercially available at the time of the Lab's macroporous resin studies, shortly

thereafter, we began to collaborate with Reilly Industries, Inc., a supplier of vinylpyridine polymers. One result of this collaboration was the development of a macroporous polyvinylpyridine resin, later designated as Reillex™ HPQ. This new resin was comparable or superior to the best commercial resins then available. We quickly incorporated Reillex™ HPQ in some of the full-scale plutonium processes at Los Alamos and, based on highly favorable results, soon replaced the resin in all remaining processes with Reillex™ HPQ. The company began marketing the resin in 1988.

As of 1997, Reillex™ HPQ had outperformed all of the dozens of other commercial resins we had tested. The resin survives the processing stream's brutal combination of nitric acid and intense radiation for at least three years and has become the standard for plutonium anion exchange in nitric acid throughout the nuclear industry. Its development did not mark the end of resin research, however. We have continued to look for ways to improve both the sorption speed and capacity of resins. Based on a variety of analytical, modeling, and chemical synthesis techniques, this research has led to a fuller understanding of how plutonium nitrate complexes bind to resins and to the development of promising new bifunctional resins.

Molecular Studies of the Pu(IV) Nitrate Complexes

The advances in anion-exchange resins made during the 1980s were based on comparatively simple experimental evaluations of the effects of the resins' bead size, porosity, and composition. In a sense, these were trial-and-error experiments guided by intuition and earlier experimental results. By 1990, we realized that further

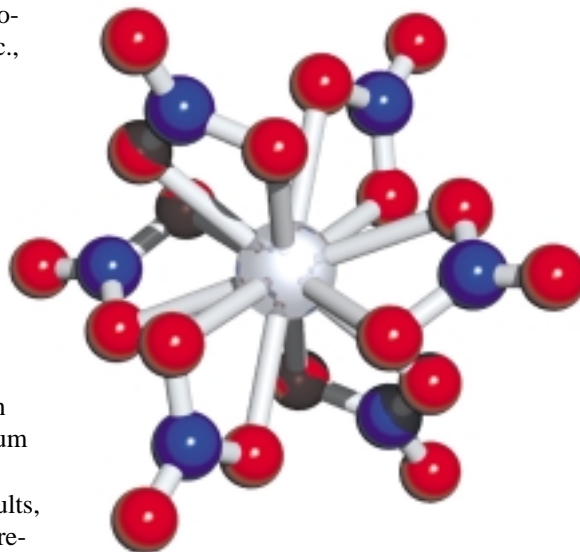


Figure 1. Molecular Model of the Pu(IV) Hexanitrate Complex

The hexanitrate complex is believed to be the one that sorbs to anion-exchange resins. A plutonium ion (silver) is at the center. Each nitrate ligand (NO_3^-) has three oxygen atoms (red) bonded to the nitrogen (blue). The nitrate bonds in a bidentate fashion, that is, two atoms from the ligand bond to the central plutonium ion.

improvements in the anion-exchange process would require a better understanding of what was occurring at the molecular level.

The earliest spectrophotometric studies of plutonium nitrate complexes, both in solution and on anion-exchange beads, were published in 1953 (Durham and Mills). Based on these light-absorption measurements of loaded resin beads and other data, Ryan concluded in 1960 that the Pu(IV) nitrate complex that sorbs on anion-

In 1990, we sought to obtain improved absorption spectra using modern instruments and data-processing techniques. We wanted not only to verify the structure of the sorbed species but also to determine the identity of the Pu(IV) complex *in solution* that most readily reacts with the anion-exchange

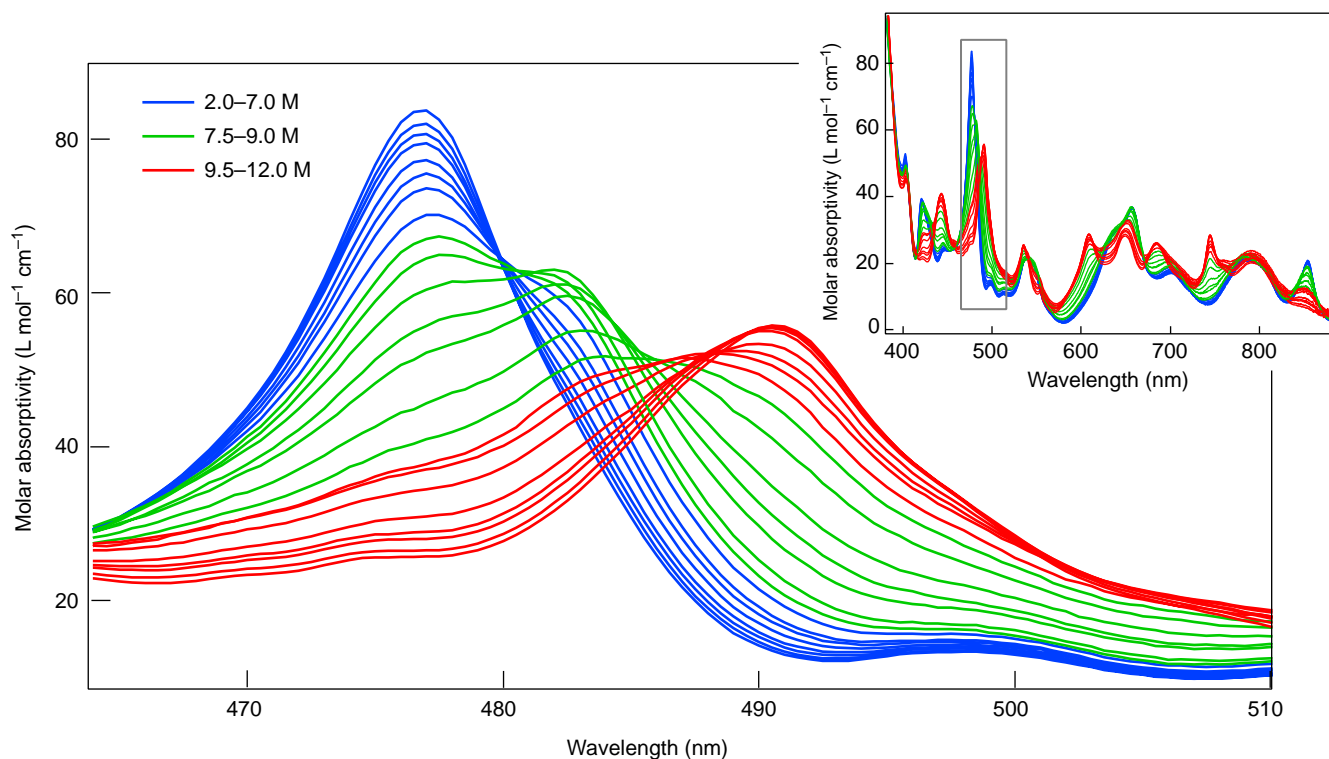


Figure 2. Absorption Spectra of Plutonium Complexes in Nitric Acid

The inset shows the absorption spectra of Pu(IV) in 2- to 12-M nitric acid solutions. The large graph is an expanded view of the region in the gray box. The blue peak at 477 nm can be assigned with confidence to the dinitrato cation $\text{Pu}(\text{NO}_3)_2^{2+}$; and the red peak at 490 nm, to the hexanitrate anion $\text{Pu}(\text{NO}_3)_6^{2-}$. The green peak at 483 nm is due to a third complex, most likely a tetranitrato neutral complex. Sequences of curves that cross at the same point (for example, the blue curves at about 480 nm and the red curves at about 488 nm) indicate that changes from one spectrum to the next are dominated by a shifting equilibrium between two plutonium complexes. The lack of such crossings for some series, such as most of those in green, indicate that three or more species are contributing to the spectra. (Graphics courtesy of J. Berg, Los Alamos National Laboratory.)

resin before becoming the sorbed hexanitrate complex. The fact that the highest concentration of this hexanitrate complex occurs at a nitric acid concentration of about 13 M but that Pu(IV) sorption is highest between 7 and 9 M indicated that the hexanitrate complex was not being sorbed directly onto the resin. Instead, it was possible that the complex was the product of a transformation that occurred during sorption.

We began studies, therefore, to produce a database of absorption spectra of Pu(IV) in varying concentrations of nitric acid, with the goal of identifying all of the plutonium species that were present. Our spectrophotometric measurements ranged from the near ultraviolet through the near infrared (300 to 1200 nanometers).

Ryan had identified two major

Pu(IV) species in nitric acid concentrations of 1 to 13 M: the positively charged dinitrato complex, $\text{Pu}(\text{NO}_3)_2^{2+}$, and the divalent hexanitrate complex, $\text{Pu}(\text{NO}_3)_6^{2-}$. For the most part, our studies agreed with Ryan's observations. We found that in dilute nitric acid, the most abundant complex was the plutonium dinitrato cation, whereas at high concentrations of nitric acid, the most abundant complex was the plutonium hexanitrate anion. We also confirmed Ryan's conclusion that the hexanitrate anion is the sorbed species.

But careful analysis of our spectrophotometric data revealed that at intermediate nitric acid concentrations of approximately 7 M, a third, previously unstudied plutonium nitrate complex reached its peak concentration (see Figure 2). Although we could not iden-

tify this third complex, it was especially interesting because as we varied the concentration of nitric acid, the absorption spectrum of the new complex in solution correlated closely with the sorption profile of Pu(IV) onto an anion-exchange resin. We therefore proposed that this new complex might be directly involved in the sorption process. Our results were presented in a Los Alamos report (Marsh et al. 1991).

Before we could confirm and perhaps exploit this hypothesis, however, we needed to identify the third plutonium species in solution that correlated so strongly with the Pu(IV) sorption profile. Unfortunately, we were unable to identify this species by our spectrophotometric measurements. Such information could only be obtained

with other spectroscopic techniques.

Previously, Fratello had used nuclear magnetic resonance (NMR) spectra of carbon, nitrogen, and oxygen in non-complexing organic liquids to observe the speciation of metal ions. Such data could then be used to infer the ions' speciation in aqueous solution. However, his technique could be used only for strongly bound ligands; weakly bound ligands exchange with the water ligands more rapidly than the timescale of NMR measurements, making it difficult to interpret the resulting signal. This problem can sometimes be overcome by acquiring NMR signals in organic solvents cooled to well below the freezing point of water, so that the rates of ligand exchange are significantly slower.

Our first NMR measurements of actinide nitrate complexes, begun in 1992, used nitric acid enriched with ^{15}N to titrate thorium in an organic solvent (deuterated acetone and CFCl_3) cooled to -100°C . We used thorium rather than plutonium because it was less hazardous and therefore easier to study and because Th(IV) has a similar chemical behavior to Pu(IV). For example, Th(IV) was known to form hexa-nitrato complexes, and the crystal structures of the thorium tetranitrato and hexanitrato salts were known to be similar to those of the comparable Pu(IV) salts. By measuring the NMR signal of ^{15}N , we observed four distinct thorium species containing—as the nitric acid concentration increased—one, two, four, and six nitrates (Figure 3). However, we observed no species containing three or five nitrates.

When we made similar NMR measurements using Pu(IV) nitrate complexes, the signal for ^{15}N indicated the presence of the hexanitrato species. The NMR signals for the other species were degraded to undetectable levels by the paramagnetism of plutonium. However, with decreasing nitrate concentration, the behavior of the NMR signal for the Pu(IV) hexanitrato complex was identical to what we had observed for Th(IV) hexanitrato. This par-

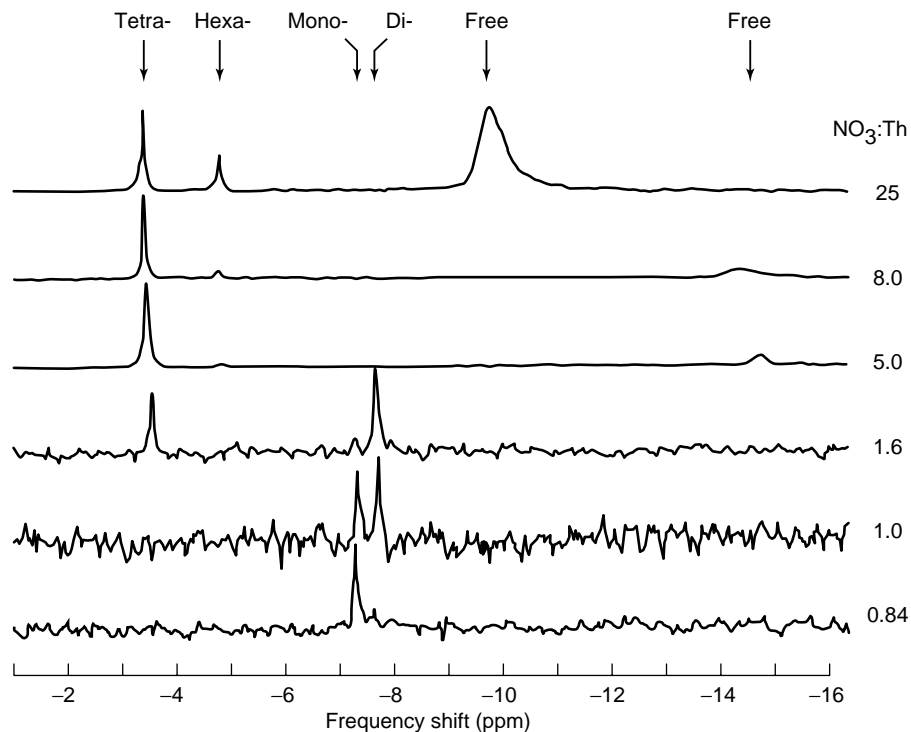


Figure 3. The NMR spectra of ^{15}N -labeled Thorium Nitrate Complexes Using thorium as a surrogate for plutonium, we were able to detect Th(IV) nitrate complexes as they formed in solution with ^{15}N -labeled NO_3^- ligands. The NMR spectra show the presence of four complexes: mononitrato (shift at -7.2 ppm), dinitrato (-7.6 ppm), tetranitrato (-3.4 ppm), and hexanitrato (-4.8 ppm). The peaks appear in order as the nitrate-to-thorium ratio increases. The thorium mononitrato complex first appears at low concentrations of nitric acid, the thorium dinitrato complex appears at higher concentrations, and so forth. Free nitrate first appears at a nitrate-to-thorium ratio of 5.0 at -14.9 ppm and shifts to -9.6 ppm as the ionic strength of the solution increases. No complexes with three or five nitrates are observed.

allelism reinforced the idea that thorium mimicked the behavior of plutonium in our solutions. Since the neutral thorium tetranitrato species $\text{Th}(\text{NO}_3)_4$ was abundant in 7-M nitric acid, we tentatively identified our third plutonium species in solution as the electrically neutral plutonium tetranitrato complex, $\text{Pu}(\text{NO}_3)_4$.

These experimental results, combined with related Raman spectroscopy done at Los Alamos and data from the literature, suggested the following Pu(IV) speciation pattern: the hexanitrato anion was the major species present in 13-M nitric acid; the dinitrato cation had the highest concentration in 2-M nitric acid; and the dinitrato, tetranitrato, and hexanitrato complexes were present at roughly equal concen-

trations in ~ 7 -M nitric acid. Later, more-sensitive experiments also supported this pattern.

As already discussed, the sorption of plutonium onto an anion-exchange resin and the concentration of the neutral tetranitrato complex both peak at ~ 7 -M nitric acid. Furthermore, the sorption of Pu(IV) as a function of nitric acid concentration parallels the concentration of the tetranitrato species. But it appeared that only the hexanitrato complex sorbed to the resin. For anion exchange to occur, then, the neutral Pu(IV) tetranitrato complex would have to acquire two more nitrate groups to become the divalent hexanitrato anion.

The spectroscopic data suggested that a pentanitrato complex was rela-

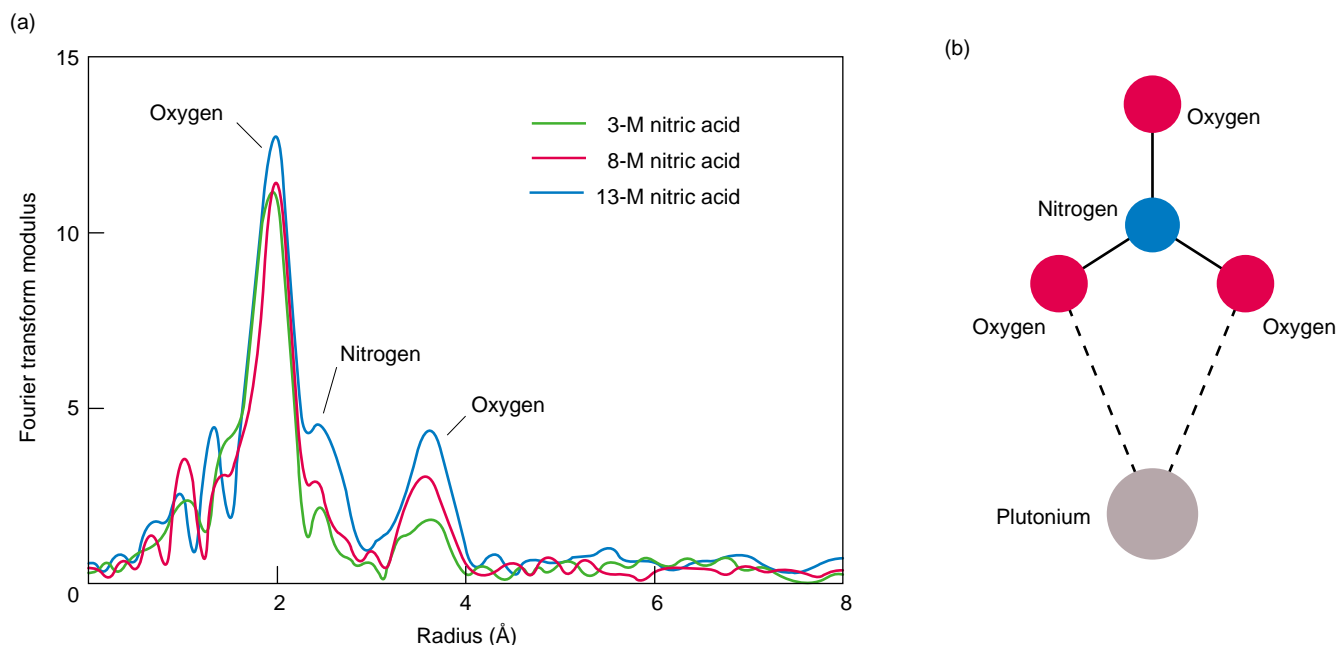


Figure 4. XAFS Studies of Pu(IV) Nitrate Species

(a) The Fourier transforms (FTs) of XAFS data reveal the relative positions and number of nearest-neighbor atoms around a central atom (in this case, plutonium). The largest peak corresponds to oxygen atoms that are located about 2.41 Å from the plutonium atom. (Because of the XAFS phase shift, peaks in the FTs are shifted to lower radii than actual distances from the plutonium ion.) The second and third peaks correspond to nitrogen atoms located about 2.97 Å from the plutonium and to a second set of oxygen atoms located about 4.15 Å from the plutonium. These distances are entirely consistent with a bidentate bonding arrangement, as illustrated in (b). The number of nitrate or water ligands that bind to the plutonium ion for different nitric acid concentrations can be obtained by comparing the intensities of the various peaks in the FT. The intensities of the third peak, for example, are in a ratio of 6:4.4:2.6 for 13-, 8-, and 3-M nitric acid, respectively. With the distribution of plutonium nitrate species obtained from XAFS absorption spectra, the expected ratio would be 6:4.3:2.5. Thus the XAFS and light-absorption data are in complete agreement.

tively unstable, which meant that the tetranitrato complex was unlikely to acquire the additional nitrates via a two-step process. Instead, the conversion requires the simultaneous convergence of the neutral $\text{Pu}(\text{NO}_3)_4$ complex and two nitrate ions, a highly unlikely event. (This unfavorable complexation reaction might explain the notoriously slow kinetics for sorbing Pu(IV) on anion-exchange resins from nitric acid.) The question was how we might facilitate the required conversion of the Pu(IV) tetranitrato complex to the Pu(IV) hexanitrato complex.

An intriguing possibility was to develop a “bifunctional” resin in which each repeating polymer unit would contain two cationic sites that were separated by a fixed distance. Such an arrangement would improve adsorption in two ways. First, two nitrate ions, bound initially to the cationic sites,

could be positioned in close proximity to each other. The neutral tetranitrato species could readily react with them to form the sorbed hexanitrato species. And second, the two positive charges on the polymer unit would hold the divalent hexanitrato complex more strongly. These properties should produce faster kinetics and higher K_d values.¹ But how should the two anion-exchange sites be spaced to achieve the best performance?

To answer that question, we needed structural information about the Pu(IV) nitrate complexes, which was minimal at the time. We were faced with a number of questions: Did one or both oxygens on each nitrate ligand bind directly to the plutonium ion? What was the coordination number for each Pu(IV) species, that is, how many nitrates and waters were coordinated with each plutonium ion? What were the

bond distances from the plutonium ion to the nitrate oxygens? Were the shapes of the bound nitrate ligands distorted from those of the free nitrate? What were the similarities and differences between the Pu(IV) hexanitrato species in solution and in the solid state?

X-ray absorption fine structure (XAFS) spectroscopy could help answer these questions, but at the time no synchrotron x-ray facility (where XAFS experiments are done) allowed plutonium-containing materials on-site. Fortunately, the forward-looking man-

¹ K_d gives a measure of the sorption affinity of the resin. It is defined as: $K_d = (1 - [B]/[A])V/M$, where $[B]$ is the concentration of the element, here Pu(IV), in solution after contact with the resin, $[A]$ is the concentration of the element in solution before contact with the resin, V is the volume of the solution in contact with the resin (in milliliters) and M is the weight (in grams) of the dry resin. The higher the K_d , the greater the sorption.

agement at the Stanford Synchrotron Radiation Laboratory (SSRL) agreed to embark with Los Alamos on an exhaustive study of the hazards involved in conducting XAFS experiments with actinides. As a result of that effort and the safe operating procedures that were developed, research groups from DOE laboratories at Los Alamos, Berkeley, Livermore, Argonne, and Richland (Washington) as well as from Australia and France now regularly study actinides at SSRL. Moreover, similar capabilities have also been developed for handling actinides at synchrotron facilities at both Berkeley and Argonne.

By 1995, XAFS spectroscopy provided all of the bond lengths and angles for the Pu(IV) hexanitrate species. Our studies of plutonium in nitric acid at concentrations of 3, 8, and 13 M dramatically confirmed the presence of inner-sphere nitrate species, yielded stoichiometries consistent with other methods, and provided precise bond distances and coordination numbers (see Figure 4). The Pu(IV) hexanitrate species in solution was found to have essentially the same structure as the hexanitrate species in the solid state. Moreover, extended x-ray absorption fine structure (EXAFS) showed that the plutonium complex sorbed on an anion-exchange resin was structurally identical to the solution species that had the highest concentration in 13 M nitric acid, that is, the hexanitrate anion, in agreement with the earlier light-absorption measurements.

First Bifunctional Anion-Exchange Resins

At this time, bifunctional anion-exchange resins were not commercially available nor, to our knowledge, had they ever been prepared in even experimental quantities. In 1996, therefore, we began to collaborate with Prof. Richard Bartsch at Texas Tech University, who was interested in developing a polymer synthesis program that could help prepare such resins. All bi-

functional resins described below were prepared at Texas Tech to our specifications.

We had several objectives for the first bifunctional resins. We wanted to (1) synthesize the new resins by modifying an existing, commercially available (hence low-cost) resin that offered superior resistance to acidic and radiolytic degradation, (2) evaluate the effect of placing different chemical groups at the second ion-exchange site, (3) vary the separation distance between the two exchange sites, that is, vary the number of hydrocarbons linking the sites, and (4) vary the rigidity of these hydrocarbon chains.

The first bifunctional resins were prepared for us in 1996 by modifying another Reilly Industries' vinylpyridine polymer resin, Reillex™ 402. This resin, seen in Figure 5(a), is easily derivatized. The new resins were synthesized by attaching different chemical groups to the nitrogen atom of the pyridine with a short hydrocarbon chain. In one resin, the other end of the chain had a trimethylammonium group— $\text{N}(\text{CH}_3)_3$ —as shown in Figure 5(b). The pyridine nitrogen provided one anion-exchange site, the nitrogen within the trimethylammonium group provided the second, and the number of hydrocarbons in the linking chain established the distance between the two sites. We prepared several such resins that differed only in the length of their hydrocarbon chains, which varied from two to six carbons. All resin polymers were cross-linked with divinylbenzene at 2 to 3 percent. (The degree of cross-linking controls the resin's rigidity, porosity, resistance to acidic and radiolytic degradation, and other properties.)

Another series of bifunctional resins was synthesized with a pyridinium group, as shown in Figure 5(c). That series had spacer chains of two to six hydrocarbons. In addition, we prepared a series of resins with a trimethylphosphonium group (with chains of two to five hydrocarbons), as well as a resin that had a trimethylammonium group

attached with an ether chain (two hydrocarbons on either side of an oxygen atom).

The resins' performance was evaluated by measuring the K_d values of Pu(IV) onto the resins in 1-, 3-, 5-, 7-, and 9-M nitric acid over contact times of 0.5, 2, and 6 hours. In all cases, resins formed with the five-carbon chains gave the highest K_d values in 7-M nitric acid. Table I compares the K_d values for several of these resins with those obtained for Reillex™ 402. The K_d values for the bifunctional resins are roughly 2 to 4 times higher than those of the base resin.² Another interesting result is that the trimethylammonium resin with the ether chain (column 4) is superior to the trimethylammonium resin with a chain of five hydrocarbons (column 3). This suggests that the increased flexibility of the oxygen spacer may contribute to the resin's improved performance.

We also tested the performance of one of our earliest resins (TTU-4, which had a trimethylammonium group attached to a spacer chain of four hydrocarbons) for removing Pu(IV) from a solution that simulated acid-dissolved sludge from the high-level nuclear waste storage tank 102-SY at the Hanford Reservation in Washington. Although the nitric acid concentration of this solution was only 0.5 M, the high concentration of dissolved nitrate salts provided a total nitrate concentration of 5 M. Our experiments again measured K_d for various solution/resin contact times but compared the results with those for Reillex™ HPQ. In all cases, the plutonium K_d values for the bifunctional resins were dramatically greater than those for Reillex™ HPQ, as evident in Table II. The fact that the K_d values for other

²The K_d values of the new resins were also as much as 14 times greater than those of Reillex™ HPQ resin. But Reillex™ HPQ is cross-linked at 25% (to give the resin mechanical strength), which substantially limits access to the cationic binding sites compared with the 2% cross-linked Reillex™ 402. Simply comparing the K_d values, therefore, is not a valid indicator of the resin's overall performance in an exchange column.

Table I. Measured K_d Values for Pu(IV) in 7-M Nitric Acid onto Resins

Contact Time	Spacer and Functional Group of Bifunctional Resin ^a				
	(h)	Reillex 402 ^a	$(\text{CH}_2)_5\text{-N}(\text{CH}_3)_3$	$(\text{CH}_2)_2\text{O}(\text{CH}_2)_2\text{-N}(\text{CH}_3)_3$	$(\text{CH}_2)_5\text{-pyridinium}$
0.5		1258	3500	4800	5700
2		2635	4300	6800	8800
6		2591	3800	6800	11000

^a K_d values measured in mL/g

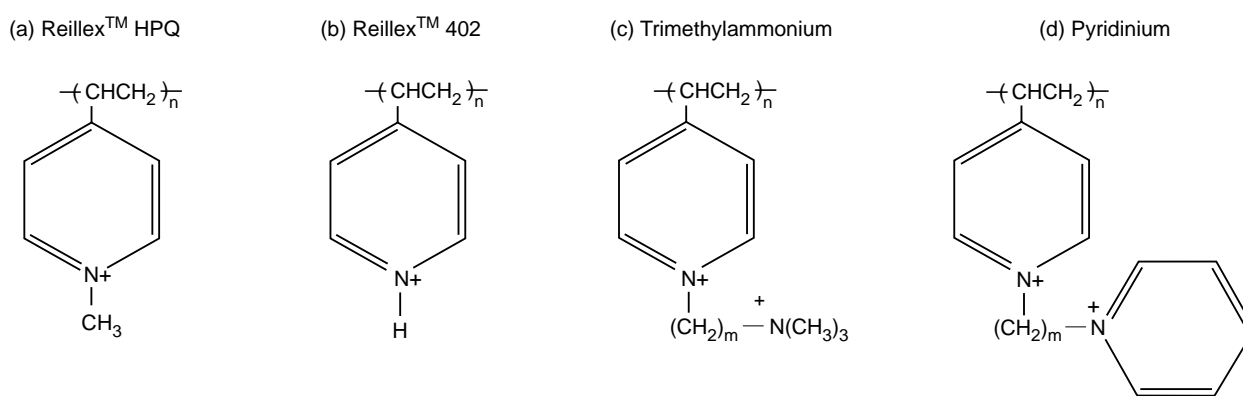


Figure 5. The First Series of Bifunctional Resins

(a) Reillex™ HPQ is a vinylpyridine polymer resin that has a methyl group, CH_3 , attached to the nitrogen atom of the pyridine. One polymer unit is shown. As seen in (b), Reillex™ 402 is similar, except that a hydrogen atom is attached to the nitrogen. Collaborators at Texas Tech University replaced that hydrogen with hydrocarbon chains of various lengths, to which were attached different chemical groups, including (c) trimethylammonium and (d) pyridinium. The chains were two to six hydrocarbons long. A plutonium hexanitrate complex should bind to the two positively charged nitrogen sites of these bifunctional resins. (e) In this cartoon, a polymer chain has numerous sites functionalized with trimethylammonium, three of which have Pu(IV) hexanitrate groups (shown as “pin-wheels”) sorbed on them. Derivatizing a polymer is not 100% efficient, so we’ve shown two sites that are not functionalized.

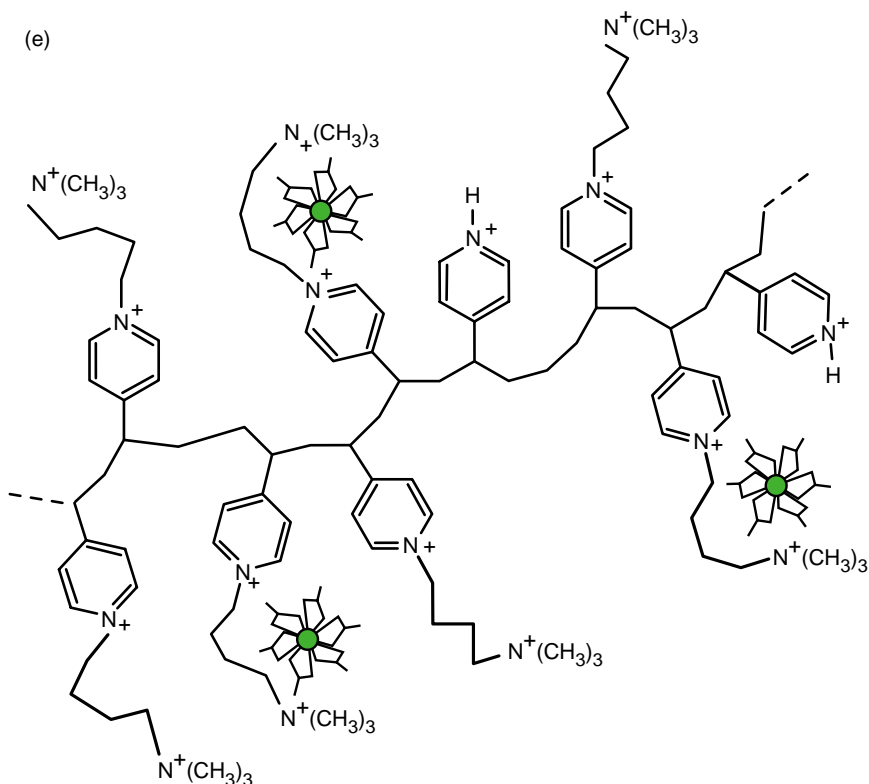


Table II. Approximate K_d Values of Several Elements to Resins in High-Level Waste Sludge

Element	Reillex HPQ ^a (mL/g)	TTU-4 ^a (mL/g)
Plutonium	78	1100
Americium	4	6
Cerium	14	23
Chromium	1	1
Cesium	1	1
Iron	1	1
Strontium	1	1
Technetium	76	24
Uranium	17	18
Yttrium	1	1
Zirconium	4	4

^aContact time of 0.5 hours

metal ions in solution were about the same for all resins demonstrated that the enhanced sorption was selective for Pu(IV), as we had envisioned.

Molecular Models

In 1998, we began to develop computer models to help us better understand how anion-exchange resins function and to guide our development of new resins. As noted, an important figure of merit for an anion-exchange resin is K_d , which can be shown from thermodynamic arguments to be proportional to what we call the “stickiness factor,” or SF.

SF is the sum of the electrostatic forces binding a plutonium hexanitrate complex to the resin’s cationic site.³ To calculate it, we must know how the electronic charge is distributed within the complex and within a polymer unit of the resin. In an exact calculation, we would solve the Schrödinger equation (with relativistic corrections) for all the electrons of all the atoms within the

³Our model does not address how the neutral Pu(IV) tetranitrate complex acquires two negatively charged nitrate ions to become the divalent Pu(IV) hexanitrate anion. The model simply examines how the hexanitrate complex binds to the resin.

hexanitrate complex and the resin. This *ab initio* (from first principles) approach would give the continuum charge distributions throughout the complex and the polymer unit, which change as the two species approach and bind to each other. The total electrostatic binding energy would then involve a double integral over the entire charge distribution. At present, however, such a calculation exceeds the capabilities of the world’s largest supercomputer!

Our approach for obtaining the SF has been to forgo a full quantum mechanical calculation and instead use a “partial charge” model consisting of point charges, which are placed at the centers of the atoms of the complex and of the polymer unit. These charges represent the average charge at each atom. Two charges within either the complex or the polymer unit interact through a linear force as if they were connected by a spring, where the spring constant represents the strength of the chemical bond. This collection of partial charges held together by chemical-bond springs is called a molecular mechanics model.

Our molecular mechanics model has everything needed to calculate the electrostatic interaction of the hexanitrate complex and the resin—that is, it contains the relative positions and magnitudes of the point charges for the entire system. Once these charge distributions are known, we need only calculate the electrostatic energy between a charge in the plutonium hexanitrate and a charge in the resin and then take the sum over all such pairs. Because of the springs, the model is mechanically flexible and to some degree can simulate how the resin’s spacers distort to better fit the hexanitrate complex.

Even with this simplified approach, however, we could not estimate the partial charges for the hexanitrate complex within a reasonable amount of computer time. As a result, we have limited ourselves to *ab initio* calculations for $\text{Pu}(\text{NO}_3)_3^{3+}$, which can be viewed as a model for one-sixth of the hexanitrate complex (see Figure 6). The results are

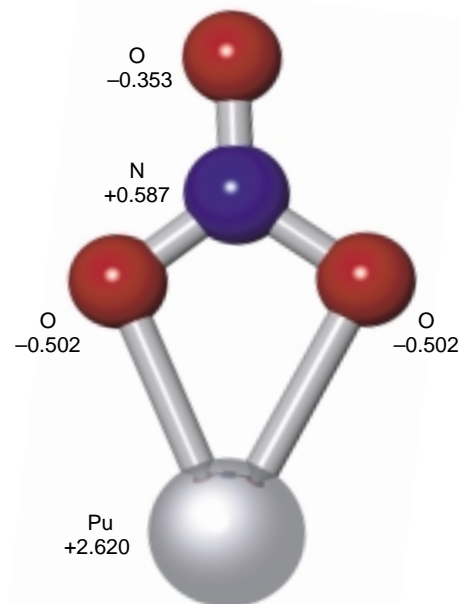


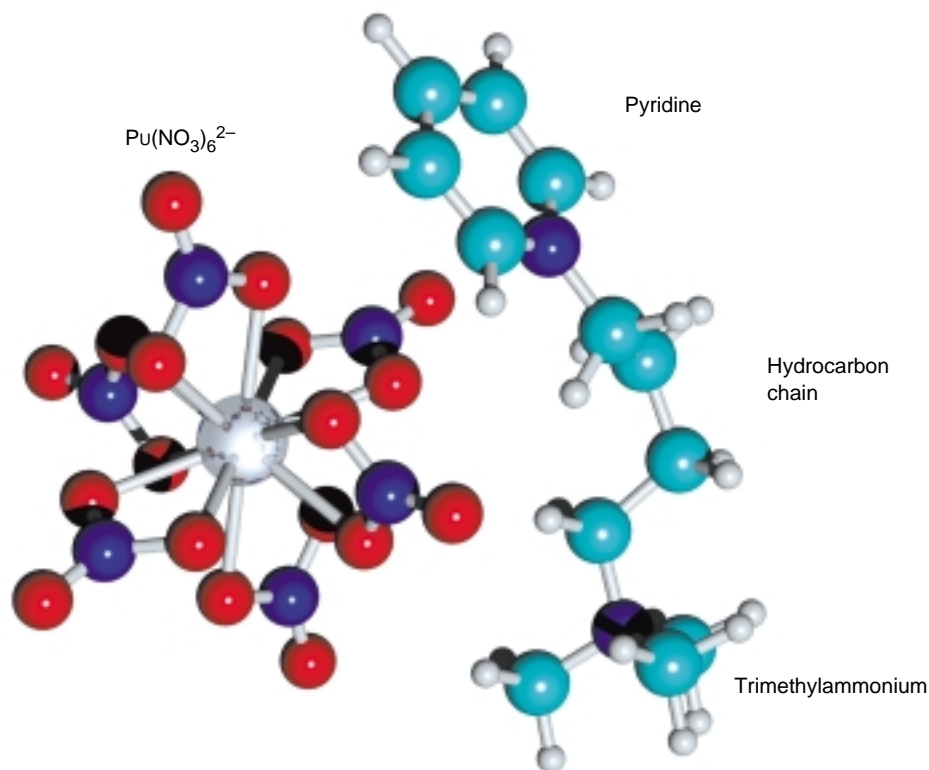
Figure 6. The Partial-Charge Model for the Pu(IV) Hexanitrate Complex
Our molecular mechanics model for the hexanitrate complex is based on calculations for the partial charges of $\text{Pu}(\text{NO}_3)_3^{3+}$, which can be viewed as one-sixth of $\text{Pu}(\text{NO}_3)_6^{2-}$. These calculations are then extrapolated to obtain the partial charges of the hexanitrate complex. This modeling procedure seems to be valid because when we compare the estimates of bond lengths and angles from our model with EXAFS data, the differences are quite small.

then extrapolated to $\text{Pu}(\text{NO}_3)_6^{2-}$. The structure of plutonium hexanitrate as derived from this model has proved to be remarkably accurate. When we overlay our molecular mechanics model of the hexanitrate complex with a ball-and-stick model obtained from EXAFS studies, differences in the positions of the atoms and their bond lengths and angles are quite small.

By using a computer code to calculate the electrostatic forces between the complex and the polymer unit as well as their resulting motions, we can watch the two species interact on a computer screen. The initial separation between the two species is 4 angstroms,

Figure 7. A Bound Complex

The Pu(IV) hexanitrate complex shown here is electrostatically bound to one polymer unit of a bifunctional resin. The chemical structure of this resin—poly(N-alkylene-trimethylammonium 4-vinylpyridine nitrate)—is also shown in Figure 5(c). In the polymer unit, the carbon atoms are bright teal, the cation-exchange sites are the two blue nitrogen atoms, and the small gray spheres are hydrogen atoms. At each exchange site, binding results from the strong electrostatic attraction between one of the polymer's positively charged nitrogen atoms and a negatively charged oxygen atom (red) on the hexanitrate complex.



but they soon drift toward each other, rotating and flexing as necessary to minimize the system's energy. Binding is complete when the two species come to rest, and a calculation of the system's electrostatic energy at that point gives the SF. Normally, binding occurs in about a thousand steps, which requires about 15 minutes on a desktop computer. A bound complex is shown in Figure 7.

This technique gives us a quick and easy means of evaluating the performance of an anion-exchange resin relative to other resins of similar composition. For example, our molecular mechanics model has been able to reproduce the experimental trends in K_d values as the values vary with spacer length when the same chemical group is used as the second ion-exchange site. (The calculations assume that the hexanitrate complex and the polymer unit are in vacuum, but the K_d values can be scaled to provide liquid-phase results. Because our model calculates only the K_d of one resin relative to another and because the solvent effects are similar for the different resins, the trends we observe should be valid.)

As our molecular modeling becomes

more sophisticated, we will be able to compare K_d values across families of resins with different types of second ion-exchange sites and with various combinations of spacer/second-site groups. Modeling will help us select—from a vast range of chemical possibilities—the most promising options for future laboratory synthesis and testing.

Our results for plutonium can also be applied to some extent to other actinide IV species that form hexanitrate complexes, such as thorium and neptunium, because the direct interaction between the plutonium ion and the resin is minimal. Instead, the major interaction is between the outer oxygens of the nitrate ligand and the cationic sites of the resin.

Future Directions for Anion-Exchange Resins

The overall performance of our bifunctional resins bodes well for the future. For the resins described in this article, the only shortcoming is a lack of mechanical strength. But we have recently developed a new series of bifunctional resins that are cross-linked

at about 20 percent. While increasing the mechanical strength, the greater cross-linking decreases the sorption, and at this point in our development project, Reillex™ HPQ remains the resin of choice for nitric acid processing.

However, we can envision different bifunctional resins that could be useful in other applications, for example, scavenging precious metals from what would normally be considered waste solutions, or removing toxic, non-radioactive metals from other industrial waste streams. Our molecular mechanics model allows us to simulate and “test” these different resins on a desktop computer in less than a day, saving the considerable time and expense required to synthesize and test them in the laboratory.

In a concurrent development program, Los Alamos researchers made rods of porous polystyrene foam as possible replacements for the beads now used to pack anion-exchange columns. The rods' porosity can be carefully controlled to provide short, optimal flow paths to functional groups attached to the polystyrene. Their use results in better sorption and better flow characteristics within a pressurized fluid

system, so they are in general a better support medium for column chromatography, including the anion-exchange process. Because the foam can be functionalized to provide two exchange sites, the rods may offer some advantages over resin beads. Initial tests of these rods have shown promising results.

Further Reading

Cleveland, J. M. 1979. *The Chemistry of plutonium*. La Grange Park, IL: American Nuclear Society.

Durham, R. W. and R. Mills. 1953. "The Adsorption of Plutonium on Anion Resins," Atomic Energy of Canada Ltd. report CEI-62.

Marsh, R. S., D. K. Veirs, and R. S. Day. 1991. "Spectrophotometric Investigation of the Pu(IV) Nitrate Complex Sorbed by Ion Exchange Resins" (June). Los Alamos National Laboratory report LA-12070.

Ryan, J. L., and E. J. Wheelwright. 1959 "The Recovery, Purification, and Concentration of Plutonium by Anion Exchange in Nitric Acid" (January). General Electric Company Hanford Atomic Products Operations report HW-55893.

Slater, M. J. 1991. *Principles of Ion Exchange Technology*. Boston: Butterworth-Heinemann Ltd.

Weigel, F., J. J. Katz, and G. T. Seaborg. 1986. Plutonium. In *The Chemistry of the Actinide Elements*, 2nd ed., Vol. 1. Edited by J. J. Katz, G. T. Seaborg, and L. R. Morss. New York: Chapman and Hall.

S. Fredric Marsh began his 39-year career at the Idaho Chemical Processing Plant, where he developed improved radioanalytical procedures for plant-support laboratories. He spent five years at the



Babcock & Wilcox Nuclear Development Center near Lynchburg, VA, focusing on radiochemical separations research, before moving on to Los Alamos National Laboratory. He was with the Laboratory for 25 years, first with the Analytical Chemistry Group, and then with the Nuclear Materials Process Development Group. Fred's contributions to plutonium ion-exchange processing were recognized by a DOE Award of Excellence in 1986 and a LANL Distinguished Performance Award in 1988. He is co-inventor of a bifunctional anion-exchange resin that is highly selective for plutonium. This new resin has been licensed to Reilly Industries, which will manufacture it as a commercial product.

D. Kirk Veirs was born in Watsonville, CA, and received his B.S. in chemistry and environmental science from Northern Arizona University in 1976. He received his Ph.D. in physical chemistry from Pennsylvania State University in 1981. As a Director's-Funded post-doctoral fellow and technical staff member at Los Alamos (1981-1985) he measured rotationally induced changes in the Raman crosssection of hydrogen isotopomers. During a brief tenure at Lawrence Berkeley Laboratory from 1985-1990, he developed a method to spectroscopically image material properties. He returned to Los Alamos in 1990 and is now a Team Leader in the Nuclear Materials Technology Division. He studied the speciation of plutonium in nitric acid and is interested in the chemical changes that occur in stored actinide materials and other related surface processes. He is a member of the NMT Division Science Leadership Council and a corecipient of the 2000 R. D. Baker Award.



Gordon D. Jarvinen received his B.S. in chemistry in 1973 from the Massachusetts Institute of Technology and his Ph.D. in inorganic chemistry in 1979 from the University of California, Los Angeles. He was a resident research fellow at E. I. Du Pont de Nemours & Company during the summer of 1973 and a Postdoctoral Fellow at the Los Alamos National Laboratory for 1979-1981, where he is currently a technical staff member. His research interests include actinide and lanthanide coordination chemistry and separation technology, design and synthesis of ligand systems for improved separation and analysis of metal ions, development of chelating and ion-exchange polymers, and membrane separations. Gordon is a member of the American Chemical Society (ACS) and the American Association for the Advancement of Science, and is Chair of the ACS Separation Science and Technology subdivision of the Industrial & Engineering Chemistry Division for 2000.



Mary Barr received her B.S. in chemistry from the University of the South-Sewanee, TN, graduating with the "Orwellian Class" of 1984. She received her Ph.D. in inorganic chemistry from the University of Wisconsin at Madison in 1991. Her Los Alamos career began in 1991 as a Director's-funded postdoctoral fellow. She has been a staff member in the Nuclear Materials Technology Division since 1993. Her recent projects include the development of improved anion-exchange resins and extractants for actinides from process and waste streams. Her previous activities have ranged from synthesizing and evaluating ion-specific chelation systems to advising the Nuclear Materials Stabilization Task Group for the Defense Nuclear Facilities Safety Board on developing procedures for removing actinides from contaminated soils.

Eddie Moody attended Union University in Jackson, TN, where he received his B.S. in chemistry in 1992. He then attended the University of Memphis, where he received his M.S. in 1994 and his Ph.D. in 1997 in inorganic chemistry. He then went on to join Los Alamos National Laboratory as a postdoctoral fellow in the Nuclear Materials Technology Division, becoming a staff member in 1999. He is primarily interested in theoretical modeling of plutonium chemistry, but is also very interested in modeling the surface interactions of different compounds. His other hobbies are scuba diving and aviation.



Yucca Mountain

Looking ten thousand years into the future

*by Roger C Eckhardt
for David L. Bish, Gilles Y. Bussod, June T. Fabryka-Martin, Schön S. Levy, Paul W. Reimus,
Bruce A. Robinson, Wolfgang H. Runde, Inés Triay, and David T. Vaniman*

It's a dry, brown, nondescript ridge near the Amargosa Desert, just north of Death Valley and west of the Nevada Test Site. The landscape is a drab mix of desert grasses, cacti, shrubs—like needleleaf rabbitbrush and Cooper goldenbush—and, of course, the occasional Yucca plant. Nothing moves but scrawny black-tailed jackrabbits and desert collared lizards. No man's land.

Yet for the past twenty years, the ridge—called Yucca Mountain but looking more like a geologic speed bump—has been scrambled over by geologists, hydrologists, volcanologists, engineers, and environmental scientists. It has been photographed from every angle and cored at hundreds of drill sites to characterize its geology and hydrology. Its plant and animal life has been cataloged, its topography charted, and its underlying volcanic tuff captured in three-dimensional computer grids.



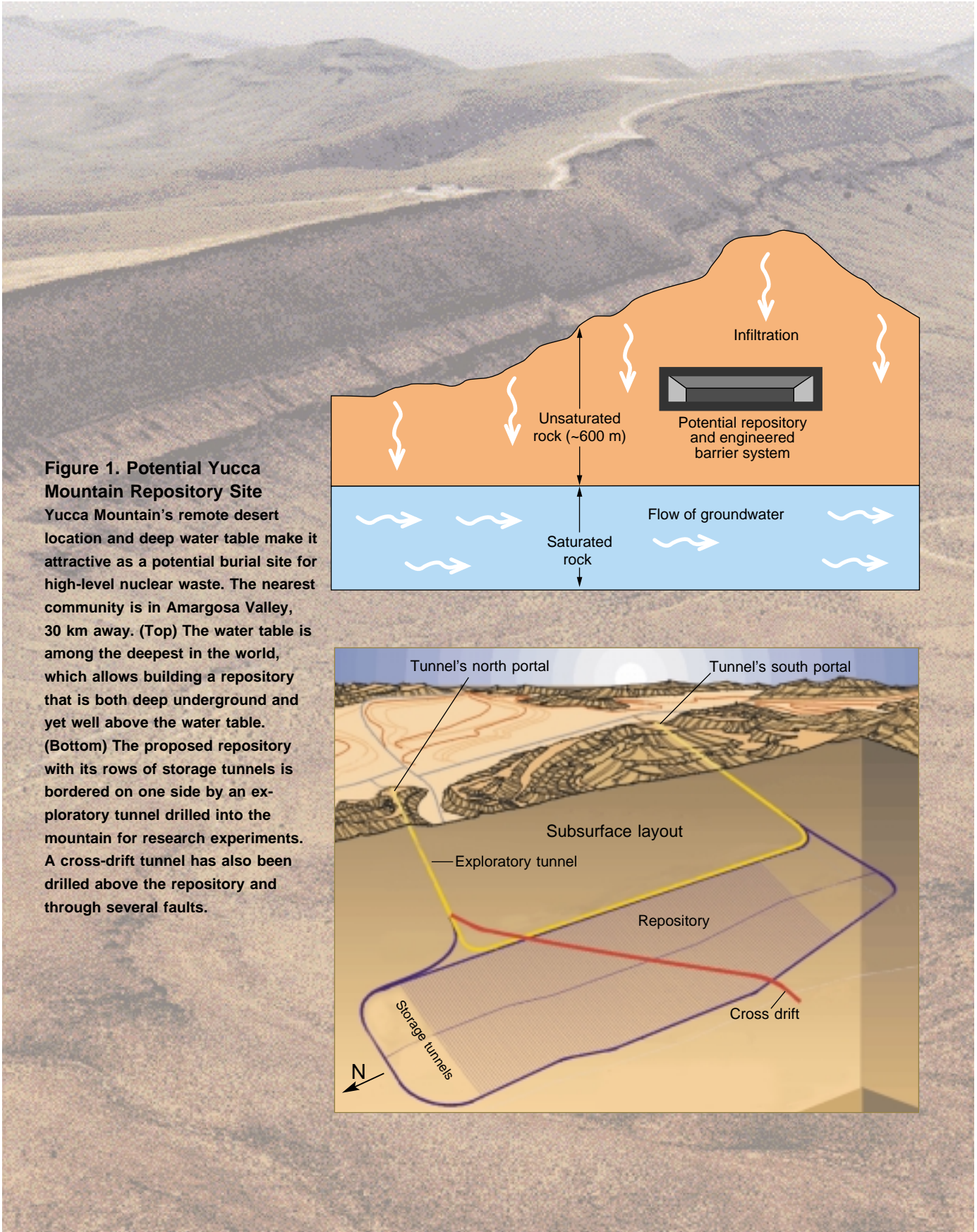


Figure 1. Potential Yucca Mountain Repository Site
 Yucca Mountain's remote desert location and deep water table make it attractive as a potential burial site for high-level nuclear waste. The nearest community is in Amargosa Valley, 30 km away. (Top) The water table is among the deepest in the world, which allows building a repository that is both deep underground and yet well above the water table. (Bottom) The proposed repository with its rows of storage tunnels is bordered on one side by an exploratory tunnel drilled into the mountain for research experiments. A cross-drift tunnel has also been drilled above the repository and through several faults.

Such intense scrutiny has resulted from the mountain's selection as a potential burial site for high-level radioactive waste. Much of this waste comes from the nation's nuclear power plants: spent fuel rods laden with highly radioactive fission products, unfissioned uranium, and plutonium. There are about a hundred commercial reactors in the United States, many operating since the sixties and seventies, and their spent fuel—some 39,000 tonnes—has been accumulating in cooling pools and dry casks with nowhere to go. By 2035, this tonnage could more than double if all power plants complete their full licensing cycles. Waste from research reactors and the Navy's nuclear fleet plus plutonium from dismantled nuclear weapons will add another 2500 tonnes. Because Congress has banned reprocessing spent fuel, all this waste must be safely stored—for eons.

A critical storage issue is the lingering radioactivity of plutonium, neptunium, and other actinides in the spent fuel. The half-lives of these elements are so long that the waste must be stored for more than 10,000 years without significant leakage to the environment. To meet Environmental Protection Agency (EPA) standards, radiation doses to the public that result from leakage must remain below 20 millirems per year (mrem/yr). These are daunting requirements for a geologic repository (see Figure 1). No matter how clever we are in engineering containment barriers—designing storage canisters and tunnels to isolate the waste—eventually, water will seep through the repository, corrode the canisters, dissolve waste radionuclides, and carry them off. When that happens, nature itself—the natural geologic barriers—will have to lend a hand in containing the waste. Studying and modeling the effectiveness of nature's barriers have been the focus of work at Los Alamos National Laboratory since the early 1980s.

In our studies, we have sought answers to a number of questions: Which radionuclides are most apt to dis-

solve and be carried off? How fast will they move through the rock? What radiation doses might citizens living in Amargosa Valley, the nearest community, receive if radionuclides reach the groundwater that feeds their wells? Will these doses stay below 20 mrem/yr, less than 10 percent of normal background radiation, for the next 10,000 years or more?

Reliable answers require amassing scientific data about the site's geochemistry and hydrology—for example, its groundwater chemistry, the sorption characteristics of site minerals, and potential groundwater flow paths—as well as about the radionuclides themselves. These data must then be combined to assess the performance of a complex physicochemical system over many millennia. Because no experiment can come close to analyzing radionuclide migration for 10,000 years or more, we have developed computer models to simulate the migration. These simulations are now being checked against data from extensive field tests.

Early in our work, we determined that neptunium was a leading “worst-case” radionuclide in terms of both the likelihood and consequences of its migration. As a result, much of our work has gone into characterizing neptunium's speciation, solubility, and sorption and modeling its transport. For the latter, we have developed a detailed picture of how water percolates through the mountain—in particular, what fraction will flow through fractures and what fraction will diffuse into the rock matrix. More recently, we identified colloidal transport as another pathway that must be incorporated in our modeling.

So far, our simulations show that it will take much longer than 10,000 years for neptunium to escape from the repository. In fact, it will take at least 100,000 years before there is any chance that radiation doses from escaping radionuclides could reach the EPA's limit of 20 mrem/yr. And we feel that these predictions are conservative. Key uncertainties in our transport parameters have been evaluated through sensitivity

analyses, and our simulations have assumed worst-case scenarios for radionuclide release and transport.

Given the challenge of predicting complex geochemical processes on geologic time scales, however, it's not surprising that scientific debate over the repository's viability is intense. There are still many uncertainties associated with our predictions, and we are just beginning to get transport data from field experiments near Yucca Mountain that will help us validate those predictions. We are also weighing other factors, such as the likelihood of climate changes that could increase rainfall in the area and the mountain's vulnerability to volcanic activity (see the box on page 492). What follows, therefore, is a summary of work in progress at Los Alamos—of how we are developing and using computer simulations to look 10,000 years into the future, and far beyond.

Yucca Mountain Repository

To date, the Department of Energy (DOE) has spent \$6 billion studying the feasibility of storing spent fuel deep within Yucca Mountain. The project involves scientists and engineers from the U.S. Geological Survey, several national laboratories, and a slew of private companies and government agencies. The task is to design a repository, characterize its site geology, and predict its reliability. By 2001, the Secretary of Energy must decide whether to recommend to the President that a repository be developed at Yucca Mountain. If the site is recommended, and if the President and Congress concur with that recommendation, then DOE will apply to the Nuclear Regulatory Commission (NRC) for a license to build the repository. As part of that application, DOE will have to present a credible case that the repository will perform as predicted.

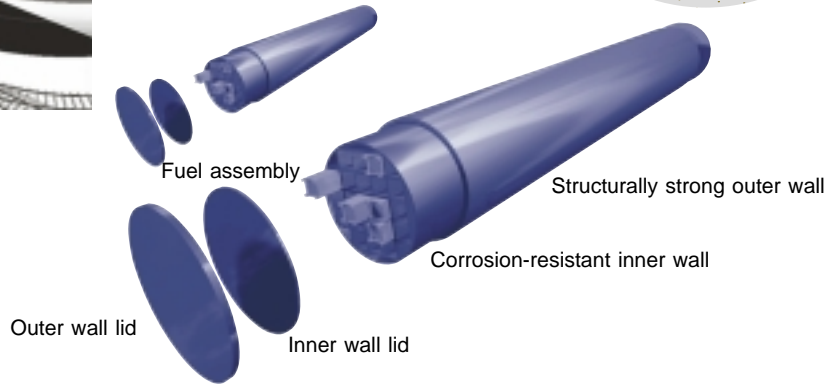
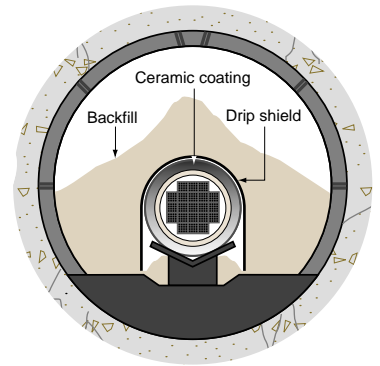
As currently envisioned, the repository is a labyrinth of tunnels some 300 meters beneath the mountain's surface (Figures 1 and 2). Waste would be placed in steel canisters 2 meters in



Figure 2. Engineered Barriers at Yucca Mountain

(a) Underground Storage Tunnels. As currently envisioned, the repository consists of about 160 km of underground tunnels with access ramps and ventilation shafts. The steel- and concrete-reinforced storage tunnels and the waste canisters they would house constitute the main engineered barriers for waste isolation. After being brought in by rail, canisters would be placed on support cradles by remotely controlled cranes.

(b) Multiple Containment Barriers. The original repository design included the tunnel, floor, and support cradle. Modifications now call for enhancing containment by adding an outer ceramic coating to the waste canisters, placing an umbrella-like drip shield over them, and backfilling the tunnels.



(c) Waste Canisters. Nuclear waste would be stored in double-walled, cylindrical canisters 2 m in diameter and up to 6 meters long. The initial design called for the canisters' inner wall to be made of a corrosion-resistant, high-nickel alloy almost 2 cm thick. For structural strength, the outer wall was to be carbon steel almost 10 cm thick. Recent modifications reverse the two layers.

diameter and up to 6 meters long, with the canisters nestled end to end along reinforced storage tunnels. Once the repository is filled with waste (at least 70,000 tonnes), remote sensors would monitor the canisters, tunnels, and surrounding rock to make sure they function as predicted. During the first 100 years, waste could be retrieved should problems arise. Eventually, all shafts, access ramps, and tunnels would be sealed.

Two key reasons for studying Yucca Mountain as a burial site for nuclear waste are its dry climate and deep water table. The first minimizes water that could seep through the repository, corroding waste canisters and carrying off radionuclides. The mountain averages only 15 centimeters of rain a year. Of this, about 95 percent evaporates quickly, and most of the rest is taken up by plants and lost via transpiration. Only 1 or 2 percent actually soaks into the ground and percolates downward.

The mountain's low water table enables building a repository that is deep underground (300 meters) yet still in the unsaturated zone, well above the water table (another 240 to 300 meters lower). For waste radionuclides to pose a danger to the public, they will have to reach the water table and, through it, infiltrate the wells supplying water to Amargosa Valley. Several hundred meters of unsaturated rock beneath the repository pose a formidable barrier to this pathway. In addition, groundwater in the region is trapped in a closed desert basin and does not flow into any rivers that reach the ocean.

Still, rock at the depth of the potential repository contains some water. When nuclear waste is first stored in the mountain, heat from its fission products will dry out the rock, pushing moisture away from the tunnels. After about a thousand years, however, the short-lived fission products will have decayed, the temperature will drop, and

water will rewet the surrounding rock. If some of the canisters have failed by then—if they have pinholes from manufacturing defects such as weak welds—dripping water could penetrate them and start dissolving radionuclides. There are many unknowns about the behavior of manmade materials subjected to heat and radiation for so long; the failure rate could accelerate, releasing more and more radionuclides into the surrounding rock.

The presence of minerals that could sop up the radionuclides is a third reason for studying Yucca Mountain as a storage site. The mountain comprises layers of volcanic tuff that were deposited millions of years ago. Many of these tuffs contain zeolites, hydrous aluminosilicate minerals that have a cagelike structure.

Zeolites are commonly used to soften hard water. Calcium and magnesium ions in water flowing through the zeolites exchange with sodium ions in the

zeolite structure and remain trapped: hard water flows in, softened water flows out. The zeolites could similarly trap radionuclides that have dissolved in groundwater. Some of the mountain's layers of zeolitic tuff also contain clay, another sorbing material. The zeolites and clay could effectively remove strontium and cesium and, to a lesser but still significant extent, uranium, plutonium, neptunium, and other transuranics that have leached into groundwater seeping through the repository and toward the water table.

Modeling the Mountain

Work at Los Alamos in developing a radionuclide transport model for Yucca Mountain began by incorporating the mountain's stratigraphy into computational grids. Using techniques that ranged from x-ray diffraction and fluorescence to microautoradiography and potassium/argon dating, we analyzed hundreds of borehole samples taken from the mountain. The picture that emerged from these and other analyses is that the mountain is composed of alternating layers of welded and nonwelded tuff—volcanic ash—that are tilted, fractured, faulted, and locally altered to zeolites and clay minerals (Figure 3).

The welded tuff consists of dense, nonporous deposits that have been hardened by heat and pressure and are typically highly fractured. By contrast, the nonwelded tuffs are soft, porous deposits that contain few fractures. Three significant zeolitic layers underlie the repository site: one in the unsaturated zone, one in the saturated zone, and one that slopes downward through both zones. A thin layer containing clay and zeolites also stretches beneath the repository.

One important finding from our rock analyses is that zeolites and clays pose effective natural barriers to radionuclide migration. Sorptive zeolites (clinoptilolite and mordenite) offer the most massive and mappable barrier. Whether their interactions are strong,

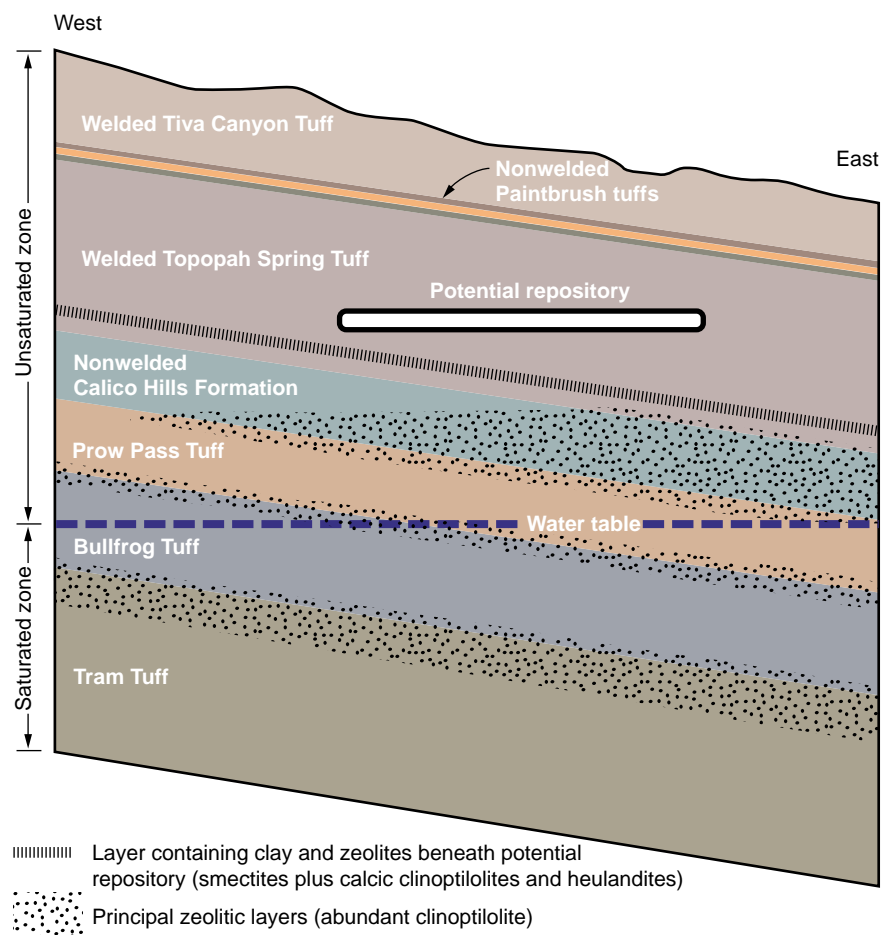


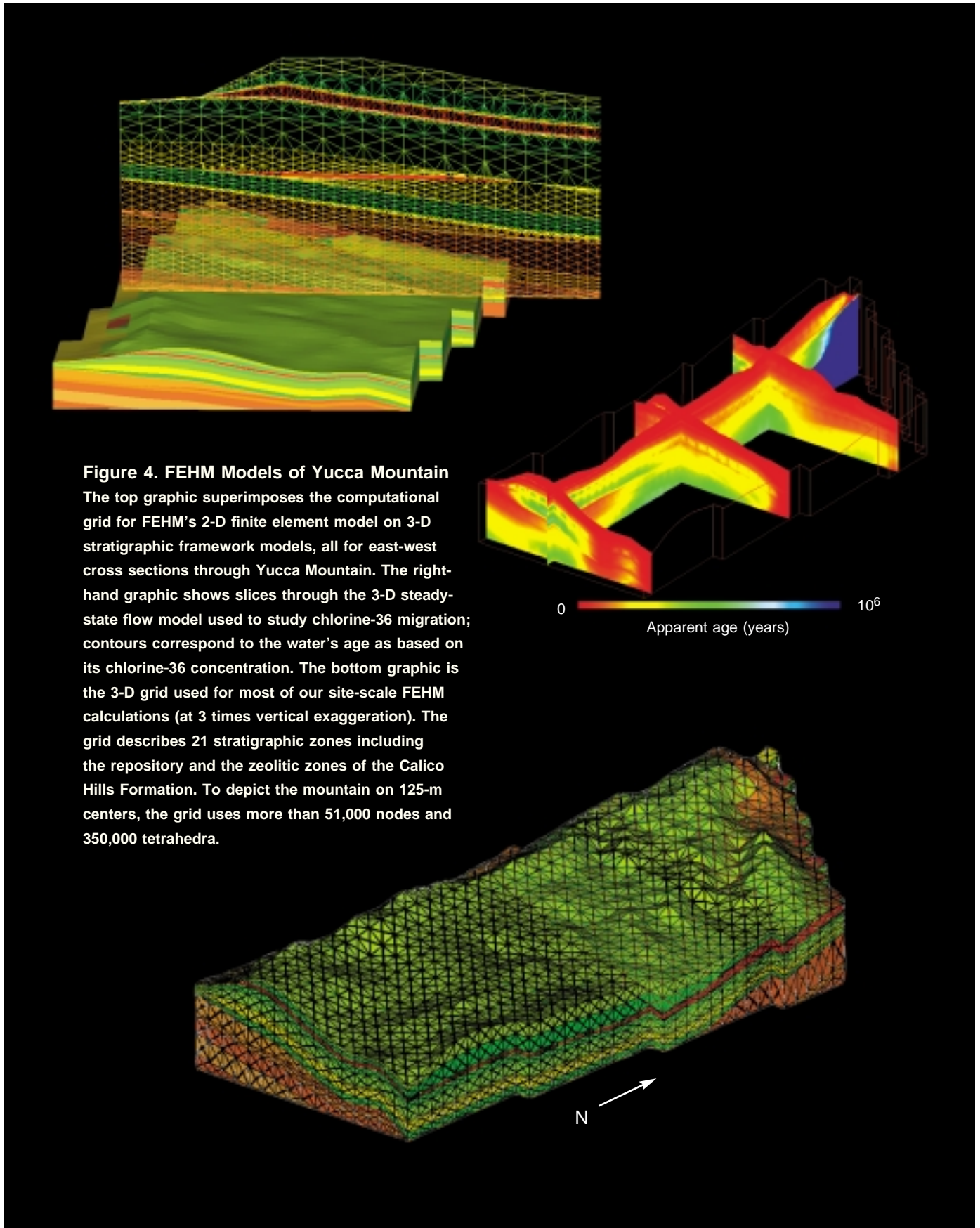
Figure 3. Yucca Mountain Stratigraphy

This east-west cross section of Yucca Mountain shows the potential repository relative to the water table and principal rock strata. The main upper layers of volcanic ash alternate between welded tuff (highly fractured, dense volcanic deposits) and nonwelded tuff (highly porous deposits with few fractures). The clay-altered layer of nonwelded Paintbrush tuffs above the repository is expected to impede the percolation of water from the mountain's surface toward the repository. The zeolitic layers beneath the repository could filter out or slow down radionuclides that escape the repository's engineered containment barriers and move toward the saturated zone. (Note: the vertical scale in this cross section is exaggerated.)

as with strontium and cesium, or weak, as with neptunium, their sheer abundance makes them a formidable obstacle to radionuclide transport. Smectite clays are not so abundant, but their widespread occurrence ensures that all transport pathways will eventually encounter them. The clays' strong affinity for plutonium and moderate affinity for neptunium make them an effective barrier. One other mineral group, manganese oxides, should also function as a barrier. Although these oxides are not

so abundant or widely distributed as the clays (and consequently not "mappable"), they commonly coat fracture surfaces in both the saturated and unsaturated zones. Their strong interaction with neptunium should impede the latter's transport through fractures.

Our transport model incorporates these various stratigraphic layers, including their mineral compositions, porosities, fault locations, and fracture densities. It also incorporates hydrological data from the U.S. Geological



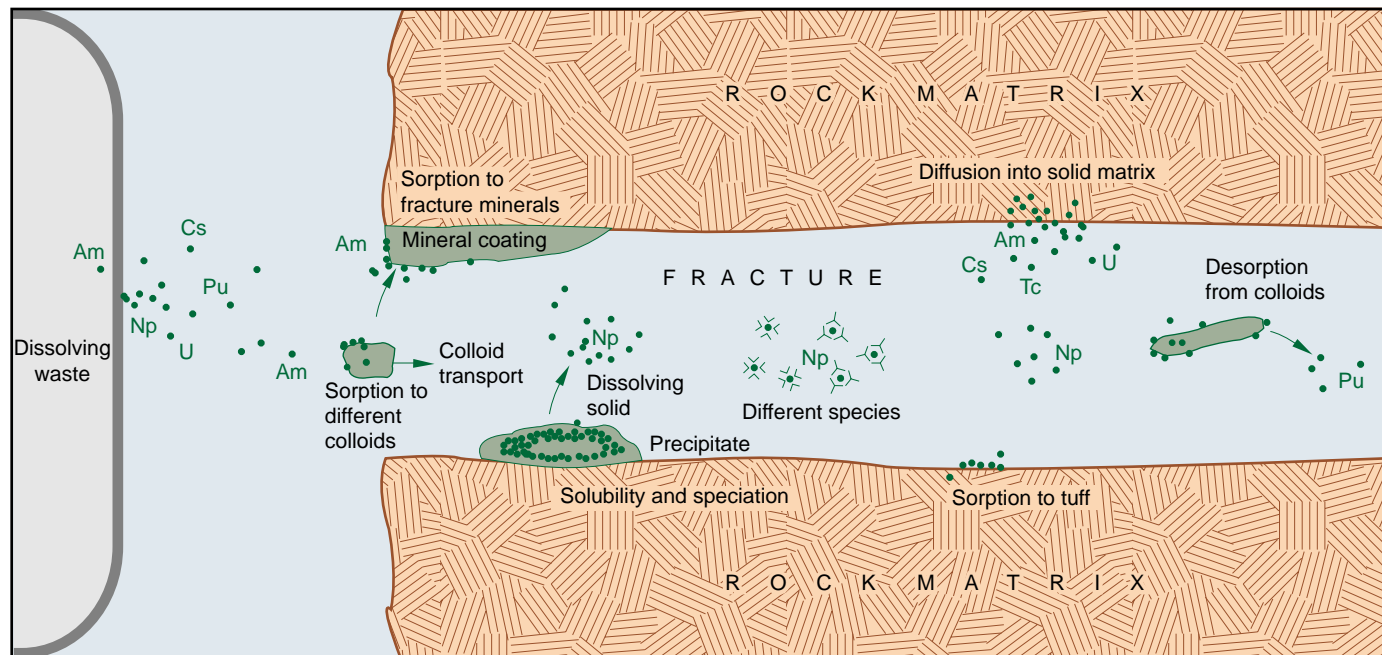


Figure 5. Geochemical Factors for Radionuclide Transport

This cartoonlike depiction of a breached waste canister shows how dissolved radionuclides could escape from the repository through water-filled rock fractures and how the surrounding rock matrix could impede their escape. To assess the effectiveness of Yucca Mountain's geologic barriers in slowing radionuclide transport, we have conducted laboratory-scale experiments to learn how soluble the radionuclides, particularly neptunium-237, would be in mountain groundwater, to what extent they would be removed from the water by sorption onto mountain tuffs and fracture minerals or by diffusion into the rock matrix, and how colloids (nanometer-sized particles) would affect their transport through rock fractures. Data from these studies are important in defining the chemical and physical parameters for our modeling.

Survey and from Lawrence Berkeley National Laboratory. These data include rock matrix and fracture permeability, residual water content in the tuff, and a spatial map of precipitation infiltration along the mountain's surface. Finally, the model incorporates radionuclide transport properties derived from extensive laboratory experiments, such as radionuclide solubilities in Yucca Mountain groundwater, sorption coefficients for the various tuffs, and diffusion coefficients for the movement of dissolved radionuclides in the rock matrix.

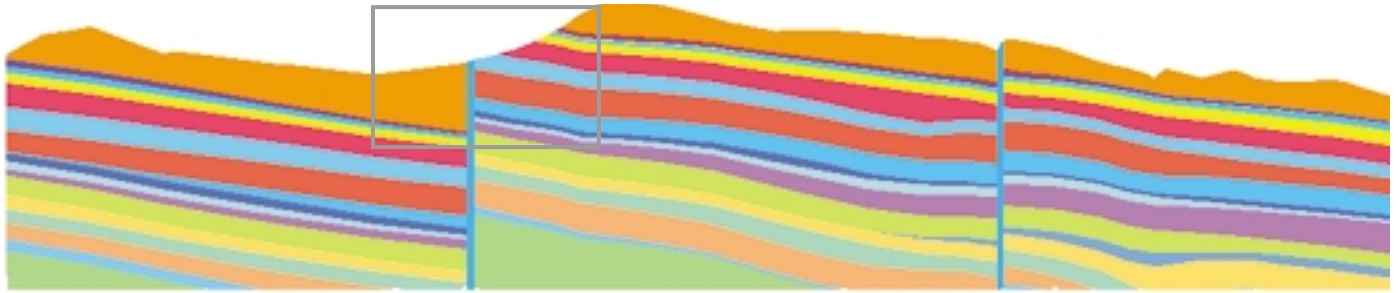
The nexus for all these data is FEHM—a finite element heat- and mass-transport code. FEHM solves the equations of heat and mass transport in porous and fractured media in two or three dimensions. The code also offers a comprehensive set of models for simulating the transport of dissolved species in either the gas or liquid phase. It

combines the capability of simulating transport using either finite element or particle-tracking solutions with a dual-permeability capability that captures the effect of fractures on flow and transport.

The code is linked to software that produces finite element computational grids that not only preserve the site's hydrostratigraphic structure but also honor the numerical conditions needed to perform accurate simulations. The grids, or meshes, are made of triangles for 2-D models and tetrahedra for 3-D models (Figure 4). Using the physical and chemical properties we have tied to each node in the calculation grids, FEHM calculates, in discrete spatial and temporal steps, the transport of individual radionuclides through the mountain. (See the box on the following two pages for an explanation of mesh generation.)

Figure 5 shows the geochemical factors for radionuclide transport that we

have focused on in assessing the effectiveness of Yucca Mountain's geologic barriers. Percolating groundwater is the primary carrier for the radionuclides, which are all soluble in water to some extent. After dissolving, they must travel through the repository's backfill and heat-altered tunnel walls, through the unsaturated rock beneath the repository, and finally through the saturated zone's groundwater flow system. In addition to the hydrologic processes that are important to radionuclide migration, transport processes such as sorption onto minerals and diffusion into dead-end rock pores will control the ultimate movement of radionuclides. Findings at the Nevada Test Site of colloid-facilitated transport for actinides have added yet another process of concern, which is discussed in the box on page 490). To be credible, our transport models must account for all these processes.



(a) Geological Model of a Cross Section at Yucca Mountain

Mesh Generation for Yucca Mountain

Carl W. Gable

To model the transport of waste radionuclides through Yucca Mountain, we must generate a grid, or mesh, on which our FEHM calculations can be run. Our primary tool for generating, optimizing, and maintaining computational meshes is LaGriT (for Los Alamos Grid Toolbox), a general-purpose software package. LaGriT is a spinoff of X3D, which was developed in the 1980s by Harold Trease.

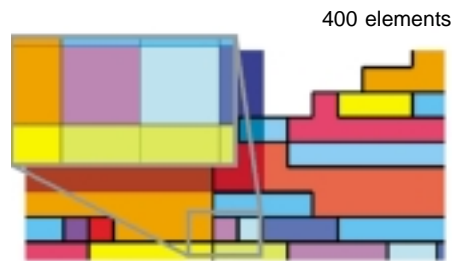
Developed in the 1990s, LaGriT is a collaborative product of the Applied Physics, Theoretical, Earth and Environmental Science, and Computing, Information, and Communications Divisions at Los Alamos. It has been used to model such varied phenomena as shock physics, combustion, semiconductor devices and processes, biomechanics, the evolution of metallic microstructure, porous flow, and seismology.¹

A mesh consists of nodes (points) at specific locations in space that are connected to form elements. These elements can be triangles or quadrilaterals in 2-D models and tetrahedra, hexahedra, prisms, or pyramids in 3-D models. The elements fit together like the pieces of a puzzle to represent physical systems such as the rock layers in Yucca Mountain, a human knee joint, or a semiconductor chip. Physical quantities such as pressure, temperature, or density, which are continuous

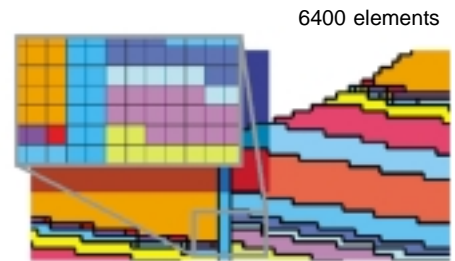
in real materials, are usually represented by discrete values at the nodes or within the elements.

Mesh generation draws on both creativity and advanced mathematical algorithms. As Thompson et al. (1999) note, grid generation is “still something of an art, as well as a science. Mathematics provides the essential foundation for moving the grid generation process from a user-intensive craft to an automated system. But there is both art and science in the design of the mathematics for . . . grid generation systems, since there are no inherent laws (equations) of grid generation to be discovered. The grid generation process is not unique; rather it must be designed.”²

a $10 \times 10 \times 10$ grid of hexahedral elements. If we double the resolution to a $20 \times 20 \times 20$ grid, the total number of elements goes from 1000 to 8000. In addition, if the calculation involves modeling the change over time of a quantity such as saturation, doubling the resolution may require cutting the time steps in half, which doubles the computer time needed. Overall, then, doubling the calculation’s resolution will increase calculation time by a factor of 16. Although high resolution best represents complex geometry and produces the most accurate physics solution, it requires more elements, which result in calculations that require more computer memory and cycles.



(b) Low-Resolution Regular Mesh



(c) High-Resolution Regular Mesh

Mesh generation can be automated but never becomes automatic. Although software like LaGriT helps automate complex “meshing” operations, generating successful meshes still rests on a series of judgment calls by an expert, who must weigh many tradeoffs. For example, imagine a calculation done on

The accompanying graphics illustrate various computational grids that could be generated for modeling Yucca Mountain. Our starting point is a geological model that represents the mountain as a sequence of sloping rock layers offset by two vertical faults (a). Focusing on the boxed area around the left-hand fault, we first create a simple mesh of square elements (b). The elements’ colors correspond to those of the cross-section layers they represent

¹More information on LaGriT is available from the software’s Web site: <http://www.t12.lanl.gov/~lagrit/>.

²*Handbook of Grid Generation*. 1999. J. F. Thompson, B. K. Soni, and N. P. Weatherill, Eds. New York: CRC Press, p. iii.

and thus also to the layers' varying material properties (such as density and porosity).

The low-resolution squares in (b) do a poor job of representing the geology. The vertical fault is lost and individual rock layers are nearly lost because the mesh is so coarse. We can improve the mesh by increasing its resolution: the squares in (c) are one-quarter the size of those in (b). Now the geology is better represented, although the interfaces between rock layers are still represented by jagged stair steps. Also, only the thickest layers are represented by contiguous elements; thin layers and small features are still lost in the grid's coarseness.

Another approach is to use variable mesh spacing, as shown in (d). Variable spacing allows us to "zoom in" with high resolution on some areas and maintain low resolution in others. However, variable spacing generally works well only for simple geometries in which the phenomena being modeled take place in a small portion of the entire computational domain and thus only a few areas require high resolution.

A more flexible approach is to adapt mesh resolution to the geometry of interest, as done in the quad-tree meshes shown in (e) and (f). These meshes allow cascading refinements: each element is subdivided into four elements, each of which is then subdivided into four still smaller elements, and so on.

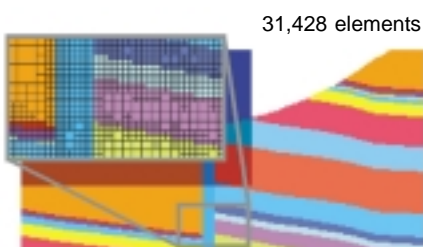
In (e) and (f), we start with the mesh of (b) and then refine only selected elements. In (e), we refine along all material interfaces by a factor of 16 but leave regions far from these interfaces at low resolution. In (f), we refine only thin rock layers by a factor of 32, increasing their resolution while maintaining lower resolution in the thick layers. In both cases, however, the number of elements is much greater than in the previous meshes, which will slow down our calculations.

Our mesh examples so far are all structured: that is, they are made of quadrilateral elements whose positions are readily defined in terms of rows and columns and whose connectivity is



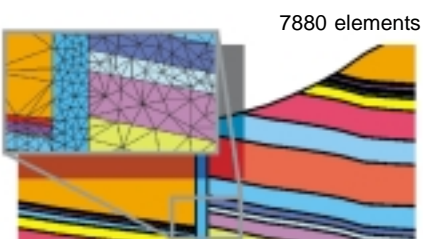
(d) Variably Spaced Regular Mesh

logical. Our last mesh examples are made of unstructured triangular elements whose connectivity is more arbitrary: for example, the nodes have varying numbers of triangles attached to them. This unstructured approach, however, allows us to create meshes that actually conform to the mountain's varied material interfaces.



(e) Quad-Tree Mesh

Both low-resolution (g) and high-resolution (h) meshes do well in representing the geologic interfaces. The high-resolution mesh, however, will do a better job solving the physics of radionuclide transport because its smaller elements can more accurately represent variations that occur over short distances. In modeling Yucca Mountain, we must also contend with phenomena that lack symmetry, have a wide range of length scales, and involve very thin

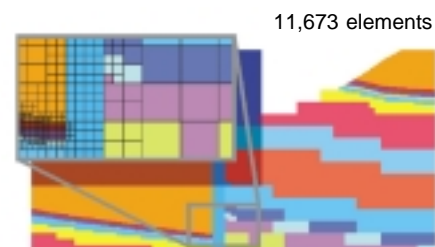


(g) Low-Resolution Triangular Mesh

layers that must be preserved as continuous. As a result, triangles in 2-D modeling and tetrahedra in 3-D modeling have been our meshes of choice.

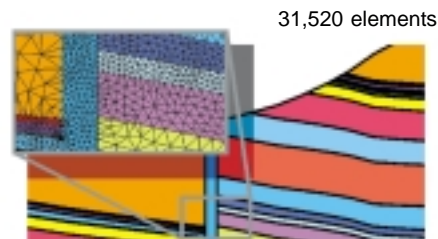
In addition to tradeoffs in how well they represent the mountain's geometry, meshes also pose tradeoffs in their suitability for different physics codes. Some codes can solve problems only on regular grids like those shown in (b)–(d). Others can use quad-tree meshes like those shown in (e) and (f) but not the unstructured meshes of (g) and (h). Thus the meshing approach must be compatible with the physics code that will be used.

Developing flow and transport models for Yucca Mountain has pushed the limits of mesh generation technology.



(f) Quad-Tree Mesh

The models' size requires us to keep the number of elements as low as possible, their complex physics requires us to accurately represent the geology of the repository site, and the need for timely results requires us to automate mesh generation whenever possible. These often conflicting demands have been met by a collaborative effort in enhancing mesh generation capabilities to meet the challenges of modeling Yucca Mountain. ■



(h) High-Resolution Triangular Mesh

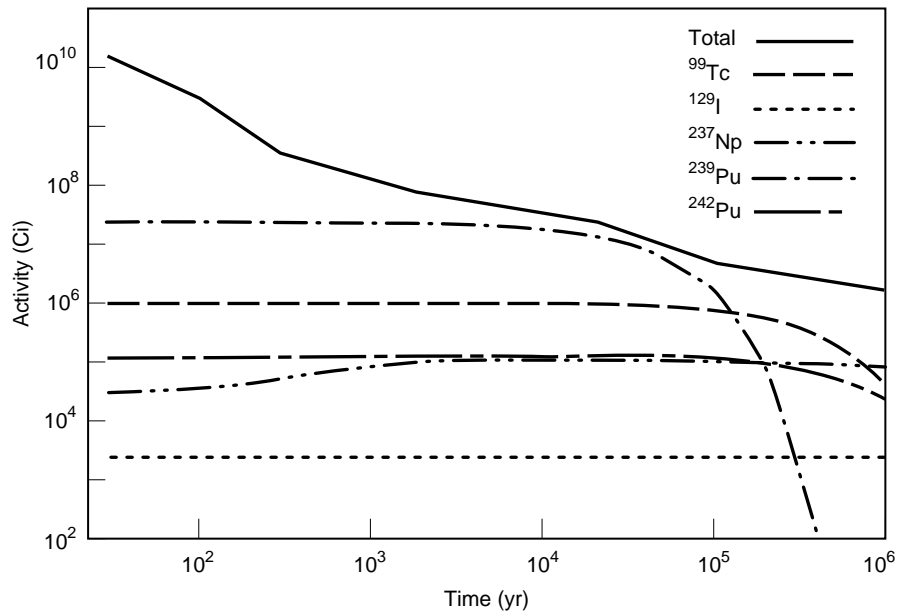


Figure 6. Radionuclide Decay Rates for Nuclear Waste

The waste's initial activity (first 1000 years) is primarily a result of short-lived fission products. Having fallen about three orders of magnitude, the remaining activity is then a result of technetium-99, iodine-129, and three long-lived actinides: neptunium-237, plutonium-239, and plutonium-242.

Neptunium Chemistry

Of the several hundred radionuclides present in spent fuel, only six are long-lived, soluble, mobile, copious, and hazardous enough to contribute significantly to calculated radiation exposures should the nuclides reach well water in Amargosa Valley. Four of them (technetium-99, iodine-129, uranium-234, and neptunium-237) could be transported by groundwater because of their high solubility and weak adsorption to minerals. The other two (plutonium-239 and plutonium-242) tend to adsorb to minerals (because of their IV oxidation state) but could be transported on or as colloids.

Although technetium-99 and iodine-129, both abundant in spent fuel, would be the dominant radionuclides to reach the valley in the first 10,000 years (Figure 6), radiation doses from them are not expected to exceed EPA limits. After 10,000 years, neptunium-237 starts to become the radionuclide of concern. While neptunium concentrations in spent fuel are small (only 0.03

percent), they will increase over time through the decay of americium-241, which has a half-life of 432.7 years. Because of its radiotoxicity, long half-life (2.14×10^6 years), high solubility, and relatively low sorption on Yucca Mountain tuffs, neptunium has been the radionuclide of prime concern in our transport calculations. Thus we have conducted extensive laboratory tests to determine its solubility, speciation, sorption, and transport. Understanding neptunium's chemical behavior is fundamental to modeling its transport.

Solubility. As in most natural aquifers, Yucca Mountain groundwater contains a number of dissolved species that can interact with the radionuclides and alter the latter's solubility. Radionuclides such as neptunium, technetium, and plutonium are also very sensitive to changes in the water's redox potential and pH. Such changes affect the stability of the radionuclides' oxidation state, which is the main parameter that controls the extent of their geochemical reactions.

Table I characterizes groundwater drawn from two saturated-zone wells and pore water found in the unsaturated zone at Yucca Mountain. Because carbonate is the predominant ligand for neptunium complexation, and because the two saturated-zone waters roughly bracket the bicarbonate concentrations found at Yucca Mountain, we have used their chemistries in our transport calculations.

Under oxidizing conditions (i.e., in water with a redox potential of >200 millivolts), neptunium will be stable in the V oxidation state, which generally has the highest solubility among actinide oxidation states. However, reducing conditions from oxygen depletion may exist in saturated-zone water at Yucca Mountain given the presence of low-valent iron. These conditions would stabilize neptunium in the IV oxidation state and reduce its solubility by several orders of magnitude. While research is still ongoing, current data strongly support the existence of some reducing groundwaters in the saturated zone at Yucca Mountain.

Carbonate concentrations, which at Yucca Mountain are in the millimolar range, will have an important effect on neptunium transport. In typical groundwaters, NpO_2^+ and the monocarbonate complex, $\text{NpO}_2\text{CO}_3^-$, are the predominant neptunium solution species. With decreasing carbonate concentration, NpO_2^+ and, to a lesser extent, the first hydrolysis product, $\text{NpO}_2\text{OH}(\text{aq})$, will dominate the solution speciation. Changes in species composition and charge will change neptunium's sorption, which in turn will alter its transport characteristics. Speciation changes may be expected in different site-specific groundwaters and when going from unsaturated- to saturated-zone water.

Under different physicochemical conditions, neptunium can either accumulate and form a precipitate after oversaturation or be transported by groundwater as dissolved or particulate species. Over time, the precipitates formed initially may transform to more thermodynamically stable and thus less

Table I. Chemistry of Yucca Mountain Groundwater

Concentrations of the major dissolved species in water from two saturated-zone wells and in pore water from the unsaturated zone. In our calculations, we have used the two saturated-zone waters to bracket the water chemistries expected at the potential repository.

Species	Saturated-Zone Well Water (mg/L)		Unsaturated-Zone Pore Water (mg/L)
Sodium	45	171	26–70
Bicarbonate	143	698	20–400
Calcium	12	89	27–127
Potassium	5	13	5–16
Magnesium	2	32	5–21
Sulfate	18	129	39–174
Nitrate	10	<0.1	0–40
Chloride	6	37	34–106
Fluoride	2	4	–
Silicon	30	30	72–100
pH	6.9	6.7	6.5–7.5
Eh (mV) ^a	340	360	400–600 ^b

^aRedox potential
^bMay be lower locally

soluble solid phases. Despite the importance of carbonate for neptunium speciation in solution, however, solid Np(V) carbonates with the general formula $MNpO_2CO_3 \cdot nH_2O$, where M is any alkali, are not likely to be stable because of the low concentrations of alkali metal cations in Yucca Mountain groundwaters. Thus, solid Np(V) oxides and/or hydroxides determine neptunium's solubility in mountain groundwaters. At redox potentials lower than about 300 millivolts, Np(IV) oxide/hydroxide is the solubility-controlling neptunium solid, with Np(V) predominating in solution.

In transport and dose calculations, our current solubility limit for neptunium is about 10^{-4} molar, with minimum and maximum values of about 10^{-6} and 10^{-3} molar, respectively. By comparison, the solubility limit for plutonium is around 10^{-8} to 10^{-7} molar, three orders of magnitude lower than that of neptunium. Plutonium's lower solubility results from the existence of Pu(IV) in the solid state. Neptunium's much greater solubility drives the search to find reducing conditions as an addition-

al barrier to neptunium transport at Yucca Mountain.

Sorption. Once groundwater dissolves the radionuclides and begins to carry them away from the repository, their sorption on mineral surfaces is the main geochemical mechanism for limiting their migration. As described earlier, Yucca Mountain is composed of a thick (>1.5 kilometers) layered sequence of volcanic tuffs and lavas (see Figure 3).

To determine the mineral composition of these layers, we analyzed thousands of core samples from the many wells that penetrate the mountain and surrounding area. These analyses show that the tuffs can be classified as vitric, devitrified, and zeolitic. Vitric tuff is composed primarily of volcanic glass fragments. Devitrified tuff, present in more than half the layers, is composed of glass fragments that have crystallized into an assemblage of feldspars and silica minerals, forming densely welded stratigraphic units. Zeolitic tuff is composed mostly of volcanic glass that has been altered to zeolites.

To characterize the transport behavior of radionuclides within these layers, we measured radionuclide sorption onto the tuffs and, for comparison, onto pure, well-characterized minerals. Crushed tuff and mineral samples were equilibrated with groundwater typical of Yucca Mountain before the radionuclides were added. From the measured amounts of radionuclides remaining in solution (C) and sorbed onto the substrate (F), we then calculated the batch sorption coefficient, $K_d = F/C$.

The K_d value (in milliliters per gram) is the ratio of moles of radionuclide per gram of solid phase to moles of radionuclide per milliliter of solution. A large K_d value indicates high sorption on the mineral or tuff.

Table II gives values for neptunium and plutonium sorption onto samples of vitric, devitrified, and zeolitic tuff and onto several minerals. As expected, the highest sorption coefficients for neptunium are obtained for zeolitic tuff and clay-bearing vitric tuff. The same sorption behavior would be expected for neptunium and plutonium ions in the same oxidation state. The fact that plutonium has a much higher retention via sorption than neptunium most likely reflects the nuclides' presence in different oxidation states: Np(V) and Pu(IV). The low sorption of neptunium is due to the small charge-to-radius ratio, the large size, and the low tendency for complexation reactions of the neptunyl ion (NpO_2^+). Because of steric effects, the sorption mechanism for neptunium onto a zeolite may be a surface reaction rather than cation exchange within the zeolite's cagelike structure.

We found that neptunium sorption for multiple tuff samples is actually rather variable. Some zeolitic, vitric, and devitrified tuff samples have almost no affinity for neptunium, whereas other samples with similar mineral compositions show sorption coefficients in the range of 5 to 10 milliliters per gram (mL/g). This variation suggests that the favorable sites for sorption are associated with some minor mineral phases, such as iron oxides or clays,

whose abundance varies in the tuff. Indeed, the largest values for neptunium sorption in Table II are for the pure minerals hematite (an iron oxide) and calcite (calcium carbonate) and for smectite (a clay). Experiments with pure clinoptilolite, a common zeolite in Yucca Mountain tuffs, and tuff samples containing significant amounts of clinoptilolite show that neptunium sorption increases with decreasing pH, contrary to the sorption of other radionuclides onto zeolites. Given the relative abundance of clinoptilolite at Yucca Mountain, we have found that a reasonable approach for predicting the sorption of neptunium onto zeolitic tuffs is to assume that clinoptilolite is the only sorptive mineral present.

Because one of the main components of Yucca Mountain groundwater is bicarbonate, we also examined how neptunium sorption is influenced by the groundwater's carbonate content and ionic strength. Although calcite showed an increase in neptunium sorption as carbonate content and ionic strength increased, zeolitic tuff showed a decrease in sorption. Such behavior is indicative of different sorption mechanisms for the two substrates.

Sorption Mechanisms. If we assume that clinoptilolite is the only sorbing phase for zeolites and calculate values of K_d divided by the solid-phase surface area, we find that neptunium sorption onto a series of tuff samples is correlated with surface area (Figure 7). This correlation again suggests that sorption is a surface reaction rather than cation exchange throughout the volume of the zeolite. Based on such data, we feel that neptunium sorption onto Yucca Mountain minerals is governed by surface complexation on a variety of oxide phases and by coprecipitation and surface adsorption involving carbonate minerals, such as calcite.

The surface-complexation mechanism appears to be relatively insensitive to variations in ionic strength, groundwater composition, and pH values between 6.5 and 8.5.

Table II. Comparison of Sorption Coefficients for Neptunium and Plutonium

Samples	K_d (mL/g) ^a		
	Neptunium		Plutonium
	pH = 7	pH = 8.5	pH = 7
Tuffs			
Zeolitic tuff	0.30	1.5	300–500
Devitrified tuff	0.007	–0.04	40–100
Vitric tuff	0.2	0.3	600–2,000
Vitric tuff with 10% clay	–8	–	–
Minerals			
Quartz	–0.1	–0.2	<10
Albite	–0.08	–0.1	3–10
Calcite	–	50	200–1,000
Hematite	70	600	>10,000
Clay			
Smectite	80	–	–
Zeolite			
Clinoptilolite	2.6	1.4	600–3,000

^aNegative values are due to uncertainties in the data (± 0.5).

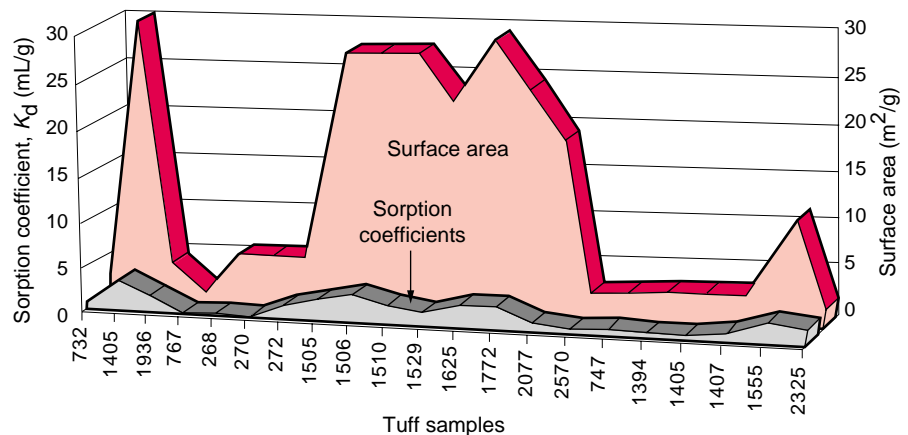


Figure 7. Correlation of Neptunium Sorption and Tuff Surface Area Comparison of the coefficients for neptunium sorption onto various tuff samples and the samples' surface area shows the two values to be correlated. The sorption coefficients are for neptunium solutions in typical Yucca Mountain groundwater under atmospheric conditions and at initial neptunium concentrations of about 10^{-7} M.

This mechanism is likely responsible for the 0.5- to 5.0-mL/g range in neptunium sorption coefficients measured in many different rock samples. The high end of this range may reflect secondary mechanisms, such as the reduction of Np(V) to Np(IV) on mineral surfaces

containing ferrous iron, making the actinide more strongly sorbing. Because of these uncertainties concerning sorption mechanisms, we have used a probability distribution for neptunium sorption coefficients in our transport calculations for Yucca Mountain.

Dynamic Measurements. In contrast to the batch sorption equilibrium measurements discussed above, the migration of radionuclides through tuff is a dynamic, nonequilibrium process. Thus, we needed to confirm our equilibrium measurements by carrying out dynamic transport experiments. We did this by eluting radionuclide solutions through columns of washed, crushed, and saturated Yucca Mountain tuff, using the same tuff as in our batch sorption experiments. (Migration through a solid rock column under unsaturated conditions would require more time than was feasible for our work.)

The arrival time for neptunium at the bottom of the column was consistent with the sorption coefficients measured in our batch sorption experiments. Consequently, we can predict the retardation of neptunium transport simply by using the equilibrium sorption coefficient. However, while the elution time was accurately predicted, the amount of eluted radionuclide differed from modeling predictions. The radionuclide did not travel uniformly through the column but arrived dispersed, probably because of variable path lengths through the rock.

A key implication of these dynamic measurements is that the use of batch sorption values in site calculations will yield conservative predictions. In other words, the predicted radionuclide transport times to the repository's site boundary (defined as 5 kilometers distant) will be shorter than actual travel times. Thus, if the simulations show that the natural rock barriers effectively impede neptunium transport, then uncertainties associated with neptunium sorption mechanisms will only improve the barriers' effectiveness over our predictions for them.

Matrix vs Fracture Flow

Another key issue for radionuclide transport is groundwater flow—how quickly will water move through the mountain and what pathways will it fol-

low? Early theories ranged from a “tin roof” scenario in which the upper thin layer of nonwelded tuffs acts as a relatively impervious barrier, diverting water laterally and drastically reducing percolation through the repository, to a scenario of rapid flow along major faults and fractures that allows water to infiltrate the repository within only a few decades. Our studies have shown the actual flow mechanisms to be a bit more complex than either of these two extremes.

To assess the movement of groundwater through Yucca Mountain, we began by looking at how water enters its upper surface. Scientists from the U.S. Geological Survey have measured infiltration rates, conducting neutron assays of soil moisture to a depth of 75 meters. By balancing such parameters as precipitation, runoff, evaporation, soil thickness, plant transpiration, and hydraulic rock properties, they developed a spatial map of infiltration across the surface of the mountain. According to this map, infiltration is highest along the crest, where rain clouds accumulate and soil cover is almost nonexistent, and much lower where thick alluvial deposits and relatively abundant plant life lead to high rates of evapotranspiration.

Next, we augmented the survey data by examining the water content in rock samples taken from deeper within the mountain. As wells were bored, we analyzed pore water trapped in core samples at various depths to determine its age and infiltration rate. Also, when an exploratory tunnel was drilled into the mountain, we collected hundreds of rock samples at regular intervals along its length. This 8-kilometer-long, U-shaped tunnel descends to the level of the potential repository and parallels the repository's eastern boundary along its own curved base (see Figure 1). The tunnel intersects major fractures in the mountain that are due to faulting, tilting, and block rotation in the distant past.

We analyzed the pore water in these rock samples for its chlorine concentration. Because chloride salts are highly

soluble, they dissolve in rainwater and move into the mountain with the infiltrating water. Once water has traveled through the upper soil zone, where it can evaporate or be taken up by plants, its chloride concentration remains relatively constant. Comparing the chloride concentration in pore water below this zone with that in rainwater yields a measure of how much water has been lost to evaporation and, thus, allows us to determine net infiltration rates for the mountain.

In addition, chlorine has a radioactive isotope, chlorine-36, that is produced naturally in the atmosphere by the interaction of cosmic rays with argon. Because the amount of chlorine-36 so generated has changed over the ages and because the isotope's half-life is 300,000 years, the ratio of chlorine-36 to stable chlorine ($^{36}\text{Cl}/\text{Cl}$) in groundwater serves as a measure of the water's age.

Looking back tens of thousands of years, we find that the $^{36}\text{Cl}/\text{Cl}$ ratio has varied because of variations in chloride deposition rates (perhaps due to climate changes) and variations in chlorine-36 production (due to changes in the earth's geomagnetic shielding). A broad-brush picture shows a bimodal distribution: a fairly constant $^{36}\text{Cl}/\text{Cl}$ ratio of about 5×10^{-13} over the last 10,000 years (the Holocene signal) and an elevated ratio of about 10×10^{-13} before that period (the Pleistocene signal). We confirmed this bimodal distribution by analyzing fossilized pack-rat middens (replete with crystallized urine) for chlorine-36 and plotting the measurements against their radiocarbon ages.

During the 1950s and early 1960s, a chlorine-36 spike occurred when atmospheric nuclear tests in the South Pacific significantly increased the isotope's production rate. The resulting $^{36}\text{Cl}/\text{Cl}$ ratio rose above 15×10^{-13} . This “bomb pulse” can be used to test for recent groundwater, such as would be expected if water infiltrated Yucca Mountain by way of fast transport paths through fractures and faults.

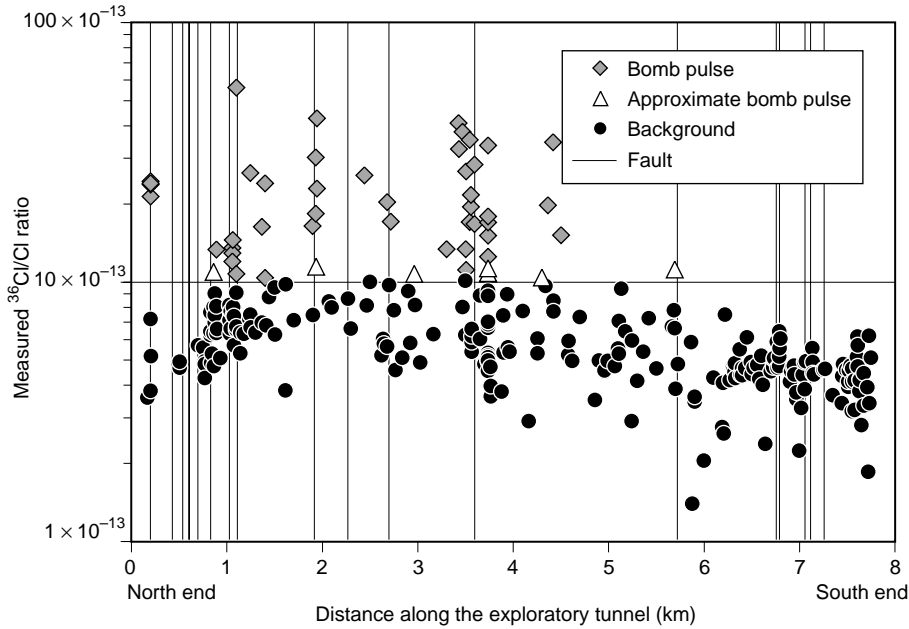


Figure 8. Distribution of $^{36}\text{Cl}/\text{Cl}$ Ratios in Pore Water from Exploratory Tunnel Rock Samples

Most bomb-pulse water is associated with faults (vertical lines). At the southern end of the tunnel, however, no bomb-pulse water was found even though faults are present. At both ends of the tunnel, but especially at the south end, the $^{36}\text{Cl}/\text{Cl}$ ratio drops off, indicating that these regions contain predominately Holocene water (<10,000 years old). By contrast, the north-central part of the tunnel has predominately Pleistocene water (>10,000 years old). These variations likely result from the changing thickness of the Paintbrush tuffs above the tunnel: where they are thicker, the travel time for water is longer.

When the pore-water data from the tunnel rock samples were examined statistically, we found four distinct sets of $^{36}\text{Cl}/\text{Cl}$ ratios. The two main ratios were the expected Holocene and Pleistocene signals. A small set of lower ratios in which chlorine-36 had noticeably decayed may represent water that is 300,000 years or more old. Finally, a small set of elevated $^{36}\text{Cl}/\text{Cl}$ ratios (12×10^{-13} and greater) represents very young bomb-pulse water.

We found a strong correlation between the distribution of bomb-pulse water and major faults (Figure 8). For example, 58 percent of the bomb-pulse samples were within 10 meters of a fault, and 75 percent were within 30 meters. We also found a strong correlation between the age of the water and the thickness of the nonwelded layer of Paintbrush tuffs that lies between the

mountain top and both the potential repository and the exploratory tunnel. Pore water at the tunnel level was younger Holocene water where the layer is thinner and older Pleistocene water where it is thicker. Thus the nonwelded tuffs, which resemble spongy, hard-packed sand, apparently impede the downward flow of water. Only where a major fault intersected this tuff layer did any young bomb-pulse water reach the tunnel.

A simulation that assumes a constant water infiltration rate of 0.5 millimeter per year (mm/yr) shows general agreement with the chlorine-36 data (Figure 9). Bomb-pulse water moves rapidly through the upper layer of welded and highly fractured Tiva Canyon Tuff, but the nonwelded Paintbrush tuffs keep most water from percolating down into the Topopah Spring Tuff, which in-

cludes the tunnel and the repository site. In the northern half of the tunnel, most water in the Topopah Spring Tuff is at least 10,000 years old. In the southern half of the tunnel, where the Paintbrush tuffs are thinner, Holocene water as young as 1000 years old is found. Exceptions to this age pattern occur at major faults, where a small fraction (1 or 2 percent) of the water in fault zones at the repository level is bomb-pulse water that moved quickly to that depth.

Despite the general agreement between the simulation and chlorine data, however, there were some discrepancies in the details. In particular, the predicted bomb-pulse signal at the southern end of the tunnel did not appear in the pore-water samples. Nor does the simulation agree with the U.S. Geological Survey data, which indicate a spatially varying water infiltration rate. In fact, when we use the survey's infiltration rate in our simulations, predictions and experimental data are even more at odds. There is no flow of bomb-pulse water along fault fractures, and the distribution of the water's age is relatively uniform throughout the tunnel rather than changing as the thickness of the Paintbrush tuff layer changes.

However, our measurements of total chloride concentrations in pore water also differ from the survey results—for instance, infiltration rates toward the southern end of the tunnel appear to be lower than those deduced from the surface measurements. Lower infiltration rates would account for the fact that no bomb-pulse signal has been detected in faults in the southern half of the exploratory tunnel.

Thus the mere presence of major faults may not, by itself, result in fast water flow. Solutes can also travel by molecular diffusion into the surrounding rock matrix, where flow rates are apt to be orders of magnitude lower. A wide body of evidence, both theoretical and experimental, suggests that matrix diffusion is an important transport mechanism in fractured media. If the

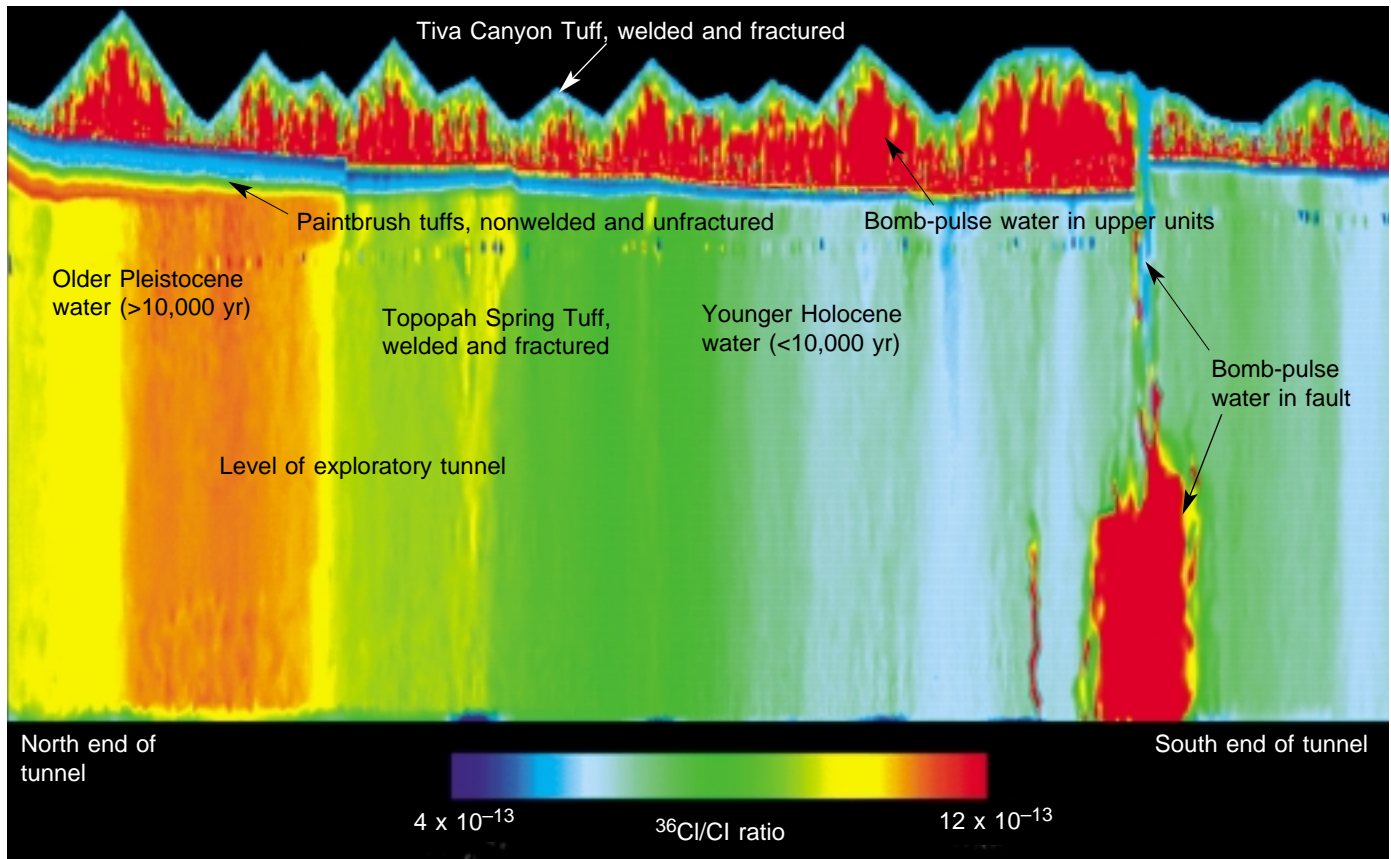


Figure 9. Simulation of $^{36}\text{Cl}/\text{Cl}$ Ratios in Yucca Mountain Groundwater

This simulation, which contains only one fault, generally agrees with analyses of the pore water in rock samples from the exploratory tunnel. Water moves rapidly through the upper Tiva Canyon layer of welded and highly fractured tuff. The next layer of nonwelded, unfractured, and porous Paintbrush tuffs, however, significantly impedes water flow. Thus, most of the young bomb-pulse water (red) remains in the Tiva Canyon Tuff. In the northern end, by the time water seeps through to the Topopah Spring Tuff—another welded, highly fractured layer—it is at least 10,000 years old (orange and yellow). Where the Paintbrush layer is thinner, the water is predominantly Holocene (blue and green). The exception occurs at a major fault, where a small amount of bomb-pulse water reaches the lower rock strata (red region on the right). Other simulations also predict bomb-pulse water at fault zones in the northern end of the tunnel.

infiltration rate is not high enough to support fracture flow, water will diffuse from fractures into the rock matrix, and downward flow may revert to slower percolation through the matrix.

It turns out that establishing the true infiltration rate, which ultimately governs the water flux through the unsaturated zone at Yucca Mountain, is much more important than showing the existence of fast-flow pathways. A neptunium atom cannot distinguish between water that is 50 years old and water that is 10,000 or 300,000 years old. Its transport toward the saturated zone will depend on the average net flux of water

through the repository. As the flux of infiltrating water increases, rock saturation increases. As rock saturation increases, the capillary suction of the rock matrix decreases, reducing the matrix's ability to pull water out of fractures. Thus the potential for water flow in fractures increases.

Through a process that weighs the various surface, chloride, and chlorine-36 data and that reexamines the hydrologic properties of the various strata (i.e., their porosity, matrix permeability, and fracture density), we are moving closer to establishing a valid flux rate for assessing repository performance.

At this point, we have found that using a spatially varying rate that averages 4 mm/yr yields reliable but conservative calculations. Ongoing field experiments at Busted Butte, discussed later, are helping us benchmark this parameter.

Laboratory transport tests indicate that fracture coatings also affect flow rates. These tests involved columns of Yucca Mountain tuff containing both natural and induced fractures. The natural fractures were coated with minerals that had been deposited over the eons; the induced fractures had no mineral coatings. By using a variety of tracers, we were able to sort out the

relative effects of flow through fractures, of matrix diffusion into rock micropores, and of sorption by fracture minerals. We found that because of sorption, neptunium arrived at the bottom of a column long after a nonsorbing tracer. Thus, minerals that appear to contribute insignificantly to sorption when they are present in trace quantities in the bulk rock may quite effectively retard transport when they are concentrated on fracture surfaces. Sensitivity studies are under way to assess the impact such sorptive minerals could have on radionuclide transport.

Unsaturated-Zone Transport

Our modeling studies of how effectively the natural barriers at Yucca Mountain will contain migrating waste radionuclides began with modeling travel times for neptunium through rock barriers in the unsaturated zone. To help us benchmark our modeling parameters, we are now conducting large-scale field experiments to measure the actual *in situ* transport properties of fractured rock. The experiments are under way at Busted Butte, about 8 kilometers southeast of the potential Yucca Mountain repository.

Unsaturated-Zone Simulations. We simulated neptunium transport from the repository to the water table with a site-scale model that accounts for speciation, sorption, diffusion, radioactive decay, repository heat, and both fracture and matrix flow. Figure 10 shows the results of a 2-D simulation for our base case, which used a spatially variable infiltration rate averaging 4 mm/yr and chemical data typical of Yucca Mountain groundwater: a pH of 8 with 150 milligrams per liter (mg/L) of bicarbonate, 125 mg/L of sodium, and 25 mg/L of calcium. The base case also assumed a repository design in which the density of waste canisters would lead to thermal loads high enough to boil water in the adjacent tunnel rock.

The first panel in Figure 10 shows the concentration of aqueous neptunium 2000 years after waste emplacement. By this time we assume that the waste canisters have begun to cool, that water has rewet the edges of the repository, and that some of the canisters have been breached by dripping water. Neptunium is dissolving and moving rapidly through the welded tuff below the repository via fracture flow. However, its migration is slowed significantly when it reaches the layer of Calico Hills nonwelded tuff (defined by the lower blue boundary), where matrix flow dominates.

The second panel, at 10,000 years, shows the transport plume after all repository rock has been rewet and all waste canisters are releasing neptunium. The third panel, at 50,000 years, shows the main neptunium plume reaching the water table. The aqueous neptunium concentrations are considerably reduced from those in the previous panel, mainly because of dilution with the percolating groundwater and sorption within the zeolitic tuffs in the Calico Hills layer. The final panel, also at 50,000 years, shows the concentration profile of immobile neptunium attached to zeolites. Comparison of the bottom two panels demonstrates that even though neptunium sorption onto zeolites is relatively small, it will still retard transport.

We have also carried out other base-case simulations to study the effect of varying assumptions for repository heat, water infiltration, and water chemistry. These studies indicate that the heat pulse from the decay of fission products in the waste does not significantly affect neptunium migration because the time scale of heat-pulse propagation is shorter than the time scales associated with neptunium release and migration. The major uncertainty in this conclusion is the possibility of rock/water interactions that permanently alter the rock's porosity, permeability, or mineralogy.

In regard to water chemistry, our studies show that the groundwater's pH and its calcium and sodium concentrations significantly affect how much the

zeolitic and clay-bearing tuffs in the unsaturated zone retard neptunium transport. For example, a rise in pH to 9 decreases neptunium solubility, which results in slower releases from the repository. However, it also decreases the sorption of neptunium on zeolites, which leads to more rapid migration. The decrease in sorption would dominate, resulting in shorter travel times to the water table and higher peak concentrations for the radionuclide.

Our studies also show that small-scale variations in the site's chemical and hydrologic properties can affect neptunium transport and that such variations are strongly dependent on mineral distributions. In particular, zeolite distributions influence the flow patterns of percolating water and the sorption of many radionuclides. Where zeolitic abundance is low (less than 10 percent) and, thus, where neptunium sorption coefficients are low ($K_d < 1$ mL/g), the permeability is large enough for flow to be matrix dominated, causing significant retardation by diffusion despite the low K_d values. When our simulations account for such correlations, we find that neptunium transport is significantly retarded. Its transport is slowed even more when we account for the presence of smectite clays in the rock matrix.

Overall, our studies indicate that zeolitic sorption of neptunium in the unsaturated zone results in travel times that are much longer than 10,000 years, and thus the repository's primary regulatory goal can be met for this important limiting actinide. However, our modeling work is based on measurements from small-scale laboratory experiments that do not characterize the effects of larger geologic features such as faults and stratigraphic boundaries. To characterize the effects of these heterogeneities in the unsaturated zone, we are conducting large-scale field experiments at Busted Butte.

Busted Butte Field Studies. We chose Busted Butte because two major tuff layers that underlie the potential repository—Topopah Spring Tuff and

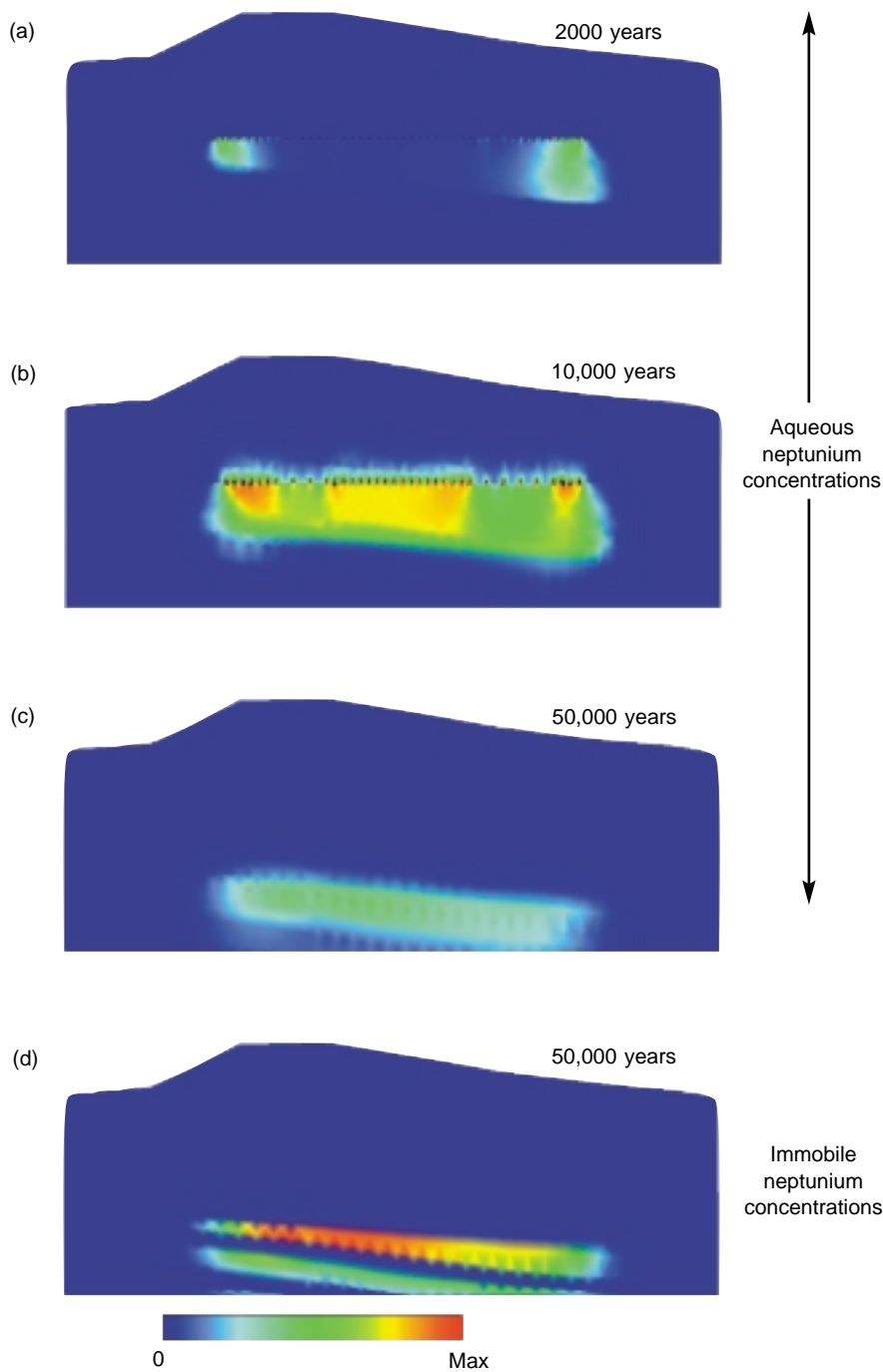


Figure 10. Simulated Neptunium Transport at Yucca Mountain
 Our base-case analysis of neptunium transport at Yucca Mountain predicts that it will take the radionuclide 50,000 years to penetrate the mountain’s rock barriers and reach the water table. The top three panels show the concentrations of aqueous neptunium as (a) the edges of the repository are rewet by water and some waste canisters begin to leak, (b) after all rock in the repository has been rewet and canisters throughout the repository are leaking, and (c) when the aqueous neptunium plume reaches the water table. Panel (d) shows the concentration of immobile neptunium sorbed onto zeolites at the same time that aqueous neptunium reaches the water table. Comparison of (c) and (d) demonstrates the effective role zeolites would play in retarding neptunium transport through sorption.

the Calico Hills Formation—are near the butte’s surface and are readily accessible. These layers are actually distal extensions of the formations beneath the repository. The Busted Butte test site is 70 meters underground and is divided into several test blocks for a series of experiments (Figure 11). The idea is to inject aqueous tracers into the rock through horizontal boreholes, mea-

sure tracer migration, and then compare those measurements with our modeling predictions.

To mimic the behavior of neptunium and other radionuclides, we are injecting a mixture of both nonsorbing and reactive tracers and synthetic microspheres. Nonsorbing, or conservative, tracers (such as bromide) move with the aqueous phase and thus track

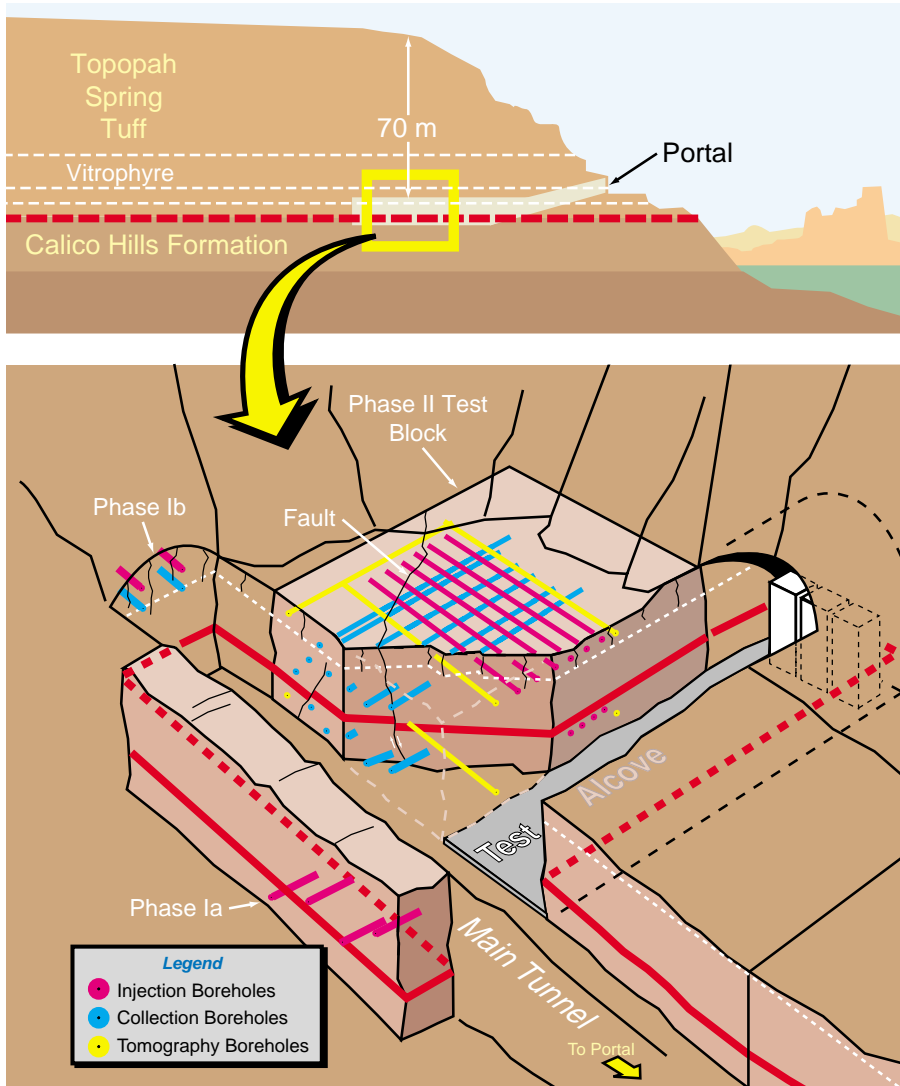


Figure 11. Busted Butte Field Test Site

Two of the repository's key unsaturated-zone tuff layers, the Topopah Spring Tuff and Calico Hills Formation, are only 70 m beneath the surface at Busted Butte. We are using these formations to measure tracer-solution transport times through large rock volumes. The site is divided into several test blocks, but the same general experimental procedure is being followed at each one: mixtures of tracers are injected through one set of horizontal boreholes and then detected either at parallel collection boreholes or by auger sampling and mineback. Comparing measured travel times for the tracers with our modeling predictions is helping us validate our transport models.

the movement of water and help determine the rock's hydrologic response. They capture processes involved in the migration of nonsorbing radionuclides such as technetium. Some of these tracers are ultraviolet fluorescent dyes (fluorescein and pyridone) that can be detected at a concentration of about 10 parts per million. Reactive

tracers (such as lithium, manganese, nickel, cobalt, samarium, cerium, and fluorescent Rhodamine WT) diffuse into the rock matrix or sorb onto minerals and are used as analogs for sorbing actinides, such as neptunium. Finally, fluorescent polystyrene microspheres mimic the transport of colloids.

Some of the Busted Butte tests will validate our flow and transport models and provide new transport data for the hydrologic Calico Hills Formation. Other tests are located in the relatively low-permeability fractured rock at the base of the Topopah Spring Tuff to provide data on fracture/matrix interactions. Phase I tests, completed this past winter, involved simple, continuous, single-point tracer injection along horizontal boreholes 2 meters long. Although designed principally to test instrumentation, these tests are also providing valuable transport data.

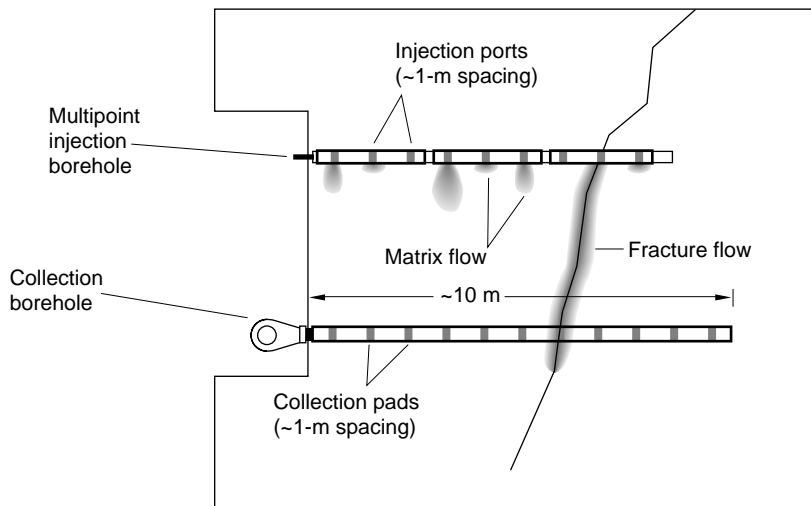
Phase II tests, currently under way, are more sophisticated and use multi-point injection systems involving eight 8.5-meter-long boreholes, each with 9 injection points (Figure 12). The large Phase II test block (7 meters high, 10 meters wide, and 10 meters deep) allows us to study how large-scale heterogeneities will affect tracer migration. The tracers are dissolved in water that has the same composition as *in situ* pore water. Injection rates vary from 1 to 50 mL/h, which correspond to infiltration rates of 30 to 1500 mm/yr. The lowest injection rates correspond to the high end of infiltration rates for Yucca Mountain; the highest injection rates are designed to obtain data on greater travel distances within the experiments' 2-year time frame.

The Phase II tests are using three geophysical techniques (based on neutron assays, ground-penetrating radar, and electrical resistance measurements) to generate 2- and 3-D images of test-block saturation before and during the experiments.

Our first results came from the Phase Ib test, which was conducted at the base of the Topopah Spring Tuff. The test used a pair of injection/collection boreholes located near a vertical fracture and an injection rate of 10 mL/h (see Figure 11). The nonsorbing tracers began arriving at the collection boreholes, which are 28 centimeters beneath the injection points, about a month after injection. For the injection rate used, pure fracture flow would have resulted

Figure 12. Multipoint Injection and Collection System for Phase II Tests

Multipoint injection and collection systems in the Phase II tests at Busted Butte are providing data on how large-scale heterogeneities, such as major fractures, affect tracer migration. The gray areas in this figure show hypothetical tracer movement, including rapid transport along a vertical fracture that intersects the injection and collection systems.



in travel times of hours to days. Although the concentration of tracers at the collection boreholes increased over the next couple of months, the tracers were detected at several collection pads on both sides of the fracture rather than just at the intercepting fracture plane.

These results indicate strong fracture/matrix interactions in the tuff, causing the tracers to diffuse from the fracture into the matrix and then move primarily by matrix diffusion. None of the reactive or colloidal tracers had reached the collection boreholes even six months after injection. Sample cores taken from the test block are currently being analyzed to determine how far these tracers traveled.

Our Phase Ia test was conducted in Calico Hills Formation tuff. In this test, we injected tracers from single points in each of four horizontal boreholes at two rates: 1 and 10 mL/h. After eight months of continuous injection, we began exposing vertical slices of the test block by mining into the rock face in stages to measure tracer migration (Figure 13). This was a “blind” test in that we used transport calculations to predict tracer movement before the mineback occurred. We are now comparing our predictions with results for the nonsorbing fluorescein tracer and are beginning to analyze samples for the reactive and colloidal tracers.

So far, it appears that strong capillary forces exist in the Calico Hills tuff



Figure 13. Mineback of Phase Ia Test in Calico Hills Tuff

In the Phase Ia test, a fluorescing tracer was injected into Calico Hills tuff from a single point in each of four horizontal boreholes (see test setup in Figure 11). After eight months of continuous injection, we exposed vertical slices of the test block by mining back the tuff in stages. In this photograph, the vertical plane passes through the injection points of the four boreholes. Ultraviolet light reveals the presence of the fluorescing tracer (yellow-green areas) around those points. The two larger fluorescent areas are a result of a 10-mL/h injection rate; the smaller areas, a 1-mL/h rate. Tracer movement appears to be mainly by diffusion through capillary flow. The upper-left borehole shows tracer diffusion in two perpendicular planes due to the presence of the left wall. The brighter yellow-green strip toward the bottom of the central fluorescent area reveals tracer accumulation at a boundary between two Calico Hills sublayers separated by 3 to 5 centimeters of silicified ash. Another boundary, this one rich in clay, passes horizontally above the upper-left borehole area, impeding upward capillary flow.

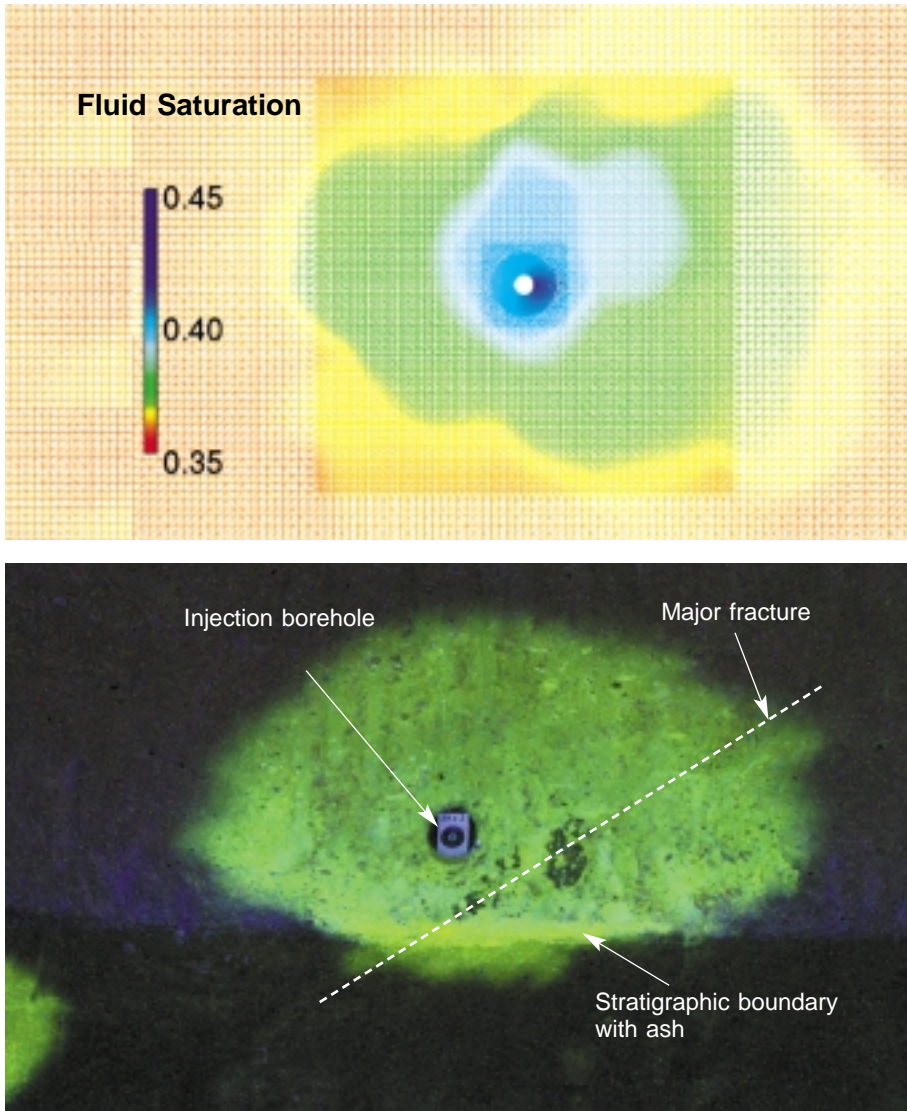


Figure 14. Capillary Flow in the Phase Ia Test vs Modeling Prediction
 The bottom photograph, which focuses on the central fluorescent area in Figure 14, shows no appreciable tracer flow along a major fracture that passes diagonally just under the injection point. The fact that the tracer has not migrated significantly along this fracture indicates that the latter is not a fast-transport pathway but instead behaves as a large pore within a porous matrix. The photo also shows tracer accumulation (brighter yellow-green strip) at a layer of ash, which impedes tracer migration. Our modeling prediction for tracer movement (top graphic) agrees well with these test results. Its asymmetrical shape for tracer migration is accurate; what was missing in our model was any provision for the stratigraphic boundary formed by the thin layer of ash. We are now modifying our codes to include the impact of such heterogeneities.

that will modulate fracture flow from overlying rock layers, thereby damping pulses of infiltrating water and providing extensive contact between radionuclides and the rock matrix. Even when injection occurs next to a fracture,

water is imbibed quickly into the surrounding matrix, and fracture flow is insignificant compared with matrix diffusion (Figure 14). Such results bode well for the performance of the repository's natural barriers: migration of

water from the fractures into the rock matrix will lead to increased contact with sorbing minerals such as zeolites and clays. The combination of matrix diffusion and sorption will lengthen radionuclide travel times.

Where no heterogeneities (such as stratigraphic boundaries) are present, our nonsorbing-tracer predictions agree very well with measurements, capturing the asymmetric migration that results from injection through a single point on one side of the borehole. Likewise, our modeling predicts the predominance of capillary flow over fracture flow in the Calico Hills vitric tuffs (see Figure 14). However, nothing was included in the model to account for boundaries between tuff sublayers; these boundaries appear to locally retard tracer migration, whether the boundary lies above or below the borehole.

The Busted Butte experiments have also uncovered two uncertainties in our modeling. In particular, we are concerned about the adequacy of continuum models to describe transport in nonwelded tuff layers with high matrix permeabilities. Our dual-permeability models appear to be more accurate in representing the flow and transport processes of an unsaturated, fractured rock mass. Another problem is how to accurately characterize the transition from fracture flow to matrix flow at boundaries between tuff layers that have different hydrogeologic properties. When completed, the Phase II tests should help us resolve such uncertainties and bring our modeling even closer to realistically describing transport in the unsaturated zone at Yucca Mountain.

Saturated-Zone Transport

Although our unsaturated-zone modeling indicates that neptunium travel times to the water table will exceed 10,000 years, radionuclides will eventually reach it, releasing a radioactive plume into the saturated zone. The second part of our modeling

work, therefore, entailed simulating neptunium transport through the saturated zone and again benchmarking our modeling parameters with field experiments.

As in the unsaturated zone, groundwater will encounter both fractured and porous media in the saturated zone (Figure 15). In fractured media, groundwater may move relatively quickly through the fractures, but some water will move into progressively smaller cracks and pores, where advection, matrix diffusion, and sorption will help retard radionuclide transport. In porous media, such as alluvium, groundwater travel times will lengthen because the water must diffuse through the matrix rather than flow along fractures. Large-scale dispersion, or dilution, will also lower radionuclide concentrations in such media.

Saturated-Zone Simulations. Transport simulations for the saturated zone were carried out to examine how long it would take for neptunium to reach the repository's site boundary, defined as 5 kilometers distant, and then travel another 15 kilometers to reach a point where it could be taken up in well water for Amargosa Valley. (This 20-kilometer point assumes that 10,000 years from now, the nearest valley population will be 10 kilometers closer to the mountain than it is today.) Our saturated-zone simulations examined how advective transport, diffusion into the rock matrix, dilution, and sorption would affect neptunium transport times.

The simulations indicate that the saturated zone could lower peak concentrations of radionuclides that bypass the unsaturated zone's natural barriers. Simply put, whenever a spike in elevated radionuclide flux reaches the water table, if the spike's duration is about the same as or less than the transport time of water through the saturated zone to the site boundary, then water in the aquifer will "dilute" the spike, both lowering its peak and stretching it out over a longer period of time. If, howev-

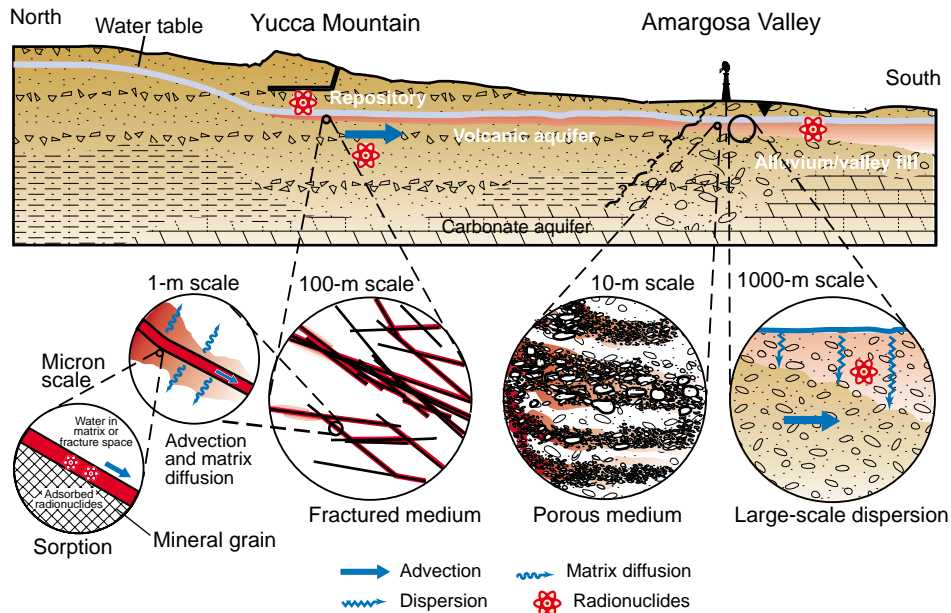


Figure 15. Conceptual Model of Radionuclide Transport in the Saturated Zone A variety of factors will affect how quickly radionuclides travel through the saturated zone. As shown on the left, advection, matrix diffusion, and sorption will help retard radionuclide transport in fractured media. As shown on the right, porous media will slow advective transport, and dispersion, or dilution, will lower the concentration of the radionuclides. Our saturated-zone simulations examine the interplay of all these factors.

er, the radionuclide flux arrives at the water table over a long period of time, dilution will not occur—the flux will act as a constant source of radionuclides to the saturated zone. Thus, the saturated zone will provide a hedge against any failures of unsaturated-zone barriers that result in sharp influxes of radionuclides to the water table.

Initially, transport through the saturated zone will be in porous, fractured tuff. Our model thus includes both fracture flow and matrix diffusion. Inclusion of the latter slows neptunium travel times to the hypothetical site boundary from about one year for pure fracture flow to thousands of years. An important aspect of matrix diffusion is that it allows the radionuclides to come in contact with minerals in the surrounding rock that may adsorb them. As shown earlier in Figure 10, even small amounts of sorption have a large impact on radionuclide travel times and peak concentrations.

Figure 16 presents simulation results for a much more pessimistic waste-leakage scenario than that of our base case. In this simulation, we assume that the first waste canister fails at 1000 years and that neptunium leaks continuously over the next 30,000 years and then stops. The upper graph plots the arrival of neptunium at the water table; the lower graph plots neptunium transport through the saturated zone to the repository's site boundary for two cases: no sorption and weak sorption (an average K_d of 2 mL/g). Note that although sorption does not reduce the maximum concentration that arrives at the boundary, even weak sorption delays the initial arrival of neptunium by about 10,000 years.

We also examined the transport of radionuclides to a point 20 kilometers away from the repository. In these calculations, we had to account for flow that would include movement through highly porous alluvium (see Figure 15).

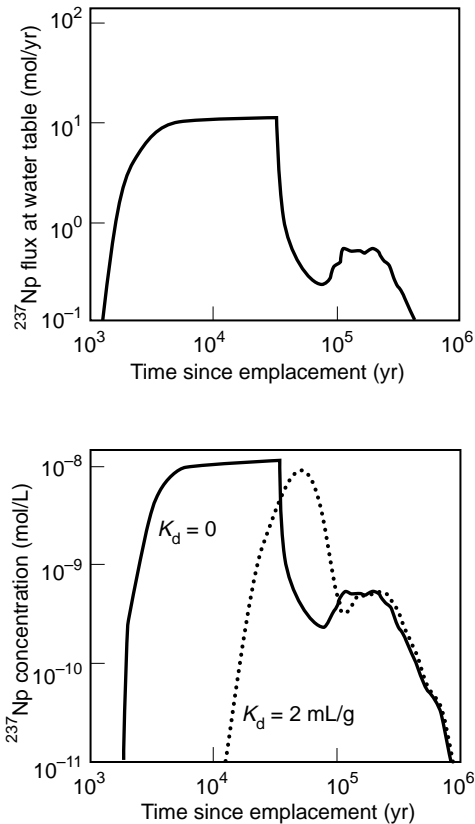


Figure 16. Neptunium Transport in the Saturated Zone

Even weak sorption significantly retards neptunium transport through the saturated zone. The two sets of graphs depict a worst-case scenario for waste leakage: the first waste canister fails at 1000 years, after which neptunium leaks continuously over the next 30,000 years. The upper graph shows the flux of neptunium-237 that crosses into the saturated zone. The lower graph shows resulting neptunium concentrations at the repository's site boundary, 5 km downstream, for two cases: no sorption (solid line) and weak sorption (dotted line).

As a result, neptunium travel times are considerably longer, with sorption in the alluvium adding from 10,000 to 50,000 years to them. As in our site-boundary calculations, sorption decreases the neptunium concentrations predicted to reach Amargosa Valley. Our calculations predict that after 100,000 years, neptunium concentrations in the valley would be no greater than 10 parts per trillion, which would pose a negligible health hazard. Thus, retardation from matrix diffusion and sorption and from the dilution effect noted above make the saturated zone an important component in the "defense in depth" provided by the mountain's natural barriers.

While encouraging, however, these calculations are not the final word. More experimental and modeling work must be done on the possibility of colloidal transport. Such transport would occur if radionuclides sorb not to stationary tuff but to particles so minute (1 nanometer to 1 micrometer in size) that they remain suspended in the groundwater and move with it. Colloidal transport became a concern when it was discovered that in just a few decades, a small amount of plutonium from an underground nuclear test had migrated more than a kilometer through the saturated zone, apparently by sorbing onto colloids. This transport process is discussed in the box on page 490.

Saturated-Zone Field Tests. To benchmark our modeling of the saturated zone, we conducted a series of field tests with tracers at a complex called the C-Wells. These wells are located about 2 kilometers southeast of the potential repository site and are drilled into fractured volcanic tuff. In terms of groundwater flow, they are directly downstream from the southern end of the repository.

In the C-Wells tests, we injected a variety of tracers into the saturated zone at one well and simultaneously pumped water out of another well about 30 meters away, establishing a recirculation loop between them. By adjusting packers in the injection well that sealed off

selected intervals along its length, we were able to test transport through distinct stratigraphic layers having different hydraulic conductivities.

The tracers used were lithium bromide (composed of a small cation and small anion), pentafluorobenzate (PFBA, a large anion), and polystyrene microspheres (simulated colloids with a negative surface charge). The microspheres were tagged with a fluorescent dye so that they could be detected with flow cytometry. The bromide and PFBA are nonsorbing solutes with different diffusion coefficients, and lithium is a weakly sorbing solute. We conducted separate laboratory tests to characterize the sorption of lithium to C-Wells tuffs and the matrix diffusion coefficients of all tracers.

Figure 17 shows tracer concentrations at the second well as a function of time for one of our field tests. The most striking feature is the curves' bimodal shape. This shape is attributed to a relatively small fraction of the tracers moving quickly between the wells through densely welded, fractured tuff, while most of the tracers passed more slowly through partially welded, less fractured tuff. These results support the concept of dual-permeability that is incorporated into our simulation models: flow occurs primarily in fractures, but a large amount of near-stagnant water is present in the rock matrix to diffuse the tracers.

Looking more closely at the curves for the two nonsorbing solutes, we see that the PFBA peaks are slightly higher than the bromide peaks, that the second bromide peak occurs later than the corresponding PFBA peak, and that the bromide curve eventually crosses over the PFBA curve. These features are all consistent with greater matrix diffusion of the bromide, which is more diffusive than the PFBA.

The lithium curve is more attenuated than the curves for the two nonsorbing tracers, which indicates sorption. The attenuation in the first lithium peak is almost exclusively a lowering of the concentration with little or no delay in

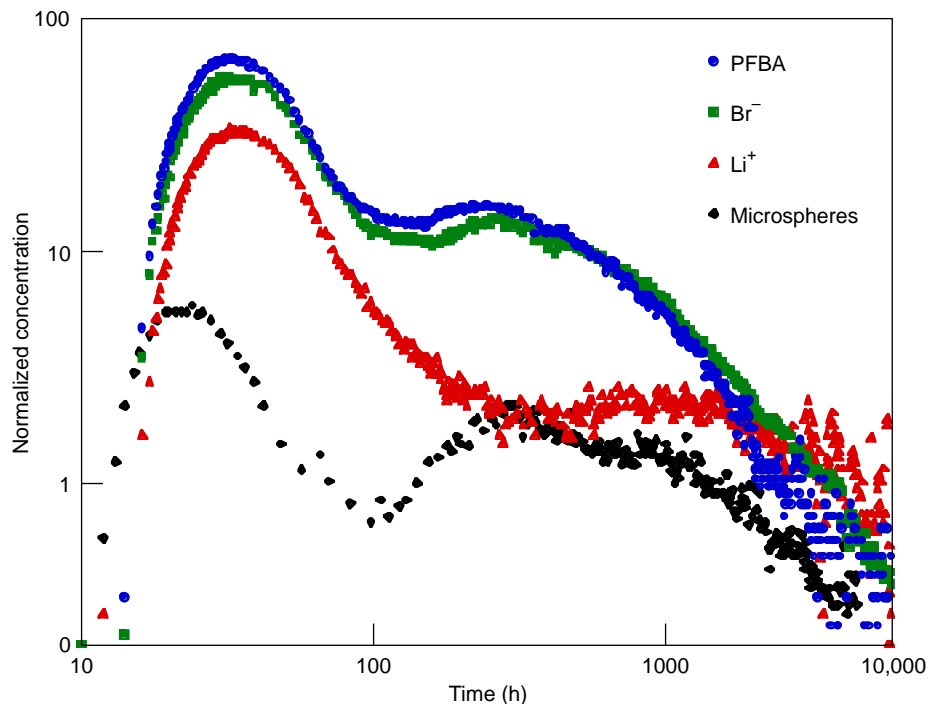


Figure 17. Saturated-Zone Field Tests at the C-Wells

A series of field tests at the C-Wells complex near the repository site helped benchmark our saturated-zone modeling parameters. The curves show the normalized concentrations of tracers injected at one well that were detected at a second well 30 m away. The data indicate multiple transport pathways for all tracers and validate matrix diffusion and sorption as important retardation mechanisms for radionuclide transport in the saturated zone.

arrival time. This reduction suggests that lithium diffuses into the matrix and is then sorbed. The attenuation in the second peak involves a clear time delay along with a dramatic lowering of concentration. This combination suggests lithium sorption in both the fractures and the matrix.

The microspheres reach the second well slightly earlier than the solutes, but their peaks are significantly attenuated. The attenuation implies that the rock matrix filters out a fraction of the microspheres, and the curve's bimodal shape suggests that two transport pathways are also available to the spheres. (These data and colloidal transport of radionuclides in general are discussed in the box on page 490.)

We were able to fit the curves of Figure 17 using a semianalytical, dual-porosity transport model, demonstrating

that our simulations are consistent with field data. One important finding was that lithium sorption measured at the C-Wells was always equal to or greater than the sorption measured in laboratory tests. This correlation increases our confidence in laboratory measurements for radionuclide sorption onto Yucca Mountain tuffs.

Will the Repository Work?

Where have our extensive research and analysis brought us? Can a Yucca Mountain repository and its natural barriers safely isolate nuclear waste for 10,000 years? What radiation doses might the residents of Amargosa Valley receive 10,000 or 100,000 years from now, and when would those doses peak? The project's performance as-

essment team is beginning to answer such questions by combining the findings of the various laboratories studying the site. Input to its performance assessment includes calculations of waste-canister failure mechanisms and rates, of the effects of a volcanic eruption at the repository, of how radionuclides dissolve and are transported in groundwater, and of how these radionuclides would disperse in the biosphere once they reach Amargosa Valley.

The team's full report will not be published until 2001. However, estimates to date for two repository designs are that radiation doses to valley residents will be only 0.1 mrem/yr 10,000 years after the repository is closed and only 30 mrem/yr 100,000 years later. The latter dose is close to the EPA's regulatory limit of 20 mrem/yr. Radiation doses will reach a peak of 200 mrem/yr 300,000 years after the repository is closed. This peak, which is two-thirds of today's background dose from natural sources such as cosmic rays, radon, and radionuclides in the soil, results primarily from weakly sorbing neptunium and, later, from colloid-transported plutonium.

But again, these estimates are not the final word. For one, data are still being collected, such as from our ongoing Busted Butte tests. In addition, the performance estimates are based on very conservative assumptions, and our studies have shown radionuclide transport to be sensitive to a range of parameters. For instance, Figure 14 shows the impact strong capillary forces have on matrix diffusion, and Figure 16 shows the impact that even weak sorption in the saturated zone can have on transport times for neptunium. More laboratory and field data should yield more realistic assumptions. Finally, there is the challenge of predicting the performance of natural and engineered barriers over geologic time scales.

As the assessment team points out, "whether these calculated annual doses will actually occur cannot be physically demonstrated or scientifically proven. The performance of a repository over

such long periods—longer than recorded human history—cannot be tested in the same way that the performance of an airplane, for example, can be tested.” *Proof* of the repository’s viability cannot be given in the ordinary sense of the word. However, the project’s iterative process of experimental measurements, modeling calculations, and analysis is moving us ever closer to a more accurate portrayal of repository performance and hence to greater confidence in our predictions.

Epilogue

We may pause at this point and ask ourselves what Yucca Mountain will look like 10,000 years from now. Will black-tailed jackrabbits and desert collared lizards still scurry across a brown, nondescript ridge, hiding behind the occasional Yucca plant? Or will the climate have changed, making the mountain greener, perhaps covered with a dense juniper forest? If a solitary hiker, reaching the ridge top, comes across a monument inscribed with hieroglyphics, will she be able to decipher the message? Will she realize that beneath her feet lies the entombed waste of the 20th century’s nuclear age?

Perhaps in her pack she’ll carry a faded graph handed down over the ages from an ancient ancestor, the computer modeler. The graph will have been passed on, parent to offspring, for generation upon generation. According to the graph, by her time in the 121st century, the total dose for all pathways and from all radionuclides should still be barely 0.1 mrem/yr.

Perhaps in her backpack she’ll also carry the instruments needed to check her ancestor’s prediction. After examining the mountain for signs of erosion, new earthquake faults, or volcanism and after checking the meteorological station for annual rainfall, perhaps she’ll return to her solar-powered vehicle and drive over to Amargosa Valley. If farmers there are still growing crops, what will she find when she pulls out

her mini-mass spectrometer and measures the concentration of neptunium in the their irrigation water? Will she grumble at the stupidity of her ancestors or smile at their wisdom? According to the statistical analysis given in the faded graph she’s carrying, there’s a 90 percent chance she’ll smile. ■

Acknowledgments

The research by Los Alamos on Yucca Mountain has so many facets and is so extensive that anyone close to the project can quickly lose the general reader in massive amounts of detail. We would like to acknowledge the difficult and important work of Judy Prono on this article. She brought the right amount of objectivity to the task, asking various investigators to explain or amplify on the material until she gradually, paragraph by paragraph, section by section, made the article much more accessible to a wide audience.

In this same vein, the article represents the work of many individuals at the Laboratory over several decades. The people listed at the beginning of the article or pictured at the end are only representative of the entire effort. Others whose work also contributed the Yucca Mountain Project include Kay Birdsell, Kathy Bower, Dave Broxton, Katherine Campbell, Dave Clark, Jim Conca, Bruce Crowe, Dave Curtis, John Czarnecki, Zora Dash, Clarence Duffy, Ned Elkins, Claudia Faunt, Dick Herbst, Larry Hersman, Stephen Kung, Ed Kwicklis, Ningpin Lu, Arend Meijer, Dave Morris, Mary Neu, Heino Nitsche, Ted Norris, Don Oakley, Jeffrey Roach, Robert Rundberg, Betty Strietelmeier, Kim Thomas, Joe Thompson, Bryan Travis, Lynn Trease, Peng-Hsiang Tseng, Greg Valentine, Kurt Wolfsberg, and Laura Wolfsberg. I would especially like to thank Chuck Harrington, Frank Perry, Tom Hirons, Ken Eggert, and Wes Meyers for supporting the work of assembling

this article, critiquing early drafts, or providing helpful material on the history of Yucca Mountain.

Further Reading

CRWMS M&O (Civilian Radioactive Waste Management System, Management and Operating) Contractor. 2000. “Analysis of Geochemical Data for the Unsaturated Zone (U0085).” CRWMS M&O report ANL-NBS-HS-000017.

———. 2000. “Calibration of the Site-Scale Saturated Zone Flow Model.” CRWMS M&O report MDL-NBS-HS-000011.

———. 2000. “Particle Tracking Model and Abstraction of Transport Processes.” CRWMS M&O report ANL-NBS-HS-000026.

———. 2000. “Saturated Zone Transport Methodology and Transport Component Integration.” CRWMS M&O report ANL-NBS-HS-000036.

———. 2000. “Unsaturated Zone and Saturated Zone Transport Properties (U0100).” CRWMS M&O report ANL-NBS-HS-000019.

New Questions Plague Nuclear Waste Storage Plan. 1999. *New York Times*. August 10 issue.

Office of Civilian Radioactive Waste Management. 1999. “Viability Assessment of a Repository at Yucca Mountain” (December). U.S. Department of Energy report DOE/RW-0508. (The full report is available on the World Wide Web at <http://www.ymp.gov/va.htm>)area

Roger Eckhardt has a Ph.D. in physical chemistry from the University of Washington but has spent a great deal of his professional life involved with science education and science writing. Most recently, he has been helping to compile and write the voluminous documents that describe the scientific work being carried out at Los Alamos for the Yucca Mountain Project.



Principal Los Alamos Contributors to the Yucca Mountain Project



Julie A. Canepa
Former project manager. Currently, program manager of LANL Environmental Restoration Project.



Paul R. Dixon
Project manager.



David L. Bish
mineralogy of Yucca Mountain tuffs.



Gilles Y. Bussod
Busted Butte unsaturated-zone transport test.



James W. Carey
Mineralogical modeling of Yucca Mountain.



Steve J. Chipera
X-ray diffraction mineralogy.



June T. Fabryka-Martin
Yucca Mountain chlorine-36 studies.



Schön S. Levy
Alteration history of volcanic rocks at Yucca Mountain.



Maureen McGraw
Modeling of colloid-facilitated transport.



Mark T. Peters
Yucca Mountain testing, including the Exploratory Studies Facility and Busted Butte experiments.



Paul W. Reimus
C-Wells studies at Yucca Mountain.



Bruce A. Robinson
Modeling of flow and transport in the unsaturated and saturated zones.



Wolfgang H. Runde
Actinide solubility and speciation at Yucca Mountain.



Wendy E. Soll
Modeling of Busted Butte hydrology.



Carleton D. Tait
Actinide solubility and speciation in Yucca Mountain groundwaters.



Inés Triay
Yucca Mountain geochemistry, including sorption, diffusion, and transport in tuffs. Currently, DOE manager for WIPP.



Jake Turin
Field hydrology for Busted Butte.



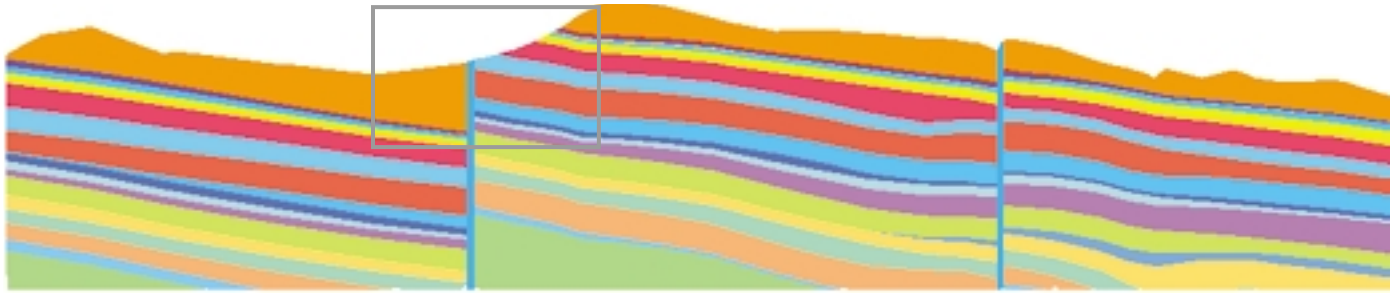
David T. Vaniman
Igneous petrology and mineralogical analysis of Yucca Mountain tuffs.



Andrew V. Wolfsberg
Modeling of colloids and chlorine-36 transport.



George A. Zyvoloski
Modeling of flow and transport in the saturated zone.



(a) Geological Model of a Cross Section at Yucca Mountain

Mesh Generation for Yucca Mountain

Carl W. Gable

To model the transport of waste radionuclides through Yucca Mountain, we must generate a grid, or mesh, on which our FEHM calculations can be run. Our primary tool for generating, optimizing, and maintaining computational meshes is LaGriT (for Los Alamos Grid Toolbox), a general-purpose software package. LaGriT is a spinoff of X3D, which was developed in the 1980s by Harold Trease.

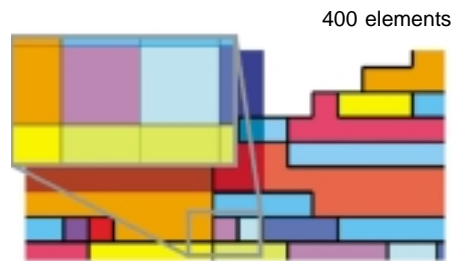
Developed in the 1990s, LaGriT is a collaborative product of the Applied Physics, Theoretical, Earth and Environmental Science, and Computing, Information, and Communications Divisions at Los Alamos. It has been used to model such varied phenomena as shock physics, combustion, semiconductor devices and processes, biomechanics, the evolution of metallic microstructure, porous flow, and seismology.¹

A mesh consists of nodes (points) at specific locations in space that are connected to form elements. These elements can be triangles or quadrilaterals in 2-D models and tetrahedra, hexahedra, prisms, or pyramids in 3-D models. The elements fit together like the pieces of a puzzle to represent physical systems such as the rock layers in Yucca Mountain, a human knee joint, or a semiconductor chip. Physical quantities such as pressure, temperature, or density, which are continuous

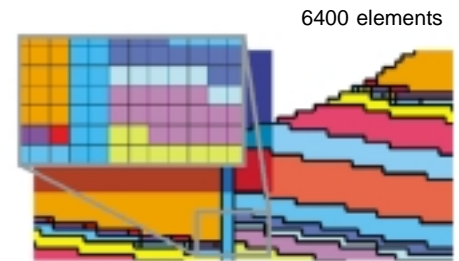
in real materials, are usually represented by discrete values at the nodes or within the elements.

Mesh generation draws on both creativity and advanced mathematical algorithms. As Thompson et al. (1999) note, grid generation is “still something of an art, as well as a science. Mathematics provides the essential foundation for moving the grid generation process from a user-intensive craft to an automated system. But there is both art and science in the design of the mathematics for . . . grid generation systems, since there are no inherent laws (equations) of grid generation to be discovered. The grid generation process is not unique; rather it must be designed.”²

a $10 \times 10 \times 10$ grid of hexahedral elements. If we double the resolution to a $20 \times 20 \times 20$ grid, the total number of elements goes from 1000 to 8000. In addition, if the calculation involves modeling the change over time of a quantity such as saturation, doubling the resolution may require cutting the time steps in half, which doubles the computer time needed. Overall, then, doubling the calculation’s resolution will increase calculation time by a factor of 16. Although high resolution best represents complex geometry and produces the most accurate physics solution, it requires more elements, which result in calculations that require more computer memory and cycles.



(b) Low-Resolution Regular Mesh



(c) High-Resolution Regular Mesh

Mesh generation can be automated but never becomes automatic. Although software like LaGriT helps automate complex “meshing” operations, generating successful meshes still rests on a series of judgment calls by an expert, who must weigh many tradeoffs. For example, imagine a calculation done on

The accompanying graphics illustrate various computational grids that could be generated for modeling Yucca Mountain. Our starting point is a geological model that represents the mountain as a sequence of sloping rock layers offset by two vertical faults (a). Focusing on the boxed area around the left-hand fault, we first create a simple mesh of square elements (b). The elements’ colors correspond to those of the cross-section layers they represent

¹More information on LaGriT is available from the software’s Web site: <http://www.t12.lanl.gov/~lagrit/>.

²*Handbook of Grid Generation*. 1999. J. F. Thompson, B. K. Soni, and N. P. Weatherill, Eds. New York: CRC Press, p. iii.

and thus also to the layers' varying material properties (such as density and porosity).

The low-resolution squares in (b) do a poor job of representing the geology. The vertical fault is lost and individual rock layers are nearly lost because the mesh is so coarse. We can improve the mesh by increasing its resolution: the squares in (c) are one-quarter the size of those in (b). Now the geology is better represented, although the interfaces between rock layers are still represented by jagged stair steps. Also, only the thickest layers are represented by contiguous elements; thin layers and small features are still lost in the grid's coarseness.

Another approach is to use variable mesh spacing, as shown in (d). Variable spacing allows us to "zoom in" with high resolution on some areas and maintain low resolution in others. However, variable spacing generally works well only for simple geometries in which the phenomena being modeled take place in a small portion of the entire computational domain and thus only a few areas require high resolution.

A more flexible approach is to adapt mesh resolution to the geometry of interest, as done in the quad-tree meshes shown in (e) and (f). These meshes allow cascading refinements: each element is subdivided into four elements, each of which is then subdivided into four still smaller elements, and so on.

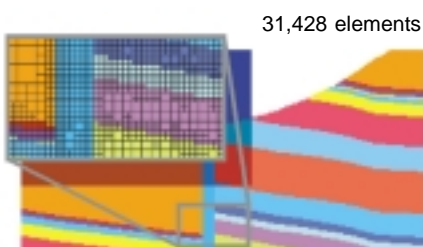
In (e) and (f), we start with the mesh of (b) and then refine only selected elements. In (e), we refine along all material interfaces by a factor of 16 but leave regions far from these interfaces at low resolution. In (f), we refine only thin rock layers by a factor of 32, increasing their resolution while maintaining lower resolution in the thick layers. In both cases, however, the number of elements is much greater than in the previous meshes, which will slow down our calculations.

Our mesh examples so far are all structured: that is, they are made of quadrilateral elements whose positions are readily defined in terms of rows and columns and whose connectivity is



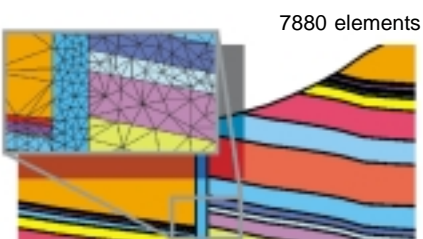
(d) Variably Spaced Regular Mesh

logical. Our last mesh examples are made of unstructured triangular elements whose connectivity is more arbitrary: for example, the nodes have varying numbers of triangles attached to them. This unstructured approach, however, allows us to create meshes that actually conform to the mountain's varied material interfaces.



(e) Quad-Tree Mesh

Both low-resolution (g) and high-resolution (h) meshes do well in representing the geologic interfaces. The high-resolution mesh, however, will do a better job solving the physics of radionuclide transport because its smaller elements can more accurately represent variations that occur over short distances. In modeling Yucca Mountain, we must also contend with phenomena that lack symmetry, have a wide range of length scales, and involve very thin

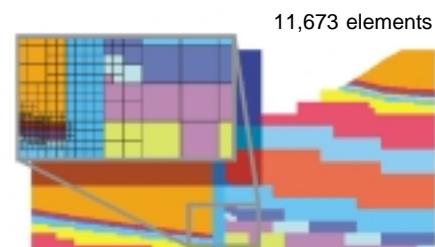


(g) Low-Resolution Triangular Mesh

layers that must be preserved as continuous. As a result, triangles in 2-D modeling and tetrahedra in 3-D modeling have been our meshes of choice.

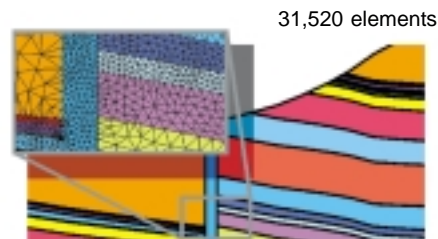
In addition to tradeoffs in how well they represent the mountain's geometry, meshes also pose tradeoffs in their suitability for different physics codes. Some codes can solve problems only on regular grids like those shown in (b)–(d). Others can use quad-tree meshes like those shown in (e) and (f) but not the unstructured meshes of (g) and (h). Thus the meshing approach must be compatible with the physics code that will be used.

Developing flow and transport models for Yucca Mountain has pushed the limits of mesh generation technology.



(f) Quad-Tree Mesh

The models' size requires us to keep the number of elements as low as possible, their complex physics requires us to accurately represent the geology of the repository site, and the need for timely results requires us to automate mesh generation whenever possible. These often conflicting demands have been met by a collaborative effort in enhancing mesh generation capabilities to meet the challenges of modeling Yucca Mountain. ■



(h) High-Resolution Triangular Mesh

Colloids

Carriers of actinides into the environment

Nearly all natural waters contain suspended colloids, submicrometer-sized particles whose concentrations depend on the physicochemical properties of the aquifer. These natural colloids are formed as a result of the weathering of rocks, plants, and soils. They are of concern as a transport mechanism at Yucca Mountain because radionuclides that sorb strongly to the mountain's volcanic tuff could also sorb strongly to suspended tuff colloids, forming radionuclide-bearing "pseudocolloids" that could move through the aquifer. Actinides with high tendencies for sorption or complexation, such as Pu(IV) and Am(III), are strong candidates to form such pseudocolloids. In addition, colloids could also form from the weathering of high-level-waste glass and spent fuel (waste-form colloids) or from the aggregation of hydrolyzed actinide hydroxides, such as those formed with Pu(IV) (intrinsic colloids). Thus, a number of possibilities exist for colloids to carry actinides away from an underground waste repository, a process known as colloid-facilitated transport.

Evidence from the Nevada Test Site confirms that some of these possibilities are also realities. The first evidence for colloid-facilitated radionuclide transport came in 1976, 11 years after the Cheshire nuclear test. Radionuclide pseudocolloids were detected in a well 300 meters to the southwest of the detonation site. In 1996, plutonium concentrations of up to 0.63 picocurie/liter were detected at the Test Site's ER-20-5 well complex. Almost all the plutonium was associated with colloids composed of silica, zeolites, and clays. The ratio of plutonium-239 to plutonium-240 indicated that the plutonium originated

from the Benham nuclear test, which was conducted in December 1968 approximately 1.3 kilometers from the ER-20-5 well complex. Thus, the plutonium traveled more than a kilometer in less than 30 years.

In both cases, however, nuclear detonations fractured saturated rock formations near the test, and the actinides were integrated into a zone of melted rock that was in direct contact with the aquifers. Further, within seconds after the detonations, actinides may have been forcefully injected through the fractures into the rock formations, although it is unlikely that such "prompt injection" is solely responsible for the migration of plutonium away from the Benham cavity. Consequently, colloid-facilitated radionuclide transport mechanisms at the Test Site may differ significantly from those at a nuclear waste repository, where the radionuclides would be isolated, at least initially, from the hydrogeologic environment.

We have conducted experiments at Los Alamos to study the formation of actinide pseudocolloids under conditions representative of those at Yucca Mountain, where nuclear spent fuel will potentially be stored in the unsaturated zone and where release scenarios involve the infiltration of groundwater. Measurements of plutonium-239 and americium-241 sorption onto hematite, smectite, and silica colloids indicate that sorption of Pu(IV) and Am(III) is completed within hours or days and is much faster than the desorption process, which occurs over months. In addition, the sorption of Pu(V) is lower than for Pu(IV) but increases with time, probably as a result of redox reactions of the Pu(V) in solution or on colloid

surfaces. The latter observation emphasizes the important connection between solution speciation and surface complexation in determining the sorption behavior of actinides onto colloids.

We also conducted field tests to investigate filtration and resuspension rates for colloids in the saturated zone at Yucca Mountain. Two sets of experiments were conducted at the C-Wells complex, which lies 2.4 kilometers east of the potential repository. In these tests, we injected tracers into the saturated zone at one well and pumped water out of a nearby well to establish flow between the wells. Polystyrene microspheres of varying sizes (280, 360, and 640 nanometers in diameter) were injected simultaneously with solute tracers into two rock formations (Bullfrog Tuff and Prow Pass Tuff) that also underlie the repository. The microspheres were selected to have sizes and surface charges that mimicked as closely as possible those of the expected pseudocolloids.

All microspheres proved mobile, but their mass recoveries at the second well were lower than those of the noncolloid tracers that were injected simultaneously. Bimodal breakthrough curves for all tracers in the Bullfrog Tuff test indicated multiple transport pathways (see Figure 17 in the preceding article). The two tests suggested that colloid transport in the two aquifers was affected by rock properties, groundwater chemistry, and colloid size. The microsphere data have enabled us to estimate rates of colloid attachment and detachment to the fractured tuff surfaces. Further field and laboratory tests are ongoing to understand colloid transport in other types of saturated media that occur at Yucca Mountain, including unfractured tuff and alluvium.

The most recent laboratory experiments have focused on measuring sorption/desorption rates and magnitudes for strongly sorbing, long-lived radionuclides onto several colloids that may be present either near the stored waste (iron oxides that result from degradation of waste canisters) or far

from it (silica and montmorillonite clay) at the mountain. These experiments show that plutonium sorbs very strongly and rapidly onto iron oxides and montmorillonite clay, while its sorption onto silica is slower and weaker. The experiments also show that the presence of other ions, such as calcium, tends to slightly suppress the sorption of plutonium.

Armed with such data from both field and laboratory experiments, modelers are using the Finite Element Heat and Mass (FEHM) transport code to simulate colloid-facilitated radionuclide transport at Yucca Mountain. Key variables are the nature and concentration of the simulated colloid, actinide sorption/desorption mechanisms and kinetics, fluid saturation, and properties of the surrounding rock matrix. In these simulations, the concentration of colloids varies with the release scenario, time, and distance from the waste packages. Accurate modeling requires information about the waste (glass or spent fuel) dissolution rates, water chemistry, and actinide distribution between solid and aqueous phases. Given the wide range of uncertainty in estimates for many of these variables, results to date are largely qualitative.

Our preliminary calculations indicate that colloid-facilitated transport is indeed possible for actinides in the III and IV oxidation states and would be associated primarily with fracture flow at Yucca Mountain. Because of the low concentration of natural colloids and the large amount of immobile rock surface area available to compete for the sorption of actinides, waste-form colloids pose the greatest risk to repository performance. Actinides are expected to be nearly irreversibly sorbed to or embedded in these colloids. However, waste-form colloids would have to travel through the unsaturated zone before reaching the saturated zone. In the unsaturated zone, filtration at air/water and rock/water interfaces should impede such transport. In the saturated zone, the high velocity of groundwater in fractures reduces the

attachment of waste-form colloids to fracture surfaces. Of the natural colloids in this zone, clay colloids will facilitate radionuclide transport more than silica colloids. However, more data are needed to accurately assess whether colloid-facilitated radionuclide transport could adversely affect the performance of a nuclear waste repository at Yucca Mountain. A quantitative evaluation of this transport mechanism awaits more knowledge about the site-specific behavior of the colloids, fundamental sorption/desorption mechanisms and kinetics, fracture-related filtration effects, and evolution of the local environment around the stored waste. ■

Analyzing Volcanic Hazards at Yucca Mountain

Frank V. Perry, Bruce M. Crowe, and Greg A. Valentine

Los Alamos researchers have also been involved in analyzing the probability and consequences of volcanic activity at the Yucca Mountain repository site. The possibility of such activity must be considered because a dozen small volcanoes lie within 20 kilometers of the mountain. All but one are within Crater Flat, a region of alluvium-filled basins to the southwest of Yucca Mountain. The twelfth, and youngest, volcano lies farther south at Lathrop Wells (Figure 1). Six of the volcanoes have erupted within the last 1 million years; the other six, within the last 4 million years.

The major goal of our volcanism studies has been to assess the probability that volcanic events will disrupt the potential repository during the 10,000-year waste-isolation period. For this assessment, we have studied the area's volcanic activity over the last 5 million years to determine its patterns. The likelihood of a volcano disrupting the repository is expressed as the annual probability of such an event over the 10,000-year period. In its simplest form, the probability is calculated by multiplying the area's recurrence rate of volcanism (volcanic events per year) by the site's intersection ratio (repository area divided by the area in which volcanism occurs), taking into account uncertainties in each value.

Volcanism Near Yucca Mountain. Volcanoes can be generally character-

ized as either basaltic or rhyolitic. Basaltic lava tends to flow easily because it erupts at high temperature and contains little silica; at the point of eruption, it often forms large scoria cones. Rhyolitic lava is more viscous and flows less readily because it erupts at lower temperatures and contains more silica. It usually erupts explosively, producing thick welded ash deposits such as those that form Yucca Mountain.

Episodes of basaltic eruptions have occurred in the Yucca Mountain region over the past 11 million years and have been the only form of volcanism since

the last rhyolitic eruptions some 7.5 million years ago. The eruption mechanisms of these basaltic volcanoes have ranged from effusive (low energy) to strombolian (violent). The youngest volcano, at Lathrop Wells, evidences the full range of activity. Lava flows that surround most of the cone attest to effusive events, while finely fragmented and highly vesicular rock attests to violent eruptions that may have spewed volcanic ash several kilometers into the air.

Probability of a Volcanic Disruption. The first Los Alamos estimates of the likelihood of volcanic activity at the repository site were made in 1980; the probability was put at about 10^{-8} events per year (Figure 2, Crowe and Carr 1980 data). This probability was at the NRC's cutoff point for concern—i.e., a

lower probability would eliminate volcanism as a regulatory issue. More recent studies sponsored by the DOE, NRC, and State of Nevada have generally bounded the disruption probability as lying between 10^{-9} and 10^{-7} events per year, while presenting alternative models of volcanism in the area and alternative statistical methods of calculating its probability.

Since volcanism near Yucca Mountain over the past million years has been relatively infrequent, one analytical approach is to estimate an upper limit on its threat by calculating the disruption

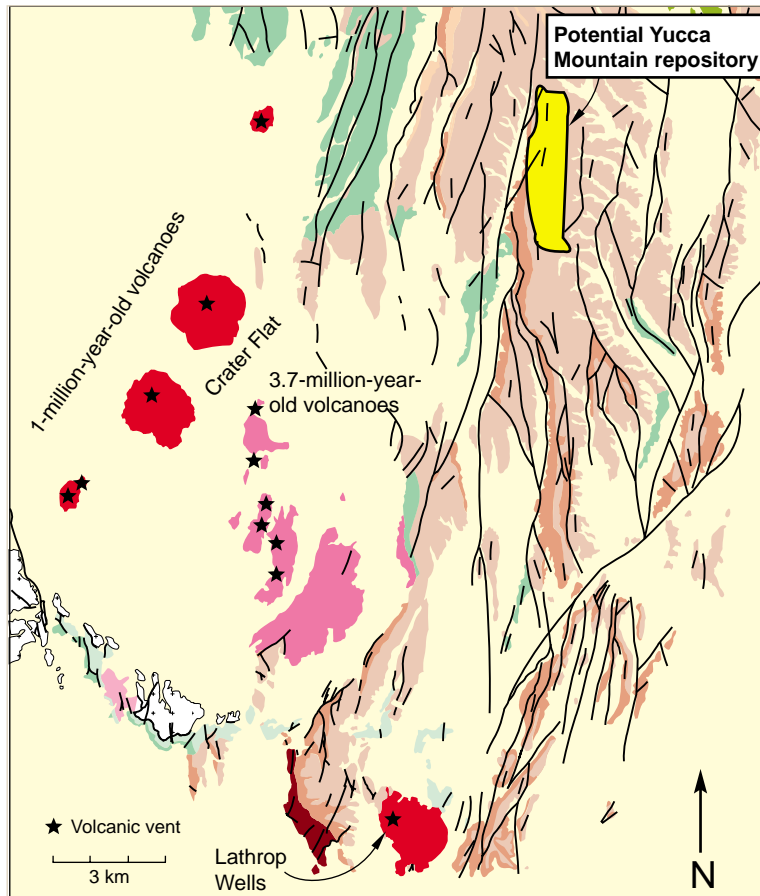


Figure 1. Volcanoes Near Yucca Mountain A dozen volcanoes are within 20 km of the potential repository site. Six have been active within the last million years; the other six, within the last 4 million years. The youngest volcano, at Lathrop Wells, is 75,000 years old.

probability of a repository placed within a more active basaltic field. The Cima Crater in central Nevada and the Lunar Crater in the Mojave Desert have been used for such comparisons (Figure 2). This method suggests a maximum disruption probability of $\sim 5 \times 10^{-6}$ events per year for the repository.

In 1995 and 1996, the DOE convened a panel of ten experts in the fields of physical volcanology, volcanic hazards, geophysics, and geochemistry to assess the mountain's vulnerability to volcanic disruption. The panel's goal was twofold: to arrive at a defensible probability distribution for volcanic disruption that reflected the latest understanding of volcanic processes in the Yucca Mountain region and to determine the uncertainty in that prediction.

Each of the ten experts independently arrived at a probability distribution. Their aggregate distribution spanned about three orders of magnitude (see lower graph of Figure 2). The mean value of this distribution was 1.5×10^{-8} events per year, with a 90 percent confidence interval between 5.4×10^{-10} and 4.9×10^{-8} (PVHA results in Figure 2). This mean value translates to a probability of about 1 in 7000 that the repository would be disrupted by volcanic activity during its 10,000-year isolation period. The panel's mean value confirmed earlier Los Alamos estimates from DOE-sponsored studies (e.g., Crowe et al. 1995).

Consequences of a Volcanic Disruption. For a full risk assessment of volcanic activity at Yucca Mountain, the probability of a disruption must be weighted with its consequences in terms of public exposure to radiation. Analysis of the consequences examines such issues as magma rise, intrusion geometry at shallow depths, hydrothermal activity, and potential eruption of nuclear waste.

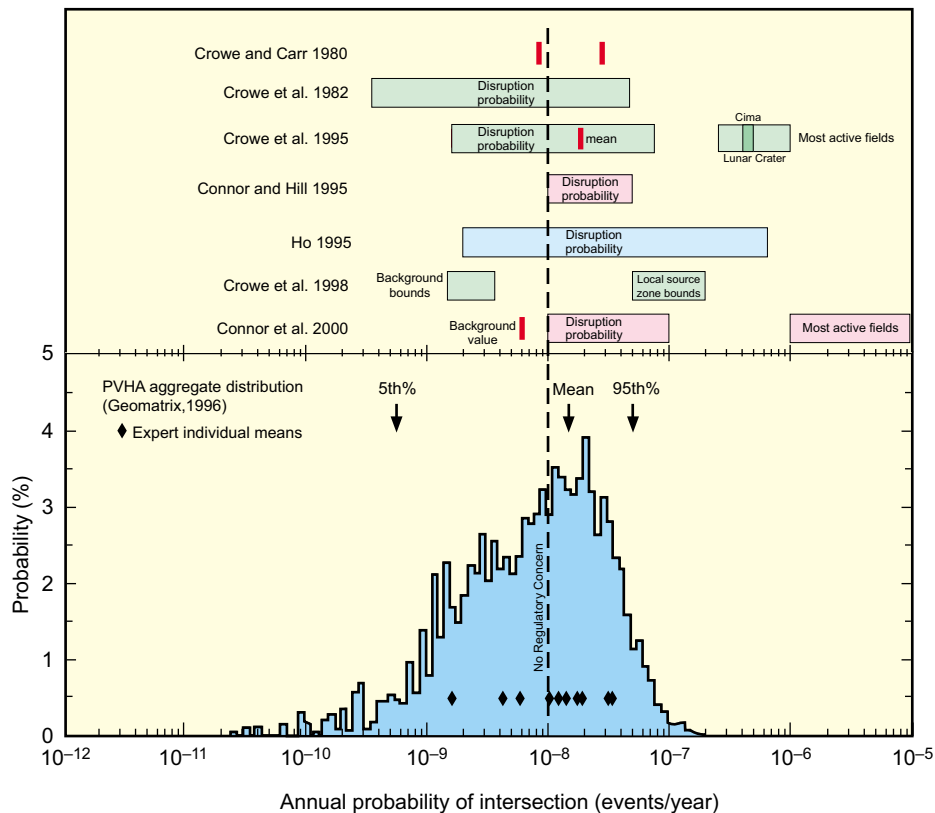


Figure 2. Probability of Future Volcanic Activity at Yucca Mountain
 A number of researchers have analyzed the likelihood of a volcano disrupting a repository at Yucca Mountain. Their probability point estimates (single lines) and ranges (rectangles) are compared here with estimates made by a panel of experts convened by the DOE to assess the hazard (PVHA distribution). The ranges labeled “Most active fields” and “Local source zone bounds” represent upper bounds for the probability and assume that the repository is placed in an active volcanic field. The background bounds and value represent lower bounds that assume the repository does not lie in an active volcanic field but lies in a region that produces only sporadic eruptions. Most estimates put the disruption probability at a little greater than 10^{-8} events per year, which translates to a 1 in 7000 chance that volcanic activity could occur during the repository's 10,000-year waste isolation period.

A recent study of the Lathrop Wells cone sponsored by the NRC reported high xenolith abundance in some strata (xenolith is underground rock that broke off and became entrained in the magma). If true, such abundance would imply that a large amount of repository debris could be ejected were a similar volcano to penetrate Yucca Mountain.

However, there is insufficient data to constrain the xenolith content of the volcano as a whole, and the study may have overestimated its abundance. Ongoing work at Sandia National Laboratories and at Los Alamos is addressing the interaction between rising magma and repository tunnels as they are specified in the current design. ■